

THE BNL EBPM ELECTRONICS, HIGH PERFORMANCE FOR NEXT GENERATION STORAGE RINGS*

K. Vetter[#], Oak Ridge National Laboratory, Oak Ridge, TN, 37831, USA

J. Mead, B. Podobedov, Y. Tian, W. Cheng, Brookhaven National Laboratory, Upton, NY, USA

Abstract

A custom state-of-the-art RF BPM (EBPM) has been developed and commissioned at the Brookhaven National Laboratory (BNL) National Synchrotron Light Source II (NSLS-II). A collaboration between Lawrence Berkeley National Laboratory (LBNL) Advanced Light Source (ALS) and BNL has proven to be a key element in the success of the NSLS-II EBPM.

High stability coherent signal processing has allowed for demonstrated 200nm RMS spatial resolution and true turn-by-turn position measurement capability. Sub-micron 24 hr. stability has been demonstrated at NSLS-II by use of 0.01°C RMS thermal regulation of the electronics racks without the need of active pilot tone correction [1, 2].

The intentional partitioning during the conceptual architecture development phase of the RF and digital processing into separate boards has enabled rapid independent development of the analog front end board (AFE) and digital front end board (DFE). The partitioning of the AFE and DFE has realized derivative instrumentation platforms including the NSLS-II Cell Controller used for Fast Orbit Feedback SVD computation and corrector actuation, the NSLS-II photo-emission X-ray BPM. A CVD diamond beamline BPM (DBPM) based on the NSLS-II Xray BPM has been developed in conjunction with Sydor Technologies via an SBIR arrangement that has been implemented on NSLS-II beamlines for local active beamline stabilization [3]. An MOU with LBNL was signed near the end of the NSLS-II EBPM development in which complete transfer of technology was provided as the basis of the LBNL ALS orbit upgrade.

INTRODUCTION

The development of the NSLS-II EBPM began in August of 2009. The development was primarily motivated in order to achieve world class performance using state-of-the-art technology with the ability of local BNL experts to optimize and evolve the EBPM.

Although funds were provided to support a development laboratory and personal, the NSLS-II project baseline was based on commercial EBPM technology. The criterion set to change the project baseline was to demonstrate to an expert external and internal review committee EBPM performance on an operational machine that sufficiently demonstrated compliance of the NSLS-II EBPM performance requirements, twelve months from the start of the development project.

A collaboration with ALS staff was quickly established

in which prototype NSLS-II EBPM beam tests would be conducted at ALS. The ALS machine was chosen as the optimal test facility as the machine RF frequency was close to NSLS-II and only required a change in the ADC sampling reference VCXO. The collaboration with the ALS staff quickly evolved into ALS staff making significant contributions to the physical design of the DFE FPGA design, which were extremely critical at the time due to the very aggressive proof-of-principal schedule that had been set. The first EBPM beam test at ALS was conducted in June of 2010, ten months after the start of the EBPM development.

Early tests were performed prior to the full development of the DFE and were structured to enable streaming of raw ADC data to file via Matlab TCP/IP connection. Capture of the raw ADC data in long data records (1Mpts or greater) allowed for detailed time and frequency analysis of the real world impairments imparted by the AFE. It was also possible to explore optimal processing algorithms with real-world impairments offline.

Rapid maturity of the EBPM AFE and DFE enabled detail studies at ALS demonstrating sub 200nm performance of 500mA dual-cam shaft user beam that served as the basis for the EBPM review committee to recommend changing the project baseline to include the custom NSLS-II EBPM.

EBPM DESIGN FOR SUB-MICRON PERFORMANCE

The design of and an EBPM for 3rd generation light sources and beyond is primarily composed of two aspects; spatial resolution, and stability. The first can be decomposed into turn-by-turn (TbT) and stored beam resolution.

User operation is typically concerned with stored beam resolution and stability, however, TbT measurements can be very useful for optimizing machine performance particularly at low bunch charge [4]. Achieving true TbT measurements is dependent on sufficient RF bandwidth to allow for the bunch energy to sufficiently decay within a single turn, and stringent coherent processing.

Stored beam spatial resolution is typically set as 10% of the beam size, qualified by projected fill patterns for nominal storage ring operation, as an RMS value. For NSLS-II early predictions assumed 80% fill of the storage ring. Experiments at ALS with 500mA dual-cam shaft bunches were a close representation of expected NSLS-II storage ring performance, scaled by the ring circumference, which closely compared with the NSLS-II booster.

Stability for synchrotrons is typically defined over time scales of 8 to 24 hrs, and qualified by the Fast Orbit Feedback (FOFB) bandwidth, often 2KHz for 3rd genera-

*Work supported by DOE contract No: DE-AC02-98CH10886

[#]vetterkg@ornl.gov

MEASUREMENT OF TUNE SHIFT WITH AMPLITUDE FROM BPM DATA WITH A SINGLE KICKER PULSE*

Yoshiteru Hidaka[†], Weixing Cheng, Boris Podobedov, Brookhaven National Laboratory, Upton, NY 11973 USA

Abstract

Measurements of amplitude-dependent tune shift are critical for understanding of nonlinear single particle dynamics in storage rings. The conventional method involves scanning of the kicker amplitude while having a short bunch train at the top of the kicker pulse. In this paper we present a novel, alternative technique that uses a long continuous bunch train, or a sequence of bunch trains, that are spread along the ring, such that different bunches experience different kick amplitudes with a single shot of a kicker pulse. With these beams, a curve of tune shift with amplitude can be extracted from the recently added new NSLS-II BPM feature called gated turn-by-turn (TbT) BPM data that can resolve bunches within a turn, either alone or together with a bunch-by-bunch BPM data. This technique is immune to pulse-to-pulse jitters and long-term machine drift.

INTRODUCTION

Third-generation light sources utilize strong focusing to achieve an electron beam emittance as small as possible. Stronger focusing leads to more negative natural chromaticity, which needs to be compensated by stronger chromatic sextupoles to have positive chromaticity. Nonlinearity in electron beam motion introduced by strong chromatic sextupoles needs to be then controlled by strong geometric sextupoles or other higher-order multipoles. Otherwise, dynamic aperture and momentum acceptance of the lattice may collapse, resulting in poor injection efficiency and reduced Touschek lifetime. Hence it is important to be able to characterize the nonlinearity of a storage ring lattice. One such nonlinear characterization metric is tune shift with amplitude (TSwA) [1].

Experimental measurement of TSwA can be performed with a single shot of a kicker pulse while obtaining turn-by-turn (TbT) data from which amplitude and tune can be extracted, if coherent damping is faster than decoherence, for example at LEP [1]. This excludes the possibility of measuring tune shift at very large amplitude, since large amplitude inevitably leads to fast decoherence. In order to measure tune shift for large amplitude, multiple shots of TbT data with different kick amplitudes are conventionally required.

CONVENTIONAL APPROACH

A conventional method to measure a TSwA curve for an electron storage ring is to place a short train of electron bunches in a ring and to kick the beam with a fast pinger

(kicker) pulse while acquiring a TbT data. Repeating this while gradually increasing the kicker strength until the beam is lost results in a TSwA curve. This multiple-shot measurement setup is depicted in Fig. 1(a). This method is prone to short-term shot-to-shot jitter as well as long-term machine drift due most likely to the limited stability of the power supplies and RF system. This sometimes makes the interpretation of the resulting TSwA curve difficult even for a state-of-the-art facility like NSLS-II, which is found to have tune jitter on the order of 10^{-4} that may not be sufficient for high-precision nonlinear lattice calibration. If we can obtain a TSwA curve with a single shot, these issues can be eliminated completely.

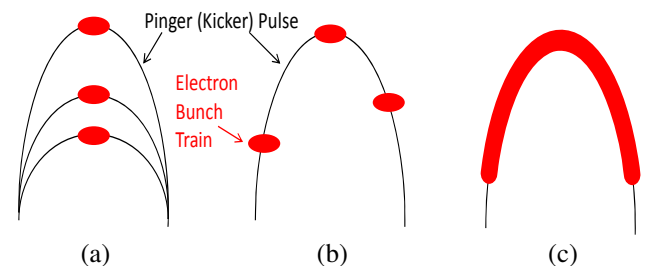


Figure 1: Various setups for measurements of tune shift with amplitude. (a) Conventional multiple-shot setup which is prone to machine jitter and drift. New single-shot setups with trains of bunches (b) discretely placed and (c) continuously placed in a storage ring.

NOVEL SINGLE-SHOT TECHNIQUE

Our single-shot method involves placing trains of bunches either discretely or continuously spread out in the ring as shown in Figs. 1(b) and (c). Due to NSLS-II ping-ers having half-sine pulses (FWHM of ~ 0.6 revolution period), these bunches experience different kick strengths. Then we save BPM ADC data from 180 regular RF BPMs

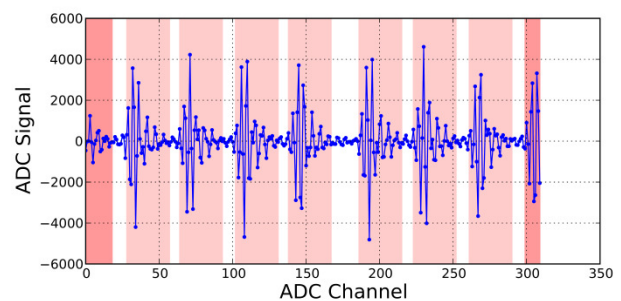


Figure 2: One turn ADC signal from a button of a BPM when 8 trains of bunches are roughly equally spread out in the ring. Shaded regions contain signals of bunch motion. Gating one of these sections and applying the standard TbT extraction process results in TbT position data only for the selected train of bunches.

* Work supported by U.S. DOE under Contract DE-SC0012704.

[†] yhidaka@bnl.gov

MICE OPERATION AND DEMONSTRATION OF MUON IONIZATION COOLING*

A. Liu[†], Fermi National Accelerator Laboratory, Batavia, USA
on behalf of the MICE collaboration

Abstract

The international Muon Ionization Cooling Experiment (MICE) will demonstrate ionization cooling, the only technique that, given the short muon lifetime, can reduce the phase-space volume occupied by a muon beam quickly enough. MICE will demonstrate cooling in two steps. In the first one, Step IV, MICE will study the multiple Coulomb scattering in liquid hydrogen (LH₂) and lithium hydride (LiH). A focus coil module will provide focusing on the absorber. The transverse emittance will be measured upstream and downstream of the absorber in two spectrometer solenoids (SS). Magnetic fields generated by two match coils in the SSs allow the beam to be matched into flat-field regions in which the tracking detectors are installed. This paper will present preliminary results and present plans for data taking of MICE Step IV, together with the design of the MICE Cooling Demonstration Step (Step DEMO), which requires addition of RF systems in the current setup.

INTRODUCTION

A stored muon beam is capable of producing a high intensity, precisely known, flavor-pure neutrino beam, and can provide a source for a multi-TeV muon collider [1–3]. The muon beam is generated from pion decay, where the pion beam is produced by bombarding a target with a high-power proton beam. Muons generated in this way occupy a large phase space volume, which is hard to accept using traditional accelerator components. In order to increase the acceptance, the beam must be cooled before acceleration. Because of the short lifetime of muons, traditional cooling methods do not suffice. In ionization cooling, all components of the muon momentum are reduced when the beam passes through an absorber. The longitudinal momentum is then restored with re-acceleration [4]. The dependence of the normalized transverse emittance of a muon beam passing through a medium is given by:

$$\frac{d\epsilon_n}{ds} \approx -\frac{1}{\beta^2} \frac{\epsilon_n}{E_\mu} \left\langle \frac{dE}{ds} \right\rangle + \frac{1}{\beta^3} \frac{\beta_\perp (0.014 \text{ GeV})^2}{2E_\mu m_\mu X_0} \quad (1)$$

where ϵ_n is the normalized transverse emittance, $\beta = v/c$, E_μ the energy in GeV, β_\perp the transverse Courant-Snyder betatron function, m_μ the muon mass in GeV/ c^2 , and X_0 the radiation length of the material. MICE will be the first experiment to demonstrate the reduction of the transverse phase space volume of a muon beam at a momentum useful for neutrino factory and muon collider applications.

* Work supported by Fermilab, Operated by Fermi Research Alliance, LLC under Contract No. DE-AC02-07CH11359 with the United States Department of Energy.

[†] aoliu@fnal.gov

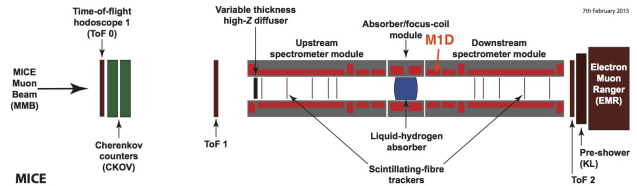


Figure 1: The schematic drawing of the MICE Step IV beam-line configuration. The red label marks the position of M1D, which will stay powered off during Step IV due to a failure in Sep. 2015.

Step IV of MICE will make detailed measurements of multiple Coulomb scattering and energy loss of muons in the absorber materials over a range of momenta from 140 to 240 MeV/ c . The collaboration also seeks to measure transverse normalized emittance reduction in a number of lattice configurations [5]. A schematic drawing of MICE Step IV is shown in Figure 1. The phase space volume of the beam is measured in the upstream and downstream spectrometer solenoids (SSU and SSD) using scintillating-fiber (Scifi) trackers. Time-of-flight (TOF) detectors upstream of SSU and downstream of SSD are used for particle identification. There are twelve coils in the channel. Three coils, E-C-E, in each of the SSs provide constant fields within the trackers. Two coils, M1 and M2, in each of the SSs provide matching into the focus coil (FC) module, and two coils in the FC module provide beam focusing onto the absorber. MICE Step IV will be operated in both flip and solenoid modes, where the direction of longitudinal magnetic field, B_z , flips across the absorber in flip mode and stays the same in solenoid mode.

In the next and final step of MICE, which is the demonstration of the ionization cooling, or Step DEMO, RF cavities and two additional absorber modules will be introduced. In this step, the unnormalized transverse emittance of the beam will be reduced with RF re-acceleration. The goals of MICE Step IV and Step DEMO are described in Table 1.

MICE STEP IV STATUS

MICE Step IV has completed its construction. Currently all the detectors described above are in place and working. MICE has developed its own comprehensive simulation software package, the MICE Analyses User Software (MAUS). MAUS was organized and written to combine the simulation requirements: to not only perform Monte Carlo (MC) simulations based on Geant4 core packages, but also to provide online monitoring and offline reconstruction of experimental data. MAUS has developed rapidly over the years and now is in version 2.6.0. In parallel, a G4beamline [6] simulation en-

COLLIDER IN THE SEA: VISION FOR A 500 TeV WORLD LABORATORY

P.M. McIntyre[†], S. Assadi, S. Bannert, J. Breitschopf, J. Gerity, J.N. Kellams, A. Sattarov
 Texas A&M University, College Station, TX USA
 Daniel Chavez, Universidad Guanajuato, Leon, Mexico
 N. Pogue, Lawrence Livermore National Laboratory, Livermore, CA USA

Abstract

A design is presented for a hadron collider in which the magnetic storage ring is configured as a circular pipeline, supported in neutral buoyancy in the sea at a depth of ~ 100 m. Each collider detector is housed in a bathysphere the size of the CMS hall at LHC, also neutral-buoyant. Each half-cell of the collider lattice is ~ 300 m long, housed in a single pipeline segment. A choice of ~ 3.2 T dipole field, 1,900 km circumference provides a collision energy of 500 TeV. Beam dynamics is dominated by synchrotron radiation (SR) damping, which sustains luminosity for >10 hours and supports bottoms-up injection to replace losses and sustain high luminosity indefinitely. We discuss how to connect and disconnect half-cell segments of the collider at-depth using remote submersibles, and how to maintain the lattice in the required alignment.

INTRODUCTION

Several scenarios are being investigated [1,2] for a future hadron collider that would extend well beyond the 14 TeV collision energy of LHC. Keil [3] showed that the beam dynamics in a hadron collider operating at 100 TeV or greater collision energy is dominated by synchrotron damping. The choice of magnetic field strength B strongly determines the cost and performance of such a collider. The radius R of the storage ring is inversely proportional to B ; the total SR power P that is radiated by the beams is proportional to B , and the achievable luminosity L is limited by P and by the beam-beam tune shift ξ :

$$L = \frac{\gamma \xi N f}{\beta_x r_p}, P = \frac{8\pi N f e^2}{3 R} \gamma^4, L = \left(\frac{3\xi}{8\pi \gamma^3 \beta_x r_p e^2} \right) P R.$$

The lowest cost/TeV superconducting dipoles ever built were those for the 3 T superferric SSC [4] and the 4 T RHIC [5]. Thus both technology cost and performance ($\sim L$) improve with decreasing field and increasing circumference. At the other pole is the choice of 15 T that would be required to achieve 100 TeV collision energy with tunnel circumference that could be built near CERN.

It is also important to keep in view the physics motivation that drives proposals for a future hadron collider – to discover new particles and new gauge fields of nature. There is a fundamental difference between the present case and the successes of the last generation – the proposal to build proton-antiproton colliders [6] was motivated by the prediction that the weak bosons should have a mass ~ 100 GeV/ c^2 , and the proposals for SSC and LHC were motivated by the prediction that the Higgs boson

should have a mass <500 GeV/ c^2 . *There is however no compelling prediction today of a mass scale for new gauge fields beyond the electroweak and Higgs scales.* This consideration suggests that the parameters for a new hadron collider should be chosen to achieve the highest possible collision energy for a given public investment.

In a previous paper [2] we presented the design of a cable-in-conduit (CIC) dual-dipole, shown in Fig. 1 that minimizes the cost/TeV of the superconducting magnets for a future hadron collider. In this paper we consider using that design in a hadron collider that with radius limited ultimately by the total synchrotron radiation heat P that can be sustainably pumped from an intermediate-temperature intercept in the cryogenics. Those parameters optimized with a magnetic field of ~ 3.2 T, a circumference of 1,900 km, and a collision energy of 500 TeV. We further consider a new option that would eliminate the tunnel: a Collider-in-the-Sea.

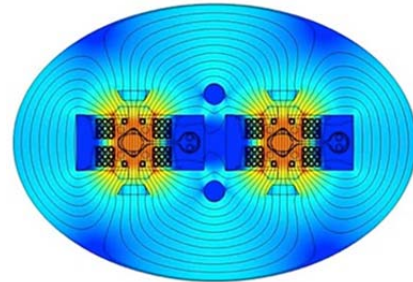


Figure 1: 4.5 Tesla C-dipole for an ultimate-energy hadron collider. Each beam tube has a side SR channel.

COLLIDER IN THE SEA

An example siting of the Collider in the Sea is shown in Fig. 2 for an example site in the Gulf of Mexico. The

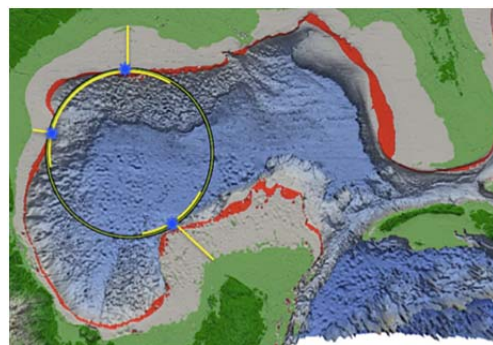


Figure 2: Bathymetry of the Gulf of Mexico, showing potential alignment of a 1,900 km circumference hadron collider. Red = 100 \rightarrow 200 m isobaths; gray = 0-100 m isobaths; blue = detectors; green = surface topography.

* Work supported by the Mitchell Family Foundation.

[†] email address: mcintyre@physics.tamu.edu

MULTIPHYSICS ANALYSIS OF CRAB CAVITIES FOR HIGH LUMINOSITY LHC UPGRADE*

O. Kononenko[†], Z. Li, SLAC National Accelerator Laboratory, Menlo Park, USA
R. Calaga, C. Zanoni, CERN, Geneva, Switzerland

Abstract

Development of the superconducting RF crab cavities is one of the major activities under the high luminosity LHC upgrade project that aims to increase the machine discovery potential. The crab cavities will be used for maximizing and leveling the LHC luminosity hence having tight tolerances for the operating voltage and phase. RF field stability in its turn is sensitive to Lorentz force and external loads, so an accurate modelling of these effects is very important. Using the massively parallel ACE3P simulation suite developed at SLAC, we perform a corresponding multiphysics analysis of the electro-mechanical interactions for the RFD crab cavity design in order to ensure the operational reliability of the LHC crabbing system.

INTRODUCTION

The high luminosity LHC upgrade project [1] aims to broaden the machine potential after 2025. To increase the accelerator luminosity beyond the design value the use of the superconducting RF crab cavities [2] is planned.

Two cavity designs, namely RFD and DQW [3], are now under development to demonstrate the beam crabbing scheme. One of the major operational concerns of this scheme is the RF field stability that is sensitive to Lorentz force and external loads. To ensure tight tolerances for the deflecting voltage and phase a good understanding of the complicated multiphysics interactions within the crab cavity is required. In particular, the electro-mechanical coupling parameters for the beam dynamics and performance analysis must be determined.

Table 1: Selected Parameters of the RFD Crab Cavity

Parameter	Value
Frequency [MHz]	400
Crabbing Voltage [MV]	3.34
Operating Temperature [K]	2

In this paper we study the RFD cavity design (see Table 1 for the list of selected relevant parameters) and use the parallel ACE3P simulation suite [4] to calculate the effect of the Lorentz force and tuner displacement on the RF frequency, determine mechanical eigenmodes as well as their coupling to electromagnetic fields.

SIMULATION MODEL

We consider the 3D mechanical model of the RFD crab cavity in a helium tank that was reconstructed based on the original drawings preserving the total mass and external dimensions, see Fig. 1 and Table 2 for more details.

* Work supported by DOE Contract No. DE-AC02-76SF00515

[†] Oleksiy.Kononenko@slac.stanford.edu

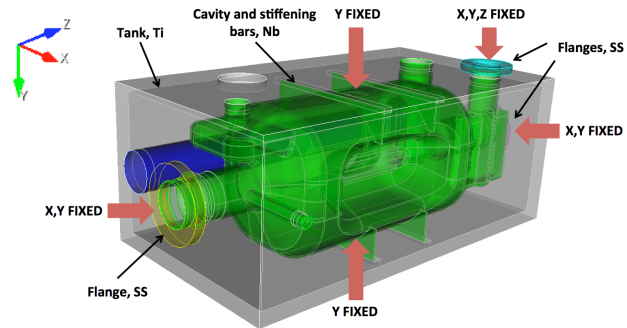


Figure 1: 3D structural model of the RFD crab cavity.

Table 2: Material Properties at 2 K

Material	Density [kg/m ³]	Poisson Ratio	Young's Modulus [GPa]
Nb	8700	0.38	118
Ti	4540	0.37	117
SS (316LN)	8000	0.29	193

The cavity mechanical interaction with the external world is a function of a complex supporting geometry, not fully designed at the time of the simulations. Same idea applies to the tuner and its frame. The boundary conditions are therefore a simplification, aimed at preserving the modes of the cavity inside the helium tank and are chosen as follows: the beam-pipe flanges are fixed in transversal plane and free longitudinally; the tuner (not shown in Fig. 1) is attached to the cavity constraining it vertically; the fundamental power coupler is fixed in all three directions.

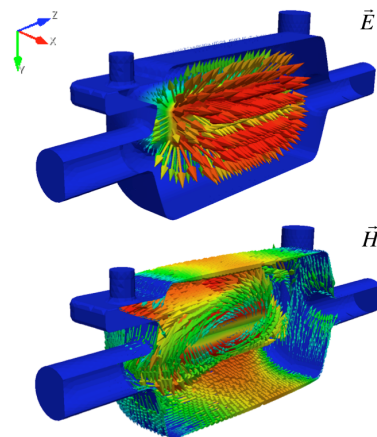


Figure 2: Electric (top) and magnetic (bottom) fields [a.u.] in the RFD cavity for the crabbing 400 MHz mode.

HIGH ENERGY COULOMB SCATTERED ELECTRONS DETECTED IN AIR USED AS THE MAIN BEAM OVERLAP DIAGNOSTICS FOR TUNING THE RHIC ELECTRON LENSES*

P. Thieberger[†], Z. Altinbas, C. Carlson, C. Chasman, M. Costanzo, C. Degen, K. A. Drees, W. Fischer, D. Gassner, X. Gu, K. Hamdi, J. Hock, A. Marusic, T. Miller, M. Minty, C. Montag, Y. Luo and A.I. Pikin, Brookhaven National Laboratory, Upton, NY 11973, USA
S.M. White, European Synchrotron Radiation Facility, BP 220, 38043 Grenoble Cedex, France

Abstract

A new type of electron-ion beam overlap monitor has been developed for the Relativistic Heavy Ion Collider (RHIC) electron lenses. Low energy electrons acquire high energies in small impact parameter Coulomb scattering collisions with relativistic ions. Such electrons can traverse thin vacuum windows and be conveniently detected in air. Counting rates are maximized to optimize beam overlap. Operational experience with the electron backscattering detectors during the 2015 p-p RHIC run will be presented. Other possible real-time non-invasive beam-diagnostic applications of high energy Coulomb-scattered electrons will be briefly discussed.

The present RHIC luminosity limitation for the collision of polarized protons, imposed by the beam-beam effect, is due to the non-linear lens effect of the macroscopic field of one bunch upon each proton in the opposite bunch. This “bad lens” causing tune-spread, emittance growth and gradual beam loss can be partially compensated with similar lenses of opposite polarity located at locations where the phase advances are integer numbers of π with respect to the pp interaction region. To accomplish this end, two electron lenses where installed in the RHIC tunnel and successfully used during the 2015 pp run [1]. To optimize the performance of such electron lenses, the electron and proton beams need to be accurately superimposed. Fig. 1 illustrates the effect of a 0.3σ horizontal misalignment ($100 \mu\text{m}$ for a $300 \mu\text{m}$ rms beam size) which is close to the maximum that can be tolerated.

To achieve such alignment with beam position monitors (BPMs) is challenging to say the least. The dc electron beam needs to be periodically interrupted which is not desirable for stable operation, and the signals thus generated are very different from the proton bunch signals, making electronic offsets practically unavoidable. It was realized at an early stage that a “luminosity” signal was required that could measure the degree of overlap directly.

At first, detecting bremsstrahlung from small impact parameter p-e collisions was considered, but it was soon

* Work supported by Brookhaven Science Associates under Contract No. DE-AC02-98CH10886 with the U.S. Department of Energy.

Most of this material appears in an article by the same authors entitled “High energy Coulomb-scattered electrons for relativistic particle beam diagnostics”, Phys. Rev. Accel. Beams 19, 041002 (2016)

[†] PT@BNL.GOV

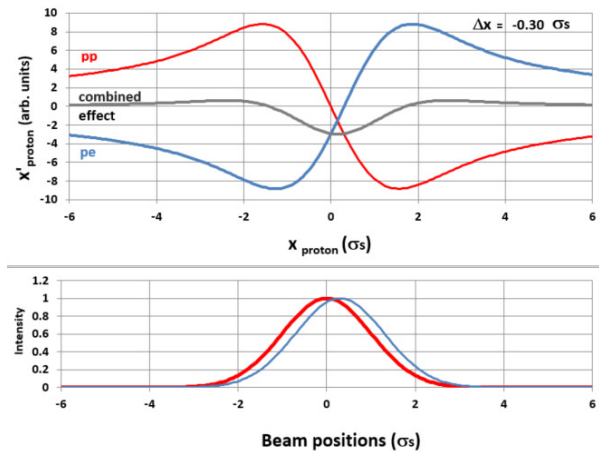


Figure 1: The radial kick from the colliding bunch (red) is partially compensated by an opposite kick from the electron lens (blue). The compensation is imperfect (grey) when the beams are misaligned. These curves are approximations obtained with simplified short beam-beam lens models for both the p-p and p-e interaction regions.

realized that the electrons participating in such collisions would acquire high enough energies to allow these to be detected instead.

The theory of small-impact parameter collisions between charged particles has been well known since 1911 [2] when Ernest Rutherford discovered the atomic nucleus by studying the scattering of alpha and beta particles from stationary targets. Our targets, the protons, far from being stationary, are moving at relativistic velocities.

Fig. 2 illustrates the fact that a small angle deflection in the proton frame leads to a backscattered high energy (up to a several MeV) electron in the lab frame.

A simple theory (see [3] and references therein) was developed for estimating energies, angles and cross sections for producing such backscattered electrons. A coordinate transformation to the proton frame allows the application of the standard equations for Rutherford scattering. The inverse transformation of the results back to the lab frame yields electron energy and scattering cross sections such as the ones shown in Fig. 3.

BUNCH SHAPE MONITOR MEASUREMENTS AT THE LANSCE LINAC*

I. Draganic[†], C. Fortgang, R. McCrady, L. Rybaryk, R. Garnett, J. O'Hara, H. Watkins, C. Taylor and D. Baros, Los Alamos National Laboratory, Los Alamos, NM, USA
A. Feschenko, V. Gaidash, and Yu. Kisselev, Institute of the Nuclear Research, Moscow, Russia

Abstract

Two Bunch Shape Monitors (BSM) have been developed, fabricated and assembled for the first direct longitudinal beam measurements at the LANSCE linear accelerator. The BSM detectors use different radio frequencies for the deflecting field: first harmonic (201.25 MHz) and second harmonic (402.5 MHz) of the fundamental accelerator radio frequency. The first BSM (BSM 201) is designed to record the H⁺ beam phase distribution after the new RFQ accelerator at the beam energy of 750 keV with a phase resolution of 1.0° and covering phase range of 180° at 201.25 MHz. The second BSM (BSM 402) is installed between DTL tanks 3 and 4 of the LANSCE linac in order to scan both H⁺ and H⁻ beams at a beam energy of ≈73 MeV with a phase resolution of 0.5° in a phase range of 90° at 201.25 MHz. Preliminary results of bunch shape measurements of both beams for different pulse lengths and repetition rates will be presented.

INTRODUCTION

The Los Alamos Neutron Science Center (LANSCE) sustains a broad user program that includes the neutron scattering studies, radioactive isotope production, basic science research and national security programs by providing multiple accelerated beams to several different experimental areas. The LANSCE linac accelerates protons (H⁺) and negative hydrogen ions (H⁻) to 800 MeV simultaneously. Accelerated H⁻ beam is delivered at 20 Hz to the proton storage ring, delivered to a moderated neutron production target for neutron-scattering experiments at the Lujan Center, at 100 Hz to an un-moderated spallation target for weapons nuclear research programs (WNR) and commercial programs, an on-demand or low repetition rate for proton radiography experiments (pRad), and at 20 Hz for ultra-cold neutron production (UCN). At present, protons are only delivered for isotope production (IPF) at 100 MeV. The LANSCE accelerator operates at 120 Hz [1, 2]. Operational parameters are listed in Table 1. All beams are delivered to the LANSCE experimental areas on a pulse-by-pulse basis, initially accelerated in separate Cockcroft-Walton-based injectors, to energy of 750 keV, and to a final beam energy of 800 MeV by a 201.25-MHz-drift tube linac (DTL) and 805-MHz coupled cavity linac.

In order to better understand longitudinal dynamics of both beams during tuning and operations we have purchased bunch-length measurement systems from the Institute for Nuclear Research of Russian Academy of Science

* Work supported by the United States Department of Energy, National Nuclear Security Agency, under contract DE-AC52-06NA25396

[†] draganic@lanl.gov

in Moscow in 2012. Both BSMs were delivered and assembled at LANSCE during summer 2014. Preliminary monitor commissioning, instrument calibrations, laboratory tests and tuning without beams were performed at that time. Based on a project review in 2015, the decision was made to install the first BSM 402 between DTL tanks 3 and 4 during the next extended maintenance period. The second BSM 201 installation is awaiting completion of the RFQ test stand. The BSM 402 detector was successfully mounted and aligned in the beam line in July 2016. First bunch monitor shape measurements of low current tuning H⁻ beam (1 mA) were recorded on August 7, 2016 during start-up of the LANSCE linac. With BSM 402 located between DTL tanks 3 & 4 we are now able to measure the bunch shapes for both beam species under variable operating conditions up to a 4-Hz repetition rate (Table 1). In this paper we discuss the first direct measurements of H⁺ and H⁻ bunch profiles.

Table 1: Typical 120-Hz LANSCE Beam Parameters

Area/Beam	Duty Factor	Chopping Specs
Lujan, H ⁻	20 Hz x 625 μs=1.25%	290 ns burst every 358 ns
WNR, H ⁻	100 Hz x 625 μs=6.25%	Single micropulse every 1.8 μs
pRad, H ⁻	1 Hz x 300 μs = 0.03%	20-30, 60 ns beam bursts, variable spacing
UCN, H ⁻	20 Hz x 625 μs = 1.25%	Variable
IPF, H ⁺	100 Hz x 625 μs=6.25%	None

BUNCH SHAPE MONITOR

The basic working concept of the bunch shape monitor is straightforward. First, the device transforms longitudinal distribution of ion beam into a spatial distribution of secondary electrons emitted from a thin wire, inserted into the beam. These electrons are then analysed using a transverse modulation from an RF deflector synchronized with the basic RF frequency of the linac, which selects a specific phase slice of the original ion beam to be sampled. The detailed description of the operation of the BSM detector is published elsewhere [3, 4]. The LANL BSMs which use two different frequencies for the RF deflecting field are shown in Fig 1. The fundamental linac frequency of 201.25 MHz is used in BSM 201 with the phase resolution of 1°. BSM 402 uses second harmonic frequency of 402.5 MHz with corresponding phase resolution of 0.5°. Both detectors have an energy-selecting bending magnet which separates low energy secondary

OPERATIONAL EXPERIENCE WITH FAST FIBER-OPTIC BEAM LOSS MONITORS FOR THE ADVANCED PHOTON SOURCE STORAGE RING SUPERCONDUCTING UNDULATORS*

J. Dooling[†], K. Harkay, V. Sajaev, and H. Shang

Advanced Photon Source, Argonne National Laboratory, Argonne, IL, USA

Abstract

Fast fiber-optic (FFO) beam loss monitors (BLMs) installed with the first two superconducting undulators (SCUs) in the Advanced Photon Source storage ring have proven to be a useful diagnostic for measuring deposited charge (energy) during rapid beam loss events. The first set of FFOBLMs were installed outside the cryostat of the short SCU, a 0.33-m long device, above and below the beam centerline. The second set are mounted with the first 1.1-m-long SCU within the cryostat, on the outboard and inboard sides of the vacuum chamber. The next 1.1-m-long SCU is scheduled to replace the short SCU later in 2016 and will be fitted with FFOBLMs in a manner similar to the original 1.1-m device. The FFOBLMs were employed to set timing and voltage for the abort kicker (AK) system. The AK helps to prevent quenching of the SCUs during beam dumps [1] by directing the beam away from the SC magnet windings. The AK is triggered by the Machine Protection System (MPS). In cases when the AK fails to prevent quenching, the FFOBLMs show that losses often begin before detection by the MPS.

INTRODUCTION

High-purity, fused silica fiber optic (FO) cables allow for fast beam loss diagnosis and their use is becoming more widespread [2–4]. They show no transmission loss up to doses of 1 MGy. This rad hardness distinguishes the high-purity fibers from radiation induced attenuation (RIA) fibers; the latter employ transmission loss as a measure of absorbed dose [5, 6]. The FO beam loss monitors (BLMs) provide fast dosimetry [7, 8].

Superconducting undulators (SCUs) have been installed in the insertion device (ID) straight sections of Sectors 1 and 6 (ID01 and ID06) of the Advanced Photon Source (APS) storage ring (SR). SCU0 has been in Sector 6 and SCU1 is in Sector 1; in September 2016, the prototype SCU0 was replaced with a full length 1-m SCU. In [9], we described calibration of the FO BLM for SCU0. The same approach was employed in ID01; however, a constant 4-mm horizontal orbit bump was required in addition to the injection kicker bump.

INSTALLATION

Both CeramOptec and FiberGuide fused-silica fiber bundles are employed; the bundles are composed of individual

200 μm silica core with 220 μm step-index silica-cladded fibers. All bundles are fabricated with a numerical aperture of 0.22. In the case of the FiberGuide cables, bundles of 7 and 61 fibers are used; whereas, the CeramOptec cables are all 61-fiber bundles. The SCU1 fiber bundles are positioned near beam elevation on either side of the vacuum chamber within the cryostat. Both internal SCU1 bundles are composed of 7 fused-silica fibers. A photograph of the upstream end of the inboard portion of the cryostat is presented in Figure 1. The end of the inboard fiber, covered with aluminum foil, is visible on the lower right-hand side (circled in white).

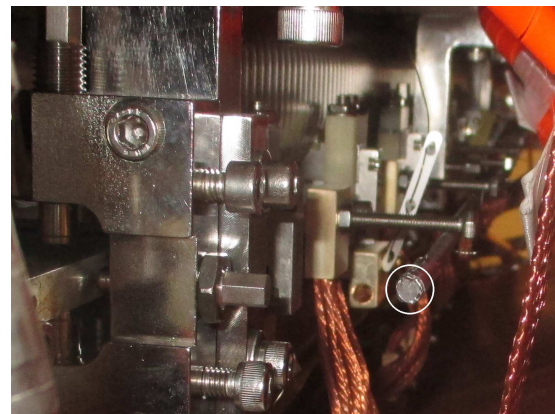


Figure 1: Looking downstream at the inboard FO bundle installed in the SCU1 cryostat (end circled in white).

ANALYSIS

Calibration is done by depositing the charge of a single bunch in the ID straight section where the fibers are located [9]. During multi-bunch fill pattern losses, the charge deposited by each loss pulse is determined from the integrated photomultiplier tube (PMT) output charge over the pulse period calibrated against the single-bunch loss data. For 24-bunch and 324-bunch uniform fill patterns, the loss pulses are clearly resolved. The SR circumference is 1104 m and the rf operates at a harmonic number of 1296 ($f_{rf} = 352$ MHz); thus, in a 24-bunch fill pattern, the loss charge is determined from summing the calibrated charge in each spacing of 54 rf buckets or 154 ns.

Calibration shows the responses of the PMTs to be nonlinear with respect to the lost (deposited) charge. The degree of saturation depends on both the intensity of light striking the PMT photocathode as well as the HV bias distributed across the dynode chain. The PMT output charge as a function of

* Work supported by the U.S. Department of Energy Office of Science, under contract number DE-AC02-06CH11357.

[†] jcdooling@anl.gov

COMMISSIONING OF THE PHASE-1 SuperKEKB B-FACTORY AND UPDATE ON THE OVERALL STATUS

Y. Ohnishi*, T. Abe, T. Adachi, K. Akai, Y. Arimoto, M. E. Biagini¹, M. Boscolo¹, K. Egawa, D. El Khechen², Y. Enomoto, J. W. Flanagan, H. Fukuma, Y. Funakoshi, K. Furukawa, S. Guiducci¹, N. Iida, H. Inuma, H. Ikeda, T. Ishibashi, M. Iwasaki, T. Kageyama, H. Kaji, T. Kamitani, T. Kawamoto, S. Kazama³, M. Kikuchi, T. Kobayashi, K. Kodama, H. Koiso, M. Masuzawa, T. Mimashi, T. Miura, F. Miyahara, T. Mori, A. Morita, S. Nakamura, T. Nakamura, H. Nakayama, T. Natsui, M. Nishiwaki, K. Ohmi, T. Oki, S. Sasaki, M. Satoh, Y. Seimiya, K. Shibata, M. Suetake, Y. Suetsugu, H. Sugimoto, M. Tanaka, M. Tawada, S. Terui, M. Tobiyama, S. Uehara, S. Uno, X. Wang, K. Watanabe, Y. Yano, S. Yoshimoto, R. Zhang, D. Zhou, X. Zhou, and Z. Zong

KEK, Tsukuba, Japan

¹also at INFN/LNF, Frascati, Italy

²also at LAL, Orsay, France

³also at University of Zurich, Zurich, Switzerland

Abstract

The SuperKEKB B-Factory at KEK (Japan), after few years of shutdown for the construction and renovation, has finally come to the Phase-1 commissioning of the LER and HER rings, without the final focus system and the Belle II detector. Vacuum scrubbing, optics tuning, and beam related background measurements were performed in this phase. Low emittance tuning techniques have also been applied in order to set up the rings for Phase-2 with colliding beams next year. An update of the final focus system construction, as well as the status of the injection system with the new positron damping ring and high current/low emittance electron gun is also presented.

INTRODUCTION

The SuperKEKB collider [1] is an asymmetric-energy and a double-ring electron-positron collider. The energy of the electron ring is 7 GeV(HER) and the positron ring is 4 GeV(LER). The collision point is one and the circumference is 3 km. The target luminosity is $8 \times 10^{35} \text{ cm}^{-2} \text{ s}^{-1}$, which is 40 times as high as the predecessor KEKB collider [2]. In order to accomplish the extremely high luminosity, a nano-beam scheme [3] is adopted. A large crossing angle and a small beam spot size in the both horizontal and vertical direction are applied in the nano-beam scheme. The crossing angle between two colliding beams is 83 mrad and the horizontal beam size is approximately $10 \mu\text{m}$. When the overlap region of two colliding beams is considered, the nano-beam scheme can exchange the coordinate x with z as:

$$\tilde{\sigma}_x^* = \sigma_z \phi_x \quad (1)$$

$$\tilde{\sigma}_z = \frac{\sigma_x^*}{\phi_x} < \beta_y^* \sim 300 \mu\text{m}, \quad (2)$$

where the $\tilde{\sigma}_x^*$ and $\tilde{\sigma}_z$ are the effective horizontal beam size at the interaction point(IP) and the effective bunch length,

* yukiyoshi.onishi@kek.jp

respectively. Because the geometrical reduction of the luminosity depends on the effective bunch length in the nano-beam scheme, it must be smaller than the vertical beta function at the IP. The low emittance and the low beta function at the IP in the horizontal direction can realize the requirement of “hourglass condition” although the real bunch length is long. The nominal bunch length, σ_z , is 6 mm in SuperKEKB. In the case of SuperKEKB, the vertical beta function can be squeezed down to approximately $300 \mu\text{m}$ from this criterion.

The famous luminosity formula is modified by replacing with the effective values as:

$$L = \frac{N_+ N_- f}{4\pi \sigma_x^* \sigma_y^*} = \frac{N_+ N_- f}{4\pi \sigma_z \phi_x \sqrt{\epsilon_y \beta_y^*}} \quad (3)$$

and the vertical and horizontal beam-beam parameter is expressed by

$$\xi_y \propto \frac{1}{\sigma_z \phi_x} \sqrt{\frac{\beta_y^*}{\epsilon_y}} \quad (4)$$

$$\xi_x \propto \frac{\beta_x^*}{(\sigma_z \phi_x)^2} \sim 0.003, \quad (5)$$

where ϕ_x is the half crossing angle. Because there is an upper limit for the beam-beam parameter, both the vertical beta function at the IP and the vertical emittance must be small with keeping their ratio constant in order to achieve the higher luminosity. The horizontal beam-beam parameter is almost constant and very small in the nano-beam scheme even though the small horizontal emittance and the small horizontal beta at the IP are realized. Consequently, the dynamic beta and the dynamic emittance becomes small.

The alternative formula of the luminosity is

$$L \propto \frac{I \xi_y}{\beta_y^*}. \quad (6)$$

In order to achieve 40 times as high luminosity as the KEKB collider, the vertical beta function at the IP is

LHC OPERATION AT 6.5 TeV: STATUS AND BEAM PHYSICS ISSUES

G. Papotti, M. Albert, R. Alemany, E. Bravin, G. Crockford, K. Fuchsberger,
R. Giachino, M. Giovannozzi, G. Hemelsoet, W. Hofle, G. Iadarola, D. Jacquet,
M. Lamont, D. Nisbet, L. Normann, T. Persson, M. Pojer, L. Ponce, S. Redaelli,
B. Salvachua, M. Solfaroli, R. Suykerbuyk, J. Wenninger
CERN, Geneva, Switzerland

Abstract

LHC operation restarted in 2015 after the first Long Shutdown, planning for a 4-year long run until the end of 2018 (called Run 2). The beam energy was fixed at 6.5 TeV. The year 2015 was dedicated to establishing operation at the high energy and with 25 ns beams, in order to prepare production for the following three years. The year 2016 was the first one dedicated to production, and it turned out to be a record-breaking year, in which the goals in both peak and integrated luminosities with proton-proton beams were achieved and surpassed.

This paper revisits 2015 and 2016, shortly highlighting the main facts in the timelines, recalling the parameters that characterized luminosity production, and sketching the main limitations and the main highlights of results for selected topics, including a particular focus on the beam physics issues.

INTRODUCTION

The year 2015 marked the restart of LHC [1] operation with beam after its first Long Shutdown (LS1) [2]. The first three months were devoted to hardware commissioning, which included the dipole training campaign to 6.5 TeV. The machine checkout interwove with the end of the hardware commissioning, and finally the first probe beams were circulated on Easter Day (5 April). Eight weeks of beam commissioning followed, which included recommissioning of all systems, including machine protection systems. The summer was devoted to a step-wise scrubbing run and intensity ramp-up: first with 50 ns, then with 25 ns beams. A total of ~ 3 weeks were dedicated to electron-cloud scrubbing at 450 GeV [3]. In September and October the intensity ramp-up with 25 ns continued, mostly limited by the heat load induced on the cryogenic system [4]. The month of August was particularly difficult as the machine availability was impaired by Single Event Effects on the Quench Protection Systems [5] and by high UFO rates (Unidentified Falling Objects, [6]), so much that most of the luminosity production happened mostly in the months of September and October.

The year 2016 required only 4 weeks of recommissioning with beam, followed directly by operation with 25 ns beams. The 2015 performance with respect to electron-cloud could be recovered with only ~ 12 hours dedicated to scrubbing at injection energy [7]. Until mid-July, operation concentrated on proton-proton physics production, in order to accumulate as much data as possible for the summer physics confer-

ences. The Machine Development (MD) program was then condensed in the second part of the year. The year was characterized by a much improved machine availability [8] that allowed integrating more than the yearly target despite a few limitations on the number of bunches and intensity.

This paper first reviews the luminosity performance achieved in 2015 and 2016, and then draws attention to the main limitations encountered, and some highlights of results for selected topics. This paper does not cover the lead ion runs (Pb-Pb in 2015 [9], and p-Pb and Pb-p in 2016), nor the special physics runs (e.g. van der Meer, high-beta, i.e. 90 m in 2015 and 2.5 km in 2016).

LUMINOSITY PERFORMANCE

The year 2015 was devoted to establishing proton-proton operation with 25 ns beams at 6.5 TeV, in order to establish a solid base for production in the rest of Run 2. The choice of β^* in ATLAS and CMS was 80 cm, which was cautious to allow some extra margins for machine protection purposes. At the end of the proton physics running period, the peak instantaneous luminosity reached $\sim 0.5 \times 10^{34} \text{ cm}^{-2} \text{ s}^{-1}$, achieved when the number of bunches per ring was maximum for the year (i.e. 2244, see Fig. 1). The main beam and machine parameters that allowed reaching such luminosity are shown in Table 1, where also the Design Report and 2016 values are shown.

Table 1: Beam and Machine Parameters from [1], and Achieved in 2015 and 2016

Parameter	Design	2015	2016
energy [TeV]	7	6.5	6.5
bunch spacing [ns]	25	25	25
β^* [m]	0.55	0.80	0.40
half crossing angle [μrad]	142.5	185	140
N_b [10^{11} ppb]	1.15	1.15	1.1
transverse emittance [μm]	3.75	3.5	2
number of bunches/ring	2808	2240	2220
L [$10^{34} \text{ cm}^{-2} \text{ s}^{-1}$] (peak)	1	0.5	1.4
pile-up μ (peak)	20	18	41
stored beam energy [MJ]	360	270	260

After the experience gained in 2015, in 2016 β^* was pushed to 40 cm. Additionally, the beam production scheme was changed from the standard one [1] to “Batch Compression, Merging and Splitting” [10], which creates brighter bunches (in particular, $\sim 2 \mu\text{m}$ emittances reach collisions, to

RHIC Au-Au OPERATION AT 100 GeV IN RUN16*

X. Gu[†], J. Alessi, E. Beebe, M. Blaskiewicz, J. M. Brennan, K. A. Brown, D. Bruno, J. Butler, R. Connolly, T. D'Ottavio, K. A. Drees, W. Fischer, C. J. Gardner, D. M. Gassner, Y. Hao, M. Harvey, T. Hayes, H. Huang, R. Hulsart, P. Ingrassia, J. Jamilkowski, J. S. Laster, V. Litvinenko, C. Liu, Y. Luo, M. Mapes, G. J. Marr, A. Marusic, G. McIntyre, K. Mernick, R. Michnoff, M. Minty, C. Montag, J. Morris, C. Naylor, S. Nemesure, I. Pinayev, V. Ranjbar, D. Raparia, G. Robert-Demolaize, T. Roser, P.W. Sampson, J. Sandberg, V. Schoefer, F. Severino, T. Shrey, K. Smith, S. Tepikian, Y. Than, P. Thieberger, J. Tuozzolo, G. Wang, Q. Wu, A. Zaltsman, K. Zeno, S. Zhang, W. Zhang
BNL, Upton, NY 11973, USA

Abstract

In order to achieve higher instantaneous and integrated luminosities, the average Au bunch intensity in RHIC has been increased by 28% compared to the preceding Au run. This increase was accomplished in part by merging bunches in the RHIC injector AGS. Luminosity levelling for one of the two interaction points (IP) with collisions was realized by continuous control of the vertical beam separation. Parallel to RHIC physics operation, the electron beam commissioning of a novel cooling technique with potential application in eRHIC, Coherent electron Cooling as a proof of principle (CeCPoP), was carried out. In addition, a 56 MHz superconducting RF cavity was commissioned and made operational. In this paper we will focus on the RHIC performance during the 2016 Au-Au run.

INTRODUCTION

The Relativistic Heavy Ion Collider (RHIC) at Brookhaven National Laboratory is a circular collider that has been operated successfully for more than a decade. It has provided heavy ion collisions of several species at different energies. In 2016, at the beginning of the FY16 physics run, RHIC provided Au-Au beam collisions at 100 GeV/n beam energy for 10 weeks, followed by 6 weeks of d-Au (Deuteron-gold) energy scan physics running. The last week of the run, which was originally devoted to the CeC PoP experiment, was eventually re-used for the 100 GeV Au-Au physics run.

INJECTION CHAIN

The Au injection chain of RHIC includes EBIS/Tandem as an injector, followed by Linac, Booster and AGS. At the beginning of Run16, eight bunches in the AGS were merged into two bunches using a bunch merge scheme of 8→4→2.

To shorten the filling time, the merge scheme of 12→6→2 (Figure 1) was tested and adopted for RHIC operation after reaching the maximum intensity (2.1×10^9) in the AGS with the 8→4→2 merge scheme. To make this scheme work, EBIS also needs to provide 12 pulses per cycle reliably; additionally the Booster merge energy has to be raised to meet the power limit from the local power grid.

* Work supported by the US Department of Energy under contract number DE-SC0012704

[†] xgu@bnl.gov

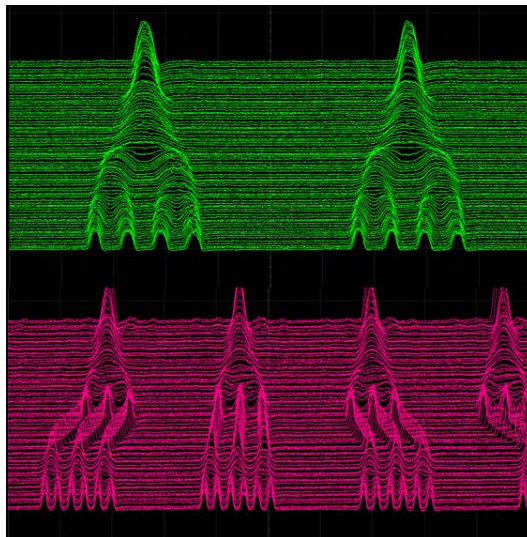


Figure 1: Merge scheme in the AGS for 8→4→2 (top) and 12→6→2 (bottom).

With the merging scheme of 12→6→2, the peak bunch intensity at AGS extraction has reached 3.15×10^9 . However, the AGS injection intensity was limited to $2.4 \sim 2.5 \times 10^9$, which was imposed by the amplifier of the RHIC Landau cavity.

With the upgrade of the Booster low-level RF, the satellite bunch intensity was only 2% of the Au intensity in Run 14, while it is around 4~5% in Run 16 because of the larger number of bunches merged. The longitudinal emittance in the AGS was about 0.7eVs, which is similar to Run 14. The normalized transverse rms emittance in the AGS was about 1.7-1.8 μ m. The duty cycle was also extended from 5.4 seconds to 6.4 seconds, although was reduced to 6 seconds later. Because of the longer cycle time, the filling time of RHIC was extended. The increase emittance growth during the extended filling time resulted in about 5% smaller ramp efficiency than Run 14.

The Tandem also achieved a record Au intensity of 2.5×10^9 and met the limited RHIC intensity requirement during EBIS outages.

RHIC LATTICE AND BEAM LOSS

The 100 GeV Au-Au lattice for Run 16 was similar to the configuration used in Run14 [1, 2]. The integer tunes were (28, 29), and the lattice had a better off-momentum

HIGH LUMINOSITY 100 TeV PROTON-ANTIPROTON COLLIDER

S. J. Oliveros*, J. G. Acosta, L. M. Cremaldi, T. L. Hart, D. J. Summers
University of Mississippi - Oxford, University, MS 38677, USA

Abstract

The energy scale for new physics is known to be in the multi-TeV range, signaling the potential need for a collider beyond the LHC. A $10^{34} \text{ cm}^{-2} \text{ s}^{-1}$ luminosity 100 TeV proton-antiproton collider is explored. Prior engineering studies for 233 and 270 km circumference tunnels were done for Illinois dolomite and Texas chalk signaling manageable tunneling costs. At a $p\bar{p}$ the cross section for high mass states is of order $10\times$ higher with antiproton collisions, where antiquarks are directly present rather than relying on gluon splitting. The higher cross sections reduce the synchrotron radiation in superconducting magnets, because lower beam currents can produce the same rare event rates. In our design the increased momentum acceptance ($11 \pm 2.6 \text{ GeV}/c$) in a Fermilab-like antiproton source is used with septa to collect $12\times$ more antiprotons in 12 channels. For stochastic cooling, 12 cooling systems would be used, each with one debuncher/momentum equalizer ring and two accumulator rings. One electron cooling ring would follow. Finally antiprotons would be recycled during runs without leaving the collider ring, by joining them to new bunches with synchrotron damping.

PROTON ANTIPROTON COLLIDER REMARKS

Physics beyond the standard model will motivate searches for new high mass states at present and future colliders for years to come. It is readily understood that direct $q\bar{q}$ annihilation processes make a significant contribution to the production cross section for high mass states, in addition to gluon splitting present in both $p\bar{p}$ and pp collisions. The presence of the anti-quark in the \bar{p} gives a significant advantage to $p\bar{p}$ colliders for production of high mass states near threshold [1–4].

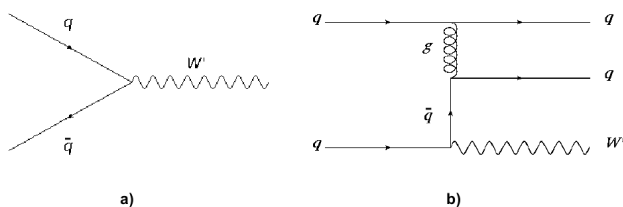


Figure 1: Feynman diagrams for W' production in (a) $q\bar{q}$ collision, and (b) qq collision (t channel). The two final state quarks cross in the u channel, which is not shown.

Figure 1 shows the Feynman diagram for W' production from $q\bar{q}$ and qq collision. Using the event generator, Madgraph [5], the W' cross section is obtained for different W'

* solivero@go.olemiss.edu

masses using proton-proton and proton-antiproton collisions at a center of mass energy of 100 TeV. The results are shown in the Fig. 2. As the mass increases the W' cross section obtained with $p\bar{p}$ collisions is greater compared to pp collisions, becoming approximately 10 times larger at higher masses.

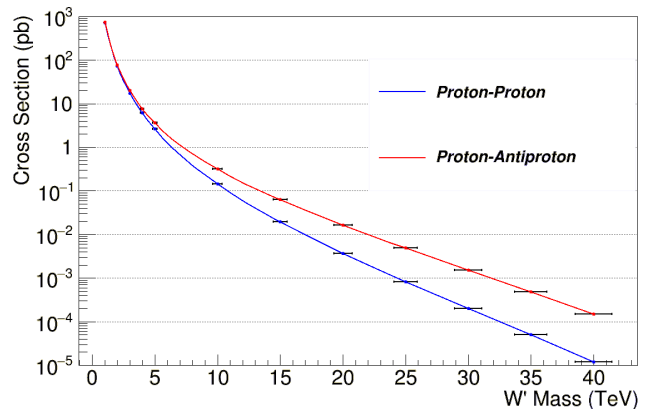


Figure 2: W' boson production cross section as a function of the mass for pp and $p\bar{p}$ collisions with a $E_{cm} = 100 \text{ TeV}$.

Synchrotron radiation (SR) effects, growing as E^4/ρ^2 , may become a serious problem in a collider's superconducting magnets and vacuum systems, but less so in $p\bar{p}$ designs. See the recent design of a 100 km high energy (100 TeV) pp collider (FCC-hh) [6]. With higher cross sections available at a $p\bar{p}$ collider it can be run at lower luminosities, with less SR effect, and even less detector pileup. Scaling to a 200 km $p\bar{p}$ ring, the SR is reduced from 35 W/m [6] to 1.75 W/m.

OBTAINING HIGH LUMINOSITY

An important goal in designing the 100 TeV $p\bar{p}$ collider will be achieving a luminosity of $10^{34} \text{ cm}^{-2} \text{ s}^{-1}$. As a starting point, taking as reference the Tevatron collider, the gain in luminosity for the 100 TeV $p\bar{p}$ collider, for which the beam energy is 50 TeV, the ring circumference is 200 km, and $\beta^* = 14 \text{ cm}$ (half of the Tevatron), the luminosity can

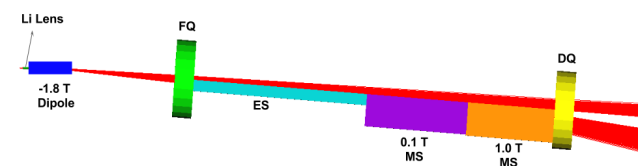


Figure 3: Configuration to divide the beam into two parts. An initial beam with momentum acceptance $p = 11.0 \text{ GeV}/c \pm 24\%$ is collected by the Li lens and dispersed by a magnetic dipole to be then divided by an electrostatic septa ES and two magnetic dipoles MS.

PERFORMANCE OF THE LOW CHARGE STATE LASER ION SOURCE IN BNL*

M. Okamura[†], J. Alessi, E. Beebe, M. Costanzo, L. DeSanto, S. Ikeda, J. Jamilkowski, T. Kaneshue, R. Lambiase, D. Lehn, C.J. Liaw, D. McCafferty, J. Morris, R. Olsen, A. Pikin, R. Schoepfer, A. Steszyn, Brookhaven National Laboratory, Upton, NY USA

Abstract

In March 2014, a Laser Ion Source (LIS) was commissioned which delivers high brightness low charge state heavy ions for the hadron accelerator complex in Brookhaven National Laboratory (BNL). Since then, the LIS has provided many heavy ion species successfully. The induced low charge state (mostly singly charged) beams are injected to the Electron Beam Ion Source (EBIS) where ions are then highly ionized to fit to the following accelerator's Q/M acceptance, like Au³²⁺. A LIS has been known as high current high charge state ion source, however we demonstrated it can provide stable long pulse low charge state heavy ion beam with a good emittance.

INTRODUCTION

Laser ion source has been used to deliver high charge state high current beams. In fact, it can provide fully stripped carbon beam with more than a few tens mA of beam current [1, 2]. In spite of the known unique features, we are developing a low charge high brightness laser ion source. In this report we introduce the laser ion source which is providing singly charged heavy ion beams to the electron beam ion source (EBIS) followed by the linacs and the chain of synchrotrons in BNL.

The new laser ion source was nicknamed as "LION" by one of the authors. We started to develop the LION in 2009 since the project was funded by NASA. The NASA has a user facility in BNL which is called as NASA Space Radiation Laboratory (NSRL) and we provide various heavy ion beams from the booster ring to simulate high energy cosmic rays in the NSRL. By installing the LION, the beam species can be switched in a minutes and the facility can operate with more versatile and more flexible modes. Before introducing LION, all the initial seed beams were provided from a set of hollow cathode ion sources [3]. The typical beam currents were only around ten microamperes with long pulses and the beam transport line from those external sources to the EBIS was designed to accommodate the range of the hollow cathode source's beam current. The LION beams also need to go through the same beam transport line comprised of electro static optics devices with the limited area of good field region. So that the LION needs to provide relatively low current comparing a standard LIS, less than a milliamper, with a very good beam emittance.

In 2014, the first beam from LION was delivered to the

* Work supported by NASA and US Department of Energy under contract number DE-SC0012704.

[†] email address okamura@bnl.gov

EBIS. The beam commissioning was very successful and since then LION has been used to provide various heavy ion beams to the NSRL. In 2015, we installed another laser and additional target to provide gold beam to relativistic heavy ion collider (RHIC). Now most of solid based species and oxygen are supplied by the LION in BNL.

FEATURES OF LASER ION SOURCE

The principle of a laser ion source is simple. In vacuum condition, a solid target is irradiated by a pulsed laser beam and a plasma is formed. The plasma is heated by successive laser irradiation and the plasma temperature becomes higher. The typical total laser pulse width is from sub-nanoseconds to several tens of nanoseconds. By controlling deposited power on the target, the plasma's temperature and expansion speed can be adjusted. For the LION development, we only need singly charged ions and the laser power density was controlled just above 10E8 W/cm². We use 850 mJ 6 ns Nd-YAG lasers [4] and the typical spot size is 3 mm to 5 mm in diameter. As we stated, the heating process is defined only by the laser and target. Other factors like effect of vacuum vessel's wall or background confinement forces do not contribute the plasma production. As long as we control the laser stability and target surface condition, stable ion beam can be easily obtained.

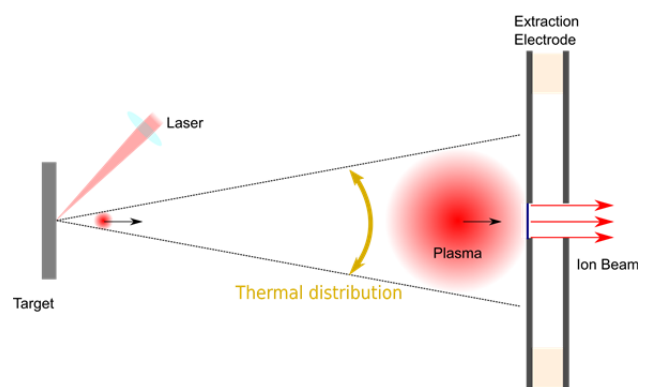


Figure 1: Expanding plasma and extracted ion beam.

Figure 1 shows expanding laser ablation plasma. The gravity centre of the plasma has a velocity perpendicular to the target surface. While the plasma travels from the target to the extraction point, it expands three dimensionally. After the heating stage, each particle in the expanding plasma can be considered to move on the straight path, and the envelope of the entire plasma has conical shape. This conical angle corresponds to the thermal distribution in the plasma. Generally, the solid angle defined by an extraction hole is much smaller than the

RECENT PROGRESS IN HIGH INTENSITY OPERATION OF THE FERMILAB ACCELERATOR COMPLEX *

M. E. Convery[†], Fermi National Accelerator Laboratory, Batavia, IL, USA

Abstract

We report on the status of the Fermilab accelerator complex. Beam delivery to the neutrino experiments surpassed our goals for the past year. The Proton Improvement Plan is well underway with successful 15 Hz beam operation. Beam power of 700 kW to the NOvA experiment was demonstrated and will be routine in the next year. We are also preparing the Muon Campus to commission beam to the g-2 experiment.

INTRODUCTION

The Fermilab accelerator complex, shown in Fig. 1, has surpassed its beam delivery goals for the past year, has demonstrated 700 kW beam power to the NOvA experiment, and is preparing the Muon Campus to begin commissioning beam to the g-2 experiment. These accomplishments would not be possible without the successful execution of the Proton Improvement Plan (PIP) which, among many other improvements, has enabled beam from the Booster at 15 Hz. Other near-term upgrades are planned for increasing beam flux to the Short Baseline Neutrino experiments. For the longer term, the PIP-II project is underway to provide protons with more than 1 MW beam power to the Long Baseline Neutrino Facility.

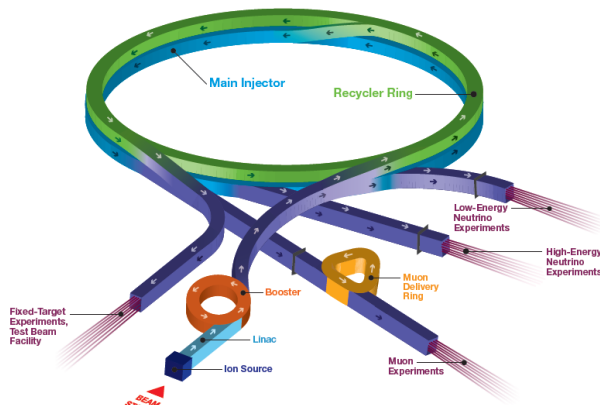


Figure 1: The Fermilab accelerator complex.

BEAM POWER OF 700 KW

Prior to the Accelerator NOvA Upgrade (ANU) in 2013, 8-GeV protons from the Booster were RF slip-stacked in the Main Injector, ramped to 120 GeV, and extracted to the NuMI target every 2.2s, for a beam power of about 320 kW. The Recycler, a ring with fixed 8 GeV kinetic energy which shares a tunnel with the Main Injec-

tor, was used for storing antiprotons for the Tevatron collider. ANU provided RF in the Recycler to allow the slip-stacking to occur there, thus reducing the cycle time of the Main Injector to only the 1.3s needed to accelerate the beam and ramp back down [1]. Along with other smaller changes, this allows us to reach 700 kW with only about a 10% increase in intensity per pulse. The biggest challenge is maintaining high efficiency and low beam losses.

Slip-stacking in the Recycler was commissioned in steps, first operating with 6 non slip-stacked bunches, and then slip-stacking in an additional 2, 4, and 6 bunches successively. At each step, the beam intensity was increased over time while tuning to decrease losses. The increase in beam power and integrated number of protons delivered to NuMI over the past two years are shown in Fig. 2. (Note that the SY120 slow-spill program takes 10% of the timeline, which reduces the beam power to NuMI accordingly. Thus the goal of 700 kW will mean operating at 630 kW when SY120 is running.) The record beam power delivered to the NuMI target averaged over an hour is 613 kW. 700 kW has also been demonstrated for less than an hour. A collimator system is currently being installed in the Recycler to capture beam losses from slip-stacking which will allow us to run routinely at 700 kW in 2017.

Challenges at High Intensity

Slip-stacking is achieved by decelerating the first set of batches before injecting the second set of six which remain on-momentum. Batches of twice the intensity are captured when the two sets overlap. Overlapping batches during the slip-stacking process interfere with the ability of the transverse dampers to pick up the beam position. The resistive wall instability is instead avoided by increasing the chromaticity. This does introduce a tune shift between the decelerated bunches and those on the central RF frequency which results in losses.

A tune shift due to space charge is also present at these high intensities, and is larger when two bunches overlap during slip-stacking. Additional details are given in [2].

PROTON IMPROVEMENT PLAN

The Proton Improvement Plan (PIP) was initiated in 2011 as a multi-year campaign funded through operations to increase the beam repetition rate from ~7 Hz to 15 Hz and double the proton source flux to more than 2×10^{17} protons/h without increasing total beam losses. Other goals are to eliminate major reliability vulnerabilities and obsolescence issues in order to ensure a useful operating life of the proton source through at least 2030.

* Operated by Fermi Research Alliance, LLC under Contract No. DE-AC02-07CH11359 with the United States Department of Energy.

[†] convery@fnal.gov

COMPLETE BEAM DYNAMICS OF THE JLEIC ION COLLIDER RING INCLUDING IMPERFECTIONS, CORRECTIONS, AND DETECTOR SOLENOID EFFECTS

G.H. Wei[†], V.S. Morozov, F. Lin, F. Pilat, Y. Zhang,
 Jefferson Lab, Newport News, VA 23606, USA
 Y.M. Nosochkov, M.-H. Wang, SLAC, Menlo Park, CA 94025, USA
 M.-H. Wang, Mountain View, CA 94040, USA

Abstract

The JLEIC is proposed as a next-generation facility for the study of strong interaction (QCD). Achieving its goal luminosity of up to $10^{34} \text{ cm}^{-2}\text{s}^{-1}$ requires good dynamical properties and a large dynamic aperture (DA) of $\sim \pm 10$ sigma of the beam size. The limit on the DA comes primarily from non-linear dynamics, element misalignments, magnet multipole components, and detector solenoid effect. This paper presents a complete simulation including all of these effects. We first describe an orbit correction scheme and determine tolerances on element misalignments. And beta beat, betatron tunes, coupling, and linear chromaticity perturbations also be corrected. We next specify the requirements on the multipole components of the interaction region magnets, which dominate the DA in the collision mode. Finally, we take special care of the detector solenoid effects. Some of the complications are an asymmetric design necessary for a full acceptance detector with a crossing angle of 50 mrad. Thus, in addition to coupling, the solenoid causes closed orbit excursion and excites dispersion. It also breaks the figure-8 spin symmetry. We present a scheme with correction of all of these effects.

IR REQUIREMENT AND CHALLENGES

Follow the step of the HERA, a new lepton-proton collider with a luminosity of several $10^{33} \text{ cm}^{-2}\text{sec}^{-1}$, which called the JLEIC, is designed to meet the new physics researches in quantum chromo-dynamics (QCD). To realize such high luminosity and physics purposes, a full-acceptance detector [1] in the first IP is designed as shown in Fig. 1.

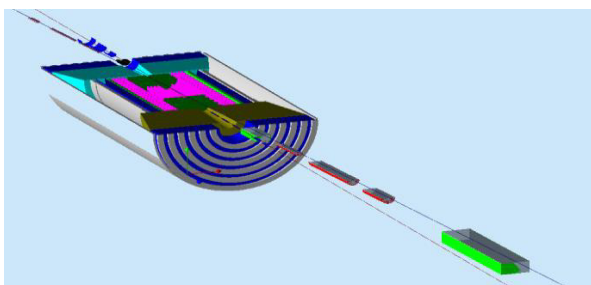


Figure 1: IR design in the first IP of the JLEIC.

[†]gwei@jlab.org

The IR design needs a long space for detector solenoid. And considering forward hadron detection, a highly asymmetric IR optics is studied as shown in Fig. 2. This new structure [2] makes a β_x^*/β_y^* of 0.1/0.02 meter at IP (Interaction Point) with very different expanded beta in upstream FFB (Final Focusing Block) and downstream FFB, ~ 750 m in upstream FFB and ~ 2500 m in downstream FFB. It would cause some design challenges on linear optics, chromaticity compensation, detector solenoid compensation, magnet quality issue, and beta squeeze etc.

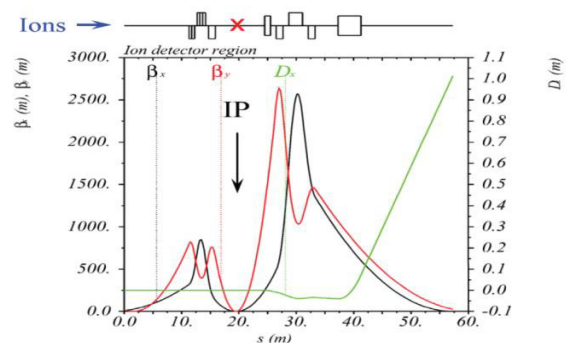


Figure 2: Asymmetric optics of IR design.

CHROMATICITY ISSUE

We use two non-interleaved $-I$ sextupole pairs (X & Y) to compensate chromatic β^* . And remaining linear chromaticity is cancelled using two-family sextupoles in arc section [3]. Final optics can be seen in Fig. 3.

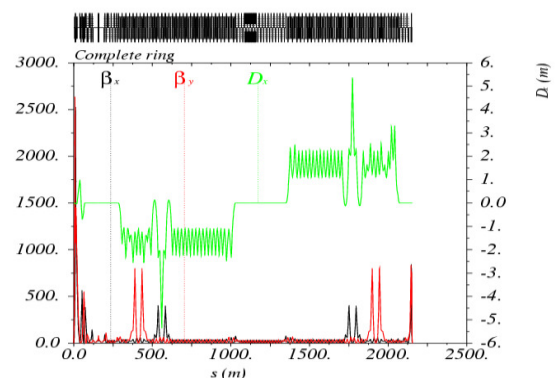


Figure 3: Beam optics of the JLEIC ion collider ring.

COMPACT CARBON ION LINAC*

P.N. Ostroumov**, A. Goel, B. Mustapha, A. Nassiri, A.S. Plastun
Argonne National Laboratory, Lemont, IL, USA

L. Faillace, S.V. Kutsaev, E.A. Savin, RadiaBeam Technologies, Santa Monica, CA, USA

Abstract

Argonne National Laboratory is developing an Advanced Compact Carbon Ion Linac (ACCIL) in collaboration with RadiaBeam Technologies. The 45-meter long linac is designed to deliver up to 10^9 carbon ions per second with variable energy from 45 MeV/u to 450 MeV/u. To optimize the linac design in this energy range both traveling wave and coupled-cell standing wave S-band structures were analysed. To achieve the required accelerating gradients our design uses accelerating structures excited with short RF pulses (~500 ns flattop). The front-end accelerating structures such as the RFQ, DTL and Coupled DTLs are designed to operate at lower frequencies to maintain high shunt impedance. In parallel with our design effort ANL's RF test facility has been upgraded and used for the testing of an S-band high-gradient structure designed and built by Radiabeam for high pulsed RF power operation. The 5-cell S-band structure demonstrated 52 MV/m acceleration field at 2 μ s 30 Hz RF pulses. A detailed physics design, including a comparison of different accelerating structures and end-to-end beam dynamics simulations of the ACCIL is presented.

INTRODUCTION

There is strong worldwide interest in carbon ion beam therapy [1, 2], but no such facility exists or under construction in the USA. A variable energy carbon beam with a maximum energy of 450 MeV/u is required for the most advanced treatment. We propose a high-gradient linear accelerator, the Advanced Compact Carbon Ion Linac (ACCIL) which includes the following main sections: a radiofrequency quadrupole (RFQ) accelerator, a drift-tube linac (DTL), coupled DTL tanks, operating at a sub-harmonic of the S-band frequency, and followed by an S-band either traveling wave or standing wave accelerating structure for the energy range from 45 MeV/u to 450 MeV/u. ACCIL is designed to accelerate the proton beam as well.

LINAC SECTIONS

In order to satisfy the requirements of compactness, reliability and efficiency we examined S-band accelerating structures and other structures operating at the sub-harmonics for the low energy section. The following criteria have defined the set of accelerating structures and their operating frequencies: a high real-estate average accelerating gradient of 20 MV/m, a reasonable heat load

(pulsed and average), less than 10^{-6} breakdowns per pulse per meter, a repetition rate of 120 Hz and a beam pulse width of 0.5 μ s.

Ion Source

The typical radiation dose for hadron therapy is delivered at the rate of $(3-10) \cdot 10^8$ carbon ions/sec and 10^{10} protons/sec [3]. This rate can be achieved at 120 Hz repetition rate, beam pulse width below 0.5 μ s, and a pulsed electric current of 13.3 μ A for $^{12}\text{C}^{5+}$ and 27 μ A for proton beam. Commercially available ECR ion sources [4] can provide the required beam intensity for both C^{5+} and protons. C^{5+} ions are preferable to avoid contamination by residual gas ions. The DC beam extracted from the ECR should be chopped into 0.5 μ s pulses. Typically, ECRs can provide carbon and proton beams with a normalized transverse emittance of 0.35 π -mm-mrad containing 90% of ions.

RFQ

To meet the alignment specifications of high frequency RFQ, we will apply high temperature furnace brazing technology [5-7]. Currently, we are considering asymmetric 4-vane structure [8] for the RFQ, which can provide a good separation of non-operational modes [9, 10]. The transverse cross-section of the RFQ is shown in Fig. 1. The RFQ accelerates the carbon $^{12}\text{C}^{5+}$ ion beam to 3 MeV/u over the length of $L = 4$ m. The operating frequency $f = 476$ MHz provides a reliable accelerating gradient, moderate field sensitivity to local random errors of resonator geometry, which scales as $(fL)^2$ [11], and sufficient beam acceptance. Right after the RFQ, the C^{5+} beam will be converted into C^{6+} by stripping with a thin carbon foil.

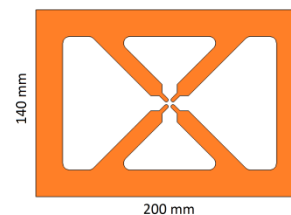


Figure 1: Transverse cross-section of the compact asymmetric 4-vane RFQ.

DTL and Coupled DTL

The effective shunt impedance per unit length of an RFQ drops as β^{-2} like in any other accelerating structure based on a TE-mode resonator. In order to provide both high efficiency and high accelerating gradient, a TM-mode is preferred in the sections following the RFQ. The most efficient TM-mode-structure in the 3 – 20 MeV/u energy range is a multi-gap DTL (also known as Alvarez

* This work was supported by the US DOE, Office of Nuclear Physics and High Energy Physics, under contract number DE-AC02-06CH11357
**Ostroumov@frib.msu.edu

ERL-RING AND RING-RING DESIGNS FOR THE eRHIC ELECTRON-ION COLLIDER *

V. Ptitsyn, Brookhaven National Laboratory, Upton, USA

Abstract

Two design options explored for eRHIC accelerator design are described: the ERL-Ring and the Ring-Ring. Both are capable to provide the luminosity level ($10^{33} \text{ cm}^{-2}\text{s}^{-1}$) required for an eRHIC Initial stage. Both options are upgradable to the Ultimate ERL-Ring design ($L \sim 10^{34} \text{ s}^{-1}\text{cm}^{-2}$). Present status of eRHIC R&D program is reported.

FROM RHIC TO ERHIC

RHIC collider at BNL has been operating from beginning of the century with heavy ion and polarized proton collisions in several experiments. The collider has been successfully fulfilling the physics goals it was built for. Experiments with heavy ion collisions led to a discovery and consequent detailed study of properties of quark-gluon perfect fluid matter, a substance existed at the very origin of the Universe. And, using collisions of polarized proton beam, the study of proton spin composition has been carried out, especially, gaining the knowledge of a gluon component of the proton spin. Besides producing remarkable nuclear physics results the RHIC collider has demonstrated consistent improvements in the machine luminosity of both heavy ion and proton collisions, literally every year. Presently, RHIC is an only place in the world with high energy polarized proton beams. It employs numerous techniques and devices throughout the injector chain and in RHIC itself to achieve high proton polarization level (up to 60%) of colliding beams at the store energy.

Present plan is to continue the experiments with heavy ion and polarized proton collision at RHIC till 2024. After that a transition to eRHIC, an electron-ion collider (EIC), can be realized. Recent US Nuclear Physics Long Range Plan [1] recommended a high-energy high-luminosity polarized EIC as the highest priority for a new NP facility construction. The transition from RHIC to eRHIC includes adding an electron accelerator to the existing RHIC ion complex. Building the EIC at BNL has a compelling advantage of using available \$2.5B RHIC ion complex. Besides the existing ion machine, eRHIC will re-use the existing infrastructure: RHIC tunnel and buildings, detector halls and cryogenic facility. eRHIC will take a full advantage of present capability of RHIC to provide polarized protons (up to 275 GeV) and heavy ions (up to Uranium).

The physics goals of the proposed electron-ion collider are well described in the EIC White paper [2], the eRHIC

Design study report [3], as well as in a EIC physics presentation made at this conference [4]. One major area or the EIC physics is related with 3D nucleon imaging and with completely resolving the nucleon spin puzzle. For these studies the high luminosity of polarized electron on polarized proton collisions is required. Other major direction of EIC exploration is related with studies of a dense gluon matter, ideally, discovering a predicted gluon saturation state, color-glass condensate. These studies are most effectively done with electron - heavy ion collisions with high center-of-mass energy (but, not necessarily requiring high luminosity).

Reaching into the gluon saturation conditions calls for highest eRHIC electron energy to be 18 GeV. In the same time the experiments require wide coverage of center-of-mass energy range, so that the electrons must be provided in the range from 5 GeV to 18 GeV. Other collider design goals are:

- Reaching $L \sim 10^{33}\text{-}10^{34} \text{ cm}^{-2}\text{s}^{-1}$ (exceeding HERA luminosity by 2 orders of magnitude).
- Providing high electron and proton polarization (>70%). Realizing complex spin pattern on the same fill.
- Satisfying full (or near full) acceptance detector, with detector elements integrated in the accelerator IR for forward particle detection.
- Minimizing the construction and operational cost of accelerator.

TWO ERHIC DESIGN OPTIONS

To achieve the accelerator design goals two design options are being evaluated, accordingly to a type of electron accelerator employed. An ERL-Ring design option uses an energy-recovery linac for electron beam acceleration. Alternative design option, Ring-Ring, considers storing high current electron beam in a storage ring.

The luminosity of ERL-Ring design is not limited by the electron beam-beam limit. This design option provides a straightforward way to high luminosity by using a small beam size at the interaction point. Application of a hadron cooling provides a simple possibility to increase the luminosity even further. This design option is also more efficient in terms of construction and operation cost. On the other side it calls for some accelerator technology beyond the present state-of-the-art, especially demanding high current polarized electron source.

The Ring-Ring design has less technological challenges than the ERL-Ring one. High luminosity is achieved by utilizing high circulating beam currents. Large synchrotron radiation power, produced by high electron current,

* Work supported by the US Department of Energy under contract number DE-SC0012704

DESIGN OF MUON COLLIDER LATTICES*

Y. Alexahin[†], Fermi National Accelerator Laboratory, Batavia, Illinois, USA

Abstract

A Muon Collider (MC) promises unique opportunities both as an energy frontier machine and as a factory for detailed study of the Higgs boson and other particles (see e.g. ref. [1]). However, in order to achieve a competitive level of luminosity a number of demanding requirements to the collider optics should be satisfied arising from short muon lifetime and relatively large values of the transverse emittance and momentum spread in muon beams that can realistically be achieved with ionization cooling. Basic solutions which make possible to achieve these goals with realistic magnet parameters are presented.

INTRODUCTION

There are a number of requirements that are either specific or more challenging in the case of a muon collider:

- Low beta-function at IP: β^* values of a few millimeters are considered for muon colliders in the c.o.m. energy range 3-6 TeV.
- Small circumference C to increase the number of turns (and therefore interactions) the muons make during their lifetime.
- High number of muons per bunch: $N_\mu \sim 2 \cdot 10^{12}$ and higher is envisaged.
- Protection of magnets from heat deposition and detectors from backgrounds produced by secondary particles.

Other requirements are specific to either high energy MC or the Higgs factory and will be analysed in the subsequent sections.

Though short muon lifetime, ~ 2000 turns, creates a number of problems, but there is a positive side of it: such short time is not enough for high-order resonances to manifest themselves. Other sources of diffusion like IBS or residual gas are also too weak to produce a halo, so if the muon beams were pre-collimated e.g. at 3σ before injection into the collider ring their distribution is likely to stay bounded by a close value. This would relax the requirements on the dynamic aperture and on the efficiency of the halo removal from the ring.

LATTICES FOR HIGH-ENERGY MC

In order not to lose much in luminosity due to the hour-glass effect (see e.g. ref. [2]) the bunch length should be small enough: $\sigma_z \leq \beta^*$. With longitudinal emittance expected from the final cooling channel this will render the momentum spread $\sigma_p/p \sim 0.001$ which is an order of magnitude higher than in hadron colliders like Tevatron or LHC. Therefore a high energy MC must have a large momentum acceptance and - to obtain small σ_z with a

reasonable RF voltage - low momentum compaction factor $|\alpha_c| \sim 10^{-5}$.

Also, for beam energies $E > 2$ TeV there is a peculiar requirement of absence of straights longer than ~ 0.5 m in order not to create "hot spots" of neutrino radiation [3]. As a consequence quadrupoles must have a dipole component to spread out the decay neutrinos. This creates difficulties with β^* -tuning sections which must allow for β^* variation in a wide range without breaking the dispersion closure.

In the following subsections we consider different parts of the ring.

Interaction Region (IR)

The dipole component in the IR quadrupoles may play a positive role sweeping away from the detector the charged secondary particles created by decays in incoming muon beam. To maximize this positive effect the strongest quadrupole in the Final Focusing (FF) multiplet - which is usually the second one from the Interaction Point (IP) - should be defocusing.

Another important requirement to the FF multiplet is that the last quadrupole was also defocusing in order to reduce the "dispersion invariant" generated by the following strong dipole used in the chromaticity correction scheme discussed later.

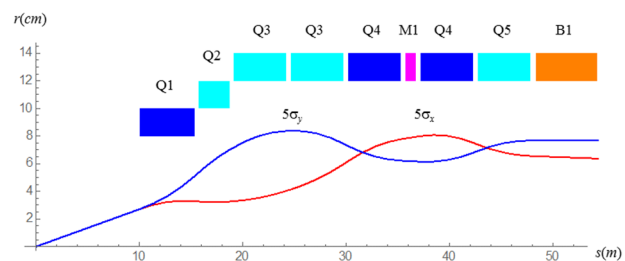


Figure 1: 6 TeV IR magnet apertures and 5σ beam envelopes for $\beta^* = 3$ mm and normalized emittance $\varepsilon_{\perp N} = 25$ (π) mm-mrad. Defocusing magnets are shown in cyan.

Table 1: 6 TeV IR Magnet Parameters

Parameter	Q1	Q2	Q3	Q4	Q5
ID (mm)	160	200	240	240	240
G (T/m)	200	-125	-100	103	-78
B_{dipole} (T)	0	3.5	4.0	3.0	6.0
L (m)	5.3	3.0	5.1	5.1	5.1

To satisfy both requirements simultaneously the multiplet should be either a doublet or a quadruplet. The first option was used in the $E_{\text{c.o.m.}} = 1.5$ TeV design [4]. For higher energies it is advantageous to use the second option which allows for much smaller β^* .

* Work supported by Fermi Research Alliance, LLC under Contract DE-AC02-07CH11359 with the U.S. DOE

[†] alexahin@fnal.gov

DESIGN OF THE ROOM-TEMPERATURE FRONT-END FOR A MULTI-ION LINAC INJECTOR*

A. S. Plastun[†], Z. A. Conway, B. Mustapha, P. N. Ostroumov¹,
Argonne National Laboratory, Lemont, USA

¹ also at FRIB, Michigan State University, East Lansing, MI, USA

Abstract

A pulsed multi-ion injector linac is being developed by ANL for Jefferson Laboratory's Electron-Ion Collider (JLEIC). The linac is designed to deliver both polarized and non-polarized ion beams to the booster synchrotron at energies ranging from 135 MeV for hydrogen to 43 MeV/u for lead ions. The linac is composed of a 5 MeV/u room temperature section and a superconducting section with variable velocity profile for different ion species. This paper presents the results of the RF design of the main components and the beam dynamics simulations of the linac front-end with the goal of achieving design specifications cost-effectively.

INTRODUCTION

A pulsed multi-ion linac with a normal conducting front-end up to 5 MeV/u and a superconducting section for higher energies as an injector for the JLab Electron-Ion Collider (JLEIC) was discussed in ref. [1, 2]. Further modifications and improvements of the front-end design are described below.

FRONT-END

A block-diagram of the injector linac is shown in Fig. 1. The JLEIC ion injector linac will consist of both heavy and light ion sources including polarized H^+ , $^2D^+$, $^3He^{2+}$, $^6Li^{3+}$ ion sources. The emittance of the polarized beams is usually larger than the emittance of heavy ion beams. For this reason, we propose to use two separate Radio-Frequency Quadrupole (RFQ) sections. The room temperature front-end consists of 2 RFQs, a Medium Energy Beam Transport (MEBT) system to accommodate and match beams from 2 separate RFQs and three tanks of 100 MHz drift tube linac (DTL) as shown in Fig. 1. The FODO lattice of the DTL provides adequate focusing and the required transverse acceptance for both heavy ions and polarized light ion beams. To minimize the overall linac cost, the transition energy between normal and superconducting sections is selected to be 5 MeV/u.

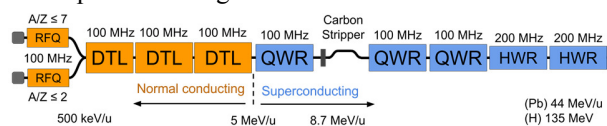


Figure 1: A schematic layout of the JLEIC ion linac.

* This work was supported by the U.S. Department of Energy, Office of Nuclear Physics, under Contract DE-AC02-06CH11357. This research used resources of ANL's ATLAS facility, which is a DOE Office of Science User Facility.

[†] email address: asplastun88@gmail.com, on leave from ITEP, Moscow

Ion Sources

Several types of ion sources are being considered: an Atomic Beam Polarized Ion Source (ABPIS), an Optically-Pumped Polarized Ion Source (OPPIS), an Electron Beam Ion Source (EBIS) and an Electron Cyclotron Resonance ion source (ECR). Table 1 provides design parameters of the beams based on the recent data [3] and the JLEIC requirements.

Table 1: Design Parameters of the Beams

Ions	Source	Current, mA	Polarization	Emittance, $\pi \cdot \text{mm} \cdot \text{mrad}$
$^1H^+$	ABPIS OPPIS	2	> 90%	1.0
$^2D^+$	ABPIS OPPIS	2	> 90%	2.0
$^3He^{2+}$	EBIS	1	70%	< 1
$^6Li^{3+}$	ABPIS	0.1	70%	< 1
$^{208}Pb^{30+}$	ECR	0.5	0	0.5

LEBT

Low Energy Beam Transport (LEBT) systems for both polarized light ion and non-polarized heavy ion beams have been designed with TRACE3D [4]. The light ion LEBT (see Fig. 2) is based on the BNL OPPIS LEBT design [5]. Two dipole magnets of opposite bend directions are used to keep the spin orientation of polarized ions. Detailed spin dynamics studies in the LEBT will be performed later.

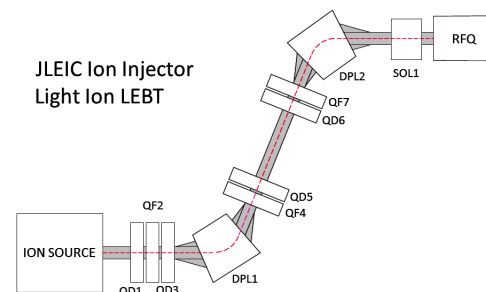


Figure 2: Light ion LEBT.

The heavy ion LEBT, presented in Fig. 3, is based on the CERN Lead Linac3 LEBT design [6]. Here two dipoles act as a mass - spectrometer separating neighbouring charge states.

TOKAMAK ACCELERATOR

Ge Li, Institute of Plasma Physics, Chinese Academy of Sciences, Anhui 230031, China

Abstract

Tokamak accelerator within plasma is analyzed to be implemented in existing machines for speeding the development of fusion energy by seeding fast particles from external high current accelerators — the so-called two-component reactor approach [J. M. Dawson, H. P. Furth, and F. H. Tenney, *Phys. Rev. Lett.* 26, 1156 (1971)]. All plasma particles are heated at the same time by inductively-coupled power transfer (IPT) within an energy confinement time. This could facilitate the attainment of ignition in tokamak by forming high-gain high-field (HGHF) fusion plasma. Tokamak as an accelerator could decrease the circulating power of fusion power plant and HVDC voltage of the external accelerators by simply inserting in-vacuum vertical field coils (IVC) within its vacuum vessel, as is suggested on Experimental Advanced Superconducting Tokamak (EAST) for designing efficiency China Fusion Engineering Test Reactor (CFETR).

INTRODUCTION

Up to 1h long-pulse accelerators with 40A beam current at 1MV are designed for externally heating ITER plasma — safety concern occurs due to its 1MV extra-high-voltage design[1]. The compressed plasma by Magnetic Compression (MC) is thus suggested as High-Gain High-Field (HGHF) plasma for efficiency tokamak heating [2]. In work here, ion accelerator within the plasma is further analyzed as the second accelerating stage for designing China Fusion Engineering Test Reactor (CFETR) with much low external accelerating voltage and circulating power. The safety problem could thus be mitigated by the two-stage accelerating scheme.

Fast particles are further accelerated by Magnetic Compression (MC) in tokamak major radius [3], as is one step of HGHF plasma. Physical process of HGHF is formulated for studying the efficiency plasma on Experimental Advanced Superconducting Tokamak (EAST). EAST can simulate the HGHF fusion plasma of CFETR for high efficiency tokamak with low circulating power requirements by upgrading EAST with MC technology.

MC ANALYSIS TO TOKAMAK ACCELERATOR

Transformer model is not only used for designing tokamak, but also used for analyzing its discharged plasma current as its second winding in real time condition. Recent study [4] suggest the ratio of its bootstrap current, i.e. the fraction of self-generated current in plasma current could reach over 85% by external heating and current drive (H&CD) — it is the nonlinear and non-inductive part of the plasma current.

DC mode of operation is thus arrived at the tokamak transformer when the fraction is driven to 100% by the inductive and non-inductive effects, i.e. external H&CD for high plasma pressure where no inductive fraction exist and plasma current is free of inductive limitation with zero-loop-voltage and VS consumptions. Limited by plasma boundary safety factor q , the flat-top amplitude of plasma current and plasma normalized pressure β determine the output power of the tokamak fusion machine where MC could save lots of expensive external H&CD power by simultaneously enhance plasma temperature, density and confinement time, as suggested for EAST in [2]. The safety factor q is the number of toroidal transits of a field line for one poloidal transit [5]. For CFETR, boundary safety factor q is designed to be ≥ 3 .

Formulas for Compressed Plasma

The equivalent circuit of compressed plasma is an inductor- series-connected with a resistor, similar to a lossless superconductor circuit while neglecting its resistance. Because the flux in such a circuit is conserved or constant [2-3], the equations specifying the conservation of toroidal and poloidal flux as well as plasma entropy are derived as

$$a^2 B_t = \text{const.} \quad (1)$$

where B_t is the toroidal field (TF) and a is the horizontal minor radius of the plasma ellipse model.

The safety factor is

$$q = \text{const.} \quad (2)$$

As the temperature and density constraints of the collisional plasma compression,

$$T n_e^{-2/3} = \text{const.} \quad (3)$$

$$L_p I_p \cong \text{const. if } R_p = 0 \quad (4)$$

where L_p and R_p are the plasma inductance and resistance in an electric circuit with plasma current I_p . $L_p = L_i + L_e$. L_i and L_e are respectively the internal and external inductances of the current bordering at the plasma boundary of its current flux [2].

After compression, other plasma variables scaling with the major (R) or minor (a) radius are derived as follows [2]:

Poloidal field (PF)

$$B_p \propto a^{-1} R^{-1} \propto C_a C_R \quad (5)$$

Where C_a and C_R are, respectively, the compression ratios of the plasma in the minor radius and major radius by external MC fields.

MAX IV AND SOLARIS LINAC MAGNETS PRODUCTION SERIES MEASUREMENT RESULTS

M. Johansson*, MAX IV Laboratory, Lund, Sweden
R. Nietubyc, NCBJ, Otwock, Poland

Abstract

The linacs of the MAX IV and Solaris synchrotron radiation light sources, currently in operation in Lund, Sweden, and Krakow, Poland, use various conventional magnet designs. The production series of totally more than 100 magnets of more than 10 types or variants, which were all outsourced to industry, with combined orders for the types that are common to both MAX IV and Solaris, were completed in 2013 with mechanical and magnetic quality assurance conforming to specifications. This article presents an overview of the different magnet types installed in these machines, and mechanical and magnetic measurement results of the full production series.

INTRODUCTION

The MAX IV Laboratory, located in Lund, Sweden, is a synchrotron radiation facility, consisting of two storage rings, 3 GeV and 1.5 GeV, and a full energy injector linac. A principle sketch of the linac is shown in Fig. 1. The choice of a linac to inject the storage rings also provides short pulse X-rays at the end the linac, and allows an upgrade path to an FEL. [1]

Whereas the MAX IV storage ring magnets are designed as “magnet blocks”, with many consecutive magnet elements machined out of a common iron block [2], all the linac and transfer line magnets are conventional designs. The different types are listed in Table 1 and some example photos are shown in Figures 3-5.

The Solaris National Synchrotron Radiation Centre, located in Krakow, Poland, consists of a 1.5 GeV storage ring identical to the MAX IV 1.5 GeV ring, and a 600 MeV injector linac using the same components as MAX IV [3]. A schematic of the facility is shown in Fig. 2.

SPECIFICATION AND PROCUREMENT

All magnets were purchased as fully assembled and tested units. Depending on whether they were new designs for MAX IV [4,5], or old re-used designs, and what

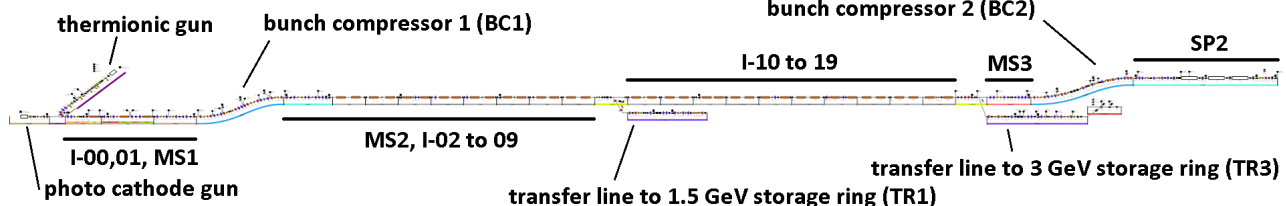


Figure 1: MAX IV linac schematic used in the control system “linac synoptic” application (illustration courtesy of J. Forsberg, MAX IV), with section names indicated. The schematic is not entirely to scale but it contains all essential features. Each “I-xx” section contains two 5 m S-band accelerator structures (except I-00 with one), giving a total of 39 S-band structures in the machine. The nominal beam path is 361.5 m from end of I-00 to entrance of SP2 beam dump.

* martin.johansson@maxiv.lu.se

material was provided from MAX-lab, the procurements can be categorized as follows,

- New magnetic design and full set of manufacturing drawings from MAX-lab.
- New magnetic design from MAX-lab. Manufacturing drawings made by supplier based on instructions in the technical specification from MAX-lab.
- Existing MAX-lab design, including drawings.
- Existing design from supplier.

Common for all cases was that the supplier was responsible for mechanical tolerances and for performing field measurements according to MAX-lab instructions, and MAX-lab was responsible for field measurement results.

The contracts were awarded to a total of five different suppliers, as listed in Table 2. All Solaris contracts were awarded to the same suppliers as chosen by MAX IV, so that each type constituted a common production series.

PRODUCTION SERIES RESULTS

Following the technical specifications/instructions that were given to the suppliers, all mechanical tolerances < 0.1 mm were verified for every yoke part of the whole series, for each magnet order, typically by 3D coordinate measurement machine. We have not made a statistical treatment of the mechanical data like for the storage ring magnets [6,7], but generally for each magnet type the tolerances listed in Table 1 were met.

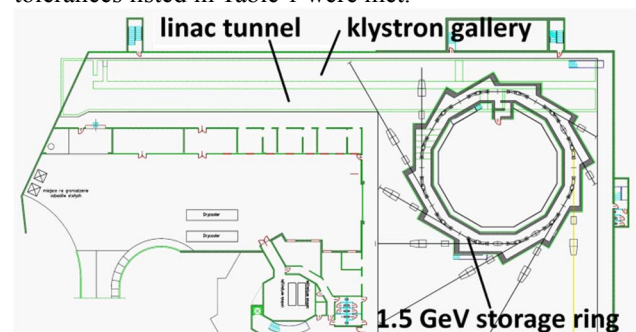


Figure 2: Solaris facility layout. The linac consists of six accelerator structures with a thermionic gun as source.

OFF-ORBIT RAY TRACING ANALYSIS FOR THE APS-UPGRADE STORAGE RING VACUUM SYSTEM

J. Carter, K. Harkay, B. Stillwell, Argonne National Laboratory, Lemont, IL, USA

Abstract

A MatLab program has been created to investigate off-orbit ray tracing possibilities for the APS-Upgrade storage ring vacuum system design. The goals for the program include calculating worst case thermal loading conditions and finding minimum shielding heights for photon absorbers. The program computes the deviation possibilities of synchrotron radiation rays emitted along bending magnet paths using discretized local phase space ellipses. The sizes of the ellipses are computed based on multi-bend achromat (MBA) lattice parameters and the limiting aperture size within the future storage ring vacuum system.

For absorber height calculations, rays are projected from each point in the discretized ellipse to the locations of downstream absorbers. The absorber heights are minimized while protecting downstream components from all possible rays. For heat loads, rays are projected until they hit a vacuum chamber wall. The area and linear power densities are calculated based on a ray's distance travelled and striking incidence angle. A set of worst case local heat loads is collected revealing a maximum condition that each vacuum component must be designed to withstand.

MOTIVATION

The goal of performing off-orbit ray tracing calculations is to better understand missteering possibilities and their consequences for the APS-U vacuum system design. It is straight forward to construct the paths of perfectly steered synchrotron rays using a 2D CAD application and this provides an initial idea of both distributed heat loads and shielding requirements for critical vacuum system components. Introducing local orbit errors [1] increases the ray path possibilities which leads to higher local heat loads and requires more conservative shielding.

Spatial and angular deviation possibilities from an ideal beam path are dictated by local phase space ellipses and present a continuum of ray path possibilities. A worst case ray path within the vacuum system is not necessarily found by choosing extreme points on the local ellipses therefore 2D CAD is not an ideal tool for investigating missteering due to the large quantity of ray possibilities which need to be constructed. More ideal would be a numerical method which discretizes each local ellipse and tests the travel of all ray possibilities within a model of the vacuum system. The approximations of the worst rays should converge towards a unique solution with increased mesh density.

METHODS

Off-orbit ray tracing possibilities can be calculated from local phase space ellipses in both the horizontal (x, x') and

vertical (y, y') phase spaces. The local ellipses are calculated for either phase space based on the Courant-Snyder parameters using equations (1) and (2) where A_x is calculated based on the half size of the limiting aperture in the storage ring and the beta function value at the limiting aperture's location. Figure 1 shows a schematic of a phase space ellipse and a corresponding mesh of ray deviation possibilities.

$$x' = -2\alpha x \pm \frac{\sqrt{(2\alpha x)^2 - 4\beta(\gamma x^2 - A_x)}}{2\beta} \quad (1)$$

$$A_x = \frac{a^2}{\beta_u} \quad (2)$$

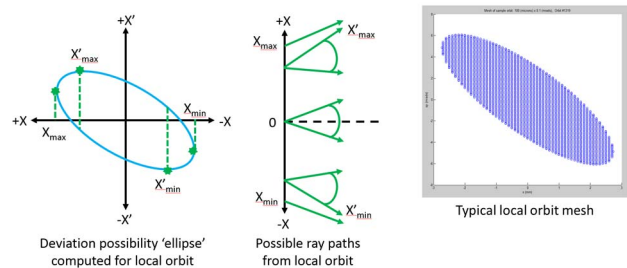


Figure 1: Local orbit ellipse concept and ray possibilities when meshed (top) and diagram of basic ray tracing schematic (bottom)

A MatLab program has been written to discretize both the horizontal and vertical local phase space ellipses along APS-U bending magnet paths and to trace out every ray in the mesh. The quantity of ellipses and their respective sizes are found using an input file containing both the global locations and Courant-Snyder parameters along finely spaced points of the APS-U magnet lattice. The rays are traced until they intersect geometric elements representing either vacuum system walls or photon absorbers.

Figure 2 shows maximum horizontal deviations from the (x, x') ellipses calculated along the APS-U bending magnet paths. The MatLab program computes the ray paths for all spatial and angular combinations within this envelope as determined by the ellipse mesh. The photon absorbers within APS-U's 22 mm I.D. multiplet vacuum chambers create an 18 mm limiting aperture for the vacuum system. The spatial deviations fit well within the typical 22 mm I.D. beam aperture found along most of the APS-U vacuum system.

STREAK CAMERA MEASUREMENTS OF THE APS PC GUN DRIVE LASER*

J. C. Dooling[†]

Advanced Photon Source, Argonne National Laboratory, Argonne, IL, USA

A. H. Lumpkin

Fermi National Accelerator Laboratory, Batavia, IL, USA

Abstract

We report recent pulse-duration measurements of the APS PC Gun drive laser at both second harmonic and fourth harmonic wavelengths. The drive laser is a Nd:Glass-based chirped pulsed amplifier (CPA) operating at an IR wavelength of 1053 nm, twice frequency-doubled to obtain UV output for the gun. A Hamamatsu C5680 streak camera and an M5675 synchroscan unit are used for these measurements; the synchroscan unit is tuned to 119 MHz, the 24th subharmonic of the linac s-band operating frequency. Calibration is accomplished both electronically and optically. Electronic calibration utilizes a programmable delay line in the 119 MHz rf path. The optical delay uses an etalon with known spacing between reflecting surfaces and is coated for the visible, SH wavelength. IR pulse duration is monitored with an autocorrelator. Fitting the streak camera image projected profiles with Gaussians, UV rms pulse durations are found to vary from 2.1 ps to 3.5 ps as the IR varies from 2.2 ps to 5.2 ps.

INTRODUCTION

To optimize beam quality, minimize emittance, and compare with simulations, we measured the pulse duration of the APS photocathode (PC) gun drive laser. Drive laser pulse duration measurements have shown conflicting results. At SLAC, the UV harmonic component was found to be greater than that of the fundamental or visible harmonics [1]; whereas, at the FNAL Laser Lab, recent data have shown the pulse duration of the UV to be comparable than that of the green [2] with a multi-pass amplifier. The non-linear dependence on fundamental wavelength power density should cause the pulse duration of the second harmonic beam to decrease [3]; however, this effect may be offset by group velocity mismatch. The last streak camera measurement of the APS drive laser was made approximately 15 years ago [4]. Before the streak camera could provide pulse duration measurements, calibration of the unit was required. Calibration data was obtained employing two methods: 1) a high-precision Colby delay generator and 2) at the visible wavelength, using an etalon cavity.

EXPERIMENTAL ARRANGEMENT

The streak camera with attenuation and focusing optics was installed in the APS Injector Test Stand (ITS); a plan

* Work supported by the U.S. Department of Energy Office of Science, under contract number DE-AC02-06CH11357.

[†] jcdooling@anl.gov

view schematic is presented in Figure 1. The dichroic filter is 99.5% reflecting at 263 nm. Roughly 5.5 orders of attenuation were required to safely and accurately measure the UV component at nominal full energy, $E_{uv} = 100 \mu\text{J}$; this energy is achieved at an IR amplifier pump current setting, $I_{set} = 170 \text{ A}$. The dichroic filter provided an optical density (OD) of 2.5 and protected the downstream optics for fourth harmonic wavelength measurements. For second harmonic measurements, the mirrors in the transport line between the Laser Room and the ITS provided an equivalent level of attenuation. In addition, the input slit to the streak camera

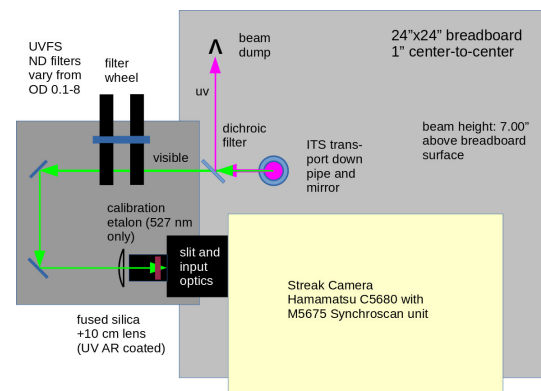


Figure 1: Streak Camera schematic.

was set at $5 \mu\text{m}$ to further limit the power density on the photocathode.

Laser

The APS PC Gun drive laser has been upgraded since first being described in Ref. [5]. The most significant modification to the CPA system was the replacement of the two flashlamp-driven amplifiers with a pair of laser diode-driven heads. The laser diodes operating at 808 nm pump electrons directly to the closely placed $^2\text{H}_{9/2}$ and $^4\text{F}_{5/2}$ excited states from which they rapidly decay to the nearby $^4\text{F}_{3/2}$ upper level of the Nd^{3+} atoms [6]. Efficient pumping results in substantially less energy deposition and reduced thermal effects in the laser rods; however, thermal lensing effects are still noticeable as rep rates or pump levels are varied. Harmonic light is generated in a pair of 1-mm-thick β -barium borate (BBO) crystals. Second harmonic (SH), visible (527 nm) green light is measured after the second doubling crystal; therefore, its temporal profile is likely to be slightly broadened.

DESIGN OF THE HGVPV UNDULATOR VACUUM CHAMBER FOR LCLS-II*

J. Lerch[†], J. Carter, P. Den Hartog, G. Wiemerslage
Argonne National Laboratory, Advanced Photon Source, Lemont, IL USA

Abstract

A vacuum chamber has been designed and prototyped for the new Horizontal Gap Vertically Polarization Undulator (HGVPV) as part of the LCLS-II upgrade project. Numerous functional requirements for the HGVPV assembly constrained the vacuum chamber design. These constraints included spatial restrictions to achieve small magnet gaps, narrow temperature and alignment specifications, and minimization of wall erosion and pressure drop within the cooling channels. This led to the design of a 3.5-meter length, thin walled, extruded aluminium chamber with interior water cooling. FEA stress analysis was performed to ensure the chamber will not fail under vacuum and water pressure. A cooling scheme was optimized to ensure water flow is sufficient to maintain temperature without the risk of erosion and to minimize pressure drop across the chamber.

INTRODUCTION

SLAC contracted the APS to design and manufacture a 3.5-meter undulator vacuum chamber (UVC) for use in an HGVPV as part of the LCLS-II upgrade project. The design process involved solving complex challenges that are becoming commonplace in next generation accelerator projects. The following is an overview of the UVC design process with an emphasis on the structural and thermal design challenges encountered.

STRUCTURAL DESIGN

Unlike most planar permanent magnet undulators, the HGVPV magnetic gap closes horizontally. This requires the UVC and its alignment fixture to be mounted directly to the HGVPV strongback in a vertical orientation (See Figure 1).

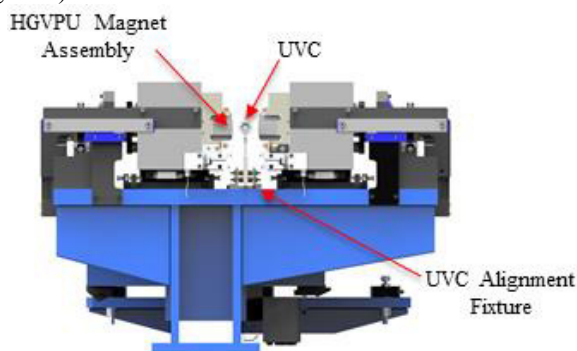


Figure 1: HGVPV and UVC final assembly.

* Sponsor: Argonne National Laboratory and Stanford Linear Accelerator Center

[†] Author Email: jlerch@aps.anl.gov

The chamber called for a straightness of $\pm 100 \mu\text{m}$ along its length and to have a vertical position adjustment precision of $< 50 \mu\text{m}$. This was accomplished by designing an extruded aluminium fixture that allowed the chamber straightness to be adjusted at 65 places along its 3.3-meter length. Tolerance control was used to maintain the vertical position precision. Figure 2 shows the final design of the alignment fixture.



Figure 2: Alignment fixture end-isometric view.

The HGVPV closed gap is 7 mm during operation. SLAC defined the vacuum aperture geometry as a 5x11 mm racetrack. This called for the wall on either side of the aperture to have a thickness of 0.5 mm (See Figure 3).

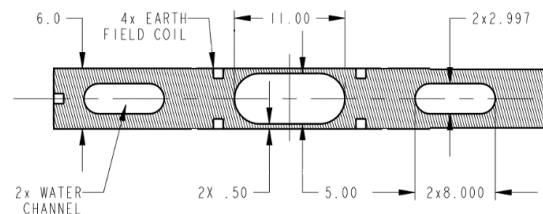


Figure 3: UVC nose cross section (dimensions are in millimetres).

To ensure that aperture wall deflection is minimized, 6063-T5 aluminium was used for the chamber material. This choice was based on previous design experience and verified using FEA (see Figure 4).

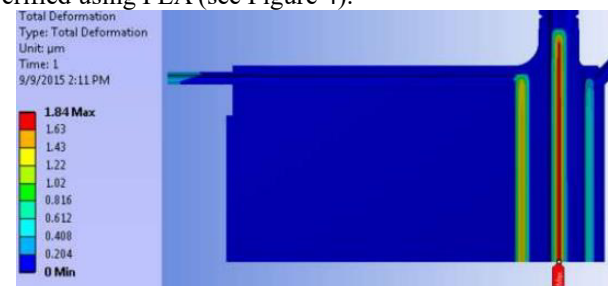


Figure 4: FEA deformation study. Max deformation found along aperture thin wall.

RESEARCH AND DEVELOPMENT ON THE STORAGE RING VACUUM SYSTEM FOR THE APS UPGRADE PROJECT*

B. Stillwell, B. Brajuskovic, J. Carter, H. Cease, R. Lill, G. Navrotski, J. Noonan, K. Suthar, D. Walters, G. Wiemerslage, J. Zientek, Argonne National Laboratory, Lemont, USA
M. Sangroula, Illinois Institute of Technology, Chicago, USA

Abstract

A number of research and development activities are underway at Argonne National Laboratory to build confidence in the designs for the storage ring vacuum system required for the Advanced Photon Source Upgrade project (APS-U) [1]. The predominant technical risks are: excessive residual gas pressures during operation, insufficient beam position monitor stability, excessive beam impedance, excessive heating by induced electrical surface currents, and insufficient operational reliability. Present efforts to mitigate these risks include: building and evaluating mock-up assemblies, performing mechanical testing of chamber weld joints, developing computational tools, investigating design alternatives, and performing electrical bench measurements. Status of these activities and some of what has been learned to date will be shared.

OVERVIEW OF THE SYSTEM DESIGN

A typical sector arc of the envisioned APS-U storage ring vacuum system is described in Figure 1. Each arc will be built of nine separable modules of four basic types which will be preassembled for rapid installation in the APS storage ring tunnel. Generally, the chambers are required to have a circular cross-section with 22 mm inner diameter and 1 mm wall thickness to fit inside of magnets. However, consideration of cost, performance, and required maintenance has led to a design by which the details of the chamber construction varies according to local spatial constraints and synchrotron radiation loading. The central "FODO" section, where intercepted bending magnet radiation is the greatest, will use tubular copper chambers with non-evaporable getter (NEG) coating and a single water channel on the outboard side. Chambers in the longitudinal gradient dipole, or "L-bend," sections will be built from bent aluminum extrusions which provide three water cooling channels and an antechamber to house NEG strips and photon absorbers. Chambers in the doublet and multiplet sections, where intercepted bending magnet radiation is relatively low, will be built from simple tubular aluminum extrusions with a single water channel. Gauges, pumps,

and valves for pump out and venting will be accommodated using crosses at five locations per arc. In addition, the system includes four RF-shielded gate valves and fourteen RF beam position monitor (BPM) assemblies which use a fixed feedthrough mounting block nested inside a pair of RF-shielded bellows.

In addition to a demanding set of performance criteria, there are a few aspects of the design that are somewhat unconventional and therefore warrant careful study. First, the design forgoes distributed pumping in some sections, exacerbating the challenge of maintaining sufficiently low pressures with such small chamber apertures. Second, while the approach to mechanical stability not unprecedented [2], it is atypical. Rather than attempting to control chamber temperatures so as to make motion of critically-aligned components like BPMs negligible, the design calls for each BPM to be mechanically decoupled from chambers using bellows. Third, because the vacuum system must be separable between modules for rapid installation and also to allow removal of BPMs without disassembly of magnets, a relatively large number of flange joints is required. To give confidence that the incidence of leaks will be sufficiently low, testing is needed to validate metallic flange joint designs and joining techniques, particularly those for dissimilar metals. Finally, the relatively large number of BPMs, bellows assemblies, and photon absorbers required to protect them requires a high degree of confidence in electrical impedance predictions for those components.

MOCK-UPS

Building and testing mock-up assemblies is helping to address many of the concerns described above. Two sets of mock-up activities are underway. The first involves fabricating, assembling, and studying a full sector arc of prototyped vacuum components. The second involves assembling integrated prototypes of vacuum, magnet, and support components for each of the four sector module types.

* Work supported by U.S. Department of Energy, Office of Science, under Contract No. DE-AC02-06CH11357.

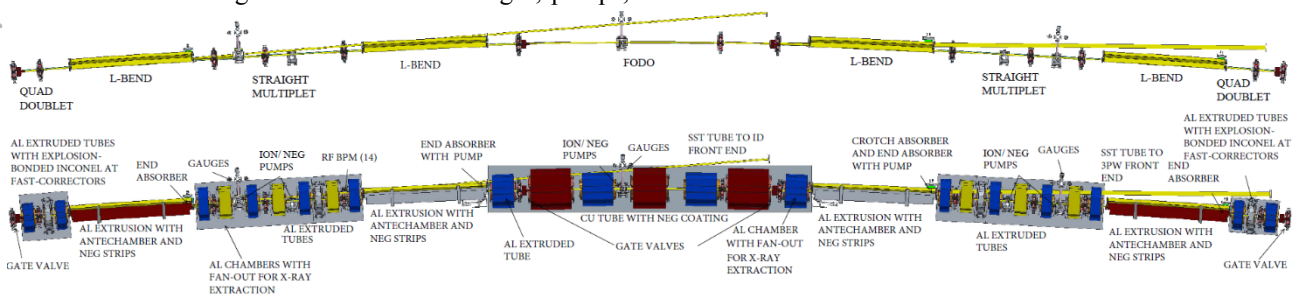


Figure 1: Layout of typical sector arc with and without magnets.

A HIGH BANDWIDTH BIPOLAR POWER SUPPLY FOR THE FAST CORRECTORS IN THE APS UPGRADE*

Ju Wang and Gary Sprau
ANL, Argonne, IL 60439, USA

Abstract

The APS Upgrade of a multi-bend achromat (MBA) storage ring requires fast bipolar power supplies for the fast correction magnets. The key requirement of the power supply includes a small-signal bandwidth of 10 kHz for the output current. This requirement presents a challenge to the design because of the high inductance of the magnet load and a low input DC voltage (40V). A prototype DC/DC power supply using a MOSFET H-bridge circuit with a 500kHz PWM control has been developed and tested successfully through the R&D program. The prototype achieved a 10-kHz bandwidth with less than 3-dB attenuation for a signal 0.5% of the maximum operating current of 15 amperes. This paper presents the designs of the power and control circuits, the component layout, and the test results.*

L_{f1}, L_{f2} : 10 μ H, C_f : 0.05 μ F, R_d : 20 Ω , C_d : 0.2 μ H
 LEM : LA 25-NP, 1000:1 current transfer ratio

The size of the input filter capacitor bank is based on the available space. This is to reduce ripple voltage and voltage fluctuations from the unregulated DC distribution that will be used in the final installation. MOSFET IRFB4620 is chosen as the switch for its low on-resistance of 11 m Ω . The output filter is a second order and damped filter. With the chosen parameters, the cut-off frequency of the filter is 160 kHz, which effectively removes the fast voltage spikes in the output without causing excessive delays and hence without affecting the speed of the power supply. A hall-effect current sensor, LEM LA 25-NP, is used to measure the current and provide the feedback signal for the current regulation.



LA 25-NP

INTRODUCTION

At IPAC2015, we reported a switching-mode bipolar power supply to be used to achieve the required high bandwidth performance [1]. Since then, we have completed the schematic designs, manufactured the PCBs (printed-circuit board), and constructed a prototype power supply. The test showed that the 10-kHz bandwidth requirement had been achieved with a load of the similar resistance and inductance to the expected magnet.

POWER CIRCUIT

The circuit, shown in Figure 1, for the fast corrector power supply is a typical four-quadrant buck converter. The circuit consists of three sections – an input filter, L_1 and C_1 ; a standard H-bridge with four MOSFET switches, $Q_1 - Q_4$, and an output filter, L_{f1} , L_{f2} , C_f , C_d , and R_d .

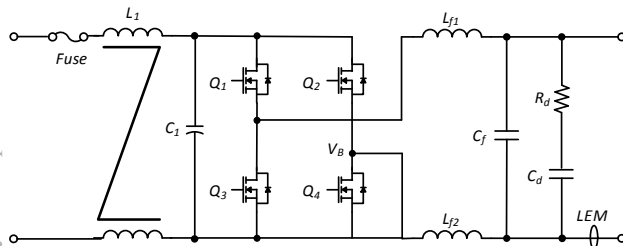


Figure 1: Power circuit.

The parameters of the components in the circuit are:

L_1 : common mode, 0.5mH, C_1 : 8000 μ F
 $Q_1 - Q_4$: IRFB4610, 100V, 73A, 11m Ω



SCHEMATIC DESIGNS

Triangular Waveform Generator

To generate the triangular waveforms for the PWM control, an 8-MHz oscillator, LTC6930CMS8-8.00 from Linear Technology, is configured to produce a 250-kHz clock signal. The clock signal then drives a MOSFET to charge and discharge an integrator through an AC coupling circuit to produce a symmetrical triangular waveform.

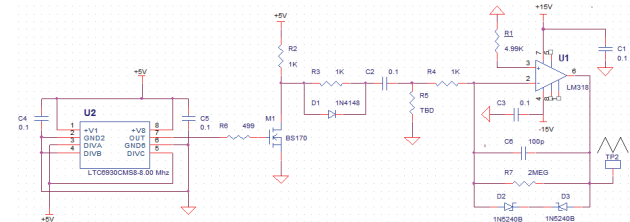


Figure 2: Triangular waveform generator.

In Figure 2, the value of R_5 can be used to adjust the amplitude of the triangular waveform. When U_2 is configured for 250kHz, R_5 is not needed to produce a 10V amplitude.

Current Sensing and Conditioning Circuit

Figure 3 shows the current sensing and conditioning circuit. The signal from the LEM sensor drives a 200 Ω burden resistor to produce a 3V signal at the full scale of 15A. This signal is filtered to reduce the unwanted ripple components and further scaled to an appropriate level before compared with the reference signal. The first stage of the circuit provides a precision gain of two with an

*This work is supported by the U.S. Department of Energy, Basic Energy Sciences, Office of Science, under contract # DE-AC02-06CH11357.

POST IRRADIATION EXAMINATION RESULTS OF THE NT-02 GRAPHITE FINS NUMI TARGET*

K. Ammigan[†], P. Hurh, V. Sidorov, R. Zwaska, FNAL, Batavia, IL 60510, USA
D. M. Asner, A. M. Casella, D. J. Edwards, A. L. Schemer-Kohn,
D. J. Senior, PNNL, Richland, WA 99352, USA

Abstract

The NT-02 neutrino target in the NuMI beamline at Fermilab is a 95 cm long target made up of segmented graphite fins. It is the longest running NuMI target, which operated with a 120 GeV proton beam with maximum power of 340 kW, and saw an integrated total proton on target of 6.1×10^{20} . Over the last half of its life, gradual degradation of neutrino yield was observed until the target was replaced. The probable causes for the target performance degradation are attributed to radiation damage, possibly including cracking caused by reduction in thermal shock resistance, as well as potential localized oxidation in the heated region of the target. Understanding the long-term structural response of target materials exposed to proton irradiation is critical as future proton accelerator sources are becoming increasingly more powerful. As a result, an autopsy of the target was carried out to facilitate post-irradiation examination of selected graphite fins. Advanced microstructural imaging and surface elemental analysis techniques were used to characterize the condition of the fins in an effort to identify degradation mechanisms, and the relevant findings are presented in this paper.

INTRODUCTION

The NT-02 neutrino target in the NuMI beamline at Fermilab produced neutrinos for the MINOS and MINERVA high energy physics experiments. The NT-02 target, 95 cm long and composed of segmented graphite fins as shown in Fig. 1, was bombarded with 340 kW beam of 120 GeV protons. During operation from 2006 to 2009 and again in 2011, it was subjected to an integrated total of 6.1×10^{20} protons on target with a Gaussian beam sigma of 1.1 mm and peak fluence of 2.5×10^{22} p/cm². With the 10 μs beam pulse length and cycle time of 1.87 s, the target experienced rapid temperature cycling from 60 °C to 330 °C during operation. The target is operated in a helium environment and the graphite fins bonded to water cooling tubes, as shown in Fig. 1.

Over the last half of the NT-02 target's lifetime, a gradual decline in neutrino yield of 10-15% was observed [1]. This performance degradation was not detected in preceding NT targets, although their lifetimes were roughly half that of the NT-02 target. The probable causes for the target performance degradation was therefore attributed to material radiation damage, cracking caused by reduction of thermal shock resistance, or localized oxidation in the heated region of

the target. The peak radiation damage in the graphite fins was estimated to be 0.63 displacements per atom (DPA), as calculated by the MARS Monte Carlo code [2].

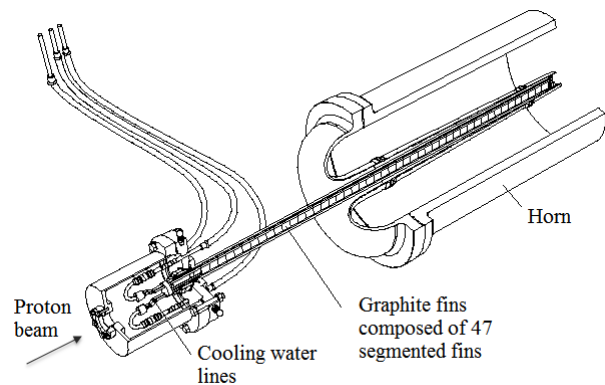


Figure 1: NuMI graphite target.

During the removal and disassembly of the NT-02 target at Fermilab, several graphite fins were discovered to be cracked near the centerline or broken away from the cooling water tubes as shown in Fig. 2. It was unclear whether the separation and fracture of the fins had occurred during the removal and disassembly operations. As a result, studies were initiated to explore the NT-02 graphite fins. The main objectives of the investigation were to determine whether the neutrino yield degradation was a result of radiation damage, by measuring bulk swelling, evaluating the fin fracture surfaces to determine whether they occurred in service or during disassembly, and finally by evaluating the microstructural condition to assess the extent of radiation damage of the POCO ZXF-5Q [3] graphite.



Figure 2: Boroscope images of NT-02 graphite fins during target autopsy. Broken fins from cooling tubes (left) and fractured fin at centerline (right).

POST IRRADIATION EXAMINATION

Four NT-02 fins were retrieved and shipped in a Type-A container to Pacific Northwest National Laboratory (PNNL),

* Work supported by Fermi Research Alliance, LLC, under Contract No. DE-AC02-07CH11359 with the U.S. Department of Energy.

[†] ammikav@fnal.gov

EXPERIMENTAL RESULTS OF BERYLLIUM EXPOSED TO INTENSE HIGH ENERGY PROTON BEAM PULSES*

K. Ammigan[†], B. Hartsell, P. Hurh, R. Zwaska, FNAL, Batavia, IL 60510, USA
 M. Butcher, M. Guinchard, M. Calviani, R. Losito, CERN, Geneva, Switzerland
 S. Roberts¹, V. Kuksenko, Oxford University, Oxford, UK

A. Atherton, O. Caretta, T. Davenne, C. Densham, M. Fitton, P. Loveridge, J. O'Dell, RAL, Didcot, UK
¹also at CCFE, Culham, UK

Abstract

Beryllium is extensively used in various accelerator beam lines and target facilities as a material for beam windows, and to a lesser extent, as secondary particle production targets. With increasing beam intensities of future accelerator facilities, it is critical to understand the response of beryllium under extreme conditions to reliably operate these components as well as avoid compromising particle production efficiency by limiting beam parameters. As a result, an exploratory experiment at CERN's HiRadMat facility was carried out to take advantage of the test facility's tunable high intensity proton beam to probe and investigate the damage mechanisms of several beryllium grades. The test matrix consisted of multiple arrays of thin discs of varying thicknesses as well as cylinders, each exposed to increasing beam intensities. This paper outlines the experimental measurements, as well as findings from Post-Irradiation-Examination (PIE) work where different imaging techniques were used to analyze and compare surface evolution and microstructural response of the test matrix specimens.

INTRODUCTION

Beryllium is currently widely used as the material of choice for critical accelerator components such as beam windows and secondary particle production targets in various accelerator beam lines and target facilities. With the increasing beam intensities of future accelerators [1], it is crucial to understand the response of beryllium to even more extreme operational environments for successful design and reliable operation of these components, without having to compromise particle production efficiency by limiting beam parameters.

One of the main challenges facing windows and targets exposed to high intensity particle beams is thermal shock [2]. These are dynamic stress waves that are generated due to the rapid expansion of the material surrounded by cooler material upon interaction with high intensity particle beams. Consequently, the material may undergo plastic deformation and eventually fail. As a result, an experiment at CERN's HiRadMat facility [3] was carried out to expose beryllium specimens to intense proton beams. The test facility aims to deliver high intensity proton beams, up to 4.9×10^{13}

protons per 7.2 μ s pulse, with Gaussian beam spot sigmas ranging from 0.1 mm to 2 mm [4]. The objectives of the experiment were to explore the onset of failure modes of beryllium under controlled conditions at highly localized strain rates and temperatures, identify any thermal shock limits, and validate highly non-linear numerical models with experimental measurements. The primary goal was to push beryllium to its limit, by imposing a temperature jump up to close to its melting point (~ 1000 °C) from a single beam pulse.

EXPERIMENTAL SET-UP

The experimental chamber is based on a double containment design to ensure containment of the beryllium specimens and mitigate any radioactive contamination upon interaction with beam. Figure 1 shows the experimental chamber attached to a vertical lift tower and positioned on the HiRadMat mobile table.

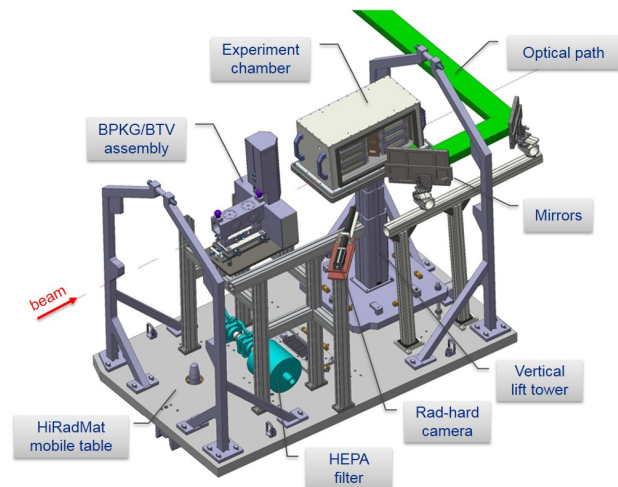


Figure 1: Experimental chamber assembled on mobile table.

The experiment contained two types of specimens: thin discs for deformation, strain, and crack/failure analyses during Post Irradiation Examination (PIE), and slugs for online measurements of strain, temperature and vibration. Strain and temperature gauges were attached to the external cylindrical surface of the slugs to measure the circumferential strain and temperature response to the pulsed beam. Dynamic radial vibrations of the cylindrical edge of the slugs were recorded with a Laser Doppler Vibrometer (LDV) sys-

* Work supported by Fermi Research Alliance, LLC, under Contract No. DE-AC02-07CH11359 with the U.S. Department of Energy.

[†] ammikav@fnal.gov

HIGHER ORDER MODES ANALYSIS OF FERMILAB'S RECYCLER CAVITY*

M. Awida[#], J. Dey, T. Khabiboulline, V. Lebedev, and R. Madrak
Fermilab, Batavia, IL 60510, USA

Abstract

Two recycler cavities are being employed in Fermilab's Recycler Ring for the purpose of slip stacking proton bunches, where 6 batches of 8 GeV protons coming from the Booster are stacked on top of 6 circulating batches. Slip stacking requires two RF cavities operating near 52.809 MHz with frequency slip of 1.26 kHz. In this paper, we report on the analysis of higher order modes in the Recycler cavity, and present their values for R/Q and shunt impedances. Knowing the frequencies and properties of higher order modes is particularly critical for understanding beam stability margins.

INTRODUCTION

Two RF cavities are utilized in Fermilab's Recycler Ring to achieve the slip stacking of proton bunches [1, 2]. Each cavity is a quarter wave resonator, as shown in Figure 1, but they are tuned to slightly different frequencies. One is operating near 52.809 MHz, while the other is detuned by -1.26 kHz. A relatively small ferrite loaded transmission line is used to electronically tune the cavity to the target resonance value. Several ports exist on the cavity. They are used for sensing the RF power with field probes and for the initial mechanical tuning of resonance frequency.

The Recycler cavities are made of copper and are designed to sustain a gap voltage of 150 kV with a maximum power of 150 kW. The designed value of shunt impedance for the fundamental operating mode is 75 k Ω , while R/Q is 13 Ω .

RF MODEL

A full 3D model for the Recycler cavity was created to analyse the cavity's higher order modes (HOM). Figure 2 illustrates the electric field of the fundamental mode resonating at 51.518 MHz. The field is scaled to produce a 150 kV gap voltage. Assuming a conductivity of 5.998e7 S/m for copper, the corresponding dissipated power is 111 kW.

The scope of this work is to compute the R/Q for the monopole modes, and the transverse R/Q_{tr} for the dipoles and quadrupoles, up to 500 MHz. In this perspective the computed quantities are defined as follows:

$$R/Q = \frac{|V|^2}{2\omega U}$$

$$R/Q_{tr} = \frac{|V_{kick}|^2}{2\omega U} \cdot k = \frac{|V_{kick}|^2}{2U \cdot c}$$

where ω is the angular frequency, U is the cavity's stored energy, k is the propagation constant, V is the longitudinal gap voltage, and V_{kick} is the transverse kick voltage.

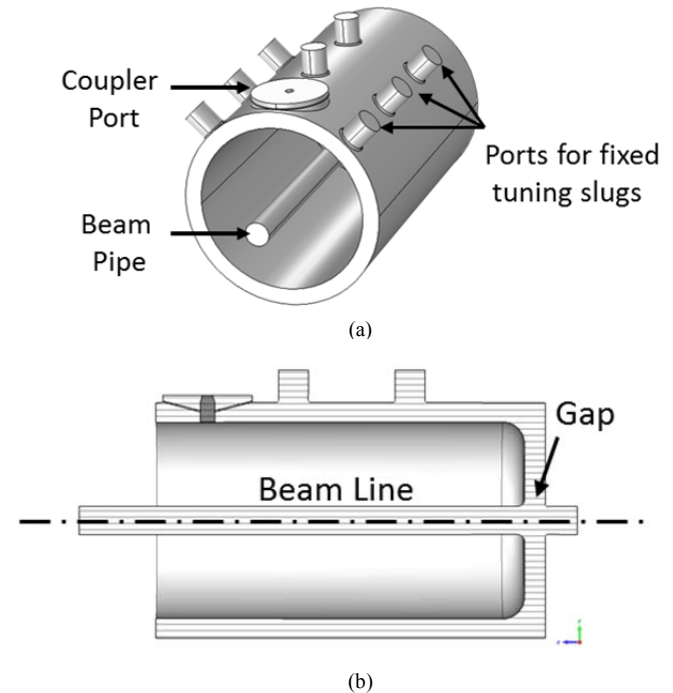


Figure 1: Fermilab's Recycler cavity. (a) 3D model. (b) Cross sectional view.

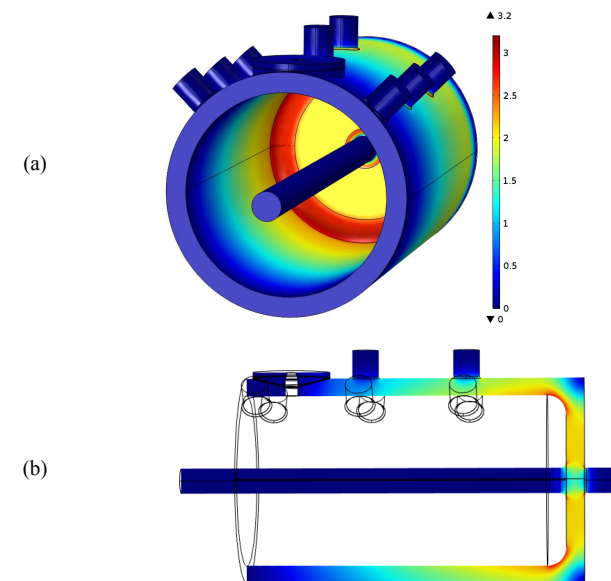


Figure 2: Surface electric field in MV/m of the fundamental mode resonating at 51.518 MHz inside the Recycler cavity. (a) 3D view. (b) Cross sectional view.

*Operated by Fermi Research Alliance, LLC, under Contract DE-AC02-07CH11359 with the U.S. DOE

#mhassan@fnal.gov

RESONANT FREQUENCY CONTROL FOR THE PIP-II INJECTOR TEST RFQ: CONTROL FRAMEWORK AND INITIAL RESULTS*

A. L. Edelen[†], S. G. Biedron, S. V. Milton, Colorado State University, Fort Collins, CO, USA
D. Bowring, B. E. Chase, J. P. Edelen, D. Nicklaus, J. Steimel, Fermilab, Batavia, IL, USA

Abstract

For the PIP-II Injector Test (PI-Test) at Fermilab, a four-vane radio frequency quadrupole (RFQ) is designed to accelerate a 30-keV, 1-mA to 10-mA, H⁻ beam to 2.1 MeV under both pulsed and continuous wave (CW) RF operation. The available headroom of the RF amplifiers limits the maximum allowable detuning to 3 kHz, and the detuning is controlled entirely via thermal regulation. Fine control over the detuning, minimal manual intervention, and fast trip recovery is desired. In addition, having active control over both the walls and vanes provides a wider tuning range. For this, we intend to use model predictive control (MPC). To facilitate these objectives, we developed a dedicated control framework that handles higher-level system decisions as well as executes control calculations. It is written in Python in a modular fashion for easy adjustments, readability, and portability. Here we describe the framework and present the first control results for the PI-Test RFQ under pulsed and CW operation.

INTRODUCTION

The resonant frequency of the RFQ may be maintained despite changes in RF heating through thermal control. For the PI-Test RFQ, we use an internal water-cooling system [1]. Both the thermal time constants and transport delays present in such systems limit the efficacy of standard PI control. The control problem is further complicated by the cavity geometry: different rates of thermal expansion and contraction of the main internal components (the walls and the vanes/pole tips) result in a large transient frequency response under changes in average RF power. At present, the resonant frequency of other RFQs is regulated with a PI loop around the vanes, while the walls are held constant [2,3]. In contrast, a joint control loop that governs both the wall and vane temperatures enables simultaneous exploitation of their individual impacts on the resonant frequency. As discussed previously [1,4,5], these system characteristics motivate the use of MPC.

In support of this, a dedicated control framework was developed to handle high-level decisions and execute control calculations. Because multiple operational modes are required, the framework is written in Python and in a modular fashion to facilitate easy modifications to the code. The framework interfaces with ACNET (Fermilab's main control system) and the RFQ/cooling system via a custom protocol generated with a novel protocol compiler [6,7]. This framework is operational for the RFQ and could be modified for similar control tasks at Fermilab.

In this paper we describe the operational needs for the RFQ, the design of the control framework, and initial control results. This work represents a first test of resonant frequency control over the RFQ, a first test of the framework, and a first test of using a dedicated Python program at Fermilab interfaced with the main control system via the protocol compiler.

SYSTEM DESCRIPTION AND OPERATIONAL GOALS

More details on the system and control challenges therein are described in [1, 5]. The low-level radio frequency (LLRF) system can compensate for detuning of the cavity only up to 3 kHz by taking advantage of the available overhead in the RF power amplifiers. This limitation translates directly to challenges for the resonance control system: detuning beyond 3 kHz occurs rapidly under changes in average RF power, particularly in CW mode, due to the frequency response of the vanes [8, 9]. In addition, the RFQ operates in both CW and pulsed RF modes, resulting in variable RF heating. Other challenges are imposed by the architecture of the water-cooling system. Transport delays and thermal time constants result in open-loop settling times on the order of tens of minutes during normal operation (e.g. see Figure 1). Finally, the coupling between the wall and vane circuits, the transient frequency response, the nonlinear valve flow curves, and fluctuations in the temperature of the cold water supply make the system more difficult to control.

The LLRF system [10] is capable of operating in either SEL mode (in which the drive frequency follows the cavity resonant frequency) or GDR mode (in which the drive frequency is set). In SEL mode, the use of RF overhead is minimized due to the changing of the drive frequency to match the RFQ, thereby also minimizing the reflected power. As such it is useful to switch into SEL mode automatically when the detuning increases beyond a tolerable threshold.

Additionally, accommodation of multiple control algorithms is desired. MPC frequency control will be the main method; however, PI frequency control using the vane valve is also desired as an auxiliary mode. In addition, for fast trip recovery it is useful to control the water temperature directly. Next, another desired mode is control of the RF forward power magnitude during a cold start or recovery from a trip. This would start out as a simple ramp, but could eventually be incorporated into an MPC routine.

In the event of an RF trip, the required recovery time for the RFQ is no more than 10x the length of the trip, with a target requirement of 2x the duration of the trip. These constraints and desired system flexibility motivate the development of a modular control system architecture

*Fermilab is operated by Fermi Research Alliance, LLC under Contract No. De-AC02-07CH11359 with the United States Department of Energy.
[†] auralee.morin@colostate.edu

ENHANCEMENT OF THE ACCELERATING GRADIENT IN SUPERCONDUCTING MICROWAVE RESONATORS*

M. Checchin^{1,2,†}, M. Martinello^{1,2}, A. Grassellino¹, A. Romanenko¹, S. Posen¹
and J. F. Zasadzinski²

¹ Fermilab, Batavia, IL 60510, USA

² Illinois Institute of Technology, Chicago, IL 60616, USA

Abstract

The accelerating gradient of superconducting resonators can be enhanced by engineering the thickness of a dirty layer grown at the cavity's rf surface. In this paper the description of the physics behind the accelerating gradient enhancement by meaning of the dirty layer is carried out by solving numerically the the Ginzburg-Landau (GL) equations for the layered system. The calculation shows that the presence of the dirty layer stabilizes the Meissner state up to the lower critical field of the bulk, increasing the maximum accelerating gradient.

INTRODUCTION

The possible enhancement of the accelerating gradient by meaning of layered structures in accelerating cavities was introduced by A. Gurevich [1]. He showed that high κ (GL parameter) superconducting layers separated by insulating layers (SIS structure) deposited at the rf surface can in principle enhance the superheating field, and allow for higher gradients.

In the same direction T. Kubo [2, 3] and S. Posen *et al.* [4] explored thoughtfully the behavior of the SIS structure. T. Kubo in particular, described also the SS structure [3, 5], i.e. a high κ (dirty) superconducting layer on top of a low κ (clean) bulk superconductor. He approached the problem in the high κ approximation by meaning of the London equations as done for the SIS structure, showing that the dirty layer can in principle enhance the superheating field even if no insulating layer is present.

In the present paper an alternative description of the SS structure is presented. The approach here is different since the calculation is carried out numerically from the GL equations, where the dirty layer is assumed to behave as a perturbation on the magnetic induction profile in the material. We show that the dirty layer stabilizes the superconductor against the vortex nucleation, and shifts the lower critical field of the whole structure up to the bulk's value, increasing the magnetic field range in which the Meissner state is stable.

THE BEAN-LIVINGSTON BARRIER FOR NON-CONSTANT κ

Let us assume a semi-infinite superconductor, where the normal to the surface directed towards the material bulk is \hat{x} ,

* Work supported by the US Department of Energy, Office of High Energy Physics.

† checchin@fnal.gov

the external magnetic field is applied along the z direction and the screening currents are flowing along the y direction. On top of such superconductor we assume the presence of a thin superconducting dirty layer with higher κ than the bulk (grown by diffusion of impurities for example), so that the κ profile of the system can be described by the analytic form:

$$\kappa(x) = -\frac{\kappa_s - \kappa_b}{1 + e^{-(x-x_0)/c}} + \kappa_s, \quad (1)$$

which corresponds to a sigmoidal function, where κ_s and κ_b are the superficial and bulk GL parameters, c is a constant that defines the steepness of the function (normally $c = 0.018$) and x_0 corresponds to the inflection point assumed as the thickness of the dirty layer.

Since we are dealing with dimensionless units $x = \text{depth}/\lambda$, with λ the penetration depth $\lambda = \lambda_0\sqrt{1 + \xi_0/l}$, l the mean free path, $x_0 = d/\lambda$, $\xi_0 = 38$ nm and $\lambda_0 = 39$ nm [6].

Forces Acting on the Vortex

The forces acting on a vortex penetrating from the surface can be calculated in first approximation by implementing the same description of C. P. Bean and J. D. Livingston [7]. The repulsive force (with respect the surface) due to the interaction of the vortex with the magnetic induction profile in the material is:

$$\mathbf{f}_f(x) = -\frac{4\pi}{\kappa(x)} \frac{\partial b_f(x)}{\partial x} \hat{\mathbf{x}}, \quad (2)$$

where $b_f(x) = a'(x)$ is calculated numerically from the GL equations modified in order to account also for the variation

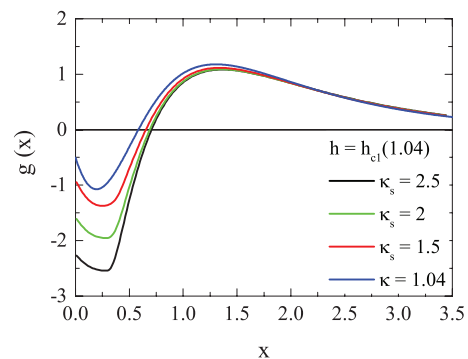


Figure 1: Gibbs free energy density as a function of x a) for different values of κ_s calculated at $h = h_{c1}(\kappa_b)$, b) for increasing applied fields, with $\kappa_s = 2.5$ and $d = 15$ nm. In both cases $\kappa_b = 1.04$.

THE RADIATION DAMAGE IN ACCELERATOR TARGET ENVIRONMENTS (RaDIATE) COLLABORATION R&D PROGRAM - STATUS AND FUTURE ACTIVITIES

P. G. Hurh[†], Fermi National Accelerator Laboratory*, Batavia IL, USA

Abstract

The RaDIATE collaboration (Radiation Damage In Accelerator Target Environments), founded in 2012, has grown to over 50 participants and 11 institutions globally. The primary objective is to harness existing expertise in nuclear materials and accelerator targets to generate new and useful materials data for application within the accelerator and fission/fusion communities. Current activities include post-irradiation examination of materials taken from existing beamlines (such as the NuMI primary beam window from Fermilab) as well as new irradiations of candidate target materials at low energy and high energy beam facilities. In addition, the program includes thermal shock experiments utilizing high intensity proton beam pulses available at the HiRadMat facility at CERN. Status of current RaDIATE activities as well as future plans will be discussed, including highlights of preliminary results from various RaDIATE activities and the high level plan to explore the high-power accelerator target relevant thermal shock and radiation damage parameter space.

INTRODUCTION

In 2012, at a Proton Accelerators for Science and Innovation Workshop (PASI) held at Fermilab, workshop participants from a range of high power accelerator facilities (high energy physics, nuclear physics, spallation sources) identified radiation damage to materials as the most cross-cutting challenge facing high power target facilities [1]. The RaDIATE collaboration was formed to address this challenge by bringing together experts from the fields of nuclear materials (fission and fusion power) and accelerator target facilities. The collaboration has grown to 11 participating institutions globally with 3 more institutions set to join this year (listed in the acknowledgements section). Some of the more significant current and planned RaDIATE activities are described here.

Radiation damage effects in materials are dependent upon several irradiation parameters including irradiation temperature, dose rate, and gas production (from transmutation). These irradiation parameters are quite different between the nuclear power environment (relatively lower dose rate, lower gas production, continuous irradiation) and the accelerator target environment (relatively higher instantaneous dose rate, higher gas production, pulsed irradiation). In addition, there are significant differences between the nuclear and accelerator applications resulting

in somewhat different material properties of interest. For instance, accelerator target and beam window are typically non-life-safety critical components and generally have localized volumes of intense cyclic irradiation (particle surrounded by cooler, non-irradiated material that challenge the limits of the material. Typical beam spot sizes range from a few millimeters to a few centimeters in radius. This gives rise to localized, cyclic thermal gradients (referred to as thermal shock), creating dynamic stress waves moving through the material. So, in the accelerator application, high-cycle fatigue and thermal diffusion are of prime concern. Whereas in a reactor application, structural materials often play a life-safety critical role, but are, during normal operation, exposed to a more uniform, continuous bulk irradiation. Reactor structural materials are only pushed to the limits by accident scenarios where they must retain damage tolerance. So, in the nuclear application, ductility and fracture toughness are of prime concern. Therefore, the differences between irradiation parameters and application-specific loading environments require research activities tailored specifically to the accelerator target and beam window application.

CURRENT RADIATE ACTIVITIES

To address these high power target research needs, a program of activities was undertaken. Recent RaDIATE activities focused upon candidate materials primarily useful for neutrino target facilities and as beam window materials for various facilities, namely graphite and beryllium. Status and highlights of major current activities are given below. Although preliminary findings are listed below, full results will be published soon in relevant scientific journals.

Graphite Studies

High-Energy Irradiation of Graphite In 2010, four grades of fine-grained, isotropic graphite, one grade of hexagonal boron-nitride, and one grade of carbon-carbon composite (3-D fiber weave) were irradiated with 181 MeV protons at Brookhaven National Laboratory's Linac Isotope Producer facility (BLIP). The resulting post-irradiation examination (PIE) of these specimens supported the target material choice for the Long Baseline Neutrino Facility (LBNF) [2]. Figure 1 shows tensile specimens being recovered after irradiation. More recently, additional PIE of these specimens has continued as part of the RaDIATE R&D program.

- Specimens were exposed to 6.7×10^{20} protons/cm² or about 0.1 DPA (displacements per atom) at an irradiation temperature of 120-150 °C.

* Operated by Fermi Research Alliance, LLC under Contract No. DE-AC02-07CH11359 with the United States Department of Energy.

[†] hurh@fnal.gov

DESIGN OF MAIN COUPLER FOR 650 MHz SC CAVITIES OF PIP-II PROJECT*

O. Pronitchev[#], S. Kazakov, FNAL, Batavia, IL 60510, USA

Abstract

Proton Improvement Plan-II at Fermilab has designed an 800MeV superconducting pulsed linac which is also capable of running in CW mode. The high energy section from 185MeV to 800MeV will be using cryomodules with two types of 650MHz elliptical cavities. Both types of cryomodules will include six 5-cell elliptical cavities. Each cavity will have one coupler. Updated design of the 650 MHz main coupler is reported.

INTRODUCTION

A multi-MW proton accelerator facility based on an H-linear accelerator using superconducting RF technology, Proton Improvement Plan-II (PIP II), is being developed at

Fermilab to support the intensity frontier research in elementary particle physics. The high energy section from 185MeV to 800MeV will be using two types of 650MHz elliptical cavities. The low beta (LB), $\beta\gamma = 0.61$ portion would accelerate proton from 185MeV-500MeV, while high beta (HB), $\beta\gamma = 0.92$ portion of the linac would accelerate from 500 to 800 MeV. Both types of cryomodules will include six 5-cell elliptical cavities. [1] Each cavity will have one coupler, see Figure 1. Coupler is compatible with both types of 650 MHz cavities. Each HB cavity requires ~100 kW CW RF power for 5 mA beam current operation This paper presents updated mechanical design of main coupler for PXIE HB and LB 650 MHz cavities.

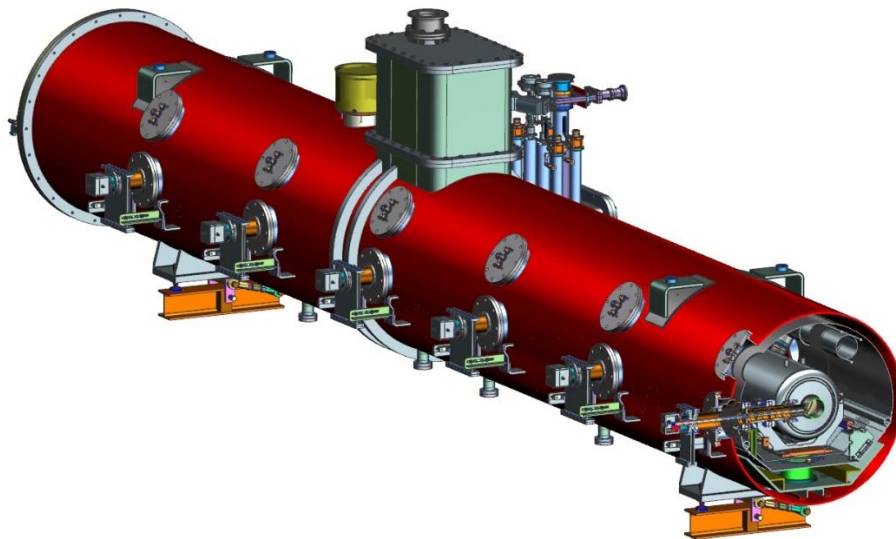


Figure 1: Cross sectional view of HB 650 MHz cryomodule.

* Work supported by DOE.

[#]olegp@fnal.gov

THE USE OF KF STYLE FLANGES IN LOW PARTICULATE APPLICATIONS*

K. R. Kendziora[†], J. Angelo, C. Baffes, D. Franck, R. Kellett, Fermi National Accelerator Laboratory, Batavia, U.S.A.

Abstract

As SCRF particle accelerator technology advances the need for “low particulate” and “particle free” vacuum systems becomes greater and greater. In the course of the operation of these systems, there comes a time when various instruments have to be temporarily attached for diagnostic purposes: RGAs, leak detectors, and additional pumps. In an effort to make the additions of these instruments easier and more time effective, we propose to use KF style flanges for these types of temporary diagnostic connections. This document will describe the tests used to compare the particles generated using the assembly of the, widely accepted for “particle free” use, conflat flange to the proposed KF style flange, and demonstrate that KF flanges produce comparable or even less particles.

INTRODUCTION

It is well established that particulate contamination can be damaging to SCRF cavities [1]. Conventionally, all-metal sealing systems with specific assembly practices are used for permanent vacuum assembly on such systems (e.g. [2]). When an accelerator with “particle free” components operates, vacuum diagnostics need to be performed. Diagnostics are used to discover the cause of strange beam behaviour, why the vacuum pressure is high, or even if the vacuum gauges are still working properly. When diagnostics need to be performed, often equipment such as RGAs, vacuum pumps, and additional gauges need to be added and then removed from the system once the diagnostics have been completed.

The preferred flange type for particle free applications at Fermilab has been a conflat flange with 316 stainless steel studs and either silicon bronze or titanium nuts. This combination provides a reliable, non-permeable seal. The drawbacks to using a conflat are the time it takes to prep the hardware, the cost of the hardware, the time required to make up the flange and more particulates are released while making up the flange. For temporary diagnostic equipment that has to be installed and removed in a relatively short time span, it would be more cost effective and time efficient to use a KF style flange. A KF style flange not only would cut down on time required to process the hardware but also in assembling the flange. This time savings becomes most critical in a “shutdown” situation where the accelerator has to be turned off for repairs, and there is a limited amount of time to perform the needed tasks. By not having to prepare 12 nuts and 6 studs (in the case of a

2.75” conflat), but only a seal and clamp, time is saved in cleaning and prep-work. Making up a conflat flange can take approximately one minute per fastener, a KF connection can be assembled in a matter of seconds.

A KF style flange can be assembled with the same, or even less particles generated in the vacuum space, as a traditional conflat flange.

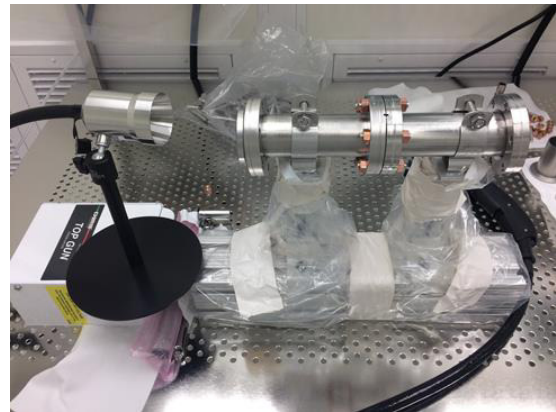


Figure 1: Test Fixture.

TEST ENVIRONMENT AND SETUP

A 2.75” conflat and a KF-40 flange were used since they are similar in size and are fairly common interfaces for vacuum diagnostic equipment. All the hardware was cleaned ultrasonically in a 1% solution of deionized (DI) water and Micro 90 for stainless steel hardware and a 1% solution of DI water and Citranox for the Si bronze hardware. The hardware was rinsed off with clean DI water. The tests were performed in a class 10 cleanroom. The KF and conflat flanges were blown off with ionized boil-off nitrogen until 0 counts were achieved on a Climet 450t particle counter. The hardware was also blown off to the same 0 count level of cleanliness. The conflat flanges were assembled on a test stand to mitigate the introduction of particles generated from the flanges rolling around on the cleanroom bench. (see Fig. 1)

To help ensure repeatable results, a torque wrench was used to tighten the nuts on the conflat flange and the clamp on the KF flange. The conflat flange nuts were tightened to 16 Nm per the manufacturer’s specification. The KF-40 flanges were tightened to 3.4 Nm to simulate finger tight since these clamps are typically tightened by hand.

* Operated by Fermi Research Alliance, LLC under Contract No. DE-AC02-07CH11359 with the United States Department of Energy.

[†] kylek@fnal.gov

SUPERCONDUCTING COIL WINDING MACHINE CONTROL SYSTEM*

J. M. Nogiec[†], S. Kotelnikov, A. Makulski, K. Trombly-Freytag, D. Walbridge
Fermi National Accelerator Laboratory, Batavia, IL 60510, USA

Abstract

The Spirex coil winding machine is used at Fermilab to build coils for superconducting magnets. Recently this machine was equipped with a new control system, which allows operation from both a computer and a portable remote control unit. This control system is distributed between three layers, implemented on a PC, real-time target, and FPGA, providing respectively HMI, operational logic and direct controls. The system controls motion of all mechanical components and regulates the cable tension. Safety is ensured by a failsafe, redundant system.

INTRODUCTION

The need to wind superconducting coils for LHC Accelerator Research Program (LARP) led to a project to equip the Spirex coil winding machine with a control system based on up-to-date technology and to provide the machine with a safety system that meets current safety policies [1].

The winder machine is about 11 m long with a bridge that moves along a track and supports a rotating boom holding a spool of cable and providing cable tension, and the mandrel supporting the coil with its winding fixture (Fig. 1).

The control system was designed to provide necessary functionality for winding coils, including automatically keeping the proper cable tension and cable spool elevation, synchronizing motors for mandrel tilt and bridge motion, and providing interlocks to prevent material or equipment damage.



Figure 1: Coil winding machine.

COMPUTERS AND INSTRUMENTATION

The computer and data acquisition (DAQ) hardware consists of a PC-based station connected via a private network to a CompactRIO (cRIO) [2] crate with I/O modules and a processor running a real-time operating system. An extension crate is connected via Ether CAT to the cRIO

* Work supported by the U.S. Department of Energy under contract no. DE-AC02-07CH11359

[†] nogiec@fnal.gov

crate. All of the control signals to and from the machine hardware are routed through an interface box, which also contains a heartbeat watchdog circuit.

Two wireless CAN transmitters are connected to the cRIO crate, allowing for control of the machine from the remote console. Vital machine parameters are displayed on two large LED displays located on both sides of the bridge.

SOFTWARE ARCHITECTURE

The control system was designed with the following layered architecture:

- HMI Layer - modules residing on the HMI computer implementing the user interface and data storage.
- Operational Logic Layer - modules that provide operational logic residing on the real-time (RT) target computer.
- Direct Control Layer - FPGA code that interfaces I/O signals and implements fast and deterministic behavior, such as motion control, motion synchronization, tension and reel regulation and interlocks.
- Hardware Layer – actual hardware elements including motors, sensors, actuators, and switches.

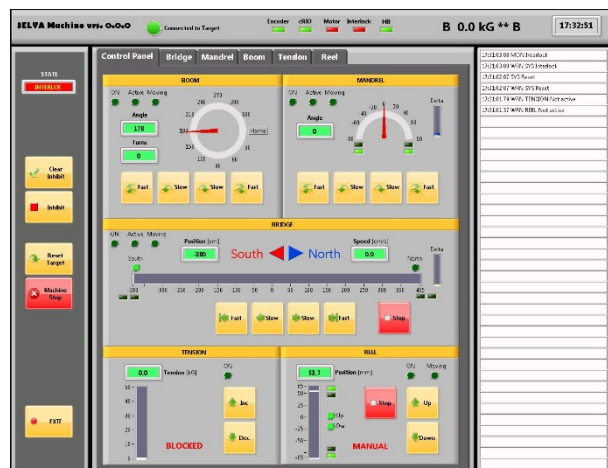


Figure 2: Touch screen user interface.

HMI Computer

The HMI computer's software starts the tension control, and provides a graphical user interface (GUI) for controlling and monitoring the machine (Fig. 2). Although the primary method of controlling the machine is via the remote console, the GUI on the HMI computer can perform a larger set of functions. The current state of the machine, including its position, tension, mandrel angle etc. can be viewed on the HMI computer display, even when the machine is being controlled by the remote console. All software exceptions as well as important events are both

PROGRESS ON THE DESIGN OF A PERPENDICULARLY BIASED 2nd HARMONIC CAVITY FOR THE FERMILAB BOOSTER*

R. L. Madrak[†], J. E. Dey, K. L. Duel, J. C. Kuharik, W. A. Pellico, J. S. Reid, G. Romanov, M. Slabaugh, D. Sun, C. Y. Tan, I. Terechkin,
Fermilab, Batavia, IL 60510

Abstract

A perpendicularly biased 2nd harmonic cavity is being designed and built for the Fermilab Booster. Its purpose is to flatten the bucket at injection and thus change the longitudinal beam distribution to decrease space charge effects. It can also help at extraction. The cavity frequency range is 76 – 106 MHz.

The power amplifier will be built using the Y567B tetrode, which is also used for the fundamental mode cavities in the Fermilab Booster. We discuss recent progress on the cavity, the biasing solenoid design and plans for testing the tuner's garnet material.

HISTORY

Perpendicularly biased prototype cavities have been constructed in the past: at LANL, where the same cavity was later shipped to TRIUMF and tested with some modifications. SSCL was planning to use a perpendicularly biased cavity for the Low Energy Booster (LEB). Both the LANL/TRIUMF and SSCL cavities were tested at high power but neither have ever operated with beam.

The required tuning range of the FNAL 2nd Harmonic cavity (76 – 106 MHz) is even larger than that of its predecessors, (46.1 – 60.8 MHz for LANL and 47.5 – 60 MHz for SSCL [1]) so the design is challenging. Among the concerns are: 1) Achieving the required tuning range using a realistic bias magnetic field, 2) Taking into account higher local permeability and heating of the garnet in areas with low magnetic field, 3) Keeping the magnetic field in the tuner as uniform as possible, 4) Transfer and removal of heat without the use of toxic materials (i.e. BeO), or those that would generate mixed waste (oil), 5) Including the power tetrode in the RF model to take into account the impact of its output capacitance and strong coupling to the cavity on the tuning range, 6) Avoiding air bubbles (which could cause sparking) in the adhesive used to fill any air gaps in the tuner, and 7) Choosing the adhesives and assembly techniques to minimize RF losses in this adhesive without compromising heat transfer.

CAVITY DESIGN

The tuner is constructed using a stack of rings of garnet (National Magnetics AL-800), for tuning, and alumina, to transfer the heat to the outer and inner surfaces, where it

will be removed by water cooling. The required gap voltage in the cavity to improve capture during injection (75 – 82 MHz) is $V_{\text{peak}} = 100$ kV. The cavity can only be useful at transition if two are available because the required voltage exceeds 100 kV. For extraction, the required voltage is smaller. In the present CST model of the cavity, the shunt impedances ($R_{\text{sh}} = V^2/P$) are 192 k Ω at 76 MHz and 361 k Ω at 106 MHz. The design has converged regarding issues 1 - 6 enumerated above. Solutions to such problems, such as the use of magnetic shimming to make the magnetic field in the tuner more uniform, are discussed in previous proceedings including [2].

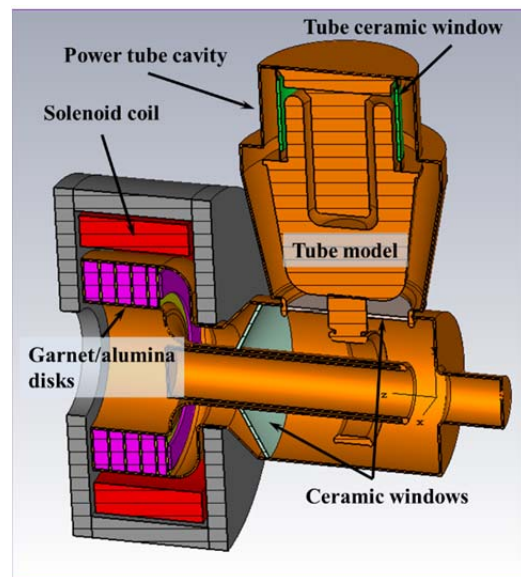


Figure 1: The present cavity design

Since the magnetic field in the garnet rings of the tuner is not uniform, it is critical to know the static permeability $\mu(B)$ and magnetic loss tangent for any bias magnetic field level within the tuner. As the vendor does not provide such data, it was necessary to measure these quantities in material samples. These first measurements are discussed in [3].

The size of the power tube and various mechanical requirements made the power tube cavity comparable in size and stored energy with the accelerating cavity itself. Implementation of the initial design of the power tube cavity in the cavity design dramatically lowered the operating frequency, and reduced the tuning range and overall effectiveness. Our attempts to take the power tube into account using simplified models with lumped elements to find a solution were not entirely successful. Progress was made after we developed a power tube model as close as

* Operated by Fermi Research Alliance, LLC under Contract No. DE-AC02-07CH11359 with the United States Department of Energy

[†]madrak@fnal.gov

MEASUREMENTS OF THE PROPERTIES OF GARNET MATERIAL FOR TUNING A 2ND HARMONIC CAVITY FOR THE FERMILAB BOOSTER*

R. L. Madrak[†], W. A. Pellico, G. Romanov, C. Y. Tan, I. Terechkin
Fermilab, Batavia, IL 60510, USA

Abstract

A perpendicularly biased 2nd harmonic cavity is being designed and built for the Fermilab Booster, to help with injection and extraction. Tunable accelerating cavities were previously designed and prototyped at LANL, TRIUMF, and SSCL for use at ~45-60 MHz (LANL at 50-84 MHz). The required frequency range for FNAL is 76 - 106 MHz. The garnet material chosen for the tuner is AL-800. To reliably model the cavity, its static permeability and loss tangent must be well known. As this information is not supplied by the vendor or in publications of previous studies, a first order evaluation of these properties was made using material samples. This paper summarizes the results of the corresponding measurements.

INTRODUCTION

A perpendicularly biased (as opposed to parallel biased) design of a second harmonic cavity has been pursued because the former should have a substantially higher shunt impedance. The cavity design and status is discussed in [1]. Various types of garnets are available and the choice of National Magnetics AL-800 (aluminum doped garnet) was based on a balance between an acceptable saturation magnetization ($4\pi M_s$) and Curie temperature. In the case of perpendicular bias, operation is in the saturation region and this results in much lower power loss than in the case of the “traditional” parallel biased ferrite.

As the magnetic bias is achieved by using a realistic solenoid, non-uniformity of the magnetic field in the garnet can have a significant impact on the local permeability and the loss tangent. If a local working point is near gyromagnetic resonance, significant local power loss can render the device non-operational if the temperature exceeds the Curie temperature, and even result in mechanical damage due to temperature gradient induced stress.

Knowing the local working point of the garnet over the whole tuning range requires reliable information about the permeability (μ), permittivity (ϵ), and loss tangents $\tan \delta_\mu$ and $\tan \delta_\epsilon$. This paper presents results of first studies of the static permeability and RF losses that were performed using existing material samples and a biasing solenoid which was already on-hand. This approach helped to deliver the necessary information, but required an elaborate (and iterative) approach. More precise measurements are planned, using witness samples of the material fabricated for the cavity.

* Operated by Fermi Research Alliance, LLC under Contract No. DE-AC02-07CH11359 with the United States Department of Energy.

[†] madrak@fnal.gov

MATERIAL PROPERTIES

The ability to accurately model the cavity is key to the success of the design. In particular, it is necessary to know the permeability as a function of magnetic field. The real and imaginary parts μ' and μ'' determine the tuning range and losses, respectively. The magnetic field in the tuner is never perfectly uniform, and in order to properly model the device, these properties must be known at every point in the tuner for all bias settings. In the following sections, we describe our measurements of the static permeability and the loss tangent using the available set of AL-800 garnet rings (3.0” OD, 0.65” ID, and 0.5” thick).

STATIC PERMEABILITY

The static magnetization curve was extracted by iteratively adjusting the magnetization curve used in the simulation of the setup, until the simulation results matched measurements. The initial $\mu(B)$ curve was a guess based on the vendor’s data for the initial permeability (~ 50) and a theoretical value for large B .

A sketch of the setup is shown in Fig. 1. The ten stacked rings are placed inside of the solenoid, which has a flux return on the bottom and sides, made from CMD-10 and G4 ferrite. The solenoid’s length, ID and OD are 177.8 mm, 100 mm, and 305 mm, respectively. The number of turns is 112. A steel plug was inserted on top to improve the uniformity of the magnetic field within the samples.

Three different magnetometer/hall probe pairs were available for measurement, and they were cross calibrated inside of the solenoid with no garnet. The hall probes were placed between rings, on the top, bottom, and middle of the stack. Magnetic field was measured with each probe as a function of solenoid current.

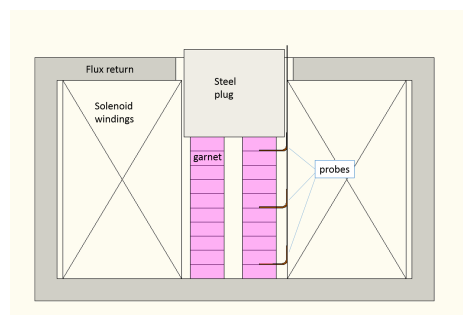


Figure 1: Setup concept for the measurement of the static magnetization.

The iteratively obtained magnetization curve was gradually changed starting with low current. At each new current

DEVELOPMENT AND COMPARISON OF MECHANICAL STRUCTURES FOR FNAL 15 T Nb₃Sn DIPOLE DEMONSTRATOR*

I. Novitski, A.V. Zlobin[#], FNAL, Batavia, IL 60510, USA

Abstract

Main design challenges for 15 T accelerator magnets are large Lorentz forces at this field level. The large Lorentz forces generate high stresses in the coil and mechanical structure and, thus, need stress control to maintain them at the acceptable level for brittle Nb₃Sn coils and other elements of magnet mechanical structure. To provide these conditions and achieve the design field in the FNAL 15 T dipole demonstrator, several mechanical structures have been developed and analysed. The possibilities and limitations of these designs are discussed in this paper.

INTRODUCTION

Nb₃Sn magnets with a nominal operating field of 15-16 T are being considered for the LHC energy upgrade (HE-LHC) and a post-LHC Very High Energy pp Collider (VHEppC) [1]. To demonstrate feasibility of the 15 T accelerator quality magnets, FNAL has started the development of a single-aperture Nb₃Sn dipole demonstrator based on a 4-layer graded cos-theta coil with 60 mm aperture and cold iron yoke [2].

Main design challenges for 15 T accelerator magnets include large Lorentz forces at this field level. The large Lorentz forces generate high stresses in the coil and mechanical structure and, thus, need stress control to maintain them below 150 MPa, which is acceptable for brittle Nb₃Sn coils. To provide these conditions and achieve the design field in the FNAL 15 T dipole demonstrator, several mechanical structures have been developed and analyzed. The possibilities and limitations of these designs are discussed in this paper.

BASELINE MAGNET DESIGN

The baseline design of the 15 T dipole demonstrator being developed at FNAL is described in [3]. It consists of a 4-layer 60-mm aperture graded coil and cold 587 mm ID iron yoke separated from the coil by 2 mm spacer. The baseline mechanical structure of the dipole demonstrator is shown in Fig. 1. The coil uses two 15 mm wide cables with 28 strands in the two innermost layers and 40 strands in the two outermost layers. The inner and outer cables are based on 1.0 mm and 0.7 mm Nb₃Sn strands respectively. The magnet maximum design bore field is 15.61 T at 4.2 K and 17.04 T at 1.9 K.

The coil assembly is surrounded by a 2 mm thick stainless steel spacer and supported by a vertically split iron yoke locked by aluminum clamps. The yoke is surrounded by a 12 mm thick stainless steel skin. The I-shaped clamps interleave with the iron yoke laminations

in the top and bottom sectors of the iron yoke, thus reducing the iron filling factor in these areas to ~50%.

The axial Lorentz forces are supported by two thick end plates connected by eight stainless steel tierods placed in the dedicated holes in the iron yoke. This support structure provides better stress management than the original concept with stainless steel C-clamps and a thick skin [4]. The cold mass transverse size is 610 mm. It is limited by the inner diameter of the FNAL test cryostat.

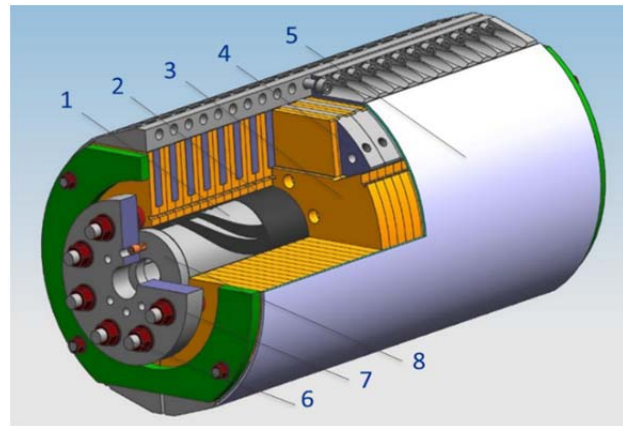


Figure 1: Baseline mechanical structure of FNAL 15 T dipole demonstrator: 1 – Nb₃Sn coil; 2 – stainless steel coil-yoke spacer; 3 – iron yoke laminations; 4 – aluminum I-clamp; 5 – stainless steel bolted skin; 6 – axial tie rod; 7 – stainless steel end plate with instrumented bullets; 8 – pusher ring.

The average transverse (azimuthal) stress in the pole and mid-plane turns of the coil layers after assembly, cooldown and at the design bore field of 15 T is shown in Table 1. The peak equivalent stress after assembly and after cooldown in pole 1 turn is 133 and 176 MPa respectively. The increase of pre-stress in the pole turns after cooldown is achieved by optimizing the gap between the two iron yoke halves during assembly. The gap is closed after cooldown and stays closed up to 15 T. At the design bore field of 15 T, the peak equivalent stress is in the innermost layer mid-plane turns and is less than 170 MPa.

ALTERNATIVE STRUCTURE

Mechanical structure based on cold iron blocks inside a thick aluminium cylinder and key&bladder assembly technique was selected as an alternative mechanical structure for the FNAL 15 T dipole demonstrator [5]. This structure concept was used for the HD magnet series at LBNL [6] and by US-LARP for several large-aperture high-field quadrupole models [7].

* Work supported by Fermi Research Alliance, LLC, under contract No. DE-AC02-07CH11359 with the U.S. Department of Energy

[#] zlobin@fnal.gov

DESIGN AND TEST OF THE PROTOTYPE TUNER FOR 3.9 GHz SRF CAVITY FOR LCLS II PROJECT

Y. Pischalnikov, E. Borissov, J. C. Yun, FNAL, Batavia, IL 60510, USA

Abstract

Fermilab is responsible for the design of the 3.9 GHz cryomodule for the LCLS-II that will operate in continuous wave (CW) mode [1]. The bandwidth of the SRF cavities will be in the range of 180 Hz. In the tuner design, the slow tuner-mechanism slim blade tuner was adopted, which was originated by INFN for the European XFEL 3.9 GHz [2]. The bandwidth of the SRF cavities for LCLS II will be in the range of 180 Hz and fine/fast tuning of the cavity frequency required. A fast/fine tuner made with 2 encapsulated piezos was also added to the design. The first prototype tuner has been built and went through testing at warm conditions. Details of the design and summary of the tests are presented in this paper.

REQUIREMENT FOR THE TUNER

3.9 GHz Cryomodules (and cavities) designs for the LCLS II Project accumulated its best features from the previous 3.9 GHz cryomodule designed and built by FNAL (for DESY/FLASH) [3] and by INFN for EuXFEL [2]. Parameters of the 3.9 GHz cavity for LCLS II project are presented in the Table 1. The significant difference is in the bandwidth of the cavity. For the LCLS II project half bandwidth must be 90 Hz and peak detuning (with active resonance control) must be less than 30 Hz.

TUNER DESIGN

Schematics of the tuner design are shown in Figure 1. The coarse tuner is a slim blade tuner (with a 1:20 ratio) with a design that is very close to the design of the tuner developed by the INFN for EuXFEL 3rd harmonics cryomodules [2].

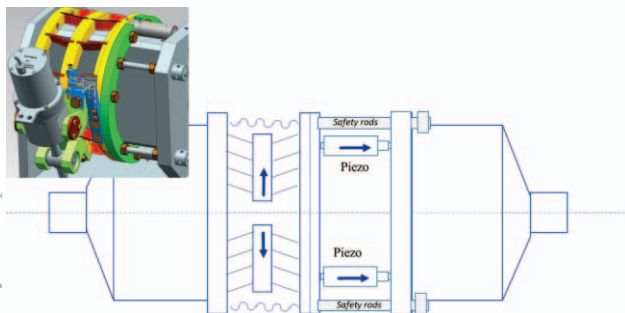


Figure 1: Schematic of the 3.9GHz SRF cavity tuner.

Table 1. 3.9 GHz SRF Cavity and Tuner Parameters

RF frequency	3900	MHz
Operating temperature	2	K
Total voltage available (16 cavities)	80	MV
Average operating gradient	14.5	MV/m
Average Q_0	2.0×10^9	-
Cavity length (L)	0.346	M
R/Q (r/Q)	750 (2168)	Ω (Ω/m)
Geometry constant (G)	275	Ω
<i>Longitudinal Cavity Stiffness</i>	5.4	kN/mm
<i>Cavity Tuning Sensitivity</i>	2.3MHz	mm
Coarse (slow) tuner range	750	kHz
Fine (fast) tuner range	~1	kHz
HOM damped Q value (monopole and dipole)	$\leq 10^6$	-
Lorentz detuning	≤ 0.6	Hz/(MV/m) ²
Number of cryomodules	2	-
Number of cavities per CM	8	-
Cavity alignment requirements (RMS)	0.5	mm
Peak detune (with piezo tuner control)	30	Hz
Required cavity field amplitude stability [†]	0.01	% (rms)
Required cavity field phase stability [†]	0.01	deg (rms)
Q_{ext}	2.2×10^7	-
<i>Half bandwidth of the cavity</i>	90	Hz
Active length of 9 cells	345.96	mm
RF beam power per cavity (@300 μ load)	1.5	kW
RF power needed per cavity	1	kW
Cavity dynamic load	17	W

The major modification of this tuner design introduced by FNAL is adding a fast/fine tuner. Two piezo-stacks have been installed between the slow/blade tuner and the ring welded to the He-vessel. Safety rods have been designed between the cavity end flange and main lever of the tuner. These safety rods protect the cavity during transportation and from non-elastic deformation during cavity/helium vessel system pressure tests.

Set-screws and special washers were included to prevent loosening of the assembly screws during warmup and cool-down cycles [4].

The 3.9 GHz SRF cavity tuner will include the same active components (electromechanical actuators and piezo-stacks) as used on the 1.3 GHz cavity tuner. [4,5]. The electromechanical actuator LVA 52-LCLS II-UHVC-X1 built by Phytron per FNAL specification was found to

*This manuscript has been authorized by Fermi Research Alliance, LLC under Contract N. DE-AC02-07CH11359 with U.S. Department of Energy.
#pischaln@fnal.gov

LCLS-II TUNER ASSEMBLY FOR THE PROTOTYPE CRYOMODULE AT FNAL

Y. Pischalnikov, E. Borissov, T. Khabiboulline, J.C. Yun
FNAL, Batavia, IL 60510, USA

Abstract

The tuner design for LCLS-II has been thoroughly verified and fabricated for used in the LCLS-II prototype modules [1,2]. This paper will present the lessons learned during the installation of these tuners for the prototype module at FNAL, including installation procedures, best practices, and challenges encountered.

TUNER COMPONENTS QC AND PREPARATION STEPS BEFORE INSTALLATION INTO CM

SRF cavity tuner frames arrived from vendor pre-assembled (Figures 1, 2). As the first Quality Control (QC) step tuner frame installed on the cavity/He vessel mock-up" frame (Figure 2). As preparation step for installation on the cavities string tuner frame dis-assembled on three large components (Figure 2).

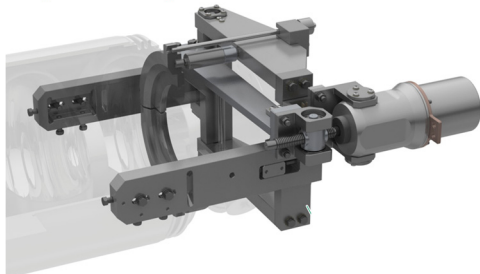


Figure 1: 3-D model of LCLS II tuner.

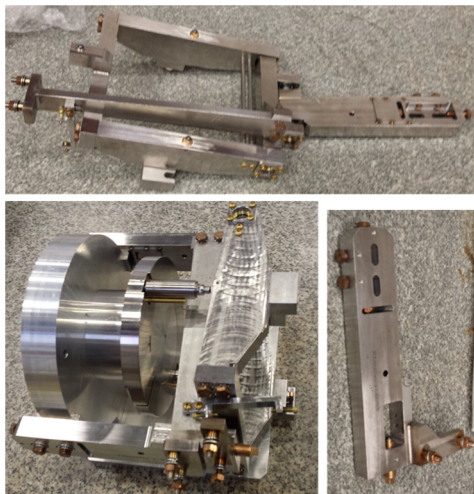


Figure 2: Tuner frame assembled on the aluminium fixture. Partially disassembled tuner before installation on pCM.

The electromechanical actuator LVA 52-LCLS II-UHVC-X1 (and two limit switches) [1, 2] terminated to rad-hard Hypotronics connectors at FNAL (Figure 3). Each actuator tested at FNAL before installation on the tuner. For production cryomodule Phytron, Inc will terminate motor and limit switches wires to 9 pin Hypotronics connectors. Company will also conduct details test of each actuators (including testing each units at LN2 temperature).

The 16 piezo-actuators P-844K075 [1, 2] were terminated to rad-hard Hypotronics connectors and tested at FNAL before to be install on prototype cryomodule (pCM). Each piezo-capsule has two $10*10*18 \text{ mm}^3$ piezo-stack and following parameter was measured for each 19 mm long piezo-stack: capacitance, dissipation factor, stroke for $V=60 \text{ V}$.

For production cryomodule Physik Instrumente (PI) will supply piezo-capsules already terminated to connector and tested. Protocol for testing agreed between PI and LCLS II project.



Figure 3: Active components of the tuner: electromechanical actuator and piezo-capsule.

TUNERS INSTALLATIONS AND CHALLENGES

Tuners installed many times on the single dressed cavity but installation on the cold mass was much challenging adventure: tight space, significant amount of the other cavity components.

Our previous experience reflected into travellers / tuner installation procedure. It roughly divided into several steps (Figure 4):

1. Removing safety brackets (that protect cavity during previous production steps)
2. Installation on the He vessel right tuner arm and main levers around beam pipe (Figure 4 (A))
3. Installation on the He vessel tuner left arm and connecting together left and right side of tuner (Figure 4 (B))

*This manuscript has been authorized by Fermi Research Alliance, LLC under Contract N. DE-AC02-07CH11359 with U.S. Department of Energy.

#pischaln@fnal.gov

DESIGN OF THE LBNF BEAMLINER TARGET STATION*

S. Tariq[†], K. Ammigan, K. Anderson, S. A. Buccellato, C. F. Crowley, B. D. Hartsell, P. Hurh, J. Hylen, P. Kasper, G. E. Krafczyk, A. Lee, B. Lundberg, A. Marchionni, N. V. Mokhov, C. D. Moore, V. Papadimitriou, D. Pushka, I. Rakhno, S. D. Reitzner, V. Sidorov, A. M. Stefanik, I. S. Tropin, K. Vaziri, K. Williams, R. M. Zwaska, Fermilab, Batavia, IL 60510, USA
C. Densham, STFC/RAL, Didcot, Oxfordshire, OX11 0QX, UK

Abstract

The Long Baseline Neutrino Facility (LBNF) project will build a beamline located at Fermilab to create and aim an intense neutrino beam of appropriate energy range toward the DUNE detectors at the SURF facility in Lead, South Dakota. Neutrino production starts in the Target Station, which consists of a solid target, magnetic focusing horns, and the associated sub-systems and shielding infrastructure. Protons hit the target producing mesons which are then focused by the horns into a helium-filled decay pipe where they decay into muons and neutrinos. The target and horns are encased in actively cooled steel and concrete shielding in a chamber called the target chase. The reference design chase is filled with air, but nitrogen and helium are being evaluated as alternatives. A replaceable beam window separates the decay pipe from the target chase. The facility is designed for initial operation at 1.2 MW, with the ability to upgrade to 2.4 MW, and is taking advantage of the experience gained by operating Fermilab's NuMI facility. We discuss here the design status, associated challenges, and ongoing R&D and physics-driven component optimization of the Target Station.

INTRODUCTION

The Target Station is a central component of the LBNF Beamline and it is expected to produce the highest power neutrino beam in the world. The driving physics consideration is the study of long baseline neutrino oscillations. The initial operation of the facility will be at a beam power of 1.2 MW on the production target, however some of the initial implementation will have to be done in such a manner that operation at 2.4 MW can be achieved without major retrofitting [1]. In general, components of the Target Station which cannot be replaced or easily modified after substantial irradiation at 1.2 MW operation are being designed for 2.4 MW, mainly the shielding around the target chase and the associated remote handling equipment. Approximately 40% of the total beam power is deposited in the target chase and surrounding shielding. Experience gained from operating Fermilab's NuMI target facility [2] is being extensively employed in the design of the LBNF facility.

The Target Station design has to implement a stringent radiological protection program for the environment, workers and members of the public. The relevant radiological concerns: prompt dose, residual dose, air activation, and water activation are being extensively modelled (to-

gether with NuMI benchmarking) and the results incorporated in the system design. Tritium build-up in the shielding infrastructure has to be managed and the choice of gas in the target chase has to be selected taking into consideration the impact on air emissions plus any corrosion related issues due to the ionizing radiation. The replaceable beam window separating the target chase from the helium-filled decay pipe needs to seal reliably and adequately between these two beamline volumes.

The reference design utilizes a NuMI-style two horn system and a two-interaction length carbon fin target. Further physics-driven component optimization work has shown that a three horn focusing system with a longer target provides improvements in the neutrino flux.

Radiation damage, cooling of elements, radionuclide mitigation, remote handling and storage of radioactive components are all essential considerations for the design of the LBNF Target Station. This paper gives a snapshot of the present design status of the Target Station and discusses the associated challenges, ongoing R&D, and physics-driven optimization of the target and horn system.

STATUS OF THE TARGET STATION DESIGN

LBNF/DUNE obtained CD-1 approval in November 2015 for the reference design. A longitudinal section through the reference LBNF Target Station design is shown in Fig. 1. It closely follows the design of the NuMI focusing system where components are loaded from the top. It includes in order of placement (1) a beryllium window that seals off and separates the evacuated primary beamline from the neutrino beamline, (2) a baffle collimator assembly to protect the target and the horns from mis-steered beam, (3) a 95 cm long target, (4) two magnetic horns. The LBNF horns operate at higher current (230 kA) and lower pulse width (0.8 ms) compared to NuMI. These elements are all located inside a heavily shielded, air-filled, air/water-cooled chamber, called the target chase, that is isolated from the decay pipe at its downstream end by a replaceable, thin, metallic window. The target chase has sufficient length and cross-section to accommodate an optimized focusing system (currently being studied). In order to mitigate potential corrosion issues and release of air-borne radionuclides we are studying alternative gases (nitrogen and helium) for the target chase atmosphere, and a complete conceptual design is currently being developed for the nitrogen-filled option. The remote handling facilities in the Target Hall include a shielded work-cell for remotely exchanging radioactive components and a storage rack

* Work supported by Fermi Research Alliance, LLC under Contract No. DE-AC02-07CH11359 with the United States Department of Energy.

[†] tariq@fnal.gov

DESIGN OF THE HIGH BETA 650 MHz CRYOMODULE - PIP II *

V. Roger[†], T. H. Nicol, Y. Orlov

Fermi National Accelerator Laboratory, Batavia, IL 60510, USA

Abstract

In this paper the design of the high beta 650 MHz cryomodule will be presented. This cryomodule is composed of six 5-cell 650 MHz elliptical cavities, designed for $\beta=0.92$. These cryomodules are the last elements of the Super Conducting (SC) linac architecture which is the main component of the Proton Improvement Plan-II (PIP-II) at Fermilab.

This paper summarizes the design choices which have been done. Mechanical, thermal and cryogenic analyses have been performed to ensure the proper operation. First the concept of having a strong-back at room temperature has been validated. Then the heat loads have been estimated and all the components have been integrated inside the cryomodule by designing the supports, the beam line, the thermal shield and the cryogenic lines. All these elements and the calculations leading to the design of this cryomodule will be described in this paper.

INTRODUCTION

The high beta 650 MHz cryomodule is based on the design of the SSR1 325 MHz cryomodule with a strong-back at room temperature supporting the cavities [1]. These two cryomodules are parts of the SC linac architecture of PIP II in order to accelerate a beam current in the energy range 11 MeV - 800 MeV. The high beta 650 MHz cryomodule is composed of six superconducting 5-cell 650 MHz elliptical cavities. One particularity of these cavities is that the chimney makes an angle with the vertical axis. This requirement comes from the test station for which without this angle the cavity would not fit.

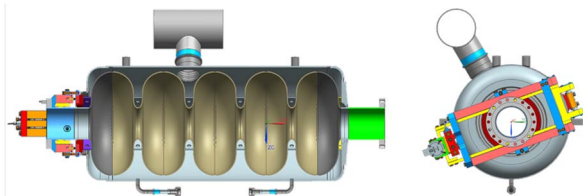


Figure 1: Cross section of the high beta 650 MHz dressed cavity with its tuner.

These cavities will be operated at 2K. Cryogenics lines have been designed in order to meet the requirements according to heat-loads and flux trapping during the cool-down.

This cryomodule is 9.8 m long with a diameter of 1.2 m. Thus insertion tooling of the cold mass inside the vacuum vessel has been designed and particular attention has been

taken considering the shrinkage of the material during the cool down.

MECHANICAL DESIGN

This cryomodule shares several elements of design with the SSR1 cryomodule in order to minimize the design cost and to use similar tooling and procedures during the assembly and operation.

Description of the Cryomodule

Figure 2 presents the cryomodule with its main components. One of the main issues during the design stage was to integrate the two phase helium pipe with the chimney. For this a custom elbow with a belled connection has been used in order to be able to weld the chimney once the cold mass is inside the vacuum vessel.

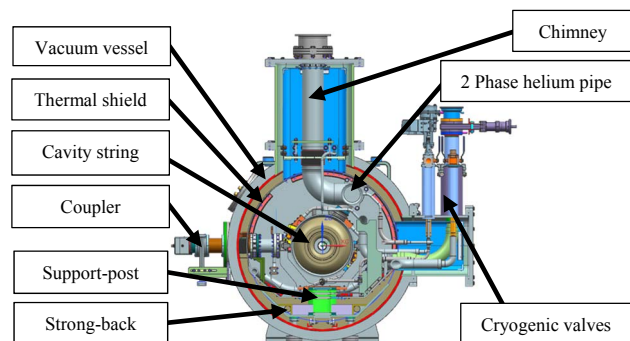


Figure 2: Cross-section of the high beta 650 MHz cryomodule.

Vacuum Vessel Design

Two big openings are located in the middle of the vessel. The first one is dedicated to the cryogenic valves and the other one to the chimney and the heat exchanger in order to reach 2K. Other ports are dedicated to the coupler, tuner, instrumentation, and relief valve.

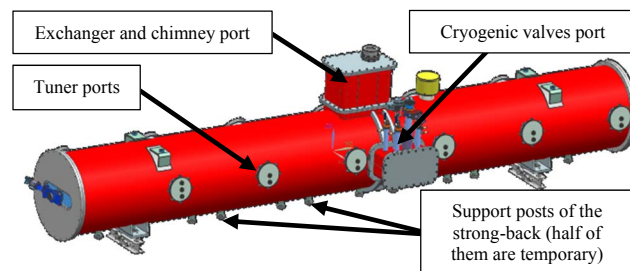


Figure 3: Vacuum vessel.

The alignment of the cavities will be done on the strong-back outside the vacuum vessel. To keep the alignment the strong-back needs to be supported in the exact same way when it will be inside the vessel. For this laser trackers will

* Work supported by Fermi Research Alliance, LLC under Contract No. DE AC02 07 CH11359 with the United States Department of Energy
[†] vroger@fnal.gov

A 600 VOLT MULTI-STAGE, HIGH REPETITION RATE GaN FET SWITCH*

D. Frolov, H. Pfeffer, G. Saewert[†], Fermilab, Batavia, USA

Abstract

Using recently available GaN FETs, a 600 Volt three-stage, multi-FET switch has been developed having 2 nanosecond rise time driving a 200 Ohm load with the potential of approaching 30 MHz average switching rates. Possible applications include driving particle beam choppers kicking bunch-by-bunch and beam deflectors where the rise time needs to be custom tailored. This paper reports on the engineering issues addressed, the design approach taken and some performance results of this switch.

INTRODUCTION

Currently available gallium nitride (GaN) transistors are at least a factor of five times both lower in capacitance and faster in switching speed than MOSFETs. This technology enables drivers for particle beam deflecting devices to be built that achieve new performance levels in terms of speed. Although the development of this switch was targeted for driving a particular beam deflector at Fermilab, pulse generators in general employ switches with which high switching speed and high voltage are desired.

One requirement at Fermilab for which a hard-switching driver has been proposed is a fast beam chopper in the 2.1 MeV Medium Energy Beam Transport (MEBT) section of what is now referred to as PIP-II Injector Test facility at Fermilab [1]. This is to be a CW operating LINAC delivering unique beam patterns concurrently to numerous experiments. Bunch pattern creation will be done on a bunch-by-bunch basis by the MEBT chopper having 6.15 ns bunch spacing (162.5 MHz). Operational requirements include greater than 500 Volts on each traveling wave kicker plate, more than 80% beam chopped out, and particle removal to better than 10^{-4} of each chopped-out bunch [2]. The ramifications on a hard-switching circuit as the driver for this chopper are to have an absolute worst case 4.0 ns rise/fall time (5-95%), be able to switch at 81.25 MHz in 100 ns bursts at 1 μ s intervals and handle average switching rates of more than 30 MHz when the PIP-II LINAC eventually operates CW.

Having the ability to build a switch in house is convenient for building deflection plate drivers that must ramp linearly at controlled rates rather than simply turn on as fast as possible. A version of this switch is under development for an electron beam profiler in the Fermilab Main Injector [3]. A pair of deflection plates needs to be ramped to plus and minus 500 V linearly in 18 ns to sweep an electron beam longitudinally across proton bunches.

A previous attempt had been made to build a fast switch

for this PIP-II MEBT chopper using a different design approach. This paper reports on achieving better results by driving each FET stage individually and the employment of different GaN FETs rated for higher voltage.

DESIGN REQUIREMENTS

This switch was designed to meet several requirements that include:

- (1) Operation to voltages of at least 500 V,
- (2) Turn-on transition times of 2 ns,
- (3) The capability of switching at tens of megahertz CW and hopefully over 30 MHz,
- (4) Pulse patterns of virtually any duty factor
- (5) Pulse widths down to 2 ns at flat top.

Additionally, understanding that to operate at such high CW switching rates, the switch needs to be constructed of multiple FETs in series to share the power dissipation. So the design needed to include the ability to assure that multiple FETs can be made to be timed simultaneously and held to small fractions of a nanosecond. Development of this switch thus far were constructions of 2- and 3-FET assemblies.

Certainly lead inductance needs to be minimized. So this switch design needs to be physically as small as possible.

DESIGN ISSUES

A number of design issues must be addressed besides switching fast. Foremost are switching losses. At tens of megahertz and 600 Volts these losses are high even for GaN to use only one FET as a switch. A FET's internal dissipation when discharging its own drain-to-source (Cds) capacitance is $0.5C_{ds}V^2f = 108$ W; where $C_{ds} = 20$ pF, and $f = 30$ MHz switching CW. We are referring to parameters for the GS66502 GaN FET from GaN Systems, Inc., used in this design. Add to this the transition switching loss that arises during turn-on and turn-off. There are 36 Watts transition switching losses with a 4.0 ns rise time driving a 3.0 A load at 30 MHz CW. (These losses drop proportionately with rise time, however.) Not a switching loss, but each FET's drain-to-source I^2R loss conducting 3 A DC is only 2 W.

It is interesting that total switching losses of a multi-FET in series are less than if the switch is comprised of only one FET. The reduction in Cds switching loss is evident from the expression for the total when three FETs are in series:

$$3 * \frac{1}{2} C_{ds} \left(\frac{V}{3}\right)^2 f = \frac{1}{3} * \frac{1}{2} C_{ds} V^2 f \text{ (Watts).}$$

Where V is the operating voltage, and f is switching rate, the total is 1/3 compared when only using one FET. Share

* Work supported by Fermi Research Alliance, LLC under Contract No. De-AC02-07CH11359 with the US Department of Energy.

[†] saewert@fnal.gov

QUENCH TRAINING ANALYSIS OF Nb₃Sn ACCELERATOR MAGNETS*

S. Stoynev[†], K. Riemer, A. V. Zlobin, FNAL, Batavia, USA

Abstract

Present Nb₃Sn accelerator magnets show long training compared to traditional NbTi magnets. It affects the required design margin or the nominal operation field resulting in higher magnet production and operational costs. FNAL has initiated a study aiming to find and explain correlations between magnet design, fabrication and performance parameters based on existing Nb₃Sn magnet training data. The paper introduces the core investigation points and shows first results.

INTRODUCTION

Nb₃Sn accelerator magnet technology has made significant progress during the past decades. Thanks to that 11-12 T Nb₃Sn dipoles and quadrupoles are planned to be used in accelerators such as LHC in near future for the luminosity upgrade [1], [2] and in a longer term for the LHC energy upgrade or a Future Circular Collider [3]. However, all the state of the art Nb₃Sn accelerator magnets show quite long training. This specific feature significantly raises the required design margin or limits the nominal operation field of Nb₃Sn accelerator magnets and, thus, increases their cost.

To resolve the problem of Nb₃Sn accelerator magnet training FNAL has launched a study aiming to analyze the relatively large amount of Nb₃Sn magnet test data accumulated at the FNAL magnet test facility. The ultimate goal of this study is to correlate magnet design and manufacturing features and magnet material properties with training performance parameters which would allow in the future optimizing the magnet design and fabrication to minimize or even eliminate magnet training. This paper describes the general strategy of the analysis, discusses the main parameters and parametrization techniques and presents first results based on partial data processing.

DATASET

At current times there are several tens of accelerator magnets based on Nb₃Sn technology produced worldwide. A big fraction of those magnets were fabricated and tested at FNAL albeit in collaboration with others. Part of the initial models suffered from unavoidable first-attempt missteps and data should be carefully vetted before accepting them for analysis. For that reason magnets that were tested latest in time are the ones to start analysing first. Currently MBHS [4] series magnets (dipoles and mirror models) are fully included and HFDA [5] (dipoles and mirror models), TQC [6], HQ [7], [8] and MQXF [2] series (quadrupoles and mirror models) are partially in-

cluded in the study. Further plans are to include data from outside FNAL, notably from LBNL and CERN tests.

TRAINING PARAMETRIZATION

To be able to correlate magnet parameters with its training, parametrization of the training evolution is needed. Figure 1 shows an example of magnet training curve and its possible parametrization. Training examples given here and later are from MBHSP02 – a dipole model from the 11 T program at FNAL [4], [9]. It is worth noting that training is sometimes conducted at different temperatures. Magnet training could be normalized to magnet short sample limit (SSL). In the analysis, those points were taken into account as well.

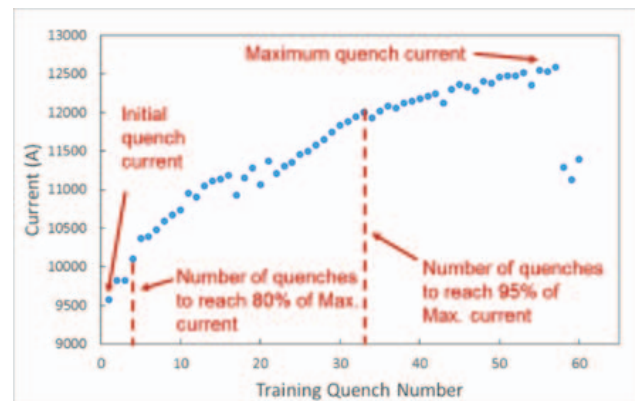


Figure 1: Magnet training and training curve parametrization.

The parametrization of magnet training curves chosen in this study includes the following parameters:

- First quench current and highest quench current

It is assumed that the magnet remembers its maximum current after the training cycle which is sometimes not completely accurate. If the magnet is far from trained or if the training was unsuccessful for other reasons (damaged cable, etc.) a careful consideration about including those data is needed.

- Number of training quenches to chosen current

Currently we work with 80% and 95% from the training plateau. The latter is considered a threshold beyond which a magnet is nearly at the plateau. The former serves as a threshold for assessing initial (typically faster) training. Both are subject to further optimization.

- Current differentials

The difference between currents in consecutive training quenches is called current differential. An example of current differentials vs. quench number is shown in Fig. 2. The points from consecutive quenches with significant magnet temperature differences (typically 1.9 K vs 4.5 K) are removed from consideration and analysed independently. Detraining quenches have negative differential

* Work supported by Fermi Research Alliance, LLC, under contract No. DE-AC02-07CH11359 with the U.S. Department of Energy

[†] stoyan@fnal.gov

FIELD QUALITY MEASUREMENTS IN THE FNAL TWIN-APERTURE 11 T DIPOLE FOR LHC UPGRADES*

T. Strauss, G. Apollinari, E. Barzi, G. Chlachidze, J. Di Marco, F. Nobrega, I. Novitski, S. Stoynev, D. Turrioni, G. Velev, A.V. Zlobin[#], FNAL, Batavia, IL 60510, USA
 B. Auchmann, S. Izquierdo Bermudez, M. Karppinen, L. Rossi, F. Savary, D. Smekens
 CERN, CH-1211 Geneva 23, Switzerland

Abstract

FNAL and CERN are developing an 11 T Nb₃Sn dipole suitable for installation in the LHC to provide room for additional collimators. Two 1 m long collared coils previously tested at FNAL in single-aperture dipole configuration were assembled into the twin-aperture configuration and tested including magnet quench performance and field quality. The results of magnetic measurements are reported and discussed in this paper.

INTRODUCTION

The development of the 11 T Nb₃Sn dipole for the LHC collimation system upgrade, started in 2011 as a collaborative effort of FNAL and CERN magnet teams [1]. The recent R&D status of the project was reported in [2]. A single-aperture 2-m long dipole demonstrator and two 1-m long dipole models have been assembled and tested at FNAL in 2012-2014. The 1 m long collared coils were then assembled into the twin-aperture configuration and tested in 2015-2016 [3]. The first magnet test was focused on the quench performance of twin-aperture magnet configuration including magnet training, ramp rate sensitivity and temperature dependence of magnet quench current [4]. In the second test performed in July 2016 field quality in one of the two magnet apertures has been measured and compared with the data for the corresponding single-aperture model. These results are reported and discussed in this paper.

MAGNET DESIGN AND PARAMETERS

The design concepts of FNAL 11 T Nb₃Sn dipole in single- and twin-aperture configurations are described in [1, 5]. Fabrication details and performance parameters of the two configurations are compared in [3, 6].

Magnet design is based on two-layer coils, stainless steel collar and cold iron yoke supported by strong stainless steel skin. The twin-aperture magnet MBHDP01 consists of two collared coils inside a common iron yoke with coils 5 and 7 around one aperture and coils 9 and 10 around the other aperture. Coil position inside the yoke and coil electrical connections in the twin-aperture magnet MBHDP01 are shown in Fig. 1. The coils 5 and 7 and the coils 9 and 10 were previously tested in single-aperture dipole models MBHSP02 and MBHSP03 respectively.

* Work supported by Fermi Research Alliance, LLC, under contract No. DE-AC02-07CH11359 with the U.S. Department of Energy and European Commission under FP7 project HiLumi LHC, GA no.284404
[#] zlobin@fnal.gov

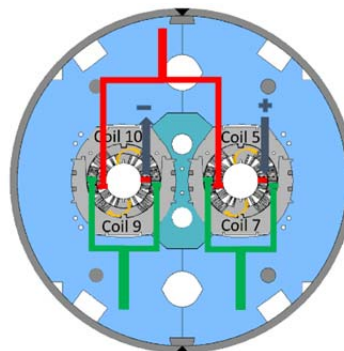


Figure 1: Coil layout and connection inside the yoke.

MAGNETIC FIELD MEASUREMENT

MBHDP01 was tested at the FNAL Vertical Magnet Test Facility. Magnetic measurements were performed using 26 mm and 130 mm long, and 26 mm wide 16-layer Printed Circuit Board (PCB) probes [7]. The probe rotation speed was 1 Hz. The resolution of magnetic measurements is estimated better than 0.5 unit. The rotating coil system was installed in the aperture with coils 9 and 10.

The field induction B in magnet aperture was represented in terms of harmonic coefficients defined in a series expansion using the complex functions

$$B_y + iB_x = B_1 10^{-4} \sum_{n=1}^{\infty} (b_n + ia_n) \left(\frac{x + iy}{R_{ref}} \right)^{n-1}, \quad (1)$$

where B_x and B_y are horizontal and vertical field components in the Cartesian coordinate system, b_n and a_n are $2n$ -pole normal and skew harmonic coefficients at the reference radius $R_{ref}=17$ mm.

RESULTS AND DISCUSSION

Figures 2-4 show the dependences of the magnet Transfer Function ($TF=b_1/I$) and low-order “normal” (b_2, b_3, b_4, b_5) and “skew” (a_2, a_3) field harmonics measured in MBHDP01 and MBHSP03 vs. the magnet current. The measurement data are compared with 2D and 3D calculations of geometrical harmonics and iron saturation effect in the twin-aperture MBHDP01 using ROXIE [8].

The measurements were done in current loops with the current ramp rate of 20 A/s. The effect of eddy currents on the field quality was studied previously in single-aperture models MBHSP02 and 03 by performing measurements in current loops with current ramp rates up to 80 A/s. It was found that this effect is small thanks to

THYRATRON REPLACEMENT*

Ian Roth, Marcel Gaudreau, Michael Kempkes, Matthew Munderville, Rebecca Simpson,
Diversified Technologies, Inc., Bedford, MA, USA

Abstract

Semiconductor thyristors have long been used as a replacement for thyratrons in low power or long pulse RF systems. To date, however, such thyristor assemblies have not demonstrated the reliability needed for installation in short pulse, high peak power RF stations used with many pulsed electron accelerators. The fast rising current in a thyristor tends to be carried in a small region, rather than across the whole device, and this localized current concentration can cause a short circuit failure. An alternate solid-state device, the insulated-gate bipolar transistor (IGBT), can readily operate at the speed needed for the accelerator, but commercial IGBTs cannot handle the voltage and current required. It is, however, possible to assemble these devices in arrays to reach the required performance levels without sacrificing their inherent speed. Diversified Technologies, Inc. (DTI) has patented and refined the technology required to build these arrays of series-parallel connected switches. DTI is currently developing an affordable, reliable, form-fit-function replacement for the klystron modulator thyratrons at SLAC capable of pulsing at 360 kV, 420 A, 6 μ s, and 120 Hz.

BACKGROUND

The Stanford Linear Collider (SLC) has used thyratrons in its klystron modulators since its inception in 1963. While the thyratrons function, they need replacement every 10,000 hours at a cost of \$13,000 each, plus labor. Furthermore, periodic maintenance is required to adjust their reservoir heater voltage over the thyristor lifetime. As the Stanford Linear Accelerator Center (SLAC) continues to run its accelerator over the next two decades, replacing the thyratrons with a solid-state switch that would last 25 years or more, and does not need maintenance, would provide significant savings – both in the avoided cost of thyratrons as well as the labor in replacing and adjusting them.

SLAC is presently funding the development of a solid-state switch, based on thyristor technology to replace the thyratrons (Figure 1), meeting the requirements of existing klystron modulators (Table 1). The difficulty is that a fast rising current in a thyristor tends to be carried in a small region, rather than across the whole device, and this localized current concentration can cause a short circuit failure.

*Work supported by DOE under contract DE-SC0011292



Figure 1: DTI solid-state replacement for the L-4888 thyristor used at SLAC. The switch, which operates at 48 kV and 6.3 kA, fits in the same location as the legacy thyristor assembly.

Table 1: ESS Klystron Modulator Requirements

Specification	
Voltage	48 kV
Current	6.3 kA
Pulse Width	6 μ s
Risetime	1 μ s, 10 A/ μ s
Frequency	120 Hz

DESIGN

An alternate solid-state device, the insulated-gate bipolar transistor (IGBT), can readily operate at the speed needed for the accelerator, but commercial IGBTs cannot handle the voltage and current required. It is, however, possible to assemble these devices in arrays to reach the required performance levels without sacrificing their inherent speed. Diversified Technologies, Inc. (DTI) has patented and refined the technology required to build these arrays of series-parallel connected switches. DTI has shipped more than 500 systems leveraging this tech-

7: Accelerator Technology Main Systems

T31 - Subsystems, Technology, and Components, Other

DESIGN AND OPERATION OF PULSED POWER SYSTEMS BUILT TO ESS SPECIFICATIONS

Ian Roth, Marcel Gaudreau, Michael Kempkes, Matthew Munderville, Rebecca Simpson
Diversified Technologies, Inc., Bedford, MA, USA

Julien Domenge, Jean-Luc Lancelot, SigmaPhi Electronics, Vannes, France

Abstract

Diversified Technologies, Inc. (DTI), in partnership with SigmaPhi Electronics (SPE) has built three long pulse solid-state klystron transmitters to meet spallation source requirements. Two of the three units are installed at CEA Saclay and the National Institute of Nuclear and Particle Physics (IN2P3), where they will be used as test stands for the European Spallation Source (ESS). The systems delivered to CEA and IN2P3 demonstrate that the ESS klystron modulator specifications (115 kV, 25 A per klystron, 3.5 ms, 14 Hz) have been achieved in a reliable, manufacturable, and cost-effective design. There are only minor modifications required to support transition of this design to the full ESS Accelerator, with up to 100 klystrons. The systems will accommodate the recently-determined increase in average power (~660 kW), can offer flicker-free operation, are equally-capable of driving Klystrons or MBIOTs, and are designed for an expected MTBCF of over ten years, based on operational experience with similar systems.

INTRODUCTION

Diversified Technologies, Inc. (DTI), in partnership with SigmaPhi Electronics (SPE), has designed and installed advanced, high voltage solid-state modulators for European Spallation Source (ESS)-class klystron pulses (Figure 1). These klystron modulators use a series-switch driving a pulse transformer, with an advanced, patent-pending regulator to maintain a precise cathode voltage as well as a constant load to the external power grid. The success of the design in meeting the ESS pulse requirements (Table 1) is shown in Figure 2.



Figure 1: DTI's prototype solid-state ESS-class klystron modulator, developed under a DOE SBIR grant.

Table 1: ESS Klystron Modulator Requirements

Specification	
Voltage	-115 kV
Current	25 A per Klystron
Pulse Width	3.5 ms
Frequency	14 Hz (max)
Average Power	160 kW (per Klystron)
Droop	< 1%
Pulse Repeatability	< 0.1%

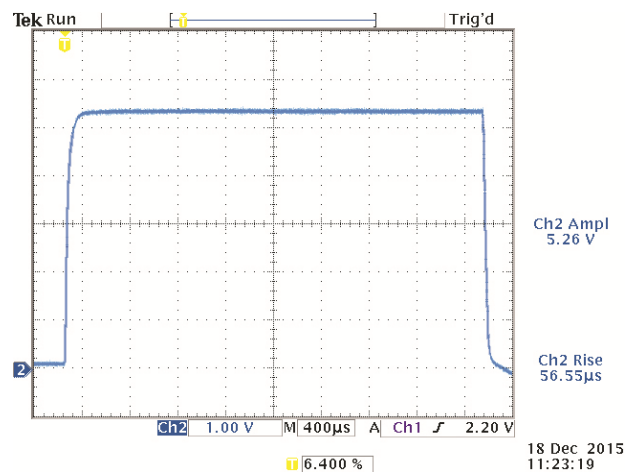


Figure 2: Modulator pulse at 108 kV, 3.5 ms, 0.07% flat-top into a Thales TH2179A klystron during site acceptance testing at IN2P3, 18 December 2015.

The DTI/SPE klystron modulator is now a fully proven design, delivering significant advantages in klystron performance through:

- Highly reliable operation, demonstrated in hundreds of systems worldwide, and predicted to significantly exceed ESS requirements
- Flicker- and droop-free operation over a range of operating parameters
- All active electronics in air for easy maintenance

With the delivery of these initial modulators, the transition to production for the ESS system itself is straightforward.

DESIGN

The heart of the DTI/SPE modulator design is a high voltage solid-state switch driving a pulse transformer. The switch is made of seven series-connected IGBT modules, and operates at 6.7 kV. This design enables a measured

BEAM COUPLING IMPEDANCE CHARACTERIZATION OF THIRD HARMONIC CAVITY FOR ALS UPGRADE*

T. Luo[†], K. Baptiste, M. Betz, J. Byrd, S. De Santis,
S. Kwiatkowski, S. Persichelli, Y. Yang, LBNL, Berkeley, CA 94720, USA

Abstract

The ALS upgrade to a diffraction-limited light source (ALS-U) depends on the ability to lengthen the stored bunches to limit the emittance growth and increase the beam life time. In order to achieve lengthening in excess of four-fold necessary to this end, we are investigating the use of the same passive 1.5 GHz normal-conducting RF cavities currently used on the ALS. While the upgraded ring RF parameters and fill pattern make it easier as long as the beam-induced phase transient is concerned, the large lengthening factor and the strongly non-linear lattice require particular attention to the cavities contribution to the machine overall impedance budget. In this paper we present our estimates of the narrow-band impedance obtained by numerical simulation and bench measurements of the cavities' resonant modes.

INTRODUCTION

The ALS upgrade to a diffraction-limited light source (ALS-U) [1] depends on the ability to lengthen the stored bunches to limit the emittance growth and increase the beam life time. In order to achieve lengthening in excess of four-fold necessary to this end, we are investigating the use of the same passive 1.5 GHz normal-conducting RF cavities currently used on the ALS. While the upgraded ring RF parameters and fill pattern make it easier as long as the beam-induced phase transient is concerned [2], the large lengthening factor and the strongly non-linear lattice require particular attention to the cavities contribution to the machine overall impedance budget. In this paper we present our estimates of the narrow-band impedance obtained by numerical simulation and bench measurements of the cavities' resonant modes.

The short range wake of the cavity has been discussed in [3]. In this paper, we will focus on the narrow band impedance below the beam pipe cutoff frequency.

To characterize the beam coupling impedance of the cavity, we have simulated its wakefield and beam coupling impedance with CST [4] to identify the resonant modes with significant contribution to the beam impedance. Low power RF bench measurement has been carried out on three cavities identical to the ones currently installed in the ALS. Combining the CST simulation and the bench measurement results, we have estimated the beam coupling impedances of the undamped TM110 modes in the cavity.

* Work supported by the Office of Science, U.S. Department of Energy under DOE contract number DE-AC02-05CH11231

[†] tluo@lbl.gov

NUMERICAL RF SIMULATION

To identify the higher order modes with considerable impedances, we have carried out the wakefield simulation with CST Particle Studio. The cavity model is built from the mechanical drawings with piston tuner and two HOM dampers, as shown in Figures 1 and 2. In the wakefield simulation, the beam is placed 5 mm away in the x direction from the cavity center. The longitudinal and transverse wakefields are integrated along the cavity center. Since the beam pipe cutoff frequencies are 3.5 GHz for TE01 mode and 4.6 GHz for TM11 mode, we have limited the analysis to frequencies under 5 GHz, as shown in Figures 3 and 4.

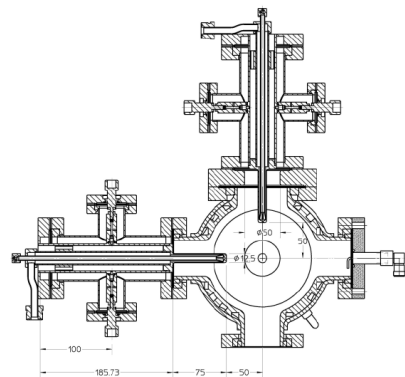


Figure 1: Mechanical drawing of 3rd harmonic cavity.

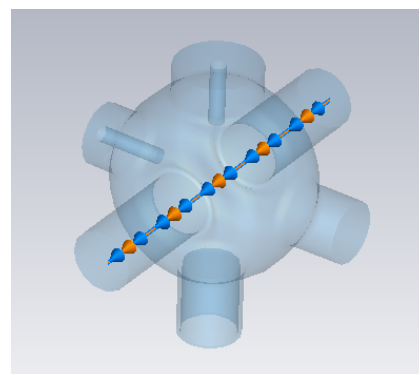


Figure 2: CST simulated model (wakefield solver).

From the wakefield simulation results, we can see that:

1. Without the HOM damper, the major contributors to the beam coupling impedances are longitudinal modes TM011 at 2.3 GHz and transverse modes TM110 at 2.3 GHz, TM120 at 2.9 GHz and TM121 at 3.4 GHz.
2. The fundamental mode TM010 at 1.5 GHz is little affected by HOM dampers.
3. The HOM dampers effectively suppresses the longitudinal mode TM011, and transverse modes TE111,

PERSISTENT CURRENT EFFECTS IN RHIC Arc DIPOLE MAGNETS OPERATED AT LOW CURRENTS*

X. Wang[†], S. Caspi, S. A. Gourlay, G.L. Sabbi, LBNL, Berkeley, CA 94720, USA
A. K. Ghosh, R. C. Gupta, A. K. Jain, P. Wanderer, BNL, Upton, NY 11973, USA

Abstract

The Relativistic Heavy Ion Collider (RHIC) arc dipoles at Brookhaven National Laboratory are operated at low field for low energy Au-Au studies. Indications of strong nonlinear magnetic fields have been observed at these low currents due to the persistent current effects of superconducting NbTi filaments. We report the details of the measurement and calculation of the field errors due to persistent current effect. The persistent current induced field errors calculated with a model based on the strand magnetization data agree well with the measurements of a spare arc dipole magnet. The dependence of the persistent current effects on the park current is calculated based on the validated model.

INTRODUCTION

The arc dipole magnets of the Relativistic Heavy Ion Collider (RHIC) at Brookhaven National Laboratory (BNL) are operated at low currents (112 to 218 A) for low energy Au-Au studies. Strong non-linear magnetic fields have been observed at these low currents. These non-linear fields result from the magnetization of superconducting filaments in the magnet conductor (persistent current effect). To understand the magnetization effects and achieve the best machine performance, the field errors were measured using a spare arc dipole magnet at low currents and compared to a computational model. Here we describe the model and the comparison with measurements. With the validated model, we calculate the dependence of the persistent current effect on the park current from which the current starts ramping up toward the operation current after the down ramp. Adjusting the park current can be an option to optimize the RHIC performance at low operation energy.

The RHIC arc dipole was wound with Rutherford cables made of multifilamentary NbTi strands. Table 1 summarizes the NbTi strand parameters relevant for the persistent current effects. Reference [1] reviews the RHIC magnet system, including the conductor, cable and arc dipole.

MAGNETIC MODEL

Several models have been developed to calculate the persistent current effects for superconducting accelerator magnets based on NbTi and Nb₃Sn conductors [2–8]. Here we use an analytic approach based on the critical state model [9, 10] to calculate the persistent current effects [2].

* The work at BNL was supported by Brookhaven Science Associates, LLC under Contract Number DE-AC02-98CH10886 and DE-SC0012704 with the U.S. Department of Energy (DOE). The work at LBNL was supported by the U.S. DOE under Contract Number DE-AC02-05CH11231.

[†] xrwang@lbl.gov

Table 1: Main Parameters for the NbTi Strands Used in the RHIC Arc Dipole Magnets

Item		Value
Wire diameter (mm)	d_W	0.648
Filament diameter (μm)	d_F	6
Filament number in a strand	N_F	3510
Cu/Non-Cu ratio	λ	2.25
Strand number in a cable	N_S	30

The magnetic field in the straight section of a long dipole magnet is two dimensional (2D). On the 2D magnet cross section, each strand is approximated as a line current located at the strand center. The field on each strand is first determined by summing the field generated by all other strands using the Biot-Savart law. This field then determines the induced persistent current in each filament of the strand. The sum of the fields generated by the persistent current in each filament gives the strand contribution to the persistent current effect.

Two parameters are required to determine the persistent current effect from each filament. The first one is the shape of the shielding currents in the superconducting filament before it is fully penetrated by the external magnetic field. We approximate the central region in the filament, initially current free, to an ellipse using Wilson's model [2, 11]. The eccentricity of the ellipse, ϵ , can be determined by

$$B_s = -\frac{\mu_0 J_c d_F}{\pi} \left(1 - \sqrt{1 - \epsilon^2} \frac{\arcsin \epsilon}{\epsilon} \right), \quad (1)$$

where B_s is the field generated by the shielding current at the center of the filament to cancel the applied field [2]. J_c is the critical current density of the NbTi filament and d_F is the filament diameter (Table 1). The eccentricity can be determined based on a series expansion of the tangent function [12, 13].

The second parameter is the filament J_c as a function of applied field, which can be determined from the strand magnetization [14]. For a filament fully penetrated by external magnetic field, its magnetization and J_c can be related through

$$M(B) = \frac{2}{3\pi} J_c(B) d_F \frac{1}{1 + \lambda}, \quad (2)$$

where λ is the Cu/Non-Cu ratio (Table 1) [2]. Two sets of $J_c(B)$ data can be obtained from the measured strand magnetization: one from the up-ramp branch with increasing applied magnetic field and the other from the down-ramp branch. We then approximate the $J_c(B)$ data with the

HIGH-EFFICIENCY 500-W RF-POWER MODULES FOR UHF*

F. H. Raab†, Green Mountain Radio Research, Boone, Iowa, USA

Abstract

This RF-power module is a building block for a multi-kilowatt high-efficiency power amplifier system. The module employs five GaN-FET class-F RF power amplifiers with a low-loss Gysel splitter and combiner. Envelope Elimination and Restoration is used to maintain efficiency over a wide range of amplitudes. Efficiencies from 79 to 83 percent are obtained for power outputs from 500 to 600 W, and high efficiency is maintained over most of the range of outputs.

INTRODUCTION

Linear (particle) accelerators can use megawatts of RF power to accelerate protons or electrons, and typically operate on a 24/7 basis. Operation over a 3 to 10-dB amplitude range is needed to compensate for vibrations, heating, and other effects. Klystrons are currently the most widely used means of generating RF power for linear accelerators. Unfortunately, the peak efficiency of the klystrons is barely higher than 55 percent, and the efficiency varies with output power, much like that of a class-A amplifier. This results in significant power consumption and cooling requirements, which in turn result in significant operating costs.

The new system described here produces the required RF power with significantly higher efficiency, which is maintained over a wide range of outputs. Its key components are:

- Class-F RF power amplifiers (PAs) using GaN FETs,
- Gysel splitters and combiners, and
- Envelope Elimination and Restoration (EER, Kahn Technique).

Use of this system has the potential to lower operating costs significantly.

A significant advantage of this approach is that the RF PAs are always saturated. This allows them to achieve the maximum possible efficiency while eliminating the effects of gain variations due to heating and other factors, stability problems, and the like.

The "500-W module" shown in Figure 1 is the building block for multi-kW RF power-amplifier systems. It includes a driver, a Gysel power splitter, five RF PAs, a Gysel combiner, and an optional circulator. Prototypes have been developed for 325, 352, 650, and 704 MHz.

Class-F operation [1] is readily implemented at UHF and offers the maximum output power for given device ratings. These amplifiers use 120-W GaN HEMT made by Cree or Qorvo. GaN FETs are preferred to LDMOS FETs at UHF MHz because their higher-frequency capability

results in better waveform shaping, hence higher efficiency.

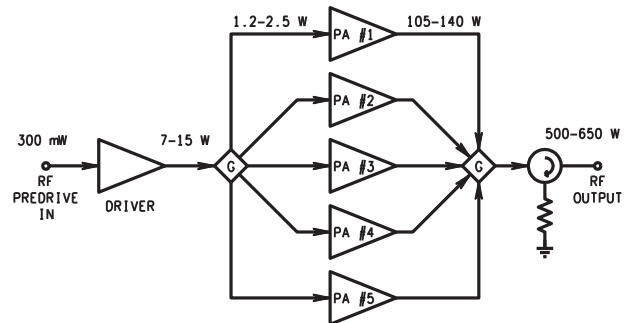


Figure 1: Block diagram.

RF POWER AMPLIFIER

A simplified circuit of the class-F power amplifier is shown in Figure 2. The output incorporates quarter-wavelength stubs for the second and third harmonics to shape the drain waveforms and thereby improve the efficiency. The GaN FET is biased near the threshold of conduction. A harmonic resonator on the input line shapes the gate-drive waveform for improved switching. The positions of the stubs are optimized experimentally, after which load pull is used to determine the fundamental-frequency matching.

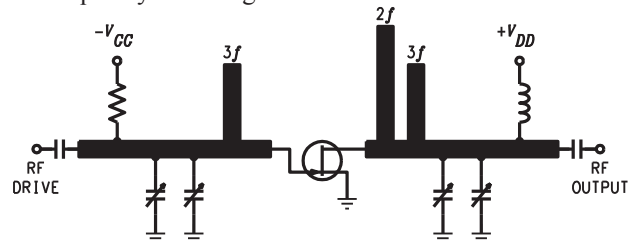


Figure 2: Class-F power amplifier.

The amplifiers are tuned to produce 120 W with maximum overall efficiency (output power divided by dc-input power plus drive power). The resultant variations of overall efficiency with output power are shown in Figure 3. The amplifiers produce 120 W with overall efficiencies from 80.5 to 87 percent. The efficiency is 70 percent or better for outputs above 7 to 12 W, depending upon the frequency. Output power is controlled by varying the supply voltage, and for these tests the drive is held constant (1.2 to 2.5 W).

Operation of the RF PAs in saturation results in excellent amplitude-modulation linearity, as shown in Figure 4. Typically, the relationship of the RF-output voltage to dc-input voltage fits a straight line within 1 percent rms. For constant drive of 1.2 to 2.5 W, the drive feedthrough is 32 to 148 mW (29 dB or more below the 120-W output). However, the addition of partial drive modulation [2] allows the level of the output to be reduced as close to

* Grants DOE-SC0002548, 6200, 6237 plus IR&D.

† f.raab@ieec.org.

DIELECTRIC LOADED HIGH PRESSURE GAS FILLED RF CAVITIES FOR USE IN MUON COOLING CHANNELS*

B. Freemire[†], Y. Torun, Illinois Institute of Technology, Chicago, IL, USA
 M. Backfish, D. Bowring, A. Moretti, D. Peterson, A.V. Tollestrup, K. Yonehara, FNAL, Batavia, IL, USA
 R. Johnson, Muons, Inc., Batavia, IL, USA
 A. Kochemirovskiy, University of Chicago, Chicago, IL, USA

Abstract

High brightness muon beams require significant six dimensional cooling. One cooling scheme, the Helical Cooling Channel, employs high pressure gas filled radio frequency cavities, which provide both the absorber needed for ionization cooling, and a means to mitigate RF breakdown. The cavities are placed along the beam's trajectory, and contained within the bores of superconducting solenoid magnets. Gas filled RF cavities have been shown to successfully operate within multi-Tesla external magnetic fields, and not be overcome with the loading resulting from beam-induced plasma. The remaining engineering hurdle is to fit 325 and 650 MHz single cell pillbox cavities within the bores of the magnets using modern technology while minimizing the peak RF power per unit length. Partially filling the cavities with a dielectric material and making them slightly reentrant accomplishes the goal of fitting shrinking the diameter of the cavities. Alumina (Al_2O_3) is an ideal dielectric, and the experimental test program to determine its performance under high power in a gas filled cavity has concluded.

INTRODUCTION

Muon cooling channels based on ionization cooling have been studied extensively over the past decade and a half. Maximizing cooling efficiency dictates strong magnetic fields (>1 T) at the location of absorbers within the cooling lattice. Radio frequency cavities are used to replace the longitudinal energy lost in the absorbers, and are therefore subject to strong magnetic fields as well. Early studies immediately observed degradation in the accelerating field of traditional vacuum cavities in magnetic fields up to 5 T [1,2].

To mitigate breakdown induced by external magnetic fields, the idea of filling cavities with a high pressure gas was introduced [3]. Given a suitable choice of gas (i.e. hydrogen), this has the additional benefit of providing the cooling medium. Such a technique has been shown to mitigate breakdown [4].

A beam traversing a gas filled RF cavity will ionize the gas, and the resulting plasma serves as a mechanism to transfer energy from the cavity to the gas; known as plasma loading. Experiments were performed to characterize the relevant processes in such an environment [5,6]. The results have been used to simulate and predict the amount of plasma loading in a cooling channel based on gas filled cavities, which

steers the design parameters [6,7]. Plasma loading is believed to be manageable for the beam intensities envisioned to meet the luminosity requirements for a muon collider.

HELICAL COOLING CHANNEL

The cooling scheme based on gas filled RF cavities is the Helical Cooling Channel (HCC) [3]. The HCC provides six dimensional cooling through ionization cooling (for which hydrogen gas is the cooling medium) and emittance exchange. This is accomplished by placing gas filled cavities within the bores of superconducting solenoid magnets, and arranging them in a helix. The helix is in turn placed within a larger, external solenoid, and the magnet system provides the necessary B_ϕ , B_z and dB_ϕ/dr field components.

Three dimensional and cross sectional views of the HCC are shown in Figs. 1 and 2. Optimization of the magnet and RF cavity parameters remains to be done, which will be described in more detail in the following sections.

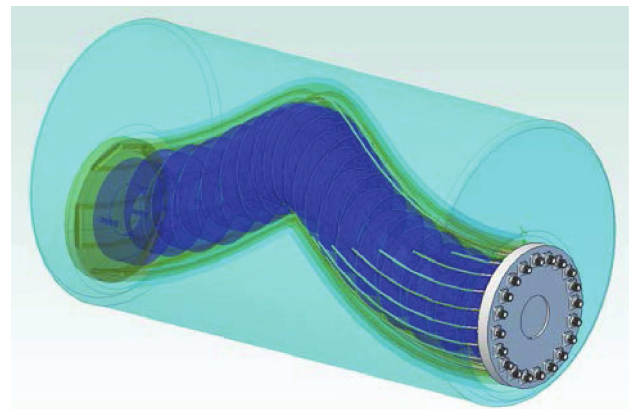


Figure 1: Three dimensional view of one cooling cell of the HCC utilizing dielectric loaded high pressure gas filled cavities [8].

Magnets for the HCC

The Helical Cooling Channel is divided into sections, each with a higher magnetic field than the previous. The early and middle sections utilize either NbTi or YBCO tape, and prototypes have been modeled and fabricated [9–11]. Higher field sections require Nb_3Sn , which presents the additional complication of requiring a reaction cycle to a temperature of 650 °C, limiting the material choice for coil support. A collaring concept was introduced to address this, mechanical

* Work supported by Fermi Research Alliance, LLC under contract No. DEAC0207CH11359.

[†] freeben@hawk.iit.edu

SIMULATION OF PING-PONG MULTIPACTOR WITH CONTINUOUS ELECTRON SEEDING*

Moiz Siddiqi[†], Rami Kishek

Institute for Research in Electronics and Applied Physics, University of Maryland, College Park

Abstract

Multipactor is a discharge resulting from secondary-electron emission. A new form of resonant multipactor combining emission from two surfaces has been studied. Initial simulations of this ping-pong mode agree with theoretical predictions of its cutoff only over a certain range. In this study, we assess the effect of the electron seeding method in the simulation on the discrepancies observed for extremely narrow and extremely wide gaps. Second, we apply techniques from non-linear dynamics to develop a new, global approach for analysing higher-periodicity multipactor. Simulation results with WARP will be discussed.

PING-PONG MULTIPACTOR THEORY

Multipactor is a discharge induced by the impact of electrons on a surface due to radio-frequency (RF) electromagnetic fields and secondary-electron emission (SEE). Depending on the impact energy and RF phase of the incident electron, a growth in the electron density is possible. Multipactor can lead to device breakdown in many applications, such as particle accelerator structures, RF systems, satellite communication equipment, and microwave components. Theoretical studies of multipactor traditionally focus on either single-surface multipactor or two-surface multipactor. A new study has been done on a combined emission from single-surface and two-surface impacts, known as ping-pong multipactor. This concept is illustrated in Figure 1. For sufficient electric fields, electrons are returned to the surface with a low impact energy [1]. These electrons can produce secondaries which then propagate to the other surface.

For small gaps between the surfaces, the ping-pong modes are found to extend the region of parameter space for multipactor growth [1]. Ping-pong multipactor is subject to the resonance condition that the total transit time for all the impacts in one period is N RF half-periods [1]. Here, N is the order of the multipactor and is constrained to be an odd integer. Additionally, the product of SEE yields (the average number of emitted secondary electrons per incident primary electron) over one period must exceed unity for multipactor growth. It is important to note that the theory and simulation makes use of the normalized variables: $\tau = \omega t$, $\bar{x} = x/D$, $\bar{v} = v/\omega D$, $\bar{E}_0 = eE_0/mD\omega^2$, for the time, position, velocity, and electric field respectively [1]. In the above equations, D is the gap separation between the plates, ω is the RF electric-field frequency, e is the electron charge, and m is the electron mass.

* Work supported by National Science Foundation

[†] msiddiqi@umd.edu

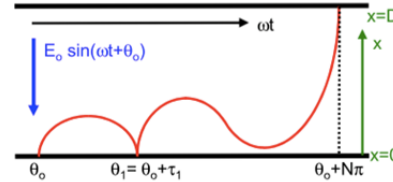


Figure 1: Particle orbits in a period-2 ping-pong multipactor [1].

SIMULATION OF PING-PONG MODES

To test the ping-pong theory, we set up a 3D Simulation using the WARP particle-in-cell code. WARP uses the POSINT library to model SEE, which includes detailed SEE parameters for any given material [1]. For the simulations, unbaked-copper surfaces are chosen, which has a peak SEE yield of 2.1 occurring at an electron impact energy of 271 eV [1]. Additionally, the code assumes a velocity distribution consistent with experimental measurements. The geometry consists of two parallel plates (0.125 mm thick, 23 x 23 mm wide) separated by a distance D , which is varied throughout the simulation. A gap impedance of 50 ohms is assumed [1]. An RF sinusoidal electric-field is present between the gap with a frequency of 0.5 GHz.

Initial simulations uniformly seed the particles between the gap prior to the start of the simulation. A series of simulations are run in a gap range of 0.75 mm – 15.0 mm by varying \bar{v}_0 for a fixed material and fixed RF electric-field frequency. The simulations are run for 5 RF periods, which is sufficient to indicate multipactor growth or decay [1]. For each gap, the simulations scan the electric-field strength and then interpolates the results to find fields that give unity gain [1]. The results of the simulation scan are shown in Figure 2. The simulation and upper period-2 ping-pong cutoff bound agree nicely for intermediate normalized velocities in the range [0.1,0.2]. However, for small and large normalized velocities, corresponding to large and small gap heights respectively, a discrepancy is seen between the upper cutoff bound and the simulation [1].

To better understand this discrepancy, a new electron seeding method is introduced where electrons are continuously injected over one RF period. This is in contrast to the uniform seeding method used in the initial simulations, where the seed electrons are placed in the gap prior to the start of the electric-field. For this new seeding method, electrons are seeded every fourth time step during the first RF period. The number of seed electrons injected per time step is chosen to ensure that the total density of seed electrons by the end of the simulations equate for the two seeding mechanisms.

SUPERFERRIC Arc DIPOLES FOR THE ION RING AND BOOSTER OF JLEIC*

J. Breitschopf[†], T. Elliot, R. Garrison, J. Gerity, J. Kellams, P. McIntyre, A. Sattarov
 Department Physics & Astronomy Texas A&M University, College Station, TX, USA
 D. Chavez Univesidad de Guanajuato, Guanajuato, Guanajuato, Mexico

Abstract

The Jefferson Laboratory Electron Ion Collider (JLEIC) project requires 3 Tesla superferric dipoles for the half-cells in the arcs of its Ion Ring and Booster. A superferric design using NbTi conductor in a cable-in-conduit package has been developed. A mockup winding has been constructed to develop and evaluate the coil structure, manufacture winding tooling and evaluate winding methods, and measure errors in the position of each cable placement in the dipole body.

INTRODUCTION

The accelerator research lab at Texas A&M University College Station, TX has been tasked to design and build a 1.2m mock dipole magnet for the figure-eight shaped Ion Collider project at Jefferson Lab[1]. The figure-eight design has two 260° arcs coupled by two strait sections. In each arc, there are 32 half-cells which consist of two 4m long dipole magnets per half-cell along with other components. The dipole magnets are required to have a 3 T uniform field, and a beam aperture of 10cm x 6cm[1].

A 15 strand NbTi cable-in-conduit design is used for the superconductor to meet the demands of field strength and stability. Precision milled G-11 forms ensure accurate placement of the cable in order to achieve the desired field quality. To evaluate the bending and winding procedures for the dipole magnet, a mock cable (empty refrigeration tubing) was used to assemble a prototype magnet. Once the mock cable was bent and placed into the form, each cable placement was measured.

CABLE AND FORM DESIGN

Cable-In-Conduit (CIC)

The CIC superconductor design originated from a concept developed by Hoenig M O and Montgomery [2]. The general style of CIC used in this project has been previously developed by the International Accelerator Facility at GSI-Darmstadt[3]. However, the specific design used in JLEIC dipole is made of 15 1.2 mm Cu-NbTi strands shown in Fig. 1. The coolant, helium for the JLEIC dipole, flows within an inner tube and the superconductor is wrapped on the outside of this tube. Then there is a seamlessly welded sheath that is formed on the outside of the superconducting strands. This provides a stable package for all the strands, and can be easily shaped.

* Work was funded in part by a contract from Jefferson Science Associates, and by grant DE-SC0016243 from the US Dept. of Energy.

[†] jeff.breitschopf@gmail.com



Figure 1: Cross-section of cable in conduit design.

Form Design

The cables are properly located in the body of the magnet by channels in the form in a block-coil configuration. This form consists of a central winding form and three layers of cables on each side, separated by segments of milled G-11 blocks. Each segment is removable so that each layer can be formed and put into place. Figure 2 shows a body cross section of the dipole with different layers and the end regions where the ion beam enters and exits the dipole.

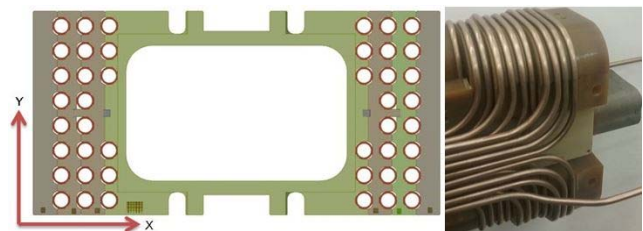


Figure 2: Body cross section of dipole (left) showing separate G-11 layers. End region form showing vertical bends (Right).

The G-11 blocks have their fiber orientation lying normal to the XY plane, with the Z axis as the beam axis. This orientation mitigates effects of thermal expansion of the block pieces. The X and Y expansion coefficients are about the same, $1.4 \times 10^{-5} \text{ K}^{-1}$ and $1.2 \times 10^{-5} \text{ K}^{-1}$ respectively, and the Z component is $7.0 \times 10^{-5} \text{ K}^{-1}$ [4].

CONSTRUCTION

Bending

In Fig. 2. (left) the cable in the winding form runs from the left hand side of the magnet to the right continuously. It must also be bent out of the way of the beam aperture. Therefore the cable must be bent 180 degrees then another 90 degrees see Fig. 2. (right) for clarity.

ROOM TEMPERATURE MAGNETS IN FRIB DRIVER LINAC*

Y. Yamazaki[#], N. Bultman, E. Burkhardt, F. Feyzi, K. Holland, A. Hussain, M. Ikegami, F. Marti, S. Miller, T. Russo, J. Wei, Q. Zhao, Facility for Rare Isotope Beams, Michigan State University, East Lansing, MI 48824, USA
 W. Yang, Q. Yao, Institute of Modern Physics, Lanzhou, China

Abstract

The FRIB Driver Linac is to accelerate all the stable ions beyond 200 MeV/nucleon with a beam power of 400 kW. The linac is unique, being compactly folded twice. In this report, the room temperature magnets, amounting 147 in total, after Front End with a 0.5-MeV RFQ, are detailed, emphasizing the rotating coil field measurements and fiducialization.

INTRODUCTION

The driver linac of the Facility for Rare Isotope Beams (FRIB) [1, 2] is to accelerate all the stable ions (including uranium) up to or beyond 200 MeV/nucleon (MeV/u) with a beam power of 400 kW (5×10^{13} ^{238}U /s). The linac is twice folded as shown in Fig. 1 in order to make it sufficiently compact to be located in the university campus, and to reuse the existing experimental facility. The linac is divided into seven segments; Front End (FE), Linac Segment (LS) 1, Folding Segment (FS) 1, LS2, FS2, LS3, and Beam Delivery Segment (BDS). Figure 1 is also showing the segments where the room temperature (RT) magnets to be reported here are located. The other segments were filled out by accelerating cyomodules (CMs), to which superconducting (SC) solenoids attached with horizontal and vertical dipoles are installed for transverse focusing and steering.

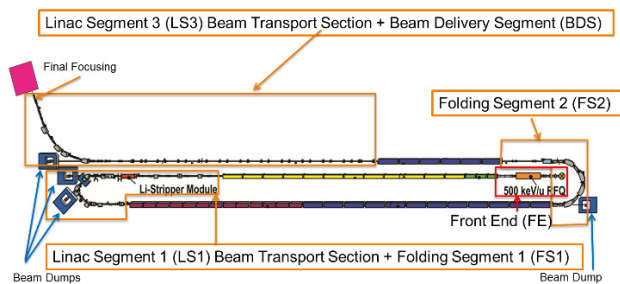


Figure 1: FRIB driver linac showing the segments (boxed in orange) where the RT magnets to be reported here are placed.

Figure 2 shows all the magnets to be used for the FRIB driver linac. The beam transport sections are equipped with the standard quadrupole magnets Q1s and the standard corrector magnets C2s. Most of C2s (44 of 46) are from Lawrence Berkeley National Laboratory (LBNL), being not reported here. A dog leg consisting of four 5-degree dipole D1s is located on each side of the liquid lithium charge stripper in order to protect SC cavi-

*Work supported by the U.S. Department of Energy Office of Science under Cooperative Agreement DE-SC0000661 and the National Science Foundation under Cooperative Agreement PHY-1102511.
[#]yamazaki@frib.msu.edu

ties from any lithium sputtering. In total, 151 RT magnets are completed or under construction by an outside vendor, including 4 spare Q1s to be used for the case of one CM missing. Note that H stands for hexapole (sextupole).

Figure 2: Magnets for the FRIB driver linac.

Originally, it was planned to use combined function magnets of quadrupole and sextupole for FS1 and BDS. After the separate function solution was found [3], all the linac RT magnets become quite common ones. Then, the manufacturing and the testing of these common magnets need no technical challenges. On the other hand, due care is still necessary for these magnets to guide the high power beams to be focused on the target with small emittances and sizes. Also, any project always need good value engineering (separate function rather than combined function was most effective example).

FIELD MAPPING RESULTS

Even if all the magnets have easily obtainable performance, we need to verify that all the magnets have required performance. The field mapping is performed by means of a all probe for one magnet of each type of quadrupoles and sextupoles and for all the dipole magnets. The absolute integrated field measured so far were compared with the requirement in Table 1. All the measurement results with the specified currents exceed the required values.

Table 1: Integrated Fields

Magnet Type	Required	Measured
Q1	≥ 8.7 T/m	9.5 T/m
Q2	≥ 7.8 T/m	8.5 T/m
Q6	≥ 3.0 T/m	3.2 T/m
H3	≥ 3.0 T/m ²	3.9 T/m ²
C1	≥ 0.0060 T	0.0063 T
C3	≥ 0.0160 T	0.0160 T

FREQUENCY DOMAIN SIMULATIONS OF RF CAVITY STRUCTURES AND COUPLER DESIGNS FOR CO-LINEAR X-BAND ENERGY BOOSTER (CXEB) WITH ACE3P

T. Sipahi, S. V. Milton, S. G. Biedron, Department of Electrical & Computer Engineering, Colorado State University (CSU), Fort Collins, CO 80523, USA

Abstract

Due to their higher intrinsic shunt impedance X-band accelerating structures offer significant gradients with relatively modest input powers, and this can lead to more compact light sources. At the Colorado State University Accelerator Laboratory (CSUAL) we would like to adapt this technology to our 1.3-GHz, L-band accelerator system using a passively driven 11.7 GHz traveling wave X-band configuration that capitalizes on the high shunt impedances achievable in X-band accelerating structures in order to increase our overall beam energy in a manner that does not require investment in an expensive, custom, high-power X-band klystron system. Here we provide the frequency domain simulation results using the ACE3P Electromagnetic Suite's OMEGA3P and S3P for our proposed Co-linear X-band Energy Booster (CXEB) system that will allow us to achieve our goal of reaching the maximum practical net potential across the X-band accelerating structures while driven solely by the beam from the L-band system.

GENERAL CONCEPT

The CSU Accelerator Facility [1] will initially focus on the generation of long-wavelength, free-electron lasers pulses, as well as the development of electron-beam components and peripherals for free-electron lasers and other light sources. It will also serve as a test bed for particle and laser beam research and development.

One of the most important parts of this accelerator is the linac that was constructed by the Los Alamos National Laboratory for the University of Twente TEU-FEL Project [2]. In addition to the capabilities of this linac we would like to further increase the electron beam energy without additional significant investments. Our idea is to utilize the electron beam from the L-Band RF gun as a drive source for a passive X-band linac structure thus allowing us to increase the beam energy by using the L-band power together with the inherent high shunt impedance of the X-band structure.

Figure 1 presents the general layout of our proposed CXEB system. We started with the power extraction mechanism using the beam from the L-band linac passing through the power extraction cavity (PEC). This power is then delivered to the X-band main accelerating cavity (MAC) structures. Then, when a bunch periodically passes

through the whole system we can achieve significantly higher beam energies. This is done by simple switching of the photocathode drive laser pulses and shifting the phase onto the cathode such that it puts the bunch into the accelerating phase of all accelerator structures.

X-BAND PEC STRUCTURE

In our previous studies [3,4] we described the general idea that can provide us some additional electron beam energy via an inexpensive and compact way using our proposed X-band Co-linear energy booster (XCEB) at CSU. In this concept we used two different types of X-band traveling wave (TW) RF cavity structures. The first one is designed as a power extraction cavity (PEC) that can provide us the needed power via our L-band system. The second one, the main accelerating cavity (MAC) [5], is designed for lower group velocity for efficient RF power deposition to the electron beam in the cavity. In our previous studies we have presented the electromagnetic field mapping of the PEC and MAC structures using SUPERFISH, the Maxwell solver of LANL's code group [6].

In here we provide the results of more advanced 3D simulations that we performed using the parallel computing capabilities of the National Energy Research Scientific Computing Center (NERSC) [7] as well as SLAC's Advanced Computational Electromagnetics Code Suite ACE3P (Advanced Computational Electromagnetics 3D Parallel) [8]. The 3D CAD modeling and visualization were done using the Telis [9] and Paraview [10] software, respectively.

We started our simulations studying how different boundary conditions effects the PEC parameters and because we would like to increase our CPU time efficiency on the super computing facility. In this part of the study, while we were applying traveling wave boundary conditions at the both ends of the half and quarter PEC single cell geometries, we kept the mesh size constant and similar to what we used for the whole cell. The parameter comparison results and the magnitude of the electric and magnetic fields for the each symmetry of the single cell of our TW X-band PEC using OMEGA3P [11], eigen frequency solver of ACE3P are given in Table 1 and Figure 2.

WAKEFIELD EXCITATION IN POWER EXTRACTION CAVITY OF CO-LINEAR X-BAND ENERGY BOOSTER IN TIME DOMAIN WITH ACE3P

T. Sipahi, S. V. Milton, S. G. Biedron, Colorado State University (CSU),
Electrical & Computer Engineering Dept., Fort Collins, CO 80523, USA

Abstract

We provide the general concept and the design details of our proposed Co-linear X-band Energy Booster (CXEB). Here, using the time domain solver T3P of the ACE3P Suite we provide the single bunch and multiple bunch wakefield excitation mechanism for the power build up when using a symmetric Gaussian bunch distribution in our traveling wave (TW) X-band power extraction cavity (PEC). Finally, we determine the achievable X-band power at the end of the PEC structure.

POWER EXTRACTION FOR X-BAND PEC

When a bunch passes through an unfilled RF cavity it interacts with the cavity and deposits some of its kinetic energy. This energy is converted into RF fields that can be decomposed into the resonant modes of the RF cavity. If a steady stream of bunches is passed through the cavity and the spacing of the bunches is such that they are precisely in phase with one of the cavity modes, then this mode gets reinforced and can grow to large values. As time progresses the field builds up, as does the impact on the passing electron bunch until equilibrium is reached where the power being dissipated is equal to the power delivered. In the case of power extraction, this power can be delivered to another device and be used as desired.

In order for the mode excitation to be coherent and therefore constructive, the bunch spacing T_b needs to be a multiple of the mode period and the mode phase velocity needs to be equal to the speed of the relativistic bunches. The bunch separation time T_b , however, must be shorter than the cavity passage time of the excited RF mode in order that several bunches can contribute to the build up of the voltage V_a .

At the equilibrium condition, the induced voltage generated by the following bunch compensates the voltage drop experienced between bunches.

In our X-band Co-linear Energy Booster system, presented in our previous studies [1,2,3], the resonant frequency of the power extraction cavity (PEC) is 11.7 GHz. Our Ti:Sapp laser is capable of producing 81.25 MHz pulses, therefore the X-band RF oscillates 144 times for each passage of an electron bunch.

Equation 1 gives the steady-state power level at the structure output when neglecting the internal wall losses [4]:

$$P = \frac{\omega}{4c} \left(\frac{R}{Q}\right) L^2 \left(\frac{q_b}{T_b}\right)^2 \frac{1}{(\beta_g - 1)} F^2(\sigma) \quad (1)$$

or in terms of the field attenuation factor per unit length (α) for a constant shunt impedance traveling wave cavity we can write the Equation 1 as [5]:

$$P = \frac{\omega}{4c} \left(\frac{R}{Q}\right) L^2 I^2 \frac{1 - e^{-\alpha L}}{\alpha L} F^2(\sigma) \quad (2)$$

where

$$\alpha = \frac{w}{2Qv_g} \quad (3)$$

ω is the frequency, Q is the quality factor of the cavity, v_g is the cavity group velocity, L is the length of the cavity, R is the cavity resonant mode shunt impedance, and $F(\sigma)$ is the form factor for a bunch of length σ . This equation is used as an initial estimate for performance and as a check of the simulation.

We performed our time domain beam dynamics simulations using the NERSC (National Energy Research Scientific Computing Center [6]) parallel computing sources and SLAC's Advanced Computational Electromagnetics Code Suite ACE3P's (Advanced Computational Electromagnetics 3D Parallel) [7] time domain solver T3P [8]. The 3D CAD modeling and visualization were done using the Trellis [9] and Paraview [10] software, respectively. Some of the important X-band PEC structure parameters that are presented in another paper of this conference were simulated using OMEGA3P are given in Table 1 [11].

Table 1: Parameters for TW X-Band PEC

Parameter	Value
Frequency [GHz]	11.7001
Phase advance per cell [Radians]	$2\pi/3$
Inner radius to wavelength ratio	0.10
Quality factor	6458
Cell length [mm]	8.5411
Shunt Impedance M Ω /m	110

GAUSSIAN BEAM OPTIMIZATION FOR CONSTRUCTIVE WAKEFIELD EXCITATION IN X-BAND PEC STRUCTURE

For an efficient and successful power extraction at the end of the X-band PEC our longer drive beam needs to be optimized. We can calculate the power using the formula for the maximum current with a very thin bunch size

EDDY CURRENT CALCULATIONS FOR A 1.495 GHz INJECTION-LOCKED MAGNETRON*

S. A. Kahn[†], A. Dudas, R. P. Johnson, M. Neubauer, Muons, Inc., Batavia, IL., USA
H. Wang, Jefferson Lab., Newport News, VA, USA

Abstract

An injection-locked amplitude modulated magnetron is being developed as a reliable, efficient RF source that could replace klystrons used in particle accelerators. The magnetron amplitude is modulated using a trim magnetic coil to alter the magnetic field in conjunction with the anode voltage to maintain the SRF cavity voltage while the cavity is experiencing microphonics and changing beam loading. Microphonic noise can have frequency modes in the range 10-50 Hz. Eddy currents will be induced in the copper anode of the magnetron that will buck the field in the interaction region from the trim coil. This paper will describe the magnetic circuit of the proposed magnetron as well as the calculation and handling of the Eddy currents on the magnetic field.

INTRODUCTION

A magnetron with injection locking and amplitude modulation is being proposed as an efficient alternative to klystrons. The project plans to build and test a prototype 1497 MHz magnetron that could be used as an RF source for JLab. Using an injection phase-locked magnetron as an alternate RF source is described in Ref. [1]. Amplitude modulation is planned to control microphonics in the superconducting RF cavities. The current in the magnetron interaction region is modulated by varying the magnetic field over the electron cloud. The magnet system consists of a DC solenoid that provides the nominal field over the interaction region. An additional coil surrounds the anode which can provide a variable $\pm 10\%$ field to modulate the current. The magnet system is described in the next section. The JLab superconducting cavities have microphonic noise modes in the frequency range 10-50 Hz [2].

MAGNET SYSTEM

Figure 1 shows a diagram of the magnetron which illustrates the magnet configuration. The larger outer solenoid coils provide 0.25 T field. A trim coil is present surrounding the anode to provide an additional variable field that can be used to modify the field in the interaction region. Surrounding the coils is a steel magnetic circuit to conduct the flux to the magnetron interaction region. This configuration provides a uniform magnet field over the interaction region. Table 1 shows parameters describing the trim coil. The decay constant associated with the coil

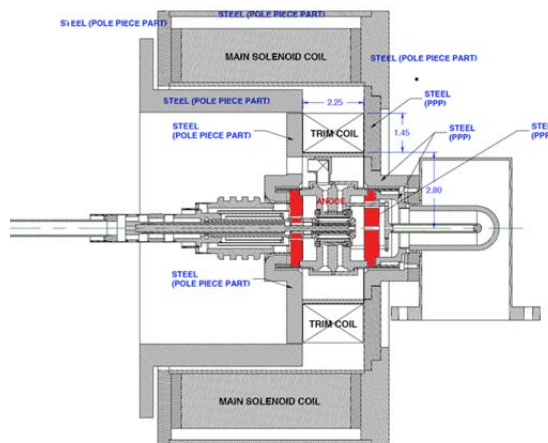


Figure 1: Diagram of magnetron showing the magnet configuration.

Table 1: Trim Coil Parameters

Parameter	Value
Maximum Field	0.025 T
Number of turns	248
Current per turn	5 A
Inductance	0.028392 h
Coil Resistance	0.279 Ω
Time Decay Constant	100 ms
Cross Section Area	21.05 cm ²

coil inductance is 100 ms. This number is independent of the number of turns as long as the coil cross section is fixed. The decay constant may be too long to react to very short time spikes. The decay constant can be further reduced with an external resistance in series with the trim coil, however that resistance must be compatible with the 5 A current and may be limited by the power supply.

EDDY CURRENT SHIELDING

The time varying currents in the trim coil will induce transient currents in the magnetron anode which is made of copper. The Eddy current in the anode will produce a field in the interaction region that opposes the field from the trim coil. We used the Opera 2D finite element simulation code [3] to model the magnetic geometry configuration of the magnetron. The anode in the R-Z is represented by a cylinder with radial thickness corresponding to the part of the anode that would allow the current to circulate the full 360° since that is the region that contributes significantly to the Eddy currents. The analysis uses a sinusoidal drive current in the trim coil with frequen-

* Work supported by U.S. D.O.E. SBIR grant DE-SC0013203

[†] email address: kahn@muonsinc.com

MAGNET DESIGN FOR THE SPLITTER/COMBINER REGIONS OF CBETA, THE CORNELL-BROOKHAVEN ENERGY-RECOVERY-LINAC TEST ACCELERATOR

J.A. Crittenden, D.C. Burke, Y.L.P. Fuentes, C.E. Mayes and K.W. Smolenski
CLASSE* Cornell University, Ithaca, NY 14853, USA

Abstract

The Cornell-Brookhaven Energy-Recovery-Linac Test Accelerator (CBETA) will provide a 150-MeV electron beam using four acceleration and four deceleration passes through the Cornell Main Linac Cryomodule housing six 1.3-GHz superconducting RF cavities. The return path of this 76-m-circumference accelerator will be provided by 106 fixed-field alternating-gradient (FFAG) cells which carry the four beams of 42, 78, 114 and 150 MeV. Here we describe magnet designs for the splitter and combiner regions which serve to match the on-axis linac beam to the off-axis beams in the FFAG cells, providing the path-length adjustment necessary to energy recovery for each of the four beams. The path lengths of the four beamlines in each of the splitter and combiner regions are designed to be adapted to 1-, 2-, 3-, and 4-pass staged operations. Design specifications and modeling for the 24 dipole and 32 quadrupole electromagnets in each region are presented. The CBETA project will serve as the first demonstration of multi-pass energy recovery using superconducting RF cavities with FFAG cell optics for the return loop.

INTRODUCTION

The Cornell Laboratory for Accelerator-based Sciences and Education (CLASSE) and the Brookhaven National Laboratory have begun collaboration on the design, construction and commissioning of a four-pass 150-MeV electron accelerator based on a superconducting, six-cavity linac with energy recover, using 106 fixed-field alternating-gradient (FFAG) cells as the return loop [1–3]. Figure 1 shows the layout comprising the injector, the main linac cryomodule, the splitter section, the FFAG return loop, the combiner, and the beam dump section. The FFAG cells carry four beams of 42, 78, 114 and 150 MeV in a vacuum chamber with interior dimensions of 84x24 mm. The splitter and combiner regions, labeled SX and RX in Fig. 1 serve to adjust the path length of each beam for energy recovery. Figure 2 shows the splitter region SX. The 24 dipole magnets and 32 quadrupole magnets in each of the splitter and combiner sections must cover a wide range of excitations and accommodate an extruded aluminum vacuum chamber of inner dimensions 34x24 mm with 3-mm thick walls. Here we describe magnet model development for the dipole and quadrupole magnets in these sections.

* Supported by NSF award DMR-0807731, DOE grant DE-AC02-76SF00515, and New York State.

MAGNET PARAMETERS AND MODELING

The splitter and combiner optics designs [1] each specify 24 dipole magnets with fields ranging from about 1.5 kG to 9 kG and 32 quadrupole magnets with field gradients ranging from about 0.1 T/m to 4 T/m (see Fig. 3) to be accommodated on a girder of surface area approximately 4x2 m², imposing stringent constraints on the magnet geometries, limiting the horizontal extent to about 20 cm and the length to 20 cm for most of the magnets. Given the limited space for coil pockets, we have constrained the power supply voltage, current and dissipated-power parameters to ensure availability of commercially available units.

The chosen quadrupole poleface and yoke design derives from a large-aperture design developed at the Cornell Electron Storage Ring (CESR) in 2004 [4]. Figure 4 shows surface color contours of the field magnitude on the iron for the 4.0 T/m excitation. A model scaled to a 40-mm bore diameter, resulting in a 12.3-cm square outer cross section, was found to exhibit excellent linearity up to an excitation of 4.0 T/m with the central field and field integral nonuniformities shown in Fig. 5, as modeled with the Vector Fields Opera 18R2 software [5].

An H-magnet design was chosen for the dipoles in order to minimize stray fields given the close proximity of the four beamlines. The maximum field is restricted to 6 kG in order to limit flux leakage out of the central pole iron. This arises from the height of the magnet, bounded below by the need for space for the coil and the number of conductor turns required to permit use of an 80-A power supply. Figure 6 shows the resulting field and field integral uniformity.

Table 1 shows an overview of geometrical, electrical and cooling parameters of the dipole and quadrupole magnet designs. The 30-cm H-dipole is intended for use in the seven cases where the lattice specifies fields greater than 6 kG (see Fig. 3). The table also shows that the non-linearity in the field/current relationship between 4.5 kG and 5.937 kG is 1.1%. Modeling shows the dipole design to be linear at the 10⁻⁴ level for lower excitations. The linearity of the quadrupole design is modeled to a similar accuracy for the field gradients below 4.0 T/m, permitting this design to be used for all 64 quadrupoles in the splitter and combiner.

SUMMARY

We have presented a first-pass design study for the magnets required for the splitter and combiner regions of the Cornell-Brookhaven ERL Test Accelerator. Stringent space

PERFORMANCE OF THE CORNELL MAIN LINAC PROTOTYPE CRYOMODULE FOR THE CBETA PROJECT*

F. Furuta[†], N. Banerjee, J. Dobbins, R. Eichhorn, M. Ge, D. Gonnella[‡], G. Hoffstaetter, M. Liepe, T. O'Connell, P. Quigley, D. Sabol, J. Sears, E. Smith, V. Veshcherevich, CLASSE, Cornell University, Ithaca, New York, USA

Abstract

The Cornell Main Linac Cryomodule (MLC) is a key component in the Cornell-BNL ERL Test Accelerator (CBETA) project, which is a 4-turn FFAG ERL under construction at Cornell University. The MLC houses six 7-cell SRF cavities with individual higher order-modes (HOMs) absorbers, cavity frequency tuners, and one magnet/BPM section. Here we present final results from the MLC cavity performance and report on the studies on the MLC HOMs, slow tuner, and microphonics.

INTRODUCTION

The Cornell-BNL ERL Test Accelerator (CBETA) is a collaboration project between BNL and Cornell to investigate eRHIC's non-scaling Fixed Field Alternating Gradient (NS-FFAG) optics and its multi-turn Energy Recovery Linac (ERL) by building a 4-turn, one-cryomodule ERL at Cornell (Fig. 1 top) [1, 2, 3]. CBETA will be built with many components that have been developed at Cornell under previous R&D programs for a hard x-ray ERL [4]. The main accelerator module, one of the key components for CBETA, will be the Cornell Main Linac Cryomodule (MLC) which will provide 36MeV energy gain for a single-turn beam of the CBETA. The MLC was built as a prototype for the Cornell hard x-ray ERL project and designed to operate in CW at 1.3GHz, 2ps bunch length, 100mA average current in each of the accelerating and decelerating beams, normalized emittance of 0.3mm-mrad, and energy ranging from 5GeV down to 10MeV, at which point the spent beam is directed to a beam stop [5]. In this paper, we report the performance test results of the MLC, such as cavity RF test, measurements and analysis of HOMs in the MLC cavities, slow tuner test, and microphonics studies on the MLC.

MAIN LINAC CRYOMODULE PROTOTYPE

Figure 1 (bottom) shows an image of the Cornell ERL Main Linac Cryomodule (MLC) prototype. The design of the MLC for the Cornell ERL has been completed in 2012. It is 9.8 m long and houses six 1.3 GHz 7-cell superconducting cavities, three of them are stiffened cavities, another three are un-stiffened, with individual HOM beamline absorbers located between the cavities. Each cavity has a single 5kW coaxial RF input coupler, which transfers power from a solid-state RF power source

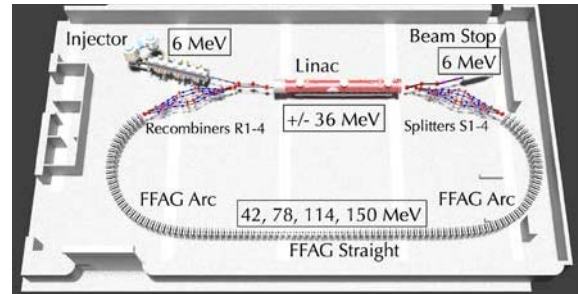


Figure1: The layout of CBETA project (top) and the MLC prototype (bottom).

to the cavity (the design Q_{ext} is 6.0×10^7). The MLC cavity surface preparation consists of bulk Buffered Chemical Polishing (BCP, 140 μ m), degassing (650degC, 4days), cavity frequency tuning, light BCP (10 μ m), low temperature baking (120degC, 48hrs), and HF rinse. The fabrication and testing of MLC components (cavity, high power input coupler, HOM dampers, tuners, etc.) and assembly of the MLC cold mass have been completed in 2014 [6, 7, 8]. RF tests with different cool down conditions, including the first cool down, have been performed in 2015 [9].

RF tests of the MLC cavities

We performed one-by-one RF test of all six cavities at 1.8K after 1) the initial cooldown from room temperature [10], 2) a thermal cycle with "fast cool down" with cool down rates of ~ 36 K/min., with large vertical spatial temperature gradient ($dT_{vertical}$) of 36K when the cavities passed the critical temperature T_c of niobium (9.2K), and 3) after a thermal cycle with "slow cool down" maintaining cool down rate of 0.23mK/min. on average, and a small horizontal spatial temperature gradient ($dT_{vertical}$) of 0.6K from 15K to 4K. The 7-cell cavities in the MLC on average have successfully achieved the specification values of 16.2MV/m with Q_0 of 2.0×10^{10} at 1.8K. Figure 2 summarizes the maximum field gradient performance and the cavity quality factor Q_0 (1.8K) of the MLC cavities.

* Work is supported by NSF awards NSF DMR-0807731 and NSF

[†]ff97@cornell.edu PHY-1002467

[‡] Now at SLAC National Accelerator Laboratory

UPDATES OF VERTICAL ELECTROPOLISHING STUDIES AT CORNELL WITH KEK AND MARUI GALVANIZING CO. LTD*

F. Furuta, M. Ge, T. Gruber, J. Kaufman, M. Liepe, J. Sears,
CLASSE, Cornell University, Ithaca, New York, USA,

H. Hayano, S. Kato, T. Saeki, KEK, High Energy Accelerator Research Organization,
Tsukuba, Ibaraki, Japan

V. Chouhan, Y. Ida, K. Nii, T. Yamaguchi, Marui Galvanizing Co. Ltd., Himeji, Hyogo, Japan

Abstract

Cornell, KEK, and Marui Galvanizing Co. Ltd have started a Vertical Electro-Polishing (VEP) R&D collaboration in 2014 to improve removal uniformity. MGI and KEK have developed their original VEP cathode named i-cathode Ninja[®], which has four retractable wing-shape parts per cell. One single cell cavity has been processed with VEP using the i-cathode Ninja at Cornell. Cornell also performed a vertical test on that cavity. Here we present process details and RF test result at Cornell.

INTRODUCTION

Electro-Polishing (EP), especially Horizontal EP, is applied on niobium SRF cavities in many projects as a high-performance surface treatment procedure. As an alternative, Cornell's SRF group has led the development of Vertical Electro-Polishing (VEP) which requires a much simpler setup and is less expensive compared with the conventional Horizontal EP [1]. Cornell has successfully demonstrated the capability of VEP on high gradient cavities for the ILC project, which require cavity specification for the accelerating field (E_{acc}) of $>35\text{MV/m}$ with cavity quality factor (Q_0) $>0.8 \times 10^{10}$ at 2K [2]. In addition, VEP was done on the high-Q cavities for the LCLS-II project at SLAC, which requires $Q_0 > 2.7 \times 10^{10}$ at $E_{acc} = 16\text{MV/m}$, 2K [3]. The EP process in vertical direction is affected by gravity, resulting in a removal difference between upper and lower half cells. In addition, the top cell of a multi-cell cavity during the VEP has a much larger removal than the end cell located on the bottom. To compensate for the removal non-uniformity, the cavity needs to be flipped and additionally processed after finishing half of the target removal. Marui Galvanizing Co. Ltd (Marui) has focused on VEP application targeted mass-production and has been developing their original cathode named "i-cathode Ninja[®]" (Ninja cathode) to improve polishing quality, especially removal uniformity during the VEP process [4]. Marui's work matches Cornell's research on VEP removal uniformity, and a collaboration between Cornell and KEK-Marui was started in 2014 to improve removal uniformity. In this paper, we present VEP processes using two types of the Ninja cathode at Cornell on a single cell cavity in addition to the result of a RF test. [5].

* Work is supported by JFY2015 US/Japan Program for Cooperation in High Energy Physics
#ff97@cornell.edu

VEP SYSTEM AT CORNELL

Figure 1 shows a 1.3GHz TESLA shape single-cell cavity installed into the Cornell VEP system with the Ninja-cathode. Two types of the Ninja cathode and top and bottom EP sleeves were shipped from Marui to Cornell. The Cornell VEP system received a couple of upgrades to enable acid circulation during the VEP process.



Figure 1: Cornell VEP system with "Ninja" cathode.

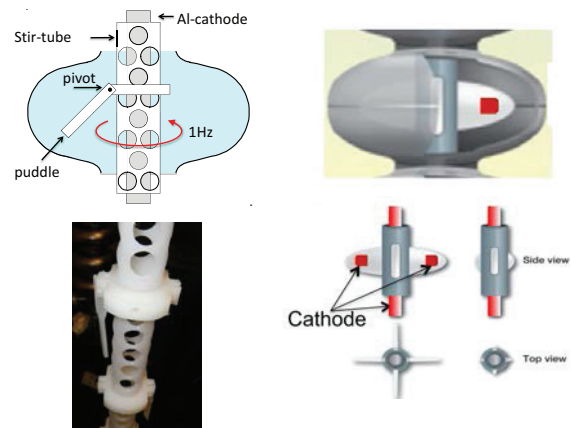


Figure 2: Images of Cornell VEP cathode (left), Images of Marui's i-cathode Ninja type-I and retractable wings (right).

SRF HALF WAVE RESONATOR ACTIVITIES AT CORNELL FOR THE RAON PROJECT*

M. Ge[†], F. Furuta, T. Gruber, S. Hartman, C. Henderson, M. Liepe, S. Lok, T. O'Connell, P. Pamel, J. Sears, V. Veshcherevich, Cornell University, Ithaca, New York, USA
J. Joo, J.W. Kim, W.K. Kim, J. Lee, I. Shin, Institute for Basic Science, Daejeon, Korea

Abstract

The RAON heavy-ion accelerator requires ninety-eight 162.5MHz Half-Wave-Resonators (HWR) with a geometrical $\beta=0.12$. Cornell University will test a prototype HWR as well as develop a frequency tuner for this cavity. In this paper we report on the progress in designing, fabricating, and commissioning of new HWR preparation and testing infrastructure at Cornell. The HWR infrastructure work includes new input and pick-up couplers, a modified vertical test insert with a 162.5MHz RF system, a new High-Pressure-Water-Rinsing (HPR) setup, and a modified chemical etching system.

INTRODUCTION

RAON, which will be a heavy-ion accelerator based In-flight Fragment (IF) and Isotope Separation On-Line (ISOL) facility, is now under construction in Korea [1, 2]. The name "RAON", which comes from a pure Korean word, can be literally interpreted as delight and happiness [3]. The accelerator consists of two Superconducting Linac (SCL) sections which require in total of ninety-eight 162.5MHz Half-Wave-Resonators (HWR) with a geometrical $\beta = 0.12$ [4].

The prototype HWR for the RAON project has been designed by the Institute for Basic Science (IBS) [5]. The cavity is now under fabrication in Research Instruments (RI). The surface treatments of the cavity will be done by RI as well. The cavity, after the fabrication, will be firstly treated with 150 μm Buffer-Chemical-Polishing (BCP), followed by 625 $^{\circ}\text{C}$ baking for 10 hours in a high-vacuum furnace; after a light BCP (5-10 μm), the cavity will be High-Pressure-Water-Rinsed (HPR) and cleanly assembled. A 120 $^{\circ}\text{C}$ baking is not adopted for the recipe because the intrinsic quality factor (Q_0) of such low-frequency cavity is dominated by the residual resistance (R_0) instead of the BCS resistance (R_{BCS}); but the 120 $^{\circ}\text{C}$ baking can increase R_0 [6], which would cause the HWR Q-degradation. In a HWR test, a Q-degradation has been observed after a 120 $^{\circ}\text{C}$ baking [7].

The cavity will be shipped to Cornell University under vacuum for vertical tests to evaluate its performance. Cornell will test 1) the bare HWR cavity without helium tank; 2) the dressed cavity with helium tank; 3) the frequency tuner for the dressed HWR. If the cavity performance is unsatisfactory after the test 1) or 2), the cavity can be retreated at Cornell. The geometry of the HWR cavity is complex and quite different from a regular 9-cell SRF cavity, thus the current cavity preparation and testing facilities at Cornell have to be modified for this project.

* Work supported by the Ministry of Science, ICT, MSIP and NRF. Contract number: 2013M7A1A1075764.

[†] mg574@cornell.edu

PREPARATION OF PERFORMANCE TESTING

Input and Pick-up Couplers

The external quality factor (Q_e) of the input coupler should match up the Q_0 of the HWR, i.e. $\beta \equiv \frac{Q_0}{Q_e} \approx 1$, $Q_e \approx Q_0$, to obtain unity coupling during the measurements. The cavity will be measured at temperature 2-4.2K; hence the R_{BCS} corresponding to the temperature range is 0.3-18n Ω for the un-baked case, computed by the SRIMP code [8, 9] which is based on the BCS theory [10, 11]. The estimation of R_0 is complicated because it relates to many factors. But since the HWR has a low-frequency and is only treated by BCP, the R_0 has less sensitivity to flux trapping from ambient magnetic fields [12]. Therefore the R_0 of the HWR mainly comes from the surface treatments. Based on this analysis and the MLC 7-cell SRF cavity experiences [13, 14], we can give a good approximation of the R_0 with 3-10n Ω , thus the surface resistance is 3.3-28 n Ω . The geometry factor of the HWR is 36 Ω , from which it can be calculated that the highest Q_0 (or Q_e) can be $\sim 1.1 \times 10^{10}$. During the test, multipacting is likely to occur at very low fields [15, 16], which can be removed by RF processing. The RF processing requires strong coupling to fill and drain RF power quickly, i.e. $\beta > 100$, $Q_e \sim 1 \times 10^7$. In summary, the range of the Q_e should be at least from 1×10^7 to 1.1×10^{10} .

We designed an electric-coupler which has a straight antenna and will be mounted in the middle section of the cavity. The Q_e vs. insert depth curves simulated by Microwave Studio are shown in Fig. 1. The total travel range of the coupler is 50mm, which can tune the Q_e from $\sim 1 \times 10^7$ to $\sim 1 \times 10^{11}$ and give adequate margins for the measurements.

The 3D model of the input coupler is shown in Fig. 2 a). When the drive gears rotate, they turn the threaded shafts to drive the moving plate in linear motion. The threaded shafts are symmetrically placed around the below; the torque is evenly delivered from the input shaft to the three threaded shafts by the gears. Hence, symmetrical forces are applied on the moving plate to avoid binding with the traveling guides. A photograph of the input coupler is displayed in Fig. 2 b). The pickup coupler is a fix coupler with $Q_e \sim 1 \times 10^{13}$ to match the required power level of the LLRF system. A feedthrough, displayed in Fig. 3 middle insert plot, is mounted on an adaptor to match the cavity flange. The 3D model and the photo-

IMPACT OF COOLDOWN PROCEDURE AND AMBIENT MAGNETIC FIELD ON THE QUALITY FACTOR OF STATE-OF-THE-ART Nb₃Sn SINGLE-CELL ILC CAVITIES*

Daniel L. Hall[†], Mingqi Ge, John J. Kaufman, Matthias Liepe, Ryan D. Porter
Cornell Laboratory for Accelerator-Based Sciences and Education (CLASSE),
Ithaca, NY 14853, USA

Abstract

Single-cell Nb₃Sn cavities coated at Cornell University have demonstrated quality factors of $>1 \times 10^{10}$ at 16 MV/m and 4.2 K in vertical tests, achieving the performance requirements of contemporary modern accelerator designs. In this paper, we present results demonstrating the impact of the cooldown procedure and ambient magnetic fields on the cavity's ability to achieve these quality factors and accelerating gradients. The impact of the magnetic fields from thermoelectric currents, generated by thermal gradients across the cavity during cooldown, are shown to be equivalent to the impact of magnetic fields trapped from ambient sources. Furthermore, the increase in the residual surface resistance due to trapped magnetic flux, from both ambient sources and thermoelectric currents, is found to be a function of the applied RF magnetic field amplitude. A hypothesis for this observation is given, and conclusions are drawn regarding the demands on the cooldown procedure and ambient magnetic fields necessary to achieve quality factors of $>1 \times 10^{10}$ at 4.2 K and 16 MV/m or higher.

INTRODUCTION

Niobium cavities coated with Nb₃Sn at Cornell University have shown high quality factors of $Q > 1 \times 10^{10}$ at 4.2 K and 16 MV/m [1–5]. To achieve these record performances, a correctly executed cooldown through the transition temperature T_c is crucial. Due to the bimetallic interface of Nb₃Sn on niobium, thermal gradients along the boundary will result in thermoelectric currents, which in turn generate magnetic fields that will become trapped in the Nb₃Sn layer, resulting in increased losses and a lowered cavity efficiency.

In this paper we present the first results from a systematic study of the impact of the thermal gradients on the cavity performance, correlated with measurements of the increase in surface resistance from an increased amount of ambient trapped flux. The sensitivity to trapped flux is found to be dependent on amplitude of the RF field, regardless of the source of trapped flux being ambient magnetic fields or those generated by thermocurrents. From this measurement, the maximum amount of flux that can be trapped while still achieving a $Q > 10^{10}$ at 4.2 K and at a stated peak RF magnetic field is given.

* This work supported by U.S. DOE award DE-SC0008431.

[†] dlh269@cornell.edu

EXPERIMENTAL SETUP

A single-cell 1.3 GHz ILC-style cavity, designated LTE1-7, was used for the purpose of measuring the impact of thermal gradients and external magnetic fields on Nb₃Sn-coated cavities. The cavity preparation and performance has previously been presented in Ref. [3]. The cavity was tested in one of Cornell's vertical test cryostats; a simplified diagram of the experimental setup within the test insert is shown in Fig. 1. A Helmholtz coil was mounted on the cav-

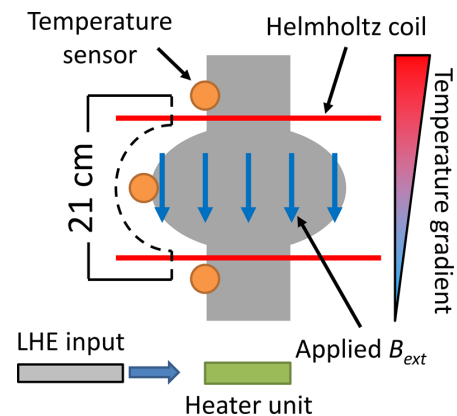


Figure 1: A simplified diagram of the experimental setup. A Helmholtz coil is used to apply a uniform external magnetic field during cooldowns that require ambient flux trapping. A heater located at the base of the cryostat is used to heat the helium entering the cryostat and establish a temperature gradient across the cavity, which is measured using the temperature sensors located at the irises and equator.

ity for the purpose of applying an external magnetic field, whose magnitude was monitored using flux gate magnetometers mounted on the cavity irises. The thermal gradient across the cavity during cooldown was controlled using a combination of a heater mounted at the base of the cryostat and another heater located in the helium delivery line. The temperature gradient across the cavity was monitored using temperature sensors mounted at the upper and lower irises and the equator.

For the purposes of this experiment, two different cooldown styles were used: the first, focussed on thermal gradients, was done in no externally applied magnetic field while establishing a thermal gradient across the cavity during the transition through T_c . The second, focussed on ambient trapped flux, was done by cooling the cavity in as small a thermal gradient as possible while applying an external

INVESTIGATION OF THE ORIGIN OF THE ANTI-Q-SLOPE*

J. T. Maniscalco[†], M. Ge, D. Gonnella, and M. Liepe

CLASSE, Cornell University, Ithaca, NY, 14853, USA

Abstract

The surface resistance of a superconductor, a property very relevant to SRF accelerators, has long been known to depend on the strength of the surface magnetic field. A recent discovery showed that, for certain surface treatments, microwave cavities can be shown to have an inverse field dependence, dubbed the “anti-Q-slope”, in which the surface resistance decreases over an increasing field. Here we present an investigation into what causes the anti-Q-slope in nitrogen-doped niobium cavities, drawing a direct connection between the electron mean free path of the SRF material and the magnitude of the anti-Q-slope. Further, we incorporate residual resistance due to flux trapping to calculate an optimal mean free path for a given trapped flux.

INTRODUCTION

Nitrogen doping of niobium, a hot topic in the field of superconducting radio-frequency (SRF) accelerator physics, has sparked much interest due to the observed phenomenon of the so-called “anti-Q-slope”. Cavities are treated with nitrogen gas in a furnace, which diffuses nitrogen into the RF penetration depth of the material. The result, as initially observed at Fermilab [1], is a field-dependent BCS surface resistance that tends to *decrease* as RF field strength increases, in contradiction to the behavior typically shown in SRF cavities. As a result, the quality factor of these cavities, inversely proportional to the surface resistance R_s , tends to increase with the RF field strength.

Recent theoretical work [2] offers an explanation for this phenomenon. According to the theory, the high-frequency oscillating field impinging on the surface changes the density of states of the quasiparticles in such a way that their number density tends to decrease with increasing field strength. This decreased density leads to decreased RF power dissipation and thus decreased surface resistance.

This effect is mediated, however, by the overheating of the Bogoliubov quasiparticles: they absorb energy from the RF field and dissipate the energy through their coupling with the lattice phonons. A lag in the energy transfer away from the quasiparticles causes them to increase in temperature relative to the lattice; this increase in turn results in an increase in the surface resistance.

In this work, we seek to find a link between this overheating phenomenon and the electron mean free path ℓ , the quantity typically used to quantify the level of nitrogen doping for a particular sample or cavity. Once armed with such a link, we seek to find an optimal mean free path to balance

the effects of the anti-Q-slope with the increased sensitivity to trapped magnetic flux observed in nitrogen-doped cavities [3]. This study is an expansion on work previously shown at IPAC 2016 [4].

QUASIPARTICLE OVERHEATING

For this study, we considered RF test data for nine separate nitrogen-doped cavity tests, with mean free path ℓ ranging from 4 to over 200 nm. These tests measured the temperature-dependent BCS surface resistance R_{BCS} as a function of peak surface magnetic field B_{pk} at a range of temperatures, typically between 1.6 K and 2.1 K. Circles in Fig. 1 show typical experimental data of this type. All cavities tested were 1.3 GHz single-cell TESLA-shape cavities, using a vertical test setup.

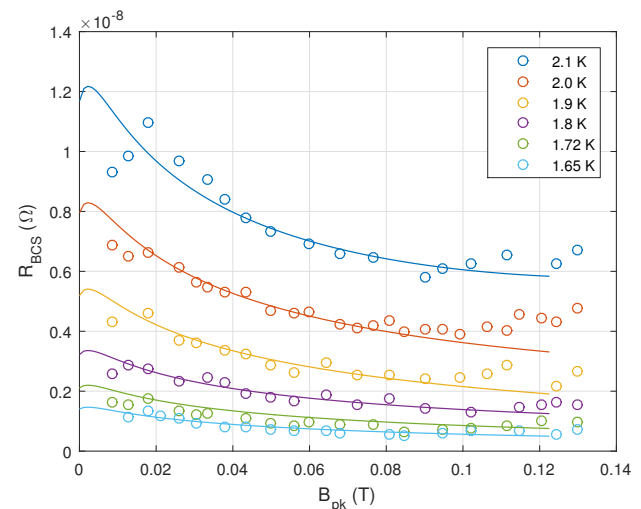


Figure 1: Typical R_{BCS} vs. B_{peak} test results for a nitrogen-doped cavity, with theoretical fits overlaid. The mean free path for this cavity was measured to be 34 ± 10 nm, with the fitted overheating corresponding to $\alpha(2.1 \text{ K}) = 0.44$.

For each temperature, theoretical predictions were fitted to experimental data by adjusting the “overheating parameter” α , which controls the extent to which the quasiparticles overheat under the RF field. Also shown in Fig. 1 are the fit results for the given cavity test data.

With our fitted values of α for each cavity at each temperature, we calculated the “normalized overheating parameter” α' , given by Eqs. (1)–(3). Here, T_0 is the experimental bath temperature, T is the quasiparticle temperature, R_{s0} is the low-field surface resistance, B_c is the thermodynamic critical field, Y quantifies the electron-phonon energy transfer rate, d is the thickness of the cavity wall, κ is the thermal

* This work supported by NSF award PHY-1416318.

[†] jtm288@cornell.edu

A NEW METHOD FOR GRAIN TEXTURE MANIPULATION IN POST-DEPOSITION NIOBIUM FILMS

J. Musson[†], L. Phillips, K. Macha, Thomas Jefferson National Accelerator Facility,
Newport News, VA, USA

H. Elsayed-Ali, W. Cao, Old Dominion University, Norfolk, VA, USA

Abstract

Niobium films are frequently grown using forms of energetic condensation, with modest substrate temperatures to control grain structure. As an alternative, energetic deposition onto a cold substrate results in a dense amorphous film, with a much larger energy density than the re-crystallized state. Re-crystallization is then performed using a pulsed UV (HIPPO) laser, with minimal heating to the substrate. In addition, a graded interface between the substrate and Nb film can be created during the early stages of energetic deposition. Experimental approach and apparatus are described, and preliminary surface analyses are presented..

INTRODUCTION

As a result of the increased interest of high-energy particle accelerators, extensive research has been performed on the creation of superconducting (SC) accelerator cavity designs which exploit the application of thin films. Typical penetration depths of ~28 nm have encouraged decades of institutions to perfect the thin film formula, but have been met with disappointment with respect to cavities fabricated from bulk niobium [1,2].

The primary methods used to grow niobium films have been hetero-epitaxial growth, and fiber growth, encouraged by careful elevated substrate temperature manipulation. In this work, a third method is explored, utilizing re-crystallization of an amorphous film. Specifically, niobium is sputtered onto a 77 K substrate as a thick (~1 μm) amorphous layer. While not in the desired form, it is subsequently re-crystallized, using a localized thermal source (eg. 5 W UV laser), producing a bulk-like structure with larger grain size. The propensity of copper substrate diffusion into the Nb film is of concern, and mitigated by the 77 K substrate, as well as the short pulse and raster control of the laser. The objectives of this method include minimization of the substrate surface energy by cooling to 77 K (LN₂), maximizing the internal energy of the condensate (by minimizing diffusivity), carefully controlling film thickness during deposition, and precisely controlling temperature conditions during re-crystallization. Protecting the substrate from high temperatures during re-crystallization is important in order to preserve the graded interface, as well as to eventually minimize the diffusion of copper into the SC Nb film. Anticipated benefits of re-crystallization include

simplicistic deposition for manufacturability, grain texture*
 Authored by Jefferson Science Associates, LLC under U.S. DOE Contract No. DE-AC05-06OR23177. The U.S. Government retains a non-exclusive, paid-up, irrevocable, world-wide license to publish or reproduce this manuscript for U.S. Government purposes. manipulation (per precise heat source) for detailed studies, and maximizing the film-substrate adhesion by *ion stitching*.

ENERGETIC CONDENSATION

This process, known as energetic condensation, begins with a niobium plasma source, such as a cathodic arc, or high-power pulse power magnetron sputtering (HiPPMS), which provides a combination of neutral metal atoms, as well as ions [3]. While the kinetic energy of neutral metal atoms and ions is relatively low (~5-10 eV), the ionization potential energy of the Nb⁺ ions (~60 eV) is added to the kinetic energy, and deposited in the first few monolayers of the film. This results in large thermal spikes, and atomic displacement, characterized as *subplantation*. [4,5,6]. In addition, electron cyclotron resonance (ECR) has been used with good results, as well as a process known as coaxial energetic deposition (CED) [7]. Most recently, a technique known as modulated pulse-power magnetron sputtering (MPPMS) was introduced, which is similar to HiPPMS, but utilizes a train of shaped pulses, but with a lower operating voltage, to produce the ionic content [8].

MPPMS

The success of HiPPMS is, in part, due to the availability of high voltage/current insulated gate bipolar transistors (IGBT), which are capable of > 2000 V at 1000 A with a < 1% duty factor. However, this still represents state of the art, and the modulators tend to be expensive (\$100k), and rather inflexible. Alternately, MPPMS delivers a modest ~600 V pulse train, with up to 10% duty cycle, using moderately priced IGBTs (\$1k), and also increasing the deposition rate. In the case of niobium, MPPMS has been compared to HiPPMS and DCMS, with respect to voltage, current, average power, and relative ion content [8]; while HiPPMS still retains the highest ion/neutral ratio, MPPMS is attractive for low-cost, extreme flexibility, and ability to be produced in most laboratories. Films exhibiting high density (especially during first monolayers), minimal fiber

[†]musson@jlab.org

WIRE STRETCHING TECHNIQUE FOR MEASURING RF CRABBING/DEFLECTING CAVITY ELECTRICAL CENTER AND A DEMONSTRATION EXPERIMENT ON ITS ACCURACY*

Haipeng Wang[#], Thomas Jefferson Lab, Newport News, VA 23606, USA

Abstract

A new wire stretching technique combining with the RF measurement on the cavity dipole modes has been developed and demonstrated on the bench to detect less than 10 μ m offset and 0.1mrad tilt angle resolutions on the RF signal when the wire is deviated away from the ideal electric centre line. The principle of this technique and its difference from the use in other applications are reviewed and compared. Empirical formula, simulation and experiment results on the RF signal responses to the E-centre line offset and titling angle have been developed.

INTRODUCTION

First two types of LHC Superconducting crab cavities, RF Dipole (RFD) developed by ODU and Double Quarter Wave (QWR) developed by BNL have arrived at Jefferson Lab for further Electron Beam Welding (EBW), Buffer Chemistry Polishing (BCP), High Temperature Bake (HTB) and finally vertical qualification cold tests. The specified accuracies for cavity fabrication, tuning and component assembly alignment are very restricted due to the requirement of crabbing beams for the Large Hadron Collider High Luminosity Upgrade [1]. Like the cavity rotation is <0.3° per cavity, 3 cavities systematically are < 1.0°. The cavity beam axis offset in the crabbing plane is <0.5 mm. It is very hard for the crab cavity fabrication process to achieve this requirement since the cavity is formed by niobium sheet metal. Even the cavity dies could be machined very accurately, the spring back after the stamping can be very precisely controlled, the later EBW and BCP processes can deteriorate these accuracies easily due to unknown welding shrinkage, chemistry bath temperature et al. In addition, the cavity's crabbing or deflecting electric centre is not well defined, so the cavity's mechanical axial centre has been used as the ideal beam line centre due to the cavity has been designed with structure symmetry relative to the perpendicular plane of the crab crossing. However any additional change by the assembly of couplers, tuner's unsymmetrical tuning deformation, cryomodule cooldown et al., the actual electric centre could be changed later.

Precision 3-D bead-pulling measurement and laser scanner survey tool have been tried out. Their achievable accuracies are questionable due to the bead vibration and accumulated errors on the portable device. Their associated costs are also high.

* Authored by Jefferson Science Associates, LLC under U.S. DOE Contract No. DE-AC05-06OR23177 and US LARP grant.

haipeng@jlab.org

TECHNIQUES HISTORY

The Single Stretched Wire (SSW) has been used for the magnet electric centre survey and multipole filed measurement [2]. By measuring the integrated flux changes with various types of wire motion, the magnetic centre accuracy can be achieved in the displacement of ~30 μ m and the field direction in 0.1mrad.

The Wire Position Monitor (WPM) has been also used for the SRF cryomodule components alignment [3]. A 50 Ω strip-line BPM with the wire-carried RF signal can be processed to live monitor the cavity reference line change during cooldown. Meanwhile this BPM can be also used as the microphonic measurement with a cavity shaker. Its accuracy in displacement can be <7 μ m [4].

The Wire Method (WM) is also widely used for the coupling impedance of beam devices [5]. This method is not entirely reliable because the stretched wire perturbs the boundary conditions, introducing a TEM wave with a zero cut-off frequency. Below the pipe cut-off frequency, this WM produces an additional power loss which drastically lowers the high Q resonance of the device. Above the cut-off frequency, the impact of the wire is not as dramatic as below the cut-off. The Mode Matching (MM) technique like tapering cones is then used. A large discrepancy appears below cut-off frequency, while above cut-off, for certain ranges of parameters, an acceptable agreement can be found. For dipole mode impedance, a Twin-Wire (TW) and hybrids are used to measure the transverse impedance.

A surface wave signal transmits through a stretching wire with horn launcher and receiver is also used to calibrate BPMs [6]. The Goubau line can be made with a thin dielectric coating or a surface roughness on the wire to transmit RF slow-wave in an open space. A thin Tungsten wire (0.25mm dia.) used for Electrical Discharge Machining (EDM) is a good Goubau-line. It has been used for the CEBAF strip-line type BPM calibration. Its accuracy is about 100 μ m in 2cm \times 2cm grid area. The same line has been used for the following wire stretching setup.

WIRE STRETCHING SETUP

A 499 MHz RFD cavity has been used for this demonstration experiment as it shown in Figure 1. The EDM wire passing through the cavity beam pipe flanges was held in tension by two RF connectors on the table anchored X-Y stations. Each X-Y stage can be step-motor controlled in x (crabbing direction) and y in 1 μ m resolution. By moving wire position (x_1 , y_1) and (x_2 , y_2),

CONSIDERATION ON DETERMINATION OF COUPLING FACTORS OF WAVEGUIDE IRIS COUPLERS*

Sung-Woo Lee, Yoon W. Kang, Mark Champion
Oak Ridge National Laboratory (ORNL), Oak Ridge, TN

Abstract

Waveguide iris couplers are frequently used to power accelerating cavities in low beta sections of ion accelerators. In ORNL Spallation Neutron Source (SNS), six drift tube linac (DTL) cavity structures have been operating. An iris input coupler with a tapered ridge waveguide and a waveguide ceramic disk window feeds each cavity. The original couplers and cavities have been in service for more than a decade. Since all DTL cavity structures are fully utilized for neutron production, none of the cavity structures is available as a test cavity or a spare. Maintaining spares of the iris couplers for operations and future system upgrade without using the full DTL structure, a test setup for precision tuning is needed. A smaller single-cell cavity may be used for pretuning of the coupling irises as the test cavity and high power RF conditioning of the iris couplers as the bridge waveguide. In this paper, study of using a single-cell cavity for the iris tuning and the conditioning is presented with 3D simulations. A single-cell test cavity has been built and used for low power bench measurement with the iris couplers to demonstrate the approach.

INTRODUCTION

Six DTL cavities have been in operation for continuous neutron beam production in SNS since the commissioning of the system in 2006. The waveguide iris couplers are employed to power the cavities with 2.5MW klystrons at 402.5MHz in 8% duty cycle. In order to prepare spare couplers to support the current operation and future SNS system upgrade such as the second target station (STS) project [1], it is desirable to have a simple systematic method to evaluate and test performance of the couplers. Utilizing a single-cell test cavity was considered [2] for pretuning of the iris openings at low power in a single port configuration and for high power RF conditioning in a dual port setup.

In this paper, considerations in preparing a single-cell test cavity and methods of evaluating waveguide iris couplers are discussed in the context of ongoing work. Determining the scale factors of coupling coefficients is needed for each DTL cavity to use the test cavity. This requires accurate RF field information at the iris-cavity interface. RF simulation of SNS DTL structures in 3D involves modeling of the details in the cavity structures, which is challenging. Field flatness needs to be achieved

by aligning drift tubes properly to precisely estimate the magnetic field at the coupler location in the cavity.

SNS DTLs were built in two different tank diameters (Table 1) that resulted in two slightly different iris couplers in their iris surface curvatures. The slight mechanical mismatch that can be introduced to use a single-cell cavity with the iris couplers has been examined in this study for improved accuracy. For the single-cell cavity, two types of single cell test cavities can be built: a reentrant pillbox cavity and a simple pillbox cavity. They are compared with simulation results. A prototype single-cell test cavity was built for low-power bench measurements to compare with the simulation results.

RF MODELING CONSIDERATIONS

Utilizing a simple test cavity to find the iris dimensions for the desirable couplings in DTL structures, accurate scale factors of the coupling coefficients are required. The scale factor can be obtained from the ratios of the total surface losses and the wall magnetic fields on the location of the coupling iris [2, 3].

$$\alpha_{ms} \triangleq \beta_m / \beta_s = \left[\frac{H_1^2}{P_c} \right]_m / \left[\frac{H_1^2}{P_c} \right]_s, \quad (1)$$

where m denotes the full multi-cell cavity, s for the single-cell test cavity and H_1 , P_c are the cavity magnetic field on the coupling iris area without the coupler and the cavity power loss, respectively.

Longitudinal Field Flatness

Field flatness of the cavities with many cells is sensitive to the longitudinal alignments of cell geometries that include the drift tubes and their gaps. The SNS DTLs have various numbers of drift tubes depending on the particle beam velocity. Although mechanical tuning was performed in a structure, the model for the simulation has to be tuned again numerically to perform the study. This process provides a proper longitudinal field flatness in a cavity that is needed to find the magnetic fields on the coupler location. Numerical optimizations on the drift tube dimensions are performed to achieve field flatness using the eigenmode solver of CST MWS [4].

Table 1: Numbers of Drift Tubes and Tank Diameters of SNS DTLs

	DTL 1	DTL 2	DTL 3	DTL 4	DTL 5	DTL 6
Number of Drift Tubes	60	48	34	28	24	22
Diameter (inch)	17.109		17.871			

*This material is based upon work supported by the U.S. Department of Energy, Office of Science, Office of Basic Energy Sciences, under contract number DE-AC05-00OR22725. The research used resources of the Spallation Neutron Source, which is a DOE Office of Science User Facility.

UPDATE ON CW 8 kW 1.5 GHz KLYSTRON REPLACEMENT*

A.V. Smirnov[#], R. Agustsson, S. Boucher, D. Gavryushkin, J.J. Hartzell, K.J. Hoyt, A. Murokh, T.J. Villabona, RadiaBeam Systems Inc., Santa Monica, CA 90404 USA
 R. Branner, K. Yuk, University of California, Davis, Davis, CA 95616 USA
 S. Blum, MACOM Lincoln Lab, Lincoln, RI 02865 USA
 V. Khodos, Sierra Nevada Corporation, Irvine, CA 92618 USA

Abstract

JLAB upgrade program requires a ~8 kW, 1497 MHz amplifier operating at more than 55-60% efficiency, and 8 kW CW power to replace up to 340 klystrons. One of possibilities for the klystron replacement is usage of high electron mobility packaged GaN transistors applied in array of highly efficient amplifiers using precise in-phase, low-loss combiners-dividers. Design features and challenges related to amplifier modules and radial multi-way dividers/combiners are discussed including HFSS simulations and measurements.

INTRODUCTION

The original RF power system at the Thomas Jefferson National Accelerator Facility (JLab) operates at 1497 MHz frequency and consists of 340 klystrons (model VKL7811). The VKL7811 klystron upgrade proposed by CPI foresees adding a solenoid magnet and its power supply, making the system so large that it will not fit in existing locations. Inductive Output Tubes (IOTs) were considered as a replacement [1]. However, IOTs are not available at 1.5 GHz, would need to be redesigned to avoid solenoid coils, and require a booster (preamp driver) as they have ~15 dB lower gain than a klystron.

High-power vacuum tubes are employed ubiquitously in radars, accelerators, and material processing industries. Although the technology is well defined and established for many decades, there are also a number of disadvantages. Among those that impose certain risks for JLab future operations are relatively low efficiency (presently 33% [1]) and shrinking market for the tube that implies growing production and refurbishing costs.

As an alternative to klystrons and other vacuum tubes, RadiaBeam is developing high-power amplifiers based on gallium nitride (GaN) high electron mobility field effect transistors (HEM FET) which offer significant potential to higher efficiencies than vacuum tube devices. Although each individual device operates at much lower power, its compact size potentially enables many of them to be operated in parallel to achieve the power needed to replace klystrons.

However, such a replacement presents a number of challenges. Most of known high power S-band or L-band transistors are traditionally designed for a pulse mode (usually for radar applications), whereas combined CW operation to our knowledge has never been demonstrated in L-band at such high, multi-kW power levels. Drain

efficiency is significantly lower than that for pulsed operation, because of various charge trapping and self-heating effects enhanced by much higher internal FET thermal resistance in CW mode of operation. Also combining efficiency tends to drop quickly with number of combining ways (faster than linear [2]). Yet another challenge is that GaN high power transistors are vulnerable to instabilities especially in CW and presence of cross-talk (insufficient isolation) between the combining ways. Depletion mode devices cannot be operated without specialized control system enabling proper bias sequencing through discretionary access control (DAC), thermal compensation, and independent fine adjustment of bias voltages and temperature slope. Additional requirements for the control system include stable (tolerable to supply voltage variations) driving of large capacitive loads and impedances in a wide dynamic range. Note, kW-range solid-state amplifier systems are industrially available in S- or L- bands. However, specific (volumetric) power density for these state-of-the-art systems is about one order lower than that for klystrons, whereas efficiency is moderate (~52% in L-band [3]). Higher density of packaging is limited by cooling, need in high, low-impedance capacitances to be connected to the amplifier modules, bulky combiner-dividers (especially in L-band), and need in eased access to the replaceable modules.

UPDATE ON ACTIVE MODULES

Here we take a broader look on L-band CW performance for transistors from different vendors. In Table 1 we summarized most of important datasheet characteristics HEM GaN MOSFETs that have been considered for the active modules. In US the transistors are currently presented by four US vendors: WolfSpeed, Qorvo, MACOM, and NPT Semiconductors. The data related specifically to CW operation are underlined in Table 1. The data are extracted from datasheets for 1.5 GHz frequency, with exception of QPD1823 data given for ~1.8 GHz frequency. Note unlike CGHV14250 and CHV14500 FETs, the CGHV14800 transistor duty factor is limited by 10% or less. Therefore it is not applicable to CW operation.

We performed CW measurements of conventional Class AB test boards supplied with intense water cooling. Some of the results are given in Table 2 for four different transistors. The performance is a somewhat lower than that (voltage) probably because we used a lowered drain voltage. Nevertheless one can see CGHV14500 FET maximum CW power and efficiency are below than that we obtained for CGHV14250 test setup in CW at ~1.5 GHz frequency. Also we faced issues related to gain

* Work supported by the U.S. Department of Energy (award No. DE-SC0013136)

[#] email address: asmimov@radiabeam.com

FIELD EMISSION DARK CURRENT SIMULATION FOR eRHIC ERL CAVITIES

Chen Xu, Ilan Ben-Zvi¹, Yue Hao, Vadim Ptitsyn¹, Kevin Smith, Binping Xiao, Wencan Xu
Brookhaven National Laboratory, Upton, New York 11973-5000, USA

¹ also at Stony Brook University, Stony Brook, New York 11794, USA

Abstract

The eRHIC project will be a electron and proton collider proposed in BNL. These high repetition rates will require Super-Conducting Radio-Frequency cavities with fundamental frequency of 650MHz for high current applications. Each with a string of two of those cavities. The strong electromagnetic fields in the SRF cavities will extract electrons from the cavity walls and will accelerate those. Most dark current will be deposited locally, although some electrons may reach several neighbour cyromodules, thereby gaining substantial energy before they hit a collimator or other aperture. Simulation of these effects is therefore crucial for the design of the machine. Track3P code was used to simulate field-emission electrons from different SRF cavities setup to optimize the field emission dark current characterizes..

INTRODUCTION

eRHIC project requires to build an electron linac ring on top of the existing RHIC ring. One of the design proposed by BNL is that an ERL based accelerator to increase electrons energy to collision energy $\sim 18\text{GeV}$ and extract their energy after collision with proton. The accelerator would be equipped with Superconducting Radiofrequency resonators to achieve the energy boost and recover the RF energy. Currently, the proposed frequency is 647.5MHz. The low frequency SRF cavities usually have larger iris and apertures than the high frequency cavities. These large apertures help damp the malicious RF energy out of the RF structure but also facilitates more field emission electrons to escape the RF structures. On the other hand, the SRF surfaces areas are inversely proportional to the fundamental frequency. A larger surface area supplies more possible emission sites due to the cleaning capability. Therefore, understanding the field emission electron characterizations will be a critical to estimate the dark current, to evaluating the radiation dosage and to prevent further propagation.

The estimation on radiation would give several malicious effects. 1, cryogenic loss; 2. RF waste on dark beam loading; 3. Radiation damage on cables and electronics; 4. Beamline vacuum deterioration and Beamline activation.

A CAVITY EMISSION

Currently, we plan to use beam pipe absorbers as our eRHIC HOM damping scheme. Room temperature absorbers will be placed on side of each. The distance

between SRF cavity and RT beam pipe damping would be longer because of the temperature gradient and evanescent fundamental mode.

The cavity geometry net length is 1.96m which is 4.228 times of the wavelength of 647MHz. The cavity schematic is shown in Figure 1. [1]

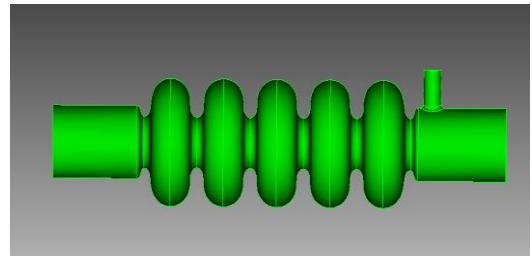


Figure 1: Cavity scheme for current eRHIC project.

Once the surface electric field is higher than the work function, surface electrons will escape the surface energy barrier and the emission current density is well-defined by Fowler–Nordheim equation in DC case. Empirically, field emission can occur when accelerator gradient is quite low. [2] Not all the SRF surfaces have high E field to emission. At the 18MeV/m accelerating gradient, the emission sites are plotted in Figure 2. The field emission dark current estimation is simulated in Omega 3P suite.

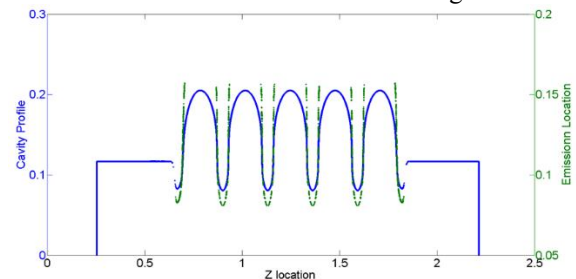


Figure 2: The initial field emission site on SRF cavity

The local surface electric field can be enhanced by geometrically protrusions. The typical enhancement factor is 120 in the tracking simulation.

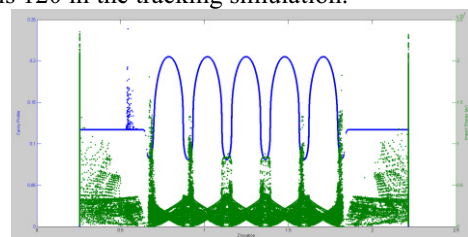


Figure 3: The impact site of field emission on SRF cavity.

Work supported by the US Department of Energy under contract number DE-SC0012704

7: Accelerator Technology Main Systems

T07 - Superconducting RF

DEPOSITION OF NON-EVAPORATIVE GETTERS R&D ACTIVITY FOR HEPS-TF

D. Z. Guo, P. He, B. Q. Liu, Y. S. Ma[†], Y. C. Yang, L. Zhang, IHEP, CAS, Beijing, P.R. China

Abstract

Non Evaporable Getter(NEG) coating technology was widely used around the world's ultra-low emittance storage rings. It will provide the distributed pumping which is the obvious solution to solve the conductance limitation of narrow vacuum chamber at small magnet aperture. The HEPS-TF is the R&D project of HEPS (High Energy Photon Source), it will cover all of the key technology for HEPS accelerator system and beamlines. In order to meet the small aperture vacuum chamber distributed pumping requirement, the NEG coating R&D for HEPS vacuum chamber is under the way. Getter films deposited on the inner surface of the chamber would transform the vacuum chamber from an outgassing source into a pump. The coating test bench will be shown here and coating procedure will be presented.

INTRODUCTION

The HEPS-TF is the R&D project of HEPS (High Energy Photon Source), it will cover all of the key technology for HEPS accelerator system and beamlines. To further develop the technologies necessary for diffraction-limited storage rings based light source, it involves many areas: vacuum system/non-evaporable getter (NEG) coating of small chambers, fast injection/pulsed magnets, RF systems/bunch lengthening, magnets/radiation production with advanced radiation devices(insertion devices), high precision power supply, beam diagnostics, mechanical support, and beam physics design(lattice) optimization.

The HEPS 6 GeV storage ring (1296 m in circumference) will be an ultra-low emittance ring (bare lattice emittance below 0.1 nm-rad) based on multi-bend achromat (MBA) magnet concept. Due to the compact lattice design and applied small magnet aperture of 25 mm, so the majority of the vacuum chambers are designed as circular tubes of 22 mm inside diameter and 1 mm wall thickness. This will cause the conductance limitation problem for the vacuum pumping. To reduce ring vacuum pressure, some of the conductance limited chambers are planned to be coated with non-evaporable getter (NEG) film of TiZrV. The use of NEG (Non-Evaporable Getter) thin film deposited onto the components used in a vacuum system has revolutionized the design of vacuum systems. The NEG film brings pumping to sources of gasloads; it provides distributed pumping in a space-limited environment and has a very low outgassing rate. The coating is deposited by magnetron sputtering method that was developed at CERN [1] and is used in other synchrotron light facilities around the world. In recent years, different getter materials have been investigated [2,3,4].

In this context, our work will focus on the progress of the deposition of NEG coatings in very narrow chambers, as well as engineering and physics challenges they face today.

NEG COATING TEST BENCH

The TiZrV NEG films were deposited using the DC Magnetron Sputtering technique. The DC Magnetron Sputtering technique was employed due to its simplicity and lower sputtering gas pressure. A schematic diagram of the experimental setup for NEG deposition is shown in Figure 1. The vacuum chamber is a 1.5 m long, 22 mm inner diameter copper cylindrical tube. The cathode was made by twisting three wires of high-purity (99.95%) titanium, vanadium and zirconium, each of 1 mm diameter, using an electric drill machine. Ti-V-Zr type was chosen because of its lowest activation temperature among ternary getters. The tube sample is electrically isolated mounted to the chamber in the direction of gravity. The cathode wire runs through the tube sample and is positioned approximately along the axis of the tube. The bottom end of the cathode wire was connected to a high voltage feed through, and the top end was mounted to a blank flange. Two edge-welded bellows, each with three springs mounted in between its flanges, apply tensile force to the cathode wire to keep it straight, preventing short circuit. Gas inlet was mounted on the top of the system, and the vacuum pumps are mounted in the bottom. A solenoid was mounted outside and coaxial to the sample tube, providing a magnetic field parallel to the tube.

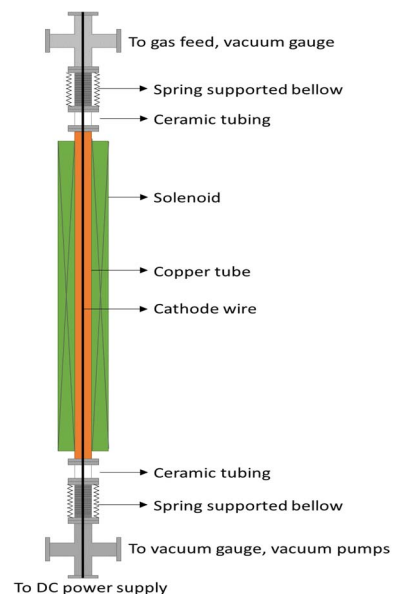


Figure 1: Test bench set-up.

STATUS REPORT ON THE SPIRAL2 FACILITY AT GANIL

E. Petit, GANIL, Caen, France
on behalf of the SPIRAL2 collaboration

Abstract

The GANIL SPIRAL2 project is based on the construction of a superconducting ion CW LINAC with two experimental areas named S3 (“Super Separator Spectrometer”) and NFS (“Neutron For Science”). This status will report the construction of the facility and the first beam commissioning results.

The perspectives of the SPIRAL2 project, with the future construction of the low energy RIB experimental hall called DESIR and with the construction of a new injector with $q/A > 1/6$ or $1/7$, will also be presented.

INTRODUCTION

Officially approved in May 2005, the GANIL SPIRAL2 radioactive ion beam facility (Fig. 1) was launched in July 2005, with the participation of many French laboratories (CEA, CNRS) and international partners. In 2008, the decision was taken to build the SPIRAL2 complex in two phases : a first one including the accelerator, the Neutron-based research area (NFS) and the Super Separator Spectrometer (S3), and a second one including the RIB production process and building, and the low energy RIB experimental hall called DESIR [1,2].

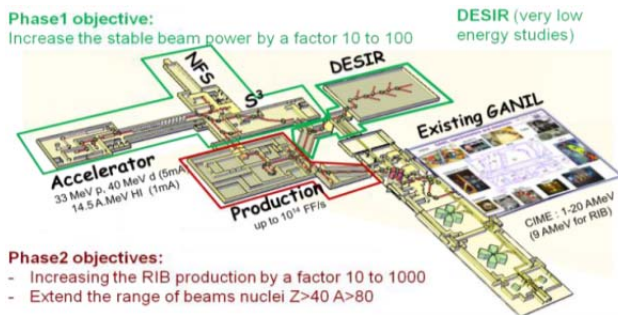


Figure 1: SPIRAL2 project layout, with experimental areas and connexion to the existing GANIL.

In October 2013, due to budget restrictions, the RIB production part was postponed, and DESIR was planned as a continuation of the first phase.

The extension of the SPIRAL2 facility, with the construction of a new injector with $q/A > 1/6$ or even $1/7$ heavy ions connected to the LINAC, is also evaluated. This new injector will increase the competitiveness of the SPIRAL2 facility by producing higher beam intensity and also heavier ion species.

The SPIRAL2 facility is now built, the accelerator installation, connecting tasks are almost achieved and the beam commissioning have started with very good results with the goal of the first beam for physics (NFS) in 2017 [3,4].

ACCELERATOR-NFS-S3 BUILDING

The construction permit of the accelerator-NFS-S3 building was obtained in October 2010. The construction of the building started in January 2011. After a difficult excavation work (Fig. 2) and geotechnical/geologic studies, the first concrete started in September 2011 (Fig. 3). The building with the conventional utilities was officially received by the end of 2014 (Fig. 4).

Significant key figures of the SPIRAL2 building construction are:

- 14 000 m³ of concrete poured,
- 2 200 T of steel reinforcement used,
- 450 000 work hours,
- Up to 120 workers on site.



Figure 2: End of excavation work mid 2011.



Figure 3: First concrete in September 2011 and the foundation stone ceremony in October 2011.



Figure 4: Completion of the accelerator building (October 2014). The beam axis is 8 meters underground.

TECHNOLOGICAL CHALLENGES ON THE PATH TO 3.0 MW AT THE SNS ACCELERATOR*

Kevin W. Jones[†], Oak Ridge National Laboratory, Oak Ridge, TN, USA for the SNS Team

Abstract

The Spallation Neutron Source (SNS) is a ~ 1 GeV pulsed hadron linear accelerator (linac) and accumulator ring capable of delivering ~ 23.3 kJ, 700 ns pulses of protons at 60 Hz to a mercury spallation target to produce intense pulses of thermal and cold neutrons. Oak Ridge National Laboratory (ORNL) proposes to build an innovative Second Target Station (STS) at SNS to meet the U.S. demand for neutrons. The current STS design requires 46.7 kJ, 700 ns pulses at 10 Hz to meet the needs of the scientific program[1]. The Proton Power Upgrade (PPU) project aims to double the available accelerator complex power from 1.4 MW to ~ 3.0 MW to meet these needs. This paper describes the technological challenges that must be addressed to achieve this objective.

STS CAPABILITIES

The STS as envisaged would be value engineered to provide the world's highest peak brightness neutron source to meet five high-level requirements:

- Provide cold neutrons with enhanced beam focusing and neutron spin manipulation to address nanoscale to mesoscale phenomena and slow material dynamics.
- Provide intense pulses at 10 Hz to limit heat deposition in a compact target and moderator assembly, enable utilization of wavelength dispersive methods, permit simultaneous access to a wide range of length and time scales, and sufficient flux to support extreme sample environments with limited angular access.
- Utilize high performance computing for real-time manipulation and visualization of massive data sets, and to combine and interpret multi-technique data.
- Provide innovative neutron scattering instrument concepts with multi-modal and flexible configurations that provide order of magnitude performance gains compared to current and currently envisaged capabilities.
- Provide high peak neutron brightness to enable in-situ sample synthesis, non-equilibrium studies, reaction kinetics, microspot scanning and parametric studies.

The envisaged pulse structure for one particular neutron wavelength compared to that currently available at the SNS First Target Station (FTS), the Japan Proton Accelerator Research Complex (J-PARC) and the European

Spallation Source (ESS) currently under construction is shown in Figure 1.

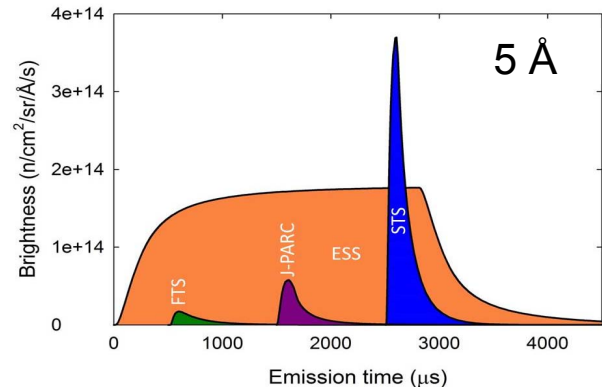


Figure 1: Temporal flux of 5 Å neutrons from SNS-FTS, J-PARC, ESS and SNS-STs.

CURRENT SNS MACHINE PERFORMANCE

To fully appreciate the technological challenges related to doubling the current available beam power it is helpful to understand current machine performance and capability. The SNS has delivered a remarkable 33.844 GW-Hr of proton beam to target over the past ~ 10.5 years and has demonstrated sustained operation at beam power levels up to 1.4 MW. Since 2012 overall reliability against schedule has been affected principally by mercury target vessel performance, varying from 72.5% to 89.5%. However if target end-of-life events are removed, basic accelerator and accumulator ring reliability varies from 89.6 to 93.2% over the same period, with only one year below 90%. Beam power and total energy delivered since commissioning are illustrated in Figure 2.

For the SNS, the average beam power is derived from the peak current injected into the RFQ, the chopping fraction, RFQ transmission, the final beam energy, and the RF duty factor.

Duty Factor

The SNS has achieved stable long-term performance at a repetition rate of 60 Hz and a beam pulse width of 965 μ s for a macroscopic beam duty factor of 5.79%. Note that the RF duty factor is somewhat higher to allow structures to fill and stabilize before the beam is accelerated.

* This material is based upon work supported by the U.S. Department of Energy, Office of Science, Office of Basic Energy Sciences under contract number DE-AC05-00OR22725.

[†] joneskw@ornl.gov

SIMULATION OF BEAM DYNAMICS IN A STRONG FOCUSING CYCLOTRON*

K. E. Badgley[†], Fermilab, Batavia, Illinois

J. Gerity, P. McIntyre, A. Sattarov, Texas A&M University, College Station, Texas

S. Assadi, HiTek ESE LLC, Madison, Wisconsin

N. Pogue, Lawrence Livermore National Lab, Livermore, California

Abstract

The strong-focusing cyclotron is an isochronous sector cyclotron in which slot geometry superconducting cavities are used to provide sufficient energy gain per turn to fully separate orbits. Each orbit travels through superconducting beam transport channels, located in the aperture of each sector dipole, to provide strong focusing and control betatron tune. The SFC offers the possibility to address several effects that limit beam current in a CW cyclotron: space charge, bunch-bunch interactions, resonance crossing, and wake-fields. Simulation of optical transport and beam dynamics entails several new challenges: the combined-function fields in the sectors must be properly treated in a strongly curving geometry, and the strong energy gain induces continuous mixing of horizontal betatron and synchrotron phase space. We present a systematic simulation of optical transport using modified versions of MAD-X and Synergia. We report progress in introducing further elements that will set the stage for studying dynamics of high-current bunches.

INTRODUCTION

Commercial facilities for medical isotope production, material irradiation by spallation neutrons, and accelerator driven subcritical core for spent nuclear fuel destruction or energy production [1-3] are a few examples where high beam current accelerators are required. The production of high current beams in cyclotrons has several challenges, including: space charge effects, turn to turn separation and total number of turns. It has been shown that the maximum achievable current increases as the inverse cube of the number of turns in the cyclotron [4]. To overcome the challenges of high intensity cyclotrons, The Accelerator Research Lab of Texas A&M University is developing a Strong Focusing Cyclotron (SFC) [5-7] that incorporates two technological innovations developed in the laboratory: low profile tapered superconducting RF-cavities, that are capable providing up to 3MV accelerating voltages, and superconducting strong focusing/defocusing (FD) beam transport channels (BTC) that should allow full control of the beam. Figure 1a) shows the 6 sector 100 MeV SFC and its main components: 4 tapered low profile SRF cavities and BTCs along the design path. The arrangement of the BTC on the face of the pole piece of the sector magnet and the BTC quadrupole and window-frame correction dipole windings are

* This work was supported by the Accelerator Stewardship Program of the US Dept. Energy, grant DE-SC0013543.

[†] email address karie.email@gmail.com

shown in Figure 1 b)-c). Figure 1 d) shows an example cross section of BTC producing a 7.5 T/m quadrupole. The main parameters of the cyclotron are given in Table .

Table 1: Main Parameters of the Cyclotron

Parameter	Value
Number of sectors	6
Sector Angle, degrees	54.42
Injection Energy, MeV	6.5
Injection Radius, m	1.1
Extraction Energy, MeV	100
Extraction radius, m	4.3
Harmonic number, h	25
Number of Turns	14
Cavity Frequency, MHz	117
Maximum Quad Strength, T/m	7.5
Correction dipole field, mT	20

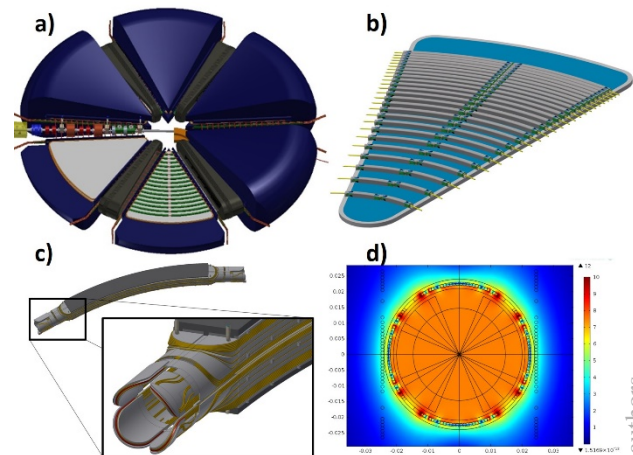


Figure 1: 100MeV SFC and its main elements.

REFERENCE ORBIT AND SECTOR MAGNETS FOR THE SFC

Beam dynamics and particle tracking require knowledge of the equilibrium orbit and elements of the accelerator. In a cyclotron, the equilibrium orbit and parameters of the accelerator elements are often found from a series of closed orbits. For the strong focusing cyclotron described here, the equilibrium orbit, and corresponding elements, must follow a spiral to stay within the BTCs, so the closed orbit method will not work. The remaining accelerator codes were designed for circular machines, or

CONCEPTUAL DESIGN OF A RING FOR PULSE STRUCTURE MANIPULATION OF HEAVY ION BEAMS AT THE MSU NSCL*

Alfonse N. Pham[†], Michael J. Syphers¹, Chun Yan Jonathan Wong, Steven M. Lund², Roy Ready
National Superconducting Cyclotron Laboratory, Michigan State University, East Lansing, MI, USA

¹ Department of Physics, Northern Illinois University, DeKalb, Illinois, USA

² Facility for Rare Isotope Beams, Michigan State University, East Lansing, MI, USA

Abstract

The Reaccelerator (ReA) Facility at the National Superconducting Cyclotron Laboratory (NSCL) located at Michigan State University (MSU) offers the low-energy nuclear science community unique capabilities to explore wider ranges of nuclear reactions and the structure of exotic nuclei. Future sensitive time-of-flight experiments on ReA will require the widening of pulse separation for improved temporal resolution in single bunch detection while minimizing loss of rare isotopes and cleaning of beam decay products that might pollute measurements. In this proceedings, we present a preliminary design of a heavy ion ring that will address the task of bunch compression, bunch separation enhancement, satellite bunches elimination, cleaning of decay products, beam loss mitigation, and improvement of beam transmission.

INTRODUCTION

The Coupled Cyclotron Facility (CCF) at the NSCL [1–3] utilizes two superconducting cyclotrons to accelerate primary ion beams up to 160 MeV/u at 1 kW beam power on a production target for rare isotope beam (RIB) production for use in nuclear physics experiments. Secondary RIBs from the target are delivered to one of three main experimental areas. In the fast-beam experimental area, the shortest-lived RIBs are delivered with energies >150 MeV/u to experiments. In the stopped-beam experimental area, delivered RIBs are thermalized (~eVs) in either gas cells or a cyclotron gas stopper before transport to the trap and laser spectroscopy area. Lastly, in the ReA experimental area shown in Fig. 1, thermalized RIBs are captured and rapidly ionized in an Electron Beam Ion Trap (EBIT) charge breeder [?, 4]. The 12 keV/u [6] RIBs emerging from the EBIT then undergo separation in a Q/A achromatic spectrometer (operational range of $0.2 \leq Q/A \leq 0.5$), are bunched in a multi-harmonic buncher (MHB), injected into a radio-frequency quadrupole (RFQ) for pre-acceleration to 600 keV/u, and finally injected into the superconducting linear accelerator (LINAC) for final acceleration up to 6 MeV/u. Upgrade plans exist to accelerate RIBs up to 12 MeV/u by adding more superconducting cryomodules.

The ReA RFQ and LINAC are designed to operate at 80.5 MHz. This allows ReA to serve as a testbed for Facility for the Rare Isotope Beam (FRIB) RFQ and superconducting RF (SRF) technology. The EBIT charge breeder produces

* Research supported by Michigan State University, MSU NSCL, ReA Project, and NSF Award PHY-1415462.

[†] pham@nsl.mscl.msu.edu

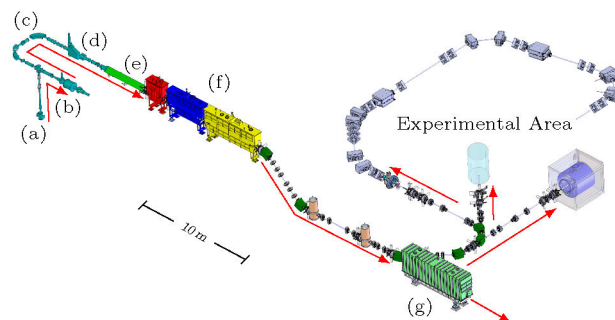


Figure 1: Diagram of the ReA facility where (a) thermalized RIBs are injected into (b) the EBIT charge breeder, undergo (c) A/Q separation after extraction, (d) matched and bunched with a MHB, (e) accelerated by a RFQ, and (f) finally injected into the SRF LINAC. Further acceleration (g) in a second LINAC section is possible.

Table 1: Properties of RIBs extracted from the ReA EBIT.

EBIT Parameters	Values
Extraction Kinetic Energy W_s	12 keV/u
Total Bunch Length σ_z	100 ns - 10s μ s
Energy Spread $\Delta W/W_s$	< 0.5%
RMS Transverse Emittance ϵ_x, ϵ_y	< 10 mm-mrad

high-charge state RIBs for ReA. Typical extracted beam properties of the EBIT are given in Table 1. The time structure of the bunch emerging from the EBIT depends strongly on the extraction scheme implemented [7]. To achieve optimal beam transmission through the RFQ, a MHB using three harmonics is utilized in the beam transport line [8]. For time-of-flight (TOF) measurements, the existence of satellite bunches at integer multiples of 12.4 ns from the primary pulse formed in the bunching process creates uncertainties in the measurements. Due to the short bunch pulse separation, the satellite bunches create ambiguity in the pulse time spread at the location of the detector as well as in the bunch detection. Figure 2 shows the bunched beam just before injection into the RFQ with non-linear tails overlapping the neighboring buckets of the RFQ. This results in the satellite bunches that were measured at the exit of the LINAC after acceleration. We present a conceptual design of a flexible buncher ring for heavy ions to address bunching challenges in ReA. The limited acceptance of the ring will also “clean” the RIBs of decay products that can confound measurements of interest of very short-lived isotopes.

OPERATING SYNCHROTRON LIGHT SOURCES WITH A HIGH GAIN FREE ELECTRON LASER

S. Di Mitri[†], M. Cornacchia, Elettra – Sincrotrone Trieste S.C.p.A., Basovizza, Trieste I-34149

Abstract

The peak current required by a high gain free electron laser (FEL) is not deemed to be compatible with the multi-bunch filling pattern of synchrotrons. We show that this problem can be overcome by virtue of magnetic bunch length compression in a ring section and that, after lasing, the beam returns to equilibrium conditions without beam quality disruption. As a consequence of bunch length compression, the peak current stimulates a high gain FEL emission, while the large energy spread makes the beam less sensitive to the FEL heating and to the microwave instability. The beam large energy spread is matched to the FEL energy bandwidth through a transverse gradient undulator. Feasibility of lasing at 25 nm is shown for the Elettra synchrotron light source (SLS) at 1 GeV. Viable scenarios for the upgrade of existing or planned SLSs to the new hybrid insertion devices-plus-FEL operational mode are discussed, while ensuring little impact on the standard beamlines functionality [1].

CONCEPT

The 260-m long Elettra circumference may internally host a by-pass undulator line ~60 m long at most, with ~20 m left for beam extraction, optics matching to the undulator line and re-injection into the ring. With the one-dimensional (1-D) TGU–SASE model introduced in [2,3], we estimate a saturation length of around 50 m for an FEL radiating at 25 nm, and driven by ~450 A peak current, ~1% relative energy spread beam. The FEL fundamental wavelength is shown in Fig.1-left plot as a function of the beam energy, and defined by the resonance condition $\lambda = (\lambda_u / 2\gamma^2) (1 + K^2/2)$, where γ is the relativistic Lorentz factor for the beam energy, λ_u is the undulator period length, $K = eB_0\lambda_u / (2\pi m_e c)$, typically in the range 1–5, is the so-called undulator parameter for a planar undulator, B_0 is the undulator peak magnetic field, e , m_e and c are the electron charge, rest mass and speed of light in vacuum, respectively. The Elettra horizontal equilibrium emittance is shown in the same plot as a function of beam energy ($\epsilon_x \propto E^2$) and number of dipole magnets in an achromatic cell ($\epsilon_x \propto 1/N_b^3$; $N_b=2$ for the actual lattice). At $\lambda=25$ nm, the diffraction limit $\epsilon_x = \lambda / (4\pi) \approx 1.8$ nm is reached at $E=1.0$ GeV (see intersection of solid blue and red curve in Fig.1)

We assume to install an S-band RF cavity in a straight section of the ring, and to run it at the phase of zero-crossing. A linear correlation in the electron longitudinal phase space (z, E) is established, and the bunch length is shortened by means of the momentum compaction α_c of the downstream ring section, in our example one half of the Elettra circumference. The following relationship has

to be fulfilled by the energy chirp h , the RF peak voltage V , the bunch length compression factor C and $R_{56} = \alpha_c C R / 2$ of half the circumference length C_R :

$$h \equiv \left(\frac{1}{C} - 1 \right) \frac{1}{R_{56}} = \frac{1}{E} \frac{dE}{dz} = \frac{2\pi}{\lambda_{RF}} \frac{eV \cos \phi_{RF}}{E_0 + eV \sin \phi_{RF}} \approx \frac{\sqrt{\sigma_{\delta cor,0}^2 + \sigma_{\delta unc,0}^2}}{\sigma_{z,0}} \quad (1)$$

In Eq. 1, λ_{RF} is the RF wavelength, ϕ_{RF} ($= 0$) the RF phase (at zero-crossing), $\sigma_{\delta cor,0}$, $\sigma_{\delta unc,0}$, and $\sigma_{z,0}$, the energy spread correlated with z , the uncorrelated energy spread and the bunch length *before* compression, respectively. In our example, $R_{56}=0.21$ m, $\sigma_{\delta unc,0}=0.1\%$ and $\sigma_{z,0}=2.7$ mm. The chirp that provides minimum bunch length, *i.e.*, maximum peak current at the end of compression is $h = -1/R_{56} = -4.8$ m⁻¹. The shortest bunch length we can achieve is $R_{56}\sigma_{\delta unc,0} = 210$ μ m, and therefore the maximum effective compression factor is $C = \sigma_{z,0}/(R_{56}\sigma_{\delta unc,0}) \approx 13$. With a bunch charge $Q=0.8$ nC, a peak current $I = CQc/(\sqrt{2\pi}\sigma_{z,0}) = 450$ A is provided at the undulator.

Linear compression is guaranteed as long as the correlated energy spread is larger than the uncorrelated one; the latter evolves during compression according to $\sigma_{\delta unc} = C\sigma_{\delta unc,0}$, because of longitudinal emittance preservation (*i.e.*, the bunch length is shortened by a factor C , whereas the uncorrelated energy spread increases by the same factor). Hence, we require $\sigma_{\delta cor,0} \gg \sigma_{\delta unc}$, where $\sigma_{\delta unc} = \sigma_{\delta unc,0} = 0.1\%$ at equilibrium, and where $\sigma_{\delta unc}$ approaches 1.3% when $C \rightarrow 13$. At the same time, $\sigma_{\delta cor,0}$ has to be not much larger than the synchrotron momentum acceptance, nominally 3% in Elettra, to avoid particle losses. With the parameters above, Eq.1 specifies $V \approx 76$ MV and $\sigma_{\delta cor,0} \approx 1.3\%$. Fig.1-right plot is the analytical representation of Eq.1, and it suggests that, for any C and $\sigma_{z,0}$, a large R_{56} is desirable to minimize h . A large R_{56} , however, is usually in conflict with the requirement of a low-emittance beam, which is the prerequisite for efficient lasing at short wavelengths.

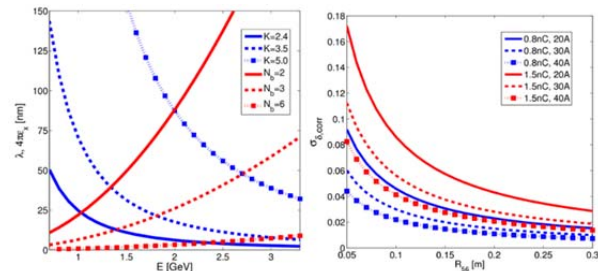


Figure 1: Elettra equilibrium horizontal emittance for different number of dipoles per cell (red), and FEL wavelength for different undulator parameters (blue), vs. beam energy. Right: rms relative correlated energy spread vs. R_{56} , to reach 450 A starting from an initial peak current of 20–40 A. Copyright of NJP (2015) [1].

[†] simone.dimitri@elettra.eu

ALS-U: A SOFT X-RAY DIFFRACTION LIMITED LIGHT SOURCE*

C. Steier[†], A. Anders, J. Byrd, K. Chow, R. Duarte, J. Jung, T. Luo, H. Nishimura, T. Oliver, J. Osborn, H. Padmore, C. Pappas, S. Persichelli, D. Robin, F. Sannibale, S. De Santis, R. Schlueter, C. Sun, C. Swenson, M. Venturini, W. Waldron, E. Wallen, W. Wan, Y. Yang
LBNL, Berkeley, CA 94720, USA

Abstract

Improvements in brightness and coherent flux of about two orders of magnitude are possible using multi bend achromat lattice designs [1]. These improvements can be implemented as upgrades of existing facilities as in the case of the Advanced Light Source Upgrade (ALS-U). ALS-U will reuse much of the existing infrastructure, thereby reducing cost and time needed to reach full scientific productivity. This paper summarizes the accelerator design progress as well as some details of the ongoing R+D program.

INTRODUCTION

The ALS-U design replaces the existing triple-bend achromat with a stronger-focusing multi-bend achromat [2, 3] aiming at producing round beams of approximately 50 pm-rad emittance, about 40 times smaller than the horizontal emittance of the existing ALS, and thus leading to a big increase in coherent flux. The current baseline design is a nine-bend achromat. ALS-U was evaluated in June 2016 by a Basic Energy Sciences Facility Upgrade Prioritization Subcommittee as 'Absolutely Central' to contribute to world leading science and as 'Ready to Initiate Construction' and received approval of Mission Need (CD-0) from DOE/BES in September 2016. Table 1 summarizes the main parameters and Figure 1 shows the nine bend achromat as well as the new accumulator ring.

Table 1: Parameter List Comparing ALS with ALS-U

Parameter	Current ALS	ALS-U
Electron energy	1.9 GeV	2.0 GeV
Beam current	500 mA	500 mA
Hor. emittance	2000 pm-rad	~50 pm-rad
Vert. emittance	30 pm-rad	~50 pm-rad
rms beam size (IDs)	251 / 9 μm	$\leq 10 / \leq 10 \mu\text{m}$
rms beam size (bends)	40 / 7 μm	$\leq 5 / \leq 8 \mu\text{m}$
Energy spread	9.7×10^{-4}	$\leq 9 \times 10^{-4}$
bunch length (FWHM)	60–70 ps (harm. cavity)	120–200 ps (harm. cavity)
Circumference	196.8 m	~196.5 m
Bend angle	10°	3.33°

One of the consequences of producing a small emittance is a small dynamic aperture, although the momentum accep-

* This work was supported by the Director, Office of Science, Office of Basic Energy Sciences, of the U.S. Department of Energy under Contract No. DE-AC02-05CH11231.

[†] CSteier@lbl.gov

2: Photon Sources and Electron Accelerators

A05 - Synchrotron Radiation Facilities

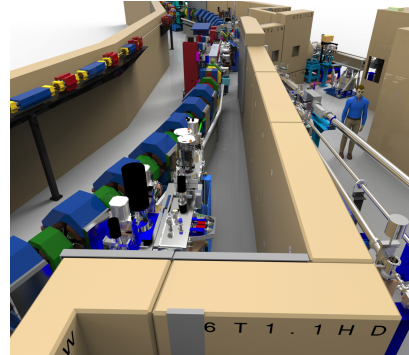


Figure 1: CAD model of ALS-U showing the existing accelerator tunnel with the new storage and accumulator rings.

tance will remain large enough for acceptable beam lifetime. To overcome this challenge, ALS-U will use on-axis swap-out injection to exchange bunch trains between the storage ring and an accumulator ring. Swap-out also makes it possible to employ very small, round chambers in the straight sections, enabling higher-performance undulators. ALS-U will provide a higher coherent flux than any other ring, whether in operation or planned, up to a photon energy of 3.5 keV, which covers the entire soft x-ray regime (see Fig. 2).

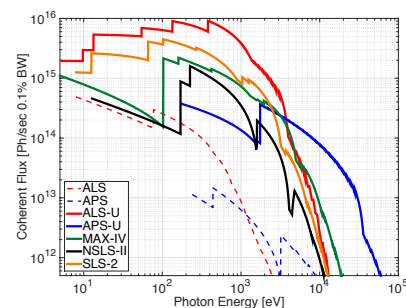


Figure 2: Coherent flux produced by selected storage-ring-based x-ray facilities.

LATTICE OPTIMIZATION

The lattice design has to balance competing goals like radiation output requirements, technological limitations, and operational demands. The most fundamental tradeoff is between small emittance and sufficient injection efficiency and lifetime. Following a now-common trend, we have been employing multi objective genetic algorithms to simultaneously optimize the linear and non-linear lattice for the lattice design. The new ALS-U ring will have the same periodic-

AWAKE - A PROTON DRIVEN PLASMA WAKEFIELD ACCELERATION EXPERIMENT AT CERN

Allen Caldwell*, Max Planck Institute for Physics, Munich, Germany
on behalf of the AWAKE Collaboration

Abstract

It is the aim of the AWAKE project at CERN to demonstrate the acceleration of electrons in the wake created by a proton beam passing through plasma. The proton beam will be modulated as a result of the transverse two-stream instability into a series of micro bunches that will then drive strong wakefields. The wakefields will then be used to accelerate electrons with GV/m strength fields. The AWAKE experiment is currently being commissioned and first data taking is expected this year. The status of the experimental program is described as well as first thoughts on future steps.

PATH TO AWAKE

It has been known for some time that plasmas can support very large electric fields, and can therefore be used for accelerating particles to relativistic energies [1]. Initially, laser driven plasma wake field acceleration was considered in the literature [2], and experimental verification of the ideas followed [3]. Detailed simulations of the process are now available which have predicted the production of electron beams with interesting characteristics. In recent experiments, gradients in the range 10-100 GV/m have been achieved. These have so far been limited to distances of a few cm, but the progress has been very impressive [4]. In order to accelerate an electron bunch to 1 TeV, these gradients would have to be maintained over distances of tens of meters, or many acceleration stages would have to be combined. Both of these options are very challenging, both because of dephasing and energy conservation issues.

It was later recognized that plasmas could also be excited by a bunch of electrons [5]. Given an intense enough bunch of electrons, the plasma is both created [6] and excited by the passage of the bunch. Very large electric fields were predicted and later observed [7]. In the case of electron driven plasma wakefield acceleration (PWA), a gradient of 50 GV/m was achieved and sustained at SLAC for almost 1m [8]. However, the maximum energy that can be transferred to a particle in the witness bunch is limited by the transformer ratio and is at most 2 for longitudinally symmetric drive bunches [9]. This upper limit can in principle be overcome by asymmetric bunches [10], but this will be technically very difficult to realize. Energy issues also dictate that an electron-bunch driven PWA would require a large number of stages to reach the TeV scale, and therefore be quite complex.

The scheme proposed for study in the AWAKE experiment is based on proton-driven PWA [11]. The principle advantage of using protons to driving the wake is that proton

bunches are today accelerated to high energies, and so have enough energy to bring a bunch of electrons to the TeV scale in a single acceleration stage. However, the length of existing proton bunches requires the use of a bunching scheme to drive the plasma wakefield in such a way as to produce GV/m fields.

Self-Modulation Instability

The angular frequency ω_P of the plasma wave is fixed by the local plasma density n_0 via

$$\omega_P = \sqrt{\frac{4\pi n_0 e^2}{m_e}},$$

where m_e is the electron mass and e is the elementary charge. On the time scale of a few wave oscillations, the much heavier plasma ions can be considered immobile. The plasma wave or wake follows the drive bunch, and its phase velocity v_{ph} is close to that of the drive bunch [12]. Its wavelength is therefore approximately $\lambda_P = \frac{2\pi c}{\omega_P}$. The maximum amplitude of the longitudinal electric field in the wave is on the order of the wave-breaking field $E_0 = \frac{m_e c \omega_P}{e}$ [13].

The extremely short driver length required for efficient excitation of the plasma wave (a small fraction of λ_P generally is required) presents a serious obstacle to the realization of the concept. The CERN proton bunches available today are approximately 10 centimeters long (the root-mean-square length) and are therefore ineffective at driving large wakefield amplitudes. Various bunch compression schemes have been studied in the early stages of studying proton-driven plasma wakefield acceleration [14]. While technically feasible, the concepts developed will be costly and require extensive amounts of space.

An alternative to extreme bunch compression is multi-bunch wave excitation. In this scheme the plasma wave is resonantly driven by a train of short micro bunches spaced one wakefield period apart. It is exactly this scheme that was first proposed as the plasma wakefield accelerator in [5]. In our application, the long proton bunch is converted into a stream of micro bunches, each short on the scale of the plasma wavelength, by an instability. The instability of interest is the self-modulation instability (SMI), which can be viewed as the axisymmetric mode of the transverse two-stream (TTS) instability. The SMI is a convective instability that grows both along the bunch and along the plasma. Analytical calculations and three-dimensional simulations [15] predicted an exponentially fast growth of the SMI and confirmed that non-axisymmetric modes of the TTS instability are also suppressed if the seed perturbation is strong enough.

* caldwell@mpp.mpg.de

A NOVEL TECHNIQUE OF POWER CONTROL IN MAGNETRON TRANSMITTERS FOR INTENSE ACCELERATORS*

G. Kazakevich[#], R. Johnson, M. Neubauer, Muons, Inc, Batavia, IL 60510, USA
V. Lebedev, W. Schappert, V. Yakovlev, Fermilab, Batavia, IL 60510, USA

Abstract

A novel concept of a high-power magnetron transmitter allowing dynamic phase and power control at the frequency of locking signal is proposed. The transmitter compensating parasitic phase and amplitude modulations inherent in Superconducting RF (SRF) cavities within closed feedback loops is intended for powering of the intensity-frontier superconducting accelerators. The concept uses magnetrons driven by a sufficient resonant (injection-locking) signal and fed by the voltage which can be below the threshold of self-excitation. This provides an extended range of power control in a single magnetron at highest efficiency minimizing the cost of RF power unit and the operation cost. Proof-of-principle of the proposed concept demonstrated in pulsed and CW regimes with 2.45 GHz, 1kW magnetrons is discussed here. A conceptual scheme of the high-power transmitter allowing the dynamic wide-band phase and mid-frequency power controls is presented and discussed.

INTRODUCTION

SRF cavities of the modern superconducting accelerators are typically manufactured from thin sheets of niobium to allow them to be cooled at minimized power of cryo-facilities. Fluctuations of helium pressure, acoustic noise caused by liquid He flux, etc., all cause mechanical oscillations of the cavity walls changing the cavity resonant frequency. This results in parasitic amplitude and phase modulation of the accelerating field in the cavity. The cavity detuning caused by the mechanical oscillations is typically a few tens of Hz [1, 2]. At very high external quality factor of the SRF cavities, Q_E , the bandwidth of the fundamental mode of the RF oscillation in the cavities has the same order as the detuning value. This causes deviations of the accelerating field phase and amplitude. The parasitic modulations are not associated with instability of the RF source; they exist even if the RF source is ideally stable. Thus, only the dynamic phase and power control of the RF sources locking phase and amplitude of the RF field in the SRF cavity [3], allows keeping stable phase and amplitude of the accelerating field in the cavity. The bandwidth of the power and the phase control of the RF source is determined by necessary suppression of the amplitude and phase deviations; e.g., for suppression of the amplitude modulation to deviations level of <1% at the deviations of ~140% one needs suppression >40 dB, at the bandwidth of the control ~10 kHz.

The traditional RF sources (klystrons, IOTs, solid-state

amplifiers) can provide such control; however the capital cost of the RF system of the large-scale superconducting accelerator will be a significant part of the project cost. The magnetrons controlled by the phase-modulated resonant driving RF signal may provide dynamic phase and power control with the capital cost in a few times less than the traditional RF sources [4, 5] at a higher efficiency. This will also reduce the cost of operation of the RF sources.

Two methods allowing power control in magnetron transmitters were suggested recently: using power combining from two magnetrons with a 3-dB hybrid [ibid.]; or by an additional modulation of the depth of phase-modulated signal driving a single magnetron [6]. The last one is applicable at a very high Q_E value. The average relative efficiency in the range of power control of ~10 dB for the both methods is about of 50%.

We propose a novel technique of power control which keeps a wide bandwidth for the phase control and provides the range of the power control up to 10 dB by variation of current in the extended range [7]. For such a range the minimum magnetron current has to be much less than the minimum current available in free run. This is realized in the magnetron driven by a resonant wave and fed by the voltage less than threshold of self-excitation [7]. Note, that the proposed technique is applicable for any value of Q_E .

The proposed technique of the magnetron power control provides highest efficiency in comparison with methods described in Refs. [4-6]. This will allow significantly decrease the capital and operating costs of the ADS class projects. The proposed method increasing the transmitter efficiency at power control in magnetrons can be used in combination with methods described in Refs. [4-6] maximizing efficiency at the wideband power control.

The concept of a controllable operation of the magnetron fed by the voltage less than the threshold of self-excitation was substantiated by a developed kinetic model [7]. Demonstration of proof-of-principle of the proposed method of the wide-range power control in magnetrons is presented and discussed here.

A WIDE-RANGE POWER CONTROL IN PRE-EXCITED CW MAGNETRONS

Proof-of-principle of the developed technique of the power variation in pre-excited magnetrons was demonstrated in experiments with 2.45 GHz, 1 kW tubes. In pulsed regime the CW magnetron type OM75P(31) with a permanent magnet was fed by a pulsed modulator at pulse duration of 1.2 ms. Before the experiments, the magnetron was in use for about of 8 years, thus it could provide output power up to ~500 W.

* Supported by Fermi Research Alliance, LLC under Contract No. De-AC02-07CH11359 with the United States DOE in collaboration with Muons, Inc.

[#]e-mail: gkazakevitch@yahoo.com; grigory@muonsinc.com

VACUUM BREAKDOWN AT 110 GHz

S. C. Schaub*, M. A. Shapiro, R. J. Temkin
Massachusetts Institute of Technology, Cambridge, MA, USA

Abstract

A 1.5 MW, 110 GHz gyrotron is used to produce a linearly polarized quasioptical beam in 3 μ s pulses. The beam is concentrated in vacuum to produce strong electric fields on the surfaces of dielectric and metallic samples, which are being tested for breakdown threshold at high fields. Dielectrics are tested in the forms of both windows, with electric fields parallel to the surface, and sub-wavelength dielectric rod waveguides, with electric fields perpendicular to the surface. Currently, visible light emission, absorbed/scattered microwave power, and vacuum pressure diagnostics are used to detect discharges on dielectric surfaces. Future experiments will include dark current diagnostics for direct detection of electrons. Dielectrics to be tested include crystal quartz, fused quartz, sapphire, high resistivity float-zone silicon, and alumina. Metallic accelerator structures will also be tested in collaboration with SLAC. These tests will require shortening of the microwave pulse length to the nanosecond scale.

INTRODUCTION

Research has begun to test the feasibility of RF linear accelerators operating at W-band frequencies and above (>100 GHz). Experiments have been performed at SLAC to test metallic wakefield structures in which W-band and higher frequency fields are excited [1, 2]. At MIT, we are beginning to experimentally test breakdown limits of materials and cavities subject to intense W-band RF, in high vacuum conditions (10^{-8} Torr). A 1.5 MW, 110 GHz gyrotron is used to power the experiments with 3 μ s RF pulses. Ongoing experiments are testing multipactor breakdown thresholds of various dielectric materials. Future experiments will test breakdown thresholds of metallic cavities.

EXPERIMENT DESIGN

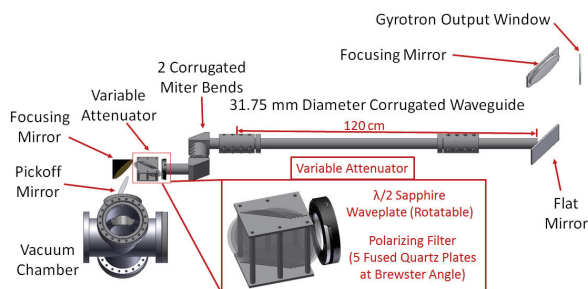


Figure 1: Experimental Apparatus

The overall configuration of the experiment is laid out in Fig. 1. The 110 GHz, 1.5 MW gyrotron outputs a linearly

* sschaub@mit.edu

polarized, gaussian beam. The beam is focused into a length of 31.75 mm diameter corrugated waveguide. The output from the waveguide (a 98% gaussian beam) is fed through a variable attenuator, then focused into a vacuum chamber, where structures under test are placed. Two structures have been designed to be installed in the vacuum chamber for testing dielectric materials. They are described in the following subsections.

Parallel E Configuration

To test multipactor breakdown thresholds with RF E-fields parallel to the surface of dielectric samples, a Fabry-Pérot cavity was constructed. The cavity is formed between a dielectric mirror and a metal mirror. The dielectric mirror consists of multiple, optically polished, 25.4 mm diameter, dielectric wafers clamped at the edges. The end of the cavity is a 6 mm focal length spherical mirror in an optical mount that allows fine axial translation, for frequency tuning. A half-wavelength thick dielectric sample is placed at the second field maximum within the cavity. This structure is shown in Fig. 2. The RF gaussian beam is focused to a 2 mm spot size on a dielectric mirror. The electric field of the incident gaussian beam is polarized in the y direction.

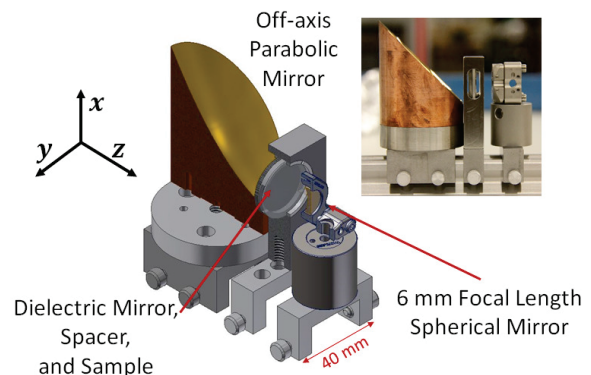


Figure 2: Section view and photograph of parallel E-field dielectric testing configuration.

The complex magnitude of the electric field in the Fabry-Pérot cavity is shown in Fig. 3. The maximum field on the surface of the sample, with 1 MW of power delivered to the dielectric mirror, is 150 MV/m. In Fig. 3, dashed lines show the locations of the boundaries in the dielectric mirror. Dotted lines show the boundary of the sample under tests, a sapphire wafer in this example. The solid curve at the right of the image indicates the location of the spherical mirror at the end of the cavity.

The Fabry-Pérot cavity has been assembled and tested at low power. The measured S_{11} is shown in Fig. 4. Coupling of 30 dB was achieved, with a 52 MHz 3 dB bandwidth and a

ACCELERATOR PHYSICS CHALLENGES IN THE DESIGN OF MULTI-BEND-ACHROMAT-BASED STORAGE RINGS

M. Borland, Argonne National Laboratory, Argonne, USA

R. Hettel, SLAC National Laboratory, Menlo Park, USA

S. C. Leemann, MAX IV Laboratory, Lund, Sweden

D. S. Robin, Lawrence Berkeley National Laboratory, Berkeley, USA

Abstract

With the recent success in commissioning of MAX IV, the multi-bend achromat (MBA) lattice has begun to deliver on its promise to usher in a new generation of higher-brightness synchrotron light sources. In this paper, we begin by reviewing the challenges, recent success, and lessons learned of the MAX IV project. Drawing on these lessons, we then describe the physics challenges in even more ambitious rings and how these can be met. In addition, we touch on engineering issues and choices that are tightly linked with the physics design.

INTRODUCTION

Third generation storage ring light sources brought unprecedented X-ray brightness and flux from insertion device photon sources to the synchrotron radiation scientific community. However a growing number of applications would benefit from even higher brightness beams and their enhanced transverse coherence, including nanometer imaging applications, X-ray correlation spectroscopy and spectroscopic nanopores, diffraction microscopy, holography and ptychography.

Given that photon spectral brightness $B(\lambda)$ is inversely proportional to the convolved photon-electron emittance $\Sigma_{x,y}(\lambda)$ at wavelength λ for each transverse plane x and y (i.e. $B(\lambda) \propto (\Sigma_x(\lambda)\Sigma_y(\lambda))^{-1}$, $\Sigma_{x,y}(\lambda) = \epsilon_r(\lambda) \oplus \epsilon_{x,y}(e-)$), there is an ongoing effort to reduce electron emittance in storage ring light sources towards the diffraction limited photon emittance $\epsilon_r(\lambda) \approx \lambda/4\pi \sim \lambda/2\pi$, depending on photon source properties, or ~ 8 pm-rad to 16 pm-rad for $\lambda = 1\text{\AA}$ for wavelengths of interest to reach maximal brightness. Along with the increase in brightness, the percentage of transversely coherent photons also increases as electron emittance is reduced, approaching a maximum of 100% when the electron emittance drops below $\epsilon_r(\lambda)$.

While diffraction limited emittance for angstrom-wavelength X-rays can be routinely reached in the vertical plane by reducing the horizontal-vertical emittance coupling to very small values, the horizontal emittance for 3rd generation machines is typically in the 1–10 nm-rad range. This level of emittance is the result of the typical implementation of double- and triple-bend achromat (DBA and TBA) lattices using storage technology that has been developed over a few decades. However it is known that the emittance of a storage ring scales as $F(\nu, \text{cell})E^2(N_s N_d)^{-3}$, where $F(\nu, \text{cell})$ is a function of ring horizontal tune ν and lattice type, E is the electron energy, and N_s lattice sectors (with intervening

insertion device straight sections) each have N_d dipoles. For a given lattice cell type, a larger ring circumference C will accommodate more sectors and emittance is reduced by C^{-3} . Light source lattice cells are typically achromatic, or nearly so, to minimize the increase in effective beam emittance in ID straights caused by electron energy spread.

The concept of increasing N_d to create multibend achromat lattices is not new [1], but it is only in the last several years that developments in precision magnet design, vacuum technology and advanced tools for simulating and optimizing highly nonlinear lattice designs have been made to actually build rings having affordable size (i.e. of order 1 km for 6 GeV, 0.5 km for 3 GeV, and 0.2 km for 2 GeV) with emittances substantially lower than the 3rd generation. The 3 GeV, 528 m MAX IV ring, discussed below, is the first pioneering implementation of such a “4th generation” storage ring light source, having a 7-bend achromat (7BA) lattice having the order of 300 pm-rad emittance that is now in operation, and in construction is the Sirius Light Source in Brazil with a 5BA lattice and similar size and emittance to MAX IV. In the meantime the high energy ESRF and APS light sources are in the process of upgrading their lattices to modified 7BA lattices, exploiting longitudinal gradient dipoles to obtain further emittance reduction, and in the case of the APS, using a “reverse bend” design [2,3] for a reduction in emittance to 41 pm-rad (the diffraction limit for 2.5–5 Å photons) at 6 GeV. Other facilities, including SPring-8, ALS, SLS and others also planning lattice upgrades sometime in the future, while IHEP is planning a new MBA ring comparable in size and performance to the APS and SPring-8. In the case of the APS and the ALS (a 9BA lattice), emittance is reduced to the point that the dynamic aperture will not support off-axis injection with accumulation; on-axis “swap-out” injection will be used. In the future, given that the science case is justified, rings having ~ 2 km circumference might be built having order 10 pm-rad emittance (e.g. PETRA-IV at DESY).

The physics and engineering challenges associated with implementing these state-of-the-art 4th generation light sources are daunting and are discussed in the following.

LESSONS OF MAX IV

Commissioning of the MAX IV 3 GeV storage ring started in August 2015 and is ongoing. A report of the commissioning status can be found in [4]. Here we only summarize a couple of key issues relevant to the design and commissioning of future MBA-based storage rings.

ADVANCED CONCEPTS FOR SEEDED FELS

Eugenio Ferrari*, Enrico Allaria, Elettra - Sincrotrone Trieste SCpA, Trieste, Italy

Abstract

The experiments enabled by ultrashort XUV/X-rays FELs, e.g. coherent control of quantum phenomena, nonlinear optics, etc., require the knowledge, and possibly the control, of the spectro-temporal content of individual pulses. While spatial coherence is also a property of FELs based on SASE, the capability of generating temporally coherent pulses is a distinctive feature of seeded FELs. Indeed, this is a natural consequence of the principle on which a seeded FEL relies: before emitting radiation, electrons interact with a coherent source, the seed, and, under given conditions, the latter transmits its coherence properties to the FEL light. In the following, we demonstrate the use of interferometry in the frequency domain to investigate the properties of the seeded FEL pulses. Moreover, we provide the first direct evidence of the temporal coherence of a seeded FEL working in the extreme ultraviolet spectral range and show the way to control the light generation process to produce Fourier-limited pulses.

INTRODUCTION

Seeded FELs have the potential to produce spatially and temporally fully coherent pulses [1]. However, the ability to generate fully coherent pulses and shape their spectro-temporal content with high stability on a shot-to-shot basis is extremely challenging, due to the difficulties in precisely controlling the light generation process [2]. In addition to amplification, several factors contribute to the evolution of the electric field during the FEL process. A linear frequency chirp $d\omega/dt$ in the seed affects the emission process, causing a broadening of the spectral envelope [3]. Furthermore, before interacting with the seed, electrons are accelerated and can acquire a time-dependent energy profile. A curvature $d^2\gamma(t)/dt^2$ in the electron energy $\gamma(t)$ produces the same effect as a linear frequency chirp in the seed [4,5] and causes an additional linear frequency offset during amplification due to varying $d\gamma(t)/dt$ along the electron beam [6]. The interplay between these effects determines the FEL temporal phase, which has an impact on the spectral content of the radiated light [7].

PHASE-LOCKED FEL PULSES

In a coherent control experiment, light pulses are used to guide the real-time evolution of a quantum system. This requires the coherence and the control of the pulses' electric-field carrier waves. In the following we demonstrate the generation of two time-delayed phase-locked XUV pulses from a seeded FEL. The pulses are produced by two seed replicas locked in phase. The adopted approach also pro-

vides a method to investigate the longitudinal coherence of a seeded FEL.

Experimental Setup

The experiment was performed on FEL-1 [8] and exploits the capability of the seed laser to trigger and drive the FEL process and generate coherent and controllable XUV pulses.

Figure 1 shows the experimental setup for the generation of two time-delayed phase-locked pulses implemented at FERMI. The twin seed pulses are produced from a single pulse of the third harmonic of a Ti:Sa laser and temporally split into two pulses after transmission through a birefringent plate. The thickness of the birefringent plate and the group velocity difference for the two plate's orthogonal axes, rotated at 45° with respect to the laser polarization, determine the time delay τ between the two seed pulses. The polarization of both pulses is then adjusted to be parallel to the modulator one using adequate optical components. This ensures optimum seed-electron coupling in the modulator.

The relative phase between the carrier waves of the twin seed pulses $\Delta\phi_{seed}$ is controlled by fine tuning the incidence angle on the plate using a motorized rotation stage with minimum phase step of about $\lambda_{seed}/30$. The two seeds interact with the relativistic electron beam inside the modulator and give rise to a periodic energy modulation at the seed wavelength, which is confined to the position of the two seed pulses within the electron beam (see Fig. 1).

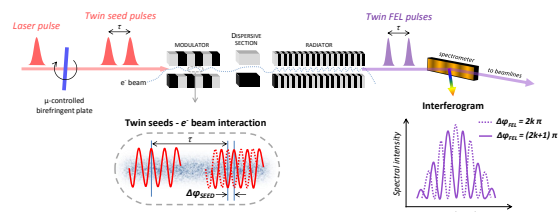


Figure 1: HGHG FEL in the two phase-locked pulses configuration. Two time-delayed seed pulses are created by transmission of a single laser pulse through a birefringent plate. The plate is motorized to precisely control the relative phase $\Delta\phi_{seed}$ between the two carrier waves of the twin seeds, which interact with the relativistic electron beam in the modulator. Image reproduced from [9].

Interferogram Creation and Measurements

Two mutually coherent pulses delayed in time produce a spectral interference pattern [10]. This configuration can be regarded as the temporal equivalent of the Young's double slit interferometer where the time-delayed pulses play the role of the spatially separated slits, and the spectrometer is the equivalent of the far-field screen. The interference arises in the frequency domain instead of the spatial one.

* eugenio.ferrari@psi.ch

FOKKER-PLANCK ANALYSIS OF TRANSVERSE COLLECTIVE INSTABILITIES IN ELECTRON STORAGE RINGS*

R. R. Lindberg, ANL, Argonne, IL 60439, USA

Abstract

We analyze single bunch transverse instabilities due to wakefields using a Fokker-Planck model. We expand on the work of Suzuki [1], writing out the linear matrix equation including chromaticity, both dipolar and quadrupolar transverse wakefields, and the effects of damping and diffusion due to the synchrotron radiation. The eigenvalues and eigenvectors determine the collective stability of the beam, and we show that the predicted threshold current for transverse instability and the profile of the unstable agree well with tracking simulations. In particular, we find that predicting collective stability for high energy electron beams at moderate to large values of chromaticity requires the full Fokker-Planck analysis to properly account for the effects of damping and diffusion due to synchrotron radiation.

INTRODUCTION

Understanding, predicting, and controlling collective instabilities is an important part of storage ring design and operation. Single bunch transverse instabilities are of particular importance in high-energy electron storage rings, as they typically set the limit on the maximum achievable current. The standard analysis of these instabilities decomposes the linearized Vlasov equation into normal modes, and then stability is determined by comparing the maximum growth rate with the transverse synchrotron and Landau damping rates (see, e.g., [2–6]). However, synchrotron emission results in both damping and diffusion in phase space, so that when synchrotron radiation provides the dominant damping mechanism it can render the Vlasov model incomplete. This is often the case for high energy electron storage rings, in which case a Fokker-Planck description must be employed to accurately predict stability. Here we build on the work of Ref. [1] to develop a more complete Fokker-Planck analysis of transverse stability, where particular attention is paid to the dynamics at large chromaticity.

MODEL EQUATIONS

Our starting point is very similar to the Hamiltonian models in the textbooks [4, 5], but it includes the Fokker-Planck damping and diffusion associated with synchrotron radiation. Hence, the distribution function F obeys the equation

$$\frac{\partial F}{\partial s} + \{F, \mathcal{H}\} = \frac{2}{c\tau_z} \left[\sigma_\delta^2 \frac{\partial^2 F}{\partial p_z^2} + p_z \frac{\partial F}{\partial p_z} + F \right] + \frac{2}{c\tau_x} \left[\varepsilon_0 \mathcal{J} \frac{\partial^2 F}{\partial \mathcal{J}^2} + \frac{\varepsilon_0}{4\mathcal{J}} \frac{\partial^2 F}{\partial \Psi^2} + (\varepsilon_0 + \mathcal{J}) \frac{\partial F}{\partial \mathcal{J}} + F \right]. \quad (1)$$

* Work supported by the U.S. Department of Energy, Office of Science, Office of Basic Energy Sciences, under Contract No. DE-AC02-06CH11357.

Here $(z, p_z) = (ct - s, -\delta)$ are the longitudinal variables, (\mathcal{J}, Ψ) are the transverse action-angle variables, τ_z is the longitudinal damping time, σ_δ is the equilibrium energy spread, τ_x is the transverse damping time, ε_0 is the natural emittance, and $\{, \}$ denotes the Poisson bracket. We assume that the Hamiltonian \mathcal{H} is comprised of the linear synchrotron and betatron motion, the first order chromaticity nonlinearity, and the lowest order effects of the dipolar wakefield. The basic procedure to simplify Eq. (1) is to

1. linearize with respect to perturbations about the self-consistent equilibrium;
2. assume that the transverse motion is described by dipole oscillations at the (chromaticity-corrected) betatron frequency
3. expand the longitudinal perturbation as a sum of linear modes in longitudinal action and angle;
4. solve the resulting eigenvalue problem to determine normal modes and complex frequencies as a function of current I and chromaticity ξ_x .

Mathematically, the first two steps can be expressed as

$$F = f_0(\mathcal{J})g_0(\mathcal{H}_z) + f_1(\Psi, \mathcal{J}; s)g_1(z, p_z; s), \quad (2)$$

where the equilibrium is a negative exponential in action,

$$f_0(\mathcal{J})g_0(\mathcal{H}_z) = \frac{e^{-\mathcal{J}/\varepsilon_0}}{2\pi\varepsilon_0} \frac{e^{-I/\langle I \rangle}}{2\pi\langle I \rangle}, \quad (3)$$

while the perturbation is a product of a simple dipole oscillation in the transverse dimension [2], with all the wakefield-driven complexity in the longitudinal perturbation g_1 :

$$F_1 \propto -\sqrt{\mathcal{J}}/2 f'_0(\mathcal{J}) e^{-i[\Omega - (\Psi + k_\xi z) + \omega_\beta s/c]} g_1(z, p_z). \quad (4)$$

Here, $(\Psi + k_\xi z)$ represents the chromaticity corrected betatron oscillation phase, with the head-tail phase $k_\xi \equiv \omega_0 \xi_x / \alpha_c c$ [7], while Ω is the complex frequency, and instability is characterized by $\Im(\Omega) > 0$.

We insert the perturbation (4) into the Eq. (1) and isolate the betatron oscillations by multiplying by $\sqrt{\mathcal{J}} e^{-i\Psi}$ and integrating over the transverse dimensions. When the dust clears the transverse part of the Fokker-Planck operator reduces to a simple damping term with damping time τ_x . This is because we have assumed that there is no interesting structure in the transverse plane; in contrast to this, we will find that the longitudinal Fokker-Planck damping and diffusion will depend on the longitudinal mode profile.

The next step is to linearize the problem for $|g_1| \ll 1$ and apply Sacherer's linear mode formalism by expanding g_1 as a sum of orthogonal linear modes

$$g_1(\Phi, r) = \sum_{q=0}^{\infty} \sum_{n=-q}^{\infty} a_q^n \frac{r^{n/2} L_q^n(r)}{\sqrt{(q+n)!/q!}} \frac{e^{-r}}{2\pi} e^{in\Phi}. \quad (5)$$

CORRUGATED STRUCTURE INSERTION TO EXTEND SASE BANDWIDTH UP TO 3% AT THE EUROPEAN XFEL

I. Zagorodnov*, G. Feng, T. Limberg, Deutsches Elektronen-Synchrotron, Hamburg, Germany

Abstract

The usage of x-ray free electron laser (XFEL) in femtosecond nanocrystallography involves sequential illumination of many small crystals of arbitrary orientation. Hence a wide radiation bandwidth could be useful in order to obtain and to index a larger number of Bragg peaks used for determination of crystal orientation.

Considering the baseline configuration of the European XFEL in Hamburg, and based on beam dynamics simulations, we demonstrate here that usage of corrugated structures allows for a considerable increase in radiation bandwidth. It allows for data collection with a 3% bandwidth, a few microul radiation pulse energy, a few fs pulse duration, and a photon energy 5.4 keV.

INTRODUCTION

The usage of x-ray free electron laser (XFEL) in femtosecond nanocrystallography involves sequential illumination of many small crystals of arbitrary orientation and a wide radiation bandwidth could be useful for determination of crystal orientation. With nominal scenario for beam compression and transport at the European XFEL [1] the radiation bandwidth is quite narrow, on the level of several permilles.

It was shown in [2] that a strong beam compression could be used to increase the correlated energy spread of the electron beam and as consequence to increase the radiation bandwidth up to 2% at photon energy 6 keV. In this paper we study another possibility: we use over-compression of the electron beam at the last chicane and insert corrugated structures before the undulator section to generate strong wakefields [3].

Based on beam dynamics simulations, we demonstrate here that the usage of corrugated structures allows for a tenfold increase in radiation bandwidth.

nm. The layout of the accelerator (with the undulator line SASE1) is shown in Fig. 1. Beam dynamics in the accelerator with nominal set of parameters is described in [4].

In this paper we consider a special scenario with over-compression of the electron bunch in the last bunch compressor (BC2 in Fig. 1). The over-compression allows to obtain a bunch with lower particle energy at the tail. This energy difference will be enhanced later on by strong wake fields of the corrugated structures.

The setup of simulations can be found in [5]. For the numerical modeling of the linac we have used two codes: code ASTRA [6] for straight sections and code CSRtrack [7] for curved parts of the beam trajectory. Code ASTRA allows to take into account three dimensional space-charge fields, but it neglects the radiation. Code CSRtrack is used to model coherent synchrotron radiation in the dispersion sections. In order to include the effect of the vacuum chamber we have applied the concept of wake fields. The wake functions for a point charge at different linac components are obtained with the code ECHO [8]. The impact of wake fields has been modeled through discrete kicks at several positions along the linac.

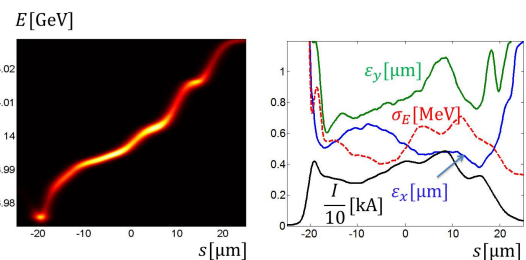


Figure 2: Beam after collimator.

The longitudinal phase space and the slice parameters of the beam after collimator section are shown in Fig. 2. The tail has an energy drop of about 55 MeV.

It is well known, that the spectrum bandwidth of self-amplified spontaneous emission (SASE) radiation is approximately equal to the doubled energy bandwidth in the electron beam. For the final beam energy of 14 GeV the relative energy bandwidth in the electron beam is about 0.4% and we can hope to have the SASE radiation bandwidth of 0.8%. In order to increase the bandwidth up to several percents we will use a chain of corrugated structures. In our studies the corrugate structure has the parameters suggested at SLAC.

WAKE IN CORRUGATED STRUCTURE

The geometry of the corrugated structure is shown in Fig. 3. Here $p = h = 2t = 0.5\text{mm}$, plate halfwidth $w = 6\text{mm}$

BEAM DYNAMICS IN LINAC

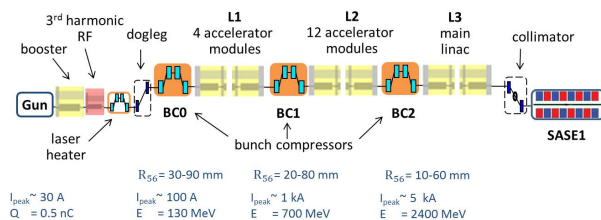


Figure 1: Layout of the European XFEL.

The European XFEL is under construction now in Hamburg. It contains several photon lines to produce extremely short and bright light pulses with wave length down to 0.04

* Igor.Zagorodnov@desy.de

STUDY ON THz IMAGING BY USING THE COHERENT CHERENKOV RADIATION

M. Nishida[†], M. Brameld, M. Washio, RISE, Waseda University, Tokyo, Japan
K. Sakaue, WIAS, Waseda University, Tokyo, Japan
R. Kuroda, Y. Taira, AIST, Ibaraki, Japan

Abstract

THz frequency is a special electromagnetic wave which is categorized between a radio wave and a light wave. It can pass through the various materials like a radio wave and can be transported with optical components like a light wave. Thus, it is suitable for imaging application of materials. At Waseda University, we have a high-quality electron beam by Cs-Te photocathode RF-gun and generate the coherent Cherenkov radiation using the tilted electron beam by RF-deflector. We successfully observed a high peak power coherent THz light. Our target is to obtain the three-dimensional THz images. So, we performed the cross-section images as a pre-stage of three-dimensional imaging.

INTRODUCTION

Recent technological innovation brought about the applied study using the THz light. The THz light is applied to various fields including industry, medical care, agriculture, and the security. As an imaging tool, the X-ray is well known for the baggage check at the airport and X-ray examination at the hospital. The THz light has the same property as the X-ray at a point to obtain transparent images in non-destruction. But the advantage of the THz light is safety to the human body because energy is extremely low in comparison with the X-ray [1]. So, we can detect the weapons such as a knife or the handgun which a person hides in irradiating the THz light to the human body. Furthermore, as well as transmission imaging, we can obtain reflection imaging by using the property of the light wave. So, we can detect the crack of the concrete, the rust of the vehicle body under the painting.

We generated the coherent Cherenkov radiation, and succeeded in observing a high power THz light using Cs-Te photocathode RF-gun that we own. In this paper, we report the outline of generating the THz Cherenkov radiation, results of the three-dimensional THz imaging of materials and future prospects.

GENERATION OF THE THz LIGHT

Coherent Cherenkov Radiation

Cherenkov radiation that appears while the electron beam travels in a media with a velocity that exceeds the speed of light in the media is investigated and widely used in particle detectors for nuclear physics. The radiation cone in transparent medium is defined by

following condition:

$$\cos \theta_c = \frac{1}{\beta n} \quad (1)$$

where θ_c is the radiation angle, β is the electron velocity in the speed of light units, n is the refractive index [2]. Moreover, the degree of the coherent effect depends not only on the longitudinal size of the electron beam but also on the emittance, or transverse size and the angular divergence of the electron beam. The total radiation intensity is defined by following:

$$P = \begin{cases} NP_0 & (\text{incoherent limit}) \\ N^2 P_0 & (\text{coherent limit}) \end{cases} \quad (2)$$

where P is the total radiation intensity, P_0 is the intensity emitted by a single electron, N is the number of the electron. In the case of coherent radiation, the total radiation intensity is known to be proportional to square of the number of the electron [3]. In this way, the intensity of the coherent radiation is much higher.

Observation of the THz Light

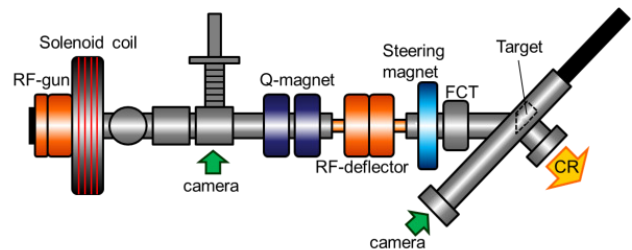


Figure 1: Schematic of the electron beam line layout.

Figure 1 shows the beam line layout at Waseda University. Our accelerator system is very compact which is approximately 3m in total. In this experiment, the accelerated electron beam is tilted by RF-deflector [4] and passed TOPAS [5] as a target. TOPAS is one of the polymer and has characteristic that the refractive index hardly changes in the THz region ($n=1.52$). Therefore, the Cherenkov radiation angle in the THz region is approximately 48.9deg from Eq.1. Also, Fig.2 shows the principle of generating the coherent Cherenkov radiation. When the electron beam is tilted the same angle as the Cherenkov radiation angle by RF-deflector, the beam size from the view of radiation angle is much smaller. Furthermore, phase matched THz light is generated to overlap the phase of the wave with each point. So, we can generate high peak power coherent THz light [6].

[†] m-nishida.mari@ruri.waseda.jp

DEVELOPMENT OF A FIBER LASER FOR IMPROVING THE PULSE RADIOLYSIS SYSTEM *

Y.Saito^{†, A)}, Y.Soeta^{A)}, Y.Hosaka^{A)}, K.Sakae^{B)}, M.Washio^{A)}

^{A)} Research Institute for Science and Engineering, Waseda University

^{B)} Waseda Institute for Advanced Study, Waseda University

Abstract

At Waseda University, we have been developing a pulse radiolysis system in order to clarify the early chemical reactions by ionizing radiation with S-band Cs-Te photo cathode RF-gun. According to our measurement, sample deterioration was observed even in the low absorption dose. Thus we need a high power and stable pulsed laser as a probe light. We constructed and tested Er fiber laser oscillator as a new probe laser. In this conference, we will introduce our Er fiber laser, experimental results of pulse radiolysis with Er fiber laser as a probe light and future prospective.

INTRODUCTION

In these days, the radiation is applied in various fields, for example semiconductor integrated circuit manufacturing. Semiconductor integrated circuit is conducted by transferring circuit pattern master called photomask on silicon wafer. To make this photomask, electron lithography is used. In this process, a resist material, which is high reactivity with the radiation, is used but most of resist's reaction mechanism was not proved yet.

When material is irradiated, a short-lived and highly reactive substance, radical, ion and excited states etc, called intermediate active species are made (fs-ps). Then the intermediate active species react with around substances (ps-μs). In this phase a principal chemical reaction is determined by intermediate active species in early process. So proving the behavior of intermediate active species is important for understanding and controlling radiation chemical reaction. A pulse radiolysis is one of the methods to measure the behavior of intermediate species by using an electron beam pulse. At Waseda University, we are using a Cs-Te RF electron gun for the radiation chemical analysis.

Now we introduce a purpose to investigate a Supercontinuum ray (SC ray) as a probe ray to improve pulse radiolysis system. In pulse radiolysis we measure a light absorption by intermediate active species. As a probe light, we have investigated a SC ray using Yb fiber laser and PCF (Photonic Crystal Fiber). But we haven't achieved a stable probe light in the visible region^[1]. Therefore we built Er fiber laser oscillator as new probe ray source. Now we succeeded in generating a second harmonic of Er fiber laser and measuring of hydrated electron in ns time resolution. In this paper, we report current results about generation SC ray in the visible region, improvement of Er fiber for measurement of ps time resolution and analysis of dose rate effect against the hydrated electron.

PULSE RADIOLYSIS

Pulse radiolysis experiment consists of sample, radiation (producing intermediate active species) and probe light. We use the Cs-Te cathode RF electron gun as a radiation source. An intermediate active species are produced by irradiating an electron beam on the sample. And the probe light, simultaneously incident to the sample, is absorbed depends on the intermediate active species concentration. Specifically, we measure the temporal change of O.D. (Optical Density) :

$$O. D. \equiv \log \frac{I_0}{I} = \epsilon c l \quad (1)$$

where, I_0 , I , ϵ , c , l are the incident light intensity, transmitted light intensity, the molar absorption coefficient, the active main concentration and the interaction length, respectively. From this O.D. we can obtain the amount of intermediate active species. We evaluate our pulse radiolysis system by measuring hydrated electrons. The hydrated electron is the free electrons that have been stabilized by coordination of water molecules. This has the broadband transient absorption around 720 nm and about 1 μs decay time. Relationship of the dose and decay time of hydrated electron is shown in Figure 1. We used Xe flash lamp as a probe light. As shown in Figure 1, the decay time of the hydrated electron changes immediately in the low absorbed dose. In particular, the decay time change of the high charge beam was significant in this pulse radiolysis system. It means that the sample deteriorates due to electron beam. When water is irradiated, many kinds of reactions occur. After a series of reaction final products (H_2O_2 , H_2 , etc) are generated and accumulated in water. Especially H_2O_2 reacts with hydrated electron well. So as more water is irradiated, the decay time of hydrated electron descends. On the other hands, the relationship of the dose and peak O.D. of hydrated electron is shown in Figure 2. Figure 2 shows that peak O.D. is constant against the dose. This also means that we can use the peak O.D. of hydrated electron to evaluate this system even from a deteriorated sample. However, it should be reduced the number of irradiations during the measurement (average number of times). To this purpose, the high intensity and stable probe light is required. Also, from the viewpoint of chemical reaction analysis, broadband and short pulse is required for the probe light. Thus, we have developed a SC light as the probe light. SC light is a broadband pulse laser. SC light is produced by ultra-short pulse IR laser from Yb fiber laser oscillator with a non-linear optical effect in PCF. The center oscillation

[†] email address y.saito@fuji.waseda.jp

IoT APPLICATION IN THE CONTROL SYSTEM OF THE BEPCII POWER SUPPLIES*

C.H. Wang[†], L.F.Li[#], X.L.Wang, Institute of High Energy Physics, Beijing 100049, China
P. Chu, Michigan State University, East Lansing, MI 48824, USA

Abstract

In recent years with the development of Internet technology, the Internet of things (IoT) has begun to apply to each domain. The paper introduces the idea how to apply IoT to the accelerator control system and take the existing control system of the BEPCII power supplies as an example for IoT application. It not only introduce the status of the control system of the BEPCII power supplies, but also present a solution how to apply IoT to the existing control system. The purpose is to make the control system more intelligent and automatically identify what and where the problem is when the alarm of the control system of the power supplies occurs. That means that IoT can help to automatically identify which chassis and which module inserted in the chassis and the connection cables. It is great convenient for the maintainer to use a mobile phone to diagnose faults and create the electronic maintenance record.

INTRODUCTION

In general, a modern accelerator is a complex facility which consists of many systems and a large amount of equipment such as magnets, power supplies, RF and vacuum devices, and so on. Various equipment and cables are placed dispersedly with a long distance. During the construction and installation as well as running of an accelerator, a huge number of data and information related to the equipment are created. So, it's very important for a large accelerator to collect, save and manage such large data. With the benefit of the Internet of things, these problem can be solved nicely. The idea of IOT application in the accelerator is that every object is connected, and people and objects are also linked together; there should be setup model of two-sided direct interconnecting and interworking networks. It's possible to use RFID[1] in the accelerator to construct a sensing layer as shown in Figure 1.

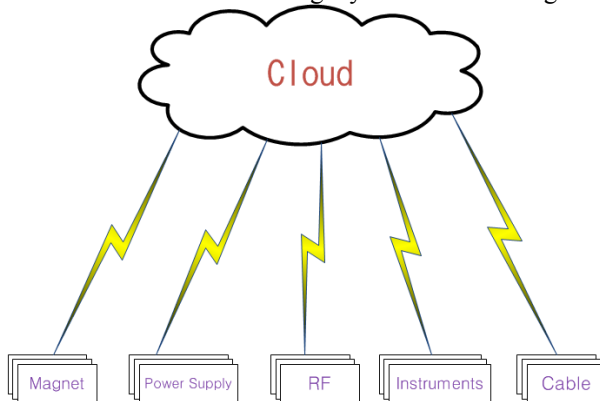


Figure 1: IOT with RFID in the accelerator.

* Work supported by NFSC (project No.:1137522)

[†] Email address: wangch@ihep.ac.cn

[#] on leave from IHEP

The goal is to automatically track the information of the accelerator equipment and devices as well as the cables with RFID. So, we will take a mature system as an example of IoT like the BEPCII power supply control system.

POWER SUPPLY CONTROL SYSTEM IN THE BEPCII

The control system of the BEPCII[2] power supplies follows the “three-layer” standard model [3] of a distributed architecture as shown in Figure 2. The front-ends consist of VME-64x crates, Motorola PowerPC750 CPU boards (MVME5100s as IOCs) and PSC/PSI modules as shown as in the figure 2. A workstation/Linux and a PC/Linux are used for the EPICS development. There are 17 IOCs (10000 points) implementing the controls and monitors for more than 400 magnet power supplies in the two rings and the transport line. The control system of the BEPCII power supplies has run well for ten years since it was put into operation and running in September of 2006.

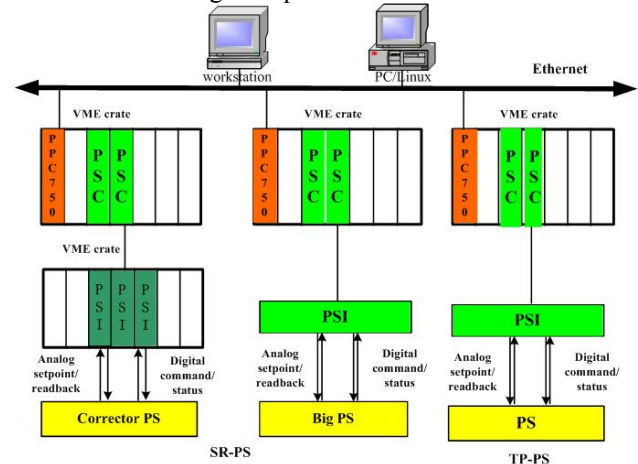


Figure 2: BEPCII PS Control System Architecture.

During the maintenance of the BEPCII control system, there are many different kinds of control devices and various, thousands of cables, it's not so easy for the engineers to maintain, even there are labels on the control crates and control modules as well as the cables; it's easy to forget after a while. Therefore, it is very important for the electronic information with RFID of all equipment (cabinets, chassis, plug-ins, cables, etc.) to be automatically identified. This will greatly improve the control system intelligence, operation maintenance convenience, fault location identification and automatic maintenance logging.

Layout of the Power Supply Control Station

There are four local stations for the power supply control in the BEPCII. There are many cabinets, chassis, plug-ins,

CYCLOTRONS FOR ACCELERATOR-DRIVEN SYSTEMS*

Tae-Yeon Lee[†], Seunghwan Shin and Jaeyu Lee, Pohang Accelerator Laboratory, Pohang, Korea
Chul Un Choi and Moses Chung, UNIST, Ulsan, Korea

Abstract

Accelerator-Driven system (ADS) can transmute long lived nuclear waste to short lived species. For this system to be fully realizable, a very stable high energy and high power proton beam (typically, 1 GeV beam energy and 10 MW beam power) is required, and preparing such a powerful and stable proton beam is very costly. Currently, the most promising candidate is superconducting linear accelerators. However, high power cyclotrons may be used for ADS particularly at the stage of demonstrating proof of principle of ADS. This paper discusses how cyclotrons can be used to demonstrate ADS.

INTRODUCTION

The accelerator-driven system (ADS) [1][2][3] in which a nuclear reactor is set up sub-critical and extra neutrons required for sustainable power generation is provided by neutrons emitted from high energy proton beam hitting a heavy metal target had long been considered to be a safe nuclear power generation system. In this scheme, the accelerator plays the role of safety key, turning off the accelerator which is very sensitive to perturbations and leaving the reactor in shortage of neutrons, so that the nuclear chain reaction can immediately stop. However, the nuclear disaster of Fukushima demonstrated that even ADS would not have avoided the Fukushima accident which occurred due to failure of cooling system after the reactor became subcritical. The status of ADS as a safe power generation system was shaken just as much as the conventional reactor was. In this regard, the idea that the thorium molten salt reactor adopts air cooling and, therefore, there will be no chance of Fukushima-type accident has been suggested. Although this ADS-based thorium reactor is promising, it is still in the early stage of development and the realization will take long time. We may have to wait for quite some time until the ADS-based thorium reactor will be fully developed, if we want to use fully safe nuclear power generation. In other words, power generation using the uranium-based ADS, let alone nuclear power in general, may not be highly supported by the public.

However, in spite of being unable to provide perfect safety against Fukushima-type accidents, nuclear energy has a strong advantage to protect environment that it is the only base load energy from emitting negligible amount of carbon dioxide, the greenhouse gas. Such renewable energy forms such as solar photovoltaic and wind energy cannot play the role of base load energy because these energy forms vary sensitively in large scale to the weather condition. These renewable energy forms

cannot be a serious candidate for the base load power until a huge scale of energy storage system is developed. It is important to note that the global warming due to the greenhouse effect is on-going right now and we have to try to stop it promptly. One of the methods is to construct nuclear power plants instead of coal power plants, and perhaps that is why nuclear power plants are still being constructed as several countries including Vietnam, Bangladesh, United Arab Emirates, Turkey and Belarus began to build the first nuclear power plant (NPP) of each country in 2012 while Jordan and Saudi Arabia began in 2013. Regarding this, ADS has a very helpful function, besides safe power generation, which is transmutation of spent fuel from long-lived materials (of the order of tens of thousands years) such as actinides to short lived materials (of the order of few hundred years). How to dispose or process nuclear spent fuel is a still unsolved problem of all countries with nuclear reactors. ADS proposes so far the best method of disposal, transmutation of minor actinides having hundred thousand year level half lifetime to nuclear species having 2~3 hundred year half lifetime. The critical fast reactors are also capable of transmuting minor actinides while generating power. Compared to critical fast reactors that incorporate uranium in the fuel, ADS can in principle operate on pure minor actinides (MA) feed as a dedicated transmutation system and thus is safer and can transmute more MA in a given time. The power required for the transmutation-dedicated ADS can be provided by making use of the massive heat generated from transmuting MA for electricity generation, although it may not be enough for commercial purpose.

With the current technology level, transmutation of spent fuel by ADS seems more feasible than power generation by ADS. Korea is one of the countries that face impeding spent fuel problem and ADS can be a serious candidate for solving the problem. Although this transmutation dedicated ADS cannot provide perfect safety against the Fukushima-type cooling accidents, this may still be studied and built extensively because the primary purpose of the transmutation-dedicated ADS is not the safety but removal of the toxic long-lived nuclear waste. This paper discusses possible schemes of ADS for transmutation of spent fuel. Focus will be put on economic aspect and currently available technologies.

ADS AND CYCLOTRONS

The ADS scheme adopts a sub-critically designed reactor and a target system which is designed to emit many neutrons when hit by protons. As it requires fast neutrons not thermal neutrons, the ADS does not use moderator including water. With the neutrons from the target added, the reactor can maintain criticality necessary for sustaining the reactor. The ADS scheme was proposed long time

* Work supported by Basic Science Research Program through the National Research Foundation of Korea (NRF-2015R1D1A1A01060049).

AN UPDATED LLRF CONTROL SYSTEM FOR THE TLS LINAC

C. Y Wu*, Y. S. Cheng, P. C. Chiu, K. H. Hu, K. T. Hsu, Demi Lee, C. Y. Liao
NSRRC, Hsinchu 30076, Taiwan

Abstract

The amplitude and phase of the RF field at the linear accelerator (LINAC) decides the beam quality. To study and to improve the performance of the LINAC system for Taiwan Light Source (TLS), a new design of a low-level radio-frequency (LLRF) control system was developed and set up for the TLS LINAC. The main components of the LLRF control system are an I/Q modulator, an Ethernet-based arbitrary waveform generator, a digital oscilloscope and an I/Q demodulator; these are essential parts of the LLRF feed-forward control. This paper presents the efforts to improve the LLRF control system. The feasibility of the RF feed-forward control will be studied at the linear accelerator of TLS.

INTRODUCTION

The beam quality of a 50-MeV linear accelerator (LINAC) is determined by the flatness of the RF field amplitude and phase. Both parameters depend primarily upon the performance of the klystron modulator and the beam-loading effects. A well-tuned pulse-forming network is not achieved easily but is essential to produce an effective microwave pulse for the linear accelerator. To eliminate tedious tuning of the pulse-forming network, a RF feed-forward system might be another, and alternative, solution to improve the performance. Not only beam-loading effects can be compensated but also the effects of slow drift due to various causes can be removed with a RF feed-forward control [1-3]. The feasibility of RF feed-forward control was studied recently at the linear accelerator of Taiwan Light Source. The efforts will continue as R&D topics to study the control algorithm and the RF control hardware development. Improvement of the operational performance of the injector to support top-up operation of TLS requires further exploration.

LINAC SYSTEM

The pre-injector of TLS consists of a 140-kV thermionic gun and a 50-MeV linear accelerator system of traveling-wave type. A synoptic view of the pre-injector is shown in Fig. 1. The microwave system was composed of a multiplier that generates 2998 MHz from 499.654 MHz, a 1-kW GaAs solid-state RF amplifier, and a high-power klystron amplifier. The high-power klystron is powered with a 80-MW modulator based on a pulse-forming network (PFN). The PFN is charged with a switching power supply. An analogue I/Q modulator is placed in front of the GaAs amplifier to control the amplitude and phase of the RF field fed into the linear accelerator. An analogue I/Q demodulator is used to

detect the RF signal from the outlet of the linear accelerator.

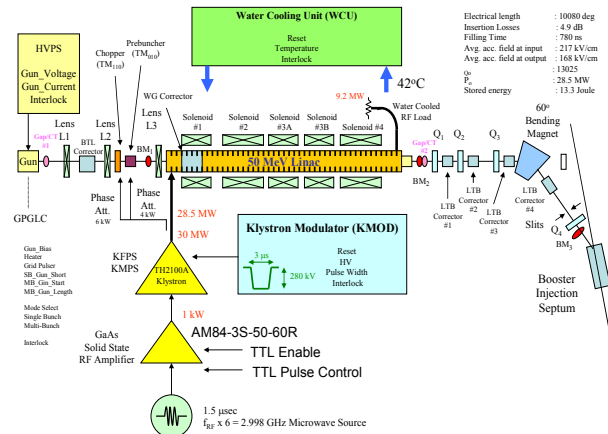


Figure 1: Synoptic of the 50-MeV linear accelerator system at TLS.

DESCRIPTION OF THE LLRF SYSTEM

Overview

A functional block diagram of the low-level RF system for the linear accelerator of TLS is shown in Fig. 2. This system consists of a clock generator, an arbitrary waveform generator (AWG), an analogue-type I/Q modulator, a GaAs solid-state RF amplifier, a high-power klystron and a klystron modulator, an analogue-type I/Q demodulator and a digital oscilloscope.

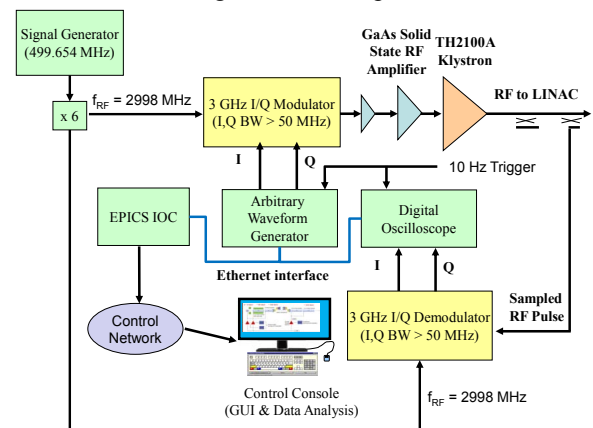


Figure 2: Block diagram of the updated low-level RF system for the 50-MeV linear accelerator; it is a feed-forward-enable system.

The arbitrary waveform generator serves to generate an in-phase (I) and a quadrature-phase (Q) control waveform as an input to the I/Q modulator. The pickup RF signal at the LINAC output is detected with the I/Q demodulator to

*chunyiwu@nsrrc.org.tw

FIRST TEST RUN FOR HIGH DENSITY MATERIAL IMAGING EXPERIMENT USING RELATIVISTIC ELECTRON BEAM AT THE ARGONNE WAKEFIELD ACCELERATOR

Y.R. Wang, Z.M. Zhang[#], S.C. Cao, Q.T. Zhao, X.K. Shen, IMP, CAS, Lanzhou 730000, China
 M. Conde, D.S. Doran, W. Gai, W. Liu, J.G. Power, C. Whiteford, E.E. Wisniewski
 ANL, Argonne, IL 60439, USA
 J.Q. Qiu, Euclid Techlabs, LLC, Solon, USA

Abstract

Argonne Wakefield Accelerator (AWA), has been commissioned and in operation since last year. It can provide beam of several bunches in a train of nano-seconds and 10s of nC with energy up to 70 MeV. In addition, the AWA can accommodate various beamlines for experiments. One of the proposed experiments is to use the AWA beam as a diagnostics for time resolved high density material, typically a target with high Z and time dependent, imaging experiments. When electron beam scatters after passing through the target, the angular and energy distribution of beam depend on the density and thickness of the target. A small aperture is used to collimate the scattered electron beam for off axis particles, and the target image will be detected by imaging screen. By measuring the scattered angle and energy at the imaging plate would yield information of the target. In this paper, we report on the AWA electron imaging (EI) system setup, which consist of a target, imaging optics and drift. The AWA EI beam line was installed on June, 2016 and the first test run was performed on August, 2016. This work will have implication on the high energy density physics and even future nuclear fusion studies. The details of AWA EI experiment setup, results, analysis and discussions are presented here.

INTRODUCTION

High energy density physics aims to study the properties of matter under extreme states of high temperature and high pressure. A new scheme based on high-energy electron beam as a probe was proposed for time-resolved imaging measurement of high energy density materials, especially for high energy density matter and inertial confinement fusion (ICF) [1, 2]. Comparing with proton and other x-ray diagnostics systems, electron imaging based on photo injector linear accelerator systems (LIN-AC) is expected to gain high spatial and temporal resolution at lower cost. Los Alamos National Lab developed the first high-energy electron radiography concept [3] with a 30 MeV electron beam achieving a resolution of 100 μm . The first test run for high density material imaging experiment using relativistic electron beam at AWA was done. The imaging system was based on the AWA drive beamline with 50 MeV beam. The highest beam

energy of AWA drive beam is 70 MeV, but for the electron imaging experiment, the energy of 50 MeV is chosen for stable running.

DESCRIPTION & OPTICS DESIGN OF AWA ELECTRON IMAGING SYSTEM SETUP

The first run for EI experiment in AWA was performed using drive beam. Figure 1 shows a schematic of the AWA drive beamline. The drive beam is generated by a photocathode RF gun running at 1.3 GHz. The drive gun is followed by 6 linac tanks (1.3 GHz) that bring the beam energy up to 70 MeV. The beam after 6 linac tanks is transported into dogleg which consists of two dipoles. For simplicity, the dogleg section is not designed for electron imaging experiment purposely. The dogleg is followed by AWA electron imaging experiment system which showed in Figure 2. It consists of two quadruples, target, one triplet, collimator and imaging plate.

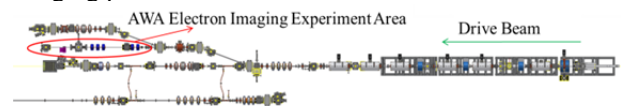


Figure 1: AWA drive beamline layout.

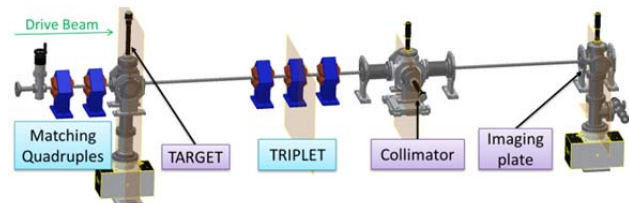


Figure 2: AWA electron imaging experiment system.

In AWA electron optical imaging system design, the beam energy of 50 MeV was chosen because of the power limitation of dogleg. The first two quadruples before target is used to matching the beam. The target crossing composed of a YAG screen, a bowtie shape mask with 10 mm long and 2.43 mm height segments, and a 200 μm thick aluminium triangle part. The details of target cross are showed in figure 3.

The optical imaging system starts from target to imaging screen, which consists of one triplet and drift sections. The optical imaging system design is the key part in EI beamline, which was optimized by Transport code [4]. For electron imaging system, two conditions need to be

[#] zzm@impcas.ac.cn

AN INTERNET RACK MONITOR-CONTROLLER FOR APS LINAC RF ELECTRONICS UPGRADE

Hengjie Ma, Alireza Nassiri, Terry Smith, Yine Sun, Argonne National Laboratory, Argonne, USA
Lawrence Doolittle, Alex Ratti, Lawrence Berkeley National Laboratory, Berkeley, USA

Abstract

To support the research and development in APS LINAC area, the existing LINAC rf control performance needs to be much improved, and thus an upgrade of the legacy LINAC rf electronics becomes necessary. The proposed upgrade plan centers on the concept of using a modern, network-attached, rackmount digital electronics platform –Internet Rack Monitor-Controller (or IRM-C) to achieve the goal of modernizing the rf electronics at a lower cost. The system model of the envisioned IRM-C is basically a 3+1 tier stack with a high-performance DSP in the mid-layer to perform the core tasks of real-time rf data processing and controls. The Digital Front-End (DFE) attachment layer under the DSP bridges the application-specific digital front-ends to the DSP. A network communication gateway, together with an event receiver (EVR) in the top layer merges the Internet Rack Monitor-Controller node into the networks of the accelerator control infrastructure. Although the concept of the IRM-C is very much in trend with today’s Internet-of-Things (IoT), this implementation has actually been used in the accelerators for over two decades.

CHALLENGES

The APS LINAC rf electronics covers the functions of rf control, monitoring, as well as the equipment protection in general as a typical “Low-level rf” (LLRF) system does. However, upgrading the electronics with an aim at improving the rf performance in precision has a set of challenges mainly due to two factors. The first is the use of SLED (SLAC LINAC Energy Doubler) in the rf power source as an economical method of boosting the rf power. The second has to do with an adopted strategy of operating the klystrons in saturated conditions for the purposes of prolonging the klystron life and minimizing the rf over-power trips. Both the choice of SLED and the operation strategy are appropriate for the given mission of the LINAC merely as a beam injector. However, that also has created some challenges to the future electronics upgrade for the rf improvement. Specifically,

1. The rf output from the SLED pulse compressor has a very narrow, and rapidly decaying pulse waveform which lacks the desirable flat-top that the waveforms from a non-SLED rf source normally have. The accelerating structures typically have a rf filling time of ~800nS. Over that time period, the SLED rf power drops by more than 80% from its peak as shown by the yellow scope trace in Figure 1, and it results in a severely lopsided rf field distribution in the accelerat-

ing structures (or A-S) indicated by the A-S output waveform (red trace). It is very difficult to accurately measure the rf level and phase with such dynamic waveforms, and would require in the new electronics to use the digitizers of ultra-high speed and high-resolution, and clocked with a very low-jitter timing. The very-high peak power of the severely lopsided SLED rf waveforms puts a lot of stress on the high-power rf components, and has created the need in enhancing the rf protections.

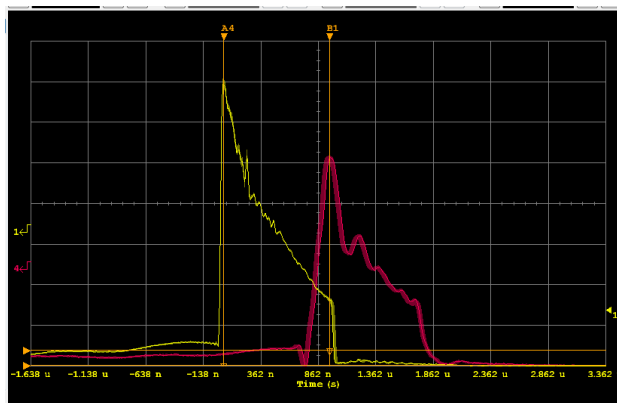


Figure 1: Rapidly decaying rf waveforms of APS LINAC rf driven by a SLED-based rf source, A-S Input rf power (yellow trace) and A-S Output Power (red trace).

2. Operating the klystrons in saturation has a significant impact on the rf control. Under such conditions, the klystrons work like Class-C amplifiers, and that has two implications. 1) the normal capability of effectively controlling the klystron output power through changing the rf input level is lost, and so goes the capability of fast rf power control. 2) The klystron output rf phase would change dramatically as the rf operating power level is changed. The result is that the rf power and phase cannot be independently adjusted, which makes the beam operation difficult. Correcting this undesirable rf power-phase coupling requires some very fast and sophisticated DSP technology.
3. With the existing rf system, the SLED timing jitter gets translated into the beam energy jitter. Because of the rf power-phase coupling issue, APS has adopted an alternative way of the controlling the rf “power” without affecting the phase. That is done by timing the A-S rf filling such that when the beam passes through, the A-S is only partially rf-filled as shown in the scope picture in Figure 2. By adjusting the SLED timing to change the degree of the partial rf-fill, the total amount of rf power that the beam experiences

A VME AND FPGA BASED DATA ACQUISITION SYSTEM FOR INTENSITY MONITORS*

J. Diamond[#], A. Ibrahim, N. Liu, E. S. McCrory, A. Semenov, Fermilab, Batavia, Illinois, USA

Abstract

A universal data acquisition system supporting toroids, DCCTs, Faraday cups, scrapers and other types of instrumentation has been developed for reporting beam intensity measurements to the Fermilab Accelerator Controls System (ACNet). Instances of this front end, supporting dozens of intensity monitor devices have been deployed throughout the Fermilab accelerator complex in the Main Injector, Recycler, Fermilab Accelerator Science and Technology (FAST) facility and the PIP-II Injector Experiment (PXIE). Each front end consists of a VME chassis containing a single board computer (SBC), timing and clock module and one or more 8 to 12-channel digitizer modules. The digitizer modules are based on a Cyclone III FPGA with firmware developed in-house allowing a wide range of flexibility and digital signal processing capability. The front end data acquisition software adds a list of new features to the previous generation allowing users to: take beam intensity measurements at custom points in the acceleration cycle, access waveform data, control machine protection system (MPS) parameters and calculate beam energy loss.

INTRODUCTION

Beam intensity instrumentation is a critical part of every particle accelerator. The Fermilab Accelerator Division Instrumentation department is tasked with developing world-class beam instrumentation that can support the laboratory's growing complex of diverse particle accelerators. To meet these demands, a VME digitizer module has been designed in-house for acquiring signals from toroids, DCCTs, and other types of beam instrumentation. The module's firmware also provides enhanced digital signal processing capability that can be customized to unique situations.

Data acquisition software developed at Fermilab and proven in one situation is often put to use in another with some degree of modification. In the past, each deployment of a beam intensity data acquisition system was managed as a separate software project even though each descended from a common code base (a practice known to software developers as forking). The problem with this approach is that each instance (a fork) of the common software does not benefit when a bug fix or new feature is applied to another. Diligent management and time-consuming development were necessary to ensure that software and firmware changes were made to each fork of the code base and tested properly.

* This work was supported by the DOE contract No. DEAC02-07CH11359 to the Fermi Research Alliance LLC.
jdiamond@fnal.gov

Faced with a rapidly increasing demand across the laboratory for beam intensity monitors based on the in-house designed digitizer module, the decision was made to coalesce the data acquisition software development into a single unit that is flexible enough to be used in all situations. Instead of each deployment of an intensity monitor data acquisition system running custom software, all deployments will run the same software configured individually for the application.

DIGITIZER MODULE

The beam intensity data acquisition system was developed to utilize two variations of an in-house designed 6U VME digitizer module. One variation of the digitizer module samples at 125 MS/s and supports 8 channels and another samples at 250 MS/s and supports 12 channels. Both variations are equipped with 192 MB of DDR2 SDRAM for data buffering and a Cyclone III FPGA for signal processing (see Fig. 1).

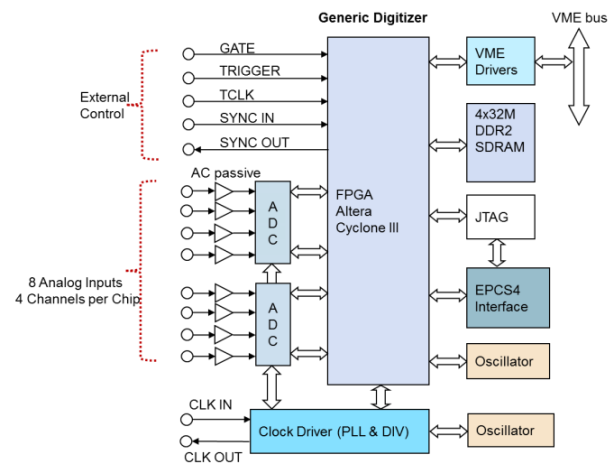


Figure 1: 125MS/s 8-channel VME Digitizer Module.

The FPGA firmware can be divided into two sections. One section supports the basic infrastructure required for any general application: an ADC data receiver, a VME bus driver, a memory driver, a serial port interface and a sync signal decoder for smart triggering. The section other supports application specific algorithms including the intensity calculation.

Beam intensity is calculated by the digitizer module's firmware and presented to the data acquisition software in raw ADC counts over the VME bus. When beam current is measured the digitizer module also provides a calculation of the beam pulse length. Scaling to beam intensity

A LONGITUDINAL DIGITAL MODE DAMPER SYSTEM FOR THE FERMILAB BOOSTER*

N. Eddy[#], W. Pellico, A. Semenov, D. Voy, A. Waller, Fermilab, Batavia, IL 60510, USA

Abstract

The Fermilab Booster accelerates bunches and accelerates proton beams from 400 MeV to 8 GeV. During the acceleration the Radio Frequency (RF) cavities are swept from 38MHz to 52.8MHz and requires crossing through transition where accelerating phase is shifted 90 degrees. In order to keep the beam stable and minimize losses and emittance growth a longitudinal damping system is required. This has traditionally been done by dedicated analog electronics designed to operate on specific beam modes for frequencies of instabilities. A complete digital implementation has been developed for this same purpose. The new digital system features and performance are detailed.

INTRODUCTION

The longitudinal damper is required to suppress coupled bunch instabilities in the Fermilab Booster and is a critical component of the high intensity machine operation [1]. The damper operates by detecting an oscillation feeding it back on the beam with the appropriate phase to create negative feedback. For a longitudinal instability these show up as synchrotron tune lines about the revolution harmonics. As the Booster is an $h=84$ machine, the instabilities can appear in any of the 84 revolution harmonics often referred to as modes. The approach taken in the Booster has been to build dedicated electronics to suppress each mode which has caused problems. The new digital system can be configured to provide diagnostics and damping on any of the 84 modes via software control.

DAMPER SYSTEM

An overview of the Booster longitudinal damper system is shown in Fig. 1. In the Booster the pickup is a Resistive Wall Current Monitor. In principle, the digital system can operate on any of the 84 modes, but damping requires appropriate hardware, typically a cavity, to apply the correction signal. There are currently two options in the Booster. The accelerating RF cavities are used for damping mode 1 and 2. A dedicated cavity with a center frequency of 80MHz and bandwidth of 10MHz. This is able to damp modes 42-54. A second dedicated cavity at 65 MHz is also installed but is not currently used as no destructive modes have been observed in this frequency range.

Digital Damper Hardware

A custom VME/VXS board is the heart of the damper

* This work was supported by the DOE contract No.DEAC02-07CH11359 to the Fermi Research Alliance LLC.

[#] eddy@fnal.gov

system. It was developed for generic feedback applications and is shown in Fig. 2. It consists of 4

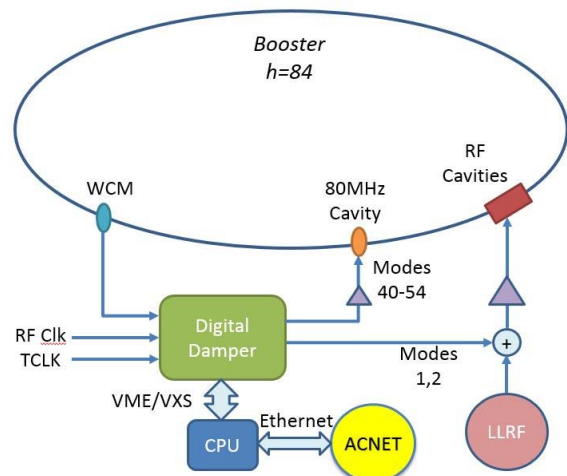


Figure 1: Overview of the Booster longitudinal damper system.

channels of 250 MS/s 14 bit ADCs and 4 channels of 500 MS/s 16 bit DACs which are connected to an Altera Cyclone V FPGA. Timing for the board is handled through a lower jitter PLL based clock distribution chip so that ADC, DAC, and logic can be synchronized with an external reference clock.

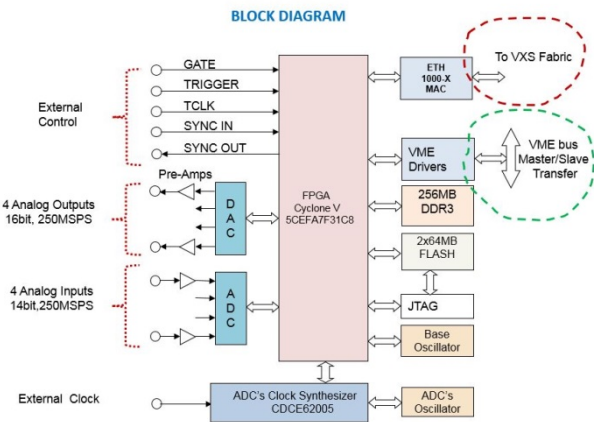


Figure 2: Block diagram for custom VME/VXS digital feedback board developed at Fermilab.

Digital Damper Firmware

A single damper board has 16 down converter channels as shown in Fig. 3. In principle, each channel can be programmed to provide either a drive or correction signal on any mode with some limitations due to hardware and system configuration. There are 4 DACs on the board and each channel can only be assigned to 1 DAC to insure

LOW LEVEL RF CONTROL FOR THE PIP-II INJECTOR TEST RFQ

J. P. Edelen[#], B. E. Chase, E. Cullerton, J. Einstein-Curtis, and P. Varghese Fermilab, Batavia, IL

Abstract

The PIP-II injector test radio frequency quadrupole (RFQ) arrived at Fermilab in the fall of 2015. The RFQ is a 162.5MHz H- accelerator with a nominal drive power of 100kW, which produces a bunched H- beam at 2.1MeV. In this paper we discuss commissioning, operational performance, and improvements to the low level RF (LLRF) control system for the RFQ. We begin by describing the general system configuration and initial simulation results. We will then highlight temperature related issues in the high power RF system, which necessitate active control over the phase balance of the two amplifiers. Finally we demonstrate performance of the RF feedback and feed-forward compensation needed to meet specification during a 20-microsecond beam pulse.

INTRODUCTION

The PIP-II injector test radio frequency quadrupole (RFQ) was commissioned at Fermilab in January 2016. The RFQ operates at 162.5MHz with a nominal drive power of 100kW. The RFQ accelerates H- to an energy of 2.1MeV and can be operated in both pulsed and CW mode. In order to meet the machine requirements for PIP-II the LLRF system is required to achieve 10^{-3} regulation in the amplitude and 0.1 degrees in phase, and investigate areas for improvement.

The LLRF system is comprised of both analog and digital components. The analog RF components are used to translate the 162.5 MHz signals from the cavity and the directional coupler an intermediate frequency of 13MHz. The signals are then digitized and converted to base-band using the FPGA. The FPGA then performs control calculations on these signals to generate the output signal that is converted back to the intermediate frequency and then up to 162.5 MHz to drive RF amplifiers.

The controller can be operated in three modes: Feed-forward only, feedback (with feed-forward as needed), and frequency-tracking mode. In feed-forward only mode the LLRF system drives the amplifier with a fixed signal level. In feedback mode the LLRF system includes proportional and integral control calculations in order to regulate the cavity amplitude and phase to a desired set point. In the frequency-tracking mode, the LLRF system adjusts the drive frequency proportional to the error in the cavity phase. Additionally, due to the high average power of this RFQ, two solid-state amplifiers are used to power the cavity. To avoid two competing PI loops, the cavity is regulated with a single controller that has two drive outputs. These outputs have independent amplitude and phase calibrations to account for uneven RF distribution systems and unequal amplifier gains.

In this paper we discuss initial simulations of the feedback system and compare with measured data obtained during the system commissioning. Following this, we will discuss the necessary amplifier calibrations to ensure a proper match into the RFQ. Next we discuss temperature related issues in the RF system and an additional controller necessary to compensate for temperature drifts. Finally we demonstrate 10^{-3} performance of the RF system during a 20-microsecond beam pulse.

SYSTEM MODELING

The RFQ was modelled using Matlab's Simulink simulation environment [2]. By using a low-pass-filter model of the RF cavity and neglecting the RF distribution system, we can simulate the controller performance and compare with a measured RF envelope. Figure 1 shows a simplified block diagram of the LLRF system model created in Simulink [2].

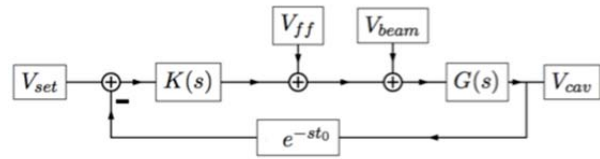


Figure 1: Block diagram of the LLRF simulation model.

Figure 2 shows the simulated RF pulse in the RFQ compared with the measured pulse obtained during RFQ commissioning.

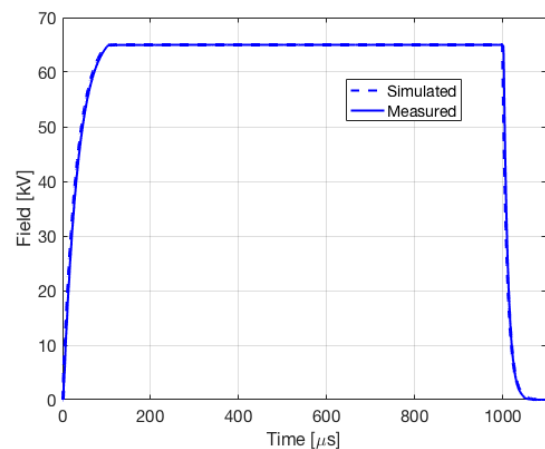


Figure 2: Comparison of measured RF pulse to simulated RF pulse in the RFQ. Proportional and integral gains were 9.0 and $8.0e5$ respectively.

In Figure 1, $K(s) = K_p + K_i/s$, $G(s) = \frac{\omega_0}{2Q_L} \left(s + \frac{\omega_0}{2Q_L} \right)$, and t_0 is the feedback delay of the system, 2 microseconds was used for our simulations in Figure 2.

50-MeV RUN OF THE IOTA/FAST ELECTRON ACCELERATOR*

D. Edstrom, Jr.#, C. Baffes, C. Briegel, D.R. Broemmelsiek, K. Carlson, B. Chase, D.J. Crawford, E. Cullerton, J. Diamond, N. Eddy, B. Fellenz, E. Harms, M. Kucera, J. Leibfritz, A.H. Lumpkin, D. Nicklaus, E. Prebys, P. Prieto, J. Reid, A. Romanov, J. Ruan, J. Santucci, T. Sen, V. Shiltsev, Y. Shin, G. Stancari, J.C. Thangaraj, R. Thurman-Keup, A. Valishev, A. Warner, S. Wesseln (FNAL, Batavia, IL), P. Kobak (BYU-I, Rexburg, ID), W. Rush (KU, Lawrence, Kansas), A. Green, A. Halavanau, D. Mihalcea, P. Piot (NIU, DeKalb, IL, USA)
J. Hyun (Sokendai, Ibaraki, Japan)

Abstract

The low-energy section of the photoinjector-based electron linear accelerator at the Fermilab Accelerator Science & Technology (FAST) facility was recently commissioned to an energy of 50 MeV. This linear accelerator relies primarily upon pulsed SRF acceleration and an optional bunch compressor to produce a stable beam within a large operational regime in terms of bunch charge, total average charge, bunch length, and beam energy. Various instrumentation was used to characterize fundamental properties of the electron beam including the intensity, stability, emittance, and bunch length. While much of this instrumentation was commissioned in a 20 MeV running period prior, some (including a new Martin-Puplett interferometer) was in development or pending installation at that time. All instrumentation has since been recommissioned over the wide operational range of beam energies up to 50 MeV, intensities up to 4 nC/pulse, and bunch structures from ~1 ps to more than 50 ps in length.

INTRODUCTION

The Fermilab Accelerator Science & Technology (FAST) facility team is constructing a 300 MeV electron linac based on superconducting RF (SRF) technology [1]. Once complete, the beamline will be used to inject 150 MeV electrons into the Integral Optics Test Accelerator (IOTA) ring currently being built to test integrable nonlinear inserts [2,3], electron lenses for space-charge compensation [4,5], and other advanced accelerator technologies [6,7]. The low electron injector duty factor required for IOTA (i.e. a single pulse train to be injected on demand every few minutes) allows for a beamline-based test program run in parallel to make use of the large, stable operational parameter space provided by the electron injector as summarized in Table 1. The injector itself comprises a number of components including a photoinjector-based electron gun, a 25-meter-long low-energy (≤ 50 MeV) beamline shown in Fig. 1, and an 100-meter-long high-energy (≤ 300 MeV) beamline. The IOTA ring is being built at the end of the high energy section near the high-energy absorber. Here we address commissioning of first beam to the full 50 MeV energy of the low energy beamline to the low energy absorber.

* This work was supported by the DOE contract No. DEAC02-07CH11359 to the Fermi Research Alliance LLC.
edstrom@fnal.gov

LOW ENERGY BEAMLIN

The electron gun is a normal-conducting, 1.5-cell copper cavity operating at 1.3 GHz. A train of pulsed UV from the drive laser strikes a Cs₂Te-coated Mo cathode in the gun cavity resulting in a train of electron bunches with bunch charge of up to 4 nC/bunch. A 4.5 MeV electron beam from the gun passes through a short (~1 m) low-energy diagnostic section before acceleration in two consecutive superconducting RF structures referred to as capture cavities, CC1 and CC2. Each capture cavity in its own cryostat is a 9-cell, 1.3 GHz (L-Band), Nb accelerating structure cooled nominally to 2 K. Following acceleration, the electron beam passes through the low-energy beam transport section, which includes steering and focusing elements, an optional chicane for bunch compression and beam transforms, as well as a host of instrumentation. It is then directed into the low-energy absorber ahead of the high-energy section still under construction. This begins with a TESLA Type IV ILC-style cryomodule, which has been conditioned previously to 31.25 MeV/cavity to provide ~300 MeV beam to the high-energy absorber, planned for 2017 [1].

Primary instrumentation in the low-energy beamline is named for its position, between 100 and 125, where the gun defines the beginning of the beamline at 100 and the cryomodule defines the end of the low-energy beamline at 126, and it includes beam position monitors (BPMs), two toroids, two wall current monitors, loss monitors, a ceramic gap [8], and transverse profile monitors (TPMs). The last is a modular component that is used to insert a cerium-doped YAG screen or OTR foil into the beam path. The YAG screens and many of the OTR foils are monitored with cameras, allowing for a direct measurement of the transverse electron beam profile, but one of the OTR foils (in the TPM at instrumentation cross X121) provides signal to a Hamamatsu C5680 streak camera and the Martin-Puplett interferometer (MPI).

With the exception of the MPI, the instrumentation noted above had already been used to characterize the electron beam in the 20-MeV low-energy commissioning run in 2015 [9]. In that run, CC1 had not been installed, limiting the energy and presenting a longer drift between the gun and CC2. Measurements made in this commissioning run included beam energy measurements using the path

BEAM INTENSITY MONITORING SYSTEM FOR THE PIP-II INJECTOR TEST ACCELERATOR*

N. Liu[#], J. Diamond, N. Eddy, A. Ibrahim, N. Patel, A. Semenov, Fermilab, Batavia, IL 60510, USA

Abstract

The PIP-II injector test accelerator is an integrated systems test for the front-end of a proposed CW-compatible, pulsed H⁻ superconducting RF linac. This linac is part of Fermilab's Proton Improvement Plan II (PIP-II) upgrade. This injector test accelerator will help minimize the technical risk elements for PIP-II and validate the concept of the front-end. Major goals of the injector accelerator are to test a CW RFQ and H⁻ source, a bunch-by-bunch MEBT beam chopper and stable beam acceleration through low-energy superconducting cavities. Operation and characterization of this injector places stringent demands on the types and performance of the accelerator beam diagnostics. This paper discusses the beam intensity monitor systems as well as early commissioning measurements of beam transport through the Medium-Energy Beam Transport (MEBT) beamline.

INTRODUCTION

The beam intensity, or number of charged particles in the beam, has to be monitored and must be kept within predetermined safety and operational envelopes. To ensure that, beam intensity monitors with magnetically-coupled toroidal pickups are used as a non-interceptive method to measure the total transferred intensity in the PIP-II H⁻ linac. The beam intensity monitor system consists of the toroid assembly, the signal conditioning circuit as well as the data acquisition electronics (see Fig. 1). The toroid pickup is inserted around the beam tube with a ceramic insulator.

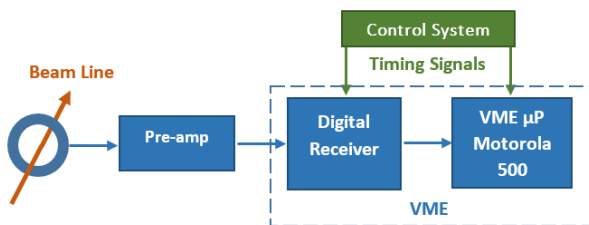


Figure 1: Toroid-based beam intensity monitor system.

A low-pass filter / gain stage follows. An in-house designed digitizer module is used for data acquisition and digital signal processing. The digitizer is a 6U VME module and has 8 analog input channels with selectable AC or DC coupling. On-board ADC chips are capable of a sampling rate up to 125MS/s. A programmable clock distribution circuit offers flexible timing configurations. Other elements on the board are the Cyclone III FPGA chip

*Work supported by the Fermi National Accelerator laboratory, operated by Fermi Research Alliance LLC, under contract No. DE-AC02-07CH11359 with the US Department of Energy #ningliu@fnal.gov

for signal processing, and 192 MB of DDR2 memory for data buffering (see Fig. 2). A Motorola 5500 VME microprocessor is used for data buffering and communication with Fermilab's Accelerator Controls System (ACNet).

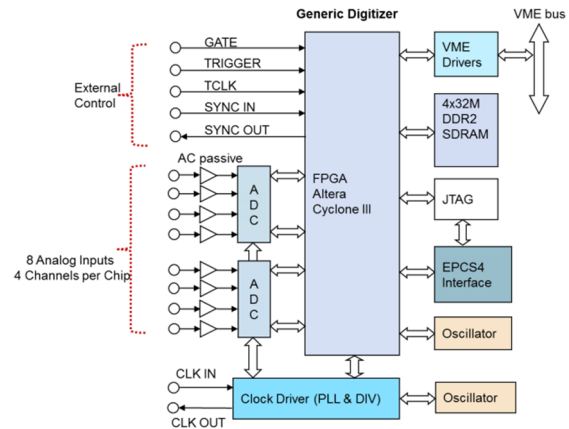


Figure 2: 8-channel 125 MS/s VME digitizer.

TOROID SYSTEM

At PIP-II beam intensity is detected using several magnetically-coupled toroidal pickups along the transport line, to provide a non-destructive method to measure the total transferred intensity.

- The first part of the monitor is the beam pickup, i.e. the toroid, including its mechanical assembly, ceramic gap, shielding, etc., as part of the beam line within the tunnel enclosure. A ceramic insulator provides an electric break in the metallic vacuum chamber. The toroid couples to the magnetic field components of the beam, i.e. detects the beam intensity. The support and shielding structure provides a well-defined path of low impedance for the wall currents.
- Following the pickup are the preamp and digital electronics which are discussed in following sections.

The toroidal pickup follows the basic transformer theory. Passing through the center of the toroid, the beam forms a single-turn primary coil of the transformer. An N-turn secondary coil is wound around the core, and the induced voltage is measured across a load resistor which terminates the secondary winding.

The toroidal pickups installed at PIP-II have a limited bandwidth substantially lower than the RF beam spectrum. As a result, most of the bunch time structure, i.e. bunch-by-bunch information, is lost. Thus the waveform of the toroid signal reflects the “envelope” of the beam pulse (Fig. 3). Using both *Ohm's* law and transformer relationships, the amplitude of macro-pulse is linear with

INITIAL DEMONSTRATION OF 9-MHz FRAMING CAMERA RATES ON THE FAST DRIVE LASER PULSE TRAINS*

A. H. Lumpkin[#], D. Edstrom Jr., and J. Ruan
Fermi National Accelerator Laboratory, Batavia, IL 60510 USA

Abstract

We report the configuration of a Hamamatsu C5680 streak camera as a framing camera to record transverse spatial information of green-component laser micropulses at 3- and 9-MHz rates for the first time. The latter is near the time scale of the ~ 7.5 -MHz revolution frequency of the Integrable Optics Test Accelerator (IOTA) ring and its expected synchrotron radiation source temporal structure. The 2-D images are recorded with a Gig-E readout CCD camera. We also report a first proof of principle with an OTR source using the linac streak camera in a semi-framing mode.

INTRODUCTION

Although beam centroid information at the MHz-micropulse-repetition rate has routinely been achieved at various facilities with rf BPMS, the challenge of recording beam size information at that rate is more daunting due to limitations in data-transfer rates. This is also near the time scale of the 7.5-MHz revolution frequency of the Integrable Optics Test Accelerator (IOTA) ring being constructed at the Fermilab Accelerator Science and Technology (FAST) Facility [1]. To simulate the expected IOTA optical synchrotron radiation (OSR) source temporal structure, we have used the green component of the FAST drive laser [2]. This is normally set at 3 MHz, but has also been run at up to 9 MHz. To circumvent the need to readout the 2D images in less than a few microseconds, we have configured our Hamamatsu C5680 streak camera as a framing mode camera using a slow vertical sweep plugin unit with the dual axis horizontal sweep unit. A two-dimensional array of images sampled at the MHz rate can then be displayed on the streak tube phosphor and recorded by the CCD readout camera at up to 10 Hz.

Demonstrations of the tracking of the beam size and position of consecutive green micropulses are shown, although there are gaps in the displayed pulse train for a given trigger delay. As an example, by using the 10 microsecond vertical sweep with the 100 microsecond horizontal sweep ranges, 49 of the 300 micropulses at 3 MHz are displayed for a given trigger delay. The whole pulse train dynamics are shown by recording only six sets of images with the appropriate stepped delays. Spatial resolutions of better than 15 microns seem possible for beam profiling and would be even better for beam centroids. Example 2D image arrays with profiling examples will be presented.

*Work supported under Contract No. DE-AC02-07CH11359 with the United States Department of Energy.

[#]lumpkin@fnal.gov

EXPERIMENTAL ASPECTS

Two main aspects of the experiment are the drive laser as the source of a visible-light, 3-MHz pulse train and the Hamamatsu streak camera configured as a framing camera.

The Drive Laser & FAST Electron Accelerator

The drive laser is based on a Calmar seed laser, consisting of a Yb-doped fiber laser oscillator running at 1.3 GHz that was then divided down to 81.25 MHz before amplification through a set of fiber amplifiers as shown in Fig.1. The seed output of 81.25 MHz packets of 1054 nm infrared (IR) laser is then reduced to the desired pulse train frequency (nominally 3 MHz) with a Pockels cell before selection of the desired pulse train with two additional Pockels cells and amplification through a series of YLF crystal-based single pass amplifiers (SPAs) and a Northrup-Grumman amplifier, which nominally yields 50 μ J of IR per pulse before the two frequency-doubling crystal stages generate the green and then the UV components with a total nominal efficiency of 10% [2]. The pulse train selected is between a single pulse per machine cycle (nominally 1 Hz) and 1 ms (3000 pulses at the nominal 3 MHz pulse train frequency) [2]. The UV drive laser pulse train is used to generate an electron pulse in the FAST IOTA electron injector, an SRF-based linear accelerator tested thus far to 50 MeV [3].

In the initial framing camera studies we observed the green component remaining from UV-conversion at 3 and 9 MHz pulse train frequencies with the laser lab streak camera, but we have also recently applied the principle to optical transition radiation (OTR) from an Al-coated Si substrate foil with subsequent transport to a beamline streak camera.

The Streak Camera Systems

Commissioning of the streak camera system was facilitated through a suite of controls centered around ACNET, the Fermilab accelerator controls network. This suite includes operational drivers to control and monitor the streak camera as well as Synoptic displays to facilitate interface with the driver. Images from the readout cameras, Prosilica 1.3 Mpixel cameras with 2/3" format, may be analyzed both online with a Java-based ImageTool and an offline MATLAB-based ImageTool processing program [4,5]. Bunch-length measurements using these techniques have been reported previously from the A0 Facility [6] and FAST first commissioning at 20 MeV [7].

INITIAL OBSERVATIONS OF MICROPULSE ELONGATION OF ELECTRON BEAMS IN A SCRF ACCELERATOR*

A. H. Lumpkin[#], D. Edstrom Jr., J. Ruan, J. Santucci, and R. Thurman-Keup
Fermi National Accelerator Laboratory, Batavia, IL 60510 USA

Abstract

Commissioning at the SCRF accelerator at the Fermilab Accelerator Science and Technology (FAST) Facility has included the implementation of a versatile bunch-length monitor located after the 4-dipole chicane bunch compressor for electron beam energies of 20-50 MeV and integrated charges in excess of 10 nC. The team has initially used a Hamamatsu C5680 synchroscan streak camera to assess the effects of space charge on the electron beam bunch lengths. An Al-coated Si screen was used to generate optical transition radiation (OTR) resulting from the beam's interaction with the screen. The chicane bypass beamline allowed the measurements of the bunch length without the compression stage at the downstream beamline location using OTR and the streak camera. We have observed electron beam bunch lengths from 5 to 16 ps (σ) for micropulse charges of 60 pC to 800 pC, respectively. We also report a compressed sub-ps micropulse case.

INTRODUCTION

One of the more obvious effects of space-charge forces acting within micropulses in photoinjectors and SCRF linacs is the elongation of the electron bunch compared to the initial drive laser bunch length [1,2]. During the initial 20-MeV commissioning run of the Fermilab Accelerator Science and Technology (FAST) facility [3], we took advantage of a 1.5-m drift between the photoinjector rf gun and the initial accelerating capture cavity CC2. Recently, another cavity, CC1, has been installed in this drift space so that the beam is accelerated to higher energies (~50 MeV) immediately following the photoelectric injector and gun diagnostics station [4]. We now have a direct comparison available of the observed electron beam bunch lengths for different micropulse charges and the two accelerator configurations: both with the full 1.5 m drift and with the much shorter drift following installation of the additional ~1 m of accelerating structure.

The chicane bypass beamline allowed the measurements of the bunch length without the compression stage at the downstream beamline location using OTR and the streak camera. The UV component of the drive laser had previously been characterized with a Gaussian fit σ of 3.5-3.7 ps. However, the uncompressed electron beam was observed to elongate as expected due to space-charge forces in the 1.5-m drift from the gun to the first SCRF accelerator cavity in this initial configuration. We also report our results with the CC1 cavity installed. A preliminary ASTRA-Elegant prediction is noted. Finally,

* This work was supported by the DOE contract No. DEAC02-07CH11359 to the Fermi Research Alliance LLC.

[#] lumpkin@fnal.gov

we report generation of sub-ps micropulses at FAST for the first time using the 4-dipole bunch compressor (chicane, see Fig. 1).

EXPERIMENTAL ASPECTS

Two main aspects of the experiment are the injector as the source of the electrons in a 3-MHz pulse train and the Hamamatsu C5680 streak camera configured with the 81.25 MHz synchroscan plugin unit. The beam generates the OTR at the X121 converter screen. These topics will be discussed in this section.

The Injector Linac

The high-power electron beams for the FAST facility [3] are generated in a photoelectric injector (PEI) based on a UV drive laser and the L-band rf photocathode (PC) gun cavity. The PEI drive laser is comprised of multiple stages including a Calmar Yb fiber oscillator and amplifier, several YLF-based amplification stages, a final Northrup Grumman IR amplification stage, and two frequency-doubling stages that result in a UV component at 263 nm with a nominal 3-MHz micropulse bunch structure [5]. The UV component is transported from the laser lab through the UV transport line to the photocathode of the gun for generation of the photoelectron beams for use in the SC rf accelerator.

The low-energy section of the facility and part of the first cryomodule are schematically shown in Fig. 1. After the L-band rf PC gun, the beam is accelerated through two L-band superconducting cavities resulting in a beam energy of up to 50 MeV, though initially this was limited to 20 MeV due to the absence of CC1. We will report the bunch length elongation observed downstream for both configurations.

The Streak Camera System

The linac streak camera consists of a Hamamatsu C5680 mainframe with S20 PC streak tube and can accommodate a vertical sweep plugin unit and either a horizontal sweep unit or blanking unit. The UV-visible input optics allow the assessment of broadband OTR. A M5675 synchroscan unit with its resonant circuit tuned to 81.25 MHz from the Master Oscillator (MO) and a M5679 horizontal sweep unit were used for these studies. The low-level rf is amplified in the camera to provide a sine wave deflection voltage for the vertical plates that results in low jitter (~1ps) of the streak camera images and allows for synchronous summing of a pulse train of OTR. The temporal resolution is about 2.0 ps (FWHM), or 0.8 ps (σ), for NIR photons at 800 nm. When combined with the C6878 phase locked loop (PLL) delay box we can track phase effects at the ps level over several

FROM RELATIVISTIC ELECTRONS TO X-RAY PHASE CONTRAST IMAGING*

A. H. Lumpkin^{1#}, A. B. Garson², and M. A. Anastasio²

¹Fermi National Accelerator Laboratory, Batavia, IL 60510 USA

²Washington University in St. Louis**, St. Louis, MO 63130 USA

Abstract

We report the initial demonstrations of the use of single crystals in indirect x-ray imaging for x-ray phase contrast imaging at the Washington University in St. Louis Computational Bioimaging Laboratory (CBL). Based on single Gaussian peak fits to the x-ray images, we observed a four times smaller system point spread function (21 μm (FWHM)) with the 25-mm diameter single crystals than the reference polycrystalline phosphor's 80- μm value. Potential fiber-optic plate depth-of-focus aspects and 33- μm diameter carbon fiber imaging are also addressed.

INTRODUCTION

X-ray phase contrast (XPC) imaging is an emerging technology that holds great promise for biomedical applications due to its ability to provide information about soft tissue structure [1]. The need for high spatial resolution at the boundaries of the tissues is noted for this process. Based on results on imaging of relativistic electron beams with single crystals [2], we proposed transferring single-crystal imaging technology to this bio-imaging issue. We report initial indirect x-ray imaging tests that demonstrated improved spatial resolution with single crystals compared to the $\text{Gd}_2\text{O}_2\text{S:Tb}$ polycrystalline phosphor in a commercial, large-format CCD system. Using the Washington University microfocus x-ray tube as a source of 17 keV x-rays and the exchangeable phosphor feature of the camera system, we compared the point spread function (PSF) of the system with the reference phosphor to that with several rare-earth-garnet single crystals of varying thickness borrowed from the Fermilab and Argonne National Laboratory (ANL) linac labs.

We used a series of x-ray collimators which ranged in diameter from 400 to 25 microns. These were placed on the camera's Be entrance window to explore the PSF effects. Based on single Gaussian peak fits to the x-ray images, we observed a four times smaller system PSF (21 microns (FWHM)) with the 25-mm diameter single crystals than with the reference polycrystalline phosphor's 80-micron value. Initial images of 33-micron diameter carbon fibers have also been obtained with the system. The tests with a full-scale 88-mm diameter single crystal which would be fiber optically coupled to the CCD sensor with 86-mm diameter are being planned.

*Work partly supported under Contract No. DE-AC02-07CH11359 with the United States Department of Energy.

**Work at Washington University in St. Louis was supported in part by NSF CBET1263988.

#lumpkin@fnal.gov

TECHNICAL CONSIDERATIONS

The improved spatial resolution with single crystals over polycrystalline or powder samples had been previously noted in the imaging of relativistic electron beams [2]. Examples are shown in Fig. 1 as deduced from results at various laboratories, and the concept is being applied to indirect x-ray imaging in this research.

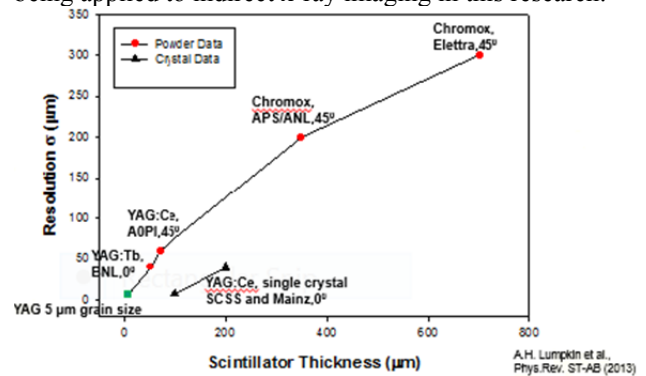


Figure 1: Summary of spatial-resolution values for different polycrystalline and single-crystal sample thicknesses for relativistic electron beams.

The CBL Facility

The CBL XPC lab [3] includes the microfocus x-ray source, a high precision stage and rail system, and the high resolution Quad-RO x-ray camera as schematically shown in Fig. 2. The x-ray source is a KeveX PXS10-65W with cone beam, tungsten anode, 7-100 micron spot sizes, and 45-130 kV tube voltages. The Thorlabs rail system was used, but not the computer controlled stages. The Quad-RO-4096 is a Peltier cooled (-40 degrees C) CCD, with 15 micron pixel pitch for a 4096 x 4096 array [4]. It has 14 bit intensity quantization and a PSF to be determined (generally 30-40 microns was ascribed).

We placed sequentially the collimators from the Amptec x-ray spectrometer set, on a lead plate with a hole drilled in it smaller than the W disc diameter. This plate was leveled with shims against the outer flange surface of the Quad-RO camera and positioned for the x-ray images to fall in the central area of one of the four quadrants of the CCD array. The set included collimators of 400, 200, 100, 50, and 25 μm in diameter. We estimated the rms size by dividing by the SQRT 12, and we multiplied by 2.35 to obtain the FWHM of the effective x-ray source size as tabulated in Table 1. The x-ray source was run at 7- μm spot size, at 25 or 60 kV tube voltage, at 150 μA current, 3.8 W, and located 0.9 m from the camera. Typical image integration times were 30s, and we averaged over five frames. Data were dark current

FEASIBILITY OF OTR IMAGING FOR LASER-DRIVEN PLASMA ACCELERATOR ELECTRON-BEAM DIAGNOSTICS*

A. H. Lumpkin^{1#}, D.W. Rule², M.C. Downer^{3**}

¹Fermi National Accelerator Laboratory, Batavia, IL USA

²Silver Spring, Maryland, USA, ³University of Texas, Austin, Texas, USA

Abstract

We report the initial considerations of using linearly polarized optical transition radiation (OTR) to characterize the electron beams of laser plasma accelerators (LPAs) such as at the Univ. of Texas at Austin. The two LPAs operate at 100 MeV and 2-GeV, and they currently have estimated normalized emittances at ~ 1 -mm mrad regime with beam divergences less than $1/\gamma$ and beam sizes to be determined at the micron level. Analytical modeling results indicate the feasibility of using these OTR techniques for the LPA applications.

INTRODUCTION

Recent measurements of betatron x-ray emission from quasi-monoenergetic electrons accelerating to 500 MeV within a laser plasma accelerator (LPA) enabled estimates of normalized transverse emittance well below 1 mm-mrad and divergences of order $1/\gamma$, where γ is the Lorentz factor [1]. Such unprecedented LPA beam parameters can, in principle, be addressed by utilizing the properties of optical transition radiation (OTR). In particular, the linearly polarized features of that radiation provide additional beam parameter sensitivity. We propose a set of complementary measurements of beam size and divergence with near-field and far-field OTR imaging, respectively, on LPA electron beams ranging in energy from 100 MeV [2] to 2 GeV [3]. The feasibility is supported by analytical modeling for beam size sensitivity and divergence sensitivity. In the latter case, the calculations indicate that the parallel polarization component of the far-field OTR pattern is sensitive to rms divergences (σ_θ) from 0.1 to 0.4 mrad at 2 GeV, and it is similarly sensitive to rms divergences from 1 to 5 mrad at 100 MeV.

We anticipate the signal levels from charges of 100 pC will require a 16-bit cooled CCD or scientific CMOS camera. Other practical challenges of utilizing these techniques with the LPA configurations will also be discussed. These include the fundamental requirement to deflect the high power laser component with a foil while scattering the electron beam less than its intrinsic divergence. This may be achieved with a replaceable foil.

*Work partly supported under Contract No. DE-AC02-07CH11359 with the United States Department of Energy.

**Work at the Univ. of Texas supported by DOE grant DE-SC0011617. #lumpkin@fnal.gov

TECHNICAL CONSIDERATIONS

Two main aspects of the proposed experiments are to install OTR stations with near-field and far-field imaging options in the LPAs to assess electron beam size and divergence. A brief summary of the two LPAs at the University of Texas at Austin will be described with current diagnostics, and then the proposed OTR techniques will be addressed.

The Laser Plasma Accelerators

The Texas PW LPA schematic is shown in Fig. 1. The PW laser is focused onto the gas jet of 7-cm extent. At plasma electron densities of 3 to 5 $\times 10^{17}$ cm⁻³ strong plasma wake field acceleration occurred, and the electrons attained quasi-monoenergetic energies of 2 GeV [3]. Normally a dipole magnet is used to provide a dispersive effect in the x-plane for energy and energy spread measurements as detected by a downstream LANEX phosphor screen, imaging plate, or other. The vertical beam divergence is measured by evaluating the vertical beam size at the known drift location. A summary of the beam parameters for the PW LPA is given in Table 1. A similar process occurs with a TW LPA driven by a 30 TW laser to provide energies of 100 MeV [2], or 0.1 GeV, as summarized in Table 2.

Table 1: Summary of some PW LPA electron beam properties. The estimated parameters are indicated*.

Parameter	Units	Value	Range
Energy	GeV	2	1-2
Emittance*	mm mrad, norm.	1	0.1-2
Beam size*	μm	1	0.1-2
Divergence	mrad (FWHM)	0.3	0.2-0.4
Charge	pC	100	10-100
Duration*	fs	10	10-30

Table 2: Summary of some TW LPA electron beam properties. The estimated parameters are indicated*.

Parameter	Units	Value	Range
Energy	GeV	0.100	.050-0.100
Emittance*	mm mrad, norm.	1	0.1-1
Beam size*	μm	1	0.1-2
Divergence	mrad FWHM	4	2-5
Charge	pC	100	10-100
Duration*	fs	10	10-30

BEAM POSITION MONITORING SYSTEM FOR THE PIP-II INJECTOR TEST ACCELERATOR*

N. Patel[#], C. Briegel, J. Diamond, N. Eddy, B. Fellenz, J. Fitzgerald, V. Scarpine
FNAL, Batavia, IL 60510, USA

Abstract

The Proton Improvement Plan II (PIP-II) injector test accelerator is an integrated systems test for the front-end of a proposed continuous-wave (CW) compatible, pulsed H⁻ superconducting RF linac. This linac is part of Fermilab's PIP-II upgrade. This injector test accelerator will help minimize the technical risk elements for PIP-II and validate the concept of the front-end. Major goals of the injector accelerator are to test a CW RFQ and H⁻ source, a bunch-by-bunch Medium-Energy Beam Transport (MEBT) beam chopper and stable beam acceleration through low-energy superconducting cavities. Operation and characterization of this injector places stringent demands on the types and performance of the accelerator beam diagnostics. A beam position monitor (BPM) system has been developed for this application and early commissioning measurements have been taken of beam transport through the beamline.

INTRODUCTION

A BPM system is required for providing transverse position, relative intensity, and relative phase measurements for the MEBT linac as shown in Figure 1. A 4-button BPM system is implemented to provide such measurements for beam parameters shown in Table 1.

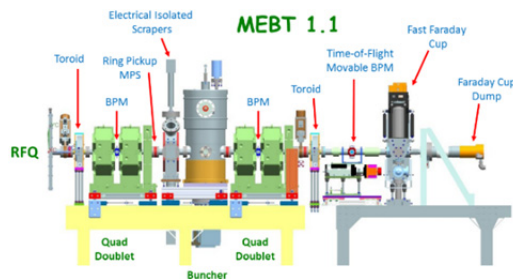


Figure 1: First Two BPMs in MEBT beamline.

Table 1: Typical Beam Parameters

Ion type	H ⁻
Beam Energy	2.1 MeV
Particles per bunch, nominal	2x10 ⁸
Max rms beam size, x/y	4 / 4 mm
Max rms bunch length in MEBT	15° of 162.5 MHz
Maximum rms bunch length in SC cryo-modules	6° of RF frequency
Bunch/RF frequency in MEBT	162.5 MHz CW
β	0.067
rms bunch length (sigma)	120 psec

For position, the relative accuracy indicates the allowable deviation, at large averaging, of linearity between the

* This work was supported by the DOE contract No. DEAC02-07CH11359 to the Fermi Research Alliance LLC.
[#]npatel@fnal.gov

reported and actual beam positions over ±5 mm range. The system should be able to subtract in software an absolute offset of BPM pickups and electronics up to 1mm.

For phase, the relative accuracy indicates the allowable deviation of linearity between the reported and actual beam phases, at large averaging, over ±5°.

DESIGN OVERVIEW

The BPM system block diagram is shown in Figure 2. Each BPM has 4 ports corresponding to each of the pickups. Figure 3 shows a picture of an individual uninstalled pick-up which is 20mm in diameter. The button pick-up is modified version of a design used by J. Crisp at FRIB [1]. Higher levels of assembly are shown in Figures 4 and 5. Superflex Helix coaxial cable with SMA terminations is connected to each of the ports. This cable was selected due to its shielding performance, flexibility, durability and low signal attenuation. At about 100 to 200 feet in length, the RF cables are then connected to a rack which houses all the BPM electronics. Within the rack, the BPM signals connect to an in-house designed 4-channel analog signal conditioning transition module, whose picture is shown in Figure 6 and block diagram in Figure 7. One highlight of this module is that a bandpass filter is placed on a daughter card. This allows for a compact, yet flexible design where a filter change with different footprint would only require a new daughter card assembly. The current bandpass filter selects the fundamental frequency of the bunch train. Several analog bandpass filters, both commercial off the shelf (COTS) and custom designs were evaluated. The “SXBP-161R5+” Mini Circuits filter was selected for performance, package size, cost and the advantage of being COTS.

As a result, the output of each channel from this module is a 162.5MHz tone. Twenty transition modules are able to fit in a 5U high crate having a custom backplane. Therefore, one crate can support up to 20 BPMs.

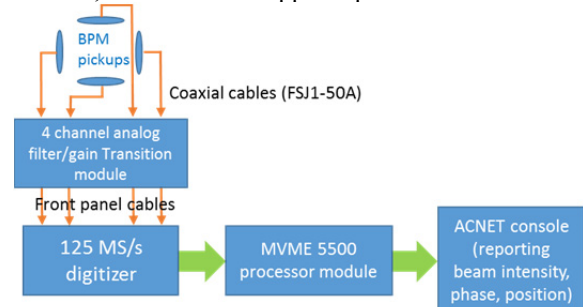


Figure 2: BPM system block diagram.

FERMILAB SWITCHYARD RESONANT BEAM POSITION MONITOR ELECTRONICS UPGRADE RESULTS*

T. Petersen[†], P. S. Prieto, A. Watts, J. Diamond, N. Liu, D. Slimmer, Fermi National Accelerator Laboratory

Abstract

The readout electronics for the resonant beam position monitors (BPMs) in the Fermilab Switchyard (SY) have been upgraded, utilizing a low noise amplifier transition board and Fermilab designed digitizer boards. The stripline BPMs are estimated to have an average signal output of between -110 dBm and -80 dBm, with an estimated peak output of -70 dBm. The external resonant circuit is tuned to the SY machine frequency of 53.10348 MHz. Both the digitizer and transition boards have variable gain in order to accommodate the large dynamic range and irregularity of the resonant extraction spill. These BPMs will aid in auto-tuning of the SY beamline as well as enabling operators to monitor beam position through the spill.

INTRODUCTION

The Fermilab Switchyard Stripline beam position monitors (BPMs) have been outfitted with new electronics. They consist of a transition board, VME processor (MVME 2401 or 5500), and an 8-channel, 125 MHz digitizer board. The transition boards condition the incoming signal before it arrives at the digitizers. This ensures that the signal is the appropriate magnitude to be read by the digitizer, as well as ensuring that only the frequency of interest is being detected. The large dynamic range and adjustable gain are the most considerable upgrades to the electronics system [1].

SYSTEM OVERVIEW

Resonant BPMs

The Switchyard BPMs have an external coil which in conjunction with the plate capacitance acts as a resonant circuit at 53 MHz. This increases the low intensity levels observed during slow spill. These signal levels are expected to be between -110 dBm to -80 dBm [2], with peak levels reaching higher due to the nature of the spill.

Transition Board

The transition board electronics were designed with a large dynamic range in mind, with three 23 dB gain low noise amplifiers (LNAs) and a programmable attenuator with up to 31.5 dB of attenuation (in 0.5 dB steps) for an effective gain of 37.5-69 dB. This is shown in Figure 1. In addition the signal passes through a bandpass filter (BW of 5 MHz, centered at 53.10348 MHz) in order to increase the signal to noise ratio. This analog path also taps the signal after the first LNA to be read through a logarithmic amplifier, allowing the implementation of a control loop

to determine the appropriate attenuation level for a given incoming RF power level. This is important so that the analog signal falls within the dynamic range of the Digitizer's ADC.

The digital portion of the transition board is controlled via a microcontroller. This is used to read in the incoming power level from the log amp, set the digital attenuator value, and communicate with the VME processor card through CAN bus protocol.

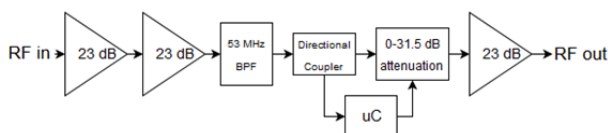


Figure 1: Block diagram of transition board.

Digitizer and DSP Chain

The analog signal is read into an 8 channel digitizer with a sampling rate of 122.163 MHz. This was chosen to be above the Nyquist rate for the RF of interest (2.3 times the machine RF), and this clock signal is supplied via a PLL that is locked to the SY RF. The BPM pickup signal is digitally processed in an FPGA, with the DSP chain being detailed in Figure 2.

The ADC signal is down-converted from 53.10348 MHz to near base-band via mixing with an NCO produced signal, which produces an I&Q pair. This is done in order to get the signal close to DC, and still preserve phase data for magnitude calculation. When the NCO frequency was too close to the machine frequency of 53.10348 MHz, the down-converted frequency could be seen modulating the position readout. This was determined to be caused by truncation errors in the data chain, and was mitigated by choosing the down-converted frequency such that it could be easily notched out by the moving average filter.

Since the Switchyard slow spill lasts for approximately 4 seconds, the number of total samples for the spill needed to be reduced in order to effectively read out the data. The bulk of the sampling rate reduction was done by using a decimating CIC filter, with a decimation rate of 2048. The CIC filter has the benefit of decimation while also averaging the data. This is beneficial since the spill is not uniform, and the averaging assures that all power is accounted for in the accumulated intensity readout.

The following two FIR filters also have a decimation rate of 2, for a total decimation value of 8192 and final sampling frequency of 14.9 kHz. This is the rate at which the magnitude data (as seen in Figure 2) is reported. The intensity is calculated as the square root of the sum of squares of the two magnitudes. This value is reported separately from the individual magnitude data, which is further processed once it is passed to ACNET, Fermilab's Accelerator

* Work supported by the Fermi National Accelerator Laboratory, operated by Fermi Research Alliance LLC, under contract No. DE-AC02-07CH11359 with the US Department of Energy

[†] tpeterse@fnal.gov

FERMILAB CRYOMODULE TEST STAND RF INTERLOCK SYSTEM*

T. Petersen[†], J. S. Diamond, D. McDowell, D. Nicklaus, P. S. Prieto, A. Semenov,
Fermi National Accelerator Laboratory, Batavia, IL 60510, USA

Abstract

An interlock system has been designed for the Fermilab Cryo-module Test Stand (CMTS), a test bed for the cryo-modules to be used in the upcoming Linac Coherent Light Source 2 (LCLS-II) project at SLAC. The interlock system features 8 independent subsystems, one per superconducting RF cavity and solid state amplifier (SSA) pair. Each system monitors several devices to detect fault conditions such as arcing in the waveguides or quenching of the SRF system. Additionally each system can detect fault conditions by monitoring the RF power seen at the cavity coupler through a directional coupler. In the event of a fault condition, each system is capable of removing RF signal to the amplifier (via a fast RF switch) as well as turning off the SSA. Additionally, each input signal is available for remote viewing and recording via a Fermilab designed digitizer board and MVME 5500 processor.

INTRODUCTION

Fermilab has been designated as one of the laboratories to test a number of cryo-modules for SLAC's upcoming Linac Coherent Light Source 2 [1]. In order to provide facilities for this test, an RF interlocks system has been designed (using previous interlock systems as a template). The interlocks are designed to remove the low level RF (LLRF) within 120 nsec from detection of an RF fault. This is done by monitoring a number of signal sources when an abnormal state is detected, a fast GaAs switch interrupts the LLRF delivered to the SSA. All analog signals are digitized at up to 80 MHz with a 16 channel Fermilab-designed board. The RF interlocks will operate in pulse mode first, then move to continuous wave (CW) mode.

SYSTEM DESCRIPTION

The full RF interlock system consists of 8 SSA-Coupler pairs controlled by dedicated RF interlocks. Each RF interlock system consists of 5 VME 64X boards which contain analog circuits to process the analog signals and an FPGA to communicate via the VME bus with the crate controller. The interlock boards are organized by function as a System Control board, an 8-channel FWR/REFL PWR board, a 6-channel Field Emission Probe board, a 6-channel Photo-multiplier board, and a Digitizer board. These boards can be seen (in the order listed above) in Figure 1. In addition to these boards there is a Relay-Latch board that is used to fan out some auxiliary input signals to the 8 subsystems such as vacuum and temperature trips. A PLC also processes IR and RTD sensors from the couplers and provides an input to the System Control board.

* Work supported by the Fermi National Accelerator laboratory, operated by Fermi Research Alliance LLC, under contract No. DE-AC02-07CH11359 with the US Department of Energy

[†] tpeterse@fnal.gov

The block diagram given below in Figure 2 illustrates a full system of interlock permits each System Controller monitors. Communication between the RF Interlocks and the Accelerator Controls is done through an MVME 5500 processor, which monitors each board for trips and displays these trips through an EPICS GUI. The controller is also used to remotely sets trip limits (each board has a hard, potentiometer set trip limit as well as a software set, DAC trip limit), and transfer digitizer data.

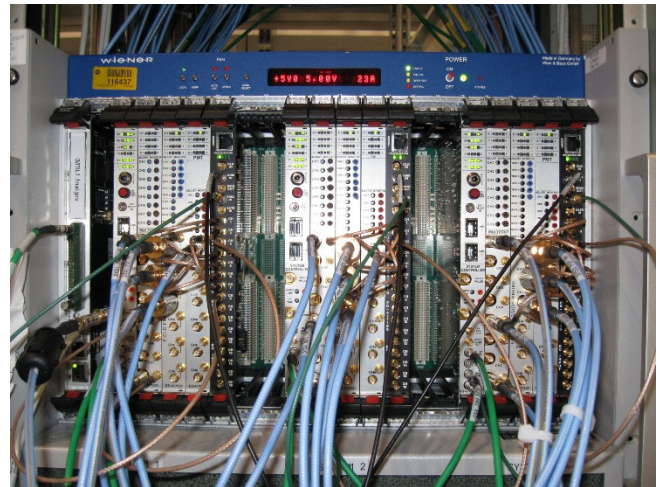


Figure 1: Three full systems in a VME crate with processor and digitizers.

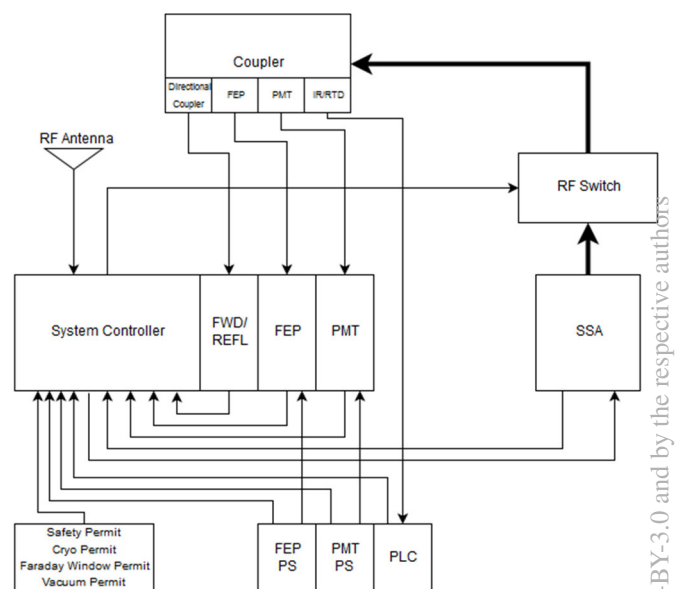


Figure 2: This block diagram details the various signals, permits, and components in each system. Digitizer and MVME 5500 excluded.

COMPUTED TOMOGRAPHY OF TRANSVERSE PHASE SPACE*

A. Watts[†], C. Johnstone[‡], J. Johnstone[§]
Fermilab, Batavia, IL, USA

Abstract

Two computed tomography techniques are explored to reconstruct beam transverse phase space using both simulated beam and multi-wire profile data in the Fermilab Muon Test Area ("MTA") beamline. Both Filtered Back-Projection ("FBP") and Simultaneous Algebraic Reconstruction Technique ("SART") algorithms [1] are considered and compared. Errors and artifacts are compared as a function of each algorithm's free parameters, and it is shown through simulation and MTA beamline profiles that SART is advantageous for reconstructions with limited profile data.

BEAM PROJECTION

Computed tomography reconstructs an N-dimensional object out of many (N-1)-dimensional projections, examples of which are pictured in Fig. 1. Similarly, a transverse beam profile is a one-dimensional projection of the two-dimensional phase space. Computed tomography is thus the reverse of the projection process, i.e. integrating many (N-1)-dimensional projections into a reconstructed N-dimensional image. For a full reconstruction, profile data must exist through a viewing angle range of π radians [1]. However, to use any computed

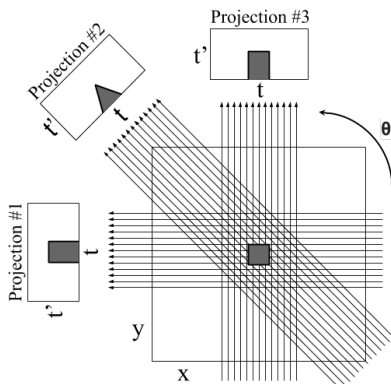


Figure 1: 1-D projection of a 2-D object. Traditional tomography is the reverse of the projection process.

tomography algorithm, an analogy must be made between such projections of a physical object and beam profiles [2]. For the projection in Fig. 1, the coordinate systems of the image and a projection are related by:

$$\begin{pmatrix} t \\ t' \end{pmatrix} = \begin{pmatrix} \cos\theta & \sin\theta \\ -\sin\theta & \cos\theta \end{pmatrix} \begin{pmatrix} x \\ x' \end{pmatrix} \quad (1)$$

So the projection onto the t axis of a ray passing through pixel (x, x') of the original image at angle θ is:

$$t = x\cos\theta + x'\sin\theta \quad (2)$$

Thus Equation 3 describes the general projection $P(t, \theta)$ onto axis t at viewing angle θ of two-dimensional object $f(x, y)$.

$$P(t, \theta) = \iint dx dy f(x, y) \delta(x\cos\theta + y\sin\theta - t) \quad (3)$$

Similarly, neglecting dispersion, the phase space coordinates for a particle at two locations in a beamline with only linear forces are related by:

$$\begin{pmatrix} x_2 \\ x'_2 \end{pmatrix} = \begin{pmatrix} R_{11} & R_{12} \\ R_{21} & R_{22} \end{pmatrix} \begin{pmatrix} x \\ x' \end{pmatrix} \quad (4)$$

By defining the phase orientation angle $\theta = \tan^{-1}(\frac{R_{12}}{R_{11}})$ and scaling factor $s = \sqrt{R_{11}^2 + R_{12}^2}$, such that $R_{11} = s\cos\theta$ and $R_{12} = s\sin\theta$ the beam projection can be rewritten as:

$$P(x_2, \theta) = \iint dx dx' f(x, x') \delta(s[x\cos\theta + x'\sin\theta - \frac{x_2}{s}]) \quad (5)$$

For beam, each projection $P(x_2, \theta)$ is a profile measured with instrumentation like a multi-wire detector. Thus computed tomography algorithms may be used to reconstruct beam transverse phase space if each profile is scaled horizontally by $\frac{1}{s}$ and vertically by s , and if the appropriate scaling factor and phase orientation angle for each profile are known. Whereas traditional tomography involves rotating a camera around a fixed object, beam tomography rotates the phase space distribution while taking projections (i.e. beam profiles) at the same location in the beamline.

BEAM SIMULATION

To test the efficacy of the computed tomography algorithms, a simple linear particle tracking Python code was used to build profile data while varying the phase orientation angle of a simple FODO channel beamline. A deliberately non-elliptical and asymmetric beam distribution was generated particle-by-particle, each of which being passed through the beamline using the thick-lens linear transfer matrix.

A multiwire profile monitor was simulated by taking a histogram of all particle 'x' values with 48 bins spaced 1 mm apart; this is typical for the number of wires and spacing for Fermilab SEM multiwires. For every quadrupole value in the scan of phase rotation angle ranging π radians, a histogram profile is taken at the end of the beamline. The initial beam distribution is pictured in Fig. 2 in two-dimensional histogram form. Reconstruction of this simulated data at the beginning of the beamline was carried out using the "scikit-image" Python library [3].

* Work supported by Fermi Reserach Alliance, LLC under Contract no. DE-AC02-07CH11359 with the United States Department of Energy.

[†] awatts@fnal.gov

[‡] cjj@fnal.gov

[§] jjohnstone@fnal.gov

REAL-TIME MAGNETIC ELECTRON ENERGY SPECTROMETER FOR USE WITH MEDICAL LINEAR ACCELERATORS

P. E. Maggi[†], K. R. Hogstrom, K. L. Matthews II,
Louisiana State University, Baton Rouge, LA 70803, USA
R. L. Carver, Mary Bird Perkins Cancer Center, Baton Rouge, LA 70809, USA

Abstract

Accelerator characterization and quality assurance is an integral part of electron linear accelerator (linac) use in a medical setting. The current clinical method for radiation metrology of electron beams (dose on central axis versus depth in water) only provides a surrogate for the underlying performance of the accelerator and does not provide direct information about the electron energy spectrum. We have developed an easy to use real-time magnetic electron energy spectrometer for characterizing the electron beams of medical linacs. Our spectrometer uses a 0.57 T permanent magnet block as the dispersive element and scintillating fibers coupled to a CCD camera as the position sensitive detector. The goal is to have a device capable of 0.12 MeV energy resolution (which corresponds to a range shift of 0.5 mm) with a minimum readout rate of 1 Hz, over an energy range of 5 to 25 MeV. This work describes the real-time spectrometer system, the detector response model, and the spectrum unfolding method. Measured energy spectra from multiple electron beams from an Elekta Infinity Linac are presented.

INTRODUCTION

Many cancer centers have multiple medical linear accelerators (linacs) used for treating patients. The linacs produce beams of photons or electrons; typical electron energies range from 4 MeV to 25 MeV. If all of the linacs at a cancer center have matched beams, which include matched dose vs depth curves, patients can be treated with any machine at the facility without the need to recalculate machine specific treatment plans. This is especially beneficial if a treatment machine is out of operation, as the patient can easily and immediately be treated on another machine.

The depth-dose curve of a therapeutic electron beam strongly depends on the energy distribution of the incident beam, primarily the mean energy and most probable energy [1]. Depth-dose curves are typically measured using a large water tank with a small diode or ion chamber that is positioned at different depths in the tank. The depth-dose curve reflects only specific features of an energy spectrum, such as peak mean energy (E_p), average energy, and FWHM, but not the spectrum as a whole. Efforts have been made to analytically back calculate the energy spectra from this data [2] or via matching of depth-dose curves with iterative Monte Carlo simulations [3]. These predicted spectra are generated assuming only a Gaussian spectrum that is not excessively broad (e.g. less than 15% FWHM). However it is widely understood

that there is a low-energy tail present in the spectrum [1] as a result of beam conditioning for therapeutic use. Additionally, measurements by Kok et al [4] have shown that spectra for certain traveling-wave linacs (Elekta, Phillips) can have further spectral deviations violating the Gaussian assumption; this is due to accelerator tuning parameters (e.g. High Powered Phase Shifter) relating to the RF recycling system. A magnetic spectrometer has the potential to simplify beam measurements, reduce the time needed for beam matching, and provides more information about the electron beam.

SPECTROMETER HARDWARE

We have developed an easy to use real-time magnetic electron energy spectrometer for characterizing the electron beams of medical linacs. Our spectrometer system is constructed around a 0.57 T (effective field strength) dipole magnet block as the dispersive element; this magnet block was used by McLaughlin et al [5] as part of a passive spectrometer system. The magnet poles measure 15.23 cm x 46.99 cm x 2.63 cm, with a 2.54 cm separation (Fig. 1), and are held apart by steel and aluminium plates. The electron beam enters the magnet block via a 6.35 mm diameter aperture in the steel mounting face. The electrons exit the magnet block at the detector plane, which is the face parallel to both the central axis of the incident electron beam and the direction of the magnetic field.

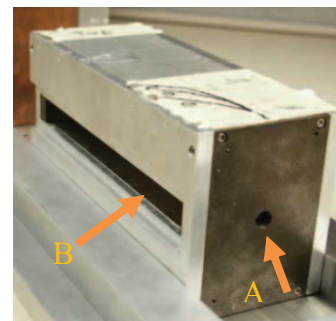


Figure 1: Photograph of magnet block showing the entrance aperture (A) and exit window (B).

The detector system uses a row of 60 1 mm x 1 mm square BCF-20 green scintillating fibers (Saint-Gobain, Malvern, PA) oriented vertically; this provides a one-dimensional position sensitive detector. The fiber ribbon is rearranged to a square bundle to be imaged by a Pixlink PL-8955 monochromatic CCD camera (Fig 2). This design was initially proposed by Gahn et al. [6] for use in high intensity laser plasma studies.

[†] pmaggi1@lsu.edu

LOW NOISE DIGITIZER DESIGN FOR LCLS-II LLRF*

G. Huang^{1†}, L. R. Doolittle¹, J. Yang^{2,1}, Y. Xu^{2,1}

¹LBNL, Berkeley, CA 94720, USA

²Tsinghua University, Beijing, China

ABSTRACT

Modern accelerators use a digital low level RF controller to stabilize the fields in accelerator cavities. The noise in the receiver chain and analog to digital conversion (ADC) for the cavity probe signal is critically important. Within the closed-loop bandwidth, it will eventually become part of the field noise seen by the beam in the accelerator. Above the open-loop cavity bandwidth, feedback processes transfer that noise to the high power drive amplifiers. The LCLS-II project is expected to use an undulator to provide soft X-rays based on a stable electron beam accelerated by a superconducting linac. Project success depends on a low noise, low crosstalk analog to digital conversion. We developed a digitizer board with 8 ADC channels and 2 DAC channels. The broadband phase noise of this board is measured at <-151 dBc/Hz, and the adjacent channel crosstalk is measured at <-80 dB. In this paper we describe the digitizer board design, performance test procedures, and bench-test results.

INTRODUCTION

In the LCLS-II low level RF system design, every half cryomodule (four cavities) use one Precision Receiver Chassis (PRC) and two RF station (RFS) for the field control loop. [1–4] The PRC is the receiver side of the loop and the RFS implement the control algorithm and generate the drive signal. The error signal is transferred from the PRC to the RFS over fiber link in digital domain. In the PRC, we convert four cavity pickup signals and two phase reference line signals. In each RFS, we convert forward, reflected and cavity drive loop back signal from the RF system of two cavities. Including the cavity drive requirements of the RFS, this leads to a requirement for a module with at least six inputs and two outputs.

The digitizer board is carefully tuned to meet specific needs of the LCLS-II LLRF system: the input IF is 20 MHz with an ADC sample rate of 94.3 MS/s, and the output IF is 145 MHz with a DAC sample rate of 188.6 MS/s. All input and output frequencies are coherent. With possible small changes to passive components, the hardware could be used with other frequencies.

We take advantage of the FMC standard for the high speed interface to the digital pins from FPGA. We chose the LPC (low pin count) FMC connector to avoid excessive layer count on the circuit board.

* Work supported by the LCLS-II Project and the U.S. Department of Energy, Contract DE-AC02-76SF00515

† ghuang@lbl.gov

Besides the core ADC and DAC functions, many small features have been added to the digitizer board to support the specific needs of the LCLS-II LLRF system.

- Synchronous clock to all the ADC and DAC channels, derived from the LO
- Provide an LO/8 signal for up converter
- Electrically compatible with FMC FPGA boards
- SMA connector for analog input and output
- Some GPIO out from FMCs
- Monitor board voltage, current, temperature
- Provide additional slow ADCs and DACs
- Synchronizable switch regulators

DIGITIZER DESIGN

Board Design

The block diagram of the digitizer board is shown in Figure 1, and a picture of the board is shown in Figure 2.

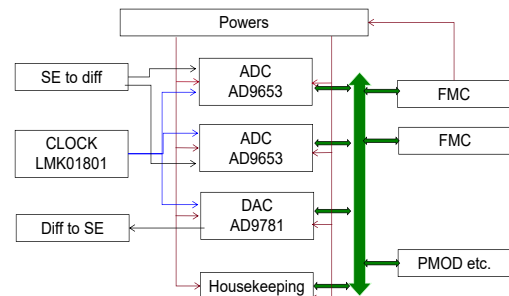


Figure 1: digitizer board hardware modules.

An LMK01801 dual clock divider chip takes the system's LO and divides down to generate the ADC clock, DAC clock, and an offset LO used in the upconversion chain. Bank A is assigned to the ADC/DAC clocks, and Bank B is used for other outputs.

We selected from three modern ADC chips, LTC2174, AD9653 and AD9268, starting by building test boards. [5] During this board development, we evaluated different low-noise regulator configurations for ADC power supplies and reference voltage. We also developed layout sub-pcbs for the modules, and the basic FPGA firmware module for the high speed LVDS serdes.

The AD9563 uses high-speed LVDS lanes like the LTC2174, but has lower noise. Its noise is similar to the AD9268, but its interface uses fewer FMC/FPGA pins.

Both the test boards and the final board are powered by the FPGA carrier board through the FMC connector. The

FPGA CONTROL OF COHERENT PULSE STACKING*

Y. Xu[†], R. Wilcox, J. Byrd, L. Doolittle, Q. Du, G. Huang, W. Leemans, Y. Yang,
Lawrence Berkeley National Laboratory, Berkeley, CA 94720, USA

A. Galvanauskas, J. Ruppe, University of Michigan, Ann Arbor, MI 48109, USA

J. Dawson, Lawrence Livermore National Laboratory, Livermore, CA 94550, USA

[†]also at Department of Engineering Physics, Tsinghua University, Beijing 100084, China

Abstract

Coherent pulse stacking (CPS) is a new time-domain coherent addition technique that stacks several optical pulses into a single output pulse, enabling high pulse energy from fiber lasers. Due to advantages of precise timing and fast processing, we use an FPGA to process digital signals and do feedback control so as to realize stacking-cavity stabilization. We develop a hardware and firmware design platform to support the coherent pulse stacking application. A firmware bias control module stabilizes the amplitude modulator at the minimum of its transfer function. A cavity control module ensures that each optical cavity is kept at a certain individually-prescribed and stable round-trip phase with 2.5 deg rms phase error.

INTRODUCTION

Investing in advanced kW-class ultrafast lasers will have a very significant impact on particle accelerator systems [1]. However, high pulse energy is achieved at low repetition rate currently [2]. Coherent stacking of several short pulses into a single output pulse in the fiber amplifier system is a promising technique combining high average power and high repetition rate. This Joule-kHz coherent pulse stacking system will revolutionize accelerator applications like LPAs and FELs.

In our experimental coherent pulse stacking system, the oscillator generates a 1064nm optical beam at 400MHz repetition rate with 10 ps pulse width, which is subsequently coupled into a polarization-maintaining single-mode fiber. An amplitude modulator then generates a pulse burst, followed by a phase modulator imprinting the required phase. The first pulses of the tailored optical pulse burst enter the reflecting resonant cavity and interfere destructively at the cavity output port, thus storing optical energy inside the resonant cavity. Later, the final pulse in the burst produces a constructive interference with the previous intra-cavity pulses at the output port, so that all stored energy is extracted from the resonant cavity into a single output pulse [3]. Properly configured sequences of multiple optical cavities will achieve a higher peak-power enhancement factor.

Timing and synchronization are essential for ultrafast pulse addition, and scalable controls are needed for a complex optical system. Here we develop a hardware and

firmware design platform to support the coherent pulse stacking application. The ML605 FPGA board processes digital signals captured by high-speed ADC and then sends feedback signals to the modulator and the cavity actuator. A bias control module stabilizes the bias operating point of the modulator while a cavity control module locks the optical cavity phase for pulse stacking. The FPGA outputs the feedback control signal to optical cavities at kHz frequency, to support kHz repetition rates.

HARDWARE INFRASTRUCTURE

The ML605 is an FPGA based digital signal processing board which enables us to create designs targeting the Virtex-6 FPGA. The ML605 addresses the FPGA to commodity-CPU boundary through Gigabit Ethernet and supports GMII (Gigabit Media Independent Interface) from the FPGA to the PHY (physical layer). The FMC110 and the XM105 are added to ML605 through FMC HPC connector and FMC LPC connector respectively.

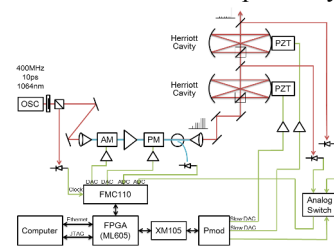


Figure 1: Hardware infrastructure of coherent pulse stacking system.

Figure 1 shows the hardware infrastructure of coherent pulse stacking. The FMC110 is a dual-channel 12-bit A/D (ADS5400) and dual-channel 16-bit D/A (DAC5681Z) FMC daughter card. The sampling clock, which is the master clock signal, is supplied externally by the laser oscillator so as to enable simultaneous sampling at a rate of 400 Msp/s. A trigger signal at kHz repetition rate, which is derived from the master clock, determines the feedback control frequency (that is the repetition rate described above) and system bandwidth. The XM105 Debug Card is designed to provide a number of multi-position headers and connectors which output FPGA interface signals to slow DACs (which drive the cavity PZTs or modulator bias) and analog switch (which selects signals from multiple photodiodes to one single ADC).

FIRMWARE INFRASTRUCTURE

The FPGA firmware can be divided into three layers: the bottom layer is hardware-dependent drivers, the inter-

* Work supported by the Director, Office of Science, Office of High Energy Physics, of the U.S. Department of Energy under Contract No. DE-AC02-05CH11231.

[†] yilunxu@lbl.gov

MULTICAVIDY COHERENT PULSE STACKING USING HERRIOTT CELLS*

Y. Yang[†], R. Willcox, J. Byrd, L. Doolittle, Q. Du, G. Huang, Y. Xu
Lawrence Berkeley National Laboratory, Berkeley, CA 94720, USA

Abstract

Coherent Pulse Stacking provides a promising way to generate a single high-intensity laser pulse by stacking a sequence of phase and amplitude modulated laser pulses using multiple optical cavities. Optical misalignment and phase stability are two critical issues that need to be addressed. Herriott cells are implemented for their relaxed alignment tolerance and a phase stabilization method based on cavity output pattern matching has been developed. A single pulse with intensity enhancement factor over 7.4 has been generated by stacking 13 modulated pulses through a four-cavity stacking system. This can be a possible path for generating TW KHz laser pulses for a future laser-driven plasma accelerator.

INTRODUCTION

Laser-driven wakefield acceleration has become an emerging concept for a future accelerator facility, which could offer a far-more compact and cost-efficient approach compared with conventional accelerators [1]. However, one of the issues for developing a laser-based accelerator that has practical application is that the driving laser requirement is beyond current technology capability, particularly in terms of repetition rate. The state-of-the-art Joule-level sub-ps or fs laser amplifier can only operate at several hertz. Generation of 1 J to over 10 J laser at a repetition rate of kHz to 10 kHz, can bring laser-based acceleration from a lab-based concept into a facility which can benefit users.

Fiber-based amplifiers have seen significant increase in both average power and efficiency in recent years. However, the peak intensity is limited by optical damage or nonlinear effects. To overcome these limits, spatial and temporal coherent combination offers a possible solution [2]. A research collaboration among University of Michigan, LBNL and LLNL has been formed to explore the possibility of generating both high average power and high peak intensity laser systems based on fiber.

This paper focuses on a recently-proposed temporal combination scheme, called Coherent Pulse Stacking (CPS), which makes use of passive optical cavities to coherently stack a sequence of amplitude and phase modulated pulses into one high-intensity laser pulse [3]. Misalignment tolerance and phase stability are two challenges for CPS. We consider using Herriott cells to relax misalignment tolerance and fast photodiodes to detect the cavity phases for active

feedback control. A four-cavity stacking system with FPGA-based control platform has been established [4]. An intensity enhancement factor of 7.4 has been achieved with a 13-pulse input. This could be a promising technique for generating high-intensity laser pulses based on fiber amplifiers.

MULTICAVIDY STACKING CONCEPT AND SETUP

The optical cavity used for Coherent Pulse Stacking is shown in Fig. 1. It is an interferometer with a low-reflectivity input/output mirror, and a cavity length equal to the pulse repetition period. The preceding pulses can interfere with following pulses at the low-reflectivity mirror. The phase delay in the optical resonator will determine whether the interference is constructive or destructive. Constructive interference will cause the input pulse to remain in the cavity, while destructive interference will make the stored pulse exit the cavity. As is also shown in Fig. 1, when a sequence of equal-amplitude pulses enters the cavity, the corresponding output pulse amplitude will be either enhanced or reduced due to interference. With the amplitudes and phases of input pulses appropriately modulated, one can find certain cavity phases at which all the input pulses before the last one will remain in the cavities, and the last pulse can extract all the stored energy out of the cavities, thus being amplified to a considerable extent. A detailed theoretical description can be found in Ref. [3]. The highest intensity enhancement through a single cavity is 2.6. A sequence of cavities can stack more input pulses and extract more energy. This paper focuses on the four-cavity case, where numerical calculation shows an intensity enhancement around 7.8 can be achieved with a input of 13 modulated pulses.

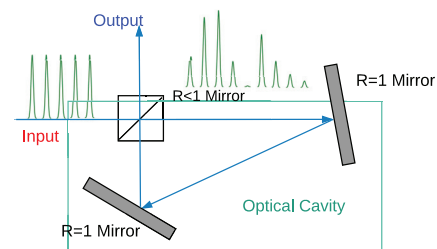


Figure 1: The optical cavity schematic used for Coherent Pulse Stacking.

The schematic of our four-cavity CPS experiment is shown in Fig. 2. A burst of 13 pulses are amplitude and phase modulated before entering the four-cavity stacking system. At certain phase delays of the four cavities ($\Phi_1, \Phi_2, \Phi_3, \Phi_4$),

* Work supported by Office of Science, Office of High Energy Physics, of the U.S. Department of Energy under Contract No. DE-AC02-05CH11231

[†] yaweyang@lbl.gov

FUTURE PROSPECTS OF RF HADRON BEAM PROFILE MONITORS FOR INTENSE NEUTRINO BEAM*

Q. Liu[†], Case Western Reserve University, Cleveland, OH 44106, USA

M. Backfish, A. Moretti, V. Papadimitriou, A. V. Tollestrup, K. Yonehara, R. M. Zwaska,
Fermilab, Batavia, IL, 60510, USA

M. A. Cummings, R. Johnson, G. Kazakevich, Muons, Inc., Batavia, IL 60510, USA
B. Freemire, Illinois Institute of Technology, Chicago, IL 60616, USA

Abstract

A novel beam monitor based on a gas-filled multi-RF-cavity is proposed to measure the precise profile of secondary particles for neutrino experiments. It promises to be radiation robust in extremely high-radiation environment. When a charged beam passes through a gas-filled microwave RF cavity, it produces electron-ion pairs in the cavity, which shifts the gas permittivity. The beam profile can thus be reconstructed from the signals from individual RF cavity built into the beam profile monitor. To help with the demonstration tests, the temperature dependence of the monitor and a new cavity geometry for the monitor are discussed.

INTRODUCTION

A novel beam monitor based on a gas-filled RF resonator is proposed to measure the precise profile of secondary particles downstream of a target in the LBNF beam line at high intensity. The RF monitor is designed to be radiation robust in extremely high-radiation environment. When a charged beam passes through a gas-filled microwave RF cavity, it produces electron-ion pairs in the cavity. The induced plasma changes the gas permittivity in proportion to the beam intensity. This permittivity shift can be measured by the modulated RF frequency and the quality factor. The beam profile can thus be reconstructed from the signals from individual RF cavity built into the beam profile monitor [1]. A demonstration test is underway, and the current results have shown technical feasibility. The next phase to validate the RF monitor concept consists of two steps: step (1) is to build and test a new multi-cell 2.45 GHz RF cavity that can be used for the NuMI beamline, and step (2) is to build and test a new multi-cell 9.3 GHz RF cavity that can be put in service in a future beamline at the LBNF for spatial resolution. Higher frequency makes smaller cavity and makes finer spatial resolution in the beam profile measurement, which is needed for LBNF. These two resonant frequencies are chosen since they are the standard frequencies for magnetron RF source.

One of the intrinsic issues on the RF monitor is the temperature increment due to the energy deposition of the incident beam. In order to promote increased accuracy in beam profile measurement, a new geometry of the cavity is considered, with simulation results supporting of its feasibility.

* Work supported by Fermilab Research Alliance, LLC under Contract No. DE-AC02-07CH11359 and DOE STTR Grant, No. DE-SC0013795.

[†] qx1104@case.edu

TEMPERATURE DEPENDENCE

As a particle beam is incident on and passes through the RF monitor wall, it deposits energy to the monitor. The mean stopping power can be obtained using the Bethe-Bloch formula. Assuming that all of the net energy deposition of the incident beam goes into Joule heating, this would create a temperature increment of the monitor. The rate of this energy deposition of the beam is defined as the beam power.

In order to see how this temperature increment would affect the monitor's performance, it is necessary to first find an analytic function that describes the behavior of the monitor's temperature. To simplify the problem, following assumptions are made:

- The main source of power input into the monitor is the beam power while the deposited power is removed by the natural convection of the room air.
- The beam profile is in the form of a delta function. That is to say that the beam distribution and particle interaction are not considered.
- The room of beam enclosure is treated as a heat reservoir, with constant temperature 300 K. This is critical for setting up the boundary condition later in the problem.
- The material properties of the cavity wall, such as the thermal and electrical conductivity, are independent of the temperature.

According to the assumption that the net energy deposition would all go into Joule heating, the following energy balance equation can be written:

$$P - hA[T(t) - 300] = cM \frac{dT(t)}{dt} \quad (1)$$

where P is the power deposition by the incident beam, h is the heat transfer coefficient, A is the surface area of the monitor, c is the specific heat of the monitor wall, M is the total mass of the monitor, and $T(t)$ is the temperature of the monitor as a function of time, t .

The size of rectangular RF gas monitor is $20 \times 210 \times 10$ mm³. It is made of aluminum, since it is a lightweight yet durable metal. Table 1 shows the parameters to evaluate Eq. (1) for each building material of the RF gas monitor. The major particle to deposit the energy is high energy protons. The average momentum of protons is 120 GeV/c in this calculation.

The first order linear differential equation produces asymptotic solutions, which will reach an equilibrium as time goes

DEVELOPMENT OF A PYTHON-BASED EMITTANCE CALCULATOR AT FERMILAB SCIENCE & TECHNOLOGY (FAST) FACILITY

^{1,2}A.T. Green #, ^{1,2}Y.M. Shin

¹Department of Physics, Northern Illinois University, DeKalb, IL 60115, USA

²Fermi National Accelerator Laboratory (FNAL), Batavia, IL 60510, USA

Abstract

Beam emittance is an important characteristic describing charged particle beams. In linear accelerators (linac), it is critical to characterize the beam phase space parameters and, in particular, to precisely measure transverse beam emittance. The quadrupole scan (quad-scan) is a well-established technique used to characterize transverse beam parameters in four-dimensional phase space, including beam emittance. A computational algorithm with Python scripts has been developed to estimate beam parameters, in particular beam emittance, from experimental results using the quad-scan technique in the photoinjector-based electron linac at the Fermilab Accelerator Science and Technology (FAST) facility. This script has been benchmarked against ELEGANT simulation and implemented in conjunction with an automated quad-scan tool (also written in Python) and has decreased the time it takes to perform a single quad-scan from an hour to a few minutes. From the experimental data, the emittance calculator quickly delivers several results including, but not limited to, geometrical and normalized transverse emittance, Courant-Snyder parameters, and plots of the beam size versus quadrupole field strength.

INTRODUCTION

Emittance is an intrinsic quality of charged particle beams in particle accelerators and needs to be fully characterized in order to assure that the beamline is operational. This beam parameter quantifies the volume of six-dimensional phase space (x, p_x) occupied by the dynamically moving particles in the beam. Beam emittance is also related to the smallest achievable spot size and divergence:

$$\sigma = \sqrt{\beta \epsilon_g} \propto \sqrt{\epsilon_g} \quad (1)$$

$$\sigma \sigma' = \epsilon \rightarrow \frac{\epsilon}{\sqrt{\beta \epsilon_g}} \propto \sqrt{\epsilon_g}, \quad (2)$$

where σ is the beam size, σ' is the divergence, β is a Courant-Snyder parameter, and ϵ_g is the geometrical emittance [1].

A common way of measuring the beam emittance is via the quad-scan technique. By this method, an experimenter scans the quadrupole field strength k over a desired range and records the beam size at some location downstream.

The quadrupole magnet fields strength and beam size measurements, along with the precise knowledge of the accelerator configuration, are all that are needed to calculate the beam emittance. Under conservative forces, beam emittance is a conserved quantity and as such, calculating the emittance at one location along the beamline will describe the emittance anywhere along the accelerator.

FERMILAB SCIENCE AND TECHNOLOGY (FAST)

It is at the FAST facility at Fermilab where this emittance calculator has been employed. FAST is an advanced superconducting (SRF) accelerator laboratory currently under construction at Fermilab. The goal of this facility is to provide cutting edge R&D and infrastructure critical to the research and development of both current and future accelerators. A schematic of the main components of the FAST beamline are depicted in Fig. 1 (from left-to-right):

- Low-energy beamline (red) – RF gun, bucking solenoid, main solenoid, and two superconducting booster cavities (CC-1 and CC-2) capable of accelerating electrons up to 50 MeV.
- CM2 (light blue) – Cryomodule 2, an ILC-type cryomodule, for accelerating electrons up to 300 MeV.
- RFQ (dark blue) – Radio frequency quad capable of accelerating protons up to 2.7 MeV.
- IOTA (blue ring) – Integrable Optics Test Accelerator electron/proton storage ring for 150 MeV electron-based experiments and 2.5 MeV proton-based experiments.

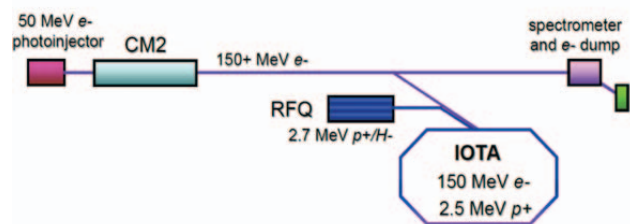


Figure 1: Sketch showing the main components of the FAST beamline [2].

Table 1 gives a brief view of the achieved beam parameters during the 50 MeV commissioning phase. It should be noted that the beam parameters marked with an asterisk were verified prior to the 50 MeV run.

This work was supported by the DOE contract No. DEAC02-07CH11359 to the Fermi Research Alliance LLC.
#cravatta83@gmail.com

DEVELOPMENT OF SHORT UNDULATORS FOR ELECTRON-BEAM-RADIATION INTERACTION STUDIES*

P. Piot^{1,2}, M. B. Andorf¹, G. Fagerberg³, M. Figora⁴, A. Sturtz⁴

¹ Department of Physics and Northern Illinois Center for Accelerator & Detector Development, Northern Illinois University DeKalb, IL 60115, USA

² Fermi National Accelerator Laboratory, Batavia IL 60510, USA

³ Department of Physics, Northern Illinois University DeKalb, IL 60115, USA

⁴ College of Liberal Art & Science, Northern Illinois University DeKalb, IL 60115, USA

Abstract

Interaction of an electron beam with external field or its own radiation has widespread applications ranging from coherent-radiation generation, phase space cooling or formation of temporally-structured beams. An efficient coupling mechanism between an electron beam and radiation field relies on the use of a magnetic undulator. In this contribution we detail our plans to build short (11-period) undulators with ~ 7 -cm period refurbishing parts of the ALADDIN U₃ undulator [1]. Possible use of these undulators at available test facilities to support experiments relevant to cooling techniques and radiation sources are outlined.

INTRODUCTION

Over the recent years there have been a wide interest in laser-photon interaction. The motivations for such explorations include the manipulation of electron bunches [2], the generation of coherent radiation [3] along with the possible phase-space cooling based on optical-stochastic cooling [4, 5] (OSC) or on chromatic coupling [6]. Additionally, undulator radiation enables the indirect measurement of the electron-beam parameter [7].

Motivated by such opportunities along with developing an experimental program centered on the optical control and phase-space cooling of electron beams, we recently acquired an undulator magnet which is being reconfigured as three short undulator magnets (henceforth dubbed as “micro-undulators”). One of the magnets is foreseen to be installed at the Fermilab Accelerator Science & Technology (FAST) facility to initiate tests of subsystem relevant to a planned proof-of-principle experiment at the Integrable-Optics Test Accelerator (IOTA) ring [8].

UNDULATOR DESIGN & STATUS

Our group has recently acquired an undulator available as surplus from the decommissioned ALADDIN storage ring at University of Wisconsin, Madison. This magnet dubbed as undulator U₃ is a current-sheet-equivalent-material (CSEM) undulator composed of Nd-B-Fe permanent magnets [1].

The U₃ undulator was nominally configured as a variable-gap undulator and the peak magnetic field is parametrized as a function of the gap g with the formula $B(g) = B_0 \exp\left[-g\left(\frac{\pi}{\lambda_u} + \frac{1}{d}\right)\right]$ where the coefficients $B_0 = 2.2692298$ T and $d = 2453.705 \times 10^{-3}$ m were obtained from a fit to the measurements carried by the ALADDIN team [9]. The latter parameterization is valid for gap $g \in [10, 150]$ mm corresponding to undulator parameters $K \equiv \frac{eB\lambda_u}{2\pi mc}$ field in the range $K \in [0.02, 9.60]$ (here e and m are the electronic charge and mass and c the velocity of light).

The expected radiation-wavelength range for energy available at several Midwestern accelerator facilities is shown in Fig. 1. The wavelength spans the near infrared to ultraviolet wavelengths. For reference Fig. 1 also displays the wavelengths associated to several laser media available at some of the considered accelerator facilities.

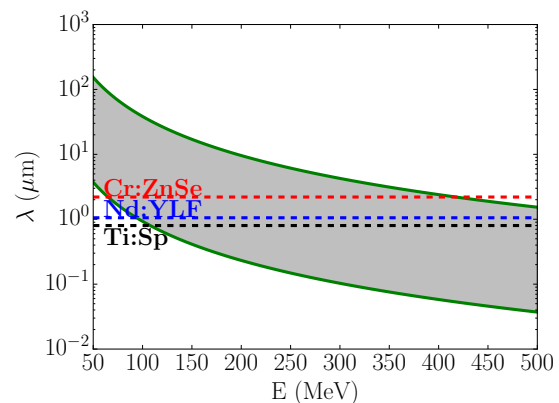


Figure 1: Range of wavelengths (shaded area) attainable with various electron-beam energies available at Midwestern accelerator facilities using the U₃ undulator. The horizontal dashed lines with associated labels represents the wavelength of lasers available at FAST and illustrate that optical pulses formed by these laser media could be coupled to the electron beam in the U₃ undulator.

The U₃ undulator was delivered to NIU in May 2016 and disassembled during the Summer. A new frame is currently being designed and we expect the first micro-undulator to be undergoing magnetic measurement before the end of 2016. We eventually will build three micro-undulators from U₃

* Work supported by the by the US Department of Energy (DOE) contract DE-SC0013761 to Northern Illinois University. Fermilab is operated by the Fermi research alliance LLC under US DOE contract DE-AC02-07CH11359.

A HIGH-LEVEL PYTHON INTERFACE TO THE FERMILAB ACNET CONTROL SYSTEM*

P. Piot^{1,2} and A. Halavanau^{1,2}

¹ Department of Physics and Northern Illinois Center for Accelerator & Detector Development, Northern Illinois University, DeKalb, IL 60115, USA

² Fermi National Accelerator Laboratory, Batavia, IL 60510, USA

Abstract

This paper discusses the implementation of a PYTHON-based high-level interface to the Fermilab ACNET control system. The interface has been successfully employed during the commissioning of the Fermilab Accelerator Science & Technology (FAST) facility. Specifically, we present examples of applications at FAST which include the interfacing of the ELEGANT program to assist lattice matching, an automated emittance measurement via the quadrupole-scan method and transverse transport matrix measurement of a superconducting RF cavity.

INTRODUCTION

The ACNET accelerator-control system was originally developed for the start of TEVATRON operations in 1983 [1]. It was eventually extended into a comprehensive unified control system for the accelerators in operation at Fermilab. Over the years ACNET has undergone substantial improvement [2]. Additionally, ACNET is complemented with the Accelerator Command Language (ACL), a scripting environment developed as a versatile scripting tool for developing high-level application involving ACNET devices [3].

The ACL environment is extensively used at the Fermilab Accelerator Science and Technology (FAST) facility and while it provides excellent capabilities in accelerator control, it may be challenging for non experts to learn. Additionally, ACL does not enjoy the simplicity, large user base, and extensive open-source packages available from high-level scripting languages such as PYTHON. Based on these observations we have developed a PYTHON interface to ACL. The interface – dubbed PYACL – enables control of accelerator devices within the PYTHON framework (as a script or an IPYTHON notebook). Such a development enables the rapid scripting of high-level applications by non-ACL experts while interfacing the accelerator control and data analysis with the extensive set of available PYTHON packages.

IMPLEMENTATION

Our current implementation of PYACL consists of a PYTHON-based interface providing a set of elementary functions to directly execute ACL commands via operating-system calls; see overview in Fig. 1. Our current tests were per-

formed under the linux operating system but PYACL is platform independent. The PYACL package currently consists of a `acnet.py` toolbox which provides a set of elementary functions to read and write into ACNET devices (either to single devices or a list of devices). Another functionality of `acnet.py` is to handle image acquisition (from a frame grabber) and storage of corresponding arrays as python NUMPY arrays.

In the context of the FAST facility, an additional toolbox (`fast.py`) was developed to include functions specific to the FAST accelerator. These especially include magnet-specific current-to-strength conversion (e.g. I to k_1 for quadrupole) and other functions relevant to beam-dynamics calculations or often use during operation (e.g. automated single-magnet degaussing procedure). Likewise, the script can also write input files for the ELEGANT program [4] thereby providing on-line beam-dynamics modeling of the FAST beamline. In the following sections we present examples of successful application of the PYACL toolbox.

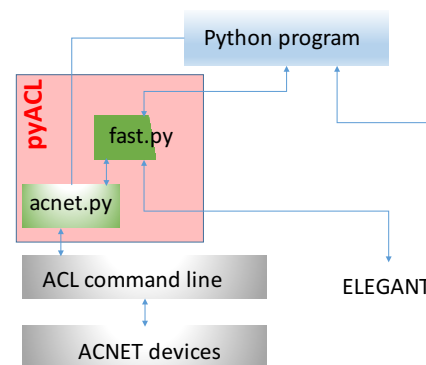


Figure 1: Overview of the interfacing of PYTHON scripts with the Fermilab's ACNET control system.

AUTOMATED SCANS

A simple example of the application of PYACL involves scanning routine commonly used in accelerators. For instance, consider a simple example of hysteresis removal for a dipole or quadrupole magnet. In low-energy accelerators such a hysteresis removal (or “degaussing”) is accomplished with an oscillating exponential decaying current excitation. The current is varied in time as $I_k = I_0 \exp(-k/\tau) \cos[(-)^k \pi]$, where $k \in N$ is the step

* Work supported by the by the US Department of Energy (DOE) contract DE-SC0011831 to Northern Illinois University. Fermilab is operated by the Fermi research alliance LLC under US DOE contract DE-AC02-07CH11359.

A GENERAL MODEL OF VACUUM ARCS IN LINACS

Jim Norem[#], Nano Synergy Inc., Downers Grove IL 60516, USA
Zeke Insepov, Purdue University, West Lafayette IN 47907, USA

Abstract

We are developing a general model of breakdown and gradient limits that applies to accelerators, along with other high field applications such as power grids and laser ablation. We have considered connections with failure modes of integrated circuits, sheath properties of dense, non-Debye plasmas and applications of capillary wave theory to rf breakdown in linacs. In contrast to much of the rf breakdown effort that considers one physical mechanism or one experimental geometry, we find an enormous volume of relevant material in the literature that helps to constrain our model and suggest experimental tests.

INTRODUCTION

Although 115 years have elapsed, and high electric fields in the presence of metals have been under continuous study, there seems to be no agreement about the mechanisms and parameters involved in vacuum arcs. This is particularly strange since arcing and associated processes are important factors in accelerator R&D goals, failure modes in high-density integrated circuits, fusion power systems, micrometeorite impacts and high energy density systems such as laser ablation, all of which are well-supported research interests.

Our effort, which started from a study of x rays from rf systems and has evolved into modeling arcs, models mechanisms involved in various stages of arc evolution using numerical methods. We believe that our model is simpler and more generally applicable than other explanations and in this paper we describe increasingly precise calculations, other possible uses and applications of the model and also comment on some other models [1-3].

OUR MODEL

Extensive measurements of x-rays and surface damage from rf systems convinced us that local fields were enhanced by surface asperities, and the fields could be measured using the parameters from Fowler Nordheim field emission. We found the magnitude of these enhanced fields was sufficient to produce Coulomb explosions and initiate breakdown. Our model, supported by a number of numerical calculations, is outlined in Fig. 1. The model describes the arcing process in four stages: 1) Coulomb explosions, aggravated in part by electromigration, produce neutral gas near the surface. We have modeled the Coulomb explosion, both for smooth surfaces and for cubes with sharp corners, using MD. 2) The neutral gas ‘fragments’ are ionized by field emission of electrons, enhanced by plasma ions near the surface

that increase both the surface field and field emission. PIC codes were used to show how field emission currents combined with local neutral atoms would produce an ion cloud, while increasing the local fields driving the field emission. 3) Evolution of the plasma whose density increases due to self-sputtering, is modeled. MD was used to model the detailed properties of the sheath as the density was increased above the nonlinear plasma limit, while separate MD calculations have shown how self-sputtering would produce a secondary yield above 10 for dense plasmas above molten metal surfaces insuring a rapid density increase. 4) The effects on the turbulent surface due to plasma pressure and surface field have also been modeled. After the plasma is gone, surface damage is produced during cooling and smoothing due to damped capillary waves and cracking of the thermally contracting surface. We have also shown how high field enhancements can be produced on an otherwise smooth surface by a combination of damped capillary waves and cracking [1,2].

We have found that two phenomena seem to dominate the physics of arcs: unipolar arcs, and surface cracking, and the study of these arcs seems to focus in these issues.

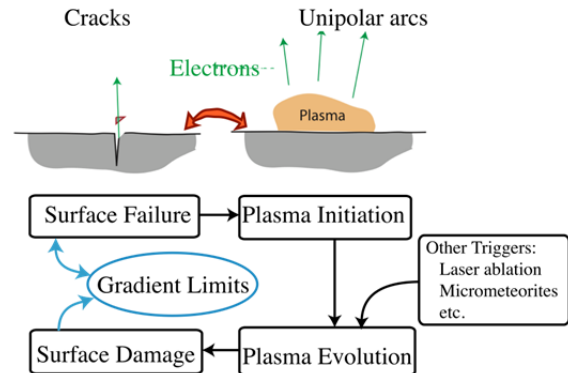


Figure 1: The four stages of a discharge describe evolution of cracks and unipolar arcs [1].

MODELING ELECTROMIGRATION

We have recently looked in more detail at electromigration as a factor in the initial surface failure. Electromigration is one of the primary causes of mass transport induced failure in electronic materials, and the effect is proportional to the local current density, j , where experimental data shows the dependence is $j^{1.6}$ [4]. We have found that current densities, both in field emission and in arcs, can be in the range of $>10^{11}$ A/m², and this current density is also associated with bulk transport of metal atoms in electronic systems [1,2,3,4]. We assume field emission and breakdown occurs at the corners of crack junctions and that electromigration would transport

[#]norem.jim@gmail.com

FIRST STEPS TOWARD INCORPORATING IMAGE BASED DIAGNOSTICS INTO PARTICLE ACCELERATOR CONTROL SYSTEMS USING CONVOLUTIONAL NEURAL NETWORKS

A.L. Edelen[†], S.G. Biedron^{1,2}, S.V. Milton², Colorado State University, Fort Collins, CO
J.P. Edelen, Fermilab^{*}, Batavia, IL

¹also at University of Ljubljana, Ljubljana, Slovenia ²also at ElementAero, Chicago, IL

Abstract

At present, a variety of image-based diagnostics are used in particle accelerator systems. Often times, these are viewed by a human operator who then makes appropriate adjustments to the machine. Given recent advances in using convolutional neural networks (CNNs) for image processing, it should be possible to use image diagnostics directly in control routines (NN-based or otherwise). This is especially appealing for non-intercepting diagnostics that could run continuously during beam operation. Here, we show results of a first step toward implementing such a controller: our trained CNN can predict multiple simulated downstream beam parameters at the Fermilab Accelerator Science and Technology (FAST) facility's low energy beamline using simulated virtual cathode laser images, gun phases, and solenoid strengths.

INTRODUCTION

Recently, convolutional NNs (CNNs) have yielded impressive results in the area of computer vision, especially for image recognition tasks [1]. They are also starting to be used in physics-related applications, such as automatic classification of galaxies [2] and neutrino events [3]. Given the present success of CNNs, it may now be possible to use them as a means of incorporating image diagnostics directly into particle accelerator control systems. While this could be done in a variety of ways (e.g. even just using traditional control methods with extracted image information), the avenue we have chosen to pursue is to create a NN controller that directly processes image data using some initial convolutional layers.

In support of this, we are investigating automated control over the photocathode electron gun at the Fermilab Accelerator Science and Technology (FAST) facility [4,5], specifically focused on automated beam alignment and tuning of the solenoid strength and gun phase. For a given laser system it is not always easy to produce a top-hat transverse laser profile, and any asymmetries in the initial laser distribution can impact the electron beam parameters. As such, it could be useful to train a controller to take a measured laser distribution image (here, the virtual cathode image) and yield optimal gun phase and solenoid strength settings (as determined by downstream beam parameters). In principle, if one had fine control over the transverse laser distribution itself, one could also include it as a controllable parameter.

To develop this type of controller, the first step is ensuring that a NN can adequately predict the beam parameters from various input distribution images, the gun phase settings, and the solenoid strengths. This process model can then be used to help train a NN controller. To this end, we have created a NN model that uses physics-based simulations of FAST as training data. It is also worth noting that by using simulation data to train the NN, we've created a fast-executing representation of the dynamics that could also be used in model predictive control, offline optimization studies, or quick tests in the control room without perturbing the machine. In this paper, we discuss our simulation studies, provide an overview of the NN architecture, and show the NN's performance in predicting beam parameters at the exit of the gun and the second capture cavity.

PARMELA SIMULATIONS

Simulations of the first 8 meters of the FAST low energy beamline were conducted using PARMELA [6]. Included in the simulations are the electron gun, both superconducting capture cavities, and the intermediate beam-line elements. The locations of the cavities and beam-line elements were taken from a Fall 2015 mechanical survey. Two sets of simulation scans were conducted: one set of fine scans to predict beam parameters after the gun, and one set of coarse scans to predict beam parameters after the second capture cavity (CC2). The gun phase was scanned from -180° to 180° in 10° and 5° steps, and the solenoid strength was scanned from 0.5 to 1.5 in 10% and 5% steps, where 1.0 represents the nominal setting that produces the peak axial field of 1.8 kGauss. Prior to scaling of the field maps, the bucking coil was tuned to produce zero magnetic field on the cathode. The field maps of the solenoid assembly, gun, and capture cavities used for the PARMELA simulations were generated using Poisson Superfish [7].

For the gun studies, we used three initial top-hat beam distributions with different radii. For the simulations up through CC2, we used nine different beam distributions. Three of these were the same top-hat distributions used for the gun simulations, and the other six were Gaussian transverse distributions with different RMS widths in x and y . These distributions were also converted into the simulated virtual cathode images (e.g. Figure 1) that were later used in training the NN. Prior simulation results using initial beam distributions derived from measured virtual cathode images suggest this is a sound approach.

* Fermilab is operated by Fermi Research Alliance, LLC under Contract No. De-AC02-07CH11359 with the United States Department of Energy.

[†] auralee.morin@colostate.edu

UPDATES TO THE LOW-LEVEL RF ARCHITECTURE FOR FERMILAB *

J. A. Einstein-Curtis[†], B. E. Chase, E. Cullerton, P. Varghese, Fermilab, Batavia, IL, USA
 S. Biedron¹, S. Milton, Colorado State University, Fort Collins, CO, USA
 D. Sharma², RRCAT, India

¹also at Faculty of Electrical Engineering, University, Ljubljana, Slovenia

²also at Fermilab, Batavia, IL, USA

Abstract

Fermilab has teamed with Colorado State University on several projects in LLRF controls and architecture. These projects include new LLRF hardware, updated controls techniques, and new system architectures. Here we present a summary of our work to date.

BACKGROUND

The Fermilab multi-cavity field controller (MFC) is a VXI-based LLRF controller designed for precision vector control of accelerating cavities [1]. The design has been used on several test stands at Fermilab, as well as in several parts of the main accelerator network. The design and its variants consist of a digital signal processor (DSP) for handling scaling values sent to a control system, a complex programmable logic device (cPLD) to handle the bus communications and board management, and a field programmable gate array (FPGA) to handle signal processing.

A newer design was proposed to replace the MFC as several components were being obsoleted and better performing components became available. One of the major updates was switching to a system-on-chip (SoC) module, where the control system front-end software can be run on the same chip as the signal processing logic. This leads to significant possible savings in interconnect, power, and board space usage, but also leads to other design challenges.

This new design requires a multi-disciplinary development effort, as we are developing for systems at every level of the systems design process, from firmware simulation and development up through new techniques for data transfer to the Fermilab control system. The control system is based on older technologies, so interfacing with newer developments in controls and data transfer requires a careful balance between the capabilities of the control system and the requirements of the project.

While moving away from a crate architecture provides for more flexibility and opportunities in high-performance design, it also requires more design effort up front to create a standardized system that can easily be iterated and debugged. Creating the interfaces between each internal subsystem is the greatest challenge, as they all need to be tested and verified along with their required dependencies.

* Operated by Fermi Research Alliance, LLC under Contract No. De-AC02-07CH11359 with the United States Department of Energy.

[†] jeinstei@fnal.gov, also at Colorado State University, Fort Collins, CO, USA



Figure 1: An example of a SoC MFC Board.

HARDWARE DESIGN

The SoC-based MFC design, as shown in Fig. 1, introduces several levels of complexity to an already complex system. When developing a system with discrete components, work is easily parsed out to individual developers. The SoC complicates such design flows as every function resides on the same chip. The traditional FPGA development flow relies on having well-defined boundaries and interfaces between different levels, such that each level builds on the previous.

For the Fermilab SoC design, the design builds on existing experience, but still needed to be integrated in to a new control architecture as a network-attached device (NAD) instead of a card in a crate.

Additional thought went in to using a system-on-module (SoM) for the FPGA and embedded processor component to allow for future upgrades using a standardized platform. Several companies now make SoMs that incorporate an SoC, including Critialink and Novtech. A Novtech SoM design is shown in Fig. 2.

The SoC design provides a Linux-based development framework for controls system interfacing and low-level systems debugging, which is much more flexible than a traditional crate-based architecture. In addition to the high-level protocols, the SoC architecture allows for standard interconnect technologies to be used inside the chip for data transfer, such as AXI and Altera's Qsys interconnect.

PIP-II LLRF SYSTEM DESIGN

The Proton Improvement Plan-II (PIP-II) is Fermilab's plan for improving beam intensity, generate more neutrinos, and upgrade the Fermilab accelerator complex. At the heart of this plan is a new superconducting linear accelerator. The Fermilab LLRF group has been working on new

EXAMINATION OF OUT-OF-FIELD DOSE AND PENUMBRAL WIDTH OF FLATTENING FILTER FREE BEAMS IN MEDICAL LINEAR ACCELERATORS

L.C. Bennett, O.N. Vassiliev, University of Texas MD Anderson Cancer Center, Houston, Texas, U.S.A.

Abstract

Until recently, medical linear accelerators (LINACS) have been equipped with a flattening filter in the beam line in order to make the intensity of the photon beam uniform at a specified depth. This makes calculation of patient dose simpler, but has the drawback of introducing additional scatter in peripheral regions of the photon field, leading to increased dose in regions outside the primary target and enhanced risk of developing secondary malignancies and other complications. All leading manufacturers of linacs have introduced a Flattening Filter Free (FFF) mode in their most recent linacs, with the flattening filter completely removed from the beam-line. We show that the FFF modes on a TrueBeam™ linac (Varian Medical Systems, Palo Alto, CA) exhibit a clinically relevant reduction in peripheral and out-of-field dose when compared to flattened beams with similar depth-dose distributions.

INTRODUCTION

Flattening Filter Free beams are a relatively new modality in radiation oncology, with Varian Medical systems releasing the TrueBeam™ medical linear accelerator with FFF options in 2010 and Elekta (Stockholm, Sweden) following with the Versa HD in 2013. The use of flattening filters was traditionally favoured due to the uniformity of the intensity of the photon beam they produce, resulting in “flat” dose profiles; the introduction of intensity-modulated radiotherapy (IMRT) and multi-leaf collimation (MLC), however, have allowed physicians to generate unique fields that modulate photon fluence to achieve optimal dose distributions without using a flattening filter.

Removal of the flattening filter generates beams that are characterized by a “peaked” profile, with a higher photon intensity towards the center of the beam and a lower intensity towards the periphery. Because the beam is unflattened, the average energy of the photon spectra is lower; for this reason, an FFF beam with nominal energy of 10 MV will have a similar depth-dose distribution to a flattened (FF) beam with nominal energy 6 MV. FFF beams are capable of delivering a higher dose rate by upwards of a factor of 2.3 for 6 MV beams and 5.5 for 18 MV beams, allowing treatment times to be reduced and thus reducing the opportunity for intrafractional variation due to patient movement; additionally, the removal of a

flattening filter greatly reduces the amount of scattered and leakage radiation generated during treatment [1].

Previous studies have demonstrated through the use of Monte Carlo models and measurements that FFF beams have the potential to reduce dose in peripheral regions of the photon field [2][3]. It is believed that this effect could be a result of the reduction in scatter caused by elimination of the flattening filter. We investigated various profile measurements from the Varian Representative Data set, examining penumbral width (distance between 80% and 20% central axis dose) and relative dose at various distances from the field edge (defined as 50% central axis dose) in this study.

For this investigation, we compared beam profiles for the energy pairing of 10 MV FFF and 6 MV FF. This beam energy pairing was chosen in order to compare the standard of care (6 MV FF) to a beam of similar depth dose distribution. Profiles were compared for field sizes of 3x3 cm², 4x4 cm², 6x6 cm², 8x8 cm², and 10x10 cm². Each field size was also examined at depths in water of 5 cm, 10 cm, 20 cm, and 30 cm. Relative dose was examined at distances of 2 mm, 5 mm, 10 mm, 30 mm, and 50 mm from the field edge.

NORMALIZATION OF PROFILES

Because of the different shapes of the FF and FFF profiles, normalization of FFF beams had to be done in such a way that the penumbral regions of the FF and FFF beams could be more fairly compared. Methods for normalizing FFF beams have been developed using both the inflection point of the FFF profile as well as the spatial differences between the doses at 80% and 20% of the normalized central axis FF dose; however, these methods either fail to achieve optimal coverage of a target or result in excessive dose along the central axis of the FFF beam [4], [5]. For this reason, we normalized the FF profiles such that central axis dose was 110%; the dose of the FFF beam at the location of 100% FF dose was then used to normalize the FFF beam. This allowed us to examine the profiles and penumbra under clinically relevant conditions, as the hypothetical target volume would be neither underdosed nor overdosed using this method.

USING HIGH PRECISION BEAM POSITION MONITORS AT THE CORNELL ELECTRON STORAGE RING (CESR) TO MEASURE THE ONE WAY SPEED OF LIGHT ANISOTROPY

W. F. Bergan*, M. J. Forster, N. Rider, D. L. Rubin, D. Sagan, Cornell University, Ithaca, NY, USA
 B. Wojtsekhowski, Carnegie Mellon University, Pittsburgh, PA, USA
 B. Schmookler, Massachusetts Institute of Technology, Cambridge, MA, USA

Abstract

The Cornell Electron Storage Ring (CESR) has been equipped with a number of high-precision beam position monitors which are capable of measuring the orbit of a circulating beam with a precision of a few microns. This technology will enable a precision measurement of deviations in the one-way speed of light. An anisotropic speed of light will alter the beam momentum as it travels around the ring, resulting in a change of orbit over the course of a sidereal day. Using counter-circulating electron and positron beams, we will be able to suppress many of the systematics such as those relating to variations in RF voltage or magnet strength. We show here initial feasibility studies to measure the stability of our beam position monitors and the various systematic effects which may hide our signal and discuss ways in which we can minimize their impact.

INTRODUCTION

The isotropy of the speed of light forms a cornerstone of modern physics. However, theories of quantum gravity suggest that this symmetry may not hold exactly, so it is possible that the speed of light may not be wholly isotropic. Although very good measurements have been done on the two-way speed of light, accurate measurements of the one-way speed are significantly more difficult. A recently proposed way to precisely test the isotropy of the one-way speed of light is to examine the behavior of counter-circulating electrons and positrons in the Cornell Electron Storage Ring (CESR) [1,2]. If the speed of light is anisotropic, the relationship between velocity and momentum will be direction-dependent. Particle momenta will vary around the storage ring, causing the orbits to vary over the course of a sidereal day. The fractional change in orbit is enhanced by a relativistic factor of γ^2 relative to the the fractional change in the speed of light. Since we are using 5.3 GeV beams, this means that we may obtain a limit of the speed of light anisotropy of one part in 10^{16} with an orbit measurement accurate to one part in 10^8 . To reduce systematics, we will look at the difference between the positron and electron orbits. Any change in the operating parameters of the accelerator will result in different orbit shifts for the two species only insofar as the electrons and positrons have different energies at different parts of the ring, and so will be greatly suppressed. Meanwhile, our signal will be enhanced because, if the energy of the electrons is increased in one part of the ring due to a speed of light

anisotropy, the positron energy will be reduced by the same amount since they are traveling in the opposite direction.

We present here a number of studies in simulation and actual experiment. We first use BMAD, an accelerator simulation program, to simulate a signal from the speed of light anisotropy as well as the effects of changes in dipole strength or RF voltage [3]. We next examine data taken at CESR where we put electron and positron beams in the ring and changed the RF voltage. Finally, we observe the stability of the beam position monitors (BPMs) and see that there is a current-dependent effect. Simulations show that this may be due to some current-dependent gains in the BPM buttons.

ACCELERATOR LATTICE

Single counterrotating bunches of electrons and positrons collide at diametrically opposed interaction points in the storage ring. A colliding beam lattice was designed to minimize the effect of the collisions on both closed orbit and lifetime. The strength of the beam-beam collision is characterized by the tune shift parameter $\xi = \frac{N}{2\pi\gamma} \frac{\beta_i}{\sigma_i(\sigma_x + \sigma_y)}$, where $i = x, y$ gives the horizontal and vertical tune shifts respectively. Since $\sigma_x \gg \sigma_y$, we minimize vertical tune shift by minimizing β_y . Horizontal beam size is given by $\sigma_x = \sqrt{\epsilon\beta_x + (\eta\delta)^2}$. To minimize horizontal tune shift, we minimize horizontal beta and maximize emittance and horizontal dispersion. The relevant lattice parameters at the two interaction points are given in Table 1. The beam energy is 5.3 GeV. The beam position monitors are most accurate in the current range of 0.5-1.0 mA/bunch. Beam beam parameters at the two interaction points (IP) in the table are computed for $N = 10^{10}$ particles per bunch (0.6 mA).

Table 1: Beam Parameters at Interaction Points

IP	β_x (m)	β_y (m)	η_x (m)	$\xi_x \times 10^{-3}$	$\xi_y \times 10^{-3}$
south	6.1	3.94	0.99	1.66	4.86
north	5.5	4.38	1.00	1.51	5.04

The beam-beam parameter is well below the limit measured at all electron-positron colliders. Because the electrons and positrons do not collide head-on as a result of the energy scallop, and perhaps other effects, there the beam-beam kick may introduce a current dependent distortion of the closed orbit. This effect is shown in simulation to cause orbit shifts at the micron level.

* wfb59@cornell.edu

MINIMIZATION OF EMITTANCE AT THE CORNELL ELECTRON STORAGE RING WITH SLOPPY MODELS

W. F. Bergan*, A. C. Bartnik, I. V. Bazarov, H. He, D. L. Rubin, J. P. Sethna
Cornell University, Ithaca NY, USA

Abstract

Our current method to minimize the vertical emittance of the beam at the Cornell Electron Storage Ring (CESR) involves measurement and correction of the dispersion, coupling, and orbit of the beam and lets us reach emittances of 10 pm, but is limited by finite dispersion measurement resolution. For further improvement in the vertical emittance, we propose using a method based on the theory of sloppy models. The storage ring lattice permits us to identify the dependence of the dispersion and emittance on our corrector magnets, and taking the singular value decomposition of the dispersion/corrector Jacobian gives us the combinations of these magnets which will be effective knobs for emittance tuning, ordered by singular value. These knobs will permit us to empirically tune the emittance based on direct measurements of the vertical beam size. Simulations show that when starting from a lattice with realistic alignment errors which has been corrected by our existing method to have an emittance of a few pm, this new method will enable us to reduce the emittance to nearly the quantum limit, assuming that vertical dispersion is the primary source of our residual emittance.

INTRODUCTION

The Cornell Electron Storage Ring (CESR) is a 768 m circumference storage ring at Cornell University using electron and positron beams of up to 5.6 GeV. Among other uses, it is a testbed for beam dynamics relevant to damping rings of future linear colliders, including low-emittance tuning. It is instrumented with roughly 100 Beam Position Monitors (BPMs) and a large number of independently-controllable corrector magnets, of which 85 (the vertical kickers and skew quadrupoles) are useful for reducing the vertical emittance. Currently, we minimize the vertical emittance at CESR by identifying and correcting the sources of emittance, such as dispersion and coupling, enabling us to obtain vertical emittances of order 10 pm. The effectiveness of this method is limited by finite dispersion resolution, forcing us to take a different approach in order to proceed further [1].

One method is to make use of sloppy models. These are models which nominally depend on a large number of parameters, but, if we transform to a basis of eigenparameters, the corresponding eigenvalues show an exponential falloff when written in decreasing order [2, 3]. Therefore, only a few of these eigenparameters will be sufficient to describe most of the behavior of the system. In our case, these sloppy eigenparameters will be various linear combinations of the corrector magnets which affect our vertical emittance. To obtain improved emittances, it would be useful to identify

which combinations of our corrector magnets have the largest impact on the emittance. We may then adjust those magnet combinations by hand and monitor the vertical emittance directly in order to bring further reductions in emittance. This is similar to the RCDS method successfully employed at SLAC by Huang *et al.* [4, 5].

The utility of the eigencombinations depends on our ability to monitor vertical emittance and closed orbit. CESR is equipped with an xray beam size monitor that provides real time measurement of the vertical beam size with resolution corresponding to emittance 0.5 pm-rad. A visible light interferometer measures horizontal beam size. The closed orbit is continuously monitored with the 100 distributed beam position monitors referred to above.

PROCEDURE

To first order, the vector of dispersions measured at each of our N BPMs, \vec{d} , will be equal to $J\vec{c}$, where \vec{c} is the vector of our M corrector magnets and J is the $N \times M$ dispersion/corrector Jacobian matrix. This may be found from simulations of the ideal CESR lattice using the BMAD accelerator-simulation program. [6] We may take its singular value decomposition (SVD) in order to identify its right singular vectors, \vec{v}_i , which correspond to different magnet combinations, and their associated singular values, which tell us their effectiveness at changing the dispersion. Since our vertical emittance is strongly dependent on the vertical dispersion, we expect that these magnet combinations should give us large emittance effects as well. We may check that this model shows sloppy behavior by examining the singular values of our dispersion/corrector Jacobian, which are plotted in Fig. 1. We immediately see that the singular values drop roughly exponentially, indicating that this model is sloppy.

To evaluate the effectiveness of these sloppy directions, we used BMAD simulations. We generated a lattice with random magnet alignment errors consistent with our measurement resolution in CESR. We then applied our standard emittance tuning procedure including measurement errors corresponding to our BPM resolution, obtaining a few pm emittance. [1] At this point, we applied our sloppy model algorithm by sequentially varying each of our magnet combinations found above in order of decreasing singular value to obtain a minimal emittance. We repeated this procedure for an ensemble of 83 misaligned lattices to obtain a sense of the utility of our method. We see in Fig. 2 the mean emittance across our ensemble of lattices after tuning different numbers of singular directions. Note that we are able to reduce the emittance by a factor of 3 with just 10 magnet combinations, and by more than a factor of 5 with 25 such

* wfb59@cornell.edu

SUCCESSFUL LABORATORY-INDUSTRIAL PARTNERSHIPS: THE CORNELL-FRIATEC SEGMENTED INSULATOR FOR HIGH VOLTAGE DC PHOTOCATHODE GUNS

K.W. Smolenski*, B. Dunham, CLASSE[†] Cornell University, Ithaca, NY, USA

D.L. Barth, M. Muehlbauer, S. Wacker, Friatec AG Division Frialit-Degussit, Mannheim, Germany

J.M. Maxson, University of California, Los Angeles (UCLA), CA, USA

Abstract

High voltage DC photocathode guns currently offer the most reliable path to electron beams with high current and brightness. The performance of a photocathode gun is directly dependent on its vacuum and high voltage capabilities, determined in large part by the ceramic insulators. The insulator must meet XHV standards, bear the load of pressurized SF₆ on its exterior, support the massive electrode structures as well as holding off DC voltages up to 750 kV. The Cornell-Friatec insulator was designed collaboratively between the industrial and laboratory teams and has now been produced in quantity for projects at Cornell University and elsewhere. Stray electron tracking has guided the design of internal collector rings to ameliorate punch-through failures that have plagued earlier guns.

INTRODUCTION

Many future linac and ERL based accelerator facilities require sources of high current and brightness electrons. Over the past 15 years the Cornell ERL injector project has led to advancements in the performance and reliability of DC gun technology enabling these new accelerators [1]. These guns have proven themselves by setting world records for high-average current from a high brightness photoinjector [2]. These guns are now being used as the electron source for two new projects: LReC, an electron cooler at RHIC [3], and for the Cornell-Brookhaven Electron-Recovery-Linac Test Accelerator (CBETA). Cornell and Brookhaven National Lab have begun collaboration on the design, construction and commissioning of a four-pass 150 MeV electron accelerator based on a superconducting, six-cavity linac with energy recovery, using 106 fixed-field alternating gradient (FFAG) cells as the return loop [4, 5]. This accelerator will be based on the existing Cornell ERL Injector with an upgraded DC gun as shown in Fig. 1.

DESIGN

DC guns suffer from the problem of controlling field emitted electrons from the high voltage surfaces. These electrons can land on the insulator, and if the charge builds up, punch-through can occur, causing a vacuum leak to the high pressure SF₆ space. In past guns we have used monolithic cylindrical insulators with an internal resistive coating to

* kws4@cornell.edu

[†] Supported by NSF award DMR-0807731, DOE grant DE-AC02-76SF00515, and New York State.

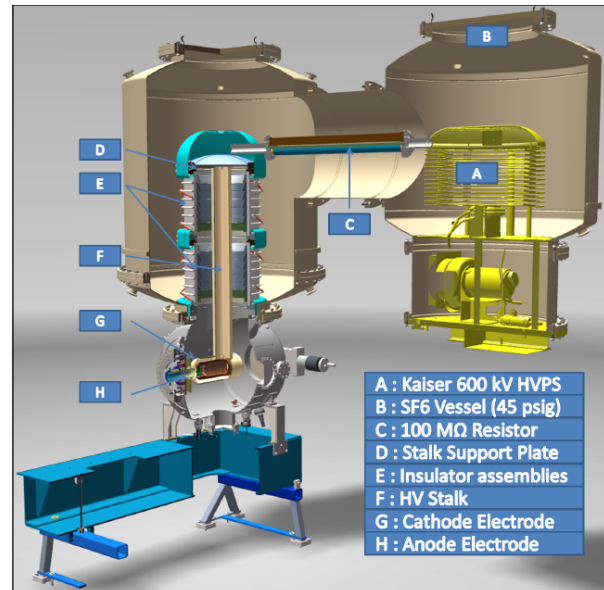


Figure 1: DC gun utilizing the Friatec segmented insulator (E) is shown on the left, inside an SF₆ pressure vessel. The HVPS (A) is on the right, inside a common SF₆ vessel.

bleed off these electrons, but it has only been successful up to 450 kV during processing, above which punch-through failure occurs. In addition, the coating has not adhered well, depositing a layer of particulate on the electrodes, certain demise for reaching higher voltages. Two such insulators were built and tested with similar damage occurring to both. A second batch of insulators were built with a doped alumina material with a known resistance, sufficient to drain electrons without drawing excessive current from the power supply, but unfortunately similar failures occurred.

These setbacks have led to the use of more complex segmented insulators with internal shields. These insulators were designed in a partnership between Cornell University and Friatec AG, with Cornell responsible for the high voltage design and Friatec responsible for the vacuum design and fabrication. The new insulator has internal guard rings to block any field emitted electrons ejected off the central support tube from reaching (and potentially damaging) the insulator. The diameter of the insulator is increased in order to reduce the maximum field on the central tube to 10 MV/m at 750 kV. At 500 kV, this will result in a reasonable field level of 6.7 MV/m.

INTEGRATED CONTROL SYSTEM FOR AN X-BAND-BASED LASER-COMPTON X-RAY SOURCE *

D. J. Gibson[†], R. A. Marsh, G. G. Anderson, C. P. J. Barty
Lawrence Livermore National Laboratory, Livermore, CA 94550, USA

Abstract

LLNL's compact, tunable, laser-Compton x-ray source has been built around an advanced X-band photogun and accelerator sections and two independent laser systems. In support of this source, the control system has developed into an integrated architecture that continues to grow to simplify operation of the system and to meet new needs of this research capability. In addition to a PLC-based machine protection component, a custom, LabView-based suite of control software monitors systems including low level and high power RF, vacuum, magnets, and beam imaging cameras. This system includes a comprehensive operator interface, automated arc detection and rf processing to optimize rf conditioning of the high-gradient structures, and automated quad-scan-based emittance measurements to explore the beam tuning parameter space. The latest upgrade to the system includes a switch from real-time OS to FPGA-based low-level RF generation and arc detection. This offloads processing effort from the main processor allowing for arbitrary expansion of the monitored points. It also allows the possibility of responding to arcs before the pulse is complete.

INTRODUCTION

A compact laser-Compton x-ray source based on x-band accelerator hardware has recently been commissioned at LLNL [1]. While the accelerator was being built and brought online, a remote control system was developed in parallel to run it, with features added on demand as the accelerator grew in complexity and as tasks amenable to automation became apparent. For this control system, National Instruments LabView was chosen as the basis for the bulk of the control system, with PLC logic supplementing it to provide basic IO and machine protection functionality. Other platforms, such as EPICS, were considered but not selected as they generally have a steeper entry curve getting the first devices online with no local experience. Using LabView, basic functionality was able to be provided rapidly. Also, given the relatively small scale of the system, the highly distributed nature of EPICS was unnecessary. Once the platform was chosen and the software grew in complexity, there has not been a need to reconsider that path.

In this paper, we present an overview of the key components of the control system: the RF control chassis, the machine protection system (specifically with regards to breakdown damage), and the auxiliary support system controls.

* This work was performed under the auspices of the U.S. Department of Energy by Lawrence Livermore National Laboratory under Contract DE-AC52-07NA27344.

[†] gibson23@llnl.gov

RF SOURCE

Low level RF control, and all RF monitoring, is performed using a National Instruments (NI) PXI system running the real-time version of LabView. User interface is provided by a comprehensive front panel that communicates with the real time controller through a mix of shared variables and network streams. Figure 1 gives the detailed clocking diagram driving the accelerator system. The master timing reference is an MXO-PLMX from Wenzel Associates, which relies on an 11.9 MHz reference oscillator coupled with a low noise frequency multiplier that provides a 2.586 GHz master clock. This 2.586 GHz signal is used by the MenloSystems electronics to phase-lock the 81.6 MHz oscillator to the RF clock and generate a synchronized 10 Hz trigger.

Low-level RF Pulse Generation

The master clock is multiplied by a factor of 4 to provide the 11.424 GHz X-band RF used in the accelerator. This RF signal is then modulated via an IQ mixer with greater than 100 MHz of bandwidth. The I & Q ports are driven by an Active Technologies AT-1212 2-channel, 14-bit arbitrary function generator (AFG) connected to an NI PXI-7954R Flex-RIO board. Performance of this system is detailed in Ref. [2]. Currently, a simple square pulse is generated, but once a planned RF pulse compressor is installed, more complicated shaping (such as a phase flip in the signal) will be easily implementable. This shaped pulse is supplied to the traveling wave tube and klystron for amplification to ~50 MW.

Modulator Control

The klystron is powered by a Scandinova K2-3X modulator, providing 420 kV, 330 A pulses. The modulator is equipped with its own manufacturer-supplied control hardware and software, which provides network-based access to all necessary controls and readbacks. This system also controls the klystron solenoid magnets and monitors water flow through the system. The relay-logic based facility personnel safety system ties directly into the modulator, preventing the high-voltage circuits from being energized without a permissive signal supplied by the facility.

A custom interface screen was created in LabView to simplify operator interaction with the modulator and avoid having to manually adjust operating parameters, such as the cathode filament current, each time the system was turned on and off. This also allows the built-in LabView datalogging capabilities to monitor the performance of the modulator and keep a log of beam operating time.

PRELIMINARY STUDY OF ADVANCED LLRF CONTROLS AT LANSCE FOR BEAM LOADING COMPENSATION IN THE MaRIE X-FEL *

A. Scheinker[†], M. Prokop, J. Bradley III, P. Torrez, L. Castellano, S. Kwon, D. Knapp, J. Lyles, S. Baily, J. Hill, D. Rees, Los Alamos National Laboratory, Los Alamos, USA

Abstract

The analog low level RF (LLRF) control system of the Los Alamos Neutron Science Center is being upgraded to a Field Programmable Gate Array (FPGA)-based digital system (DLLRF). In this paper we give an overview of the FPGA design and the overall DLLRF system. We also present preliminary performance measurements including results utilizing model-independent iterative feedforward for beam-loading transient minimization, which is being studied for utilization in the future MaRIE X-FEL [1], which will face difficult beam loading conditions.

INTRODUCTION

A digital low level RF (DLLRF) system upgrade has been in development at the Los Alamos Neutron Science Center (LANSCE) proton linear accelerator for many years [2], to replace the existing analog feedback control system. Although the simple analog system has performed reliably over the years, the move towards a digital control system was inspired by many factors including the possibilities of: remote control tuning via ethernet, the ability to quickly switch between controller setups for various beam types, and to implement iterative updates to controller outputs in-hardware to implement exotic adaptive control algorithms (during the ~ 8 milliseconds between RF pulses, as demonstrated in this work). This transition is made possible by the availability of affordable, fast (> 100 MS/s), high resolution (16 bit) analog to digital converters (ADC) and fast (~ 125 MHz) field programmable gate arrays (FPGA).

The ability to switch between multiple controllers between beam pulses is especially important for LANSCE where a large variety of beam types, each of which has its own influence on the RF cavity fields via various levels of beam loading. The LANSCE experimental facilities include: 1) The Lujan Center, which requires short high intensity proton bunches in order to create short bursts of moderated neutrons with energies in the meV to keV range. 2) The Proton Radiography (pRad) Facility, which provides movies of dynamic phenomena in bulk material (for example, shock wave propagation) via 50 ns proton bursts, repeated as frequently as 358 ns with programmable burst repetition intervals. 3) The Weapons Neutron Research (WNR) Facility, which provides unmoderated neutrons with energies in the keV to MeV range. 4) The Isotope Production Facility (IPF), which produces medical radioisotopes for US hospitals. 5). The Ultra Cold Neutrons (UCN) Facility, which creates neutrons with en-

ergies below μeV for basic physics research. The various beam flavors at LANSCE are summarized in Table 1.

Table 1: Parameters of LANSCE 625 μs Pulse Width Beams at 800 MeV, H^- , and 100 MeV, H^+ (IPF)

Beam	Ave Current [μA]	Rep Rate [Hz]	Ave Power [kW]
Lujan	100 – 125	20	80 – 100
pRad	< 21	~ 1	< 1
WNR	< 2	100	~ 3.2
UCN	< 5	20	< 4
IPF	460	100	46

The ability to handle various beam loading conditions, some of which are extreme, will also be crucial for the Matter-Radiation Interactions in Extremes (MaRIE) X-FEL linac currently being designed [1].

MaRIE X-FEL LLRF REQUIREMENTS

The MaRIE X-FEL linac will accelerate electrons up to 12 GeV via superconducting (SC) 1.3 GHz TESLA-type cavities, with the goal of producing 42 keV X-rays with electron bunches of 8 mA average current over macropulse lengths of 69 ns – 700 μs . The MaRIE linac will also produce short, intense pulses for electron radiography (eRad). The spacing of electron bunches will be customizable. Typical X-Ray FEL bunches will be 0.2 nC. The average current will be 8 mA over the entire macropulse, with drastically decreasing bunch spacing, down to 2.3 ns, for the final 230 ns of the pulse. The eRad experiments will require 2 nC micropulses which will be interleaved within the same macropulse as the X-ray FEL bunches, with a separation of 24 ns after individual eRad micropulses. The extreme beam loading caused by closely spaced high current bunches will require the use of much faster (lower Q) normal conducting cavities to make up for the energy droop introduced in the SC sections, whose extremely high Qs would require prohibitively large klystron power inputs for beam loading compensation [3, 4].

DIGITAL LLRF OVERVIEW

Signal Processing

The cavity and master oscillator (MO) RF signals, both at a frequency $f_{\text{RF}} = 201.25$ MHz, are sampled via standard IQ sampling. First the signals are down-converted to $f_{\text{IF}} = 25$ MHz by mixing with a local oscillator (LO) signal at

* Work supported by Los Alamos National Laboratory

[†] ascheink@lanl.gov

EFFECTS OF LOW FREQUENCY BUNCHER (LFB) FIELD VARIATION ON AN H⁻ BEAM PHASE-ENERGY*

Prabir K. Roy[†] and Yuri K. Batygin

Los Alamos National Laboratory, AOT-OPS, Mailstop: H812, Los Alamos, NM 87545, USA

Abstract

We examined the correlation between phase-space distribution of a 750 keV H⁻ beam and amplitude set-point of a low frequency (16.77 MHz) buncher (LFB) cavity. The beam current, x–y dimension, and Courant–Snyder twiss parameters are reported for variation of LFB amplitude set-point. Measured data indicated that a tuned peak voltage of LFB is essential to optimize the beam bunch and current.

INTRODUCTION

With RF linacs, phase-energy bunching of the beam is necessary to accumulate particles inside the separatrix [1]. This bunching is different than temporal compression [2] (used to obtain higher compression ratio). The phase-energy bunch must be optimum before injection into RF Drift Tube Linac (DTL) to ensure: (1) the beam capture rate, (2) reduced beam loss, (3) improved final beam quality, and (4) reduced radiation spill.

The Los Alamos Neutron Science Center (LANSCE) accelerator simultaneously utilizes H⁺ and H⁻ beams to support multiple user sites [3, 4], such as the isotope production (IPF), Weapon Neutron Research (WNR), and Proton radiation (PRad). Cockroft-Walton based injectors are used to accelerate H⁻ and H⁺ beams up to 750 keV. The long pulsed beams are then converted into bunches and passed onto the Drift Tube Linac (DTL) cavities. After traversing all four DTL tanks, the bunch energy is increased to 100 MeV. The H⁺ species are deflected into the IPF line, while the H⁻ continue on to the Couple Cavity Linac (CCL). The 44 modules of the CCL are used to increase beam energy to 800 MeV. The final beam is then delivered to Lujan, WNR and PRad facilities.

For the WNR facility, linac micropulses are initially formed in the low energy transport section. A part of this section is shown schematically in Fig. 1. The segment, consists of a signal pattern generator chopper (not shown); a 16.77 MHz Low Frequency Buncher (LFB) and the 201 MHz Main Buncher (MB). The chopper cuts the initial 625 μs beam into 347 mini pulses. Each of these chopped 20 nsec pulses are space by 1780 nsec. The beam energy is sinusoidally modulated by the buncher gap voltage. Once the beam crosses this bunching occurs at a distance as beam drifts downstream. The regular spacing between linac microbunches is 1.8 μs. Therefore, these micropulses predominantly depend upon the 16.77 MHz low frequency buncher field.

The drift distance at which a maximum bunch change is expected, changes, if the LFB RF voltage set-point is not optimized. Additional tuning is required to compensate for variations. The beam tuning is optimized, based on hardware and software utilization properly. The LANL developed TRACE model [5] was used to calculate the required strength of focusing magnets at the low energy (750 keV) transport to DTL sections. Experimental measurement of Twiss parameters α , beta (β); and emittance (ϵ) are utilized to run the code [5]. Therefore, it is of considerable interest to verify the Twiss parameters stability with minor or major change of LFB amplitude set-point.

In this proceeding, modulation of a cavity peak voltage, and change of drift length for a given peak voltage are addressed. The low frequency buncher instrument set-point calibration is presented. The beam emittance, current, and profile are reported. Finally, the beam phase-energy variation with variation of cavity peak voltage is analyzed using a computational code PARMILA [6].

MODULATION OF RF PEAK VOLTAGE AND BUNCH LENGTH

The phase-energy bunch is defined by the field of RF. The cavity field applies a kick to the energy of the pulse. As a result, the phase projection of the phase-energy coordinates is affected, and a narrower bunch is shaped at some drift distance; based on correlation of time and off-momentum particles coordinates [7]. A modulated voltage (V) of cavity is written as,

$$V = V_0 \sin(\omega t), \quad (1)$$

where, V_0 is the peak voltage; $\omega = 2\pi f$, is angular frequency of the cavity field for RF frequency (f); and t is the time. The RF phase (ϕ) is ignored in above equation as a net gain of energy not expected. Figure 2 shows modulated voltage ramps with time for variation of peak voltages. A phase-energy bunching distance, L , from a cavity, is written by [1],

$$L = \frac{\lambda}{2\pi} \frac{mc^2 \beta^3 \gamma^3}{qV_0}, \quad (2)$$

where, λ is the RF wave-length (a ratio of light velocity to RF frequency); m , c , q have its usual meaning of mass, velocity of light, and charge of a particle; γ is the Lorentz factor, and β is the relativistic velocity factor; V_0 is the peak voltage of cavity (a product of peak RF field (E) and length of cavity). Figure 3 shows phase-energy bunching distance vs peak voltage, calculated using the Equation (2). As seen in the graph, distance of a phase-energy bunching is perturbed once the cavity's field is altered. That means, a bunch can

* LA-UR-16-27610. This work supported by the United States Department of Energy under contract DE-AC52-06NA25396.

[†] pkroy@lanl.gov

HELIUM PRESSURE VESSEL JACKETING OF THE FERMILAB SSR1 SINGLE SPOKE SC CAVITIES

E.C. Bonnema, E.K. Cunningham, Meyer Tool & Mfg., Inc. Oak Lawn, IL, USA

Abstract

Meyer Tool recently completed the welding of the liquid helium pressure vessel jackets around ten (10) superconducting single spoke niobium cavities for Fermilab. The SSR1 cavities are intended for use in the PIP-II Injector Experiment Cryomodule. Meyer Tool's scope of supply included review of the Fermilab Pressure Rating Analysis Document, the development of fabrication details and a fabrication sequence, and the actual jacketing of the cavities. This paper will focus on the development of the sequence and how the sequence evolved over the course of welding of the ten (10) jackets. As the frequency of these cavities is critical, the fabrication sequence accommodated numerous in-process frequency checks, a frequency tuning step prior to the final weld, the use of thermal cameras to monitor weld heat input into the cavity, and post welding final machining of critical features. Lessons learned from this fabrication will be discussed.

PRESSURE RATING ANALYSIS

Fermilab provided Meyer Tool with a pressure rating analysis document which "is a partial report on the extensive campaign of calculations and finite element analysis performed with the intent of verifying compliance to the 2010 ASME Boiler and Pressure Vessel Code Section VIII for the dressed SSR1 resonator of 3rd generation (SSR1 G3)."[1] Prior to fabrication Meyer Tool reviewed this document for Code compliance and possible stamping.

The Fermilab report utilized a mix of requirements from Division 1 and 2 of the ASME BPV Code Section VIII in developing the analysis. Our opinion was that while the mix of Division 1 and 2 analysis and fabrication details did not compromise the pressure safety of the helium jacket, the design did not fully meet the requirements of either Division 1 or 2 of Section VIII. Without changes to weld design details and the addition of the NDE requirements that would have added significant cost and unnecessary fabrication risk, the helium jackets could not be stamped. Fermilab elected not to make these changes and the helium jackets were not Code stamped.

JACKET COMPONENTS

The helium jacket was constructed of eight main components. These main components were fit and welded together to form the pressure vessel that surrounds the SSR1 cavity. Figure 1 identifies these main components in the vessel assembly.

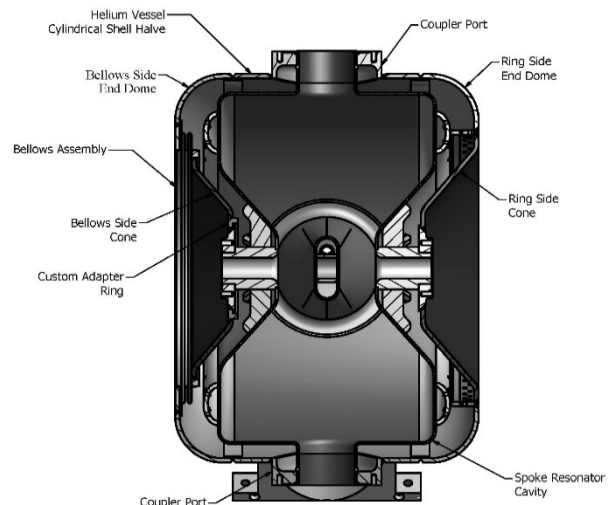


Figure 1: Helium jacket components.

These components consisted of: (1) A single rolled cylinder, made from 316LSS 0.25" plate and split into halves. (2) Two spun formed end domes, constructed of 316LSS 0.25" plate. These end domes were custom machined to fit each cavity and bellows. (3) Two spun formed conical heads, again constructed from 316LSS 0.25" plate. These conical heads also had to be custom machined to each cavity and bellows. (4) A single bellows assembly provided by Fermilab. (5) A 316LSS adapter ring. The adapter ring was added during fabrication of the first SSR1 cavity helium jacket to adjust for the variations in cavities and weld shrinkage and distortion. The bellows, bellows side cone, and custom adapter ring were welded as a subassembly prior to fit up to the cavity. The counterbore detail on the backside of the adapter ring, which interfaced with the beam tube flange on the cavity, was left unmachined until all other welding was complete. This allowed customization of adapter ring in final fit up to eliminate undue stress on either the cavity or the bellows.

INITIAL WELD DESIGN

Eleven welds were necessary to complete the helium jacket after fit up. They are identified in Figure 2. Backing strips, either integral to mating stainless steel components on the cavity or consisting of 316L sheet install behind weld seams, were used behind all the welds made on the helium jacket components assembled around the cavity.

DESIGN, SIMULATIONS AND EXPERIMENTAL DEMONSTRATION OF AN INTRA-PULSE RAMPED-ENERGY TRAVELLING WAVE LINAC FOR CARGO INSPECTION*

S.V. Kutsaev, R. Agustsson, A. Arodzero, R. Berry, S. Boucher, Y. Chen, J. Hartzell, B. Jacobson, A. Laurich, A. Murokh, E. Savin, A.Yu. Smirnov, A. Verma
 RadiaBeam Technologies, LLC, Santa Monica, CA, 90404, USA

Abstract

Novel radiographic imaging techniques [1] based on adaptive, intra-pulse ramped-energy short X-ray packets of pulses, a new type of fast X-ray detectors, and advanced image processing are currently some of the most promising methods for real-time cargo inspection systems. RadiaBeam Technologies is developing the high-speed Adaptive Railroad Cargo Inspection System (ARCIS), which will enable better than 5 mm line pair resolution, penetration greater than 450 mm of steel equivalent, material discrimination over the range of 6 mm to 250 mm, 100% image sampling rate at speed up to 45 km/h, and minimal average dose.

One of the core elements of ARCIS is a new S-band travelling wave linac with a broad range of energy control. The linac allows energy ramping from 2 to 9 MeV within a single 16 μ s RF pulse using the beam loading effect. RadiaBeam Technologies has designed, built and tested the ARCIS accelerator prototype. In this paper, we will discuss the linac design approach and its principal components. The results of the experimental demonstration of intra-pulse energy ramping will be presented. We will also provide a detailed comparison of beam dynamics simulations in Hellweg2D and CST Studio codes with experimental measurements, including transient beam loading effects.

INTRODUCTION

Adaptive Rail Cargo Inspection System (ARCIS) is an innovative X-ray cargo inspection technique being developed by RadiaBeam Technologies, LLC [1,2]. Conventional dual energy radiography systems cannot meet the requirements of the security market needs for high throughput rail cargo radiography inspection systems, which include:

- better than 5 mm line pair imaging resolution;
- penetration beyond 450 mm steel equivalent;
- maximum scanning speed with material discrimination (four levels of Z) 45 km/h;
- low dose and small radiation exclusion zone.

The ARCIS technical concept relies on linac-based, adaptive, ramped energy source of packets of short X-ray pulses sampled by a new type of fast X-ray detectors with rapid hardware processing for intelligent linac control, and advanced radiography image processing and material discrimination analysis.

*This work has been supported by the US Department of Homeland Security, Domestic Nuclear Detection Office, under competitively awarded contract HSHQDC-13-C-B0019. This support does not constitute an express or implied endorsement on the part of the Government.

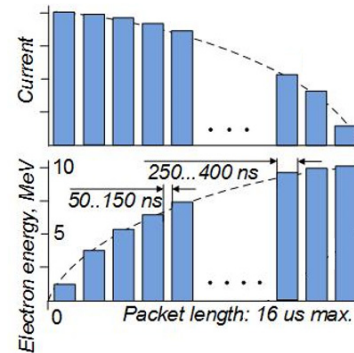


Figure 1: Energy and current temporal profiles of packet of short X-ray pulses.

To ensure ARCIS imaging performance a new S-band travelling wave linac with deep energy control has been designed. This linac will provide the packet of thirty-two 400 ns X-ray pulses separated by the 100 ns gap with pulse energy ramping within packet from 2 to 9 MeV and a total beam power of up to 2 MW (see Figure 1). The detailed description of the ARCIS system can be found in the paper [2].

LINAC DESIGN

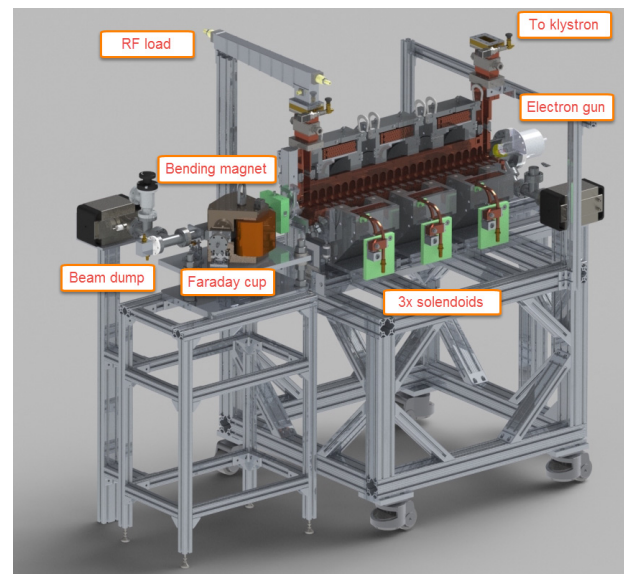


Figure 2: 3D design and physical layout of the ARCIS linac.

The discussion on linac parameters justification and detailed linac design can be found in the paper [3]. The design of the ARCIS linac consists of the following components (see Figure 2):

BEAM STABILITY DURING TOP OFF OPERATION AT NSLS-II STORAGE RING*

Weixing Cheng[#], Belkacem Bacha, Yongjun Li, Yuke Tian, Om Singh
NSLS-II, Brookhaven National Laboratory, Upton, NY 11973

Abstract

NSLS-II storage ring started top off operation since Oct 2015. User operation current has been gradually increased to 250mA. Observations of beam stabilities during top-off operations will be presented. Total beam current was typically maintained within +/-0.5% and bunch to bunch current variation was less than 20%. Injection transition during top-off was measured with bunch by bunch (BxB) digitizer, and BPM to analyze the orbit motion at various bandwidths (turn by turn, 10kHz and 10Hz rate). Coupled bunch unstable motions were monitored. As the vacuum pressure improves, fast-ion instability is not as severe compared to early stage of commissioning /operation, but still observed as the dominant instability. Resistive wall instability is noticed as more in-vacuum-undulator (IVU) gaps closed. xBPM measured photon stability and electron beam stability at top off injection have been evaluated. Short term and long term orbit stabilities will be reported.

TOP OFF OPERATION STATUS

NSLS2 is a newly constructed synchrotron light source with electron energy of 3GeV, emittance of 1nm.rad/8pmrad (H/V). The storage ring circumference is ~792m with 30 DBA cells. Three damping wigglers are available symmetrically to decrease the horizontal emittance below 1nm.rad. NSLS-II storage ring has been commissioned in 2014 and start user operation in 2015. Top off operation has been realized since October 2015. User operation current has been gradually increased to the current level of 250mA.

Typical lifetime during 250mA is ~10 hours, top off injection period of 140 seconds maintains the total beam current within +/-0.5%. Bunch to bunch current is measured on the fill pattern monitor [1]. As shown in Fig. 1 is the typical fill pattern during 250mA operation. A long bunch train with 2ns bunch separation was filled followed by the ion cleaning gap. There is a single bunch filled in the gap to continuous monitoring the tune. Ignore the rise edge, bunch to bunch current variation is within 20%.

Fill pattern monitor scope was triggered at top-off injection and 100 turns of data were saved. The trigger delay was adjusted to have first 33 turns before the injecting beam arrives. Top image in Fig. 1 shows the fill pattern before and after injection. About 100 bunches coming from injector were filled at target bucket #648. Total beam current increased by ~1.1mA for this particular injection.

NSLS-II in-house developed digital BPM electronics is capable to measure the beam positions in turn by turn (TbT, 378kHz for NSLS-II storage ring), fast acquisition

(FA, 10kHz) and slow acquisition (SA, 10Hz rate) mode. The waveform data can be synchronized with the injection trigger to see the position transient due to mismatch of pulse kickers.

As the injection kicker pulse is short, different bunches may see different kick amplitude. Ideally if the four injection kickers are perfectly matched, the stored beam will be bumped locally in the injection section. However, it's not possible to match the four kicker pulses perfectly and each bunch may see different kicking amplitude, even outside the injection bump. To see the bunch to bunch position oscillation due to the injection mismatch, bunch by bunch feedback system data can be used. Coupled bunch stability can be analyzed using bunch by bunch data. To cross check and calibrate the bunch by bunch feedback measured positions, a 20GHz sampling rate scope has been used to sample the four button broadband signals and process the bunch to bunch positions. The bunch to bunch diagnostic tools are very useful to study the injection mismatch, as well as other advanced beam measurement like bunch to bunch tune measurement.

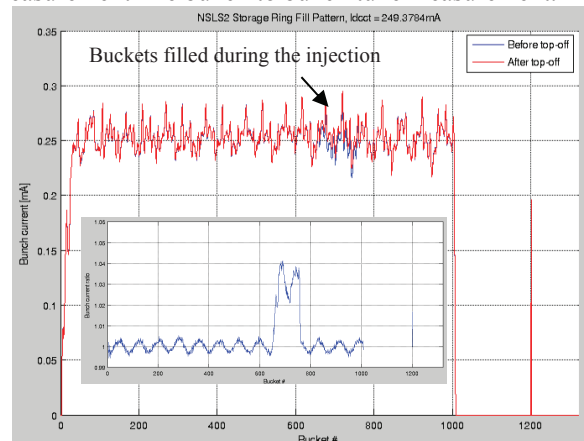


Figure 1: Fill pattern during 250mA top off injection. 100 bunches were injected at target bucket #648-750. The image shows the fill pattern before (blue) and after (red) the injection. Embedded image shows the bucket current change in percentage. ~3% current on top of 0.25mA was filled at the target bunches.

BUNCH BY BUNCH POSITION MONITOR

Bunch by bunch feedback system has been in operation since early stage of the storage ring commissioning [2]. The system proves to be critical to suppress the transverse coupled bunch instability as well as single bunch TMCI instability. The digitizer sampled ADC values is determined by the bunch position and bunch current, it will be affected if the bunch phase changed relative to the detection phase and front end electronics attenuator settings.

*Work supported by DOE contract No: DE-SC0012704

[#]chengwx@bnl.gov

COMMISSIONING AND FIRST RESULTS FROM CHANNELING RADIATION AT FAST*

A. Halavanau[†], D. Mihalcea, NIU, DeKalb, IL, USA
 D. Broemmelsiek, D. Edstrom Jr., T. Sen, A. Romanov, J. Ruan, V. Shiltsev,
 FNAL, Batavia, IL, USA
 P. Kobak, BYU-I, Rexburg, ID, USA
 W. Rush, KU, Lawrence, KS, USA
 J. Hyun, Sokendai, Ibaraki, Japan

Abstract

X-rays have widespread applications in science and industry, but developing a simple, compact, and high-quality X-ray source remains a challenge. Our collaboration has explored the possible use of channeling radiation driven by a 50 MeV low-emittance electron beam to produce narrowband hard X-rays with photon energy of 40 to 140 keV [1-3]. Here we present the simulated X-ray spectra including the background bremsstrahlung contribution, and a description of the required optimization of the relevant electron-beam parameters necessary to maximize brilliance of the resulting X-ray beam. Results are presented from our test of this, carried out at the Fermilab Accelerator Science & Technology (FAST) facility's 50-MeV low-energy electron injector. As a result of the beam parameters, made possible by the photo-injector based SRF linac, the average brilliance at FAST was expected to be about one order of magnitude higher than that in previous experiments.

INTRODUCTION

Crystal channeling presents the possibility of developing an easily disseminable, compact, and high-quality X-Ray source, which could be useful in a number of areas of science and industry (e.g. lithography and adhesive curing). Because of the conditions for crystal channeling, a low-emittance electron beam is necessary for significant X-ray production. The Fermilab Accelerator Science & Technology (FAST) facility's photoinjector-based SRF linac is ideal for testing this. Details of the UV Drive laser, photocathode-based electron gun, and other current machine parameters have been noted elsewhere [4].

The crystal channeling test setup consisted of a diamond crystal mounted in a goniometer (provided by HZDR via Vanderbilt University, see Fig. 1) near the end of the low-energy linac section tested during the 50-MeV commissioning run this past summer (2016). An open channel or Al foil target may also be used, selected with the goniometer translation axis. Once a channel is found by adjusting the pitch and yaw axes of the diamond crystal with the goniometer, the electrons oscillating within the crystal channel generate a co-linear X-ray beam. The

* This work was seeded by the DARPA AXIS program award AXIS N66001-11-1-4196 to Vanderbilt University & Northern Illinois University. Fermilab is operated by the Fermi research alliance LLC under US DOE contract DE-AC02-07CH11359.

[†] aliaksei@fnal.gov

electrons were then swept downward into the low-energy beam absorber, but the X-rays were allowed to pass through a diamond window at the end of the low energy beamline for detection.

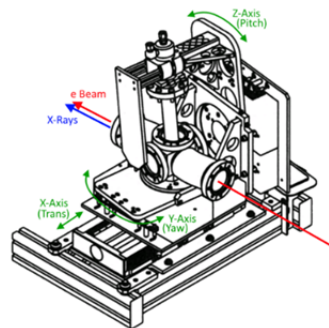


Figure 1: The goniometer from Helmholtz Zentrum Dresden Rossendorf (HZDR) used in the crystal channeling efforts during the 50-MeV run [5].

Detector Commissioning

To observe channeling two detectors were proposed: a forward or primary-beam detector (FwD) and a Compton-scattering detector (CSD) as seen in Figure 2. Both single-photon Amptek X-ray spectrometers, the FwD was located roughly 2 m from a channeling crystal. Because of the sensitivity of the detectors, a piece of PVC was placed in the path of the expected X-ray trajectory at 45° roughly 1.5 m from the diamond crystal to serve as a Compton scattering surface with the CSD 1 m from that to detect the much lower-intensity scattered X-ray beam expected from the scattering surface (7 orders of magnitude below the primary beam), allowing the CSD to operate at higher electron bunch charges. Installation and alignment of both detectors has been described previously [6]. Specifications for the detectors are listed in Table 1.

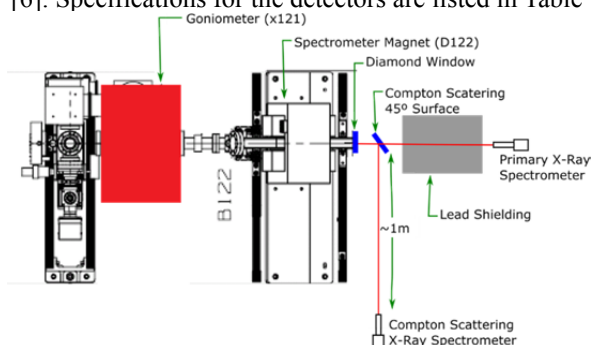


Figure 2: Forward and 90-deg (Compton scattering) detector configuration.

THE DESIGN AND CONSTRUCTION OF A RESONANCE CONTROL SYSTEM FOR THE IOTA RF CAVITY

G. Bruhaug, Idaho State University, Pocatello, USA
K. Carlson, Fermilab, Batavia, USA

Abstract

The IOTA ring will be an advanced storage ring used for non-linear beam dynamics experiments to assist in the construction of future accelerators. This ring is being built in conjunction with the FAST electron LINAC and the HINS RFQ proton source for injection into the ring. These accelerators will generate +150 MeV electron beams and 2.5 MeV proton beams respectively. As the beams are injected into the IOTA storage ring their longitudinal profile will begin to smear out and become more uniform. This will prevent detection of beam position with a Beam Position Monitoring system (BPM). To combat this a ferrite loaded bunching cavity is being constructed. This paper details the design and construction of an automatic resonance control system for this bunching cavity.

INTRODUCTION

At the New Muon Laboratory (NML) at Fermilab, the Fermilab Accelerator Science and Technology (FAST) electronic LINAC is being constructed along with the Integral Optics Test Accelerator (IOTA) storage ring and the HINS RFQ proton source. FAST will generate beams of 150-300 MeV electrons that will be injected into the IOTA storage ring for non-linear beam dynamics experiments. In addition, a 2.5 MeV proton beam will be injected into the storage ring at a separate time to test space charge effects. To detect the position of the particles inside of the IOTA storage ring, a Beam Position Monitor (BPM) will be used. However, the BPM requires the beam to be bunched, and after several turns throughout the storage ring the beam will have lost its initial bunching. Thus a bunching system needed to be developed to allow the BPM to detect the position of the particles inside of the storage ring. Due to the nature of the BPM, bunching the beam at 30.62 MHz, $h=56$, would be the preferred frequency for this bunching system. This arrangement will work fine for the electron beam, but previous work [1] showed that it would not be suitable for the proton beam. The cavity is limited to 1 kV or less on the accelerating gap, and as such could not suitably bunch the proton beam. The solution was then to bunch the proton beam at $h=4$, 2.19 MHz, and modulate the bunched beam with the 30.62 MHz RF cavity that is also used to bunch the electron beam [1]. The cavity is an anodized aluminum pillbox that was taken from the now decommissioned Antiproton Source. Inside of the pillbox housing there is a piece of beam pipe with two ceramic breaks, which are used as the accelerating gaps. In addition, the housing is split into two with a copper and aluminum separator. This separator decouples the 30.62 MHz bunching side from the 2.19 MHz bunching side.

The cavity housing also contains several ferrite disks to further tune the accelerating cavities to the correct frequencies [2]. The final tuning will be done with two large, variable capacitors to align the cavities resonant frequency with that of the incoming RF power. These variable capacitors will be controlled via stepper motors to tune the bunching cavities. It was decided that an automatic tuning system would be helpful in this case. The following paper details the design, construction, and preliminary implementation of such a system.

EXPERIMENT DETAILS

The project consisted of two major components; software design, and integrated systems testing. In addition, the software design focused on the integration of the PLC control software with the Fermilab Accelerator Controls Network (ACNET), along with the development of a controls loop for the automatic RF tuning. The hardware for this project consisted of a P2-550 Programmable Logic Controller (PLC), Two STP-DRV-4850 stepper motor drivers, a P2-AD08 Analog to Digital Converter, and two P2-SCM serial communication modules all of which are from Automation Direct. In addition, two LP-100A Vector RF Wattmeters along with two ten-turn potentiometers and the requisite power supplies. The system configuration can be seen in Figure 1.

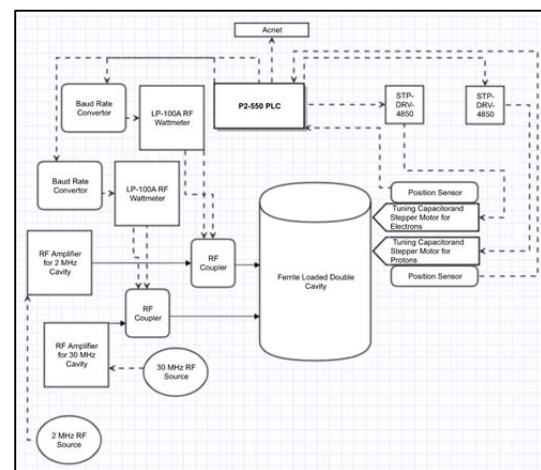


Figure 1: IOTA bunching cavity controls system.

Software Design

To continuously keep the IOTA bunching cavity at the same resonance frequency as the incoming RF power, a controls loop had to be built. In addition, this controls loop had to be integrated with the Fermilab ACNET system and allow for operator intervention, along with sending the operators alerts and updated data about the state of

COMPACT RING-BASED X-RAY SOURCE WITH ON-ORBIT AND ON-ENERGY LASER-PLASMA INJECTION

Marlene Turner^{1*}, CERN, Geneva, Switzerland

Jeremy Cheatam, Auralee Edelen, CSU, Fort Collins, Colorado, USA

Osip Lishilin, DESY Zeuthen, Zeuthen, Germany

Aakash Ajit Sahai, Imperial College Physics, London, Great Britain

Andrei Seryi, JAI, Oxford, Great Britain

Brandon Zerbe, MSU, East Lansing, MI, USA

Andrew Lajoie, Chun Yan Jonathan Wong, NSCL, East Lansing, MI, USA

Kai Shih, SBU, Stony Brook, New York

James Gerity, Texas A&M University, College Station, TX, USA

Gerard Lawler, UCLA, Los Angeles, CA, USA

Kookjin Moon, UNIST, Ulsan, Korea

¹also at Technical University of Graz, Graz, Austria

Abstract

We report here the results of a one week long investigation into the conceptual design of an X-ray source based on a compact ring with on-orbit and on-energy laser-plasma accelerator (mini-project 10.4 from [1]). We performed these studies during the June 2016 USPAS class "Physics of Accelerators, Lasers, and Plasma..." applying the art of inventiveness TRIZ [2]. We describe three versions of the light source with the constraints of the electron beam with energy 1 GeV or 3 GeV and a magnetic lattice design being normal conducting (only for the 1 GeV beam) or superconducting (for either beam). The electron beam recirculates in the ring, to increase the effective photon flux. We describe the design choices, present relevant parameters, and describe insights into such machines.

INTRODUCTION

Laser wakefield acceleration [3] experiments (LWFA) achieved GeV electron energies in cm-scales using plasma waves [4–6]. In this paper we explore a compact synchrotron light source, that uses a laser wakefield accelerated electron beam in combination with a conventional lattice. We outline a design that produces 0.4 keV (water-window) or 10 keV photons and we estimate the design parameters of the compact light source, the achievable brilliance, and we discuss the feasibility and challenges of the design. Our design uses the state of the art technology including a laser plasma gas-jet accelerator, a quadrupole doublet to focus and confine the beam, four 90 degree dipole bending magnets (superconducting or normal conducting) to keep the beam on a periodic lattice, and a 2 m long wiggler magnet to produce the desired radiation. We do not study the radiation emitted by the bending magnets, or the betatron oscillations of the electron beam in the plasma bubble.

A schematic of the design is in Fig. 1, and the investigated design criteria are detailed below:

* marlene.turner@cern.ch

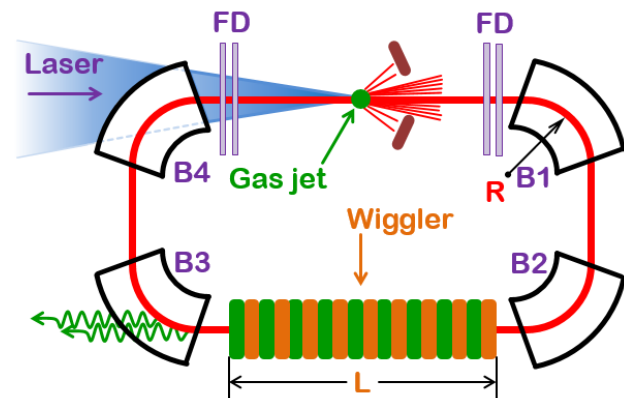


Figure 1: Schematics of the compact ring design. The laser beam enters through a window in the B4 dipole bending magnet, ionizes the gas jet and creates strong plasma wakefields to self-inject and accelerate electrons. Furthermore the produced electron beam gets parallelized with a quadrupole focusing doublet (FD). The electron beam is held on a circular trajectory by four 90-degree bending magnets (B1–B4). Opposite to the plasma injector, a Wiggler magnet produces the desired radiation. A second FD is used to refocus the circulated beam.

- 0.4 keV photons produced by a 1 GeV electron beam and normal-conducting magnets.
- 0.4 keV photons produced by a 1 GeV electron beam and super-conducting magnets.
- 10 keV photons produced by a 3 GeV electron beam and super-conducting magnets.

DESIGN OF THE MACHINE

Plasma Based Self-injected Electron Accelerator

The laser wakefield acceleration with self-guiding and self-injection provides the electron beam for the compact ring. An intense 500 TW-class Ti:Sapphire CPA system is

COMMISSIONING OF THE MAX IV LIGHT SOURCE

P. F. Tavares[†], E. Al-Dmour, Å. Andersson, M. Eriksson, M. Grabski,
M. Johansson, S.C. Leemann, L. Malmgren, M. Sjöström, S. Thorin
MAX IV Laboratory, Lund University, Lund, Sweden

Abstract

The MAX IV facility, currently under commissioning in Lund, Sweden, features two electron storage rings operated at 3 GeV and 1.5 GeV and optimized for the hard X-ray and soft X-ray/VUV spectral ranges, respectively. A 3 GeV linear accelerator serves as a full-energy injector into both rings as well as a driver for a short-pulse facility, in which undulators produce X-ray pulses as short as 100 fs.

In this paper, we briefly review the overall facility layout and design concepts and focus on recent results obtained in commissioning of the accelerators with an emphasis on the ultralow-emittance 3 GeV storage ring, the first light source using a multibend achromat.

INTRODUCTION

A central aspect of the MAX IV design concept is the notion that the diverse needs of the user community are difficult to satisfy with a single source without compromising performance. The MAX IV approach to the common dilemma of simultaneously providing high brightness hard and soft radiation as well as extremely short radiation pulses consists in having a facility featuring three different accelerators, each of which is optimized for a different range of applications (Fig. 1):

- (i) Two electron storage rings operating at different energies (1.5 GeV and 3 GeV) in order to cover a wide photon energy range in an optimized way with short-period insertion devices.
- (ii) A linear accelerator which acts as a full-energy injector into both rings and provides electron pulses with duration below 100 fs to produce X-rays by spontaneous emission in the undulators of a short-pulse facility (SPF).

The 3 GeV storage ring [1-3] employs a multibend achromat (MBA) lattice to achieve a bare lattice emittance of 0.33 nm rad. The technical implementation of the MBA lattice raises several engineering challenges: the large number of strong magnets per achromat requires a compact design with small-gap combined-function magnets and the small apertures lead to a low-conductance vacuum chamber design that relies on the chamber itself as a distributed copper absorber for the heat deposited by synchrotron radiation, while non-evaporable getter (NEG) coating provides for reduced photodesorption yields and distributed pumping. Finally, a low main frequency (100 MHz) is chosen for the RF system yielding long bunches, which are further elongated by passively operated third-

harmonic cavities. These long bunches are a crucial ingredient to overcome both incoherent (intrabeam scattering) and coherent collective effects and allow operation at high currents while maintaining good Touschek lifetime [4].

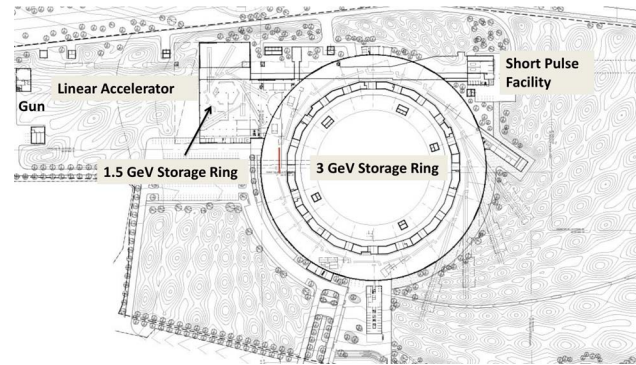


Figure 1: Overview of the MAX IV facility.

The 1.5 GeV storage ring [1] replaces the MAX II and MAX III rings, whose operation was officially concluded on December 15th, 2015 after nearly two decades of continuous service to the scientific community. Despite having about the same circumference as MAX II, the 1.5 GeV storage ring delivers a smaller emittance through the use of the same compact magnet design as in the 3 GeV storage ring. An exact copy of the 1.5 GeV storage ring was built and successfully commissioned at the Polish laboratory Solaris [5].

In this paper, we focus on commissioning results and operational experience with those accelerator subsystems that present most of the innovations brought about by the MAX IV design. In fact, as the first realisation of a light source based on the MBA concept, the MAX IV 3 GeV storage ring offers an opportunity for validation of concepts that are likely to be important ingredients of future diffraction-limited light sources.

INJECTOR LINAC

The MAX IV linear accelerator [2] is used for both full energy injection and top-up to the storage rings and as a high brightness driver for a Short Pulse Facility (SPF) [6]. It consists of 39 warm S-band linac sections together with 18 RF units, each consisting of a 35MW klystron and a solid state modulator and a SLED energy doubler.

For injection to the storage rings a thermionic gun with a pulse train chopper system is used [7]. The chopper can be used to either produce a 500 MHz time structure convenient to enhance the signal-to-noise ratio for single pass beam position monitor electronics during early commis-

[†]pedro.fernandes_tavares@maxiv.lu.se

OVERVIEW OF ELECTRON SOURCE DEVELOPMENT FOR HIGH REPETITION RATE FEL FACILITIES*

F. Sannibale, Lawrence Berkeley National Laboratory, 94720 Berkeley, CA, USA

Abstract

An increasing science demand for high-repetition rate (MHz-class) FEL facilities, from IR to X-rays, has been pushing institutions and groups around the world to develop proposals addressing such a need, and some of them have been already funded and are under construction. Such facilities require the development of high-brightness high-repetition rate electron guns, and a number of groups worldwide started to develop R&D programs to develop electron guns capable of operating at this challenging regime. Here we describe the approaches and technologies used by the different programs and discuss advantages and challenges for each of them. A review of the present achievements is included, as well as a brief analysis to understand if the present technology performance is sufficient to operate present and future high repetition rate FEL facilities.

INTRODUCTION

After the success of FEL facilities operating at relatively low repetition rates (~ 100 Hz) an increasing science demand for high-repetition rate (MHz-class) FEL facilities, from IR to X-rays, has been pushing institutions and groups around the world to develop proposals addressing such a need. Some of them (notably the LCLS-II at SLAC) are already funded and under construction.

It is well known that the ultimate performance of an FEL is already defined at the injector and at its electron gun in particular. The high repetition rate requirement significantly impacts the technological choices for the injector, and while for most of its components solutions already exist, for the electron gun that is not completely true. The low repetition rate successful technology, based on normal-conducting (NC) high-frequency ($> \sim 1$ GHz) RF, cannot be scaled to rates higher than a few kHz because of the increasing power that needs to be dissipated on the structure. In response to that, a number of groups started R&D programs to develop alternative electron guns capable of operating at this difficult regime.

Technologies used and investigated include DC guns, superconducting RF (SRF) guns, normal-conducting (NC) low frequency RF gun, and a hybrid DC-SRF configuration. Figure 1 shows some of the main active groups in the field and their location around the world.

This paper, after an initial analysis of which parameters mainly affect the performance of an electron gun, continues by describing the different technologies used and discusses advantages and challenges for each of them.

A (incomplete) review of the present achievements is also included, and in the final part, the question if the present technology performance is sufficient to operate present and future high repetition rate FEL facilities is discussed.

MAIN PARAMETERS DRIVING THE GUN BRIGHTNESS PERFORMANCE

In FELs, the emittance (ε) to wavelength (λ) matching condition for the transverse emittance

$$\varepsilon \approx \frac{\lambda}{4\pi} \Rightarrow \frac{\varepsilon_n}{\beta\gamma} \approx \frac{\lambda}{4\pi}$$

indicates that small normalized emittances (ε_n) should be pursued to keep the energy of the linac as low as possible (β, γ in the equation are the relativistic Lorentz factors). For X-ray machines ($\lambda < \sim 1$ nm) and present gun performance, GeV-class electron beam energies are required. In the case of high repetition rate FELs, such energies are obtained by using long and expensive superconducting linacs.

Emittance appears also in the equations regulating the FEL gain and in general, the optimization of the FEL performance requires high peak currents (kA-class) and normalized transverse emittances as small as possible.

At the injector exit, the beam is relativistic enough to make space charge forces negligible. At this point the emittances are “frozen” and their value define the ultimate transverse brightness that the linac can achieve.

The emittance at the injector exit is given by the quadratic sum of a number of different independent terms:

$$\varepsilon_n = \sqrt{\varepsilon_{nTherm.}^2 + \varepsilon_{nBz@Cat.}^2 + \varepsilon_{nSpace Charge}^2 + \varepsilon_{nAberr.}^2 + \varepsilon_{nRF}^2}$$

where we can recognize the contributions due to the: cathode thermal emittance; presence of a solenoidal field at the cathode; space charge; optics aberrations; and RF.

The optimization game in injectors consists in getting the cathode thermal contribution small and making all the other emittance contributions possibly negligible.

The cathode thermal emittance is given by:

$$\frac{\varepsilon_{nTherm.}}{\sigma_r} = \sqrt{\frac{\Delta E_c}{3mc^2}} \quad \text{with } \sigma_r \equiv \text{rms beam size @ cathode} \\ \text{and } \Delta E_c \equiv \text{excess energy}$$

with m the electron rest mass and c the speed of light. The electron excessive energy depends on the cathode material and on the emission process. For example, in the case of photoemission, the excess energy is equal to the difference between the photon energy and the effective work function of the material (including the Schottky barrier reduction induced by the gun accelerating field).

*Work supported by the Director of the Office of Science of the US Department of Energy under Contract no. DEAC02-05CH11231

†fsannibale@lbl.gov

DEMONSTRATION OF FRESH SLICE SELF-SEEDING IN A HARD X-RAY FREE ELECTRON LASER*

C. Emma, C. Pellegrini, UCLA, Los Angeles, CA 90095 USA

A. Lutman, M. Guetg, A. Marinelli, J. Wu, SLAC, Menlo Park, CA 94025, USA

Abstract

We discuss the first demonstration of fresh slice self seeding, or Enhanced Self-Seeding (ESS) in a hard X-ray Free Electron Laser (XFEL). The ESS method utilizes a single electron beam to generate a strong seed pulse and amplify it with a small energy spread electron slice. This extends the capability of self seeded XFELs by producing short pulses, not limited by the duration set by the self-seeding monochromator system, with high peak intensity. The scheme relies on using a parallel plate dechirper to impart a spatial chirp on the beam, and appropriate orbit control to lase with different electron beam slices before and after the self-seeding monochromator. The performance of the ESS method is analyzed with start-to-end simulations for the Linac Coherent Light Source (LCLS). The simulations include the effect of the parallel plate dechirper and propagation of the radiation field through the monochromator. We also present results of the first successful demonstration of ESS at LCLS. The radiation properties of ESS X-ray pulses are compared with the Self-Amplified Spontaneous Emission (SASE) mode of FEL operation for the same electron beam parameters.

INTRODUCTION

X-ray Free Electron Lasers (XFELs) are tunable sources of coherent X-rays capable of generating high intensity pulses from nanometer down to sub-angstrom wavelengths [1]. The extraction efficiency and the bandwidth of typical Self Amplified Spontaneous Emission (SASE) [2] XFELs is characterized by the FEL parameter ρ , typically around 10^{-3} . The bandwidth can be narrowed, among other methods, via self-seeding [3], and the intensity can be increased via tapering of the undulator magnetic field [4] [5] [6] [7]. One major limitation of self-seeded tapered XFELs is the trade-off between seed power and energy spread at the start of the seeded undulator section. This trade-off limits the output power of tapered self-seeded systems. It has recently been shown that for high efficiency XFELs aiming to reach multi-TW peak powers, the output power can be greatly enhanced by generating a strong seed pulse and amplifying it with a small energy spread electron beam. This can be accomplished by using two different electron beam slices, one to generate the seed signal and the other to amplify it after the self-seeding monochromator in a tapered undulator. This method, termed fresh slice or Enhanced Self-Seeding (ESS), proposed in Ref. [5] has recently been experimentally demonstrated at the Linac Coherent Light Source (LCLS) [8]. Multi-color lasing using the fresh slice scheme has recently been reported in Ref. [9]. We present experimental results

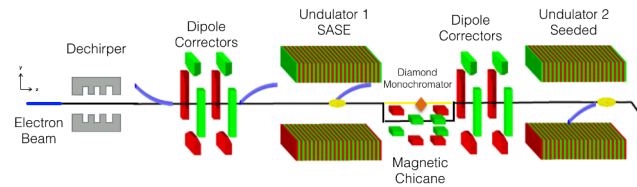


Figure 1: Schematic of the ESS experimental demonstration setup with the parallel plate dechirper installed at the LCLS. The beam travels off-axis through the vertical dechirper and acquires a quadratic spatial chirp. Dipole correctors are used to steer the tail on-axis in the SASE section and the core (head) on-axis in the seeded section. The X-ray seed pulse (yellow) is overlapped with the core (head) in the second section by adjusting the magnetic chicane delay.

of ESS demonstration comparing the performance of the ESS scheme with SASE at the same photon energy. We also compare experimental ESS data with start-to-end simulations using the same LCLS machine parameters as the experimental demonstration.

ENHANCED SELF-SEEDING EXPERIMENTAL RESULTS

A schematic of the demonstration experiment for ESS at the LCLS is shown in Fig. 1. The electron beam parameters are 4kA current (core), 11.1 GeV energy, normalized transverse emittance $0.4 \mu\text{m}$ and 180 pC charge. The resonant photon energy is 5.5 keV. In our experiment the electron beam lases in the tail slices during the first SASE section and the seed pulse is amplified on the core slices in the seeded section after the monochromator. Selective lasing is achieved by imparting a spatial chirp on the electron beam and using appropriate orbit control to steer the tail and core slices on axis in the SASE and seeded section respectively. The spatial chirp is imparted on the electron beam in a passive manner by making use of the transverse wakefields of the parallel plate dechirper recently commissioned at LCLS [10] [11]. We adjust the dechirper jaw such that the beam travels off-axis near the vertical jaw and the dipole wake imparts a head-tail quadratic spatial chirp on the beam. We use vertical dipole correctors before the first undulator section to steer the tail on-axis and generate a saturated SASE pulse before the diamond monochromator. The photon beam travels through the diamond monochromator which transmits a wide bandwidth SASE pre-pulse and a long narrow bandwidth tail. The electron beam passes through the chicane around the diamond monochromator and dipole correctors are used to steer the core slices on axis in the undulator section downstream. The chicane delay is

* Work partially supported by: DOE Grant Number DE-SC0009983

A NEW THERMIONIC RF ELECTRON GUN FOR SYNCHROTRON LIGHT SOURCES *

S.V. Kutsaev¹, R. Agustsson¹, J. Hartzell¹, A. Murokh¹, A. Nassiri², E. Savin^{1,3}, A.V. Smirnov¹, A.Yu. Smirnov¹, Y. Sun², A. Verma¹, G. Waldschmidt², and A. Zholents²

¹RadiaBeam Systems, LLC, Santa Monica, CA, 90404, USA

²Argonne National Laboratory, Lemont, IL, 60439, USA

³also at National Research Nuclear University « MPhI », Moscow, Russia

Abstract

A thermionic RF gun is a compact and efficient source of electrons used in many practical applications. RadiaBeam Systems and the Advanced Photon Source at Argonne National Laboratory collaborate in developing of a reliable and robust thermionic RF gun for synchrotron light sources which would offer substantial improvements over existing thermionic RF guns and allow stable operation with up to 1A of beam peak current at a 100 Hz pulse repetition rate and a 1.5 μ s RF pulse length. In this paper, we discuss the electromagnetic and engineering design of the cavity and report the progress towards high power tests of the cathode assembly of the new gun.

INTRODUCTION

Electron guns are used in electron microscopes, electron beam welders, and as sources for particle accelerators. Thermionic RF electron guns were developed at SLAC/SSRL for the Stanford Positron Electron Accelerating Ring (SPEAR) Project [1]. Conventional RF guns can offer high average beam current, which is necessary for synchrotron light and THz radiation sources facilities, as well as for industrial accelerators. Most of the light sources worldwide are storage ring based, and thus rely on thermionic guns for their operation. Unfortunately, they have decades-old thermionic RF gun technology, and it is due for an upgrade.

The current RF gun is a 1.6-cell side-coupled structure, operating at 2856 MHz frequency. Typically, the RF gun is powered with \sim 1.5 MW pulsed power but can sustain up to 7 MW via an end-coupled waveguide. The cathode used is a tungsten dispenser cathode with a diameter of 6 mm. The gun can produce peak beam kinetic energies of up to 4.5 MeV and peak macro pulse currents of up to 1.3 A. Practical operating RF pulse parameters are \sim 1 μ s at a repetition rate of \sim 15 Hz. More details of gun parameters may be found in [2].

Recently, RadiaBeam Technologies has developed and demonstrated a compact source of narrow bandwidth free space THz radiation [3] using the actual APS gun at the Injector Test Stand (ITS) facility. A thermionic injector generates an electron beam, which is compressed in an alpha magnet and propagated through a few cm-long corrugated pipe radiator. A prototype system was

commissioned at Argonne National Laboratory, and demonstrated a strong signal ($>$ 100 kW peak power), at 500 μ m wavelength, in \sim 5% bandwidth. While the initial commissioning of this THz source has so far been very encouraging, pushing the system performance envelope beyond 2 THz requires an update of the RF gun performance.

Given the immediate requirements of these two applications, RadiaBeam in collaboration with APS are developing the new reliable and robust thermionic RF gun with the parameters specified in Table 1.

Table 1: Design Parameters of the RF Gun

Parameter	Value
Operating frequency	2856 MHz
Output energy	up to 3 MeV
Accelerated current	up to 1A
RF power	5 MW
Repetition rate	up to 100 Hz

ELECTROMAGNETIC DESIGN

Conventional thermionic RF gun design implements a side coupling cell [4]. This cell is required to tune the field ratio between main cells and to increase frequency mode separation in the cavity. However, such design has several significant drawbacks. First, an additional cell complicates the engineering design and fabrication process. Second, it breaks the symmetry of the structure. Finally, due to the sharp edges in the area where accelerating cells connect to the coupling cell, the peak surface magnetic field can be strong in this area. Strong magnetic field increases the pulsed heating temperature gradient and limits the performance of the RF gun both by reducing the maximum gradient and by limiting the pulse length [5].

In our design, we propose to remove the coupling cell and add magnetic coupling holes to the iris between the cells to provide required mode separation and similar dimensional sensitivity without any change to the electrodes shape (see Figure 1). In this case, the structure will operate in π -mode, and magnetic field will provide the coupling. Pin tuners in each cell will allow the tuning of the field ratio. The magnetic coupling holes cause the longitudinal field asymmetry in the full cell. To compensate this effect, we reduced the blending radius of one side of the cavity. We kept the original design of the electrodes, so the beam quality remains the same as in the existing APS gun.

* This work is supported by the U.S. Department of Energy, Office of Basic Energy Science, under contract DE-SC0015191 and contract No. DE-AC02-06CH11357

LOADING OF WAKEFIELDS IN A PLASMA ACCELERATOR SECTION DRIVEN BY A SELF-MODULATED PROTON BEAM

V. K. Berglyd Olsen*, E. Adli (University of Oslo, Oslo, Norway)

P. Muggli (Max Planck Institute for Physics, Munich, Germany and CERN, Geneva, Switzerland)

J. M. Vieira (Instituto Superior Technico, Lisbon, Portugal)

Abstract

Using parameters from the AWAKE project and particle-in-cell simulations we investigate beam loading of a plasma wake driven by a self-modulated proton beam. Addressing the case of injection of an electron witness bunch after the drive beam has already experienced self-modulation in a previous plasma, we optimise witness bunch parameters of size, charge and injection phase to maximise energy gain and minimise relative energy spread and emittance of the accelerated bunch.

INTRODUCTION

The AWAKE experiment at CERN proposes to use a proton beam to drive a plasma wakefield accelerator with a gradient on the order of 1 GeV/m to accelerate an electron witness beam [1, 2].

In this paper we present two simulation configurations with a modified proton drive beam based on the baseline parameters for the AWAKE experiment. The drive beam is delivered from the SPS accelerator at CERN at an energy of $400 \text{ GeV}/c$, a bunch length $\sigma_z = 12 \text{ cm}$, and $\sigma_{x,y} = 200 \mu\text{m}$. [3].

The baseline plasma electron density n_{pe} for AWAKE is $7 \times 10^{14} \text{ cm}^{-3}$. The corresponding plasma wavelength $\lambda_{pe} = 2\pi c/\omega_{pe} = 1.26 \text{ mm}$, where $c/\omega_{pe} = 200 \mu\text{m}$ is the plasma skin depth, and ω_{pe} is the plasma frequency given as $[n_{pe}e^2/m_e\epsilon_0]^{1/2}$.

In order to generate a suitable wakefield, the drive beam must be shorter than λ_{pe} . This is not achievable for the SPS proton beam. In order to use such a beam to drive a wakefield we exploit the self-modulation instability (SMI) that can occur when the beam travels through a plasma and $\sigma_z \gg \lambda_{pe}$. The SMI modulates the beam at a period of $\approx \lambda_{pe}$ [4], allowing us to inject the witness beam in an optimal bucket between two such proton micro bunches.

BEAM LOADING

A particle beam at high energy travelling through a plasma will excite a plasma wave in its wake, and the plasma can sustain a very high accelerating gradient [5]. It is possible to accelerate a secondary beam by extracting energy from this wakefield, thus transferring energy from a drive beam to a trailing witness beam. Such an accelerator design was first proposed by Chen in 1985 [6]. However, there are some challenges in this transfer of energy from drive to witness beam.

* v.k.b.olsen@fys.uio.no

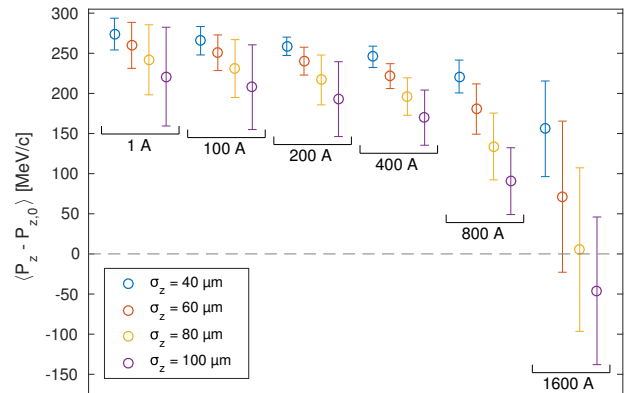


Figure 1: Energy gain and spread for a series of witness beams after $\approx 1.1 \text{ m}$ of plasma. The initial momentum of the witness beam is $217.8 \text{ MeV}/c$. Mean momentum and RMS spread is calculated for all macro particles in the PIC simulation.

One such challenge stems from the witness beam generating its own field, modifying the E_z -field behind it such that the particles in the tail will be accelerated less than those in the front. This causes an increase in energy spread in the beam [7]. This effect can in theory be corrected for by shaping the witness beam. An optimally shaped and positioned beam, such as a triangular beam, can flatten the wakefield such that change in energy spread is effectively zero [8]. However, this requires beam shapes that are difficult to produce experimentally.

BEAM LOADING OF SMI WAKEFIELDS

For AWAKE, most of the SMI evolves during the first stage of $z < 4 \text{ m}$ [2]. This evolution results in a phase change of the wakefields that causes the optimal point for acceleration to drift backwards relative to the witness beam [9, 10].

In our current study we have restricted ourselves to Gaussian witness beams, and seek to demonstrate through simulations how small energy spread can still be achieved by optimally loading the field. The first set of simulations presented uses a subset of 26 micro bunches resulting from the self-modulation that occurs in the previous plasma stage. The pre-modulated beam does undergo further evolution as the envelope function does not fully match the SMI beam, but we only look at the first $\leq 3 \text{ m}$ of this stage, before the phase change starts to dominate [11]. All simulations have been done using OSIRIS 3.0 [12].

SIMULATION OF HIGH-POWER TUNABLE THz GENERATION IN CORRUGATED PLASMA WAVEGUIDES*

Chenlong Miao[†], IREAP, University of Maryland, College Park 20740, USA

John P. Palastro, Naval Research Laboratory, Washington DC 20375, USA

Thomas M. Antonsen, IREAP, University of Maryland, College Park 20740, USA

Abstract

Intense, short laser pulses propagating through inhomogeneous plasmas generate terahertz (THz) radiation. We consider the excitation of THz radiation by the interaction between an ultra short laser pulse and a miniature plasma waveguide. Such corrugated plasma waveguides support electromagnetic (EM) channel modes with subluminal phase velocities, thus allowing the phasing matching between the generated THz modes and the ponderomotive potential associated with laser pulse, making significant THz generation possible. Full format PIC simulations and theoretical analysis are conducted to investigate this slow wave phase matching mechanism. We find the generated THz is characterized by lateral emission from the channel, with a spectrum that may be narrow or broad depending on laser intensities. A range of realistic laser pulses and plasma profile parameters are considered with the goal of maximizing the conversion efficiency of optical energy to THz radiation. These studies are the first to investigate ponderomotively driven THz self-consistently in the interesting situations in which the interaction occurs over a scale many wavelengths long.

INTRODUCTION

Terahertz radiation (THz) lies between microwave and infrared in the electromagnetic spectrum and typically spans frequencies from 300 GHz to 20 THz. A wide variety of applications [1] can be found including time domain spectroscopy (TDS), remote detection, medical and biological imaging and so on. One of the most commonly seen examples is that most airports use millimeter wave/THz scanners for human body security checking. Existing small scale THz sources based on laser-solid interaction are limited to μJ /pulse levels due to material damage [2] although the recent discovery using optical rectification (OR) [3–5] in organic crystals can exceed this limit. This has led to the consideration of THz generation via laser-plasma interactions [6–8] and THz peak energy of tens of μJ can be achieved. Higher energy THz pulses can be generated at accelerator facilities via synchrotron [9] or transition radiation [10]. Such facilities are relatively large and expensive to operate. This motivates research interest in small-scale, high efficiency terahertz sources.

A scheme involving laser pulses propagating through axially corrugated plasma channels has been proposed by Antonsen et al. [11]. This slow wave structure supports electromagnetic modes that have subluminal phase velocities,

thus providing the possibility of phase matching between the excited modes and the driver. Here, with a combination of theory and simulation, we investigated the ponderomotively driven THz generation via the slow wave phase matching process by laser pulses propagating through corrugated plasma waveguides. These waveguides have been realized in laboratory [12, 13].

THz GENERATION

The set up of the THz generation mechanism is schematically shown in Fig. 1.

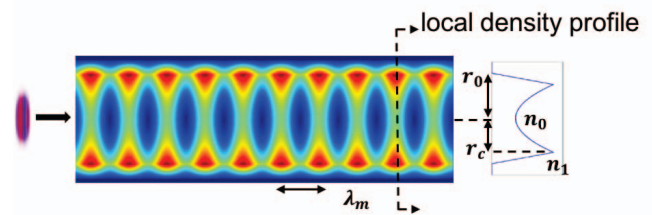


Figure 1: System setup of THz generation in corrugated plasma waveguides. An intense, ultra-short laser pulse propagates through the preformed corrugated plasma channels and drives lateral THz emission.

Corrugated Plasma Waveguides

We consider the corrugated plasma waveguides as shown in Fig. 1 to be cylindrical symmetric, with electron densities described by the following,

$$\frac{n(r, z)}{n_0} = \begin{cases} n_0 + (n_1 - n_0) \frac{r^2}{r_c^2} & r \leq r_c \\ n_1 \frac{r_0 - r}{r_0 - r_c} & r_c < r < r_0 \\ 0 & r \geq r_0 \end{cases} \quad (1)$$

where n_0 is the normalized density. The channel has a density modulation period of λ_m and the modulation wavenumber is defined as $k_m = 2\pi/\lambda_m$. The axially modulated z dependence is carried through the parameters n_0 , n_1 , r_c and r_0 . The quantity $n_0(z)$ is the normalized on-axis density and $n_1(z)$ is normalized density at $r = r_c$ as shown in Fig. 1. The quantities n_0 and n_1 are both axially modulated, $n_0 = 1 + \delta \sin(k_m z)$ and $n_1 = \bar{n}_1 + \delta_1 \sin(k_m z)$, respectively. δ is the density modulation amplitude of on-axis density n_0 . The quantity \bar{n}_1 is the average transverse peak density and δ_1 is the density modulation amplitude of n_1 . The density

* Work supported by DoE and NRL

[†] clmiao@umd.edu

STATUS OF THE LOS ALAMOS MULTI-PROBE FACILITY FOR MATTER-RADIATION INTERACTIONS IN EXTREMES*

J. L. Erickson, R. W. Garnett[†], Los Alamos National Laboratory, Los Alamos, NM, USA

Abstract

The Matter-Radiation Interactions in Extremes (MaRIE) project will provide capability that will address the control of performance and production of materials at the mesoscale. MaRIE will characterize the behavior of interfaces, defects, and microstructure between the spatial scales of atomic structures and those of the engineering continuum where there is a current capability gap. The mission need is well-met with an x-ray source, coherent to optimize disordered imaging capability, brilliant and high-rep-rate to provide time-dependent information, and high enough energy to see into and through the mesoscale of materials of interest. It will be designed for time-dependence from electronic motion (picosecond) through sound waves (nanosecond) through thermal diffusion (millisecond) to manufacturing (seconds and above). The mission need, the requirements, a plausible alternative reference design of a 12-GeV linac-based 42-keV x-ray free-electron laser, and the status of the project will be described.

THE MISSION NEED

One of the main objectives of the National Nuclear Security Administration is to enable new and more rigorous science-based approaches to manufacturing and certification without the need for nuclear tests. Los Alamos has been pursuing a next-generation signature facility based on multi-probe capabilities to address this control of performance and production of weapons materials at the mesoscale for quite some time. Many of the uncertainties that remain in the assessment of weapon safety, security, and performance arise from uncertainties in material properties governed at the spatial scales between atomic structures and those of the engineering continuum (the mesoscale) [1]. The Matter-Radiation Interactions in Extremes (MaRIE) facility would provide this new capability by aiding our ability to test materials response at resolutions necessary to understand the links between materials microstructure and performance in weapons-relevant extreme environments through new and more rigorous science-based approaches to manufacturing and certification as part of science-based stewardship.

Experimental data from MaRIE would improve the understanding of interfaces, defects, and microstructure in the mesoscale and provide the ability to offer time-dependent control of processes, structures, and properties. Materials will be characterized at the mesoscale, and their dynamic behavior studied in time-dependent extreme conditions through the use of both imaging and diffractive

scattering with multiple probes at multiple spatial and time scales. Exascale computing will be combined with experimental results from the MaRIE facility to enable rapid and confident deployment of new components and systems through more cost-effective and more rigorous science-based approaches.

The scientific community has identified that the challenge to accelerated discovery and use of new materials with enhanced and optimized properties is at the mesoscale, where new tools and approaches are needed to understand this regime [2]. It has become clear that in many important areas the functionality that is critical to macroscopic behavior begins not at the atomic or nanoscale but at the mesoscale, where defects, interfaces, and non-equilibrium structures dominate materials behavior [3]. Measurements are needed of scattering off the periodic structure of the material (phase, texture, orientation) as well as imaging of non-periodic structures (defects, material interfaces, and microstructures) to resolve these materials behaviors. These measurements are possible with a brilliant, high-repetition-rate, coherent X-ray source such as proposed for the MaRIE facility.

MaRIE would fill a critical gap in length scale between the integral scale addressed by hydrotest facilities such as DARHT and Scorpius and facilities for materials phenomena at smaller scale such as NIF and Z. The reference design assumes the MaRIE facility would be sited at the Los Alamos Neutron Science Center (LANSCE). The LANSCE facility has been the flagship facility for large-scale science at Los Alamos for many decades.

THE MARIE FACILITY

The proposed MaRIE facility includes a new 12-GeV electron linac driving a 42-keV X-ray free-electron laser (XFEL), coupled with the existing capabilities of the LANSCE 1-MW capable, 800-MeV proton linear accelerator (linac), a new experimental hall, and materials fabrication and characterization facilities. The LANSCE accelerator complex currently supports a broad user base including the neutron scattering community, basic science, and national security programs by providing multiple beams to several experimental areas. MaRIE builds upon LANSCE to transform the science of microstructure, interfaces, and defects of materials in extremes. This will be accomplished by providing the necessary extreme environments (pressure, temperature, radiation, etc.) coupled with multiple probes including, charged particles (protons and/or electrons), optical laser photons, coherent X-rays, and state-of-the-art diagnostics. Figure 1 shows a pre-conceptual layout of the MaRIE facility at LANSCE.

* Work supported by the United States Department of Energy, National Nuclear Security Agency, under contract DE-AC52-06NA25396.

[†] rgarnett@lanl.gov

ACCELERATOR TECHNICAL PROGRESS AND FIRST COMMISSIONING RESULTS FROM THE EUROPEAN XFEL*

R. Wichmann[†], Deutsches Elektronen-Synchrotron, Hamburg, Germany
on behalf of the European XFEL Accelerator Consortium

Abstract

The European XFEL under construction in Hamburg, Northern Germany, aims at producing X-rays in the range from 260 eV up to 2 keV out of three undulators that can be operated simultaneously with up to 27,000 bunches per second. The FEL is driven by a 17.5 GeV super-conducting linac. Installation of this linac is now finished and commissioning is next. First lasing is expected for spring 2017. This paper summarizes the status of the project. First results of the injector commissioning are given

INTRODUCTION

The accelerator complex of the European XFEL [1] is being constructed by an international consortium under the leadership of DESY. Seventeen European research institutes contribute to the accelerator complex and to the comprehensive infrastructure in-kind [2]. DESY coordinates the European XFEL Accelerator Consortium but also contributes with many accelerator components, and the technical equipment of buildings, with its associated general infrastructure. The main milestones of the European XFEL project with focus on the accelerator are as follows:

- 07/2006: XFEL TDR [1] published
- 01/2009: start of underground construction
- 08/2014: start installation of accelerator components
- 12/2015: start of injector commissioning
- 10/2016: cool-down of XFEL linac, start of commissioning
- 07/2017: start user operation.

LAYOUT OF THE EUROPEAN XFEL

In the following the overall layout of the European XFEL is given with emphasis on the different sections of the accelerator complex as depicted in Figure 1.

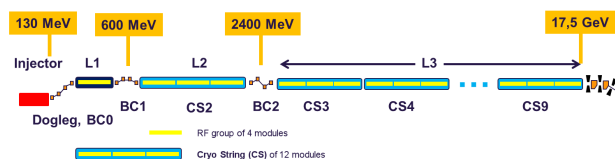


Figure 1: Schematic layout of the major sections of the XFEL accelerator.

* Work supported by the respective funding agencies of the contributing institutes; for details please see <http://www.xfel.eu>

[†] riko.wichmann@desy.de

Introduction to the Accelerator

The European XFEL with its total facility length of 3.4 km follows the established layout of high performance single pass Self-Amplified Spontaneous Emission (SASE) FELs. A high bunch charge, low emittance electron gun is followed by some first acceleration to typically 100 MeV. In the following, magnetic chicanes help to compress the bunch and therefore increase the peak current. This happens at different energies to take care of beam dynamic effects which would deteriorate the bunch emittance in case of too early compression at too low energies. Thus the linac is separated by several of such chicanes. The European XFEL main linac accelerates the beam in three sections L1, L2, and L3, following the first acceleration in the injector.

The XFEL linac was designed with an electron beam energy of 17.5 GeV provided by 100 super-conducting (s.c.) modules (plus 1 in the injector) of 12.2 m length suspended from the tunnel ceiling, operated at 1.3 GHz. Each module houses 8 s.c. cavities of about 1 m length. 4 such modules are forming 1 standard RF unit consisting of a modulator (outside the tunnel), a pulse transformer and 10 MW multi-beam klystron [3] (both located in the tunnel underneath the accelerator modules, see Fig. 2). 3 RF units (consisting of a total of 12 accelerating modules) form 1 standard cryogenic unit called a cryo-string (CS2 to CS9 in Fig. 1). With a design gradient of 23.6 MV/m 1 RF unit with 4 accelerator modules was intended as spare.

Injector

The injector design of the European XFEL is visibly affected by the need of long bunch trains which are required for the efficient use of s.c. linac technology. Like many other FELs it starts with a normal-conducting 1.6 cell radio frequency (RF) electron gun delivering 600 μ s long trains followed almost immediately by a first s.c. accelerator section which allows efficient acceleration of bunch trains. This first linac section consists of a standard XFEL module, followed by a harmonic 3.9 GHz module. Unlike the standard RF units described above, the 2 klystrons for the injector module are located outside the injector tunnel. The 3rd harmonic system is needed to manipulate the longitudinal beam profile together with the later bunch compression in magnetic chicanes. Beam diagnostics is used to verify the electron beam quality at energy of about 130 MeV. A transverse deflecting system is installed which consists of a 550 mm long 3 GHz RF structure, able to streak individual bunches out of the bunch train vertically. These bunches will be kicked to the off axis screens to examine the longitudinal profile and slice emittance. The in total 50 m long injector installation ends

OPTIMIZATION OF COMPTON SOURCE PERFORMANCE THROUGH ELECTRON BEAM SHAPING*

A. Malyzhenkov^{†1}, N. Yampolsky, Los Alamos National Laboratory, Los Alamos, NM 87545, USA
¹also at Northern Illinois University, Dekalb, IL 60115, USA

Abstract

We investigate a novel scheme for significantly increasing the brightness of x-ray light sources based on inverse Compton scattering (ICS) - scattering laser pulses off relativistic electron beams. The brightness of these sources is limited by the electron beam quality since electrons traveling at different angles, and/or having different energies, produce photons with different energies. Therefore, the spectral brightness of the source is defined by the 6d electron phase space shape and size, as well as laser beam parameters. The peak brightness of the ICS source can be maximized then if the electron phase space is transformed in a way so that all electrons scatter off the x-ray photons of same frequency in the same direction. We describe the x-ray photon beam quality through the Wigner function (6d photon phase space distribution) and derive it for the ICS source when the electron and laser rms matrices are arbitrary. We find the optimal uncorrelated electron beam phase space distribution resulting in the highest brightness of the ICS source for the simple on axis case as an example.

INTRODUCTION

Currently there is a strong national need for high quality light sources at hard X-rays [1]. The quality of a light source is characterized by its brightness, or photon density in phase space. Larger brightness corresponds to radiation with a higher degree of coherency and thus permits higher resolution in imaging experiments. Relativistic electron beams are routinely used to generate radiation above optical frequencies. Over the past 50 years light sources based on synchrotron radiation have improved their average brightness by over 15 orders of magnitude [2, 3]. The 3rd and 4th generation light sources produce radiation via magnetic devices known as undulators – arrays of alternating permanent magnets which wiggle the electron trajectory. The wavelength of radiation generated by relativistic beams in these devices is on the order of $\lambda_{x\text{-ray}} \sim \lambda_u/(2\gamma^2)$. The undulator wavelength λ_u is limited to ~ 1 cm for practical devices. As a result, generating X-rays with wavelengths < 1 nm requires multi-GeV electron beams. Since the accelerator size and cost scales with energy, the facilities are correspondingly large and expensive.

A large-amplitude electromagnetic wave can also serve to undulate the trajectory of an electron beam. The electron trajectory in the wave field deviates from the straight line motion in a manner similar to that of an undulator, resulting

in radiation. Alternatively, this process can be viewed as inverse Compton scattering (ICS) in which photons increase their energy after scattering off the relativistic electrons [4,5]. Regardless of viewpoint, the end result is the potential to generate hard X-rays using optical wavelength light and 0.1 GeV-range electron beams. X-ray ICS sources have been proposed and demonstrated over the past decade [6–8]. It produces photons with energies of tens of keV. Estimates for the peak brightness of these sources are close to each other and are on the order of $10^{20} - 10^{22}$ ph/mm²/mrad²/s/0.1% BW, more than 10 orders of magnitude below the estimate for hard x-ray free electron lasers (FELs). As a result, ICS sources based on current technology cannot compete with FELs [9]. Significant increases in brightness are needed to make ICS sources more attractive.

The spectrum of a single-particle ICS radiation strongly depends on its energy γ and angle at which it travels in respect to the axis $x' = dx/dz$ (plots (a) and (b) in Fig. 1). As a result, angular divergence and energy spread of the electron beam increase the bandwidth $\Delta w/w$ of the backscattered radiation as $(\gamma\Delta x')^2$ and $2\Delta\gamma/\gamma$, respectively [10, 11]. For example, both effects result in the same 1% ICS bandwidth for the following beam parameters: 50 MeV beam having 250 keV energy spread, 10 μm normalized emittance, and 100 μm rms spot size. However, the beam phase space may be conditioned by redistributing electrons in the phase space so that high energy electrons travel at large angles and low energy electrons at small angles. In this case all the electrons emit photons of the same energy in some direction (plot (c) in Fig. 1) and ICS peak brightness may reach the limit of a single-electron radiation. Collimation of emitted radiation at this angle would result in a significant increase in ICS source quality compared to the normal, unconditioned case.

In this manuscript we demonstrate the brightness of an ICS source as a function of the 6-dimensional electron distribution in the phase space. In addition, we show how it behaves for the simple uncorrelated electron beam with an observer located on z -axis.

6D WIGNER FUNCTION

First, we introduce the 6D Wigner function as an auto-correlation function of the radiated electric field to characterize the distribution of emitted photons in the phase space, based on the Quantum Mechanical Wigner function

* Work supported by the Laboratory Directed Research and Development (LDRD) program at LANL

[†] malyzhenkov@lanl.gov

PROGRESS ON THE MAGNETIC PERFORMANCE OF PLANAR SUPERCONDUCTING UNDULATORS *

M. Kasa[†], C. Doose, J. Fuerst, Y. Ivanyushenkov, and E. Gluskin, Advanced Photon Source, Argonne National Laboratory, Argonne, IL, USA

Abstract

One of the primary goals of the superconducting undulator (SCU) program at the Advanced Photon Source (APS) is to achieve a high quality undulator magnetic field without the need for magnetic shimming to tune the device. Over the course of two years, two SCUs were designed, manufactured, assembled, and tested at the APS. Both SCUs were one meter in length with a period of 1.8 cm. After magnetic measurements of the first undulator were completed, several design changes were made in order to improve the quality of the undulator magnetic field. The design modifications were implemented during construction and assembly of the second SCU. The details of the design modifications along with a comparison of the magnetic measurement results will be described.

INTRODUCTION

Several superconducting undulators (SCUs) have been constructed and tested at the Advanced Photon Source (APS). Two of these undulators were built to the same specifications and constructed two years apart. Lessons learned from the magnetic performance of the first undulator, referred to as SCU18-1, were used to modify the assembly of the second SCU, referred to as SCU18-2. The primary goal of the modifications to the second assembly was to improve the uniformity of the magnetic field quality in order to obtain phase errors below 5 degrees RMS over the entire operating range without the need for magnetic shimming. Both SCUs were designed and built to the specifications listed in Table 1.

Table 1: SCU18-1 and SCU18-2 Specifications

Parameter	Value
Cryostat length, m	2.06
Magnetic length, m	1.1
Undulator period, mm	18
Magnetic gap, mm	9.5
Beam vacuum chamber vertical aperture, mm	7.2
Undulator peak field, T	0.97
Undulator parameter, K	1.63
Operating Current, A	450

* Work supported by the U.S. Department of Energy, Office of Science, under Contract No. DE-AC02-06CH11357.

[†] kasa@anl.gov

MECHANICAL DESIGN

General Layout

The undulator field of an SCU is generated by energizing NbTi superconductor coils in grooves that are precisely machined on a magnetic core made of low carbon steel [1].

The quality of the magnetic field, i.e. repeatability of the peak magnetic field from one undulator period to another along the full device, strongly depends on the precision of grooves, quality of winding, and the uniformity of the magnetic gap. The high quality of APS SCU winding has already been reported [2]. In this paper we concentrate on the method of precise control of the SCU gap and results of the SCU performance when all three critical factors are well controlled. The specification of the machining tolerances of each core was determined through the use of simulation software where various geometrical errors were introduced and the effect on the phase errors could be determined [3]. Following winding and epoxy impregnation, two cores are assembled together and the magnetic gap is defined by precision-machined spacers, as shown in Fig. 1. The gap spacers are placed at locations where the poles extend outside of the body of the cores.

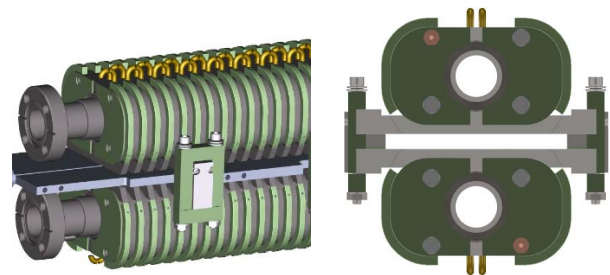


Figure 1: Assembly of two cores separated by the precision gap spacers.

Details of the Assembly of SCU18-1 and SCU18-2

After each core is manufactured, the flatness of the pole surface is measured to verify that it meets specifications. The flatness that is typically achieved after the final grinding process is 10 μm RMS with a peak-to-peak variation of 33 μm . The coil winding groove dimensions are also verified, typically within 50 μm and an RMS value of 15 μm . The periodicity is measured to verify there are no accumulated errors, typically 10 μm RMS and a maximum of 30 μm .

DEVELOPMENT OF THE METHOD FOR EVALUATION OF A SUPERCONDUCTING TRAVELING WAVE CAVITY WITH A FEEDBACK WAVEGUIDE

R. Kostin^{1,2†}, P. Avrakhov², A. Kanareykin^{1,2}, V. Yakovlev³, N. Solyak³

¹ also at St. Petersburg Electrotechnical University LETI, St. Petersburg, Russia

² also at Euclid Techlabs, Bolingbrook, IL

³ also at Fermilab, Batavia, IL

Abstract

Euclid Techlabs is developing a superconducting traveling wave (SCWT) cavity with a feedback waveguide [1] and has demonstrated a traveling wave at room temperature [2] in a 3-cell SCTW cavity [3]. A special method described in this paper was developed for cavity evaluation. It is based on an S-matrix approach. The cavity tuning procedure based on this method is described.

INTRODUCTION

The accelerating gradient in RF cavities plays a key role in high energy accelerators [4], since the cost of the project is highly dependent on the overall length of the machine. Euclid Techlabs proposed [1] a superconducting traveling wave cavity with a feedback waveguide which can provide 20% - 40% percent higher accelerating gradient than conventional standing wave cavities with the same surface fields [5].

The first approach to a TW cavity was a single cell cavity. It was manufactured to prove the feasibility of cleaning the feedback waveguide. The cavity was cleaned at Argonne National Lab and tested at Fermilab at the vertical test stand in liquid helium. A 26 MV/m accelerating gradient was reached [5], which is comparable to Tesla single cell cavities with the same treatment. This opened the way to build a next generation TW cavity – a 3-Cell SCTW cavity [3] to demonstrate operation in the TW regime in a superconducting cavity with a high gradient. Two 3-cell SCTW cavities were built. Traveling wave operation was successfully achieved at room temperature [2]. The cavity during room temperature testing is depicted in Fig. 1.

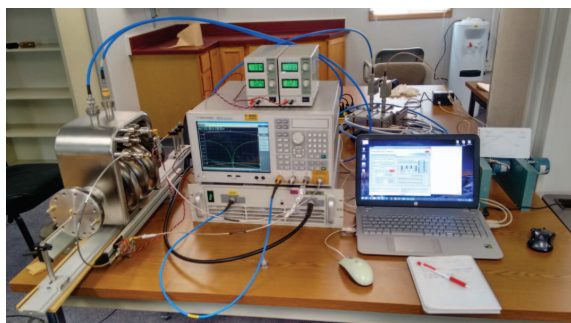


Figure 1: 3-Cell traveling wave niobium cavity room temperature test layout.

Waveguide stiffening is required for cryogenic high power tests because of the small bandwidth during the test. The welding process is almost finished; cavity processing and testing will be started before the end of the year 2016.

A special model based on the S-matrix approach was used for cavity development. It is faster, easier and more accurate. In some cases, it is not possible at all to analyze the cavity with finite element modeling (FEM) software. The model can also include such features as sensitivity to microphonics, Lorentz force, and waveguide deformation by a tuning element. An analytical model was built and used first for traveling wave adjustment in 1 coupler ring. The analytical model was checked with FEM simulation of a full 3D model which showed the same result and thus, verified the analytical model. The same method was used for the 2 coupler superconducting traveling wave cavity analysis. It was also successfully compared to a full 3D FEM simulation.

COUPLER TRAVELING WAVE RING

The method of evaluation of a traveling wave cavity with a feedback waveguide was started from the simplest case of a rectangular waveguide ring with one coupler. This model does not have any corrugated parts for particle acceleration but derivation of the required parameters for traveling wave adjustment becomes simpler. Particle accelerating sections can be inserted afterwards. Reflections introduced into the ring can be canceled by placing a reflecting element $\lambda/4 + N \cdot \lambda/2$ away from the corrugated section. The waveguide ring is depicted schematically in Figure 2.

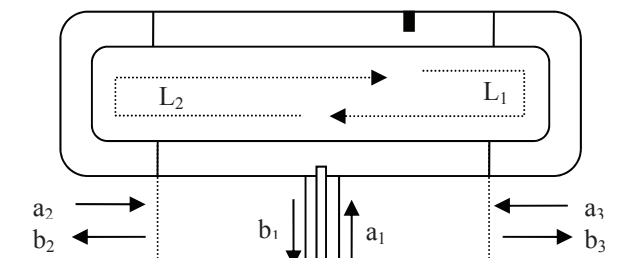


Figure 2: Schematic of the waveguide ring with a coupler and a reflection element.

The ring consists of a coax-waveguide transition, two 180 degree bends and a straight waveguide with a discontinuity. The analytical S-matrix forms of the elements can be found in [6]. Their S-matrices are shown below:

A MORE COMPACT DESIGN FOR THE JLEIC ION PRE-BOOSTER RING*

B. Mustapha[†] and P. Ostroumov[‡], Argonne National Laboratory, Argonne, IL, USA
 B. Erdelyi, Northern Illinois University, DeKalb, IL, USA

Abstract

The original design of the JLEIC pre-booster was a 3-GeV figure-8 synchrotron with a circumference of about 240 m. In the current baseline design, the 3-GeV pre-booster was converted into an 8-GeV booster of the same shape and size but using super-ferric magnets with fields up to 3 Tesla. In order to reduce the foot-print of the JLEIC ion complex, we have designed a more compact and cost-effective octagonal 3-GeV ring about half the size of the original design. At 3 GeV, the figure-8 shape is not required to preserve ion polarization; Siberian snakes with reasonable magnetic fields can be used for spin correction. As the ion collider ring requires higher injection energy, we propose to use the existing electron storage ring, which is part of the electron complex, as a large booster for the ions up to 12 GeV. The design optimization of the pre-booster, leading to a final octagonal ring design is presented along with preliminary beam simulation results.

INTRODUCTION

In an effort to lower the risk and reduce the footprint of the JLEIC ion accelerator complex, we have proposed an alternative design approach [1]. An essential part of the alternative approach is to replace the 8-GeV figure-8 booster of the current baseline design [2] with a more compact 3-GeV pre-booster ring and to use the electron storage ring (e-ring) as large ion booster up to 12 GeV or higher. The current 8-GeV booster was based on the original 3-GeV figure-8 pre-booster design [3] where super-ferric magnets [4] replaced the original room-temperature magnets. At 3 GeV, the figure-8 shape is not required for spin preservation as Siberian snakes with reasonable magnetic fields can be used. After a brief review of the original figure-8 pre-booster design, we present the design iterations for a race-track type ring which have led to the selection of an octagonal design with half the circumference of the original figure-8.

THE ORIGINAL FIGURE-8 DESIGN

The layout of the original 3-GeV accumulator and pre-booster ring is shown in figure 1. The design parameters are listed in table 1. The main requirements for this original design were to accumulate and accelerate ion beams from the linac for injection to a large booster. The design uses room-temperature magnets and the spin polarization is preserved by its figure-8 shape.

* This work was supported by the U.S. Department of Energy, Office of Nuclear Physics, under Contract No. DE-AC02-06CH11357 for ANL.

[†] Corresponding author: brahim@anl.gov

[‡] Now at MSU.

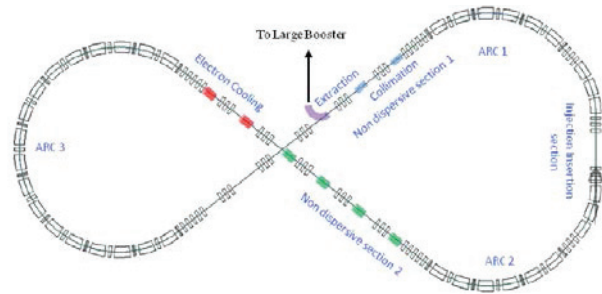


Figure 1: Layout of the original 3-GeV pre-booster.

Table 1: Design parameters of the original 3-GeV pre-booster.

Parameter	Value
Circumference, m	234
Maximum β_x , m	16
Maximum β_y , m	32
β_x at injection, m	14.9
Maximum dispersion, m	3.4
Normalized dispersion at injection	2.5
Tune in X	7.96
Tune in Y	6.79
Transition γ	5
Extraction γ (at 3 GeV)	4.22
Momentum compaction factor	0.04
Number of Quadrupoles	94
Quadrupole length, n	0.4
Quadrupole half aperture, cm	5
Maximum quadrupole field, T	1.1
Number of dipoles	36
Dipole bend radius, m	9
Dipole angle, deg	~ 14
Dipole full gap, cm	3
Maximum dipole field, T	1.5

AN ALTERNATIVE APPROACH FOR THE JLEIC ION ACCELERATOR COMPLEX*

B. Mustapha[†], P. Ostroumov[‡], A. Plastun and Z. Conway, ANL, Argonne, IL, USA,
V. Morozov, Y. Derbenev, F. Lin and Y. Zhang, JLab, Newport News, VA, USA

Abstract

The current baseline design for the JLab EIC (JLEIC) ion accelerator complex is based on a 280 MeV pulsed superconducting linac, an 8-GeV booster and a 20-100 GeV ion collider ring. We are considering an alternative design approach to lower the risk of the project and reduce the footprint of the ion complex. The proposed approach also includes the possibility of staging. In order to reduce the footprint of the ion complex, we propose to use a more compact 130 MeV linac, a compact 3-GeV pre-booster, and to consolidate the electron storage ring (e-ring) as a large booster for the ions. Considering the current parameters of PEP-II magnets, to be used for the e-ring, protons could reach 12 GeV. With new magnets, proposed for an alternative low-emittance design of the e-ring, the energy could reach 15 GeV. In these options, room-temperature magnets are used in the pre-booster and e-ring. The ion collider ring could be staged, first with room-temperature magnets for proton energy up to 60 GeV then later upgraded with either 3 T super-ferric magnets up to 100 GeV or with 6 T fully superconducting magnets up to 200 GeV. A brief description of the proposed alternative ion complex and a preliminary parameter study of the e-ring as an ion booster are presented. More detailed studies are underway to investigate the feasibility and evaluate the different options.

THE BASELINE DESIGN OF JLEIC

The layout of the current baseline design for the Jefferson Lab Electron-Ion Collider (JLEIC) [1] is shown in Fig. 1. The ion complex consists of a pulsed superconducting linac with 280 MeV proton energy, an 8-GeV booster ring and a 20-100 GeV collider ring. Both the booster and collider rings are based on 3 Tesla super-ferric magnets [2]. The electron complex consists of the existing CEBAF machine as a full-energy injector to a new storage ring at 3-10 GeV. The electron ring (e-ring) re-uses the magnets and RF system from the decommissioned PEP-II e+e- collider at SLAC.

* This work was supported by the U.S. Department of Energy, Office of Nuclear Physics, under Contract No. DE-AC02-06CH11357 for ANL and by Jefferson Science Associates, LLC under U.S. DOE Contract No. DE-AC05-06OR23177

[†] Corresponding author: brahim@anl.gov

[‡] Now at MSU

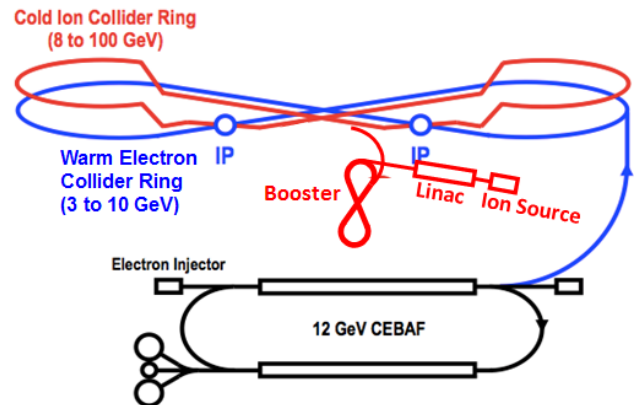


Figure 1: Layout of the current JLEIC baseline design.

MOTIVATIONS FOR AN ALTERNATIVE APPROACH

The main driving factors for considering an alternative design approach for the JLEIC ion complex are:

- Lower the risk of the project by using the proven technology of room-temperature (RT) where possible, with the possibility of upgrade with super-ferric (SF) or superconducting magnets (SC).
- Reduce the footprint of the ion complex for potential cost savings by using more compact linac and pre-booster ring, and consolidate the electron storage ring as large booster for the ions.
- Consider the possibility of staging the ion collider ring, first with RT magnets up to 60 GeV, then later with SF magnets up to 100 GeV or SC magnets up to 200 GeV.

THE PROPOSED ALTERNATIVE OPTION

The layout of the proposed alternative design is shown in Fig. 2. It consists of:

- A more compact 130 MeV linac [3].
- A more compact 3-GeV pre-booster using RT magnets [4]. At this energy, the figure-8 shape is not required, Siberian snakes with reasonable fields could be used for spin corrections.
- The e-ring as large ion booster, up to 12 GeV protons with PEP-II magnets or 15 GeV with new magnets.
- The ion collider ring with RT magnets could reach a proton energy of 60 GeV, or with 6 T SC magnets up to 200 GeV.

ACCOMPLISHMENTS OF THE HEAVY ELECTRON PARTICLE ACCELERATOR PROGRAM*

D. Neuffer[†], D. Stratakis, Fermilab, Batavia IL 60510, USA, M. Palmer, BNL, Upton, NY 11973, J-P Delahaye, SLAC, Menlo Park, CA 60439, USA, D. Summers, U. Miss., Oxford MS 38655, USA, R. Ryne, LBNL, Berkeley CA 94720, USA, M. A. Cummings, Muons, Inc.

Abstract

The Muon Accelerator Program (MAP) has completed a four-year study on the feasibility of muon colliders and on using stored muon beams for neutrinos. That study was broadly successful in its goals, establishing the feasibility of heavy lepton colliders (HLCs) from the 125 GeV Higgs Factory to more than 10 TeV, as well as exploring using a μ storage ring (MSR) for neutrinos, and establishing that MSRs could provide factory-level intensities of ν_e ($\bar{\nu}_e$) and $\bar{\nu}_\mu$ (ν_μ) beams. The key components of the collider and neutrino factory systems were identified. Feasible designs and detailed simulations of all of these components have been obtained, including some initial hardware component tests, setting the stage for future implementation where resources are available and the precise physics goals become apparent.

INTRODUCTION

Initial concepts for muon colliders and muon storage rings were proposed in ~1980[1-4], and research toward these concepts intensified in the 1990's in the search for feasible high-energy accelerator projects. In 2011, muon accelerator R&D in the United States was consolidated into a single entity, the Muon Accelerator Program (MAP) [5]. The purpose of MAP was to perform R&D in heavy electron (μ) accelerator technologies and to perform design & simulation to demonstrate the *feasibility* of concepts for neutrino factories and muon colliders [6,7,8]. MAP established that general feasibility, and awaits the development of physics motivations before proceeding to full implementation. The design studies have been accompanied by technology R&D, establishing the feasibility of key scenario components. Though MAP did not include detailed engineering studies, the design studies were performed with an awareness of gradient and field limits, and space requirements for hardware, etc. The following highlights some key accomplishments under MAP in design concepts for muon-based accelerators for neutrino factories and muon colliders.

DESIGN OVERVIEW

The key components of collider and neutrino factory systems were identified and are displayed in block diagram form in Figure 1. These are a high-intensity proton source, a multi-MW target and transport system for π capture, a front end system for bunching, energy compression and initial cooling of μ 's, muon cooling systems

* supported by Fermi Research Alliance, LLC under Contract No. De-AC02-07CH11359 with the U. S. Department of Energy.

[†] neuffer@fnal.gov

to obtain intense μ^+ and μ^- bunches, acceleration up to multi-TeV energies, and a collider ring with detectors for high luminosity collisions. For a neutrino factory a similar system could be used but with a racetrack storage ring for ν production and without the cooling needed for high luminosity collisions. The Proton Driver, Target, Front End, and Acceleration linac, are common to both facilities.

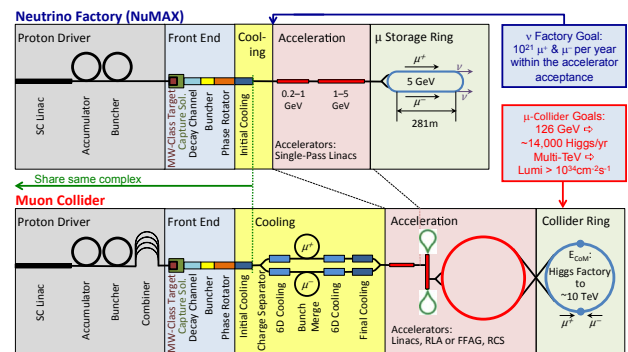


Figure 1: Block diagram of neutrino factory and muon collider facilities, as studied under MAP.

PROGRESS IN MUON ACCELERATOR DESIGN UNDER MAP

Though MAP existed for only 4 years, there has been tremendous progress in the design concepts. Some highlights include:

Proton Driver: Under MAP, designs were developed for the accumulator and compressor rings of the Proton Driver, based on the expected parameters of the Project-X linac [9]. Potential instabilities were analyzed and initial studies were performed of injection stripping and of the beam to target delivery system for the HLC design. Meanwhile, JPARC has directly demonstrated that a proton source can operate at MAP-required parameters. A proton driver based on a JPARC-style linac + rapid-cycling synchrotron is an attractive possibility [10].

Target & Front End: MAP has explored several target designs, including a design based on a solid carbon target and on a liquid Mercury target [11, 12]. The target parameters have been optimized [13]. The Front End designs use a novel rf buncher and phase-energy rotator to form the beam into a train of μ^+ and μ^- bunches that can be cooled, and accelerated by downstream systems [13, 14]. An energy deposition control system using a chicane and downstream absorber was also invented [15, 16].

Cooling: Muon cooling designs matured greatly under MAP. Figure 2 shows how the horizontal and vertical emittances evolve as the muons travel through the cooling

CONSIDERATIONS ON ENERGY FRONTIER COLLIDERS AFTER LHC*

V. Shiltsev[#], Fermilab, Batavia, IL 60510, USA

Abstract

Since 1960's, particle colliders have been in the forefront of particle physics, 29 total have been built and operated, 7 are in operation now. At present the near term US, European and international strategies of the particle physics community are centered on full exploitation of the physics potential of the Large Hadron Collider (LHC) through its high-luminosity upgrade (HL-LHC). The future of the world-wide HEP community critically depends on the feasibility of possible post-LHC colliders. The concept of the feasibility is complex and includes at least three factors: feasibility of energy, feasibility of luminosity and feasibility of cost. Here we overview all current options for post-LHC colliders from such perspective (ILC, CLIC, Muon Collider, plasma colliders, CEPC, FCC, HE-LHC) and discuss major challenges and accelerator R&D required to demonstrate feasibility of an energy frontier accelerator facility following the LHC. We conclude by taking a look into ultimate energy reach accelerators based on plasmas and crystals, and discussion on the perspectives for the far future of the accelerator-based particle physics. This paper largely follows previous study [1] and the presentation given at the ICHEP'2016 conference in Chicago [2].

INTRODUCTION

Colliding beam facilities which produce high-energy collisions (interactions) between particles of approximately oppositely directed beams have been on the forefront of particle physics for more than half a century and twenty nine reached operational stage [3]. Their energy has been on average increasing by a factor of 10 every decade until about the mid-1990's. Notably, the hadron colliders were 10-20 times more powerful. Since then, following the demands of high energy physics (HEP), the paths of the colliders diverged: to reach record high energies in the particle reaction the Large Hadron Collider was built at CERN, while new $e+e-$ colliders called "particle factories" were focused on detailed exploration of phenomena at much lower energies. The Tevatron, LEP and HERA established the Standard Model of particle physics. The current landscape of the high energy physics is dominated by the LHC. The next generation of colliders is expected to lead the exploration of the smallest dimensions beyond the current Standard Model.

While the development of energy frontier colliders over the past five decades initiated a wide range of innovation in accelerator physics and technology which

resulted in 100-fold increase in energy (for both hadron and lepton colliding facilities) and 10^4 - 10^6 fold increase of the luminosity, the progress in the maximum c.o.m. energy has drastically slowed down since the early 1990's and the lepton colliders even went backwards in energy to study rare processes – see, e.g., Fig.1 in [4]. Moreover, the number of the colliding beam facilities in operation has dropped from 9 two decades ago to 7 now (2016). The future of accelerator-based HEP beyond LHC has been recently debated by several authors in [4-7, 3] and many technical details discussed in the collective book "Challenges and Goals for Accelerators in the XXI Century" [8]. Here we bring an economical (financial) perspective to the discussion on feasible colliders beyond the LHC and show that options based on traditional acceleration technologies are very much limited. Only "... technological quantum leaps...will drive the long-term progress of the field. We can expect that these ambitions and far sighted R&D programmes in accelerator technology will redefine the field of high-energy physics in the XXI century..." (M.Mangano, [8], p.21). In general, the discussion on the "beyond the LHC" energy frontier accelerators comes to the question of the right balance between the physics reach of the future facilities and their feasibility which usually assumes the feasibility of their energy reach (whether it is possible to reach the design c.o.m. energy), feasibility of the performance (how challenging is the declared design luminosity) and cost feasibility (is it affordable to build and operate?). While the first two criteria (energy and performance reach) are relatively easy to address on the base of the current state-of-the-art accelerator technology (of, e.g., normal- and superconducting magnets, RF, etc) and beam physics, the feasibility of the cost requires analysis of both the perspective available resources and the facility cost range. In the analysis below we will use the cost of LHC - about 10B\$ at today's prices - as a reference for a globally affordable future facility and compare it with the resources required to build "beyond the LHC" colliders, including "near future" facilities with possible construction start within a decade - such as the international $e+e-$ linear collider in Japan (ILC) [9] and circular $e+e-$ colliders in China (CepC) [10] and Europe (FCC-ee) [11]; "future" colliders with construction start envisioned 10-20 years from now – such as linear $e+e-$ collider at CERN (CLIC) [12], muon collider [13], and circular hadron colliders in China (SppC) [10], Europe (HE-LHC [14] and FCC-pp [11]) and USA (VLHC [15]); and an ultimate "far future" colliders with time horizon beyond the next two decades based on beam-plasma [16], laser-plasma [17] and crystal-plasma [18, 4] acceleration technologies.

*Fermi Research Alliance, LLC operates Fermilab under contract No. DE-AC02-07CH11359 with the U.S. Department of Energy
#shiltsev@fnal.gov

BEAM EXTRACTION FROM THE RECYCLER RING TO P1 LINE AT FERMILAB*

M. Xiao[†], Fermilab, Batavia, IL 60540, USA

Abstract

The transfer line for beam extraction from the Recycler ring to P1 line provides a way to deliver 8 GeV kinetic energy protons from the Booster to the Delivery ring, via the Recycler, using existing beam transport lines, and without the need for new civil construction. It was designed in 2012. The kicker magnets at RR520 and the lambertson magnet at RR522 in the RR were installed in 2014 Summer Shutdown, the elements of RR to P1 Stub (permanent quads, trim quads, correctors, BPMs, the toroid at 703 and vertical bending dipole at V703 (ADCW) were installed in 2015 Summer Shutdown. On Tuesday, June 21, 2016, beam line from the Recycler Ring to P1 line was commissioned. The detailed results will be presented in this report.

INTRODUCTION

In the post-Nova era at Fermilab complex, shown in Fig. 1, the protons are directly transported from the Booster ring to the Recycler Ring (RR) rather than the Main Injector (MI) [1]. For Mu2e and g-2 projects, a new beamline, shown in RED in Fig. 1, was designed in 2012 [2] and completed in the installation in 2015. This new beamline provides a way to deliver 8 GeV kinetic energy protons from the Booster to the Delivery ring, via the Recycler, using existing beam transport lines (P1, P2 line), and without the need for new civil construction. Fig. 2 presents the schematic layout of the transfer line from the Recycler Ring to the P1, P2 line. Shown in Blue in Fig. 2 are the kicker magnets RRRICK and the lambertson magnet RRLAM in the RR, which were installed in 2014 Summer Shutdown.

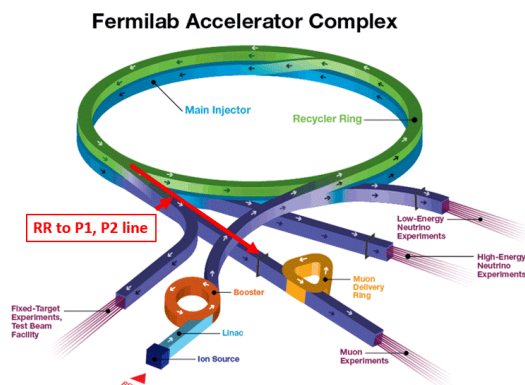


Figure 1: Fermilab Complex.

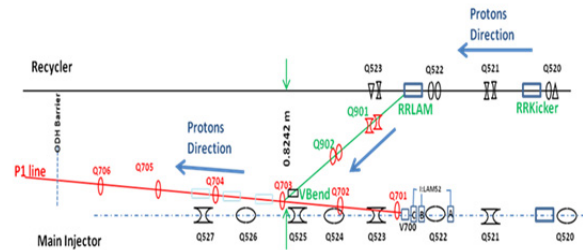


Figure 2: Schematic layout of the transfer line.

The Stub from the RR to P1 line (shown in green in Fig. 2), including permanent quads, trim quads, correctors, BPMs, the toroid at 703 and vertical bending dipole at V703 (ADCW), was installed in 2015 Summer Shutdown. A new 2.5 MHz RF system, which will be used to rebunch a 4×10^{12} of protons from Booster into 4 bunches of 10^{12} protons in the Recycler, is being installed during 2016 Summer Shutdown. The commissioning for the beam extraction was done at the end of June 2016, the protons were extracted successfully from the Recycler ring to P2 line. The detailed results will be presented in this report.

DEVICES AND PARAMETER SCANS

The main devices and their best values for RR to P1 line extraction are shown in Fig. 3. The parameter R:KPS5A is the voltage for the kicker magnets RRRICK, R:LAM52 is the current for the lambertson magnet and R:V703 is the current for the vertical bending. Trim dipoles R:VT701 and R:HT702, trim quads R:QT701 and R:QT702 were not used at first run. These best values left in the parameter page R65 are based on the parameter scan for R:KPS5A and R:LAM52.

```

PC: R65 RR30 Extron Param:New(P1-CU20) (02)
R65 RR P1 STUB SET D/A A/D Com-U PTools
-<FTP>+ *SA X-A/D X=TIME Y=R:DCCT ,I:TOR714,R:KPS5A
COMMAND BL-- Eng-U I= 0 I= 0 , 0 , 0
-<10>+ r_93 AUTO F= .36 F= .4 , .4 , 4
kickers timers correctors diagnost power supp RR_9TUNING

-R:KPS5A RR->DR Xfer Kicker 2.1 .295 kV ...+
-R:LAM52 LAM52 MEASURED I 588 587.2 Amps ..
-R:VT701 RR-P1 Vertical Trim @ 701 0 .003 Amps ET
-R:HT702 RR Horz Trim @ 702 0 -.018 Amps ET
-R:QT701 RR-P1 Quad Trim @ 701 0 .058 Amps E.
-R:QT702 RR-P1 Quad Trim @ 702 0 -.012 Amps ET
-R:V703 V703 MEASURED I 486.2 487 Amps ..
    
```

Figure 3: Best values of the devices for beam extraction.

The scans were done with the changes of the values of R:KPS5A and R:LAM52, by monitoring 3 loss monitor

*Work supported by U.S. Department of Energy under contract No. DE-AC02-76CH03000.

[†] meiqin@fnal.gov

SOLID-STATE PULSED POWER SYSTEM FOR A STRIPLINE KICKER

Neal Butler, Fred Niell, Marcel Gaudreau, Michael Kempkes, Rebecca Simpson,
Matthew Munder-ville, Diversified Technologies, Inc., Bedford, MA, USA

Abstract

Diversified Technologies, Inc. (DTI) has designed, built, and demonstrated a prototype pulse amplifier for stripline kicker service capable of less than 5 ns rise and fall times, 5 to 90 ns pulse lengths, peak power greater than 13.7 MW at pulse repetition rates exceeding 100 kHz, and measured jitter under 100 ps. The resulting pulse is precise and repeatable, and will be of great interest to accelerator facilities requiring electromagnetic kickers. The pulse generator is based on the original specifications for the NGLS fast deflector. DTI's planar inductive adder configuration uses compensated-silicon power transistors in low inductance leadless packages with a novel charge-pump gate drive to achieve unmatched performance. The prototyping efforts guided the design of the full unit, however the magnetics and transmission line effects of the system were not revealed until the entire unit was assembled. The unit was brought to LBNL, compared with other researcher's efforts, and was judged very favorably. A number of development prototypes have been constructed and tested, including a successful 18.7 kV, 749 A unit. The modularity of this design will enable configuration of systems to a wide range of potential applications in both kickers and other high speed requirements, including high performance radars, directed energy systems, and excimer lasers.

INTRODUCTION

Diversified Technologies, Inc. (DTI) recently completed an SBIR effort under a grant from the US Department of Energy to research kicker drivers for the Next Generation Light Source (NGLS) injectors. The NGLS specification required a 10 kV, 200 Ampere pulse into 50 Ω , with a 2 ns rise time (10-90%), a highly repeatable flattop with a pulsewidth from 5-40 ns, and a fall time less than 1 μ s (defined as down to 10^{-4} of the peak value). DTI chose a novel derivative of the classic inductive adder circuit which has demonstrated not only the required pulse rise times required by NGLS, but also the pulses required by the Advanced Light Source (ALS) upgrade at Lawrence Berkeley National Lab (LBNL), and a number of other commercial, medical, and other non-accelerator-based applications.

DESIGN

Inductive adders have been used for decades in the accelerator physics community to create ultra-high voltage, short rise time deflection pulses in beams. The inductive adder approach can be thought of as a number of pulse transformers with the primary windings in parallel and the

secondary windings in series. Such approaches are not typically used in high-PRF applications, and have not shown the fast rise times required for the NGLS kicker. DTI's improvements to the classic inductive adder design include:

- Multiple cores on a single circuit board
- Secondary return current path on the circuit board
- State-of-the-art 650 V rated compensated MOSFETs
- Low inductance leadless flat packages
- Push-pull double voltage drive
- Low inductance backswing clamp
- High performance low delay charge pump gate drives

Re-arranging the circuitry of the classic inductive adder by placing several cores and drive circuits on a single circuit board allows the secondary return current to flow through the ground plane on the circuit board, which minimizes the secondary stray inductance (Figure 1).

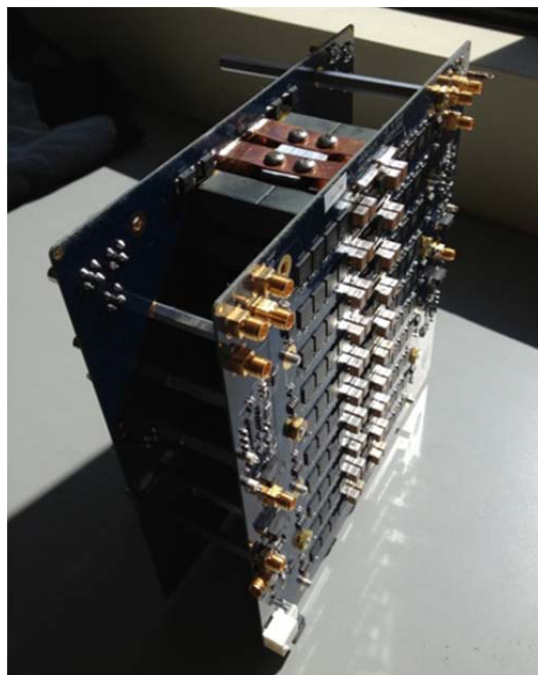


Figure 1: Dual PCB high speed pulser kicker driver system developed by DTI for the NGLS program. This kicker uses commodity 650 V transistors to switch nearly 17 MW, 700 A in 5 ns.

The best figure of merit power transistors are 650 V rated compensated silicon MOSFETs. These are available

1: Circular and Linear Colliders

T12 - Beam Injection/Extraction and Transport

QUANTIFICATION OF OCTUPOLE MAGNETS AT THE UNIVERSITY OF MARYLAND ELECTRON RING*

H. Baumgartner[†], S. Bernal, I. Haber, T. Koeth, D. Matthew, K. Ruisard, M. Teperman,
B. Beaudoin, University of Maryland, College Park, USA

Abstract

It is particularly important to manage beam loss in high intensity accelerators, because the large beam current can result in heating, damage, and activation of components. A lattice of strong nonlinear magnets is predicted by theory to damp resonances while maintaining dynamic aperture. Results of rotating coil measurements and magnetic field scans will be presented, quantifying the multipole moments and fringe fields of PCB octupoles in UMER's nonlinear lattice experiments.

INTRODUCTION

The University of Maryland Electron Ring (UMER) is a 10 keV, 11.52 meter electron ring for the study of intense beam dynamics. UMER is embarking on a new effort to investigate integrable nonlinear optics, which is a promising area of research in high-intensity ring design [1]. To this end, a quasi-integrable octupole lattice will be incorporated into the existing FODO ring structure [2]. Currently, the entire UMER ring utilizes air-core dipole and quadrupole magnets constructed from flexible printed circuits (Fig. 1). These PCBs are inexpensive to manufacture and can be made with a quick turnaround time. The 2oz copper thickness can easily sustain currents of 2A with no additional cooling, or up to 10A with water cooling. The thin profile of the flexible PCB opens up the possibility of stacking multiple PCBs into one mount, or even utilizing the multi-layer capabilities of circuit board manufacturing to make a single PCB with different magnets on different PCB layers.

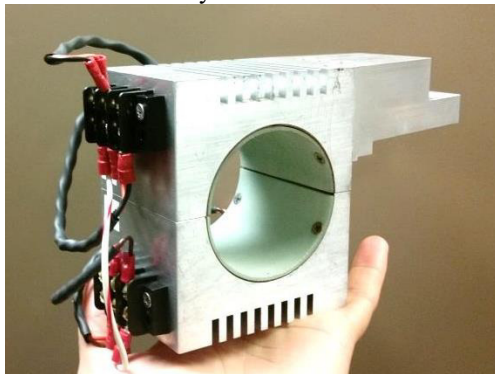


Figure 1: Assembled PCB magnet showing the aluminium housing and G10 liner. The flex PCB is underneath the liner. The magnet length is 2.3" and the bore diameter is 2.2".

A magnet is comprised of two PCBs that form its top and bottom half. Each magnet half is mounted into an aluminum housing, aligned with pins and held in place with a formed G10 liner. The two halves of the magnet are then placed around the beam pipe and bolted together.

Recently, octupole PCB magnets were designed for the UMER nonlinear optics project [3]. This paper presents the results of numerical calculations and empirical measurements of the PCB octupole magnets.

MAGNET DESIGN

The magnetic multipole expansion is given by [4] is

$$B_y + iB_x = \sum_{n=1} (b_n + ia_n) \left(\frac{x+iy}{r_0} \right)^{n-1} \quad (1)$$

Multipoles can be created by an angularly dependent current distribution given by Eq. 2 [4], where z is the longitudinal coordinate, a is an adjustable parameter, L is magnet length and n is the pole order.

$$\sin(n\theta) = 1 - \left(\frac{2z}{aL} \right)^2 \quad (2)$$

In the UMER PCB magnets, this azimuthally varying current distribution is achieved by creating spiral traces of varying density and length, as shown in Figure 2. Conductors parallel to the beam axis, forming the diamond shape, contribute to the field, while conductors perpendicular to the beam axis are simply return traces.

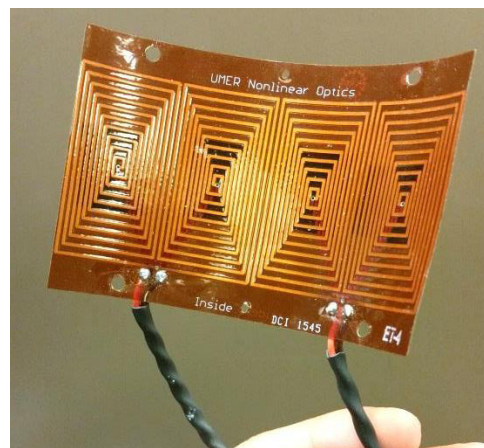


Figure 2: The flex PCB containing the windings of the octupole magnet.

Because of the small aspect ratio of these magnets, they are dominated by fringe fields. As such, it is especially important to characterize the magnet with good longitudinal resolution.

* Supported by DOE-HEP and the NSF Accelerator Science Program.

[†] heidib@umd.edu

EXPERIMENTAL PLANS FOR SINGLE-CHANNEL STRONG OCTUPOLE FIELDS AT THE UNIVERSITY OF MARYLAND ELECTRON RING *

K. Ruisard[†], H. Baumgartner, B. Beaudoin, I. Haber, M. Teperman, T. Koeth

Institute for Research in Electronics and Applied Physics, University of Maryland College Park, MD, USA

Abstract

Nonlinear quasi-integrable optics is a promising development on the horizon of high-intensity ring design. Large amplitude-dependent tune spreads, driven by strong nonlinear magnet inserts, lead to decoupling from incoherent tune resonances. This reduces intensity-driven beam loss while quasi-integrability ensures a well-contained beam. In this paper we discuss on-going work to install and interrogate a long-octupole channel at the University of Maryland Electron Ring (UMER). This is a discrete insert that occupies 20 degrees of the ring, consisting of independently powered printed circuit octupole magnets. Transverse confinement is obtained with quadrupoles external to this insert. Operating UMER as a non-FODO lattice, in order to meet the beam-envelope requirements of the quasi-integrable lattice, is a challenge. We discuss efforts to match the beam and optimize steering solutions. We also discuss our experiences operating a distributed strong octupole lattice.

INTRODUCTION

Beam resonances that drive particle losses and beam halo present a significant challenge for high intensity accelerators, limiting beam current due to risk of damage and/or activation. While Landau damping can control resonant effects, the addition of weak nonlinearities to a linear lattice can introduce resonant islands and chaotic phase space orbits, which reduce dynamic aperture and lead to destructive particle loss. Theory predicts that lattices with one or two invariants and sufficiently strong nonlinear elements should suppress tune and envelope resonances without loss of stable phase space area [1].

The small-angle Hamiltonian for transverse particle motion in the normalized frame is given by

$$H_N = \frac{1}{2} (p_{x,N}^2 + p_{y,N}^2 + x_N^2 + y_N^2) + \kappa U(x_N, y_N, s)$$

with general nonlinear contribution U . (Normalized coordinates are $x_N = \frac{x}{\sqrt{\beta(s)}}$ and $p_N = p\sqrt{\beta(s)} - \frac{\alpha x}{\sqrt{\beta(s)}}$)

In order for U to be an invariant quantity and for H_N to be conserved, $\beta_x = \beta_y$ inside the nonlinear element and the nonlinear element strength parameter $\kappa(s)$ depends on $\beta(s)$. In particular, for an octupole element $\kappa \propto \frac{1}{\beta(s)^3}$. External focusing is provided by a linear lattice, which should reduce to an integer π phase advance between nonlinear inserts, as depicted in Fig. 1.

* Funding for this project and travel is provided by DOE-HEP, NSF GRFP and NSF Accelerator Science Program

[†] kruisard@umd.edu

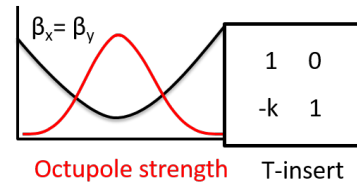


Figure 1: Simple quasi-integrable system: FOFO focusing with nonlinear insert.

Parallel work at the IOTA ring [2] will test a fully integrable nonlinear solution. The focus of the UMER nonlinear optics program is on the quasi-integrable case of the octupole lattice (with 1 invariant of motion), with the goal of experimentally observing transverse stability and halo mitigation.

EXPERIMENT

UMER is an 11.52 m circumference ring with a dense FODO lattice of printed circuit magnets (72 quads, with cell length 32 cm). The arrangement of quadrupoles in the standard UMER lattice can be seen in Fig. 2. All UMER magnets are flexible printed circuit boards (PCBs). The first generation of PCB octupoles for nonlinear optics experiments have been manufactured and characterized [3].

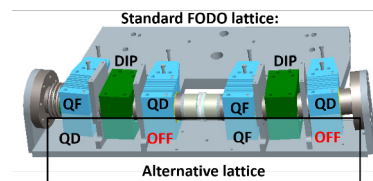


Figure 2: 20° of UMER, consisting of 2 dipoles and 4 quadrupoles in a FODO arrangement. A custom section is being designed to accommodate a single long octupole mount.

To meet the requirements of a quasi-integrable lattice as described above, UMER must operate as a non-FODO lattice. The nonlinear insert will occupy a single 20° section of the ring, with quadrupole strengths modified to obtain envelope and tune requirements. Previous flexibility of the UMER lattice has been demonstrated in the alternative lattice, which uses a lengthened FODO cell of 64 cm [4]. The UMER quadrupoles are each individually powered with unique polarity switches, allowing for any imaginable combination of families and lattice functions.

Characterization of the "single-channel" octupole lattice will be made monitoring beam loss and profile evolution of

SIMULATIONS OF SPACE CHARGE NEUTRALIZATION IN A MAGNETIZED ELECTRON COOLER

James Gerity, Peter M. McIntyre, Texas A&M University, College Station, Texas

David Leslie Bruhwiler, Christopher Hall, RadiaSoft LLC, Boulder, Colorado

Vince Jan Moens, EPFL, Lausanne, Chong Shik Park, Giulio Stancari, Fermilab, Batavia, Illinois

Abstract

Magnetized electron cooling at relativistic energies and Ampere scale current is essential to achieve the proposed ion luminosities in a future electron-ion collider (EIC). Neutralization of the space charge in such a cooler can significantly increase the magnetized dynamic friction and, hence, the cooling rate. The Warp framework is being used to simulate magnetized electron beam dynamics during and after the build-up of neutralizing ions, via ionization of residual gas in the cooler. The design follows previous experiments at Fermilab as a verification case. We also discuss the relevance to EIC designs.

INTRODUCTION

The nuclear physics community has identified the construction and operation of a high-luminosity polarized electron-ion collider (EIC) as a top priority in answering pressing questions about the structure of nuclear matter [1]. In the United States, the design of both Jefferson Lab's JLEIC [2] and Brookhaven's eRHIC [3] rely on electron cooling to reach their target luminosity. The novel strategies these projects employ for high-energy cooling (bunched cooling and coherent cooling, respectively) are promising, but also represent substantial R&D risk, motivating detailed study of possible improvements to DC electron cooling at intermediate energies. In particular, strong magnetization of the electron beam enhances cooling [4] by transverse confinement of electrons, so that the Coulomb interactions with the ion beam effectively only see the longitudinal degree of freedom. This enhancement is useful up to a "drift velocity" stability limit that shears the beam apart due to the combined effects of magnetization and strong space-charge, which scales with $\vec{E}_{s.c.} \times \vec{B}$. If the electron beam space charge is neutralized, this limit can be removed, enabling the use of stronger magnetization and higher electron beam current. A previous proposal [5] makes the case for using an intense beam of neutralized and magnetized electrons for cooling in an EIC.

IONIZATION

Warp includes an Ionization class that handles ionization interactions between arbitrary species, producing arbitrary secondaries. The implementation in the most recent version uses the total ionization cross-section when randomly deciding if an ionization occurs between particles on any particular check. A full treatment of these interactions necessitates the use of differential cross-

incident and emitted species as well as the angle of emission, as described in [6] and [7].

To this end, an extended Ionization class has been developed as part of rswarp [8] to allow for this more complete description of ionization physics. The extended class allows the user to specify the energy distribution of emitted species as arbitrary functions of incidence parameters. Also included is an implementation for sampling the differential cross-section described in [6, 7] using an algorithm originally developed for XOOPIIC [9]. Several of the solvers included with Warp do not include native routines for exporting particle and field data for offline analysis, and the rswarp module also includes classes for exporting these data in a format compliant with the OpenPMD standard [10].

PRELIMINARY RESULTS

A validation case* was simulated in the form of a 10 mA beam of 116 keV electrons traveling over a 1 m drift with a periodic field constraint on the longitudinal boundaries. The beam was generated with a transverse KV distribution and Gaussian velocity distribution with $\Delta p/p = 1e-3$. The electron beam spatial profile is shown in Fig. 1. All species were absorbed at the boundaries of the computational domain.

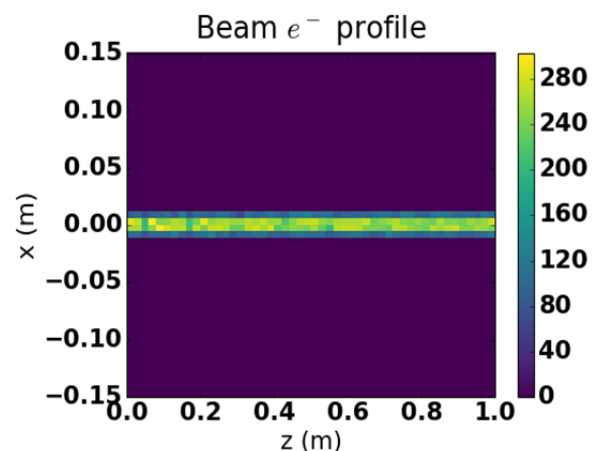


Figure 1: Beam profile at 0.5 μ s, binned by macroparticle count. The single-pass beam is not noticeably disrupted by its interaction with the background gas.

The beam was simulated both with and without ionization of a background H_2 gas enabled, and the resulting beam self-fields were compared to assess the neutralizing effect of the ionized gas (see Fig. 2). Ionization caused by emitted secondary electrons was not considered in the interest of simulation runtime. As shown in Fig. 3, fast

* Full source code for this simulation is freely available as part of the rsc cooler repository [11]. See the *10mA_DC_ionization* example.

AN ACCURATE AND EFFICIENT NUMERICAL INTEGRATOR FOR PAIR-WISE INTERACTION

A. Al Marzouk*, B. Erdelyi, Northern Illinois University, DeKalb, IL 60115, USA

Abstract

We are developing a new numerical integrator based on Picard iteration method for Coulomb collisions. The aim is to achieve a given prescribed accuracy most efficiently. The integrator is designed to have adaptive time stepping, variable order, and dense output. It also has an automatic selection of the order and the time step. We show that with a good estimation of the radius of convergence of the expansion, we can obtain the optimal time step size. We also show how the optimal order of the integration is chosen to maintain the required accuracy. For efficiency, particles are distributed over time bins and propagated accordingly.

INTRODUCTION

Many numerical integrators exist to solve the ordinary differential equations (ODEs) of the n-body problem. The goal of any numerical integrator is to achieve a given prescribed accuracy most efficiently. The main parameters controlled to accomplish this goal are the time step size and the order of the integration. Accuracy is usually attained by using either a very small time step size or a very high order, and both parameters are kept fixed during the simulation. Hence, the available integrators face efficiency challenges while trying to maintain accuracy.

Aiming to achieve both accuracy and efficiency, we developed our numerical integrator to be adaptive, variable order and with dense output. The integrator is proposed to deal with the electrostatic n-body problem. It is based on Picard iteration method combined with differential algebra (DA) [1]. The DA is a powerful tool to deal with ODEs since its structure is based on truncated power series algebra (TPSA) with well defined basic and analytic operations [2]. It has been proven that numerical methods based on Picard iteration can be competitive when implemented with the advanced differential algebra [3]. Here, we present features of our integrator that enable accomplishing accuracy and efficiency with some examples.

THE NUMERICAL INTEGRATOR

Our Picard-based numerical integrator is adaptive, variable order with dense output. Adaptive variable order means that it uses a time step that is as large as possible while varying the order. This allows to maintain efficiency by reducing the order when a small time step is required, and to attain accuracy by increasing the order if a large time step is allowed. This adaptivity was shown to be the most efficient way to achieve the required accuracy [4]. Time stepping is performed using time bins where each particle

is propagated with the appropriate time step size. Particles' time step sizes are automatically selected to increase efficiency. The dense output generated by the integrator is important for computations efficiency of time stepping, especially in the very high accuracy regime in certain applications.

System of Equations

Our integrator deals with a system of ODEs (1) that we derived from a net Coulomb force of all the particles in the system. For particle i , there are six differential equations, three for position derivatives, and three for momentum derivatives. Therefore, for N particles, we have $6N$ ODEs to be integrated. Particles can be non-relativistic as well as relativistic.

$$\frac{d\hat{Y}_i}{d\hat{t}} = \left(\frac{dx_i}{d\hat{t}}, \frac{dy_i}{d\hat{t}}, \frac{dz_i}{d\hat{t}}, \frac{d\hat{p}_{x_i}}{d\hat{t}}, \frac{d\hat{p}_{y_i}}{d\hat{t}}, \frac{d\hat{p}_{z_i}}{d\hat{t}} \right) \quad (1)$$

where:

$$\frac{dx_i}{d\hat{t}} = \hat{v}_{x_i} = \frac{\hat{p}_{x_i}}{\sqrt{f_i^2 + \hat{p}_{x_i}^2 + \hat{p}_{y_i}^2 + \hat{p}_{z_i}^2}},$$

$$\frac{d\hat{p}_{x_i}}{d\hat{t}} = \frac{q n_i}{mc^2} \left[\frac{q}{4\pi\epsilon_0} \sum_{\substack{j=1 \\ j \neq i}}^N \frac{n_j (x_i - x_j)}{\gamma \left[(x_i - x_j)^2 + (y_i - y_j)^2 + \gamma^2 (z_i - z_j)^2 \right]^{3/2}} \right],$$

$\frac{dy_i}{d\hat{t}}$ and $\frac{dz_i}{d\hat{t}}$ have the same form as $\frac{dx_i}{d\hat{t}}$. $\frac{d\hat{p}_{y_i}}{d\hat{t}}$ and $\frac{d\hat{p}_{z_i}}{d\hat{t}}$ are similar to $\frac{d\hat{p}_{x_i}}{d\hat{t}}$.

$$\hat{\mathbf{p}} = \frac{\mathbf{p}}{mc}, \quad \hat{t} = tc, \quad f_i = \frac{m_i}{m}, \quad n_i = \frac{q_i}{q}, \quad i = 1, 2, \dots, N$$

m = mass of particle, q = charge of particle, and c = speed of light.

In case there is an external field (electric and/or magnetic), the components of $\frac{q n_i}{mc^2} (\mathbf{E} + c\mathbf{v} \times \mathbf{B})$ will be added to the the respectful components of the momentum derivatives $\frac{d\hat{\mathbf{p}}}{d\hat{t}}$.

Optimal Time Step Size and Optimal Order

Á. Jobra and M. Zou presented two main requirements for the optimal selection of the time step size and the order [5]. The integrator must have a truncation error of the order of a given prescribed accuracy, and it should use the minimum total number of arithmetic operations. In order to meet these requirements, [5] provided a theorem for the optimal selection of the time step size h and the order p up to which Taylor series has to be computed. According to the

* aalmarzouk@niu.edu

IMPLEMENTING THE FAST MULTIPOLE BOUNDARY ELEMENT METHOD WITH HIGH-ORDER ELEMENTS

A. Gee*, B. Erdelyi†

Physics Dept., Northern Illinois University, DeKalb, IL 60115, USA

Abstract

The next generation of beam applications will require high-intensity beams with unprecedented control. For the new system designs, simulations that model collective effects must achieve greater accuracies and scales than conventional methods allow. The fast multipole method is a strong candidate for modeling collective effects due to its linear scaling. It is well known the boundary effects become important for such intense beams. We implemented a constant element fast boundary element method (FMBEM) [2] as our first step in studying the boundary effects. To reduce the number of elements and discretization error, our next step is to allow for curvilinear elements. In this paper, we will present our study on a quadratic and a cubic parametric method to model the surface.

INTRODUCTION

Beam applications have grown in the last few decades as has the need for precise control, particularly for high-intensity beams. However, collective and boundary effects become significant at such intensities. Conventional lattices are insufficient to prevent undesirable behavior. To facilitate future lattice designs, simulation models such as N -body solvers are being developed for large scale problems. In particular, the fast multipole method (FMM) is a strong candidate as a N -body solver due to its $O(N)$ scaling.

It is well known effects due to the beam pipe become important for high-intensity beams. To include boundary conditions for complicated structures, the boundary element method (BEM) has shown excellent results in various fields. However, the dense system matrix of size M can lead to $O(M^3)$ scaling in the worst scenario. The FMM has been used to accelerate the BEM, improving the scaling significantly [1]. In previous work, we combined our FMM module with a constant element BEM [2]. However, our results suggested the accuracy is strongly limited by the discretization error from flat panel elements. Parametric curvilinear elements are expected to improve the accuracy and performance of the FMBEM. We evaluated an analytical quadratic patch [3] and a constructive cubic patch [4] which use unit normals.

THEORY

Our constant element BEM in [2] was implemented using the single layer potential formulation, which leads to an ill-conditioned system [1]. We chose to continue using the

double layer potential and the single layer field for Dirichlet and Neumann type BC, respectively. Equations 1 and 2 give the discretized integral equations with $\frac{\partial G}{\partial n_y} \equiv \mathbf{n}(\mathbf{y}) \cdot \nabla_y G$.

$$\phi(\mathbf{x}_i) = \sum_{j=1}^M \int_{\Gamma_j} \frac{\partial G}{\partial n_y}(\mathbf{x}_i, \mathbf{y}_j) \eta(\mathbf{y}_j) d\Gamma(\mathbf{y}) \quad (1)$$

$$\frac{\partial \phi}{\partial n_x}(\mathbf{x}_i) = \sum_{j=1}^M \int_{\Gamma_j} \frac{\partial G}{\partial n_x}(\mathbf{x}_i, \mathbf{y}_j) \sigma(\mathbf{y}_j) d\Gamma(\mathbf{y}) \quad (2)$$

From Eqs. 1 and 2 and the parametric area element, $\left| \frac{\partial \mathbf{x}}{\partial u} \times \frac{\partial \mathbf{x}}{\partial v} \right|$, it is imperative our parametrization gives accurate normals on the element and interpolates the normals at the vertices for continuity. We decided on two methods given in [3] and [4].

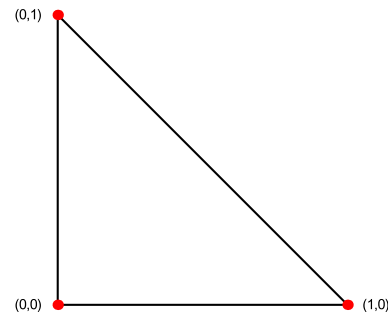


Figure 1: Triangle in (u, v) with vertices $\mathbf{x}_1 = \mathbf{x}(0, 0)$, $\mathbf{x}_2 = \mathbf{x}(1, 0)$, $\mathbf{x}_3 = \mathbf{x}(0, 1)$ and corresponding normals.

The quadratic patch in [3] fits an order 2 polynomial of form $\mathbf{x}(u, v) = \mathbf{a}_{00} + \mathbf{a}_{10}u + \mathbf{a}_{01}v + \mathbf{a}_{20}u^2 + \mathbf{a}_{11}uv + \mathbf{a}_{02}v^2$ given vertices $\mathbf{x}_1, \mathbf{x}_2, \mathbf{x}_3$ and normals $\mathbf{n}_1, \mathbf{n}_2, \mathbf{n}_3$. For a triangle as in Fig. 1, the coefficients are given in Eq. 3. $\mathbf{c}(\mathbf{d}_{ij}, \mathbf{n}_i, \mathbf{n}_j)$ in Eq. 3 is termed the curvature parameter in [3] and can be calculated by Eq. 4. [3] gives details on the derivation.

$$\begin{aligned} \mathbf{d}_{ij} &\equiv \mathbf{x}_j - \mathbf{x}_i \\ \mathbf{c}_{ij} &\equiv \mathbf{c}(\mathbf{d}_{ij}, \mathbf{n}_i, \mathbf{n}_j) \\ \mathbf{a}_{00} &= \mathbf{x}_1 & \mathbf{a}_{20} &= \mathbf{c}_{12} \\ \mathbf{a}_{10} &= \mathbf{d}_{12} - \mathbf{c}_{12} & \mathbf{a}_{11} &= \mathbf{c}_{12} + \mathbf{c}_{13} - \mathbf{c}_{23} \\ \mathbf{a}_{01} &= \mathbf{d}_{13} - \mathbf{c}_{13} & \mathbf{a}_{02} &= \mathbf{c}_{23} \end{aligned} \quad (3)$$

$$\begin{aligned} \mathbf{v} &= \frac{\mathbf{n}_i + \mathbf{n}_j}{2} & d &= \mathbf{d}_{ij} \cdot \mathbf{v} & c &= 1 - 2\Delta c \\ \Delta \mathbf{v} &= \frac{\mathbf{n}_i - \mathbf{n}_j}{2} & \Delta d &= \mathbf{d}_{ij} \cdot \Delta \mathbf{v} & \Delta c &= \mathbf{n}_i \cdot \Delta \mathbf{v} \\ \mathbf{c}(\mathbf{d}_{ij}, \mathbf{n}_i, \mathbf{n}_j) &= \begin{cases} \frac{\Delta d}{1 - \Delta c} \mathbf{v} + \frac{d}{\Delta c} \Delta \mathbf{v} & c \neq \pm 1 \\ \mathbf{0} & c = \pm 1 \end{cases} \end{aligned} \quad (4)$$

* agee1@niu.edu

† berdelyi@niu.edu

A SIMPLE METHOD FOR MEASURING THE ELECTRON-BEAM MAGNETIZATION*

A. Halavanau^{1,2}, G. Qiang^{3,4}, E. Wisniewski³, G. Ha⁵, J. Power³, P. Piot^{1,2}

¹ Department of Physics and Northern Illinois Center for Accelerator & Detector Development, Northern Illinois University, DeKalb, IL 60115, USA

² Fermi National Accelerator Laboratory, Batavia, IL 60510, USA

³ Argonne Wakefield Accelerator, Argonne National Laboratory, Lemont, IL, 60439, USA

⁴ Accelerator laboratory, Department of Engineering Physics, Tsinghua University, Beijing, China

⁵ POSTECH, Pohang, Kyungbuk, 37673, Korea

Abstract

There are a number of projects that require magnetized beams, such as electron cooling or aiding in “flat” beam transforms. Here we explore a simple technique to characterize the magnetization, observed through the angular momentum of magnetized beams. These beams are produced through photoemission. The generating drive laser first passes through microlens arrays (fly-eye light condensers) to form a transversely modulated pulse incident on the photocathode surface [1]. The resulting charge distribution is then accelerated from the photocathode. We explore the evolution of the pattern via the relative shearing of the beamlets, providing information about the angular momentum. This method is illustrated through numerical simulations and preliminary measurements carried out at the Argonne Wakefield Accelerator (AWA) facility are presented.

CHARACTERIZATION OF THE MAGNETIZED BEAM

When electron beam is born in presence of an axial magnetic field, it forms a “magnetized” beam state. Such beams have a variety of applications in electron cooling and can lead to the formation of beams with asymmetric transverse emittances or “flat” beams [2].

According to Busch’s theorem the total canonical angular momentum (CAM) of a charged particle in axially symmetric magnetic field is conserved and given by [3]:

$$L = \gamma m r^2 \dot{\theta} + \frac{1}{2} e B_z(z) r^2, \quad (1)$$

where (r, θ, z) are cylindrical coordinates.

We now specialize on the case of the Argonne Wakefield Accelerator (AWA) “witness” beamline illustrated in Fig. 1. The beamline includes a L-band RF gun with a Mg photocathode on its back plate. The gun is surrounded by a bucking and focusing solenoids, configured such that they nominally yield a vanishing magnetic field B_{0z} at the photocathode surface. When the solenoids are tuned to provide a

non-vanishing axial magnetic field B_{0z} at the cathode, the electrons acquire a canonical angular momentum (CAM); see Eq. (1). The conservation of the CAM L yields that the mechanical angular momentum (MAM) of the beam in the magnetic-field-free zone is:

$$|\mathbf{L}| = \gamma m |\mathbf{r} \times \frac{d\mathbf{r}}{dt}| = \frac{1}{2} e B_{0z} r_0^2, \quad (2)$$

where is the field at the cathode surface, r_0 is the particle coordinate at the cathode and r is the particle coordinate at the measurement location downstream of the cathode. The norm of $|\mathbf{L}|$ can be computed as $L = |\mathbf{r} \times \mathbf{p}| = x p_y - y p_x$. The particle’s total momentum $\vec{p} = p_r \hat{\mathbf{r}} + p_\theta \hat{\boldsymbol{\theta}} + p_z \hat{\mathbf{z}}$ has non-zero $\hat{\boldsymbol{\theta}}$ -component $p_\theta = \gamma m_e r \dot{\theta}$ resulting in CAM-dominated beam. The associated beam dynamics can be treated via envelope equation formalism, which in the case of magnetized beam takes form [3, 4]:

$$\sigma'' + k_l^2 \sigma - \frac{K}{4\sigma} - \frac{\epsilon_u^2}{\sigma^3} - \frac{\mathcal{L}^2}{\sigma^3} = 0, \quad (3)$$

where $k_l = e B_z(z)/2\gamma m c$ is Larmor wavenumber, $K = 2I/I_0\gamma^3$ is the perveance, I and I_0 are the beam and Alfvén current respectively, ϵ_u - geometric emittance and magnetization $\mathcal{L} \equiv \langle L \rangle / 2\gamma m c$. Magnetized state is achieved when $\mathcal{L} \gg \epsilon_u$.

Since the last two terms in Eq. (3) can be combined, magnetized beams are characterized by eigen-emittance concept, where eigen-emittances are the eigen values of 4×4 transverse beam matrix Σ , and 4D emittance is $\epsilon_{4D} \equiv \gamma |\Sigma|^{1/4}$.

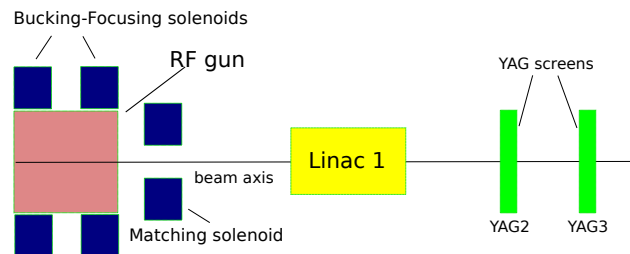


Figure 1: Overview of the AWA witness beamline. The overlap of two solenoid fields produces CAM-dominated beams.

* This work was supported by the US Department of Energy under contract No. DE-SC0011831 with Northern Illinois University. The work by the AWA group is funded through the U.S. Department of Energy, Office of Science, under contract No. DE-AC02-06CH11357.

SIMULATIONS IN SUPPORT OF WIRE BEAM-BEAM COMPENSATION EXPERIMENT AT THE LHC

A. Patapenka*, Northern Illinois University, DeKalb; FNAL, Batavia, IL 60510, USA
Y. Papaphilippou, R. De Maria, CERN, Geneva, Switzerland
A. Valishev, FNAL, Batavia, IL 60510, USA

Abstract

The compensation of long-range beam-beam interaction with current wires is considered as a possible technology for the HL-LHC upgrade project. A demonstration experiment is planned in the present LHC machine starting in 2018. This paper summarizes the tracking studies of long range beam-beam effect compensation in the LHC aimed to aid in planning the demonstration experiment. The impact of wire compensators is demonstrated on the tune footprints, dynamic aperture, beam emittance and beam intensity degradation. The simulations are performed with SIXTRACK code. The symplectic transport map for the wire element, its verification and implementation into the code are also discussed.

INTRODUCTION

The performance of the Large Hadron Collider (LHC) is limited by electromagnetic interactions between proton beams and their surroundings. In particular, one of these effects is the long range beam-beam interaction (LRBBI), which occurs between two beams passing the common beam pipe and when the transverse offset is much larger than the beam sizes. The interaction strength scales as an $1/r$ EM field. The LRBBI can lead to beam emittance growth and beam losses. A straight current carrying wire generates an identical $1/r$ field and it was originally proposed for the LHC to compensate LRBBI effects [1].

The wire compensators' location should be chosen based on optics considerations [2]. Locality is important, as the long range effects occur in a phase advance of $\pi/2$ from the IP. In this respect, the wires should be located as close as possible to these interactions. Considering that the interactions near the IR are the strongest ones, it was initially thought that the "ideal" positions can be found in lattice locations of equal beta functions (aspect ratio of 1) [3], which can be found ± 104.9 m from IR1 and IR5 and are since marked as BBC (Beam Beam Compensator) in the equipment database. A later study has shown that actually there are fixed aspect ratios depending on the IR layout where the wires can eliminate all excited resonance driving terms excited by the BBLRI [4]. In any case, the BBC locations are in an area where the beams share a common beam pipe, and it is quite difficult to integrate wires, in between them. In this respect, it was proposed [2], that wires are embedded in the jaws of Tertiary Collimators (TCT) in IR5 and IR1, for performing experimental tests in 2017-2018. In this

paper we describe the wire model that is implemented into SIXTRACK and tracking studies are undertaken for TCT locations.

WIRE MODEL

We assume that the wire is a finite straight conductor with infinitely small thickness. Although, a single wire cannot physically exist, we can consider an electric loop as a set of straight wires and there is no objection in the construction of a Hamiltonian and the calculation of a first order symplectic map for each of the elements.

The vector potential of a straight finite thin wire, in Cartesian coordinates, can be described by 4 parameters: the current I , two tilt angles a and b and its length L . Making a natural parametrisation along the wire and using as integration range $(-L/2, +L/2)$, it is possible to obtain, from Biot-Savart law, a generic formula for the vector potential components:

$$A_i(x, y, z) = \frac{I\mu_0 \cos(c_i)}{4\pi} \left[\sinh^{-1} \left(\frac{\frac{L}{2} - a}{\sqrt{b^2 - a^2}} \right) + \sinh^{-1} \left(\frac{\frac{L}{2} + a}{\sqrt{b^2 - a^2}} \right) \right]. \quad (1)$$

The index i corresponds to x , y or z , c_i to the direction cosines and it could be expressed from the tilt angles, $a = x \cos(c_x) + y \cos(c_y) + z \cos(c_z)$ and $b^2 = x^2 + y^2 + z^2$.

First Order Transport Map

The Hamiltonian parameterized by s (longitudinal coordinate) of single elements that is also used by the SIXTRACK code [5], is represented as :

$$H = -\sqrt{\beta_0^2 p_s^2 + 2p_s - (p_y - a_y)^2 - (p_x - a_x)^2 + 1} + p_s - a_s$$

The field (1) of the wire is s -dependent. To take into account the effect of fringe field, an additional parameter must be introduced, the integration length L_{int} . By considering that the integration limits are $[-L_{int}/2, +L_{int}/2]$ assuming the wire parallel to longitudinal axis, and applying the Lie operator, the following equations for the momentum kick,

* andrei.patapenka@cern.ch

BEAM TEST OF MASKED-CHICANE MICRO-BUNCHER*

^{1,2}Y. M. Shin[#], ^{1,2}A. Green, ²R. Thurman-Keup, ²A. H. Lumpkin, ²J. C. Thangaraj, ²D. Crawford,
²D. R. Edstrom Jr., ²J. Santucci, ²J. Ruan, and ²D. Broemmelsiek

¹Department of Physics, Northern Illinois University, Dekalb, IL, 60115, USA

²Fermi National Accelerator Laboratory (FNAL), Batavia, IL 60510, USA

Abstract

Masking a dispersive beamline segment such as a dogleg or a chicane is a simple way to shape a beam in the longitudinal and transverse space. This technique is often employed to generate arbitrary bunch profiles for beam/laser-driven accelerators and FEL undulators or even to reduce background noise from dark currents in electron linacs. We have been investigating a beam-modulation of a slit-masked chicane at the electron injector beamline of the Fermilab Accelerator Science and Technology (FAST) facility. With the chicane design parameters (bending angle of 18°, bending radius of 0.95 m and $R_{56} \sim -0.19$ m) and a nominal beam of 3 ps bunch length, Elegant simulations showed that a slit-mask with slit period 900 μm and aperture width 300 μm induces a modulation with bunch-to-bunch space of about 187 μm (0.25 nC), 270 μm (1 nC) and 325 μm (3.2 nC) with 3 ~ 6% correlated energy spread: An initial energy modulation pattern has been observed in the electron spectrometer downstream of the masked chicane using a micro-pulse charge of 270 pC and 40 micro-pulses. The first Optical Transition Radiation (OTR) signals of the longitudinally modulated beam were measured with a Martin-Puplett interferometer and a synchro-scan streak camera at a station between the chicane and spectrometer.

INTRODUCTION

One of the easiest ways to achieve the beam-modulation is to mask the beam in a chicane with a slit-mask or a wire-grid. The basic concept was first suggested by D. C. Nguyen and B. Carlsten in 1996 in the effort to reduce the length of FEL undulators [1]. Also, Brookhaven National Laboratory (BNL) demonstrated the generation of a stable train of micro-bunches with a controllable sub-ps delay with the mask technique using a wire-grid. The main advantage of the masking technique is to facilitate control of micro-structured density profiles, including the energies and phases. We have implemented the masked chicane method in the 50-MeV electron injector at the Fermilab Accelerator Science and Technology (FAST) facility [2,3]. Downstream of the FAST 50-MeV photoinjector beamline, a magnetic bunch compressor consisting of four rectangular dipoles was installed with a slit-mask inserted into the middle section (see Fig. 1). Based on this slit-masked chicane, the bunching performance and sub-ps microbunch generation

were studied. In order to evaluate bunching performance with nominal beam parameters [4], the masked chicane has been analyzed against linear bunching theory in terms of both bunch-to-bunch distance and microbunch length and verified through Elegant [5]. For Elegant simulations, bunch charge distribution and the beam spectra were investigated principally with three different bunch charges, 0.25 nC, 1 nC, and 3.2 nC, under two RF-chirp conditions of minimum and maximum energy spreads. We took initial data from masked-chicane micro-buncher at the FAST 50-MeV beamline with the plan to demonstrate beam-shaping control, in particular temporal modulation, of FAST linac and to check micro-bunching effects on angle-dependent energy-shifts of channeling beam via crystalline targets.

THEORETICAL ANALYSIS

The bunch-compressing chicane consists of four dipoles and a slit mask. The mask with slit spacing, W , and aperture width, a , is inserted in the middle of the bunch compressor (dispersion region). The configuration of such a masked chicane is shown with the phase-space plots in Fig. 1. Before the beam is injected into the masked chicane, a positive linear energy-phase correlation is imposed by accelerating the beam off the crest of the RF wave in the linear accelerator. The chicane disperses and re-aligns the particles with respect to their energies in phase space. The input beam is then compressed and the phase space ellipse is effectively rotated to lower the bunch length while increasing the momentum spread. In the middle of the chicane, the beam is partially blocked by the transmission mask and holes are introduced in the energy-phase ellipse. The second half of the chicane refocuses the beam in the longitudinal direction and the beam ellipse is slightly rotated past the vertical. In this step, the linear energy-phase correlation is preserved by over-bunching, accompanied with a steeper phase-space slope.

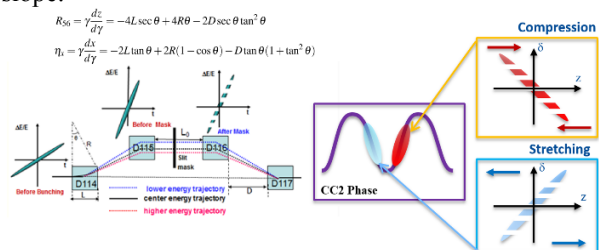


Figure 1: Time-tagged beam ellipse diagram (L) of bunch modulation process through the masked chicane with respect to RF-phase conditions (R).

* This work was supported by the DOE contract No. DEAC02-07CH11359 to the Fermi Research Alliance LLC.

[#] youngmin@fnal.gov

FEL WIGGLER BUSSBAR FIELD COMPENSATION*

Bing Li^{†1,2}, Hao Hao^{‡2}, Jingyi Li¹, Ying K. Wu²

¹NSRL, University of Science and Technology of China, Anhui, 230029, China

²DFELL/TUNL, and Department of Physics, Duke University, NC, 27708 USA

Abstract

The Duke storage ring is a dedicated driver for the storage ring based free-electron laser (FEL) and the High Intensity Gamma-ray Source (HIGS). The high intensity gamma-ray beam is produced using Compton scattering between the electron and FEL photon beams. The beam displacement and angle at the collision point need to be maintained constant during the gamma-ray beam production. The magnetic field of the copper bussbars carrying the current to the FEL wigglers can impact the beam orbit. The compensation scheme in-general is complicated. In this work, we report preliminary results of a bussbar compensation scheme for one of the wiggler and power supply configurations. Significant reductions of the orbit distortions have been realized using this compensation.

INTRODUCTION

The Duke free electron storage ring is a dedicated driver for the storage ring based free-electron laser (FEL) [1] and the High Intensity Gamma-ray Source (HIGS) [2]. The facility operates three accelerators: (1) a 0.16–0.27 GeV linac pre-injector; (2) a 0.16–1.2 GeV full-energy, top-off booster injector; and (3) a 0.24–1.2 GeV electron storage ring [3]. The operation of the FEL system uses various configurations of the six available wigglers including two planar OK-4 wigglers and four helical OK-5 wigglers, located in the south straight section of the Duke storage ring. The nearly monochromatic gamma-ray beam is produced using Compton scattering between the electron beam and FEL photon beam. The electron beam orbit displacement and its angle at the collision point are two essential factors which can impact the quality of the gamma-ray beam.

The helical FEL system of the Duke storage ring can use up to four electromagnetic OK-5 wigglers which are powered by two power supplies, named TREX2 and TREX3, respectively. The upstream OK-5A and OK-5B wigglers share the use of power supply TREX3, the other two wigglers (OK-5C and OK-5D) share TREX2. The DC currents are carried to various wigglers using long copper bussbars with the longest ones running about 24 m under the beamline. The DC current induced direct bussbar magnetic fields can impact the beam orbit, therefore affecting the quality of the gamma-ray beam. To maintain a consistent e-beam orbit for a wide range of FEL wiggler currents and electron beam energies, the bussbar field needs to be properly compensated. Because a variety of the FEL wiggler configurations (see

Fig. 1) are used, the field compensation scheme is complicated. As an example, the compensation scheme for one of the wiggler power supplies TREX2 which powers two downstream OK-5 wigglers (OK-5C and OK-5D) is described in this paper.

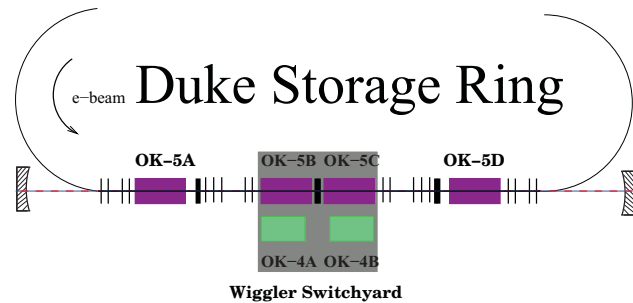


Figure 1: The schematic layout of the Duke FEL system with four helical OK-5 wigglers.

ORBIT COMPENSATION SCHEME

Consider a corrector at a location s_0 , strength $\theta(s_0)$, the changes of the closed orbit at some other location s in the storage ring can be described as [4]

$$\Delta u_{co} = G(s, s_0)\theta(s_0),$$

where u is the orbit change in either the horizontal or vertical direction, and the Green function of Hill's equation is $G(s, s_0) = \frac{\sqrt{\beta(s)\beta(s_0)}}{2\sin\pi\nu} \cos(\pi\nu - |\psi(s) - \psi(s_0)|)\theta(s_0)$, where β is the lattice betatron function, and ν is the betatron tune and ψ is the phase advance.

Let us consider a storage ring with N correctors and M beam position monitors (BPMs). The Green function between the i -th BPM and the j -th corrector is $G(s_i, s_j)$ denoted as a real response matrix element R_{ij} . The response matrix can be measured by recording the BPM readings while varying the strength of the correctors one by one.

The singular value decomposition (SVD) algorithm is used to decompose the response matrix R into

$$R = U\Lambda V^T, \quad (1)$$

where V^T is a real orthogonal $N \times N$ matrix with $VV^T = V^TV = I$, Λ is a rectangular $M \times N$ matrix with non-negative diagonal elements $\Lambda_{1,1} = \sqrt{\lambda_1}$, $\Lambda_{2,2} = \sqrt{\lambda_2}$, ..., and U is a real orthogonal $M \times M$ matrix with $U^TU = UU^T = I$ [4]. The real diagonal matrix Λ are ordered from the largest of the singular value to the smallest.

To keep the strengths of the correctors reasonably small while achieving an effective orbit correction, only a subset

* Work supported in part by the US DOE grant no. DE-FG02-97ER41033.

[†] bingli@fel.duke.edu

[‡] haohao@fel.duke.edu

MuSim, A GRAPHICAL USER INTERFACE FOR MULTIPLE SIMULATION CODES

Thomas J. Roberts[†], Muons, Inc., Batavia, IL, U.S.A.

Yu Bao, Muons, Inc. and University of California, Riverside, CA, U.S.A.

Abstract

MuSim [1] is a user-friendly program designed to interface to many different particle simulation codes, regardless of their data formats or geometry descriptions. It presents the user with a compelling graphical user interface that includes a flexible 3-D view of the simulated world plus powerful editing and drag-and-drop capabilities. All aspects of the design can be parameterized so that parameter scans and optimizations are easy. It is simple to create plots and display events in the 3-D viewer (with a slider to vary the transparency of solids), allowing for an effortless comparison of different simulation codes. Simulation codes: G4beamline 3.02 [2], MCNP 6.1 [3], and MAD-X [4]; more are coming. Many accelerator design tools and beam optics codes were written long ago, with primitive user interfaces by today's standards. MuSim is specifically designed to make it easy to interface to such codes, providing a common user experience for all, and permitting the construction and exploration of models with very little overhead. For today's technology-driven students, graphical interfaces meet their expectations far better than text-based tools, and education in accelerator physics is one of our primary goals.

MuSim [1]

There are dozens of simulation codes in use, and many physicists have complained about the resulting "Tower of Babel"; establishing a common graphical user interface for multiple simulation codes is a major improvement in the field. MuSim can interface to many different beam-optics and particle simulation codes since they necessarily have a common domain, with common concepts, common objects, and common operations. By abstracting these common elements, a single program can indeed interface to many simulation codes with relatively little effort.

Graphical interfaces are used throughout, making it easy to construct the system graphically, display the system with beam tracks, analyze results, and use on-screen controls to vary parameters and observe their effects in (near) real time. Such exploration is essential to give users insight into how systems behave, and is valuable to both experienced and inexperienced scientists, for both teaching and learning, and for tasks such as optimizing a system design using a variety of codes before it is built.

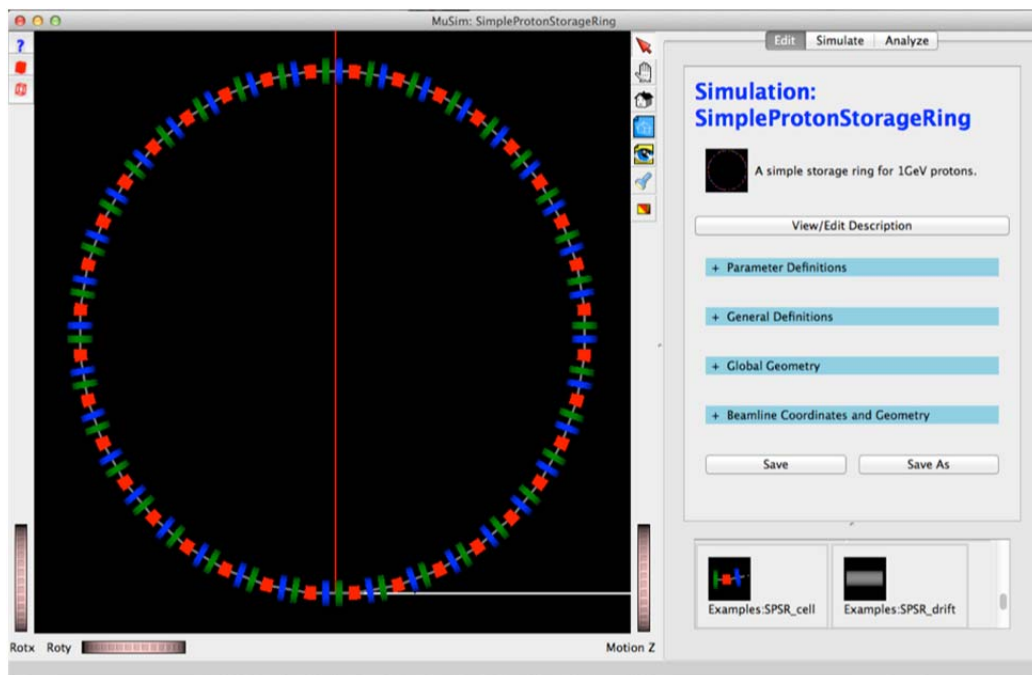


Figure 1: The MuSim main window, showing a 3-D image of the simulated world and an editing panel. At the lower right is the Library; two of its objects are visible – they can be dragged and dropped in the viewer to insert them into the world. This simulation is a simple proton storage ring: dipoles are red, focusing quads are blue, defocusing quads are green; the red and white lines are coordinate axes (the third is out-of-the-page and cannot be seen).

[†] tjrob@muonsinc.com

DEPENDENCE OF THE COUPLING OF DIPOLE MOTION FROM BUNCH TO BUNCH CAUSED BY ELECTRON CLOUDS AT CEsrTA DUE TO VARIATIONS IN BUNCH LENGTH AND CHROMATICITY*

M. G. Billing[†], L. Y. Bartnik, M. J. Forster, N. T. Rider, J. Shanks, M. Spiegel, S. Wang
CLASSE, Cornell University, Ithaca, NY, U.S.A.

R. L. Holtzapple, California Polytechnic State University, San Luis Obispo, CA, U.S.A.
E. C. Runburg, Notre Dame University, Notre Dame, IN, U.S.A.

Abstract

The Cornell Electron-Positron Storage Ring Test Accelerator (CesrTA) has been utilized to probe the interaction of the electron cloud with a 2.1 GeV stored positron beam. Recent experiments have characterized any dependence of beam–electron cloud (EC) interactions on the bunch length (or synchrotron tune) and the vertical chromaticity. The measurements were performed on a 30-bunch positron train with 14 nsec spacing between bunches, at a fixed current of 0.75 mA/bunch. The dynamics of the stored beam, in the presence of the EC, was quantified using 20 turn-by-turn beam position monitors in CESR to measure the correlated bunch-by-bunch dipole motion. In this paper we report on the observations from these experiments and analyze the coupling of dipole motion from bunches within the train to subsequent bunches, caused by the EC.

INTRODUCTION

In 2008 the storage ring CESR was converted to operate as a test accelerator CesrTA, capable of studying EC effects in the presence of trains of positron or electron bunches [1,2,3]. Early in the CesrTA project measurements were undertaken to study any dependence of electron cloud (EC) dynamics on the bunch length (equivalently synchrotron tune). The result of these studies found no significant dependence over a limited range of synchrotron tunes (see Section 6.3.2.9 in reference [4]). These results disagreed with observations and simulations made elsewhere [5]. As a consequence it was decided to revisit these measurement over as large a range of synchrotron tunes as practical as well as study the EC as a function of two vertical and horizontal chromaticities to allow for different damping rates.

In addition, gated horizontal and vertical stripline kickers were employed to excite coherent dipole motion in single bunches within the train in order to observe any coupling of the motion of these bunches to subsequent bunches through the EC. The motion is then observed at 20 monitors from the CESR beam position monitoring (CBPM) system [6], which simultaneously detect the positions of all bunches turn-by-turn for 8192 turns as the excitation was moved from one bunch to the next through the entire train. Since the growth of the EC within the bunch shifts the tunes of the bunches monotonically along

the train, the excitation frequency for the kickers was swept over a range sufficient to cause both horizontal and vertical motion in every bunch. The number of turns, observed by the CBPM system, was set to encompass 2 periods of the frequency sweep to guarantee one complete period for the excitation and decay of the dipole motion.

EXPERIMENTAL PROCEDURES

CESR was operated at 2.085 GeV in low-emittance conditions for measurements, taking place in December 2015 and April 2016. Bunch-by-bunch transverse and longitudinal dipole feedback was available; bunch-by-bunch feedback was employed during injection and it was either disabled or reduced during measurements as described below. The tunes of CESR for the first positron bunch were set to be $Q_x=14.572$ and $Q_y=9.579$, chosen to avoid placing any of bunches within the train on a resonance. After optics correction the vertical emittance was adjusted for a single bunch to be approximately 37 pm-r (for a design horizontal emittance of 3.2 nm-r). The measurement sequence was 1) to top off all bunches with all feedback on, 2) turn off transverse feedback, 3) to transversely excite in sequence 5 bunches individually while taking CBPM data for each excitation. Steps 1-3 were repeated until all 30 bunches have been excited. During the entire experiment longitudinal feedback remained on. During filling horizontal and vertical damping rates were 2700 sec^{-1} and 6100 sec^{-1} , respectively, for 0.75 mA (1.1×10^{10} particles). These are much higher than the 18 sec^{-1} transverse radiation damping rates.

During the measurements, the synchrotron tune, Q_s , and bunch length, σ_z , were adjusted to four settings as seen in Table 1. The measurements were performed at different values of vertical chromaticity $Q_v' = \partial Q_v / \partial \delta$, where δ is the fractional energy deviation. In these optics with the same vacuum chamber components (hence impedance) the change in vertical damping rates were measured in December 2014 at $\sigma_z=10.8 \text{ mm}$ as a function of Q_v' ,

$$\Delta\alpha_v = (26.2 \text{ sec}^{-1}) Q_v' \left(\frac{I_b}{1 \text{ mA}} \right)$$

yielding incremental changes in the vertical damping rates for 0.75 mA bunches of 79, 124 and 189 sec^{-1} for the three Q_v' settings in Table 1. The last column in Table 1 represents the relative amplitude of the drive sent to both the horizontal and vertical stripline kickers. It was necessary to increase the lower vertical chromaticity and to

* Work supported by U.S. NSF and DOE contracts PHY-0724867 and DE-FC02-08ER41538, respectively

[†] email address: mgb9@cornell.edu

ELECTRON CLOUD SIMULATIONS FOR THE LOW-EMITTANCE UPGRADE AT THE CORNELL ELECTRON STORAGE RING

J.A. Crittenden, Y. Li, S. Poprocki, and J.E. San Soucie
CLASSE* Cornell University, Ithaca, NY 14850, USA

Abstract

The Cornell Electron Storage Ring operations group is planning a major upgrade of the storage ring performance as an X-ray user facility. The principal modification foresees replacing the former e^-e^+ interaction region with six double-bend achromats, reducing the emittance by a factor of four. The beam energy will increase from 5.3 to 6.0 GeV and single-beam operation will replace the present two-beam e^-e^+ operation. The initial phase of the project will operate a single positron beam, so electron cloud buildup may contribute to performance limitations. This work describes a synchrotron radiation analysis of the new ring, and employs its results to provide ring-wide estimates of cloud buildup and consequences for the lattice optics.

INTRODUCTION

The Cornell Electron Storage Ring (CESR) serves as the X-ray source for the Cornell High Energy Synchrotron Source (CHESS). At present, CESR operates at 5.3 GeV with counter-rotating electron and positron beams. This two-beam operation limits CESR performance in emittance, beam lifetime, and beam current. An upgrade to single-beam operation has now progressed to the engineering and prototyping phase. The CHESS X-ray end stations will all be oriented to align with the on-axis positron beam. The positron beam energy will be increased from 5.3 to 6.0 GeV, and the normalized emittance will be reduced by a factor of four. One-sixth of the CESR storage ring, including the former interaction region for the CLEO experiment, will be replaced by six double-bend achromats, each equipped with two conventional combined-function magnets providing dipole fields of 6.4 kG and quadrupole fields of 8.8 T/m gradient [1], and with Cornell Compact Undulators (CCUs) [2]. The synchrotron radiation from this new section requires extensive additional shielding to enclose the ring throughout the large CLEO experimental hall. It will also present an additional source of electron cloud buildup, and since initial operation will be with a single positron beam, it is important for the vacuum chamber design to estimate the effect of the cloud on the beam optics. Here we present a synchrotron radiation analysis of the ring, electron cloud buildup modeling, and estimates for electron-cloud-induced betatron tune shifts.

SYNCHROTRON RADIATION ANALYSIS OF THE UPGRADED LATTICE

The vacuum chamber design in the modified south arc section of the CESR ring foresees a small vertical dimension of 5 mm in the CCUs, and a 100-mm horizontal dimension with the beam 25 mm from the outer wall, thus providing a 50-mm antechamber for electron cloud suppression. Outside of the CCUs, the vacuum chamber will be nearly elliptical with vertical side walls, as in most of the CESR ring, but reduced by a factor of two, so 45x25 mm rather than 90x50 mm. This vacuum chamber model has been implemented in the Bmad synchrotron radiation analysis [3] of the lattice. Figure 1 compares the rates of photons incident on the vacuum chamber wall in the downstream 50 m of the upgraded lattice to the rates in present operation. In contrast to the upgraded lattice, there is very little radiation in the first 15 m at present. The radiation from the combined-function bends illuminates both the bends themselves and the downstream quadrupoles and CCUs.

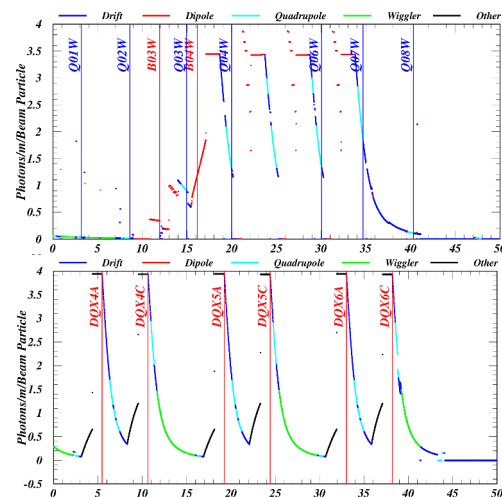


Figure 1: Calculations of synchrotron radiation incident on the vacuum chamber walls in the downstream 50 m of the modified section of the CESR ring. The upper plot shows the rates during present CHESS operation. The lower plot shows the rates expected for the upgraded lattice.

The modeling methodology for estimating coherent betatron tunes shifts employs the element-type ring occupancy fractions and the element-type-averaged rates, beta functions and beam sizes, as described in Ref. [4]. Inclusion of the field-free and dipole regions of the CESR ring suffice to accurately model present tune shift measurements. We include the combined-function magnet and CCU regions in the calculations for the upgraded lattice in order to assess

* Work supported by the National Science Foundation DMR 13-32208

OPTIMIZATION OF LINEAR INDUCTION RADIOGRAPHY ACCELERATOR WITH ELECTRON BEAM WITH ENERGY VARIATION

Yuan Hui Wu[†] and Yu-Jiuan Chen

Lawrence Livermore National Laboratory, Livermore CA, USA

Abstract

The current interest for the next generation linear induction radiography accelerator (LIA) is to generate multiple, high peak current, electron beam pulses. The beam energy and current may vary from pulse to pulse. Consequently, the transport and control of multi-pulsing intense electron beams through a focusing lattice over a long distance on such a machine becomes challenging. Simulation studies of multi-pulse LIAs using AMBER [1] and BREAKUP Code [2] are described. These include optimized focusing magnetic tune for beams with energy and current variations, and steering correction for corkscrew motion. The impact of energy variation and accelerating voltage error on radiograph performance are discussed.

INTRODUCTION

Controlling beam transport is essential for accelerator operation and future induction accelerator design. In this study, see Figure 1, we simulated a conceptual linear induction accelerator. The nominal incoming 2-MeV, 2-kA electron beam exiting from the diode injector has a uniform KV distribution with a 5 cm edge radius ($r = 5$ cm) and an 800π mm-mrad edge normalized emittance ($\epsilon = 800\pi$ mm-mrad). The incoming beam has a small energy variation ($d\gamma/\gamma$), which varies from -5% to 5% with respect to the nominal beam energy.

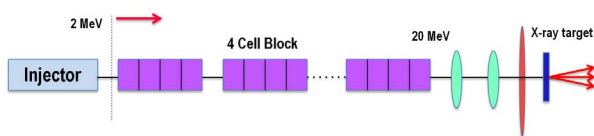


Figure 1: The conceptual accelerator configuration used in the simulations. The model has 72 cells arranged into 18 blocks, and an intercell gap of 50 cm.

[†] wu39@llnl.gov

The accelerator consists of 18 4-cell blocks, which accelerate the electron beam to 20 MeV. The intercell separation is 50 cm. The accelerating voltage in each accelerator cell (see Figure 2) is $250\text{kV}(1+dV/V)$, where dV/V varies from -5% to 5%. The downstream beamline consists of two focusing solenoids and a final focusing solenoid.

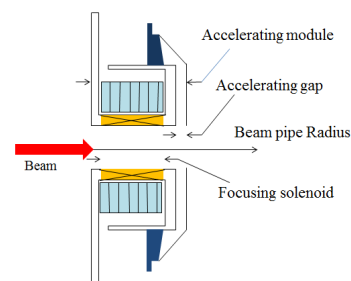


Figure 2: Schematic of simulated 250kV accelerating cell.

ELECTRON BEAM TRANSPORT AND TUNE OPTIMIZATION

To preserve the beam quality, the beam envelope oscillation needs to be minimized [3]. As shown in Figure 3, the solenoid magnetic tune is optimized to reduce the envelope oscillation for a nominal electron beam. Transport of the electron beam with different initial energy variation and accelerating voltage variation is simulated using the same magnetic tune. For the beam produced with an initial energy variation, the beam current also varies according to the Child-Langmuir's law. Electron beam slices with initial energy variations from -5% to 5% and accelerating voltage errors from -5% to 5% were simulated (Fig. 3). The beam slice with larger initial energy variation has larger envelope oscillation. Likewise, the beam slice transport through accelerator with large voltage error experiences larger envelope oscillation.

By using AMBER slice PIC code, an electron beam pulse with a given different initial energy variation was simulated by dividing the pulse into 20 slices. Each slice represents a por-

UNFOLDING ELECTRON BEAM PARAMETERS USING SPOT SIZE MEASUREMENT FROM MAGNET SCAN

Yuan Hui Wu[†], Yu-Jiuan Chen and Jennifer Ellsworth
Lawrence Livermore National Laboratory, CA, USA

Abstract

The Flash X-ray Radiography (FXR) [1] linear induction accelerator at Lawrence Livermore National Laboratory produces x-ray bursts for radiographs. The machine is able to produce x-ray spot sizes less than 2mm. The beam parameters are unfolded from electron beam radii measured during magnet scan by modelling the FXR LINAC with the simulation code AMBER [2] and the envelope code XENV [3]. These unfolded beam parameters are then used as the initial condition for forward simulations of the beam transport through the drift region to the target. Using x-ray spot size data from a scan of final focus magnet, a good agreement between data and simulation is found for the back streaming ions' neutralization factor $f=0.3$.

INTRODUCTION

The beam accelerated by the FXR linac is transported through a drift region to the x-ray conversion target (See Fig. 1). This downstream transport system consists of five magnetic solenoids (DR1, DR2, DR3, DR4 and DR5) and a final focusing solenoid (FF4). A diagnostics station is located between the DR2 and DR3 magnets. For the experiments described in this paper, the time resolved electron beam size was measured by inserting a 1mm thick aluminium coated quartz disk into the beam line at 45 degree angle and imaging the disk with a gated scientific imaging camera. The Cherenkov light captured by CCD camera in the diagnostic cross is calibrated to measure the electron beam radius.

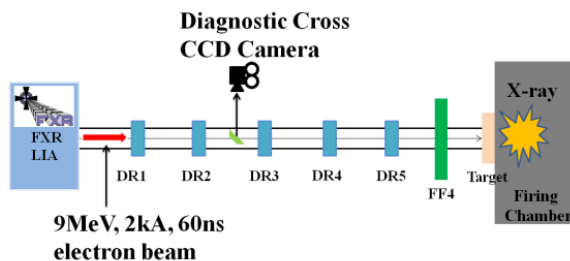


Figure 1: Schematic of FXR downstream section

UNFOLDING ELECTRON BEAM PARAMETERS

To unfold the beam parameters at a given position of the accelerator, the electron beam transport from that position to the diagnostic cross is simulated with AMBER PIC code. A global optimization algorithm [4] (Genetic Algorithm) was used to search beam parameters to match the experimental spot sizes from DR1 scan. The unfolded Lapostolle normalized emittance is 1230 mm-mrad, rms

[†] wu39@llnl.gov

radius r is 9.4 mm, rms envelope slope r' is 15.5 mrad, beam energy E is 8.85 MeV and peak current I is 1.83 kA. Using these beam parameters as initial condition, the simulated electron beam radii for the DR1 magnet scan are shown in Fig. 2. The same beam parameters then used to simulate the beam radii for a magnet scan from DR2, the comparison between the simulated beam radii and the measured beam radii for the DR2 magnet scan are shown in Fig.3. These are a good agreement. The unfolded emittance is consistent with the previously measured value [5].

As discussed in Ref. 1, FXR can produce two electron pulses with different acceleration scheme by sequentially energizing alternate cells. Each of the two pulses gains half of the full machine energy. Minimum beam envelope oscillation is important to reduce emittance growth [6]. Using the unfolded beam parameters as the initial condition for simulations, a magnetic tune is developed for two electron pulses (see Fig. 4). For this simulation, it is assumed that the injector produces two identical electron pulses. The optimized magnetic tune offers a similar final emittance for two pulses.

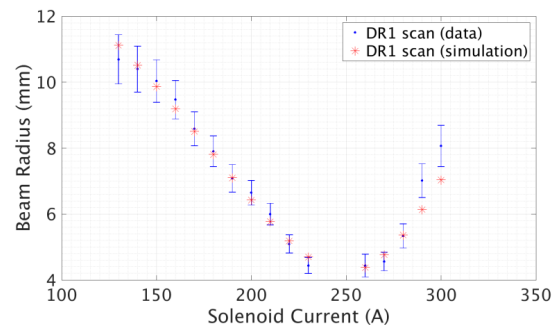


Figure 2: DR1 scan, comparison of measured and simulated beam radius.

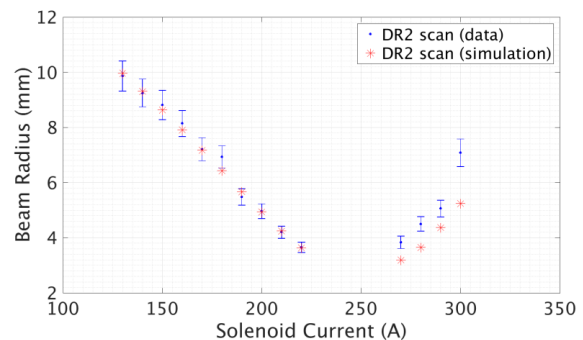


Figure 3: DR2 magnet scan, comparison of measured and simulated beam radius.

DYNAMICS OF INTENSE BEAM IN QUADRUPOLE-DUODECAPOLE LATTICE NEAR SIXTH ORDER RESONANCE*

Y. K. Batygin[#], T. T. Fronk, LANL, Los Alamos, NM 87545, USA

Abstract

The presence of duodecapole components in quadrupole focusing field results in excitation of sixth-order single-particle resonance if the phase advance of the particles transverse oscillation is close to 60° . This phenomenon results in intensification of beam losses. We present analytical and numerical treatment of particle dynamics in the vicinity of sixth-order resonance. The topology of resonance in phase space is analyzed. Beam emittance growth due to crossing of resonance islands is determined. Halo formation of intense beams in presence of resonance conditions is examined.

INTRODUCTION

An ideal quadrupole lens has a constant gradient across the aperture created by poles with infinite hyperbolic shape. Unavoidable deviations from ideal pole shape results in the appearance of higher order harmonics in the quadrupole field spectrum. The vector-potential of the magnetic field of a lens with quadrupole symmetry contains harmonics of the order $2(2m+1)$, $m = 0, 1, 2, \dots$:

$$A_z = -\left[\frac{G_2}{2}r^2 \cos 2\theta + \frac{G_6}{6}r^6 \cos 6\theta + \frac{G_{10}}{10}r^{10} \cos 10\theta + \dots\right], \quad (1)$$

where G_2 is the gradient of quadrupole lens, G_6 is the duodecapole component, G_{10} is the “20-poles” component. The vertical component of the magnetic field along abscissa is given by

$$B_y(x, 0) = G_2x + G_6x^5 + G_{10}x^9 + \dots \quad (2)$$

While traveling through a quadrupole lens of length D , particles receive a momentum kick, which contains linear and nonlinear parts:

$$\Delta \frac{dx}{dz} = -\frac{qD}{mc\beta\gamma} (G_2x + G_6x^5 + G_{10}x^9 \dots) \quad (3)$$

The presence of duodecapole harmonic in quadrupole field results in excitation of sixth-order resonance if phase advance of transverse oscillations per focusing period is close to 60° . Increase of beam losses near 60° phase advance was observed experimentally at SNS linac [1]. Minimization of duodecapole component requires specific pole shape of quadrupole lenses [2]. In present paper we estimate effect of 6th order resonance on beam expansion.

*Work supported by US DOE under contract DE-AC52-06NA25396
batygin@lanl.gov

HAMILTONIAN OF SIXTH-ORDER RESONANCE

Consider particle motion in a quadrupole channel with focusing period S in the presence of duodecapole components. The quadrupole channel is substituted by a continuous focusing channel with phase advance μ_o per period, which for FODO focusing structure is determined as

$$\mu_o = \frac{S}{2D} \sqrt{1 - \frac{4D}{3S} \frac{qG_2D^2}{mc\beta\gamma}} \quad (4)$$

Presence of duodecapole component is introduced as an additional nonlinear momentum kick, which particle receives once per focusing period. In the adopted approximations, single particle motion is described by a matrix:

$$\begin{pmatrix} x_{n+1} \\ p_{n+1} \end{pmatrix} = \begin{pmatrix} \cos \mu_o & \sin \mu_o \\ -\sin \mu_o & \cos \mu_o \end{pmatrix} \begin{pmatrix} x_n \\ p_n + \Delta p_n \end{pmatrix}, \quad (5)$$

where n is the number of focusing period, x is the particle position, p is the modified particle momentum, and Δp is the nonlinear kick due to presence of duodecapole component:

$$p = \frac{S}{\mu_o} \frac{dx}{dz}, \quad \Delta p = \delta_5 x^5. \quad (6)$$

Let us introduce action-angle variables through transformation:

$$x = \sqrt{2J} \cos \psi, \quad p = -\sqrt{2J} \sin \psi. \quad (7)$$

Normalized emittance of the beam bounded by the ellipse in phase space is related to introduced action value as

$$\varepsilon = 2J \beta\gamma \frac{\mu_o}{S}. \quad (8)$$

Analysis shows that the Hamiltonian describing slow motion near 6th order resonance is given by

$$H(J, \psi) = J\mathcal{G} - \frac{\delta_5}{4} J^3 - \frac{\delta_5}{24} J^3 \cos 6\psi, \quad (9)$$

where $\mathcal{G} = \mu_o - \pi/3$ is the deviation from “resonance” angle 60° .

Figure 1 illustrates topology of phase space structure. A particle moves either along internal phase space trajectory or along external islands with larger amplitude. In the vicinity of point J_u , particle motion is unstable. The

SIMULATIONS OF NONLINEAR BEAM DYNAMICS IN THE JLEIC ELECTRON COLLIDER RING*

F. Lin[#], Ya. S. Derbenev, V. S. Morozov, F. Pilat, G.H. Wei, Y. Zhang,
Jefferson Lab, Newport News, VA 23606, USA
Y. Cai, Y. M. Nosochkov, M. Sullivan, SLAC, Menlo Park, CA USA
M-H. Wang, Mountain View, CA 94040, USA

Abstract

The short lengths of colliding bunches in the proposed Jefferson Lab Electron-Ion Collider (JLEIC) allow for small beta-star values at the interaction point (IP) yielding a high luminosity. The strong focusing associated with the small beta-stars results in high natural chromaticities and potentially a beam smear at the IP. Rapid growth of the electron equilibrium emittances and momentum spread with energy further complicates the situation. We investigated nonlinear dynamics correction schemes that overcome these problems and allow for stable beam dynamics and sufficient beam lifetime at the highest electron energy. In this paper, we present and compare tracking simulation results for various schemes considering their emittance contributions.

INTRODUCTION

The Jefferson Lab Electron-Ion Collider (JLEIC) [1] is designed to have small beta-stars at the IP to achieve the high luminosity requirement. This unavoidably introduces large chromaticities due to the strong focusing of the final focusing quadrupoles (FFQs) and chromatic beam smear at the IP. In the JLEIC electron collider ring baseline design, the large phase advance 108° in the arc FODO cell was chosen to be close to 135° that generates a minimum emittance in a FODO cell lattice [2, 3]. Hence, in addition to the FFQs, such large phase advance requires strong focusing from quadrupoles resulting in a significant chromaticity contribution from the two arcs, $\sim 40\%$ in the baseline design. Linear chromaticities can be straightforwardly compensated using two sextupole families globally distributed in the arcs. The sextupoles are arranged to have the $-I$ phase advance to cancel the sextupole introduced non-linear geometric and chromatic effects. Compensation of the FFQs-induced non-linear chromaticities requires a local compensation system where sextupoles generate an opposite chromatic kick in phase to compensate the one from the FFQs at the IP. This local compensation system should have large beta functions and dispersion at the sextupole locations to obtain reasonable sextupole strengths and large ratio of horizontal and vertical beta functions for separate correction in two transverse planes. Again, sextupoles are

located with $-I$ phase advance to suppress the sextupole induced nonlinear resonances. Besides, the local compensation optics should be designed not to increase the electron beam emittance significantly. Several chromaticity correction systems in the electron collider ring considering the emittance control have been reviewed [4]. This paper summarizes all studied compensation schemes and reports the tracking simulation results.

COMPENSATION SCHEMES AND SIMULATION RESULTS

The JLEIC electron collider ring is designed using major PEP-II High Energy Ring (HER) magnets within their magnet specification in two arcs and straights and new magnets in special machine blocks, such as spin rotators, interaction regions, etc [2,3]. Electron equilibrium emittance is primarily determined by the arc optics design. Two arcs, consisting of regular FODO cells, spin rotators and matching sections, contribute more than 90% of the natural horizontal emittance. Phase advance 108° in the regular arc FODO cell allows one to have a 3π phase advance between sextupoles so that the sextupole introduced geometric resonance driving terms can be cancelled every 5 cells. Without any chromaticity correction optics inserted, the electron horizontal emittance is 8.9 nm-rad at 5 GeV and the natural chromaticity is $\xi_{x,y} = [-113, -120]$. Note that chromaticities and emittance vary in different chromaticity correction schemes due to the local excitation of optics functions.

Philosophy of chromatic correction is described in [4] in detail. A brief description of each studied compensation scheme is given as follows.

1. Only linear chromaticities are compensated using two sextupole families distributed in the arcs. Since no local correction, the large beta functions in the FFQs near the IP create large chromatic perturbations resulting in large non-linear momentum variations of beta functions. This leads to a beam smear at the IP affecting the luminosity. Since there is no optics modification, this scheme does not introduce any emittance growth.
2. A local chromaticity compensation block (CCB) on each side of the IP is placed for a local and independent correction of up- and downstream FFQs. Each CCB has two $-I$ interleaved sextupole pairs in each horizontal and vertical planes. The interleaved sextupoles generate residual sextupole non-linear geometric effects due to the overlap of

* Authored by Jefferson Science Associates, LLC under U.S. DOE Contract No. DE-AC05-06OR23177 and DE-AC02-06CH11357. The U.S. Government retains a non-exclusive, paid-up, irrevocable, worldwide license to publish or reproduce this manuscript for U.S. Government purposes. Work supported by the US DOE Contract DE-AC02-76SF00515.

[#] fanglei@jlab.org

SPIN FLIPPING SYSTEM IN THE JLEIC COLLIDER RING*

A. M. Kondratenko, M. A. Kondratenko, Science and Technique Laboratory Zaryad, Novosibirsk
 Yu. N. Filatov, MIPT, Dolgoprudny, Moscow Region
 V. S. Morozov, Ya. S. Derbenev, F. Lin, Y. Zhang, Jefferson Lab, Newport News, VA 23606, USA

Abstract

The figure-8 JLEIC collider ring opens wide possibilities for manipulating proton and deuteron spin directions during an experiment. Using 3D spin rotators, one can, at the same time, efficiently control the polarization direction as well as the spin tune value. The 3D spin rotators allow one to arrange a system for reversals of the spin direction in all beam bunches during an experiment, i.e. a spin-flipping system. To preserve the polarization, one has to satisfy the condition of adiabatic change of the spin direction. When adjusting the polarization direction, one can stabilize the spin tune value, which completely eliminates resonant beam depolarization during the spin manipulation process. We provide the results of numerical modeling of a spin-flipping system in the JLEIC ion collider ring. The presented results demonstrate the feasibility of organizing a spin-flipping system using a 3D rotator. The figure-8 JLEIC collider provides a unique capability of doing high-precision experiments with polarized ion beams.

INTRODUCTION

Using Spin-Flipping systems (SF systems) in colliders allows one to raise experiments with polarized beams to a new precision level. There are many papers on spin-flipping systems (see, for instance, [1–5]). Reference [6] specified the main requirements to building long-term stable SF systems by introducing small magnetic field integrals into the collider lattice. SF systems can be divided into two classes based on how the spin reversals are organized. The first class involved single-turn SF systems, which allow one to flip the spin every particle turn. Natural representatives of this class are colliders with Siberian snakes whose spin tune equals a half. Stable polarization reversals are realized by introduction into the collider of rf fields at a frequency twice lower than the particle circulation frequency. The second class includes multi-turn SF systems, which flip the spin over a large number of particle turns. A natural representative of this class is a figure-8 collider whose spin tune equals zero. An advantage of a multi-turn SF system in a figure-8 collider is the possibility of flipping the spin using quasi-static fields instead of RF ones.

Let us demonstrate how one can organize a multi-turn SF system in the JLEIC collider by introduction into its lattice of quasi-static solenoids with small field integrals.

* Authored by Jefferson Science Associates, LLC under U.S. DOE Contracts No. DE-AC05-06OR23177 and DE-AC02-06CH11357. The U.S. Government retains a non-exclusive, paid-up, irrevocable, worldwide license to publish or reproduce this manuscript for U.S. Government purposes.

ION POLARIZATION CONTROL IN THE JLEIC COLLIDER

Using figure-8 ring geometry [7] is an elegant way to preserve and control the polarization of a beam of any particle species (p, d, ^3He , ...) during its acceleration and storage at any energy. The ideal lattice of a figure-8 ring is transparent to the spin. The resulting effect of the “strong” arc dipoles on the spin dynamics is reduced to zero over one particle turn. Any spin orientation at any orbital location repeats every turn. In other words, in a figure-8 accelerator, the spin tune is zero, and there is no preferred polarization orientation because the particle is in the zero-integer spin resonance region. To stabilize the beam polarization direction at the interaction point, it is sufficient to use compact insertions for polarization control, which utilize already existing collider magnets and solenoids with small field integrals (“weak” solenoids) [8-10]. The spin tune and the polarization direction are then determined not by the “strong” structural fields of the collider but by the introduced weak solenoids. The weak solenoids do not affect the closed orbit at all and do not essentially change the beam orbital parameters. This property is universal and does not depend on the particle type. Figure-8 colliders provide a real opportunity for obtaining intense polarized deuteron beams with energies greater than a few tens of GeV.

To control the ion polarization in an ideal lattice of the JLEIC collider ring, it is sufficient to use a single 3D rotator, which consists of three modules for control of the radial n_x , vertical n_y , and longitudinal n_z beam polarization components (see Fig. 1).

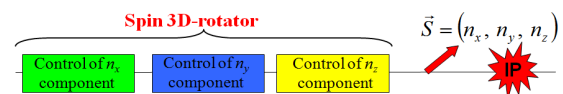


Figure 1: 3D spin rotator schematic.

Figure 2a shows the module for control of the radial polarization component n_x , which consists of two pairs of opposite-field solenoids and three vertical-field dipoles producing a fixed orbit bump. The control module for the vertical polarization component n_y is the same as that for the radial component except that the vertical-field dipoles are replaced with radial-field ones (Fig. 2b). To keep the orbit bumps fixed, the fields of the vertical- and radial-field dipoles must be ramped proportionally to the beam momentum. The module for control of the longitudinal polarization component n_z consists of a single weak solenoid (Fig. 2c).

COMPENSATION OF CHROMATICITY IN THE JLEIC ELECTRON COLLIDER RING *

Y. M. Nosochkov[†], Y. Cai, M. Sullivan, SLAC, Menlo Park, CA, USA
 Ya. S. Derbenev, F. Lin, V. S. Morozov, F. Pilat, G. H. Wei, Y. Zhang,
 Jefferson Lab, Newport News, VA, USA
 M-H. Wang, Mountain View, CA, USA

Abstract

The Jefferson Lab Electron-Ion Collider (JLEIC) is being designed to achieve a high luminosity of up to $10^{34} \text{ cm}^{-2} \text{ s}^{-1}$. The latter requires a small beam size at the interaction point demanding a strong final focus (FF) quadrupole system. The strong beam focusing in the FF unavoidably creates a large chromaticity which has to be corrected in order to avoid a severe degradation of momentum acceptance. This has to be done while maintaining sufficient dynamic aperture. An additional requirement in the electron ring is preservation of a low beam emittance. This paper reviews the development of a chromaticity correction scheme for the electron ring.

INTRODUCTION

The Jefferson Lab Electron-Ion Collider (JLEIC) [1] is being designed to achieve a high luminosity of up to $10^{34} \text{ cm}^{-2} \text{ s}^{-1}$. The latter requires a small beam size and, therefore, small beta function (β^*) at the interaction point (IP). Consequently, beta functions in the IP final focus (FF) quadrupoles are very high ($\sim 1/\beta^*$) making the FF a large source of chromaticity in the ring. Since the linear chromaticity (first order chromatic tune shift) is straightforward to cancel with conventional two-family sextupoles in the arcs, the main concern is the FF non-linear chromaticity causing a large momentum distortion of beta functions and non-linear chromatic tune shift. These effects increase the tune spread exposing the beam to more betatron resonances limiting momentum acceptance and dynamic aperture; and cause chromatic beam smear at IP resulting in a larger beam size limiting luminosity. Compensation of the FF non-linear chromaticity requires a dedicated local correction system which has been already studied for the JLEIC ion ring [2]. An additional requirement for such correction in the electron ring is that it does not significantly increase the beam emittance. This paper reviews the development of the electron ring chromaticity correction system including low emittance options.

LATTICE

The JLEIC rings have a figure-8 layout, as shown in Fig. 1 for the electron ring. The electron and ion rings are stacked vertically in the same tunnel. The baseline design includes

* Authored by Jefferson Science Associates, LLC under US DOE Contract No. DE-AC05-06OR23177 and DE-AC02-06CH11357. The US Government retains a non-exclusive, paid-up, irrevocable, world-wide license to publish or reproduce this manuscript for US Government purposes. Work supported by the US DOE Contract DE-AC02-76SF00515.

[†] yuri@slac.stanford.edu

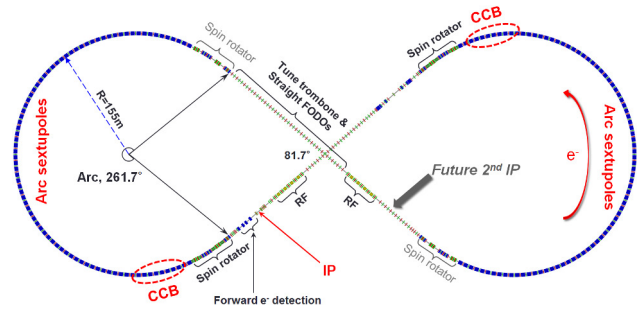


Figure 1: Top view layout of the electron ring.

one IP, where $\beta_{x,y}^* = 10 \times 2 \text{ cm}$ and the horizontal crossing angle is 50 mrad. A second IP can be added as a future upgrade. The design colliding beam energies are: 3-10 GeV for electrons, 20-100 GeV for protons, and up to 40 GeV per nucleon for ions. The figure-8 layout provides an optimal preservation of the ion polarization [3]; and the large enough circumference of $\approx 2.2 \text{ km}$ allows to use the PEP-II High Energy Ring [4] components in the electron ring.

The electron ring consists of two arcs and two long straight sections. The straights contain the interaction region (IR), spin rotators, RF-cavities, tune trombones, and a chicane for forward electron detection and polarimetry. The arc lattice is based on 15.2 m long FODO cells with 108° phase advance. The latter produces a relatively low emittance while providing conditions for cancellation of sextupole non-linear geometric and chromatic effects.

Optics of the straight section with the IR, before including the FF chromaticity correction, is shown in Fig. 2. The IR and the FF beta functions are asymmetric relative to the IP due to the detector requirements. Without the FF chromaticity correction optics, the electron ring equilibrium horizontal emittance is 8.9 nm-rad at 5 GeV from MAD8 [5] calculation, and the natural chromaticity is $\xi_{x,y} = [-113, -120]$.

CHROMATICITY CORRECTION

The chromaticity correction study for the electron ring followed a similar study performed for the ion ring [2]. A chromaticity correction block (CCB) consisting of special optics with sextupoles for FF correction is included at one end of each arc nearest to the IP, replacing the regular arc cells, as shown schematically in Fig. 1. Initially, the studied CCB design was based on the same magnet positions and bending angles as in the arc, thus preserving the ring geometry. Later, a different CCB configuration was studied based on the low emittance design developed for SuperB [6].

PROGRESS ON SKEW PARAMETRIC RESONANCE IONIZATION COOLING CHANNEL DESIGN AND SIMULATION

A. Sy[#], Y. Derbenev, V.S. Morozov, Jefferson Lab, Newport News, VA 23606, U.S.A.
 A. Afanasev, George Washington University, Washington, DC 20052, U.S.A.
 Y. Bao, University of California, Riverside, Riverside, CA 92521, U.S.A.
 R. P. Johnson, Muons, Inc., Batavia, IL 60510, U.S.A.

Abstract

Skew Parametric-resonance Ionization Cooling (Skew PIC) is an extension of the Parametric-resonance Ionization Cooling (PIC) framework that has previously been explored as the final 6D cooling stage of a high-luminosity muon collider. The addition of skew quadrupoles to the PIC magnetic focusing channel induces coupled dynamic behavior of the beam that is radially periodic. The periodicity of the radial motion allows for the avoidance of unwanted resonances in the horizontal and vertical transverse planes, while still providing periodic locations at which ionization cooling components can be implemented. Properties of the linear beam dynamics have been previously reported and good agreement exists between theory, analytic solutions, and simulations. Progress on aberration compensation in the coupled correlated optics channel is presented and discussed.

INTRODUCTION

The Parametric-resonance Ionization Cooling (PIC) [1] concept aims to enable high energy muon physics by providing muon beam emittances that are an order of magnitude smaller than those achieved using conventional ionization cooling methods. PIC uses half-integer resonances in the linear optics of its cooling channel to provide simultaneous focusing in both transverse planes, and absorbers at the naturally periodic focal points to limit the angular spread of the beam. Skew Parametric-resonance Ionization Cooling (Skew PIC) [2,3] expands on this concept by utilizing coupling of the transverse motion to shift the canonical betatron tunes away from the resonant values that destabilize the beam in the uncoupled case. Previous work described the first implementation of the Skew PIC channel and presented simulation results demonstrating the rotational behavior at periodic absorber locations that is a hallmark of Skew PIC, as well as the use of a single quadrupole family to induce a parametric resonance in the Skew PIC channel.

To be suitable as the final 6D cooling stage of a high-luminosity muon collider, a Skew PIC channel must be able to control the $p=200$ MeV/c muons from upstream stages with initial RMS momentum spread $\Delta p/p$ of 2% and initial RMS angular spread θ_{rms} of 130 mrad. The highly divergent nature of the particle distribution is very challenging for aberration compensation. Skew PIC may offer a solution by reducing the dimensionality of the aberration compensation problem to the radial dimension

[#]amysy@jlab.org

only, thereby reducing the number of compensating multipoles required. We present recent results discussing such nonlinear compensation, as well as discussions on coupling strength and implications for channel design.

EFFECTS OF COUPLING STRENGTH

The PIC and Skew PIC concepts require the correlated optics condition to be met, i.e. the canonical betatron tune in one transverse plane is an integer multiple of that in the other transverse plane. In the PIC system, this property leads multipole fields to excite nonlinear resonances. Transverse coupling in a correlated optics system, as with Skew PIC, shifts the canonical betatron tunes away from the integer values that are problematic from the aberration compensation point of view. As previously noted in [2], the magnitudes of the curvature strength K , straight quadrupole strength n , and coupling strength g are related to the rotation angle along the circular trajectory a particle traces in the x - y or x' - y' phase space at special periodic points through the relation:

$$g = -\frac{1}{2}(k_x^2 - k_y^2) \sin 2\theta$$

where

$$k_{1,2}^2 = \frac{1}{2} \left(k_x^2 + k_y^2 \pm \sqrt{(k_x^2 + k_y^2)^2 + 4g^2} \right)$$

and

$$\begin{aligned} k_x^2 &= K^2 - n \\ k_y^2 &= n \end{aligned}$$

Very large coupling strengths should be avoided to avoid the instability associated with a large rotation angle, where the dynamics can encounter a half-integer resonance. The dependence of the canonical betatron tune shift on the magnitude of the coupling strength is shown for one channel configuration in Figure 1. For this channel configuration, coupling strengths associated with tune shifts above $\Delta\nu > 0.33$ do not meet the coupled correlated optics requirement and the Skew PIC optics breaks down.

Stronger coupling may enable faster muon cooling by facilitating fast mixing of horizontal and vertical dynamic behavior. Conversely, weaker coupling may be more suitable due to constraints on the dispersion functions imposed by ionization cooling requirements. At the periodic absorber locations, the oscillating dispersion function generated by the coupled correlated optics must be small to minimize energy straggling of particles in the absorbers. A non-zero dispersion or first derivative of the

SIMULATION STUDY ON JLEIC HIGH ENERGY BUNCHED ELECTRON COOLING*

H. Zhang[†], Y. Roblin, Y. Zhang, Ya. Derbenev, S. Benson, R. Li, J. Chen,
Jefferson Lab, Newport News, VA 23606, USA
H. Huang, L. Luo, Old Dominion University, Norfolk, VA 23529, USA

Abstract

In the Jefferson Lab (JLab) Electron Ion Collider (JLEIC) project the traditional electron cooling technique is used to reduce the ion beam emittance at the booster ring, and to compensate the intrabeam scattering effect and maintain the ion beam emittance during the collision at the collider ring. Different with other electron coolers using DC electron beam, the proposed electron cooler at the JLEIC ion collider ring uses high energy bunched electron beam, provided by an ERL. In this paper, we report the new electron cooling simulation program developed at JLab to fulfil specific simulation requirements of JLEIC and some recent simulation study on how the electron cooling rate will be affected by the bunched electron beam properties, such as the correlation between the longitudinal position and momentum, the bunch size, and the Larmor emittance.

JLEIC TWO-STAGE COOLING SCHEME

To reach the frontier in Quantum Chromodynamics, the JLEIC will provide an electron beam with energy up to 10 GeV, a proton beam with energy up to 100 GeV, and heavy ion beams with corresponding energy per nucleon with the same magnetic rigidity. The center-of-mass energy goes up to 70 GeV. Two detectors, a primary one with full acceptance and a high-luminosity one with less demanding specification, are proposed. To achieve the ultrahigh luminosity close to $10^{34} \text{ cm}^{-2}\text{s}^{-1}$ per detector with large acceptance, the traditional electron cooling will be implemented strategically. [1]

The JLEIC ion complex consists of ion sources, an SRF linac, a booster ring and a collider ring, as shown in Fig 1. Since the electron cooling time is in proportion to the energy and the 6D emittance of the ion beam, which means it is easier to reduce the emittance at a lower energy, a multi-stage cooling scheme has been developed. A low energy DC cooler will be installed at the booster ring, which will reduce the emittance to the desired value for ion beams with the kinetic energy of 2 GeV/u. In the current JLEIC baseline design, An Energy-Recovery-Linac (ERL) based bunched beam cooler will be installed at the collider ring, which has 60 meter long cooling section with 2 T magnetic field inside and provides a bunched electron beam of 420 pC/bunch to compensate the intrabeam scattering (IBS) effect and maintain the emittance of the ion beam during the injection process and during the collisions. For future luminosity upgrades,

a circulator ring based bunched beam cooler is proposed, which allows to reuse the electron bunches tens of times before they finally be dumped through the ERL. Repeated

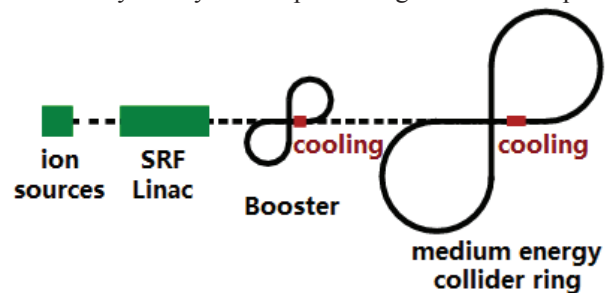


Figure 1: Components of JLEIC ion complex.

usage of the electron beam reduces the burden of the electron source, thus an electron beam up to 2 nC/bunch for stronger cooling. [1]

SIMULATION CODE DEVELOPMENT

The DC cooler is within the state-of-art. [2] But the bunched beam cooler, using high energy (up to 55 MeV) electron bunches, is out of the state-of-art, and needs significant R&D. Numerical simulation is inevitable for the design and optimization of the JLEIC electron cooling system. BETACOOOL [3] has been used in our preliminary study and it has successfully supported the JLEIC design. As the study goes more in-depth, it will be beneficial to have a more efficient and more flexible tool to fulfil some specific needs of JLEIC, and a new electron cooling simulation program has been developed at JLab. [4]

Similar with BETACOOOL, The new program calculates the evolution of the macroscopic beam parameters, such as emittances, momentum spread and bunch length. It can simulate both DC cooling and bunched beam cooling, including the IBS effect. Since BETACOOOL has provided a collection of physical models for various electron cooling simulations, we decided to follow the models in BETACOOOL, whenever they are applicable, and revise them when necessary. Martini model [5] is chosen for IBS expansion rate calculation. Martini model assumes Gaussian distribution for the ion beam, which is reasonable at least for the first order, and the absence of vertical dispersion of the lattice, which is true for JLEIC booster ring and collider ring. Parkhomchuk formula has been implemented for magnetized friction force calculation, because both the coolers at JLEIC are magnetized. Two models, the single particle model and the Monte Carlo model, are borrowed from BETACOOOL to calculate the electron cooling rate. The whole cooling process can be simulated by a four-step procedure: 1. Create sample ions; 2. Calcu-

* Work supported by the Department of Energy, under Contract No. DE-AC05-06OR23177 and DE-AC02-06CH11357.

[†] hezhang@jlab.org

DIFFUSION MEASUREMENT FROM TRANSVERSE ECHOES

Y. S. Li*, Carleton College, Northfield, MN, USA

Abstract

Beam diffusion is an important measure of stability in high intensity beams. Traditional methods of diffusion characterization (e.g. beam scraping) can be very time-consuming. In this study, we investigate the transverse beam echo as a novel technique for measuring beam diffusion. Numerical analysis of maximum echo amplitude was compared with theoretical predictions with and without diffusion. We succeeded in performing a self-consistent measurement of diffusion coefficient D_1 via a parameter scan over delay time τ . We also demonstrated the effectiveness of pulsed quadrupoles as a means to boost echo amplitude. Finally, multi-echo sequences were also briefly investigated. Results from this study will support planned experiments at the IOTA proton ring under construction at Fermilab.

INTRODUCTION

A significant barrier to the reliable operation of high intensity beams is beam diffusion due to space charge and other intensity dependent effects. The traditional method of diffusion characterization using beam scraping is a very time-intensive process that could take many hours to complete [1]. In this study, we investigate transverse beam echoes as a novel method to measure diffusion. The echo signal amplitude is extremely sensitive to any phase perturbations and more importantly, requires only several thousand turns to measure. Transverse beam echoes have been primarily observed in proton and heavy-ion rings [2]. The basic elements of an echo are the following: (a) non-linear ring elements (e.g. octupoles) to introduce action-dependence in the betatron frequency, (b) dipole kick to initiate the echo sequence and (c) quadrupole kick after delay time τ . At time 2τ , we will observe spontaneous oscillations in the beam centroid, which is an “echo” of the original dipole kick (Fig. 1). An animation of the echo sequence can be found in [3].

THEORY

Echo Characteristics

If we assume an initial Gaussian beam distribution and linear action-dependence in ω , i.e.

$$\psi_0(J) = \frac{1}{2\pi J_0} e^{-J/J_0}, \quad \omega(J) = \omega_0 + \omega' J, \quad (1)$$

where J_0 is the initial emittance, ω_0 is the base betatron frequency and ω' is the detuning parameter, then the echo amplitude is given analytically by [4, 5]

$$\langle x \rangle_{\text{ampl}}(\xi) = \frac{a}{(1 + \xi^2)^{3/2}}, \quad (2)$$

$$\text{where } a = \theta q \sqrt{\beta \beta_k} \omega' J_0 \tau. \quad (3)$$

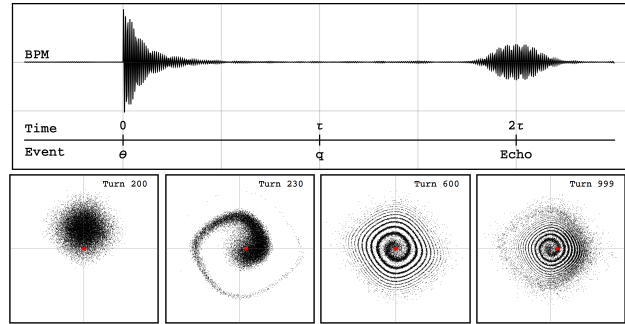


Figure 1: *Top*: Simulated BPM output for a typical echo sequence. *Bottom*: Phase space portraits a) after dipole kick, b) experiencing phase decoherence, c) after quad kick and d) at time of maximum echo amplitude. Red dot indicates beam position centroid.

Here, a is the maximum amplitude of the echo, $\xi \equiv \omega' J_0(t - 2\tau)$ is the normalized time variable and β, β_k are the betatron functions at the BPM and dipole kicker respectively. It is also useful to define the normalized maximum echo amplitude:

$$A = \frac{a}{\sqrt{\beta \beta_k} \theta}. \quad (4)$$

We expect A to have a theoretical limit of 1, since we do not expect to recover more phase information in the echo than was present right after the dipole kick. In practice, saturation effects set in much sooner, as we shall see shortly. It is also important to note that we made two key assumptions in the analysis:

1. The delay time τ is much larger than the decoherence time τ_{decoh} .
2. Both dipole kick θ and quad kick q are weak.

These assumptions impose limits on our working parameter space. A precise mathematical statement of these assumptions can be found in [5].

Diffusion

Beam diffusion is modeled by the eponymous PDE

$$\frac{\partial \psi}{\partial t} = \frac{\partial}{\partial J} \left(D(J) \frac{\partial \psi}{\partial J} \right), \quad (5)$$

$$\text{where } D(J) = D_0 + \sum_n D_n \left(\frac{J}{J_0} \right)^n, \quad n \geq 0. \quad (6)$$

Here, $\psi(J, \phi, t)$ is the beam distribution in phase space. The diffusion coefficient $D(J)$ can contain any number of linear or nonlinear terms. We will assume in this analysis that $n = 1$ (linear). The maximum echo amplitude becomes

* liy@carleton.edu

IMPLEMENTATION OF MAD-X INTO MUSIM

Yu Bao*, University of California, Riverside, Department of Physics and Astronomy, CA, USA
Tom Roberts, Fermilab, Batavia, IL 60510, USA

Abstract

MuSim is a new and innovative graphical system that allows the user to design, optimize, analyze, and evaluate accelerator and particle systems efficiently. It is designed for both students and experienced physicists to use in dealing with the many modeling tools and their different description languages and data formats. G4beamline [1] and MCNP [2] have been implemented into MuSim in previous studies. In this work, we implement MAD-X [3] into MuSim so that the users can easily use the graphical interface to design beam lines with MAD-X and compare the modeling results of different codes.

INTRODUCTION

There are many particle simulations codes available for accelerator and detector simulations. Most of them have unique and inconvenient user interfaces. The aim of MuSim is to provide a graphical user interface for the user to easily construct, simulate and compare many particle simulations. It has a 3-D viewer to display the scheme as the user constructs it. All objects, such as magnets, tubes, radio frequency cavities and detectors, can be simply dragged and dropped from the element list to the scheme. This is much more flexible and intuitive than the geometry specifications of many simulation codes using command lines. MuSim provides both global and beamline coordinates so that the user can easily choose either of them for specific systems.

MAD-X is one of the most popular codes in accelerator design and simulation. It is a general purpose accelerator and lattice design program. It reads a command line style file in which the user defines the properties of all machine elements, then calculate the optics parameters, compute the desired properties of such a machine, and simulate the beam dynamics in the designed machine. The file formats of MAD-X have been adopted by other, related simulation codes, making this interface usable for other codes as well. MAD-X has a graphic output package to output the beam parameters, but it has no graphical viewer to check the designed physical scheme.

In this work, we implement MAD-X into MuSim to combine the advantages of the two: the user can benefit from the friendly user interface of MuSim to easily design the accelerator system and use the sophisticated modules of MAD-X to simulate the beam dynamics without learning the complicated input formats of MAD-X. The users can also easily compare the simulation results between MAD-X and other simulation codes such as G4beamline and MCNP, regardless of their different input and output file formats.

* Email: yubao@ucr.edu. This work is supported by Muons Inc.

3D MAD-X

MuSim provides a unified command list to define the particle source, the beam line elements and the system coordinates for all available codes. In the "Edit" page of MuSim, the users can specify the parameters of all these elements. Figure 1 shows a single cell of a storage ring, consisting of two quadruples and a bending dipole magnet. The elements can be placed in both global coordinates and beamline coordinates, if the simulating code that the user chooses can accept them. In case of using MAD-X, only beamline coordinates can be used. The S-axis (white line) of the beamline coordinates follows the centerline of the beamline, and is bent by the bending magnets just like the reference particle; the cells are simply placed sequentially along the S axis.

Various beamline elements including drift tube, solenoid, dipole, quadruple, multiple magnet, pillbox cavity, and detectors, can be easily chosen from the command list. All their parameters are specified right after they are chosen. The command list also has several solids that MAD-X does not accept but can be used in other codes. In this case, an error message will be alarmed if the user chooses MAD-X as the simulation program.

SIMULATION CHOICES

After editing and saving the beamline elements, the user can click on the "Simulate" icon to switch to the simulation page. Figure 2 shows the simulation of a bunch of electrons passing through three quadruples. A set of detectors (yellow rings) are put along the beam line to record the beam parameters that are calculated by the simulating code. The white disk is a beam dump to stop all the particles at the end. The user can simply choose the simulating program from the drop down menu to run the simulation, and the trajectories can be displayed after the system has been simulated by a specified program.

Another advantage of MuSim are its sliders. As shown in Fig. 2, the user can vary the beam line parameters easily by either the sliders or directly the input box. The result will be shown in the 3D viewer instantly. This is a great advantage for designing beam lines.

ANALYSIS

After being simulated, the particles are recorded by the detectors along the beam line. The parameters of the particles, such as position, time, momentum, event id number, PDG id number, and field strengths (in the extended mode), are all recorded as a tree for one detector in a ROOT [4] file, regardless of which simulation code has been chosen.

Here is an example of using two codes (MAD-X and G4beamline) in MuSim to simulate a beam dynamic in a

MECHANICAL DESIGN AND MANUFACTURING OF A TWO METER PRECISION NON-LINEAR MAGNET SYSTEM*

J. D. McNevin, R. B. Agustsson, F. H. O'Shea
RadiaBeam Technologies, Santa Monica, United States

Abstract

RadiaBeam Technologies is currently developing a non-linear magnet insert for Fermilab's Integrable Optics Test Accelerator (IOTA), a 150 MeV circulating electron beam storage ring designed for investigating advanced beam physics concepts. The physics requirements of the insert demand a high level of precision in magnet geometry, magnet axis alignment, and corresponding alignment of the vacuum chamber geometry within the magnet modules to maximize chamber aperture size. Here we report on the design and manufacturing of the vacuum chamber, magnet manufacturing, and kinematic systems.

OPERATIONAL INTRODUCTION

The DOE High Energy Physics research aims to experiment with extreme high-intensity proton accelerators to observe rare processes and small deviations from the standard model, including neutrino and charged lepton oscillations [1]. RadiaBeam Technologies is developing the Integrable Optics Test Accelerator (IOTA) insert in order to produce an adequate beam for these experiments at the Advance Superconducting Test Accelerator facility at Fermi National Lab [2]. This insert employs a non-linear integrable lattice that is intended to greatly increase the stable phase space area in circular high intensity accelerators by using specifically tailored non-linear inserts of the magneto static optics with the benefit of expanding the dynamic aperture of circular machines [2].



Figure 1: IOTA Insert.

RadiaBeam Technologies is currently near the completion of a full scale prototype non-linear insert, see Fig. 1. Production of the insert has brought forth numerous notable challenges all derived from the extremely governing tolerances dictated by physics requirements. The magnets were each optimized to comply best with ideal physics. Manufacture of the magnets in turn had to closely adhere to

the optimized model so as to ensure adequate performance as well as to avoid interference with the vacuum chamber that sits inside the array of magnets. Numerous strategies were employed in the design and manufacture of the vacuum chamber to in reciprocation prevent interference with the magnet faces while simultaneously allowing for the largest internal aperture possible.

DESIGN AND MANUFACTURE OF THE MAGNET MODULES

The magnetic field strength and physical apertures size of the non-linear insert are directly related to the longitudinal distance from the center of the insert [1–3]. We have taken the approach of sectioning the insert in a manor that the physical aperture size and magnetic field properties of the magnets are constant along short partitions of the insert however very between adjacent sections along the length of the insert. This magnet section to section variance is frequent and great enough to allow the insert to comply with the physics compulsions of the integrable optics theory. The IOTA insert contains two each of nine different magnet configurations. We have assigned each configuration a name module one through module nine in order of ascending aperture size, see Fig. 2. The magnets modules are located in ascending order from the center of the insert outwards. This generates a stepwise magnetic aperture size that decreases as the beam approaches the center of the insert then increases as it exits.

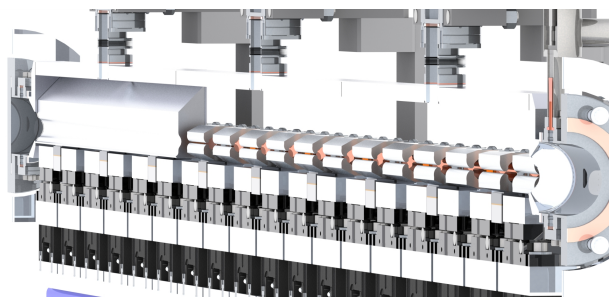


Figure 2: Array of magnets from the a bifurcated view of the insert. Portions of the vacuum chamber are hidden.

Magnet Module Physical Requirements

The design of the magnet magnets is based off of previous prototypes developed in phase one of this project wherein the level of required compliance of real geometry to idealized models was realized. The physical requirements of the magnets were evaluated by use of 2D and 3D simulations for magnetic circuit design and pole shaping [4]. This analysis

* Work supported by DOE under contract DE-SC0009531

FUNDAMENTAL PROPERTIES OF A NOVEL, METAL-DIELECTRIC, TUBULAR STRUCTURE WITH MAGNETIC RF COMPENSATION*

A. V. Smirnov[†], RadiaBeam Systems, LLC, Santa Monica, CA 90404, USA

E. Savin, National Research Nuclear University (MEPhI), Moscow, 115409, Russia

Abstract

A number of electron beam vacuum devices such as small radiofrequency (RF) linear accelerators (linacs) and microwave traveling wave tubes (TWTs) utilize slow wave structures which are usually rather complicated in production and may require multi-step brazing and time consuming tuning. Fabrication of these devices becomes challenging at centimeter wavelengths, at large number of cells, and when a series or mass production of such structures is required. A hybrid, metal-dielectric, periodic structure for low gradient, low beam current applications is introduced here as a modification of Andreev's disk-and-washer (DaW) structure. Compensated type of coupling between even and odd TE₀₁ modes in the novel structure results in negative group velocity with absolute values as high as 0.1c–0.2c demonstrated in simulations. Sensitivity to material imperfections and electrodynamic parameters of the disk-and-ring (DaR) structure are considered numerically using a single cell model.

INTRODUCTION

Industrial linac systems are employed in a wide variety of applications, from radiography to sterilization. In general, such a conventional system consists of standard, low-gradient, usually S-band, linac with beam energy from few to about ten MeVs, and average beam power in the range of few watts to 100 kW. As a rule these system are rather expensive, bulky, heavy, and not portable. The MicroLinac technology originally developed at SLAC [1] employs a compact X-band linear accelerator powered by an inexpensive, low power, pulsed magnetron [2,3]. However, to make the MicroLinac concept suitable for wider scope of applications, the conventional linac technology needs to be significantly advanced further to reduce cost, weight, and dimensions.

A biperiodic MicroLinac structure employs side [4] or on-axis [2] coupling cells enabling substantial bandwidth and number of cells to achieve beam energies exceeding 1 MeV within a single section at limited power supply (sub-MW in X-band). However, fabrication of a multi-cell, tapered MicroLinac structure remains rather expensive and time consuming. It requires significant efforts to machine the large number of different cells with very high precision. Besides, each cell usually needs to be cold-tested, some of the cells may require re-machining. A multi-step brazing is usually required along with individual tuning of the cells of the brazed assembly.

An attractive opportunity for eased fabrication of MicroLinac is using of dielectric loaded structures, in

which a smooth ceramic-lined metal tube replaces the metal periodic structure [5,6,7]. However, a wide practical implementation of this approach is prevented by a number of problems. Among them are single-wall multipactor and charging of the dielectric material capable to damage the material at practical values of pulse repetition rates and beam currents. In a MicroLinac these problems are convoluted by substantial beam loss at finite capture of a usually continuous beam injected from a thermionic injector at low energies (a few tens of keV). An additional problem is a large spread of phase velocities required for a MicroLinac lying in the range of (0.3-1)c. Shunt impedance over Q of a dielectric loaded structure at low phase velocity is noticeably lower compared to a conventional π -mode, iris loaded structure. In addition that low phase velocity implies high permittivity for dielectrics ($\epsilon > 20$), which is usually associated with elevated loss factors and thus further reduction of shunt impedance.

One interesting modification of a conventional iris (or disk) loaded traveling wave structure is related to a hybrid dielectric and iris loaded periodic accelerating structure [8]. That modification enables remarkably low (approaching to unity) overvoltage (defined as a ratio of maximum surface field to peak accelerating field) at still substantial shunt impedance and group velocity. However, this modification does not take advantage of magnetic energy stored in the dielectric to provide magnetic coupling. A modified dielectric loaded, periodic structure has been introduced to enhance coupling impedance [9]. However, that dielectric-structured approach seems to be difficult to apply for fabrication of a long, multi-cell, strongly tapered MicroLinac. It may still suffer from the issues related to dielectric exposition to the beam and multipactor similar to that in conventional dielectric-loaded and iris-loaded hybrid structures.

A hybrid metal-dielectric, periodic slow-wave structure [10] enables higher group velocities, mitigation of the charging problem, and potential simplification of structure production for a low-current, low-gradient applications. In Fig. 1 we present a schematic of a single section X-band MicroLinac for radiography source replacement.

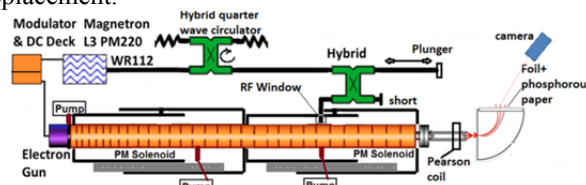


Figure 1: Schematic of a single section X-band MicroLinac system for radiography source replacement.

*Work supported by the U.S. Department of Energy (award No. DE-SC-FOA- SC0011370)

[†]asmirnov@radiabeam.com

BI-COMPLEX TOOLBOX APPLIED TO GYROMAGNETIC BEAM BREAK-UP*

A. V. Smirnov, RadiaBeam Systems, LLC, Santa Monica, CA 90404, USA

Abstract

Transverse instability of a multi-bunch beam in the presence of a longitudinal magnetostatic field and hybrid dipole modes is considered analytically within a single-section model. It incorporates resonant interaction with beam harmonics and eigenmodes, degenerated waves of different polarizations, and the Lorentz' RF force contribution. The analysis is performed in a very compact form using a bi-complex ij -space including four-component collective frequency $\tilde{\nu}$ of the instability. Rotating polarization of the collective field is determined by $\text{Im}_i \text{Im}_j \tilde{\nu}$ that is in agreement with experimental data. The other three components represent detuning of the collective frequency $\text{Re}_i \text{Re}_j \tilde{\nu}$, the "left-hand", and "right-hand" increments $\text{Im}_i \text{Re}_j \tilde{\nu} \pm \text{Im}_j \text{Re}_i \tilde{\nu}$ of the gyro-magnetic BBU effect. The scalar hyper-complex toolbox can be applied to designing of non-ferrite non-reciprocal devices, spin transport, and for characterization of complex transverse dynamics in gyro-devices such as Gyro-TWTs.

INTRODUCTION

Only a few BBU studies give detailed analysis of the instability in the presence of a longitudinal magnetic field [1,2,3]. Some experimental features of the stimulated instability in the presence of a solenoidal field [4] are not completely covered by conventional analytical models [1,3,5]. In particular, the model presented here may be helpful to explain the periodical bouncing and positive gain of stimulated dipole mode instability observed at different magnetic fields above and below the instability threshold [4].

The problem can be conveniently formulated in a 4D hypercomplex space. Conventional quaternions have been applied in physics very productively starting from the prominent Maxwell article [6]. Although the vector quaternions are used commonly, the scalar version of the quaternions is applied here to reduce the problem to a very simple scalar algebraic equation.

ANALYTICAL APPROACH

Self-consistent fields induced in a closed structure can be expanded in series of eigenmodes with variable amplitudes [7]. We apply here the approach describing long-range wake fields induced by a modulated beam in a cavities [8] and slow-wave guides in time-space domain [9,10].

*asmirnov@radiabeam.com

We treat the instability as being dominated by some complex frequency $\tilde{\omega}$ that has to be defined from a dispersion equation governing the collective process. We consider the BBU effect in the presence of two different polarizations of the dipole mode assuming conventional paraxial approximation $(p_r a)^2 \ll 1$ (where a is the aperture radius, and p_r is the transverse wavenumber of the r -th mode). We use "fast" and "slow" time variables τ and t respectively, corresponding to the bunch passage through the structure and the field amplitude evolution during the pulse.

Assuming $\tilde{\rho}$ and \tilde{C}_r are the bi-complex [11] variables, the beam transverse motion in presence of focusing is described as follows:

$$\frac{1}{\gamma} \frac{d}{d\tau} \gamma \beta_z \frac{d}{d\tau} \tilde{\rho} + j\Omega \frac{d}{d\tau} \tilde{\rho} - \Omega_{\perp} |\tilde{\rho}|_j (1+j) = -i \frac{q_0}{2m_0 \gamma} \sum_{r,\pm} D_{r,\pm} A_r \tilde{C}_r \exp\left(i(\theta_{r,\pm} \frac{\tau}{\tau_0} - \omega t)\right), \quad (1)$$

where $\tilde{\rho} = \rho_x + j\rho_y$, $\tilde{C}_r = C_r^{(x)} + jC_r^{(y)}$ are the bi-complex displacement and field slowly varying amplitudes in the two orthogonal transverse planes, $x = \text{Re}_i \text{Re}_j \tilde{\rho}$,

$y = \text{Re}_i \text{Im}_j \tilde{\rho}$, $\Omega_{\perp} = \frac{q_0 \beta_z c}{2\gamma} \frac{\partial B_z}{\partial z}$, $t = t_{ol} + \tau$ is the "slow" time

for the l -th bunch, $\Omega = \frac{q_0 B_z}{m_0 \gamma}$ is the Larmor frequency,

$\theta_{r,\pm} = kL \left(\frac{1}{\pm \beta_r} - \frac{1}{\beta} \right)$ are the phase slippages for forward and

backward waves, $\tau_0 = L/\beta c$, and L is the section length,

$$D_{r,\pm} = \frac{p_r \gamma_r^2}{2h_r} [1 \mp \beta_z \beta_r \pm \Xi_r (\beta_z \mp \beta_r)], \quad \beta_z = v_z/c,$$

$$\beta_r = k_r/h_r, \quad \gamma_r^2 = 1/(1-\beta_r^2), \quad p_r = k_r/\beta_r \gamma_r, \quad k_r = \omega'_r/c,$$

$\omega_r = \omega'_r - i\omega_r^* = \omega'_r(1-i/2Q_r)$, Q_r is the Q-factor, A_r and Ξ_r are the amplitude and hybridization coupling coefficients.

Evolution of the slowly varying field amplitudes \tilde{C}_r can be described with the Vainshtein theory [7] for a resonating structure loaded with the current $\vec{j}(\vec{r}, t)$ in the presence of stimulating signal at the frequency ω . For two degenerated eigenmodes polarized in vertical and horizontal planes we can describe the amplitude evolution as follows:

$$\frac{d\tilde{C}_r}{dt} - i(\omega - \omega_r) \tilde{C}_r = -\frac{1}{N_r} \int dV \vec{j}_{\omega} \tilde{E}_r^0, \quad (2)$$

where $\tilde{E}_r = \tilde{E}_r^{(x)} + j\tilde{E}_r^{(y)} \equiv (\tilde{E}_r^{0(x)} + j\tilde{E}_r^{0(y)}) \exp(ih_r z)$, $N_r^{(x,y)} = \epsilon_0 \int dV \tilde{E}_r^{(x,y)2}$ is the normalization factor.

At $\Delta\gamma \ll \gamma$ and $\Omega_{\perp} \ll \Omega$ equations (1) and (2) lead to the following system of homogeneous ODEs:

MAGNETIC CLOAKING OF CHARGED PARTICLE BEAMS*

K. G. Capobianco-Hogan[†], A. A. Adhyatman, G. Arrowsmith-Kron, G. Bello-Portmann, D. B. Bhatti, R. Cervantes¹, B. Coe², A. Deshpande[‡], N. Feege[‡], S. Jeffas, T. Kraulik, J. LaBounty, T. M. LaByer, A. Oliveira, H. A. Powers, R. S. Sekelsky, V. D. Shetna, H. van Nieuwenhuizen, N. Ward, Stony Brook University Physics and Astronomy, Stony Brook, NY 11794, USA

¹currently at University of Washington, Seattle, WA 98195, USA

²currently at Brookhaven National Laboratory, Upton, NY 11973, USA

Abstract

In order to measure the momentum of particles produced by asymmetric collisions in the proposed Electron Ion Collider, a magnetic field should be introduced perpendicular to the path of the beam to increase momentum resolution without bending or depolarizing it. A magnetic cloak consisting of a superconducting magnetic shield surrounded by a ferromagnetic layer is capable of shielding the interior from a magnetic field – thereby protecting the beam – without distorting the field outside of the cloak – permitting detector coverage at high pseudorapidity.

MOTIVATION

The Electron Ion Collider (EIC) is a proposed upgrade to an existing accelerator at either Brookhaven National Laboratory (BNL) or Jefferson National Laboratory (JLab) that would collide 21 GeV electrons with 250 GeV protons (or other hadron) [1]. The EIC detector built around the BaBar solenoid has been proposed as an upgrade to BNL's SPHENIX experiment if the Relativistic Heavy Ion Collider (RHIC) is upgraded to the eRHIC [2].

The addition of 1 m long 1 T homogeneous dipole fields perpendicular to the beam in the hadron going and electron going regions coupled with three position measurements with $\sigma_x = 60 \mu\text{m}$ would result in momentum resolution of $\delta p/p = p \cdot 0.2 \% \text{ GeV}^{-1} c_0$ [3]. Such dipole magnets would deflect and depolarize the electron and hadron beams as they passed through the detector. The beams can be protected from these magnetic fields using 2 m to 3 m long superconductor cylinders with diameters of 4 cm [3]. Use of such superconducting magnetic shields would distort the dipole fields near the beam line, but ferromagnetic cylinders surrounding the superconducting shields can be used to contain these distortions, creating a magnetic cloak as shown in Fig. 1.

MAGNETIC CLOAKING

Superconducting Magnetic Shield

The critical temperatures (T_c) of a superconductor is the temperature at which the superconductor transitions from the normal conducting to the superconducting states in the

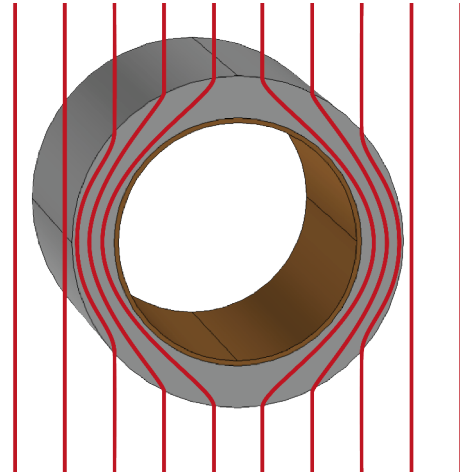


Figure 1: Diagrams the principle of magnetic cloaking, field lines shown in red [4].

when cooled in the absence of applied currents and magnetic fields. When cooled below its T_c , a type I superconductor will expel applied magnetic fields below the critical field (B_c) of the superconductor, which is a function of its temperature. Type II superconductors have two critical fields, the lower critical field (B_{c1}) and the upper critical field (B_{c2}), which are also dependant on the temperature of the superconductor. A type II superconductors can shield the majority of applied magnetic fields less than it's B_{c1} . The small leakage in this field range are due to shield geometry and magnetic flux pinning caused by microscopic impurities common in type II superconductors. Between B_{c1} and B_{c2} , a type II superconductor is in a mixed state where it will shield a portion of the applied magnetic field by allowing partial flux penetration through microscopic regions in the normal conducting state. These normal conducting regions are surrounded by vortex currents that shield the superconducting region from the magnetic field that penetrates the superconductor. Above B_{c2} , a type II superconductor will be in the normal conducting state. The critical fields of both types of superconductor are approximately given by

$$B_c(T) \approx B_c(0) \left(1 - \frac{T^2}{T_c^2}\right), \quad (1)$$

where B_{c1} and B_{c2} can be substituted for B_c .

Type II superconductors have several advantages over type I superconductors for shielding applications. Firstly, all

* Work supported by Electron Ion Collider Detector Research and Development Program funded by the DOE Office of Nuclear Physics.

[†] kyle.capobianco-hogan@stonybrook.edu, kylecapohogan@gmail.com

[‡] Faculty advisers.

FINAL 6D MUON IONIZATION COOLING USING STRONG FOCUSING QUADRUPOLES

T. L. Hart, J. G. Acosta, L. M. Cremaldi, S. J. Oliveros, and D. J. Summers
University of Mississippi, Oxford, MS 38677 USA
D. V. Neuffer, Fermilab, Batavia, IL 60510 USA

Abstract

Low emittance muon beam lines and muon colliders are potentially a rich source of BSM physics for future experimenters. A muon beam normalized emittance of $\epsilon_{x,y,z} = (280, 280, 1570)\mu\text{m}$ has been achieved in simulation with short solenoids and a betatron function of 3 cm. Here we use ICOOL and MAD-X to explore using a 400 MeV/c muon beam and strong focusing quadrupoles to achieve a normalized transverse emittance of $100\mu\text{m}$ and complete 6D cooling. The low beta regions, as low as 5 mm, produced by the quadrupoles are occupied by dense, low Z absorbers, such as lithium hydride or beryllium, that cool the beam transversely. Equilibrium transverse emittance is linearly proportional to the transverse betatron function. Reverse emittance exchange with septa and/or wedges is then used to decrease transverse emittance from 100 to $25\mu\text{m}$ at the expense of longitudinal emittance for a high energy lepton collider. Cooling challenges include chromaticity correction, momentum passband overlap, quadrupole acceptance, and staying in phase with RF.

INTRODUCTION

Ionization cooling is the only cooling technique fast enough for muons and is being tested at the MICE [1–6] experiment. The basic theory of transverse and longitudinal cooling is described in [7]. Two cooling schemes [8, 9] have been proposed to reduce muon emittances for a lepton collider [10–20]. Simulation results are shown in Table 1.

Table 1: Helical and Rectilinear Cooling Channel normalized 6D emittances ϵ_{6D} from simulations and the emittances needed for a muon collider. The channels cool by over five orders of magnitude and need less than a factor of 10 more for a collider. The 21 bunches present after initial phase rotation are also merged into one bunch during cooling [21].

	ϵ_x mm	ϵ_y mm	ϵ_z mm	ϵ_{6D} mm^3
Initial Emittance [8]	48.6	48.6	17.0	40,200
Helical Cooling [9]	0.523	0.523	1.54	0.421
Rectilinear Cooling [8]	0.28	0.28	1.57	0.123
Muon Collider [22]	0.025	0.025	70	0.044

For a given magnetic field, quadrupole focusing can achieve lower betatron functions than solenoids to reduce the equilibrium emittances below those shown in Table 1.

CHANNEL DESIGN

Low equilibrium emittance requires low $\langle \beta_{\perp} \rangle$. Strong quadrupole focusing [23, 24] can achieve β_{\perp}^* values within the required 0.5 to 2.0 cm range. A half cell is composed of four quadrupole magnets; the magnet (Q0) is a coupling quadrupole preceded by an RF (radio frequency) cavity ($L = 0.125$ m) and separated by three following RF ($L = 0.125$ m) cavities from Q1. The 650 MHz RF has a phase angle 11.5° away from zero crossing and a 27.87 MV/m gradient. The following quadrupole magnets (Q2, Q3) are separated by a short drift space to try to avoid excessive fringe field interference [25] between magnets, as shown in Fig. 1.

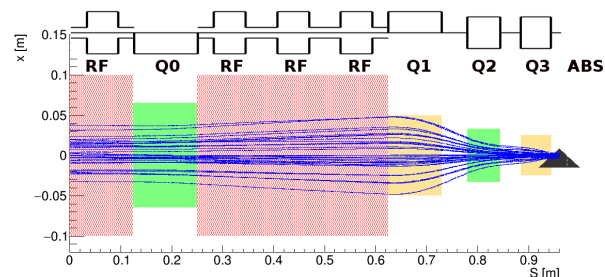


Figure 1: Half cell dimensions. Four identical RF cavities get a total of 50 cm giving a half cell length of 96 cm.

The bore diameter and length for the first quadrupole magnet Q0 is 12.5 cm. The Q0 magnet works as a coupling quadrupole reducing the betatron function maximum and allows the addition of more RF cavities to increase longitudinal synchrotron focusing. The bore diameter and length for the second quadrupole (Q1) is 10.5 cm followed by a Q2 magnet with length and diameter of 6.5 cm. A 6.0 cm long central quadrupole Q3 with 3 cm bore radius is added to reduce both the chromaticity and the minimum beta function. The 192 cm long full cell has a 3 cm drift space for an absorber. The quadrupoles Q2 and Q3 have a dipole magnetic component to produce an uniform dispersion of 4.1 mm at the absorber space [26–28].

This configuration provides strong focusing using magnetic pole tip fields of $Q0 = 0.75\text{ T}$, $Q1 = 4.69\text{ T}$, $Q2 = 9.02\text{ T}$ and $Q3 = 11.40\text{ T}$. Quadrupoles with peak fields of more than 12 T have been built with Nb_3Sn [29, 30]. The betatron function evolution for the full cell is shown in Fig. 2. The transported beam has $\beta_{x,max} \approx 2\beta_{y,max}$.

Full Cell Constraints

MAD-X [31, 32] sets magnet parameters to constrain the phase advances per 1.92 m long full cell to

1: Circular and Linear Colliders

A09 - Muon Accelerators and Neutrino Factories

A MODEL TO SIMULATE THE EFFECT OF A TRANSVERSE FEEDBACK SYSTEM ON SINGLE BUNCH INSTABILITY THRESHOLDS*

G. Bassi[†], A. Blednykh, V. Smaluk, BNL, Upton, NY 11973-5000, USA
Z. Yang, Department of Physics, Auburn University, Auburn, AL 36849, USA

INTRODUCTION

We discuss a simple algorithm to model the effect of the transverse feedback system (TFS) on beam stability based on a standard implementation of the TFS diagnostics, in which electrostatic or strip-line pickups are used as beam position monitors (BPMs) to detect the position of the beam centroid, and strip-line kickers are used to kick the momentum of the beam in order to suppress any unstable bunch centroid motion (dipole instability). This is accomplished by imposing a specific phase advance relation between the pickup and the kicker. The algorithm is implemented in the particle tracking code SPACE [1] and applied to model the NSLS-II TBS [2]. To mimic the experimental conditions, the kick induced on the bunch centroid at the kicker location requires the knowledge of the amplitude of the dipole motion at the pickup location. This is accomplished by calculating the average momentum of the bunch from the bunch centroid position at previous turns. The additional knowledge of the beta functions at the pick-up and kicker location, together with the desired damping time, completely define the kick strength.

SCHEMATICS OF THE TRANSVERSE FEEDBACK SYSTEM

The goal of a resistive TFS is to suppress betatron oscillations at a given damping rate. A schematic view of a feedback system is given in Fig. 1. A BPM detects the aver-

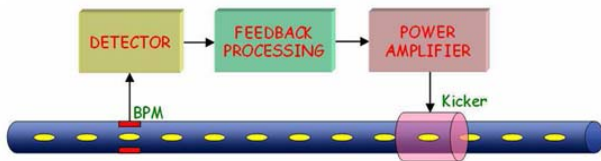


Figure 1: Schematic view of a feedback system [3]

age position of the beam acting as the detector, followed by a feedback processing to calculate the proper power, suitably amplified, to be delivered to the beam at the kicker location, where electromagnetic fields are induced on the beam with a net transfer of momentum [3]. The NSLS-II TFS is designed to provide a damping time as fast as 200 μ s to suppress transverse instabilities at the nominal current of 500mA [2].

A MODEL OF THE TRANSVERSE FEEDBACK SYSTEM

We now discuss the derivation of a simplified model of the TFS. The model is implemented in the SPACE code for our numerical analysis. Without loss of generality, we limit the discussion to the horizontal plane. We use position x and momentum $p = x'/\omega_\beta$ as phase space variables, where $\omega_\beta = c/\beta_x$ and β_x is the beta function.

Let us assume that the bunch centroids $\langle x_t \rangle = \int dx dp x f(x, p, t)$ and $\langle p_t \rangle = \int dx dp p f(x, p, t)$, where f is the transverse phase space density, perform betatron oscillations with constant β_x , then

$$\begin{aligned} \langle x_t \rangle &= \langle x_{t_0} \rangle \cos \omega_\beta (t - t_0) + \langle p_{t_0} \rangle \sin \omega_\beta (t - t_0), \\ \langle p_t \rangle &= \langle p_{t_0} \rangle \cos \omega_\beta (t - t_0) - \langle x_{t_0} \rangle \sin \omega_\beta (t - t_0). \end{aligned} \quad (1)$$

Using turn number n instead of t as independent variable, Eq.(1) can be written as a transfer map from turn n to m

$$\begin{aligned} \langle x_m \rangle &= \langle x_n \rangle \cos 2\pi\nu_x \Delta + \langle p_n \rangle \sin 2\pi\nu_x \Delta, \\ \langle p_m \rangle &= \langle p_n \rangle \cos 2\pi\nu_x \Delta - \langle x_n \rangle \sin 2\pi\nu_x \Delta, \end{aligned} \quad (2)$$

where $\Delta = m - n$ and $\nu_x = \omega_\beta/\omega_0$ is the betatron tune, where ω_0 is the revolution angular frequency. Assume now the bunch performs harmonic oscillations around the phase space origin $(0, 0)$, and let A be the amplitude of the oscillations defined as $A^2 = \langle x \rangle^2 + \langle p \rangle^2$. Then A is a constant of motion, $A_t = A_{t_0}$. Consider now the beam at turn n at a kicker location is given a kick in the momentum p according to

$$\langle x_n \rangle^- = \langle x_n \rangle^+, \langle p_n \rangle^- = \langle p_n \rangle^+ + k, \quad (3)$$

where $\langle \cdot \rangle^-$ and $\langle \cdot \rangle^+$ label quantities before after the kick respectively. Let A_K be the amplitude after the kick and A_P be the amplitude before the kick. Here the subscripts K and P refer to quantities evaluated at the kicker and pickup location respectively. It follows, for small kicks ($|k| \ll 1$), that $A_K = A_P + 2\langle p_n \rangle^- k + k^2 \approx A_P + 2\langle p_n \rangle^- k$. Thus defining $\Delta A = A_K - A_P$ and assuming $A \approx A_P \approx A_K$, it follows that $\Delta A/A = 2\langle p_n \rangle^- k/A^2$. If we label $\langle p_n \rangle^-$ as $\langle p_n \rangle_K$ (momentum at kicker location) and $\langle x_n \rangle_P, \langle p_n \rangle_P$ as position and momentum of at a pickup location preceding the kicker by the distance S , we have the transformation $\langle p_n \rangle_K = \langle x_n \rangle_P \cos \Delta\varphi + \langle p_n \rangle_P \sin \Delta\varphi$, where $\Delta\varphi = 2\pi\nu_x S/C$, with C the ring circumference. Let us assume now that the kick k is determined by the linear combination

$$k = b_0 \langle x_n \rangle_P + b_1 \langle x_{n-1} \rangle_P, \quad (4)$$

with constant coefficients b_0, b_1 . From Eq.(2) it follows that $\langle x_{n-1} \rangle_P = \langle x_n \rangle_P \cos(2\pi\nu_x) - \langle p_n \rangle_P \sin(2\pi\nu_x)$, thus, by

* Work supported by DOE contract DE-SC0012704

[†] gbassi@bnl.gov

BEAM-INDUCED HEATING OF THE KICKER CERAMICS CHAMBERS AT NSLS-II*

A. Blednykh[†], B. Bacha, G. Bassi, G. Ganetis, C. Hetzel, H.-C. Hseuh, T. Shaftan, V. Smaluk, G. Wang, BNL, NSLS-II, Upton, NY, 11973-5000, USA

Abstract

Previous experiences with the beam-induced heating of the ceramics chambers in the NSLS-II storage ring have been discussed (reference). A total five ceramics chambers are being considered for replacement due to concerns of overheating while storing $I_{av} = 500mA$ during operations. Air cooling fans have been installed as a temporarily solution to the heating problem.

INTRODUCTION

Four ceramic chambers with titanium (Ti) coating are installed in the injection straight section (Cell 30) and one additional chamber is installed in a different straight section (Cell 22) for use with the pinger magnet. The sche-

matic layout of the injection straight section is shown in Fig. 1. The kicker chambers have a ceramic length of 755 mm and octagonal profile of 76 mm (H) x 25 mm (V) which match the cross section of adjacent bellows and chambers. The original specification of the kicker ceramic chambers called for a $2\mu m$ thick coating of Ti- on the entire inner surface with $\pm 10\%$ thickness uniformity.

The Ti-coating thickness was estimated from the end-to-end resistance measurements for each chamber. It should be noted that the measured resistance before installation and after the chamber was removed from the ring, did not change, between $R \sim 3 \div 4\Omega$. It is difficult to verify the coating thickness and uniformity along the interior surface of the chambers. Work is under way to accurately characterize these thin films.

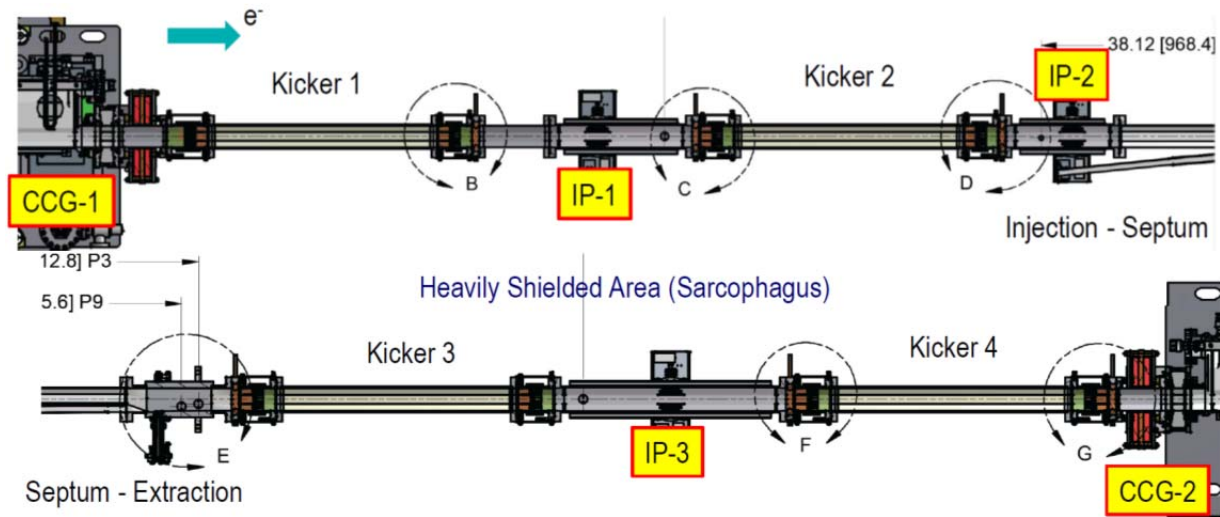


Figure 1: NSLS-II injection straight section (Cell 30).

Heating of the ceramics chambers has been observed during machine studies with an average current of $I_{av} = 375mA$ and a standard filling-pattern of $M = 1080$ bunches (Fig. 2). Several temperature RTD sensors have been installed near each transition from ceramic to stainless steel. This transition is made of Ni42 (42% of Nickel-Iron), which is used as to better match the thermal expansion of the ceramic.. It was observed that the downstream end of the kicker 2 chamber was showing a much higher temperature than the others. The maximum temperature of the Kicker2 downstream chamber as well as the other kicker chambers is shown in Fig. 2. In addition a temperature gradient was observed across the Kicker 3 chamber,

* Work supported by Department of Energy contract DE-AC02-98CH10886

[†] blednykh@bnl.gov

$T_{3,US} \sim 75^\circ C$ upstream (orange trace of Fig. 2) and $T_{3,DS} \sim 55^\circ C$ downstream (purple trace of Fig. 2). As can be seen from Fig. 2 the temperature of the chamber had not reached steady state after one hour with $I_{av} = 375mA$ (blue trace of Fig. 2) stored in the ring. The beam current was lowered due to concern of potential damage to the resulting from the unexpected heating. During beam operation at low current, we were able to collect temperature data as a function of average current. It should be noted that, between 6-7 hours are require to reach a steady-state temperature. Figure 3, shows a plot of the temperature distribution as a function of average current. This relation appears to be quadratic fitted to a curve ($T \sim I_{av}^2$). Based on this data the heating appears to be a result of resistive wall heating rather than synchrotron radiation. Tempera-

A NUMERICAL STUDY OF THE MICROWAVE INSTABILITY AT APS*

A. Blednykh[#], G. Bassi, V. Smaluk, BNL, NSLS-II, Upton, NY, 11973-5000, USA
R. R. Lindberg, ANL, Argonne, IL 60439, USA

Abstract

Two particle tracking codes, ELEGANT and SPACE, have been used to simulate the microwave instability in the APS storage ring. The total longitudinal wakepotential for the APS vacuum components, computed by GdfidL, has been used as the input file for the simulations. The numerical results have been compared with bunch length and the energy spread measurements for different single-bunch intensities.

LONGITUDINAL MICROWAVE INSTABILITY

In this paper we compare the results of numerical simulations obtained using the ELEGANT [1] and SPACE [2] codes with measurements taken at the APS storage ring. The main parameters of the APS storage ring are shown in Table 1.

Table 1: Main APS Storage Ring Parameters [3]

Energy	$E[GeV]$	7
Revolution Period	$T_0[\mu s]$	3.682
Momentum Compaction	α	2.82×10^{-4}
Energy Loss	$U [MeV]$	5.353
RF Voltage	$V [MV]$	9
Synchrotron Tune	ν_s	0.0078
Damping Time	$\tau_{x,y/s} [ms]$	9.6/4.8
Energy Spread	$\sigma_{\epsilon_0} [\%]$	0.096
Bunch Length	$\sigma_{t0} [ps]$	20

The total longitudinal wakepotential has been computed by the GdfidL code [4] for the APS vacuum components distributed around the ring. The longitudinal wakepotential for a 1mm bunch length is shown in Fig. 1. This wakepotential was simulated by Y.-C. Chae, it reflects contribution from most of the components. Based on the geometry complexity the step size for the simulations with GdfidL was probably varied, which can affect the accuracy of the simulations for different geometries. The obtained wakepotential is used to determine the instability thresholds and the numerical results are compared with the measurements. The longitudinal impedance is shown in Fig. 2 up to 150GHz. It should be noted here, that the measured results can be confirmed numerically using the numerically simulated by Y.-C. Chae the wakepotential for a shorter bunch length, 10 times shorter, than the circulating bunch in the storage ring (at low current) for longitudinal and transverse instabilities [5].

In Figs. 3 and 4 we compare the bunch length and energy spread obtained by two codes numerically with the

*Work supported by Department of Energy contract DE-AC02-98CH10886 (BNL) and ANL contract is DE-AC02-06CH11357
#blednykh@bnl.gov

measurements. The grey trace of Fig. 3 is the experimental fit of the bunch length. The blue and green dots represent the numerical results of SPACE and ELEGANT respectively.

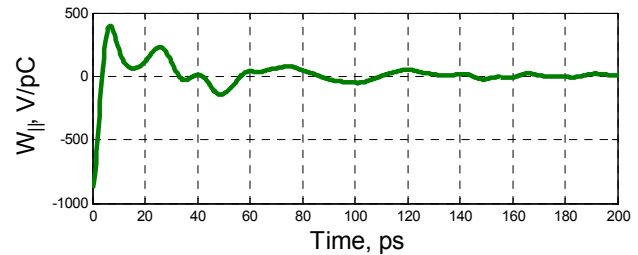


Figure 1: The total longitudinal wakepotential of the APS storage ring simulated for a 1mm bunch length, including the resistive walls and geometric changes of the vacuum components.

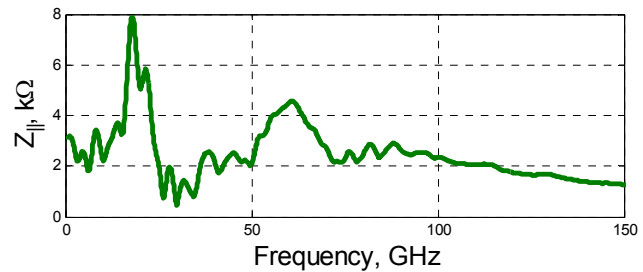


Figure 2: Modulus of the longitudinal impedance obtained by FFT of the longitudinal wakepotential presented in Fig. 1.

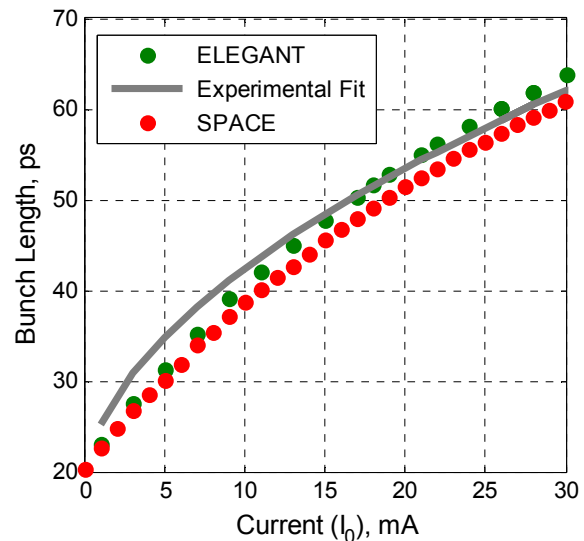


Figure 3: Bunch length vs. single bunch current at $V_{RF} = 9MV$. The experimental results are represented by the experimental fit obtained during several measurements in APS. The green and blue dots correspond to the ELEGANT and SPACE numerical results respectively.

LINEAR OPTICS CHARACTERIZATION AND CORRECTION METHOD USING TURN-BY-TURN BPM DATA BASED ON RESONANCE DRIVING TERMS WITH SIMULTANEOUS BPM CALIBRATION CAPABILITY*

Yoshiteru Hidaka[†], Boris Podobedov, Brookhaven National Laboratory, Upton, NY 11973 USA
Johan Bengtsson, J B Optima, LLC, Rocky Point, NY 11778, USA

Abstract

A fast new linear lattice characterization / correction method based on turn-by-turn (TbT) beam position monitor (BPM) data in storage rings has been recently developed and experimentally demonstrated at NSLS-II. This method performs least-square fitting iteratively on the 4 frequency components extracted from TbT data and dispersion functions. The fitting parameters include the errors for normal/skew quadrupole strength and 4 types of BPM errors (gain, roll, and deformation). The computation of the Jacobian matrix for this system is very fast as it utilizes analytical expressions derived from the resonance driving terms (RDT), from which the method name DTBLOC (Driving-Terms-Based Linear Optics Characterization/Correction) originates. At NSLS-II, a lattice corrected with DTBLOC was estimated to have beta-beating of <1%, dispersion errors of ~1 mm, and emittance coupling ratio on the order of 10^{-4} .

INTRODUCTION

There are many existing linear lattice characterization / correction methods such as LOCO [1] and other newer methods [2-4] for storage rings to name a few. As an alternative, a new algorithm called DTBLOC [5, 6] has been recently developed to characterize the linear optics from TbT data, based on linear RDTs [7-10]. TbT and dispersion data from BPMs are the only required input data for this method, which makes this tool fast. Then, the real and imaginary parts (or amplitude and phase) of two frequency components in each plane need to be extracted from TbT data by any high-precision frequency analysis method. For NSLS-II with 180 BPMs, the observation parameters consist of 1440 values from 4 complex frequency components (8 real values) per BPM and 360 values from η_x and η_y per BPM and 2 values from tunes. The fitting parameters are the integrated strength errors in normal and skew quadrupoles as well as the 4 BPM errors (horizontal & vertical gain, roll, deformation [or crunch]) for each BPM. The fitting is performed by SVD using a Jacobian matrix with analytical expressions based on RDTs.

ANALYTICAL EXPRESSIONS

In this section, we will only show the outline of the derivation and the final result of the analytical expressions used in DTBLOC to compute the Jacobian matrix of the TbT frequency components with respect to the magnet

strength errors and BPM errors. A more detailed derivation can be found in [5].

The complex Courant-Snyder variables $h_{x,-}$ and $h_{y,-}$ at turn N and at a location s in a ring can be expressed as a function of resonance driving terms (RDT) $f_{jklm}^{(s)}$ [8]:

$$h_{x,-}(s, N) = \hat{x} - i\hat{p}_x = \sqrt{2I_x} e^{i(2\pi\nu_x N + \psi_{s,x,0})} - 2i \sum_{jklm} j f_{jklm}^{(s)} (2I_x)^{\frac{j+k-1}{2}} (2I_y)^{\frac{l+m}{2}} \times e^{i[(1-j+k)(2\pi\nu_x N + \psi_{s,x,0}) + (m-l)(2\pi\nu_y N + \psi_{s,y,0})]}, \quad (1)$$

$$h_{y,-}(s, N) = y - i\hat{p}_y = \sqrt{2I_y} e^{i(2\pi\nu_y N + \psi_{s,y,0})} - 2i \sum_{jklm} l f_{jklm}^{(s)} (2I_x)^{\frac{j+k}{2}} (2I_y)^{\frac{l+m-1}{2}} \times e^{i[(k-j)(2\pi\nu_x N + \psi_{s,x,0}) + (1-l+m)(2\pi\nu_y N + \psi_{s,y,0})]}, \quad (2)$$

where the linear RDTs are defined as

$$f_{2000}(s) = \frac{\sum_w (-\Delta b_2 L^w) \beta_x^w e^{i(2\Delta\phi_x^{w,s})}}{8(1 - e^{2\pi i(2\nu_x)})},$$

$$f_{0020}(s) = \frac{\sum_w (+\Delta b_2 L^w) \beta_y^w e^{i(2\Delta\phi_y^{w,s})}}{8(1 - e^{2\pi i(2\nu_y)})},$$

$$f_{1001}^{1010}(s) = \frac{\sum_w (+\Delta a_2 L^w) \sqrt{\beta_x^w \beta_y^w} e^{i(\Delta\phi_x^{w,s} \mp \Delta\phi_y^{w,s})}}{4(1 - e^{2\pi i(\nu_x \mp \nu_y)})}.$$

From Eqs. (1) and (2), for an uncoupled lattice with focusing errors only ($\Delta b_2 L \neq 0, \Delta a_2 L = 0$), we can derive analytical expressions for \hat{x} and \hat{y} TbT positions in terms of 2 sine-cosine pair terms with 2 different frequencies as a function of RDTs responsible for β -beating (2000 and 0020). Then adding coupling errors on top of this lattice, we can obtain another set of expressions for \hat{x} and \hat{y} TbT positions as a function of all the linear RDTs (2000, 0020, 1001, and 1010). After approximation assuming small magnet strength errors, which results in small RDT values, and using the relationship $x = \sqrt{\beta_x} \hat{x}$ and $y = \sqrt{\beta_y} \hat{y}$ between the normalized coordinates (\hat{x}, \hat{y}) and the phase-space coordinates (x, y) , we can express the magnitudes and phases for the primary and secondary frequency components f_{x1}, f_{y1} and f_{x2}, f_{y2} of (x, y) TbT positions as the following:

$$|f_{x1}| = \sqrt{\{C_x^{(x)}\}^2 + \{S_x^{(x)}\}^2}, |f_{x2}| = \sqrt{\{C_y^{(x)}\}^2 + \{S_y^{(x)}\}^2},$$

$$|f_{y1}| = \sqrt{\{C_y^{(y)}\}^2 + \{S_y^{(y)}\}^2}, |f_{y2}| = \sqrt{\{C_x^{(y)}\}^2 + \{S_x^{(y)}\}^2}, \quad (3)$$

* Work supported by U.S. DOE under Contract DE-AC02-98CH10886.

[†] yhidaka@bnl.gov

USING SQUARE MATRIX TO REALIZE PHASE SPACE MANIPULATION AND DYNAMIC APERTURE OPTIMIZATION*

Yongjun Li[†], Li-Hua Yu, BNL, Upton, New York, USA

Abstract

A new method of using linear algebra technique to analyze periodical nonlinear beam dynamics is presented in ref. [1]. For a given system, a square upper triangular nonlinear transfer matrix is constructed out of the truncated power series transfer map. The square matrix is first separated into different invariant subspaces with much lower dimensions and we only focus on few invariant subspaces. An excellent action-angle approximation to the solution of the nonlinear dynamics can be obtained after applying Jordan transformation. We found that the deviation of linear action-angle invariant (i.e. Courant-Snyder invariant) from constancy of the new action provides a measure of the nonlinear of the motions. Therefore the square matrix provides a novel method to optimize the nonlinear dynamic system, and manipulate phase space as well. A chromaticity +7/+7 lattice of the NSLS-II optimized with this method was successfully commissioned. Our studies show that a basic “principle” – confining tune-shift-with-amplitude to prevent tune from crossing resonances in designing strong focusing storage rings, with which was complied by accelerator physicists for several decades, may not be an absolutely necessary condition.

INTRODUCTION

The question of the long term nonlinear behavior of charged particles in storage rings has a long history. To gain understanding, one would like to analyze particle motion under many iterations of the one turn map. The most reliable numerical approach is the use of a tracking code with appropriate local integration methods. For analysis, however, one would like a more compact and efficient representation of the one-turn-map out of which to extract relevant information. Among the many approaches to this issue we may mention canonical perturbation theory, Lie operators, power series, and normal form etc. Here, we would like to look at this problem from a somewhat different perspective, i.e., using linear algebra technique to analyze and optimize nonlinear beam dynamics. The theory on the square matrix method is explained in ref. [1]. In the following section, we only summarize this method briefly.

THEORY

For a given periodical nonlinear dynamic system, such as a particle moving in a storage ring, we use the complex Courant-Snyder variable $z = \bar{x} - i\bar{p}$, its conjugate $z^* = \bar{x} + i\bar{p}$ and powers to form a vector $\mathbf{Z} = (1, z, z^*, z^2, zz^*, \dots, z^{*n})^T$,

where T means taking the transpose of a vector. Here we use 1D motion to simplify the notation. The one turn map to transfer an initial status \mathbf{Z}_0 to its final status \mathbf{Z}_1 can be represented by a square matrix \mathbf{M} :

$$\mathbf{Z}_1 = \mathbf{M}\mathbf{Z}_0 \quad (1)$$

The matrix \mathbf{M} is upper-triangular, and has the form

$$\mathbf{M} = \begin{pmatrix} 1 & 0 & \cdots & 0 \\ 0 & \mathbf{M}_{11} & \cdots & \mathbf{M}_{1n} \\ \vdots & & \ddots & \vdots \\ 0 & 0 & \cdots & \mathbf{M}_{nn} \end{pmatrix} \quad (2)$$

Here each submatrix \mathbf{M}_{ij} has different dimensions respectively. Among them, \mathbf{M}_{ii} 's are square diagonal submatrices. A great simplification comes from a fact that the matrix is upper tridiagonal with all its eigenvalues given by its diagonal elements precisely determined by the tune, which represents the oscillation's phase advance per turn $\mu = 2\pi\nu$ solely. We can separate the full space spanned by the matrix columns into different invariant subspaces according to the eigenvalues. For example, all $z(zz^*)^k$, $k = 0, 1, \dots$ belong to a same invariant space of the eigenvalue $e^{i\mu}$. We found that the simplest invariant subspaces $e^{i\mu}$ already provides a wealth information about dynamics. In this way, the high dimension matrix is reduced to several much lower dimension ones. For example, for a 2D $x - y$ system (4D in phase space), if we truncate the square matrix up to the 7th order, its dimension is 330×330 . The reduced matrix dimension for $e^{i\mu_x}$ and $e^{i\mu_y}$ is only 10×10 respectively. Then a stable Jordan decomposition, can be obtained on the low dimension submatrices \mathbf{M}_j

$$\mathbf{N}_j = \mathbf{U}_j \mathbf{M}_j \mathbf{U}_j^{-1} = e^{i\mu_j \mathbf{I}_j + \boldsymbol{\tau}_j} \quad (3)$$

where the matrix \mathbf{N}_j with $j = 1, 2, \dots$ is the Jordan block with eigenvalue $e^{i\mu_j}$, corresponding to the j^{th} invariant subspace inside the space of vector \mathbf{Z} . \mathbf{I}_j is the identity matrix, while $\boldsymbol{\tau}_j$ is a superdiagonal matrix:

$$\boldsymbol{\tau}_j = \begin{pmatrix} 0 & 1 & 0 & \cdots & 0 \\ 0 & 0 & 1 & \cdots & 0 \\ \vdots & \vdots & \ddots & \ddots & \vdots \\ 0 & 0 & 0 & \ddots & 1 \\ 0 & 0 & 0 & \cdots & 0 \end{pmatrix} \quad (4)$$

The transfer of \mathbf{Z}_0 by the one turn map \mathbf{M} inside the j^{th} subspace can be re-written as

$$\mathbf{W}_1 = \mathbf{U}\mathbf{Z}_1 = \mathbf{U}\mathbf{M}\mathbf{Z}_0 = e^{i\mu\mathbf{I} + \boldsymbol{\tau}}\mathbf{W}_0 \quad (5)$$

* Work supported by U.S. Department of Energy under Contract No. DE-AC02-98CH10886 and DE-SC0012704

[†] yli@bnl.gov

OPTIMIZE THE ALGORITHM FOR THE GLOBAL ORBIT FEEDBACK AT FIXED ENERGIES AND DURING ACCELERATION IN RHIC*

C. Liu[†], R. Hulsart, K. Mernick, R. Michnoff, M. Minty
Brookhaven National Laboratory, Upton, NY, U.S.A.

Abstract

To combat triplets vibration, the global orbit feedback system with frequency about 10 Hz was developed and engaged in operation at injection and top energy in 2010, during beam acceleration in 2012 at RHIC. The system has performed well with keeping 6 out of 12 eigenvalues for the orbit response matrix. However, we observed corrector current transients with the lattice for polarized proton program in 2015 which resulted in corrector power supply trips. In this report, we will present the observation, analyze the cause and also optimize the feedback algorithm to overcome the newly emerged problem with the feedback system.

INTRODUCTION

RHIC comprises two circular counter-rotating accelerators in a common horizontal plane, which are oriented to intersect one another at six interaction points (IPs) with two colliding beam experiments (STAR and PHENIX) [1]. Each ring consists of three inner arcs and three outer arcs with six insertions joining them. The DX dipole magnets bring the beams together for head-on collisions at IPs for experiments. They are the only common bending magnets for both rings. The triplets (Q1, Q2 and Q3 quadrupole magnets) focus the beam for small beam sizes at IPs. The triplets and D0 magnets on the same side of IP for the two rings were installed in the same cryostat.

Horizontal orbit jitter around 10 Hz was observed in both rings in the early days by measuring the beam positions [2]. Triplets vibration was suspected since its strong focusing and the sharing of cryostat of triplets from both rings. This hypothesis was later confirmed by offline modeling and measurement by accelerometer of the triplet vibrations with frequency around 10 Hz. Later on, oscillation of Helium flow pressure around 10 Hz was measured as well [3, 4].

The orbit jitter will affect the beam parameters and machine performance in many ways [5]. The orbit jitter caused by Helium-induced triplet vibration would introduce orbital and angular jitter at the IPs, which will diminish the luminosity. The orbit jitter in sextupoles will introduce tune modulations, which would affect dynamic aperture and therefore beam lifetime. The orbit jitter at collimators and experimental area would result in oscillating background. The precision of beam measurements were dominated by the presence of 10 Hz orbit oscillation.

Several solutions were proposed to combat the orbit jitter problem over the years [6, 7]. Stiffening of the mechanical

supports of the magnet was suggested to increase the resonant frequencies of the triplet. A linear shock absorber attached to outside support can damp the triplet vibration passively. Two linear actuators connected to each end of the cold mass provide forces proportional and opposite to the velocities of both ends of the cold mass would damp the vibration actively. A local orbit feedback system with small corrector dipoles at the two ends of the cryostat to compensate both position and angle was designed and tested. The 10 Hz global orbit feedback system with correctors located close to triplets, which correct the orbit oscillation reported by fast BPMs globally was designed and implemented for operation successfully.

ORBIT FEEDBACK SYSTEM OVERVIEW

The 10 Hz global orbit feedback system [8] was designed to correct the 10 Hz horizontal beam perturbations in both rings that are caused by Helium induced triplet vibration. The full system in each ring consists of 36 BPMs, corresponding to 2 per triplet in each of the 12 triplet locations and two in each of the 6 arcs, and 1 dipole corrector at each triplet location for a total of 12 correctors. The standard RHIC BPM Integrated Front End (IFE) electronic modules were equipped with new daughter card for 10 kHz position data distribution [9]. The correctors are compact “window-frame” horizontal laminated yoke magnets due to space limitations. A small fringe field from each magnet, overlapping the opposite RHIC ring, is compensated by a correction winding placed on the opposite ring’s magnet and connected in series with the main winding of the first one [10].

ORBIT FEEDBACK ALGORITHM

The algorithm is essentially a least square fit with the goal to compensate the 10 Hz orbit oscillation by fast correctors [11]. On the left side of Eq. (1), the x_i is the measured beam positions. The x_{ig} is the goal beam position, which is the measured average position in our case.

$$\begin{pmatrix} x_1 \\ x_2 \\ \vdots \\ x_m \end{pmatrix} + \begin{pmatrix} x_{1g} - x_1 \\ x_{2g} - x_2 \\ \vdots \\ x_{mg} - x_m \end{pmatrix} = \begin{pmatrix} x_{1g} \\ x_{2g} \\ \vdots \\ x_{mg} \end{pmatrix} \quad (1)$$

To compensate the oscillation, one needs to introduce orbit offsets by assigning proper correction strength to correctors. The $m \times n$ matrix R denotes the response of the beam positions to the strength of correctors. The proper corrector

* The work was performed under Contract No. DE-SC0012704 with the U.S. Department of Energy.

[†] cliu1@bnl.gov

THE eRHIC RING-RING DESIGN *

C. Montag, G. Bassi, J. Beebe-Wang, J.S. Berg, M. Blaskiewicz, A. Fedotov, W. Fischer, Y. Hao, A. Hershcovitch, Y. Luo, R. Palmer, B. Parker, S. Peggs, V. Ptitsyn, V. Ranjbar, S. Seletskiy, T. Shaftan, V. Smaluk, S. Tepikian, F. Willeke, H. Witte, Q. Wu,
Brookhaven National Laboratory, Upton, NY 11973, USA

Abstract

The ring-ring version of the eRHIC electron-ion collider design aims at providing electron-proton collisions with a center-of-mass energy ranging from 32 to 141 GeV at a luminosity reaching $10^{33} \text{ cm}^{-2} \text{ sec}^{-1}$. This design of the double-ring collider also supports electron-ion collisions with similar electron-nucleon luminosities, and is upgradeable to $10^{34} \text{ cm}^{-2} \text{ sec}^{-1}$ using bunched beam electron cooling of the hadron beam and more bunches. The baseline luminosities are achievable using existing technologies and beam parameters that have been routinely achieved at RHIC in hadron-hadron collisions or elsewhere in e+e- collisions. This minimizes the risk associated with the challenging luminosity goal and is keeping the technical risk of the e-RHIC electron-ion collider low. The latest design status will be presented.

INTRODUCTION

The ring-ring design of the electron-ion collider eRHIC aims at an electron-proton center-of-mass energy range of 32 - 141 GeV, with luminosities in the $10^{32} - 10^{33} \text{ cm}^{-2} \text{ sec}^{-1}$ range. This is realized by adding an electron storage ring with an energy range of 5 to 18 GeV to the existing RHIC facility, which will be operated at proton energies from 50 to 275 GeV. The upper electron energy limit has been chosen to limit the total synchrotron radiation power to 10 MW while still providing high luminosities at the highest center-of-mass energies. The number of bunches is increased 3-fold over the present RHIC configuration, to 330. This necessitates new injection kickers and in-situ copper coating of the existing stainless steel beam pipes to lower the resistive wall cryo load as well as the secondary electron yield [1, 2].

The luminosity scales as

$$\mathcal{L} \propto \sqrt{I_p I_e (1 + K_x)(1 + K_y)} \left(\frac{\xi_{x,p} \xi_{y,p} \xi_{x,e} \xi_{y,e}}{\beta_{x,p}^* \beta_{y,p}^* \beta_{x,e}^* \beta_{y,e}^*} \right)^{1/4}, \quad (1)$$

where I , ξ , and β denote the beam current, beam-beam parameter, and the β -function at the interaction point (IP), while $K_x = \sigma_x/\sigma_y$ and $K_y = \sigma_y/\sigma_x$ are the ratios of horizontal and vertical beam sizes at the IP, which are equal for both beams. The beam-beam parameters ξ_p for the protons are limited to what has been achieved in proton-proton collisions in RHIC, $\xi_p < 0.015$ [3], while we assume a maximum $\xi_e < 0.1$ for the electrons, as has been achieved in KEKB [4]. As Equation 1 shows, luminosity is increased

with flat beams, $K_x = \sigma_x/\sigma_y \gg 1$. Flat beams in eRHIC are achieved by intentionally increasing the horizontal proton beam emittance in conjunction with a large β -function ratio β_x/β_y between 6 and 140.

The eRHIC physics program requires detector acceptance for forward scattered protons with transverse momenta between 200 MeV/c and 1.3 GeV/c. These protons are detected by Roman Pots that are inserted into the beam pipe downstream of the main detector. This requires the scattered protons to have a transverse amplitude of about 10σ , where σ denotes the RMS proton beam size at the location of the Roman Pot, which in turn limits the maximum allowable RMS beam divergence σ' at the IP. For a beam energy of 275 GeV, a transverse momentum of 200 MeV/c corresponds to a scattering angle $\phi = 730 \mu\text{rad}$; the maximum allowable RMS beam divergence is therefore $\sigma' = 73 \mu\text{rad}$. For given emittance this limits the IP β -function β^* , and therefore the luminosity. However, not the entire transverse momentum range has to be measured in the same machine configuration. Since events with small transverse momenta p_\perp are plentiful, operating in a configuration with good acceptance at small p_\perp , where the luminosity is limited, over a small fraction of time provides sufficient statistics for the experimental program. The majority of the time the machine can then be operated with high luminosity to detect a sufficiently large number of protons with high p_\perp . Table 1 lists the design parameters at the beam energies giving the highest luminosities.

INTERACTION REGION

High luminosity requires small β^* . Since these small β -functions increase quadratically with the distance from the IP, it is necessary to place the innermost focusing magnets as close to the IP as possible to avoid excessive contributions to the machine chromaticity from those quadrupoles, and limit their aperture and, in turn, their peak fields. The low- β magnets for both the electron and the proton beam are therefore arranged in an interleaved pattern, as depicted in Figure 1. Since the detector requires a machine-element free region of ± 4.5 m around the IP, the innermost (proton) quadrupole is located just outside the detector.

Since the eRHIC physics program requires detection of forward neutrons within a ± 4 mrad cones, a strong dipole magnet (B1) deflects the proton beam away from that neutron cone which is then detected about 25 m downstream of the IP. A second dipole (B2) then bends the proton beam back, thus forming a dogleg with B1. Between the second dipole (B2) and the fourth proton quadrupole (Q4) there is a

* Work supported by the US Department of Energy under contract number DE-SC0012704

THE ROLE OF ADAMI INFORMATION IN BEAM COOLING*

V. H. Ranjbar, BNL, Upton, NY, USA

Abstract

We re-consider stochastic cooling as type of information engine using the Adami definition of information [1]. We define information as data which can permit the cooling system to predict the individual trajectories better than purely random prediction and then act on that data to modify the trajectories of an ensemble of particles. In this study we track the flow of this type of information through the closed system and consider the limits based on sampling and correction as well as the role of the underlying model.

INTRODUCTION

The view of stochastic cooling as a type of information engine goes back to Simon Van Der Meer [2] the inventor of stochastic cooling, who cast it as a form of the famous Maxwell's demon, which is currently understood as type of information engine.

If we recall James Maxwell came up with a famous thought experiment that challenged the ideas enshrined in the second law of thermodynamics, specifically the idea that for a system of particles in thermal equilibrium, where all the fast and slow moving particles were completely mixed, no more work could be extracted. Maxwell imagined a box containing this distribution with a wall dividing it into two sides (see Fig. 1). In the wall there was a door, which was controlled by some demon that would open the door only for fast moving particles and keep it shut for the slow particles. In this way, over time, all the fast particles would come to reside on one side of the box, leaving the slow particles on the other. In this situation, a heat engine could be run from the differential in temperature, and thus extracting work in violation of the second law of thermodynamics.

For many years Maxwell's demon challenged the understanding of entropy and the second law. Later, statistical mechanics were worked into the existing thermodynamic framework and entropy was understood as representing the possible states of a given system. Finally, entropy made its way into the new field of information theory when Shannon equated the statistical definition of entropy with information [3]. Maxwell's Demon began to be understood as a class of information engines. An information engine is currently understood as a system which can turn information into work. Here information gathered by the demon concerning the velocity of each particle represented a rise in entropy. This is because this information needed to be stored on some physical medium whose initial entropic state had to be considered. So, for example, a magnetic tape, which stores information as zeros and ones, needed to be first initialized to be all zeros. This initialization placed the tape into a

* Work supported by the US Department of Energy under contract number DE-SC0012704.

† vranjbar@bnl.gov

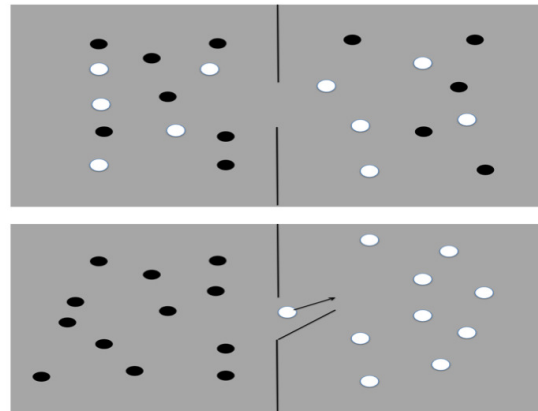


Figure 1: Fast (white) and slow (black) particle in equilibrium (top). Maxwell's Demon opens door to sort particles of different speed (bottom).

lower entropic state, which was then given up as information was recorded. In the end, the work required to reset this memory would consume more energy than was extracted, thus preserving the second law. This is known as Landauer's erasure principle [4]. More recently a physical realization of a type of Maxwell demon machine has been created using a photon circuit [5]. However, the implications of Maxwell's Demon are still somewhat unresolved and debated.

ADAMI INFORMATION

Of course the stochastic cooling system doesn't come anywhere near violating the second law of thermodynamics, since the energy consumed by the amplifiers, and kickers clearly introduce external energy to help lower the entropy of the cooled beam. However as Simon Van Der Meer recognized, the set-up is actually very similar. In the classical stochastic cooling system, there exists a pickup and kicker which operates somewhat like the demon, in that the demon (the cooling system) takes a measurement and then based on that performs an operation. In the case of stochastic cooling the demon kicks offending particles back into a lower orbit (see Fig. 2). What is important here is that this system uses 'information' together with externally supplied energy to lower the entropy and increase the order of the system, which in this case it is the beam. This is different from other standard cooling systems in that usually it involves an exchange of energy in the form of gases, liquids or particles mixing with a cool bath (as in electron cooling) that achieve the reduction of entropy. In the stochastic cooling case information about the predicted behavior of the system is a key component, without it, this type of cooling couldn't occur. Also the better one's information is the more cooling possible.

PERMANENT MAGNETS FOR HIGH ENERGY NUCLEAR PHYSICS ACCELERATORS*

N. Tsoupas[†], S. Brooks, A. Jain, F. Meôt, V. Ptitsyn, and D. Trbojevic
Brookhaven National Laboratory, Upton, NY 11973, USA

Abstract

The proposed eRHIC accelerator[1] will collide 20 GeV polarized electrons with 250 GeV polarized protons or 100 GeV/n polarized ^3He ions or other unpolarized heavy ions. The electron accelerator of the eRHIC will be based on a 1.665 GeV Energy Recovery Linac (ERL) placed in the RHIC tunnel and two Fixed Field Alternating Gradient (FFAG) recirculating rings placed alongside the RHIC accelerator. The electron bunches reach the 20 GeV energy after passing 12 times through the ERL by recirculation in the FFAG rings. After the interaction with the hadron bunches the electron bunches will give back their energy to the ERL in the form of electromagnetic radiation after passing 12 times through the ERL. The FFAG rings consist of FODO cells comprised of one focusing and one defocusing quadrupoles made of permanent magnet material. Similarly other sections of the electron accelerator will utilize permanent magnets. In this presentation we will discuss details on the design of these magnets and their advantages over the current-excited magnets.

INTRODUCTION

The proposed eRHIC accelerator [1] shown schematically in Fig. 1 consist of the hadron accelerator (blue ring in Fig. 1) and the electron accelerator comprised of a 1.665 GeV Energy Recovery Linac (ERL) and two rings (red arcs) based on the FFAG principle. The accelerator will collide 20 GeV polarized electrons with 250 GeV polarized protons or 100 GeV/n polarized $^3\text{He}^{+2}$ ions or other non-polarized heavy ions. The electron bunches reach the 20 GeV energy by passing 12 times through the ERL and by recirculating in the FFAG rings. After the interaction with the hadron bunches the ERL will retrieve the energy from the electron bunches in the form of electromagnetic radiation after the bunches pass 12 times through the ERL. One of the two modes of operation of the eRHIC accelerator is the 15.0 GeV where the low energy FFAG arc accommodates the energy range of the electron bunches from 1.685 GeV to 5.016 GeV (see inserts in Fig. 1) with the high energy arc from 6.680 GeV to 15.0 GeV and the other mode is the 20 GeV with the corresponding energy range of the electron bunches shown on Fig. 1). The experimental areas of the electron-hadron collisions are shown by the yellow rectangles. Two important concepts are involved in the electron accelerator, namely, the ERL and the FFAG concepts. The ERL concept provides 1.665 GeV of energy to the electron bunches each time they pass through the ERL for the electrons to achieve the top energy of the

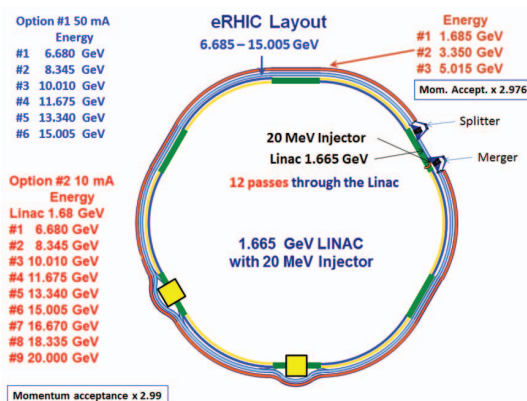


Figure 1: Schematic diagram of the eRHIC accelerator. The blue and red rings are the hadron and the electron accelerators respectively. The yellow rectangles are the experimental areas for the electron-hadron collisions.

20 GeV before the collision with the hadrons. Following the collision the electrons deliver back to the ERL the 20 GeV of energy by recirculating 12 times through the ERL, each time delivering to the ERL 1.665 GeV of energy. Since it takes 12 passes for the electrons to achieve the 20 GeV of energy, and also 12 passes to give back the energy to the ERL, the electron bunches circulating in the accelerator have 12 different energies, ranging from 1.685 to 20 GeV. The three electron bunches with the energies 1.685, 3.350 and 5.015 GeV are circulating in one FFAG arc and the rest of the bunches with energy range from 6.68 GeV to 20.0 GeV in the second FFAG arc. Thus this particular design of the FFAG places electron bunches with large energy range in a small transverse distance of ~ 22 mm in each of the FFAG arcs. The remarkable property of the FFAG is the accommodation of bunches with large energy range into a relatively small transverse space of the FODO cell.

THE FFAG CELL

The FFAG arcs of the eRHIC consists of FODO cells which can be made of a pair of quadrupoles which are displaced in the transverse direction or a pair of magnets each having a dipole and a quadrupole component. Figure 2 shows the parameters of one particular design of an eRHIC cell which is made of a pair of displaced quadrupoles. The traces on the figure are the trajectories of the central particle of the three recirculating electron bunches.

* Work supported by the US DOE under contract number DE-SC0012704

[†] tsoupas@bnl.gov

RECENT IMPROVEMENTS TO TAPAS, THE ANDROID APPLICATION FOR ACCELERATOR PHYSICS AND ENGINEERING CALCULATIONS

M. Borland*, Westmont, IL USA

Abstract

The Android application TAPAs, the Toolkit for Accelerator Physics on Androids, was released in 2012 and at present has over 300 users. TAPAs provides more than 50 calculations, many of which are coupled together. Updates are released about once a month and have provided many new capabilities. Calculations for electron storage rings are a particular emphasis, and have expanded to include CSR threshold, ion trapping, Laslett tune shift, emittance dilution, and undulator brightness curves. Other additions include helical superconducting undulators, rf cavity properties, Compton backscattering, and temperature calculations for mixing water.

INTRODUCTION

The need to perform quick, approximate calculations arises frequently in the day-to-day experience of physicists and engineers working at accelerator facilities. This can happen during informal discussions, meetings, reviews, or simply when exploring ideas at one's desk. Being able to perform a reasonably accurate calculation quickly is a great productivity aid in many situations. These days, we are more likely to have a smartphone at hand than almost any other calculation aid. It was with this in mind that the Android application TAPAs [1] was written.

The name TAPAs, "Toolkit for Accelerator Physics for Androids," is meant to bring to mind the popular Spanish cuisine, in that calculations are broken up into many relatively small "activities." The "toolkit" aspect comes into play in that these activities are linked together through sharing of certain numerical inputs and outputs. Figure 1 gives a QR code for downloading TAPAs.

NEW FEATURES AND CAPABILITIES

Calculations within TAPAs are separated into several major categories, namely, Electron Storage Rings, Undulators, Synchrotron Radiation, Electron Linear Accelerators, Electron Guns, Free Electron Lasers, Electromagnetism, Engineering, Particle Passage Through Matter, and APS-Specific Calculations. Most of these have seen improvements and additions since the original publication [1]. One general improvement is that the pop-up calculator used for data entry now consistently includes all input and output quantities under the "Val." button. It is also scrollable, which supports use in split-window mode on Android 7.

* michael.d.borland@gmail.com

Electron Storage Rings

This category has seen perhaps the most changes since the previous publication. One of the most useful activities is the Storage Ring Scaling activity, which allows scaling lattices by the number of cells and beam energy. Several built-in lattices are provided for the convenience of the user, as illustrated in Fig. 2. In addition, TAPAs now allows the user to load custom lattices. To do this, one runs `elegant` [2] for the lattices in question, followed by the script `prepareTAPAs` (distributed with `elegant`). This script prepares a file that can be transferred to one's Android device and then loaded into TAPAs.



Figure 1: QR code for obtaining TAPAs from Google Play.

Several other storage ring activities make use of lattice data as well (regardless of whether it is built-in or user-provided), based on the lattice selected in the scaling activity. Among these are three new activities: ion trapping, Laslett tune shift, and emittance dilution. The ion trapping calculation uses the s -dependent lattice functions, the natural emittance, the energy spread, and the user-specified emittance ratio to compute the fraction of the circumference over which various gas species are expected to be trapped. The functionality is equivalent to that provided by the script `ionTrapping` that is distributed with `elegant`. The Laslett tune shift activity performs integrals over the periodic cell, following [3] and [4]. In both cases, one can perform more approximate calculations even without a lattice by entering values for average beam sizes or lattice functions.

The emittance dilution activity computes transverse and longitudinal emittance dilution due to decoherence following injection of a mismatched, offset beam into a storage ring [5]. In addition, it allows estimation of the time required to damp to within a specified factor of the equilibrium beam properties.

The gas scattering lifetime activity has been improved to support both rectangular and elliptical aperture shapes. The code integrates over the aperture shape in a method similar to that outlined in [6].

BENCHMARK OF STRONG-STRONG BEAM-BEAM SIMULATION OF THE KINK INSTABILITY IN AN ELECTRON ION COLLIDER DESIGN*

J. Qiang[#], R. D. Ryne, LBNL, Berkeley, CA94720, U.S.A.

Y. Hao, BNL, Upton, Long Island, NY 11973, U.S.A.

Abstract

The kink instability limits the performance of a potential linac-ring based electron-ion collider design. In this paper, we report on the simulation study of the kink instability using a self-consistent strong-strong beam-beam model and benchmark these results with a strong-weak model and an analytical model.

INTRODUCTION

An electron-ion collider (EIC) as the highest priority from the Nuclear Physics Office long range plan recommendation has been actively studied at both BNL and Jlab. The linac-ring collider is an important option for the EIC design due to the fact that it can produce higher luminosity than the ring-ring based collider [1]. However, the beam-beam effect between the electron beam and the proton/ion beam significantly limits the final collider performance. Besides causing the electron beam mismatch at the interaction point and transverse phase space distortion, it also causes the proton/ion beam unstable and emittance blow up through the so-called kink instability [2-3]. Here, the kink instability is similar to the conventional wakefield head-tail instability except that the wakefield in the kink instability is from the electron beam-beam force excited by the small offset of the proton beam. Such an instability limits final luminosity of the linac-ring collider.

COMPUTATIONAL SETUP

All self-consistent simulations presented in this study were done using a strong-strong collision model implemented in the code BeamBeam3D [4]. The BeamBeam3D is a parallel three-dimensional particle-in-cell code to model beam-beam effect in high-energy colliders. This code includes a self-consistent calculation of the electromagnetic forces (beam-beam forces) from two colliding beams (i.e. strong-strong modeling), a linear transfer map model for beam transport between collision points, a stochastic map to treat radiation damping, quantum excitation, an arbitrary orbit separation model, and a single one-turn map to account for chromaticity effects. Here, the beam-beam forces are calculated by solving the Poisson equation using an FFT-based algorithm. The longitudinal bunch length effect is included using multiple slices during the beam-beam interaction. This makes it suitable to study the kink instability, which depends on the bunch length of the colliding beams. It can also handle multiple bunch collisions at multiple interaction points (IPs), and various

beam-beam compensation schemes. The parallel implementation is done using a particle-field decomposition method to achieve a good load balance. It has been applied to studies of the beam-beam effect at a number of high energy colliders such as RHIC, Tevatron, LHC, and KEK-B [5-8].

The parameters used in this study are given in the following table. Here, the electron bunch length is much shorter than the proton bunch length. It collides once with the proton beam, and a new electron beam is generated from the linac at the interaction point every turn while the proton beam circulating around one of the RHIC rings following a one-turn transfer map and comes back to collide with the electron beam again and again. As the electron bunch length is much shorter than the proton bunch, it undergoes the proton bunch subject to the strong beam-beam forces from the proton beam. Before carrying out detailed physics study, we checked the convergence of relevant physics with respect to the choice of the numerical parameters, especially the number of longitudinal slices for each beam. Figure 1 shows the electron beam emittances after one collision as a function of the number of slices for the proton beam using 4 and 8 slices for the electron beam. It is appears that 4 slices for the electron beam will be sufficient while 160 slices are needed for the proton beam. The macroparticle for each beam used in the simulation is about 1 million.

Table 1: Physical Parameters Used in the Simulations

Parameter	E	P
$N(10^{11})$	0.07	3
ε_n [μm]	23	0.2
β^* [cm]	5	5
Q_x		0.685
Q_y		0.675
Q_z		0.004
bunch length [cm]	0.4	5
Energy [GeV]	15.9	250
beam-beam param.	2.9	0.004

*Work supported by the Director of the Office of Science of the US Department of Energy under Contract no. DEAC02-05CH11231 and by the FP7 HiLumi LHC <http://hilumilhc.web.cern.ch>

[#]jqliang@lbl.gov

POSINST SIMULATION ON FERMILAB MAIN INJECTOR AND RECYCLER RING

Yichen Ji, Linda Spentzouris, Department of Physics, Illinois Institute of Technology, IL 60616, USA
Robert Zwaska, FNAL, Batavia, IL 60510, USA

Abstract

The Fermilab accelerator complex is currently undergoing an upgrade from 400kW to 700kW. This intensity could push operations into the region where electron cloud (e-cloud) generation could be observed and even cause instabilities. [1] The POSINST simulation code was used to study how increasing beam intensities will affect electron cloud generation. Threshold simulations show how the e-cloud density depends on the beam intensity and secondary electron yield (SEY) in the Main Injector (MI) and Recycler Ring (RR).

POSINST AND INPUT PARAMETERS

POSINST is a code that simulates the build-up and dissipation of electron cloud with realistic beam parameters and values for the externally applied magnetic field [2–5]. The electric fields due to the electron cloud are calculated in POSINST using a Particle In Cell (PIC) technique. These electric fields could be used as an input for codes that simulate beam dynamics, or for analytical calculations (for example beam instability growth rate due to field from electron cloud). POSINST simulates electron motion in 3D space, but calculates the electric field only for a 2D cross-section of the accelerator. POSINST treats externally applied magnetic fields as a predetermined uniform constant either parallel or perpendicular to the ideal beam trajectory, and thus can only simulate dipole or solenoidal fields. The secondary electron generation is based on the Furman-Pivi probabilistic model [4]. The beam parameters used in the simulations are given in Table 1. The beam fill pattern is shown by Figure 1.



Figure 1: The 588 RF buckets are grouped into 7 batches of 84 buckets. Six batches have beam in them, while the seventh batch is empty. Each batch with beam has 82 filled buckets and 2 empty buckets.

The SEY curves are generated based on a set of parameters in POSINST governing the generation of backscattered electrons, rediffused electrons, and true secondary electrons. These parameters determine the shape of the SEY curve, which is scaled by an input for the peak SEY value. The POSINST electron generation parameters were obtained by fitting the Furman-Pivi probabilistic model to a real SEY measurement of steel. [4] The SEY curves used in simulations are shown in Figure 2.

Table 1: Simulation Inputs Parameters

general parameters	
Beam energy [GeV]	8
Bunch Intensity [protons/bunch]	5.5e10 - 11.5e10
Total Intensity [protons]	2.71e13 - 5.41e13
ring circumference[m]	3319.419
revolution frequency [kHz]	90
Harmonic number	588
RF frequency [Mhz]	53
Total RF bucket filled	492
SEY	1.2-1.9
MI specific parameters	
σ_x [mm]	3
σ_y [mm]	3
σ_z [m]	0.3
σ_t [ns]	1
Bunch length [σ][m][ns]	10; 3; 10
Ellipse chamber major/minor semi-axis [cm]	5.88; 2.39
Dipole Field[T]	0.234
RR specific parameters	
σ_x [mm]	3.6
σ_y [mm]	1.6
σ_z [m]	0.75
σ_t [ns]	2.5
Bunch length [σ][m][ns]	4; 3; 10
Ellipse chamber major/minor semi-axis [cm]	4.7 2.2
Dipole Field[T]	0.137

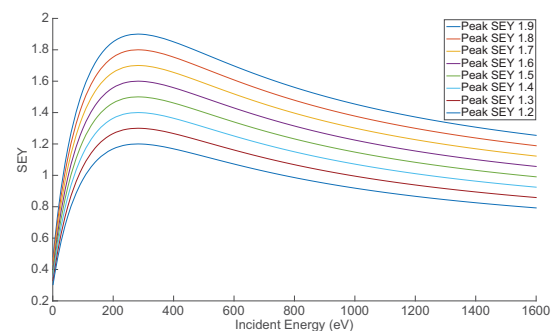


Figure 2: The SEY curves used in simulation.

THRESHOLD SIMULATION RESULT

Figure 3 shows a typical simulation of electron cloud build up at one location in the accelerator for a time duration of one revolution period of the machine. The density of the E-cloud build up matches the filling pattern. The E-cloud builds up rapidly and then saturates. After saturation is reached, the E-cloud density oscillates as bunches pass and dips as the

BEAM MEASUREMENTS AT THE PIP-II INJECTOR TEST LEBT*

J.-P. Carneiro[†], B. Hanna, L. Prost, V. Scarpine, A. Shemyakin
Fermilab, Batavia, IL 60510, USA

Abstract

This paper presents the main results obtained during a series of beam measurements performed on the PIP-II Injector Test LEBT from November 2014 to June 2015. The measurements which focus on beam transmission, beam size and emittance at various locations along the beamline are compared with the beam dynamics code TRACK. These studies were aimed at preparing the beam for optimal operation of the RFQ, while evaluating simulation tools with respect to experimental data.

INTRODUCTION

The Proton Improvement Plan II (PIP-II) is a series of upgrades planned for the Fermilab complex in order to increase the proton through-cut for its experiments. At its core is the construction of an H^- CW 800-MeV superconducting RF linac. To study the feasibility of the PIP-II front-end (the first ~ 25 -30 MeV), Fermilab has started since 2012 the construction of the PIP-II Injector Test (PI-Test) which present status is described in detail in Ref. [1]. This document presents beam measurements performed on the Low Energy Beam Transport (LEBT) and corresponding simulations.

LEBT DESIGN AND LAYOUT

The goal of the LEBT is to transport and properly inject the beam coming from the ion source into the RFQ, while avoiding beam loss and emittance growth. It includes a chopping system for commissioning purposes and Machine Protection.

LEBT Design

The originality of the PI-Test LEBT resides in its neutralization pattern. While for similar beam parameters most solenoid-based LEBTs operate in a nearly fully neutralized regime to counteract space charge effects, the PI-Test LEBT operates with a relatively long non-neutralized region upstream of the RFQ entrance. References [2] and [3] describe in detail the PI-Test LEBT design principle and report measurements validating the transport scheme chosen. In particular, a low-emittance beam with Twiss parameters close to the design ones at the end of the LEBT have been achieved. Selected beam measurements performed during the commissioning of the LEBT are also presented in Ref. [4].

LEBT Layout

Figure 1 presents a layout of the LEBT with its main elements and diagnostics as installed during the measurements

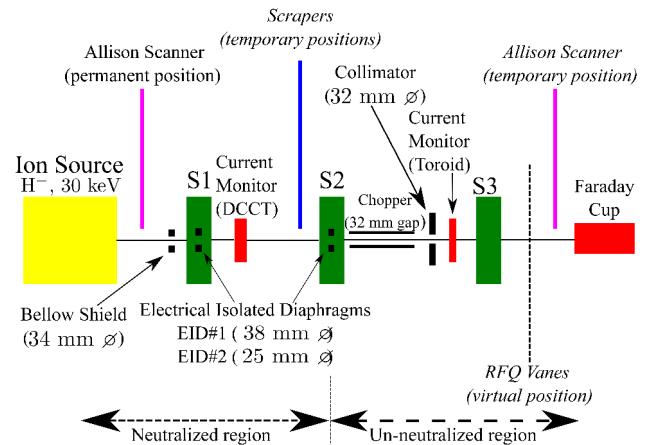


Figure 1: Layout of the PIP-II Injector Test LEBT.

presented in this document. The ion source (30 keV, 15 mA operating pulsed or DC) is followed by 3 solenoids with a Faraday Cup located at the end of the beamline. The chopper is installed downstream of the second solenoid.

Two current monitors are installed in the LEBT (downstream of the first solenoid and right after the chopper) and used for transmission studies. From November 2014 to mid-April 2015 an Allison Scanner was installed (in horizontal position) at the end of the beamline, about 20 cm downstream of the virtual position of the RFQ vanes. As indicated in Fig. 1, the Allison Scanner was eventually relocated to its final vertical position at the ion source exit. A set of 4 scrapers were installed between the two first solenoids and were used for beam size measurements. Inside the first and second solenoid, a water-cooled round Electrical Isolated Diaphragms (EID#1 and EID#2) biased to +50 V are installed with the primary goal of confining the positive ions responsible for the beam neutralization between these two solenoids. An aperture restriction of 34 mm diameter (a.k.a bellow shield) protects the bellow connecting the ion source vacuum chamber to Solenoid 1.

SIMULATION TOOLS

The code TRACK [5] is the main tool for simulations. The solenoid fields were implemented in the code as 3D fields from MWS [6] and normalized to the measured field integral. A significant effort has been carried out to implement in the code a detailed aperture profile of the beamline. The space charge effects were simulated using the 3D routine in TRACK. Neutralization from the interaction of the beam with the residual gas is modeled in TRACK by a simple flag that homogeneously decreases the current. The tracking is usually performed with 100k macro-particles on the Fermi Grid. Initial beam particle distributions were generated with

* Operated by Fermi Research Alliance, LLC under Contract No. DEAC02-07CH11359 with the United States Department of Energy

[†] carneiro@fnal.gov

PROCEDURE FOR THE ALIGNMENT OF THE BEAM IN THE ELECTRICAL AXES OF THE PI-TEST RFQ*

J.-P. Carneiro[†], L. Prost, J. Steimel
Fermilab, Batavia, IL 60510, USA

Abstract

The PI-Test Radio-Frequency Quadrupole (RFQ) has been in operation with beam at Fermilab since March 2016. The RFQ accelerates H^- beam from 30 keV to 2.1 MeV currently with 20 μ s pulses and a maximum current of 10 mA. Once fully conditioned, the RFQ is expected to enable CW operation. Simulations with the beam dynamics code TRACK predict that a misalignment of the beam at the RFQ entrance can possibly deteriorate the transverse and longitudinal emittance at the RFQ exit without necessarily impacting the beam transmission. This paper discusses the procedure developed at Fermilab to align the beam in the electrical axes of the RFQ. Experimental results are shown together with predictions from TRACK.

INTRODUCTION

The Proton Improvement Plan II (PIP-II) is a series of upgrades for Fermilab's accelerator complex, which core is the development and construction of an H^- , 800 MeV superconducting linac with the primary goal of supporting operations for the Long-Baseline Neutrino Facility (LBNF). In order to study the feasibility of the PIP-II front-end, Fermilab has started the construction of the PIP-II Injector Test (PI-Test) which status is described in detail in Ref. [1]. In its present configuration the PI-Test linac comprises a Low-Energy Beam Transport (LEBT), a Radiofrequency Quadrupole (RFQ) and a short Medium-Energy Beam Transport (MEBT). This paper presents the procedure adopted for aligning the beam to the electrical axis of the RFQ.

PI-TEST FRONT-END LAYOUT

A layout of the PI-Test linac is presented in Figure 1. The H^- ion source is able to produce up to 15 mA DC or pulsed at an energy of 30 keV. Upon exiting the ion source, the beam is transported by a LEBT made of 3 solenoids and described in detail in Refs. [2, 3]. A set of horizontal and vertical correctors is installed within each solenoid to enable beam steering. There is a chopper downstream of the second solenoid and a movable aperture (a.k.a. LEBT scraper) is located at the LEBT/RFQ interface. The 4-vanes RFQ has been in operation at Fermilab since March 2016. Recent RFQ commissioning results in pulsed and CW mode have been reported in Ref. [4]. The beam energy exiting the RFQ has been measured to be $2.11 \pm 1\%$ for 65 kV of inter-vane voltage. Upon exiting the RFQ, the beam is transported to a Faraday Cup by the MEBT made of 2 quadrupole doublets

Figure 1: Layout of the PIP-II Injector Test.

with a bunching cavity located between them. BPMs are positioned between the quadrupoles inside each doublet. Using the 2 current monitors located in the LEBT and at the RFQ exit, a direct measurement indicates $98\% \pm 3\%$ transmission through the RFQ for a 5 mA beam (short pulses) [1].

BEAM STEERING INTO THE RFQ

The solenoid and corrector fields were implemented in the codes TRACK [5] and TRACEWIN [6] as 3D fields simulated with MWS [7] and normalized to the measured field integrals. Using the matching procedure included in TRACEWIN, Solenoid 2 & Solenoid 3 correctors currents can be changed together such that, at a given position downstream (e.g.: LEBT scraper or RFQ entrance), the beam centroid angle (or position) is adjusted independently of the other degree of freedom. This tool was tested in June 2015 prior to the installation of the RFQ when an Allison scanner was positioned (in the horizontal plane) downstream of Solenoid 3. The estimated displacement accuracy is 1% between the measured and predicted horizontal position of the beam while the beam angle measurements agree to within 10% with the prediction from TRACEWIN [8].

PREDICTED MISALIGNMENT IMPACT

The RFQ has been implemented in TRACK using 3D fields from a MWS model. Figure 2 shows TRACK predicted emittance and transmission at the RFQ exit for different beam position or angle at the RFQ entrance. For these simulations, a matched 4D-Waterbag distribution with 5×10^4 macro-particles at 5 mA has been used at the RFQ entrance. The space charge effects were simulated using the 3D space charge routine. Figure 2(a) shows that a horizontal beam excursion at the RFQ entrance of ± 1 mm with respect to the axis has a negligible impact on the beam transmission but nevertheless increases the output transverse emittance by $\sim 25\%$ and the longitudinal emittance by $\sim 10\%$. The same observation applies to Fig. 2(b) for a beam entering the RFQ on axis with a horizontal angle of ± 10 mrad. These simulations confirm the importance of properly aligning the

* Operated by Fermi Research Alliance, LLC under Contract No. DEAC02-07CH11359 with the United States Department of Energy

[†] carneiro@fnal.gov

COMPUTATION OF ELECTROMAGNETIC FIELDS GENERATED BY RELATIVISTIC BEAMS IN COMPLICATED STRUCTURES

Igor Zagorodnov*, Deutsches Elektronen-Synchrotron, Hamburg, Germany

Abstract

We discuss numerical methods for computation of wake fields excited by short bunches in accelerators. The numerical methods to implement a low-dispersive scheme, conformal approximation of the boundaries, surface conductivity, and indirect wake potential integration are reviewed. The implementations of these methods in electromagnetic code ECHO for 2D and 3D problems are presented. Several examples of application of the code to important problems in the European Free Electron Laser project and in the Linac Coherent Light Source (LCLS) project are considered.

INTRODUCTION

This paper gives an overview of our research in numerical methods for electrodynamics and accelerator physics. It presents original low-dispersive numerical methods (TE/TM implicit and explicit schemes) for calculation of electromagnetic fields in accelerators. The developed algorithms allow for calculation of electromagnetic fields of ultra-short bunches in very long structures. In order to reduce the numerical errors the Uniformly Stable Conformal (USC) algorithm is developed and described. It allows for a conformal geometry modeling without time step reduction. Combination of both described approaches (the low-dispersive numerical scheme and the conformal technique without time step reduction) gives high quality results even on a coarse mesh with a large time step. Indirect method for wake potential integration is reviewed. The algorithms are implemented in code ECHO which is available at [1].

NUMERICAL METHODS

In order to simulate self-consistent dynamics of the charged particles, we need to be able to solve at least two kinds of problems: (i) to calculate the electromagnetic field for the given charges and currents and (ii) to solve equations of motion of charged particle in the given electromagnetic field. In this paper we consider the approaches to effective solution of the first problem.

Low-Dispersive Numerical Schemes

The particle-in-cell (PIC) method [2] is an effective approach for simulation of beam dynamics in accelerators. In this model one emulates nature by following the motion of a large number of charged particles in their self-consistent electric and magnetic fields. The electromagnetic fields in many PIC codes are computed using the finite-difference time domain (FDTD) method [3], [4]. As any numerical mesh approach, the FDTD method suffers from an anisotropic

numerical dispersion. The numerical wave phase speed is slower than the physical one. Hence, the high energy particles can travel in vacuum faster than their own radiation. This effect is commonly referred as numerical Cherenkov radiation [5], which (due to its accumulative character) corrupts the simulation. Hence, the electromagnetic field computation for short relativistic bunches in long structures remains a challenging problem even with the fastest computers.

Several approaches [5]- [9] have been proposed to reduce the accumulated dispersion error of large-scale three-dimensional simulations for all angles and for a given frequency range. These methods require the usage of larger spatial stencils and a special treatment of the material interfaces. The increased computational burden justifies itself for computational domains large in all three dimensions. However, in the accelerator applications the domain of interest is very long in the longitudinal direction and relatively narrow in the transverse plane. Additionally, the electromagnetic field changes very fast in the direction of bunch motion but is relatively smooth in the transverse plane. Hence, it is extremely important to eliminate the dispersion error in the longitudinal direction for all frequencies. If the numerical dispersion is suppressed then a quite coarse mesh and moderate computational resources can be used to reach accurate results. It was shown in wake field calculations by A. Novokhatski [10] and in plasma simulations by A. Pukhov [11].

As it is well known, the FDTD method at the Courant limit is dispersion free along the grid diagonals and this property can be used effectively in numerical simulations [12]. However, the only reasonable choice in this case is to take equal mesh steps in all three directions. Alternatively, a semi-implicit numerical scheme without dispersion in the longitudinal direction with a simpler conformal treatment of material interfaces and the usage of non-equidistant grids has been developed in [13]- [15].

The scheme described in [10, 14] allows to solve the scalar problem and to calculate the wake potential for fully axially symmetric problems with staircase approximation of the boundary. In [15], a three-level scheme $\mathbf{R}(\mathbf{y}^{n+1} - 2\mathbf{y}^n + \mathbf{y}^{n-1}) + \mathbf{A}\mathbf{y}^n = \mathbf{f}^n$ for the vectorial problem was suggested. Our scheme is based on a second order hyperbolic wave equation for vector potential. A modification of the USC method [16] is used to avoid the "staircase" problem and to obtain a second order convergent algorithm. However, the operator \mathbf{R} in this scheme is not self-conjugate; and therefore an "energy" conservation cannot be proven theoretically by the standard techniques [17]. Additionally, the scheme is not economical for general three-dimensional geometries. The last drawback can be overcome by splitting methods [17]. However, the absence of a theoretical proof

* Igor.Zagorodnov@desy.de

SIMULATIONS OF BOOSTER INJECTION EFFICIENCY FOR THE APS-UPGRADE*

J. Calvey, M. Borland, K. Harkay, R. Lindberg, CY Yao, ANL, Argonne, IL 60439, USA

Abstract

The APS-Upgrade will require the injector chain to provide high single bunch charge for swap-out injection. One possible limiting factor to achieving this is an observed reduction of injection efficiency into the booster synchrotron at high charge. We have simulated booster injection using the particle tracking code elegant, including a model for the booster impedance and beam loading in the RF cavities. The simulations point to two possible causes for reduced efficiency: energy oscillations leading to losses at high dispersion locations, and a vertical beam size blowup caused by ions in the Particle Accumulator Ring. We also show that the efficiency is much higher in an alternate booster lattice with smaller vertical beta function and zero dispersion in the straight sections.

INTRODUCTION

The Advanced Photon Source (APS) booster synchrotron accelerates electron bunches from 375 MeV to 7 GeV before injection into the storage ring. In the present APS, the bunch charge typically ranges from 2 - 3 nC, which is sufficient for top-up operation. However, the APS-Upgrade will use swap-out injection [1, 2], so the booster will need to provide the full charge in one shot, up to 16 nC for the 48 bunch "timing" mode. As a result, an R&D program was recently started to identify limitations to achieving reliable high-charge injection into the storage ring [3]. This paper will discuss recent progress in understanding and overcoming these limitations.

Booster Parameters

A list of booster parameters is given in Table 1. Parameters are given for two different lattices—the current operational lattice (which has 92 nm emittance [4]), and the original booster lattice (with 132 nm emittance [5]). One important difference between the two is that the 132-nm lattice has zero dispersion through the straight sections of the booster, which includes the RF cavities (Fig. 1). The 132-nm lattice has higher maximum dispersion, but a lower vertical beta function.

The booster is run off-momentum, i.e. the RF frequency does not match the booster circumference. This was a result of Decker distortion [6] in the storage ring, which shares an RF source with the booster. However, since running off-momentum results in a lower emittance (which is desirable for injection into the storage ring), we plan on retaining this feature for the upgrade.

* Work supported by the U.S. Department of Energy, Office of Science, Office of Basic Energy Sciences, under Contract No. DE-AC02-06CH11357.

Table 1: Booster Parameters

Parameter	Value
Energy	0.375 - 7.0 GeV
Ramp time	225 ms
Circumference	368 m
Revolution frequency	815 kHz
RF Voltage	0.5 - 8.0 MV

Parameter	92 nm	132 nm
Horizontal tune	13.75	11.75
Vertical tune	5.8	9.8
Avg. horizontal beta function	7.87	7.93
Avg. vertical beta function	12.57	8.53
Momentum compaction	7.14×10^{-3}	9.71×10^{-3}
Energy offset	-0.085%	-0.06%

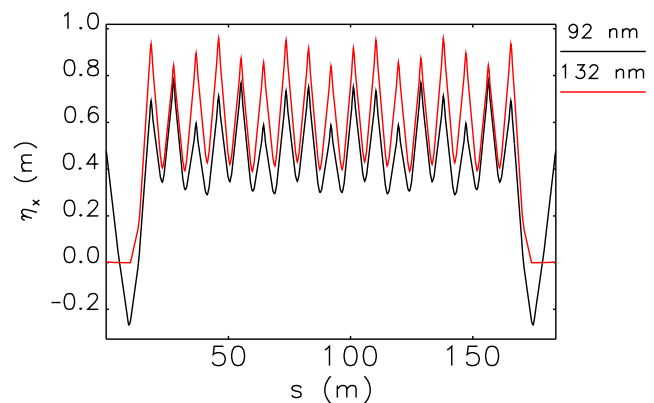


Figure 1: Horizontal dispersion for one half of the booster.

MEASUREMENTS

Initial attempts at improving the efficiency of the 92 nm lattice met with limited success. Fig. 2 (top) shows a typical example of stored current in the booster as a function of time. The 20 measurements shown were taken under nominally identical conditions, with 5-nC bunch charge. There is a significant loss of charge early in the ramp, which varies in magnitude shot-to-shot. Despite a great deal of effort (adjusting the RF voltage, chromaticity, tunes, correctors, etc.), we were not able to reliably extract more than 4 - 5 nC from the booster in this lattice. Interestingly, we found that increasing the RF voltage at injection actually made the initial losses worse.

The 132-nm lattice proved much easier to work with. As shown in Fig. 2 (bottom), the injection efficiency at 9 nC is ~90%, with only modest variation shot-to-shot.

HOLLOW ELECTRON BEAM COLLIMATION FOR HL-LHC - EFFECT ON THE BEAM CORE*

M. Fitterer[†], G. Stancari, A. Valishev, Fermilab, Batavia, IL 60510, USA
 R. Bruce, S. Papadopoulou, G. Papotti, D. Pellegrini, S. Redaelli, D. Valuch, J. F. Wagner,
 CERN, Geneva, Switzerland

Abstract

Collimation with hollow electron beams or lenses (HEL) is currently one of the most promising concepts for active halo control in HL-LHC. In previous studies it has been shown that the halo can be efficiently removed with a hollow electron lens. Equally important as an efficient removal of the halo, is also to demonstrate that the core stays unperturbed. In this paper, we present a summary of the experiment at the LHC and simulations in view of the effect of the HEL on the beam core in case of a pulsed operation.

INTRODUCTION

For high energy and high intensity hadron colliders like the HL-LHC, halo control becomes more and more relevant, if not necessary, for a safe machine operation and control of the targeted stored beam energy in the range of several hundred MJ. Past experiments at the Fermilab Tevatron proton-antiproton collider [1] demonstrated a successful halo control with hollow electron beams or hollow electron lenses (HELs) in DC mode.

Simulations of the HEL performance for LHC and HL-LHC [2–4] show a sufficiently high halo removal rate if beams are colliding, but only very low halo removal rates if the beams are separated. In order to clean the tails efficiently and in a short time-span also in case of separated beams, the halo removal rate can be increased by pulsing the HEL [2, 4, 5], where two different pulsing patterns are considered:

- **random:** the e-beam current is modulated randomly: at every turn the kick is varied between 0 and its maximum value following a uniform distribution,
- **resonant:** the e-lens is switched on only every n th turn with $n = 2, 3, 4, \dots$ and the maximum kick is applied.

One of the main reservations about pulsing the e-lens is the possibility of emittance growth due to noise induced on the beam core by the HEL.

For an ideal radially symmetric hollow electron lens with an S-shaped geometry, the beam core would experience a zero net kick and thus no noise would be induced on the core. In the presence of imperfections in the HEL bends and in the e-beam profile, the kick at the center of the beam is non-zero. First estimates of the residual kick yield 0.142 nrad from the HEL bends assuming 10% current modulation and

16 nrad due to profile imperfections based on profile measurements of the current HEL e-gun prototype [6]. In case of DC operation of the HEL the kicks are static and could thus be corrected, if even necessary. However, for a pulsed operation, the tolerable kick amplitudes are much smaller as the pulsing frequency overlaps with the frequency spectrum of the beam itself. In case of random pulsing, white noise is induced driving all orders of resonances. In case of a resonant pulsing, only certain resonances are driven, explicitly for pulsing every n th turn only the n th order resonances are driven.

In order to obtain a first estimate on the tolerable profile imperfections in case of the resonant excitation¹, an experiment including preparatory simulations was conducted in August 2016 at the LHC, of which we will present the related simulation results and also first experimental results. The excitation for the MD was generated with the transverse damper system (ADT) of the LHC [7]. Details can be found in [6].

DESCRIPTION OF THE LHC EXPERIMENT

As experiments at top energy are always not very efficient because of the long recovery times in case of beam losses, this first try was performed at injection energy. Expected effects of the resonant excitation are losses and emittance growth. To minimize the emittance growth due to intra-beam scattering, low intensity bunches are used instead of nominal bunches. For nominal single bunches with $N_b =$

Table 1: Machine and Beam Parameters for LHC Experiment

Parameter	Value	Unit
Energy	450	GeV
norm. emittance	2.5	μm
bunch length (4σ)	1.0	ns
bunch intensity	0.7×10^{11}	-
number of bunches	$12 \times 4 = 48$	-
$\beta_{IP1/5}^*$	11	m
working point (x/y)	64.28/ 59.31	-
chromaticity	15	-
octupole current (MOF)	19.6	A

1.2×10^{11} , $\epsilon_N = 1.6 \mu\text{m}$ the expected emittance growth due to IBS is around 24.3 %/hour, while for the requested low

* Fermilab is operated by Fermi Research Alliance, LLC, under Contract DE-AC02-07CH11359 with the US Department of Energy.

[†] mfittere@fnal.gov

¹ For white noise analytical formulas and measurements exist. Due to very limited time for experiments at the LHC, the priority was therefore set on the resonant excitation.

MICROWAVE INSTABILITY STUDIES IN NSLS-II*

A. Blednykh[#], B. Bacha, G. Bassi, W. Cheng, O. Chubar, K. Chen-Wiegart, V. Smaluk
BNL, NSLS-II, Upton, NY, 11973-5000, USA

Abstract

The microwave instability in the NSLS-II has been studied for the current configuration of insertion devices, 9 In-Vacuum Undulators (IVU's), 3 Elliptically-Polarized Undulators (EPU's), 3 Damping Wigglers (DWs). The energy spread as a function of single bunch current has been measured based on the frequency spectrum of IVU for X-Ray Spectroscopy (SRX) beamline, for two lattices, the bare lattice with nominal energy spread $\sigma_\delta = 0.0005$, and a lattice with one DW magnet gap closed ($\sigma_\delta = 0.0007$). In addition we did measure the energy spread from a Synchrotron Light Monitor (SLM) camera installed in a nonzero dispersive region, for the two aforementioned lattices, and for a third lattice with 3 DWs gaps closed ($\sigma_\delta = 0.00087$). The measurements have been complemented by beam spectra taken from a Spectrum Analyzer, and have been compared with numerical simulations with the particle tracking code SPACE.

MEASUREMENTS

The NSLS-II storage ring has been designed to accumulate a high-current (500 mA) electron beam with sub-nanometer (0.5 nm with all damping wigglers) horizontal emittance and diffraction-limited vertical emittance smaller than 8 pm [1]. Three pairs of damping wigglers have been installed in NSLS-II in Cells 8, 18 and 28 to decrease the horizontal emittance below 1 nm. The wigglers introduce additional strong radiation damping which increases the beam energy spread and the bunch length. The magnet gaps of the wigglers and insertion devices are controlled remotely; this allows us to vary the lattice configuration with any ID's combination.

Three different diagnostic methods have been used in parallel to determine the longitudinal microwave instability threshold in NSLS-II. Horizontal beam-profile changes vs single bunch current have been monitored by a SLM camera installed in a low dispersion area (Fig. 1). IVU of a SRX beamline has been used as a diagnostic tool to determine the energy spread based on the spectral peak of the 5th harmonic radiation as a function of current (Figs. 2, 3). A reliable estimation of the electron beam energy spread from SRX IVU photon energy spectrum became possible after careful re-alignment of the IVU magnet girders with respect to the electron beam. The third method is based on beam spectrum measurements from the stripline of a bunch-by-bunch transverse feedback system. The monitor of a spare stripline was connected to the RF- input of an ESA 4405B spectrum analyzer. The center frequency was set to the 21th RF

harmonic (10493.3136MHz) with a span of 40KHz. It was verified to be the most sensitive span for the synchrotron sidebands. This method is used at other facilities [2], besides being used at NSLS-II [3]. The longitudinal instability thresholds have been studied for three different lattices, a bare lattice (all ID's gap open), a lattice with 1DW magnet gap closed and a lattice with 3DWs magnet gap closed. By closing the DWs magnet gap we measured the microwave instability threshold current I_{th} dependence on the energy spread σ_δ at fixed RF voltage (Figs. 1-5). Based on the measurements, we observed the expected dependence $I_{th} \propto \sigma_\delta^3$. The measured I_{th} from both SLM and SRX beamline has been found to be $I_{th} \sim 0.2 - 0.3$ mA (bare lattice) [3], $I_{th} \sim 0.8 - 0.9$ mA (1 DW gap closed), and $I_{th} \sim 1.6$ mA (3 DWs gaps closed) respectively, as shown in Figs. 1 and 2. The thresholds have been confirmed from the measured beam spectra shown in Figs. 4 and 5, where the second harmonic of the synchrotron frequency f_s suddenly appears at the microwave instability threshold. Measurements from SLM for the lattice with 3 DWs gap closed are shown in Fig. 6 at $V_{RF} = 2$ MV, $V_{RF} = 2.6$ MV and $V_{RF} = 3.4$ MV.

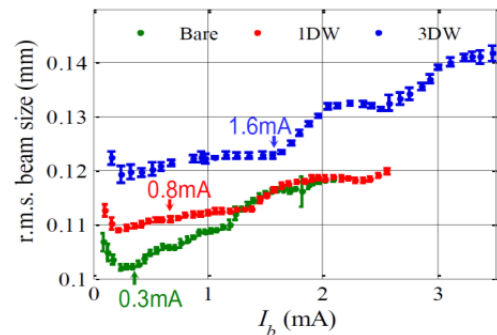


Figure 1: Horizontal beam size from SLM vs single bunch current for three different lattices at $V_{RF} = 2.6$ MV.

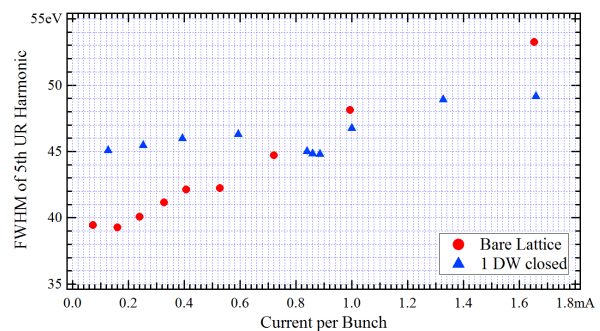


Figure 2: FWHM size of spectral peak of 5th harmonic radiation from 21-mm period IVU measured at SRX beamline at ~ 8 keV photon energy as a function of current per bunch, for bare lattice and with one DW closed.

* Work supported by Department of Energy contract DE-AC02-98CH10886

[#]blednykh@bnl.gov

INVESTIGATION OF STRUCTURAL DEVELOPMENT IN THE TWO-STEP DIFFUSION COATING OF Nb₃Sn ON NIOBIUM*

Uttar Pudasaini¹, G. Ereemeev², Charles E. Reece², J. Tuggle³, and M. J. Kelley^{1,2,3}

¹Applied Science Department, The College of William and Mary, Williamsburg, VA 23185, USA

²Thomas Jefferson National Accelerator Facility, Newport News, VA 23606, USA

³Virginia Polytechnic Institute and State University, Blacksburg, VA 24061, USA

Abstract

The potential for higher operating temperatures and increased accelerating gradient has attracted SRF researchers to Nb₃Sn coatings on niobium for nearly 50 years. The two-step tin vapor diffusion: nucleation followed by deposition appears to be a promising technique to prepare Nb₃Sn coatings on interior cavity surface. We have undertaken a fundamental materials study of the nucleation and deposition steps. Nucleation was accomplished within parameter ranges: 300 - 500 °C, 1 - 5 hrs duration, 5 mg - 1 g SnCl₂ and 1g Sn. The resulting deposit consists of (< 10%) coverage of tin particles, as determined by SEM/EDS, while XPS and SAM discovered extra tin film between these particles. Preliminary results by EBSD show no evident effect of substrate crystallography on the crystallography of the final coating. Substantial topography was found to develop during the coating growth.

INTRODUCTION

Discovered in 1954 [1], Nb₃Sn has the potential to replace traditional niobium in superconducting radio frequency (SRF) cavities. Because both the critical temperature and superheating field are nearly twice that of niobium, Nb₃Sn promises higher operating temperature and accelerating gradient than niobium SRF cavities, resulting in significant cost reduction. Despite these advantages, Nb₃Sn is a brittle material with low thermal conductivity, so its application must be restricted to coating form. Complicated cavity shapes limit the types of techniques available to prepare Nb₃Sn coatings.

The most successful coating technique thus far is tin vapor diffusion, developed at Siemens AG in the 1970s [2], and further developed at Wuppertal University [3]. The majority of research institutions currently working to develop Nb₃Sn-coated SRF cavities have adopted this technique [4-6]. The basic procedure consists of two steps: nucleation and deposition. First, tin chloride is evaporated at about 500 °C, depositing tin on the niobium surface. These tin deposits act as nucleation sites, which are assumed to grow with the influx of tin vapor during deposition at higher temperature. Deposition temperature suitable to form Nb₃Sn phase is determined by the Nb-Sn binary phase diagram [7]. An example of the Nb₃Sn coating process at Jlab is shown in Figure 1.

Although tin vapor diffusion is a promising technique for future development of Nb₃Sn SRF cavities, fundamen-

tal material studies are still needed to better understand the coating process. The goal of this research is to refine this coating technique by conducting more thorough investigations of the nucleation and deposition processes. Accordingly, we discuss the results from both nucleation experiments and complete coating experiments.

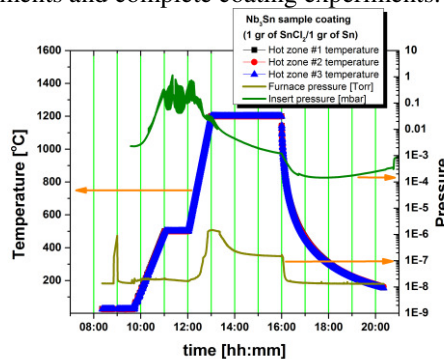


Figure 1: Temperature profile used for coating Nb₃Sn onto niobium samples. The nucleation process occurs at the first temperature plateau of 500 °C and deposition proceeds at the 1200 °C temperature plateau.

EXPERIMENTAL DESCRIPTION

High purity niobium coupon samples were prepared by electric discharge machining (EDM) 3mm-thick sheet material which is the same type of material used to fabricate SRF cavities at Jlab. All samples were subjected to buffered chemical polishing (BCP) with an expected minimum removal of 50 μm, followed by metallographic polishing, also known as nanopolishing (NP).

A detailed description of the Jlab deposition system used in this work is available in [4]. The setup of this experiment is similar to the setup described in our previous work [8]. One gram of tin (~3 mg/cm²) and one gram of tin chloride were packaged in niobium foil and placed inside a sample chamber. After mounting sample coupons inside the chamber, both ends of the chamber were covered either by niobium foils or niobium plates before it was installed in the furnace insert. Once the insert had been pumped down to a pressure of 10⁻⁵ – 10⁻⁶ Torr, the heating profile was initiated. During nucleation experiments, the temperature inside the insert was increased at a rate of 6 °C /min until it reached the desired nucleation temperature. The time period for which this temperature was maintained depended on the experiment.

A field emission scanning electron microscope (FE-SEM) with energy dispersive x-ray spectroscopy (EDS) was used to examine the nucleated samples. SEM images were taken and visible features were analyzed with EDS.

* Partially authored by Jefferson Science Associates under contract no. DEAC0506OR23177. Work at College of William & Mary supported by Office of High Energy Physics under grant SC0014475.

SURFACE IMPURITY CONTENT OPTIMIZATION TO MAXIMIZE Q-FACTORS OF SUPERCONDUCTING RESONATORS*

M. Martinello[†], M. Checchin, FNAL, Batavia, IL, USA and IIT, Chicago, IL, USA
 A. Grassellino, O. Melnychuk, S. Posen, A. Romanenko, D.A. Sergatskov, FNAL, Batavia, IL, USA
 J.F. Zasadzinski, IIT, Chicago, IL, USA

Abstract

Quality factor of superconducting radio-frequency (SRF) cavities is degraded whenever magnetic flux is trapped in the cavity walls during the cooldown. In this contribution we study how the trapped flux sensitivity, defined as the trapped flux surface resistance normalized for the amount of trapped flux, depends on the mean free path. A systematic study of a variety of 1.3 GHz cavities with different surface treatments (EP, 120 °C bake and different N-doping) is carried out. A bell shaped trend appears for the range of mean free path studied. Over-doped cavities fall at the maximum of this curve defining the largest values of sensitivity. In addition, we have studied the trend of the BCS surface resistance contribution as a function of mean free path, showing that N-doped cavities follow close to the theoretical minimum. Adding these results together we show that the 2/6 N-doping treatment gives the highest Q-factor values at 2 K and 16 MV/m, as long as the magnetic field fully trapped during the cavity cooldown is lower than 10 mG.

INTRODUCTION

Recently, a new surface treatment implemented on superconducting cavities, called nitrogen-doping, shows unprecedented values of quality-factors ($Q_0 > 4 \cdot 10^{10}$) at medium values of accelerating field ($E_{acc} = 16$ MV/m) [1]. However, it was shown that whenever external magnetic is trapped in nitrogen-doped cavities, the Q_0 degradation is more severe than in standard-treated niobium cavities such as 120 °C baked and electro-polished (EP).

To understand this peculiar behavior, it is necessary to analyze the RF surface resistance, $R_s = G/Q_0$. R_s is given by two contributions, one temperature-dependent called BCS surface resistance (R_{BCS}), and one temperature-independent called residual resistance (R_{res}).

Surprisingly, in nitrogen-doped cavities R_{BCS} decreases with the increasing of the accelerating field. This results in an increasing of Q-factor with accelerating field called anti-Q-slope [1].

The residual resistance term R_{res} is the one affected by trapped magnetic flux [2]. The amount of trapped flux depends on both the value of external magnetic field which surrounds the cavity during the SC transition, and on the cooldown details, which affects the magnetic flux trapping efficiency [3–5]. Fast cooldowns, with large thermal gradients along the cavity length, facilitate magnetic flux expulsion,

while slow and homogeneous cooling through transition leads to full flux trapping.

In this paper both the trapped flux and the BCS surface resistance contributions are studied for cavities subject to different surface treatments: electro-polishing (EP), 120 °C baking, and N-doping with different time of nitrogen exposure and EP removal. Details on the N-doping treatment can be found elsewhere [1, 6].

The findings here reported allow a better understanding of which surface treatment is required to maximize the Q-factor for a certain RF field, taking into account the external DC magnetic field trapped during the cooldown. More details of this study may be found in Ref. [7].

EXPERIMENTAL PROCEDURE

All the cavities analyzed are single cell 1.3 GHz Tesla-type niobium cavities.

In order to estimate the trapped flux surface resistance, every cavity was RF tested, at least, after two different cooldowns: i) compensating the magnetic field outside the cavity in order to minimize its value during the SC cavity transition, ii) cooling slowly the cavity with about 10 mG of external magnetic field applied.

After each of these cooldowns, the cavities were tested at the Vertical Test System (VTS) at Fermilab. Curves of Q-factor versus accelerating field were always acquired at both 2 and 1.5 K.

A schematic of the instrumentation used to characterize the trapped flux surface resistance may be found in Fig. 1 of Ref. [8]. Helmholtz coils are used to adjust the magnetic field around the cavity, Bartington single axis fluxgate magnetometers to monitor the external magnetic field at the cavity equator, and thermometers to measure the temperature distribution during the cooldown.

The residual resistance may be considered as a sum between the trapped flux surface resistance, R_{fl} , and the "intrinsic" residual resistance, R_0 , which does not depend on trapped flux.

At 1.5 K the BCS surface resistance contribution becomes negligible, therefore $R_{res} = G/Q(1.5K)$.

If during the cooldown the amount of trapped flux is successfully minimized, then: $R_{fl} \approx 0$ and $R_{res} \approx R_0$. In order to obtain very low value of trapped flux, the magnetic field outside the cavity was compensated during the cooldown through the SC transition. Alternatively, the measurement was done after a complete magnetic flux expulsion ($B_{SC}/B_{NC} \sim 1.74$ at the equator). We have observed that these two methods gave the same results within the mea-

* Work supported by the US Department of Energy, Office of High Energy Physics.

[†] mmartine@fnal.gov

CALCULATING SPIN LIFETIME *

V. H. Ranjbar[†], BNL, Upton, USA

Abstract

We have extended a lattice independent code to integrate the Thomas-BMT equation over 2 hours of beam time in the presence of two orthogonal Siberian snakes. In tandem to this we have recast the Thomas-BMT equation in the presences of longitudinal dynamics, into the parametric resonance formalism recently developed to understand overlapping spin resonances [1]

INTRODUCTION

One of the important factors effecting the net polarization integrated over during RHIC store is the polarization lifetime. This value has varied between a low of about 0.5% per hour to a high of 2% per hour. However we do not yet possess a good theory to explain these losses, neither has the community been able to simulate these losses. For example direct spin tracking to simulate 1 hour of beam time would take 300 million turns in RHIC. Even if we could do 100K turns in 1 hour (which is about 4 times faster than what I have observed) it would take 125 days to do this. Even if we would allocate the time we don't have the compute resources to do this for any kind of realistic distribution.

So in leu of this, we have turned to lattice independent spin tracking methods developed previously [2]. This approach involves integrating the T-BMT equation using only several spin resonances with a unitary 4th order Gaussian quadrature integrator. In this paper we present the results from an extension of this integrator to handle longitudinal dynamics.

SPIN DYNAMICS REVIEW

The dynamics of the spin vector of a charged particle with q charge in the laboratory frame is described by the Thomas-BMT equation,

$$\frac{d\vec{S}}{dt} = \frac{q}{\gamma m} \vec{S} \times \left((1 + G\gamma)\vec{B}_\perp + (1 + G)\vec{B}_\parallel \right), \quad (1)$$

\vec{S} is the spin vector of a particle in the rest frame, and \vec{B}_\perp and \vec{B}_\parallel are defined in the laboratory rest frame with respect to the particle's velocity. $G = \frac{g-2}{2}$ is the anomalous magnetic moment coefficient, and γmc^2 is the energy of the particle. Here we neglect the electric fields. Following a standard derivation (see for example [1]) the T-BMT equation can

be recast in a spinor form:

$$\frac{d\Psi}{d\theta} = -\frac{i}{2} \begin{pmatrix} f_3 & -\xi \\ \xi^* & -f_3 \end{pmatrix} \Psi. \quad (2)$$

Where $\xi(\theta) = F_1 - iF_2$ and $f_3 = (1 + F_3)$ with,

$$\begin{aligned} F_1 &= -\rho z''(1 + G\gamma) \\ F_2 &= (1 + G\gamma)z' - \rho(1 + G) \left(\frac{z}{\rho} \right)' \\ F_3 &= -(1 + G\gamma) + (1 + G\gamma)\rho x''. \end{aligned} \quad (3)$$

Here, θ is the orbital angle that remains constant outside the bends. Although the spinor function Ψ is similar in form to the quantum-mechanical-state function, in this case \vec{S} is a classical vector. However, as in the former case, this two-component spinor is defined,

$$\Psi = \begin{pmatrix} u \\ d \end{pmatrix}. \quad (4)$$

u and d are complex numbers representing the up- and down-components. The components of the spin vector become

$$\begin{aligned} S_1 &= u^*d + ud^* \\ S_2 &= -i(u^*d - ud^*) \\ S_3 &= |u|^2 - |d|^2. \end{aligned} \quad (5)$$

Because $H = (\vec{\sigma} \cdot \vec{n})$ is hermitian,

$$|\vec{S}| = |u|^2 + |d|^2 = \Psi^\dagger \Psi \quad (6)$$

and the magnitude of the spin-vector remains constant. We chose the normalization condition for the spinor function to be $\Psi^\dagger \Psi = 1$.

When evaluating the cumulative effect of the lattice on the spin, the standard approach is to expand $F_1 - iF_2$ into a Fourier series:

$$\xi(\theta) = F_1 - iF_2 = \sum_K \varepsilon_K e^{-iK\theta} \quad (7)$$

wherein the Fourier coefficient or resonance strength ε_K is given by the following:

$$\varepsilon_K = -\frac{1}{2\pi} \oint [(1 + G\gamma)(\rho z'' + iz') - i\rho(1 + G) \left(\frac{z}{\rho} \right)'] e^{iK\theta} d\theta. \quad (8)$$

Here, K is the resonance spin tune. Also usually the $(1 + G\gamma)\rho x''$ term is ignored to first order. Since θ is constant in a region without dipoles, it is usually clearer to express the resonance integral in terms of s :

$$\varepsilon_K = -\frac{1}{2\pi} \oint \left[(1 + G\gamma)(z'' + \frac{iz'}{\rho}) - i(1 + G) \left(\frac{z}{\rho} \right)' \right] e^{iK\theta(s)} ds. \quad (9)$$

* Work supported by the US Department of Energy under contract number DE-SC0012704. This research used resources of the National Energy Research Scientific Computing Center (NERSC), which is supported by the Office of Science of the U.S. Department of Energy under Contract No. DE-AC02-05CH11231.

[†] vranjbar@bnl.gov

INCOHERENT VERTICAL EMITTANCE GROWTH FROM ELECTRON CLOUD AT CESR TA

S. Poprocki, J.A. Crittenden, S.N. Hearsh, J.D. Perrin, D.L. Rubin, S.T. Wang
CLASSE*, Cornell University, Ithaca, NY 14853, USA

Abstract

We report on measurements of electron cloud (EC) induced tune shifts and emittance growth at the Cornell Electron-Positron Storage Ring Test Accelerator (CesrTA) with comparison to tracking simulation predictions. Experiments were performed with 2.1 GeV positrons in a 30 bunch train with 14 ns bunch spacing and 9 mm bunch length, plus a witness bunch at varying distance from the train to probe the cloud as it decays. Complementary data with an electron beam were obtained to distinguish EC effects from other sources of tune shifts and emittance growth. High resolution electric field maps are computed with EC buildup simulation codes (ECLLOUD) in the small region around the beam as the bunch passes through the cloud. These time-sliced field maps are input to a tracking simulation based on a weak-strong model of the interaction of the positron beam (weak) with the electron cloud (strong). Tracking through the full lattice over multiple radiation damping times with electron cloud elements in the dipole and field-free regions predict vertical emittance growth, and tune shifts in agreement with the measurements.

INTRODUCTION

An increase in vertical beam size due to electron cloud has been seen in many positron rings (PEP-II, KEKB, DAPHNE, and CESR). A comprehensive summary of EC studies at CESR TA is given in [1], and a description of accelerator physics R&D efforts at CESR TA with the goal of informing design work for the damping rings of a high-energy linear e^+e^- collider can be found in Refs. [2, 3]. Our goal here is to develop a model to predict emittance growth associated with electron cloud buildup. This model assumes that the emittance growth is incoherent. Particles within a bunch are treated independently and tracked through the full CESR TA lattice with custom elements in Bmad [4] that model the positron beam - electron cloud interaction. EC elements give kicks to the particles based on electric field maps derived from an EC buildup simulation. The effect of the perturbed beam on the EC is not included in this weak-strong model. Tunes are computed using the 1-turn transfer matrix or from the FFT of the turn-by-turn bunch centroid positions. Vertical and horizontal equilibrium beam sizes are obtained by tracking the bunch through 60,000 turns (multiple radiation damping times). In order to test this model, measurements were obtained for a wide range of witness bunch positions,

and bunch and train currents for both electron and positron beams.

MEASUREMENTS

This paper focuses on measurements of 0.4 mA (0.64×10^{10} bunch population) and 0.7 mA (1.12×10^{10}) trains of 30 bunches followed by witness bunches at various distances (with 14 ns spacing) and bunch currents. Note that only one witness bunch was present for each measurement. Bunch-by-bunch, turn-by-turn vertical beam size measurements were taken with an X-ray-based beam size monitor [5]. Additionally, we have collected single-shot bunch-by-bunch horizontal beam size measurements using a gated camera [6]. Bunch-by-bunch tune measurements are obtained from FFTs of position data from multiple gated BPMs [7].

Bunch-by-bunch feedback is used on all bunches for size measurements, to minimize centroid motion and associated coherent emittance growth. Feedback is disabled one bunch at a time for tune measurements. In order to minimize systematic effects of the beam-cloud interaction due to motion of the bunches, we do not use external sources to enhance the oscillation. Thus these measurements rely on the self-excitation of the bunch centroid. Indeed, under certain conditions the self-excitation produced a low signal to noise ratio, particularly in the vertical plane.

SIMULATIONS

The EC buildup simulation is based on extensions [8] to the ECLLOUD [9] code. The beam size used in these simulations is ring-averaged and weighted by the element lengths for either the 800 Gauss dipole magnets or the field-free drift regions, and roughly 730 (830) microns horizontally for dipoles (drifts) and 20 microns vertically. The large ring-averaged horizontal size is dominated by dispersion effects. In these simulations we clearly see the "pinch effect" of the beam attracting the EC (Fig. 1). Electric fields on a 15×15 grid of $\pm 5\sigma$ of the transverse beam size are obtained for 11 time slices as the bunch passes through the cloud. Figure 2 shows these field maps in a dipole for bunch number 30 in the 0.7 mA/b train during the central time slice. Since only a small fraction ($\sim 0.1\%$) of photoelectrons are within the $\pm 5\sigma$ region around the beam, it is necessary to combine the results of many ECLLOUD simulations.

The particle tracking simulations use a custom beam-cloud interaction element in Bmad overlaid on the dipole or drift elements and use the full CESR lattice. The electric fields from the different time slices are linearly interpolated to give the value of the fields at the x , y , and t of each particle. The effect of the pinch is extracted from the ECLLOUD

* Work supported by the US National Science Foundation contracts PHY-1416318, PHY-0734867, PHY-1002467, and the U.S. Department of Energy DE-FC02-08ER41538.

VLASOV ANALYSIS OF MICROBUNCHING GAIN FOR MAGNETIZED BEAMS*

C.-Y. Tsai[#], Department of Physics, Virginia Tech, VA 24061, USA

Ya. Derbenev, D. Douglas, R. Li, and C. Tennant Jefferson Lab, Newport News, VA 23606, USA

Abstract

For a high-brightness electron beam with low energy and high bunch charge traversing a recirculation beamline, coherent synchrotron radiation and space charge effect may result in the microbunching instability (MBI). Both tracking simulation and Vlasov analysis for an early design of Circulator Cooler Ring [1] for the Jefferson Lab Electron Ion Collider reveal significant MBI. It is envisioned these could be substantially suppressed by using a magnetized beam. In this work, we extend the existing Vlasov analysis, originally developed for a non-magnetized beam, to the description of transport of a magnetized beam including relevant collective effects. The new formulation will be further employed to confirm prediction of microbunching suppression for a magnetized beam transport in a recirculating machine design.

INTRODUCTION

Beam quality preservation is of general concern in delivering a high-brightness electron beam through a transport line or recirculation arc in the design of modern accelerators. During high-brightness beam transport, initial small density modulations can be converted into energy modulations due to short-ranged wakefields or high-frequency impedances. Then, the energy modulations can be transformed back to density counterparts downstream in dispersive regions. The density-energy conversion, if forming a positive feedback, can result in the enhancement of modulation amplitudes. This has been known as the microbunching instability (MBI) (see, for example, Refs. [2-4]). MBI has been one of the most challenging issues associated with beamline designs such as magnetic bunch compressor chicane for free-electron lasers or linear colliders. Moreover, it also poses difficulties in the design of transport lines for recirculating or energy-recovery-linacs (ERLs). Any dominant source of beam performance limitations in such a high-brightness electron beam transport system must be carefully examined in order to preserve beam phase-space quality. Among those, we already know the longitudinal space charge force (LSC) and coherent synchrotron radiation (CSR) can, in particular, drive MBI. The LSC effect stems from upstream ripples on top of the longitudinal charge density, and can generate an energy modulation when the beam traverses a long section of a beamline. When the beam encounters bending, CSR due to electron coherent radiation emission inside a bend can

have a significant effect upon further amplifying the induced density modulations. A typical transport line in a recirculated machine can have a long linac or straight section and a large number of bending dipoles, and thus can potentially incubate such density-energy conversion along the beamline. The successive accumulation and conversion mechanism between density and energy modulations can result in significant microbunching amplification.

In the early design of the Circulator Cooler Ring (CCR) [1] for the Jefferson Lab Electron Ion Collider (JLEIC) [5], both tracking simulations [6, 7] and Vlasov analysis [8, 9] have shown that MBI is a serious concern for the CCR design. The one-turn CSR microbunching gain (to be defined later) is found to be up to 4000 at the modulation wavelength of 350 μm and is even higher when LSC is included. This is mainly due to the high bunch charge (~ 2 nC) and relatively low energy (~ 55 MeV) of the cooling beam circulating in the CCR. Mitigation of MBI thus becomes an issue for a high-brightness beam transport in recirculating machines. Several mitigation schemes have been proposed in the literature for different machine configurations and can be in general divided into two categories: those addressing the transport lattice, and those directed at the transported beam. For the former aspect, the optics impact of beamline lattice designs on MBI has been recently investigated [10-15]. In those beamline designs, the beam is transversely uncoupled, i.e. non-magnetized. For the latter aspect, Derbenev [16] had proposed using magnetized beam to improve electron cooling performance [17] and to mitigate collective effects such as space charge [18] and MBI (our primary focus in this paper). A magnetized beam can be generated by immersing the cathode in an axial magnetic field and thus features a nonzero angular momentum. In general, the magnetized beam is a transversely coupled beam.

In the remainder of this paper, we will derive the equations governing microbunching for a transversely coupled beam. Our derivation largely follows the theoretical treatment by Huang and Kim [4] and Heifets, Stupakov, and Krinsky [3]. To characterize the general feature of a magnetized (or a otherwise coupled) beam, we use the beam sigma matrix instead of Twiss (or Courant-Snyder) parameters. We then apply the resultant integral equation to a specialized arc design for magnetized beam transport to a section of cooling solenoid. We also benchmark our developed code against particle tracking by ELEGANT [19]. Both simulation results are in good agreement.

* This material is based upon work supported by the U.S. Department of Energy, Office of Science, Office of Nuclear Physics under contract DE-AC05-06OR23177.

[#]jcytsai@vt.edu

COMPACT CRABBING CAVITY SYSTEMS FOR PARTICLE COLLIDERS*

S. U. De Silva

Center for Accelerator Science, Old Dominion University, Norfolk, VA 23529, USA

Abstract

In circular or ring-based particle colliders, crabbing cavities are used to increase the luminosity. The first superconducting crabbing cavity system was successfully implemented at KEKB electron-positron collider that have demonstrated the luminosity increase with overlapping bunches. Crabbing systems are an essential component in the future colliders with intense beams, such as the LHC high luminosity upgrade and proposed electron-ion colliders. Novel compact superconducting cavity designs with improved rf properties, at low operating frequencies have been prototyped successfully that can deliver high operating voltages. We present single cavity and multi-cell crabbing cavities proposed for future particle colliders and addresses the challenges in those cavity systems.

INTRODUCTION

Luminosity increase in particle colliders requires maximizing the number of interactions between the colliding bunches. Non-overlapping bunches limit the number of interactions to that crossing angle as given in

$$L = \frac{N_1 N_2 f_c N_b}{4\pi\sigma_x\sigma_y} \frac{1}{\sqrt{1 + \left(\frac{\sigma_z\theta_c}{2\sigma_x}\right)^2}} \quad (3)$$

where θ_c is the crossing angle. This limitation can be overcome by using crabbing cavities to enable head-on collision of bunches. The crabbing concept was first proposed by R.B. Palmer [1], in using a rf cavity to generate a transverse kick at the head and tail of the bunch that forces head-on collision at the interaction point of the colliding bunches as shown in Fig. 1.

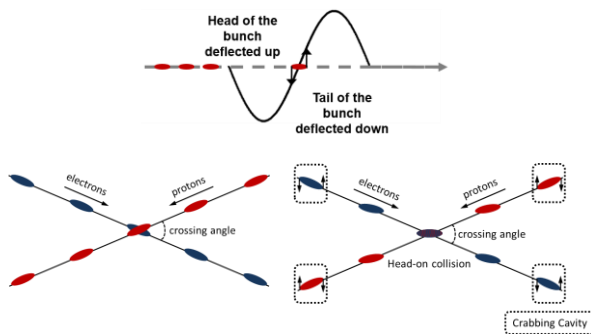


Figure 1: Transverse kick due to crabbing cavity (top) and bunch collision with and without crabbing cavities (bottom).

*Work supported by DOE via US LARP Program and by the High Luminosity LHC Project. Work was also supported by DOE Contract No. DE-AC02-76SF00515. #sdesilva@jlab.org

Crabbing cavities can be used as an rf separator in splitting a single beam to multiple beams; operating at a phase offset of $\pi/2$. These cavities operating in crabbing mode can also be used in emittance exchange in beams, x-ray pulse compression, and beam diagnostics.

TM₁₁₀-TYPE CAVITIES

Crabbing cavities operating in TM₁₁₀ mode uses the transverse magnetic field interaction with the beam to generate transverse kick as shown in Fig. 2 [2]. The TM₁₁₀ mode is degenerate in a cylindrical-shaped geometry; therefore a squashed-elliptical geometry is adapted to separate the two polarizations.

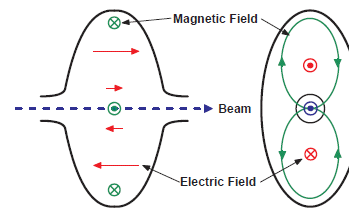


Figure 2: Squashed-elliptical crabbing cavity operating in TM₁₁₀ mode.

The squashed-elliptical cavity has a lower order mode (LOM), which is the TM₀₁₀ monopole mode present in the geometry. The narrow separation between the crabbing mode with LOM and HOMs while maintaining high R/Q for the crabbing mode makes the damping scheme very complex for these cavities. The operating frequency is inversely related to the transverse dimensions, hence these shapes are not favourable at low operating frequencies. At high operating frequencies TM₁₁₀-type cavities can deliver compact crabbing cavities that are capable of accommodating large beam apertures. The degrees of freedom in the parameter space for TM₁₁₀-type cavities are limited, which makes the suppression of higher order multipole components difficult.

1st Superconducting Crabbing Cavity

The first and only superconducting crabbing cavity has been designed and developed at KEK for the KEKB factory [3].

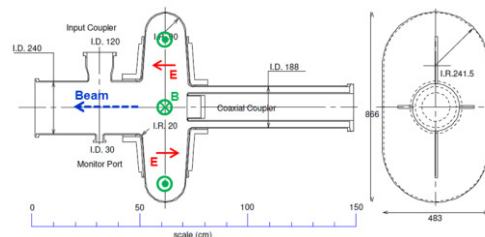


Figure 3: 508.9 MHz KEK crabbing cavity.

EFFECT OF PROTON BUNCH PARAMETER VARIATION ON AWAKE

N. Savard, University of Victoria, Victoria, Canada and TRIUMF, Vancouver, Canada

J. Vieira, Instituto Superior Tecnico, Lisbon, Portugal

P. Muggli, Max-Planck Institute for Physics, Munich, Germany and CERN, Geneva, Switzerland

Abstract

We show that the phase of the wakefields as the CERN SPS proton bunch experiences the self-modulation instability is very weakly dependent on variations of the bunch parameters by $\pm 5\%$. There is a $\approx \lambda_{pe}/4$ -wide region of the wakefields that remain accelerating and focusing for an electron witness bunch after the instability has grown and saturated, that is after ~ 4 m into the plasma with AWAKE base-line parameters. These results suggest that deterministic injection and acceleration of an electron witness bunch into these wakefields resulting from the self-modulation instability is, in principle, possible experimentally.

INTRODUCTION

Sending relativistic charged particle bunches through a plasma generates wakefields in the transverse and longitudinal direction with frequency defined by the electron plasma density n_e , frequency $\omega_{pe} = (n_e e^2 / \epsilon_0 m_e)^{1/2}$ and wavelength $\lambda_{pe} = 2\pi c / \omega_{pe}$ [1]. In the linear regime, the transverse wakefields are $\frac{\pi}{2}$ out of phase with the longitudinal ones, so there is a region within $\lambda_{pe}/4$ where the fields are both accelerating and focusing for an electron (or positron) bunch to be externally injected and accelerated over a long distance.

AWAKE is a proof-of-principle experiment which will be propagating the SPS (Super Proton Synchrotron) bunch through a plasma column of 10 m to drive wakefields and accelerate an externally injected electron bunch. With a baseline electron plasma density of $7 \times 10^{14} \text{ cm}^{-3}$, $\lambda_{pe} \approx 1.2$ mm. This is many times shorter than the longitudinal rms length of the bunch (≈ 12 cm), which causes protons along the bunch to be locally either focused or defocused by the wakefield. This is the self-modulation instability (SMI) [2]. The focused protons form micro-bunches separated by $\approx \lambda_{pe}$, which resonantly drive the wakefields to large amplitudes.

The SMI growth and the associated evolution of the proton bunch cause the wakefield phase-velocity to change with respect to the initial bunch velocity, until eventually stabilizing at the speed of the bunch. This can be seen in Fig. 1, where we see that the on-axis field E_z moves backwards within a set window of $\xi = z - ct$ of the proton bunch as it propagates within the plasma. Near 4 m, the phase stabilizes after SMI development (i.e., lines become vertical on Fig. 1), which becomes a suitable location to inject particles. Note that the transverse wakefields follow a similar evolution (not shown).

Many simulations have been performed for AWAKE using parameters of the CERN SPS bunch. However, from an experimental viewpoint we are interested in determining

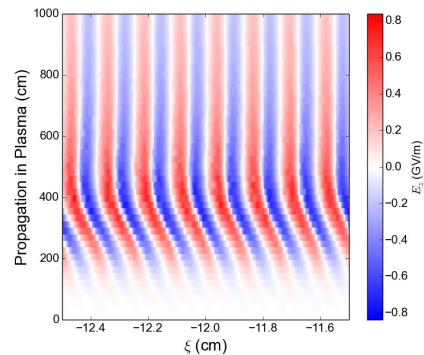


Figure 1: E_z as a function of ξ and propagation distance of the proton bunch along the plasma in a region near $\xi = -12$ cm from the proton bunch front.

how variations in the parameters of the proton bunch affect the phase change at positions ξ along the bunch, i.e., where the electrons are injected. We use a variation of $\pm 5\%$ of the bunch parameters for this study in order to obtain the trends of the wakefields phase variation. Since all particles are relativistic and there is essentially no dephasing between them over the plasma length considered here, injected electrons stay in the proper phase (accelerating and focusing) all along the acceleration process, unless the relative phase of the wakefields change.

In the experiment, the proton bunch will be co-propagating with a laser pulse at its center as it goes through rubidium (Rb) vapor. The ~ 100 fs laser pulse ionizes the Rb, creating a relativistically moving ionization front in the bunch that seeds the SMI. For the simulations, the bunch density is cut to include the sharp start of the beam/plasma interaction and for $-\sqrt{2}\pi\sigma_{zb} < \xi < 0$ is given by :

$$n_b(\xi, r) = n_{b0} \times 0.5 \left[1 + \cos \left(\sqrt{\frac{\pi}{2}} \frac{\xi}{\sigma_{zb}} \right) \right] \times e^{-\frac{r^2}{2\sigma_{rb}^2}}.$$

Here $n_{b0} = N_b / [(2\pi)^{3/2} \sigma_{rb}^2 \sigma_{zb}]$. Since the wakefields amplitude is proportional to n_b , the evolution of the wakefields (amplitude and phase) may be sensitive to its initial value n_{b0} , which itself depends on the bunch population N_b , and rms radius and length, σ_{rb} and σ_{zb} , respectively. These are parameters that may vary from event to event in the experiment.

For these studies, we use the particle-in-cell code OSIRIS [3] developed at IST in Lisbon and at UCLA. For these 2D cylindrical simulations we use a box size of 1.61 mm with 425 grid points in r and 299.89 mm with 18000 grid points in z . The number of plasma and beam particles are 6×10^6 and 5×10^5 respectively. The simulation time

PROGRESS TOWARD AN EXPERIMENT AT AWAKE

P. Muggli*

Max Planck Institute for Physics, Munich, Germany and CERN, Geneva, Switzerland
for the AWAKE Collaboration

Abstract

We briefly report on the progress towards an AWAKE experiment at CERN. First experiments are scheduled for the end of 2016 and will focus on the study of the self-modulation instability. Later experiments, scheduled for 2017-18, will study acceleration by externally injecting electrons into the the wakefields.

INTRODUCTION

The AWAKE experiment at CERN aims at studying the use of proton (p^+) bunches to drive wakefields in plasmas to accelerate electrons (e^-) [1]. The first phase of the experiment, scheduled for the end of 2016, will study the physics of the self-modulation instability (SMI) [2] of a long ($\sigma_z = 12$ cm) CERN-SPS p^+ bunch in a dense plasma, i.e., such that $\sigma_z \gg \lambda_{pe} \sim n_e^{-1/2}$. Here $\lambda_{pe} = 2\pi c/\omega_{pe}$ is the wavelength of the relativistic plasma wave or wakefields in an electron plasma of density n_e and plasma electron angular frequency $\omega_{pe} = (n_e e^2/\epsilon_0 m_e)^{-1/2}$. In a second phase, scheduled for 2017-18, a low energy e^- witness bunch (10-20 MeV) with length $\cong \lambda_{pe}$ will be injected in the plasma to sample the wakefields and potentially reach an energy >1 GeV, with a finite energy spread. We describe here the state of readiness of the major components of AWAKE for the first experiments.

FACILITY

A major component of the experiment is the facility that has been built in place of the CNGS facility. The commissioning of the facility will be completed in 2017.

PROTON BEAM LINE

The p^+ beam line consists mainly of: a final focus system; a horizontal magnetic chicane to allow for the p^+ bunch to become co-linear with a laser beam used for plasma formation and SMI seeding; three screens to measure the p^+ bunch transverse size; a number of magnetic correctors, beam position monitors, current transformers and beam loss monitors that form the standard beam line instrumentation. The first pilot p^+ bunch ($\cong 10^9 p^+$) was brought to the beam dump. The beam line was successfully commissioned and produced the expected p^+ bunch parameters: energy of $\cong 400$ GeV (SPS beam), $1-3 \times 10^{11} p^+$ /bunch, focused beam size $\sigma_r^* \cong 200 \mu\text{m}$ and $\beta^* \cong 5$ m.

* muggli@mpp.mpg.de

PLASMA SOURCE

The plasma source consists of a rubidium (Rb) vapor source and of a laser for ionization of the vapor [3].

Vapor Source

The vapor source is designed to produce an $\cong 10$ m-long column of Rb vapor with density n_{Rb} in the $1-10 \times 10^{14} \text{cm}^{-3}$ range ($7 \times 10^{14} \text{cm}^{-3}$ nominal), with a very uniform density profile ($\delta n_{Rb}/n_{Rb} < 0.2\%$) and with a sharp density edge at each end, with a drop in density by approximately two orders of magnitude in a few centimeters. The source is based on a long heat exchanger (see Fig. 1) ensuring the density uniformity by imposing a very uniform temperature along the vapor column ($\delta n_{Rb}/n_{Rb} \propto \delta T/T$ in absence of flow). The sharp density edge at each end is created by expansion of the Rb vapor into a vacuum volume through a 1 cm diameter aperture [4]. The source uses two Rb evaporation reservoirs and the vapor density is measured at each end with a relative accuracy of better than 0.5% using the anomalous optical dispersion around the D2 line of Rb at 780 nm [5]. Note that



Figure 1: Picture of the vapor source 10 m-long heat exchanger under installation in the AWAKE facility. The picture is looking towards the SPS.

since the source has two Rb reservoirs it can also generate essentially linear density gradients along the source.

Rubidium was chosen because of its low ionization potential ($\phi = 4.177$ eV for the first e^-) and its relatively large vapor pressure. Temperatures between 150 and 230 °C are sufficient to reach the desired density range. The heat exchanger satisfied the required temperature uniformity specifications and is installed in the AWAKE facility. The source ends are currently under installation and commissioning.

Laser

The laser for vapor ionization is an Erbium-doped fiber oscillator followed by a CPA Ti:Sapphire amplification chain.

SYNCHROTRON OSCILLATION DERIVED FROM THREE COMPONENTS HAMILTONIAN

Kouichi Jimbo[#], IAE, Kyoto University, Uji-city, Kyoto, Japan
Hikaru Souda, Gunma University Heavy Ion Medical Centre, Maebashi-city, Gunma, Japan

Abstract

The Hamiltonian, which was composed of coasting, synchrotron and betatron motions, clarified the synchro-betatron resonant coupling mechanism in a storage ring. The equation for the synchrotron motion was also obtained from the Hamiltonian. It shows that the so-called synchrotron oscillation is an oscillation around the revolution frequency as well as of the kinetic energy of the on-momentum particle. The detectable synchrotron oscillation is a horizontal oscillation on the laboratory frame.

INTRODUCTION

The Hamiltonian, which was composed of coasting, synchrotron and betatron motions, was derived to explain the observed horizontal betatron tune jump near the synchro-betatron resonant coupling point[1]. We discuss about the so-called synchrotron oscillation related to the Doppler effect. We show that the synchrotron oscillation derived from the Hamiltonian is longitudinal as well as horizontal oscillations.

HAMILTONIAN FOR THE ORBING PARTICLE

We assume that an on-momentum particle of mass m and momentum p_0 is circling (without oscillating motion) the reference closed orbit of the average radius R with velocity v . E_0 is the total energy and K is the kinematic energy of the on-momentum particle. We have the following relations:

$$E_0^2 = (p_0 c)^2 + (m c^2)^2, p_0 = m \gamma \beta c, \text{ and } E_0 = K + m c^2,$$

$$\text{where } \beta = \frac{v}{c}, \frac{ds}{dt} = v, \gamma = \frac{1}{\sqrt{1-\beta^2}} \text{ and } E_0 = m \gamma c^2.$$

Keeping up to the 2nd order to describe an orbiting particle of coasting, betatron and synchrotron motions, the Hamiltonian composed of three motions is given as follows from Eq.(21) of the reference 1:

$$\begin{aligned} \bar{H} = & -(1 + \delta_c + \delta_s) + \frac{1}{2} \left(\frac{\bar{p}_x}{p_0} \right)^2 + \frac{1}{2} K_x \bar{x}^2 + \frac{1}{2} (-\eta) (\delta_c + \delta_s)^2 \\ & - \frac{h q V}{2 \pi \beta^2 E_0} \{ \cos(\phi + \phi_D) - \cos(\phi_s + \phi_D) + (\phi - \phi_s) \sin(\phi_s + \phi_D) \} \end{aligned} \quad (1)$$

where δ_s is the (rationalized) fractional deviation of the kinetic energy caused by the so-called synchrotron oscillation and δ_c is the (rationalized) fractional deviation

of the kinetic energy caused by the dispersion. Both δ_s and δ_c are normalized by $\beta^2 E_0$. The coasting motion consists of the 0th (on-momentum particle) and 1st (δ_s and δ_c) order effects. η is the phase slip factor. We assume the strong focusing case $0 < (-\eta) < 1$. ϕ is the phase of the rf wave. Around the off-momentum closed orbit, \bar{x} is horizontal coordinate and \bar{p}_x is horizontal momentum of the orbiting particle. We also have $\phi_D = -\frac{D}{R} \left(\frac{\bar{p}_x}{p_0} \right) + \frac{D'}{R} \bar{x}$, and $\phi_s = \psi_s - \phi_D$. D is the dispersion and ψ_s is the phase angle for synchronous particle with respect to the rf cavity voltage V . In the following argument, we neglect the betatron oscillation.

OSCILLATION AROUND THE REVOLUTION FREQUENCY

We obtain the following equation for the so-called synchrotron oscillation from Eqs.(26) and (27) of the reference 1:

$$\delta_s = \hat{\delta} \cos \{ \nu_\eta (\theta - \theta_0) \} + \delta_0 + C \quad (2)$$

$$\nu_\eta^2 = \frac{\omega_s^2}{\omega_0^2} = \frac{h q V |\eta \cos(\phi_s + \phi_D)|}{2 \pi \beta^2 E_0} \quad (3)$$

where $\delta_0 = -\delta_c - \frac{1}{\eta}$, θ is the orbit angle ($\theta = \frac{s}{R}$), θ_0 is the orbit angle at the injection point. ω_0 is the revolution frequency, ω_s is the synchrotron frequency, ν_η is the synchrotron tune, $\hat{\delta}$ is the amplitude of oscillation and C is an integration constant.

Generally $\delta_c \ll 1$ and we can choose $\delta_c = \hat{\delta}$ at $\theta = \theta_0$. We can neglect this term. Then we consider only the reference closed orbit. Now the coasting motion consists of the on-momentum particle plus the effect of δ_s . From Eq.(2)

$$\delta_s = \hat{\delta} \cos \{ \nu_\eta (\theta - \theta_0) \} + \frac{1}{(-\eta)} + C \quad (4)$$

Neglecting the integration constant $C = 0$,

$$-\eta \delta_s = -\eta \hat{\delta} \cos \{ \nu_\eta (\theta - \theta_0) \} + 1. \quad (5)$$

[#]jimbo@iae.kyoto-u.ac.jp

DESIGN OF FRONT END FOR RF SYNCHRONIZED SHORT PULSE LASER ION SOURCE

Y. Fuwa*, Y. Iwashita, Kyoto University, Kyoto, Japan

Abstract

An laser ion source which produces short pulse ion beam is under development. In this ion source, laser plasma is produced in an RF electric field and ions are extracted from the plasma before its expansion. The ion beach can be injected into RF acceleration bucket of RFQ. For this ion source, an accelerator front end was designed.

SHORT PULSE LASER ION SOURCE

Short pulse ion beams are promising candidate as a component of a high efficiency accelerator front end. In conventional ion source, the pulse length of the extracted ion beams are longer than the RF (Radio Frequency) period of the subsequent accelerator. Therefore, the ion beams must be bunched in the front end of the accelerator such as an RFQ (Radio Frequency Quadrupole). If the beam is already bunched at the extraction area of the ion source, the beam can be injected into accelerating RF phase and directly accelerated in RFQ. Then, the bunching section of the RFQ can be omitted and the accelerating efficiency of RFQ can be improved.

For production of initially-bunched beam, laser plasma induced by ultra-short pulse laser has a promising potential. With the focused short pulse laser in a few tenth of micro meter, the volume of the interaction region are small enough to produce bunched ions, and the ions in the plasma produced by the short pulse laser are supposed to have also short pulse structure. If the short pulse ions bunch can be produces in an RF electric field, the ions can be captured by the RF bucket and the bunch structure can be kept. Therefore, the production of short pulse ion bunch can be achieved and direct acceleration of the bunched ion beam in RFQ can be realized.

PLASMA PRODUCTION CONDITION

In this section, conditions to produce short pulse ion beam is discussed.

For the extraction the ions from the laser plasma, the thickness of plasma should be smaller than Debye length. The Debye length λ_D is defined as

$$\lambda_D = \sqrt{\frac{\epsilon_0 k T}{n_e e^2}} \quad (1)$$

where ϵ_0 , k , T , n_e and e are the permittivity of vacuum, the Boltzmann constant, electron temperature, electron density, and elementary charge, respectively. The thickness of the plasma is the same order of the laser dimension at the focal

point. In our test bench, the focal spot of laser can be controlled less than 50 μm . For the practical use of ion beam, peak current of extracted microbunch should be larger than 1 mA. To achieve this current, the number of protons per microbunch is larger than 10^7 . From those condition, the temperature of plasma should be between 100 eV and 1 keV. The summary of the discussion is illustrated in Figure 1. The region colored by light green is the sufficient condition to produce short pulse ion bunch.

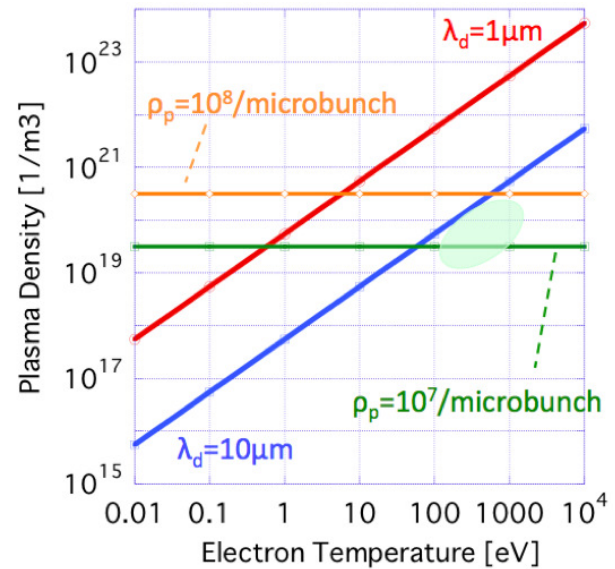


Figure 1: Condition of short pulse ion beam production. The region colored by light green is suitable for the production of short pulse ion beam.

Amplitude and frequency of applied electric field in the acceleration gap are also important. Figure 2 shows minimum amplitude of RF electric field in 1 mm acceleration gap to extract protons within half RF cycle. The minimum amplitude of the field is a function of RF frequency. For example, 5 MV/m of peak amplitude of the electric field is needed for 100 MHz RF field. There is also a limit of amplitude of electric field, known as Kilpatrick criteria,

$$f[\text{MHz}] = 1.64(E[\text{MV/m}])^2 \exp\left(-\frac{8.5}{E[\text{MV/m}]}\right). \quad (2)$$

This relation is an indication of the amplitude of the electric field which can be applied without discharge. Combined this relation and the minimum electric field to extract protons discussed above, it is supposed that the frequency of the applied electric field should be less than 200 MHz to extract protons (see Figure 2).

* fuwa@kyticer.kuicr.kyoto-u.ac.jp

EBIS CHARGE BREEDER FOR RAON FACILITY*

S. Kondrashev[†], J.W. Kim, Y.K. Kwon, Y.H. Park, H.J. Son
Institute for Basic Science, Daejeon, Korea

Abstract

New large scale accelerator facility called RAON is under design in the Institute for Basic Science (IBS), Daejeon, Korea. Both techniques of rare isotope production Isotope Separation On-Line (ISOL) and In-Flight Fragmentation (IF) will be combined within one facility for the first time to provide wide variety of rare isotope ion beams for nuclear physics experiments and applied research [1]. Electron Beam Ion Source (EBIS) charge breeder will be utilized to prepare rare isotope ion beams produced by ISOL method for efficient acceleration. Beams of different rare isotopes with masses in the range of 6 – 180 a.m.u. will be charge-bred by an EBIS charge breeder to a charge-to-mass ratio (q/A) $\geq 1/4$ and accelerated by linear accelerator to energies of 18.5 MeV/u. RAON EBIS charge breeder will provide the next step in the development of breeder technology by implementation of electron beam with current up to 3 A and utilization of wide (8") warm bore of 6 T superconducting solenoid. The design of RAON EBIS charge breeder is presented and discussed.

INTRODUCTION

EBIS charge breeder (EBIS CB) is a key element for efficient and cost effective acceleration of rare isotope beams produced by ISOL method. It serves as an interface between ISOL ion source and linear accelerator to convert a singly-charged ion beam into the highly-charged ion beam with required charge-to-mass ratio. Over the last decade EBIS CB has been established as a mature concept with demonstrated superior parameters - high breeding efficiency, short breeding times and low background of stable contaminants in charge-bred rare isotope beams. By this reason EBIS CB is now preferable choice for the most of rare isotope facilities either already operational or being under construction, including RAON. After successful demonstration of effective charge breeding and many years of reliable on-line operation of REX EBIS CB at CERN ISOLDE [2], next generation EBIT CB for MSU ReA3 [3] and EBIS CB for ANL CARIBU [4] both with higher electron beam current and electron beam current density in the ion trap have been developed and commissioned recently.

At present, the CARIBU EBIS CB is the most advanced system with up to 2 A electron beam current and 28% breeding efficiency demonstrated off-line with injected stable $^{133}\text{Cs}^+$ ion beam [5, 6]. The RAON EBIS CB will provide the next step in the development of the breeder technology further enhancing electron beam cur-

rent up to 3 A and improving overall system design and performance by implementation of the superconducting solenoid with larger (8") diameter of the warm bore.

Parameters of the RAON EBIS CB are described elsewhere [7] and its general design is presented in [8]. The RAON EBIS CB will be operated in so-called "pulsed" injection mode which provide higher breeding efficiency in comparison with "continuous" injection mode [2]. An RFQ cooler-buncher will be placed downstream of the EBIS CB to convert dc beam of selected rare isotope extracted from ISOL ion source into pulsed ion beam required for "pulsed" injection into the EBIS CB. The RFQ cooler-buncher will deliver to the EBIS CB high quality ion beams with emittance of about $3\pi\text{ mm}^2\text{mrad}$, energy spread below 10 eV and pulse duration of about 10 μs . Such RFQ cooler-buncher capable to handle high intensity ion beams (up to 10^9 ions/s) has been recently designed [9] and its manufacturing is now in progress.

DESIGN OF RAON EBIS CB

3D model of RAON EBIS CB is presented in Fig. 1. RAON EBIS CB utilize semi-immersed (into magnetic field) type e-gun with pure magnetic compression. Such electron gun has been designed and built by Budker Institute of Nuclear Physics (BINP, Novosibirsk, Russia). The e-gun is semi-immersed (into magnetic field) type e-gun with pure magnetic compression. Thermionic IrCe cathode with diameter of 5.6 mm is used to generate high quality electron beam with up to 3 A current. An electron collector is capable to dissipate up to 20 kW power of DC electron beam. The unshielded 6 T superconducting solenoid with 8" diameter of warm bore has been ordered from Tesla Engineering Ltd. with expected delivery in March of 2017.

Two diagnostics stations consisting pneumatically driven large aperture Faraday cups (FC) and pepper pot emittance probes have been designed and manufactured. The design of pepper pot emittance probe is similar to one described in [7]. A single microchannel plate (MCP) with wide dynamic range coupled to a fast P47 phosphor screen has been chosen as an imaging system for both emittance probes. Its sensitivity is high enough to measure emittance of both injected and extracted beams into/from EBIS CB with wide range of intensities.

Dumping of high power pulsed and DC 3 A electron beam into electron collector is planned as a first step of EBIS CB sub-systems commissioning prior to delivery of the 6 T superconducting solenoid.

Drift Tube Section

Detailed description of drift tube (DT) section design of RAON EBIS CB can be found in [8]. Further modifications were made to address the issue of mechanical stress

* Work supported by the Rare Isotope Science Project of Institute for Basic Science funded by Ministry of Science

[†] email address: kondrashev@ibs.re.kr

NEW COOLERS FOR ION ION COLLIDERS

V. V. Parkhomchuk, BINP, Novosibirsk, Russia

Abstract

For crucial contributions in the proof of principle of electron cooling, for leading contribution to the experimental and theoretical development of electron cooling, and for achievement of the planned parameters of coolers for facilities in laboratories around the world the 2016 *Robert R. Wilson Prize for Achievement in the Physics of Particle Accelerators* was awarded to Vasili Parkhomchuk. In this paper new future coolers for ion*ion collider will be discussed.

INTRODUCTION

The electron coolers are widely used for accumulation and cooling of heavy ions at storage rings. In 2016 the design and construction of the relativistic energy ion-ion collider NICA at Dubna were started. To obtain high luminosity at NICA it is extremely important to use powerful electron cooling of ions in collider regime for suppression of beam-beam effects at relatively low energy beams. In this report possible solution based on experience of high voltage cooler at COSY are discussed.

All modern collider will operate in bunch regime to obtain high luminosity. At beam collision point designed beta function in both transverse directions is very small and the bunch length should be less than value of beta function at collision point β^* . As was first time demonstrated by Dag Reistad in cooling experiments at CELSIUS, at this condition very dangerous phenomena called “electron heating” can develop [1]. New generation of electron coolers try to use the hollow electron beam for control the transverse and longitudinal emittances as instruments against this phenomena [2].

COOLING BUNCHED BEAM

Usually for accumulation and cooling a regime without RF is used when ions beam are uniformly distributed along the orbit. In this case high frequency mode does not excite inside vacuum chamber. All modern colliders will operate in bunch regime to obtain high luminosity. For not too deep relativism the influence of longitudinal RF field from cavity and beam space charge fields determinate the longitudinal beam bunch profile.

At this conditions cooling and sinusoidal RF voltage lead to parabolic shape of ion bunch profile with sharp edges. Figure 1 shows the longitudinal shape of a proton bunch (1.6 GeV, 0.3 A electron beam at COSY) after acceleration and after electron cooling [3]. It is easy to see that after the main bunch the additional small bunches appeared because of high order oscillations at vacuum chamber. For a low energy cooling and the high intensity proton beam same transverse oscillations were detected Fig. 2.

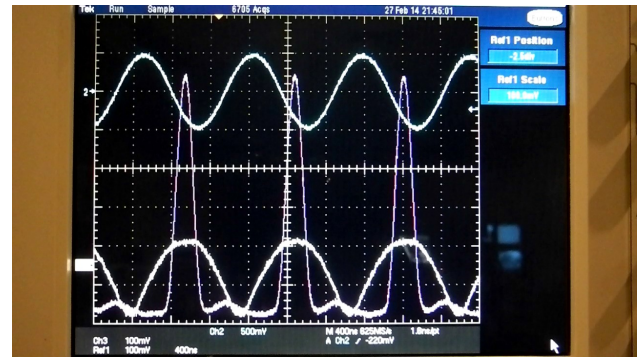


Figure 1: RF signal of proton beam profile before cooling and after cooling.

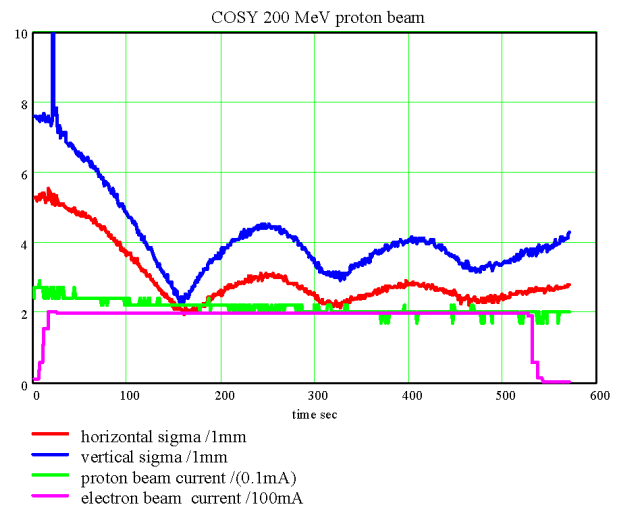


Figure 2: Periodical heating of proton beam on energy 200 MeV (COSY).

Decreasing of the proton beam intensity to less than 0.2 mA help to stop an unwanted oscillations “cooling-heating”.

LEIR COOLER

The electron cooler for LEIR was the first of a new generation of coolers being commissioned for fast phase space cooling of ion beams in storage rings. It was a state-of-the-art cooler incorporating all the recent developments in electron cooling technology (adiabatic expansion, electrostatic bend, variable density electron beam gun) and is designed to deliver up to 600 mA of electron current for the cooling and stacking of Pb^{54+} ions in the frame of the ions for LHC project (2006).

Figure 3 shows the horizontal beam size measured by the Ionization Profile Monitor during the whole LEIR cycle. As the cooling progresses the beam emittance is reduced by more than a factor of 30 at time 0.2 s. After acceleration to

NEUTRONS AND PHOTONS FLUENCES IN THE DTL SECTION OF THE ESS LINAC

L. Lari^{1#}, ESS-ERIC, Lund, Sweden and CERN, Geneva, Switzerland
 L. S. Esposito, ADAM, Geneva, Switzerland and CERN, Geneva, Switzerland
 R. Bevilacqua, R. Miyamoto, C. Pierre, L. Tchelidze, ESS-ERIC, Lund Sweden
 F. Cerutti, A. Mereghetti, CERN, Geneva, Switzerland
¹present affiliation: Fermilab, Batavia, IL, USA

Abstract

The last section of the normal conducting front end of the ESS accelerator is composed by a train of 5 DTL tanks. They accelerate the proton beam from 3.6 until 90 MeV. The evaluation of the radiation field around these beam elements gives a valuable piece of information to define the layout of the electronic devices to be installed in the surrounding tunnel area. Indeed the risk of SEE and long term damage has to be considered in order to maximize the performance of the ESS accelerator and to avoid possible long down time. A conservative loss distribution is assumed and FLUKA results in term of neutrons and photon fluence are presented.

INTRODUCTION

The European Spallation Source European Research Infrastructure Consortium ESS-ERIC is a joint European organization committed to constructing and operating the first long-pulse neutron spallation source in the world. The facility started its construction in summer 2014 and it is composed of a linear accelerator in which protons are accelerated and collide with a rotating helium-cooled tungsten target. The first beam at 572 MeV on target is foreseen for June 2019 and the nominal average linac beam power of 5 MW will be reached for 2023 [1,2].

ESS LINAC

The ESS linac accelerates 62.5 mA of protons up to 2 GeV in a sequence of normal conducting and superconducting accelerating structures.

In details the normal conducting part starts with the Microwave Discharge Ion Source that produces a proton beam transported through the Low Energy Beam Transport (LEBT) section to the Radio Frequency Quadrupole (RFQ). The RFQ accelerates, focuses and bunches the continuous 75 keV beam up to 3.6 MeV. It is followed by the Medium Energy Beam Transport (MEBT) system where beam characteristics are diagnosed and optimized for further acceleration in the Drift Tube Linac (DTL) section. The Superconducting linac follows the DTLs: 26 Double-Spoke, 36 Medium Beta and 84 High Beta cavities in cascade accelerate the beam up to 2 GeV. Finally, in the High Energy Beam Transport section, the beam is rastered on the tungsten target, using an active fast magnet beam delivery system.

llari@fnal.gov

One of the target characteristics of ESS linac is its high availability per year (95%) as following the facility users program main requirements [3]. As a consequence, a limit of 1 W/m in beam losses for the entire linac was set as design parameter in order to allow the required hands-on maintenances. This restriction means that the relative amount of losses that can be accepted are in the range of 10^{-4} : 10^{-7} per meter, with respect to the beam energy where the losses happen [4].

DTL SECTION

The DTL section is where the normal conducting structure ends. It is composed of 5 tanks, each more than 7 m long. They will be installed in the first part of the ESS linac tunnel, starting about 20 cm inside the Front End Building, where the Ion Source, the LEBT, the RFQ and MEBT will be located.

Exactly the DTLs accelerate protons from 3.62 MeV up to 86.5 MeV. The five tanks are independently powered by a 2.8 MW klystron each. Permanent Magnet Quadrupoles (PMQ) in every second drift tube provide the transverse focusing. Steerers and Beam Position Monitors (BPM) are spread out in some of the empty drift tubes to correct and measure the trajectory.

The DTL is being designed and built by the INFN-LNL, Legnaro, Italy [5].

FLUKA CALCULATIONS

The FLUKA Monte Carlo code [6,7] is used for the evaluation of the prompt radiation around the DTLs, assuming 1 W/m proton losses uniformly distributed along the DTL section, taking into account the different beam energies. As a conservative approach the emission angle is set to 3 mrad with respect to the beam direction.

In order to provide realistic results, detailed FLUKA models of the five DTLs were developed. In particular each drift tube was modelled separately and their lengths were set with respect to the last version of the ESS optics design (see Fig. 1) [8].

The DTL models were then integrated in an updated version of the FLUKA geometry of the ESS accelerator [9]. The updated FLUKA linac model can be used to support integration and operation of the machine as well as to compare results from MCNPX code (used for the low energy part until DTLs [10]) or from MARS code (used for the high energy part [11] starting from DTLs), if needed.

PROTON BEAM DEFOCUSING AS A RESULT OF SELF-MODULATION IN PLASMA

Marlene Turner,^{1*} CERN, Geneva, Switzerland

Alexey Petrenko, Edda Gschwendtner, CERN, Geneva, Switzerland

Konstantin Lotov,² Alexander Sosedkin,² Novosibirsk State University, 630090, Novosibirsk, Russia

¹also at Technical University of Graz, Graz, Austria

²also at Budker Institute of Nuclear Physics SB RAS, 630090, Novosibirsk, Russia

Abstract

The AWAKE experiment will use a 400 GeV/c proton beam with a longitudinal bunch length of $\sigma_z = 12$ cm to create and sustain GV/m plasma wakefields over 10 meters [1]. A 12 cm long bunch can only drive strong wakefields in a plasma with $n_{pe} = 7 \times 10^{14}$ electrons/cm³ after the self-modulation instability (SMI) developed and microbunches formed, spaced at the plasma wavelength. The fields present during SMI focus and defocus the protons in the transverse plane [2]. We show that by inserting two imaging screens downstream the plasma, we can measure the maximum defocusing angle of the defocused protons for plasma densities above $n_{pe} = 5 \times 10^{14}$ electrons/cm⁻³. Measuring maximum defocusing angles around 1 mrad indirectly proves that SMI developed successfully and that GV/m plasma wakefields were created [3]. In this paper we present numerical studies on how and when the wakefields defocus protons in plasma, the expected measurement results of the two screen diagnostics and the physics we can deduce from it.

INTRODUCTION

The Advanced Proton-Driven Plasma Wakefield Acceleration Experiment (AWAKE) is currently under construction at CERN. AWAKE will use a 400 GeV/c proton beam from the CERN SPS to excite GV/m plasma wakefields. The goal of AWAKE is to accelerate electrons to GeV energies in 10 m of plasma [1].

AWAKE uses a 10 m-long rubidium vapour source with a density of 7×10^{14} electrons/cm³ [4]. A 450 mJ laser (4 TW, 100 fs) [5] ionizes the outermost electron of the rubidium atom and creates a plasma with a radius of 1 mm. The 400 GeV/c proton drive bunch has a longitudinal bunch length of $\sigma_z = 12$ cm, a radial bunch size $\sigma_r = 0.2$ mm, 3×10^{11} protons per bunch and an emittance of 3.6 mm mrad.

Using the linear plasma wakefield theory and the condition of most efficient wakefield excitation: $\sigma_z = \sqrt{2}c/\omega_{pe}$, where c is the speed of light, $\omega_{pe} = \sqrt{4\pi n_{pe}e^2/m_e}$ the plasma electron frequency, n_{pe} the plasma electron density, e the electron charge and m_e the electron mass, we can estimate that the optimum plasma density for $\sigma_z = 12$ cm is $n_{pe} = 4 \times 10^9$ electrons/cm³, which corresponds to a maximum accelerating field of ≈ 6 MV/m. To create GV/m plasma wakefields AWAKE will use a plasma density of

$n_{pe} = 7 \times 10^{14}$ electrons/cm³ which corresponds to an optimum drive bunch length of $\sigma_z \approx 0.3$ mm.

The energy of the proton bunches available at CERN is enough to accelerate electrons up to the TeV range [6]. To reach GV/m wakefields, the experiment must rely on the self-modulation instability (SMI) to modulate the long proton bunch into micro-bunches spaced at the plasma wavelength λ_{pe} ($\lambda_{pe} = 1.2$ mm for $n_{pe} = 7 \times 10^{14}$ electrons/cm³). These micro-bunches can then resonantly drive plasma wakefields.

The SMI is seeded by the ionization front created by a short laser pulse overlapping with the proton bunch [6]. The transverse wakefields periodically focus and defocus protons, depending on their position ξ along the bunch; the proton bunch, while being modulated, contributes to the wakefield growth.

Inserting two imaging screens downstream of the plasma, gives the possibility to detect the protons that are focused and defocused by the SMI.

Phase 1 of the AWAKE experiment will start in late 2016. The goal is to measure and understand the development of the SMI. In AWAKE phase 2 (2017-2018) externally injected electrons with the energy ≈ 15 MeV will be accelerated to GeV energies.

In this paper, we study the wakefields that act on the defocused protons and we look at the proton trajectories. We describe the measurable quantities of the two-screen images and show how we plan to determine the saturation point of the SMI from these images.

NUMERICAL SIMULATIONS

Wakefields Acting on the Proton Drive Bunch

Plasma simulations were performed with the quasi-static 2D3v code LCODE [7,8]. All following simulations use the AWAKE baseline parameters described in the Introduction section except that we used a more realistic proton beam emittance of 2.2 mm mrad instead of 3.6 mm mrad [9].

To understand the SMI and proton defocusing, we look at the wakefields that a proton experiences when traversing the plasma. Figure 1a shows the force - the contributions from the radial electric field E_r and the azimuthal magnetic field B_ϕ - that affects the proton with the highest radial momentum p_r . The resulting force in CGS units is:

$$F_r = E_r - B_\phi \quad (1)$$

* marlene.turner@cern.ch

FREQUENCY MANIPULATION OF HALF-WAVE RESONATORS DURING FABRICATION AND PROCESSING*

Z.A. Conway[†], R.L. Fischer, C.S. Hopper, M.J. Kedzie, M.P. Kelly, S-H. Kim, P.N. Ostroumov and T.C. Reid, Argonne National Laboratory, Argonne, IL 60439, U.S.A.

V.A. Lebedev, A. Lunin, Fermi National Accelerator Laboratory, Batavia, IL 60510, U.S.A.

Abstract

Argonne National Laboratory is developing a superconducting resonator cryomodule for the acceleration of 2 mA H⁺ beams from 2.1 to 10.3 MeV for Fermi National Accelerator Laboratory's Proton Improvement Plan II. The cryomodule contains 8 superconducting half-wave resonators operating at 162.500 MHz with a 120 kHz tuning window. This paper reviews the half-wave resonator fabrication techniques used to manipulate the resonant frequency to the design goal of 162.500 MHz at 2.0 K. This also determines the target frequency at select stages of resonator construction, which will be discussed and supported by measurements.

INTRODUCTION

Argonne National Laboratory (ANL) has designed and is now fabricating a half-wave resonator (HWR) cryomodule for the Proton Improvement Plan II (PIP-II) Injector Test (PIP2IT) at Fermi National Accelerator Laboratory (FNAL) [1, 2]. The HWR cryomodule contains 8 HWRs and 8 SC solenoids, with integrated *x-y* steering and return coils, for the acceleration of a ≥ 2 mA H⁺ beam from 2.1 to 10.3 MeV. This HWR cryomodule is positioned immediately after the normal conducting radio-frequency quadrupole (RFQ) accelerator in the proposed 800 MeV linac. This linac will replace the existing 400 MeV linac as part of the PIP-II project [3, 4, 5].

Figure 1 shows the major sub-assemblies which comprise a HWR. Figure 2 shows a finished HWR. The HWRs are fabricated from bulk niobium and have no demountable joints for tuning. Because all of the formed sections are Electron Beam Welded (EBW) into the final resonator assembly the dimensions of the parts must be properly sized to attain the desired room temperature frequency of 162.581 MHz. This is a precursor to the final 2.0 K resonant frequency being 162.500 MHz. Final fine tuning is accomplished via plastic deformation of the cavity at the beam ports after the HWR assembly is welded, the helium jacket is installed and all surface polishes are finished.

In the next section the target frequency at various stages of cavity implementation are described and results are presented. This is followed with a brief review of the impact which this tuning procedure has on the cavity performance at 2.0 K and a few concluding remarks.

* This material is based upon work supported by the U.S. Department of Energy, Office of Science, Office of Nuclear Physics and High-Energy Physics, under Contract No. DE-AC02-76-CH03000 and DE-AC02-06CH11357. This research used resources of ANL's ATLAS facility which is a DOE Office of Science User Facility.

[†] zconway@anl.gov

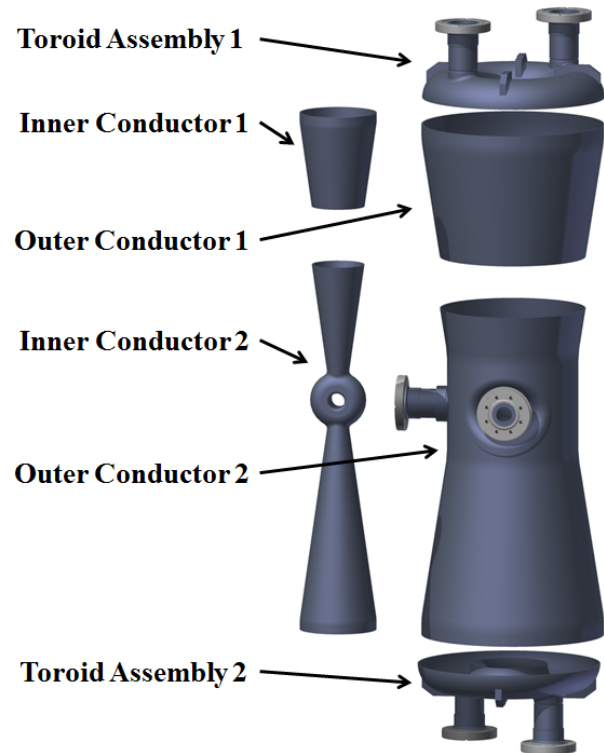


Figure 1: The major sub-assemblies which comprise a half-wave resonator. The parts shown are assembled with indium wire in all of the joints to determine the resonant frequency during the final stages of fabrication. After the frequency measurements the assembly is welded.



Figure 2: Left, two half-wave resonators in the cleanroom after final electron-beam welding. Top right, a half-wave resonator immediately prior to the final electron beam welding. Bottom right, a finished half-wave resonator. The HWR end-to-end length is 48 inches at room temperature.

INTERLEAVING LATTICE DESIGN FOR APS LINAC*

S. Shin^{†,1}, Yin-E. Sun, A. Zholents

Argonne National Laboratory, Argonne, IL, 60439, USA

¹also at Pohang Accelerator Laboratory, Pohang 37673, Korea

Abstract

The design of the lattice for the Advanced Photon Source (APS) injector linac suitable for the interleaving operation of the thermionic and photocathode rf electron guns is presented.

INTRODUCTION

The APS linac is part of the injector complex of the APS storage ring. The thermionic RF electron gun (RG) provides the electron beam that is accelerated through the linac, injected into the Particle Accumulator Ring (PAR), cooled, transferred to the Booster synchrotron, accelerated, and injected into the APS storage ring. The linac is also equipped with the state-of-the-art S-band photocathode RF electron gun (PCG) that serves as a backup to the RG. Three fast switching dipole magnets at the end of the linac (interleaving dipoles) direct the electron beam in and out of the PAR and into the Booster. Turning them off allows to bypass PAR and Booster and send electrons into the Linac Extension Area (LEA) tunnel which follows the APS linac. The existing beamline in the LEA is going to be repurposed for testing of small aperture apparatus and other beam physics experiments taking advantage of the PCG generated high brightness beam.

Typically, the beam generated from RG is used ~ 20 seconds every two minutes to support storage ring top-up operation. Fast switching (interleaving) between RG and PCG will allow operating LEA beamline during the rest of the two minutes. Because of the significantly different properties of beams produced by RG and PCG including beam energy, energy spread, bunch length, emittance and bunch charge, setting up one single lattice for the linac suitable for both beams is extremely challenging. In this paper we present a solution of this problem. Section 2 introduces optimum APS linac lattice for storage ring injection. Section 3 describes the optimum APS linac lattice for PCG and LEA experiments. A compromise interleaving lattice that conserves the high brightness of the PCG generated beam and maintains the high injection efficiency to PAR of the RG generated beam is described in Section 4.

APS LINAC LATTICE FOR INJECTION

Figure 1 shows the layout of the APS injector linac. It includes twelve S-band accelerating structures and an asymmetrical magnetic chicane containing four dipoles and two quadrupoles. One thermionic RF gun and one alpha magnet is used to inject a short train of electron micro

bunches into the linac. (An identical spare set is also installed). The PCG is installed at the front end of the linac and equipped with one additional accelerating structure. Note that alpha magnet and chicane are redundant for the operation with the RG generated beam and therefore, chicane is only dedicated to compress PCG generated beam. Table 1 shows the main beam parameters.

Satisfying the requirement for injection into the PAR, APS linear accelerator have been operated with minimal beam loss through linear accelerator after filtering low energy electrons in the alpha magnet. Figure 2 shows lattice functions for APS linear accelerator. In order to prevent beam loss, beta functions through linear accelerator are kept below 25 m. Two dispersion bumps (one in the chicane and one in the beam transport line) are present in the horizontal plane. Due to large dispersion function and beta function in the region before PAR, horizontal RMS beam size is 3.5 mm and horizontal full aperture is 16 mm in this region. However, careful trajectory control in this region is achieved to prevent beam loss. Lattice functions at the end point are matched with PAR injection point.

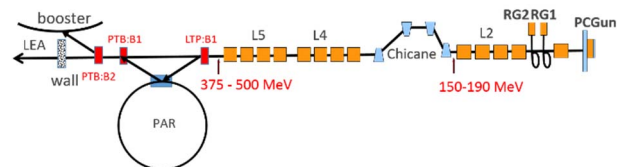


Figure 1: Layout of APS linear accelerator.

Table 1: Parameter for APS Linear Accelerator

Parameter	RG beam for Injection	PC beam for R&D
Energy	375 MeV	> 375 MeV
Emittance	15 um rad	1 um rad
Charge	1.6 nC	300 pC
Peak I	300 A	> 1 kA

APS LINAC LATTICE WITH PC GUN

The APS PC gun is a LCLS type gun [1] and is driven by a picosecond Nd:glass laser. The maximum field gradient in the gun cavity is 120 MV/m. High brightness with higher peak current (>1 kA) electron beam is produced by first increasing the electron beam energy to approximately 40-45 MeV in the first accelerating section (L1), giving energy chirp in the second accelerating section (L2) and finally rotating the particle distribution in the longitudinal phase space to reduce the bunch length via an asymmetric

* Work supported by the U.S. Department of Energy, Office of Science, under Contract No. DE-AC02-06CH11357.

[†] shin@aps.anl.gov

RF DESIGN AND SIMULATION OF A NON-PERIODIC LATTICE PHOTONIC BANDGAP (PBG) ACCELERATING STRUCTURE

N. Zhou^{#,1}, T. Wong, Illinois Institute of Technology, Chicago, USA
 A. Nassiri, Argonne National Laboratory, Lemont, USA
¹also at Argonne National Laboratory, Lemont, USA

Abstract

Photonic bandgap (PBG) structures (metallic and or dielectric) have been proposed for accelerators. These structures act like a filter, allowing RF fields at some frequencies to be transmitted through, while rejecting RF fields in some (unwanted) frequency range. Additionally PBG structures are used to support selective field patterns (modes) in a resonator or waveguide. In this paper, we will report on the RF design and simulation results of an X-band PBG structure, including lattice optimization, to improve RF performance.

INTRODUCTION

Photonic bandgap (PBG) structures for particle acceleration have the capability of single-mode confinement while damping unwanted higher order modes (HOMs). A PBG accelerating cavity employs a PBG structure in the form of a metallic or dielectric lattice with a single rod removed from the center. This periodic lattice prevents propagation of electromagnetic waves at certain frequencies through the lattice. A rejection band is created which serves to confine and localize the desired mode around the defect. The spacing of the array and the diameters of rods are adjusted so that the frequencies of unwanted higher-modes fall outside of the rejection band. In this manner, the wakefields are not confined at the center and may be extracted from the structure.

PBG RESONATOR

In any accelerating cavity, such as a pillbox cavity, there exists many HOMs, which can be excited by a beam passing through the cavity. The excited modes, and wakefields, induce unwanted transverse motion or energy spread in the beam and could produce beam emittance growth. The advantage of a PBG accelerating resonator is in the efficient and economical suppression of higher order modes wakefields [1]. This structure has a rejection band which confines and localizes the accelerating mode around the missing rod (defect) in a PBG resonator. Other frequencies will leak out to varying degrees through the PBG wall.

A simple PBG resonator schematic is shown in figure 1. It uses a two-dimensional triangular lattice where a single rod is withdrawn from the center of the lattice. A mode outside the rejection band is confined around the

defect by internal reflection from the PBG lattice. The electric field of the monopole mode for the PBG cavity is shown in figure 2.

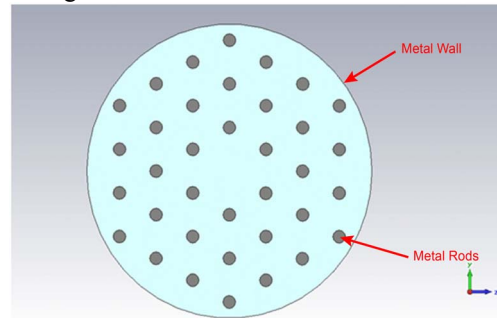


Figure 1: Strict two-dimensional triangular lattice in PBG resonator.

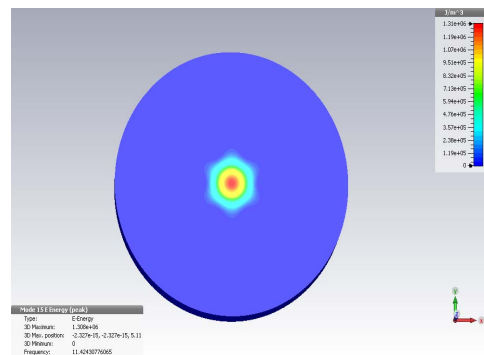


Figure 2: Electric field of the monopole mode in PBG resonator.

OPTIMIZED PBG RESONATOR

In a recent investigation [2] it was demonstrated that the possible advantages of arranging rods in according to various non-periodic geometries [3] in PBG resonators. It was shown that some rod arrangements which lacked lattice symmetry (but retained some rotational symmetry) dramatically reduced the radiative losses of the accelerating mode as compared to lattice arrangements of equal rod count [4]. In addition, simulation results indicated lower wakefields in these optimized structures [5].

The non-periodic lattice shown in figure 3 consists of three layers. On the first layer, all six metal rods are retained. For subsequent layers, radial lines are drawn from the origin through each of the rods, retained rods which are along those lines, removed the rest rods in lattice. In this case, the number of metal rods was reduced

*Work supported by the U.S. Department of Energy, Office of Science, under Contract No. DE-ACO2-O6CH11357

nzhou@aps.anl.gov

RESISTIVE WALL GROWTH RATE MEASUREMENTS IN THE FERMILAB RECYCLER

R. Ainsworth*, P. Adamson, A. Burov, I. Kourbanis, Fermilab[†], Batavia, IL USA

Abstract

Impedance could represent a limitation of running high intensity beams in the Fermilab recycler. With high intensity upgrades foreseen, it is important to quantify the impedance. To do this, studies have been performed measuring the growth rate of presumably the resistive wall instability. The growth rates at varying intensities and chromaticities are shown. The measured growth rates are compared to ones calculated with the resistive wall impedance.

INTRODUCTION

For high intensity operations in the Recycler, high chromaticity is used to help stabilise the beam against the resistive wall instability. Thus, it is important to understand the instability itself and the associated impedances.

The real part of the transverse impedance can be found by measuring the growth rate of the instability. In the case of an evenly filled ring and a coasting bunch [1], the real part of the impedance and the growth rate are related by the following

$$\frac{1}{\tau} = \frac{N_t r_0 c}{2\gamma T_0^2 \omega_\beta} \Re[Z_1^\perp(\omega_q)] \quad (1)$$

where $1/\tau$ is the growth rate, N_t is the total number of protons, c is the speed of light, γ is the relativistic factor, T_0 is the revolution time and $\omega_q = n\bar{\omega}_0 + \omega_\beta$ where $\omega_\beta = Q_v \bar{\omega}_0$ and $\bar{\omega}_0$ is the ideal angular revolution frequency. It should be noted that the measurements shown later will be for an unevenly filled ring distribution and thus there will be some differences which are discussed in the Theory section. The coasting beam approximation is justified when $\omega_q \ll 53$ MHz.

MEASUREMENTS

Four batches were injected in the Recycler with the dampers turned on and with chromaticity set to 0 in both planes. Each batch contained 81 53 MHz bunches and were separated by a gap equal to 3 bunches. The harmonic number for the Recycler is 588 meaning only 4/7 of the ring is occupied. After allowing the beam to circulate for 24250 turns, the dampers were turned off and the beam was allowed to blow up. Bpms were used to measure the growth. Data was measured at varying intensities using both 1 and 2 RF cavities.

In order to measure the growth rate, a fit is performed of the nature

$$A + Be^{\alpha x} \quad (2)$$

* rainswor@fnal.gov

[†] Operated by Fermi Research Alliance, LLC under Contract No. De-AC02-07CH11359 with the United States Department of Energy.

Table 1: Default Parameters for Recycler Measurements

Parameter	Unit	RR
Batches		4
Bunches	[bunches per batch]	81
N_b	[protons per bunch]	3×10^{10}
E	[GeV]	8.884
T_0	[μ s]	11.135
Q_h		25.4395
Q_v		24.3926
Q_s	1 RF cavity	0.0029
Q_s	2 RF cavities	0.0039
$\xi_{h,v}$		0 ± 0.5
$\epsilon_{n,95\%}$	[π mm mrad]	15
σ_t	[ns, 1 RF cavity]	1.7
$\sigma_{\delta p/p}$	[1 RF cavity]	3.3×10^{-4}

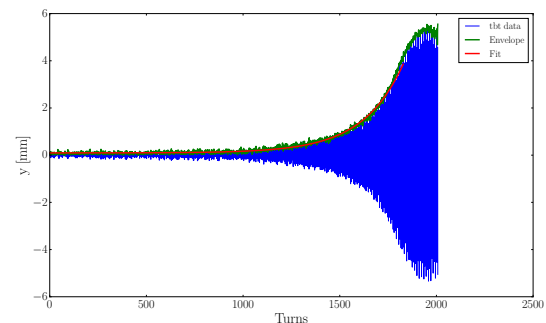


Figure 1: Turn by turn data taken showing a blow up due to the resistive wall instability. The green line shows envelope of the data and the red line shows a fit to this envelope.

where alpha is the growth rate in inverse turns. To convert to s^{-1} , one divides by the revolution time. In order to make the fit easier, the envelope is found first using a hilbert transform. An example envelope and fit is shown in Figure 1.

A linear function $y = ax + b$ was used to fit the dependence of the measured growth rate (y) on the bunch intensity (x). For 1 RF cavity, the results in the vertical plane show a dropoff in at high intensity. The beam was seen to have become unstable before the dampers were turned off. For the long-wave coupled-bunch instability sufficiently above its threshold, the growth rate has to be independent of RF voltage. Indeed, for the vertical degree of freedom the slopes dy/dx for 1 and 2 cavities agree within 4%; for the horizontal dimension, which measurement error bars are larger, this discrepancy is 15%. The constant term comes about from Landau damping resulting in a threshold intensity of the instability to occur.

INSTALLATION PROGRESS AT THE PIP-II INJECTOR TEST AT FERMILAB*

C. Baffes[†], M. Alvarez, R. Andrews, A. Chen, J. Czajkowski, P. Derwent, J. Edelen, B. Hanna, B. Hartsell, K. Kendziora, D. Mitchell, L. Prost, V. Scarpine, A. Shemyakin, J. Steimel, T. Zuchnik, Fermi National Accelerator Laboratory, Batavia IL, USA
A. Edelen, Colorado State University, Fort Collins CO, USA

Abstract

A CW-compatible, pulsed H⁺ superconducting linac “PIP-II” is being planned to upgrade Fermilab's injection complex. To validate the front-end concept, a test accelerator (The PIP-II Injector Test, formerly known as “PXIE”) is under construction. The warm part of this accelerator comprises a 10 mA DC, 30 keV H⁺ ion source, a 2 m-long Low Energy Beam Transport (LEBT), a 2.1 MeV Radio Frequency Quadrupole (RFQ) capable of operation in Continuous Wave (CW) mode, and a 10 m-long Medium Energy Beam Transport (MEBT). The paper will report on the installation of the RFQ and the first sections of the MEBT and related mechanical design considerations.

PIP-II CONTEXT

Proton Improvement Plan II (PIP-II) [1,2] is a planned upgrade to the Fermilab accelerators complex that will enable the complex to deliver >1 MW of proton beam power on target to the Long Baseline Neutrino Facility (LBNF) [3], and provide a platform for future upgrades to multi-MW/high duty-factor operations. The existing normal-conducting linac will be replaced with a new superconducting RF linac injecting into the Booster Ring at 800 MeV. The PIP-II Injector Test (here abbreviated as PI-Test) [4] is a prototype of the front end of PIP-II, including the room-temperature accelerating section, a Half-Wave Resonator Cryomodule (HWR) [5] and a Single Spoke Resonator Cryomodule (SSR1). PI-Test is designed to accelerate 2 mA of CW beam to 25 MeV.

PI-TEST STATUS AND PLANS

As of this writing, the ion source, LEBT [6] and RFQ have been fully installed. The RFQ has been conditioned with CW RF up to 100 kW input power, and commissioned with pulsed beam up to a 5 mA, 5 ms pulse at 10 Hz [7]. The MEBT [8] is evolving in stages designed to first verify RFQ requirements. The first stage (Fig. 1) included permanent components (two doublet/corrector magnet packages, designed and fabricated by Bhabha Atomic Research Centre (BARC), beam scrapers, and a bunching cavity), and instrumentation to characterize the beam coming out of the RFQ. Instrumentation included toroids for transmission measurements, a time-of-flight movable beam position monitor (TOF) to determine the beam energy, and a fast Faraday cup (FFC) for longitudinal bunch structure measurement. The transmission of

the RFQ was verified to be ~98% and the energy to be 2.11 MeV ± 1% [7], both within specification.

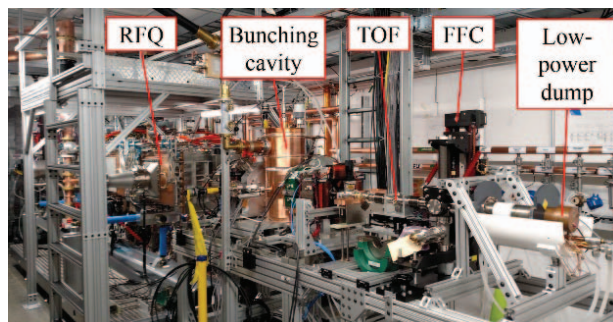


Figure 1: RFQ exit and MEBT in longitudinal diagnostic configuration for initial beam commissioning of RFQ.

During a shutdown in September 2016 the MEBT was reconfigured to accommodate CW beam from the RFQ. A prototype absorber [9] was installed to investigate the potential for blistering from H⁺ beam, and a long drift space and high-power beam dump [10] were installed to allow working with current up to 10 mA CW (Figs. 2, 4) and large beam size at the dump. As of this writing, this configuration is being commissioned in pulsed mode.

Radiation from 2.1 MeV H⁺ Beam

Measurable radiation, dominated by high energy photons (γ), has been observed from the 2.1 MeV pulsed beam incident on a Faraday cup made of copper, scrapers made of molybdenum alloy TZM and the nickel dump, and interpreted via simulation in the MARS program. Scaling these simulations/measurements up to 100% duty factor, predicted radiation levels in some areas of the enclosure are too high to permit beam-on access (e.g. ~100 mrem/hr adjacent to the dump). As a result, personnel interlocks are required for work with CW beam.

Next Steps for the MEBT

After demonstration of CW beam operation, the MEBT will be reconfigured to accommodate an Allison-type [11] emittance scanner. After measuring the transverse emittance, the MEBT will be extended to include 4 triplets (provided by BARC) and prototypes of the fast kickers designed to provide bunch-by-bunch chopping at 162.5 MHz. The final stage of the MEBT build will incorporate the Ultra-High Vacuum (UHV) low-particulate section that interfaces to the HWR cryomodule.

* This work was supported by the DOE contract No. DEAC02-07CH11359 to the Fermi Research Alliance LLC.

[†] cbaffes@fnal.gov

FERMILAB RECYCLER COLLIMATION SYSTEM DESIGN

B. C. Brown*, P. Adamson, R. Ainsworth, D. Capista, K. Hazelwood, I. Kourbanis, N. V. Mokhov, D. K. Morris, M. Murphy, V. Sidorov, E. Stern, I. Tropin, M-J. Yang, Fermilab[†], Batavia, USA

Abstract

To provide 700 kW proton beams for neutrino production in the NuMI facility, we employ slip stacking in the Recycler with transfer to the Main Injector for recapture and acceleration. Slip stacking with 12 Booster batches per 1.33 sec cycle of the Main Injector has been implemented and briefly tested while extensive operation with 8 batches and 10 batches per MI cycle has been demonstrated. Operation in this mode since 2013 shows that loss localization is an essential component for long term operation. Beam loss in the Recycler will be localized in a collimation region with design capability for absorbing up to 2 kW of lost protons in a pair of 20-Ton collimators (absorbers). This system will employ a two stage collimation with a thin molybdenum scattering foil to define the bottom edge of both the injected and decelerated-for-slipping beams. Optimization and engineering design of the collimator components and radiation shielding are based on comprehensive MARS15 simulations predicting high collimation efficiency as well as tolerable levels of prompt and residual radiation. The system installation during the Fermilab 2016 facility shutdown will permit commissioning in the subsequent operating period.

INTRODUCTION

The flagship physics program at Fermilab for the next two decades requires a robust high energy, high intensity proton source [1]. Slip stacking in the Recycler Ring [2] is a central part of that plan. The similar lattices and apertures of the Recycler compared with the Main Injector suggested that similar per cycle beam intensities could be supported. The increase in delivered proton beam power at 120 GeV is largely due to a faster repetition rate due to using the Recycler for beam accumulation while the acceleration of intense proton beams occurs in the Main Injector. In Ref. [2] one finds a description of several limitations which are being addressed, this paper will focus on the need to provide beam loss localization (collimation) to limit activation and radiation damage in the Recycler Ring.

The beam emittance available from the Fermilab Booster is large enough to produce losses due to both longitudinal and transverse emittance tails when used for slip stacking. Slip stacking in the Recycler is accomplished by stacking in the Recycler Ring but transferring the aligned bunches to the Main Injector for capture in the high voltage RF. This allows the use of the Main Injector collimation system [3] to continue to protect from the uncaptured longitudinal tails. The vertical design aperture of the Recycler beam pipe is

22 mm (half height) whereas the Main Injector beam pipe design provides 23.9 mm (half height). We have shown [4] that losses in the Main Injector were seen when this design aperture was reduced by installation issues. Many of the observed loss locations are at vertical β_{max} when the vertical aperture is reduced from the design value by installation imperfections. Additional activation locations are found at the transfer points where Lambertson magnets limit both the horizontal and vertical aperture.

The transverse beam loss in the Recycler has not been resolved into components due to the tails on the injected beam or tails due to emittance growth. Construction of a collimation system is proceeding without a such understanding. We will construct a collimation system which defines a vertical beam boundary with a primary collimator which scatters beam into the limited available vertical aperture in the local region. Studies with SYNERGIA confirm that horizontal to vertical emittance coupling will allow this to control horizontal tails.

TUNNEL LOCATION

The nominal Recycler beam height is 84" (7' or 2.13 m) above the floor of the Main Injector tunnel. Most of the tunnel is constructed with 10' wide by 8' high concrete hoops. For beam transport to the Tevatron this 8' ceiling height transitioned to 9' and then 10' for the proton (P150 line at 520) and antiproton (A150 at 620) beam transfer tunnel sections. For the Main Injector secondary collimators, we found that 23" (584 mm) of steel was suitable to contain the radiation showers from 8 GeV proton loss. With only 12" available with 8' ceilings we looked around. The 9' ceilings might be marginally usable but in the MI520 region there is too much else involved in the Recycler (P150 kickers and electrostatic septa in the Main Injector and the transfer line from RR to P150). At MI620 we have lots of instrumentation and the 9' ceiling ends too soon to be helpful for most purposes. The 520 region has two accelerators and two transfer lines while details of the Recycler lattice add complications. At the 613 cell boundary (high vertical beta) between the G613A and G613B gradient magnets there is a 9' ceiling with the transition to 10' ceiling above the G613B gradient magnet. We have placed a primary collimator at 613 and two secondary collimators in this region as a Phase I installation in the 2016 Facility Shutdown with consideration for two additional secondary collimators for a Phase II installation later.

TWO STAGE COLLIMATION

We employ a 0.125 mm molybdenum (Mo) TZM foil to define the lower edge of both the injected beam and the beam decelerated for slipping. Since we use a location with

4: Hadron Accelerators

T19 - Collimation

* bcbrown@fnal.gov

[†] Operated by Fermi Research Alliance, LLC under Contract No. DE-AC02-07CH11359 with the United States Department of Energy.

ON THE POSSIBILITY OF USING NONLINEAR ELEMENTS FOR LANDAU DAMPING IN HIGH-INTENSITY BEAMS *

Y. Alexahin, E. Gianfelice-Wendt[†], V. Lebedev, A. Valishev, Fermilab, Batavia, IL 60510, USA

Abstract

Direct space-charge force shifts incoherent tunes downwards from the coherent ones breaking the Landau mechanism of coherent oscillations damping at high beam intensity. To restore it nonlinear elements can be employed which move back tunes of large amplitude particles. In the present report we consider the possibility of creating a “nonlinear integrable optics” insertion in the Fermilab Recycler to host either octupoles or hollow electron lens for this purpose. For comparison we also consider the classic scheme with distributed octupole families. It is shown that for the Proton Improvement Plan II (PIP II) parameters the required nonlinear tune shift can be created without destroying the dynamic aperture.

INTRODUCTION

The Fermilab Recycler [1] is a 3.3 km long 8.9 GeV proton storage ring originally constructed to accumulate antiprotons for Tevatron Run II and based on permanent magnets. For supplying megawatt beams for the Long-Baseline Neutrino Facility, PIP II foresees the replacement of the 400 MeV Linac by a new 800 MeV superconducting one, while the old rings Booster, Main Injector and Recycler, are expected to undergo only minor improvements.

With PIP II parameters [2], the Recycler is expected to store at least a factor 1.5 more protons wrt current operation increasing the incoherent space charge tune shift from -0.06 to -0.09 at 1σ . Currently coupled bunch instabilities in the Recycler are controlled by dampers. However their use during slip stacking is problematic and new dampers are now under consideration.

In general, there are two contributions to Landau damping for bunched beams: the intrinsic one due to the space charge tune spread, and the external one due to machine nonlinear elements. For the PIP II Recycler with its very high space charge parameter, $\Delta Q_{sc}/Q_s$ [3], the intrinsic damping is too weak to be useful and external nonlinear lenses are needed to provide stabilization. However if the required non-linearities are large they may compromise the beam Dynamical Aperture (DA).

For the Recycler it has been evaluated that a tune shift of $\approx 1.4 \times 10^{-3}$ at 1σ is needed in presence of a damper and $\approx 5.6 \times 10^{-3}$ without it [4].

We have studied the possibility of inserting octupole magnets into the existing Recycler ring as well as the possibility of modifying the lattice for a “nonlinear integrable

optics” [5] insertion to host either octupoles or a hollow electron lens.

DISTRIBUTED OCTUPOLES

The detuning due to an octupole of integrated strength $O_3 = \frac{\partial^3 B_y}{\partial x^3} \ell / B\rho$ is

$$\Delta Q_{x,y} = \frac{O_3}{16\pi} (\beta_{x,y}^2 J_{x,y} - 2\beta_x \beta_y J_{y,x})$$

$J_{x,y}$ being the action ($2J_{x,y} = a_{x,y}$, with $a_{x,y}$ Courant-Snyder invariant). To minimize the 2nd order chromaticity and the cross-term detuning which may limit the DA the octupoles should be located where $D_x=0$ and $\beta_z^2 \gg \beta_x \beta_y$ ($z=x, y$).

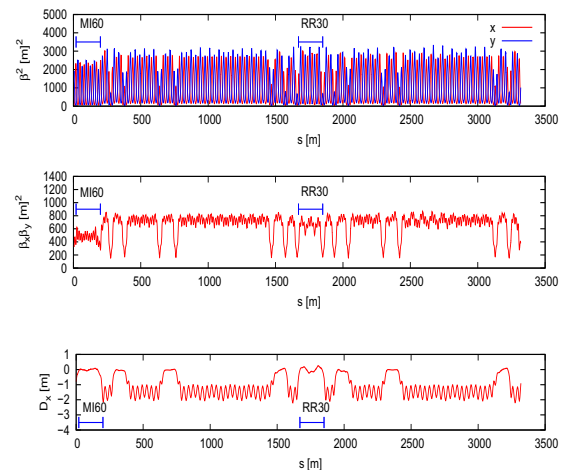


Figure 1: Recycler optics.

For minimizing the direct impact of the octupoles on DA a scheme where the phase advance between consecutive octupoles satisfies the condition $\Delta\mu_z = k\pi/N_{oct}$ ($z=x, y$) with $k=1, 2, \dots, N_{oct} - 1$ and $\Delta\mu_z \neq \pi/2$, has been considered. The only resonance excited in this case by normal octupoles is the 4th order $2Q_x - 2Q_y = \text{integer}$ one. Two families of 5 octupoles each were located in the straight section MI60 (see Fig. 1). The 9 MI60 tuning quadrupoles and the quadrupoles QD531, QF532, QF610 and QD611, assumed to be tunable, were used to move $\Delta\mu_{x,y}/2\pi$ between octupoles from 0.26 to 0.3 keeping the optics unperturbed outside. The RR30 straight section tuning quadrupoles were used for optimizing the betatron tunes and 4 quadrupoles were added for re-matching the optics. With octupole settings for a tune shifts of about 0.005 at 1σ , the on-energy DA computed with 1000 turns tracking and ignoring synchrotron motion is only about 3σ for 2.5×10^{-6} m rms normalized emittance,

* Work supported by Fermi Research Alliance LLC. Under DE-AC02-07CH11359 with the U.S. DOE

[†] eliana@fnal.gov

EXPERIMENTAL STUDIES OF BEAM COLLIMATION SYSTEM IN THE FERMILAB BOOSTER*

V. Kapin[#], S. Chaurize, N. Mokhov, W. Pellico, M. Slabaugh, T. Sullivan, R.J. Tesarek, K. Triplett,
Fermilab, Batavia, IL 60510, USA

Abstract

A two-stage collimation (2SC) system was installed in Fermilab Booster around 2004 and consists of 2 primary collimators (PrC), one for each of the horizontal and vertical planes and 3 secondary collimators (SC) each capable of acting in both planes. Presently, only SC are used as the single-stage collimation (1SC). Part of the Fermilab Proton Improvement Plan (PIP) includes a task to test 2SC for Booster operations. In this paper we describe preparatory steps to fix SC motion issues and installation of a 380 μ m thick aluminum foil PrC and post-processing software for beam orbit and beam loss measurements. The initial experimental results for 2SC in the vertical plane are also presented. The tuning of 2SC system was performed using fast loss monitors allowing much higher time-resolution than existing BLMs. Analysis of losses and beam transmission efficiency allow for the comparison of 1SC and 2SC schemes.

INTRODUCTION

The Fermilab Booster [1] is a 15Hz rapid cycling synchrotron which accelerates protons from 400 MeV to 8 GeV with the beam transmission efficiency of about 90%. Booster is made up primarily of combined function magnets and RF cavities, and it is divided into 24 equal-length periods. Approximately 10% of protons are lost during accelerating cycle; the majority of the protons are lost at the beginning of the cycle near injection energy.

The Proton Improvement Plan (PIP) [2], established in 2012, is aimed to increase the beam throughput while maintaining the present residual activation levels. One of 22 PIP tasks is a possible upgrade of the Booster collimation system installed in 2004 at its periods 5, 6 and 7.

The booster collimation system was designed as a two-stage collimation (2SC) system. However, this design was incompatible with frequent radial orbit variations inherent in the RF cogging scheme used in Booster until 2015. Therefore, the collimation system was used in a single stage (1SC) mode, while still ensuring a significant reduction in Booster activation.

Implementation of new magnetic cogging in 2015 [3] - keeps the beam on a central orbit and creates conditions to use 2SC system. The principle aim of the 2SC system is the reduction of uncontrolled beam losses generated during multiturn injection, RF capture, creation of the extraction notch and enabling the control feedback. In this paper, the collimation effectiveness of the 2SC mode for the vertical plane is measured and compared with that of

the existing 1SC mode. The sum of all 64 BLMs in the Booster is used as a figure of merit in this evaluation.

BOOSTER COLLIMATION SCHEME

Each Booster period contains two horizontally focusing magnets (F) and two horizontally defocusing magnets (D) along with a 6.0-meter "long straight" section, a 1.2-meter "short straight" section, and a 0.5-meter short drift spaces between F and D magnets. The 2SC system was installed in the unused straight sections of periods 5, 6, and 7.

Figure 1 shows layout of the 2SC system, which consists of horizontal (H-prim) and vertical (V-prim) primary collimators located in the short drift spaces nearby of Short-5 and three identical 1.2 m-long secondary collimators (or absorbers) 6A, 6B, and 7A located in Long-6 and Long-7. Near the primary and secondary collimators beam position monitors (BPM), beam loss monitors (BLM) and fast loss monitors (FLM) [4,5] are used to evaluate the beam position, radiation rate and when the collimators intercept the beam tails.

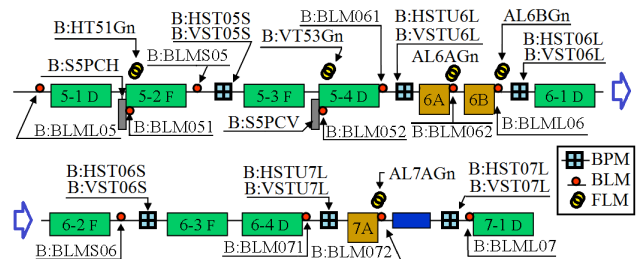


Figure 1: Layout of 2SC system in periods 5,6 and 7.

The primary collimators are movable thin scattering foils. The absorbers are movable steel cubes with square beam apertures. According to the 2004 original 2SC design [6,7] protons within 3σ are considered the beam core and the normalized 95%-emittance equal to 12π mm \cdot mrad. For collimation in the vertical plane, collimators V-prim, 6B and 7A are used. V-prim is placed at the lower edge of the beam core. The jaws of the 6B and 7A collimators are positioned with a 2mm offset from the beam core, while the jaw of collimator 6B is located below the beam and the jaw of collimator 7A is located above the beam.

In 2015, improvements were made to realize the original design of the 2SC. These improvements include: design and installation of 0.380 μ m thick aluminum primary collimators [8,9] and improvements in the accuracy and reliability of the absorber motion.

* Operated by Fermi Research Alliance, LLC under Contract No. DE-AC02-07CH11359 with the United States Department of Energy.

[#] kapin@fnal.gov

NUMERICAL SIMULATIONS OF COLLIMATION EFFICIENCY FOR BEAM COLLIMATION SYSTEM IN THE FERMILAB BOOSTER*

V.V. Kapin[#], V.A. Lebedev, N.V. Mokhov, S.I. Striganov, I.S. Tropin,
Fermilab, Batavia, IL 60510, USA

Abstract

A two-stage beam collimation (2SC) system has been installed in the Fermilab Booster more than 10 years ago. It consists of two primary collimators (horizontal and vertical) and three 1.2m-long secondary collimators. The two-stage collimation has never been used in Booster operations due to uncontrolled beam orbit variations produced by radial cogging (it is required for beam accumulation in Recycler). Instead, only secondary collimators were used in the single-stage collimation (1SC). Recently introduced magnetic cogging resulted in orbit stabilization in the course of almost entire accelerating cycle and created a possibility for the 2SC. In this paper, the 2SC performance is evaluated and compared the 1SC. Several parameters characterizing collimation efficiency are calculated in order to compare both schemes. A combination of the MADX and MARS15 codes is used for proton tracking in the Booster with their scattering in collimators being accounted. The dependence of efficiency on the primary collimators foil thickness is presented. The efficiency dependence on the proton energy is also obtained for the optimal foil. The feasibility of the 2SC scheme for the Booster is discussed.

INTRODUCTION

The Fermilab Booster [1] is a 15Hz rapid cycling synchrotron accelerating protons from 400 MeV to 8 GeV with accelerating efficiency about 90%. Booster optics is based on combined function dipoles and includes 24 equal-length periods. Totally, about 10% of protons are lost during 20,000-turn accelerating cycle. Major fraction of loss happens at the beginning of the accelerating cycle.

The Proton Improvement Plan (PIP) [2] established in 2012 is aimed to double the beam throughput, while maintaining the present residual activation levels. One of many other PIP tasks is a possible upgrade of the Booster collimation system installed in 2004. It is located in the periods 5, 6 and 7.

The booster collimation system has been designed as a two-stage collimation (2SC) system. However, this design was not compatible with uncontrolled radial orbit variations inherent to the radial cogging used in Booster till 2015. Therefore, the collimation system was used in a single stage (1SC) mode, which was still ensuring a significant reduction in Booster activation.

Implementation of new magnetic cogging in 2015 [3] resulted in a stable beam orbit and created conditions for implementation of the 2SC aimed to reduce uncontrolled

beam losses mostly generated shortly after injection. In this paper, the collimation efficiency of the 2SC in the vertical plane is evaluated and compared with that of the existing 1SC.

BOOSTER COLLIMATION SYSTEM

Each Booster period contains two horizontally focusing (F) and two horizontally defocusing magnets (D) separated by two straight lines (6.0-meter "long straight" and a 1.2-meter "short straight") and two 0.5-meter short drifts separating F and D magnets. The 2SC system has been installed in the straight sections of periods 5, 6, and 7. Figure 1 shows layout of the 2SC system. It consists of horizontal (H-prim) and vertical (V-prim) primary collimators located in the short drifts nearby of Short-5 and three identical 1.2 m-long secondary collimators (or absorbers) 6A, 6B, and 7A located in Long-6 and Long-7. Each absorber is capable to limit aperture in both planes.

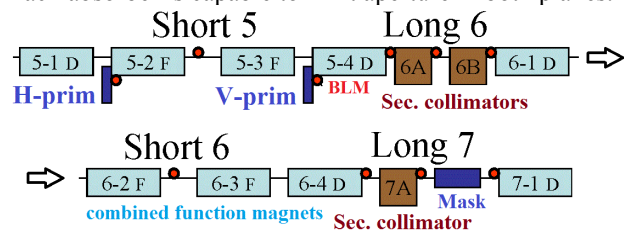


Figure 1: Layout of 2SC system in periods 5, 6 and 7.

The primary collimators are movable thin scattering foils. The absorbers are movable girders with square cross-section with square apertures in the center for beam passage. The 2004 original 2SC design [4,5] considered the beam core to be equal 3σ for normalized 95%-emittances of 12π mm-mrad. For collimation in the vertical plane, collimators V-prim, 6A and 7A are used. V-prim is placed at the lower edge of the 3σ -beam core. The jaws of the 6B and 7A collimators are positioned with a 2mm offset from the 3σ -beam core, while the jaw of collimator 6B is located below the beam and the jaw of collimator 7A is located above the beam.

The purpose of this 2SC is to localize proton losses inside the secondary collimators, so that to reduce irradiation of the rest of the machine to an acceptable level.

SIMULATION APPROACH

The 2004 original 2SC had been designed with the STRUCT code [6], which simulated a multi-turn tracking of halo protons in the Booster lattice with their scattering on collimators. Protons lost on the machine components were stored to the files for the next step of calculations with the MARS code [7], which performed full-scale

* Operated by Fermi Research Alliance, LLC under Contract No. DE-AC02-07CH11359 with the United States Department of Energy.

[#] kapin@fnal.gov

NEUTRINOS FROM A PION BEAM LINE: nuPIL *

A. Liu[†], A. Bross, Fermi National Accelerator Laboratory, Batavia, USA

J-B. Lagrange¹, J. Pasternak, Imperial College, London, UK

¹also at Fermi National Accelerator Laboratory, Batavia, USA

Abstract

The Fermilab Deep Underground Neutrino Experiment (DUNE) was proposed to determine the neutrino mass hierarchy and demonstrate leptonic CP violation. The current design of the facility that produces the neutrino beam (LBNF) uses magnetic horns to collect pions and a decay pipe to allow them to decay. In this paper, a design of a possible alternative for the conventional neutrino beam in LBNF is presented. In this design, an FFAG magnet beam line is used to collect the pions from the downstream face of a horn, bend them by ~ 5.8 degrees and then transport them in either a LBNF-like decay pipe, or a straight FODO beam line where they decay to produce neutrinos. Using neutrinos from this Pion beam Line (nuPIL) provides flavor-pure neutrino beams that can be well understood by implementing standard beam measurement technology. The neutrino flux and the resulting δ_{CP} sensitivity from the current version of nuPIL design are also presented in the paper.

INTRODUCTION

The Deep Underground Neutrino Experiment (DUNE) aims at studying long-baseline neutrino oscillation by utilizing a wide-band neutrino beam from Fermilab. In the current design, DUNE will be supported by the Fermilab Long-Baseline Neutrino Facility (LBNF), which is required to provide a 1.2 MW proton beam power, upgradable to multi-megawatt power, and detectors for various physics searches. DUNE is required to have sensitivity to CP violation of better than 3σ over more than 75% of the CP-violating phase δ_{CP} [1].

However, there are many challenges in producing a neutrino beam following the LBNF design. These include the uncertainty in secondary particle production rate and dynamics, target and horn stability, and primary proton beam targeting stability. Many of these challenges can be handled by using a magnetic beam line to transport only the secondary pions of interest to a neutrino production straight.

The neutrinos from a Pion beam Line (nuPIL) concept, as a substitution for a conventional horn and decay pipe neutrino facility, works to provide a flavor-pure neutrino beam with precisely measurable flux. The nuPIL concept can avoid the difficulties caused by dissipating large amounts of radiation underground by using a bend to collect and transport only those particles within a desired momentum

range. Uninteracted protons and high-energy secondaries are sent to an absorber located at grade.

Two types of beamlines were investigated and considered for nuPIL, a pure FODO lattice [2] and then an FFAG + FODO (hybrid) lattice. A pure FFAG lattice design is under way, but could have many challenges, such as the neutrino flux is unavoidably reduced when produced in an FFAG straight because of the “scallop angle” of the cell structure. In this paper, the present version of a hybrid lattice for nuPIL is presented. The optics design, tracking result, neutrino flux from the beamline, and the corresponding sensitivity to CP violation are presented.

OPTICS DESIGN OF THE FFAG STEERING BEND SECTION

In the current LBNF design, the neutrino beam is directed toward the Far Detector (FD) at the Sanford Underground Research Facility (SURF) by steering the primary high energy proton beam upwards on a hill, and then steering downwards at a 5.8° pitch angle with respect to the surface so that the neutrino beam points towards SURF. The target is bombarded by the proton beam, thus produce secondary pions that decay in a pipe. These pion decays produce a neutrino beam that points to the FD.

In order to prevent unwanted power from going deep underground, it is natural to bend the secondary pions to form the required 5.8° pitch angle after they are generated. The dipole field in the FFAG cells provides this pitch angle and allows one to keep either π^+ or π^- while pions with the opposite sign can be either absorbed, or potentially used by a short-baseline neutrino program, such as nuSTORM [3, 4]. The use of scaling FFAG magnets [5, 6] could increase the momentum acceptance of the pion beamline, therefore expand the neutrino energy spectrum, which is useful for the δ_δ studies [7]. Meanwhile, the Twiss β function in the steering bend section should be kept as small as possible to ensure good transmission. FFAG lattices have a large transverse acceptance, and thus are ideal for the pion beam after the collection horn, which has a large RMS emittance. The steering bend section is composed of a dispersion creator section to bring up the dispersion from 0 at the end face of the horn, followed by a dispersion suppressor to slightly reduce the dispersion for matching to a FODO straight. The optics of the FFAG section is shown in Figure 1.

HORN OPTIMIZATION BASED ON THE FFAG ACCEPTANCE

nuPIL uses a single horn with a 4 interaction lengths carbon target to produce and collect secondary pions. The

* Work supported by Fermilab, Operated by Fermi Research Alliance, LLC under Contract No. DE-AC02-07CH11359 with the United States Department of Energy.

[†] aoliu@fnal.gov

INSTALLATION AND COMMISSIONING OF AN ULTRAFAST ELECTRON DIFFRACTION FACILITY AS PART OF THE ATF-II UPGRADE*

M. A. Palmer[†], M. Babzien, M. Fedurin, C. M. Folz, M. Fulkerson, K. Kusche, J. Li, R. Malone, T. Shaftan, J. Skaritka, L. Snyderstrup, C. Swinson, F. J. Willeke
Brookhaven National Laboratory, Upton, NY 11973, USA

Abstract

The Accelerator Test Facility (ATF) at Brookhaven National Laboratory (BNL) is presently carrying out an upgrade, ATF-II, which will provide significantly expanded experimental space and capabilities for its users. One of the new capabilities being integrated into the ATF-II program is an Ultrafast Electron Diffraction (UED) beam line, which was originally deployed in the BNL Source Development Laboratory. Inclusion of the UED in the ATF-II research portfolio will enable ongoing development and extension of the UED capabilities for use in materials research. We discuss the design, installation and commissioning of the UED beam line at ATF-II as well as plans for future upgrades.

INTRODUCTION

The Accelerator Test Facility at Brookhaven National Laboratory (BNL) is a US Department of Energy Office of Science National User Facility supported by the Accelerator Stewardship Program (ASP). The ASP mission is to support fundamental accelerator science and technology R&D and disseminate accelerator knowledge and training. In its role of support the ASP, the ATF provides its users with access to a high-brightness 80-MeV electron beam as well as a Terawatt-class picosecond CO₂ laser, which can be used individually or synchronized with the electron beam for combined experimental operation. The ATF-II upgrade of the facility aims to provide expanded capabilities for the accelerator research community [1]. One of the opportunities afforded by this upgrade has been to expand the ATF electron beam portfolio to include an Ultrafast Electron Diffraction (UED) facility, which was originally developed as part of the research effort at the BNL Source Development Laboratory [2]. By integrating this facility with the ATF-II complex in BNL Building 912, accelerator researchers will be able to continue to explore ways to advance and optimize accelerator technology for UED, and also the closely associated Ultrafast Electron Microscopy (UEM) applications for the materials science research community.

Fast diffraction measurements represent a key probe of structural dynamics in a range of materials. At present ultrafast experiments based on FEL x-ray sources and electron beams enable us to probe the relevant physical processes [3-4]. An advantage of electron beams is their large interaction cross-section. However, there are challenges associated with obtaining short pulses of sufficient charge to probe processes on femtosecond timescales in a single

pulse due to the space charge effects which limit the minimum bunch lengths that can be obtained [5]. A key thrust of the planned UED research program will be to demonstrate techniques which optimize the time resolution of the device, targeting femtosecond-scale performance.

THE UPDATED UED FACILITY AT BROOKHAVEN

A formal decision to incorporate the UED facility into the ATF-II was made in November 2015. At that point, an aggressive implementation plan was put into effect which was executed with the following schedule:

- December 2015: Facility layout, as shown in Figure 1, was developed and approved. The detailed beam line layout is shown in Figure 2.
- January-February 2016: The accelerator and photocathode laser systems were deployed in BNL Building 912.
- March 2016: The RF system was commissioned and conditioned to full power. The control system was also commissioned.

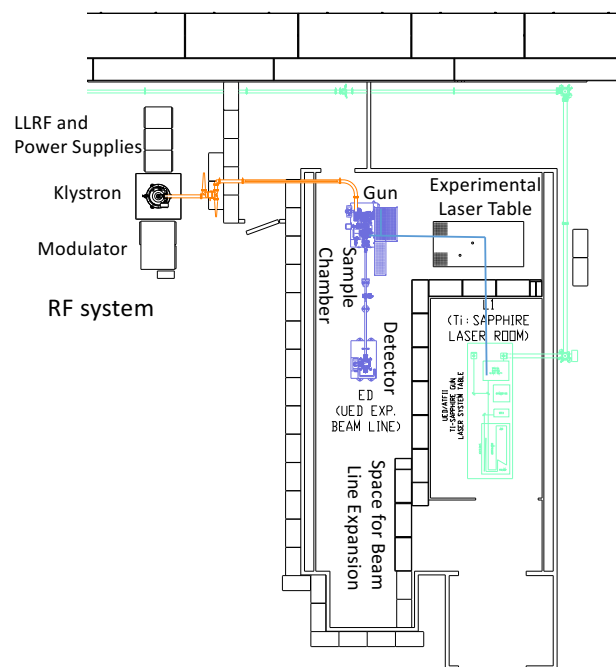


Figure 1: Layout of the UED Facility, which is housed in BNL Building 912 as part of the ATF-II expansion. A key feature is the space for beam line expansion which will enable future R&D work to optimize the parameters provided by the UED apparatus.

* Work supported by the US DOE under contract DE-SC0012704.

[†] mpalmer@bnl.gov

FERMILAB ACCELERATOR R&D PROGRAM TOWARDS INTENSITY FRONTIER ACCELERATORS : STATUS AND PROGRESS*

V. Shiltsev[#], Fermilab, Batavia, IL 60510, USA

Abstract

The 2014 P5 report indicated the accelerator-based neutrino and rare decay physics research as a centrepiece of the US domestic HEP program at Fermilab. Operation, upgrade and development of the accelerators for the near-term and longer-term particle physics program at the Intensity Frontier face formidable challenges. Here we discuss key elements of the accelerator physics and technology R&D program toward future multi-MW proton accelerators and present its status and progress.

INTENSITY FRONTIER ACCELERATORS

The 2014 Particle Physics Project Prioritization Panel (P5) report [1] identified the top priority of the domestic intensity frontier high-energy physics for the next 20-30 years to be a high energy neutrino program to determine the mass hierarchy and measure CP violation, based on the Fermilab accelerator complex which needs to be upgraded for increased proton intensity. To this end, a new beam line - the Long Baseline Neutrino Facility (LBNF) – and new experiment - the Deep Underground Neutrino Experiment (DUNE), located in the Sanford Underground Research Facility (SURF) - are being planned [2].

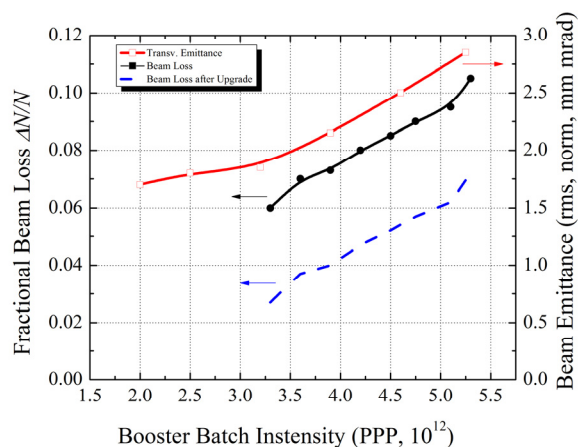


Figure 1: Fermilab Booster performance vs intensity: beam emittance (red line, right axis) and fractional beam loss now (black, left axis) and after anticipated upgrades (blue). Courtesy W.Pellico.

The P5 physics goals require about 900 kt·MW·years of the total exposure (product of the neutrino detector mass, average proton beam power on the neutrino target and data taking period) and that can be achieved assuming

*Fermi Research Alliance, LLC operates Fermilab under contract No. DE-AC02-07CH11359 with the U.S. Department of Energy
[#]shiltsev@fnal.gov

a 40 kton Liquid Argon detector and accelerator operation with the eventual multi MW beam power. At present, after commissioning of the 6+6 batch slip-stacking in the Recycler and reduction the Main Injector cycle time to 1.33s from 2.2s during the MINOS/Collider Run II era. Due to these improvements, in 2016 the Main Injector achieved world-record 615 kW average proton beam power over one hour to the NuMI beam line. On that way, the operations team increased number of batches slip-stacked in Recycler in steps (just 6 batches in late 2014, then 2+6, 4+6 and, finally, 6+6 batches in mid-2016). At each step, the increase intensity was followed by tuning for efficiency and minimization of losses. Finally, the peak power of 700 kW for one minute was demonstrated in June 2016 [3]. Sustainable routine operation at that level is expected in 2017 after an upgrade of the Recycler beam collimation system which is going to take place during the Summer 2016 shutdown.

ONGOING STUDIES AND PIP-II

There are a number of ongoing experimental beam studies, theoretical investigations, modelling and simulation efforts dedicated to understanding beam dynamics issues with high intensity beams in the existing accelerators. Those include studies of the space-charge effects in the Booster [4] – see Fig.1, theory and experiments on the coherent beam stability in the Booster, Recycler and Main Injector [5-9], electron-cloud studies which include *in situ* SEY measurements, micro-wave measurements in the Main Injector and development of the most effective vacuum pipe coating and scrubbing methods [10]; evaluation need of a transition crossing optimization in the Booster and Main Injector; investigations of beam losses and efficiency of collimation systems employed in all accelerators [11, 12].

We advance our simulation and modelling capabilities for high-intensity beams by development of a flexible beam dynamics framework on base of SYNERGIA [13] with fully 3D PIC capabilities which include space-charge and impedance, both single and multi-bunch effects, single-particle physics with full dynamics and which could run on desktops, clusters and supercomputers. Continuous development of the MARS-based energy deposition modelling tools [14] includes updates related to recent developments in nuclear interaction models; implementation of polarized particle transport and interaction, developments of radiation damage models and transfer matrix algorithms in accelerator material-free regions; and further enhancement of the geometry modules.

Numerous beam studies and upgrades are taking place in the Booster as part of the *Proton Improvement Plan (PIP)* [15]. They include studies of advanced injection schemes, efficient coggling, collimation efficiency, laser

FERMILAB MUON CAMPUS AS A POTENTIAL PROBE TO STUDY NEUTRINO PHYSICS*

R. Miceli[#], Stony Brook University, Stony Brook, NY, USA

Z. Pavlovic and D. Stratakis, Fermi National Accelerator Laboratory, Batavia, IL, USA

J. Grange, Argonne National Laboratory, Argonne, IL, USA

J. Zennaro, University of Chicago, Chicago, IL, USA

S. Kim, Cornell University, Ithaca, NY, USA

Abstract

In the next decade the Fermilab Muon Campus will host two world class experiments dedicated to the search for signals of new physics: The g-2 Experiment will determine with unprecedented precision the anomalous magnetic moment of the muon and the Mu2e experiment will improve by four orders of magnitude the sensitivity on the search for the as-yet unobserved charged lepton flavor violation process of a neutrinoless conversion of a muon to an electron. In this paper, we will discuss a possibility for extending the Muon Campus capabilities for neutrino research. In particular, with the aid of numerical simulations, we estimate the number of produced neutrinos at various locations along the beamlines as well as at the Short-Baseline Near Detector, which sits inline with a straight section of the Delivery Ring. Finally, we discuss items for future study.

INTRODUCTION

One of the recommendations adopted by the Office of Science from the 2014 HEPAP P5 report is the completion of the g-2 [1] and Mu2e [2] projects in all of the funding scenarios under consideration. Consequently, the construction and operation of a Muon Campus facility to support these experiments is a significant priority at Fermilab for the next decade. The Fermilab Muon Campus consists of a synchrotron – the Delivery Ring (DR) – and the various beamlines necessary to transport beam from the Fermilab Recycler to the DR and from the DR to the g-2 and Mu2e experiments. A layout of the Muon Campus is shown in Fig. 1.



Figure 1: Layout of the Fermilab Muon Campus. Note that AP 10 is the straight section that is well aligned with the SBND detector.

* Operated by Fermi Research Alliance, LLC under Contract No. De-AC02-07CH11359 with the United States Department of Energy.
#raffaele.miceli@stonybrook.edu

During operation of the DR for the Fermilab g-2 Experiment, a considerable number of muons will be produced through the decay of stored pions. These pion decays also produce a large quantity of neutrinos. While the vast majority of these neutrinos cannot be put to use, it just so happens that one of the DR's straight sections (straight 10) is in good alignment with the Short Baseline Near Detector (SBND) [3], one of the liquid argon time projection chamber (LArTPC) detectors in FNAL's Short-Baseline Neutrino Program [4]. This arrangement is illustrated in Fig. 2. Given the high efficiency of LArTPCs, these neutrinos could be a significant source of data for the SBND.



Figure 2: Layout showing the placement of the SBND with respect to the Delivery Ring of the Fermilab Muon Campus.

FERMILAB MUON CAMPUS LINES

Protons with 8 GeV kinetic energy are transported via the M1 beamline to an Inconel target at AP0. Within a 1.33 s cycle length, 16 pulses with 10^{12} protons and 120 ns full length arrive at the target. Secondary beam from the target will be collected using a lithium lens, and positively-charged particles with a momentum of 3.1 GeV/c ($\pm 10\%$) will be selected using a bending magnet. Secondary beam leaving the Target Station will travel through the M2 and M3 lines which are designed to capture as many muons with momentum 3.094 GeV/c from pion decay as possible. The beam will then be injected into the DR. After several revolutions around the DR, essentially all of the pions will have decayed into muons, and the muons will have separated in time from the heavier protons. A kicker will then be used to abort the protons, and the muon beam will be extracted into the new M4 line, and finally into the new M5 beamline which leads to the g-2 storage ring. Note that the M3 line, DR, and M4 line are also designed to be used for 8 GeV proton transport by the Mu2e experiment. However, the two experiments cannot run simultaneously. A detailed performance analysis of the Fermilab g-2 Experiment can be found in [5].

A RECIRCULATING PROTON LINAC DESIGN*

Kilean Hwang[†], Ji. Qiang, Lawrence Berkeley National Laboratory, Berkeley, USA

Abstract

The acceleration efficiency of the recirculating RF linear accelerator was demonstrated by operating electron machines. The acceleration concept of recirculating proton beam was recently proposed and is currently under study. In this paper, we present a 6D lattice design and beam dynamics tracking for a two-pass recirculating proton linac from 150 MeV to 500 MeV, which is the first section of the three acceleration steps proposed earlier [1]. Issues covered are optimization of simultaneous focusing of two beams passing the same structure and achromatic condition under space-charge potential.

INTRODUCTION

The recirculating electron beam of superconducting linear accelerator (LINAC) is proven to be efficient due to high construction/operation cost of the superconducting RF cavities [2, 3]. The synchronization of the multi-pass RF phases is less important factor for the relativistic electron beam due to nearly frozen longitudinal velocity. The proton beam, on the other hand, experiences relatively large velocity change through the accelerating structure, and requires strong restriction on RF phase synchronization for multiple passes. Especially, when the beam passes LINAC only twice, Ref. [1] showed that such a synchronization can be achieved by proper choice of the separation length between the cavities. It can be understood by the following condition.

$$L(1/v_1 - 1/v_2) = nT_{RF} \quad (1)$$

where v_1 and v_2 are the longitudinal beam velocities of the 1st and 2nd passes respectively, T_{RF} is the RF time period, n is an integer number, and L is the separation length. Note that the separation length becomes larger and larger as the beam is accelerated. Such a non-periodic structure may alleviate the beam halo formation but makes the design of the focussing channel difficult.

Table 1: Parameters

Item	Value	Description
Bunch Current	20 mA	Averaged over RF period
Transverse emittance	0.23 mm-mrad	Normalized
Longitudinal emittance	3.2 deg-MeV	Normalized
SCRF Freq.	650 MHz	5 Cell

* Work supported by the Director of the Office of Science of the US Department of Energy under Contract no. DEAC02-05CH11231.

[†] kilean@lbl.gov

Another important issue of the recirculating proton LINAC is the relatively strong space-charge. Especially, the achromatic condition of the splitter and merger system can be easily violated by the space-charge induced dispersion [4].

The purpose of this paper is to assert the feasibility of the multi-pass scheme for efficient proton beams acceleration. We address the above two issues by a conceptual (but rigorous in terms of particle dynamics with full 3D space-charge simulation) design of double-pass recirculating LINAC. We adopt the input parameters similar to Project-X as shown in Table 1. The layout of the double pass recirculating LINAC is shown in Fig 1.

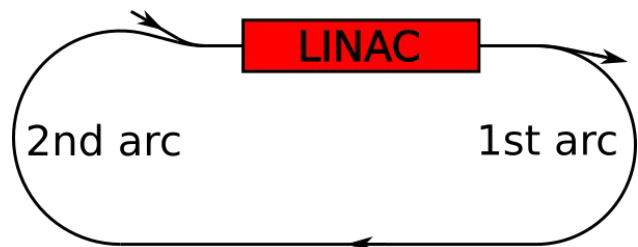


Figure 1: Layout.

LINAC

The LINAC consists of 17 superconducting RF cavities and the separation length between the cavities are chosen according to Eq. (1). The energy gains for each cavity are shown in Fig. 2 where the cavity number i and $17+i$ are pointing physically the same cavities. Passing the same structure twice, the beam is accelerated from 150 MeV to 500 MeV. All the RF phases, except the 2nd and the 4th cavities, are synchronized to -30 degree. Further phase optimization can make the energy gain even more efficient.

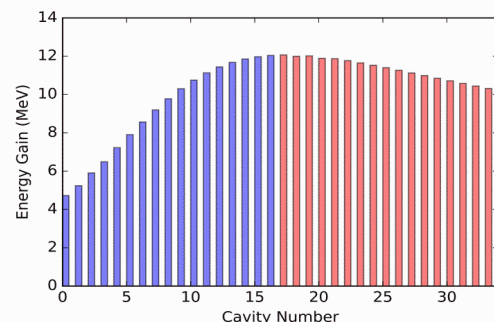


Figure 2: Energy gain of each cavities.

Focusing Channel

Figure 3 shows the separation length between cavities in regard of Eq. (1). In order to overcome the space-charge and RF defocusing and lack of the space for quadrupoles, we synchronize the RF phases of the 2nd

RECENT EXPERIMENTS AT NDCX-II: IRRADIATION OF MATERIALS USING SHORT, INTENSE ION BEAMS*

P. A. Seidl[†], Q. Ji, A. Persaud, E. Feinberg, B. Ludewigt, M. Silverman, A. Sulyman, W. L. Waldron, T. Schenkel, Lawrence Berkeley National Laboratory, Berkeley, USA
 J. J. Barnard, A. Friedman, D. P. Grote, Lawrence Livermore National Laboratory, Livermore, USA
 E. P. Gilson, I. D. Kaganovich, A. Stepanov, Princeton Plasma Physics Laboratory, Princeton, USA
 F. Treffert, M. Zimmer, TU Darmstadt, Darmstadt, Germany

Abstract

We present an overview of the performance of the Neutralized Drift Compression Experiment-II (NDCX-II) accelerator at Berkeley Lab, and summarize recent studies of material properties created with nanosecond and millimeter-scale ion beam pulses. The scientific topics being explored include the dynamics of ion induced damage in materials, materials synthesis far from equilibrium, warm dense matter and intense beam-plasma physics. We summarize the improved accelerator performance, diagnostics and results of beam-induced irradiation of thin samples of, e.g., tin and silicon. Bunches with over 3×10^{10} ions, 1-mm radius, and 2-30 ns FWHM duration have been created. To achieve these short pulse durations and mm-scale focal spot radii, the 1.2 MeV He⁺ ion beam is neutralized in a drift compression section which removes the space charge defocusing effect during final compression and focusing. Quantitative comparison of detailed particle-in-cell simulations with the experiment play an important role in optimizing accelerator performance; these keep pace with the accelerator repetition rate of $\sim 1/\text{minute}$.

INTRODUCTION

Intense pulses of ions in the MeV range enable new studies of the properties of matter ranging from low intensity (negligible heating, but active collective effects due to proximate ion trajectories in time and space), to high intensity where the target may be heated to the few-eV range and beyond. By choosing the ion mass and kinetic energy to be near the Bragg peak, dE/dx is maximized and a thin target may be heated with high uniformity, thus enabling high-energy density physics (HEDP) experiments in the warm dense matter (WDM) regime. The Neutralized Drift Compression Experiment (NDCX-II) was designed with this motivation [1-3].

Reproducible ion pulses ($N > 10^{11}$ /bunch), with bunch duration and spot size in the nanosecond and millimeter range, meet the requirements to explore the physics topics identified above. The formation of the bunches generally involves an accelerator beam with high perveance and low emittance, attractive for exploring basic beam physics of general interest, and relevant to the high-current, high-intensity ion beams needed for heavy-ion-driven inertial fusion energy [4].

Furthermore, short ion pulses at high intensity (but below melting) enable pump-probe experiments that explore the dynamics of radiation-induced defects in materials. For high peak currents and short ion pulses, the response of the material to radiation may enter a non-linear regime due to the overlapping collision cascades initiated by the incident ions. These effects may be transient (no memory effect at a subsequent pulse) and the short, intense pulses of ions provide an opportunity to observe the time-resolved multi-scale dynamics of radiation-induced defects [5-7]. In addition, by measuring the ion range during the course of the ion pulse, the effects of defects and heating on range can be observed. The time-resolved information provides insight and constraints on models of defect formation and in the design of structural materials, for example, for fission and fusion reactors.

ACCELERATOR PERFORMANCE AND BEAM MODELING

A new multicusp, multiple-aperture plasma ion source is capable of generating high purity ion beams of, for example, protons, helium, neon and argon [8]. To date, we have used it solely for the generation of He⁺ ions. Furthermore, helium at about 1 MeV is nearly ideal for highly uniform volumetric energy deposition, because particles enter thin targets slightly above the Bragg peak energy and exit below it, leading to energy loss in the target, uniform within several percent.

An ion induction accelerator is capable of simultaneously accelerating and rapidly compressing beam pulses by adjusting the slope and amplitude of the voltage waveforms in each gap. In NDCX-II, this is accomplished with 12 compression and acceleration waveforms driven with peak voltages ranging from 15 kV to 200 kV and durations of 0.07-1 μs [9]. The first seven acceleration cells are driven by spark-gap switched, lumped element circuits tuned to produce the required cell voltage waveforms. These waveforms ("compression" waveforms because of their characteristic triangular shape) have peak voltages ranging from 20 kV to 50 kV. An essential design objective of the compression pulsers is to compress the bunch to < 70 ns so that it can be further accelerated and bunched by the 200-kV Blumlein pulsers which drive the last five acceleration cells.

In the final drift section, the bunch has a head-to-tail velocity ramp that further compresses the beam by an order-of-magnitude. The space-charge forces are sufficiently high at this stage to require that dense plasma,

* PASeidl@lbl.gov Work supported by the US DOE under contracts DE-AC0205CH11231 (LBNL), DE-AC52-07NA27344 (LLNL) and DE-AC02-09CH11466 (PPPL).

HIGH-PERFORMANCE MODELING OF PLASMA-BASED ACCELERATION AND LASER-PLASMA INTERACTIONS*

J.-L. Vay[†], G. Blaclard, R. Lehe, M. Lobet, LBNL, Berkeley, CA, U.S.A.
 M. Kirchen, University of Hamburg, Hamburg, Germany
 H. Vincenti, Commissariat a l'Energie Atomique, Gif-Sur-Yvette, France
 P. Lee, Université Paris-Saclay, Orsay, France
 B. B. Godfrey, U. Maryland, College Park, MD, USA

Abstract

Large-scale numerical simulations are essential to the design of plasma-based accelerators and laser-plasma interactions for ultra-high intensity (UHI) physics. The electromagnetic Particle-In-Cell (PIC) approach is the method of choice for self-consistent simulations, as it is based on first principles, and captures all kinetic effects, and also scales easily (for uniform plasmas) to many cores on supercomputers. The standard PIC algorithm relies on second-order finite-difference discretizations of the Maxwell and Newton-Lorentz equations. We present here novel PIC formulations, based on the use of analytical pseudo-spectral Maxwell solvers, which enable near-total elimination of the numerical Cherenkov instability and increased accuracy over the standard PIC method. We also discuss the latest implementations in the PIC modules Warp-PICSAR and FBPIC on the Intel Xeon Phi and GPU architectures. Examples of applications are summarized on the simulation of high-harmonic generation with plasma mirrors and of laser-plasma accelerators.

PSEUDO SPECTRAL ANALYTICAL TIME DOMAIN (PSATD)

Maxwell's equations in Fourier space are given by

$$\frac{\partial \tilde{\mathbf{E}}}{\partial t} = i\mathbf{k} \times \tilde{\mathbf{B}} - \tilde{\mathbf{J}} \quad (1a)$$

$$\frac{\partial \tilde{\mathbf{B}}}{\partial t} = -i\mathbf{k} \times \tilde{\mathbf{E}} \quad (1b)$$

$$[i\mathbf{k} \cdot \tilde{\mathbf{E}} = \tilde{\rho}] \quad (1c)$$

$$[i\mathbf{k} \cdot \tilde{\mathbf{B}} = 0] \quad (1d)$$

where \tilde{a} is the Fourier Transform of the quantity a . As with the real space formulation, provided that the continuity equation $\partial \tilde{\rho} / \partial t + i\mathbf{k} \cdot \tilde{\mathbf{J}} = 0$ is satisfied, then the last two equations will automatically be satisfied at any time if satisfied initially and do not need to be explicitly integrated.

Decomposing the electric field and current between longitudinal and transverse components $\tilde{\mathbf{E}} = \tilde{\mathbf{E}}_L + \tilde{\mathbf{E}}_T =$

$\hat{\mathbf{k}}(\hat{\mathbf{k}} \cdot \tilde{\mathbf{E}}) - \hat{\mathbf{k}} \times (\hat{\mathbf{k}} \times \tilde{\mathbf{E}})$ and $\tilde{\mathbf{J}} = \tilde{\mathbf{J}}_L + \tilde{\mathbf{J}}_T = \hat{\mathbf{k}}(\hat{\mathbf{k}} \cdot \tilde{\mathbf{J}}) - \hat{\mathbf{k}} \times (\hat{\mathbf{k}} \times \tilde{\mathbf{J}})$ gives

$$\frac{\partial \tilde{\mathbf{E}}_T}{\partial t} = i\mathbf{k} \times \tilde{\mathbf{B}} - \tilde{\mathbf{J}}_T \quad (2a)$$

$$\frac{\partial \tilde{\mathbf{E}}_L}{\partial t} = -\tilde{\mathbf{J}}_L \quad (2b)$$

$$\frac{\partial \tilde{\mathbf{B}}}{\partial t} = -i\mathbf{k} \times \tilde{\mathbf{E}} \quad (2c)$$

with $\hat{\mathbf{k}} = \mathbf{k}/k$.

If the sources are assumed to be constant over a time interval Δt , the system of equations is solvable analytically and is given by (see [1] for the original formulation and [2] for a more detailed derivation):

$$\tilde{\mathbf{E}}^{n+1} = C\tilde{\mathbf{E}}^n + iS\hat{\mathbf{k}} \times \tilde{\mathbf{B}}^n - \frac{S}{k}\tilde{\mathbf{J}}^{n+1/2} \quad (3a)$$

$$+ (1-C)\hat{\mathbf{k}}(\hat{\mathbf{k}} \cdot \tilde{\mathbf{E}}^n) + \hat{\mathbf{k}}(\hat{\mathbf{k}} \cdot \tilde{\mathbf{J}}^{n+1/2}) \left(\frac{S}{k} - \Delta t \right), \quad (3b)$$

$$\tilde{\mathbf{B}}^{n+1} = C\tilde{\mathbf{B}}^n - iS\hat{\mathbf{k}} \times \tilde{\mathbf{E}}^n \quad (3c)$$

$$+ i\frac{1-C}{k}\hat{\mathbf{k}} \times \tilde{\mathbf{J}}^{n+1/2}. \quad (3d)$$

with $C = \cos(k\Delta t)$ and $S = \sin(k\Delta t)$.

For fields generated by the source terms without the self-consistent dynamics of the charged particles, this algorithm is free of numerical dispersion and is not subject to a Courant condition. Furthermore, this solution is exact for any time step size subject to the assumption that the current source is constant over that time step.

ALTERNATE FORMULATION IN A GALILEAN FRAME

The numerical Cherenkov instability (NCI) [3] is the most serious numerical instability affecting multidimensional PIC simulations of relativistic particle beams and streaming plasmas [4–9]. It arises from coupling between possibly numerically distorted electromagnetic modes and spurious beam modes, the latter due to the mismatch between the Lagrangian treatment of particles and the Eulerian treatment of fields [10].

A new scheme was recently proposed, in [11, 12], which completely eliminates the NCI for a plasma drifting at a

* Work supported by US-DOE Contracts DE-AC02-05CH11231 and by the European Commission through the Marie Slowdoska-Curie actions (Marie Curie IOF fellowship PICSAR grant number 624543). Used resources of NERSC, supported by US-DOE Contract DE-AC02-05CH11231.

[†] jlway@lbl.gov

NOVEL METALLIC STRUCTURES FOR WAKEFIELD ACCELERATION

Xueying Lu, Michael A. Shapiro, Richard J. Temkin, MIT, Cambridge, MA 02139, USA

Abstract

Three novel ideas for wakefield acceleration (WFA) of electrons with metallic periodic subwavelength structures are presented. The first idea is a deep corrugation structure for collinear WFA. A nominal design for the Argonne Wakefield Accelerator (AWA) is shown. The second idea is an elliptical structure with two beam holes at the two focal points for two-beam acceleration (TBA). The third idea is a metamaterial (MTM) ‘wagon wheel’ structure designed as a power extractor at 11.7 GHz for the AWA. The fundamental mode is TM-like with a negative group velocity.

INTRODUCTION

Wakefield acceleration (WFA) is a concept to achieve high accelerating gradients by using a compact high-charge relativistic drive bunch to accelerate a following low-charge witness bunch. There have been studies in the plasma and dielectric WFA, and gradients of GV/m have been reached [1,2]. A metallic WFA structure may be attractive because it is stable and less susceptible to damage. In this paper, novel ideas of WFA using metallic structures are discussed, including the idea of a metamaterial (MTM) structure. MTMs are subwavelength periodic structures with novel electromagnetic features, like negative group velocity of the lowest mode. These features give rise to new properties in the interaction of the MTMs with an electron beam [3].

This paper presents sequentially three metallic structures, a cylindrical deep corrugation structure for collinear WFA, an elliptical structure for two-beam acceleration (TBA), and a wagon wheel MTM structure for power extraction.

DEEP CORRUGATION STRUCTURE

The deep corrugation structure is an array of metallic subwavelength cylindrical cavities, as in Fig. 1. It is different from the conventional corrugated waveguide structure in the way that the corrugation depth is larger than the iris radius, and the period is much smaller than the wavelength.

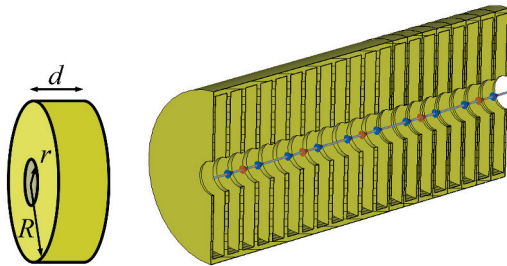


Figure 1: Deep corrugation structure. Left: a single cavity. Right: full multi-cell structure.

Two methods of analysis are adopted to study the wakefield in the structure excited by a short electron bunch. The

first one is the analytical method to calculate the wakefield in a single cavity, and the second one is the numerical method to simulate the wakefield in a multi-cell structure.

Analytical Wakefield Calculation of a Single Cell

The analytical model is a single cavity with radius R and length d excited by a point charge with charge Q traveling at velocity v_0 in the z direction. By solving the Maxwell equations in the cavity with the excitation current

$$J_z(\mathbf{r}, t) = \frac{Qv_0}{2\pi r} \delta(r) \delta(z - v_0 t), \quad (1)$$

we have,

$$E_z(r, z) = \sum_{s=1, n=0}^{\infty} \alpha_{s,n} \left(\frac{cp_s}{R} \right)^2 J_0 \left(p_s \frac{r}{R} \right) \cdot \cos \left(\frac{\pi n}{d} z \right) \left[(-1)^n \frac{\sin \left[\Omega_{s,n} \left(t - \frac{d}{v_0} \right) \right]}{\Omega_{s,n}} - \frac{\sin(\Omega_{s,n} t)}{\Omega_{s,n}} \right], \quad (2)$$

where p_s is the s^{th} zero of the J_0 function, and

$$\alpha_{s,n} = \frac{Qv_0}{\pi \epsilon_0 g_n d} \frac{1}{R^2 J_1^2(p_s)} \frac{1}{\Omega_{s,n}^2 - (\pi n v_0 / d)^2},$$

$$g_n = \begin{cases} 1, & \text{for } n = 0 \\ 0.5, & \text{otherwise} \end{cases},$$

$$\Omega_{s,n} = c \sqrt{\left(\frac{p_s}{R} \right)^2 + \left(\frac{\pi n}{d} \right)^2}.$$

When the excitation charge is changed to a Gaussian bunch with an rms length of σ_z , the wakefield $E_{z,g}$ is,

$$E_{z,g}(r, z) = \sum_{s=1, n=1}^{\infty} E_{s,n}(r, z, t, \Omega_{s,n}) \exp \left(-\frac{\Omega_{s,n}^2 \sigma_z^2}{2c^2} \right), \quad (3)$$

where $E_{s,n}(r, z, t, \Omega_{s,n})$ is the same as E_z in Eq. 2.

Numerical Simulation of a Multi-cell Structure

The CST Particle Studio Wakefield Solver is used to simulate the structure excited by a short relativistic bunch.

Fig. 2 shows the longitudinal electric field on the middle cutting plane with a bouncing pattern observed. The pattern is formed when the drive bunch initially excites a decelerating wake (in red) after it. The decelerating wake travels outward and bounces at the metal wall with a 180-degree phase shift, transforming to an accelerating wake (in blue). The accelerating wake then travels inward and is focused at the beam axis. A following witness bunch can be placed at the refocusing location in blue to be accelerated.

PROGRESS ON BEAM-PLASMA EFFECT SIMULATIONS IN MUON IONIZATION COOLING LATTICES*

J. Ellison, Illinois Institute of Technology, Chicago, IL, USA

P. Snopok, Illinois Institute of Technology, Chicago, IL, USA & Fermilab, Batavia, IL, USA

Abstract

New computational tools are essential for accurate modeling and simulation of the next generation of muon-based accelerators. One of the crucial physics processes specific to muon accelerators that has not yet been simulated in detail is beam-induced plasma effect in liquid, solid, and gaseous absorbers. We report here on the progress of developing the required simulation tools and applying them to study the properties of plasma and its effects on the beam in muon ionization cooling channels.

INTRODUCTION

Though muon accelerator simulation codes have been steadily improving over the years, there is still much room for improvement. Many single-particle processes and collective effects in vacuum and matter, such as space charge, beam-beam effects, plasma effects from ionized electrons and ions have not been implemented in any current code. These effects have to be either deemed negligible or taken into account to ensure the proper accuracy of simulations.

Ionization cooling (principle illustrated in Fig. 1) is a method by which the emittance of a muon beam can be reduced. A beam is sent through a material, losing momentum through multiple scattering and ionization processes, and reducing its emittance. By re-accelerating the beam through RF cavities, the longitudinal momentum is restored, and any lost energy is regained so that the process can be repeated.



Figure 1: Principle of ionization cooling: 1) The overall momentum is reduced through ionization where $\langle \frac{dE}{dx} \rangle$ is the mean energy loss of the muons. 2) Transverse momentum increases through multiple scattering. 3) Through re-acceleration, longitudinal momentum is regained.

The evolution of the normalized transverse emittance can be described by the following equation:

$$\frac{d\epsilon_n}{dz} \approx -\frac{1}{\beta^2} \left\langle \frac{dE_\mu}{dz} \right\rangle \frac{\epsilon_n}{E_\mu} + \frac{1}{\beta^3} \frac{\beta_\perp E_s^2}{2E_\mu mc^2 X_0},$$

where ϵ_n is the normalized emittance, z is the path length, E_μ is the muon beam energy, $\beta = v/c$, X_0 is the radiation length of the absorber material, β_\perp is the betatron function, and E_s is the characteristic scattering energy [1]. Here, two

competing effects can be seen: the first term is the cooling (reduction of phase space beam size) component from ionization energy loss and the second term is the heating (increase of phase space beam size) term from multiple scattering. For minimizing heating, a small betatron function from a strong magnetic field and a large radiation length are needed. To maximize cooling, a large stopping power is needed, $\left\langle \frac{dE_\mu}{dz} \right\rangle$. Hydrogen seems to give the best balance between a large radiation length and a large stopping power.

Muons will ionize material as they travel through absorbers. This will generate a plasma, and it is the interaction of the muon beam with the generated plasma that is studied here. Beam-plasma interaction is not taken into account currently in a majority of muon accelerator simulation codes. This interaction is especially important when simulating ionization cooling in the hybrid cooling channels with medium-to-high pressure gas-filled RF cavities (Fig. 2).

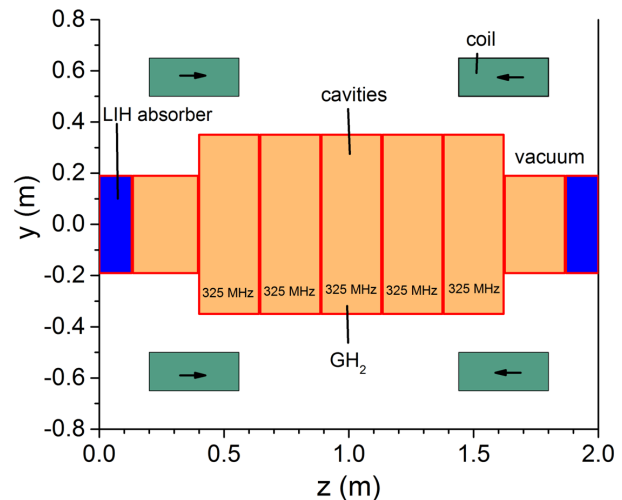


Figure 2: Example of a matter-dominated hybrid cooling channel with gas-filled RF cavities, nearly all the cell length has material: either medium-pressure gaseous hydrogen or LiH absorber. (Image courtesy of D. Stratakis)

The plasma effects have been studied by plasma physicists, but have not been studied extensively from a beam physics point of view. The plasma has been shown not to disrupt the beam or make it blow up dramatically [2], however, for ionization cooling purposes beam-plasma effects may have a large impact on the cooling rates for both charges of muons. Essentially, the head of a bunch sees a material with different properties than the tail of the bunch and whole bunches may see materials with different properties than the previous bunches. Ionization rates vary from material to material so

* Work supported by the U.S. Department of Energy.

WEDGE ABSORBERS FOR MUON COOLING WITH A TEST BEAM AT MICE*

David Neuffer,[#] Fermilab, Batavia, IL 60510 USA

J. Acosta, D. Summers, University of Mississippi, Oxford, MS 38655 USA

T. Mohayai, P. Snopok, IIT, Chicago, IL 60166 USA

Abstract

Emittance exchange mediated by wedge absorbers is required for longitudinal ionization cooling and for final transverse emittance minimization for a muon collider. A wedge absorber within the MICE beam line could serve as a demonstration of the type of emittance exchange needed for 6-D cooling, including the configurations needed for muon colliders. Parameters for this test are explored in simulation and possible experimental configurations with simulated results are presented.

INTRODUCTION

Ionization cooling has been proposed as a potentially useful method for cooling particle beams.[1, 2] It could be particularly effective in cooling muons, where cooling to emittances suitable for a high-energy lepton collider is possible, and a cooled muon beam in a storage ring could provide an intense source of muon-decay neutrinos (a “neutrino factory”). Ionization cooling could also be used in some proton and ion beam scenarios. In ionization cooling the beam passes through a material, where energy loss is opposite the direction of momentum, followed by longitudinal acceleration restoring the longitudinal momentum. This reduces transverse emittances ($\varepsilon_{i,N}$), following the cooling equation:

$$\frac{d\varepsilon_N}{ds} = -\frac{g_t}{\beta^2 E} \frac{dE}{ds} \varepsilon_N + \frac{\beta_{\perp} E_s^2}{2\beta^3 m_{\mu} c^2 L_R E}, \quad (1)$$

where the first term is the frictional cooling effect and the second is the multiple scattering heating term. Here L_R is the material radiation length, β_{\perp} is the betatron focusing function, and E_s is the characteristic scattering energy (~ 14 MeV), and g_t is the transverse partition number.

Longitudinal cooling depends on having the energy loss mechanism such that higher-energy muons lose more energy. The equation is:

$$\frac{d\varepsilon_L}{ds} = -\frac{\partial \left(\frac{dE_{\mu}}{ds} \right)}{E_{\mu}} \varepsilon_L + \frac{\beta\gamma \beta_L}{2} \frac{d \left\langle \left(\frac{\delta p}{p} \right)^2 \right\rangle}{ds} \quad (2)$$

The dependence of energy loss with energy is antidamping for $p_{\mu} < 350$ MeV/c, and only weakly damping for higher energy. However, the longitudinal cooling rate is enhanced when absorbers are placed at non-zero dispersion and the absorber density or thickness depends upon position, such as in a wedge absorber. With wedge cooling, the longitudinal and transverse partition numbers are coupled, exchanging transverse and longitudinal cooling rates:

$$g_L \Rightarrow g_{L,0} + \frac{\eta\rho'}{\rho_0}; g_x \Rightarrow 1 - \frac{\eta\rho'}{\rho_0} \quad (3)$$

where ρ'/ρ_0 is the change in density with respect to transverse position, ρ_0 is the reference density associated with dE/ds , and η is the dispersion ($\eta = dx/d(\Delta p/p)$). This coupling is essential to obtaining effective longitudinal cooling and is therefore needed in any multistage system requiring large cooling factors.

High-luminosity $\mu^+ \mu^-$ colliders also require a “final cooling” stage in which transverse emittance is reduced, while longitudinal emittance may increase. This may be done by explicit emittance exchange techniques and energy loss in a wedge absorber is a particularly promising one [4,5].

The goal of the MICE experiment is to explore the conditions for ionization cooling and to demonstrate the effectiveness of components of a μ cooling system. Wedge absorber emittance exchange is an essential component of many cooling systems and the MICE demonstration would be greatly enhanced by a wedge demonstration.

Large exchanges can be obtained within a single wedge and readily measured within the limited scope of the MICE experiment. In this note we explore use of single polyethylene wedges to demonstrate the basic principles of emittance exchange within ionization cooling.

WEDGE EXCHANGE FORMALISM

A transport matrix based formalism can be used to estimate the exchange effects of a single wedge.[6] Figure 1 shows a stylized view of the passage of a beam with dispersion η_0 through a wedge absorber. The wedge is approximated as an object that changes particle momentum offset $\delta = \Delta p/P_0$ as a function of x , and the wedge is shaped such that that change is linear in x . (The change in average momentum P_0 is ignored in this approximation, as well as energy straggling and multiple scattering.) The rms beam properties entering the wedge are given by the transverse emittance ε_0 , betatron amplitude β_0 , dispersion η_0 and relative momentum width δ_0 . (To simplify discussion the beam is focussed to a betatron and dispersion waist at the wedge: $\beta_0', \eta_0' = 0$.) The wedge transforms the δ of particles depending on position x :

$$\frac{\Delta p}{p} = \delta \rightarrow \delta - \frac{2(dp/ds) \tan \frac{\theta}{2}}{P_0} x = \delta - \delta' x$$

dp/ds is the momentum loss rate in the material ($dp/ds = \beta^1 dE/ds$). $2x \tan \theta/2 \equiv x \tan \theta$ is the wedge thickness at transverse position x (relative to the central orbit at $x=0$), and $\delta' = 2dp/ds \tan \theta/2 / P_0$ indicates the change of δ with

*Work supported by FRA Associates, LLC under DOE Contract No. DE-AC02-07CH11359.

[#]neuffer@fnal.gov

SIMULATED MEASUREMENTS OF BEAM COOLING IN MUON IONIZATION COOLING EXPERIMENT*

Tanaz Angelina Mohayai^{†1}, Illinois Institute of Technology, Chicago, IL, USA

David Neuffer, Fermilab, Batavia, IL, USA

Chris Rogers, STFC Rutherford Appleton Laboratory, Oxfordshire, UK

Pavel Snopok¹, Illinois Institute of Technology, Chicago, IL, USA

for the MICE Collaboration

¹also at Fermilab, Batavia, IL, USA

Abstract

Cooled muon beams are essential to high-luminosity Muon Collider and the production of high-flux and pure neutrino beams at the Neutrino Factory. When pions decay into muons, they form beams with large phase-space volumes. To optimize muon yield and fit the beam into cost-effective apertures, the beam phase-space volume needs to be reduced. Ionization cooling is the only technique that can reduce the beam phase-space volume within the short muon lifetime, and the international Muon Ionization Cooling Experiment (MICE) will be the first experiment to demonstrate this. A figure of merit for beam cooling is the transverse root-mean-square (RMS) emittance reduction. However, RMS emittance can be sensitive to non-linear effects in beam optics. This paper studies an alternative measure of cooling where a direct measurement of phase-space density and volume is made through the novel application of the Kernel Density Estimation (KDE) method.

INTRODUCTION

Ionization cooling in MICE Step IV (the current experimental configuration, Fig. 1) is achieved by passing the beam through a low- Z absorber where the beam's transverse momentum is reduced through energy loss, ultimately resulting in the desired reduction in the beam's phase-space volume. Two trackers are located upstream and downstream of the absorber, forming the cooling channel. Each tracker comprises five scintillating-fiber stations each with three doublet fiber layers. The Spectrometer Solenoids housing the trackers are each made of five superconducting coils, with two used for beam matching at the absorber (Match 1 and Match 2) and three for maintaining constant solenoidal fields in the tracking volumes (End 1, Center, and End 2) [1]. On September 2015, the Match 1 coil of the downstream Spectrometer Solenoid failed during magnet commissioning, and the current running configurations are designed to take this into account.

Phase-space density and volume are important concepts in describing the state of a system of particles. The phase-space density can be described as the probability density function

(PDF) in phase space, where the PDF is the probability of finding a particle within a particular volume. With non-linear beam optics and beam distributions with a long tail, defining a parametric model for the distribution becomes challenging. The underlying PDF of such distributions can then be found using density estimation (DE) techniques. In non-parametric DE, no assumptions are made about the distribution parameters. KDE is an example of such a method which uses kernel functions to estimate the density.

KERNEL DENSITY ESTIMATION TECHNIQUE

In general, a six dimensional position-momentum phase space can be used to represent the individual muons in a MICE beam profile. In MICE Step IV, there is a particular interest in measuring the four dimensional transverse phase space. These coordinates are coupled in the presence of solenoidal fields. Muons in the beam distribution can be individually reconstructed in the trackers [2] obtaining position and kinetic momentum values for $\vec{X}_i = (x_i, p_{x_i}, y_i, p_{y_i})$, where i runs from 1 to n and n represents the total number of muons in the beam sample under study. When the Kernel Density Estimation (KDE) technique is applied in four dimensions to the MICE beam sample, Gaussian kernel functions in the form of multi-dimensional ellipses of variances $h = h_f \Sigma$ are centered at each muon. h and h_f are the bandwidth parameter and factor discussed in the next section, and Σ is the covariance matrix of the data set whose elements represent the amount of variances of each of the \vec{X}_i coordinates. In MICE, dimension variable d is set to 4, representing the dimension of the transverse phase-space vector. The estimated density, \hat{f} , at an arbitrary point $\vec{x} = (x, p_x, y, p_y)$ in phase space is then determined by summing the contributions of the transverse coordinates \vec{X}_i of all muons [3],

$$\hat{f}(\vec{x}) = \frac{|\Sigma|^{-1/2}}{nh_f^d \sqrt{(2\pi)^d}} \sum_{i=1}^n \exp \left[-\frac{(\vec{x} - \vec{X}_i)^T \Sigma^{-1} (\vec{x} - \vec{X}_i)}{2h_f^2} \right]. \quad (1)$$

A kernel function which acts as a weighting function, should satisfy a certain set of conditions for its sum to result in a PDF [4]: it should be non-negative and should integrate to 1. In addition, it should be symmetric about its center and its second moment should be finite [5]. The bandwidth parameter, h acts as the variance of the assigned

* Work supported by DOE, INFN, STFC, DOE SCGSR under contract No. DE-AC05-06OR23100, and IIT Irwin Fieldhouse Fellowship. We thank D. Kaplan and J. S. Berg for the valuable discussions.

[†] tmohayai@hawk.iit.edu

HYBRID METHODS FOR SIMULATION OF MUON IONIZATION COOLING CHANNELS*

J. Kunz[†], P. Snopok^{‡§}, Illinois Institute of Technology, Chicago, IL, USA
M. Berz, Michigan State University, East Lansing, MI, USA

Abstract

COSY Infinity is an arbitrary-order beam dynamics simulation and analysis code. It uses high-order transfer maps of combinations of particle optical elements of arbitrary field configurations. New features have been developed and implemented in COSY to follow charged particles through matter. To study in detail the properties of muons passing through a material, the transfer map approach alone is not sufficient. The interplay of beam optics and atomic processes must be studied by a hybrid transfer map–Monte Carlo approach in which transfer map methods describe the average behavior of the particles including energy loss, and Monte Carlo methods are used to provide small corrections to the predictions of the transfer map, accounting for the stochastic nature of scattering and straggling of particles. This way the vast majority of the dynamics is represented by fast application of the high-order transfer map of an entire element and accumulated stochastic effects. The gains in speed simplify the optimization of muon cooling channels which are usually very computationally demanding. Progress on the development of the required algorithms is reported.

INTRODUCTION

A prime example of why matter-dominated lattices are relevant comes from the prospect of a neutrino factory or a muon collider [1]. As muon branching fractions are 100% $\mu^- \rightarrow e^- \bar{\nu}_e \nu_\mu$ and $\mu^+ \rightarrow e^+ \nu_e \bar{\nu}_\mu$, there are obvious advantages of a muon-sourced neutrino beam. Also, because muons are roughly 200 times heavier than electrons, synchrotron radiation is not an issue. As a result, a high-energy muon collider ($\sqrt{s} \approx 6$ TeV) could be built on a compact site. Such energy levels are experimentally unprecedented in the leptonic sector, since a circular electron accelerator is restricted by synchrotron radiation. At lower energy, a muon collider could serve as a Higgs Factory ($\sqrt{s} \approx 126$ GeV), with possible new physics via the observation of Higgs to lepton coupling. This is advantageous since the Higgs coupling to leptons scales as mass squared.

However, muon-based facilities are not without their challenges. Synthetic muon creation comes from the collision of protons with a fixed target. The resultant spray of particles largely contains kaons (which decay primarily into pions and muons), pions (which decay primarily into muons), and rogue protons. High-intensity collection entails a large initial phase space volume. The resultant cloud of muons must be

collected, focused, and accelerated well within the muon lifetime ($2.2 \mu\text{s}$ at rest). The only technique that is fast enough to be relevant on that time scale is ionization cooling [2].

For a neutrino factory only a modest amount of cooling is required, predominantly in the transverse plane. However, neutrino factories could benefit from full six-dimensional cooling, where in addition to the transverse cooling emittance exchange is used to reduce longitudinal beam size in addition to transverse. Current muon collider designs assume a significant, $O(10^6)$, six-dimensional cooling.

Cooling channels required for a high-energy high-luminosity muon collider could be up to a thousand meters long. Designing, simulating, and optimizing performance of those channels involves using high-performance clusters and multi-objective genetic optimizers. Typically, the codes used for simulations belong to the class of particle-by-particle integrators, where each particle is guided through the length of the cooling channel independently. That takes its toll on genetic optimizers, especially with a large number of particles per run. Transfer map methods could solve this problem, since the nonlinear map of the system is calculated once, and then can be applied to any number of particles at a very low computational cost. On the other hand, the transfer map approach alone is not sufficient to study the passage of muons through a material. This study implements a hybrid transfer map–Monte Carlo approach in which transfer map methods describe the deterministic behavior of the particles, and Monte Carlo methods are used to provide corrections accounting for the stochastic nature of scattering and straggling of particles.

COSY INFINITY

COSY Infinity (COSY) [3] is a simulation tool used in the design, analysis, and optimization of particle accelerators, spectrographs, beam lines, electron microscopes, and other such devices, with its use in accelerator lattice design being of particular interest here. COSY uses the transfer map approach, in which the overall effect of the optics on a beam of particles is evaluated using differential algebra. Along with tracking of particles through a lattice, COSY includes many analysis and optimization tools.

Currently supported elements in COSY include various magnetic and electric multipoles (with fringe effects), homogeneous and inhomogeneous bending elements, Wien filters, wigglers and undulators, cavities, cylindrical electromagnetic lenses, general particle optical elements, and *deterministic* absorbers of intricate shapes described by polynomials of arbitrary order, with the last element being of particular interest for this study. This element only takes into

* Work supported by the U.S. Department of Energy

[†] Also at Anderson University, Anderson, IN, USA

[‡] psnopok@iit.edu

[§] Also at Fermilab, Batavia, IL, USA

OPTICALLY BASED DIAGNOSTICS FOR OPTICAL STOCHASTIC COOLING*

M. B. Andorf¹, V. A. Lebedev², P. Piot^{1,2}, J. Ruan²

¹ Department of Physics and Northern Illinois Center for Accelerator & Detector Development, Northern Illinois University DeKalb, IL, USA

² Fermi National Accelerator Laboratory, Batavia, IL, USA

Abstract

An Optical Stochastic Cooling (OSC) experiment with electrons is planned in the Integrable Optics Test Accelerator (IOTA) ring currently in construction at Fermilab. OSC requires timing the arrival of an electron and its radiation generated from the upstream pickup undulator into the downstream kicker undulator to a precision on the order of less than a fs. The interference of the pickup and kicker radiation suggests a way to diagnose the arrival time to the required precision.

INTRODUCTION

Fermilab is currently preparing a proof-of-principle of Optical Stochastic Cooling (OSC) using 100 MeV electrons at the Integrable Optics Test Accelerator (IOTA). In OSC a particle emits radiation in a pickup undulator. The light from the pickup is then transported, and in the presence of an optical amplifier, amplified, to a kicker undulator located downstream and identical to the pickup undulator. Therefore the particle follows a curved path in a magnetic bypass chicane such that it arrives at the entrance of the kicker just as the light from the pickup is also arriving [1, 2]. For the reference particle the arrival time of radiation and particle in the kicker is such that it receives no kick. Particles with a nonzero synchrotron or betatron coordinate are displaced relative to the reference particle by an amount $\Delta s = M_{51}x + M_{52}\theta + M_{56}(\Delta p/p)$ and receive a longitudinal kick given as

$$\frac{\delta p}{p} = -\xi_0 \sin(k\Delta s). \quad (1)$$

In the above M_{ij} are the elements of the 6×6 transfer matrix from pickup to kicker, $k \equiv 2\pi/\lambda$ is the radiation wave-number, and $(\delta p)/p$ is the relative momentum change of the particle after a single pass through the cooling section. The kick normalized amplitude is $\xi_0 = 2E_0\sqrt{G}/(pc)$ where E_0 corresponds to, in the case of a sufficiently small undulator parameter, the energy radiated in a single undulator, G is the gain in power from the optical amplifier (if present), p the design momentum and c the velocity of light. When the dispersion function is non vanishing at the kicker undulator location a horizontal kick is also applied thereby resulting in horizontal cooling. Likewise, introducing coupling between

the two transverse phase spaces provides a path for cooling along all three degrees of freedom.

Table 1: Undulator Parameters for the OSC in IOTA

parameter	value	unit
U_o	100	MeV
K	1.04	-
period	11.06	cm
λ (at zero angle)	2.2	μm
Total length	77.4	cm

In IOTA, the OSC proof-of-principle experiment will be accomplished in two phases. In a first stage, we will not have an amplifier and rely on passive cooling: the optical system will consist of a telescope composed of three lenses chosen so that the optical transfer matrix between the pickup and kicker undulators is $-I$ where I is identity matrix. The telescope can transport $\sim 90\%$ of the energy from the pickup to the kicker. Parameters for the undulators can be found in Table 1 and yield a value for the kick amplitude, $\xi_0 = 8.5 \times 10^{-10}$. Simulations show that the kick is further reduced by roughly 10 % due to dispersion in telescope [3]. In the second stage, a 7-dB Cr:ZnSe optical amplifier (with an operating band from 2.2 – 2.9 μm) will be installed and is expected to double the cooling rates over the passive cooling scheme.

In this paper we explore how to measure the timing error between the arrival of the pickup signal and the particle in the kicker. The timing precision needs to be < 1 fs in order to fully optimize the cooling rates. We propose a technique that uses optical interference between the pickup and kicker radiation signals. Before detailing the measurement technique we first consider in the impact of arbitrary timing error on the OSC process.

LONGITUDINAL TIMING

Cooling Rates and Transit Time Error

The damping decrements λ_i ($i \in [x, s]$) for small betatron and synchrotron amplitudes are given by [4]

$$\begin{bmatrix} \lambda_x \\ \lambda_s \end{bmatrix} = \frac{k\xi_0}{2} \begin{bmatrix} M_{56} - S_P \\ S_P \end{bmatrix}, \quad (2)$$

where $S_P = M_{51}D_p + M_{52}D'_p + M_{56}$ is the partial slip factor such that a particle with a momentum deviation $\Delta p/p$ will be

* Work supported by the by the US Department of Energy (DOE) contract DE-SC0013761 to Northern Illinois University. Fermilab is operated by the Fermi research alliance LLC under US DOE contract DE-AC02-07CH11359.

THEORETICAL AND NUMERICAL STUDY ON PLASMON-ASSISTED CHANNELING INTERACTIONS IN NANOSTRUCTURES

Young-Min Shin, Department of Physics, Northern Illinois University, Dekalb, IL, 60115, USA
also at Fermi National Accelerator Laboratory (FNAL), Batavia, IL 60510, USA

Abstract

A plasmon-assisted channeling acceleration can be realized with a large channel possibly at the nanometer scale. Carbon nanotubes are the most typical example of nano-channels that can confine a large amount of channeled particles and confined plasmons in a coupling condition. This paper presents a theoretical and numerical study on the concept of laser-driven surface-plasmon (SP) acceleration in a carbon nanotube (CNT) channel. An analytic description of the SP-assisted laser acceleration is detailed with practical acceleration parameters, in particular with specifications of a typical tabletop femto-second laser system. The maximally achievable acceleration gradients and energy gains within dephasing lengths and CNT lengths are discussed with respect to laser-incident angles and CNT-filling ratios.

INTRODUCTION

Laser accelerations based on photon-matter interactions typically take advantage of intense driving lasers with excessively high power at the level of Tera-watt or even Peta-watt to quickly ionize a gas target (or often solid targets) and to raise particle energies to the MeV scale. Such femto-second laser systems occupy a large physical space, while the acceleration medium/target itself is relatively much smaller than the driving source, and, in spite of their exceptionally large field strengths, downside of using a solid target for the laser-acceleration is that the targets become vulnerable to intense laser-matter interactions and could be readily destroyed under the impact of a short pulse driving source. The system size and limited reproducibility have refrained laser-accelerations from being adapted to accelerator-based systems. It would be more practical to increase laser-target coupling efficiency and/or repetition rate, while keeping the laser intensity sufficiently low, perhaps below the target ionization threshold. In particular, affordable laser intensities would be more compatible with systems in practically applicable sizes. In such a way, structuring a target can improve the acceptance of channeling particles and field confinements in the acceleration region, which would increase laser-plasma coupling efficiency. A CNT, synthetic nanostructure consisting of honeycomb unit cells based on *sp*-2 carbon-bonding, is well suited for laser-driven acceleration since oscillatory plasma waves (SPs) are readily generated by a photo-excitation in such a structured negative index material [1, 2]. If the optical wavelength of a driving laser is close enough to a plasma wavelength of the CNTs, the laser would strongly perturb a density state of conduction electrons on the tube and excite surface plasmons at the photon-plasmon coupling

condition. The optical properties and coupling condition can be effectively controlled by CNT parameters such as the diameter and aerial density. In this condition, it is regarded that the laser is coupled into an effective metallic substrate with homogenized optical parameters (plasma frequency, permittivity, refractive index, and absorption coefficient) that are averaged over an area of the laser wavelength on a target implanted with sub-wavelength CNTs.

SYSTEM DESCRIPTION

Figure 1 depicts the concept of the laser-driven SPP acceleration in a nanotube. In the substrate target, particles channeled in the nanotube are repeatedly accelerated and focused by confined fields of the laser-excited SPP along the CNTs embedded in the nano-holes under the phase-velocity matching condition. The energy gain of accelerated particles, if any, is limited by the dephasing length. Continuous phase velocity matching between particles and SP waves can be extended by tapering the longitudinal plasma density in a target. In a CNT-target, the longitudinal plasma density profile can be controlled by selectively adjusting tube dimensions. When an intense short pulse laser illuminates the near-critical density plasma, the inductive acceleration field moves with a speed v_g , which is less than v_p , depending on the plasma density: $v_g = c\sqrt{1 - \omega_p^2/\omega^2}$, where c is the speed of light, ω_p is the electron plasma frequency, and ω is the laser frequency. The accelerating ions have a progressively higher speed along the targets, so the inductively accelerated ions are kept accelerating for a long time inside the near-critical density plasma target. The distance between the two adjacent targets are also adjusted accordingly.

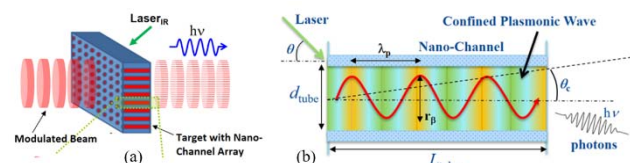


Figure 1: (a) Conceptual drawing of laser-pumped CNT-acceleration and (b) photo-excited plasmonic wave interacting with CNT-channelling electrons.

The acceleration mechanism of the laser-excited sub- λ plasmon is conceptually depicted in Fig. 1, illustrating accelerating particles in a laser-pumped CNT channel [3, 4]. The laser irradiated on a target modulates the electron density of the CNT and quickly induce a plasma oscillation at a photon-plasmon coupling condition. The photo-excited density fluctuation induces electromagnetic fields in a

CONSTRUCTION STATUS OF A RF-INJECTOR WITH A CNT-TIP CATHODE FOR HIGH BRIGHTNESS FIELD-EMISSION TESTS

^{1,2}Young-Min Shin, ¹Greg Fagerberg, ¹Michael Figora, ¹Andrew Green

¹Department of Physics, Northern Illinois University, Dekalb, IL, 60115, USA

²Fermi National Accelerator Laboratory (FNAL), Batavia, IL 60510, USA

Abstract

We have been constructing an S-band RF-injector system for field-emission tests of a CNT-tip cathode. A pulsed S-band klystron is installed and fully commissioned with 5.5 MW peak power in a 2.5 microsecond pulse length and 1 Hz repetition rate. A single-cell RF-gun is designed to produce 0.5 – 1 pC electron bunches in a photo-emission mode with duration 3 ps at 0.5 – 1 MeV. The measured RF system jitters are within 1% in magnitude and 0.2 degree in phase, which would induce 3.4 keV and 0.25 keV of energy jitters, corresponding to 80 fs and 5 fs of temporal jitters, respectively. Our PIC simulations indicate that the designed bunch compressor reduces the time-of-arrival (TOA) jitter by about an order of magnitude. Emission current and beam brightness of the field-emitted beam are improved by implanting CNT tips on the cathode surface, since they reduce the emission area, while providing high current emission. Once the system is commissioned in field-emission mode, the CNT-tip cathode will be tested in terms of klystron-power levels to map out its current-voltage (I-V) characteristics in pulse emission mode.

INTRODUCTION

Complex dynamics is concomitant with charged particles traveling through periodic lattice structures. When ions interact with scattering sites in a periodic structure, their interactive characteristics vastly change depending upon the condition of the interaction such as spatial distribution, composition, and energy-states of the scatterers, and energy-momentum distributions of the charged particles. If an interactive medium under the particle interaction is in a non-equilibrium state, for instance a lattice structure illuminated by a high power energy source, the dynamics would be even more complicated. Spatiotemporal variation of the interaction parameters would also have a strong dependence on the nature of the external driving source. A precise measurement technique with a sub-atomic scale spatial resolution is required to characterize this kind of charge-matter interaction occurring at the quantum mechanical level. Electron diffraction is a widely used technique for crystallography and combining it with an ultrafast pump laser provides temporal information of structural variations [1 – 3]. The electron pump-probe technique is typically capable of providing sub-angstrom spatial resolution and 100 fs of temporal resolution, which is sufficient for our experiments. We will investigate the interaction mechanism and particle dynamics in nanostructured crystals using this diagnostic method. The

planned experiments need a bright, mono-energetic, non-divergent electron beam for precise electron radiation/scattering measurements with a low signal-to-noise ratio. It is crucial to push the beam emittance down to the channel acceptance of an interacting medium. An ultra-cold electron source with a high brightness, ideally up to the quantum limit, is a key element for the experiments because it supplies a sufficient number of coherent electrons to the phase space of the interaction-channel and eventually to a detector. One of our major plans is to develop a high brightness electron source with a CNT cold-cathode [4].

SIMULATION INVESTIGATION OF CNT-TIP COLD-CATHODE

We investigated field-emission characteristics of a nanotube array with finite-element-algorithm (FEA) simulations [5] combined with a modified Fowler-Nordheim (FN) model. A ratio of field distortion due to the presence of a charged object(s) in the space is parameterized by the electric field enhancement factor $\beta = E/E_0$, where $E_0 (= U/L)$ is the electric field between the electrodes (U and L : the anode-cathode voltage and distance, respectively). For theoretical analysis, the local electric field, E , was approximated by various analytic forms (e.g. $\beta \approx \rho(1 + d/D)$, where D is the tip-to-tip distance) of the field enhancement factor, β . In principle, as the aspect ratio ($\rho = l/d$) of CNTs exceeds 1000, field emission from nanotubes would occur at a much lower applied voltage than typical field-emitters. Static field simulations can provide very accurate solutions of the local field distribution, E . The transverse emittances and intrinsic energy spread of the electron bunch emitted from a cathode are mostly determined by initial beam conditions, when electrons are created at a cathode surface.

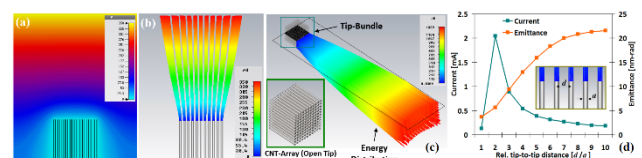


Figure 1: CNT-tip array cathode model (a) electrostatic field analysis with multiple tips (b)/(c) field-emission simulation with the static field (d) emission current and normalized emittance versus tip-to-tip distance (d/a).

Our field-emission simulation (Fig. 1) indicated that a 100 nm wide and 2 μ m long CNT tip creates a beam with a high emission current density and small normalized emittance (a few tens of nanometers) due to the small

RF DESIGN OF A 1.3-GHz HIGH AVERAGE BEAM POWER SRF ELECTRON SOURCE

N. Sipahi, S. V. Milton², S. G. Biedron^{1,2}, Colorado State University, Fort Collins, CO, USA
I. Gonin, R. Kephart, T. Khabiboulline, N. Solyak, V. Yakovlev, Fermilab, Batavia, IL, USA

¹Faculty of Electrical Engineering, University of Ljubljana, Ljubljana, Slovenia

²Element Aero, Chicago, IL 60643 USA

Abstract

There is a significant interest in developing high-average power electron sources, particularly those integrated with Superconducting Radio Frequency (SRF) accelerator systems. Even though there are examples of high-average-power electron sources, they are not compact, highly efficient, or available at a reasonable cost. Adapting the recent advances in SRF cavities, RF power sources, and innovative solutions for an SRF gun and cathode system, we have developed a design concept for a compact SRF high-average power electron linac. This design will produce electron beams with energies up to 10 MeV. In this paper, we present the design results of our cathode structure integrated with modified 9-cell accelerating structure.

GENERAL CONCEPT

The use of SRF cavities may allow linear accelerators (linacs) that are less than 1.5 meters in length to create electron beams above 10 MeV with average beam powers measured in 10's of kW. Such compact SRF accelerators can have high wall-plug power efficiencies and, for example, may be compact enough to be readily transported to and operated at local sites [1].

DESIGN OF THE GUN STRUCTURE

In an electron source, the electron gun and the cathode system are critical components for achieving stable intensity and high-average powers. In our gun design, the gun cavity is integrated into the first cell of the 9-cell standard ILC/XFEL (International Linear Collider/European X-Ray Free Electron Laser) cavity [2], resulting in a modified 9-cell accelerating structure. The 1st cell (gun cell) of this structure is redesigned to match the desired parameters and the length is 0.4 of a regular-sized cell. The remaining eight cells are the standard, well-known ILC/XFEL cavity parameters. This integrated design feature is key to a compact design. The first cell is designed on the basis of RF field calculations.

The detailed study of the accelerator design was recently presented [3]. Figure 1 shows the design of 8.4-cell gun structure with the frequency matched to 1.3 GHz. The field in the 0.4-cell has been maximized based on the design conditions. These simulations were performed using CST Microwave Studio [4].

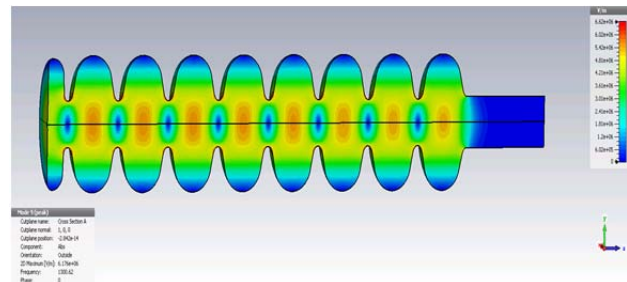


Figure 1: The 8.4-cell geometry design with the modified gun cell and the contour plot of the fields using CST MWS.

In Table 1, we summarize the design parameters of 8.4-cell accelerator structure.

Table 1. The Results of CST MWS Simulations for the Modified Gun Structure

Parameters	CST MWS results
First Cell Ratio	0.4
Frequency [MHz]	1300.6
E_{peak} , [MV/m]	22.5
B_{peak} , [mT]	44.6
$B_{\text{peak}}/E_{\text{peak}}$ [mT/(MV/m)]	1.98
R/Q [Ω]	936

DESIGN OF THE CATHODE STRUCTURE

We have chosen a thermionic cathode for our design. Since a thermionic cathode by its very nature has a high temperature, one might assume that within a SC environment this could present an issue. The black-body radiation is quite low for the size of the cathode radius (~3 mm) we intend to use; therefore, much of this can be shadowed from the superconducting surfaces.

Choosing a thermionic cathode system creates a challenge for proper gating of the electrons from the cathode, as the electrons should be gated only during favorable RF phase conditions. This condition limits the potential of electrons striking the cold superconducting surfaces. According to this condition, we have incorporated an additional space behind the cathode plane of the half-cell that is designed to be resonant at the second harmonic of the main frequency, i.e. at 2.6 GHz, and this region will be held at a DC bias. The combination of this structure design will allow us to gate the electrons over the desired range of RF phase.

SIMULATIONS OF HIGH CURRENT MAGNETIC HORN STRIPLINES AT FERMILAB

T. Sipahi, S. V. Milton², S. G. Biedron^{1,2}, Department of Electrical & Computer Engineering,
Colorado State University (CSU), Fort Collins, CO, 80523, USA

¹also at Faculty of Electrical Engineering, University of Ljubljana, Slovenia

²also at Element Aero, Chicago, IL 60643 USA

R.M. Zwaska, J. Hysten, FNAL, Batavia, IL 60510, USA

Abstract

Both the NuMI (Neutrinos and the Main Injector) beam line, that has been providing intense neutrino beams for several Fermilab experiments (MINOS, MINERVA, NOVA), and the newly proposed LBNF (Long Baseline Neutrino Facility) beam line, which plans to produce the highest power neutrino beam in the world for DUNE (the Deep Underground Neutrino Experiment), need pulsed magnetic horns to focus the mesons that decay to produce the neutrinos. The high-current horn and stripline design has been evolving as NuMI reconfigures for higher beam power and to meet the needs of the future LBNF program. We evaluated the two existing high-current striplines for NuMI and NOvA at Fermilab by producing Electromagnetic simulations of the magnetic horns and the required high-current striplines. In this paper, we present the comparison of these two designs using the ANSYS Electric and ANSYS Maxwell 3D codes with special attention on the critical stress points. These results are being used to support the development of evolving horn stripline designs to handle increased electrical current and higher beam power for NuMI upgrades and for the LBNF experiment.

GENERAL CONCEPT

Neutrino beam production from proton accelerators can be described as follows. First, the protons are accelerated to a suitable energy in a particle accelerator. The accelerated protons are extracted from the accelerator and directed on to a target where the protons interact with the target material, producing a large number of secondary pions among other particles. Shaped magnetic fields created by focusing horns are used to select out pions of the preferred charge, and focus them into a collimated beam. This pions subsequently decay to muons and the muons decay into an intense neutrino beam. The horns are fed high current, necessary to generate the required field, through striplines as shown in Fig. 1.

Realistic simulations of the horns and striplines are required. These will be used to study both the performance of the system as well as the potential for stress induced structural damage to the striplines and the horn structure.

In this paper our main interest is focused on the evaluation of the existing fatigue failure of the 700-kW high-current stripline and comparison of it with the 400-kW design. Each of these two stripline designs were

operated on horn 1 for the NuMI and NOvA at Fermilab experiments.

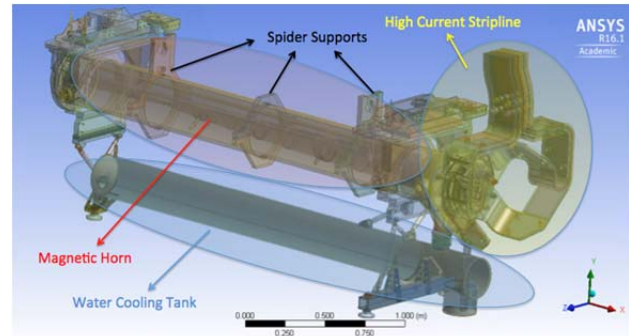


Figure 1: 3D model of the attached magnetic horn 1 (red section), the 700-kW high current stripline (yellow section), water cooling tank (blue section) and spider supports.

400 kW AND 700 kW HIGH-CURRENT STRIPLINE GEOMETRIES

Figures 2 and 3 show two different geometries for the connections between the striplines and the horns and each have their advantages and disadvantages. The stripline shown in Fig. 2 (400-kW design) is an older and larger version; it has proven itself durable in fatigue resistance and overall robustness. The stripline shown in Fig. 3 (700-kW design) has been designed as a more compact structure to accommodate a larger radius on the beam axis, reducing beam heating and increasing air cooling. In comparison to the older design this new design exhibits less symmetry. Also the L-shaped flag plates have been changed to chamfered plates in the new design.

As seen in Figs. 2 and 3 the high-current striplines are constructed as parallel conductors to minimize the magnetic fields external to the horn. However, this electric current does create a local magnetic field and force that has a significant impact on the long-term performance of the striplines; therefore, one needs to evaluate this magnetic field and determine its effect on the striplines.

ACCELERATION SYSTEM OF BEAM BRIGHTNESS BOOSTER

V. Dudnikov[#], Muons, Inc. Batavia, IL, USA
A. Dudnikov, BINP, Novosibirsk

Abstract

The brightness and intensity of a circulating proton beam can now be increased up to the space charge limit by means of charge exchange injection or by electron cooling, but cannot be increased above this limit. Significantly higher brightness can be produced through charge exchange injection with space charge compensation [1]. The brightness of the space charge compensated beam is limited at low level by the development of electron-proton (e-p) instability. Fortunately, e-p instability can be self-stabilized at a high beam density. By development of surface plasma sources (SPS) with cesiation and RFQ, an H⁻ beam injector was prepared with intensity ~0.1 A. Now we are ready to produce a “superintense” circulating beam with intensity and brightness far above the space charge limit. A beam brightness booster (BBB) for significant increase of accumulated beam brightness is discussed. An accelerating system with a space charge compensation is proposed and described. The superintense beam production can be simplified through the development of a nonlinear, nearly integrable focusing system with broad spread of betatron tune and a broadband feedback system for e-p instability suppression [2].

INTRODUCTION

Charge Exchange Injection (CEI) was developed to increase a circulating beam's intensity and brightness above injected beam parameters by multiturn injection of beam into the same transverse phase space areas (Non **liuvillian** injection) [3,4,5]. At that time, the intensity of the H⁻ beam from the plasma source was below 5 mA, with a normalized emittance of $\sim 1 \pi$ mm mrad. The intensity of the H⁻ beam from charge exchange sources went up to 15 mA, but the brightness B of this H⁻ beam was ~ 100 times less than the brightness of a primary proton beam because only 2% of proton beam was converted into H⁻ ions. In this situation, increase of the circulating beam's brightness by up to 100 times was necessary to reach the brightness of the primary proton beam, which can be used for one or several turn injection. The intensity and brightness of H⁻ ion beams was increased by orders of magnitude by the admixture of a trace of cesium into gas discharges (cesiation effect) [6]. After development of surface plasma source (SPS) with cesiation, H⁻ beam intensity was increased up to 0.1 A with emittance $\sim 0.2 \pi$ mm mrad, [7,8] and the brightness of the injecting beam became close to the space charge limit of a real accelerator such as the Fermilab booster [9]. With such a beam, it is impossible to further increase

circulating beam brightness, but CEI is routinely used for rising the circulating beam intensity for many orders by injection into different parts of the transverse phase space (painting in the transverse phase space) [5,9,10]. Further increasing circulating beam brightness is possible by using multiturn CEI with space charge compensation by particles with opposite charge (electrons or negative ions) [1,11,12]

Unfortunately, such a possibility is complicated by strong transverse two beam instability, which is driven by beam interaction with accumulated compensating particles in the circulating beam.

The strong instability with fast loss of bunched beam was discovered in 1965 at a small scale proton storage ring (PSR) during the development of charge exchange injection, and was stabilized by feedback [3, 4, 5, 12, 13]. This instability was explained in [4] as an inversed variant of the strong transverse instability of a circulating electron beam caused by interaction with compensated ions (beam- ion instability) predicted in 1965 by B. Chirikov [14]. An analogue of this instability, electron proton (e-p) instability, was observed experimentally with very low threshold at the same time during accumulation of a coasting beam [1, 5, 11-13]. The e-p instability of the coasting beam was in a good agreement with theory [14,15].

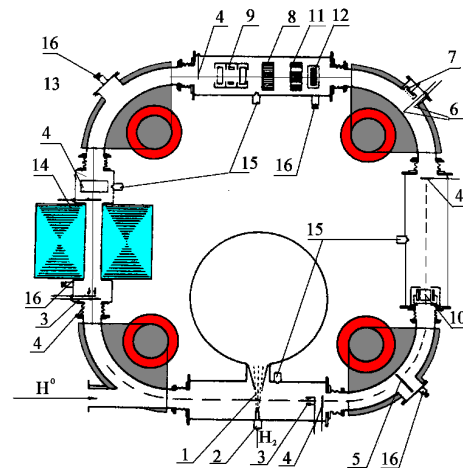


Figure 1: Schematic of a storage ring with diagnostics and control.

1-stripping gas target; 2-gas pulser; 3-Faraday Cup; 4-Quartz screen; 5, 6-moving targets; 7-ion collectors; 8-current monitor; 9-Beam Position Monitor; 10-Quadrupole pick ups; 11-magnetic BPM; 12-beam loss monitor; 13-detector of secondary particles density; 14-inductor core; 15-gas pulses; 16-gas leaks.

[#] Vadim@muonsinc.com

POSITIVE AND NEGATIVE IONS RADIO FREQUENCY SOURCES WITH SOLENOIDAL MAGNETIC FIELD*

V. Dudnikov[#], R. Johnson, Muons, Inc., Batavia, IL, USA

B. Han, S. Murrey, T. Pinnisi, C. Piller, M. Santana, C. Stinson, M. Stockli, R. Welton,
ORNL, Oak Ridge, TN, USA

G. Dudnikova, UMD CP, MD, USA; ICT SBRAS, Novosibirsk, Russia

Abstract

Operation of Radio Frequency Surface Plasma Sources (RF SPS) with a solenoidal magnetic field are described. RF SPS with solenoidal and saddle antennas are discussed. Dependences of beam current and extraction current on RF power, gas flow, solenoidal magnetic field and filter magnetic field are presented. H⁺ beam current up to 100 mA. Efficiency 100 mA/kW. H⁻ beam current up to 30 mA. Efficiency up to 6 mA/kW.

INTRODUCTION

Efficiency of plasma generation in Radio Frequency (RF) ion source can be increased by application of a solenoidal magnetic field [1-9]. A specific efficiency of positive ion generation was improved by the solenoidal magnetic field from 5 mA/cm² kW to 200 mA/cm² kW [8,9]. Chen [10] present explanation for concentration of a plasma density near the axis by magnetic field through a short circuit in a plasma plate. Additional concentration factor can be a secondary ion-electron emission initiated by high positive potential of plasma relative the plasma plate. The secondary emission can be increased by cesiation-injection of cesium for increase of the secondary negative ion emission [11-14], increasing a secondary electron and photo emission.

RF ION SOURCE IN SNS TEST STAND

RF ion source was installed in Spallation Neutron Source (SNS) test stand. A design of ion source and Low Energy Transportation channel (LEBT) is shown in Fig. 1. The RF ion source consist of AlN ceramic chamber with a cooling jacket from keep. At a left side is attached an RF assisted Triggering Plasma Gun (TPG). At a right side is attached a plasma electrode with an extraction system. The discharge chamber is surrounded by a saddle (or solenoidal) antenna. The LEBT at right side consist of accelerator electrode and two electrostatic lenses focusing a beam into a hole of 7.5 mm diameter in a chopper target. The second lens consists of four electrically insulated quadrants, which allow for chopping the beam to form an extraction gap inside the accumulator ring. In addition, the voltages on the quadrants can be varied individually to steer the beam for improving the transmission through the RFQ [15]. In more detail extraction system is presented in Fig. 2. The plasma plate (1) have a collar (2) with a conical converter surface. Cs oven (3) for decomposition of

Cs₂CrO₄ cartridges is attached to the collar. The extractor electrode (5) is attached to the plasma plate through ceramic insulator (4). Permanent magnet bars (6) is inserted into the water cooled plasma electrode (5). A ferromagnetic insert (8) can be used for shaping the magnetic field. Accelerating electrode (7) is used for accelerating of extracted ions up to 65 keV.

A plasma is generated by a current in antenna. Solenoidal magnetic field is concentrate the plasma on the axis. A transverse magnetic field generated by permanent magnet (6) located inside the water cooled extractor (5), bend the plasma flux, preventing electrons to escape the plasma. A configuration of the transverse magnetic field is shown in Fig. 1 (below). The plasma outside a 6 mm diameter impacts on the conical surface of a Mo converter, where H⁻ ions are formed. The H⁻ production is enhanced by lowering the Mo work function by adding a partial monolayer of Cs. Negative ions that drift into the source outlet are extracted by its potential of the extractor-electron dump. The extractor, which has a 6 mm aperture, is have a potential up to 8 kV. The 1 kG dipole field integrated into the extractor drives the co-extracted electrons sideways. Most of them are intercepted by the electron dump, which is kept near -57 kV with a +8 kV supply located on the -65 kV platform. The -65 keV H⁻ beam emerges from the extractor and is focused by two electrostatic lenses into the hole of diameter 7.5 mm in a chopper target.

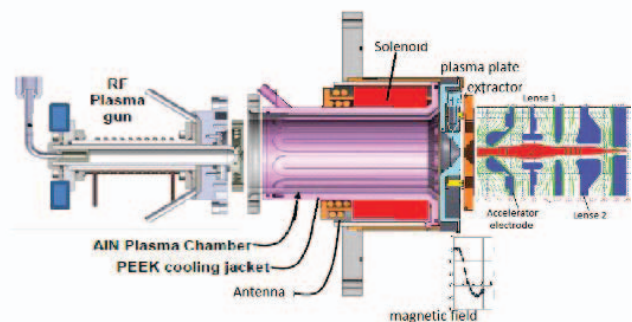


Figure 1: Design of RF Ion Source and LEBT.

EXPERIMENTAL RESULTS

Typically, 200 W from a 600 W, 13 MHz amplifier generates a TPG continuous low-power plasma. Cathode TPG is biased at 310 V with a current ~10 mA. The high current beam pulses 1 ms, up to 60 Hz are generated by up to 50 kW from a pulsed 80 kW, 2 Mz amplifier, connected to the antenna through insulating transformer and matching network. A discharge is triggered at pulsed power $P_{rf} = 3.8$ kW, antenna current $I_{ant} = 120$ A, antenna

* Work supported in part by US DOE Contract DE-AC05-00OR22725 and by STTR grant, DE-SC0011323.

[#] email address: Vadim@muonsinc.com

THE MUON INJECTION SIMULATION STUDY FOR THE MUON g-2 EXPERIMENT AT FERMILAB*

S. Kim[†] and D. Rubin, Cornell University, Ithaca, NY, USA
 D. Stratakis, Fermi National Accelerator Laboratory, Batavia, IL, USA
 N. S. Froemming, University of Washington, Seattle, WA, USA

Abstract

The new experiment, under construction at Fermilab, to measure the muon magnetic moment anomaly, aims to reduce measurement uncertainty by a factor of four to 140 ppb. The required statistics depend on efficient production and delivery of the highly polarized muon beams from production target into the g-2 storage ring at the design "magic"-momentum of 3.094 GeV/c, with minimal pion and proton contamination. We have developed the simulation tools for the muon transport based on G4Beamline and BMAD, from the target station, through the pion decay line and delivery ring and into the storage ring, ending with detection of decay positrons. These simulation tools are being used for the optimization of the various beam line guide field parameters related to the muon capture efficiency, and the evaluation of systematic measurement uncertainties. We describe the details of the model and some key findings of the study.

INTRODUCTION

The Muon g-2 Experiment, at Fermilab [1], will measure the muon anomalous magnetic moment, α_μ to unprecedented precision: 0.14 parts per million. This four-fold improvement in experimental precision compared to Brookhaven's experiment [2], could establish beyond doubt a signal for new physics if the central value of the measurement remains unchanged. To perform the experiment, a polarized beam of positive muons is injected into a storage ring with a uniform magnetic field in the vertical direction. Since the positron direction from the weak muon decay is correlated with the spin of the muon, the precession frequency is measured by counting the rate of positrons above an energy threshold versus time. The g-2 value is then proportional to the precession frequency divided by the magnetic field of the storage ring.

Achieving the targeted precision requires optimum transmission of polarized muons within the g-2 storage ring acceptance. The goal of this paper is to develop a simulation model for the Fermilab g-2 experiment. While emphasis in our previous work [3] was given to the beam-lines upstream to the storage ring, here we detail our injection to the storage ring scheme as well as evaluate the performance of the ring after multi-turn operation.

* Supported by DOE DE-SC0008037.

[†] sk2528@cornell.edu

MUON CAMPUS BEAMLINE

Protons with 8 GeV kinetic energy are transported via the M1 beamline to a Inconel target at AP0. Within a 1.33 s cycle length, 16 pulses with 10^{12} protons and 120 ns full length for each, are arriving at the target. Secondary beam from the target will be collected using a lithium lens, and positively-charged particles with a momentum of 3.1 GeV/c ($\pm 10\%$) will be selected using a bending magnet. Secondary beam leaving the Target Station will travel through the M2 and M3 lines which are designed to capture as many muons with momentum 3.094 GeV/c from pion decay as possible. The beam will then be injected into the Delivery Ring (DR). After several revolutions around the DR, essentially all of the pions will have decayed into muons, and the muons will have separated in time from the heavier protons. A kicker will then be used to abort the protons, and the muon beam will be extracted into the new M4 line, and finally into the new M5 beamline which leads to the (g-2) storage ring (Fig. 1). Note that the M3 line, DR, and M4 line are also designed to be used for 8 GeV proton transport by the Mu2e experiment.



Figure 1: Layout of the Fermilab Muon Campus.

Detailed numerical simulations [3] indicate that at the end of M5, the number of muons per proton on target (POT) within the acceptance $\Delta p/p = \pm 0.5\%$ is $\approx 2.0 \times 10^{-7}$. The beam is centered at 3.091 GeV/c with a spread $\Delta p/p = 1.2\%$ and is 96% polarized.

MUON BEAM INJECTION INTO THE STORAGE RING

The M5 beamline leads the muon beam to the entrance of the muon storage ring. The storage ring is a dipole magnet which provides the 1.451 T, uniform magnetic field (B_0) over the muon storage region. The radius of the storage ring is 7.112 m (R_0) by the center position of the

UPDATE ON PHOTONIC BAND GAP ACCELERATING STRUCTURE EXPERIMENT

J. Upadhyay and Evgenya I. Simakov

Los Alamos National Laboratory, Los Alamos, NM 87545, USA

Abstract

Photonic band gap (PBG) structures have great potential for filtering higher order modes (HOMs) without perturbing the fundamental mode and for suppressing the wakefields. An efficient PBG structure would help to improve the beam quality for high beam current future particle accelerators. A new design of X-band normal conducting PBG accelerating structure with inner elliptical rods is presented. This new optimized PBG structure would be fabricated and tested for RF breakdown at SLAC. The wakefield suppression experiment at Argonne Wakefield Accelerator (AWA) test facility is planned. The status of the experiment is reported.

INTRODUCTION

The future more compact particle accelerator with higher intensity, higher power will require higher frequency structures. The problem associated with the high frequency structures are higher order modes (HOM), excited by high current electron beam. These higher order modes interact with high current beam and disrupt them. The beam disruption or beam break up (BBU) instability is one of the biggest obstacles on the path to high current accelerators. High beam current accelerators are needed for future light sources and higher luminosity colliders. The photonic band gap accelerating structure provides a possibility to absorb HOMs and suppress the wakefields.

PBG structures are periodic structure (metallic, dielectric or both) which allows to confine the drive mode and damp higher order modes. PBG structures must be tested for acceleration and wakefield suppression [1, 2].

WAKEFIELD EXPERIMENT

A room temperature traveling-wave PBG accelerating structure operating at 11.700 GHz was built and successfully tested for wakefield suppression at Argonne wakefield accelerator (AWA) facility at Argonne national lab. This is a 16 cell travelling wave $2\pi/3$ mode PBG structure which has 9 times the operational frequency of the AWA facility. The PBG structure is electroformed and could not be brazed due to internal stresses, a vacuum compatible epoxy was used to attach the components. Due to the use epoxy the vacuum chamber containing the PBG structure could not reach ultra-high vacuum. To isolate and protect the cesium telluride photocathode used in the photo injector in AWA facility the vacuum chamber containing the PBG structure is separated from the beamline with a thin Beryllium (Be) window (178 micron). The experiment on the wakefield suppression

experienced a strong noise due to the scattering of electron beams through this Be window. The iris diameter of the PBG structure is 6.3 mm and the transverse rms size of the electron beam could be up to a few millimetres.

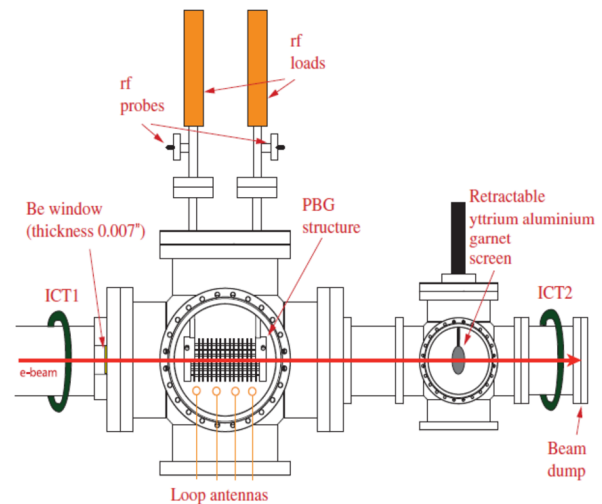


Figure 1: The experimental setup on the beam line at Argonne Wakefield Accelerator.

In the original wakefield experiment a good fraction of electron beam was hitting the front of the PBG structure and not entering the beam pipe of PBG structure. The experimental setup to do the wake field suppression experiment at AWA is shown in Figure 1. In order to understand how to send the beam through the PBG structure a series of experiment were done at AWA facility with three different thickness (30, 75, 127 micron) Be window. The beam size was measured before and after these window with different charges and different beam energies.

Based on these experiments (Table 1), a 30 micron Be window is chosen and another wakefield suppression experiment is planned. We will also demonstrate the beam acceleration/deceleration by powering the PBG structure and placing a spectrometer after the PBG structure.

MODELING AND SIMULATION OF RFQS FOR ANALYSIS OF FIELDS AND FREQUENCY DEVIATIONS WITH RESPECT TO INTERNAL DIMENSIONAL ERRORS *

Y. W. Kang, S.-W. Lee, ORNL, Oak Ridge, TN, USA

Abstract

Performance of radio frequency quadrupole (RFQ) is sensitive to the errors in internal dimensions which shift resonance frequency and distort field distribution on the beam axis along the structure. The SNS RFQ has been retuned three times to compensate the deviations in frequency and field flatness with suspected dimensional changes since the start of the project for continuous operation with H⁻ ion beams. SNS now has a new RFQ as a spare that is installed in beam test facility (BTF), a low energy test accelerator. In order to understand and predict the performance deviation, full 3D modeling and simulation were performed for the SNS RFQs. Field and frequency errors from hypothetical transverse vane perturbations, and vane erosion (and metal deposition such as Cesium introduced by the ion source operation) at the low energy ends are discussed.

INTRODUCTION

SNS project now has two RFQ structures: the first one being used in the SNS linac that was built and delivered at the beginning of the project in 2002 and the second one built as a spare and delivered in 2014. The new RFQ is now installed in BTF that is a separate low energy test accelerator for full tests of the new RFQ with beam and future science [1]. Both RFQs have the vanes designed for the same particle beam dynamics. Figures 1(a) and 1(b) show the cross sections of the two RFQs. The first SNS RFQ has a square wall cross section in two layers, outer layer in GlidCop for strength and the inner layer in OFHC copper. The second RFQ has an octagonal wall cross section in a single layer copper structure. The first RFQ was built with PISLs while the second one employed end-wall rods for dipole mode stabilization.

An RFQ is tuned for the design field distribution and the resonance frequency of the quadrupole mode after manufacturing. In this tuning process, bead-pull measurements [2] are usually performed in the four RFQ quadrants near vane gaps (point A) or near the wall (close to point C) as indicated in Figure 2(b) since the narrow gap length on the beam axis between the vanes (point B) makes it hard to pull a bead. Slug tuners shown in Figures 1(a) and 1(b) are used to tune the measured fields to the design fields. Magnetic pickup probes measure the fields with magnetic fields near the cavity wall at point C in each quadrant as shown in Figure 2(b).

In 2003 and 2009, the RFQ was found detuned with the

distorted fields and the shifted resonance. The incidents caused investigation of the problems using computer simulations of the structure [3]. Then, distorted fields were found in 2013 with unknown reason. Slight degradation of performance of the RFQ led to the findings. The RFQ structure was retuned successfully and reused for operation every time. In the third incident, the field error resembled the fields expected with reduced capacitance at the low energy end of the vanes. Thus, for suspected erosion of the vane ends at the low energy end, 3D RF simulation was performed. Borescope image of the vanes at the low energy entrance of the RFQ is shown in Figure 2. The image is not clearly showing if vane erosion occurred in the RFQ. Figures 2(b) and 2(c) show the vane erosions modeled for the 3D RF simulation.

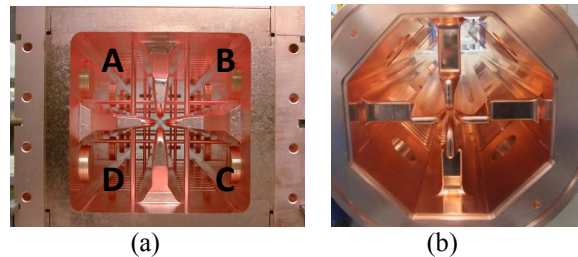


Figure 1: Internal views of the two SNS RFQs at the low energy end: (a) first RFQ being used for neutron production and (b) new RFQ installed in BTF.

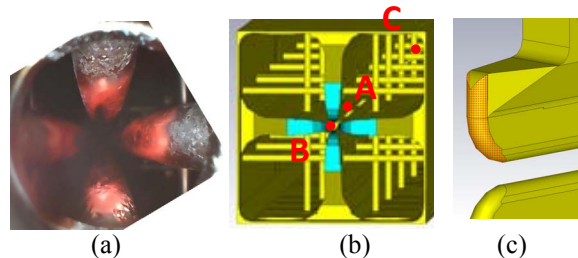


Figure 2: (a) Borescope image of the vane ends at the low energy entrance (2015) of the first RFQ. (b), (c) The models setup for the 3D RF simulations of the RFQs.

Figure 3(a) shows the initial fields and the fields after the two incidents of detuned RFQ that distorted the field flatness up to $\pm 15\%$ and shifted the resonance by -420 kHz and -230 kHz, respectively. The averages of the fields in four quadrants are shown. The four quadrants are numbered following the definition in Figure 1. Figures 3(b) – 3(e) show the third finding of the field error in 2013 and subsequent retuning for the field flatness in the RFQ structure. Figure 3(b) shows the retuned fields in 2009 and Figure 3(c) shows the tilted field found in 2013. The field error was tuned again for a better field flatness (Fig 3(d)). This time the tuning was performed by using

* ORNL is managed by UT-Battelle, LLC, under contract DE-AC05-00OR22725 for the U.S. Department of Energy. This research was supported by the DOE Office of Science, Basic Energy Science, Scientific User Facilities.

SIMULATION OF A SKEW PARAMETRIC RESONANCE IONIZATION COOLING CHANNEL

Yu Bao*, University of California, Riverside, CA 92535, USA

R. P. Johnson, Muons, Inc., Batavia, IL 60510, USA

A. Sy, Y. Derbenev, V.S. Morozov, Jefferson Lab, Newport News, VA 23606, USA

A. Afanasev, George Washington University, Washington, DC 20052, USA

Abstract

Skew Parametric-resonance Ionization Cooling (Skew-PIC) is designed for the final 6D cooling of a high-luminosity muon collider. Tracking of muons in such a channel has been modeled in MAD-X in previous studies. However, the ionization cooling process has to be simulated with a code that can handle matter dominated beam lines. In this paper we present the simulation of a Skew-PIC channel using G4beamline. We implemented the required magnetic field components into G4beamline and compared the tracking of muons by the two different codes. We optimized the cooling channel and present the muon cooling effect in the Skew-PIC channel for the first time.

INTRODUCTION

A muon collider has many advantages comparing to electron-positron colliders and hadron colliders: muons are 207 times heavier than electrons so the synchrotron radiation is small when the muons are accelerated in a ring; muons are leptons and their colliding interactions are cleaner than those in hadron colliders which involves many protons colliding over a wide range of energies.

Ionization cooling is the most effective method to cool the muon beam from the large initial emittance. In order to reach the required luminosity of $10^{34} \text{ cm}^{-2} \text{ sec}^{-1}$, the muons are cooled in a series of cooling stages and the final cooling stage requires an extremely strong magnetic field. The parametric resonance ionization cooling (PIC) method [1] is designed to avoid such a strong magnetic field while providing a significant cooling effect. It induces a parametric resonance in the cooling channel, and focuses the beam in both horizontal and vertical planes with the period of the channel's free oscillations.

The theory and analytic calculations of the PIC channel has been developed. A twin-helix cooling scheme [2] has been designed and simulated to practice the PIC channel. However, it is found that the non-linear resonance caused by the multipole fields introduces an instability to the beam. To overcome the non-linear resonance problem, the concept of Skew-PIC has been developed: the canonical betatron tunes are shifted from their resonant values and the point-to-point focusing needed for PIC is preserved.

Figure 1 shows an example of the Skew-PIC channel. The magnetic field in the channel consists of dipole, quadrupole and skew quadrupole components (in the coupled case), and

the muon dynamics in such a channel with high-order fields correction is simulated in in MAD-X [3]. However, the cooling effect of the Skew-PIC channel requires involvement of beam-matter interactions, which MAD-X can not handle. In this work we implemented the required magnetic fields into G4beamline [4], and compared the tracking of muons by G4beamline and MAD-X. We then present the cooling effect of the Skew-PIC channel and outline further improvement steps for future work.

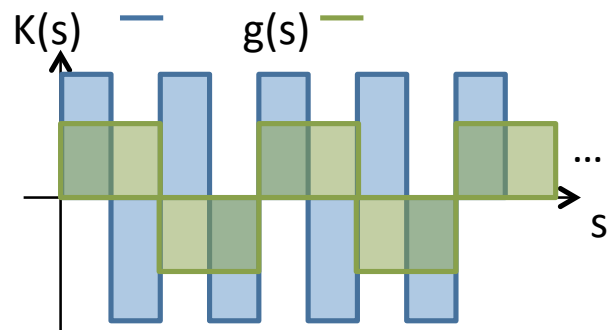


Figure 1: Curvature $K(s)$ and skew quadrupole coefficient $g(s)$ along the skew-PIC cooling channel's length s .

MULTIPOLE FIELDS IN G4BEAMLINE

Since Skew-PIC channel requires high-order fields in a bent magnet, we implement a magnetic field expansion in such a channel. In reference [5] this expansion is calculated in a bent solenoid up to the octupole order, and ready-to-use expressions for the magnetic field is given. We implemented this expansion into G4beamline and benchmarked the code with MAD-X simulations.

Figure 2 shows the trajectory of the reference particle in the uncoupled PIC channel simulated by MAD-X (upper plots) and G4beamline (lower plots). In MAD-X, the reference particle follows the centerline perfectly since MAD-X integrates the transportation matrix. However, the reference particle oscillates around the centerline in G4beamline: as the tracking distance becomes longer, the tracking error becomes greater. This is because G4beamline is tracking the particle step by step, and each step has a small error, which causes the overall error after a long distance. But this error (less than 1 mm in 160 m long channel) is acceptable.

Figure 3 shows the tracking of a gaussian distributed muon beam in the above PIC channel. The beam information is recorded at certain s positions along the channel. The

* Email: yubao@ucr.edu. This work is supported by Muons Inc.

MODULATOR SIMULATIONS FOR COHERENT ELECTRON COOLING

J. Ma¹, G. Wang², X. Wang¹, R. Samulyak^{1,2}, V. N. Litvinenko^{1,2}, K. Yu²

¹Stony Brook University, Stony Brook, New York 11794, USA

²Brookhaven National Laboratory, Upton, New York 11973, USA

Abstract

Highly resolved numerical simulations of the modulator, the first section of the proposed coherent electron cooling (CEC) device, have been performed using the code SPACE. The beam parameters for simulations are relevant to the Relativistic Heavy Ion Collider (RHIC) at Brookhaven National Laboratory (BNL). Numerical convergence has been studied using various numbers of macro-particles and mesh refinements of computational domain. A good agreement of theory and simulations has been obtained for the case of stationary and moving ions in uniform electron clouds with realistic distribution of thermal velocities. The main result of the paper is the prediction of modulation processes for ions with reference and off-reference coordinates in realistic Gaussian electron bunches with quadrupole field.

INTRODUCTION

Coherent electron cooling (CEC) [1,2] is a novel technique for rapidly cooling high-energy, high-intensity hadron beams. CEC consists of three sections: a modulator, where the ion imprints a density wake on the electron distribution, an amplifier, where the density wake is amplified, and a kicker, where the amplified wake interacts with the ion, resulting in dynamical friction for the ion. Figure 1 illustrates a general schematic of CEC.

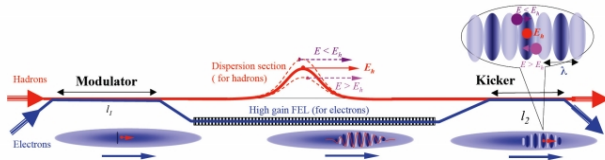


Figure 1: Schematic of coherent electron cooling concept.

Table 1: Parameters of Electron and Ion Beams

	Electron	Ion, Au ⁺⁷⁹
Beam energy	$\gamma=42.9$	$\gamma=42.9$
Peak current	100 A	
Bunch intensity	10 nC	1e+9
Bunch length	10 ps (full)	2 ns (r.m.s)
R.M.S. emittance	5π mm mrad	2π mm mrad
R.M.S. energy spread	1e-3	
Beta function	4 m	

Beam parameters for numerical simulations are relevant to Relativistic Heavy Ion Collider (RHIC) at the

Brookhaven National Laboratory (BNL), which are listed in Table 1.

METHODS AND TOOLS

SPACE, a parallel, relativistic, 3D electromagnetic Particle-in-Cell (PIC) code [3] has been used for the study of plasma dynamics in a dense gas filled RF cavities [4], and the study of mitigation effect by beam induced plasma [5]. SPACE contains modules for solving equations in electrostatic approximation. The module was used in present work as the modulation problem is electrostatic in co-moving frame. This module employs two different approaches. One is traditional PIC method for Poisson-Vlasov equation, which is effective for uniform beam and periodic boundary condition. The other is adaptive Particle-in-Cloud (AP-Cloud) method [6] that replaces traditional PIC mesh with an adaptively chosen set of computational particles, which is beneficial for non-uniform beams, geometrically irregular computational domains and mixed type boundary conditions.

Mechanism for modulation process is Coulomb interactions between ions and surrounding electrons. For relativistic beam energy, the relative density modulation of electrons due to their interaction with ions is orders of magnitudes smaller than unity. Therefore it is viable to treat each ion individually and use superposition principle to obtain net responses of electrons to all ions in the beam. Analytical solution of electrons' response to a moving ion exists for electrons with uniform spatial distribution [7]. For spatially non-uniform electrons, numerical approaches are employed either by solving the Vlasov equation [8], or by direct macro-particle simulation [9]. One of the difficulties in a macro-particle simulation is the fact that the modulation signal is too weak compared to the shot noise resulting from the discreteness of macro-particles. To extract modulation signal from shot noise, we perform two simulations with identical initial electron distribution. One simulation operates only with electron beam while the other simulation contains the electron beam and an ion. With the assumption that the Coulomb force from an ion only slightly changes the trajectories of the electrons over modulator, the influences of the ion can be obtained by taking difference in the final electron distributions of the two simulations. Similar approach has been successfully applied to simulate the FEL amplification process in the presence of shot noise [10].

NUMERICAL CONVERGENCE

Various numbers of macro-particles and refinements of computational domain are used to study the numerical convergence. Typical results are shown in Fig. 2.

DESIGN OF RFQ LINAC TO ACCELERATE HIGH CURRENT LITHIUM ION BEAM FROM LASER ION SOURCE FOR COMPACT NEUTRON SOURCE

S. Ikeda*, T. Kaneshue, and M. Okamura,
Brookhaven National Laboratory, Upton, NY 11973, USA

Abstract

To develop a high flux neutron source, we propose a linear accelerator systems with lithium beam generated by laser ion source. Because of the higher velocity of center of mass than that in the case of proton beam injection, generated neutrons are directed, and hence the flux is expected to be higher. In this research, we designed RFQ linac optimized to accelerate a high current lithium ion beam.

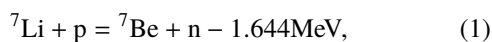
INTRODUCTION

Because the more opportunity of the usage of neutron source are required, compact neutron sources are developed for more conveniently and/or on the spot with lower cost than other neutron sources, such as nuclear reactors and spallation sources and spallation sources. The compact sources can be used to conduct nuclear data measurement [1], non-destructive inspection [2, 3] such as nuclear or explosive material detection in luggage size or cargo size container for security and the defect detection of buildings, and boron neutron capture therapy (BNCT) [4].

As compact neutron sources, there are small neutron generator using D-T reaction, electron linac for photoneuclear reaction, and MeV class proton accelerator with Li or Be target. Among them, the proton accelerator are for high flux neutron generation compared with the others. Linear accelerators are used and developed for the production of MeV class proton beam [5–7]. Typically, the energy range are from 2 MeV to 10 MeV and the current range are from 0.1 mA to 30 mA.

COMPACT NEUTRON SOURCE WITH LASER ION SOURCE

To provide higher neutron flux than conventional sources based on proton accelerators, we propose the linear accelerator using laser ion source. The conceptual design is shown in Fig. 1. The following reaction [8] is used for neutron production,



but lithium ions are injected into a target with protons. The advantage of the lithium injection is the larger center-of-mass velocity compared with proton injection. When proton beam is injected, neutrons are emitted in all direction. Meanwhile, if the lithium beam injected, the neutron scattering angle becomes smaller because the larger center-of-mass velocity

is added to the neutrons, which is expected to lead to higher flux within a solid angle.

The energy threshold of proton for the reaction ${}^7\text{Li}(p,n){}^7\text{Be}$ is 1.881 MeV [8]. Therefore, the energy of lithium needs to be more than 13.1 MeV. In this energy range, IH-Linac is used after RFQ linac typically. For example, the ions are accelerated to 300 keV/u by 3.2-m RFQ, and then 2 MeV/u by 2.5-m linac in injector line for RHIC in Brookhaven National Laboratory [9].

A solid lithium target are placed in the plasma production chamber as shown in Fig. 1. Ablation plasma containing Li^{3+} is produced by irradiation on the target with focused pulsed laser. The advantage of laser ion source is capability of producing 10 mA-class beam of fully stripped ion. In previous work, it was found that Li^{3+} can be produced by a table top laser.

After the production, the plasma drifts in the direction normal to the target surface and then is injected into the RFQ linac directly without low energy beam transport line. Since the plasma production chamber is charged up, the ion beam is extracted at the entrance of the RFQ linac. Typically, low energy transport line between ion source and RFQ linac is the problem for high current heavy ion beam acceleration. The space charge problem is avoided by injecting the drifting plasma into the RFQ linac directly. In a previous work, 20 mA of C^{6+} was accelerated using this scheme [10].

The accelerated beam is focused and bunched in MEBT line before injected into IH-linac in which the ions are accelerated to 13 MeV or more. Then the beam is injected in to the target containing proton, such as hydrogen gas, water, or Titanium hydride to produce neutron beam.

As a first step, we designed the RFQ linac to accelerate for high current beam of ${}^7\text{Li}^{3+}$ to 300 keV/u prioritizing output current rather than transmission. We used the simulation code, PARMTEQ.

RFQ DESIGN VALUES AND CALCULATION RESULTS

Table 1 shows the summary of the RFQ design parameters. The frequency was set as 100 MHz for high current beam acceleration. The input energy was determined from the previous laser ion source experiments in which the extraction voltage was 60 kV. The energy is also close to the typical RFQ injection energy. Mass to charge of ${}^7\text{Li}^{3+}$ is 3/7. Input transverse normalized total emittance was set as 1π mm mrad, and particle distribution was assumed to be four dimensional water bag. Input twiss parameter β was determined as the beam radius was the same as the minimum

* siked@bnl.gov

STABILIZED OPERATION MODE OF LASER ION SOURCE USING PULSED MAGNETIC FIELD

S. Ikeda*, M. Costanzo, T. Kanesue, R. Lambiase, C-J. Liaw, and M. Okamura,
Brookhaven National Laboratory, Upton, NY 11973, USA

Abstract

Laser ion source produces many types of ions with the electron beam ion source for experiments in Brookhaven National Laboratory. One laser and steady solenoidal magnetic field were used in the last run. For next run, we will employ two laser at the same time to improve the beam stability. In addition, we will use a pulsed magnetic field to control the beam profile flexibly. We measured the beam current at several points from the laser ion source to the following booster ring to compare the beam stabilities between the last and next run settings. The ratio of the standard deviation to the mean value of the total charge within a single beam pulse was found to be smaller at all measurement points with the next run setting.

INTRODUCTION

Many types of ion species are used for nuclear physics experiment at Relativistic Heavy Ion Collider and cosmic ray simulation at NASA Space Radiation Laboratory in Brookhaven National Laboratory. The ions are provided by the laser ion source (LIS) and the electron beam ion source (EBIS). Figure 1 shows the layout of the injector line. Singly charged ions are injected from the laser ion source into the EBIS where the ions are ionized to highly charged states. The ions are accelerated by RFQ accelerator and IH linac to 2 MeV/u, and then injected to the booster ring through the bending magnet.

In the laser ion source, the plasma is produced by laser ablation process in vacuum chamber and then drifts to the extraction electrodes through the drift section where the plasma extends to a certain width that determines the pulse width of the extracted beam. In the last run, one laser pulse for one beam pulse and 3 m solenoid to guide the plasma were used. The carbon beam was not stable compared with other species. The cause might be that the laser energy was as small as the ablation threshold and the solenoidal magnetic field was strong to meet the requirement of the higher beam currents than the design value. For the next run, we will employ two laser pulses at the same time to increase the laser energy. In addition, we installed a coil to produce pulsed magnetic field for more flexible control of the plasma and the beam profile while the steady solenoidal magnetic field will be decreased or not used. The purpose of this study is to examine whether the beam stability is improved with the next run setting. We measured the beam current at the current transformer 1 (CT 1), CT 2, CT 3, and the Faraday cup as shown in Fig.1. Then we compared the

standard deviation of the total charge within a single beam pulse.

DEVICES IN INJECTOR LINE AND THE EXPERIMENTAL CONDITIONS

Laser Ion Source

Figure 2 shows the schematic of the laser ion source. The detail is described in the reference [1]. Several types of solid targets placed in the vacuum chamber are irradiated with laser (Quantel Brilliant B TWINS, 1064 nm, 6 ns). Between the target and the extraction electrodes, the 3 m long solenoid used in the last run and the coil that will produce pulsed magnetic field from the next run are placed. The specifications of the magnets are shown in Table 1. The coil current is driven by a pulsed circuit composed of 7.5 μ F capacitor to rise the magnetic field during the time when the plasma passes through the coil. The equivalent circuit is shown in Fig.3. The current in the coil as a function of time is shown in Fig. 4.

Table 1: Magnet specifications used in laser ion source

	Last run	Next run
Magnet length	3 m	45 mm
Inner diameter	76 mm	80 mm
Turns	5728	330
Time structure	Steady	7 μ s rise time

For the experiment, graphite was used as target. As the last run settings, single laser with the energy of 550 mJ and 3 m long solenoid with the magnetic field of 2.3 mT were used. Meanwhile, as the next run settings, we irradiated the same spot on the target at the same time with two laser pulses. The total energy was 920 mJ. The pulsed magnetic field was triggered at the laser irradiation. The maximum field was 9.0 mT. For both cases, the laser spot size was 0.10 cm². The platform voltage of the laser ion source was 19 kV with respect to the laboratory ground, and the intermediate electrode voltage for extraction was -3.5 kV with respect to the platform voltage.

Electron Beam Ion Source

As explained in the reference [2], the EBIS is mainly composed of electron gun, high voltage tubes, and superconducting solenoid. The gun immersed in a magnetic field has capability of producing current up to 20 A. The electron beam goes through the high voltage tube that is surrounded by the solenoid with the magnetic field of 5 T. The diameter of the electron beam in the tubes is adjusted by changing

* siked@bnl.gov

DESIGN CONSIDERATIONS FOR THE FERMILAB PIP-II 800 MeV SUPERCONDUCTING LINAC*

A. Saini[†], Fermi National Accelerator Laboratory, Batavia, IL, USA

Abstract

Proton Improvement Plan (PIP)-II is a proposed upgrade of existing proton accelerator complex at Fermilab. It is primarily based on construction of a superconducting (SC) linear accelerator (linac) that would be capable to operate in the continuous wave and pulsed modes. It will accelerate 2 mA H⁺ ion beam up to 800 MeV. Among the various technical and beam optics issues associated with high beam power ion linacs, beam mismatch, uncontrolled beam losses, halo formation and potential element's failures are the most critical elements that largely affect performance and reliability of the linac. This paper reviews these issues in the framework of PIP-II SC linac and discusses experience accumulated in the course of this work.

INTRODUCTION

The Proton Improvement Plan –II is an aspiring program proposed for further enhancement of the existing Fermilab accelerator complex to support a world leading neutrino program and rich variety of high intensity frontier particle physics experiments at Fermilab. The most important part of the PIP-II is to build a new superconducting (SC) linear accelerator that would be capable to operate in the continuous wave (CW) regime.

A schematic of the linac baseline configuration is shown in Fig. 1. It consists of a room temperature front-end and an accelerating SC linac. The front-end is composed of a low energy beam transport (LEBT) section, an RFQ and, a medium energy beam transport (MEBT) section. The main accelerating part of the linac utilizes five families of superconducting cavities to accelerate the H⁺ ion beam from kinetic energy of 2.1 MeV to 800 MeV. On the basis of these families, SC linac is segmented into five sections i.e. half wave resonator, single spoke resonator (SSR) 1 & 2, low beta (LB) and high beta (HB). Each section in Fig. 1 is represented by optimal beta of respective cavities except LB and HB sections which are shown for geometrical beta of corresponding cavities. A detailed description of the PIP-II is presented elsewhere [1, 2].

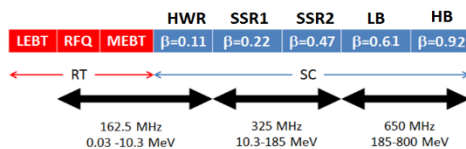


Figure 1: A schematic of acceleration scheme in the PIP-II SC linac. Red-coloured sections operate at room temperature while blue-coloured sections operate at 2K.

* Work supported by Fermi Research Alliance, LLC under Contracts No. De-Ac02-07CH11359 with the DOE, USA.

[†] asaini@fnal.gov

GENERAL

One of the major concerns related with the high intensity ion-linacs is the uncontrolled beam loss. An excessive beam loss might result in radio-activation that leads to interruptions in hands on maintenance, hazard to personal health and environment. This, in turn, keeps stringent limit on tolerable beam loss along the linac. A cumulative experience with high intensity beam operation at existing facilities such as LANSCE [3] was utilized to set a threshold limit of beam loss. An average beam loss below 1W/m at beam energy of 1GeV is considered a safe-operational limit across the accelerator community over the world.

LINAC DESIGN CONSIDERATIONS

A rigorous study is required to obtain a robust design of the ion linac that not only preserves the beam quality but also deals with different mechanisms which induce beam loss along the linac. In this paper we discuss the high intensity ion linac design considerations based on our experience gained over the years for a quest of a robust design of the PIP-II SC linac. Those considerations assist to control implications of principal beam loss mechanisms such as halo formation, beam mismatch, beam stripping, fault scenario etc.

SC Linac Acceptance

Acceptance of the linac is determined by the largest beam size that can be transmitted through the linac without any beam loss. Thus, acceptance is a vital parameter to measure the linac tolerances against potential errors. A large acceptance suggests less possibility of the uncontrolled beam loss and therefore, achieving a large acceptance is one of the primary considerations of the linac design.

Longitudinal Acceptance In an ion-linac, longitudinal acceptance is primarily outlined by its low energy part where beam is non-relativistic and bunch length is relatively longer. In order to achieve large acceptance, a strong adiabatic longitudinal focusing is required. Longitudinal phase advance (k_z) per meter for a non-relativistic ion beam is given as:

$$k_z^2 = \frac{2\pi q E_0 T_s \sin(-\phi_s)}{(\beta\gamma)^3 mc^2 \lambda}, \quad (1)$$

where β , γ are Lorentz factors for synchronous particle, ϕ_s , T_s are synchronous phase, transit time factor for synchronous particle respectively and, E_0 is accelerating field gradient. It can be noticed from eq. (1) that accelerating cavities need to be operated at large synchronous phases to avoid the phase slippage. Figure 2 shows synchronous

THE CENTER FOR BRIGHT BEAMS*

J. R. Patterson[†], G. H. Hoffstaetter, Cornell University, Ithaca, NY, USA
Y. K. Kim, University of Chicago, Chicago, IL, USA

Abstract

The Center for Bright Beams (CBB) is a new National Science Foundation Science and Technology Center. CBB's research goal is to increase the brightness of electron beams by a factor of up to 100 while reducing the cost and size of key technologies. To achieve this, it will join the capabilities of accelerator physicists with those of physical chemists, materials scientists, condensed matter physicists, plasma physicists, and mathematicians. This Center has the potential to increase the brightness of electron sources through better photocathodes, the efficiency and gradient of SRF cavities through deeper understanding of superconducting compounds and their surfaces, and better understanding of beam storage and transport and the associated optics by using new mathematical techniques. The Center currently involves ten universities and three national labs in the US and Canada, including a large and diverse team of students and postdocs.

INTRODUCTION

The NSF *Science and Technology Center (STC): Integrative Partnerships* program supports “innovative, potentially transformative, complex research and education projects that require large-scale, long-term awards.” The **Center for Bright Beams (CBB)** is a new STC with the mission to gain the fundamental understanding required to increase electron beam brightness by a factor of up to 100 while decreasing the size and cost of the key underlying technologies. The goal is to remove the brightness barriers to progress for a broad range of electron beam applications in science and industry, including FELs and synchrotron light sources, particle colliders, electron microscopes, and semiconductor fabrication and quality assurance. For each of these applications, the available beam brightness (current/emittance) limits progress.

In order to achieve its goal, CBB will combine the expertise of accelerator physicists, physical chemists, materials scientists, condensed matter physicists, plasma physicists, and mathematicians. It will tackle areas where better understanding of the underlying science has the potential for significantly improving the design or treatment of devices such as photoemission sources, superconducting cavities, and nonlinear optics. CBB will also focus on accelerator workforce development and increasing the diversity of accelerator scientists.

CBB is a collaboration of Brigham Young University, University of California Los Angeles, University of Chicago, Chicago State University, Clark Atlanta University, Cornell University (CU) (lead), University of Florida, University of Maryland at College Park, Morehouse

*Work supported by National Science Foundation Award #1549132

[†]jrp3@cornell.edu

College, University of Toronto, Fermi National Accelerator Laboratory, Lawrence Berkeley National Laboratory and TRIUMF.

RESEARCH PROGRAM

CBB has three Research Themes: Beam Production, Beam Acceleration, and Beam Storage and Transport.

Beam Production

The *Beam Production* theme will increase the brightness of electron sources by up to a factor of 100 by advancing the science of photocathodes. In a bright photoemission source, the electrons are emitted with small mean transverse energy (MTE) and experience a large accelerating field E_z . The transverse emittance $\epsilon_{2D,n}$ and 4-D brightness B_{4D} are given by

$$\epsilon_{2D,n} = \sigma_x \sqrt{MTE/mc^2} \propto \sqrt{MTE}$$

and

$$B_{4D} \propto \frac{E_z}{MTE}$$

respectively. CBB has identified four photocathode objectives shown in Fig. 1. At each stage, it will conduct beam tests. The ultimate goal will be a proof of principle experiment that uses record coherence length beams for ultrafast electron diffraction.

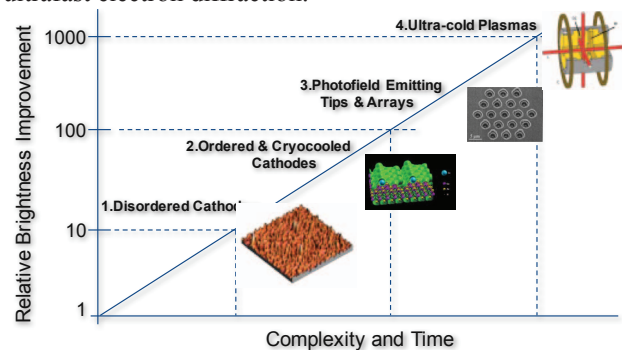


Figure 1: The Beam Production objectives, shown in order of increasing risk. In addition to these, CBB will demonstrate high resolution ultrafast electron diffraction.

Achieving these objectives requires an interdisciplinary approach. For example, materials scientist Hennig (Florida) will screen candidate photocathode materials, condensed matter physicist Arias (CU) will apply density functional theory to predict performance, Bazarov (CU) and physical chemists Hines (CU) and Padmore (LBNL) will synthesize photocathodes, and condensed matter physicists Muller (CU) and Shen (CU), together with Hines (CU), will characterize them using Scanning Tunneling Microscopy and ARPES respectively. Musumeci

EMITTANCE GROWTH FROM MODULATED FOCUSING IN BUNCHED BEAM COOLING

M.Blaskiewicz*

BNL, Upton, NY 11973, USA

Abstract

The low energy RHIC electron cooling (LEReC) project at Brookhaven employs a linac to supply electrons with kinetic energies from 1.6 to 2.6 MeV. Along with cooling the stored ion beam the electron bunches create a coherent space charge field which can cause emittance growth. This is the primary source of heating when the cooling is well tuned. An analytic theory of this process is presented and compared with simulations.

INTRODUCTION

The low energy RHIC electron cooling project is currently under construction at BNL. The goal is to improve RHIC luminosity at very low energies, aiding in the study of the equation of state of the quark-gluon plasma near its phase boundary. We are using an electron linac with bunch lengths of a few centimeters to cool gold beams with lengths of several meters. Figure 1 shows the relative scale of the electron and ion bunches. Previous work [1] has shown one

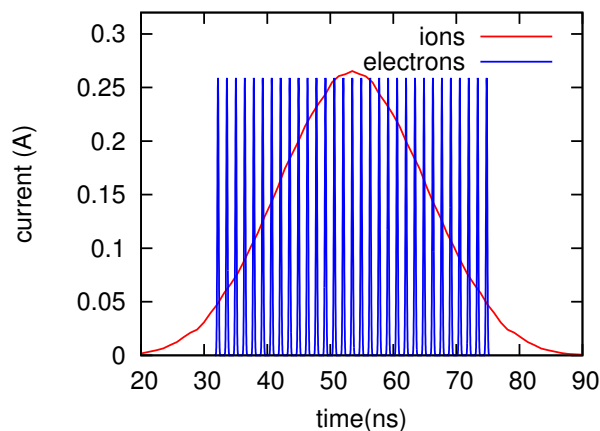


Figure 1: Longitudinal bunch structure for ions and electrons during cooling.

needs stable relative timing of the electron and ion bunches to avoid transverse heating of the ions. When the timing is stable the dominant ion heating mechanism is due to a combination of the space charge force from the electrons with the longitudinal intrabeam scattering (IBS) of the ions [2]. The idea is that longitudinal IBS causes the longitudinal action, and hence the synchrotron frequency, to vary. As the synchrotron tune varies the ions cross a variety of synchrotron resonances driven by the bunch structure of the

electron beam resulting in emittance growth. Figure 2 shows qualitative simulations of the beam emittance for early times and Figure 3 shows a more extensive simulation.

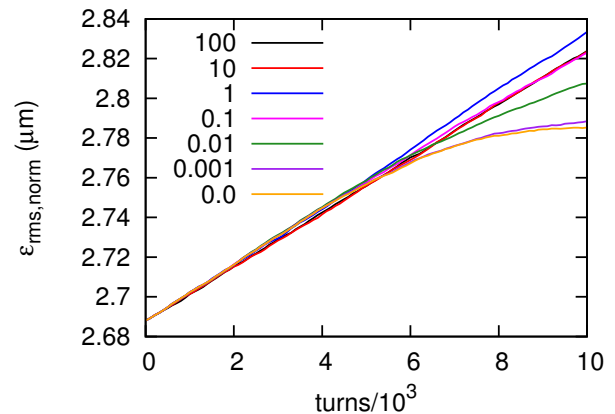


Figure 2: Emittance growth with electron bunches of 10 times nominal charge for a range of longitudinal IBS rates. The nominal IBS growth time is 650 seconds, labeled by 1. The labels are proportional to the rates, and saturation occurs for the nominal rate and faster rates.

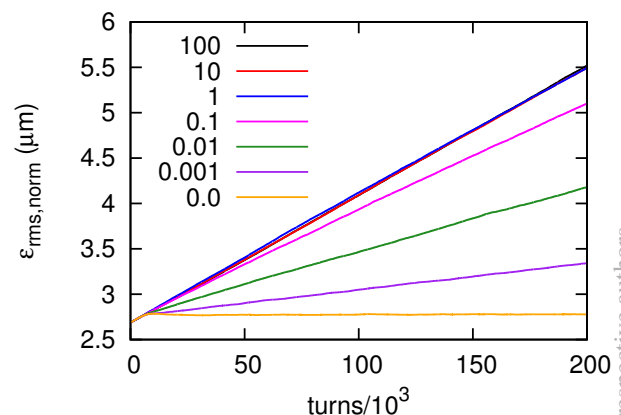


Figure 3: Emittance growth with electron bunches of 10 times nominal charge for a range of longitudinal IBS rates. This is an extended plot of the simulations in Figure 2

For the first few thousand turns IBS rates from zero through 100 times the nominal rate all yield the same rms emittance growth. After that the emittance growth rate depends weakly on the IBS rate. This effect as well as the detailed dependence of early emittance growth on various dynamical parameters can be explained.

* Work supported by the US Department of Energy under contract number DE-SC0012704

START-TO-END BEAM DYNAMICS OPTIMIZATION OF X-RAY FEL LIGHT SOURCE ACCELERATORS*

J. Qiang[#], LBNL, Berkeley, CA, 94720, USA

Abstract

State-of-the-art tools have been developed that allow start-to-end modeling of the beam formation at the cathode, to its transport, acceleration, and delivery to the undulator. Algorithms are based on first principles, enabling the capture of detailed physics such as shot-noise driven micro-bunching instabilities. The most recent generation of the IMPACT code, using multi-level parallelization on massively parallel supercomputers, now enables multi-objective parametric optimization. This is facilitated by recent advances such as the unified differential evolution algorithm. The most recent developments will be described, together with applications to the modeling of LCLS-II.

INTRODUCTION

High brightness, coherent x-ray free electron laser (FEL) light sources provide an invaluable tool for scientific discovery in biology, chemistry, physics, and material science. Most of these FEL light sources use an accelerator beam delivery system to generate high quality electron beam needed for coherent x-ray radiation in an undulator. In order to achieve the desired electron beam quality within a reasonable cost, the accelerator system needs to be carefully designed. Typically, the accelerator system consists of a photo-injector as a front end to produce a high brightness electron beam, a linear accelerator (or equivalent accelerator) to accelerate the electron beam to the designed energy and to compress the beam to high peak current, and a final beam transport system to deliver the beam for different radiation undulator stations. As the quality of the electron beam such as emittance, peak current, energy spread plays a critical role in the production of the coherent x-ray radiation, it is important to optimize the electron beam quality during the accelerator design. In past studies, the accelerator design was typically divided into two sections, the injector section and the linear accelerator (linac) section. The injector was designed using the theory of space-charge emittance compensation and the multi-objective beam dynamics optimization [1-8]. After the injector optimization, an optimal solution from the injector output was selected as an input to the downstream linear accelerator. Using the electron beam information from the injector, the linear accelerator was then designed using analytical model, single pass tracking, and multi-objective optimization [9-12]. However, it turns out that final beam quality does not only depend on the linear accelerator settings, but also depend on the initial electron beam distribution. An optimal solution from the injector

does not necessarily mean the best solution for the final beam quality. For example, the final electron beam longitudinal phase space distribution does not depend only on the peak current of the electron beam out of the injector, but also on its longitudinal phase space distribution. A highly nonlinear phase space distribution cannot be easily compressed in the linac to a high peak current at the end of the accelerator. In this paper, we report on start-to-end beam dynamics optimization using a multi-objective global optimization method and show an application to a future x-ray FEL light source LCLS-II accelerator design.

PARALLEL MULTI-OBJECTIVE OPTIMIZATION METHOD

In accelerator community, multi-objective genetic algorithm (MOGA) such as NSGA-II has been widely used for beam dynamics optimization [13]. In this study, we developed a new multi-objective optimization algorithm based on a differential evolution method. The differential evolution method is a simple yet efficient population-based, stochastic, evolutionary algorithm for global parameter optimization [14]. In a number of studies, the differential evolution algorithm performed effectively in comparison to several stochastic optimization methods such as simulated annealing, controlled random search, evolutionary programming, the particle swarm method, and genetic algorithm [14-16].

The differential evolution algorithm starts with a population initialization. A group of NP solutions in the control parameter space is randomly generated to form the initial population. This initial population can be generated by sampling from a uniform distribution within the parameter space if no prior information about the optimal solution is available, or by sampling from a known distribution (e.g., Gaussian) if some prior information is available. After initialization, the differential evolution algorithm updates the population from one generation to the next generation until reaching a convergence condition or until the maximum number of function evaluations is reached. At each generation, the update step consists of three operations: mutation, crossover, and selection. The mutation and the crossover operations produce new candidates for the next generation population and the selection operation is used to select among these candidates the appropriate solutions to be included in the next generation. During the mutation operation stage, for each population member (target vector) x_i , $i = 1, 2, 3, \dots, NP$ at generation G , a new mutant vector v_i is generated by following a mutation strategy. In past studies, multiple mutation strategies (>10) were proposed in the literature.

*Work supported by the Director of the Office of Science of the US Department of Energy under Contract no. DEAC02-05CH11231.

[#]jqliang@lbl.gov

IMPEDANCE CHARACTERIZATION AND COLLECTIVE EFFECTS IN THE MAX IV 3 GeV RING*

F. J. Cullinan[†], R. Nagaoka, Synchrotron SOLEIL, 91192 Gif-sur-Yvette, France
G. Skripka, Å. Andersson, P. F. Tavares,
MAX IV Laboratory, Lund University, SE-221 00 Lund, Sweden

Abstract

Collective instabilities in the MAX IV 3 GeV storage ring are enhanced by combination of high beam current, ultralow emittance and small vacuum chamber aperture. To mitigate instabilities by Landau damping and improve lifetime three passive harmonic cavities are installed to introduce synchrotron tune spread and bunch lengthening respectively. We present the results of the studies of collective effects driven by the machine impedance. Bunch lengthening and detuning were measured to characterize the machine impedance and estimate the effect of the harmonic cavity potential. Investigations of collective effects as a function of parameters such as beam current and chromaticity are discussed.

INTRODUCTION

The study of collective effects in a particle accelerator is of high importance because they can lead to a deterioration in the machine performance. The MAX IV 3 GeV machine [1] is based on a multibend achromat lattice where the emittance is pushed down to a bare-lattice value of 0.33 nm rad, which is further reduced to 0.2 nm rad when loaded with insertion devices. Achieving such a small emittance requires strong-focusing, small-bore magnets which necessitate the use of a small nominal vacuum chamber aperture (11 mm radius). This, in turn, leads to a large machine impedance and enhanced collective effects.

Numerical characterization of beam instabilities is typically done using an impedance model describing the machine in the frequency domain followed by particle tracking accounting for this impedance.

In this paper we present the first experimental results of longitudinal and transverse instability studies on the MAX IV 3 GeV machine and compare them to numerical results obtained with the particle tracking code *mbtrack* [2]. The geometric impedance model of the complete MAX IV 3 GeV ring was created and processed to be used in the tracking. Description of the machine impedance budget and simulations of possible longitudinal and transverse instabilities can be found in [3] and [4]. Here we will compare the results to measured values for the potential-well bunch lengthening and tune shift with bunch current and discuss the TMCI,

head-tail, resistive-wall and ion-driven instabilities present in the machine.

The MAX IV 3 GeV ring is equipped with a diagnostic beam line for beam size measurements [5] using the visible synchrotron radiation emitted from the center of a dipole magnet. This beam line was used for the bunch length measurements presented below and for observation of the transverse beam profile and any beam blow-up indicating that the beam is unstable. For more accurate measurements of transverse instabilities, the bunch-by-bunch feedback system from Dimtel [6] was used as a diagnostic tool. At the time of the measurements, only two in-vacuum insertion devices were installed and these were left in the open position. Round vacuum chambers were installed at all other straight sections.

LONGITUDINAL SINGLE-BUNCH

A single, high-current bunch was obtained by injecting a train of nine bunches into the ring and then using the bunch-by-bunch feedback system to clean eight and leave only one bucket filled. By using an optical sampling oscilloscope resolving the time structure of synchrotron light, the bunch length could be measured as the current was decreased in steps by scraping. The synchrotron tune was measured to be 0.00157 and the other parameters of the MAX IV 3 GeV ring were assumed to be at their design values during the experiment, i.e. momentum compaction $\alpha_c = 3.07 \times 10^{-4}$ and energy spread $\sigma_E = 7.82 \times 10^{-4}$.

The measured bunch lengthening due to potential well distortion is presented in Figure 1 and compared to simulation. The length of each error bar is equal to the standard

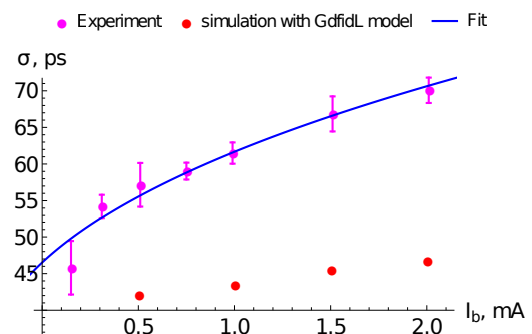


Figure 1: Bunch length vs. current: measurements in magenta (set of five measurements), simulations with *mbtrack* with full numerical machine impedance in red and fit including a single broadband resonator in blue.

deviation of 5 bunch length measurements using the oscillo-

* The authors are grateful for financial support through the Swedish Research Council funded Cooperation in the field of synchrotron light research between SOLEIL and MAX IV. The research leading to these results has received funding from the European Commission under the FP7 Research Infrastructure project EuCARD-2, grant agreement no. 312453.

[†] francis.cullinan@synchrotron-soleil.fr

SRF DEVELOPMENT AND CRYOMODULE PRODUCTION FOR THE FRIB LINAC*

T. Xu[†], H. Ao, B. Bird, N. Bultman, E. Burkhardt, F. Casagrande, C. Compton, J. Crisp, K. Davidson, K. Elliott, A. Facco¹, R. Ganni, A. Ganshyn, P. Gibson, W. Hartung, K. Hosoyama⁵, M. Ikegami, M. Kelly³, P. Knudsen, R. Laxdal⁴, S. Lidia, I. Malloch, S. Miller, D. Morris, P. Ostroumov, M. Reaume, J. Popielarski, L. Popielarski, M. Shuptar, G. Shen, S. Stark, K. Saito, J. Wei, J. Wenstrom, M. Wiseman², M. Xu, Y. Xu, Y. Yamazaki and Z. Zheng
 Facility for Rare Isotope Beams, Michigan State University, East Lansing, MI, 48824, USA
¹ also at INFN - Laboratori Nazionali di Legnaro, Legnaro (Padova), Italy
² also at Thomas Jefferson National Accelerator Facility, Newport News, VA 23006, USA
³ also at Argonne National Laboratory, Lemont, IL 60439, USA
⁴ also at TRIUMF, Vancouver, Canada
⁵ also at High Energy Accelerator Research Organisation, Tsukuba, Japan

Abstract

The Facility for Rare Isotope Beams' heavy ion continuous-wave (CW) linac extends superconducting RF to low beam energy of 500 keV/u. 332 low-beta cavities are housed in 48 cryomodules. Technical development of high performance subsystems including resonator, coupler, tuner, mechanical damper, solenoid and magnetic shielding is necessary. In 2015, the first innovatively designed FRIB bottom-up prototype cryomodule was tested meeting all FRIB specifications. In 2016, the first full production cryomodule is constructed and tested. The preproduction and production cryomodule procurements and in-house assembly are progressing according to the project plan.

INTRODUCTION

The Facility for Rare Isotope Beams (FRIB) driver linac consist of 332 low-beta superconducting RF cavities is designed to accelerate all ions up to 200 MeV/u or higher and will be the largest low-beta superconducting linac in the world [1]. Work on the first superconducting cyclotron at MSU began in 1982. Since then, MSU has been at

the frontier of superconducting technology for accelerator applications and associated R&D, as shown in Fig 1. In 2000, the National Superconducting Cyclotron Laboratory (NSCL) at MSU started SRF development work in collaboration with Jefferson Lab and INFN-Legnaro for the Rare Isotope Accelerator (RIA) [2, 3]. Early work was focused on elliptical cavities for medium β , coaxial resonators (QWRs and HWRs) for low β , and prototype cryomodules [4, 5]. In 2006, an ion re-accelerator (ReA3) was funded by MSU as an NSCL experimental facility and test bed for a future driver linac [6]. In 2014, the third ReA3 cryomodule was commissioned [7]. The first ReA3 experiment with a rare isotope beam was conducted in 2015. At the end of 2015, the first FRIB $\beta=0.085$ QWR production cryomodule was completed, and cryomodule mass production began. In 2014, a state-of-the-art SRF facility was built to support FRIB cryomodule production [8]. Two linacs, a total of 51 SRF cryomodules, and over 300 superconducting magnets will be in service at MSU when the FRIB is completed in 2022.

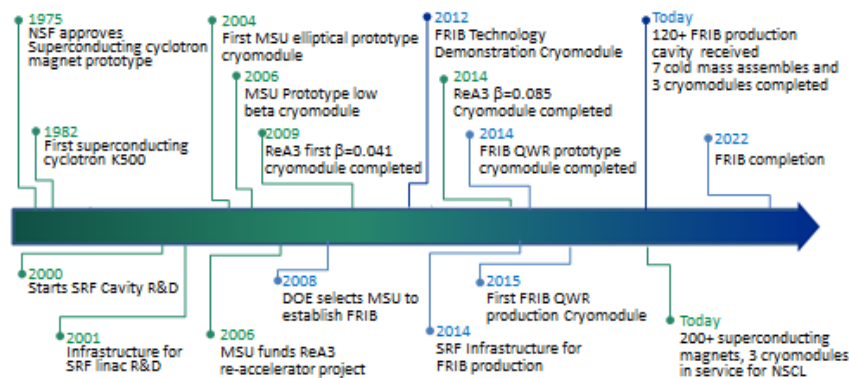


Figure 1: Time line of superconducting and accelerator technology development at MSU.

* Work supported by the U.S. Department of Energy Office of Science under Cooperative Agreement DE-SC0000661

[†] xuti@frib.msu.edu

FIRST TEST RESULTS OF THE 150 MM APERTURE IR QUADRUPOLE MODELS FOR THE HIGH LUMINOSITY LHC*

G. Ambrosio[†], G. Chlachidze, Fermilab, Batavia, IL USA

P. Wanderer, BNL, Upton, NY USA

P. Ferracin, CERN, CH

G. Sabbi, LBNL, Berkeley, CA USA

on behalf of the LARP-CERN collaboration for HL-LHC

Abstract

The High Luminosity upgrade of the LHC at CERN will use large aperture (150 mm) quadrupole magnets to focus the beams at the interaction points. The high field in the coils requires Nb₃Sn superconductor technology, which has been brought to maturity by the LHC Accelerator Research Program (LARP) over the last 10 years. The key design targets for the new IR quadrupoles were established in 2012, and fabrication of model magnets started in 2014. This paper discusses the results from the first single short coil test and from the first short quadrupole model test. Remaining challenges and plans to address them are also presented and discussed.

INTRODUCTION

With two successful tests the US LARP (LHC Accelerator Research Program) and CERN have closed the design phase for the High Luminosity LHC (HL-LHC) [1] IT quadrupoles and started the demonstration phase. The HL-LHC requires Inner Triplet quadrupoles with 150 mm aperture and 133 T/m gradient (MQXF) [2]. In developing these quadrupoles, LARP and CERN are basing design and technology on the successful demonstration of 90-mm and 120-mm aperture quadrupoles by LARP.

The successful tests of a single short coil (MQXFSM1) and of the first short quadrupole (MQXFS1) have demonstrated the validity of several MQXF magnet design and technology choices. In this paper we present and discuss these test results. Subsequently we discuss the main challenges in front of MQXF development, and the plans to address them.

MQXF MAIN DESIGN PARAMETERS

MQXF is a cos²θ quadrupole comprised of four double-layer coils assembled in a shell-based mechanical support structure. The design concept and main features are described in [3-4]. The conductor and performance parameters specific to the MQXFS1 assembly are summarized in Table 1.

The superconducting cable, which incorporates a stainless steel core to control the dynamic effects, was fabricated using 0.85 mm diameter Nb₃Sn strands of the OST-RRP design. Of the four coils used in MQXFS1, two were

fabricated by LARP using the 108/127 wire layout and two by CERN using the 132/169 wire layout.

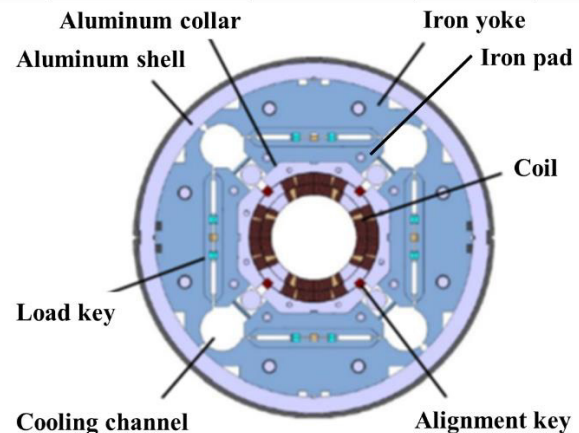


Figure 1: MQXF cross-section.

As shown in Fig. 1, the four quadrants are assembled using bolted aluminum collars, then aligned using keys inserted into each pole piece. The resulting coil pack is surrounded by bolted iron pads, inserted in a yoke-shell sub-assembly, and loaded using water-pressurized bladders and interference keys. Four tensioned aluminum rods are connected to stainless steel end plates to provide axial pre-load to the coils. Further details about MQXF magnet design and fabrication are provided in [5-6].

Table 1: MQXFS1 Cable and Magnet Parameters

Parameter	Unit	Value
Strand diameter	mm	0.85
Number of strands		40
Cable width	mm	18.094
Cable mid-thickness	mm	1.529
Core width/thickness	mm	12/0.025
Turn insulat. thickness	mm	0.15
Coil aperture	mm	150
No. turns in layer 1/2		22/28
Operational gradient	T/m	132.6
Operational current (I_{op})	kA	16.48
Peak coil field at I_{op}	T	11.4
Stored energy at I_{op}	MJ/m	1.17
Short sample current	kA	21.5

* Work supported by the US Department of Energy through the US LHC Accelerator Research Program (LARP) and by the High Luminosity LHC project at CERN.

[†] Giorgioa@fnal.gov

650 MHz ELLIPTICAL SUPERCONDUCTING RF CAVITIES FOR PIP-II PROJECT *

V. K. Jain^{†1}, I. V. Gonin, C. Grimm, S. Kazakov, T. N. Khabiboulline, V. Lebedev, C. S. Mishra, N. K. Sharma,¹ E. Borissov, Y. Pischalnikov, A. Rowe, D. Mitchel, T. Nicol, V. P. Yakovlev

Fermi National Accelerator Laboratory, Batavia, IL, USA

¹on leave from Raja Ramanna Centre for Advanced Technology, Indore, MP, India

Abstract

Proton Improvement Plan-II at Fermilab is an 800 MeV superconducting pulsed linac which is also capable of running in CW mode. The high energy section operates from 185 MeV to 800 MeV instigated using 650 MHz elliptical cavities. The low-beta (LB) $\beta_G = 0.61$ portion will accelerate protons from 185 MeV-500 MeV, while the high-beta (HB) $\beta_G = 0.92$ portion of the linac will accelerate from 500 to 800 MeV. The development of both LB and HB cavities is taking place under the umbrella of the Indian Institutions Fermilab Collaboration (IIFC). This paper presents the design methodology adopted for both low-beta and high-beta cavities starting from the RF design yielding mechanical dimensions of the cavity cells and, then moving to the workable dressed cavity design. Designs of end groups (main coupler side and field probe side), helium vessel, coupler, and tuner are the same for both cavities everywhere where it is possible. The design, analysis and integration of dressed cavity are presented in detail.

INTRODUCTION

Proton Improvement Plan-II (PIP-II) is Fermilab's project aimed for future development of the accelerator complex. In particular, it should provide LBNE (Long Baseline Neutrino Experiment) operations with beam power on target of at least 1 MW [1]. The central element of PIP-II is a new superconducting (SC) 800 MeV 2 mA CW linac initially operating in a pulsed regime to support beam injection into the 8 GeV Booster. PIP-II will use five types of SC cavities: 162.5 MHz half-wave resonators (HWR), two families of single-spoke resonator operating at 325 MHz (SSR1 and SSR2), and two families of elliptical cavities (LB650 and HB650) operating at 650 MHz. The layout of the PIP-II linac, (Fig. 1) shows the transition energies between accelerating structures, and their frequencies [2]. In this paper, the designs of the elliptical SC cavities for LB650 and HB650 are presented.

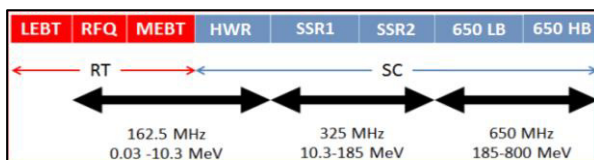


Figure 1: Layout of PIP-II injector linac.

DESIGN METHODOLOGY

Based on physics requirements for PIP-II, the functional requirement specifications (FRS) of the HB and

* Operated by Fermi Research Alliance, LLC under Contract No. DE-AC02-07CH11359 with the United States Department of Energy.

[†] vjain@fnal.gov

7: Accelerator Technology Main Systems

T07 - Superconducting RF

LB elliptical cavities are defined [3,4]. Cavity shapes for end-cells and mid-cells are developed using RF simulations which satisfy the parameters of the FRSs as shown in Fig. 2. The cavity dimensions are computed for operating temperature of 2K. The cold RF shape is recomputed to the room temperature dimensions by using the coefficient of thermal expansion of the niobium. Additional thickness is added to this RF profile to account material removal during processing. The cavity dimensions after processing are used for mechanical simulations. However, for fabrication purposes only the warm inner profile without material removal is used. Fig. 2 illustrates general design practices for electromagnetic, RF and mechanical simulations and iterative process between them indicated by chain dotted lines. Mechanical design such as cavity/tuner stiffness and vessel design uses RF design input [5]. The coupler, tuner and magnetic shield designs are done separately, however they also contribute indirectly to cavity RF and mechanical designs.

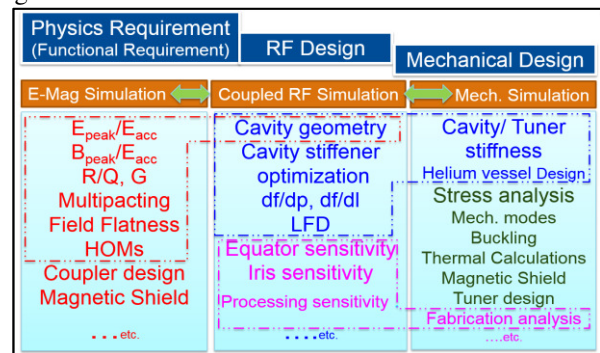


Figure 2: SC cavity design methodology.

650 MHz RF DESIGN

A requirement for both pulsed and CW operations significantly complicates the cavity design. The goal of the cavity shape optimization is to minimize both surface electric, E_{surf} , and magnetic, B_{surf} , fields.

Table 1: PIP-II Parameters of 650 MHz Cavities [3,4]

Cavity Parameters	LB650	HB650
β_G	0.61	0.92
β_{opt}	0.65	0.97
$R/Q(\beta_G)$, Ohms	327.4	576
$E_{surf}/E(\beta_G)$	2.43	2.1
$B_{surf}/E(\beta_G)$, mT/MV/m	4.6	3.94
G , Ohms	187	260
Energy gain per cavity MeV	11.7	19.9

INTRINSIC LANDAU DAMPING OF SPACE CHARGE MODES AT COUPLING RESONANCE*

Alexandru Macridin, Alexey Burov, Eric Stern, James Amundson, Panagiotis Spentzouris, Fermilab, Batavia, Illinois, USA

Abstract

Using Synergia accelerator modeling package and Dynamic Mode Decomposition technique, the properties of the first transverse dipole mode in Gaussian bunches with space charge are compared at transverse coupling resonance and off-resonance. The Landau damping at coupling resonance and in the strong space charge regime is a factor of two larger, while the mode's tune and shape are nearly the same. While the damping mechanism in the off-resonance case fits well with the classical Landau damping paradigm, the enhancement at coupling resonance is due to a higher order mode-particle coupling term which is modulated by the amplitude oscillation of the resonance trapped particles.

INTRODUCTION

Landau damping (LD) mechanism [1] is an important research topic in plasma and accelerator physics. The damping is caused by the energy exchange between a coherent mode and the particles in resonance with the mode. In the typical picture, LD requires the coherent resonance line to lie within the incoherent spectrum. Our numerical investigation of the transverse space charge (SC) modes in bunched beams reveals a novel damping mechanism at the coupling resonance (CR), *i.e.*, when the horizontal and the vertical tunes are close. In contrast with the usual LD mechanism, the tunes of the LD-responsible particles, *i.e.*, the particles which absorb the mode energy, have a wide spread. This happens due to the oscillatory behavior of the amplitudes of the CR trapped particles, which modulates the mode-particle coupling.

The transverse SC modes in bunched beams away from the CR were calculated in Refs [2–4]. Their intrinsic LD in the strong SC regime was suggested in Ref [2, 3]. Predicted damping rates were confirmed by numerical simulations [5–7]. The linear CR influence on LD was addressed in Ref [8].

In our study there is no linear coupling term between the transverse planes since the SC force introduces only higher-order coupling terms. The main resonance is the fourth-order Montague resonance [9] resulting from the term proportional to x^2y^2 in the SC potential. The particles trapped in the resonance islands are characterized by an oscillatory energy exchange between the transverse planes. Their transverse amplitudes are oscillating with typical trapping frequencies. The mode-particle coupling is therefore modulated by the trapping frequency since it is dependent on the particle's amplitudes. Because the trapping frequencies are particle dependent, the tunes of the LD-responsible particles are particle dependent also.

We compare the properties of the first SC mode both on and off the CR. We find that the LD is larger in the former case. By investigating the properties of the particles exchanging energy with the mode, we conclude that the off-resonance case well fits the conventional LD scenario characterized by LD-responsible particles with an incoherent tune spectrum at the coherent tune. At CR the damping enhancement is caused by the presence of the modulated coupling between the mode and the trapped particles. Our approach does not assume any analytical model; it is solely based on numerical simulations of a bunch propagating through a lattice.

FORMALISM

The mode-particle interaction equation can be written [10]

$$\ddot{x} + \omega_0^2(Q_{0x} - \delta Q)^2 x = -2\omega_0^2 Q_{0x} \delta Q \bar{x} \quad (1)$$

The SC mode enters in Eqs. 1 and 2 as $\bar{x}(t) = e^{-i\omega_0 \nu t} \bar{x}[z(t)]$, where ν is the mode tune. For the first mode, $\bar{x}[z] \approx \sin[\pi z/4\sigma_z]$ [2, 3]. Taking into account the synchrotron oscillations of $z(t)$, the Bessel function expansion of $\bar{x}(t)$ yields the mode-particle main resonant exchange tune at $\nu - Q_s$, where Q_s is the synchrotron tune. The tune shift $\delta Q(z, J_x, J_y)$ is proportional to the line charge density and is dependent on the particle transverse actions. To a good approximation, J_x and J_y are constants of motion. The resonant energy exchange between the mode and the particle occurs when the particle tune is close to $\nu - Q_s$.

The situation is different at the CR. In the proximity of the resonance, the sum $J_s = J_x + J_y$ is a constant of motion, while the difference $J_d = J_x - J_y$ oscillates around the stable point. Using the J_d expansion of the mode-particle coupling term, $2\omega_0^2 Q_{0x} \delta Q = A + B J_d$, Eq. 1 can be written as

$$\ddot{x} + \omega_0^2 Q_x(z, J_s, J_d)^2 x = -A(z, J_s) \bar{x} - B(z, J_s) J_d \bar{x}. \quad (2)$$

The trapping frequency $\omega_0 Q_t$, *i.e.*, the frequency of the J_d oscillations at CR, is particle dependent [9]. The oscillations of J_d contribute to the damping in two ways. First, the dependence of $Q_x(z, J_s, J_d)$ on J_d yields satellites spaced by harmonics of Q_t in the incoherent spectrum. These satellites are resonant with the particle-mode coupling term $A \bar{x}$ when their tune is at $\nu - Q_s$. Second, the J_d oscillations modulate the particle-mode coupling term $B J_d \bar{x}$, yielding a novel damping mechanism. If in the conventional picture, the LD requires particles with an incoherent spectrum covering the mode frequency, *i.e.*, $\bar{Q}_x \approx \nu - Q_s$, where \bar{Q}_x is the particle's main tune, the $B J_d \bar{x}$ term implies mode-resonant particles when $\bar{Q}_x \approx \nu - Q_s - Q_t$. Because Q_t is particle dependent, \bar{Q}_x of the particles participating to the parametric LD is particle dependent, too, and may spread over a large range.

* Work supported by U.S. Department of Energy contract DE-AC02-07CH11359.

ACCELERATOR PHYSICS DESIGN REQUIREMENTS AND CHALLENGES OF RF BASED ELECTRON COOLER LEReC

A.V. Fedotov[#], M. Blaskiewicz, W. Fischer, D. Kayran, J. Kewisch, S. Seletskiy, J. Tuozzolo
Brookhaven National Laboratory, Upton, NY 11973, U.S.A.

Abstract

The Low Energy RHIC electron Cooler (LEReC) is presently under construction at BNL to improve the luminosity of the Relativistic Heavy Ion Collider (RHIC). Required electron beam and its acceleration will be provided by the photoemission electron gun and the RF linear accelerator. As a result, LEReC will be the first bunched beam electron cooler. In addition, this will be the first electron cooler to cool beams under collisions. In this paper, we describe accelerator physics requirements, design considerations and parameters, as well as associated challenges of such electron cooling approach.

INTRODUCTION

Mapping the Quantum-Chromo-Dynamics (QCD) phase diagram is one of the fundamental goals in the heavy-ion collision experiments. The QCD critical point is a distinct feature of the phase diagram, the existence of which is predicted by various QCD models. The beam energy scan phase-I (BES-I) runs for physics, motivated by the search of the QCD critical point, were successfully conducted at RHIC in 2010-11. Driven by physics and the BES-I results, the future physics program called BES-II is proposed. However, required event statistics is much higher than previously achieved and relies on significant luminosity improvement in RHIC with the help of electron cooling [1].

Although maximum required electron energy is not very high, and typical electrostatic DC acceleration is an option (which was considered in the past [2]), an approach based on the RF acceleration was chosen. Such a scheme of cooling with bunched electron beam is also a natural approach for high-energy electron cooling which requires RF acceleration. As such, LEReC is also a prototype for future high-energy electron coolers, both in physics and technology.

COOLER REQUIREMENTS

The LEReC design is based on the non-magnetized cooling approach with zero magnetic field on the cathode and no magnetic field in the cooling region. For non-magnetized cooling to be effective one needs to have strict control not only of the longitudinal velocity spread of electrons as in typical low-energy magnetized coolers but also of the transverse electron velocities (both the

velocity spread and the average beam velocity), similar to the FNAL cooler [3].

The friction force acting on the ion with charge number Z inside a non-magnetized electron beam with velocity distribution function $f(v_e)$ is

$$\vec{F} = -\frac{4\pi n_e e^4 Z^2}{m} \int \ln\left(\frac{\rho_{\max}}{\rho_{\min}}\right) \frac{\vec{V}_i - \vec{v}_e}{|\vec{V}_i - \vec{v}_e|^3} f(v_e) d^3 v_e, \quad (1)$$

where e and m are the electron charge and mass, V and v_e are the ion and electron velocities respectively, and n_e is electron density in the particle rest frame (PRF). The Coulomb logarithm $\ln(\rho_{\max}/\rho_{\min})$ is kept under the integral because the minimal impact ρ_{\min} parameter depends on electron velocity.

Table 1: Electron Beam Parameters for Cooling

Electron beam energy, MeV	1.6-2.6
Charge per single bunch, pC	130-200
Number of bunches in macrobunch	30-24
Total charge in macrobunch, nC	3-5
Average current, mA	30-55
RMS normalized emittance, μm	< 2.5
Angular spread, mrad	< 0.15
RMS energy spread	< 5×10^{-4}
RMS bunch length, cm	2-3
Length of cooling sections, m	20

To maximize cooling power and not to overcool a core of ion distribution, which is important for colliding beams, electron beam rms velocity spreads are chosen close to those of the ion beam. The ion beam has rms momentum spread in the range of $\sigma_p = 4-5 \times 10^{-4}$. This sets the requirement for the rms momentum spread of electron beam to $< 5 \times 10^{-4}$.

For the rms normalized emittance of the ion beam, 2.5 μm at $\gamma=4.1$, and 30 m beta function in the cooling section, the ion beam rms angular spread in the lab frame is 0.14 mrad. This gives the requirement for the electrons angular spread θ in the cooling section < 0.15 mrad.

For electron beam parameters in Table 1 the temperature of the longitudinal degree of freedom is

$$T_{\parallel} = mc^2 \beta^2 \left(\frac{\Delta p}{p} \right)^2 \approx 0.12 eV$$

and the transverse degree of freedom

*Work supported by the US Department of Energy under contract No. DE-SC0012704

#fedotov@bnl.gov

RF CALIBRATION OF CEBAF LINAC CAVITIES THROUGH PHASE SHIFTS*

A. Carpenter[#], J. Benesch, C. Slominski, Jefferson Lab, Newport News, VA, USA

Abstract

This paper describes a new beam-based method of cavity energy gain calibration based on varying the cavity phase. This method can be fully automated and allows a larger range of momentum excursions during measurement than previous calibration approaches. Monte Carlo simulations suggest that a calibration precision of 2-3% could be realistically achieved using this method. During the commissioning of the Continuous Electron Beam Accelerator Facility's (CEBAF) energy upgrade to 12 GeV, 876 measurements were performed on 375 of the 400 linac cavities in Fall 2015 and applied December 2015. Linac optics appears to be closer to design as a result. The resulting ensemble proved to be 2% over the value needed to get the desired energy in the arcs. Continued offline analysis of the data has allowed for error analysis and better understanding of the process.

CEBAF 1995-2012

CEBAF is a recirculating electron accelerator using superconducting RF. It consists of an injector which provides fully relativistic electrons (130 MeV), two linacs of equal momentum gain, and ten recirculating arcs. The injector and linac energies are in the ratios: 0.1128:1:1 so electrons in arc 2 have ~90% more momentum compared to arc 1. With fully relativistic electrons, the extreme relativistic limit applies, so momentum measurements in the recirculating beam transport arcs are proportional to energy.

For 1995-2012 a momentum balance method was used to calibrate the cavity gradients (energy gain per unit length). The highest energy-gain cavity in each linac was calibrated against the magnets in the downstream arc using optics with dispersion ~6 m. The reference cavity in a given linac was then set to produce a 1.5 MeV/c change in momentum in the downstream arc. The gradient for the cavity under test was nominally set to produce a compensating 1.5 MeV/c change or turned off, and the reference cavity was used to restore the original orbit in the following arc. The change in the reference cavity's gradient was used to calibrate the gradient in the cavity under test. The associated momentum gain per cavity ranged from 1.5 to 6 MeV/c. Repeated arc 1 measurements on individual cavities in linac 1 had an RMS span of 5%. Measurements in arc 2 had a 9% RMS span as the momentum in the arc is higher but the change due to a single cavity is not. The RF control system is not

stable for gains corresponding to 1.5 MeV/c or less. These errors were adequate for the forgiving optics of the original CEBAF layout and minimal emittance growth due to synchrotron radiation.

PHASE SHIFTS

In late 2014, it was realized that using the phase control on each cavity would allow a larger momentum shift than the gradient balance method as the cavity could be moved to a decelerating phase. This would increase the shift to almost twice the nominal or the maximum allowed by the following arc's acceptance. With assistance [1] Root was used for a Monte Carlo evaluation of the process. For momentum shifts limited to 0.4%, energy RMS errors were in the range 1.9-2.5% for all linac 1 cavities and for linac 2 cavities providing more than 2.5 MeV/c gain. For lower gain linac 2 cavities, amplitude RMS error was projected to reach 4.6% at 1.5 MeV/c. The cavity phase shift-based algorithm is summarized below. The analysis that follows considers cavities with nominally "low" (~1.5 MeV/c) to "medium" (~6 MeV/c) operating gradients and those with nominally "high" operating (~10.5 MeV/c) cavity gradients. This classification scheme distinguishes between the older, lower capability cavities, and the newer, higher capability cavities fabricated for the recent CEBAF upgrade.

Calibration and Shift Calculation Algorithm

Calibration of RF cavity gradient settings and proper phasing is achieved by shifting a cavity's phase and measuring the change in energy (momentum) in the nearest downstream dispersive region (beam transport arc). Since the only element changing is the phase of a single cavity, the change in energy can be calculated using the following model,

$$dE_i = E_i - E_{orig} = A \cos(\theta + \varphi_i) - A \cos \theta$$

where

- dE_i \equiv change in energy measured in the nearest downstream dispersion region for shift φ_i
- A \equiv amplitude (MeV) of the cavity energy cosine function to be estimated
- θ \equiv cavity phase angle error to be estimated
- φ_i \equiv the i^{th} cavity phase shift

This formula can be recast as $\delta E_i = X_{1i} \beta_1 + X_{2i} \beta_2$ where $\beta_1 = A \cos \theta$, $\beta_2 = A \sin \theta$, $X_1 = \cos \varphi_i - 1$, and $X_2 = -\sin \varphi_i$. Using measurements made at multiple phase shifts, this model can be fit using ordinary least squares regression. Once estimates for β_1 and β_2 have been found, it is trivial to solve for A and θ where

* Notice: Authored by Jefferson Science Associates, LLC under U.S. DOE Contract No. DE-AC05-06OR23177 and DE-AC02-06CH11357. The U.S. Government retains a non-exclusive, paid-up, irrevocable, world-wide license to publish or reproduce this manuscript for U.S. Government purposes.

[#] adamc@jlab.org

100 kW VERY COMPACT PULSED SOLID-STATE RF AMPLIFIER: DEVELOPMENT AND TESTS

G. B. Sharkov^{†1}, A. A. Krasnov, S. A. Polikhov, NIITFA, 115230 Moscow, Russia
R. Cisneros, R. J. Patrick, TMD Technologies Ltd., Hayes, Middlesex UB3 1DQ United Kingdom
¹also at ITEP, 117218 Moscow, Russia

Abstract

Solid-state RF power amplifier (SSPA) technology has developed significantly over recent years [1]. Powers of hundreds of kilowatts are being achieved, driven by the developments of LDMOS and other transistor technologies [2]. The price and size of SSPA still correlate with the output power (due to the number and cost of transistors), which is not the case for vacuum tube based devices. In order to be competitive with tetrodes, klystrons, IOT's and other tubes at higher levels of power and frequency, SSPA's should be designed to be more compact and cheaper than current offerings, using the high efficiency and reliability of modern transistors to produce highly available amplifier systems. The scalability of SSPA output power is achieved by a modular architecture based on several ~1kW transistors; this gives an important advantage over vacuum tubes.

In order to meet challenging demands for high power, efficient, reliable, compact and cost effective RF amplifiers, a novel architecture of SSPA is employed and a 100 kW prototype has been developed (Fig. 1). The complete system fits into one 19" cabinet. It is developed according to the requirements of the ESS project's "low-beta" part of the Linac: 400 kW, 352 MHz, 3.5 msec pulse at 14 Hz repetition rate, <5 m² footprint [3].

ARCHITECTURE

The main idea of the proposed architecture is to reduce the manufacturing cost, especially removing hand assembly and tuning and the need for highly skilled personnel. Since the materials costs are mainly driven by the costs of transistors and matching elements, which are hard to reduce, the labour costs is the main manageable cost driver. To achieve this goal one needs to standardise all subsystems for any frequency within roughly 20 – 1300 MHz and any output power from 10 to 1500 kW, such that each new specification will not cause significant redesign and R&D. The system should be modular, so that changes to the working frequency will lead to the redesign of a minimum set of subsystems. Ideally this would be limited to the PCB's with RF transistors and the power combiners. All subsystems should fit into one 19" cabinet, so that one cabinet can serve as a standalone RF amplifier comprising individual PA modules and power combiner and respective ancillary systems*. Increasing the required output power will then be implemented by providing complete cabinet amplifiers with a final stage power

combiner mounted above the cabinets. This approach provides a fully scalable system. The low level modularity of the system together with the ability to work without all of the PA modules functional and the ability to "hot swap" units allows very high availability (potentially 99.9%) to be achieved which is unachievable by single vacuum tube systems.

Commercial-off-the-shelf (COTS) components are used as much as possible to reduce the R&D scope to the core technology only. Sub-Systems such as high reliability DC power sources, cooling water distribution and the 19" cabinet can be bought freely. The main modules of the control system (CS) can be developed once for all specifications, so that only frequency specific modules will be changed for each application.

Transistor evaluation boards, which are usually taken as building blocks for SSPA development [4], become quite bulky for high power systems, where hundreds of transistors are needed. Consequently the power amplifier building block should contain at least two transistors (four might be an option for pulsed systems to minimize the cost of connectors, PCB's, etc.). One should avoid designing the matching circuits using coaxial wires since they require laborious hand work. A flat transformer on a PCB is a good choice to reach the needed precision and repeatability (taking into account the possible overheating issues).



Figure 1: 100 kW 352 MHz pulsed SSPA prototype.

[†] gbsharkov@niitfa.ru

* For systems with high average power or for CW operation the DC power supplies may be placed in separate cabinet

LOWER EMITTANCE LATTICE FOR THE ADVANCED PHOTON SOURCE UPGRADE USING REVERSE BENDING MAGNETS*

M. Borland, Y. Sun, V. Sajaev, R. R. Lindberg, T. Berenc, ANL, Argonne, IL 60439, USA

Abstract

The Advanced Photon Source (APS) is pursuing an upgrade to the storage ring to a hybrid seven-bend-achromat design [1]. The nominal design provides a natural emittance of 67 pm [2]. By adding reverse dipole fields to several quadrupoles [3, 4] we can reduce the natural emittance to 41 pm while simultaneously providing more optimal beta functions in the insertion devices and increasing the dispersion function at the chromaticity sextupole magnets. The improved emittance results from a combination of increased energy loss per turn and a change in the damping partition. At the same time, the nonlinear dynamics performance is very similar, thanks in part to increased dispersion in the sextupoles. This paper describes the properties, optimization, and performance of the new lattice.

INTRODUCTION

APS is pursuing a major upgrade of our 7-GeV storage ring, replacing the double-bend structure with a 6-GeV multi-bend achromat [5] in order to achieve much lower emittance. The nominal lattice, based on a hybrid seven-bend achromat [1], achieves a natural emittance of 67 pm [2] and reasonable nonlinear dynamics performance [2, 6, 7]. In an effort to reduce the emittance further, we explored the option of converting several quadrupoles into combined-function weak reverse bending magnets [3, 4].

The use of reverse bends (RBs) has several potential advantages: it increases the energy loss per turn, thus potentially reducing emittance much as a damping wiggler would; it allows manipulation of the damping partition numbers; it provides additional means of manipulating the dispersion function; and it reduces constraints on the lattice quadrupoles, potentially allowing more optimized beta functions at the straight sections.

LINEAR OPTICS

Linear optics design started from the 67-pm lattice. The four quadrupoles in the high-dispersion region and the central FODO-like region were all converted into gradient dipoles with zero bending angle. The parallel hybrid simplex optimizer [8] in Pelegant [9, 10] was then allowed to vary the angles of both the normal and reverse bending dipoles and the quadrupole gradients. After several iterations, it became clear that only three of the RBs were in fact effective, namely, those replacing the central two quadrupoles in each high-dispersion region and the central two quadrupoles in the FODO region; this is a total of six RBs per sector.

* Work supported by the U.S. Department of Energy, Office of Science, Office of Basic Energy Sciences, under Contract No. DE-AC02-06CH11357.

Instead of merely attempting to minimize the emittance, we attempted to maximize the approximate brightness for an 18-mm-period, 3.7-m-long superconducting undulator tuned for 20 keV at the 3rd harmonic. This automatically incorporates the fact that maximizing brightness depends not only on lowering the emittance, but also on having closer-to-ideal beta functions. The lattice functions are shown in Fig. 1, while Table 1 lists several properties of the lattice in comparison to the 67-pm lattice. In addition to the significantly lower emittance, the beta functions at the IDs are both smaller, which further enhances the x-ray brightness. The maximum dispersion is 20% larger, which helps reduce the strength of the sextupoles.

Table 1: Comparison of the 67-pm and 41-pm lattices.

	67pm	41pm
ν_x	95.125	95.091
ν_y	36.122	36.165
$\xi_{x,nat}$	-139	-130
$\xi_{y,nat}$	-108	-123
Nat. emittance (pm)	66.9	41.4
Energy spread (%)	0.096	0.129
Horiz. damping time (ms)	12.1	7.2
Long. damping time (ms)	14.1	19.6
Energy loss (MeV/turn)	2.27	2.80
Momentum compaction	5.7×10^{-5}	3.8×10^{-5}
Damping partition J_x	1.61	2.20
Damping partition J_δ	1.39	0.80
Max. η_x (m)	0.074	0.090
@ ID Straight Sections:		
β_x (m)	7.0	4.9
η_x (mm)	1.11	1.47
β_y (m)	2.4	1.9
$\epsilon_{x,eff}$ (pm)	67.0	41.8

NONLINEAR DYNAMICS OPTIMIZATION

Nonlinear dynamics optimization was performed using a tracking-based multi-objective genetic algorithm (MOGA) [11, 12] (similar to [13, 14]) based on dynamic acceptance (DA) and Touschek lifetime obtained from the local momentum acceptance (LMA) [15, 16]. One refinement is that the rf voltage is adjusted for each trial configuration to be no larger than the maximum LMA, which ensures the lowest voltage and longest bunch possible.

As with the 67-pm lattice, the DA is only large enough for on-axis injection, but the LMA is larger, approaching $\pm 5\%$ in some cases. The momentum tune footprint of the

SIMULATION OF SWAP-OUT RELIABILITY FOR THE ADVANCED PHOTON SOURCE UPGRADE*

M. Borland, ANL, Argonne, IL 60439, USA

Abstract

The proposed upgrade of the Advanced Photon Source (APS) to a multibend-achromat lattice relies on the use of swap-out injection to accommodate the small dynamic acceptance, allow use of unusual insertion devices, and minimize collective effects at high single-bunch charge. This, combined with the short beam lifetime, will make injector reliability even more important than it is for top-up operation. We used historical data for the APS injector complex to obtain probability distributions for injector up-time and down-time durations. Using these distributions, we simulated several years of swap-out operation for the upgraded lattice for several operating modes. The results indicate that obtaining very high availability of beam in the storage ring will require improvements to injector reliability.

INTRODUCTION

An important reliability consideration for the APS Upgrade is whether the APS injector is able to provide pulses for swap-out [1, 2] at an interval of 5 to 15 seconds. We can get some indication of this by looking at the top-up downtime performance of the injector. This is an imperfect measure because the top-up interval is typically 60-120 seconds. Downtime shorter than this, e.g., a momentary trip that is quickly reset, may be invisible. However, we think it is relatively rare that trips are reset rapidly compared to the 8 s data logger interval for the relevant quantities.

Drawing on data collected since 2004, we computed three quantities: (1) The injector unavailability, defined as the ratio of the time during which the injector failed to provide beam for top-up to the total planned for top-up operation. (2) The durations of all top-up outages. (3) The durations of all periods of continuous top-up. The details of analyzing the data from the data logs to reconstruct the required probability distributions are highly APS-specific and may lack general interest. Hence, here we only quote some results of the analysis. As shown in Fig. 1, we found that the injector unavailability has been fairly constant over more than a decade, with occasional excursions to the high and low side. The median unavailability within a run is 1.1%. The worst is over 5%, while the best is below 0.2%.

The unavailability results are interesting, but they don't tell us whether we have many short-duration events or a few long-duration events. To analyze this, we perform additional analysis, which involves finding the duration of all continuous segments for which top-up is disabled when it should have been enabled. This is shown in Fig. 2. The

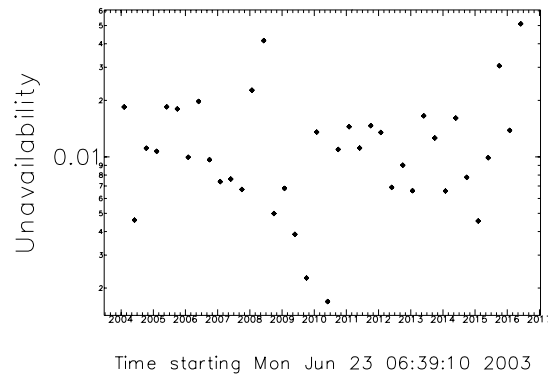


Figure 1: APS injector top-up unavailability over 3-month-long runs starting in 2004.

median outage duration is 150 s, much longer than the expected 5-15 s interval between swap-out injections needed for APS-U. Hence, with present performance we can expect to have to make up the beam current by injecting at a higher rate for a while after each outage. A typical 150 s outage will require injecting at 1 Hz for 10 to 30 s to make up the missed shots. A related quantity is the length of uninterrupted top-up, the distribution for which is shown in Fig. 3. Note that the archive has data sampled every 8s, so the cumulative distributions start there.

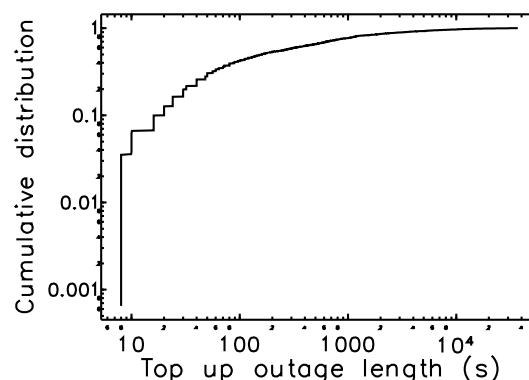


Figure 2: Cumulative distribution of top-up outage duration for all APS runs from 2004 to present.

SIMULATION OF SWAP-OUT

Combining the probability distributions shown in Figs. 2 and 3 allows simulating swap-out operation. To do this, we wrote a C-language program `swapOutSim`, with which

* Work supported by the U.S. Department of Energy, Office of Science, Office of Basic Energy Sciences, under Contract No. DE-AC02-06CH11357.

MAGNETIC MEASUREMENTS OF STORAGE RING MAGNETS FOR THE APS UPGRADE PROJECT*

C. Doose[†], R. Dejus, M. Jaski, W. Jansma, J. Collins, A. Donnelly,
J. Liu, H. Cease, G. Decker, Argonne National Laboratory, Argonne, IL 60439, USA
A. Jain, Brookhaven National Laboratory, Upton, NY 11973, USA
J. DiMarco, Fermilab, Batavia, IL 60510, USA

Abstract

Extensive prototyping of storage ring magnets is ongoing at the Advanced Photon Source (APS) in support of the APS Multi-Bend Achromat (MBA) upgrade project (APS-U) [1]. As part of the R&D activities four quadrupole magnets with slightly different geometries and pole tip materials, and one sextupole magnet with vanadium permendur (VP) pole tips, were designed, built, and tested. Magnets were measured individually using a rotating coil and a Hall probe for detailed mapping of the magnetic field. Magnets were then assembled and aligned relative to each other on a steel support plate and concrete plinth using precision-machined surfaces to gain experience with the alignment method chosen for the APS-U storage ring magnets. The required alignment of magnets on a common support structure is 30 μm RMS. Measurements of magnetic field quality, strength, and magnet alignment after subjecting the magnets and assemblies to different tests are presented.

INTRODUCTION

A 3D rendering of the magnets on the support steel plate of the Demonstration Modular Multiplet (DMM) is shown in Fig. 1. The magnet lengths are based on the design version 3 of the MBA lattice but differ only slightly from the magnet lengths in more recent versions of the lattice [2]. All quadrupoles are 269 mm long and have the same pole tip shape but differ slightly in other manufacturing details:

- Quadrupole A001 has a symmetric yoke and steel pole tips that do not extend beyond the yoke in the longitudinal direction (short tips).
- Quadrupole A002 also has short steel pole tips but has a left-right asymmetric yoke to provide an opening in the core for a photon beam extraction chamber.
- Quadrupole A003 has a set of VP short pole tips.
- Quadrupole A004 has a set of “mushroom” steel pole tips that extend out of the yoke up to the coil ends, a design feature to gain extra field integral value.

All quadrupoles have also vertical and horizontal corrector coils but these will be eliminated in the final version of the design due to field quality issues. The

* Work supported by U.S. Department of Energy, Office of Science, under contract numbers DE-AC02-06CH11357, DE-SC0012704 for work at Brookhaven National Laboratory, and DE-AC02-07CH11359 for work at Fermilab.

[†] doose@aps.anl.gov

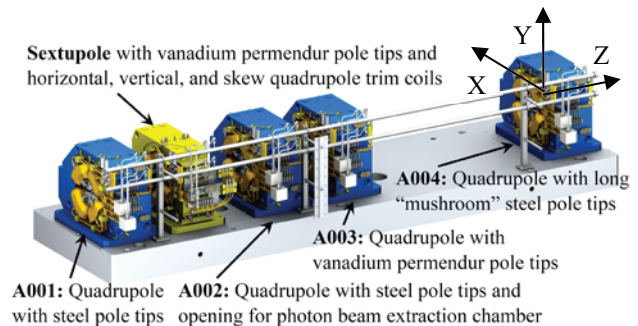


Figure 1: A 3D rendering of the DMM magnet layout on the support plate. The quadrupoles (in blue colour) are referred to as A001 thru A004 from left to right.

sextupole magnet is 235 mm long and has VP pole tips. It also has vertical, horizontal, and skew quadrupole corrector coils. All pole tips were machined using electrical discharge machining (EDM) after bolting to the core to obtain a $\pm 10 \mu\text{m}$ machining tolerance.

Among the many purposes for building the DMM assembly, checking for the following aspects was key:

- Mechanical tolerance stack up and its effect on magnetic performance.
- Accuracy of magnetic design calculations.
- Crosstalk between neighbouring magnets.
- Alignment methods, alignment accuracy, and repeatability under disassembly/reassembly of magnets to simulate vacuum chamber installations.
- Alignment stability after transportation of a magnet assembly on a plinth.

MAGNETIC MEASUREMENT RESULTS

The field harmonics in all of the DMM magnets were measured using a radial rotating coil built using printed circuit technology. The coil also provided signals bucked for the dipole and the quadrupole terms (DQ bucked) and bucked for the dipole, quadrupole and sextupole terms (DQS bucked) to ensure measurements free of spurious harmonics in the quadrupoles and the sextupole. The main coil had an outer radius of 11.35 mm and the field harmonics were expressed at a reference radius of 10 mm. Typical noise in the measurement of harmonics was below 10 ppm of the main field (0.1 unit). The axial field profiles were measured in the horizontal midplane at several excitation currents using an IIA series Senis Hall probe [3].

BEAMLINE-CONTROLLED STEERING OF SOURCE-POINT ANGLE AT THE ADVANCED PHOTON SOURCE*

L. Emery, G. Fystro, H. Shang, and M. Smith, ANL, Argonne, IL 60439, USA

Abstract

An EPICS-based steering software system has been implemented for beamline personnel to directly steer the angle of the synchrotron radiation sources at the Advanced Photon Source. A script running on a workstation monitors "start steering" beamline EPICS records, and effects a steering given by the value of the "angle request" EPICS record. The new system makes the steering process much faster than before, although the older steering protocols can still be used. The robustness features of the original steering remain. Feedback messages are provided to the beamlines and the accelerator operators. Underpinning this new steering protocol is the recent refinement of the global orbit feedback process whereby feedforward of dipole corrector set points and orbit set points are used to create a local steering bump in a rapid and seamless way.

INTRODUCTION

In order to give beamlines more convenient (and faster) control of their source points, APS has implemented in June 2016 direct source-point angle steering using EPICS in concert with a workstation-based server script.

The Advanced Photon Source (APS), like many other light sources, has been providing a steering request system to the beamlines to effect a local change in the source angle or (rarely) source position. Because the light source has a large number of beamlines, APS has implemented in 1995 a formal protocol between the beamlines and the accelerator control room using an intermediary floor coordinator (FC) contacted by pager and telephone (Fig. 1). Needless to say, the process of communicating back and forth by these means to iterate to a final steering condition took time and became too onerous to use frequently.

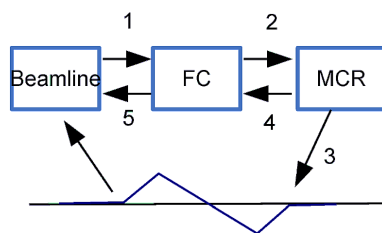


Figure 1: Original request protocol. Numbers indicate the telephone communication flow through FCs. Step 3 represent the actual source angle steering process for a particular beamline. Time to completion was 3 to 10 minutes.

* Work supported by the U.S. Department of Energy, Office of Science, Office of Basic Energy Sciences, under Contract No. DE-AC02-06CH11357.

In Jan 2016, a new (and somewhat bridging) steering request protocol was implemented, in which the beamlines communicated with the Main Control Room (MCR) operators directly using a web page form, reducing the turn-around time for steering requests to a few minutes.

Before the roll-out of the web page protocol a new algorithm for performing a local steering was developed and implemented, in which the switching between the "slow" global orbit feedback and a local bump feedback was replaced by the same global orbit feedback but with insertions of feedforward bumps for beam position monitor (bpms) set points and dipole corrector current set points. The design goal of the new algorithm was both to eliminate micron-step orbit changes of the original method and to make it possible to automate.

This feedforward algorithm was implemented in an operations GUI ("operator" steering) in Dec. 2015, permanently replacing a long-standing steering procedure, and then later, as a workstation-based server using EPICS ("beamline" steering) (Fig. 2) in June 2016. Both these methods are available for use now.

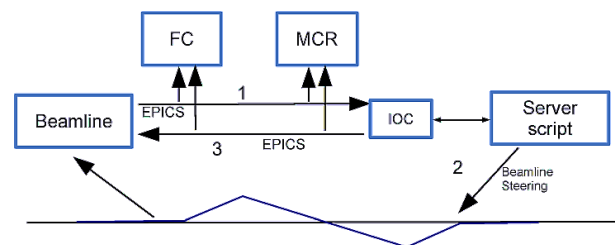


Figure 2: Direct steering protocol. The flow is through the EPICS control system. Time to completion is 5 to 20 seconds.

STEERING REQUEST BY WEB PAGE

Though superseded by the new direct steering some details of this protocol is reported here since some non-EPICS beamlines have not yet connected with the new steering PVs with an EPICS client. This protocol is used to request insertion device (ID) and bending magnet (BM) source angle steering in addition to two other user-run operational activities, beamline intensity optimization and x-ray bpm calibration, not yet implemented as a beamline-controlled activity.

A series of web pages were created for requests and responses between a beamline's console and an operator's console. The beamline staff types in an angle value and a direction for one or both planes. The beamline user presses a "Send" button, which causes an audible notification in the MCR's web page. After the MCR operators execute the

OPERATIONAL EXPERIENCE WITH BEAM ABORT SYSTEM FOR SUPERCONDUCTING UNDULATOR QUENCH MITIGATION*

Katherine C. Harkay[#], Jeffrey C. Dooling, Vadim Sajaev, Ju Wang, ANL, Argonne, IL 60439, USA

Abstract

A beam abort system has been implemented in the Advanced Photon Source storage ring. The abort system works in tandem with the existing machine protection system (MPS), and its purpose is to control the beam loss location and, thereby, minimize beam loss-induced quenches at the two superconducting undulators (SCUs). The abort system consists of a dedicated horizontal kicker designed to kick out all the bunches in a few turns after being triggered by MPS. The abort system concept was developed on the basis of single- and multi-particle tracking simulations using *elegant* and bench measurements of the kicker pulse. Performance of the abort system—kick amplitudes and loss distributions of all bunches—was analyzed using beam position monitor (BPM) turn histories, and agrees reasonably well with the model. Beam loss locations indicated by the BPMs are consistent with the fast fiber-optic beam loss monitor (BLM) diagnostics described elsewhere [1,2]. Operational experience with the abort system, various issues that were encountered, limitations of the system, and quench statistics are described.

INTRODUCTION

Protection against beam-loss-induced quenches is a well-known issue in high-energy proton accelerators that use superconducting magnets. Superconducting wigglers and SCUs employed at synchrotron light sources have quench-detection interlocks to protect the magnet; however, characterizing and mitigating beam-loss-induced quenches is reported only at APS [3] and Canadian Light Source [4]. At APS, both SCUs were found to quench sometimes during beam dumps triggered by the Machine Protection (MPS) or Personnel Safety (PSS) Systems, with ID6 SCU (a.k.a. SCU0 [5]) quenching more often than ID1 SCU (a.k.a. SCU1) (SCUs are powered off prior to manual beam dumps). Quenches can occur when less than 1 nC is lost in the coils, which is less than 0.3% of the total stored beam. The beam is lost mostly on the smallest aperture, which is the 5-mm gap insertion device ID4 vacuum chamber, but beam losses are also clearly observed at the SCU locations [1,2]. For both SCUs, quench recovery is typically fast enough to allow them to be operated once the beam is restored; however, such quenches are best minimized.

In January 2016, a new beam abort system was implemented at APS that works in tandem with the existing

beam dump system. Its purpose is to control the beam loss location away from the IDs and SCUs and, thereby, minimize beam loss-induced quenches. The abort system consists of a dedicated horizontal kicker that stays charged during user operation, and its discharge is triggered by MPS. Should the abort kicker fail to fire, MPS would dump the beam as usual. Using a peak kick ≥ 1 mrad, the entire beam is lost on the chamber walls within a few turns. The design loss location is the injection straight section (Sector 39) vacuum chamber [6].

ABORT KICKER

The abort kicker (AK) design was described previously [3], and is based on the APS injection kickers. In order to kick out the entire beam, the kicker pulse waveform must be sufficiently long. Figure 1 shows the free-wheeling diode that was added to stretch the pulse.



Figure 1: Photo showing free-wheeling diode added to stretch the abort kicker pulse.

The kicker waveform was determined experimentally by recording the motion of a single bunch whose position relative to the 0th rf bucket (i.e., fixed reference on the pulse waveform) was scanned in steps of 108 buckets (corresponding to every other bunch in a 24-bunch fill pattern). For every measurement, the kick amplitude was determined by comparing the measured trajectory with simulation. A significant complication is beam position monitor (BPM) saturation for trajectories greater than 5 mm, whereas the peak trajectory for a kicker voltage setpoint of 10 kV (corresponding to a peak kick of 1.3 mrad) is 10 mm—this is close to the requirement for beam abort, as discussed in the next section. Therefore, the fit was based on trajectories less than 5 mm, where the measured and simulated trajectories agree well. The kicker waveform extends over several turns, so where possible the kicks on three consecutive turns was extracted.

Figure 2 shows the measured kicker profile. On this plot, one turn corresponds to 24 bunches. This plot also shows the waveform obtained in the bench measurements of the

*Work supported by U. S. Department of Energy, Office of Science, under Contract No. DE-AC02-06CH11357.
#harkay@aps.anl.gov

PARAMETERIZATION OF HELICAL SUPERCONDUCTING UNDULATOR MAGNETIC FIELD*

S.H. Kim[†], Argonne National Laboratory, Argonne, IL 60439, USA

Abstract

Using a scaling law, the magnetic fields of helical superconducting undulators (HSCUs) for a period range of 10 – 50 mm are parameterized from the field calculations of one reference HSCU with a period of 30 mm. The on-axis fields are calculated at the critical current densities of the *NbTi* and *Nb₃Sn* superconducting coils at 4.2 K. The parametrized on-axis fields for the period range are expressed in terms of the period and inner radius of the helical coils. The corresponding critical current densities and coil maximum fields are also included. The parameterization procedures are described in detail and some field deviations are discussed.

INTRODUCTION

During the early phase of insertion device development, Halbach has provided the analytically derived on-axis field as a function of the pole gap and magnetic period for the use of pure permanent magnet blocks [1]. He also derived another on-axis field relation for the use of optimized samarium-cobalt alloy poles and magnet dimensions [2].

Using a wire of an infinitesimal cross section, the transverse field of a single helix is given by Smythe [3]. Kincaid has extended the field on the axis due to a pair of current carrying wires wound on a bifilar helix [4]. Assuming that the field pattern has a sinusoidal variation along the axis and no higher harmonics are present, Blewett and Chasman have derived the spiraling transverse field. [5].

The first helical superconducting undulator (HSCU) with a period of 30 mm was constructed by Elias and Madey in 1979 for an early free-electron laser experiment [6]. In recent years, short period HSCUs are under development at the Advanced Photon Source, Argonne National Laboratory, and several other institutions.

The on-axis field B_0 for the helical undulator with specific coil dimensions is expressed as

$$B_0 = \frac{2\mu_0 j \lambda}{\pi} \sin\left(k \frac{a}{2}\right) \int_{r_0}^{r_0+b} \{krK_0(kr) + K_1(kr)\} \frac{dr}{\lambda}. \quad (1)$$

Here μ_0 is the permeability in free space, j is the current in the coil pack on radius r_0 , $k = 2\pi/\lambda$ with λ as the undulator period along the z -axis, and K_0 and K_1 are modified Bessel functions [7]. The coil dimensions a and b are specified in Fig. 1.

Equation (1) suggests that when the undulator dimensions are scaled according to a period ratio and the $j\lambda$ is kept as a constant, the on-axis field B_0 remains unchanged. The more important aspect is that the whole field distribution remains unchanged even with non-linear magnetic poles. The scaling law must hold also for other electromagnets [8]. The units used in this paper are: length (mm), current (kA), and magnetic field (T).

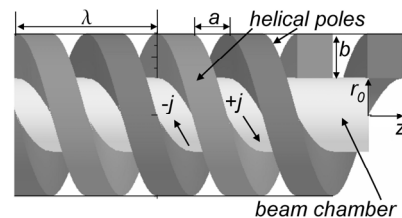


Figure 1: A model helical undulator: a double-helix steel coil is shown as magnetic poles on the outer surface of a beam chamber. In the empty space between the steel poles, helical coils of current densities, $+j$ and $-j$, are to be wound with r_0 as the inner radius of the coils, a and b as the coil dimensions.

THE SCALING LAW APPLICATION

As indicated in Eq. (1), when two undulator geometries are scaled, for example, 3:2, and the magnitude of the $j\lambda$ is kept as a constant, the undulators will have the same field distribution. For the reference undulator ($\lambda = 30$, $r_0 = 12$), the on-axis fields B_0 and the corresponding maximum field B_m in the superconducting (SC) coils in Fig. 2, along with the one that has been scaled down by a factor of 2/3 ($\lambda = 20$, $r_0 = 8$).

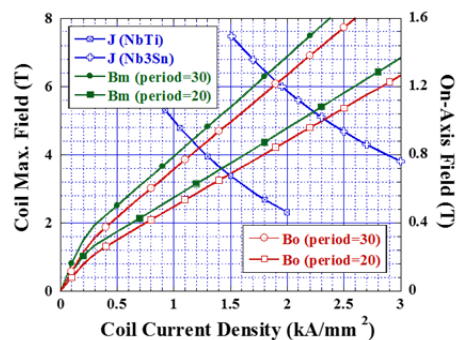


Figure 2: On-axis fields B_0 and maximum fields B_m in the coils are plotted as a function of coil (engineering) current density J for the two undulators with periods of 30.0 and 20.0.

*Work supported by the U.S. Department of Energy, Office of Science, under Contract No. DE-AC02-06CH11357

Associate of Seville, Advanced Photon Source

[†]shkim@aps.anl.gov, shkim242@gmail.com

DIELECTRICALLY-LOADED WAVEGUIDE AS A SHORT PERIOD SUPERCONDUCTING MICROWAVE UNDULATOR*

R. L. Kustom, G. Waldschmidt, A. Nassiri, and K. J. Suthar
Argonne National Laboratory, Argonne, IL 60439

Abstract

The HEM₁₂ mode in a cylindrical, dielectrically-loaded waveguide (WG) provides E and H fields on the central axis that are significantly higher than the fields on the conducting walls. This waveguide structure could be designed to operate near the cutoff frequency of the HEM₁₂ mode where the wavelength and phase velocity vary significantly to enable tuning of the equivalent undulator wavelength by changing the frequency. A typical frequency range would be from 18 – 24 GHz. It would be possible to generate high-energy, 45 to 65 keV, x-rays on the fundamental mode which are tunable by changing the source frequency while maintaining a constant equivalent undulator field strength on axis field of 0.5-T. The x-ray brightness of the microwave undulator would be up to 4 to 7 times higher than what is available with the APS 1.8 cm period Superconducting Wire Undulator.

INTRODUCTION

The benefits of a tunable high-energy x-ray source at the Advanced Photon Source (APS) were summarized in a workshop that was held at the APS in August of 2004 [1]. Presently, x-rays at energies greater than 25-keV are generated on the higher harmonics of permanent magnet undulators, or more recently on the APS superconducting wire undulators (SWU) [2]. Ultimately, the magnetic undulator is limited in generating x-rays on the fundamental mode to 20 to 30-keV because the undulator periods required are near, or under, 1-centimeter, which results in restrictively small vacuum apertures on the order of a fraction of a centimeter to achieve a reasonable deflecting field on axis.

If a superconducting microwave undulator can be realized, it would provide the advantage of larger vacuum apertures up to 5 cm, x-ray generation on the fundamental mode of the undulator, and a constant brightness.

Microwave undulators were first proposed by Shitake at KEK [3] and Batchelor at BNL [4] in 1983 using rectangular waveguides. Recent studies have been directed towards open-mode structures, over-moded waveguides (WGs), ridge WGs, square WGs, corrugated WGs, and elliptical WGs [5,6,7,8]. The SLAC group have built a room temperature microwave undulator that operates in pulsed mode with tens of MW of input power [6]. The device generates a 0.65-T equivalent undulator field.

A short model of a superconducting microwave undulator using an elliptical WG operating at 6-GHz was built and tested in a cryostat at Frascati [8]. It achieved

an equivalent undulator field of 330-gauss with a 10-watt heat loss. The field was limited by the size of the amplifier.

The challenge of these geometries is finding one that achieves high fields on axis with minimal losses on the conducting walls to minimize power requirements from the source. This is especially true if continuous wave (CW) operation is desired at superconducting temperatures. Since the loss factor of sapphire is very low at cryogenic temperatures, it is possible to consider using it in a dielectrically-loaded WG as a superconducting microwave undulator.

HEM₁₂ MODE

The HEM₁₂ mode in the dielectrically-loaded WG is the sum of a TE and TM mode for which the velocity of propagation is identical for each mode and for which the fields are matched at the dielectric boundary. The WG structure is a cylindrically symmetric tube with an inner radius of the dielectric, a , and the outer radius, b . The conducting boundary of the WG structure is at radius b . The electric and magnetic fields in the vacuum region of the WG are listed in Eq. 1 through 6.

$$E_z = E_0 J_1(x_{np} \rho) \cos(\phi) \quad [1]$$

$$H_\rho = -j \{E_0 \omega \epsilon_0 J_1(x_{np} \rho) \sin(\phi)\} / (h^2 \rho) \quad [2]$$

$$H_\phi = -j \{E_0 \omega \epsilon_0 J_1'(x_{np} \rho) \cos(\phi)\} / h \quad [3]$$

$$E_\rho = (\beta H_\phi) / (\omega \epsilon_0) \quad [4]$$

$$E_\phi = (-\beta H_\rho) / (\omega \epsilon_0) \quad [5]$$

$$\beta = [\omega^2 \mu_0 \epsilon_0 - h^2]^{1/2} \quad [6]$$

where E_0 is a constant, $\omega = 2\pi f$, ϵ_0 is the free space permittivity, $J_1(x_{np} \rho)$ is the Bessel function of order 1, $J_1'(x_{np} \rho)$ is the derivative of $J_1(x_{np} \rho)$ with respect to its argument, $(x_{np} \rho)$, x_{np} is the zero of the Bessel function, and $h = x_{np} / a$.

Figure 1 shows the E & H fields for an example structure where the radius $a = 2.15$ -cm, the radius $b = 2.2$ -cm, and the dielectric is sapphire with a permittivity 9.9. The frequency of the propagating wave is 18-GHz. The E_z and H_z fields are zero at the origin. The magnitudes of the H_ϕ and H_ρ add on the origin, as do the magnitudes of the E_ϕ and E_ρ field components to generate strong H_y and E_x fields in the transverse Cartesian plane. Fig. 2 is a Microwave Studio [9] computer generated plot of the transverse H-field for the same HEM₁₂ mode at 18-GHz in Fig.1.

*Work supported by the U.S. Department of Energy, Office of Science, under Contract No. DE-ACO2-O6CH11357.

COLLECTIVE EFFECTS AT INJECTION FOR THE APS-U MBA LATTICE *

R. Lindberg and M. Borland, ANL, Argonne, IL 60439, USA
A. Blednykh, BNL, Upton, Long Island, NY 11973, USA

Abstract

The Advanced Photon Source has proposed an upgrade to a multi-bend achromat (MBA) with a proposed timing mode that calls for 48 bunches of 15 nC each. In this mode of operation, we find that phase-space mismatch from the booster can drive large wakefields that in turn may limit the current below that of the nominal collective instability threshold. We show that collective effects at injection lead to emittance growth that makes ordinary off-axis accumulation very challenging. On-axis injection ameliorates many of these issues, but we find that transverse feedback is still required. We explore the role of impedance, feedback, and phase-space mismatch on transverse instabilities at injection.

INTRODUCTION

The Advanced Photon Source (APS) Multi-Bend Achromat (MBA) upgrade [1] plans to replace the existing 3rd generation storage ring with a 7-bend achromat. The nominal APS-U lattice is based on the design from Ref. [2], and aggressively pushes the emittance to 67 pm [3]. This results in strong nonlinearities and limited the dynamic aperture, such that on-axis swap-out injection [4, 5] is the only option. Recent work has investigated more forgiving alternate lattices that sacrifice the smallest emittance in exchange for a larger dynamic aperture and Touschek lifetime. The resulting 90 pm alternate lattice [6] has a dynamic aperture that appears to be suitable for accumulation. Since all conclusions regarding dynamic aperture are drawn from single particle tracking, here we discuss the extent to which collective effects may reduce injection efficiency and the charge-dependent (effective) dynamic aperture for the APS-U.

The APS-U plans to operate with an average current of 200 mA in one of two modes: the first is a “high brightness” mode that stores 324 bunches, while the second is a “timing mode” with 48 equally-spaced bunches. In the 324-bunch mode there is 2.4 nC/bunch, which is low enough that single-bunch collective effects typically do not play a major role. On the other hand, the timing mode has 15.3 nC/bunch, and collective effects can play a large role.

Our main focus will be how collective effects at injection reduce injection efficiency during accumulation in the 90-pm lattice. We will show that collective effects can result in significant emittance growth and particle loss within a few hundred turns of injection, so that the shared-oscillation method of top-up injection does not appear feasible at high charge with the assumed ± 4 -mm physical aperture. We

then make a few comments for on-axis injection in the 67 pm lattice, showing that non-equilibrium effects can drive collective oscillations at injection that need to be controlled with appropriate feedback.

COLLECTIVE EFFECTS DURING ACCUMULATION

As mentioned previously, simulations indicate that the 90-pm lattice can be filled with traditional accumulation when operated in the 324 bunch mode, albeit only if residual oscillations are shared between the stored and injected beams. On the other hand, we find that collective effects can significantly reduce the injection efficiency in the timing mode that has ~ 15 nC/bunch. These simulations are based on element-by-element tracking with Pelegant [7, 8], and use the impedance model described in [9] divided into 16 local impedance elements per sector.

In the simplest case where we assume no transverse feedback, collective effects combined with nonlinearities result in phase space filamentation and emittance growth over the first hundred turns. This in turn leads to an effective spread in oscillation amplitudes to the point where a significant fraction of the beam is lost on the physical aperture. We show transverse phase space plots that illustrate the beam size growth and subsequent loss on the aperture at $x = -4$ mm in Fig. 1. The corresponding reduction in current as a function of pass number is included in the last panel.

Figure 1 shows that transverse wakefields substantially increase the spread in oscillation amplitudes during the first ~ 100 passes; the initially nearly point-like beam at pass 0 becomes a broad smear by pass 56. Subsequent evolution continues to spread the beam outwards, leading to significant particle loss between pass 63 and 84. After this point the beam is left with less than 75% of its initial charge, and it continues to lose particles for the next few hundred turns.

We have found that qualitatively similar dynamics also occurs at lower initial charge. For example, if the initial current is 3 mA the beam filaments in a similar manner but to a lesser degree, with losses greater than 10%. Only when the charge is reduced by one-half to an initial single bunch current of 2.1 mA do we find that the losses drop below the amount of injected charge.

Applying transverse feedback is one potential way to limit the stored beam oscillations and subsequent filamentation. To assess whether this possibility might work in practice, we implemented elegant’s transverse feedback element TFBPICKUP with a 6-turn FIR filter. In the first trial run we allowed the feedback system to have unlimited strength, and chose the gain to be approximately 0.3 of its ideal. Perhaps

* Work supported by the U.S. Department of Energy, Office of Science, Office of Basic Energy Sciences, under Contract No. DE-AC02-06CH11357 (ANL) and DE-AC02-98CH10886 (BNL).

FIELD QUALITY FROM TOLERANCE STACK UP IN R&D QUADRUPOLES FOR THE ADVANCED PHOTON SOURCE UPGRADE*

J. Liu[†], M. Jaski, R. Dejus, C. Doose, A. Donnelly, J. Downey, M. Borland

Argonne National Laboratory, Argonne, IL 60439, USA

A. Jain, Brookhaven National Laboratory, Upton, NY 11973, USA

Abstract

The Advanced Photon Source (APS) at Argonne National Laboratory (ANL) is planning to upgrade the existing Double-Bend Achromat (DBA) 3rd generation storage ring lattice to a 4th generation Multi-Bend Achromat (MBA) lattice [1]. In this paper we present a novel method to determine fabrication and assembly tolerances for quadrupole magnets through combined magnetic and mechanical tolerance analyses. We performed mechanical tolerance stack-up analyses using the Teamcenter Variation Analysis package [2] to determine part and assembly fabrication tolerances and finite element analyses (FEA) using OPERA [3] to estimate the effect of fabrication and assembly errors on magnetic field quality and to set tolerances to achieve desired magnetic performances. We present our analysis results and make comparison to magnetic measurements of fabricated R&D magnets in this paper.

INTRODUCTION

The APS upgrade project (APS-U) is preparing to replace the existing storage ring lattice with a hybrid seven-bend-achromat lattice that provides dramatically enhanced hard x-ray brightness and coherent flux [4]. Tight manufacturing and alignment tolerances will be required for the new storage ring magnets. For example, the multipole components of the low order harmonics, at a reference radius of 10 mm, are required to be less than 10 units (0.1% of the main field). Further the magnet-to-magnet alignment within a girder needs to be better than 30 μm RMS.

We present results of joint mechanical tolerance stack-up analyses and 2D magnet simulation using code OPERA of an R&D quadrupole magnet. The mechanical tolerance stack-up analyses allocate tolerances to parts and assemblies based on magnet alignment requirements. The FEA 2D magnetic analyses are performed to determine multipole errors and their distributions under different tolerance conditions. Our results led us to find out key factors for the magnet performance and to develop a new magnet design which can achieve high magnetic field quality but does not require high precision machining.

MECHANICAL TOLERANCE ANALYSIS

The R&D quadrupole magnets are made of a top and a bottom two-piece solid steel yoke with removable pole bases and pole tips [5]. The Teamcenter Variation

Analysis software randomly generates parts within specified mechanical tolerances, virtually assembles parts using specified procedures, and virtually measures parts at specified locations. An example of distribution of a measurement is shown in Fig. 1(a). Two fabrication methods were simulated in detail: i) with the four pole tips assembled to the yoke and then machined tip profile using electrical discharge machining (EDM), and ii) with the four pole tips machined separately using regular CNC machine and then assembled to the yoke. The magnet mechanical center in the horizontal (X) direction are shown in Fig. 1(b) for two assembly tolerances: 20 μm and 50 μm (labeled A20 and A50, respectively) and three pole tip profile tolerances: $\pm 15 \mu\text{m}$, $\pm 25 \mu\text{m}$, and $\pm 50 \mu\text{m}$ (labeled P30, P50, and P100, respectively). The results for the vertical (Y) center are similar.

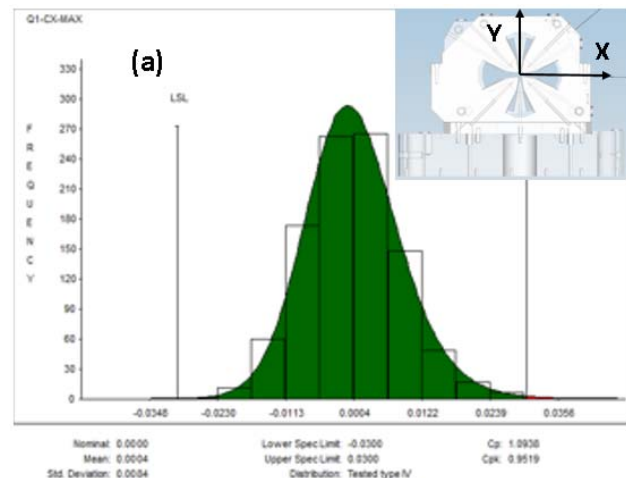


Figure 1: (a) Example of distribution of a measurement in mechanical tolerance analysis.

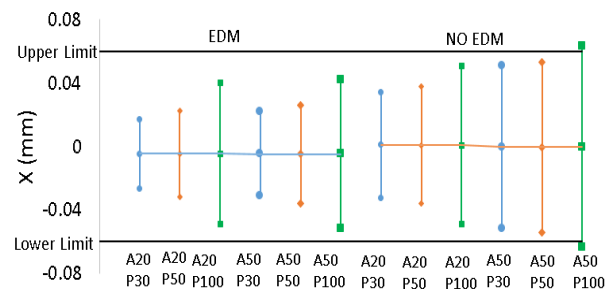


Figure 1: (b) Distribution of mechanical centers in X.

It was found in this study that the assembly tolerances for mating surfaces need to be better than 20 μm if EDM machining is not used. This in turn will be expensive and difficult to achieve for a series of production magnets. The assembly tolerances can be relaxed to 50 μm if EDM machining is used but this is expensive too and associated

* Work supported by U.S. Department of Energy, Office of Science, under contract numbers DE-AC02-06CH11357 and DE-SC0012704 for work at Brookhaven National Laboratory.

[†] jliu@aps.anl.gov

SIMULATION STUDY OF THE HELICAL SUPERCONDUCTING UNDULATOR INSTALLATION AT THE ADVANCED PHOTON SOURCE*

V. Sajaev, M. Borland, Y.-P. Sun, A. Xiao, ANL, Argonne, IL 60439, USA

Abstract

A helical superconducting undulator is planned for installation at the APS. Such an installation would be first of its kind, since a helical undulator was never installed in synchrotron light source before. Due to its reduced horizontal aperture, a lattice modification is required to accommodate large horizontal oscillations during injection. We describe details of the lattice change and show results of experimental tests of the new lattice. To understand the effect of the undulator on single-particle dynamics, we first computed kick maps using different methods. We have found that often-used Elleaume formula [1] for kick maps gives incorrect results for this undulator. We then used the kick maps obtained by other methods to simulate the effect of the undulator on injection and lifetime.

INTRODUCTION

Advanced Photon Source has been methodically developing superconducting undulators (SCU) for a number of years. Presently, two planar SCUs are in operation at APS [2]. As a next step, a helical superconducting undulator is in development, with installation planned for next year [3]. The main parameters of the undulator are given in Table 1. In an ordinary planar undulator, the vertical gap of the vacuum chamber is usually made as small as possible to reduce the distance between the magnet arrays and to increase the vertical magnetic field, while the horizontal gap is not important and is usually made comparatively large. This works well for the traditional injection design where large horizontal acceptance is required to capture the injected beam. In a helical undulator, the poles and coils form a circle around the vacuum chamber, and therefore both vertical and horizontal aperture is small. With a horizontal inside diameter of of 26

Table 1: Main Parameters of the Helical SCU

Cryostat length	1.85 m
Magnetic length	1.2 m
Undulator period	31.5 mm
Undulator field $B_x = B_y$	0.4 T
Undulator parameter	1.2
Magnetic bore diameter	31 mm
Full vacuum chamber gap	26 × 8 mm

mm, the helical undulator will become the smallest aperture in the ring. To avoid reduction of the horizontal acceptance, the beta functions at the SCU location must be changed.

* Work supported by the U.S. Department of Energy, Office of Science, Office of Basic Energy Sciences, under Contract No. DE-AC02-06CH11357.

In this paper, we describe the required lattice modification and simulate the effect of the helical undulator on the beam dynamics.

LATTICE MODIFICATIONS

The original APS lattice is made of 40 nearly-identical sectors, each of which has a 5-m-long straight section for insertion device (ID) installation. The Twiss parameters at the standard ID center are $\beta_x = 19.5$ m, $\beta_y = 2.9$ m, and $\eta_x = 0.17$ m. To better serve the user program at sector 32, a few years ago the beta functions there were modified to $\beta_x = 3.6$ m, $\beta_y = 5.0$ m, and $\eta_x = 0.07$ m, which allowed for the horizontal beam size reduction by a factor of 2.3. The effect of this single-sector symmetry breaking on the nonlinear dynamics was minimal and did not require any special sextupole optimization. This lattice is now in operation full time.

From the previous experience with planar SCUs we know that excessive beam losses at the SCU location can lead to magnet quenches [4]. Since the HSCU horizontal gap of ± 13 mm will be the smallest horizontal physical aperture in the ring, to avoid beam losses inside the device the beta functions must be modified to increase acceptance at this location. The following conditions were considered for lattice modification: (1) the HSCU vacuum chamber extends from +0.7 m to +2.2 m relative to the center of the sector 7 straight section and has a gap of ± 13 mm × ± 4 mm; (2) the HSCU chamber acceptance should be larger than the two smallest existing acceptances; (3) the smallest existing acceptance is sector 4 ID chamber with gap of ± 15 mm × ± 2.4 mm that extends from -2.5 m to +2.5 m relative to the center of the ID straight section; (4) the second smallest acceptance is a number of ID chambers with gap of ± 18 mm × ± 3.5 mm that have the same length as the sector 4 chamber; (5) the horizontal dispersion at HSCU needs to scale with the horizontal limiting aperture locations (ID4 and other IDs) to preserve Touschek lifetime; (6) the modified beta functions should deviate from the standard sectors as little as possible.

A lattice that satisfies all the above conditions was designed using the optimizer in `elegant` [5]. The lattice functions at the entrance of sector 7 were fixed, and all 10 quadrupoles in sector 7 were used in optimization. The quadrupoles in sector 8 were then set to provide mirror symmetry around the end of sector 7 (middle of the sector 7 ID straight section) to return the lattice functions back to the original values at the exit of sector 8. The lattice functions of sectors 7 and 8 are shown in Figure 1. The drift spaces at the left and right ends of the plot correspond to the standard ID straight sections while the drift space in the middle of the plot is the straight section with modified beta functions.

TUNING OF THE APS LINAC ACCELERATING CAVITIES AFTER STRUCTURAL RE-ALIGNMENT*

T.L. Smith, G. Waldschmidt
ANL, Argonne, IL 60439, USA

Abstract

A new S-band LCLS type Photo-cathode (PC) gun was recently installed in the APS linac. As a consequence, it was recognized that many of the linac accelerating structures were out of their 1 mm straightness tolerance. In order to reduce the effects of wakefield on the beam and increase the quality of the beam transport, several of the misaligned structures were straightened. This paper discusses the bead-pull RF measurements, the effect of the straightening efforts on the rf performance and the cell-to-cell retuning efforts that were performed.

INTRODUCTION

To take full advantage of the improved beam quality produced by the new photocathode gun recently installed in the linac, an effort has been initiated to straighten the accelerating structures. Due to physical connections made to the structures in the APS tunnel, they were found to have been deformed by up to ~6 mm. Two of the thirteen structures in the linac and two spares have been straightened, at this time, with a worst-case of 5.4 mm total deformation [1] before straightening.

Initial mechanical straightening of the structures to within the $\pm 200 \mu\text{m}$ specification resulted in significant impact on the rf properties of the structures. The most apparent impact was found on the input match which changed from -30 dB to -12 dB on the first structure. This effect was also closely related to the degradation of the cell-to-cell phase advance. The source of the degradation of the rf performance as well as the methodology used to measure and recover the structure for optimal operation will be discussed.

BEAD-PULL RF TUNING METHOD

A bead-pull method using a non-resonant perturbation algorithm [2] was used on the linac structures. With this approach, the complex electric field values were measured thereby accommodating field amplitude and phase advance calculations. Assuming a small perturbation (copper cylinder = 2 mm diameter x 5 mm length), the change in input reflection at the position of the bead is proportional to the sum of the square of the magnitude of the electromagnetic field components. Bead-pull algorithms such as this are commonly available for traveling wave accelerating cavities [3] as well as for deflecting cavities [4,5]. This method is capable of making amplitude and cell-to-cell phase measurements in real time for fast and accurate tuning of an APS linac accelerating structures shown in Fig. 1.

* Work supported by U.S. Department of Energy, Office of Science, under Contract No. DE-AC02-06CH11357.

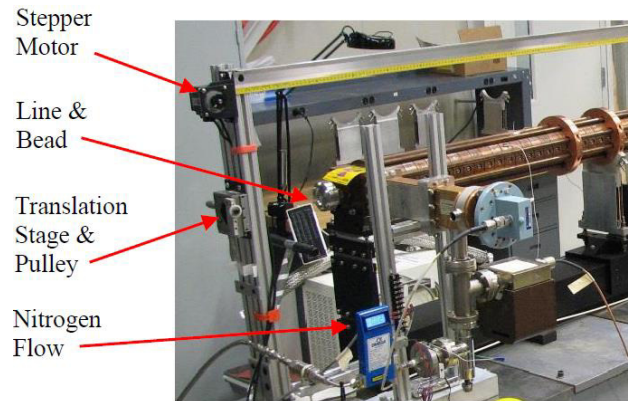


Figure 1: Linac structure with bead-pull setup.

The perturbing bead is supported on a $90 \mu\text{m}$ diameter nylon fish line and pulled through the structure using a servo motor which is controlled by a LabVIEW program. The bead is pulled at a constant speed with continuous data acquisition to quickly and efficiently measure each structure. Phase advance measurements were made using the electric field values at the same relative locations in each of the interior cells. These locations were determined by searching for the peak electric field value within a cell and performing a least squares fit to compensate for noisy data [4]. The phase advance of a given cell was calculated using the electric field in the current cell and in both neighboring cells.

The local reflection coefficients (LRCs) are derived from the electric field in each cell and are used to create a quantitative measure of the amount of tuning required in an individual cell to compensate for any deviation of the cell from the desired cell-to-cell phase advance. In effect, the LRC guides the extent of the deformation which needs to be applied to the tuning apparatus of each cell. Conveniently, the LRC is defined at each cell and can be referenced back to the global reflection coefficient measured by a network analyzer. The tuning of an individual cell can be performed by appropriately interpreting the global reflection coefficient and tuning only a moderate percentage (~40%) of the reflection at each cell. Tuning of the interior cells typically requires several passes over the entire structure to get it within specifications of $120^\circ \pm 1^\circ$.

STRUCTURE STRAIGHTENING AND BEAD-PULL RF MEASUREMENTS

Before any tuning, the structure is mounted onto the strong back along with supports and saddles. The mechanical straightening process is performed by applying pressure on the structure at the four different support locations as shown in Fig. 2. The saddle's width is

MULTI-OBJECTIVE ONLINE OPTIMIZATION OF BEAM LIFETIME AT APS*

Yipeng Sun[†], ANL, Argonne, IL 60439, USA

Abstract

In this paper, online optimization of beam lifetime at the APS (Advanced Photon Source) storage ring is presented. A general genetic algorithm (GA) is developed and employed for some online optimizations in the APS storage ring. Sextupole magnets in 40 sectors of the APS storage ring are employed as variables for the online nonlinear beam dynamics optimization. The algorithm employs several optimization objectives and is designed to run with topup mode or beam current decay mode. Up to 50% improvement of beam lifetime is demonstrated, without affecting the transverse beam sizes and other relevant parameters. In some cases, the top-up injection efficiency is also improved.

OVERVIEW

Multi objective optimization methods and techniques are widely used [1] (see a review in [1]) in many aspects of engineering and physics studies, including the genetic algorithms [2, 3]. Starting in 2005 [4, 5], accelerator and beam applications became widespread. For storage rings, the dynamic acceptance, local momentum acceptance and Touschek lifetime, and other nonlinear terms were optimized using genetic algorithms in tracking simulations [6–10].

Online machine-based single- or multi-objective optimizations were also performed on operating storage rings [11, 12]. For example, beam loss rate was employed to minimize average vertical beam sizes in SPEAR3 ring by applying the genetic algorithms [11]. Dynamic apertures of the SPEAR3 ring was optimized by tuning sextupole magnets with online optimizations [12]. Here online optimization of beam lifetime at the APS (Advanced Photon Source) storage ring is presented, which is similar to the study of Huang [12]. The online machine-based optimizations of nonlinear beam dynamics may have an advantage over nominal simulation-based techniques, as it is applied with the accelerator models replaced by the real accelerators.

The Advanced Photon Source storage ring is a third-generation synchrotron radiation light source, with a circumference of 1104 meters [13], 40 sectors and an effective beam emittance of 3.13 nm [14]. The main operational lattice has reduced horizontal beam size (RHB) at one ID straight. The linear optics in one of the 38 nominal sectors is shown in Fig. 1, where the starting and ending point are the insertion device (ID) center. In the following sections, some experimental results of lifetime optimization are presented and discussed. The nominal bunch fill pattern is 24

equi-spaced bunches, with a total beam current up to 102 mA.

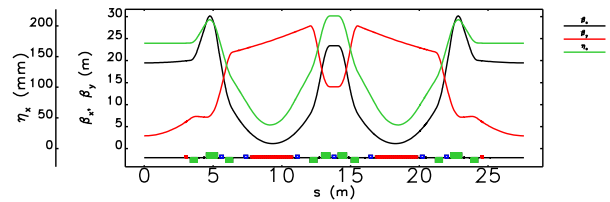


Figure 1: Twiss parameters in one arc section of APS storage ring. Green blocks represent quadrupoles, red blocks represent dipoles, and blue blocks represent sextupoles.

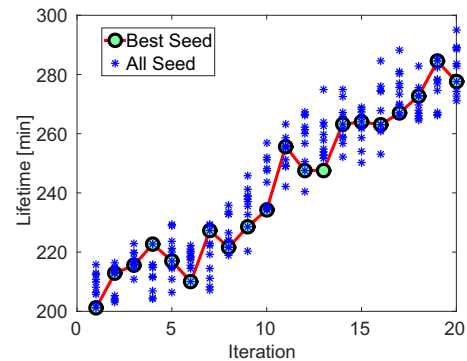


Figure 2: Lifetime (calculated using DCCT current measurements) at each iteration. A total of 20 iterations (finished in a short time), and 10 seeds for each iteration. Starting point is optimized sextupoles from MOGA simulation [7] [15] on the high chromaticity lattice ($\xi = 11$).

OPTIMIZATION ALGORITHM

A genetic algorithm was developed and employed for some online optimizations in APS storage ring. Compared with nonlinear beam dynamic optimization through numerical tracking simulations, online machine-based optimization targets the measured, rather than predicted, real accelerator performances. Possible optimization objectives include the beam lifetime, injection efficiency, beam loss [11], and transverse beam sizes measured at the pinhole camera. The optimization variables may include the quadrupole magnet strengths, skew quadrupole magnet strengths, sextupole magnet strengths [12], and upstream injectors.

For the lifetime optimization, sextupole magnets in up to 40 sectors of the APS storage ring were employed as tuning knobs. There are seven sextupole magnets in each sector which are usually powered as seven families for more

* Work supported by the U.S. Department of Energy, Office of Science, Office of Basic Energy Sciences, under Contract No. DE-AC02-06CH11357.

[†] yisun@aps.anl.gov

ONLINE MINIMIZATION OF VERTICAL BEAM SIZES AT APS*

Yipeng Sun[†], ANL, Argonne, IL 60439, USA

Abstract

In this paper, online minimization of vertical beam sizes along the APS (Advanced Photon Source) storage ring is presented. A genetic algorithm (GA) was developed and employed for the online optimization in the APS storage ring. A total of 59 families of skew quadrupole magnets were employed as knobs to adjust the coupling and the vertical dispersion in the APS storage ring. Starting from initially zero current skew quadrupoles, small vertical beam sizes along the APS storage ring were achieved in a short optimization time of one hour. The optimization results from this method are briefly compared with the one from LOCO (Linear Optics from Closed Orbits) response matrix correction.

OVERVIEW

Multi objective optimization techniques are useful tools in finding optimum solutions in many complex systems [1] with many optimization targets and variables/knobs, including applications of genetic algorithms [2,3]. On accelerator and beam-related topics, the genetic algorithm was implemented in 1992 on optimizing sequences of permanent magnet segments of wiggler magnets [4]. Such algorithm was then used for dc-gun photoinjector design optimizations [5], the International Linear Collider damping rings design [6], and electron storage ring nonlinear beam dynamics optimizations based on numerical tracking simulations [7–11].

Recently machine-based online single-objective or multi-objective optimizations were also performed experimentally on operating storage rings, to optimize the dynamic aperture (DA) in SPEAR3 storage ring [12], also to minimize vertical beam sizes along SPEAR3 ring [13]. It was proposed by Tian et al. [13] to employ specific physics quantities that could be measured instantly on an operating accelerator, while it may take a long time to compute such physics quantities in the numerical tracking simulations. For accelerator-based particle colliders, an example of such a physics quantity is the luminosity of two colliding beams [13]. To optimize the photon brightness via reducing average beam sizes at IDs, it is proposed to employ the total beam loss rates [13] as the optimization objective since it is inversely proportional to average beam intensity along the ring. As pointed out by Franchi et al. [14], smaller horizontal-vertical-coupling has three potential advantages: enabling smaller vertical-gap-IDs with higher fields, hence enhancing the photon flux; improving the photon brightness given it is not limited by energy spread; improving injection efficiency for off-axis accumulation schemes. On the other

hand, it is also noted [14] that reduced vertical beam sizes may introduce some reductions on Touschek lifetime which may have negative impact on photon users.

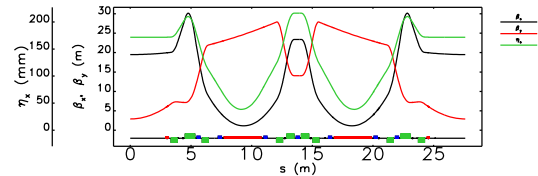


Figure 1: Twiss parameters in one arc section of APS storage ring. Green blocks represent quadrupoles, red blocks represent dipoles, and blue blocks represent sextupoles.

In this paper, online minimization of beam sizes along the APS (Advanced Photon Source) storage ring is presented, which is similar to the study of Tian et al. [13]. The Advanced Photon Source storage ring light source has a circumference of 1104 meters [15] with an effective beam emittance of 3.13 nm [15, 16]. The nominal operation mode employs the so-called reduced horizontal beam size (RHB) lattice where horizontal beta function is reduced at one specific insertion device. The linear optics in one of the normal sectors is shown in Figure 1 above. In the following sections, experimental results of beam sizes minimization in APS ring are presented. The bunch fill pattern is 24 or 324 bunches that are evenly distributed in the storage ring.

OPTIMIZATION ALGORITHMS

As the online machine-based optimization method is applied on real accelerators, and uses the real accelerator performances as the optimization targets, it may have an advantage over the nominal simulation based techniques. A total of 59 families of skew quadrupole magnets were employed as knobs to adjust the coupling and vertical dispersions in APS storage ring. A general genetic algorithm was developed and employed for online machine-based optimization studies in the APS storage ring. For the online minimization of beam sizes along the ring, the algorithm could employ one or more of the following evaluation objectives.

- Beam loss rate monitor readings [13]
- Horizontal and vertical beam sizes (measured at sector 35 pinhole location)
- Lifetime calculated using DCCT measurements
- Total beam current measured from DCCT

The following operation bunch modes are available, with some possible advantages and disadvantages listed below.

- 24-bunch mode, with a single bunch current up to 4.1 mA. This bunch mode has a higher beam loss rate and a stronger impact from collective effects.
- 324-bunch mode, single bunch current up to 0.3 mA. Beam loss rates may be more noisy for this mode.

* Work supported by the U.S. Department of Energy, Office of Science, Office of Basic Energy Sciences, under Contract No. DE-AC02-06CH11357.

[†] yisun@aps.anl.gov

APS-U LATTICE DESIGN FOR OFF-AXIS ACCUMULATION*

Yipeng Sun[†], Michael Borland, Ryan Lindberg, and Vadim Sajaev, ANL, Argonne, IL 60439, USA

Abstract

A 67-pm hybrid-seven-bend achromat (H7BA) lattice is being proposed for a future Advanced Photon Source (APS) multi-bend-achromat (MBA) upgrade project. This lattice design pushes for smaller emittance and requires use of a swap-out (on-axis) injection scheme due to limited dynamic acceptance. Alternate lattice design work has also been performed for the APS upgrade to achieve better beam dynamics performance than the nominal APS MBA lattice, in order to allow off-axis accumulation. Two such alternate H7BA lattice designs, which target a still-low emittance of 90 pm, are discussed in detail in this paper. Although the single-particle-dynamics performance is good, simulations of collective effects indicate that surprising difficulty would be expected accumulating high single-bunch charge in this lattice. The brightness of the 90-pm lattice is also a factor of two lower than the 67-pm H7BA lattice.

OVERVIEW ON ALTERNATE LATTICE DEVELOPMENT

The equilibrium emittance is aggressively pushed to a low value in the nominal lattice design [1] of the Advanced Photon Source (APS) Multi-Bend Achromat (MBA) upgrade. To achieve low emittance, seven bending magnets with either transverse or longitudinal gradients, plus strong quadrupole focusing are employed in each of the 40 arc cells [2]. The strong nonlinearities introduced by the chromaticity correction sextupoles make the dynamic acceptance (DA) insufficient for beam accumulation, given the large injected beam size from the booster and the assumed 2-mm septum thickness. The on-axis swap-out injection scheme [3, 4] is the only option for this lattice.

Alternate lattices have also been studied with relaxed goals for the equilibrium emittance, which aim to achieve better beam dynamics performance than the nominal lattice, and allow possibility for traditional off-axis accumulation injection scheme. There are some advantages and requirements of adopting off-axis accumulation

- Requires minimal changes to the existing systems (injectors, control system, timing system, etc.).
- Does not require new capabilities as for the on-axis injection scheme (very fast stripline kickers, high-charge-booster, a new beam dump system, etc.).
- Requires better magnet quality, alignment precision, power supply stability, and beam trajectory plus orbit control.

- May require some additional octupole magnets and the power supplies for these magnets, in order to achieve larger dynamic acceptance.
- Needs special optics design (smaller β_x) at some insertion devices (ID) to accommodate small horizontal gap IDs (helical undulator etc.).

Three types of lattice design, from five-bend achromat (5BA) to 8BA, were investigated and compared in terms of the requirements on the technical systems (magnets, power supply, vacuum) and the nonlinear beam dynamics performance, as listed below. The MAX-IV style: uniform TME cells with many families of sextupoles [5]; the ESRF-II style: high dispersion bump with -I phase separation [2]; the SIRIUS-inspired style [6]: a combination of MAX-IV and ESRF-II styles. Reverse bending fields in some focusing quadrupole magnets [7, 8] are also studied and employed in the lattice design. In the following sections, two 90-pm Hybrid-7BA lattice design are presented in some detail. The general APS-U lattice design considerations plus hard constraints are employed [1].

LINEAR AND NONLINEAR OPTICS

To achieve a high dispersion bump and a smaller emittance, two longitudinal gradient dipoles (LGD) with three uniform-length segments each are adopted at both sides of the dispersion bump. The maximum bending field is 0.44 T in the LGDs, while it is 0.72 T in the central transverse gradient bending magnet. There are 16 quadrupole magnets per sector, with a maximum gradient of 81 T/m. All the quadrupole magnets are matched [9, 10] to be within engineering design limits with at least 10% margin, while all the sextupole magnets are within 20% margin of engineering design limits. The maximum pole-tip fields for the magnets are: 1 T for quadrupoles; 0.6 T for sextupoles; 0.3 T for octupoles.

Compared to the nominal APS-U lattice, the alternate 90pm lattice has several potential advantages:

- Uniform-section-length LGD dipole magnets may be easier to produce and operate than the five-section, variable-section-length dipoles for the nominal lattice.
- There are 2.5 meters free space next to the two LGDs inside the dispersion bump available in each sector for other components (e.g., traditional injection kickers, skew quadrupoles magnets, steering magnets, etc.).
- There are four additional 0.32 m spaces available for octupoles inside the dispersion bump in each sector.
- The ID straight length is increased from 5.8 m to 6.1 m, which can accommodate two additional harmonic sextupoles for nonlinear optics tuning.

The Twiss parameters for one sector of 90pm alternate lattice are shown in Fig. 1. Four injection kickers and one injection septum are employed in one unmodified 90pm lat-

* Work supported by the U.S. Department of Energy, Office of Science, Office of Basic Energy Sciences, under Contract No. DE-AC02-06CH11357.

[†] yisun@aps.anl.gov

COMPARISON OF NONLINEAR DYNAMICS OPTIMIZATION METHODS FOR APS-U*

Yipeng Sun[†], Michael Borland, ANL, Argonne, IL 60439, USA

Abstract

Many different objectives and genetic algorithms have been proposed for storage ring nonlinear dynamics performance optimization. These optimization objectives include nonlinear chromaticities and driving/detuning terms, on-momentum and off-momentum dynamic acceptance, chromatic detuning, local momentum acceptance, variation of transverse invariant, Touschek lifetime, etc. In this paper, the effectiveness of several different optimization methods and objectives are compared for the nonlinear beam dynamics optimization of the Advanced Photon Source upgrade (APS-U) lattice. The optimized solutions from these different methods are preliminarily compared in terms of the dynamic acceptance, local momentum acceptance, chromatic detuning, and other performance measures.

OVERVIEW

Next-generation storage ring light sources, such as the Advanced Photon Source (APS) Multi-Bend Achromat (MBA) upgrade, will improve the x-ray brightness by roughly two orders of magnitude. For APS upgrade (APS-U), the equilibrium emittance is pushed from the current 3 nm to below 100 pm. To achieve this low emittance, the original double-bend achromat lattice is replaced by a hybrid seven-bend-achromat (H7BA) lattice [1], where seven bending magnets with either transverse or longitudinal gradients, plus strong quadrupole focusing, are employed in each of the 40 arc cells. The strong nonlinearities introduced by the chromaticity sextupoles make it hard to achieve large dynamic acceptance (DA) and long Touschek lifetime, even for the on-axis swap-out injection scheme [2].

A direct-tracking-based multi-objective genetic algorithm (MOGA) [3–6] is employed to vary the linear optics and optimize the nonlinear elements (typically sextupoles, but also octupole magnets) for better beam dynamics performance. The optimization objectives include: DA; Touschek lifetime computed from local momentum acceptance (LMA); and the desired positive chromaticity for high bunch charge mode. The algorithm can include realistic errors and find robust solutions. The disadvantage is that the LMA simulation takes significant computing time.

In this paper, several alternate optimization objectives are explored which may be faster and yet provide good nonlinear optics solutions. These optimization objectives include: analytically calculated nonlinear chromaticities and driving/detuning terms; on-momentum and off-momentum

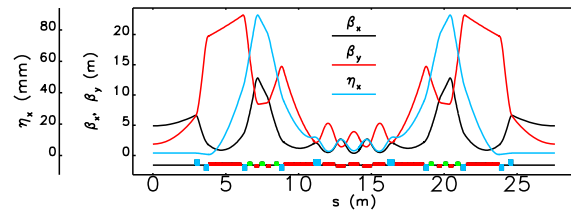


Figure 1: Twiss parameters in one sector of a 41-pm, H7BA lattice design for APS-U. Blue blocks represent quadrupoles, red blocks represent dipoles, and green blocks represent sextupoles.

dynamic acceptance [7, 8]; and minimization of variation of the Courant-Snyder invariant [9] [10, 11]. Consideration of the chromatic detuning is also included in most of these cases. In the following sections, details are presented on the applications of these nonlinear optics optimization methods.

OPTIMIZATION KNOBS

For all the nonlinear optics optimizations, a same APS-U H7BA lattice is employed which emittance is 41 pm with reverse bending fields [12]. The TWISS parameters are shown in Figure 1 for one sector. The nominal betatron tunes are (95.1, 36.1) and the linear chromaticities are all corrected to be (5, 5) for the high bunch charge mode. For the hybrid achromat lattice scheme [1], there are 3 pairs of sextupole magnets in each sector, with betatron phase advance of $\Delta\nu_x = 3\pi$ and $\Delta\nu_y = \pi$ between each pair (designed to cancel geometric aberrations [1]). Usually a two-sector translational symmetry is adopted, giving a maximum of 12 families of sextupoles. Octupole fields may be integrated in the 8-pole fast corrector magnets. The algorithms are allowed to vary up to 10 families of sextupole magnets, with two families reserved for the linear chromaticity, plus up to 4 families of octupole magnets. Simulation is performed with ELEGANT [13].

OBJECTIVE: DA AND LMA

The nominal optimization method is a direct-tracking-based MOGA [5, 6]. It is employed to directly optimize the Touschek lifetime (through local momentum acceptance) and the injection efficiency (through dynamic acceptance with physical apertures). Recently chromatic detuning from direct tracking is also included as another optimization objective. The optimized solutions are robust in ensemble evaluations after commissioning simulation [2]. The disadvantage is that the local momentum acceptance takes a long time to compute. A MOGA optimization process is

* Work supported by the U.S. Department of Energy, Office of Science, Office of Basic Energy Sciences, under Contract No. DE-AC02-06CH11357.

[†] yisun@aps.anl.gov

SIMULATION STUDIES OF A PROTOTYPE STRIPLINE KICKER FOR THE APS-MBA UPGRADE*

X. Sun[†], C. Yao, ANL, Argonne, IL 60439, U.S.A.

Abstract

A prototype dual-blade stripline kicker for the APS multi-bend achromat (MBA) upgrade has been designed and developed. It was optimized with 3D CST Microwave Studio. The high voltage (HV) feedthrough and air-side connector were designed and optimized. The electromagnetic fields along the beam path, deflecting angle and high electric fields with their locations were calculated with 15 kV differential pulse voltage applied to the kicker blades through the feedthroughs. The beam impedance and power dissipation on different parts of the kicker and external loads were studied for a 48-bunch fill pattern. Our simulation results show that the prototype kicker with its HV feedthroughs meets the specified requirements. The results of TDR (time-domain reflectometer) test, high voltage pulse test and beam test of the prototype kicker assembly agreed with the simulations.

INTRODUCTION

A fast kicker is needed for swap-out injection in APS-MBA Upgrade [1-2]. The kicker assembly consists of the stripline kicker and high voltage feedthrough, as shown in Fig. 1.

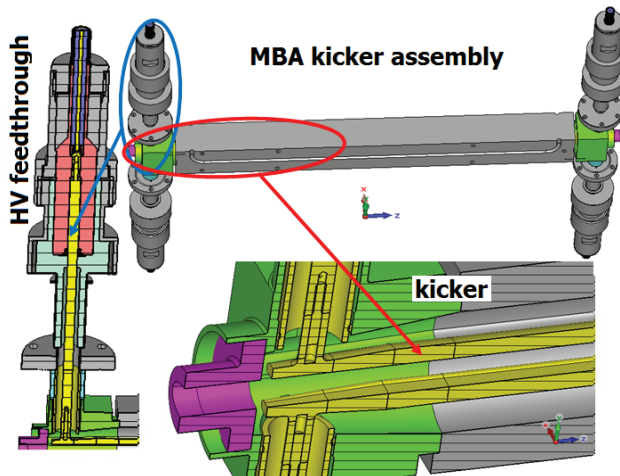


Figure 1: The MBA kicker assembly.

The stripline kicker and high voltage feedthrough with air-side connector need to be designed for impedance matching throughout the structure to achieve the maximum kicker strength, reduce local high voltage concentration, which can lead to breakdown, and minimize the beam impedance. The kicker and feedthrough with air-side connector were designed and optimized to match 50 Ω impedance. Then the electromagnetic fields, wake impedance, beam power loss and power dissipation on the metals and external loads were analysed.

* Work supported by the U. S. Department of Energy, Office of Science, Office of Basic Energy Sciences, under Contract No. DE-AC02-06CH11357.

[†] xiang@aps.anl.gov

2D STRIPLINE KICKER MODEL

The main part geometry of the kicker was designed with a 2D modelling program [3]. It was optimized to match the differential impedance as close as possible to 50 Ω while allowing some mismatch in the common-mode impedance. “D” shaped blades were adopted to improve field uniformity in the good field region. The tapered sections were added to both ends of the kicker to improve impedance matching to the feedthroughs.

The optimized geometry is shown in Fig. 2.

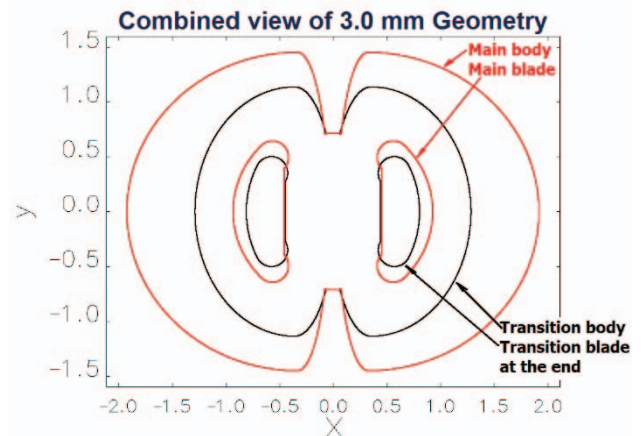


Figure 2: 2D modelling result geometry.

3D SIMULATION OF THE KICKER

A 3D kicker model was developed based on 2D simulation results, as shown in Fig. 3, and CST Microwave (MWS) [4] was applied.

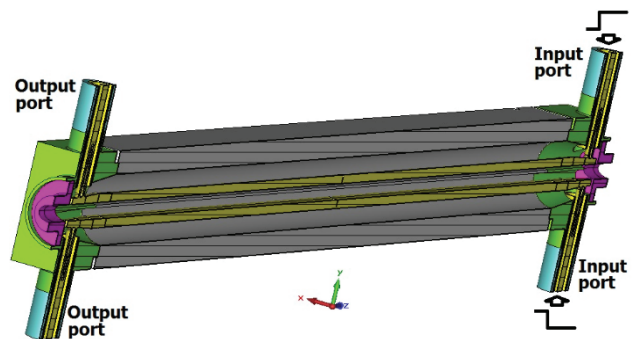


Figure 3: 3D prototype kicker model.

The 3D simulation verified the 2D results and further optimized the tapered part of the stripline kicker. The optimization of the tapered blades and body minimized the reflecting and improved the interface to the feedthrough.

The kicker differential and common-mode impedances were calculated and shown in Fig. 4. The optimized geometry gives a differential-mode impedance of 50 Ω with

BEND MAGNET HEAT LOADS AND OUT OF ORBIT SCENARIOS*

Timothy Valicenti^{1†}, Kamlesh Suthar[‡], Jason Carter, and Patric Den Hartog

Argonne National Laboratory, Lemont, U.S.

¹ also at Brown University, Providence, U.S.

Abstract

This paper presents an analytical calculation of the spatial power spectrum emitted from relativistic electrons passing through a series of bend magnets. Using lattice files from the software Elegant, both the ideal and missteered trajectories taken by the beam are considered in determination of the power profile. Calculations were performed for the Advanced Photon Source Upgrade multi-bend-achromat storage-ring. The power distribution and integrated total power values are in agreement with Synrad, a monte-carlo based program developed at CERN, within one percent error. The analytic solution used in this software gives a both quick and accurate tool for calculating the heat load on a photon absorber. The location and orientation can be optimized in order to reduce the peak intensity and thus the maximum thermal stress. The program can be used with any optimization or FEA software and gives rise to a versatile set of uses. [1]

INTRODUCTION

Problem Statement

When accelerated through a magnetic field, relativistic electrons emit synchrotron radiation. As shown in Figure 1, this radiation creates a spatial power distribution on intercepting surfaces which may be used to calculate the resultant heat load. The problem may be broken up into several simpler steps. These involve computing the ideal trajectory that the bunch of electrons take; adding real orbital errors to this trajectory; ray tracing the emitted photons; and determining the intensity of the power where each ray lands.

Solution

A parameterization of the ideal path is used; thus discrete time steps are chosen. MATLAB was used with N_t equidistant time steps that each create a ray that impacts the input photon absorber per analysed bend magnet. For each of these rays, a vertical spread of N_y points is created and the full power spectrum is calculated. This gives a mesh of varying density and $N_t * N_y$ points.

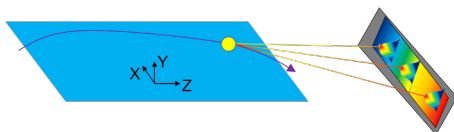


Figure 1: Problem setup.

* Work supported by Argonne National Laboratory and the DOE

† timvalicenti@gmail.com

‡ Corresponding Author: suthar@anl.gov

Many initial values such as the magnetic field strength, geometrical constants of the magnets, and beam energies are taken from a lattice file created by the program Elegant.

THEORY AND METHOD

Ideal Trajectory

To solve for the proper electron trajectory, values in the Elegant output file are used – given at the end of the previous element (denoted by subscript 0). In a dipole field, the path taken follows an arc of a circle. This can be done using a parameterization with a radius of curvature given by Eq. (1) [2].

$$\rho = \frac{m(\gamma)v}{q_e B} \text{ m} \quad (1)$$

In order to place the trajectory in the proper location in global ZXY-position space, the curve must be oriented and translated according to the initial conditions of the beam. If θ is the angle that the beam enters a dipole field at with respect to the Z-axis, then Eq. (2). gives the ideal path. The second term is the initial position found by translating the end coordinates of the previous element by the drift length, δs . Here $\bar{R}_{\bar{Y}}(\theta_0)$ is a counterclockwise rotation matrix about the vertical direction \bar{Y} by the angle θ_0 . This parameterization is solely for the trajectory of the electron within dipole magnets.

$$\bar{r}(t) = \bar{R}_{\bar{Y}}(\theta_0) \begin{bmatrix} \rho \sin(\frac{v}{\rho}t) \\ \rho(\cos(\frac{v}{\rho}t) - 1) \\ 0 \end{bmatrix} + \begin{bmatrix} Z_0 + \delta s \cos \theta_0 \\ X_0 + \delta s \sin \theta_0 \\ 0 \end{bmatrix} \quad (2)$$

Off Orbit Trajectories

The lattice files give Courant-Snyder (or Twiss) parameters (α and β) which can be used to define two phase space ellipses - one for errors along the local x-axis and one for errors along the local y-axis. To achieve the values at the start of the magnet, they must be taken from the previous element in the lattice file and translated across the drift length (Eq. (4) and Eq. (5)) [3,4].

$$\alpha_1 = \alpha_0 - \gamma_0 \delta s \quad (3)$$

$$\beta_1 = \beta_0 - 2\alpha_0 \delta s + \gamma_0 \delta s^2 \quad (4)$$

$$A_u = \gamma_{x,1} x^2 + \alpha_{x,1} x x' + \beta_{x,1} x'^2 \quad (5)$$

$$A_u = \gamma_{y,1} y^2 + \alpha_{y,1} y y' + \beta_{y,1} y'^2 \quad (6)$$

For each missteered path, one selects a point within each ellipse corresponding to the orbital errors. The trajectory is

SUMMARY OF Cs₂Te PHOTOCATHODE PERFORMANCE AND IMPROVEMENTS IN THE HIGH-GRADIENT, HIGH-CHARGE AWA DRIVE GUN

E.E. Wisniewski, M. Conde, D.S. Doran, W. Gai,
W. Liu, J.G. Power, and C. Whiteford, ANL/HEP, Argonne, IL USA
S.P. Antipov, C.Jing, Jiaqi Qiu ANL/HEP Argonne, IL; Euclid TechLabs, LLC, Solon, OH USA

Abstract

The AWA L-band, high-charge photoinjector for the 70 MeV drive beamline has been operating for almost 3 years at the Argonne Wakefield Accelerator (AWA) facility. at Argonne National Laboratory (ANL). The gun operates at high-field (85 MV/m peak field on the cathode) and has a high quantum efficiency (QE) Cesium telluride photocathode with a large area (30 mm diameter). It produces high-charge, short pulse, single bunches ($Q > 100$ nC) as well as long bunch-trains ($Q > 600$ nC) for wakefield experiments (high peak current). During the first two years of operation, photocathode performance was evaluated and areas of improvement were identified. After study, consideration and consultation, steps were taken to improve the performance of the photocathode. So far, in total, three photocathodes have been fabricated on-site, installed and operated in the gun. Improvements made to the photocathode plug, vacuum system, and gun operation are detailed. The results include vastly improved conditioning times, better cathode performance, and QE above 4% for over 11 months.

THE ARGONNE WAKEFIELD ACCELERATOR (AWA) DRIVE PHOTOCATHODE GUN

The AWA L-band drive gun for the new 75 MeV drive linac has been commissioned and is operating. The 1.3 GHz photo-injector operates at high gradient (85 MV/m). The 31 mm dia. Cesium telluride photocathode, specifically designed for the production of high charge, is fabricated on-site. The method of fabrication used at AWA was based on and developed from methods published by researchers at LANL and INF-LASA and described in detail elsewhere [1, 2]. Using those sources for guidance, the AWA Cs₂Te photocathode is fabricated in a UHV chamber with a base pressure of 1.5×10^{-10} Torr and transported to the drive gun for installation in a UHV load-lock chamber.

The photoinjector generates high-charge, short pulse, single bunches ($Q > 100$ nC) and bunch-trains ($Q > 450$ nC) for wakefield (and other) experiments. The photocathode requirements at AWA were determined by the drive beam parameters. The AWA drive beam parameters are summarized in Table 1 [3].

Table 1: AWA Drive Beam Cathode Operating Parameters

Cathode peak RF field	>85 MV/m
RF pulse length	$\approx 7.6 \mu\text{s}$
Average dark current	<5 nC/RF pulse
QE%	>1%
QE lifetime	>1 month
Laser pulse width	1.5 – 8 ps FWHM
Single-bunch charge	100pC to >100nC
Multi-bunch mode:	<ul style="list-style-type: none"> • up to 50 nC/bunch • 2 to 32 bunches • bunch spacing = 770 ps • Max charge = 0.6 μC

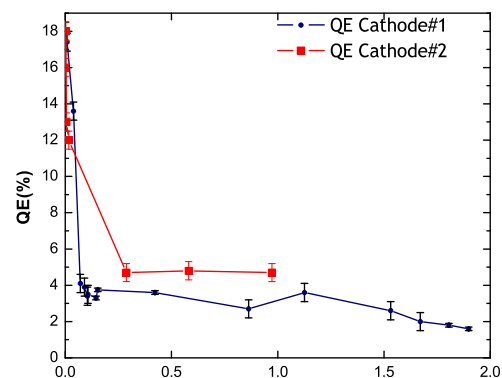


Figure 1: QE vs. time for the two AWA drive gun photocathodes installed since August 2013. QE drops sharply during RF conditioning to 88 MV/m and stabilizes to about 4% during subsequent operation.

PHOTOCATHODE PERFORMANCE SUMMARY

After initial RF conditioning to 88 MV/m, the QE of Cathode1 stabilized at a solid 3.5%, 3.5 times the requirement. Single bunch and bunch-train QE phase scans were flat, an indication that there was no field enhancement of QE analogous to the Schottky effect observed in metal photocathodes. Data taken for bunch charge from 1 nC to 100 nC

MULTIPLE SCATTERING EFFECTS ON A SHORT PULSE ELECTRON BEAM TRAVELLING THROUGH THIN BERYLLIUM FOILS

E.E. Wisniewski, M. Conde, D.S. Doran, W. Gai,
W. Liu, J.G. Power, and C. Whiteford, ANL/HEP, Argonne, IL USA
S. P. Antipov, C.-J. Jing ANL, Argonne, IL USA; Euclid TechLabs, LLC, Solon, Ohio, USA
Qiang Gao, ANL, Argonne, Illinois; TUB, Beijing
G. Ha, POSTECH, Pohang, Kyungbuk, S. Korea and ANL/HEP, Argonne, IL USA

Abstract

The Argonne Wakefield Accelerator beamlines have stringent vacuum requirements (100 picotorr) necessitated by the Cesium telluride photoinjector. In direct conflict with this, the structures-based wakefield accelerator research program sometimes includes worthy but complex experimental installations with components or structures unable to meet the vacuum standards. A proposed chamber to sequester such experiments safely behind a thin beryllium (Be) window is described and the results of a study of beam-quality issues due to the multiple scattering of the beam through the window are presented and compared to GEANT4 simulations via G4beamline. Three thicknesses of Be foil were used: 30, 75 and 127 micron, probed by electron beams of three different energies: 25, 45, and 65 MeV. Multiple scattering effects were evaluated by comparing the measured transverse rms beam size for the scattered vs. unscattered beam. The experimental results are presented and compared to simulations. Results are discussed along with the implications and suggestions for the future sequestered vacuum chamber design.

MOTIVATION FOR USE OF BE WINDOWS AT AWA

The Argonne Wakefield Accelerator (AWA) beamlines have a demanding vacuum environment to preserve the drive gun Cs₂Te photocathode. Such photocathodes require vacuum pressures on the order 10⁻¹⁰ torr. The strict vacuum requirements have a large impact on experimental design, severely limiting material choices to those that are UHV compatible. In addition, the UHV requirement prevents easy access to experimental structures after installation and usually prohibits the possibility of altering experimental setups within the timeframe of an experiment. Thus, the experiment must work "as installed". If it does not, at best, the consequences can include lengthy downtime while the experimental area is vented and equipment is uninstalled, modified, cleaned, and re-installed. Once this occurs, the offending sector of the beamline must be pumped to attain UHV vacuum pressure before the operations and the experiment may resume. This can take several days to more than one week.

Compromise: Separate vacuum regimes

One way of easing the vacuum requirement and allowing quick and easy access to make changes to the experimental

setup is to place a vacuum chamber sequestered behind a Be window at the end of the beamline (discussed previously in [1]). The vacuum requirement in the "dirty" vacuum chamber can be relaxed to 10⁻⁸ torr, which can be attained in a matter of hours with much fewer restrictions. Of course, there is a cost: beam quality suffers due to multiple scattering as the beam passes through the Be window. An electron beam traveling through matter primarily interacts with the nuclei via the Coulomb force. Electrons experience many mostly small deflections as they scatter multiple times within the media. The distribution of scattering events is described by Moliere's theory. The details of the theory are beyond the scope of this paper. However, it is important to point out that the predictions of scattering theory become increasingly less reliable as the foil thickness is decreased. Hence, it is important to gather some experimental data in order to understand what to expect. The foils used in these studies are very thin: 127, 75 and 30 micron.

The studies described here were designed to develop guidance that can be used in simulations and planning for experiments using such an installation in the near future. It was hoped to use the results of these studies to develop guidance to be used in planning such installations in the future by trying to measure the effects on the beam transverse size and understand how well it is matched to numerical and analytical predictions.

AWA has already had some experience with this limiting effect of the increase in beam transverse size and emittance due to a Be window. Two experiments (one involving an RF choke cavity and another involving a photonic-band-gap (PBG) structure [2]) come to mind. Both devices had an aperture I.D.=6 mm and also required the beam to be moved within the aperture from an on-axis position to off-axis without significant beam loss inside the structure. In other words, a tightly focused beam was required with a fairly constant transverse size much less than the aperture I.D. Performing these experiments with a beam scattering through a Be window was indeed a challenge.

TESTING SEVERAL THIN BE FOILS AT AWA

A motorized actuator was equipped with a custom Be foil holder designed to hold foils of three different thicknesses, 127 μm, 75 μm, and 30 μm probed by electron beams of three different energies: 25, 45, and 65 MeV. The laser pulse length was 6 ps FWHM.

BENCHMARKING OF TOUSCHEK BEAM LIFETIME CALCULATIONS FOR THE ADVANCED PHOTON SOURCE*

A. Xiao, B. Yang, ANL, Argonne, IL 60439, USA

Abstract

Particle loss from Touschek scattering is one of the most significant issues faced by present and future synchrotron light source storage rings. For example, the predicted, Touschek-dominated beam lifetime for the Advanced Photon Source (APS) Upgrade lattice in 48-bunch, 200-mA timing mode is only ~ 2 h. In order to understand the reliability of the predicted lifetime, a series of measurements with various beam parameters was performed on the present APS storage ring. This paper first describes the entire process of beam lifetime measurement, then compares measured lifetime with the calculated one by applying the measured beam parameters. The results show very good agreement.

INTRODUCTION

Many physical processes can cause particle loss from a stored beam, such as quantum effects, gas scattering effect, Touschek scattering effect, beam-beam collisions, etc. The total beam lifetime t is given by

$$\frac{1}{t} = \frac{1}{t_1} + \frac{1}{t_2} + \dots \quad (1)$$

where t_1, t_2, \dots are beam lifetime from each individual physical process. For a low emittance machine like the APS storage ring [1], compared to the Touschek scattering effect—which gives a beam lifetime ~ 10 hours when running at the 24-bunch, 100-mA mode—contributions from all other physical processes give a beam lifetime ~ 200 hours, which is negligible. This presents a great opportunity for benchmarking our Touschek beam lifetime calculation, which is a crucial topic for our future APS upgrade [2, 3].

The particle scattering rate depends on the bunch distribution, which is given by beam parameters and optical functions that vary with location s . Scattered particles with a larger momentum error may be lost due to large betatron and synchrotron oscillation amplitude. The boundary of momentum error acceptance is also localized, and is called a local momentum aperture (LMA) [4, 5].

In our experiment, the operational machine's optics are obtained from our regular LOCO fitting and optical correction [6] and the LMA is then calculated using `elegant` [7,8] based on obtained machine models and rf voltage. Other beam parameters, such as bunch current, bunch length, beam size, and coupling, are varied and measured in the experiment. The Touschek lifetime T is then calculated by applying these measured parameters to the Piwinski's formula [9]. T

is compared with measured beam lifetime T_{meas} . Our experiment results show very good agreement, which makes us more confident on the simulated lifetime for our future APS upgrade.

LIFETIME CALCULATION

The local Touschek scattering rate R is given by Eq. (31) in Piwinski's paper [9], and is rewritten here:

$$R = \frac{r_0^2 c N^2}{8\sqrt{\pi}\beta^2\gamma^4 \varepsilon_x \varepsilon_y \sigma_s \sigma_p} F(A, B, \delta_m), \quad (2)$$

where r_0 is the classical electron radius, c is the speed of light, N is the number of particles inside the bunch, β and γ are relative velocity and factor, $\varepsilon_{x,y}$ are the transverse beam emittances, σ_s and σ_p are the bunch length and energy spread, and F is the factor depends on the local optical functions A , beam parameters B , and momentum acceptance δ_m . The Touschek beam lifetime T is given by the total beam loss rate, and is averaged over the ring:

$$\frac{1}{T} = \left\langle \frac{R}{N} \right\rangle. \quad (3)$$

These calculations are performed with the program `touschekLifetime` [10], which conveniently reads required data from `elegant`.

MEASUREMENT OF INPUTS FOR LIFETIME CALCULATION

To validate Eqs. (2) and (3), optical functions and beam parameters should be known in advance and it is also preferable to vary beam parameters over a large range to check the equation's parameter dependency. In normal APS operation, the machine's optical functions are measured regularly and corrected to the designed model [6]. This corrected model is then used to determine the LMA from tracking with `Pelegant`, giving δ_m over the ring. Results show that the non-linear effects in the APS storage ring are well corrected and the LMA is only limited by the available rf voltage. Thus, the beam lifetime is measured under various conditions: including different bunch charge N ; different beam size $\varepsilon_{x,y}$ through varying coupling; different bunch length σ_s , varied together with bunch charge and rf voltage and measured by a streak camera; and different momentum acceptance δ_m , through varying of rf voltage.

Calibration of RF Voltage

To determine the actual rf voltage—as opposed to the nominal control system rf voltage readout (`TotGapVolt`)—we measured the synchrotron frequency (`synchFreq`) and

* Work supported by the U.S. Department of Energy, Office of Science, Office of Basic Energy Sciences, under Contract No. DE-AC02-06CH11357.

BEAM LOSS SIMULATION AND COLLIMATOR SYSTEM CONFIGURATIONS FOR THE ADVANCED PHOTON SOURCE UPGRADE*

A. Xiao, M. Borland, ANL, Argonne, IL 60439, USA

Abstract

The proposed multi-bend achromat (MBA) lattice for the Advanced Photon Source upgrade (APS-U) has a design emittance of less than 70 pm. The Touschek loss rate is high: compared with the current APS ring, which has an average beam lifetime ~ 10 h, the simulated beam lifetime for APS-U is only ~ 2 h when operated in timing mode ($I = 200$ mA in 48 bunches). An additional consequence of the short lifetime is that injection must be more frequent, which provides another potential source of particle loss. In order to provide information for the radiation shielding system evaluation and to avoid particle loss in sensitive locations around the ring (for example, insertion device straight sections), simulations of the detailed particle loss distribution have been performed. Several possible collimation configurations have been simulated and compared.

INTRODUCTION

A preliminary study indicates there are three major particle loss sources in the APS MBA lattice: (1) The Touschek effect, with an average Touschek lifetime ~ 2 h in 48-bunch mode [1], giving a particle loss rate of ~ 102 pA. (2) Gas scattering, with an average lifetime $\sim 10\text{h}@100\text{Ah}$ to $\sim 60\text{h}@1000\text{Ah}$ [2], giving a particle loss rate of ~ 20 pA to 3 pA. (3) Injected beam losses. Since we are doing the “swap-out” on-axis injection [3–5], the required injected bunch charge is ~ 16.6 nC/shot every ~ 15 s for timing mode. Assuming 97% injection efficiency, the particle loss rate is ~ 33 pA. The Touschek and injected beam losses are studied in this paper.

Collimators are planned in order to confine losses to a designated area. In this paper, we first describe the aperture limitations around the ring. We then present simulation results with different collimator locations and apertures. Simulation results show a good agreement between calculated beam lifetime and lifetime from a detailed scattered particles tracking study that used the methods described in [6]. Based on the simulations, a summary of loss distributions is given.

APERTURE LIMITATIONS

The physical aperture limitations around the ring in radial size (x/y) are

- Nominal arc vacuum chamber: 11/11 mm (round)
- Nominal photon absorber at each arc BPM location: 8/8 mm (round)

- Nominal ID vacuum chamber: 10/3 mm (elliptical)
- Narrow ID vacuum chamber:
 - Type I (Sector 3/7/10/14/21/24/28/31): 4/3 mm (n=6 super elliptical)
 - Type II (Sector 17/35): 4/4 mm (round)
- Stripline kicker: 6.7/4.2 mm (elliptical)
- Septum: 3.7/2.7 mm (n=6 super elliptical)

COLLIMATOR CONFIGURATIONS

There are two major concerns with any beam loss: radiation safety and protecting an insertion device (ID) from radiation damage. For radiation safety, we want stray particles to be lost in areas with a better existing shielding or where supplemental shielding can easily be added. For protecting ID, we would like particles to be lost at the downstream end of the ID straight section, so the shower propagates away from the nearest ID.

In general, to collimate Touschek scattered particles (with a large momentum error), collimators are best installed in an area with large dispersion and betatron functions. This suggests the dispersion bump generated by the longitudinal gradient dipole, as shown in Fig. 1. However, in sectors 1 through 35, this region is close to the ratchet door that gives access to the beamline front end, as shown in Fig. 2. This area has weaker radiation shielding compared to the utility region (rf/injection section) from sector 36 to 40, which has a thicker, continuous shielding wall. With all these facts in mind we explored the following collimator configurations. The collimator in this initial study has a 6x6 mm radius round aperture, and only multipole errors are included. Distances refer to Fig. 1.

- Case A: Collimators in the first dispersion bump area, from 6.32 m (entrance of AS1) to 7.04 m (exit of AQ4), in sector 20, and sector 36–40.
- Case B: Same collimator locations as Case A, but in all sectors (1–40).
- Case C: Collimators in both dispersion bump areas (6.32 m to 7.04 m and 20.56 m to 21.28 m), in all sectors.
- Case D: Extended collimator area to cover high beta-y area, 5.95 m (entrance of AQ3) to 7.24 m (entrance of AS2), all sectors.
- Case E: Add n=6 super-elliptical aperture limits at the downstream end of all ID straights (sector 1 to 35) and collimators as in Case D.

The beam loss distributions were simulated based on these collimator configurations using Pelegant [7, 8]. From Table 1, we see that having two collimators in one sector doesn't

* Work supported by the U.S. Department of Energy, Office of Science, Office of Basic Energy Sciences, under Contract No. DE-AC02-06CH11357.

PERFORMANCE OF THE 3.4-METER LONG VERTICAL POLARIZING UNDULATOR PROTOTYPE FOR LCLS-II*

N.Strelnikov¹, I.Vasserman, J.Xu, and E.Gluskin, Advanced Photon Source, Argonne National Laboratory, Argonne, Illinois 60439, USA

¹also at Budker Institute of Nuclear Physics, Novosibirsk 630090, Russia

Abstract

As part of the LCLS-II R&D program, a novel 3.4-meter long undulator prototype with a horizontal main magnetic field and dynamic force compensation — called the horizontal gap vertical polarization undulator (HGVPU) — has recently been developed at the Advanced Photon Source (APS). Initial steps of the project included designing, building, and testing a 0.8-meter long prototype [1]. Extensive mechanical testing of the HGVPU has been carried out. The magnetic tuning was accomplished by applying a set of magnetic shims. As a result, the performance of the HGVPU meets all the stringent requirements for the LCLS-II insertion device [2], which includes limits on the field integrals and phase errors for all operational gaps, as well as the reproducibility and accuracy of the gap settings. The HGVPU has been included in the baseline of the LCLS-II project for the hard x-ray undulator line.

INTRODUCTION

The absolute majority of synchrotron radiation (SR) sources, including free electron lasers (FEL), utilize insertion devices (IDs) with a vertically-oriented magnetic field. This preferential direction is the result of the strong asymmetry — the horizontal size is much larger than the vertical one — of the electron beam cross-section in the storage rings, which is the main source of SR. Although electron beams in FELs are quite symmetric in the transverse plane, ID designers have not yet taken real advantage of this. The status quo (even that of SR sources) will soon be changed because of the recent advancements in the design of ultra-small emittance storage rings. Such machines promise to operate with round electron beams and execute on-axis injection. Therefore, developments of novel planar IDs with horizontal magnetic fields will become a practical matter.

There are at least two major advantages for horizontal magnetic field IDs. One is related to the rotation of the polarization plane of emitted radiation, which results in the transformation of monochromators and experimental set-ups to the “gravity neutral” systems. In many cases it would significantly simplify the construction and operation of these set-ups. The second advantage is also related to the “gravity neutral” design, but now applies to the undulator’s mechanical system. When such a design is combined with the magnetic force compensation system, the ID gap drive mechanisms become quite compact

without sacrificing stringent requirements on the accuracy and reproducibility of the ID gap control.

Currently all FELs around the world utilize the traditional approach as to the design of the ID gap drive mechanisms, regardless of the type of IDs. These designs are loaded with very strong, often bulky, beams that are able to withstand tremendous magnetic forces without noticeable distortions, and with very precise mechanical components that permit the control of the ID magnetic gap value at the micron level. Typically, the fabrication of such devices requires unique machine tools that can process several meter beams within a few microns of precision [3, 4, 5, 6, 7].

The alternative ID design based on the “gravity neutral” concept with the dynamic compensation of magnetic forces has recently been developed at the APS. The undulator’s 2.6-cm period magnetic structures are supported by two 3.4-m long, 15-cm thick and 20-cm tall aluminium strongbacks. Each strongback is placed on two linear slides that allow independent horizontal motion. The position of the strongbacks, and therefore the gap of the undulator, is controlled by 4 linear actuators, 2 for each strongback. The linear actuators are preloaded with constant force springs at the linear slides. Special force compensation systems have been designed and constructed to closely match the magnetic force gap dependent function [1]. The HGVPU prototype system is shown in Fig. 1.

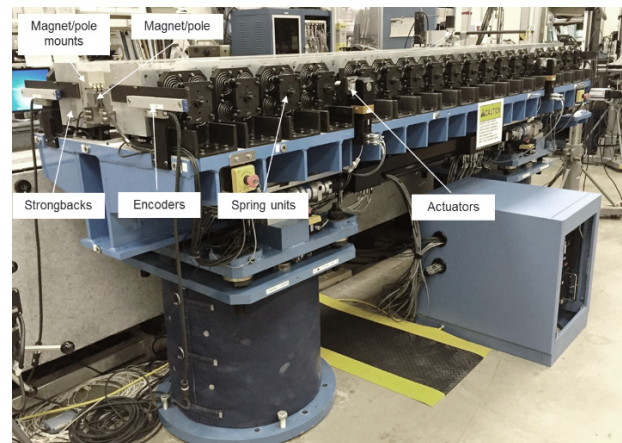


Figure 1. HGVPU at the APS ID magnet measurement facility.

HGVPU ASSEMBLY AND MECHANICAL TUNING PROCESS

The length of the prototype magnetic structure populated with magnets and poles is 3.4 meters long. The

*Work supported by the U.S. Department of Energy, Office of Science, under Contract No. DE-AC02-06CH11357.

PRELIMINARY TEST RESULTS OF A PROTOTYPE FAST KICKER FOR APS MBA UPGRADE*

C. Yao[#], L. Morrison, X. Sun, J. Wang, A. Cours, F. Westferro, A. Xiao, T. Clute, Z. Conway, G. Decker, F. Lenkszus, J. Carwardine, A. Barcikowski, R. Keane, A. Brill
ANL, Argonne, IL 60439, USA

Abstract

The APS multi-bend achromatic (MBA) upgrade storage ring plans to support two bunch fill patterns: a 48-bunch and a 324-bunch. A “swap out” injection scheme is required. In order to provide the required kick to injected beam, to minimize the beam loss and residual oscillation of injected beam, and to minimize the perturbation to stored beam during injection, the rise, fall, and flat-top parts of the kicker pulse must be within a 16.9-ns interval. Stripline-type kickers are chosen for both injection and extraction. We developed a prototype kicker that supports a ± 15 kV differential pulse voltage. We performed high voltage discharge, TDR measurement, high voltage pulse test and beam test of the kicker. We report the final design of the fast kicker and the test results.

INTRODUCTION

A prototype stripline kicker was developed for the APS MBA upgrade storage ring. Its design was reported in IPAC15 [1]. Further optimization of the kicker model was performed. Fabrication of the kicker and feedthroughs started February of 2016. The kicker was delivered recently. We performed a series of tests of the kicker. We report the final design of the kicker and the test results.

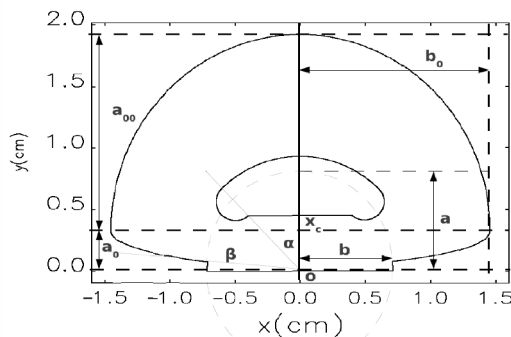


Figure 1: Geometry of the stripline kicker 2-D model. With these parameters: $a=7.8$ mm, $b=7.14$ mm, $\alpha = 43.83^\circ$, $a_0=2.87$ mm, $a_{00}=15.91$ mm, $b_0=14.54$ mm, blade thickness=3.0 mm.

*Work supported by the U.S. Department of Energy, Office of Science, under Contract No. DE-AC02-06CH11357.

[#]cyao@aps.anl.gov

FINAL KICKER GEOMETRY

CST Microwave Studio [2] was employed in the optimization simulation of the kicker and feedthrough. We used its frequency domain solver to perform 3D impedance and field simulation, and optimization of the matching of the interface between the feedthroughs and the kicker blades. We also use its time-domain tool to evaluate the impedance of a Gaussian beam bunch. CST MW studio has TDR simulation. We compared its results with TDR measurement of the kicker [3]. A final geometry was selected. Figure 1 shows the main cross-section of the final geometry and its parameters. Figure 2 shows a 3D model of the kicker.

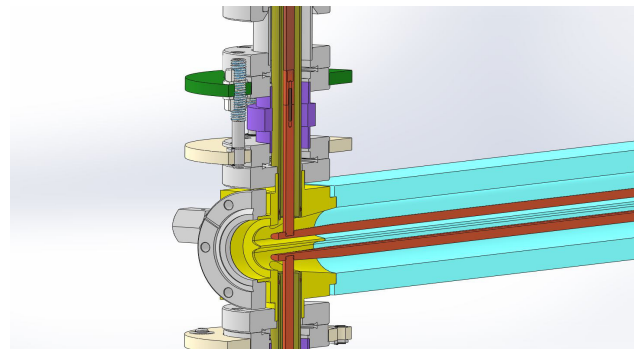


Figure 2: A plot of the kicker design model.

FEEDTHROUGH DESIGN

The feedthroughs are critical components. They serve as insulator, vacuum seal and blades support. Their impedance must match to 50Ω . Because of the location of the kickers, they must be able to sustain bake-out at 150°C and high radiation. The air-side breakdown voltage is of particular concern. We decided to collaborate with COSMOTEC to develop the feedthroughs. Figure 3 shows a plot of the final feedthrough model. Figure 4 shows a photo of a feedthrough.

KICKER FABRICATION AND ASSEMBLY

The kicker was designed with collaboration of APS and Argonne Physics Department. Argonne Physics Department assembled the kicker. The kicker assembly was delivered on August 18. Testing of the kicker started right after that. Figure 5 shows a photo of the installed kicker assembly.

ANALYTICAL MODELING OF ELECTRON BACK-BOMBARDMENT INDUCED CURRENT INCREASE IN UN-GATED THERMIONIC CATHODE RF GUNS

J. P. Edelen*, Fermilab, Batavia, IL, Y. Sun, Argonne National Lab, Lemont, IL
J. R. Harris, AFRL, Albuquerque, NM, J. W. Lewellen, LANL, Los Alamos, NM

Abstract

In this paper we derive analytical expressions for the output current of an un-gated thermionic cathode RF gun in the presence of back-bombardment heating. We provide a brief overview of back-bombardment theory and discuss comparisons between the analytical back-bombardment predictions and simulation models. We then derive an expression for the output current as a function of the RF repetition rate and discuss relationships between back-bombardment, field-enhancement, and output current. We discuss in detail the relevant approximations and then provide predictions about how the output current should vary as a function of repetition rate for some given system configurations.

INTRODUCTION

Thermionic cathodes are widely known as a robust source. When used in un-gated RF guns they result in a simple electron injector that is robust and suitable for a wide range of applications. However, one primary drawback of this system is that the gun will accelerate electrons whenever the field on the cathode is negative. As a result, some electrons that are emitted late relative to the RF period will not gain enough energy to exit the cathode cell. These electrons will be decelerated when the field changes sign and eventually accelerated back towards the cathode surface. These so-called back-bombarded electrons deposit their energy on the cathode surface in the form of heat. This back-bombardment heating impedes the ability to regulate the output current of the gun.

Recent work developed scaling laws relating back-bombardment power to different gun design parameters [1,2,3]. These scaling laws can be used for initial gun design and trade-space optimization prior to a detailed simulation-based design. While instructive, these models do not provide any estimates for how the output current will be affected by gun designs with different back-bombardment power levels. In order to address this, we combined the analytic models for back-bombardment power with the Richardson-Dushman equation to study the effect of gun design parameters on the output current. For a fixed geometry, there are three parameters which directly affect the back-bombardment power levels: the initial output of the cathode, the field on the cathode, and the RF duty factor.

In this paper we will address how changing the RF duty factor and the peak field on the cathode will affect the output current of the gun in the presence of back-bombardment

heating. While this work is concerned with estimating the change in output current due to back-bombardment heating for a general class of thermionic guns, the Advanced Photon Source (APS) injector test stand gun will be used as an example to provide justification for the necessary approximations. For a different gun, the approximations made here would need to be re-evaluated. We will begin with a brief overview of the existing back-bombardment power models, and discuss their range of validity. Then we derive the relationship between repetition rate and output current in the presence of back-bombardment heating, followed by a discussion of how field enhancement in these guns changes the back-bombardment effect.

OVERVIEW OF BACK-BOMBARDMENT THEORY

The back-bombardment power for a particular gun design is defined by Equation 1 [1].

$$P_{ave} = \frac{3IE_0c^2}{4v_{eff}f\alpha^2}TKD_F \quad (1)$$

In Equation 1, I is the average beam current, E_0 is the peak field gradient, c is the speed of light in vacuum, f is the RF frequency of the gun, α is the normalized gap length of the cathode cell, defined by $\alpha = c/(fL_{gap})$, T is the transit time factor, v_{eff} is the effective velocity (Equation 2), K is the normalized field strength (Equation 3), and D_F is the duty factor of the RF system.

$$v_{eff} = c\sqrt{1 - \left(1 + \frac{qE_0\lambda}{2m_0c^2\alpha}\right)^{-2}} \quad (2)$$

$$K = \frac{\int_0^{L_{gap}} E(z)dz}{E_0\lambda/\alpha} \quad (3)$$

For the APS Injector test stand, the geometry parameters α , T , and K , are given by Table 1. Equation 1 has been demonstrated to match simulation and measurement of back-bombardment power to order of magnitude accuracy for

Table 1: Geometry Parameters for the APS Gun

Parameter	Symbol	Value
Transit Time Factor	T	0.73
Normalized Gap Voltage	K	0.80
Alpha	α	3.36

* jedelen@fnal.gov

OBSERVATION OF REPETITION-RATE DEPENDENT EMISSION FROM AN UN-GATED THERMIONIC CATHODE RF GUN

J. P. Edelen[#], Fermilab, Batavia, IL
 Y. Sun, Argonne National Lab, Lemont, IL
 J. R. Harris, AFRL, Albuquerque, NM
 J. W. Lewellen, LANL, Los Alamos, NM

Abstract

Recent work at Fermilab in collaboration with the Advanced Photon Source and members of other national labs, designed an experiment to study the relationship between the RF repetition rate and the average current per RF pulse. While existing models anticipate a direct relationship between these two parameters we observed an inverse relationship. We believe this is a result of damage to the barium coating on the cathode surface caused by a change in back-bombardment power that is unaccounted for in the existing theories. These observations shed new light on the challenges and fundamental limitations associated with scaling an un-gated thermionic cathode RF gun to high average current.

INTRODUCTION

Thermionic cathodes are widely known as a robust source of electrons. When used in un-gated RF guns they result in a simple electron injector that is suitable for a wide range of applications for accelerators [1,2,3]. However, one primary drawback of this system is that the cathode will emit whenever the field is appropriately signed. Therefore, some electrons that are emitted late relative to the RF phase will not gain enough energy to exit the cathode cell. These electrons will be decelerated when the field changes sign and eventually accelerated back towards the cathode surface. These so-called back-bombarded electrons deposit their energy on the cathode surface in the form of heat. Because of the cathode's finite thermal mass this additional heating impedes the ability to regulate the output current of the gun. In order to improve our understanding of how changing the back-bombardment heating will affect the beam current, we conducted an experimental study at the Advanced Photon Source Injector Test Stand.

For a gun with a fixed geometry, the back-bombardment power can be varied by changing three parameters: 1) the cathode heater power which changes the cathode current, 2) the peak field in the gap which changes the peak energy of back-bombarded electrons, and 3) the RF duty factor which changes the total amount of energy deposited per second. The cathode heater is slow to respond and therefore changing the heater power does not produce step changes in the back-bombardment power. Changing the peak field in the gap also changes the level of field-enhanced emission causing both a change in the energy of back-bombarded particles and a change in the current, which are difficult to decouple. However, changing the RF repetition rate does not have a

slow time response and it does not come with any obvious second order effects.

To study how back-bombardment will impact the output current of the gun, we observed the change in current caused by a change in repetition rate for a variety of conditions. In this paper we will show some initial results for how the output current changed with repetition rate for different values of peak field. We provide an analysis of our measurements and finally a hypothesis for the mechanism that produces the observed dependence of output current on repetition rate.

EXPERIMENTAL SETUP

The section of the injector test stand used for this experiment has a 1.5 cell room temperature electron gun, two pairs of quadrupoles, two corrector magnets, a current monitor (Bergoz ICT), a bend, a screen, and a fast-Faraday cup, Figure 1. The gun is powered by a klystron capable of delivering up to 4MW of peak power to the gun. The pulse width of the RF system is 1.05 micro-seconds and the repetition rate can be varied at uneven intervals between 2Hz and 30Hz (2Hz, 4Hz, 6Hz, 8Hz, 10Hz, 12Hz, 15Hz, 20Hz, 30Hz).

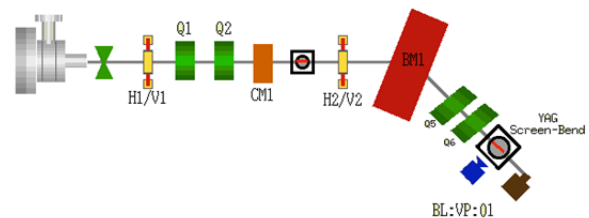


Figure 1: Diagram of the injector test stand used for these experiments, courtesy of the APS control system synoptic display. From left to right, 2.856GHz thermionic gun, gate valve, horizontal/vertical corrector, quadrupole 1, quadrupole 2, current monitor, YAG screen, bending magnet, quadrupole 5, quadrupole 6, YAG screen, and a Faraday cup.

Through the control system we can collect 1Hz data on the average current, magnet settings, forward and reflected power, vacuum pressure, and other diagnostics as needed. Additionally we can periodically collect raw waveform data from the ICT, the faraday cup, and from the RF system using a remotely triggered oscilloscope.

INITIAL RESULTS

The initial experiment was to vary the repetition rate for several values of peak field at a single heater power.

MODIFICATION OF 3RD HARMONIC CAVITY FOR CW OPERATION IN LCLS-II ACCELERATOR*

T. N. Khabiboulline[†], M. H. Awida, I. Gonin, A. Lunin, N. Solyak, V. Yakovlev
Fermi National Accelerator Laboratory, Batavia, IL, USA

Abstract

A 3.9 GHz 3rd harmonic cavity was developed at FNAL and it is currently used in the FLASH accelerator at DESY in order to improve FEL operation. The European XFEL accelerator in Hamburg also adapted the same cavity design for a pulsed linac operation. The 3rd harmonic cavity for the LCLS-II accelerator at SLAC will operate in a continuous wave (CW) regime. A CW operation and a high average current in the LCLS-II linac result in increased heat loads to main and HOM couplers of the cavity. Several cavity design modifications were proposed and investigated for improving a cavity performance in the CW regime. In this paper we present results of the design review for proposed modifications.

INTRODUCTION

The LCLS-II superconducting linac consists of thirty five 1.3 GHz, 8-cavity cryomodules (CM), and two 3.9 GHz, 8-cavity cryomodules. Third harmonic superconducting cavities are used for increasing a peak bunch current and for linearizing the longitudinal beam profile. Table 1 shows main parameters of the 3.9 GHz cavity and cryomodule developed for the LCLS-II linac [1].

Table 1: Main parameters of the 3.9 GHz CM and cavity.

	Nominal	Min	Max
Average Q0 at 2K	2.0x10 ⁹	1.5x10 ⁹	-
Average gradient, MV/m	13.4	-	14.9
Beam to RF phase, deg.	-150	-90	-180
Cavity R/Q	750 Ω	-	-
G factor	273 Ω	-	-
FPC, Q _{ext}	2.7x10 ⁷	-	-

A continuous wave (CW) operation of the 3.9 GHz cavity in LCLS-II linac at gradient of 14.9 MV/m sets an extra requirement on possible overheating of the HOM coupler feedthrough [2]. We revised the design of the 3.9 GHz cavity and proposed minimal improvements in order to keep the geometry of cavity cells unchanged.

In the original design of the 3.9 GHz cavity we observed a trapped dipole mode in the power coupler of the cavity, where the cut-off frequency for the dipole TE₁₁ mode is close to the frequency of the operating mode. This trapped dipole mode affects on RF fields in the HOM coupler at the

operating frequency as well. Therefore we proposed a reduction of the beam pipe diameter from 40 mm to 38 mm. This modification allowed to move the frequency of the trapped dipole mode away from the operating frequency, which simplifies HOM coupler notch frequency tuning and reduces the leakage of RF power at operating frequency.

Another concern was a thermal quench of HOM antenna at about 20 MV/m observed during a vertical test (VT) in the CW regime. In the VT setup all components are submerged into a superfluid helium and therefore cooling of the HOM feedthrough is significantly better than in the cryomodule. The HOM feedthrough antenna is made of a solid Niobium, which does not produce significant amount of RF losses until its temperature is below critical. Operating mode RF fields may initiate a thermal runaway process and cause a quench in HOM feedthrough antenna in case of pure cooling [3]. In order to avoid such a scenario and reduce the antenna RF heating we proposed to move the antenna away from the f-part and use a shorter antenna tip by increasing the height of the f-part snag. As a result, the length of antenna tip is decreased from 5 mm to 1 mm and the height of the f-part snag is increased to 7.8 mm.

Previously few cavities developed a vacuum leak on the HOM coupler can after a bulk BCP processing. Consequently the original thickness of the can was increased from 1 mm to 1.15 mm for XFEL cavities. For ensuring a good safety margin we decided on a further increase of the HOM can thickness. Mechanical stress analysis demonstrates a feasibility of 1.3 mm thickness.

The 3.9 GHz cavity in LCLS-II linac can emit on HOM coupler up to 5 W of average RF HOM power. Additionally up to 1 W of RF power can leak by the operating mode. In order to make a correct choice of RF cables for HOM coupler a thermal analysis was performed.

BEAM PIPE MODIFICATION

A conical tapering of the NbTi transition ring was accepted for the beam pipe aperture reduction from 40 mm to 38 mm (see Fig. 1).

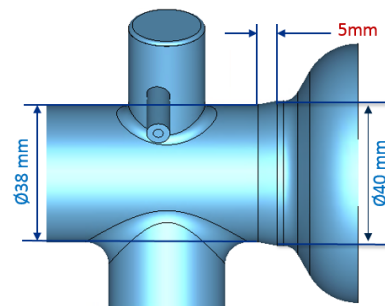


Figure 1: New beam pipe and transition ring.

*Operated by Fermi Research Alliance, LLC under Contract No. DE-AC02-07CH11359 with the United States Department of Energy

[†] khabibul@fnal.gov

MODELING OF DARK CURRENT GENERATION AND TRANSPORT USING THE IMPACT-T CODE*

J. Qiang[#], K. Hwang, LBNL, Berkeley, CA94720, U.S.A.

Abstract

Dark current from unwanted electrons in photoinjector can present significant danger to the accelerator operation by causing damage to photocathode and power deposition onto conducting wall. In this paper, we present numerical models of dark current generation from the field emission and from the electron impact ionization of the residual gas that were recently developed in the IMPACT-T code and a test application to the LCLS-II like injector.

INTRODUCTION

Dark current is normally referred as unwanted electrons in an accelerator. Those electrons lost onto photocathode, cavity wall or beam pipe can cause damage to the cathode material, increased heat load to superconducting surfaces, radioactivity beyond acceptable levels, and even other machine damage. It is one of limiting factors in the photoinjector design and operation, and has to be studied in these facilities [1-3]. In this paper, we report on the numerical modeling of the dark current generation and transport in a parallel beam dynamics code, IMPACT-T [4]. Here, the dark current includes two contributions: one is from the field emitted electrons, and another is from the electron impact ionization of the residual gas.

COMPUTATIONAL MODELS

We first present the numerical model for the dark current generation from the field emission electrons. The production of the dark current due to the field emission can be approximated using the Fowler-Nordheim equation [5]:

$$I = A_e \cdot 1.54 \cdot 10^{-6} \cdot 10^{4.52\phi - 0.5} \cdot \frac{\beta_0^2 E^2}{\phi} \cdot \exp\left(-\frac{6.53 \cdot 10^9 \phi^{1.5}}{\beta_0 E}\right) \cdot 1 \text{ A}$$

where \square is the enhancement factor of the electric field due to microscopic surface irregularities, A_e is the effective emitting area in units of m^2 , \square the work function of the material in units of eV, and E the macroscopic electric field applied to the material surface in units of V/m. Using the above equation and the time-dependent information of the electric field, we can obtain the time-dependent initial distribution of the dark current $I(t)$ in the tracking simulation. We assume that the electron are uniformly generated within the emitting surface area A_e with a Gaussian momentum distribution in a plane transverse to the surface normal direction, and a semi-Gaussian momentum distribution along the normal direction. These spatial coordinates and momenta are then transformed from the local coordinate system of the emitting surface to the global accelerator coordinate system for macroparticle tracking study.

*Work supported by the Director of the Office of Science of the US Department of Energy under Contract no. DEAC02-05CH11231.

[#]jqliang@lbl.gov

Another source of the dark current comes from the electron impact ionization of the residual gas, which can be important in a high average current injector. The electron beam colliding with the background residual gas can generate electrons through electron-impact ionization. Those electrons from the impact-ionization will be repelled by the space-charge forces of the electron beam and can move to large amplitude to become halo particles. The generation of these electrons can be simulated using a Monte Carlo method given a model for the impact-ionization probability of the residual gas. Here, the probability of production of an electron by the electron impact ionization during a time interval dt is given by [6]:

$$P_i = 1 - e^{-n_{\text{gas}}\sigma v dt}$$

where n_{gas} is the density of background residual gas, σ is the electron impact ionization cross-section, and v is the relative speed between the electron and the gas molecule. Given the ionization probability for an electron, a uniformly distributed random number r is generated. If $r < P_i$, then ionization occurs and an electron particle is generated. Once a dark current electron is generated, it will be subject to both the external forces of accelerating/focusing fields and the space-charge forces from the electron beam. The space-charge forces among the halo electrons and the space-charge forces on the main electron bunch due to the dark current electrons are neglected, given the fact that the number of these electrons is much less than the number of electrons in the main electron bunch. The initial spatial location of a dark current electron is assumed to be the same as that of the electron that produces the ionization. The initial velocity of the dark current electron is sampled from a Gaussian distribution with a given initial gas temperature.

APPLICATION TO A PHOTOINJECTOR

As a test of the dark current computational model in the IMPACT-T code, we simulated dark current generation and transport in an LCLS-II like photoinjector. The LCLS-II as a next generation high repetition rate x-ray free electron laser (FEL) light source is being actively studied [7-8]. The electron source for this accelerator comes from an injector that is schematically shown in Fig. 1 [9-10]. This injector consists of a 187 MHz low RF frequency photo-gun that accelerates an electron beam to about 750 keV, a solenoid magnet, a 1.3 GHz buncher cavity, another solenoid, and eight 1.3 GHz TESLA like superconducting cavities that accelerates the electron beam to about final 100 MeV energy. The designed repetition rate of the injector is 1 MHz with a plan to operate 20pC, 100pC and 300pC of electron charges.

SIMULATION OF THE SHOT-NOISE DRIVEN MICROBUNCHING INSTABILITY EXPERIMENT AT THE LCLS *

J. Qiang[#], LBNL, Berkeley, CA, U.S.A.

Y. Ding, P. Emma, Z. Huang, D. Ratner, T. Raubenheimer, F. Zhou, SLAC, Menlo Park, CA, U.S.A.

Abstract

The shot-noise driven microbunching instability can significantly degrade electron beam quality in next generation light sources. Experiments were carried out at the Linac Coherent Light Source (LCLS) to study this instability. In this paper, we will present start-to-end simulations of the shot-noise driven microbunching instability experiment at the LCLS.

INTRODUCTION

The microbunching instability [1-5], seeded by shot noise and driven by collective effects (primarily space-charge), can significantly degrade the quality of the electron beam before it enters the FEL undulators. Recently, a series of experiments were carried out at the LCLS to study the microbunching instability [6]. With the help of x-band transverse deflecting cavity (XTCAV), the longitudinal phase space can be imaged at the end of the accelerator revealing the detailed structure arising from the microbunching instability. To better understand these experimental results, we have done start-to-end macroparticle simulations using real number of electrons on a high performance large scale computer. This also provides a validation of the computational model used in the simulation.

COMPUTATIONAL SETUP

All simulations presented in this study were done using a 3D parallel beam dynamics simulation framework IMPACT [7-8]. It includes a time-dependent 3D space-charge code module IMPACT-T to simulate photo-electron beam generation and acceleration through the s-band photo RF gun and a traveling wave boosting cavity L0, and a position-dependent 3D space-charge code module to simulate electron beam transport through the traveling wave linac system. Besides the 3D space-charge effects, the simulation also includes coherent synchrotron radiation (CSR) effects through a bending magnet, incoherent synchrotron radiation inside the bending magnet, the longitudinal wakefield of the RF structures, and the longitudinal resistive wall wakefields of the long transport lines. All simulations were done using the real number of electrons (1.1×10^9) for the 180-pC bunch charges, to capture the initial shot noise of the beam, which can have important impact on the final beam quality and FEL performance due to the microbunching instability [9-10]. The total computational time takes about 10 hours on thousands of processors at the NERSC supercomputer center [11].

*Work supported by the Director of the Office of Science of the US Department of Energy under Contract no. DEAC02-05CH11231 and DEAC02-76SF00515.

[#]jqiang@lbl.gov

SIMULATION RESULTS

Figure 1 shows a schematic plot of the LCLS accelerator layout used for the microbunching instability experiment. It consists of a photoinjector (not shown in the plot), a short section of linac (L0) before the laser heater, two bunch compressors and three linac sections. The bunch compressor two (BC2) is used to control the final peak current while the linac section 3 (L3) is used (in this case) to de-accelerate electron beam from 5 GeV down to 4.3 GeV. The simulation starts from the emission of the photo-electrons at the cathode. The real number of electrons (180pC) was used in the simulation to model the

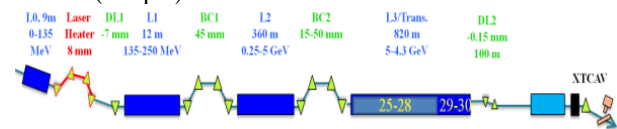


Figure 1: A schematic plot of LCLS accelerator layout.

initial shot-noise of the beam. The initial transverse laser profile is a Gaussian distribution with 1 mm rms size and truncated at 0.5 sigma, the longitudinal profile also has a Gaussian distribution with 1ps rms bunch length and truncated at 2.5 sigma. The initial normalized thermal emittance is about 0.2 μm . Figure 2 shows the kinetic energy evolution of the electron beam inside the accelerator. It is accelerated to 250 MeV before bunch compressor one, 5 GeV before bunch compressor two, and de-accelerated down to 4.3 GeV at the end of the accelerator. Figure 3 shows the transverse rms size and the longitudinal rms bunch length evolution through the accelerator. The transverse size is reasonably well matched in the accelerator with less than 100 μm rms size. The longitudinal bunch length out of the injector is about 0.5 mm and is compressed to about 0.06 mm after the bunch compressor one and further compressed to about 0.02 mm after the BC2. The compression factor at BC1 is

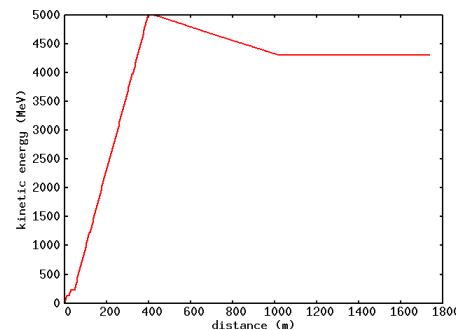


Figure 2: Electron beam kinetic energy evolution through the accelerator.

DARK CURRENT STUDY OF A STANDING WAVE DISK-LOADED WAVEGUIDE STRUCTURE AT 17 GHz*

H. Xu[†], M. A. Shapiro, and R. J. Temkin

Massachusetts Institute of Technology, Cambridge, MA, USA

Abstract

We present calculations of the dark current in a high gradient accelerator with the intent of understanding its role in breakdown. The initial source of the dark current is the field emission of electrons. For a 17 GHz single-cell standing wave disk-loaded waveguide structure, the 3D particle-in-cell simulation shows that only a small portion of the charge emitted reaches the current monitors at the ends of the structure, while most of the current collides on the structure surfaces, causing secondary electron emission. In the simulation, a two-point multipactor process is observed on the side wall of the cell due to the low electric field on the surface. The multipactor approaches a steady state within nanoseconds when the electric field is suppressed by the electron cloud formed so that the average secondary electron yield is reduced. This multipactor current can cause the ionization of the metal material and surface outgassing, leading to breakdown. We report first results from an experiment designed to extract dark current directly from an accelerator cell from the side through two slits. First results show that the dark current behavior deviates from the field emission theory.

INTRODUCTION

One of the factors that are considered to affect the performance of a normal conducting high gradient accelerator is dark current. Once captured, dark current can become part of the beam that is being accelerated by the cavities and degrade the beam quality. Also, secondary electrons and X-ray photons can be generated by the collision of dark current electrons onto the structure surfaces.

Dark current in an accelerator cavity is initiated by field emission, and processes such as secondary electron emission (SEE) and multipactor (MP), assuming an average secondary electron yield (SEY) above unity, can add to the ultimate dark current measured in experiments. Our study investigates MP driven by the electric field on the surface of the accelerator structure side wall. The RF electric field on the side wall surface is perpendicular to the surface, but the parallel field turns on where there is a displacement away from the side wall. When the field emission electrons hit the side wall, secondary electrons can be expelled by the perpendicular field, accelerated by the parallel field, and pulled towards the side wall again with a period of half an RF cycle.

The dark current from an accelerator cavity is often measured by current monitors at the ends of the structure, and the results are usually fitted using the Fowler-

Nordheim (FN) formula for field emission to acquire estimation for field enhancement factor. However, assuming the dark current is only generated through field emission, only a small fraction of the current makes it to the current monitors and the fractional value can vary with the gradient level. On the other hand, whether the current being measured all comes from field emission can be questioned. A more direct measurement of the dark current from a high gradient accelerator cell can provide us with more distinct information about the dark current generation mechanism.

The particle-in-cell (PIC) simulation method serves as an efficient way to study the dynamics of dark current, including the generation of SEE and the formation of MP. All of the PIC simulations mentioned in this work were carried out in CST Particle Studio [1].

SIMULATION

A 3D model of the standing wave single cell structure with a resonant frequency of 17.1 GHz is built, based on the MIT Disk-Loaded Waveguide (MIT-DLWG) structure [2], as shown in Fig. 1. The TM_{01} mode microwave power is fed in from the left through the circular waveguide and the ratio of the peak amplitude of the electric field on the beam axis in the three cells is about 1:2:1. SEE using Furman's model [3] is calculated only for the central cell (within the red rectangle), since the field strength is low in the other cells. On the surface of each of the irises facing the central cell, we create a source of electrons by selecting a ring shaped area (indicated by arrows) which sees the maximum of the electric field when the cavity is under high gradient operation. The emission current is decided by FN field emission theory.

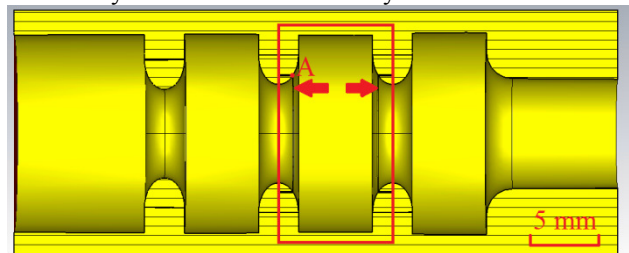


Figure 1: MIT-DLWG structure model.

The field enhancement factor β value is determined from the previous high power test of the MIT-DLWG structure. An immediate calculation using the downstream dark current monitor (placed at the right end in Fig. 1) measurement result gives a β value of 81. However, the escape ratio, which is defined as the percentage of the field emission electrons that reach the current monitors at the ends of an accelerator structure, needs to be considered to correct this calculation. Fig. 2 shows the escape

* Work supported by the U.S. Department of Energy, Office of High Energy Physics, under Grant No. DE-SC0015566

[†] haoranxu@mit.edu

PERFORMANCE OF A COMBINED SYSTEM USING AN X-RAY FEL OSCILLATOR AND A HIGH-GAIN FEL AMPLIFIER *

L. Gupta[†] University of Chicago, Chicago IL 60637 USA
R. Lindberg, K-J. Kim, Argonne National Lab, Lemont IL USA

Abstract

The LCLS-II at SLAC will feature a 4 GeV CW superconducting (SC) RF linac [1] that can potentially drive a 5th harmonic X-Ray FEL Oscillator to produce fully coherent, 1 MW photon pulses with a 5 meV bandwidth at 14.4 keV [2]. The XFELO output can serve as the input seed signal for a high-gain FEL amplifier employing fs electron beams from the normal conducting SLAC linac, thereby generating coherent, fs x-ray pulses with TW peak powers using a tapered undulator after saturation [3]. Coherent, intense output at several tens of keV will also be feasible if one considers a harmonic generation scheme. Thus, one can potentially reach the 42 keV photon energy required for the MaRIE project [4] by beginning with an XFELO operating at the 3rd harmonic to produce 14.0 keV photons using a 12 GeV SCRF linac, and then subsequently using the high-gain harmonic generation scheme to generate and amplify the 3th harmonic at 42 keV [5]. We report extensive GINGER simulations that determine an optimized parameter set for the combined system.

INTRODUCTION

Free electron laser (FEL) technology is developing in many labs around the world, for its use in fundamental science research in fields including biological, material, and other physical sciences. An FEL is capable of creating partially coherent, bright x-ray radiation, unlike many other modern machines. Although many FELs are currently operating around the world, there is a continued push for improvement in the field, in order to produce another generation of FEL machines that can provide fully coherent x-rays.

Many current FELs create bright x-rays with limited temporal coherence due to the Self-Amplified Spontaneous Emission (SASE) method of x-ray production. A SASE FEL can achieve significant amplification from shot noise to provide GW x-ray beam with wavelengths on the order of Angstroms for users, but these beams are temporally chaotic. Some machines plan to use self-seeding methods, in which SASE x-ray pulses are sent through a monochromator, in order to purify the spectrum. This light is then amplified in a second portion of the machine, thereby delivering a high-power beam of reduced bandwidth x-rays, as compared to the SASE spectrum. The bandwidth ($\Delta\lambda/\lambda$) from a SASE FEL is order 10^{-3} , where $\Delta\lambda/\lambda$ for the self-seeded FEL is order 10^{-5} [6].

Another FEL design is the x-ray FEL oscillator (XFELO). The XFELO is a low-gain device, in which a coherent radiation signal is built up in a cavity consisting of diamond Bragg crystals. The crystals reflect the x-rays, that then copropagate with an electron bunch in an undulator within the cavity. The copropagating x-rays act as a seed signal, and stimulate radiation from the electron bunch at the same wavelength. The signal grows, while reducing in bandwidth, due to the narrow bandwidth of the diamond crystals reflectivity. As such, an XFELO can produce light with bandwidth on the order of 10^{-7} [7].

While the theory of XFELs is well known, an XFELO machine has yet to be built. The LCLS-II is an ideal project with which an XFELO could be driven, in order to create TW power radiation. The superconducting, 4GeV upgrade of LCLS-II would allow an XFELO to be driven at the 5th harmonic to create 1MW, 14.4keV x-ray pulses, which could then be used to stimulate and amplify radiation from the 14.35GeV LCLS-I beam. A tapered solution, simulated in GINGER [8], is presented here.

Further, due to the coherence and brightness of XFELO x-rays, we propose that a harmonic generation machine with an XFELO seed laser could be used in the Matter-Radiation Interactions in Extremes (MaRIE) experiment at Los Alamos National Laboratory. The MaRIE experiment requires narrow bandwidth, bright x-rays at 42keV or higher photon energies. This paper also outlines a general scheme by which 42keV x-rays could be produced for the MaRIE experiment, in an XFELO driven harmonic generation machine.

TERAWATT POWER RADIATION AT LCLS-II

In order to produce a bright, terawatt power x-ray laser at LCLS-II, an XFELO could be used to create a seed signal to be amplified in a high-gain FEL. Specifically, the 4GeV LCLS-II beam could be used to drive an XFELO at the 4th harmonic, to generate a 1MW, 14.4keV radiation beam, with as low as 5.0meV bandwidth. The laser would then be used to stimulate emission from an LCLS-I amplifier, driven by a 14.35 GeV electron beam. GINGER was used to simulate such an amplifier, and a tapered solution of the LCLS-I type amplifier is presented in Fig. 1. The resulting radiation beam would be extremely stable, because the XFELO is able to produce a fully coherent seed laser for a high-gain amplifier such as the LCLS-I.

The solution presented in Fig. 1 relies on undulator tapering so that the resonance condition is maintained within the undulator as the beam energy decreases. Simulation parameters for these results are listed in Tab. 1. The radiation

* Work supported by US department of Energy contract DE-AC02-06CH11357.

[†] lipigupta@uchicago.edu

LLNL LASER-COMPTON X-RAY CHARACTERIZATION*

Y. Hwang[†], T. Tajima, University of California, Irvine, CA USA 92697
G. Anderson, D. J. Gibson, R. A. Marsh, C. P. J. Barty,
Lawrence Livermore National Laboratory, Livermore, CA USA 94550

Abstract

30 keV Compton-scattered X-rays have been produced at LLNL. The flux, bandwidth, and X-ray source focal spot size have been characterized using an X-ray ICCD camera and results agree very well with modeling predictions. The RMS source size inferred from direct electron beam spot size measurement is $17\ \mu\text{m}$, while imaging of the penumbra yields an upper bound of $42\ \mu\text{m}$. The accuracy of the latter method is limited by the spatial resolution of the imaging system, which has been characterized as well, and is expected to improve after the upgrade of the X-ray camera later this year.

INTRODUCTION

X-ray and γ -ray generation by laser-Compton scattering (LCS) is being studied worldwide for its potential as a compact synchrotron quality X-ray source [1–5]. At LLNL, an X-band linac has been built and is in operation to produce laser-Compton scattered X-rays [6]. Important features including flux and bandwidth of the X-rays have been characterized using an X-ray CCD camera and simulations [7]. X-ray flux was measured with a calibrated camera and matched the value expected from simulations.

For bandwidth demonstration, a $50\ \mu\text{m}$ silver foil was placed in front of the camera and the beam energy was tuned to produce X-rays with peak energy just above the K absorption edge of silver (25.5 keV). Due to Doppler shifting, X-ray energy decreases as observance angle deviates from the axis of the electron beam. This energy-angle correlation creates a dark disc in the center where the X-ray energy is above the K-edge and therefore highly attenuated, surrounded by a bright background where energy is below the K-edge. The steepness of contrast is directly related to the bandwidth of the X-rays, and simulation was able to reproduce the image extremely well with expected parameters, as shown in Figure 1.

Small X-ray source size is a characteristic of Compton light sources that is of particular importance in several imaging applications such as phase contrast imaging [8], but accurate source size measurement has yet to be achieved due to the limited imaging capability of the current setup.

* This work performed under the auspices of the U.S. Department of Energy by Lawrence Livermore National Laboratory under Contract DE-AC52-07NA27344.

[†] yoonwooh@uci.edu

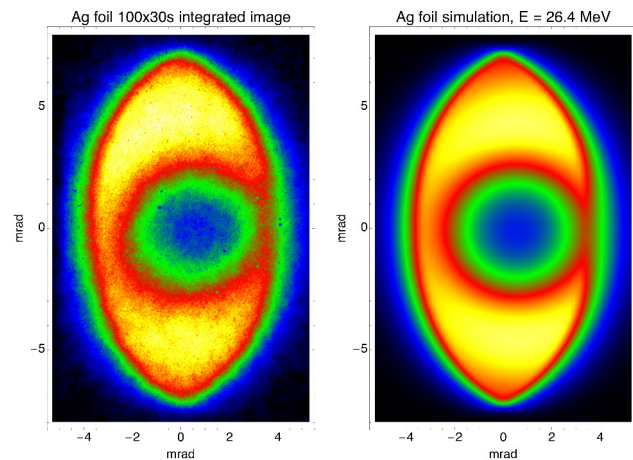


Figure 1: 3,000 second integration image of $50\ \mu\text{m}$ Ag foil K-edge hole (left) and its simulation (right).

SPATIAL RESOLUTION AND SOURCE SIZE

The spatial resolution of a radiograph depends strongly on both the source size and the imaging system's resolving power. The source size of our X-ray beam is similar to the size of the electron spot size at the interaction point, since the electron spot size is smaller than the laser spot size. The RMS source focal spot size σ_s can be defined from the geometric unsharpness formula $\sigma_s = \sigma_p a/b$, where σ_p is the RMS penumbra size, a is the source to object distance and b is the object to detector distance. Modeling of radiographs using the image simulation code described in [7] shows excellent agreement of the above-defined source size and the electron beam spot size.

Single shot OTR images of the electron beam spot at the interaction point show an RMS size of $14\ \mu\text{m}$ in horizontal and $11\ \mu\text{m}$ in vertical, with jitter around $5\ \mu\text{m}$ by $3\ \mu\text{m}$ [9]. The integrated image of 1,000 overlapped shots (Figure 2) yields $16.7\ \mu\text{m}$ by $12.8\ \mu\text{m}$ and is very close to Gaussian in profile (Figure 3).

Therefore, in order to measure the penumbra and the X-ray source size directly, a very high resolution imaging device is necessary; otherwise the blur from the imaging system will dominate the resolution of the result, rendering source size determination impossible. The large field-of-view Andor X-ray CCD camera that was used to characterize the beam's flux and bandwidth is not capable of resolving small details necessary for the source size measurement, due to scintillator thickness, 3:1 demagnification fiber optic taper and multiple fiber optic relays, in addition to dimmed and non-uniform

UPGRADE OF THE CORNELL ELECTRON STORAGE RING AS A SYNCHROTRON LIGHT SOURCE*

D. L. Rubin, J. A. Crittenden, J. P. Shanks, S. Wang
CLASSE, Ithaca, NY, USA

Abstract

The planned upgrade of the Cornell Electron Storage Ring as an X-ray source for CHESS will include an increase in beam energy and decrease in emittance from 100 nm-rad at 5.3 GeV to 30 nm-rad at 6 GeV, increase in beam current from 120 to 200 mA, continuous top-off injection of the single circulating beam, and four new zero dispersion insertion straights that can each accommodate a pair of canted undulators. The existing sextant of the storage ring arc that serves as the source for all of the CHESS X-ray beam lines will be reconfigured with 6 double-bend achromats, each consisting of two pairs of horizontally focusing quadrupoles, and a single pair of combined-function gradient bend magnets. The chromaticity will be compensated by the existing sextupoles in the legacy FODO arcs. We describe details of the linear optics, sextupole distributions to maximize dynamic aperture and injection efficiency, and characterization of magnetic field and alignment error tolerance.

INTRODUCTION

The Cornell High Energy Synchrotron X-ray Source (CHESS) was originally developed to operate parasitically with the particle physics electron-positron colliding beam program at the Cornell Electron/Positron Storage Ring (CESR). X-ray beam lines were constructed to take advantage of radiation from both electron and positron beams in the sextant (the south arc) of the ring that is accessible. (The remainder of the ring circumference of 768 m is in an underground tunnel.) The lattice and layout of the south arc were designed to generate high luminosity. An upgrade is now underway to reconfigure the south arc for X-ray science. The plan is to replace the 100m arc [1] with six double-bend achromats and seven low-beta, zero-dispersion straights. Five of the straights will be equipped with undulator or wiggler insertion devices. All of the beam lines will be rearranged to intercept X-rays from a single clockwise beam, eliminating the complexity associated with two-beam operation [2]. The beam energy will be increased from 5.3 to 6 GeV. The horizontal emittance, heretofore limited by the FODO structure in the south arc and the lattice constraints imposed by two beam operation, will be reduced from 100 nm at 5.3 GeV to 30 nm at 6 GeV. The 13.7-m long achromats are compact. In order to save space for correction magnets and beam instrumentation, the vertical focusing in the achromat is derived from the field gradient in the bending magnets. Flexibility to tune and correct optics and orbits is provided by four independently powered horizontally focusing quadrupoles and horizontal and vertical dipole

correctors. Matching of the achromat optics into the legacy FODO structure in the CESR arcs is accomplished with the addition of a single pair of quadrupoles in the transition region.

LATTICE

The operational parameters of CHESS at present are compared to the new machine in Table 1. A comparison of pin-hole flux for CHESS, APS and the CHESS post-upgrade is shown in Fig. 1. With a 3.5 m undulator, pin-hole flux at CHESS will exceed that of APS with undulator A.

Table 1: CHESS and Post-upgrade Parameters

Parameter	Present CHESS	Post Upgrade
Particle beams	2 Counter-rotating	Single (clockwise)
Insertion devices	One pair undulators	Five pairs undulators
E_{beam} [GeV]	5.3	6.0
I_{beam} [mA]	125 X 125	200
Bunches	20 e^+ X 45 e^-	100
ϵ_x [nm]	100	30
ϵ_y [nm]	1	0.1 \rightarrow 1
Injection	Top-off e^+ /5 min Refill e^- /2 hrs	Top-off/3 min \rightarrow const I

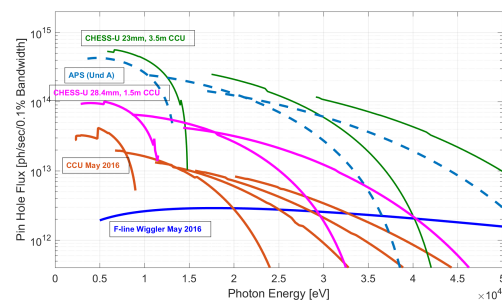


Figure 1: Pin-hole flux [photons/sec/0.1% Bandwidth]. Red lines are CHESS 1.5 m compact undulator May 2016. Purple - CHESS post-upgrade with 1.5 m compact undulator. Dashed blue - APS undulator A, and green - CHESS post-upgrade with 3.5 m undulator.

Achromat

The achromat shown in Fig. 2, consists of four horizontally focusing quadrupoles, and a pair of defocusing gradient bends. Beam parameters at midpoint of the ~4 meter straight are $\beta_x = 11.2$ m, $\beta_y = 2.6$ m and $\eta = 0$ m. β_x is limited from below by the separation of the quad (Q_1) at the end of the straight from the adjacent gradient-bend. If the zero-dispersion condition is relaxed by varying the quadrupole strengths, horizontal beta can be reduced to $\beta_x = 3.8$ m,

* Work supported by the National Science Foundation DMR 13-32208

PHOTO-INJECTOR OPTIMIZATION AND VALIDATION STUDY WITH THE OPAL BEAM SIMULATION CODE

L. D. Duffy*, K. A. Bishofberger, J. W. Lewellen, S. J. Russell, D. Shchegolkov,
Los Alamos National Laboratory, Los Alamos, NM, USA

Abstract

A 42 keV x-ray free electron laser (XFEL) is a plausible technology alternative for the Matter Radiation Interactions in Extremes (MaRIE) experimental project, a concept developed by Los Alamos National Laboratory. An early pre-conceptual design for such an XFEL calls for 100 pC electron bunches with very low emittance and energy spread. High fidelity simulations that capture all beamline physics will be required to ensure a successful design. We expect to use the beam simulation code OPAL as one of the tools in this process. In this study, we validate OPAL as a photo-injector design tool by comparing its performance with published PITZ experimental data and simulations.

This photo-injector configuration was experimentally demonstrated to have a minimum transverse emittance of $0.696 \pm 0.020 \mu\text{m}$ in 2011. For 100 pC, the bunch charge anticipated for a MaRIE XFEL, PITZ demonstrated $0.212 \pm 0.006 \mu\text{m}$, with ASTRA predicting a projected transverse emittance of $0.173 \mu\text{m}$ [2]. Given that PITZ is designed to meet the European XFEL requirement of $0.9 \mu\text{m}$ for a 1 nC bunch in the injector, the PITZ design represents a promising starting point for a photo-injector design to meet the MaRIE XFEL concept requirement of $0.1 \mu\text{m}$ for a 100 pC bunch charge. As such, simulations of the PITZ photo-injector were selected for the photo-injector optimization study to validate the performance of the OPAL code.

INTRODUCTION

The design of a 42 keV XFEL is driven by the requirement that there is good overlap between the electron beam and x-ray phase spaces. The Los Alamos National Laboratory XFEL preliminary concept for the MaRIE project has a 12 GeV electron linac producing 42 keV photons from the wiggler. The phase-space overlap requirement limits the normalized transverse emittance of the electron beam at the wiggler entrance to $\epsilon_n \leq \beta\gamma\lambda_x/4\pi$, where β and γ are the electron beam's relativistic factors, and λ_x is the x-ray wavelength. The normalized transverse emittance goal for the MaRIE XFEL concept is $0.20 \mu\text{m}$ at the wiggler entrance. Such a small transverse emittance leaves little space for emittance growth throughout the linac, and places stringent demands on the transverse emittance from the photo-injector. The MaRIE concept goal transverse emittance from the photo-injector is less than $0.1 \mu\text{m}$ for a 100 pC electron bunch. Ensuring a successful photo-injector design concept requires high-fidelity simulations. We have selected the OPAL beam dynamics code [1] for our simulations, due to its fully 3D space charge algorithm, and our ability to incorporate necessary physics into the OPAL code through our local OPAL code developers.

In this proceedings, we present our results validating the OPAL code from published results of optimization of the PITZ (Photo Injector Test facility at DESY, Zeuthen site) photo-injector [2].

PITZ PHOTO-INJECTOR

The PITZ photo-injector is designed to minimize the transverse emittance for a 1 nC bunch. Simulations with the ASTRA [3] code have predicted a minimum projected transverse emittance of $0.607 \mu\text{m}$ for this bunch

SIMULATIONS AND OPTIMIZATION APPROACH

The OPAL simulations we performed were based on previous, publicly available ASTRA simulations of the PITZ photo-injector and Poisson/Superfish input files for the PITZ photo-injector and PITZ solenoid taken from the 37th ICFA Advanced Beam Dynamics Workshop on Future Light Sources PITZ benchmark problem [4]. It should be noted that these simulations are not exactly equivalent to those used in Ref. [2], to which we compare our results. Thus, it is natural to expect that these results will not be exactly the same as the numbers we compare to in Ref. [2], however the results should be similar.

The PITZ photo-injector consists of a 1.6 cell L-band normal conducting RF cavity, with a Cesium Telluride cathode. The combination of a large, main solenoid, and a bucking solenoid provide the magnetic field for emittance compensation, and prevent magnetic field at the cathode. A cut disk structure booster cavity, specially designed for PITZ, is located with its first iris at 3.24 m from the cathode. A beam monitor is located at 5.74 m from the cathode, and it is at this location that emittance measurements have been taken to determine the minimum transverse projected emittance [2]. Similarly, our simulations specifically aimed to minimize the emittance at this location.

Starting with the ASTRA simulation input, the goal was to optimize the settings of a PITZ-like photo-injector for injector bunch charges of 0.02, 0.1, 0.25, 1 and 2 nC. Simple linear optimization of parameters was used, as basic tools were available to perform such a scan. More advanced optimization methods, such as automated Pareto Front optimization, are desirable and likely more efficient in terms of person-hours. Different charge runs were performed by different authors, to obtain the best optimization for each

* ldd@lanl.gov

QUALITY FACTOR IN HIGH POWER TESTS OF CRYOGENIC COPPER ACCELERATING CAVITIES*

A. Cahill[†], J. Rosenzweig, UCLA, Los Angeles, California

V.A. Dolgashev, M. Franzi, S. Tantawi, S. Weathersby, SLAC, Menlo Park, CA

Abstract

Recent SLAC experiments with cryogenically cooled 11.4 GHz standing wave copper accelerating cavities have shown evidence of 250 MV/m accelerating gradients with low breakdown rates. The gradient depends on the circuit parameters of the accelerating cavity, such as the intrinsic and external quality factors (Q_0 , Q_E). In our studies we see evidence that Q_0 decreases during rf pulse at 7-70 K. This paper discusses experiments that are directed towards understanding the change of Q_0 at high power.

MOTIVATION

Accelerating gradient is important for future rf linacs, larger gradients decreases the accelerator length. RF breakdown is one of the major factors limiting the operating accelerating gradient. The statistical nature of rf breakdowns was discovered during work on NLC/GLC [1–4]. For several kilometer long linacs, the breakdown probability needs to be very small, $< 10^{-6}$ /pulse/meter[5]. Presently, X-band structures are the most studied in terms of rf breakdowns [4, 6–9]. We know that breakdown statistics depend on pulse heating [10] and a numerous list of other factors, such as the peak electric field, the peak magnetic field [11], and the peak Poynting vector[12].

One of the current hypotheses explains the statistical behavior of rf breakdowns in X-band accelerating structures by generation and movement of dislocations under stresses created by rf magnetic and electric fields [13]. This dislocation movement should dramatically change at cryogenic temperatures and this should be reflected in the statistical behavior of the breakdown rate. Recent experiments at SLAC were performed with copper accelerating cavities cooled to cryogenic temperatures to investigate this claim. These experiments have shown preliminary evidence of 250 MV/m accelerating gradients and 500 MV/m peak surface electric fields with 10^{-3} per pulse per meter breakdown rates at 45 K[14]. The cavity was designed using rf surface resistance measured at low temperature and low power[15, 16]. During high power measurements we noticed a reduction of Q_0 . This change in Q_0 brings uncertainty to our calculation of the gradient. To know the gradient precisely we need to understand the physics of the reduction in Q_0 . In this paper we discuss our experimental work directed towards this understanding.

* Work Supported by DOE/SU Contract DE-AC02-76-SF00515 and DOE SCGSR Fellowship

[†] acahill@physics.ucla.edu

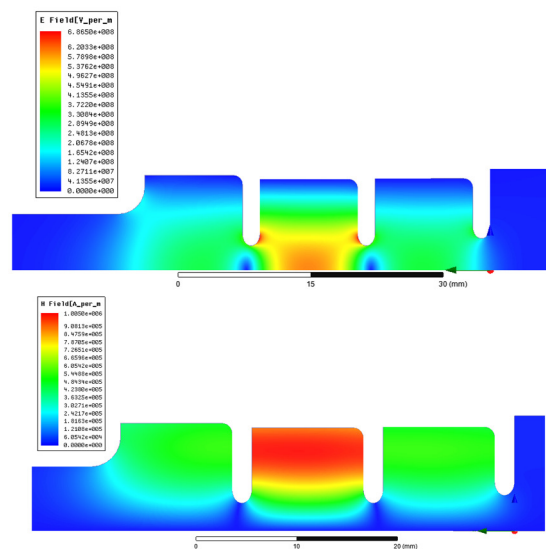


Figure 1: Electric and magnetic fields. 10 MW input at 95K.

EXPERIMENTAL METHODS

In this experiment we used the same cavity as described in [17]. To localize rf breakdowns to a single cell, one cell of the test structure has high electric and magnetic fields, to mimic those of a full length accelerating section [5]. There are two cells on each side of the test cell to remove any effects from the coupling to the waveguides on either end of the structure. The ratio of the radius of the irises adjacent to the central cell, to the wavelength is, $a/\lambda = 0.105$. The electric field on axis in the middle cell was tuned to be twice that of the outer cells. A diagram and field map of the cavities is shown in Fig. 1. RF power is coupled into the structure by a TM_{01} mode launcher, connected by a circular waveguide. The cavity can be cooled to 7 K when placed inside the cryostat.

Low Power Measurements

After an initial run at high power to study breakdown statistics as mentioned previously, the cavity was disconnected from the klystron. At this time we measured the rf properties of the cryo cavity using a network analyzer. The network analyzer was attached to a WR-90 rf window that was connected to the TM_{01} mode launcher and coupled to the cavity. To find the Q_0 from the frequency scan of the network analyzer we fit the data with a resonant circuit model. There was also a dispersion term to account for the effect from the waveguide connecting the network analyzer to the accelerating cavity. Figure 2 shows the fitted Q_0 versus temper-

HIGH GRADIENT S-BAND CRYOGENIC ACCELERATING STRUCTURE FOR RF BREAKDOWN STUDIES*

A. Cahill[†], A. Fukasawa, J. Rosenzweig, UCLA, Los Angeles, California
G. B. Bowden, V.A. Dolgashev, S. Tantawi, SLAC, Menlo Park, CA

Abstract

Operating accelerating gradient in normal conducting accelerating structures is often limited by rf breakdowns. The limit depends on multiple parameters, including input rf power, rf circuit, cavity shape, cavity temperature, and material. Experimental and theoretical study of the effects of these parameters on the breakdown physics is ongoing at SLAC. As of now, most of the data has been obtained at 11.4 GHz. We are extending this research to S-band. We have designed a single cell accelerating structure, based on the extensively tested X-band cavities. The setup uses matched TM_{01} mode launcher to feed rf power into the test cavity. Our ongoing study of the physics of rf breakdown in cryogenically X-band accelerating cavities shows improved breakdown performance. Therefore, this S-band experiment is designed to cool the cavity to cryogenic temperatures. We use operating frequencies near 2.856 GHz. We present the rf design and discuss the experimental setup.

INTRODUCTION

Accelerating gradient is important for future rf linacs, larger gradients decreases the accelerator length. RF breakdown is one of the major factors limiting the operating accelerating gradient. The statistical nature of rf breakdowns was discovered during work to develop NLC/GLC [1–4]. For several kilometer long linacs, the breakdown probability needs to be very small, $< 10^{-6}$ /pulse/meter[5].

Presently, most of the data on rf breakdowns is obtained with X-band accelerating structures[4, 6–9]. We know that breakdown statistics depend on pulse heating [10], the peak electric and magnetic field [11], and the peak Poynting vector[12]. However, properties of rf breakdown at other frequencies has not been satisfactorily studied. For example, at S-band, there has been relatively few experiments with published breakdown rates [13, 14].

One of the current hypotheses explains the statistical behavior of rf breakdown in X-band accelerating structures by generation and movement of dislocations under stresses created by rf magnetic and electric fields [9, 10]. This dislocation movement should dramatically change under cryogenic temperatures and this should be reflected in the statistical behavior of the breakdown rate. Recent experiments at SLAC were performed with copper accelerating cavities cooled to cryogenic temperatures to investigate this claim. These experiments have shown evidence of 250 MV/m accelerat-

ing gradients and 500 MV/m peak surface electric fields in X-band copper cavities at 45 K[15].

The TOPGUN collaboration would like to apply these findings to an ultra-high gradient S-band rf photoinjector [16]. With a significantly larger gradient the beam brightness of an electron photoinjector will be improved by over an order of magnitude. To design and build a practical S-band photoinjector, we first need to extend the knowledge on rf breakdowns to this frequency. We designed an experimental setup that includes a cryogenically cooled copper single-cell-SW accelerating structure.

DESIGN CONSIDERATIONS

In our breakdown experiments, we have tested more than 50 single-cell accelerating cavities at X-band[5]. We propose to use the same approach at S-band.

To reduce price and complexity for the test setup, the cavity will be fed by a TM_{01} mode launcher[17], that is connected to the cavity by a circular waveguide with radius of 1.81 in. The mode launcher will serve as the rf coupler. We propose to use the same configuration in the TOPGUN S-band photoinjector[18].

To localize rf breakdowns to a single cell, one cell of the test structure has high electric and magnetic fields, to mimic those of a full length accelerating section [5]. There are two cells on each side of the test cell to remove any effects from the coupling to the waveguides on either end of the structure. The ratio of the radius of the irises adjacent to the central cell, to the wavelength was kept the same as in the X-band cryo experiments, $a/\lambda = 0.105$. The electric field on axis in the middle cell was tuned to be twice that of the outer cells.

The difference between the cryo S-band and cryo X-band cavities are two-fold: the outer diameter of the cells in the S-band design are rounded to increase the Q_0 , and the S-band design is more overcoupled. The choice of the coupling value will be discussed later.

DESIGN PARAMETERS

SUPERFISH[19], a 2D finite element electric field solver, was used to design the geometry of the S-band accelerator cavity, and verified with HFSS[20], a 3D finite element electric field solver. The geometry is shown in Fig. 1. The on-axis electric field in the cavity for the π mode are shown in Fig. 2. The peak axis in the middle cell is twice that of the outer cells. Table 1 lists the dimensions shown in Fig. 1

* Work Supported by DOE/SU Contract DE-AC02-76-SF00515 and DOE SCGSR Fellowship

[†] acahill@physics.ucla.edu

DEVELOPMENT OF A SHORT PERIOD CRYOGENIC UNDULATOR AT RADIABEAM*

F. H. O'Shea[†], R. Agustsson, Y.-C. Chen, A. J. Palmowski, and E. Spranza,
RadiaBeam Technologies, Santa Monica, CA, USA

Abstract

RadiaBeam Technologies has developed a 7-mm period length cryogenic undulator prototype to test fabrication techniques in cryogenic undulator production. We present here our first prototype, the production techniques used to fabricate it, its magnetic performance at room temperature and the temperature uniformity after cool down.

INTRODUCTION

The goal of this project was to build a cryogenic undulator that used praseodymium-iron-boron magnets and textured dysprosium (TxDy) poles. The latter material is being developed at RadiaBeam using an in-house formula for production that shows a great deal of promise for increasing the gap field strength of short period undulators, while the magnets were purchased from a vendor. Both the material development and undulator design goals have been discussed in previous publications [1–4].

Because dysprosium's Curie temperature is approximately 90 K, the undulator is necessarily cryogenic. The choice of praseodymium based magnets is because of a spin-axis re-orientation in neodymium magnets [5], and they are stronger than samarium cobalt magnets.

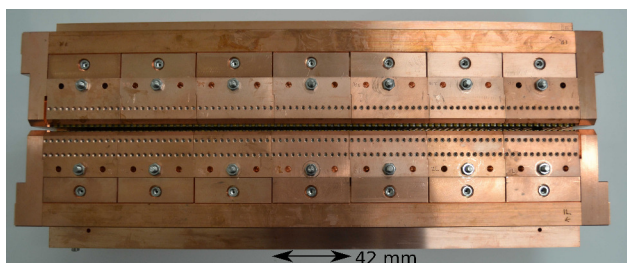


Figure 1: Image of the cryogenic undulator.

We met with much success in understanding the TxDy and have developed a strong understanding of the features of its performance. Unfortunately, we also had considerable difficulty attaining our desired level of batch-to-batch consistency in the textured dysprosium [2, 3]. Without regular access to a cryogenic hysteresisgraph or vibrating sample magnetometer the turn around time for sample production and testing made exploration of production parameters impractical. Eventually, we had to cease the development of the textured dysprosium.

While the TxDy was being developed, the undulator design became quite advanced and showed promise for func-

tioning as a room temperature undulator using vanadium permendur (VP) poles. In order to test the engineering design of the undulator and take advantage of further development of the TxDy we hope to pursue in the future, we built a 42 period undulator using VP poles instead of TxDy. The undulator is shown in Fig. 1. The prototype undulator performed favorably compared to our desired specifications [1–4].

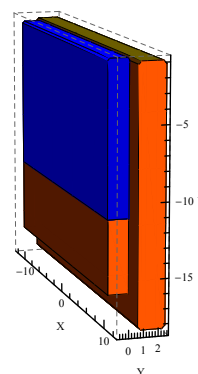


Figure 2: Layout of the minimum element representation of the undulator in Radia. The orange objects are permanent magnets and the blue object is the pole. The backing magnet can be seen below the pole. All axes have units of mm. The electron beam travels along the \hat{y} -axis at $x = z = 0$.

MAGNETIC DESIGN

The work discussed in the section was performed before the switch from TxDy to VP. It nonetheless describes the motivation for the design decisions made for the undulator that was produced.

We used Radia to design the undulator [6]. The Radia representation of the minimum magnetic element is shown in Fig. 2. The magnetic properties for the dysprosium were taken from a vibrating sample magnetometer measurement made on an initial sample [2]. The material properties for the magnets were taken from measurements of the hybrid praseodymium-neodymium based magnets available commercially [7]. The design gap of the undulator was fixed at 2 mm to allow access with a Hall probe.

A full design study was performed including managing demagnetization (or lack thereof), magnetic and mechanical tolerances and magnetic field strength optimization. The results for the dimensions and tolerances of the magnetically active objects is shown in Table 1. The low initial permeability of TxDy ($\mu_i \sim 10^2 \mu_0$) as compared to VP

* Work supported by DOE under contracts DE-SC0006288 and NNSA S5AA DE-NA0001979.

[†] oshea@radiabeam.com

THz AND SUB-THz CAPABILITIES OF A TABLE-TOP RADIATION SOURCE DRIVEN BY AN RF THERMIONIC ELECTRON GUN*

A. V. Smirnov[#], R. Agustsson, S. Boucher, T. Campese, Y. Chen, J. Hartzell, B. Jacobson, A. Murokh, F.H. O'Shea, E. Spranza, RadiaBeam Technologies Inc., Santa Monica, CA 90404, USA
 W. J. Berg, M. Borland, J. Dooling, L. Erwin, R. Lindberg, S. Pasky, N. S. Sereno, Y. Sun and A. A. Zholents, Advanced Photon Source, Argonne National Laboratory, Argonne, IL-60439, USA
 W. Bruns, Warner Bruns Feldberechnungen, Berlin 10551, Germany
 B. van der Geer and M. de Loos, Pulsar Physics, Eindhoven 5614 BC, The Netherlands

Abstract

Design features and experimental results are presented for a sub-mm wave source [1] based on APS RF thermionic electron gun. The setup includes compact alpha-magnet, quadrupoles, sub-mm-wave radiators, and THz optics. The sub-THz radiator is a planar, oversized structure with gratings. Source upgrade for generation frequencies above 1 THz is discussed. The THz radiator will use a short-period undulator having 1 T field amplitude, ~20 cm length, and integrated with a low-loss oversized waveguide. Both radiators are integrated with a miniature horn antenna and a small ~90°-degree in-vacuum bending magnet. The electron beamline is designed to operate different modes including conversion to a flat beam interacting efficiently with the radiator. The source can be used for cancer diagnostics, surface defectoscopy, and non-destructive testing. Sub-THz experiment demonstrated a good potential of a robust, table-top system for generation of a narrow bandwidth THz radiation. This setup can be considered as a prototype of a compact, laser-free, flexible source capable of generation of long trains of Sub-THz and THz pulses with repetition rates not available with laser-driven sources.

INTRODUCTION

To generate narrow bandwidth, sub-THz beams a resonant Cherenkov radiation is proved can be effective and compact alternative to coherent undulator radiation especially at beam energies as low as few MeVs produced by a thermionic RF Gun followed by a magnetic compression [1]. Classical coherent Cherenkov radiation is usually produced [2] in rather dispersive (low group velocity), closed resonant structures having electrically small (in wavelength scale) apertures. The radiation is usually driven by a monopole, essentially single mode, long-range wakefields. The coherent radiation frequency is determined by the resonant synchronism between phase and electron beam velocities. Therefore, for relativistic electron beams frequency adjustment is very limited to be practical for such a "resonant Cherenkov" source. We overcome this issue by using an overmoded, high group velocity, slow-wave structure employed as a radiator. Performance specifics of such a tuneable, oversized, side-

open, planar experimental structure are discussed below.

Another fundamental problem related to Coherent Vavilov-Cherenkov radiation is limited maximum frequency when using low-energy, low-brightness driving electron beams. Since the interaction gap is still proportional to wavelength even for oversized, overmoded structures, the transmitted beam current drops dramatically. Besides, micro-bunching capabilities of magnetic compression remain limited resulting in rapid reduction of bunching factor at higher frequencies. These issues make such a source impractical above ~1 THz. Therefore, for 1 THz frequency and above we consider below a compact undulator instead of Cherenkov radiator using basically the same beamline.

RBT-APS EXPERIMENT OUTLINES

Experimental setup of the sub-THz source [1] was developed jointly by RadiaBeam Technologies, LLC and the Accelerator Systems Division of Advanced Photon Source (APS) at Argonne National Laboratory (ANL). It is deployed on the Injector Test Stand (ITS) of the APS. We briefly outline here three novel features of the source: a) rather wide tunability of the frequency and the radiation spectrum; b) capability to determine effective microbunch length from the spectra taken; and c) relatively low α -magnet extra strength required to make up the microbunch space charge.

Originally the side-open, oversized, planar radiator was designed for ~504 GHz frequency (at 0.986c phase velocity). Nevertheless we have produced spectra tuned across two frequency ranges: (476–584) GHz with close to theoretical 7% instantaneous FWHM (see Figure 1a), and also (311–334) GHz with 38% instantaneous bandwidth. Both single line (for each band) and two-line spectra (see Figure 1) are producible in a well controllable way. Tuning has been accomplished with the following means: a) kinetic beam energy variation (2.5-2.9) MeV; and b) alpha-magnet gradient (2.15-2.71) T/m. Additional, fine tuning was done by varying pitch angle related to aligning of the radiator assembly with respect to the beamline axis. The spectrum peak frequency was tuned mostly with beam energy, whereas the intensity of each of these frequency components was controlled relatively independently from zero to maximum by fine tuning of the beam transport (steering) within the structure. The interferometric results indicate that at higher electron beam energies the spectrum peak frequency is lower. This

*Supported by the U.S. Department of Energy (award No. DE-SC-FOA-0007702).

[#]asmirnov@radiabeam.com

LCLS INJECTOR LASER PROFILE SHAPING USING DIGITAL MICROMIRROR DEVICE

S. Li*, S. Alverson, D. K. Bohler, A. Fry, S. Gilevich, Z. Huang, A. Miahnahri, D. Ratner, J. Robinson, F. Zhou, SLAC National Accelerator Laboratory, Menlo Park, USA

Abstract

In the Linear Coherent Light Source (LCLS) at SLAC, the injector laser plays an important role as the source of the electron beam for the Free Electron Laser (FEL). The emittance of the beam is highly related to the transverse profile of the injector laser. Currently the LCLS injector laser has undesired features, such as hot spots, which carry over to the electron beam. These undesired features increase electron emittance, degrade the FEL performance, and complicate operations. The injector laser shaping project at LCLS aims to produce arbitrary electron beam profiles, such as cut-Gaussian, uniform, and parabolic, and to study the effect of spatial profiles on beam emittance and FEL performance. Effectively it also allows easy transition between the two spare lasers, where the operators can use the spatial shaper to achieve identical profiles for the two lasers. In this paper, we describe the experimental methods to achieve laser profile shaping and electron beam profile shaping respectively, and demonstrate promising results.

INTRODUCTION

The injector laser at LCLS consists of a Ti:Sapphire laser system, producing a 2 ps pulsed laser at 760 nm with a repetition rate of 120 Hz. The infrared laser is then converted to ultraviolet wavelength (253 nm) via nonlinear process in a frequency tripler. The UV laser then strikes a copper photocathode which emits photo-electrons due to the photo-electric effect [1]. Past studies have shown that certain laser profiles lead to lower electron beam emittance [2, 3]. Figure. 1 is a typical example of the transverse profile of the LCLS injector laser (left) and electron beam profile (right) near cathode. Hot spots and non-uniformities in the laser profile and photocathode quantum efficiency lead to non-uniformities in the electron beam. Therefore, with spatial shaper optics, we can address and remove the non-uniformities and achieve arbitrary profiles.

In this paper, we briefly discuss the hardware choice and experimental setup. We describe the experimental methods to achieve accurate shaping of the laser and the electron beam profiles. We also demonstrate promising results obtained at LCLS.

HARDWARE AND EXPERIMENTAL SETUP

There are many commercially available adaptive optics. J. Maxson et al. [4] have used liquid-crystal-on-silicon (LCoS) spatial light modulators (SLM) to spatially modulate laser

* siqili@slac.stanford.edu

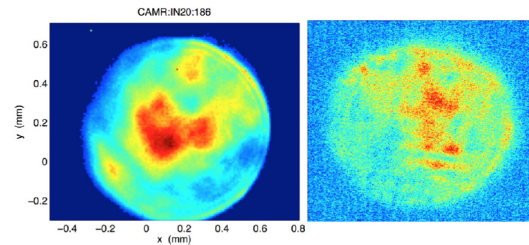


Figure 1: Example of LCLS injector laser transverse profile (left). Example of electron beam emission profile (right) near cathode.

and electron beam with the green photocathode at Cornell. However, LCoS based SLMs are not compatible with UV lasers for our case. A. Halavanau et al. [5] have used a microlens array to experimentally characterize and shape the beam transverse profile. Other relevant studies can be found in [6, 7, 8]. After extensive damage tests on various materials [9], we choose to work with digital micromirror device (DMD) from Texas Instruments [10]. Unfortunately, there is no DMD available to work in deep UV as our laser wavelength, so we resort to a third-party company for replacing the window on the chip in order to transmit UV. Damage tests have shown that a converted UV DMD can sustain up to 90 μJ laser power with beam size 1 cm (damage threshold varies with beam size), when the laser pulse is placed after the micromirrors have just stabilized into a new state for each period (see details in [10]).

The model we use is DLP 7000 DMD which consists of 768×1024 micromirrors with size $13.68 \mu\text{m}$. The micromirrors can flip into two states, ON or OFF corresponding to $\pm 12^\circ$, given an input voltage. Due to the nature of the DMD design, laser intensity reduction is achieved by grouping the individual micromirrors into macropixels and turning off a fraction of randomly-distributed micromirrors in each macropixel to reduce intensity by a certain amount. The device is programmable through an API in Matlab, which we incorporate into the LCLS EPICS control system.

A technical subtlety is the pulse front tilt introduced by the DMD, as from a grating. The pulse front tilt is effectively a correlation between the time coordinate and the transverse position coordinate. In the case of the DMD, or a grating, the correlation results in an elongated pulse length. We compensate this effect by introducing a diffraction grating upstream of the DMD (Fig. 2), which cancels the pulse front tilt from the DMD. The compensation is confirmed by measuring the electron bunch length in comparison to the regular setup without DMD, which shows $< 10\%$ difference.

COMPUTATION OF SYNCHROTRON RADIATION

Dean Andrew Hidas*, Brookhaven National Laboratory, Upton, NY, USA

Abstract

This presentation introduces a new open-source software development for the computation of radiation from charged particles and beams in magnetic and electric fields. The computations are valid in the near-field regime for both relativistic and non-relativistic scenarios. This project is being developed, and is currently in use, at Brookhaven National Laboratory's National Synchrotron Light Source II. Primary applications include, but are not limited to, the computation of spectra, photon flux densities, and power density distributions from undulators, wigglers, and bending magnets on arbitrary shaped surfaces in 3D making possible detailed study of sensitive accelerator and beam-line equipment. Application interfaces are available in Python, Mathematica, and C. Practical use cases are demonstrated and benchmarked. Additionally, future upgrades will be elaborated on.

INTRODUCTION

Open Source Code for Advanced Radiation Simulation (OSCARS) [1] is a new open source software developed at Brookhaven National Laboratory (BNL). OSCARS is a general purpose code for the calculation of radiation of charged particles in motion. Primary uses are for synchrotron and accelerator facilities where photon density distributions and heat loads on accelerator and beam-line equipment is of great interest. This software allows for the calculation of these properties on arbitrary shaped surfaces in 3 dimensions.

At its core OSCARS is a numerical discretization of derived equations from the Liéard-Wiechert potentials, which are valid for relativistic and non-relativistic particles alike and includes the so-called near-field contributions. These calculations are based off of the particle trajectory, which in OSCARS is calculated from the well known relativistic Lorenz force given in equation 1. The particle trajectory propagation is determined in 3D using a 4th-order Runge-Kutta method to solve the second order equations of motion. Other methods, such as adaptive step, are easily implemented and of potential future interest depending on use cases.

$$\frac{d\vec{p}}{d\tau} = q(\vec{E} + \vec{v} \times \vec{B}) \quad (1)$$

CORE CAPABILITIES

OSCARS is capable of computing charged particle trajectories, power density distributions, flux density distributions, and spectra for charged particles and charged particle beams in arbitrary magnetic field configurations. This includes multi-particle simulations of mixed-particle type beams of native or user defined particle types. OSCARS is capable of computing power density and flux density distributions on

arbitrary surfaces in 3 dimensions. OSCARS also allows for the easy definition of surface planes and arbitrary objects in 3D, with simple utilities to translate and rotate them in space, making it versatile and extendible to many applications at accelerator facilities.

Utilities are built-in for modern large scale computing. A typical user will benefit from an easy python MPI [2] implementation to achieve moderate gains in speed on their desktop, workstation computer, or cluster. For **very** large-scale simulations OSCARS is also designed to be run on any modern grid/cloud computing infrastructure such as the Department of Energy and National Science Foundation supported Open Science Grid [3], where it has already been run extensively.

OSCARS is capable of reading in 1D, 2D, and 3D field configurations of various formats. In the case of 1D data, irregularly spaced points are interpolated to form a uniform grid to maximize the speed of trajectory calculations. Additionally OSCARS has utilities built-in for generating dipole, Gaussian, undulator, and wiggler fields. These fields are not discretized which allows for high precision calculations. A user may also input any functional form in the same manner by simply creating any python function which describes the field of interest.

The core code is written in C++ for speed and has a python extension. The main application programming interface is written in Python for ease of use and integrability by the larger scientific community. Currently the extension is available for python 2.7 and is forthcoming for python versions ≥ 3.4 . No additional packages are required to run the core of OSCARS. The user is free to choose any visualization platform. As of writing this a modest package for visualization exists for OSCARS based on matplotlib [4] which is non-essential, but perhaps convenient.

SPECTRUM & FLUX DENSITY

The electric field is calculated in the frequency domain directly from equation 2, which is derived by taking the Fourier transform of the Liéard-Wiechert potentials. This derivation and different formulations can be found in many texts [5–7]. The spectrum is calculated for the idealized planar undulator U49 ($\lambda_m = 49$ [mm], $N_{periods} = 55$, and $B_v^{max} = 1$ [T]) for both the case of a filament beam (single-particle) and for the NSLS-II design parameters in a 6.6 [m] straight section at its final operating current of 500 [mA]. The beam parameters used are $\epsilon_v = 0.008$ [nm rad], $\epsilon_h = 0.9$ [nm rad], $\beta_v = 0.8$ [m], $\beta_h = 1.5$ [m], $E = 3$ [GeV], and $\Delta E/E = 0.001$. Figure 1 shows the on-axis spectrum and flux density at 30 [m] around the 3rd harmonic in the spectrum. The computation of the flux density on a grid of 200×200 takes less than 4 seconds on a modest laptop (with 2.8 GHz Intel Core i7).

* dhidas@bnl.gov

DC PHOTOGUN GUN TEST FOR RHIC LOW ENERGY ELECTRON COOLER (LEReC)*

D. Kayran[#], Z. Altinbas, D. Beavis, S. Bellavia, D. Bruno, M. Costanzo, A. V. Fedotov, D. Gassner, J. Halinski, K. Hamdi, J. Jamilkowski, J. Kewisch, C.-J. Liaw, G. Mahler, T. A. Miller, S. K. Nayak, T. Rao, S. Seletskiy, B. Sheehy, J. Tuozzolo, Z. Zhao
Brookhaven National Laboratory, Upton, NY 11973, U.S.A.

Abstract

Non-magnetized bunched electron cooling of low energy RHIC requires electron beam energy in range of 1.6-2.6 MeV, with average current up to 45 mA, very small energy spread, and low emittance [1]. A 400 kV DC gun equipped with photocathode and laser delivery system will serve as a source of high quality electron beam. Acceleration will be achieved by an SRF 704 MHz booster cavity and other RF components that are scheduled to be operational in early 2018. The DC gun testing in its installed location in RHIC will start in early 2017. During this stage we plan to test the critical equipment in close to operation conditions: laser beam delivery system, cathode QE lifetime, DC gun, beam instrumentation, high power beam dump system, and controls. In this paper we describe the gun test set up, major components, and parameters to be achieved and measured during the gun beam test.

INTRODUCTION

The LEReC uses a replica of the DC photocathode gun used in the Cornell University prototype injector, which has already been producing record high-brightness, high average current electron beams [2]. The gun has been built and is currently HV conditioning Cornell University. The gun will be operated with a multi-alkali NaK2Sb (or CsK2Sb) photocathode, which will be illuminated with green (532 nm) laser light with an oscillator frequency of 704 MHz. The 400 keV electron beam from the gun is transported via a 704 MHz SRF booster cavity and 2.1

GHz 3rd harmonic linearizer normal conductive cavity. Electron beam is accelerated to maximum kinetic energy of 2.6 MeV. In drift space electron bunch is stretched to required bunch length. Before entering the cooling section accumulated energy chirp is compensated by normal conductive 704 MHz cavity. Two dogleg-like mergers and mirror dipole are used to combine and to separate electron cooler electron beam with/from RHIC ion beams. The layout of LEReC is shown in Fig. 1. The optics of entire transport line has been designed and optimized to delivery electron bunches for different operation energies with quality satisfied electron cooling requirement (Table 1) [3].

Table 1: LEReC Electron Beam Requirements

Kinetic energy, MeV	1.6	2.0	2.6
Bunch Charge, pC	130	160	200
Bunches per train	30	27	24
Macro bunch charge, nC	3.9	4.3	4.8
Macro bunch rep. f, MHz	9.3	9.3	9.3
Total beam Current, mA	36	40	45
Normalized Emittance, μ	< 2.5	< 2.5	< 2.5
Energy spread, 10^{-4}	< 5	< 5	< 5

PURPOSE OF LEREC GUN TEST

The gun beam test (see Fig. 2) is the first stage of LEReC commissioning. Our aim is to test critical LEReC equipment in close to operation condition. This will demonstrate that the DC gun with photocathode meets its performance specifications and can work reliably.

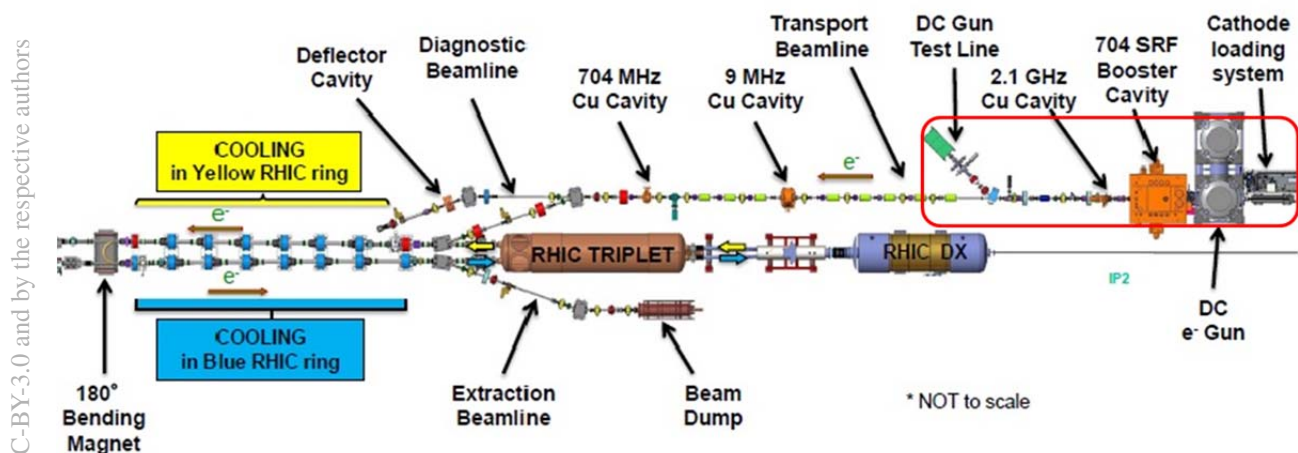


Figure 1: Layout of LEReC accelerator. Red contour box indicates DC gun test area.

*Work supported by the US Department of Energy under contract No. DE-SC0012704.

[#]dkayran@bnl.gov

SIMULATION OF STRAY ELECTRONS IN THE RHIC LOW ENERGY COOLER

J. Kewisch,[#] Brookhaven National Laboratory, Upton, NY 11973, U.S.A.

Abstract

The Low Energy RHIC electron Cooler [1], under construction at BNL, accelerates electrons with a 400 kV DC gun and a 2.2 MeV SRF booster cavity. Electrons which leave the cathode at the wrong time will not be accelerated to the correct energies and will not reach the beam dump at the end of the accelerator. They may impact the beam pipe after incorrect deflection in dipoles or after being slowed down longitudinally in the booster while the transverse momentum is not affected. In some cases their direction is reversed in the booster and they will impact the cathode.

We simulated the trajectories of these electrons using the GPT tracking code [2]. The results are qualitative, not quantitative, since the sources and numbers of the stray electrons are unknown.

INTRODUCTION

There are various reasons for the emission of electrons from the cathode at the wrong time: they may be created by stray laser light, or they may be secondary particles from cosmic rays or back-bombarding ions or other electrons.

We tracked a bunch with half a million particles and the length of a full RF wave length until all particles are lost. Since we are mostly interested in beam loss near the SRF cavity we did not consider electrons that survive the first 4 meters. Figure 1 shows that part of the beam line. The stray electrons are by definition not inside the regular electron bunch, so the space charge calculation is turned off.

The first calculation starts with a 3 mm radius beam from the center of the cathode holder. From the half million 50% of the electrons make it through the 4 meter mark, 8% return to the cathode, and the remaining 42% are lost on the beam pipe somewhere in between. Again, this assumes that the electrons are created in a continuous stream, which is most likely not correct.

LOCATION OF THE BEAM LOSSES

Figure 2 shows where the 42 % of the electrons are lost. We distinguish between forward going electrons (red curve) and backwards going particles (black curve).

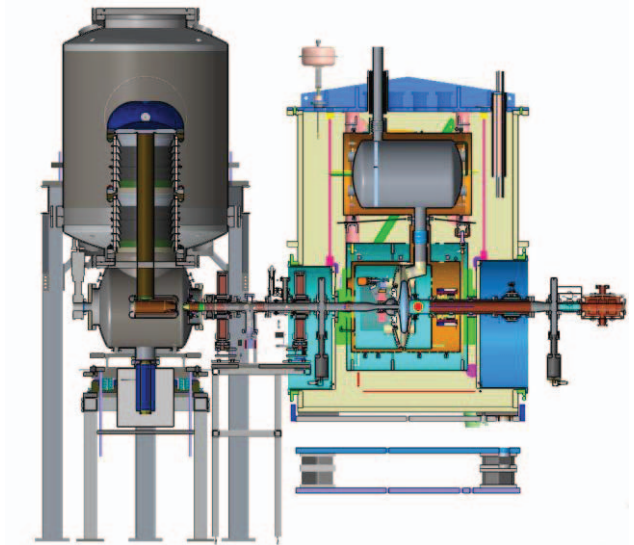


Figure 1: Section of the LEReC considered in this simulation.

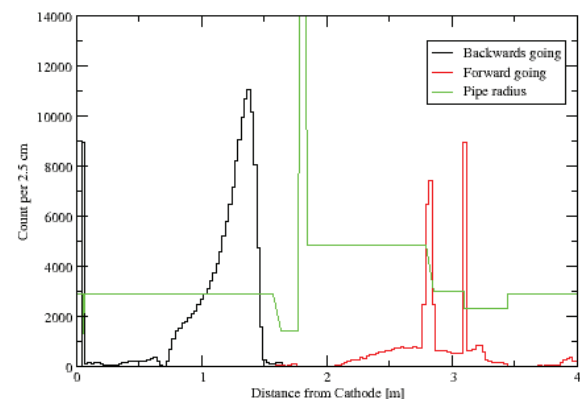


Figure 2: Location of electron losses. Backward going electrons are counted in black, forward going in red.

The green curve shows the beam pipe radius (in arbitrary units, to guide the eye). The spike in the green curve indicates the position of the SRF cavity, which is shown in light blue in Figure 1. The spike in the number of backwards traveling electrons at 0.05 m is caused by electrons impacting the anode of the DC gun.

There are only small losses inside the cryostat. The booster cavity was built as an SRF electron gun which was converted into a cavity by removing the cathode insert. At the location of this cathode insert the beam pipe

2: Photon Sources and Electron Accelerators

A08 - Linear Accelerators

BEAM OPTICS FOR THE RHIC LOW ENERGY ELECTRON COOLER (LEReC)**

J. Kewisch[#], A.V. Fedotov, D. Kayran, S. Seletskiy
Brookhaven National Laboratory, Upton, NY 11973, U.S.A.

Abstract

A Low-energy RHIC Electron Cooler (LEReC) [1] system is presently under construction at Brookhaven National Laboratory. This device shall enable gold ion collisions at energies below the design injection energy with sufficient luminosity. Electron beam with energies between 1.6, 2.0 and 2.6 MeV are necessary. This machine will be the first to attempt electron cooling using bunched electron beam, using a 703 MHz SRF cavity for acceleration. Special consideration must be given to the effect of space charge forces on the transverse and longitudinal beam quality. We will present the current layout of the cooler and beam parameter simulations using the computer codes PARMELA [2].

INTRODUCTION

The nuclear physics program for the Relativistic Heavy Ion Collider (RHIC) for the 2019 and 2020 run periods concentrates on the search for the QCD phase transition critical point. Gold-gold collisions at energies between 2.9 and 4.8 GeV are required for this program, which is well below the design injection energy of RHIC of 10.5 GeV. At those energies intra-beam scattering is strong and

a significant luminosity improvement in RHIC with the help of electron cooling is necessary.

Unlike all existing electron coolers the LEReC will use bunched electron beams for cooling. This introduces strong longitudinal space charge forces and the electron beam must not only be optimized for a low transverse emittance but also for a low energy spread in order to achieve efficient cooling.

Table 1: Electron Beam Parameters and Requirements

Energy [MeV]	1.6	2.0	2.6
Bunch Charge for Cooling [pC]	100	120	150
Accelerated bunch Charge [pC]	130	160	200
Bunches per train	30	27	24
Total beam Current [mA]	40	40	44
Normalized Emittance [μ]	< 2.5	< 2.5	< 2.5
Energy spread $\cdot 10^{-4}$	< 5	< 5	< 5

In the calculation of the beam quality we take advantage of the fact that electrons that are too hot (i.e. have a too high velocity in the co-moving frame) do not contribute to the cooling but do not harm either. For the calculation at 1.6 MeV 130 pC bunches are tracked, and

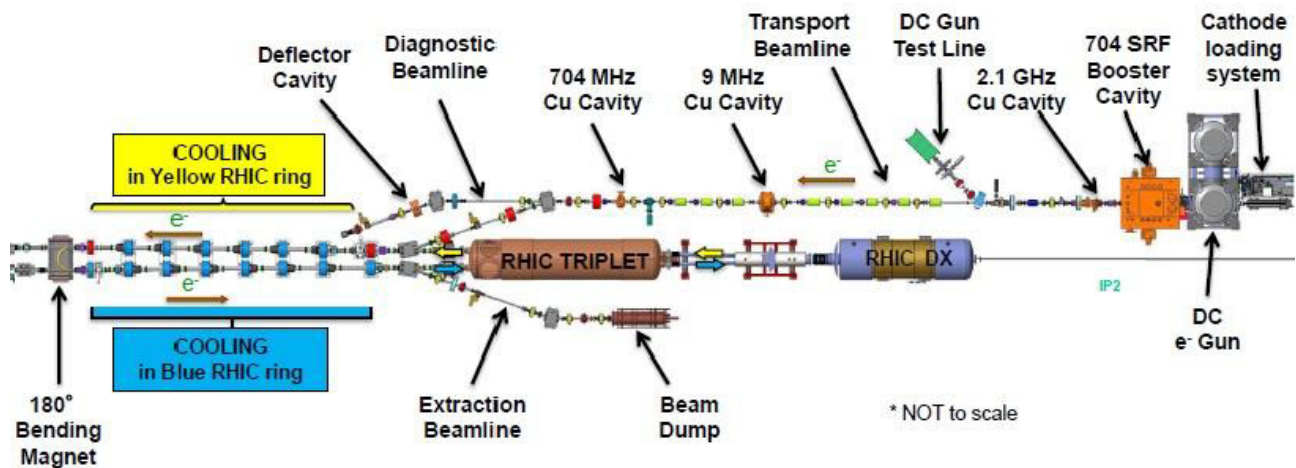


Figure 1: Layout of LEReC accelerator.

100 pC (electrons with the lowest energy deviation) are used for the evaluation of the beam parameters.

DESIGN OF THE LEREC

The layout of the LEReC is shown in Figure 1. The electron bunches will be created using a DC photocathode electron gun to be built for LEReC by Cornell University, which will operate at 400 kV. A similar gun at Cornell University has already delivered beams exceeding the required quality (300 pC, 50 mA, $\epsilon_n=1\mu$). The SRF gun used in the Brookhaven ERL will be transformed into

a cavity (then called “SRF booster”) and will provide an energy boost up to 2.25 MeV.

The SRF booster is too tall to be installed in the RHIC tunnel. It has to be placed in the 2 o’clock experimental hall. A transport beam line will bring the electrons to the “warm section” of RHIC.

The SRF booster will not only accelerate the electrons,

*Work supported by the US Department of Energy under contract No. DE-SC0012704.

#jorg@bnl.gov

MAGNETIC OPTIMIZATION OF LONG EPUS AT NSLS-II

C. Kitegi,[†] P. Cappadoro, O Chubar, T. Corwin, H. Fernandes, D. Harder, D. Hidas, M. Musardo, W. Licciardi, J. Rank, C. Rhein and T. Tanabe

Energy Sciences Directorate, Brookhaven National Laboratory, Upton, NY 11973, USA

Abstract

The Soft Inelastic X-ray scattering (SIX) and the Electron-Spectro-Microscopy (ESM) are two beamlines under construction at National Synchrotron Light Source-II (NSLS-II). The specifics of these two beamlines required the use of two long Advanced Planar Polarized Light Emitter-II (APPLE-II) undulators, as a source that provides both circularly and vertically polarized radiation. Thus, we designed 3.5 m and 2.7m long APPLE-II type undulators for SIX and ESM. The NSLS-II ID group is responsible for the magnetic optimization of these two long undulators. In this paper, we first summarize the APPLE-II magnetic and mechanical design. Then, we discuss the magnetic performance of the first APPLE-II achieved with the shimming performed at BNL.

INTRODUCTION

NSLS-II is in operation since February 2015. With 17 beamlines already in operation and at least 6 more scheduled for next year, the NSLS-II beamline development timeline is very aggressive [1]. To support this ambitious planning, the Insertion Devices procurement strategy is quite diverse. During the NSLS-II construction, all the insertion devices were ordered as turnkey devices. Now simple devices such as 3 Poles Wigglers are fully constructed, assembled and shimmed in-house. In a few cases, devices previously installed in other facilities are refurbished before being installed at NSLS-II [2]. For the construction of more complex devices, we rely on our industrial suppliers. However when the magnetic correction is a clearly identified risk, it can trigger the decision of performing the magnetic assembly and the shimming in-house.

We currently use this strategy for the delivery of two APPLE-II type undulators to the NEXT project [3]. Because of their length and their period, these devices are challenging to shim within the NSLS-II specifications. Thus, the two devices were procured as turnkey devices similarly to the other NSLS-II devices but the magnetic optimization was excluded from the scope of the contract. In this approach, the selected vendor is responsible for the delivery of the mechanical frame, the control system and sorting and mounting magnets in M3 and M5 modules. Still in order to demonstrate that the devices are properly functioning under magnetic load and the required field is achieved at minimum gap, the magnetic assemblies have to be temporarily installed on the mechanical frames for the Factory Acceptance Test. The contract for the two devices was awarded to Kyra in October 2014.

At NSLS-II we use “IDBuilder”, a genetic algorithm based computer code for the assembly and the magnetic tuning of undulators [4]. This versatile software was developed at SOLEIL and has been used for the assembly and the tuning of most of the APPLE-II type undulators and In-Vacuum Undulators installed at SOLEIL. In the next section, the magnetic and mechanical design of the 2 APPLE-II is discussed. We first received the SIX EPU, on March 1. Its large number of periods, almost 60, makes its assembling and disassembling a long and tedious process. Therefore it was agreed that for SIX only, the supplier would perform a best effort assembly using their software [5] and ship the device as is. The magnetic performance of the SIX EPU, achieved after magnetic correction was done at NSLS-II, is reviewed in this paper.

LONG EPUS DESIGN

Magnetic Design

The NSLS-II ID group provided to the supplier a magnetic reference design for the SIX EPU57 and ESM EPU105. While most of the parameters were fixed, the supplier was able to further improve the magnetic end section design, by adding an air gap between the last magnet of the end section and the first main magnet of the periodic structure. The main parameters of the two long EPUS are listed in Table 1. The name of the end section magnets uses the convention defined in [6]. The air gaps s1, s2 refer to the spaces between end section magnets as detailed in [6] and s3 is the added air space proposed by the supplier.

Table 1: Magnetic Design Main Parameters

	ESM EPU105	SIX EPU57
Period	105 mm	57
Nb of Periods	24	59
Minimum Gap	16mm	16mm
Length	2.7m	3.5m
Vert. and Hor.	1.14T	0.83T
Peak Field	0.7T	0.57T
Main Mag.	34mm x 34mm x	34mm x 34mm
Geom.	26.2mm	x 14.2mm
HW/W/HL	7.9mm/13mm	4.3mm/7.1mm
Thickness	/17mm	/8.7mm
Air gaps	5.5mm/7.6mm	5.6mm/4.1mm
s1/s2/s3	/3mm	/3.1mm
Remanence	1.25T	1.25T
Intrinsic	2.5T	2.5T
Coercive field		

* Work supported by DOE under contract DE-SC0012704

[†] ckitegi@bnl.gov

CATHODE PUCK INSERTION SYSTEM DESIGN FOR THE LEReC PHOTOEMISSION DC ELECTRON GUN

C.J. Liaw, J. Tuozzolo, T. Rao, M. Mapes, A. Steszyn, K. Hamdi, V. De Monte, L. DeSanto, J. Walsh, Brookhaven National Laboratory, Upton, New York, USA
K. Smolenski, Cornell University, Ithaca, New York, USA

Abstract

The operation of LEReC is to provide an electron cooling to improve the luminosity of the RHIC heavy ion beam at lower energies in a range of 2.5-25 GeV/nucleon. The electron beam is generated in a DC Electron Gun (DC gun) designed and built by the Cornell High Energy Synchrotron Source Group. This DC gun will operate around the clock for at least two weeks without maintenance. This paper presents the design of a reliable cathode puck insertion system, which includes a multi-pucks storage device, a transfer mechanism, a puck insertion device, a vacuum/control system, and a transport scheme.

INTRODUCTION

The operation of Low Energy RHIC Electron Cooling (LEReC) at Brookhaven National laboratory (BNL) is to provide an electron cooling to improve the luminosity of the RHIC heavy ion beam at low energies in a range of 2.5 -25 GeV/nucleon. The design goals [1] of the electron beam generator are (1) to generate a high average current (up to 50 mA) and low emittance electron beam and (2) to operate the generator around the clock, through a 6 months RHIC run, with 8 hours maintenance periods every two weeks. A DC photoemission gun (DC gun) is currently under construction at BNL, which adopted the successful DC gun technology for the new ERL X-Ray facility at Cornell [2, 3] and was developed to generate an average beam current up to 100 mA.

The high current operation of a DC gun will cause ion back-bombardment, which had been shown as the main reason for the degradation of the performance of a photocathode [3]. To obtain good operational lifetimes, in addition to keep the vacuum level in the gun as low as possible, the spent high average current photocathode will need to be cleaned and replaced regularly. In the past, the reported lifetime of a photocathode varied from 200 hours [4] (with a 1 μ A average beam current) to a couple minutes [5] (with a 10 mA average beam current). Recently the gun development result at Cornell [6] showed that the lifetime of their CsK₂Sb photocathode could generate up to 60 mA beam current with 30 hours 1/e lifetime. Development for a much higher average beam current still continues. This short lifetime necessitates the design and construction of a rapid Cathode Puck Insertion System (CPIS) for the LEReC's operation. We are building a system which can store, transfer, exchange and insert 12 cathode pucks, one at a time, into the gun reliably

without breaking the vacuum. In this paper, a CPIS design is presented, which includes a Multi-Pucks Storage Device (MPSD), a transfer mechanism, a Puck Insertion Device, a vacuum/control system, and a system transporting scheme.

CATHODE PUCK INSERTION SYSTEM DESIGN

A 3-D model of the developed CPIS design is shown in Fig. 1, which includes a mobile and a stationary portion.

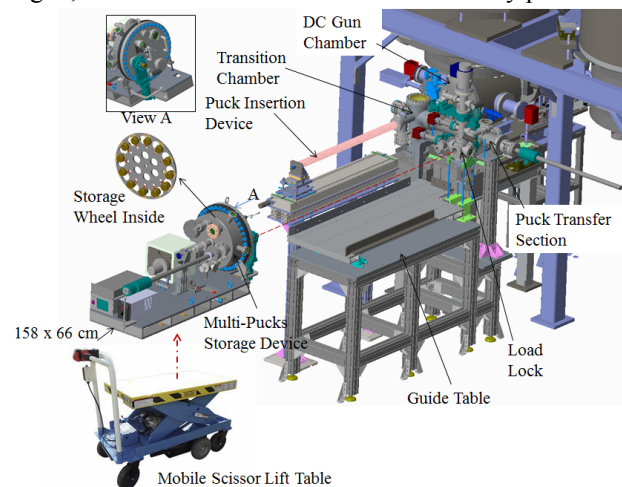


Figure. 1: Model of the cathode puck insertion system.

The former, which is used to transport the cathode pucks to the DC gun, inside the RHIC tunnel, includes a MPSD, a puck manipulating mechanism, a mobile scissor lift table, and the associated vacuum equipment. The latter, which is attached to the rear of the gun, includes a Load Lock, a Puck Transfer Section (including a puck transfer mechanism), a Puck Insertion Device, a Guide Table (for the alignment with the mobile portion), and the associated vacuum equipment. Designs of four major system components are described below:

Multi-Pucks Storage Device

The cathode puck, which will be used in the BNL's DC gun, is made of arc cast molybdenum with a size of 51 mm in diameter and 45 mm in length. (See Fig. 2.)

* This work is supported by Brookhaven Science Associates, LLC under Contract No. DE-SC0012704 with the U.S. DOE.

PERFORMANCE OF CEC POP GUN DURING COMMISSIONING*

I. Pinayev#, W. Fu, Y. Hao, M. Harvey, T. Hayes, J. Jamilkowski, Y. Jing, P. Kankiya, D. Kayran, R. Kellermann, V.N. Litvinenko, G. Mahler, M. Mapes, K. Mernick, T. Miller, G. Narayan, M. Paniccia, W. Pekrul, T. Rao, F. Severino, B. Sheehy, J. Skaritka, K. Smith, J. Tuozzolo, E. Wang, G. Wang, W. Xu, A. Zaltsman, Z. Zhao, BNL, Upton, NY 11973, USA
K. Mihara, I. Petrushina, SBU, Stony Brook, NY, USA

Abstract

The Coherent Electron Cooling Proof-of-Principle (CeC PoP) experiment [1, 2] employs a high-gradient CW photo-injector based on the superconducting RF cavity. Such guns operating at high accelerating gradients promise to revolutionize many sciences and applications. They can establish the basis for super-bright monochromatic X-ray and gamma ray sources, high luminosity hadron colliders, nuclear waste transmutation or a new generation of microchip production. In this paper we report on our operation of a superconducting RF electron gun with a record-high accelerating gradient at the CsK₂Sb photocathode (i.e. ~ 20 MV/m) generating a record-high bunch charge (above 3 nC). We give short description of the system and then detail our experimental results.

INTRODUCTION

The purpose of the coherent electron cooling experiment is to demonstrate reduction of the energy spread of a single hadron bunch circulating in the relativistic heavy ion collider (RHIC). A superconducting RF gun operating at frequency of 113 MHz serves as a source of the electron beam. The CsK₂Sb photocathode is illuminated by 532 nm laser. The designed electron beam parameters are shown in the Table 1.

Table 1: Design Parameters of the Electron Beam

Parameter	Value
Energy	2 MeV
Bunch charge	1-5 nC
Normalized emittance	< 5 mm mrad

GUN DESIGN

The CeC PoP gun has quarter-wave structure and its design is shown in the Fig. 1. The gun cavity is placed inside cryostat with thermal and magnetic shields. The cathode stalk is inserted inside the cone and is kept at room temperature as well as CsK₂Sb cathode. Such design allows preservation of quantum efficiency of the photocathode. The stalk itself serves as a cavity field pick-up.

The hollow fundamental power coupler (FPC) is insert-

ed from the flat side of the cavity and let the generated beam go outside. 2-kW solid-state amplifier provides the RF power. The FPC is surrounded by a gun solenoid, which is the first focusing element.

Two manual tuners are used for coarse tuning of the cavity while the fine frequency change is performed with help of the FPC, which is placed on a translation stage.

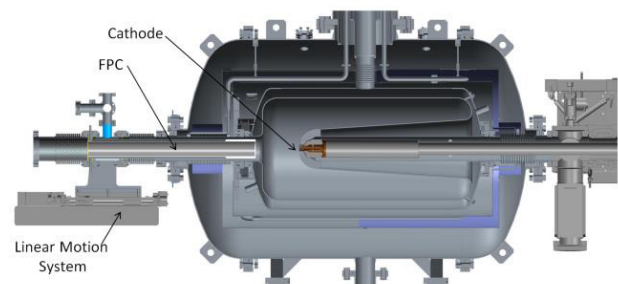


Figure 1: Layout of the superconducting gun.

The fundamental power coupler is followed by a laser cross which serves for launching of the drive laser beam onto the cathode.

EXPERIMENTAL SET-UP

The tests were performed with fully installed equipment and the low energy beam line components are shown in Fig. 2. The main systems components are:

- cathode manipulation system with “garage”, which serves for storage and insertion of the photocathodes.
- the gun itself.
- six solenoids for the beam focusing.
- two copper 500 MHz cavities for energy chirp.
- 704 MHz accelerator cavity.
- dipoles and quadrupoles in the high energy part.
- beam diagnostics.
- drive laser.

The brief description of the systems is below.

Drive Laser

The drive laser is built by NuPhotons. It generates up to 0.5 μ J pulse at 532 nm wavelength. The pulse duration is variable from 100 ps to 1 ns and maximal repetition rate is 78 kHz.

* Work supported by U.S. Department of Energy under contract number DE-SC0012704.
#pinayev@nsl.gov

COMMISSIONING OF CeC PoP ACCELERATOR*

I. Pinayev#, Z. Altinbas, J.C. Brutus, A. Curcio, A. DiLieto, C. Folz, W. Fu, D. Gassner, Y. Hao, M. Harvey, T. Hayes, R. Hulsart, J. Jamilkowski, Y. Jing, P. Kankiya, D. Kayran, R. Kellermann, V.N. Litvinenko, G. Mahler, M. Mapes, K. Mernick, R. Michnoff, K. Mihara, T. Miller, G. Narayan, P. Orfin, M. Paniccia, D. Phillips, T. Rao, F. Severino, B. Sheehy, J. Skaritka, L. Smart, K. Smith, V. Soria, Z. Sorrell, R. Than, J. Tuozzolo, E. Wang, G. Wang, B. Xiao, W. Xu, A. Zaltsman, Z. Zhao
BNL, Upton, NY 11973, USA

I. Petrushina, SBU, Stony Brook, NY 11974, USA

Abstract

Coherent electron cooling is new cooling technique to be tested at BNL. Presently we are in the commissioning stage of the accelerator system. In this paper we present status of various systems and achieved beam parameters as well as operational experience. Near term future plans are also discussed.

INTRODUCTION

The coherent electron cooling experiment is expected to demonstrate cooling of a single hadron bunch circulating in the relativistic heavy ion collider (RHIC) [1]. The system layout is shown in Fig. 2. A superconducting RF gun operating at 113 MHz frequency generates the electron beam. 500-MHz normal conducting cavities provide energy chirp for ballistic compression of the beam. 704 MHz superconducting cavity will accelerate beam to the final energy. The electron beam merges with the hadron beam and after cooling process is steered to a dump. The FEL-like structure enhances the electron-hadron interaction. The electron beam parameters are shown in the Table 1.

Table 1: Parameters of the Electron Beam

Parameter	Value
Energy	22 MeV
Bunch charge	1-5 nC
Normalized emittance	< 5 mm mrad
Energy spread	< 10^{-3}

TEST OF THE EQUIPMENT IN THE COMMON SECTION

One of the first tasks was to measure the effect of the CeC PoP equipment installed in the common section on the hadron beams circulating in RHIC. The motivation was verify ability to commission systems in the background mode without substantial disturbance to RHIC operations.

Eight quadrupoles placed in the common section were energized to the extremes and tunes and orbit were monitored. The results of the experiment are shown in the

* Work supported by U.S. Department of Energy under contract number DE-SC0012704.
#pinayev@nnl.gov

Fig. 1. The tune change at injection energy from an individual quadrupole was 0.005. This requires that currents in the quadrupoles were changed simultaneously and then influence of focusing and defocusing quadrupoles will compensate each other.

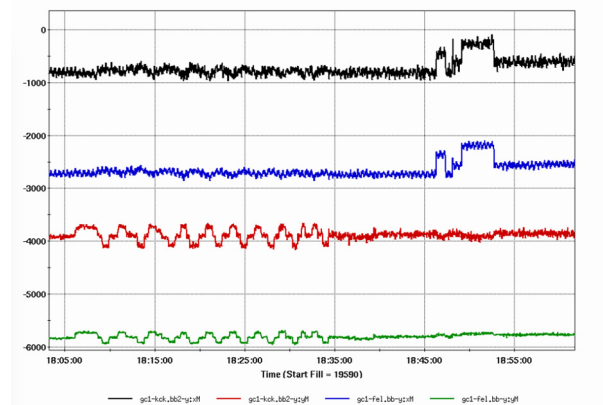


Figure 1: Effect of the CeC quadrupoles and dipoles on RHIC beam. The measurements were performed at injection energy where two hadron beams are separated vertically and beam motion is more prominent.

We also checked the influence of the dipoles used for merging electron and hadron beams (the rigidity of which differs substantially). We have installed two compensating dipole that should limit the orbit disturbance to the interaction region. The measurements confirmed the utilized approach but we also observed change of the tunes due to the fringe fields. The change value was found tolerable for operations.

GUN COMMISSIONING

The CeC PoP gun has quarter-wave structure and operates at 113 MHz. It has manual tuners for coarse set of the resonant frequency, while fine-tuning is performed by a fundamental power coupler (FPC).

Gun commissioning started with conditioning of the FPC for multipacting [2]. Then we performed helium condition of the cavity suppress dark current an increase cavity voltage. At the end we were able operate at 1.25 MW in CW mode and 1.7 MV in the pulsed mode.

Gun conditioning was done with molybdenum puck identical to the cathode but without photoemissive coating. Upon completion of the conditioning we inserted photocathode and scanned cavity phase [3].

MAGNETIC SHIELDING OF LEReC COOLING SECTION*

S. Seletskiy[†], A. Fedotov, D. Gassner, D. Kayran, G. Mahler, W. Meng
BNL, Upton, USA

Abstract

The transverse angle of the electron beam trajectory in the low energy RHIC Electron Cooling (LEReC) accelerator cooling section (CS) must be much smaller than 100 urad. This requirement sets 2.3 mG limit on the ambient transverse magnetic field. The maximum ambient field in the RHIC tunnel along the cooling section was measured to be 0.52 G. In this paper we discuss the design of the proposed LEReC CS magnetic shielding, which is capable of providing required attenuation.

REQUIREMENTS TO LEReC CS SHIELDING

The LEReC accelerator [1, 2] consists of 400 keV photo-gun followed by the SRF Booster accelerating beam to 1.6-2.4 MeV, the transport beamline, the merger that brings the beam to the two cooling sections (in the Yellow and in the Blue RHIC rings), the two 20 m long CSs separated by the 180° bending magnet and the extraction to the beam dump. The LEReC also includes two dedicated diagnostic beamlines: the DC gun test line and the RF diagnostic beamline.

The LEReC layout is schematically shown in Fig. 1.

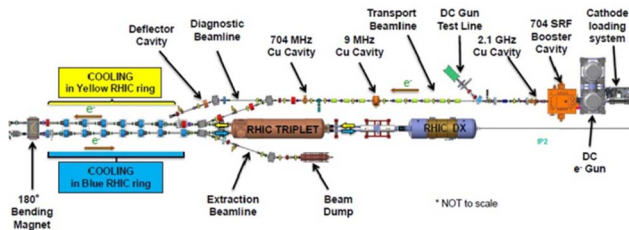


Figure1: LEReC layout.

Each CS includes 6 solenoids separated by drifts. There is a bellow, a beam position monitor (BPM) and a flange located downstream of each solenoid.

The transverse angle of the electron beam trajectory in the LEReC CS must be much smaller than $\theta_{max} = 100$ urad. Since the smallest e-beam energy is going to be 1.6 MeV ($B\rho = 68.3$ G·m), the ambient transverse magnetic field must be suppressed to:

$$B_{\perp} \ll \frac{B\rho\theta_{max}}{L} = 2.3 \text{ mG} \quad (1)$$

where $L=3$ m is the solenoid-to-solenoid distance in the cooling section.

The maximum ambient field in the RHIC tunnel along the cooling section was measured to be 0.52 G [3]. Assuming that 1 mG residual transverse field is low enough we find the required attenuation factor S to be 520.

From Fermilab Electron Cooler experience [4], due to mechanical joints of the shields, actual attenuation of

* Work supported by the US Department of Energy under contract No. DE-SC0012704

[†] seletskiy@bnl.gov

magnetic shielding can be almost two times smaller than the designed one. Therefore, we suggest adding a safety factor of two to our model making design $S=1040$.

COMPARING ANALYTIC FORMULAS TO 3D SIMULATIONS

The systematic studies of shielding of the magnetic fields with cylindrical shells of high permeability material [5] were summarized in the form of simple analytic formulas [6, 7].

The attenuation factor of the long cylinder with diameter D , thickness d and magnetic permeability μ is:

$$S = 1 + \mu \frac{d}{D} \quad (2)$$

For two cylindrical layers with diameters D_1 and D_2 and with respective attenuations S_1 and S_2 :

$$S = S_1 S_2 \left(1 - \left(\frac{D_1}{D_2} \right)^2 \right) + S_1 + S_2 + 1 \quad (3)$$

The general formula for N layers is:

$$S = 1 + \sum_{n=1}^N S_n + S_N \prod_{n=1}^{N-1} S_n \left[1 - \left(\frac{D_n}{D_{n+1}} \right)^2 \right] \quad (4)$$

Applying (2)-(4) to 4 different shielding setups and comparing obtained attenuations with results of 3D simulations we see that the formulas agree with simulations with $\sim 10\%$ precision (results of the comparison are given in Table 1). Therefore, we will use these formulas for initial optimization of the design parameters for LEReC CS shielding.

Table 1: Comparison of S found from analytic formulas (row 6) and S found from 3D simulations (row 7). The second and the third columns correspond to Opera [8] simulations of two possible LEReC setups. The fourth and the fifth columns correspond to the test and the final Fermilab setups [9].

	LEReC1	LEReC2	Fermi1	Fermi2
μ	15000	11000	15000	11000
N layers	2	2	3	3
$D_{1,2,3}$, mm	300, 400	300, 400	219, 233.4, 267.2	219, 241.2, 266.6
d , mm	1	1	1	1
S_{formula}	950	537	7538	3356
$S_{\text{simulation}}$	877	485	7400	3000

ABSOLUTE ENERGY MEASUREMENT OF THE LEReC ELECTRON BEAM *

S. Seletskiy †, M. Blaskiewicz, A. Fedotov, D. Kayran, J. Kewisch, T. Miller, P. Thieberger
BNL, Upton, USA

Abstract

The goal of future operation of the low energy RHIC Electron Cooling (LEReC) accelerator is to cool the RHIC ion beams. To provide successful cooling, the velocities of the RHIC ion beam and the LEReC electron beam must be matched with $1E-4$ accuracy. While the energy of ions will be known with the required accuracy, the e-beam energy can have an initial offset as large as 5%. The final setting of the e-beam energy will be performed by observing either the Schottky spectrum of debunched ions co-traveling with the e-beam or the recombination signal. Yet, to start observing such signals one has to set the absolute energy of the electron beam with an accuracy better than $1E-2$, preferably better than $5E-3$. In this paper we discuss how such accuracy can be reached by utilizing the LEReC 180 degree bend as a spectrometer.

LEREC LAYOUT

The LEReC accelerator [1, 2] consists of a 400 keV photo-gun followed by the SRF Booster, which accelerates the beam to 1.6-2.4 MeV, the transport beamline, the merger that brings the beam to the two cooling sections (in the Yellow and in the Blue RHIC rings), the cooling sections separated by the 180° bending magnet and the extraction to the beam dump. The LEReC also includes two dedicated diagnostic beamlines: the DC gun test line and the RF diagnostic beamline.

The LEReC layout is schematically shown in Fig. 1.

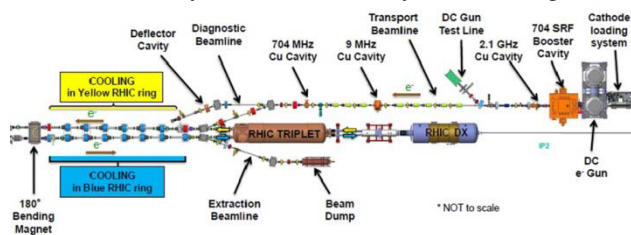


Figure 1: LEReC layout.

To set the absolute energy of the electron beam with an accuracy better than $5 \cdot 10^{-3}$ we plan to utilize the 180° bending magnet as a spectrometer.

The 180° bend setup is schematically shown in Fig. 2.

The 180° bend is located between the first and the second LEReC cooling sections. It is designed to have a bending radius $\rho_0 = 0.35$ m. The entrance to the magnet is equipped with two BPMs (one of them hybrid [3]) and its exit is equipped with one hybrid BPM. BPM-to-BPM distances are defined by precision requirements of the

* Work supported by the US Department of Energy under contract No. DE-SC0012704

† seletskiy@bnl.gov

energy regulation and were set in dedicated optical simulations.

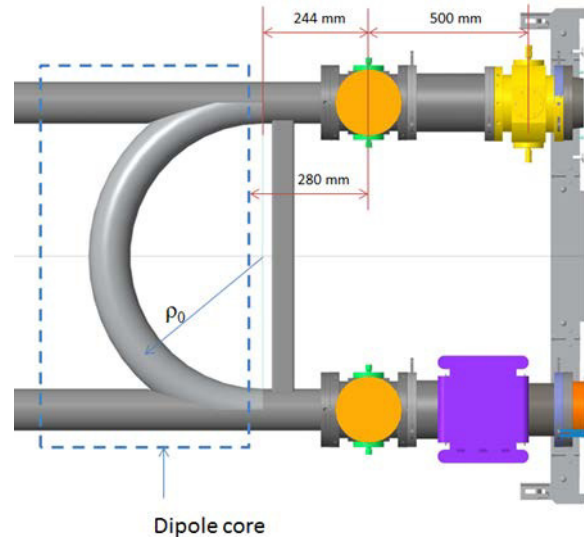


Figure 2: Schematics of 180° bend.

HARD EDGE APPROXIMATION OF THE 180° BEND

In the hard-edge approximation the horizontal e-beam displacement (x_{out}) at the exit of 180° bend is given by:

$$x_{out} = -x_{in} + 2\rho_0 - 2\rho \cos \theta_{in} \quad (1)$$

The notation used in (1) is explained in Fig. 3.

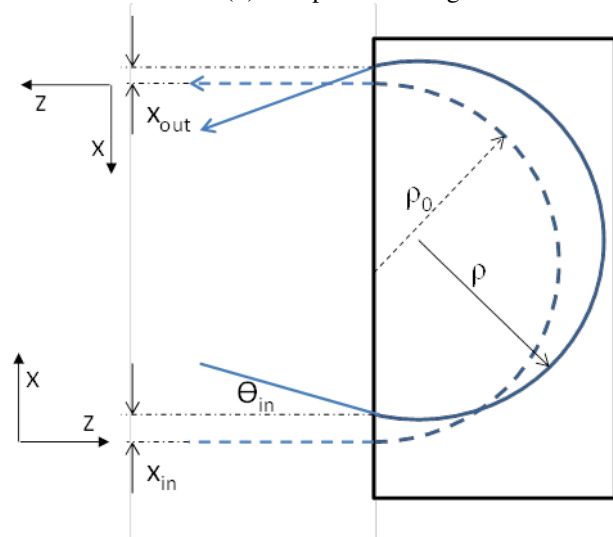


Figure 3: Beam trajectory in 180° bend.

To measure beam energy (E) in the 1.6-2.6 MeV range with the accuracy required for LEReC one must perform proper Taylor expansion of the exact expression for magnetic rigidity:

EXPERIMENTS OF LOSSLESS CROSSING - RESONANCE WITH TUNE MODULATION BY SYNCHROTRON OSCILLATIONS*

G-M. Wang[†], T. Shaftan, J. Rose, V. Smaluk, Y. Li, B. Holub
Brookhaven National Laboratory, Upton, NY

Abstract

It had become a standard practice to constrain particle's tune footprint while designing the storage ring lattice so that the tunes fit between harmful resonances that limit ring dynamic aperture (DA). However, in recent ultra-bright light source design, the nonlinearities of storage ring lattices are much enhanced as compared with the 3rd generation light source one. It is becoming more and more difficult to keep the off-momentum tune footprint confined and even more, the solution cannot be found to confine off-energy tune footprint in certain cases. The questions have been asked whether crossing of a resonance stopband from off-momentum particle will necessarily lead to particle loss. In NSLS-II, we modified the lattice working point to mimic machine tune footprint crossing half integer with beam synchrotron oscillation excitation and demonstrated that beam can cross a resonance without loss with control of stopband width and high order chromaticity.

INTRODUCTION

It had become a standard practice to constrain the particle's tune footprint while designing storage ring lattice so that the particle tunes fit between harmful resonances that limit ring dynamic aperture (DA) [1]. This approach, known as "tune confinement", puts tight limits on the magnitude of the tune shifts with amplitude and with momentum. The latter requires labor-intensive optimization of the off-momentum DA and the corresponding tune footprint for the large momentum deviations to achieve reasonable lifetime.

As nonlinearities of the modern ring lattices are much enhanced as compared with the previous generation synchrotrons, it is becoming more and more difficult to keep the off-momentum tune footprint confined [2, 3]. In certain cases when the lattice solution with the confined off-momentum tune footprint cannot be found, one may ask whether the crossing of a resonance stopband from an off-momentum particle leads to a beam loss.

Recently modern synchrotrons advanced to Multi-Bend Achromat lattices featuring small dispersion and low beta functions, and, as a result, high nonlinearity of the particle motion. In certain cases, the tune spread for on-energy beam was successfully minimized, but the off-momentum tunes swing across the major resonances. Surprisingly, the tracking result does not show particle loss. Authors of [2] explained this phenomenon by rapid transition through the stopband together with substantial tune shifts

with amplitude that help to drive particles off the resonance during the transition. Results of our studies presented in the paper indicate that this explanation is adequate.

Significance of the finding from the analysis presented in [2] advances the modern lattice design beyond the principles of the "tune confinement", while posing an important question: under which conditions does the chromatic tune footprint not need to be confined? In NSLS-II, we modified the lattice working point to mimic machine tune footprint crossing half integer with beam synchrotron oscillation excitation and demonstrated that beam can cross a resonance without loss with control of stopband width and high order chromaticity.

DYNAMICS OF THE PARTICLE CROSSING A STATIC RESONANCE STOPBAND

We will consider a storage ring model with large chromatic tune shift with momentum deviation $\delta = \Delta p/p$ up to the second order as:

$$\nu(\delta) = \nu_0 + \xi_1 \delta + \xi_2 \delta^2 + O(\delta^3), \quad (1)$$

where ξ_1 and ξ_2 are linear and 2nd order chromaticities. In the following we constrain our analysis to the 2-dimensional case of ν and δ . For our experiments we maximized the 2nd order chromaticity of the lattice, so that $\xi_{1\nu} = +1$ and $\xi_{2\nu} = +300$ (similar to [2, 3]) by changing ring sextupoles while maintaining small tune shifts with amplitude.

Next we assume that the particle energy oscillates with the maximum deviation δ_0 and this synchrotron oscillation for simplicity is taken as $\delta(t) = \delta_0 \sin(2\pi\nu_s n)$, where ν_s is the synchrotron tune and n is the number of turns around the ring. A cartoon illustrating the problem under consideration is shown in the plot of Fig. 1. As one can see, the betatron tune of a longitudinally oscillating particle crosses the resonance $\nu = \nu_R$, which is not infinitely thin in presence of quadrupole errors. The resonance is characterized by a stopband with the width $\Delta\nu_R$, which is heuristically defined as the boundary of the tune range where the peak beta-beat $\Delta\beta/\beta = \frac{\beta - \beta_0}{\beta_0}$ reaches 100% [4].

Here β_0 is the reference beta function calculated from the unperturbed lattice model, and β is the measured beta function obtained from coherent beam oscillations excited by a pulse kick and measured by beam position monitors distributed around the ring [5].

We define $\delta_R = \delta(\nu_R)$ as the value of energy deviation where the particle's tune crosses the resonance ν_R . The energy boundaries corresponding to the resonance stopband $\Delta\nu_R$ are (neglecting the contribution from ξ_1):

*This manuscript has been authored by Brookhaven Science Associates, LLC under Contract No. DE-SC0012704 with the U.S. Department of Energy.

[†] gwang@bnl.gov

NLSLS-II POST MORTEM FUNCTION DEVELOPMENT AND DATA ANALYSIS OF BEAM DUMP*

G-M. Wang[†], L. Doom, K. Ha, R. Smith, W. Cheng, J. Choi, J. Tagger, Y. Tian, T. Shaftan
Brookhaven National Laboratory, Upton, NY, USA
R. Madelon, Orleans University, France

Abstract

The National Synchrotron Light Source II (NSLS-II) is a state of the art 3 GeV third generation light source at Brookhaven National Laboratory. The storage ring was commissioned in 2014 and transitioned to routine operations in the December of the same year. At this point the facility hosts 16 operating beam lines with beam current up to 250 mA. During beamline operation, various sources (protection system or subsystem malfunction) may cause beam dump. To identify the beam trip sources and improve the operation reliability, post mortem function was developed in NSLS-II to capture the subsystems status and beam information prior and after beam dump, including RF system, power supply, BPMs and active interlock system. Most of the trip events have been identified and related source was improved. In this paper, we'll present the post mortem function development and data application to diagnose beam dump source.

INTRODUCTION

The National Synchrotron Light Source II (NSLS-II) is a new 3 GeV third generation light source at Brookhaven National Laboratory [1]. It can deliver a broad band of light with the brightness of 1022 photons/s/mm²/mrad²/0.1%BW to support 60-70 beam lines at full built-out.

The storage ring was commissioned in 2014 and began its routine operations in the December of the same year. In 2015-2016 we have been continuously installing and commissioning new insertion devices, their front-ends and beamlines. At this point the facility hosts 16 beamlines in routine operation. Over past year we have been steadily increasing beam current to 250 mA with all ID gaps closed with two SRF cavity in operation. During beam studies we accumulated beam current up to 400 mA.

High operation reliability is always desirable. So it is important to understand each beam trip reason, fix the potential problems and avoid unnecessary beam trip. In the following section, we'll present the beam protection system, post mortem function development and post mortem data applications in NSLS-II.

ACTIVE INTERLOCK SYSTEM

The active interlock system (AIS) [2] is one of the major machine protection systems from the synchrotron radiation. The main purpose of AIS is to protect the

*This manuscript has been authored by Brookhaven Science Associates, LLC under Contract No. DE-SC0012704 with the U.S. Department of Energy

[†] gwang@bnl.gov

insertion device (ID), frontend and storage ring vacuum chamber due to mis-steered synchrotron radiations from IDs (ID-AI) and Dipole magnets (BM-AI).

The required ID-AI system response time is within 1 ms, because through 1 ms duration damping wiggler (DW) aluminum vacuum chamber will increase the surface temperature to 100 C. System engaged beam current threshold is 2 mA. The safe beam envelope defined for device protection are beam position offset within 0.5 mm, and beam angle offset within 0.25 mrad at insertion device center both plane.

The required BM-AI system response time is within 10 ms. System engaged beam current threshold is 50 mA. The safe beam envelope is beam position offset along the ring within 5 mm in x plane and within 3 mm in y plane.

AI system trip source includes beam out of ID-AI or BM-AI envelope, external device failures or global communication glitch detected. It also includes fail-safe function to protect the system from unexpected faults condition, such as AIS Timing trigger error, Cell controller timing error, BPM fault condition (PLL unlock and ADC saturation, ID bpm, and BM bpm), PLC heartbeat status fault (1 Hz), DCCT system fault, DCCT PLC heartbeat status (5 Hz). AI system keeps monitoring these input signals and will dump the beam by turning off RF system under any abnormal condition.

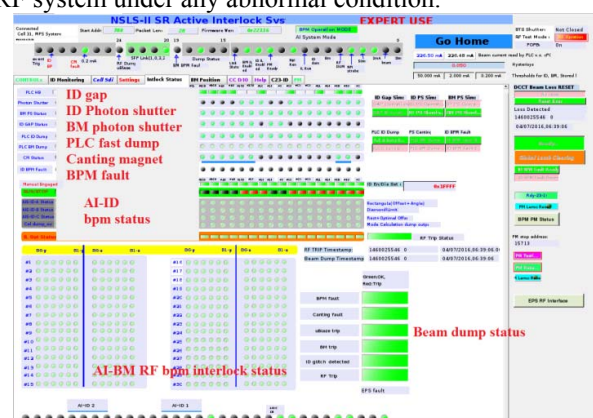


Figure 1: AI system expert page for monitoring all of the AI system status monitoring.

AIS also latched its input signal status during beam dump and displayed them for operation purpose, as shown in Fig. 1. These top level status signals are very useful and convenient to direct the beam dump source, such as ID trip or canting magnet trip or BPMs out of envelope. However, AIS detected dump source can be the leading reason or can be the result of other system fail. One

K₂CsSb PHOTOCATHODE PERFORMANCE IN QWR SRF GUN*

E. Wang#, T. Rao, Y. Hao, Y. Jing, V. Litvinenko, I. Pinayev, J. Skaritka, G. Wang, T. Xin
Brookhaven National Laboratory, Upton, NY, USA

Abstract

In 2016 run of Coherent Electron Cooling (CeC), we have successfully tested the performance of a number of K₂CsSb cathodes. These cathodes with QE of 6%-10% were fabricated in Instrumentation Division, a few miles away, transported to RHIC tunnel under UHV conditions, attached to the CeC gun, kept in storage and inserted in the gun as needed. A maximum bunch charge of 4.6 nC was generated in the gun when the QE was 1.8%. With careful conditioning at increasing accelerating fields, it was possible to maintain the QE of several cathodes for more than a week. For the cathodes that experienced degradation, the primary cause was multipacting when the power into the gun reached certain level. For subsequent measurement, the substrate was masked to coat only the central 9 mm of substrate. By optimizing the procedure for boosting the power to the gun and covering all viewports to minimize dark current, we were able to overcome multipacting. In this paper, we discuss the cathode preparation, transfer to the gun and operational experience with the cathode in 112 MHz gun.

INTRODUCTION

In order to achieve high luminosity, eRHIC will need an electron cooling to reduce the ion beam emittance which is increased by intra-beam scattering. Currently, BNL is carrying on a Proof of Principle experiment to demonstrate an advance cooling scheme called coherence electron cooling (CeC) which needs high charge bunch 5 nC with a repetition frequency of 78 kHz. A 112 MHz superconducting quarter-wave resonator (QWR) with high quantum efficiency photocathode will generate this beam to cool one of the ion bunches in RHIC. Figure 1 shows the 112 MHz gun layout.

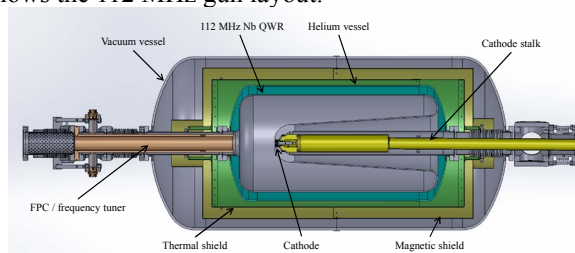


Figure 1: Plane view layout of the 112 MHz QWR gun.

In 112 MHz gun, we chose K₂CsSb as the photocathode material because of its high QE at green light and relatively long lifetime at 10⁻¹⁰ torr vacuum. With QE above 1%, the cathode can deliver more than 3 nC bunch charge. Typically, the fresh K₂CsSb cathode QE is in range of 8% ~12%.

* Work supported by Brookhaven Science Associates, LLC under Contract No. DE-SC0012704 with the U.S. Department of Energy.

wange@bnl.gov

The most challenging step in this experiment is compatibility of cathode and superconducting RF gun. Very strong multipacting was observed in 112 MHz gun after the insertion of cathodes. It was also observed in other SRF gun. By optimizing the power boost procedure, we were able to run the gun in CW mode in gun voltage around 1.2 MV.

CATHODE PREPARATION AND TRANSFER

Cathode Preparation

The cathodes are deposited at a deposition chamber described in [1] and shown in Fig. 2. The procedure of the cathode preparation is presented in [1].

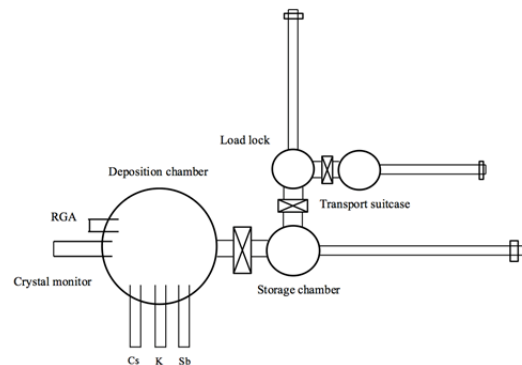


Figure 2: A schematic of the Instrumentation Division's K₂CsSb photocathode deposition system.

In 2015 run, the entire Molybdenum substrate pucks were exposed to alkali vapor. The alkali-coated cathode surface has relatively low work function and has very high secondary emission yield. This created favorable conditions for strong multipacting around cathode. The hard multipacting barrier only existed when the multi-alkali cathode was inserted into the gun. We developed a technique using excimer laser to remove the active cathode material from the puck's edge. However, the initial QE of 4.2% significantly degraded, to less than 0.0001%, due to outgassing during the laser ablation process. The pressure during cleaning process was in the 10⁻⁸ to 10⁻⁷ torr range, typically. We heated up the cathode to 80°C for two hours and rejuvenated it to a stable QE of 0.8%. This cathode maintained almost same QE in the gun and generated high charge beam in 112 MHz gun with CW operation.

The laser ablation takes time and also damages cathode. The rejuvenation process did work, but did not recover to the original QE. Simulations indicated that there are two multipacting sensitive zones, one in a narrow gap between the side surface of the puck and the inside surface of cathode stalk, another one between cathode edge and gun

DESIGN AND SIMULATION OF EMITTANCE MEASUREMENT WITH MULTI-SLIT FOR LEReC *

C. Liu[†], A. Fedotov, J. Kewisch, M. Minty, Brookhaven National Laboratory, Upton, NY, U.S.A.

Abstract

To improve the luminosity of beam energy scan of low energy Au-Au collision, a electron machine is under construction to cool ion beams in both RHIC rings with pulsed electron beam. Over the course of the project, a multi-slit device is needed to characterize the transverse beam emittance of three energies, 0.4, 1.6 and 2.6 MeV. This report shows the optimization and compromise of the design, which include the slit width, slit spacing, and drift space from the multi-slit to the downstream profile monitor.

INTRODUCTION

Mapping the QCD phase diagram is one of the fundamental goals of heavy-ion collision experiments [1]. In the past, Au-Au collision with various energies (Beam Energy Scan/BES-I) has been provided for the experiments in RHIC [2]. Driven by the physics and BES-I results, future physics program with higher luminosity goals called BES-II is proposed for Au-Au center-of-mass energy below 20 GeV [3]. The role of electron cooling [4] for the lowest energy points is to counteract intrabeam scattering (IBS): this prevents transverse emittance growth and intensity loss from the RF bucket due to the longitudinal IBS.

An electron accelerator (Fig. 1) is being constructed to provide Low Energy RHIC electron Cooling (LEReC) and will provide a beam to cool both the blue and yellow RHIC ion beams by co-propagating a 10~50 mA electron beam of 1.6~2.6 MeV [5] with the ion beams. The electron accelerator consists a DC gun which provides 0.4 MeV beam and a Booster cavity which provides an energy gain of either ~1.2 or ~2.2 MeV.

Over the course of the project, beam emittance measurement is required for three beam energies, 0.4, 1.6 and 2.6 MeV in the injection line [6]. Due to space and budget limitation, it's desirable to use a single device for all the measurements. Since the beam is space charge dominated, the multi-slit and single slit options are considered to avoid the complication of space charge force.

EMITTANCE MEASUREMENT OVERVIEW

The principle of emittance measurement with multi-slit was presented in [7]. The electron beam was intercepted by the multi-slit flag so that emittance dominated beam-lets pass through and project onto the downstream profile monitor (PM). Based on the width of the individual stripes on

the profile monitor and some geometrical information, the beam emittance at the flag can be reconstructed.

With a single slit device, one can either move the slit across the beam or move the beam relative to the slit and record multiple snap shots of the projected stripe on the downstream monitor. The advantage of a single slit device is that the step size (equivalent to the slit spacing in multi-slit device) is adjustable, and there is no concern of stripes overlapping with each other on the profile monitor like for the multi-slit case. However, it requires additional hardware to move the beam or the flag with good precision.

SIMULATION

To optimize a multi-slit design common for all the three energies, we started to optimize the individual design for each energy. In the following simulations, the beam distributions were from the output of PAMELA simulation with space charge.

There are some general design considerations for optimization of the multi-slit device. The thickness of the flag should be large enough to stop most of the particles. The slit width should be small, negligible compared to the size of the stripes on profile monitor. The ratio of slit width to thickness should not be smaller than the divergence of the beam. The drift space should be enough for beam-lets to diverge, not too much that the stripes on the profile monitor overlap with each other. The downstream profile monitor should be large enough for diverged beam-lets.

The projection of the stripes on the profile monitor and its multiple Gaussian peak fit for energy of 0.4 MeV are shown in Fig 2. Only 7 main beam stripes were projected in the horizontal plane. The slit width was 0.15 mm, slit spacing was 2.5 mm and the drift space was 2 m. A 2 inch size profile monitor is required at this energy to accommodate the entire beam.

The projection of the stripes on the profile monitor and its multiple Gaussian peak fit for energy of 1.6 MeV are shown in Fig. 3. The slit width was 0.15 mm, slit spacing was 1.2 mm and the drift space was 1 m. The particles with large horizontal displacement have larger uncorrelated beam divergence due to space charge force. The drift length was chosen so that the visible stripes are not overlapping with each other. The stripes even further away from the center will overlap.

The projection of the stripes on the profile monitor and its multiple Gaussian peak fit for energy of 2.6 MeV are shown in Fig. 4. The slit width was 0.15 mm, slit spacing was 2 mm and the drift space was 2 m. With higher energy, the beam divergence is smaller so that with limited drift length

* The work was performed under Contract No. DE-SC0012704 with the U.S. Department of Energy.

[†] cliu1@bnl.gov

IMPEDANCE SIMULATION FOR LEREC BOOSTER CAVITY TRANSFORMED FROM ERL GUN CAVITY*

C. Liu[#], BNL, Upton, NY 11733, U.S.A.

Abstract

Wake impedance induced energy spread is a concern for the low energy cooling electron beam. The impedance simulation of the booster cavity for the LEReC projection is presented in this report. The simulation is done for both non-relativistic and ultra-relativistic cases. The space charge impedance in the first case is discussed. For impedance budget consideration of the electron machine, only simulation of the geometrical impedance in the latter case is necessary since space charge is considered separately.

INTRODUCTION

Low energy RHIC electron cooling (LEReC) is designed to cool low energy ion beams at RHIC, which is crucial for beam energy scan for searching the critical point on the QCD phase diagram [1]. The electron beam energy is 1.6 MeV for the first phase, and will be increased to 2.6 MeV on the second phase to match the velocity of higher energy ions. The electron beam will be mostly accelerated by the booster cavity on the first phase. The ERL gun cavity will be modified to be used as the booster cavity. The ERL gun cavity is shown in Fig. 1.

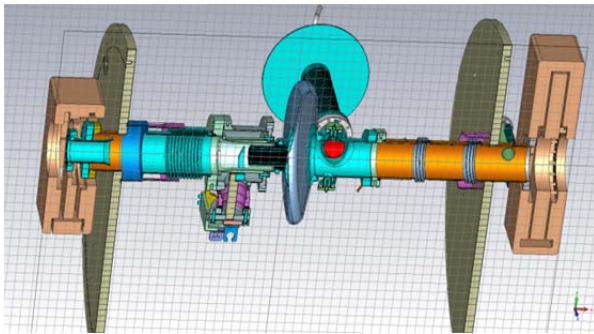


Figure 1: Three dimensional drawing of the ERL gun cavity.

For effective cooling, the allowable energy spread of the electron beam is very small (relative RMS energy spread $\sim 5E-4$). Therefore, the budget of wake impedance introduced by various components in the electron machine is very tight. The sum energy spread due to resistive wall and geometrical impedance should be no greater than space charge induced energy spread [2]. A new insert was designed on the cathode side of the ERL gun in the effort of reducing geometrical impedance. The simulation of impedance of this booster cavity with the insert (Fig. 2) will be presented in the following.

*The work was performed under Contract No. DE-SC0012704 with the U.S. Department of Energy.

[#]cliu1@bnl.gov

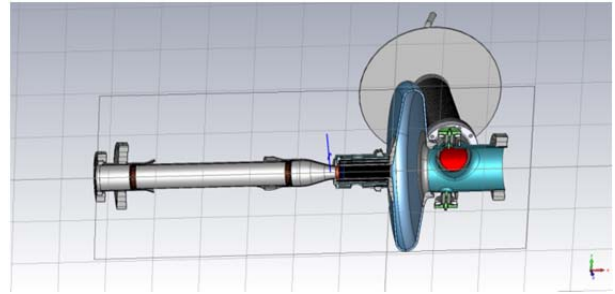


Figure 2: Three dimensional view of the booster cavity design with new insert.

SIMULATION SETUP

Electron beam parameters for the simulation are listed here. Beam energy is 400 keV, so that Lorentz $\beta=0.8279$. Bunch charge is 100 pC. Bunch rms length is 10 mm. Repetition rate of micro bunches and the fundamental frequency of the cavity is 704 MHz. Bunch spacing is 0.43 m. Repetition rate of bunch train is ~ 9 MHz. The following results are for single bunch simulation.

All cavity material was assigned to be PEC (perfect electrical conducting). All other materials were assigned to be “normal”, which essentially means vacuum. Integration method is “Direct”, because others are not applicable for non-relativistic beams [3]. The boundary was “open” at both end of the structure. The structure is symmetric with respect to the horizontal and vertical plane.

SIMULATION RESULTS

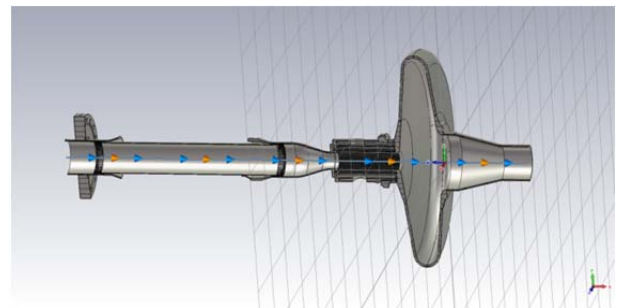


Figure 3: Simplified booster cavity structure in CST simulation.

The impedance simulation was carried out for a simplified structure, which only keeps the essential parts for electromagnetic fields. The structure in CST simulation is shown in Fig. 3. On the right hand side, a

MECHANICAL STRAIGHTENING OF THE 3-m ACCELERATING STRUCTURES AT THE ADVANCED PHOTON SOURCE

D. Bromberek, W. G. Jansma, T. Smith, G. Waldschmidt, Advanced Photon Source Argonne National Laboratory, Argonne, USA

Abstract

A project is underway at the Advanced Photon Source to mechanically straighten the thirteen 3-meter accelerating structures in the Linear Accelerator (Linac) in order to minimize the transverse wake-field, and improve charge transport efficiency and beam quality. Flexure supports allow positioning of the structures in the X and Y directions. Mechanical design of the flexure support system, straightening techniques, mechanical measurement methods, and mechanical and RF results will be discussed.

flex support and halo to move the structure in the desired X, Y and XY directions.

INTRODUCTION

The Linac of the Advanced Photon Source at Argonne National Laboratory is composed of thirteen S-Band accelerating structures operating at 2856MHz. The thirteen accelerating structures are in the process of being mechanically straightened off-line to reduce transverse wake-field and improve beam performance with thermionic and photocathode guns. Using a modified SLAC design [1], flexure (flex) supports are used on a strong-back to mechanically straighten the structures with a goal of within $\pm 200 \mu\text{m}$ in the X (horizontal), and Y (vertical) directions. Prior to straightening, the deformation of the operational structures was greater than 1 mm in X, and greater than 6 mm in Y. It is believed that rigid water connections to the structures contributed to the gross deformation in the Y direction. The location of quadrupole (quad) magnets vary for each structure which requires that the flex supports are locatable on the strong-back to accommodate different configurations. The magnets can also hinder achieving the $\pm 200 \mu\text{m}$ tolerance throughout the entire 3-m length due to restricted access for straightening hardware. An operational structure prior to straightening and without the new support system is shown in Fig. 1.



Figure 1: Original Linac structure located in the APS with quad magnets and rigid water lines.

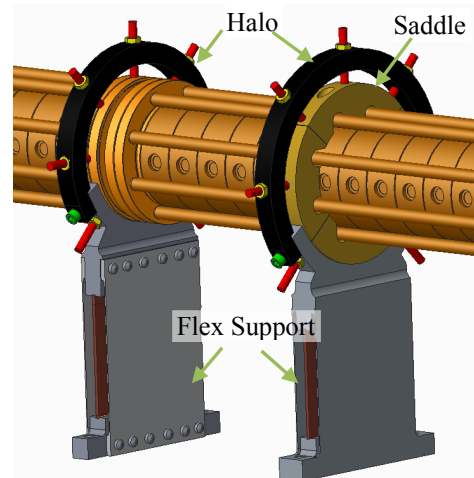


Figure 2: Section of Linac structure with supports: left - SLAC riveted assembly, right - ANL EDM assembly.

FLEXURE SUPPORT DESIGN

The flex supports are a modified SLAC design with locatable pedestals, halos, and cell saddles, which can be mounted at a desired location on the strong-back, depending on the deformation profile of the structure and the position of quad magnets at the chosen installation location. The SLAC flex support consists primarily of a 5-piece riveted assembly while the ANL version is a 2-piece electrical discharge machined (EDM) assembly, as shown in Fig. 2. In both designs, thin wall side plates allow movement in the Z direction while a phosphor bronze center plate strives to maintain the Y elevation, and minimize X tilt and Z twist. Setscrews are provided on the

STRAIGHTENING TECHNIQUES AND MECHANICAL MEASUREMENT METHOD

X and Y base-line profiles are established using a portable articulating arm coordinate measuring machine (CMM) [2]. Eight points are taken around the circumference of the cells and 2D and 3D axes are created using the CMM measurement software. A base-line 2D XY profile for structure 008 is shown in Fig. 3. A typical 3D profile for a structure is shown in Fig. 4. With the base-line profiles established, the support pedestals are mounted to a strong-back. Support pedestal positions are determined

RESULTS OF THE 2015 HELIUM PROCESSING OF CEBAF CRYOMODULES*

M. Drury[†], F. Humphry Jr., L. King, M. McCaughan, A. Solopova
Thomas Jefferson National Accelerator Facility, Newport News, VA 23606

Abstract

Many conference series have adopted the same The CEBAF accelerator at Jefferson Lab consists of an injector and two linacs connected by arcs. Each linac contains 25 cryomodules that are designed to deliver an integrated energy of 2.2 GeV per pass to an electron beam in order to meet 12 GeV energy requirements. Helium processing is a processing technique that is used to reduce field emission (FE) in SRF cavities. Helium processing of the 50 installed linac cryomodules was seen as necessary to support 12 GeV energy requirements. This paper will describe the processing procedure and summarize the results of this effort.

BACKGROUND

In the summer of 2015, Jefferson Lab undertook a program to helium process all of the cavities in cryomodules that were installed in the CEBAF linacs. This work was deemed necessary to establish a robust SRF energy gain in support of high availability 12 GeV operations [1].

Reducing field emission from the SRF cavities would have several benefits. First, in the case of the original CEBAF cryomodules (denoted as C20's), a reduction in field emission would lead to a reduction in the rate of periodic window arcing. This is a phenomenon associated with the fundamental power coupler design used in these cryomodules. Field emission in the cavity causes electrostatic charging of the cold RF window which, in turn, causes periodic arcing. The rate of arcing is directly related to the magnitude of field emission [2]. Thus, reducing fields emission levels and increasing the field emission onset gradient would allow higher operating gradients in these older cryomodules. In 2015, there were 30 of the original C20 cryomodules installed in the linacs and injector. In addition, there were 11 refurbished C20 cryomodules (C50's) and 11 new high gradient cryomodules (C100's) installed during the 12 GeV upgrade.

Second, a reduction in field emission would, in many cases, result in a reduction in the dynamic heat load for a given cavity. This could, in some cases, lead to higher operating gradients for the C50 and C100 cavities. Finally, the radiation levels around the C100 cryomodules are high enough to cause damage to materials such as cable insulation and to electronics that are located near the C100 cryomodules. High radiation levels also appear to be responsible for deteriorating beamline vacuums in the C100 zones. Reducing field emission would help to mitigate these problems and allow the C100 cryomodules to operate at higher gradients.

* Work supported by US DOE Contract No. DE-AC05-06OR23177
drury@jlab.org

SET UP AND EQUIPMENT

The program was allotted a 4-month time span during the summer maintenance shutdown in 2015. Based on the amount of time available, it was decided to set up four processing stations; two in each of the linacs that comprise the CEBAF accelerator. Each processing station consists of a pumping cart located in the tunnel adjacent to the cryomodule and a control and data acquisition station upstairs in the service building.

Pumping Carts

The pumping carts contain all of the hardware necessary to safely introduce and monitor gaseous helium into the beamline of cold cryomodule (See Figure 1). Using these carts, 99.9999% pure helium is introduced into the cryomodule beamline vacuum through a 0.003 μm filter and a variable leak metering valve. A residual gas analyzer (RGA) is used to measure the partial pressure of helium in the beamline. The RGA is backed up by two full range vacuum gauges. A turbo pump is included for pumping out helium at the end of the processing phase.

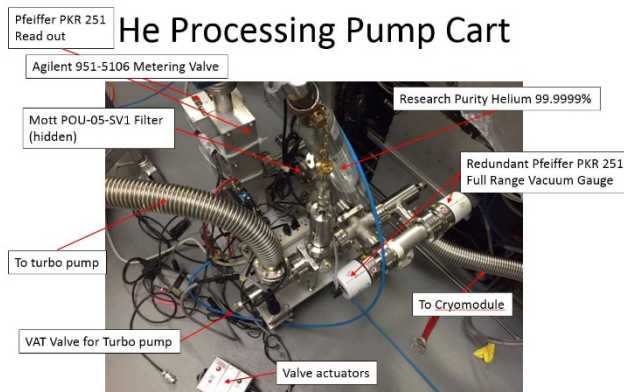


Figure 1: Pump Cart.

Control Stations

Each control station upstairs includes a PC running Windows and Labview. Each PC is able to communicate with a Field Control Chassis (FCC), power meters, a frequency counter, and the accelerator control system (EPICS). Radiation monitoring is accomplished using the DecaRad system. The DecaRad is a ten channel data acquisition system that connects to ten channels of Geiger-Mueller (GM) tubes and monitored via EPICS. The set of ten GM tubes are positioned around a cryomodule according to the diagram in Figure 2.

The top layout is used for the C100 cryomodule design. The bottom layout is for original design C20 and C50 cryomodules.

MAX IV AND SOLARIS 1.5 GeV STORAGE RINGS MAGNET BLOCK PRODUCTION SERIES MEASUREMENT RESULTS

M. Johansson*, MAX IV Laboratory, Lund, Sweden
 K. Karas, Solaris NSRC, Krakow, Poland
 R. Nietubyc, NCBJ, Otwock, Poland

Abstract

The magnet design of the MAX IV and Solaris 1.5 GeV storage rings replaces the conventional support girder + discrete magnets scheme of previous third-generation synchrotron radiation light sources with an integrated design having several consecutive magnet elements precision-machined out of a common solid iron block, with mechanical tolerances of ± 0.02 mm over the 4.5 m block length. The production series of 12+12 integrated magnet block units, which was totally outsourced to industry, was completed in the spring of 2015, with mechanical and magnetic quality assurance conforming to specifications. This article presents mechanical and magnetic field measurement results of the full production series.

INTRODUCTION

The MAX IV Laboratory, located in Lund, Sweden, is a synchrotron radiation facility, consisting of two storage rings, 3 GeV and 1.5 GeV, and a full energy injector linac. [1]. The Solaris National Synchrotron Radiation Centre, located in Krakow, Poland, consists of a 1.5 GeV storage ring identical to the MAX IV 1.5 GeV ring, and a 600 MeV injector linac [2]. These 1.5 GeV rings have a double bend achromat (DBA) lattice, consisting of 12 achromats, with a circumference of 96 m.

Each DBA is realized as one integrated “magnet block” (example photo shown in Fig. 1) conceptually identical to the MAX IV 3 GeV ring magnets [3], so that the ring consists of 12 such units, containing a total of 156 magnet elements.¹ The different magnet element types that are present in the magnet blocks are listed in Table 1. Detailed magnet design was made using the Opera-3d FEM code [4], with a model of the full magnet block being simulated (see Fig. 2). The magnet design was iterated against the lattice design [5], with the final magnet design that went into production being the 4th iteration [6].

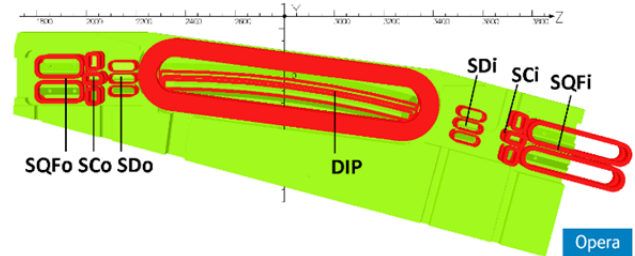


Figure 2: Opera-3d model “MAXIV1,5GeVmagnetblock, MJ130711-36.opc”, with magnet element names indicated.

Table 1: List of 1.5 GeV Ring Magnet Elements, with Nominal Field Strengths from Design Lattice [5].

magnet	No [pcs]	l [m]	r _{pole} [mm]	B [T]	B' [T/m]	B''/2 [T/m ²]
DIP ²	24	1.19	14	-1.310	6.749	
	pfcs				$\pm 5\%$	
SQFo	24	0.2	17.5		-28.71	-219.5
SQFi	12	0.4	23.5		-25.03	-142.4
SDo	24	0.1	25.5			510.1
SDi	24	0.1	25.5			370.7
SCo	24	0.05	18.6			32.0
	corr x			± 0.25 mrad		
	corr y			± 0.25 mrad		
	skew q				-3.6	
SCi	24	0.07	24.5			67.2
	corr x			± 0.25 mrad		
	corr y			± 0.25 mrad		
	skew q				-2.145	

Specification and Procurement

The 1.5 GeV ring magnet block procurement was similar to the preceding MAX IV 3 GeV ring magnet procurement [3], with a supplier being responsible for mechanical tolerances and for performing field measurements according to MAX-lab instructions, and MAX-lab being responsible for field measurement results, but with

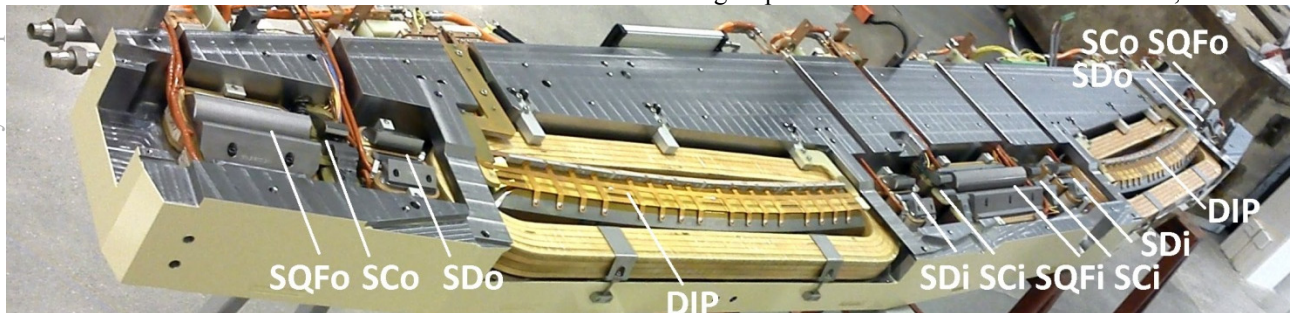


Figure 1: 1.5 GeV ring DBA magnet block #023 bottom half, with magnet element names indicated.

* martin.johansson@maxiv.lu.se

¹ 300 elements if counting SCo/SCi x, y, and skew q windings separately.

² DIP is defined in the lattice as consisting of 30 longitudinal slices, total length = 1.19 m (effective l = 1 m). Fields stated here are central slice.

PERSISTENT CURRENT EFFECT IN 15 - 16 T Nb₃Sn ACCELERATOR DIPOLES AND ITS CORRECTION*

V.V. Kashikhin, A.V. Zlobin[#], FNAL, Batavia, IL 60510, USA

Abstract

Nb₃Sn magnets with operating fields of 15-16 T are considered for the LHC Energy Doubler and a future Very High Energy pp Collider. Due to large coil volume, high critical current density and large superconducting (SC) filament size the persistent current effect is very large in Nb₃Sn dipoles at low fields. This paper presents the results of analysis of the persistent current effect in the 15 T Nb₃Sn dipole demonstrator being developed at FNAL, and describes different possibilities of its correction including passive SC wires, iron shims and coil geometry.

INTRODUCTION

Commercially produced Nb₃Sn composite wires provide high critical current density J_c which is sufficient to increase the operation field in accelerator magnets up to 15-16 T. Magnets with this level of nominal field are considered for the LHC Energy Doubler and a future Very High Energy pp Collider [1].

The persistent current effect in superconducting (SC) accelerator magnets degrades the magnet field quality and, thus, reduces the accelerator dynamic aperture and the operation field range which complicates the field correction system. In a new generation of accelerator magnets based on Nb₃Sn superconductor the persistent current effect is considerably larger than in traditional NbTi magnets due to higher J_c and larger SC filament size d_{eff} [2]. Due to the large coil volume the persistent current effect becomes even larger and, therefore, more important in 15-16 T Nb₃Sn dipoles. This paper presents the results of analysis of the coil magnetization effect in the 15 T Nb₃Sn dipole demonstrator being developed at FNAL and describes different correction options including coil geometry, iron shims and passive SC wires.

MAGNET DESIGN AND PARAMETERS

The design of the 15 T dipole demonstrator being developed at FNAL is described in [3], [4]. It consists of a 4-layer graded coil with 60-mm aperture and a cold iron yoke with 587 mm outer diameter separated from the coil by a 2 mm spacer. The coil cross-section is shown in Fig. 1. The coil is based on two 15 mm wide cables. The 28-strand inner and 40-strand outer cables use 1.0 mm and 0.7 mm Nb₃Sn strands respectively. The strand and cable parameters are reported in [5]. The magnet maximum design bore field is 15.61 T at 4.2 K and 17.04 T at 1.9 K.

*Work supported by Fermi Research Alliance, LLC, under contract No. DE-AC02-07CH11359 with the U.S. Department of Energy

[#] zlobin@fnal.gov

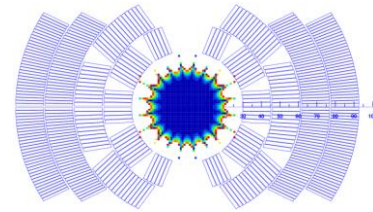


Figure 1: Coil cross-section. The dark colored zone in the aperture represents a field uniformity better than 2×10^{-4} .

COIL MAGNETIZATION EFFECT

The allowed “normal” B_n^Y and “skew” B_n^X field harmonics ($n=1, 3, 5, \dots$) produced by the coil magnetization M are represented as follows

$$B_n^Y + iB_n^X = -\frac{nR_{ref}^{n-1}}{2\pi} \int_S M(z) \left(\frac{e^{ia(z)}}{z^{n+1}} - \frac{z^{*n-1}e^{-ia(z)}}{R_{Fe}^{2n}} \right) dS, \quad (1)$$

where $z=x+iy$, $z^*=x-iy$, $\alpha(z)$ is the angle between the vector M and axis Y , S is the coil cross-section, R_{Fe} is the iron yoke ID, and R_{ref} is the reference radius in the magnet aperture.

The coil magnetization related to the persistent currents in SC filaments is represented as follows

$$M(B, T) = -\mu_0 \frac{2}{3\pi} \lambda_{coil} \varepsilon(B) J_c(B, T) d_{sc}, \quad (2)$$

where λ_{coil} is the coil filling factor with superconductor, $J_c(B)$ is the superconductor critical current density, d_{sc} is the effective SC filament diameter, and $\varepsilon(B)$ is the function describing the field profile inside the SC filaments.

Formulas (1) and (2) show correlations of the field harmonics related to the coil magnetization with the magnet design and superconductor parameters.

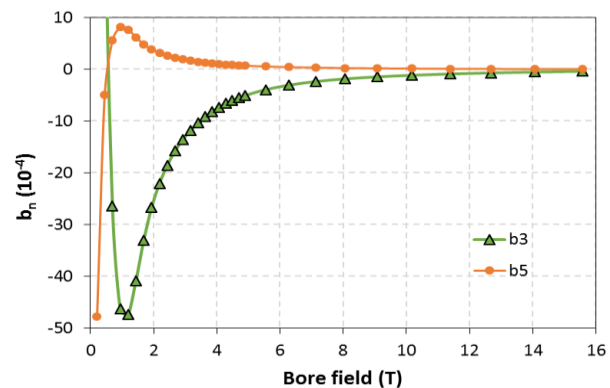


Figure 2: Calculated normal sextupole b_3 and decapole b_5 vs. the bore field in FNAL 15 T Nb₃Sn dipole.

THERMAL MODELING AND CRYOGENIC DESIGN OF A HELICAL SUPERCONDUCTING UNDULATOR CRYOSTAT*

Y. Shiroyanagi[†], J. Fuerst, Q. Hasse, and Y. Ivanyushenkov
Argonne National Laboratory, Argonne, IL USA

Abstract

A conceptual design for a helical superconducting undulator (HSCU) for the Advanced Photon Source (APS) at Argonne National Laboratory (ANL) has been completed. The device differs sufficiently from the existing APS planar superconducting undulator (SCU) design to warrant development of a new cryostat based on value engineering and lessons learned from the existing planar SCU. Changes include optimization of the existing cryocooler-based refrigeration system and thermal shield, as well as cost reduction through the use of standard vacuum hardware. The end result is a design that provides a significantly larger 4.2 K refrigeration margin in a smaller package for greater installation flexibility in the APS storage ring. This paper presents ANSYS-based thermal analysis of the cryostat, including estimated static and dynamic (beam-induced) heating, and compares the new design with the existing planar SCU cryostat.

BACKGROUND

Two planar superconducting undulators (SCU) are currently in operation at APS. The cryogenic system was designed in conjunction with the Budker Institute of Nuclear Physics in Novosibirsk, Russia, based upon design concepts used on their superconducting wigglers [1, 2]. In the past, ANSYS thermal analysis for a planar undulator was conducted based on the cryocooler load lines and estimated heat loads. Calculated excess cooling capacity was matched to the measurement for the operating planar SCU (SCU1) [3]. Based on the same principle, the thermal model of HSCU cryostat was built.

COOLING SCHEMATIC

The overall cooling schematic for the current planar SCU and HSCU cryostat are shown in Fig. 1 and Fig. 2, respectively. For both the planar SCU and HSCU cryostat, the magnet assembly is thermally isolated from the beam chamber. Magnets are indirectly cooled by LHe flowing through the channels inside the magnet assembly. The cryostat is operated in zero-boiloff mode.

The current planar SCU has three thermal circuits. All four cryocooler 1st stages (RDK-408S and RDK-415D) are connected to the outer thermal shield, the warm section of the current leads, and the beam chamber stainless steel transition. Arrows 1, 2, 3, and 4 of Fig. 1 represent the heat flow of this circuit. The 2nd stages of the two RDK-408S cryocoolers are connected to the inner thermal shield and the Al beam chamber section passing through

the magnets. Arrows 5 and 6 represent heat flow within this cooling circuit. The third circuit is the connection of the 2nd stage of the two RDK-415D to the LHe tank and

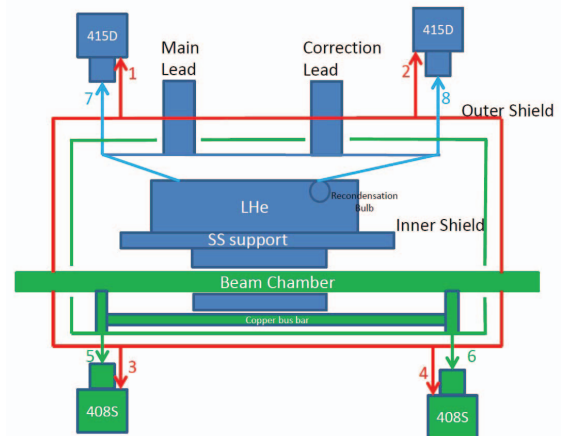


Figure 1: Cooling schematic of the planar SCU Cryostat.

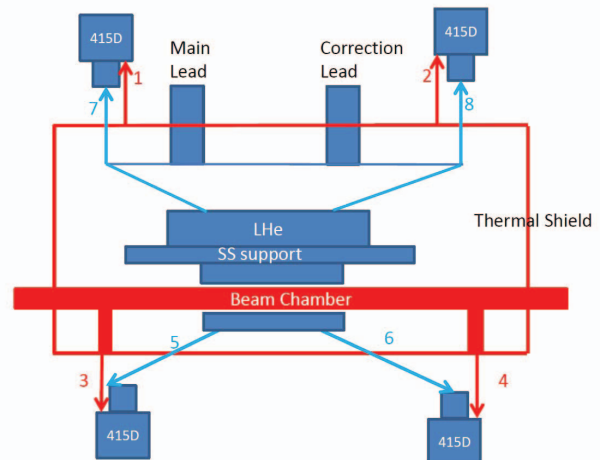


Figure 2: Cooling schematic of HSCU cryostat.

HTS current leads. Arrows 7 and 8 represent the heat flow within this circuit.

The HSCU has only two thermal circuits: the thermal shield cooling circuit and the magnet cooling circuit. The first stages of all four RDK-415D cryocoolers are connected to the warm magnet current leads, the thermal shield, and the beam chamber stainless steel transition sections. Arrows 1, 2, 3, and 4 of Fig. 2 represent the heat flow within this circuit (thermal shield circuit). The 2nd circuit is the connection of all four cryocooler 2nd stages to the HTS section of the current leads and the magnet / LHe tank assembly. Arrows 5, 6, 7, and 8 of Fig. 2 represent the heat flow within this circuit (magnet cooling circuit). The dedicated intermediate thermal shield and

*Work supported by the U.S. Department of Energy, Office of Science, under Contract No. DE-AC02-06CH11357.

[†] email address yshiroyanagi@aps.anl.gov

STATUS OF THE DEVELOPMENT OF SUPERCONDUCTING UNDULATORS FOR STORAGE RINGS AND FREE ELECTRON LASERS AT THE ADVANCED PHOTON SOURCE *

Y. Ivanyushenkov[†], C. Doose, J. Fuerst, K. Harkay, Q. Hasse, M. Kasa, Y. Shiroyanagi, D. Skiadopoulos, E. Trakhtenberg, and E. Gluskin,
Advanced Photon Source, Argonne National Laboratory, Argonne, IL, USA
P. Emma, SLAC, Menlo Park, CA94025, USA

Abstract

Development of superconducting undulator (SCU) technology continues at the Advanced Photon Source (APS). The experience of building and successfully operating the first short-length, 16-mm period length superconducting undulator SCU0 paved the way for a 1-m long, 18-mm period device— SCU18-1— which has been in operation since May 2015. The APS SCU team has also built and tested a 1.5-m long, 21-mm period length undulator as a part of the LCLS SCU R&D program, aimed at demonstration of SCU technology availability for free electron lasers. This undulator successfully achieved all the requirements including a phase error of 5° rms. Our team has recently completed one more 1-m long, 18-mm period length undulator— SCU18-2— that is replacing the SCU0. We are also working on a helical SCU for the APS. The status of these projects will be presented.

INTRODUCTION

Magnetic simulations suggest that superconducting undulator technology outperforms other undulator technologies in terms of undulator peak field for a given magnetic gap and period length [1]. The higher undulator field leads to generation of higher photon fluxes, especially at higher photon energies. This predicted advantage of SCU technology was demonstrated at the APS by operational performance of the first superconducting undulator, SCU0. While only having a magnetic length of 0.3 m, this device generates a higher photon flux than a 2.4-m long hybrid undulator at the photon energies above 80 keV [2].

In addition, the SCU technology allows for the realization of various types of undulators, including planar and circular polarizing devices. This makes the SCU technology very attractive for both storage ring light sources and free electron lasers (FELs).

PLANAR UNDULATORS

Undulators SCU18-1 and SCU18-2 for APS

After the completion of SCU0, the APS team built two more planar undulators for the APS: SCU18-1 and SCU18-2. These devices are similar in design and use similar cryostats. Their parameters are given in Table 1. The SCU18-

1 undulator is in operation in Sector 1 of the APS since May 2015, and the SCU18-2 replaced SCU0 in Sector 6 in September 2016.

Table 1: SCU18-1 and SCU18-2 Parameters

Parameter	Value
Cryostat length, m	2.06
Magnetic length, m	1.1
Undulator period, mm	18
Magnetic gap, mm	9.5
Beam vacuum chamber vertical aperture, mm	7.2
Undulator peak field, T	0.97
Undulator parameter K	1.63
Operating current, A	450

LCLS R&D undulator

This undulator was built as a part of LCLS SCU R&D project aimed at demonstrating that SCU technology can achieve challenging specifications for FEL undulators [3]. The parameters of this device is given in Table 2.

Table 2: Parameters of LCLS R&D Undulator

Parameter	Value
Cryostat length, m	2.06
Magnetic length, m	1.5
Undulator period, mm	21
Magnetic gap, mm	8.0
Beam vacuum chamber vertical aperture, mm	5.7
Undulator peak field, T	1.67
Undulator parameter K	3.26
Operating current, A	588

* Work supported by the U.S. Department of Energy, Office of Science, under Contract No. DE-AC02-06CH11357.

[†] yury@aps.anl.gov

SPECIFICS OF ELECTRON DYNAMICS IN HIGH ENERGY CIRCULAR e+e- COLLIDERS*

Q. Qin[†], J. Gao, H.P. Geng, P. He, D. Wang, N. Wang, Y.W. Wang, Y. Zhang,
Institute of High Energy Physics, Chinese Academy of Sciences, Beijing, P.R. China

Abstract

As the demands of high energy physics, especially the newly found Higgs boson at the LHC, lepton circular collider looks much more promising than linear collider. But the energy will be 20% higher than the LEP operated about 20 years ago. Compare to the relative low energy electron circular collider, the high energy lepton collider has its special features, which influences the design of the whole machine and the beam dynamics. Specifics of beam dynamics, from linear lattice design to dynamics aperture, from beam-beam interaction to collective effects, will be discussed in this paper, together with the study of high energy circular collider CEPC and the FCC.

INTRODUCTION

The Higgs boson was declared to be discovered at the LHC 3 years ago with a mass of ~ 126 GeV/ c^2 , which is only about 20 GeV higher than the beam energy of LEP2. In Sept. 2012, two months later than the discovery of Higgs boson, IHEP announced a plan of building a circular electron positron collider (CEPC) as a Higgs factory in the next decade to study the features of Higgs, and some precise measurements on the Higgs particle. The CEPC can be converted to a super proton proton collider (SppC) in the same tunnel of CEPC. Meanwhile, TLEP, which was re-organized as FCC-hh, and $-ee$, were proposed by CERN as a future project after the LHC. In the following years, IHEP made some progresses on the pre-CDR study on the CEPC, including theory, machine and detector. In this paper, some specifics of the high energy electron positron collider will be discussed, and compared to the low energy e+e- collider like Beijing electron positron collider (BEPC).

BEAM-BEAM INTERACTION

In a circular e+e- collider, luminosity is determined by the beam-beam interaction to a great extent, which is often characterized as the so-called beam-beam parameter, ξ_y . In the design of the BEPC, the maximum design ξ_y is 0.04, and was achieved with optimizing other beam parameters in the luminosity tuning. At the large collider with high beam energy, the beam-beam parameter can be achieved as high as 0.08 or even 0.1[1]. In a round beam operation, ξ_y can even reach 0.15[2].

On the other hand, beam-beam interaction determines not only the luminosity, but the design, operation, and even the interaction region design of a collider. The colliding bunch current or the luminosity performance will be limited by this effect, which is called the beam-beam limit.

The desire to achieve high luminosity leads one naturally to specify high currents and/or small beam sizes. These tend to make the beam-beam interaction stronger, which, in turn, may lead to beam blow-up, coherent oscillations, or fast particle losses that could defeat the purpose of the initial specification. The beam-beam parameter is defined as

$$\xi_{x,y} = \frac{r_e \beta_{x,y} N_b}{2\pi\gamma\sigma_{x,y}(\sigma_x + \sigma_y)}, \quad (1)$$

where γ denotes the relativistic Lorentz factor of the colliding particle, r_e the classical electron radius, N_b the bunch population of the each beam, $\beta_{x,y}$ the beta functions at the interaction point (IP), and finally, σ_x and σ_y the horizontal and vertical rms beam sizes of the opposing beams at the IP, respectively. The parameter ξ roughly corresponds to the linear beam-beam tune shift experienced by a particle at small amplitude. The transverse beam-beam deflection could be shown as that got from the BEPCII luminosity on-line tuning in Fig. 1:

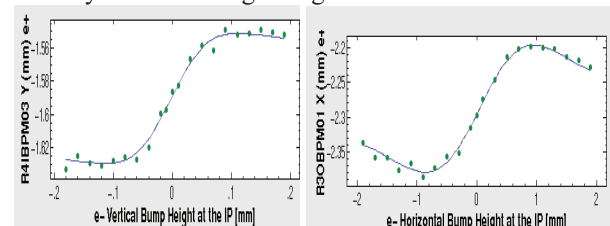


Figure 1: Beam-beam deflection at the BEPCII.

As to the case with crossing-angle at the IP, the bunch length effect due to transverse beam-beam forces could not be neglected when the beams are focused extensively. The transverse kick depends on the longitudinal position as well as on the transverse position. To keep the symplecticity, we should expect, at the same time, an energy change which depends on the transverse coordinates [3].

Large crossing angle at IP can avoid the parasitic collisions when bunch spacing is shortened for more collision bunches in high energy e-e+ colliders. But for large crossing angle, an instability due to synchro-betatron resonances will limit the performance of colliders. The so-called synchro-beam map for a particle-slice interaction, which provides us a 6x6 symplectic map, enables us to install the beam-beam interaction in 6-dimensional weak-strong simulations. Simulation studies show that crossing with a large angle has less serious detrimental effects that is usually believed [4]. The luminosity reduction is only of geometrical, and thus, collision with a crossing angle is popular, such as KEKB, DAFNE and BEPCII, in which horizontal crossing schemes are applied with Piwinski angles of 0.5–1. For a Piwinski angle $\phi \gg 1$, the betatron resonance dominates, but for $\phi < 1$, the synchro-betatron resonance will dominate.

* Work supported by the innovation foundation of IHEP Y4545240Y2, 2015, and the National Foundation of Natural Sciences 11505198.

[†] qinq@ihep.ac.cn

HIGH GRADIENT PM TECHNOLOGY FOR ULTRA-HIGH BRIGHTNESS RINGS

G. Le Bec^{*}, J. Chavanne, European Synchrotron Radiation Facility, Grenoble, France

Abstract

Permanent magnets have long been major components in accelerator-based light sources, particularly as a part of insertion devices. However, their use as main lattice magnets (dipoles, quadrupoles) has been so far somewhat limited. The present trend towards small magnet apertures, exemplified by various multibend achromat designs currently under commissioning or design/construction opens up the discussion once more on the large-scale use of permanent magnets as a means to achieve extremely high gradients in future diffraction-limited storage rings. This paper will review the current R&D programs on the use of permanent magnets in the lattice of high brightness storage rings.

INTRODUCTION

Projects of ultra-small emittance storage rings have been launched around the world. The Max-IV project in Sweden is the first storage ring of this new generation [1]: a 330 pm-rad emittance at 3 GeV is targeted with a 7-bend achromat lattice and 40 T/m gradients. The European Synchrotron Radiation Facility – Extremely Brilliant Source (ESRF-EBS) project, in France [2], aims to reach an emittance of 135 pm-rad at 6 GeV, while the Advanced Photon Source Upgrade (APS-U) targets 70 pm-rad at 6 GeV [3]. The ESRF-EBS project is in the procurement phase and the APS-U is in an advanced development stage. In these two projects the quadrupole gradients reach almost 100 T/m, which appears to be the upper limit of standard electromagnet technology. Such high gradients have been enabled by the shrinking of the vacuum chamber aperture: in all these projects, the magnet bore diameter is about 25 mm.

The theoretical minimum emittance obtainable on an electron storage ring has been presented in various papers [4, 5]. It appears that i) ultra-low emittance machines should have an increased number of (small angle) dipoles, and ii) the horizontal beta function should reach a minimum value inside the dipoles. The second statement implies either increasing the circumference of the ring for inserting focusing elements with standard gradients, or increasing the gradients. It should be noted here that the highest gradient magnets have been developed for upgrading rings with existing buildings and beamlines. Generally speaking, it seems more cost-efficient to increase the magnet gradients than to increase the length of the rings.

Focusing magnets used in ultra-high brightness rings are subject to specific design constraints. They should be high gradient and compact, as mentioned above. The

gradients should be reasonably tunable, e.g. within $\pm 5\%$ for the high gradient quadrupoles of the ESRF-EBS. The homogeneity of the gradient should be sufficient to preserve a acceptable dynamic aperture and lifetime. Synchrotron radiation must escape from the ring: a slot free of magnetic material should be available around the horizontal symmetry plane. Finally, storage ring magnets must be reliable, cost effective, and low in power consumption.

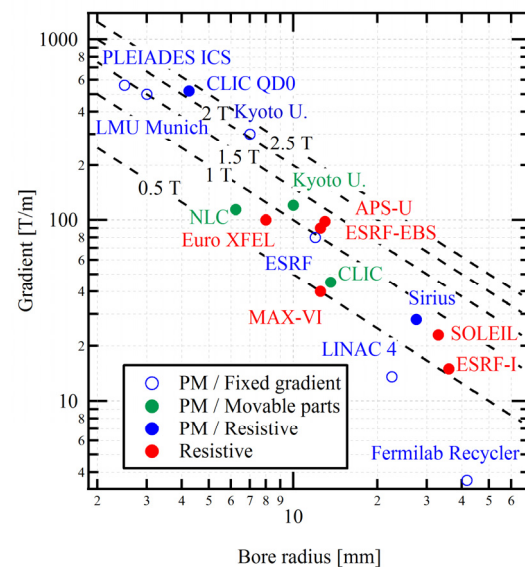


Figure 1: Examples of quadrupole gradients vs magnet bore radius for different technologies, including resistive magnets [12, 13], hybrid PM/resistive magnets [8, 11], tunable PM magnets with movable parts [10, 14-16] and fixed gradient PM magnets [6, 9, 17-19]. The dashed lines indicate the equivalent pole tip field defined as the radius times the gradient.

Figure 1 shows the gradient of a few examples of quadrupoles of different technologies. Ultra-high gradients are reached at bore radii smaller than 5 mm, which seems not compatible with the light source storage ring constraints mentioned above. All devices with a radius below 10 mm have been designed for linear accelerators [6-8]. At the opposite corner of the figure, the quadrupoles of the Fermilab Recycler are low gradient, low field and large aperture [9]. This accelerator should be mentioned as the first large scale ring with magnets entirely energised with ferrite PM blocks. The quality of the magnetic field, i.e. the gradient homogeneity, does not appear in the figure. It should be noted that the only magnets with field quality suitable for storage rings are below the 1.5 T line. Tunable, moderate gradient PM Quadrupoles (PMQs) prototypes have been developed for large scale applications like CLIC [10] or Sirius [11]. The

* lebec@esrf.fr

NEW 1.4 CELL RF PHOTOINJECTOR DESIGN FOR HIGH BRIGHTNESS BEAM GENERATION*

E. Pirez[†], J. Maxson, P. Musumeci

Department of Physics and Astronomy, UCLA, Los Angeles, California 90095, USA

D. Alesini, INFN/LNF, Frascati (Roma), Italy

Abstract

The new electromagnetic and mechanical designs of the S-band 1.4 cell photoinjector are discussed. A novel fabrication method is adopted to replace the brazing process with a clamping technique achieving lower breakdown probability. The photoinjector is designed to operate at a 120MV/m gradient and an optimal injection phase of 70° to improve the extraction field by a factor of 1.9 compared to standard 1.6 cell designs with the same peak field. New geometries and features are implemented to improve beam quality for the demand of high brightness beam applications.

INTRODUCTION

For decades radiofrequency (RF) photoinjectors have been the state-of-the-art in terms of high brightness electron sources. They have played a key role in the development of applications such as short wavelength high gain free electron lasers, ultra-fast electron diffraction, inverse Compton scattering, high power THz generation, among others [1–4]. Although several improvements in photoinjector design have been made over the years, the achieved beam brightness is at least five orders of magnitude lower than the theoretical quantum limit for a fully coherent electron source [5]. Significant improvements on beam brightness must be made to further advance high brightness beam applications.

Improving the beam brightness can be done through different methods. These include minimizing the velocity spread of the electrons during photo-emission by either fine-tuning the laser wavelength [6–9] or modifying the characteristics (a.g. work function) of the photocathode [10]. In this paper we will focus on improving beam brightness by increasing the accelerating electric field E_0 the electrons see as they are emitted from the cathode surface, the extraction field. A higher extraction field has several advantages. Particles quickly accelerate away from the cathode reducing the space charge effects that limit peak brightness. It allows for very high current densities from a small area on the photocathode simultaneously reducing the initial emittance.

How the beam brightness scales with the extraction field depends on what definition one uses as many exist in literature [11]. But regardless of the operating regime, maximizing the extraction field at the cathode achieves brighter beams [12–14]. Increasing the peak field involves significant redesign of the RF structures and resolving fundamental material breakdown issues. A simple alternative is to limit the phase slippage due to the fact that the photo-emitted

particles are not relativistic. The optimal phase (to reach maximum energy and minimum energy spread) for launching particles in typical 1.6 cell RF guns is close to 30 degrees and much lower than 90 degrees so that the launch field is significantly smaller than the peak achievable field in the gun [15]. Without a drastic redesign of RF photoinjectors, the optimal launch phase can be increased by simply shortening the first cell which minimizes the slippage leading to a higher extraction field.

DESIGN OF THE 1.4 CELL PHOTOGUN

The new RF design is based on the design of the 1.6 cell RF structure developed by the SPARC lab of the National Institute of Nuclear Physics (LNF-INFN) [16]. The 1.6 cell photoinjector is currently operating at the Pegasus lab at UCLA at a gradient of 120MV/m. Inspired by the 1.6 cell photoinjector design and fabrication techniques, we have developed a new 1.4 cell photoinjector with a shortened first cell to improve extraction field and therefore increasing beam brightness. In this section we discuss further improvements to the electromagnetic and mechanical design.

Typical 1.6 photoinjectors have an optimal launching phase of $25^\circ - 35^\circ$ depending on the input RF power. The 1.6 cell photoinjector has a first cell of 36.45mm optimal launching phase of 30° . The 1.4 cell photoinjector first cell has a length of $d_{half} = 22\text{mm}$ which gives an optimal launching phase of 70° . The higher launching phase increased the extraction field by a factor of $\sin(70^\circ)/\sin(30^\circ) = 1.9$.

In Fig. 1a, we show the energy dependence on the injection phase for the 1.6 and the 1.4 cell structure at a 120MV/m gradient. The optimal launching phase is the one for which the maximum output energy is achieved. The 1.4 cell photoinjector has a lower output energy than the SPARC photoinjector due to the shortening of the accelerating region. Many applications of high brightness beams are not critically affected by final electron beam energy. In Fig. 1b, we

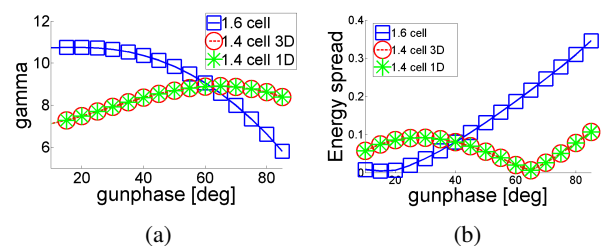


Figure 1: Comparison between the 1.6 cell (3D map) and the 1.4 cell (1D and 3D maps) photoinjector. (a) Gamma vs. phase. (b) Energy spread.

* Work supported by NSF grant 145583

[†] eylenepirez@gmail.com

BENCH MEASUREMENTS OF A MULTI-FREQUENCY PROTOTYPE CAVITY FOR THE FAST KICKER IN THE JLEIC CIRCULATOR COOLER RING*

Y. Huang^{†,1,2,3}, H. Wang³, R.A. Rimmer³, S. Wang³, J. Guo³

¹Institute of Modern Physics, Chinese Academy of Sciences, Lanzhou 730000, China

²University of Chinese Academy of Sciences, Beijing 100049, China

³Thomas Jefferson National Accelerator Facility, Newport News, VA 23606, USA

Abstract

A multi-frequency copper prototype cavity with 5 odd harmonic modes (from 95.26 MHz to 857.34 MHz) has been fabricated and bench measured at JLab. This quarter wavelength resonator (QWR) based deflecting cavity is a half scale prototype of the five-mode cavity (from 47.63 MHz to 426.67 MHz) in the QWRs group developed for the ultrafast harmonic RF kicker in the proposed Jefferson Lab Electron Ion Collider (JLEIC, formerly MEIC). With this prototype cavity, several RF measurements were performed and the results showed good agreement with the simulation results.

INTRODUCTION

A group of quarter wavelength resonator (QWR) based deflecting cavities have been developed to generate 10 harmonic modes for an ultrafast harmonic RF kicker in the proposed Jefferson Lab Electron Ion Collider (JLEIC, formerly MEIC) [1-3]. To validate the electromagnetic characteristics of the cavity from numerical simulation, a half scale copper prototype cavity with 5 odd multiple harmonics of 95.26 MHz has been fabricated and measured. Fig.1 shows the copper prototype cavity with its cross section cut CAD view.

SOME FABRICATION DETAIL

The outer conductor was fabricated from a commercial copper water pipe line. The inner conductor, five tuner pipes, five tuning stubs, one input coupler pipe, two beam pipes and all flanges are all made from oxygen free copper. All the welding processes were performed with the electron beam welding (EBW) including joints of those pipes to the outer conductor, the inner conductor to the end plate where the RF current is the strongest. The electric end flange with the pickup port is welded together and its flange is bolted to the cavity body which makes it possible for further near-beam structure optimization and a replacement with other end structures to reduce the multipole fields and longitudinal impedance. Fig.2 shows the cavity components before the final welding of the end plate to the outer conductor.

*Work supported by Jefferson Science Associates, LLC under U.S.DOE Contract No. DE-AC05-06OR23177

[†]yulu@jlab.org

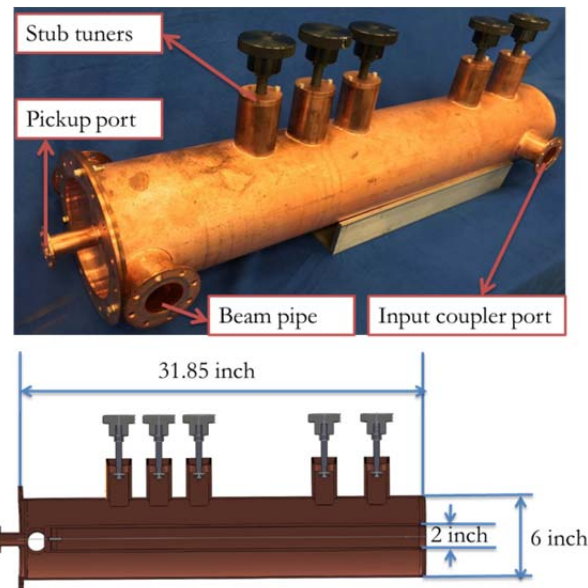


Figure 1: The copper prototype cavity with five odd multiple harmonic modes of 95.26 MHz (top) and the cross section view of this prototype (bottom).



Figure 2: Cavity components before the final welding of the end plate to the outer conductor.

In the first round of measurements (without RF fingers installed in the tuner ports), the harmonic frequencies with stub tuning process, unloaded Q factors and bead-pulling measurements were performed. Then the mode combination experiments were carried out. All of them have shown good agreement with the simulation results. Then the cavity was sent to the machine shop to repair the

PRODUCTION OF MEDICAL ISOTOPES WITH ELECTRON LINACS*

D. A. Rotsch[†], K. Alford, J. L. Bailey, D. L. Bowers, T. Brossard, M. A. Brown, S. D. Chemerisov, D. Ehst, J. Greene, R. G. Gromov, J. J. Grudzinski, L. Hafenrichter, A. S. Hebden, W. Henning, T. A. Heltemes, J. Jerden, C. D. Jonah, M. Kalensky, J. F. Krebs, V. Makarashvili, B. Micklich, J. Nolen, K. J. Quigley, J. F. Schneider, N. A. Smith, D. C. Stepinski, Z. Sun, P. Tkac, G. F. Vandegrift, M. J. Virgo, K. A. Wesolowski, A. J. Youker
Argonne National Laboratory, Argonne, IL, USA

Abstract

Radioisotopes play important roles in numerous areas ranging from medical applications to national security and basic research. Radionuclide production technology for medical applications has been pursued since the early 1900s both commercially and in nuclear science centers. Many medical isotopes are now in routine production and are used in day-to-day medical procedures. Despite these advancements, research is accelerating around the world to improve the existing production methodologies as well as to develop novel radionuclides for new medical applications. Electron linear accelerators (linacs) represent a unique method for the production of radioisotopes. Even though the basic technology has been around for decades, only recently have electron linacs capable of producing photons with sufficient energy and flux for radioisotope production become available. Housed in Argonne National Laboratory's Low Energy Accelerator Facility (LEAF) is a newly upgraded 55 MeV/25-kW electron linear accelerator, capable of producing a wide range of radioisotopes. This talk will focus on the work being performed for the production of the medical isotopes ⁹⁹Mo (⁹⁹Mo/^{99m}Tc generator), ⁶⁷Cu, and ⁴⁷Sc.

INTRODUCTION

Medical isotopes are generally categorized as therapeutic, diagnostic, or both (theranostic/theragnostic). Radiation therapy relies on the destructive effects of radiation to disable unwanted cells and tissues in a biological system – ideally to combat cancer [1]. Beta-emitting nuclides of the appropriate energy and half-life such as ⁴⁷Sc, ⁶⁷Cu, ¹⁸⁶Re, and ¹⁸⁸Re are of interest. A general rule for a beta-therapy is that ~0.2 mm of tissue (~2-20 cells) is penetrated per 100 keV, making the β_{\max} energy a crucial factor when treating diseases. Diagnostic procedures rely on the penetrating gamma or an annihilation induced by the injected radioisotope (such as ¹⁸F, ⁴⁴Sc, ⁶⁴Cu, or ^{99m}Tc). Current medical single photon emission diagnostic cameras (SPECT) are optimized for ^{99m}Tc (140 keV) energies and as such, gamma emissions similar to 140 keV are most desired for these procedures. Positron emission tomography (PET) detects the dual 511 keV annihilation emission from positron emitters.

*Work supported by NNSA Materials Management and Minimization, Office of Science Isotope Program, and Argonne National Laboratory's under U.S. Department of Energy contract DE-AC02-06CH11357

[†]rotsch@anl.gov

Radioisotopes that have image-able gamma emissions and alpha or beta emissions suitable for localized cell destruction are referred to as theranostic agents and are of extreme interest to the medical community. Theranostic agents help minimize healthcare costs, hospital visits, and inconveniences to the patients as they allow for real-time assessment of the treatments.

The electron linac is useful for producing radioisotopes having high specific activity with increased yields. In particular, exploration of the (γ,p) reaction may be able to overcome the shortcomings of the low specific activity usually associated with neutron transmutation.

Argonne National Laboratory's Low Energy Accelerator Facility (LEAF) houses a newly upgraded 55 MeV/25-kW electron linear accelerator (linac), capable of producing a number of medical isotopes through photonuclear reactions that are difficult or otherwise impossible to make [2-4]. Parameters of the linac are provided in Table 1.

Table 1: Parameters of the Argonne Linac

Parameter	Value	Unit
Maximum beam energy	55	MeV
Minimum beam energy	20	MeV
Maximum average beam power	25	kW
RF frequency	1300	MHz
Repetition rate	240	Hz
Length of RF pulse	6.5	μ s
Maximum beam pulse width	5	μ s
Beam energy spread	3	%

ELECTRON LINAC PRODUCED RADIOISOTOPES

Photonuclear-reaction yields of radioactive isotopes depend on the production of high-energy photons generated by interactions of high-energy electrons with a high-Z material (i.e., a converter) to produce Bremsstrahlung radiation. Production yields are controlled by the electron beam flux, target size, length of irradiation, and reaction cross section. The reaction cross section is one of the most important parameters for estimating efficacy and efficiency of photonuclear reactions. A great deal of work has been done to create experimental cross-sectional data bases for (γ,n) reactions (usually leading towards low specific activity radioisotopes); however, even this database is still incomplete [5-7]. The (γ,p) reactions (that lead to high specific activity radioisotopes) is much less extensively investigated and requires considerable additional investigation.

FULFILLING THE MISSION OF BROOKHAVEN ATF AS DOE'S FLAGSHIP USER FACILITY IN ACCELERATOR STEWARDSHIP*

I. V. Pogorelsky, I. Ben-Zvi, M. A. Palmer, Accelerator Test Facility,
Collider Accelerator Department, Brookhaven National Laboratory, Upton, NY 11973 USA

Abstract

The Accelerator Test Facility (ATF) at Brookhaven National Laboratory has served as a user facility for accelerator science for over a quarter of a century. In bringing advanced accelerator-science and technology to individual users, small groups of researchers, and large collaborations, the ATF offers a unique combination of a high-brightness 80-MeV electron beam synchronized to a Terawatt-class picosecond CO₂ laser. The ATF is now the flagship user facility of the Accelerator Stewardship program of the DOE OHEP. In this role, it will also provide opportunities for small businesses to develop accelerator-based products, running the full gamut from the laboratory to the applications. At this juncture, the ATF has embarked upon a transformational upgrade of its capabilities designed to meet ever-growing demands of the user community. We describe our plan for greatly expanding the ATF's floor space along with critical enhancement of our laser and electron accelerator capabilities to enable forefront research for advanced acceleration techniques and radiation sources. We will discuss emerging opportunities for scientific breakthroughs in several areas of R&D enabled by the ATF upgrade.

INTRODUCTION

25 years ago, a newly created Brookhaven Accelerator Test Facility (ATF), sponsored by the U.S. Department of Energy (DOE) Office of High-Energy Physics (OHEP), pioneered the concept of a proposal-driven user facility for advanced accelerator research using lasers and electron beams. Since then, the ATF has become an internationally recognized destination for researchers who benefit from free access to unique scientific capabilities not otherwise affordable to individual institutions and businesses.

We explore several examples that demonstrate the tremendous productivity of collaborative user research utilizing the ATF's unique accelerator capabilities and professional staff. Researchers from academia, industry and national laboratories have successfully investigated a wide range of topics at the ATF: from free electron lasers (FEL) to their opposites – inverse FEL accelerators; from x-ray Compton scattering by colliding laser- and electron-beams to THz radiation generated by beams interacting with tiny radiation structures; from testing radiation damage to electronics for space missions to the study of wakefields in plasmas and dielectric capillaries; and finally

*Work supported by the US Department of Energy under contract number DE-SC0012704.

the investigation of novel methods of accelerating electrons and ions without using RF cavities.

The ATF, which was designated a DOE Office of Science National User Facility in 2015, serves as the flagship research facility for the Accelerator Stewardship Program. ATF continues to broaden its user community by reaching out to federal agencies, universities, and industrial users. It serves as a community catalyst and incubator for new creative ideas.

Building on the success of the ATF user research program, DOE has begun investment in the upgrade of both the electron beam and laser capabilities of the facility. We describe how the ATF-II upgrade will transform the facility's science reach and productivity by offering new opportunities for innovative research in strong-field physics and advanced accelerator design with a range of parameters not previously accessible. By enabling first-of-kind technical demonstrations and workforce training, ATF-II will fulfil a broad Accelerator Stewardship mission and will support a wide variety of user needs.

ACCELERATOR STEWARDSHIP: FROM CONCEPT TO IMPLEMENTATION

Much of the U.S. effort in accelerator science and engineering takes place in the Department of Energy's National Laboratories. However, researchers from universities and small businesses play a vital role in advancing the field. An important question is how can these diverse groups afford to undertake state-of-the-art experimental research to explore bold new ideas, test new techniques, and prove theoretical models? The answer is clear: It lies in the ready availability of modern user facilities. Indeed, user facilities are the mainstay of many sciences, and, by hosting a free service for users, they deter waste and duplication of effort. They are invaluable in that they enable investigators with a small research budget to carry out their experimental work using high-performance accelerators and lasers, supported by experts dedicated to this task. To understand how the Accelerator Stewardship Program developed into a strategic direction for accelerator science and technology (AST), we must go back in the history of accelerator R&D, starting from the 1980 recommendations of the M. Tigner Panel on the Long Range Accelerator R&D at OHEP. The members of this panel were largely responsible for establishing the proposal-based program that has supported long-range accelerator R&D over the past few decades. The ATF was established in mid-1980s as a part of this program.

The "accelerator stewardship" concept emerged in 1994 recommendations of the J. Marx Panel. Established

MAXIMUM BRIGHTNESS OF LINAC-DRIVEN ELECTRON BEAMS IN THE PRESENCE OF COLLECTIVE EFFECTS

S. Di Mitri[†], Elettra – Sincrotrone Trieste S.C.p.A., Basovizza, Trieste I-34149

Abstract

Linear accelerators capable of delivering high brightness electron beams are essential components of a number of research tools, such as free electron lasers (FELs) and elementary particle colliders. In these facilities the charge density is high enough to drive undesirable collective effects (wakefields) that may increase the beam emittance relative to the injection level, eventually degrading the nominal brightness. We formulate a limit on the final electron beam brightness, imposed by the interplay of geometric transverse wakefield in accelerating structures and coherent synchrotron radiation in energy dispersive regions. Numerous experimental data of VUV and X-ray FEL drivers validate our model. This is then used to show that a normalized brightness of 10^{16} A/m², promised so far by ultra-low charge beams (1-10 pC), can in fact be reached with a 100 pC charge beam in the Italian FERMI FEL linac, with the existing machine configuration.

INTRODUCTION

In this article we recall a limit on the maximum brightness of an ultra-relativistic electron beam achievable in a single-pass linac when collective effects are part of the dynamics [1]. The limit is determined by the interplay of the dispersion strength (*e.g.*, bunch length compression factor) with the linac geometric transverse wakefield (GTW) and coherent synchrotron radiation (CSR) effect on the transverse emittance. We validate our model by means of a systematic comparison of theoretical predictions with experimental data in the linac of FERMI FEL [2-4]. We show that the effects of GTW and CSR on the final beam quality, which has traditionally been treated separately in the archival literature, are coupled by the variation of the bunch length along the beam line. Hence, GTW and CSR should be considered simultaneously during machine design.

Without aiming to replace powerful and sophisticated numerical codes, the analysis proposed in this paper purports to be useful as an exploratory and fast tool to maximize the beam brightness. It is worth to mention that, in principle, the brightness can always be improved by brute force, *e.g.* increasing the beam energy, thus with a direct impact on the accelerator size and cost. Our analysis, instead, aims to maximize the brightness by improving the accelerator performance once the beam line is given, thus with no additional costs.

MODELLING COLLECTIVE EFFECTS

By using the beam matrix formalism, one finds that the CSR-induced normalized emittance growth in the bending plane is [5]:

$$\Delta\gamma_0\varepsilon_{i,0} \cong \gamma_0\varepsilon_{i,0} \left[\sqrt{1 + \frac{\tilde{\beta}\theta^2\sigma_{\delta,CSR}^2}{\varepsilon_{i,0}}} - 1 \right] \equiv \gamma_0\varepsilon_{i,0} \left[\sqrt{1 + X_{CSR}} - 1 \right], \quad (1)$$

where γ_0 and $\varepsilon_{i,0}$ are, respectively, the relativistic Lorentz factor and the unperturbed geometric emittance at the dispersive insertion, θ is bending angle, $\tilde{\beta}$ is the minimum value of β in the insertion, and $\sigma_{\delta,CSR}$ is the CSR-induced RMS energy spread relative to the beam mean energy. The latter is [6]:

$$\sigma_{\delta,CSR} = 0.2459 \frac{r_e}{e} \frac{Q}{\gamma} \left(\frac{l\theta^2 C^4}{\sigma_{z,0}^4} \right)^{1/3}, \quad (2)$$

where we introduced the electron classical radius r_e and the electron charge e , Q is the bunch total charge, l the dipole magnet length, $\sigma_{z,0}$ the initial RMS bunch length and C the (linear) compression factor, *i.e.* the ratio of the initial over the final bunch length:

$$C = \frac{\sigma_{z,0}}{\sigma_{z,f}} = \frac{1}{1 + hR_{56}} \approx \frac{1}{1 + (\sigma_{\delta,0}/\sigma_{z,0})R_{56}}. \quad (3)$$

Here $\sigma_{\delta,0}$ is the relative energy spread imparted to the beam by the upstream RF off-crest acceleration. The longitudinal transport matrix element R_{56} is determined by the dispersive insertion geometry and is, for a four dipoles, achromatic and symmetric chicane with $\theta \ll 1$,

$$R_{56} \cong -2\theta^2 \left(L_{12} + \frac{2}{3}l \right), \quad \text{where } L_{12} \text{ is the drift length}$$

between the two outer bending magnets. In our convention, a negative R_{56} compresses the bunch duration if the linearly correlated energy chirp h is positive.

The single-bunch transverse wakefield instability [7], which happens when the bunch travels at a distance Δ from the linac electric axis, generates a displacement of the trailing particles respect to the bunch head; this displacement is correlated with the longitudinal coordinate along the bunch. The trailing particles start a betatron oscillation around a new dispersive trajectory, therefore increasing their Courant-Snyder invariant. Such an effect can be removed by finding a “golden” trajectory which makes the wakefield’s kicks cancel each other (emittance bumps) [8–10]. In analogy with the CSR case, the transverse emittance dilution at the linac end is [9]:

$$\Delta\gamma_f\varepsilon_{f,0} \cong \gamma_f\varepsilon_{f,0} \left[\sqrt{1 + 2 \left(\frac{\pi r_e}{Z_0 c e} \right)^2 \frac{Q^2 \bar{W}_1^2 \Delta^2 L_{FODO} L_{tot} \bar{\beta}}{\gamma_f \varepsilon_{f,0} \sqrt{\gamma_0 \gamma_f}}} - 1 \right] \equiv \quad (4)$$

$$\equiv \gamma_f \varepsilon_{f,0} \left[\sqrt{1 + X_w} - 1 \right],$$

where $Z_0 = 377 \Omega$ is the vacuum impedance, c is the speed of light in vacuum, γ_f and $\varepsilon_{f,0}$ are, respectively, the relativistic Lorentz factor and the unperturbed geometric emittance at the linac end, $\bar{\beta}$ the average betatron function

[†] simone.dimitri@elettra.eu

INTRABEAM SCATTERING IN HIGH BRIGHTNESS ELECTRON LINACS

S. Di Mitri[#], Elettra Sincrotrone Trieste, 34149 Basovizza, Trieste, Italy

Abstract

Intra-beam scattering (IBS) of a high brightness electron beam in a linac has been studied analytically, and the expectations found to be in reasonable agreement with particle tracking results from the Elegant code. It comes out that, under standard conditions for a linac driving a free electron laser, IBS plays no significant role in the development of microbunching instability. A partial damping of the instability is envisaged, however, when IBS is enhanced either with dedicated magnetic insertions, or in the presence of an electron beam charge density at least 4 times larger than that produced by present photo-injectors.

INTRODUCTION

The question to which extent intra-beam scattering (IBS) affects the properties of high brightness electron bunches in linacs was posed in [1,2], with attention to the interplay of IBS and microbunching instability (MBI). Following our study in [3], here we aim to provide a quantitative answer and an outlook, by comparing the analysis and particle tracking runs of the ELEGANT code [4], whereas IBS was simulated following prescriptions given in [2,5].

In particular, we wonder whether IBS could play a role when the beam transverse dimension is squeezed with strong focusing (“low-beta”) FODO cells, so to increase the IBS longitudinal growth rate. At first glance, the idea of using IBS to increase the energy spread of an electron bunch traveling in a dedicated FODO channel seems to be attractive for the following reasons: i) IBS heats the beam by avoiding cost, complexities and maintenance of a laser heater (LH) system [6]; ii) the heating level is tuneable with the quadrupoles’ focusing strength; iii) it provides longitudinally uncorrelated energy spread, thus avoiding any side effect associated to the energy modulation induced in a LH at the infrared laser wavelength (*e.g.*, the so-called trickle heating) [7]. We will see however that, to be as effective as a LH, the enhancement of IBS requires a long and densely packed FODO channel. An alternative compact lattice in which the beam recirculates through low-beta FODO channels is investigated. This solution, however, turns out to be not practical because of the coherent synchrotron radiation (CSR) instability that develops through the arcs.

THEORETICAL BACKGROUND

Ultra-relativistic electron bunches in modern accelerators generally have much smaller velocity spread in the longitudinal direction of motion than in the transverse planes owing to the relativistic contraction by the Lorentz factor γ : $\sigma_\delta/\gamma \ll \sigma_{x'}, \sigma_{y'}$, where σ_δ is the beam rms fractional energy spread and $\sigma_{x'}, \sigma_{y'}$ the rms angular divergence. If the bunch’s charge density is high

enough and the bunch travels a long path, multiple Coulomb scattering tends to redistribute the beam momenta from the transverse degree of freedom to the longitudinal one. This process is called IBS and its longitudinal growth rate may be comparable to the beam damping time in low emittance electron storage rings. The instantaneous growth rate of the energy spread of a bunched beam circulating in a ring was given in [8,9]. Since there are no synchrotron oscillations in a linac, the formula for a coasting beam should be used here (which results in a growth rate a factor 2 larger than that of a bunched beam) [8]:

$$\frac{1}{\sigma_\delta} \frac{d\sigma_\delta}{dt} \approx \frac{r_e^2 c N}{8\gamma^2 \varepsilon_{n,x} \sigma_x \sigma_z \sigma_\delta^2} \ln \left(\frac{\Delta\gamma_{\max}}{\Delta\gamma_{\min}} \right) \quad (1)$$

Here r_e is the electron classical radius, $\beta c \approx c$ the electron velocity, N the number of electrons in the bunch, $\varepsilon_{n,x} = \varepsilon_{n,y}$ the rms normalized transverse emittance of a round beam, and σ_z the rms bunch length. The argument of the Coulomb logarithm is the ratio of the maximum and the minimum energy exchange due to a single scattering event, and $\Delta\gamma_{\max} \propto \gamma^2 \sigma_{x'}$, $\Delta\gamma_{\min} \propto r_e / (\sigma_x \sigma_{x'}) \approx \gamma r_e / \varepsilon_{n,x}$ [1].

Following an argument made in [10], we consider that the IBS energy distribution has a nearly Gaussian core with a long tail. Since we are mostly interested in the energy spread of the Gaussian core, we set the maximum energy transfer to $\Delta\gamma_{\max} = \gamma \cdot 10^{-5}$ as also done in [1], and find that the logarithm is of the order of 10 for a normalized emittance of $\sim 1 \mu\text{m}$. Then, Eq.1 can be integrated and it yields to the final fractional rms energy spread in the presence of IBS cumulated over the distance Δs [3]:

$$\sigma_\delta \approx \sqrt{\sigma_{\delta,0}^2 + \frac{2r_e^2 N}{\gamma^2 \varepsilon_{n,x} \sigma_x \sigma_z} \Delta s} \equiv \sqrt{\sigma_{\delta,0}^2 + \sigma_{\delta,IBS}^2} \quad (2)$$

with $\sigma_{\delta,0}$ the initial rms fractional incoherent energy spread. Equation 2 is an approximate expression for smooth betatron oscillations, neither energy dispersion nor particle acceleration. If we apply Eq.2 to the low energy part of a linac, we find that an electron beam from a state-of-the-art photo-injector, *e.g.* with beam charge $Q = 0.5 \text{ nC}$, $\sigma_z = 750 \mu\text{m}$, $\varepsilon_n = 0.6 \mu\text{m rad}$, $\sigma_x = 150 \mu\text{m}$ and $\gamma = 300$, collects an absolute rms energy spread $\sigma_{E,IBS} \approx 3 \text{ keV}$ over $\Delta s \sim 30 \text{ m}$. This is comparable to the typical value of $\sigma_{E,0} \approx 2 \text{ keV}$ out of the photo-injector [11], and still far from the amount of heating required to suppress MBI in an FEL-driver [12,13]. Then, if we assume that the bunch length is magnetically compressed by a factor of, say, $C \sim 30$, $\sigma_{E,IBS}$ may grow up to $\sim 100 \text{ keV}$ over hundreds of meters, but its contribution to Landau damping of MBI remains small for two reasons. First, in the linac region immediately following the compressor, $\sigma_{E,IBS}$ is negligible compared to

[#]Work supported by the FERMI project of Elettra Sincrotrone Trieste.
#simone.dimitri@elettra.eu

CSR-IMMUNE Arc COMPRESSORS FOR RECIRCULATING ACCELERATORS DRIVING HIGH BRIGHTNESS ELECTRON BEAMS

S. Di Mitri[†], M. Cornacchia, Elettra – Sincrotrone Trieste S.C.p.A., Basovizza, Trieste I-34149

Abstract

The advent of short electron bunches in high brightness linear accelerators has raised the awareness of the accelerator community to the degradation of the beam transverse emittance by coherent synchrotron radiation (CSR) emitted in magnetic bunch length compressors, transfer lines and turnaround arcs. We reformulate the concept of CSR-driven beam optics balance, and apply it to the general case of varying bunch length in an achromatic cell. The dependence of the CSR-perturbed emittance to beam optics, mean energy, and bunch charge is shown. The analytical findings are compared with particle tracking results. Practical considerations on CSR-induced energy loss and nonlinear particle dynamics are included. As a result, we identify the range of parameters that allows feasibility of an arc compressor in a recirculating accelerator driving, for example, a free electron laser or a linear collider.

INTRODUCTION

In spite of the relatively high beam rigidity from hundreds of MeV up to multi-GeV energies, the electron beam energy-normalized projected emittance may be degraded in the bending plane at the $\sim 1 \mu\text{m}$ rad level and above, when the beam is bent in dipole magnet-chicanes that act as bunch length compressors [1–4], in multi-bend transfer lines [5] and in turnaround arcs [6–11]. Initially thought for a constant bunch length along the line [12], a specific linear optics design has recently been revisited to minimize [5] or even cancel [13] the emittance disruption in double bend achromatic (DBA) lines, and then in a periodic [14] and a non-periodic arc [15], in which the bunch length is notably compressed. Turnaround arcs have been considered as magnetic bunch length compressors for energy-recovery linac (ERL) designs, in the 0.1–1 GeV energy range [6–11]. In [8,9] some degree of optics control was exercised in order to minimize the CSR effect following the theoretical prescriptions given in [16], but in all cases the CSR effect was effectively suppressed by limiting the bunch charge below 0.15 nC. To date, when arcs are included in the accelerator geometry, bunch length is kept constant through them by isochronous paths, or lengthened before entering the arc (CSR effect is weaker for longer bunches), and re-compressed at its end. In this article, we follow [17] and recall the range of validity of the linear optics analysis and investigate the robustness of the proposed arc compressor lattice for a realistic range of beam parameters, where a normalized emittance at the arc's end at the $0.1 \mu\text{m}$ rad level is promised, for compression factors of up to ~ 45 , applied to a 0.5 nC beam, at 2.4 GeV.

[†] simone.dimitri@elettra.eu

LINEAR OPTICS FORMALISM

The periodic, achromatic 180 deg arc compressor introduced in [14] is made of 6 identical DBA cells. The single DBA magnetic lattice and its periodic optics solution is shown in Fig.1. We assume optics symmetry w.r.t. the DBA central axis, which implies π betatron phase advance (in the bending plane) between the dipoles [18], and expand the trigonometric terms up to the 3rd order in the bending angle, $\theta \ll 1$. Following the mathematics in [17], we calculate the expression of the single particle Courant-Snyder (C-S) invariant at the end of the second dipole magnet for arbitrary C-S parameters in the dipoles, by considering a dependence of the CSR kick factor on the rms bunch length $k \sim 1/\sigma_z 4/3$, so that $k_2 = k_1 \times C^4/3$, where C is the bunch length compression factor through the DBA cell. The particle invariant is minimized by the following C-S parameters in the second dipoles [17]:

$$\alpha_{2,opt} = -\frac{\beta_2}{\left(\frac{l_b}{6}\right)} \frac{(C^{4/3} + 1)}{|C^{4/3} - 3|}, \quad (1)$$

$$\beta_{2,opt} = \left(\frac{l_b}{6}\right) \frac{\sqrt{(C^{4/3} - 1)^2 + \alpha_2^2 (C^{4/3} - 3)^2}}{(C^{4/3} + 1)}$$

We notice that a solution with $\alpha_2 = 0$, e.g. adopted in [14], does not minimize J_3 in absolute sense, although it may be practical from the optics design point of view.

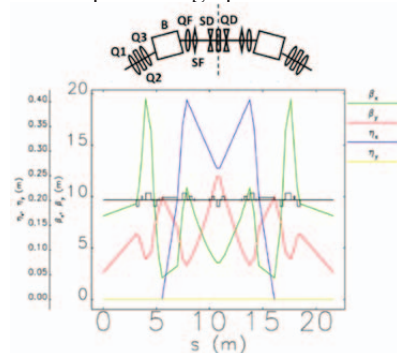


Figure 1: Linear optics functions and DBA cell layout including dipole magnets (B), focusing (QF, Q1 and Q3) and defocusing (QD, Q2) quadrupole magnets, focusing (SF) and defocusing sextupole magnets (SD). Copyright of Elsevier (2016) [17].

LINEAR COMPRESSION FACTOR

The linear compression factor is defined by $C=1/|1+hR_{56}|$, where R_{56} is the transfer matrix element of the DBA cell, identical in all cells, and h is the incoming linear energy chirp, $h=dE/(Edz)$, E being the beam mean energy. Bunch length compression is achieved as far as the energy spread correlated along the bunch, typically imparted to the beam by an upstream RF section running

PROBABILISTIC ESTIMATION OF LOW ENERGY ELECTRON TRAPPING IN QUADRUPOLES

K. G. Sonnad, J. A. Crittenden, CLASSE, Cornell University, Ithaca, NY, USA

Abstract

Electron cloud formation in quadrupoles is important for storage rings because they have the potential of being trapped for a time period that exceeds the revolution period of the beam. This can result in a turn by turn build up of cloud, that could potentially interfere with beam motion. Using the theory on the motion of particles in nonuniform magnetic fields, we describe a method to estimate the probability distribution of trapping across the cross-section of a quadrupole for a given field gradient and electron energy. Such an estimate can serve as a precursor to more detailed numerical studies of electron cloud build and trapping in quadrupoles.

INTRODUCTION

The trapping of electrons in quadrupoles has been observed in positron as well as proton rings [1, 2]. Calculation of trajectories of single electrons in quadrupoles has shown that they can indeed remain trapped indefinitely provided certain initial conditions are satisfied. [3, 4]. The motion of a charged particle travelling in a non-uniform magnetic field is said to be adiabatic if the condition $|\nabla B|/B|r_c \ll 1$, where B is the magnitude of the magnetic field and r_c is the cyclotron radius corresponding to this magnetic field. Under these conditions, the magnetic moment given by $\mu = mv_{\perp}^2/2B$ is an adiabatic invariant and is a conserved quantity, where v_{\perp} is the component of the velocity perpendicular to the magnetic field. The energy $\mathcal{E} = 1/2m(v_{\perp}^2 + v_{\parallel}^2)$ is always a conserved quantity. As the particle migrates to a region of higher magnetic field, the parallel component of the velocity v_{\parallel} reduces and a point may reach when it goes to zero, in which case the particle reverses its path. Based on this phenomenon, one can specify a so called loss cone drawn in velocity space. The axis of the cone is along v_{\parallel} . It can then be shown (see for example Ref [5]) that the angle of this cone θ_c satisfies $\sin^2 \theta_c = B_0/B_e$, where B_0 is the magnitude of the magnetic field at the initial point, and B_e corresponds to the field at the escape point, along the field line. If at the initial point, the particle lies outside the loss cone, it would reverse its path before reaching the escape point. Due to the symmetry in a quadrupole field pattern, it is guaranteed that two such "mirror" points occur along a field line, between which a particle may remain trapped. For trapping to occur, it is sufficient for two conditions to be satisfied. (1) The motion needs to remain adiabatic all along the field line, and (2) the particle needs to lie outside the loss cone at the given point on the field line. Reference [3] studied the nature of the particle trajectories and their escape when either conditions (1) or (2) were individually violated.

METHOD OF COMPUTING THE TRAPPING PROBABILITY

If the magnetic moment $\mu = mv_{\perp}^2/2B$ is conserved, then the perpendicular velocity of a particle travelling from point 1 to 2 can be traced, and is given by

$$v_{\perp}(2) = v_{\perp}(1) \left(\frac{B(2)}{B(1)} \right)^{1/2} \quad (1)$$

For a quadrupole field, the magnetic field is given by $B_x = ky$, $B_y = kx$, or $|\nabla B| = k$. Thus, condition for adiabatic motion to exist is

$$\frac{r_c |\nabla B|}{B} = \frac{v_{\perp} m k}{e B^2} \ll 1 \quad (2)$$

If the angle made by the particle with respect to the "perpendicular" direction is ϕ , then we have

$$v_{\perp} = v \cos(\phi) \quad (3)$$

For a particle to remain trapped, it is necessary that the motion remains adiabatic all along the field line. It is sufficient for this condition to satisfy if the motion is adiabatic at the point where the magnitude of magnetic field is a minimum. Using this, the condition for adiabatic motion to sustain along a field line may be obtained by combining equation (1) and (2). This is

$$\frac{v \cos(\phi) m k}{e B_o^{1/2} B_{min}^{3/2}} \ll 1 \quad (4)$$

Where B_o is field at the reference point, and B_{min} is the minimum field value along that field line. While there is no rule that demarcates between adiabatic and nonadiabatic motion, it would be reasonable for our purposes to make an assumption that the motion is adiabatic if the left side is less than a predefined empirical parameter $\eta \ll 1$. With this, Eq(4) will lead to the condition

$$\cos(\phi) < \frac{\eta e B_o^{1/2} B_{min}^{3/2}}{m v k} \quad (5)$$

We will now define another cone in velocity space whose axis is parallel to v_{\perp} , with angle ϕ_a , such that for all points lying inside this cone, the above condition is violated. Under our assumptions, these points correspond to cases where the particle motion will eventually cease to remain adiabatic. This gives us,

$$\cos(\phi_a) = \begin{cases} \frac{\eta e B_o^{1/2} B_{min}^{3/2}}{m v k}, & \text{if } \leq 1 \\ 0, & \text{otherwise} \end{cases} \quad (6)$$

TRANSFORMER RATIO ENHANCEMENT EXPERIMENT BASED ON EMITTANCE EXCHANGER IN ARGONNE WAKEFIELD ACCELERATOR

Qiang Gao^{1,2,*}, Chunguang Jing³, Sergey P. Antipov³, Jiaru Shi¹, Huaibi Chen¹, Wei Gai^{1,2}, John Goham Power², Manoel Conde², Charles Whiteford², Eric Edson Wisniewski², Wangming Liu², Darrell Scott Doran²,

¹ Tsinghua University, Beijing 100084, China,

² Argonne National Laboratory, Lemont, IL 60439, USA,

³ Euclid TechLabs, Solon, Ohio 44139, USA

Abstract

The transformer ratio is an important figure of merit in collinear wakefield acceleration, it indicates the efficiency of energy transferring from drive bunch to witness bunch. Higher transformer ratio will significantly reduce the length of accelerator thus reducing the cost of accelerator construction. However, for the gaussian bunch, this ratio has its limit of 2. To obtain higher transformer ratio, one possible method is to tailor the beam current profile to specific shapes. One method of beam shaping is based on emittance exchange, which has been demonstrated at the Argonne Wakefield Accelerator. Its principle is to tailor the beam transversely using a mask then exchange the beam's transverse profile and longitudinal profile. In this paper, we describe our efforts to optimize the beamline and mask in order to generate a triangular beam with quadratic head, which has a transformer ratio of 6.4. We also present our design of a dielectric slab based accelerating structure to measure the transformer ratio. Finally, we discuss an experiment for this high transformer ratio at Argonne Wakefield Accelerator Laboratory.

INTRODUCTION

Transformer ratio (TR) is an important figure of merit in the collinear wakefield acceleration. It is defined as the ratio of maximum energy gain by witness beam to the maximum energy loss by the drive beam. This ratio indicates the efficiency of energy transferring from drive bunch to witness bunch. The higher transformer ratio it is, the higher energy gain that witness bunch has when the drive bunch energy is fixed. However, it can be proved that TR is less than 2 for a drive beam with a symmetric longitudinal current profile, such as a gaussian[1]. Two main techniques have been explored by scientist to enhance the TR recent years. One of them is to utilize a ramped bunch train which had been demonstrated at Argonne to obtain TR as high as 3.4 [2] while another methods shape the drive bunch current profile. This can be done by tailoring the beam transversely then exchange its longitudinal profile with transverse profile. Recently an experiment has demonstrated that inserting a mask into one dogleg can obtain a triangle bunch which has TR as

high as 3.5 [3]. Now we design and optimize an experiment to enhance the transformer ratio utilizing emittance exchange (EEX) beamline at Argonne Wakefield Accelerator Laboratory.

PRINCIPLE

The concept of EEX was first come up with in 2002 [4]. Then scientist found that it can be used for beam longitudinal shaping [5]. The crucial components of EEX are that two identical doglegs and one deflecting cavity which is inserted between the two doglegs. The linear transport matrix of EEX beamline can be expressed as following equation when taking the thin-lens assumption,

$$\begin{bmatrix} x_f \\ x'_f \\ z_f \\ \delta_f \end{bmatrix} = \begin{bmatrix} 0 & 0 & \kappa L/2 & \eta + \kappa\xi L/4 \\ 0 & 0 & \kappa & \kappa\xi/2 \\ \kappa\xi/2 & \eta + \kappa\xi L/4 & 0 & 0 \\ \kappa & \kappa L/2 & 0 & 0 \end{bmatrix} \begin{bmatrix} x_i \\ x'_i \\ z_i \\ \delta_i \end{bmatrix} \quad (1)$$

So the beam longitudinal profile after EEX is only determined by the initial transverse phase space. It means that we can obtain arbitrary longitudinal profile if we tailor the beam transversely with mask [6].

When a charged drive bunch traverses a dielectric waveguide it will excite the wakefield inside and behind the bunch. The TR can be calculated as ratio of the maximum accelerating voltage behind the drive bunch to the maximum decelerating voltage inside the drive bunch. Figure 1 shows the current profile of a gaussian bunch and its wakefield.

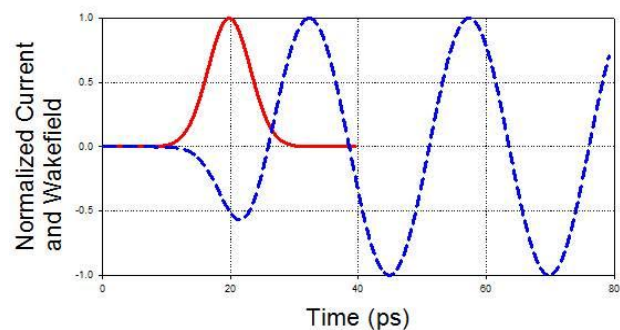


Figure.1: The current profile and wakefield of a gaussian bunch. The red solid line is the current profile and blue line is the wakefield.

*gaoq08thu@gmail.com

MODELING OF DIPOLE AND QUADRUPOLE FRINGE-FIELD EFFECTS FOR THE ADVANCED PHOTON SOURCE UPGRADE LATTICE *

M. Borland, R. R. Lindberg, ANL, Argonne, IL 60439, USA

Abstract

The proposed upgrade of the Advanced Photon Source (APS) to a multibend-achromat lattice requires shorter and much stronger quadrupole magnets than are present in the existing ring. This results in longitudinal gradient profiles that differ significantly from a hard-edge model. Additionally, the lattice assumes the use of five-segment longitudinal gradient dipoles. Under these circumstances, the effects of fringe fields and detailed field distributions are of interest. We evaluated the effect of soft-edge fringe fields on the linear optics and chromaticity, finding that compensation for these effects is readily accomplished. In addition, we evaluated the reliability of standard methods of simulating hard-edge nonlinear fringe effects in quadrupoles.

INTRODUCTION

The APS Upgrade (APS-U) project plans to replace the existing 3rd-generation storage ring with a multi-bend achromat (MBA) design [1] that will reduce the emittance to less than 70 pm [2, 3]. The goal is to replace the existing storage ring and return to user operation within 12 months. One important factor in achieving this will be thorough understanding of the lattice and beam dynamics with realistic models of the magnets. This paper reports progress on this issue with respect to modeling of quadrupole and dipole magnets.

The integrated quadrupole strength for low-emittance lattices scales like N_d , where N_d is the number of dipoles per sector [4]. One strategy for dealing with this is to use smaller magnet apertures, which may impact field quality. Magnets may also be operated in a more highly-saturated condition. The latter condition in particular will increase the difficulty of modeling linear and nonlinear edge effects.

The APS-U lattice includes several types of dipole magnets, including two types of 5-segment longitudinal gradient dipoles. The former are quite unfamiliar and hence merit close attention. Of interest is ensuring that the trajectory through the magnets is correct, assessing the effect on linear optics, and understanding the impact on chromaticity and other nonlinear properties.

QUADRUPOLE MODELING

The initial design of the APS-U quadrupoles made use of “mushroom” pole tips, which extend under the coils in order to increase the effective length of the magnets. This allowed operating with higher magnetic efficiency for a given integrated gradient, without unduly increasing the magnet core

length. It also allowed making most magnets of identical lengths, with nearly identical cores and coils. However, the resulting gradient profile shape depended strongly on the level of excitation as shown in Fig. 1. With the exception of the 98% efficiency case, corresponding to an integrated gradient of ~ 12 T, the profiles are very unusual.

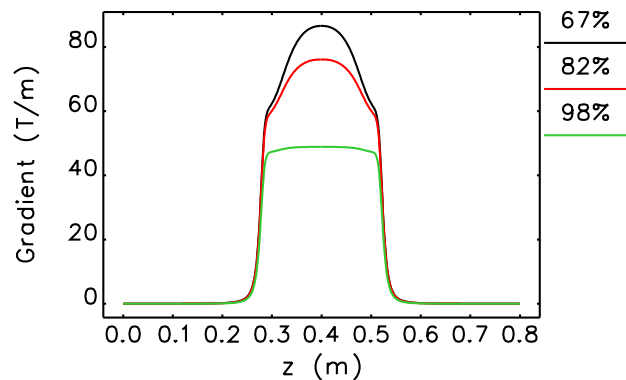


Figure 1: Gradient profiles for initial APS-U quadrupoles at various levels of magnetic efficiency.

Our first task was to assess the impact of such profiles on beam transport. This was done using the approach described in [5, 6] for modeling soft-edge effects. For the hard-edge nonlinear effects, we followed the standard approach [7, 8] with extensions to higher order [9]. We compared the results of these models, as implemented in the KQUAD element in Pelegant [10, 11], with direct integration of particles through a 3D field map generated with OPERA, using Pelegant’s BMXYZ element. The agreement of the linear matrix elements for a single quadrupole was within 0.01%. In spite of the unusual appearance of the gradient profiles, subsequent rematching of the linear optics succeeded in reducing the changes in the linear optics functions to under 2%, with exact restoration of the tunes. The required changes in magnet excitation were less than 0.6%.

Although the linear optics based on [6] agreed very well with integration through the field map, the nonlinearities showed poor agreement. After some investigation, we concluded that this resulted from the non-Maxwellian character of the 3D field map, which is partly a result of limitations of the magnet code and partly a result of the use of linear interpolation of the field map during integration. Hence, we switched to use of a generalized gradient expansion [12, 13], albeit using a non-symplectic integration technique for expediency. (This is available as the BGGEXP element in the next release of elegant/Pelegant.) Although the generalized gradient expansion (GGE) uses data from the same OPERA simulations, the GGE guarantees that the fields in the interior of the analysis cylinder satisfy Maxwell’s equations.

* Work supported by the U.S. Department of Energy, Office of Science, Office of Basic Energy Sciences, under Contract No. DE-AC02-06CH11357.

ION EFFECTS IN THE APS PARTICLE ACCUMULATOR RING*

J. Calvey, K. Harkay C. Yao, ANL, Argonne, IL 60439, USA

Abstract

Trapped ions in the APS Particle Accumulator Ring (PAR) lead to a positive coherent tune shift in both planes, which increases along the PAR cycle as more ions accumulate. This effect has been studied using an ion simulation code developed at SLAC. After modifying the code to include a realistic vacuum profile, multiple ionization, and the effect of shaking the beam to measure the tune, the simulation agrees well with our measurements. This code has also been used to evaluate the possibility of ion instabilities at the high bunch charge needed for the APS-Upgrade.

INTRODUCTION

Ion trapping can occur when a negatively charged beam ionizes residual gas in an accelerator, and the resulting positively charged ions become trapped in the beam's potential. If the ion density becomes sufficiently high, coupled oscillations between the beam and ions can result. Ions can also lead to tune shifts and emittance growth.

Ion trapping has been observed in the APS Particle Accumulator Ring [1], though it does not impact normal operation. However, the planned APS-Upgrade will require much higher bunch charge to be stored in the PAR, so there is a renewed concern about ion effects. This paper describes a recent effort to study trapped ions in the PAR using coherent tune shift measurements.

Basic Theory

If the displacement of the bunch relative to the center of the ion column is small compared to the beam size, the focusing effect of the ions is linear with the displacement, and the ions' effect on the bunch can be estimated using a wakefield formalism. In particular, a coherent tune shift can readily be calculated [2]:

$$\Delta\nu_y = \frac{r_e}{3\pi\gamma} \int \frac{\beta_y \lambda_{ion}}{\sigma_y(\sigma_y + \sigma_x)} ds \quad (1)$$

Here r_e is the classical electron radius, γ is the relativistic factor, β_y is the vertical beta function, λ_{ion} is the ion line density, σ_x and σ_y are the horizontal and vertical beam sizes, and the integral is done around the ring. Assuming the ions are trapped, the line density is given by Eq. (2), where σ_{ion} is the ionization cross section, P is the pressure, k is the Boltzmann constant, T is the temperature, and n_b is the number of bunches that have passed.

$$\lambda_{ion} = \sigma_{ion} \frac{P}{kT} N_e n_b \quad (2)$$

* Work supported by the U.S. Department of Energy, Office of Science, Office of Basic Energy Sciences, under Contract No. DE-AC02-06CH11357.

PAR PARAMETERS

Some basic parameters of the PAR are given in Table 1.

Table 1: PAR Parameters

Parameter	Value
Energy	375 MeV
Design bunch charge	1 - 6 nC
Circumference	30.7 m
Rev. period	102 ns
Natural emittance	233 nm-rad
Average β_y	8.36 m
Average β_x	2.80 m
Bunch length (damped)	52 - 177 mm

The PAR cycle lasts 500 ms. At the start of the cycle, linac pulses of approximately 1 nC charge are accumulated, with a new pulse being added every 33 ms. Approximately half way through the cycle, the 12th harmonic RF cavity is turned on, reducing the bunch length by a factor of ~ 3 . The bunch is extracted into the PTB transfer line at 483 ms, leaving the PAR empty for 17 ms.

Because there is only one bunch in the PAR, it may seem strange to talk about ion trapping. But because of the large beam size ($\sigma_y \approx 200 \mu\text{m}$, $\sigma_x \approx 800 \mu\text{m}$) and short revolution time in the PAR, most ions will not be able to escape between revolutions. From the ion's point of view, the PAR cycle looks like a very long bunch train, with bunch spacing 102 ns, lasting for 483 ms. This gives the ions plenty of time to accumulate.

MEASUREMENTS

The primary evidence for ion trapping in the PAR comes from coherent tune shift measurements. The tune is measured using the bunch cleaning system [3]. The beam is excited and its spectrum is measured using a pickup stripline. An HP 89440 VSA is used to control the frequency range of the excitation, and to record the beam response. The beam is excited continuously over the cycle, but the measurement trigger can be varied using a DG535 digital delay generator. This allows us to measure the tunes at different times in the PAR cycle. Figure 1 shows the vertical tune shift as a function of charge (measured near the end of the cycle). We also measured a positive horizontal tune shift of $4 \times 10^{-4}/\text{nC}$. Additionally, we found the vertical tune shift increased when we disabled most of the PAR ion pumps, leading to higher pressure. All of these measurements point towards the presence of ions. This tune shift is not necessarily dangerous (assuming we are not near any resonances), but the ions could cause a beam instability at higher charge.

ADAPTIVE SPACE CHARGE CALCULATIONS IN MADX-SC*

Y. Alexahin[†], V. Kapin, A. Valishev, FNAL, Batavia, IL 60510, USA
F. Schmidt, R. Wasef, CERN, Geneva, Switzerland

Abstract

Since a few years MADX allows to simulate beam dynamics with frozen space charge à la Bassetti-Erskine. The limitation of simulation with a fixed distribution is somewhat overcome by an adaptive approach that consists of updating the emittances once per turn and by recalculating the Twiss parameters after certain intervals, typically every 1,000 turns to avoid an excessive slowdown of the simulations. The technique has been benchmarked for the PS machines over 800,000 turns. MADX-SC code developments are being discussed that include the re-introduction of acceleration into MADX and more advanced beam sigma calculations that will avoid code interruptions for the Twiss parameters calculation.

INTRODUCTION

With the demand for ever higher intensities [1, 2] and the SC tuneshifts already exceeding 0.5 there is a need in reliable tools for simulations which take into account the specifics of the lattice including imperfections. The PIC codes use more detailed information on the SC forces but are quite slow.

On the other hand there are codes (see references in [3, 4]) that use a predefined beam shape (usually Gaussian) for the SC kick calculations. Though this is only an approximation to the real SC distribution it greatly increases the speed making such codes suitable for simulations studies of various factors e.g. the strategy of the optics correction. It is also important that they use exact formulas for the chosen beam shape making the SC kick manifestly symplectic (at least in the 4D case), hence these codes can be referred to as *symplectic codes*.

Depending on whether the beam sizes used for the SC calculations are fixed or updated according to the evolution of the tracking particle ensemble, the model is called either *frozen* or *adaptive*. Both models are available with MADX-SC.

In the present report we discuss the MADX-SC present status and future developments.

MADX-SC CODE FEATURES

MADX-SC uses for SC simulations the BEAMBEAM elements providing kicks according to the Bassetti-Erskine formula for Gaussian bunches. The simulations take a few steps:

- preparation of the lattice (at present no name longer than 8 characters is allowed),

- insertion of the BB elements using an external program which cuts – if necessary – long elements,
- finding self-consistent optics functions and beam sizes with linear SC forces,
- tracking an ensemble of particles with *nonlinear* SC forces modulated by the particle synchrotron motion. The latter feature is activated with command *option, bb_sxy_update=true* before entering the TRACK module [5].

The requirement for the existence of the self-consistent closed optics limits the applicability of the present approach. The way to overcome this limitation is discussed in the last section.

Some new features were recently introduced in MADX-SC e.g. option *bucket_swap* which returns particle leaving the RF bucket at one end to the other end like it happens in a train of bunches.

Space Charge Kick

In order to represent the space charge kick accumulated over distance L_n the number of particles N_n in a fictitious colliding beam must be set as:

$$N_n = B_f \frac{N L_n}{C (\gamma^2 - 1)}, \quad (1)$$

where $B_f = I_{\text{peak}} / I_{\text{average}} > 1$ is the bunching factor, N is the total number of particles in the beam, C is the machine circumference and γ is the relativistic mass factor. Eq. (1) was obtained for ultra-relativistic BB elements, to work correctly with the latest versions of MADX command *option, bb_ultra_relati=true* should be issued.

Emittance Update

The tracking can be performed with either frozen or adaptive SC. Both methods have their pros and cons. The frozen SC method is faster but usually underestimates the emittance blowup and particle losses since the tunes of individual particle do not change. On the other hand, the adaptive method can strongly overestimate the blowup and the losses as the reduction in the SC tuneshift can drive new and new particles onto a resonance while in the case of frozen SC they would remain stable.

The effect of the SC tuneshift reduction will be exacerbated in simulations if the beam sizes are computed with the r.m.s. emittances which are dominated by halo particles with large amplitudes. Therefore the suppression of the halo contribution is necessary but in such a way that the core contribution was not affected.

Presently the following algorithm is implemented in MADX which uses the self-consistent optics functions to calculate the action variable values J (half the Courant-

* Work supported by Fermi Research Alliance, LLC under Contract DE-AC02-07CH11359 with the U.S. DOE

[†] alexahin@fnal.gov

GASEOUS H₂-FILLED HELICAL FOFO SNAKE FOR INITIAL 6D IONIZATION COOLING OF MUONS*

Y. Alexahin[†], FNAL, Batavia, IL 60510, USA

Abstract

H₂ gas-filled channel for 6D ionization cooling of muons is described which consists of periodically inclined solenoids of alternating polarity with 325MHz RF cavities inside them. To provide sufficient longitudinal cooling LiH wedge absorbers are placed at the minima of transverse beta-function between the solenoids. An important feature of such channel (called Helical FOFO snake) is that it can cool simultaneously muons of both signs. Theoretical considerations as well as results of simulations with G4beamline are presented.

INTRODUCTION

Ionization cooling is the only method fast enough for cooling of muons which is essential for realization of muon collider, muon beam-based neutrino factories and other experiments involving muons (see e.g. Ref. [1]). Unfortunately the longitudinal motion is naturally anti-damped in the most suitable momentum range (2-300 MeV/c) since the ionization losses decrease with momentum.

Two basic schemes were proposed in order to achieve longitudinal cooling by forcing muons with higher momentum to take a longer path in the absorber so that they lose more energy. This can be realized by creating dispersion in particle positions (without significant path lengthening) and using wedge absorbers (so called RFOFO channel [2]) or by creating sufficiently large path lengthening with momentum and using a homogeneous absorber (Helical Cooling Channel [3]).

The early versions of the so-called Helical FOFO (HFOFO) snake [4] used a third possibility: locally large path lengthening in slab absorbers due to a large slope of the dispersion function there. This allowed the FOFO snake to cool muons of both signs simultaneously.

Here we present a later version of the HFOFO snake which incorporates wedge absorbers in such a way that simultaneous cooling of μ^- and μ^+ is still possible. This allowed for smaller “snake” amplitude and improved transmission.

BASIC PRINCIPLES

The helical FOFO snake is based on the following principles: alternating solenoid focusing, periodic rotating dipole field and resonant dispersion generation [4].

The focusing magnetic field is created by a sequence of solenoids with alternating polarity and gaps between them (the name FOFO reflects the fact that solenoid focusing does not depend on polarity since it is quadratic in

magnetic field). Emittances of the two transverse normal modes** are swapped with each change of polarity so that both modes are cooled.

The transverse magnetic field component necessary for dispersion generation can be created by periodical inclination of solenoids. The idea of the HFOFO snake is to make a rotating dipole field by inclining solenoids in rotating planes $x \cdot \cos(\phi_k) + y \cdot \sin(\phi_k) = 0$, $\phi_k = \pi(1-2/N_s)(k+1)$, $k=1, 2, \dots, N_s$, N_s being the number of solenoids/period.

If $N_s=2(2j+1)$ then μ^- in solenoid $k = k_1$ see exactly the same forces as μ^+ in solenoid $k = k_1 + N_s/2$ since these solenoids have the same inclination but opposite polarity. In the result μ^- and μ^+ orbits have exactly the same form with longitudinal shift by half period ($N_s/2$ solenoids) but are not mirror-symmetric as one might expect. This allows us to find such orientation of wedge absorbers (with periodicity = 2) that they provide longitudinal cooling for both μ^- and μ^+ at the same time

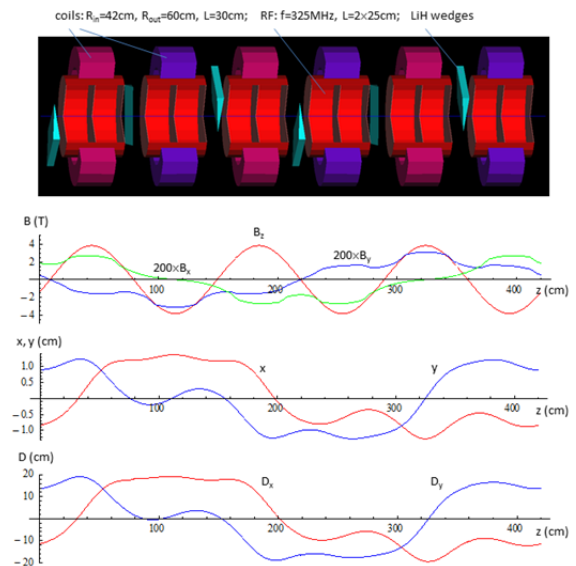


Figure 1: Top to bottom: layout of one HFOFO period, magnetic field for $p_0 = 230$ MeV/c, μ^+ equilibrium orbit and dispersion.

Large dispersion can be generated if the transverse tune Q_{\perp} is close to a resonant value. To obtain a positive momentum compaction favorable for longitudinal cooling it must be above the resonant value $Q_{\perp} > n + Q_s$, Q_s being the longitudinal mode tune. Despite closeness to a resonance the momentum acceptance of such channel can be sufficiently large owing to higher order chromatic effects.

* Work supported by Fermi Research Alliance, LLC under Contract DE-AC02-07CH11359 with the U.S. DOE

[†] alexahin@fnal.gov

** In an axisymmetric field they are cyclotron (Larmor) and drift modes (see e.g. Ref [5])

COMPUTING EIGEN-EMITTANCES FROM TRACKING DATA*

Y. Alexahin[†], Fermi National Accelerator Laboratory, Batavia, Illinois, USA

Abstract

In a strongly nonlinear system the particle distribution in the phase space may develop long tails which contribution to the covariance (sigma) matrix should be suppressed for a correct estimate of the beam emittance. A method is offered based on Gaussian approximation of the original particle distribution in the phase space (Klimontovich distribution) which leads to an equation for the sigma matrix which provides efficient suppression of the tails and cannot be obtained by simply introducing weights. This equation is easily solved by iterations in the multi-dimensional case. It is also shown how the eigen-emittances and coupled optics functions can be retrieved from the sigma matrix in a strongly coupled system.

INTRODUCTION

Finding normal mode emittances (eigen-emittances) or just second order moments from experimental or simulations data is needed for many applications, most notably in analysis of particle cooling. In the cooling process the non-Gaussian tails can develop producing a significant contribution to the second moments of the distribution. Of course we can make cuts but since the emittances are not known in advance the procedure is ambiguous.

Furthermore, besides suppression of the halo contribution, an acceptable method must also provide the exact result in absence of the halo. In the next section it is shown how to do this.

In the third section we show – using the theory developed by V. Lebedev & A. Bogacz [1] – how to find eigen-emittances and optics functions from a known covariance matrix in the case of coupled oscillations.

Finally, in the Appendix we make an estimate of the error in eigen-emittances if the mechanical momenta are used instead of the canonical ones.

GAUSSIAN FIT OF THE KLIMONTOVICH DISTRIBUTION

First let us introduce notation conventions: underlined characters will denote (column) phase space vectors, whereas upright capital letters will be used to designate matrices.

Following [2] let us choose the path length s along the reference orbit as the independent variable and dynamical variables in the form:

$$\underline{z} = \{x, P_x, y, P_y, s - c\beta_0 t, \delta\} \quad (1)$$

where $P_{x,y}$ are canonical momenta normalized by the

* Work supported by Fermi Research Alliance, LLC under Contract DE-AC02-07CH11359 with the U.S. DOE

[†] alexahin@fnal.gov

reference value $p_0 = mc\beta_0\gamma_0$:

$$P_x = (p_x + \frac{e}{c} A_x) / p_0 \quad (2)$$

with $p_{x,y}$ and $A_{x,y}$ being the components of the mechanical momentum and magnetic vector potential respectively (we use Gaussian units). Finally,

$$\delta = (\gamma - \gamma_0) / \beta_0^2 \gamma_0 \quad (3)$$

Suppose that from measurements or simulations we have a set of N particles positions in the phase space, $\underline{z}^{(k)}$, $k = 1, \dots, N$, and our task is to find the normal mode emittances. Let us first assume that the given distribution does not contain long tails (outliers) and therefore we can use simple averaging to find elements of the covariance matrix Σ :

$$\Sigma_{i,j} = \frac{1}{N} \sum_{k=1}^N \zeta_i^{(k)} \zeta_j^{(k)}, \quad \underline{\zeta}^{(k)} = \underline{z}^{(k)} - \underline{a}, \quad \underline{a} = \frac{1}{N} \sum_{k=1}^N \underline{z}^{(k)} \quad (4)$$

Now consider particle distribution in the phase space which is sometimes referred to as the Klimontovich distribution:

$$G(\underline{z}) = \frac{1}{N} \sum_{k=1}^N \delta_{6D}(\underline{z} - \underline{z}^{(k)}) \equiv \frac{1}{N} \sum_{k=1}^N \prod_{i=1}^6 \delta(z_i - z_i^{(k)}) \quad (5)$$

where δ_{6D} is the six-dimensional Dirac's δ -function.

Our task is to approximate distribution (5) with a smooth function. We will employ Gaussian distribution, though other functions (e.g. parabolic) can be used:

$$F(\underline{\zeta}) = \frac{\eta}{(2\pi)^{n/2} \sqrt{\det \Sigma}} \exp[-\frac{1}{2}(\underline{\zeta}, \Sigma^{-1} \underline{\zeta})] \quad (6)$$

where n is the dimensionality of the problem ($n = 6$ in our case) and $(\underline{a}, \underline{b})$ means a scalar product. Parameter η can be considered as the fraction of particles in the beam core.

For a moment let us replace point-like particles in distribution G with spheres of radius ρ so that G was integrable with square and later put $\rho \rightarrow 0$. Keeping ρ finite, the fitting can be formulated as a minimization problem,

$$\int_{-\infty}^{\infty} \dots \int_{-\infty}^{\infty} |F - G|^2 dz_1 \dots dz_n = \int_{-\infty}^{\infty} \dots \int_{-\infty}^{\infty} (F^2 - 2FG) dz_1 \dots dz_n + \int_{-\infty}^{\infty} \dots \int_{-\infty}^{\infty} G^2 dz_1 \dots dz_n \rightarrow \min \quad (7)$$

SIMULATING BATCH-ON-BATCH SLIP-STACKING IN THE FERMILAB RECYCLER USING A NEW MULTIPLE INTERACTING BUNCH CAPABILITY IN SYNERGIA

J. F. Amundson*, E. G. Stern, Q. Lu, R. Ainsworth, Fermilab, Batavia, Illinois

Abstract

The Recycler is an 8 GeV/c proton storage ring at Fermilab. To achieve the 700 MW beam power goals for the NOvA neutrino oscillation experiment, the Recycler accumulates 12 batches of 80 bunch trains from the Booster using slip-stacking. One set of bunch trains are injected into the ring and decelerated, then a second set is injected at the nominal momentum. The trains slip past each other longitudinally due to their momenta difference. We have recently extended the multi-bunch portion of the Synergia beam simulation program to allow co-propagation of bunch trains at different momenta. In doing so, we have expanded the applicability of the massively parallel multi-bunch physics portion of Synergia to include new categories of bunch-bunch interactions. We describe the new batch-batch capability in Synergia and present preliminary results from our first application of these capabilities to batch-on-batch slip stacking in the Recycler.

INTRODUCTION

The Fermilab accelerator complex is currently being re-configured and upgraded to meet the needs of the U.S. high-energy physics research community as defined by the Particle Physics Project Prioritization Panel (P5) report of 2014 [1]. Several steps are being taken to increase the delivered intensity from the complex. The step we study in this work is slip-stacking in the Fermilab Recycler.

THE FERMILAB RECYCLER AND SLIP-STACKING

The Recycler is a 3.3 km long permanent magnet storage ring. Being based on permanent magnets, it has only a limited energy acceptance, but it can be used to accumulate protons, through the slip-stacking procedure, during which the Recycler will receive six *batches* of 80 *bunches* each from the Fermilab Booster at its central momentum. These batches will be decelerated to a lower momentum by detuning one of two RF cavities in the Recycler. Because the batches are lower in momentum than the design momentum, their position in the ring will slip backwards relative to bunches at the design momentum. Six more batches will then be injected at the design momentum. As the batches at different momenta slip through each other, they will interact with their near neighbors through the space-charge effect. At the moment when the two sets of six batches slip into alignment they can be considered to be six double-strength batches instead of twelve single-strength batches. At that time, they will be extracted from the Recycler and injected

into the Main Injector where higher voltage RF cavities will merge and combine the different momentum bunches. See Figure 1.

Since the slip-stacking in the Recycler involves low energies and high intensities, space charge effects are of particular concern. They are also quite complex – during slip-stacking the lead bunch in Batch A passes through/near each bunch in Batch B. The second bunch in Batch similarly interacts with all but one bunch from Batch B, and so forth. By the time the two batches are combined into a new, high-intensity batch, each bunch will have a history different from every other bunch. Simulating this procedure requires significant computing resources, particularly massively parallel computing resources.

SYNERGIA

The simulation package for this work is Synergia [2, 3], an accelerator simulation framework designed to scale from desktop computer to massively parallel supercomputers. Synergia supports fully symplectic particle tracking through linear and non-linear lattice elements with arbitrary apertures. It specializes in combining single-particle tracking with a variety of collective effects for the simulation of intensity-dependent physics.

The currently released version of Synergia supports the calculation of space charge and wakefield effects in both single bunches and a train of bunches (*i.e.*, a batch.) Collective effects are incorporated in Synergia simulations using the split-operator method [4]. In general, the Hamiltonian describing the beam dynamics can be separated into single-particle and collective pieces,

$$\mathcal{H} = \mathcal{H}_{single} + \mathcal{H}_{collective}.$$

The time evolution mapping for a time step τ can be approximated:

$$\mathcal{M}(\tau) = \mathcal{M}_{single}\left(\frac{\tau}{2}\right)\mathcal{M}_{collective}(\tau)\mathcal{M}_{single}\left(\frac{\tau}{2}\right) + \mathcal{O}(\tau^3)$$

Thus the beam propagation is reduced to simulating a series of time steps. The step length τ should be chosen small enough to ensure the convergence of the results.

Single-bunch simulations

Single-bunch simulations are at the core of Synergia. A bunch of particles is evolved through the successive application of single-particle and collective operators. The single-particle operators are applied to each particle in the bunch individually, while the collective operators operate on the

* amundson@fnal.gov

DESIGN CONSIDERATIONS FOR PROPOSED FERMILAB INTEGRABLE RCS

J. Eldred and A. Valishev, FNAL, Batavia, IL 60510, USA

Abstract

Integrable optics is an innovation in particle accelerator design that provides strong nonlinear focusing while avoiding parametric resonances. One promising application of integrable optics is to overcome the traditional limits on accelerator intensity imposed by betatron tune-spread and collective instabilities. The efficacy of high-intensity integrable accelerators will be undergo comprehensive testing over the next several years at the Fermilab Integrable Optics Test Accelerator (IOTA) and the University of Maryland Electron Ring (UMER). We propose an integrable Rapid-Cycling Synchrotron (iRCS) as a replacement for the Fermilab Booster to achieve multi-MW beam power for the Fermilab high-energy neutrino program. We provide an overview of the machine parameters and discuss an approach to lattice optimization. Integrable optics requires arcs with integer- π phase advance followed by drifts with matched beta functions. We provide an example integrable lattice with features of a modern RCS - long dispersion-free drifts, low momentum compaction, superperiodicity, chromaticity correction, separate-function magnets, and bounded beta functions.

INTRODUCTION

Integrable optics is a development in particle accelerator technology that enables strong nonlinear focusing without generating parametric resonances [1]. A promising application of integrable optics is in high-intensity rings, where it is necessary to avoid resonances associated with a large betatron tune-spread while simultaneously suppressing collective instabilities with Landau damping. The efficacy of accelerator design incorporating integrable optics will undergo comprehensive experimental tests at the Fermilab Integrable Optics Test Accelerator (IOTA) [2] and the University of Maryland Electron Ring (UMER) [3] over the next several years. In this paper we discuss a potential Fermilab integrable rapid-cycling synchrotron (iRCS) as a high-intensity replacement for the Fermilab Booster.

At Fermilab, a core research priority is to improve the proton beam power for the flagship high-energy neutrino program [4]. In the current running configuration, a 700 kW 120 GeV proton beam is delivered to a carbon-target for the NuMI beamline that supports the NOvA, MINERvA, and MINOS neutrino experiments. Next, the Proton Improvement Plan II (PIP-II) will replace the 400 MeV linac with a new 800 MeV linac that will increase the 120 GeV proton power of the Fermilab complex to 1.2 MW [5].

The next flagship neutrino experiment at Fermilab will be the LBNF/DUNE [6]. The P5 Report referred to LBNF as “the highest priority project in its lifetime” and set a benchmark for a 3σ measurement of the CP-violating phase over

75% the range of its possible values [7]. The P5 benchmark for the CP-violating phase corresponds to a 900 kt·MW·year neutrino exposure requirement [4, 6]. For a 1.2 MW proton power and a 50 kt LAr detector, 15 years are required to meet that benchmark. For a 3.6 MW proton power and a 36 kt LAr detector, 7 years are required.

In order to achieve a 120 GeV proton power significantly beyond the 1.2 MW delivered by PIP-II, it will be necessary to replace the Fermilab Booster with a modern RCS [4]. The Fermilab Booster is over 45 years old and faces limitations from its magnets and its RF alike. There is no beampipe inside the dipoles and the magnet laminations generate an impedance instability. The impedance instability provides $\sim 200k$ deceleration during transition crossing at current beam intensities [8]. The Booster dipoles are combined function magnets which constrain tunability and amplify electron cloud instabilities [9]. The Booster RF cavities underwent a refurbishment process and cooling upgrade in order to achieve a 15-Hz Booster ramp rate [10] but the ramp rate will not be able to exceed 20-Hz without replacing the Booster RF entirely.

Figure 1 shows one of several siting options for an iRCS replacement for the Fermilab Booster. Neither the RCS circumference nor the injection linac length are constrained by the siting.

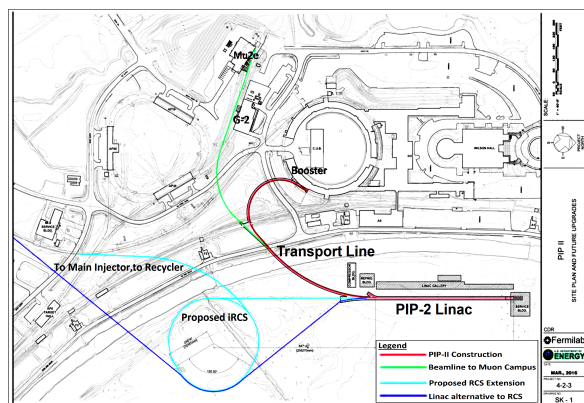


Figure 1: Site location for the proposed iRCS, relative to the PIP-II linac, muon campus, and Main Injector [11].

RCS DESIGN CONSIDERATIONS

If the PIP-II era Booster were to fill the Main Injector without slip-stacking, there would be 0.5 MW available at 120 GeV. Table 1 shows how different parameters of a replacement RCS could modify that beam power. The bolded parameters correspond to the particular scenario that relies on integrable optics and a small increase in aperture to achieve 3.6 MW of beam power.

5: Beam Dynamics and EM Fields

SIMULATION OF MULTIPACTING WITH SPACE CHARGE EFFECT IN PIP-II 650 MHz CAVITIES*

G. Romanov[#], Fermilab, Batavia, Illinois, USA

Abstract

The central element of the Proton Improvement Plan -II at Fermilab is a new 800 MeV superconducting linac, injecting into the existing Booster. Multipacting affects superconducting RF cavities in the entire range from high energy elliptical cavities to coaxial resonators for low-beta part of the linac. The extensive simulations of multipacting in the cavities with updated material properties and comparison of the results with experimental data are routinely performed during electromagnetic design at Fermilab. This work is focused on multipacting study in the low-beta and high-beta 650 MHz elliptical cavities. The new advanced computing capabilities made it possible to take the space charge effect into account in this study. The results of the simulations and new features of multipacting due to the space charge effect are discussed.

INTRODUCTION

Proton Improvement Plan-II [1] at Fermilab is a plan for improvements to the accelerator complex aimed at providing a beam power capability of at least 1 MW on target at the initiation of LBNE (Long Base Neutrino Experiment) operations. The central element of the PIP-II is a new 800 MeV superconducting linac, injecting into the existing Booster. A room temperature (RT) section of the linac accelerates H⁻ ions to 2.1 MeV and creates the desired bunch structure for injection into the superconducting (SC) linac. The superconducting part of the linac explores five superconducting cavity types operating at three different frequencies

Multipacting can affect practically all accelerating RF cavities and their components in the entire range energies and frequencies. Therefore we routinely perform the extensive simulations of multipacting (MP) as a part of RF design in each SC and RT cavities and other RF components under development (excepting SC half wave resonators since they are developed for PIP-II by other institution [2]). Also we use every opportunity to compare MP simulations with experimental data to evaluate overall reliability and accuracy of our simulation technique.

In present simulations of MP in high beta (HB, $\beta=0.9$) and low beta (LB, $\beta=0.6$) 650 MHz cavities with the use of CST Particle Studio we followed in general our practical approach described in [3]. At the same time the new advanced computing and software capabilities made it possible to take space charge effect into account in this study.

It is shown in [4] that the space charge effects play a prominent part in the secondary electron resonance dis-

charge, i.e. multipacting. In the elementary theory of multipacting and in the most MP simulation codes the space charge effect is neglected, which results in infinite growth of electron number in the calculations or in the simulations (a growth is typically exponential, but not always). Such MP dynamics is representative for the initial stages of multipacting development, and, actually, the multipacting thresholds predicted by the models without space charge effect usually are in a good agreement with the experiments. However, for the quantitative parameters of developed multipacting process such as discharge current, power, energy spectrum etc. the predictions of the elementary theory are not reliable or even cannot be done.

In principle developed multipacting is essentially a space charge limited process, and its first phenomena is a saturation of the discharge current density. During developed multipacting there are one or several bunches of electrons in RF device volume (number depends on MP order), which are well formed by phase focusing mechanism. Space charge of an electron bunch pushes peripheral particles out from phase stability interval (and possibly from area where dynamic conditions for multipacting exist). Therefore, a number of electrons constantly go out of the game. This loss of electrons is compensated by secondary electrons re-emitted at each RF cycle. Finally a dynamic equilibrium is established between losses and re-emission, and the process comes to the steady state regime in which discharge current density stops at certain level, and no infinite growth of particle number occurs [4, 5, 6].

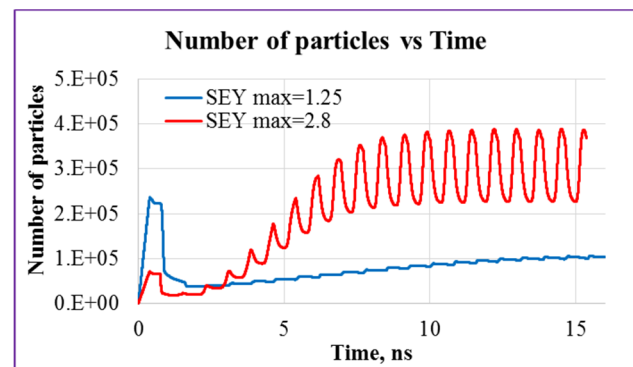


Figure 1: Typical behaviour of particle number in PIC simulations of multipacting with space charge ON. Level of particle number saturation depends on maximal SEY of the walls (simulated in PIP-II low beta 650 MHz cavity).

Following this speculation discharge current density saturation level should depend on secondary emission yield of material – the higher SEY, the higher current density. Indeed, one can see that in the simulations (see Fig.1), and that was confirmed in the experiments [7]. There is also a global limit of discharge current density, which cannot be

*Operated by Fermi Research Alliance, LLC under Contract No. DE-AC02-07CH11359 with the United States Department of Energy.

[#]gromanov@fnal.gov

MULTIPACTING IN HOM COUPLER OF LCLS-II 1.3 GHz SC CAVITY*

G. Romanov[#], A. Lunin and T. Khabiboulline, Fermilab, Batavia, Illinois, USA

Abstract

During high power tests of the 1.3 GHz LCLS-II cavity on the test stand at Fermilab an anomalous rise of temperature of the pickup antenna in the higher order mode (HOM) coupler was detected in accelerating gradient range of 5-10 MV/m. It was suggested that the multipacting in the HOM coupler may be a cause of this temperature rise. In this work the suggestion was studied, and the conditions and the location, where multipacting can develop, were found.

INTRODUCTION

During high power tests of the 1.3 GHz cavity for Linac Coherent Light Source (LCLS-II, [1]) on the test stand at Fermilab an anomaly rise of temperature of the pickup antenna in the higher order mode (HOM) coupler was detected in accelerating gradient range of 5-10 MV/m, while nominal gradient is 16 MV/m. It was suggested that multipacting (MP) in the HOM coupler may be a cause of this temperature rise due to energy deposition of MP electrons at bombardment sites. The multipactor (MP) in the HOM couplers of TESLA-type cavities is a known phenomenon that was studied already in a number of works (see [2, 3, 4] for example). Apparently the MP is not very powerful, since there is no noticeable temperature rise of other parts of HOM coupler besides the antenna. On the other hand the pickup antenna has much less effective cooling compare to the HOM coupler in general, so even a small energy deposition can heat it and be a reason of thermal runaway. Therefore we were searching MP in the given interval of accelerating gradients that would deposit energy directly on the antenna body.

The search of the MP was performed with the use of CST Studio Suite. The electromagnetic fields inside the coupler were calculated by eigenmode solver. Then the properly scaled fields were imported into PIC solver and the particle tracking was performed using our usual approach [5]. The eigenmode HOM coupler model and the fields imported into PIC solver model are shown in Fig.1.

MP IN THE NOMINAL HOM COUPLER GEOMETRY

At first the search of MP was performed in the HOM coupler of nominal geometry. In this geometry a gap of the HOM feedthrough ("coupling" gap) is 0.5 mm corresponding to the drawings. Other important gap ("filter" gap) is used to tune filtering properties of the HOM coupler. This gap is about 2 mm (the end wall is not flat, so the distance is approximate). Both gaps are shown in Fig.2.

*Operated by Fermi Research Alliance, LLC under Contract No. DE-AC02-07CH11359 with the United States Department of Energy.
[#]gromanov@fnal.gov

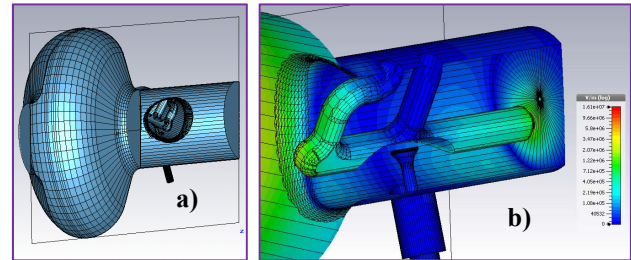


Figure 1: a) Eigenmode model of HOM coupler; b) Electric field imported into PIC model.

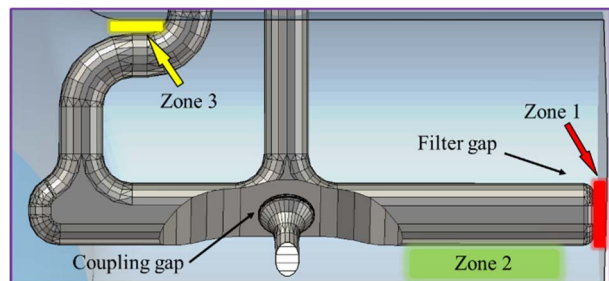


Figure 2: The known zones of multipacting.

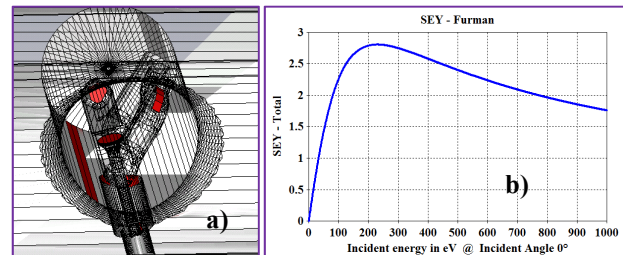


Figure 3: a) Locations of the particle sources; b) Total SEY of the wet treated niobium from CST material library.

The sources of primary electron were placed in all possible locations of MP as shown in Fig.3a. Secondary emission yield curve (SEY, also shown in Fig.3b) was taken from the CST material library. It corresponds to wet treated niobium. Obviously, a real surface is much better cleaned, but the wet treatment data was chosen deliberately because high SEY helps to find all dynamically possible MP cases.

In general, the simulations just confirmed what was found in the previous studies [2, 3, 4]: namely, there are three zones, where multipacting develops at different accelerating gradients (see Fig.2). The result in the form of $\langle \text{SEY} \rangle$ vs accelerating gradient is shown in Fig.4, where $\langle \text{SEY} \rangle$ is a ratio of total emission current to total collision current averaged over last 5 RF periods of simulation. Value of $\langle \text{SEY} \rangle$ greater than 1 indicates particle multiplication. Only one new addition to the known results is a non-resonant MP [5, 6, 7], which develops in zone 2 at $E_{\text{acc}} = 5-10$ MV/m. Usually this kind of multipacting is missed if the simulations are performed with single-trajectory tracking codes.

LINEAR LATTICE AND TRAJECTORY RECONSTRUCTION AND CORRECTION AT FAST LINEAR ACCELERATOR

A. Romanov[†], D. Edstrom, Fermilab, Batavia, IL, USA
A. Halavanau, Northern Illinois University, DeKalb, IL, USA

Abstract

The low energy part of the FAST linear accelerator based on 1.3 GHz superconducting RF cavities was successfully commissioned [1]. During commissioning, beam based model dependent methods were used to correct linear lattice and trajectory. Lattice correction algorithm is based on analysis of beam shape from profile monitors and trajectory responses to dipole correctors. Trajectory responses to field gradient variations in quadrupoles and phase variations in superconducting RF cavities were used to correct bunch offsets in quadrupoles and accelerating cavities relative to their magnetic axes. Details of used methods and experimental results are presented.

INTRODUCTION

Many of the experiments planned at the FAST linear accelerator require a beam with low emittances and well-known beam parameters along the line. Proper element positioning and calibration ensures good experimental lattice agreement with the model, but in order to finely tune the lattice parameters, beam-based methods are necessary. For example, steering the beam trajectory as close as possible to the magnetic axis of the elements not only gives better emittances, but also minimizes beam movements caused by changes in element parameters, coupled to their focusing strengths. After achieving the desired trajectory configuration, responses of the beam positions at BPMs to the corrector variations coupled with beam size analysis can give precisely tuned element parameters and determined initial conditions of the beam which allows to have relevant model of particles' distribution along the accelerator.

METHOD

Trajectory and lattice corrections consist of two independent tasks. The first task is to find the difference between the real configuration and the model. The second is to find an optimal compensation schema. Both of these tasks can be formulated as inverse problems, where the goal is to find model parameters p_i that minimize the difference between some experimental data V_{exp} and the same values calculated from the model $V_{mod}=M(p_i)$.

To find trajectory position relative to the magnetic axes of the focusing elements, it is possible to use trajectory responses to variations in the focusing strength as V_{exp} and parameters p_i are relative coordinates of the trajectory. For short elements only two coordinates can be found. For long elements with significant variation of trajectory inside the element, such as strong solenoids or strings of

RF cavities, it is possible to reconstruct both the position and the angle. At the second step, found trajectory distortions act as experimental data V_{exp} and parameters p_i are strengths of the correctors.

Lattice reconstruction is a more difficult task because of the larger amount of experimental data and number of lattice parameters involved. The following experimental data was used for the FAST lattice analysis:

- Trajectory responses to dipole correctors
- Beam second moments measured along the line

The following variable parameters of the FAST model were used:

- Gradients of magnetic fields in quadrupoles
- RF voltages in capture cavities
- RF phases in capture cavities
- Calibrations of correctors
- Calibrations of BPMs

Corrections of the lattice were straightforward, since parameters of quadrupoles and capture cavities can be adjusted individually.

DETERMINING INITIAL CONDITIONS

The minimal normalized emittances of the beam are determined by the gun configuration and can't be decreased without damping, therefore it is important to have optimal gun parameters. In an uncoupled lattice, effective transverse emittances can be easily increased by a non-zero solenoidal field at the cathode [2].

Gun setup at the FAST linear accelerator, as well as at many others, has two solenoids: main solenoid for focusing and bucking solenoid for cancelling the solenoidal field at the cathode. Gun configuration at FAST has field values in iron yokes well below saturation level and by obtaining one setting with zero field, it is possible to derive favourable conditions for a wide range of settings by keeping the found proportion.

Consider a toy model where the focusing in the gun is determined by the main solenoid and the effective emittance is determined by the bucking solenoid. In this model, the smallest spot size at some screen separated from the gun only by the drift is achieved when the field at the cathode is equal to zero. FAST setup has X101 screen for the beam size measurements separated by about 90cm drift with the gun. Realistic ASTRA simulations of FAST for the beam size at the screen X101 during main and backing solenoids scan, shown on Figure 2, confirm toy model predictions. Figure 1 shows experimental dependence of the beam size on the currents in the main and the bucking solenoids and the point of minimal size that corresponds to zero solenoidal field at the cathode.

[†] aromanov@fnal.gov

ADAPTIVE MATCHING OF THE IOTA RING LINEAR OPTICS FOR SPACE CHARGE COMPENSATION*

A. Romanov[†], A. Valishev, Fermilab, Batavia, IL, USA
D. L. Bruhwiler, N. Cook, C. Hall, RadiaSoft LLC, Boulder, CO, USA

Abstract

Many present and future accelerators must operate with high intensity beams when distortions induced by space charge forces are among major limiting factors. Betatron tune depression of above approximately 0.1 per cell leads to significant distortions of linear optics. Many aspects of machine operation depend on proper relations between lattice functions and phase advances, and can be improved with proper treatment of space charge effects. We implement an adaptive algorithm for linear lattice re-matching with full account of space charge in the linear approximation for the case of Fermilab's IOTA ring. The method is based on a search for initial second moments that give closed solution and, at the same time, satisfy predefined set of goals for emittances, beta functions, dispersions and phase advances at and between points of interest. Iterative singular value decomposition based technique is used to search for optimum by varying wide array of model parameters.

INTRODUCTION

The Integrable Optics Test Accelerator (IOTA) is under construction at Fermilab [1-3]. Figure 1 shows the IOTA ring with its main components. First stage experiments with electrons will allow to study in detail single particle dynamics in proposed nonlinear lattices. Second stage experiments with high intensity proton beams will demonstrate benefits of integrable insertions in case of operations with intense beams. Space charge forces alter the lattice structure and without proper adjustments can break the integrability of the accelerator. This work describes a re-matching method that allows to find lattice configurations in which optimal conditions for nonlinear

insertions are achieved for some predefined strength of space charge forces.

MATCHING METHOD

Only linear effects are considered in this work, which is applicable either to specially prepared bunches with Kapchinskij-Vladimirskij distribution or to particles from the core of the beam. The goal is to find such lattice configuration that will have a closed solution for a given emittance and current in presence of space charge forces. At the same time, the lattice should satisfy requirements needed for integrability.

Strong space charge effects can make intrabeam dynamics unstable in a ring tuned for a beam with negligible space charge forces. Therefore, many traditional fitting software fail at the first step of calculation of initial closed solution. There are several workarounds, for example one can gradually increase beam current while fitting necessary parameters at each step, but such approaches require a lot of manual manipulations. To overcome initial stability issues, the algorithm was developed to treat the ring lattice as a channel with some initial guess on the beam's second moments at the beginning M_{start} . In order to have a closed solution, the set of goal parameters necessary for proper ring operation is expanded with requirement to have the same second moments at the beginning of the lattice and at the end:

$$M_{start} - TM_{start}T^t \rightarrow 0, \quad (1)$$

where T is a transport matrix of a full lattice with self-forces accounted.

In case of arbitrarily coupled beam, full matrix of second moments must be matched to have a closed solution (1). For the coasting beam there is no constraints on the time correlations and, therefore, elements in the fifth row and the fifth column can differ:

$$(M_{start} - TM_{start}T^t) \cdot \text{Diag}[1,1,1,1,0,1] \rightarrow 0, \quad (2)$$

For a coasting beam in a ring without transverse coupling, the proposed approach adds 6 free and 6 goal parameters: beta functions (β_x, β_y), horizontal dispersion (D_x) and its primes at the beginning and the end of the treated lattice.

Experiment with one nonlinear magnet in IOTA ring has a set of requirements to the linear lattice, including exact values of lattice functions in the middle of the nonlinear insertion. Moving the beginning of the lattice to the

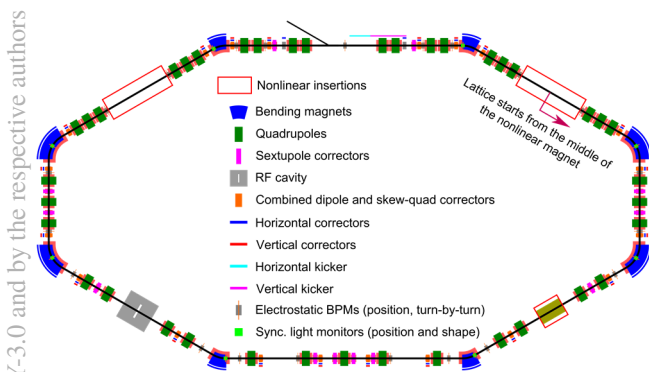


Figure 1: Schematic IOTA layout with its main components

*This work was partially supported by the US DOE Office of Science, Office of High Energy Physics, under Award Number DE-SC0011340.

[†] aromanov@fnal.gov

TESTING OF ADVANCED TECHNIQUE FOR LINEAR LATTICE AND CLOSED ORBIT CORRECTION BY MODELING ITS APPLICATION FOR IOTA RING AT FERMILAB

A. Romanov[†], Fermilab, Batavia, IL

Abstract

Many modern and most future accelerators rely on precise configuration of lattice and trajectory. The Integrable Optics Test Accelerator (IOTA) at Fermilab that is coming to final stages of construction will be used to test advanced approaches of control over particles dynamics. Various experiments planned at IOTA require high flexibility of lattice configuration as well as high precision of lattice and closed orbit control. Dense element placement does not allow to have ideal configuration of diagnostics and correctors for all planned experiments. To overcome this limitations advanced method of lattice analysis is proposed that can also be beneficial for other machines. Developed algorithm is based on LOCO approach, extended with various sets of other experimental data, such as dispersion, BPM-to-BPM phase advances, beam shape information from synchrotron light monitors, responses of closed orbit bumps to variations of focusing elements and other. Extensive modeling of corrections for a big number of random seed errors is used to illustrate benefits from developed approach.

INTRODUCTION

The Integrable Optics Test Accelerator (IOTA) is under construction at Fermilab. Its primary goal is to test advanced techniques for the stabilization of high intensity beams with highly nonlinear but integrable lattice designs. One set of experiments will be based on the use of a special nonlinear magnet that will create a big tune spread with two integrals of motion [1]. The second set of experiments will use an electron lens as a source of non-linearity [2].

Simulations show that in order to benefit from nonlinear insertions, the linear lattice should be precisely tuned. Maximal errors for the main linear parameters of the lattice are listed in Table 1. Precise measurement and correction of the ring parameters will be done with beam-based model-dependent techniques. Figure 1 shows the IOTA ring with its main components.

Table 1: Maximal Errors of the IOTA Lattice for the Integrable Optics Experiments

Parameter	Max error
Betas at the insertion	1 %
Beta beating	3 %
Dispersion	1 cm
Closed orbit at <u>insertion</u>	0.05 mm
Phase advance between insertions	0.001

aromanov@fnal.gov

To get the perfectly tuned linear lattice, IOTA will have a wide range of tools:

- Individual main quadrupole corrections
- Handy mechanical alignment design
- 20 combined X, Y and skew-quadrupole correctors
- 8 X-correctors in main dipoles
- 2 Y-correctors for the injection bump of the closed orbit
- 21 electrostatic pickups with precision of 1 μm
- Beam profile and position measurement monitors based on synchrotron light from main dipoles

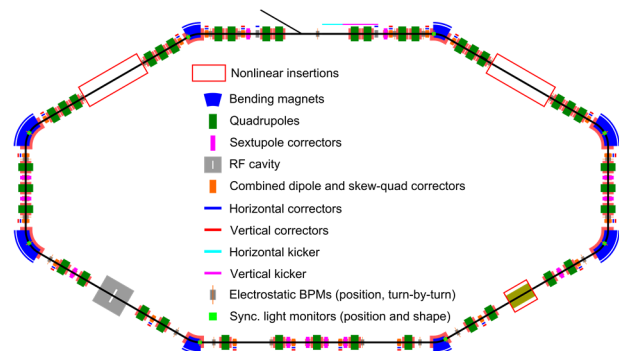


Figure 1: Schematic IOTA layout with its main components.

CORRECTION MODELING

Statistical analysis on a number of corrections applied to lattices with randomly introduced errors allows to study possible issues with the linear lattice and the closed orbit. "Sixdsimulation" software was used to analyze IOTA's configurations for all planned experiments with the nonlinear integrable systems.

The most important step in the study algorithm is the fit of pseudo-experimental data that can be done automatically or manually. In the manual mode, there are interactive tools for detailed analysis of the fit procedure. It is also possible to simulate several rounds of consecutive corrections, by using the corrected lattice at one iteration as the input for the next step.

Fitting Algorithm

Both tasks of closed orbit and linear lattice corrections can be formulated as inverse problems when some set of experimental data $V_{exp,j}$ is available and the goal is to find the parameters P_i of the model $M_j(P_i)$ that best describe the measurements. To find the approximate solution, the iterative method is used. The model parameters at iteration (n) are:

ANALYSIS OF THE TRANSPORT OF MUON POLARIZATION FOR THE FERMILAB G-2 MUON EXPERIMENT*

D. Stratakis[†], K. E. Badgley, M. E. Convery, J. P. Morgan, M. J. Syphers¹, J. C. T. Thangaraj,
Fermi National Accelerator Laboratory, Batavia IL, USA
J. D. Crnkovic, W. M. Morse, Brookhaven National Laboratory, Upton NY, USA
¹also at Northern Illinois University, DeKalb IL, USA

Abstract

The Muon g-2 Experiment at Fermilab aims to measure the anomalous magnetic moment of the muon to a precision of 140 ppb — a fourfold improvement over the 540 ppb precision obtained in BNL experiment E821. Obtaining this precision requires controlling total systematic errors at the 100 ppb level. One form of systematic error in the measurement of the anomalous magnetic moment occurs when the muon beam injected and stored in the ring has a correlation between the muon's spin direction and its momentum. In this paper, we first analyze the creation and transport of muon polarization from the production target to the g-2 storage ring. Then, we detail the spin-momentum correlations and their evolution at various beamline positions. Finally, we outline mitigation strategies that could potentially circumvent this problem.

INTRODUCTION

The Muon g-2 Experiment, at Fermilab [1], will measure the muon anomalous magnetic moment, a_μ to unprecedented precision: 0.14 parts per million. This four-fold improvement in experimental precision compared to Brookhaven's experiment [2], could establish beyond a doubt a signal for new physics if the central value of the measurement remains unchanged. To perform the experiment, a polarized beam of positive muons is injected into a storage ring with a uniform magnetic field in the vertical direction. Since the positron direction from the weak muon decay is correlated with the spin of the muon, the precession frequency is measured by counting the rate of positrons above an energy threshold versus time. The g-2 value is then proportional to the precession frequency divided by the magnetic field of the storage ring.

Most of the new experiment improvements will be based on increased statistics. Therefore, achieving the targeted precision requires optimum transmission of polarized muons within the g-2 storage ring acceptance. The goal of this paper is to develop a detailed simulation model for the Fermilab Muon g-2 experiment. In particular in this study, we analyze numerically and theoretically the creation and transport of muon polarization from the production target up to the entrance of the g-2 storage ring.

* Operated by Fermi Research Alliance, LLC under Contract No. DE-AC02-07CH11359 with the United States Department of Energy.

[†] diktys@fnal.gov

MUON CAMPUS OVERVIEW

Protons with 8 GeV kinetic energy are transported via the M1 beamline to an Inconel target at AP0. Within a 1.33 s cycle length, 16 pulses with 10^{12} protons and 120 ns full length, are arriving at the target. Secondary beam from the target will be collected using a lithium lens, and positively-charged particles with a momentum of 3.1 GeV/c ($\pm 10\%$) will be selected using a bending magnet. Secondary beam leaving the Target Station will travel through the M2 and M3 lines which are designed to capture as many muons with momentum 3.094 GeV/c from pion decay as possible. The beam will then be injected into the Delivery Ring (DR). After several revolutions around the DR, essentially all of the pions will have decayed into muons, and the muons will have separated in time from the heavier protons. A kicker will then be used to abort the protons, and the muon beam will be extracted into the new M4 line, and finally into the new M5 beamline which leads to the (g-2) storage ring. Note that the M3 line, DR, and M4 line are also designed to be used for 8 GeV proton transport by the Mu2e experiment.



Figure 1: Layout of the Fermilab Muon Campus showing the beamlines for the Muon g-2 Experiment and Mu2e Experiment.

Detailed numerical simulations [3] indicate that at the end of M5, the number of muons per proton on target (POT) within the ring acceptance $\Delta p/p = \pm 0.5\%$ is $\approx 2.0 \times 10^{-7}$. The beam is centered at 3.091 GeV/c with a spread $\Delta p/p = 1.2\%$ and is 96% polarized.

TRANSPORT OF POLARIZATION

The primary purpose of the DR [4] is to allow enough time for all pions to convert into muons. The DR is a rounded 505 m long triangle and is divided into 6 sectors numbered 10-60. Each sector contains 19 quadrupoles and 11 dipoles. Other magnetic devices include correction dipoles and sextupoles. There are three straight sections — 10, 30, and 50, which are located directly beneath service buildings AP10, 30 and 50 respectively. The straight sec-

PIP-II TRANSFER LINES DESIGN*

A. Vivoli[†], Fermilab, Batavia, IL 60510, USA

Abstract

The U.S. Particle Physics Project Prioritization Panel (P5) report encouraged the realization of Fermilab's Proton Improvement Plan II (PIP-II) to support future neutrino programs in the United States. PIP-II aims at enhancing the capabilities of the Fermilab existing accelerator complex while simultaneously providing a flexible platform for its future upgrades. The central part of PIP-II project is the construction of a new 800 MeV H⁻ Superconducting (SC) Linac together with upgrades of the Booster and Main Injector synchrotrons. New transfer lines will also be needed to deliver beam to the downstream accelerators and facilities. In this paper we present the recent development of the design of the transfer lines discussing the principles that guided their design, the constraints and requirements imposed by the existing accelerator complex and the following modifications implemented to comply with a better understanding of the limitations and further requirements that emerged during the development of the project.

INTRODUCTION

PIP-II project envisions the construction of a new SC Linac, able to run in pulsed and CW mode, to increase the proton beam intensity available at Fermilab for its future experiments [1]. The project includes upgrades of the current synchrotrons chain (Booster, Recycler and Main Injector) and transfer lines to connect the new Linac to the rest of the accelerator complex. In particular, the main transfer line we present in this paper will transport the beam from the end of the SC Linac to the Booster. A second line is also presented to transport the beam to a possible upgrade of Mu2e experiment [2], to be built in the future.

A first design of the transfer lines was already presented [3], but a better understanding of the constraints and limitations raising with the development of the project made some modifications necessary. The main changes discussed here are the revision of the design of the transfer line to the Booster to resolve interferences with existing beamlines and infrastructures at Fermilab, design of the Dump line and revision of the switching system to support beam based energy stabilization and redirection of the beam to Mu2e future upgrade and consequent modifications of the transport line to Mu2e upgrade.

TRANSPORT TO BOOSTER

A CAD drawing of the SC Linac, including ion source and warm front end, with the transfer lines on the picture of the Fermilab site is presented in Fig. 1.

The first part of the transfer line is reserved for the pos-

sible future upgrade of the PIP-II Linac and is located in the straight extension of the Linac tunnel. The lattice consists of 4 doublet periods of the same length of the periods of the last section of the SC Linac, where cryomodels are installed between doublets, such that it is possible in the future to install additional cryomodels to increase the final energy of the SC Linac from 800 MeV to 1.2 GeV. The 4 doublets in this section can be used for matching the beam to the downstream line.

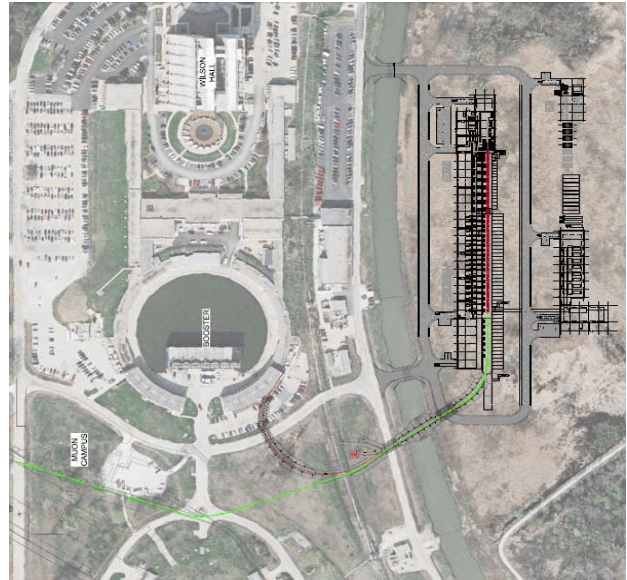


Figure 1: Drawing of SC Linac and transfer lines on the Fermilab site.

The injection into the Booster is vertical, with the final part of the transfer line being aligned with the injection straight of the Booster. At the beginning of this section the beam is brought at an elevation of 33.6 cm above the Booster plane by a magnetic dog-leg created by 2 dipole magnets and at the end of the section a vertical C-dipole bends the beam into the Booster injection magnets.

Between the energy upgrade and the injection sections the beam is transported by a FODO lattice. In the previous design the first 4 cells had dipoles between the quadrupoles forming the 1st arc, followed by 2 cells with no bends forming a straight transport and other 12 cells with bends forming the 2nd arc. The cell length was determined by the geometry of the accelerator complex and the strengths of the quadrupoles were chosen to have 90 deg. phase advance both horizontally and vertically. The dipole magnets were planned to be 2.45 m long and have a magnetic field of 2.36 kG. This was just below the value of 2.39 kG, fixed as a safe limit to avoid Lorentz stripping [4]. Note also that the choice of the phase advances per cell ensured both of the arcs to be achromatic.

With the development of the project, studies of possible interferences of the PIP-II design with existing accelera-

* Work supported by Fermi Research Alliance, LLC under Contract No. DE-AC02-07CH11359 with the United States Department of Energy.

[†] vivoli@fnal.gov

SCHARGEV 1.0 - STRONG SPACE CHARGE VLASOV SOLVER *

T. Zolkin[†], A. Burov, Fermilab, Batavia IL 60510, USA

Abstract

The space charge (SC) is known to be one of the major limitations for the collective transverse beam stability. When space charge is strong, i.e. SC tune shift \gg synchrotron tune Q_s , the problem allows an exact analytical solution. For that practically important case we present a fast and effective Vlasov solver SCHARGEV (Space CHARGE Vlasov) which calculates a complete eigensystem (spatial shapes of modes and frequency spectra) and therefore provides the growth rates and the thresholds of instabilities. SCHARGEV 1.0 includes driving and detuning wake forces, and, any feedback system (damper). In the next version we will include coupled bunch interaction and Landau damping. Numerical examples for FermiLab Recycler and CERN SPS are presented.

INTRODUCTION

SCHARGEV 1.0 is based on SSC theory developed in [1–3]. In this section we will briefly summarize its results for a single bunch with longitudinal distribution function $f(\tau, v)$ where τ is the position along the bunch measured in radians and v is the particle longitudinal velocity. Solutions describing transverse modes for zero-wake case (SSC harmonics $[v_k, Y_k(\tau)]$) form an orthonormal basis $\int \rho(\tau) Y_l(\tau) Y_m(\tau) d\tau = \delta_{lm}$ and satisfy

$$\begin{cases} \frac{1}{Q_{\text{eff}}(\tau)} \frac{d}{d\tau} \left(u^2(\tau) \frac{dY(\tau)}{d\tau} \right) + v Y(\tau) = 0, \\ \left. \frac{d}{d\tau} Y(\tau) \right|_{\tau=\pm\infty} = 0, \end{cases}$$

where Q_{eff} is the effective space charge tune shift

$$Q_{\text{eff}}(\tau) = Q_{\text{eff}}(0) \frac{\rho(\tau)}{\rho(0)},$$

ρ is the normalized line density

$$\rho(\tau) = \int f(\tau, v) dv : \quad \int \rho(\tau) d\tau = 1,$$

and temperature function u^2 is the average square of particle longitudinal velocity

$$u^2(\tau) = \int f(\tau, v) v^2 dv \Big/ \rho(\tau).$$

The modified dynamic equation including the wake and the damper is

$$\frac{1}{Q_{\text{eff}}(\tau)} \frac{d}{d\tau} \left(u^2(\tau) \frac{d\mathcal{Y}(\tau)}{d\tau} \right) + \omega \mathcal{Y}(\tau) = \left[\varkappa (\widehat{W} + \widehat{D}) - i g e^{i\psi} \widehat{G} \right] \mathcal{Y}(\tau).$$

The operators of wake forces are defined in terms of driving and detuning wakes, respectively

$$\begin{aligned} \widehat{W} Y(\tau) &= \int_{\tau}^{\infty} W(\tau - \sigma) \rho(\sigma) Y(\sigma) e^{i\zeta(\tau - \sigma)} d\sigma, \\ \widehat{D} Y(\tau) &= Y(\tau) \int_{\tau}^{\infty} D(\tau - \sigma) \rho(\sigma) d\sigma, \end{aligned}$$

where the lower limit guarantees the causality, i.e. $\sigma > \tau$. $\zeta = -\xi/\eta$ is the negated ratio of conventional chromaticity, ξ , and a slippage factor, $\eta = \gamma_1^{-2} - \gamma^{-2}$.

$$\varkappa = N_b \frac{r_0 R_0}{4\pi \gamma \beta^2 Q_\beta}$$

where N_b is the number of particles per bunch, r_0 is the classical radius of the beam particle, R_0 is the average accelerator ring radius, Q_β as the bare betatron tune, γ is Lorentz factor and β is the ratio of particle velocity to speed of light.

The operator of damper is defined through the pickup $P(\tau)$ and kicker $K(\tau)$ functions

$$\widehat{G} Y(\tau) = K(\tau) \int_{-\infty}^{\infty} P(\sigma) \rho(\sigma) Y(\sigma) e^{i\zeta(\tau - \sigma)} d\sigma.$$

g and ψ are the dimensionless gain and the damper's phase. The convention is such that resistive damper defined as $g > 0$ and $\psi = 0$, and, $\psi = \pm\pi/2$ are focusing and defocussing reactive dampers respectively.

Expansion over the zero-wake basis of SSC harmonics

$$\mathcal{Y}_k(\tau) = \sum_{i=0}^{\infty} \mathbf{C}_i^{(k)} Y_i(\tau)$$

leads to the eigenvalue problem $\mathbf{M} \cdot \mathbf{C}^{(k)} = \omega_k \mathbf{C}^{(k)}$ where the matrix \mathbf{M} depends on head-tail phase ζ

$$\mathbf{M}_{lm} = v_l \delta_{lm} + \varkappa \left[\widehat{W}_{lm}(\zeta) + \widehat{D}_{lm} \right] - i g e^{i\psi} \widehat{G}_{lm}(\zeta)$$

with matrix elements being

$$\begin{aligned} \widehat{W}_{lm} &= \int_{-\infty}^{\infty} \int_{\tau}^{\infty} d\sigma d\tau \\ &\quad W(\tau - \sigma) \rho(\tau) \rho(\sigma) Y_l(\tau) Y_m(\sigma) e^{i\zeta(\tau - \sigma)}, \\ \widehat{D}_{lm} &= \int_{-\infty}^{\infty} \int_{\tau}^{\infty} d\sigma d\tau D(\tau - \sigma) \rho(\tau) \rho(\sigma) Y_l(\tau) Y_m(\tau), \\ \widehat{G}_{lm} &= K_l(\zeta) P_m^*(\zeta), \quad \text{where} \\ P_k &= \int_{-\infty}^{\infty} d\tau P(\tau) \rho(\tau) Y_k(\tau) e^{i\zeta\tau}, \\ K_k &= \int_{-\infty}^{\infty} d\tau K(\tau) \rho(\tau) Y_k(\tau) e^{i\zeta\tau}. \end{aligned}$$

For the sake of convenience we will separate real and imaginary parts of eigenvalues and denote them as $\omega_k = \Delta_k + i\Gamma_k$.

* Fermi National Accelerator Laboratory (Fermilab) is operated by Fermi Research Alliance, LLC, for the U.S. Department of Energy under contract DE-AC02-07CH11359.

[†] zolkin@fnal.gov

SECTOR MAGNETS OR TRANSVERSE ELECTROMAGNETIC FIELDS IN CYLINDRICAL COORDINATES *

T. Zolkin[†], Fermilab, Batavia IL 60510, USA

Abstract

Laplace's equation in normalized cylindrical coordinates is considered for scalar and vector potentials describing electric or magnetic fields with invariance along the azimuthal coordinate [1]. A series of special functions are found which when expanded to lowest order in power series in radial and vertical coordinates ($\rho = 1$ and $y = 0$) replicate harmonic homogeneous polynomials in two variables. These functions are based on radial harmonics found by Edwin M. McMillan forty years ago. In addition to McMillan's harmonics, a second family of radial harmonics is introduced to provide a symmetric description between electric and magnetic fields and to describe fields and potentials in terms of the same functions. Formulas are provided which relate any transverse fields specified by the coefficients in the power series expansion in radial or vertical planes in cylindrical coordinates with the set of new functions.

This result is important for potential theory and for theoretical study, design and proper modeling of sector dipoles, combined function dipoles and any general sector element for accelerator physics and spectrometry.

INTRODUCTION

The description of sector magnets, any curved magnet symmetric along its azimuthal (longitudinal) cylindrical coordinate, is an important issue. Every modern accelerator code includes such elements, the most important being combined function dipoles. A widely used method, which goes back to Karl Brown's 1968 paper [2], is based on a solution of Laplace's equation for a scalar potential using a power series in cylindrical coordinates. A similar approach applied to Laplace's equation for the longitudinal component of a vector potential can be found for example in [3]. The same approach appears in more recent books, e.g. [4].

Two major bottlenecks should be noticed. First, if one looks for a solution in the form of a series, then these series must be truncated. In our case truncation means that potentials no longer satisfy Laplace's equation. Of course potentials can "satisfy" Laplace's equation up to any desired order by keeping more and more terms in the expansion, but they are not exact. More importantly, the recurrence equation is undetermined: in every new order of recurrence one has to assign an arbitrary constant, which will affect all other higher order terms. This ambiguity leads to the fact that there is no preferred, unique choice of basis functions; it makes it difficult to compare accelerator codes, since differ-

ent assumptions might be used for representations of basis functions.

This indeterminacy has a simple geometrical illustration. Looking for a field with e.g. pure normal dipole component on a circular designed equilibrium orbit in lowest order, one can come up with an almost arbitrary shape of the magnet's north pole if its south pole is symmetric with respect to the midplane. In the case of a dipole, the series can be truncated by keeping only its dipole component. For higher order multipoles in cylindrical coordinates truncation without violation of Laplace's equation is not possible.

While working on an implementation of sector magnets for Synergia, I found assumptions which let me sum series for pure electric and magnetic skew and normal multipoles. Looking further for symmetry in the description allowed me to generate a family of solutions in which all the series could be summed, so that no truncation was required. While discussing my results with Sergei Nagaitsev, he brought my attention to an article by McMillan written in 1975 [5]. As I found later, the same result was independently obtained by S. Mane and published in the same journal about 20 years later [6] without citing McMillan's original work. It made me to write this article in order to bring attention back to these forgotten results.

Joining my results to McMillan's, I would like to present a new representation for multipole expansions in cylindrical coordinates. Any transverse field can be expanded in terms of these functions and related to power series expansions in horizontal or vertical planes. The new approach does not contradict previous results but embraces them. The ambiguity in choice of coefficients and the problem of truncation are resolved. Thus it can be employed for theoretical studies, design and simulation of sector magnets.

The expansion of static electromagnetic fields with rotational symmetry about vertical axis, y , is derived in right-handed normalized cylindrical coordinates $(\hat{\mathbf{e}}_\rho, \hat{\mathbf{e}}_y, \hat{\mathbf{e}}_\theta)$. Sometimes sector coordinates $(\hat{\mathbf{e}}_x, \hat{\mathbf{e}}_y, \hat{\mathbf{e}}_\theta)$ are used instead. They defined as another orthogonal right-handed normalized system of coordinates with $\rho = x + 1$. It is in sector coordinates scalar potential Φ and only one nonvanishing component of vector potential A_θ , when expanded at $x, y = 0$, reproduce harmonic homogeneous polynomials in the lowest order of expansion.

The paper is structured as follows. In first section we consider pure transverse electric or magnetic fields in cylindrical coordinates. In the second one we compare new results with traditional approach of power series ansatz. Tables 1–2 are supplementary materials with sector harmonics and its relationship with power series expansion of fields.

* Fermi National Accelerator Laboratory (Fermilab) is operated by Fermi Research Alliance, LLC, for the U.S. Department of Energy under contract DE-AC02-07CH11359.

[†] zolkin@fnal.gov

SENSITIVITY OF THE MICROBUNCHING INSTABILITY TO IRREGULARITIES IN CATHODE CURRENT IN THE LCLS-II BEAM DELIVERY SYSTEM*

C. Mitchell[†], J. Qiang, M. Venturini, LBNL, Berkeley, CA 94720, USA
P. Emma, SLAC, Menlo Park, CA 94025, USA

Abstract

LCLS-II is a high-repetition rate (1 MHz) Free Electron Laser (FEL) X-ray light source now under construction at SLAC National Accelerator Laboratory. During transport to the FEL undulators, the electron beam is subject to a space charge-driven microbunching instability that can degrade the electron beam quality and lower the FEL performance if left uncontrolled. The present LCLS-II design is well-optimized to control the growth of this instability out of the electron beam shot noise. However, the instability may also be seeded by irregularities in the beam current profile at the cathode (due to non-uniformities in the temporal profile of the photogun drive laser pulse). In this paper, we describe the sensitivity of the microbunching instability to small-amplitude temporal modulations on the emitted beam current profile at the cathode, using high-resolution simulations of the LCLS-II beam delivery system.

INTRODUCTION

The microbunching instability plays a significant role in the dynamics of electron beam transport for 4th generation light sources, and much of the LCLS-II design effort [1] has been devoted to understanding microbunching phenomena seeded by the electron beam shot noise in the LCLS-II beam delivery system [2]. The present LCLS-II design has been well-optimized to control these effects through careful tuning of the local momentum compaction of the lattice [3], but irregularities in the temporal profile of the emitted bunch current at the photocathode may also seed the instability [4], originating from non-uniformities of the photocathode drive laser pulse (if the beam is generated using a single pulse) or pulse-to-pulse variations of drive laser power (if the beam is generated through longitudinal stacking).

Table 1 describes the nominal 100 pC beam that is used in this study. The nominal emitted current profile is uniform along the bunch, with linear rise and fall over a 2 ps interval at either end. We investigate the effect of adding a small-amplitude modulation to the initial current profile, so that the bunch current is described by ($\chi \ll 1$):

$$I(t) = I_0(1 + \chi \cos(2\pi t/\tau)), \quad \tau \in [1, 9] \text{ ps}. \quad (1)$$

All simulations are performed using the IMPACT code suite [5, 6], and begin with initialization of the electron beam at the photocathode. To correctly resolve the beam shot noise, we use a number of simulation particles equal to the

number of electrons in the physical bunch (625M), with a grid resolution of $64 \times 64 \times 2048$.

Table 1: Parameters describing the nominal 100 pC beam used for single-bunch cathode-undulator tracking. Final values are provided at the entrance to the first hard X-ray FEL undulator.

Parameter	Value
Bunch charge	100 pC
Transverse beam size at the cathode (rms)	0.192 mm
Thermal emittance at the cathode (rms)	1 $\mu\text{m}/\text{mm}$
Initial bunch duration (FWHM)	33 ps
Final kinetic energy	4.1 GeV
Final peak current (beam core)	714 A
Final slice emittance $\epsilon_{x,n}$ (rms, beam core)	0.48 μm
Final slice emittance $\epsilon_{y,n}$ (rms, beam core)	0.38 μm
Final slice energy spread (rms, beam core)	562 keV

MICROBUNCHING IN THE PHOTOINJECTOR

Figure 1 illustrates the amplitudes of the density and energy modulations present on the bunch at the exit of the first cryomodule (~ 100 MeV). The results are quite linear in the amplitude of the cathode-applied modulation up to $\chi = 5 - 10\%$. The results using 5M and 625M simulation particles are similar, suggesting that the applied modulation dominates the effect of shot-noise seeded microbunching in this region. Ballistic compression in the photoinjector system is expected to contribute to enhanced spatial bunching [4]. However, simulations indicate that any short-wavelength density modulation present on the bunch at the first RF cavity entrance is damped rapidly during acceleration, reappearing as increased modulation in the bunch slice energy profile.

Adiabatic Phase Damping of Plasma Oscillations

The transformation of modulations from density profile to energy profile during acceleration is closely related to the phenomenon of adiabatic synchrotron phase damping, and can be understood as follows. We model microbunching in the cryomodule using the integral equations in [7], assuming

* Work supported by the U.S. Department of Energy under Contract Nos. DE-AC02-76SF00515, DE-AC02-05CH11231, and the LCLS-II Project.

[†] ChadMitchell@lbl.gov

A PRELIMINARY BEAM IMPEDANCE MODEL OF THE ADVANCED LIGHT SOURCE UPGRADE AT LBL*

S. Persichelli[†], J. M. Byrd, S. De Santis, D. Li, T. Luo, J. Osborn, C. A. Swenson, M. Venturini, Y. Yang, LBL, Berkeley, CA, USA

Abstract

The proposed upgrade of the Advanced Light Source (ALS-U) consists of a multi-bend achromat ultralow emittance lattice optimized for the production of diffraction-limited soft x-rays. A narrow-aperture vacuum chamber is a key feature of the new generation of light sources, and can result in a significant increase in the beam impedance, potentially limiting the maximum achievable beam current. While the conceptual design of the vacuum system is still in a very early development stage, this paper presents a preliminary estimate of the beam impedance using a combination of electromagnetic simulations and analytical calculations. We include the impedance of cavities, select vacuum-chamber components and resistive wall in a multi-layered beam chamber with NEG coating.

INTRODUCTION

ALS-U is a proposed upgrade to the Advanced Light Source (ALS) at LBNL. Operating at beam energy of 2 GeV and current of 500 mA, the intent of ALS-U is to produce soft x-ray coherent flux that is orders of magnitude higher than at the existing machine at LBNL and well beyond the coherent flux at any operating light source. The upgrade program includes the replacement in the storage ring of the existing triple-bend achromat with a multi-bend achromat lattice, keeping the same footprint, symmetry and length of the straight sections of ALS. Moreover, a new low emittance accumulator ring will be installed in the existing tunnel, with the purpose of enabling swap-out injection using fast magnets. In order to improve the performances of insertion devices and allow for the larger focusing gradients needed for low emittance, extremely small vacuum chamber apertures are a key feature of ALS-U which will enhance the sensitivity to instabilities driven by collective effects. In this paper we start to address the problem by calculating the beam coupling impedance contributed by the resistive wall, main and harmonic cavities and the vacuum-chamber egresses collecting the radiation fan from the undulators.

RESISTIVE WALL

In ALS-U, the triple-bend achromat magnetic lattice of ALS is replaced with a stronger focusing multi-bend achromat. The high focussing strength and compact magnet design is achieved by using a small circular, or nearly circular, vacuum chamber of the order of 10 mm radius or less. The

* Work supported by the Director, Office of Science, of the U.S. Department of Energy under Contract No. DE-AC02-05CH11231

[†] spersichelli@lbl.gov

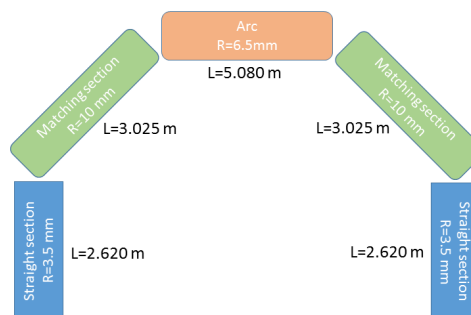


Figure 1: A sketch of an ALS-U sector.

limited conductance and pumping speed is mitigated by using non-evaporable getter (NEG) coated vacuum chambers. The vacuum chamber of ALS-U is designed with apertures about 2.5 times smaller than the current ALS in the vertical direction and much smaller in the horizontal. Therefore, the transverse resistive wall (RW) impedance is expected to be critical for the new machine performance. Ensuring good vacuum will require NEG coating ideally in the whole machine. In this approach, the whole vacuum chamber acts like a fully distributed vacuum pump, achieving good vacuum pressures with the small apertures required from ALS-U. In this section we are presenting the results of resistive wall impedance calculations, taking into account the effect of the NEG coating. To this end, we considered a simplified model of the ALS-U circular vacuum chamber consisting of three different radii: 3.5 mm for the insertion devices in the straight sections (total length 62.88 m), 10 mm radius in matching sections (total length 72.60 m) and 6.5 mm in the arcs (total length 60.96 m). A sketch of an ALS-U sector is shown Fig. 1. It is worth noting that while the longitudinal RW impedance is inversely proportional to the beam pipe radius, the transverse impedance has a strong third-power scaling with the inverse of the radius. Due to the very small radius of the chamber, we expect the insertion device sections to have a dominant impact in the transverse impedance budget. Longitudinal and transverse RW impedance has been computed with the code *ImpedanceWake2D* developed at CERN [1]. The code calculates coupling impedances and wake functions in multilayer axi-symmetric two-dimensional structures. We considered a round vacuum chamber made of copper, coated with a 1 μm thickness layer of NEG. Resistivity of copper is $1.7 \cdot 10^{-8} \Omega\text{m}$, while the NEG resistivity is assumed to be $1.5 \cdot 10^{-6} \Omega\text{m}$ [2]. In Figures 2 and 3, the real and imaginary part of the longitudinal and transverse RW impedance are shown. At the nominal ALS-U bunch length of about 200 ps, the imaginary part of the longitudi-

ANALYSIS OF MICROBUNCHING STRUCTURES IN TRANSVERSE AND LONGITUDINAL PHASE SPACES*

C. -Y. Tsai[#], Department of Physics, Virginia Tech, VA 24061, USA
R. Li, Jefferson Lab, Newport News, VA 23606, USA

Abstract

Microbunching instability (MBI) has been a challenging issue in high-brightness electron beam transport for modern accelerators. Our Vlasov analysis of MBI is based on single-pass configuration [1-3]. For multi-pass recirculation or a long beamline, the intuitive argument of quantifying MBI, by successive multiplication of MBI gains of sub-beamline sections, was found to underestimate the effect [4]. More thorough analyses based on concatenation of gain matrices aimed to combine both density and energy modulations for a general beamline [4]. Yet, quantification still focuses on characterizing longitudinal phase space; microbunching structures residing in (x, z) or (x', z) was observed in particle tracking simulation. Inclusion of such cross-plane microbunching structures in Vlasov analysis shall be a crucial step to systematically characterize MBI for a beamline complex in terms of concatenating individual beamline segments. We derived a semi-analytical formulation to include the microbunching structures in longitudinal and transverse phase spaces. Using these generalized formulas, we studied an example lattice [5] and found the microbunching gains calculated from multiplication of concatenated gain matrices can be considered as upper limit to the start-to-end gains.

INTRODUCTION

Theoretical formulation of MBI has been developed both in single-pass [1-3] and in storage-ring [6,7] systems. Hetfeis *et al.* [2] derived a linear integral equation in terms of the density modulation (or, the bunching factor). Huang and Kim [3] obtained the integral equation in a more concise way and outlined the microbunching due to initial energy modulation. This has become the building block for our work.

To quantify MBI in a beam transport system, we estimate the microbunching amplification factor (or, gain) along the beamline. For a long transport line of a recirculation machine, people tend to treat the microbunching problem as a single-pass system. More commonly, concatenations of sub-beamline sections were studied and the overall microbunching gain is speculated as the multiplication of gains from individual subsections [2, 8]. Though this concatenation approach seems intuitive, we need a more rigorous and detailed justification of its validity. Our previous work [4], which

takes both density (z) and energy (z, δ) modulations in longitudinal beam phase-space distribution, had shown that a mere product of microbunching gains from individual subsections could underestimate the overall effect (i.e. smaller than the start-to-end gain).

In this paper, we take a further step, consider the situation where microbunching structures residing in transverse-longitudinal dimension (x, z) or (x', z) can be quantified, and derive a set of governing equations for the microbunching evolution in terms of density, energy, transverse-longitudinal modulations along a general linear lattice. Then we study an example of recirculating beamline [5]. From the simulation results, we have some interesting observations and have found such combined analysis can give more information than the previous treatment. Although the formulation still appears incomplete, the gains calculated from multiplication of concatenated gain matrices can be considered as upper limit to the start-to-end gains. Comparison of the results with ELEGANT tracking [9] has given qualitative agreement. Extension of this study to include more aspects of microbunching can be possible future work.

THEORY

From the (linearized) Vlasov equation, the evolution of the phase-space distribution function is governed by [3]

$$f(X; s) = f_0(X_0) - \int_0^s d\tau \frac{\partial f_0(X_\tau)}{\partial \delta_\tau} \frac{d\delta}{d\tau} \quad (1)$$

where the energy change due to collective effect can be induced by density modulation

$$\frac{d\delta}{d\tau} = -\frac{Nr_e}{\gamma} \int \frac{dk_1}{2\pi} Z(k_1; \tau) b(k_1; \tau) e^{ik_1 z_\tau} \quad (2)$$

Here f is the beam phase-space distribution function, $X(s) = (x, x', z, \delta; s)$ the 4-D phase-space variable, N the number of particles, γ the Lorentz factor, $Z(k)$ the longitudinal impedance per unit length, k the modulation wavenumber, and $b(k)$ the density modulation.

More specifically, let us define the following quantities for subsequent analysis.

$$b(k_z; s) = \frac{1}{N} \int dX f(X; s) e^{-ik_z(s)z_s} \quad (3)$$

$$p(k_z; s) = \frac{1}{N} \int dX (\delta_s - h z_s) f(X; s) e^{-ik_z(s)z_s} \quad (4)$$

$$a_x(k_z; s) = \frac{1}{N} \int dX (x_s) f(X; s) e^{-ik_z(s)z_s} \quad (5)$$

$$a_{x'}(k_z; s) = \frac{1}{N} \int dX (x'_s) f(X; s) e^{-ik_z(s)z_s} \quad (6)$$

Figure 1 illustrates the modulations described by Eqs. (3-6), shown in (a) to (d), respectively.

* This material is based upon work supported by the U.S. Department of Energy, Office of Science, Office of Nuclear Physics under contract DE-AC05-06OR23177.
#jcytsai@vt.edu

STUDY OF 2D CSR EFFECTS IN A COMPRESSION CHICANE

C. C. Hall*, RadiaSoft, Boulder, CO, USA

S. G. Biedron, S. V. Milton, Colorado State University, Fort Collins, CO, USA

Abstract

The study of coherent synchrotron radiation (CSR) has been an area of great interest because of its negative impact on FEL performance. The modeling of CSR is frequently performed using a 1D approximation, as 2D and 3D models can become extremely computational intensive. While experimental evidence is lacking in this area most studies show reasonable agreement between 1D and 2D CSR models for beam parameters in existing accelerators. In this work we focus on 2D modeling of CSR in a four-dipole chicane lattice based on the Jefferson Lab FEL. Comparison is shown between several models and measurement for energy loss due to CSR in the chicane. While good agreement is generally observed we also present investigation of several key differences observed in simulation. In particular, showing how the 1D and 2D CSR models deviate in regards to CSR and beam interaction within the drift spaces of the chicane and the downstream drift at the chicane end.

INTRODUCTION

Particle accelerator based light sources such as free-electron lasers (FELs) have made possible the production of extremely intense, short-wavelength light at UV and x-ray wavelengths. The FEL relies on the collective emission of the electron bunch to produce coherent light to reach very high intensities. However, the electron bunches are also susceptible to undesirable coherent effects during transport, which may lead to a reduction in lasing efficiency during the FEL process. Coherent synchrotron radiation (CSR) is one such collective effect that can cause undesirable rises in emittance and energy spread of the bunch. CSR may also be a concern in the proposed electron-ion collider project [1,2], where it may drive the microbunching instability in the electron beam for the ion cooler section [3].

Modeling of CSR in accelerators is complicated by the fact that it is a collective effect that arises from the interaction of particles in a bunch. A brute force calculation of the Lienard–Wiechert fields governing this interaction is far too slow even when using a modest number, on the order of $1E4$, of macroparticles. Because of this it is common to adopt a 1D approximation [4] that assumes the bunch may be modeled as a projection of the density onto a line parallel to its longitudinal propagation. This model simplifies the calculation of the CSR field to a single integral which may be easily computed numerically. Good agreement between simulation utilizing the 1D model and experiment has been shown in a number of experiments [5–7].

However, this 1D model may be prone to overestimating the impact of CSR. By condensing the bunch down to a line

charge and removing any transverse extent from the calculation the interaction of electrons may be overestimated. This is particularly of concern since CSR is often being generated in magnetic compression chicanes where dispersion from the dipoles will cause the bunch to be spread out in the bending plane.

In this work we will show results using a 2D CSR simulation in the XZ plane performed with the code CSRtrack. Results with the 2D simulation are compared against previous work studying energy loss through the chicane of the Jefferson Laboratory ERL FEL driver [7]. Overall, good agreement is still observed between 1D and 2D CSR models from CSRtrack and simulations with the particle tracking code ELEGANT. A closer look at how the bunch is losing energy as it passes through the chicane shows several peculiarities which seem to be uniquely 2D effects and are not captured in the 1D CSR simulations.

Table 1: Parameters for the Chicane and Bunch used in Simulation

Parameter	Value
Chicane R_{56}	0.52 m
Bunch energy	135 MeV
Bunch charge	135 pC
Bunch length at max compression	150 fs

DESCRIPTION OF THE SIMULATIONS

For these simulations we use the parameters of the JLab IR FEL optical cavity chicane [8], which are given in Table 1. Our goal is to look at energy loss of the bunch due to CSR as a function of the level of compression the bunch achieves at the end of the chicane. By varying the chirp on the bunch, defined as

$$h = \frac{1}{E_{avg}} \frac{dE}{dz}, \quad (1)$$

or by varying the linear momentum compaction, R_{56} , the bunch length at the chicane entrance σ_{z0} will be changed by

$$\sigma_{zf} = (1 - hR_{56})\sigma_{z0}. \quad (2)$$

When the quantity $hR_{56} > 1$ the bunch will not achieve full compression at the end of the chicane and the bunch is said to be under-compressed. For values of $hR_{56} < 1$ the bunch passes through full compression before growing longer at the chicane exit and the bunch is said to be over-compressed. Of course, when $hR_{56} = 1$ the bunch will achieve maximum compression at the end of the chicane and we will refer to this as critically compressed.

* chall@radiasoft.net

SIMULATIONS OF HOLE INJECTION IN DIAMOND DETECTORS*

G. I. Bell[†], D. Dimitrov, C.D. Zhou, Tech-X Corp, Boulder, CO, 80303, USA
 I. Ben-Zvi, J. Smedley, T. Rao, Brookhaven National Lab, Upton, NY, 11973, USA
 E. Muller, M. Gaowei, Stony Brook University, Stony Brook, NY, 11794, USA

Abstract

We present simulations of a semiconductor beam detector using the code VSim. The 3D simulations involve the movement and scattering of electrons and holes in the semiconductor, voltages which may be applied to external contacts, and self-consistent electrostatic fields inside the device. Electrons may experience a Schottky barrier when attempting to move from the semiconductor into a metal contact. The strong field near the contact, due to trapped electrons, can result in hole injection into the semiconductor due to transmission of electrons from the valence band of the semiconductor into the metal contact. Injected holes are transported in the applied field leading to current through the detector. We compare our simulation results with experimental results from a prototype diamond X-ray detector.

INTRODUCTION

Diamond is a promising material for use in X-ray and particle detectors [1–4]. The experimental setup for an X-ray detector is shown in Figure 1, it consists of a thin diamond sheet 90 μm thick which is placed in an X-ray beam line. On either side of the diamond sheet are metal contacts which can be held at different voltages, resulting in a voltage bias across the sheet. The bias is considered positive when the voltage is higher on the metal contact to the side of the beam (right).

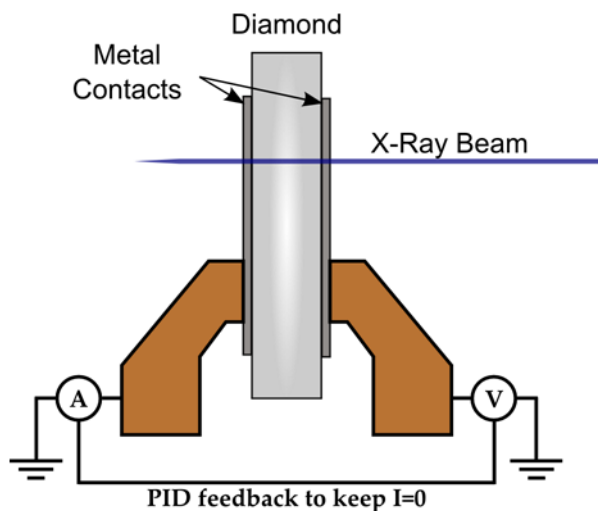


Figure 1: Schematic of an experimental X-ray detector.

When an X-ray photon passes through the thin diamond sheet, it may be absorbed, creating an electron-hole pair.

* This work is supported by the US DOE Office of Science, department of Basic Energy Sciences, grant number DE-SC0007577.

[†] gibell@txcorp.com

The electron and hole scatter inelastically in diamond, creating many more secondary electrons and holes. Further relaxation of low energy charge carriers is dominated by scattering with phonons. Under positive bias, electrons will tend to drift to the right and holes to the left, leading to separation of these charge carriers.

In these experiments an X-ray beam generates holes and electrons continuously inside the diamond detector. The experimental data of electron and hole responsivity versus bias shows a marked difference between electrons and holes. As holes are generated, they diffuse to the right under the negative bias, and are able to pass without difficulty into the right metal contact. The responsivity of holes increases when a negative bias is applied, but eventually saturates at a maximum value [3]. The maximum current is the rate at which holes are generated by the X-ray beam.

The resistivity of electrons under positive bias also shows an increase with the applied bias. The rate of increase is lower than that of holes, this was attributed to trapping of electrons inside the diamond, and to a lesser extent the different diffusion characteristics of holes versus electrons. As the bias is increased further, no saturation occurs; the current continues to increase with the bias.

The current eventually exceeds that generated by the beam. This is possible if electrons become trapped in the diamond, making it negatively charged. This could lead to holes being injected into the diamond from the right contact, where they drift across the diamond plate and pass into the left contact. Since these holes are not created by the beam, the current is not limited by the rate of hole production by the beam.

The hole current does not appear uniformly across the plate, but is isolated to small regions [5] with scale on the order of 50 μm . This supports the theory that the current is due to electron trapping localized in these small regions, perhaps due to surface defects. When electrons become trapped in these isolated regions near the right contact, they result in an increase in the electrostatic field in these regions, which can lead to hole injection. When holes are injected near the defect, they pass all the way through the diamond to the opposite contact in a well-defined current spike.

SIMULATION SETUP

The models for charge transport in diamond are described in Ref. [6]. To model electrons transmission across the potential barrier of a diamond interface (e.g., with a metal or vacuum) we use the transfer matrix method [7, 8], which has been implemented in VSim [9].

Our 3D simulations of the diamond detector use a domain of size $30 \times 500 \times 500 \mu\text{m}$. The thickness of the plate is $d = 30 \mu\text{m}$. We use periodic boundaries in y and z . The

3D MODELING AND SIMULATIONS OF ELECTRON EMISSION FROM PHOTOCATHODES WITH CONTROLLED ROUGH SURFACES*

D. A. Dimitrov, G. I. Bell, D. Smithe, C. Zhou, Tech-X Corp., Boulder, CO 80303, USA
 I. Ben-Zvi, J. Smedley, BNL, Upton, NY 11973, USA
 S. Karkare, H. A. Padmore, LBNL, Berkeley, CA 94720, USA

Abstract

Developments in materials design and synthesis have resulted in photocathodes that can have a high quantum efficiency (QE), operate at visible wavelengths, and are robust enough to operate in high electric field gradient photoguns, for application to free electron lasers and in dynamic electron microscopy and diffraction. However, synthesis often results in roughness, ranging from the nano to the microscale. The effect of this roughness in a high gradient accelerator is to produce a small transverse accelerating gradient, which therefore results in emittance growth. Although analytical formulations of the effects of roughness have been developed, a full theoretical model and experimental verification are lacking, and our work aims to bridge this gap. We report results on electron emission modeling and 3D simulations from photocathodes with controlled surface roughness similar to grated surfaces that have been fabricated by nanolithography. The simulations include both charge carrier dynamics in the photocathode material and a general electron emission modeling that includes field enhancement effects at rough surfaces. The models are being implemented in the VSIm code.

INTRODUCTION

Successful operation of modern X-ray light sources, free electron laser (FEL), and linear accelerator facilities depends on providing reliable photocathodes [1] for generation of low emittance, high-brightness, high-current electron beams using conventional lasers.

Developments in materials design and synthesis have resulted in photocathodes that can have a high quantum efficiency (QE), operate at visible wavelengths, and are robust enough to operate in high electric field gradient photoguns, for application to free electron lasers and in dynamic electron microscopy and diffraction. However, synthesis often results in roughness, ranging from the nano to the microscale. Thus, the effects on roughness on emittance are of significant importance to understand.

Recent advances in material science methods have been demonstrated to control the growth of photoemissive materials (e.g. Sb) on a substrate to create different types of rough layers with a variable thickness of the order of 10 nm. An example of such photoemissive layer with controlled sinusoidal roughness is shown in Fig. 1 together with the overall diagram of momentatron experiments developed [2] to measure transverse electron momentum and emittance.

* We are grateful to the U.S. DoE Office of Basic Energy Sciences for supporting this work under the grant DE-SC0013190.

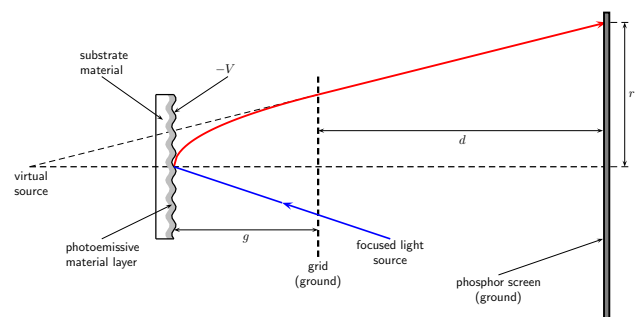


Figure 1: Diagram (not to scale) of momentatron experiments for measurement of transverse momentum of emitted electrons using rough (shown) and flat photocathode surfaces.

Feng *et al.* [3] showed recently how data from momentatron experiments can be used to investigate the thermal limit of intrinsic emittance of metal photocathodes.

Although analytical formulations of the effects of roughness have been developed, a full theoretical model and experimental verification are lacking, and our work aims to bridge this gap. We report results on electron emission modeling and 3D simulations from photocathodes with controlled surface roughness similar to grated surfaces that have been fabricated by nanolithography and investigated in momentatron experiments. The simulations include both charge carrier dynamics in the photocathode material and a general electron emission modeling with field enhancement effects at rough surfaces.

MODELING

The overall modeling capabilities needed (within the framework of a Particle-in-Cell (PIC) code) to simulate electron emission from photocathodes with controlled rough surfaces consist of: (i) electron excitation in a photoemissive material in response to absorption of photons with a given wavelength, (ii) charge dynamics due to drift and various types of scattering processes, (iii) representation of rough interfaces, (iv) calculation of electron emission probabilities that takes into account image charge and field enhancement effects across rough surfaces, (v) particle reflection and emission updates and efficient 3D electrostatic (ES) solver for a simulation domain that has sub-domains with different dielectric properties separated by piece-wise continuous rough interfaces.

Electron excitation is modeled with exponential decay of absorbed laser light intensity relative to positions on the photocathode surface. Here, we implemented and used a

IN-SITU SECONDARY ELECTRON YIELD MEASUREMENT AT FERMILAB MAIN INJECTOR

Yichen Ji, Linda Spentzouris, Department of Physics, Illinois Institute of Technology, IL 60616, USA
Robert Zwaska, FNAL, Batavia, IL 60510, USA

Abstract

Studies of in-situ Secondary electron yield (SEY) measurements of material samples at the Main Injector (MI) beam pipe wall location started in 2013. [1, 2] These studies aimed at understanding how the beam conditioning of different materials evolve if they function as MI vacuum chamber walls. The engineering run of the SEY measurement test stand was finished in 2014. From 2014 to 2016 the Fermilab accelerator intensity has increased from 24×10^{12} to 42×10^{12} protons. Beam conditioning of SS316L and TiN coated SS316L has been observed throughout this period. [3] Improvement of the data acquisition procedure and hardware has been performed. A deconditioning process was observed during the accelerator annual shut down in 2016.

THE SAMPLES AND TEST STAND

Two samples are studied in the experiment, stainless steel 316L (SS316L), the same material as the MI vacuum chamber, and Titanium Nitride (TiN) coated SS316L. The samples were installed in September 2014 and kept in the accelerator vacuum chamber ever since. They are curved pieces that are mounted on a floating arm. The samples make up part of the accelerator vacuum chamber wall so they are directly exposed to the operating accelerator and experience conditioning directly from the Electron Cloud generated. During measurements, the sample is retracted into the electrically isolated arm. A Kimball physics ELG-02 electron gun, kept in the same vacuum, directs an electron beam onto the sample and a Keithley 6487 Pico-Ammeter is used to measure the SEY of the sample.

During a measurement bias voltage is applied to the sample. The primary current I_p is measured by applying a +150V bias voltage to the sample that ensures recapture of all secondary electrons. The total current I_t is measured by applying a -20V bias voltage to the sample that repels all low energy secondary electrons. Then the secondary emission current is given by $I_{SEY} = I_t - I_p$. Then, the SEY can be calculated by the following equation.

$$SEY = \frac{I_{SEY}}{I_p} = \frac{I_t - I_p}{I_p} \quad (1)$$

Typical I_p , I_t and SEY vs incident energy from an actual measurement are shown in figure 1. This measurement was performed on September 2nd 2016 on SS316L. The system measures I_p at one point since I_p should only be determined by the electron guns. The I_t current is measured as the position of the gun electrons are varied across a 3×3 grid on the sample surface.

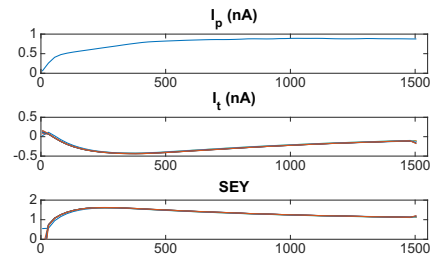


Figure 1: Typical I_p (nA), I_t (nA) and SEY vs incident energy (eV).

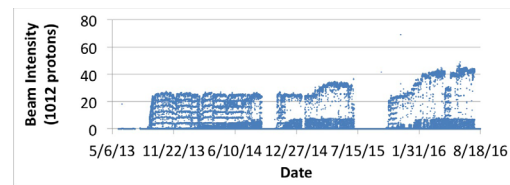


Figure 2: MI intensity from late May 2013 to Sep 2016.

The bias voltage induced leakage current is the major source of inaccuracy in this set up and has to be compensated. A long term study of the leakage current was performed and the result will be discussed later this paper.

SEY MEASUREMENT RESULTS

This measurement aimed to understand how the SEY evolves under the operation of MI. The peak SEY was measured at different typical operational MI beam intensities. These measurements also allowed the SEY to be known as a function of the MI integrated intensity (total exposure). The peak SEY was calculated by averaging all of the nine data points at each incident energy and then finding the maximum. The operational intensity of the MI over time is shown in figure 2. The intensity was steady during the first half of 2014 and started to gradually increase during the second half of 2014. There are two month annual shutdowns every year. In May of 2016, an accident happened that brought down the intensity, it was resolved and the intensity went back up.

Figure 3 shows the peak SEY data over time. The peak SEY decreased over time as expected. The 2015 annual shut down happened between July and November. Major deconditioning was observed during the annual shut down. The samples were kept in the MI vacuum chamber for the whole period. The SEY increased from 1.32 to 1.89 for TiN and from 1.55 to 1.97 for SS316L. When the intensity of the MI went down in May of 2016 to 28×10^{12} protons, a gentle

BENCHMARK OF RF PHOTOINJECTOR AND DIPOLE USING ASTRA, GPT, AND OPAL*

N. R. Neveu^{†1}, L. K. Spentzouris, Illinois Institute of Technology, Chicago, USA

J. G. Power,¹ Argonne National Laboratory, Argonne, USA

P. Piot², Fermi National Accelerator Laboratory, Batavia, USA

²Department of Physics and Northern Illinois Center for Accelerator & Detector Development, Northern Illinois University, DeKalb, USA

C. Metzger-Kraus, Helmholtz-Zentrum Berlin, Berlin, Germany

S. J. Russell, Los Alamos National Laboratory, Los Alamos, USA

A. Adelman, Paul Scherrer Institut, Villigen, Switzerland

G. Ha, POSTECH, Pohang, South Korea

Abstract

With the rapid improvement in computing resources and codes in recent years, accelerator facilities can now achieve and rely on accurate beam dynamics simulations. These simulations include single particle effects (e.g. particle tracking in a magnetic field) as well as collective effects such as space charge (SC), and coherent synchrotron radiation (CSR). Using portions of the Argonne Wakefield Accelerator (AWA) as the benchmark model, we simulated beam dynamics with three particle tracking codes. The AWA rf photoinjector was benchmarked, primarily to study SC, in ASTRA, GPT, and OPAL-T using a 1 nC beam. A 20° dipole magnet was used to benchmark CSR effects in GPT and OPAL-T by bending a 1nC beam at energies between 2 MeV and 100 MeV. In this paper we present the results, and discuss the similarities and differences between the codes.

INTRODUCTION

The AWA group has used several beam codes in the past including: T-STEP/PARMELA [1], ASTRA [2], and GPT [3]. In order to take advantage of computing resources offered by Argonne National Laboratory (ANL), an effort was made to investigate OPAL [4], an open source and parallel code that comes in two flavours; OPAL-CYL and OPAL-T. The latter was installed on the Blues cluster at the Laboratory Computing Resource Center (LCRC) provided by ANL [5]. Since no members of AWA had experience with OPAL-T, this benchmark was done to compare results to GPT and ASTRA.

There are three main collective effects of interest to the AWA: SC, CSR, and wakefields. The AWA facility houses a 70 MeV RF photoinjector [6] with a large dynamic range: 20 pC to 100 nC. In many cases, the beam is SC dominated. In the AWA's Emittance Exchange (EEX) beamline [7], CSR has a large effect on the beam as it passes through the dipoles, and wakefields are present in the two beam acceleration (TBA) beam line [8]. ASTRA, GPT, and OPAL-T are capable of simulating 3D SC, and wakefield effects. The latter two codes also include a CSR model, making them a good fit for the AWA.

* Work supported by DE-SC0015479 and DE-AC02-06CH11357

[†]nneveu@hawk.iit.edu

CODE COMPARISON

ASTRA, GPT, and OPAL-T are capable of modelling RF photoinjectors, linacs, and XFEL beamlines (excluding undulators). There are also several differences between the codes, some of which are listed in a short comparison of code features done in Table 1.

Table 1: Features of ASTRA, GPT, and OPAL-T

Feature	GPT	OPAL-T	ASTRA
Runs on Windows	Yes	No	Yes
Runs on Mac	Yes	Yes	Yes
Runs on Linux	Yes	Yes	Yes
Open Source	No	Yes	No
Parallel	Yes	Yes	No#
Autophase	No	Yes	Yes
Adaptive Time Step	Yes	No	No
3D SC Algorithm	Yes	Yes	Yes
1D CSR Algorithm	Yes*	Yes	No
Wakefield Algorithm	Yes*	Yes	Yes

*In-house modules added to the AWA version of GPT

#A parallel version is available from DESY

Although, CSR and wakefield algorithms do not come in the standard installation of GPT, users can install modules as needed. A CSR routine was written by the authors of [9] and ported to the windows version of GPT for use at the AWA. A wakefield module was also written. It is based on the model in ELEGANT [10].

SIMULATION OF THE GUN

The SC algorithms were probed using the AWA photoinjector, a 1.5 cell copper standing-wave cavity at 1.3 GHz, with bucking, focusing, and matching solenoids. The rf gun and solenoid fields seen by the beam are shown in Fig. 1. Note, in the remainder of this paper, the word gun is used in place of photoinjector.

The simulation parameters were chosen to approximately generate the canonical “1 μm at 1 nC” case. The initial beam parameters were based on gun operations at PITZ [11], due to the similarities between the PITZ and AWA rf guns. The PITZ parameters came close to achieving the 1 μm target without any optimization. A coarse 1D minimization of the emittance was done to

MODEL OF ELECTRON CLOUD INSTABILITY IN FERMILAB RECYCLER

S. A. Antipov, The University of Chicago, Chicago, IL 60637, USA

A. Burov, S. Nagaitsev, Fermilab, Batavia, IL 60510, USA

Abstract

An electron cloud instability might limit the intensity in the Fermilab Recycler after the PIP-II upgrade. A multi-bunch instability typically develops in the horizontal plane within a hundred turns and, in certain conditions, leads to beam loss. Recent studies have indicated that the instability is caused by an electron cloud, trapped in the Recycler index dipole magnets. We developed an analytical model of an electron cloud driven instability with the electrons trapped in combined function dipoles. The resulting instability growth rate of about 30 revolutions is consistent with experimental observations and qualitatively agrees with the simulation in the PEI code. The model allows an estimation of the instability rate for the future intensity upgrades.

FAST INSTABILITY

In 2014 a fast transverse instability was observed in the proton beam of the Fermilab Recycler. The instability acts only in the horizontal plane and typically develops in about 20-30 revolutions. It also has the unusual feature of selectively impacting the first batch above the threshold intensity of $\sim 4 \cdot 10^{10}$ protons per bunch (Fig. 1). These peculiar features suggest that a possible cause of the instability is electron cloud. Earlier studies by Eldred et. al. [1] indicated the presence of electron cloud in the Recycler and suggested the possibility of its trapping in Recycler beam optics magnets.

The fast instability seems to be severe only during the start-up phase after a shutdown, with significant reduction being observed after beam pipe conditioning [2]. It does not limit the current slip-stacking operation up to 700 kW of beam power, but may pose a challenge for a future PIP-II intensity upgrade [3].

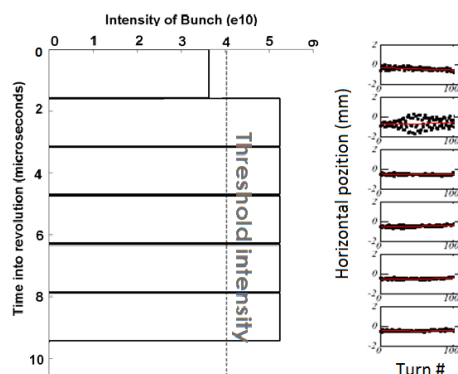


Figure 1: The first batch above the threshold intensity suffers the blow-up after injection into the ring [2].

ELECTRON CLOUD TRAPPING

The most likely candidates for the source of electron cloud in Recycler are its combined function magnets. They occupy about 50% of the ring's circumference. In a combined function dipole the electrons of the cloud move along the vertical field lines, but the gradient of the field creates a condition for a 'magnetic mirror'—an electron will reflect back at the point of maximum magnetic field if the angle between the electron's velocity and the field lines is greater than:

$$\theta > \theta_{\max} = \cos^{-1}(\sqrt{B_0 / B_{\max}}). \quad (1)$$

Particles with angles $\theta_{\max} < \theta \leq \pi/2$ are trapped by the magnetic field. For Recycler magnets (Table 1), Eq. (1) implies $\sim 10^{-2}$ of electrons in the cloud are trapped, assuming uniform distribution. A more detailed description of the trapping process is given in [4].

According to numerical studies with the PEI code [4,5], the trapping mechanism allows the electron cloud to gradually build up over multiple turns, reaching a final density orders of magnitude greater than in a pure dipole. The resulting cloud distribution is a stripe along the magnetic field lines, with higher particle density closer to the walls of the vacuum chamber (Fig. 2). The width of the stripe is about the size of the beam. Knowledge of the electron cloud build-up and its distribution allows the construction of a simple model of the electron cloud instability in Recycler.

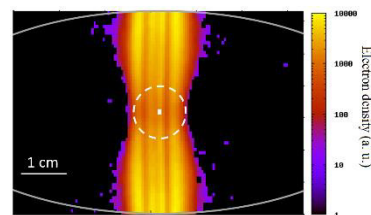


Figure 2: Electron cloud forms a stripe inside the vacuum chamber; the beam center and its 2 rms size are shown in white [4].

MODEL OF THE INSTABILITY

First, consider a round coasting proton beam travelling in a ring, uniformly filled with electron cloud. Let us denote the position of the beam centroid at an azimuthal angle θ at time t as $X_p(t, \theta)$. Further, assume that the beam travels at a constant azimuthal velocity around the ring ω_0 and use a smooth focusing approximation with betatron frequency ω_β .

ELECTRON CLOUD TRAPPING IN RECYCLER COMBINED FUNCTION DIPOLE MAGNETS

S. A. Antipov, The University of Chicago, Chicago, IL 60637, USA
S. Nagaitsev, Fermilab, Batavia, IL 60510, USA

Abstract

Electron cloud can lead to a fast instability in intense proton and positron beams in circular accelerators. In the Fermilab Recycler the electron cloud is confined within its combined function magnets. We show that the field of combined function magnets traps the electron cloud, present the results of analytical estimates of trapping, and compare them to numerical simulations of electron cloud formation. The electron cloud is located at the beam center and up to 1% of the particles can be trapped by the magnetic field. Since the process of electron cloud build-up is exponential, once trapped this amount of electrons significantly increases the density of the cloud on the next revolution. In a Recycler combined function dipole this multi-turn accumulation allows the electron cloud reaching final intensities orders of magnitude greater than in a pure dipole. The multi-turn build-up can be stopped by injection of a clearing bunch of 10^{10} p at any position in the ring.

FAST INSTABILITY

In 2014 a fast transverse instability was observed in the proton beam of the Fermilab Recycler. The instability acts only in the horizontal plane and typically develops in about 20-30 revolutions. It also has the unusual feature of selectively impacting the first batch above the threshold intensity of $\sim 4 \cdot 10^{10}$ protons per bunch (Fig. 1). These peculiar features suggest that a possible cause of the instability is electron cloud. Earlier studies [1, 2] indicated the presence of electron cloud in the ring and suggested the possibility of its trapping in Recycler combined function magnets.

The fast instability seems to be severe only during the start-up phase after a shutdown, with significant reduction being observed after beam pipe conditioning during beam scrubbing runs [3]. It does not limit the current operation with slip-stacking up 700 kW of beam power, but may pose a challenge for a future PIP-II intensity upgrade.

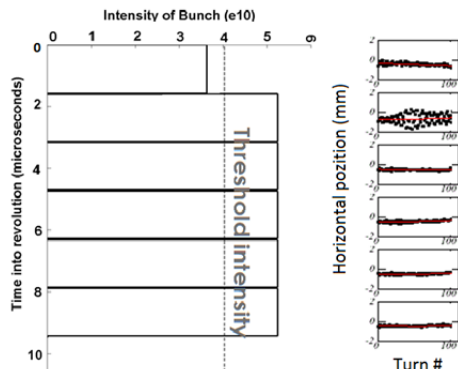


Figure 1: The first batch above the threshold intensity suffers the blow-up after injection into the ring [3].

ELECTRON CLOUD TRAPPING

In a combined function dipole the electrons of the cloud move along the vertical field lines. This motion conserves their energy E and magnetic moment

$$\mu = \frac{mv_{\perp}^2}{2B} = \text{const}, \quad (1)$$

where v_{\perp} is the component of the velocity normal to the magnetic field B . As an electron moves closer to a magnet pole it sees a higher B (Fig. 2) and it can reflect back if

$$E - \mu B = 0 \quad (2)$$

Alternatively, the electron will reflect back at the point of maximum magnetic field if the angle between the electron's velocity and the field lines is greater than:

$$\theta > \theta_{\max} = \cos^{-1}(\sqrt{B_0 / B_{\max}}). \quad (3)$$

Particles with angles $\theta_{\max} < \theta \leq \pi/2$ are trapped by magnetic field. For Recycler magnets (Table 1), Eq. (3) gives a capture of $\sim 10^{-2}$ particles of electron cloud, assuming uniform distribution.

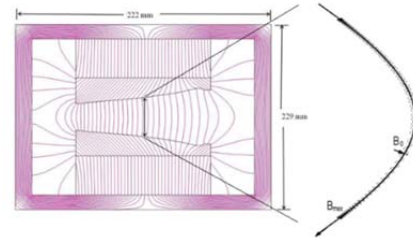


Figure 2: Electron cloud can get trapped by magnetic field of a combined function magnet.

SYMPLIFIED ANALYTICAL MODEL

Electron Capture by the Field

Let us look at the process of electron cloud trapping in more detail and consider the last two bunches of the batch. The first bunch kicks the electrons of the cloud, created by the batch. With an energy of the order of 100 eV the electrons drift along the magnetic field in the vacuum chamber, finally reaching its walls and producing secondary electrons with the energies of a few eV [4]. In the absence of the beam these secondary electrons would eventually reach the aperture and die. But the next proton bunch can stop a fraction of the secondaries, reducing their angle to $\theta < \theta_{\max}$ (Fig. 3). These electrons will remain trapped in the magnetic field after the beam is gone.

DEVELOPMENT OF AN OPTICAL CAVITY FOR LCS SOURCES AT THE COMPACT ERL

T. Akagi*, S. Araki, Y. Honda, A. Kosuge, N. Terunuma, J. Urakawa, KEK, Ibaraki, Japan
R. Hajima, M. Mori, R. Nagai, T. Shizuma, QST, Tokai, Japan

Abstract

High-energy photons from the laser Compton scattering (LCS) sources are expected to be applied in various fields in a wide range photon energies from keV to GeV. High-flux and narrow-bandwidth LCS photon beam is realized in an energy recovery linac (ERL). An electron beam of high-average current and small-emittance collides with accumulating laser pulses in an enhancement cavity for generating high-flux LCS photon beam. We have developed the high-finesse bow-tie ring cavity for the LCS experiment at the Compact ERL (cERL) in KEK. In this presentation, we will report the detail of the optical cavity.

INTRODUCTION

The photon source based on laser Compton scattering (LCS) can generate high-energy photons with relatively low-energy electrons in comparison with the synchrotron. Therefore LCS photon sources are suitable for developing the compact light sources. The LCS sources has several features such as narrow bandwidth, energy tunability, small source size, and polarization control.

Photon flux and energy bandwidth are important parameters of LCS sources. To realize a high-flux and a narrow bandwidth photon source, a high-average-current and a small emittance electron beam is essential. Energy recovery linacs (ERLs) can produce a such electron beam. On the laser system, a high-power and tightly focused laser pulse with a repetition rate that matches the electron beam is needed. We have developed an optical cavity for the LCS interaction point (IP), in which laser pulses from a mode-locked laser are stacked and enhanced. We have been developing the ERL-based LCS sources with a laser enhancement cavity at a test accelerator of ERL at KEK, the Compact ERL (cERL). We have generated 7-keV LCS X-ray in the cERL [1]. We will describe progress of development of the optical cavity.

ACCELERATOR

The cERL is a test facility constructed for the development of accelerator components and technologies necessary for future ERL-based light source. The cERL has been designed to achieve a small-emittance electron beam with a high average current.

The cERL consists of an injector, a superconducting linac, and a recirculation loop. A interaction point (IP) for the LCS is located in the straight section of the circulation loop. In the LCS experiment, the cERL is operated at a recirculation

energy of 20 MeV and a pulse repetition rate of 162.5 MHz. Recently, we have achieved to circulate 1 mA [2].

In this experiment, the beam current was limited to 1 mA, the value approved by the regulatory authority at the time. The parameters of the electron beam for the LCS experiment are listed in Table 1.

Table 1: Parameters of the Electron Beam for the LCS Experiment

Energy [MeV]	20
Bunch charge [pC]	5.5
Bunch length [ps, rms]	2
Spot size (σ_x/σ_y) [μm]	22/32
Emittance ($\varepsilon_{nx}/\varepsilon_{ny}$) [mm·mrad]	2.52/1.25
Repetition rate [MHz]	162.5

OPTICAL CAVITY

In order to produce a high-flux LCS X-ray, it is necessary to achieve a high finesse and a small laser waist size simultaneously. A 2-mirror Fabry-Perot cavity is unstable for small waist size. Therefore, we developed a 4-mirror ring cavity which consists of two plane mirrors and two concave mirrors. It is more tolerant of misalignment of mirrors than a 2-mirror cavity. A detail description of the design of the optical cavity can be found in [3]. The design parameters of the optical cavity are summarized in Table 2.

We used a commercial laser system consisting of a mode-locked oscillator and an amplifier (ARGOS, TimeBandwidth-Product) with wavelength, repetition rate, average power, pulse width (FWHM) were, 1064 nm, 162.5 MHz, 45 W and 10 ps, respectively.

Table 2: Design Parameters of the Optical Cavity

Repetition rate [MHz]	162.5
Finesse	5600
Spot size at the IP (σ_x/σ_y) [μm]	20/30
Input angle of mirrors [degree]	4.3
Diameter of mirrors [mm]	25.4
Curvature radius of mirrors [mm]	420

A photograph of the optical cavity is shown in Fig. 1. Two sets of 4-mirror cavities having a common focal point are combined symmetrically in the same structure. Only one set was used for the LCS experiment at present. Two sets cavities have been designed to produce two different polarization X-ray beams at the same time.

* akagit@post.kek.jp

IMPROVEMENT OF X-RAY GENERATION BY USING LASER COMPTON SCATTERING IN LASER UNDULATOR COMPACT X-RAY SOURCE (LUCX)

M. Fukuda^{†1}, S. Araki, Y. Honda¹, Y. Sumitomo, N. Terunuma¹, J. Urakawa, KEK, Ibaraki, 305-0801, Japan

¹also at SOKENDAI, Ibaraki, 305-0801, Japan

K. Sakaue, WIAS, Waseda University, Tokyo, 169-8050, Japan

M. Washio, RISE, Waseda University, Tokyo, 169-8555, Japan

Abstract

We have been developing a compact X-ray source based on the laser Compton scattering (LCS) at Laser Undulator Compact X-ray source (LUCX) accelerator in KEK. We have started to take X-ray images such as refraction contrast images and phase contrast imaging with Talbot interferometer. In this accelerator, 6-10keV X-rays are generated by LCS. An electron beam is produced by a 3.6cell rf-gun and accelerated to 18-24MeV by a 12cell accelerating tube. A laser pulse is stored in a 4-mirror planar optical cavity to enhance the power. To increase the flux of LCS X-rays, we perform an optimization of the beam-loading compensation, improvement of the intensity of an electron beam and a laser light at the collision point. We report the result of the X-ray generation in this accelerator.

INTRODUCTION

X-rays are utilized for a wide range of applications, for example, medical examination, biological science, material science and so on. High-flux and high-brightness X-rays are specially generated by synchrotron radiation storage rings at an order of GeV although they are generally large and expensive. On the other hand, an X-ray source via LCS is possible to generate X-rays at a similar energy by using a compact and an inexpensive accelerator because the electron-beam energy is an order of tens of MeV. For example, 10keV X-rays can be generated by LCS with 24 MeV electron beam and a 1064nm laser light.

We have been developing a LCS based X-ray source at the LUCX accelerator which has been constructed in KEK. In this accelerator, 6-10 keV X-rays are generated by LCS of a multi-bunch electron-beam with the energy of 18-24 MeV and a laser pulse with the wavelength of 1064nm. X-ray imaging experiments including absorption and refraction contrast images have been conducted since 2012. Last year, studies on a phase contrast imaging with Talbot interferometer started. The visibility of the moire fringes was about 33%[1,2]. However, the exposure time was five hours which is too long for imaging. Therefore, we improved the collision tuning to increase the X-ray flux.

[†] mfukuda@post.kek.jp

LUCX ACCELERATOR

The LUCX accelerator is a normal-conducting electron-accelerator at S-band frequency. This accelerator comprises a 3.6cell photo-cathode RF-gun[3], a 12cell standing-wave accelerating tube[3] and a 4-mirror planar optical cavity[4]. The layout is shown in Fig. 1.

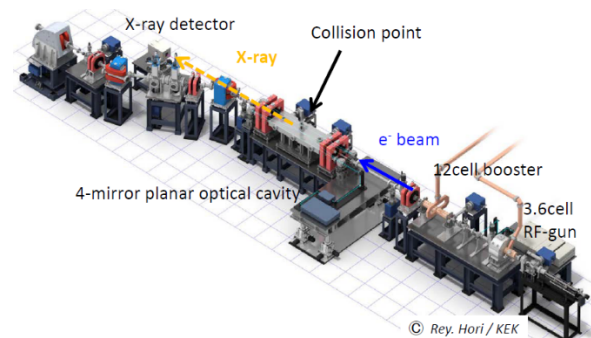


Figure 1: The beamline of the LUCX accelerator.

The RF-gun generates a 7.6MeV multi-bunch electron-beam with total charge of 600nC in 1000 bunches. And then, the accelerating tube accelerates the beam up to 24MeV. After that, the beam collided with a laser pulse stored in the optical cavity to generate X-rays by LCS. The scattered X-rays go straight through a beryllium window with the thickness of 300 μ m. On the other hand, the beam is separated from the X-rays by the first bending dipole and sent to the dump.

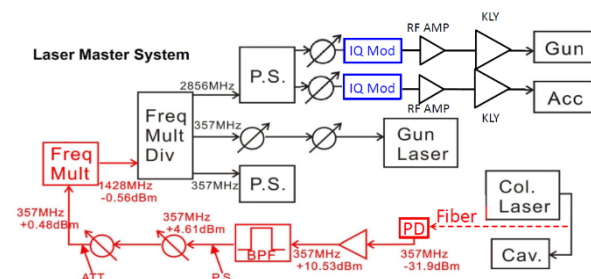


Figure 2: The diagram of the laser master system.

Figure 2 shows the diagram of the RF system. The 357MHz master clock is generated from the signal of laser pulses for the optical cavity. The devices in this accelerator is synchronized to this clock. We call this method the laser master system. The RF signal is delivered to klystrons after the frequency is converted from 357MHz to 2856MHz. And then the RF signal is chopped

A SIMULATION FOR BRIGHT THZ LIGHT SOURCE FROM WIGGLER RADIATION AT KEK LUCX

Y. Sumitomo*, S. Araki, A. Aryshev, M. Fukuda¹, M. Shevelev, N. Terunuma¹, J. Urakawa,
High Energy Accelerator Research Organization (KEK), Tsukuba, Japan
¹also at The Graduate University for Advanced Studies (SOKENDAI), Hayama, Japan
A. Deshpande, SAMEER, Mumbai, India

Abstract

We study a bright THz light source generated by a wiggler radiation at KEK LUCX THz experiment, where an injected four pre-micro-bunched electron beam with few hundreds femto-seconds separation plays a crucial role. The energy of pre-bunched beam reaches few MeV at an S-band 3.6 cell RF Gun, and hence the space-charge effect is not negligible. We simulate the beam optics by ASTRA code, a charged beam optics simulator with space-charge effect, and then the resultant particle distribution is passed to GENESIS, a FEL simulator to deal with the wiggler radiation. We also present an experimental result at KEK LUCX. The major advantage of this system is a compactness of total setup that is expected to generate a MW class peak power THz beam by the coherent radiation.

INTRODUCTION

The light source of terahertz (THz) region became an attractive frontier recent years owing to several major technical advances. The THz sources have a great potential to sense a material characteristics that can not be found with the other frequency bands (see e.g. [1]). A megawatt bright source can be generated by the help of RF accelerator and wiggler/undulator coherent radiation.

We use a THz-pulse-train photo injector where a RF-gun (S-band) accelerates a micro-bunched electron pulse train with THz separations up to few MeV, and then the pulse train enters into a wiggler after an optics system [2]. Usually, a free-electron laser (FEL) consists of long and multiple of undulators/wigglers since the micro-bunching is processed along undulators/wigglers by interactions with electromagnetic fields. In our system, the pre-micro-bunched structure of bunch train already has a high bunching factor that sources a high power electromagnetic radiation within a short distance. Hence our system is compact and costs reasonable.

The THz-pulse-train photo injector is realized in LUCX (Laser Undulator Compact X-ray project) at KEK with a pulse gun laser system [3]. Currently, the pulse laser system admits a electron train with up to four micro-bunches, where the micro-bunch length would be 50 femto-seconds (fs) at photo-cathode, and distances can be few hundreds fs. Figure 1 illustrates a rough schematic picture of LUCX alignment, where sizes and distances are not accurate for a simple illustration. Due to lack of space and coexistence with the other experiments, the wiggler is installed after the bending magnet. Since the profile of micro-bunched train

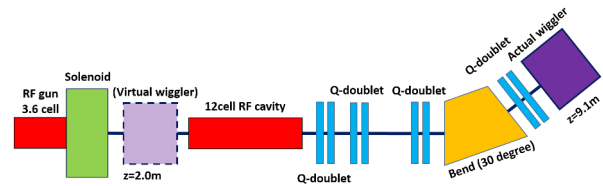


Figure 1: A rough sketch of LUCX beam alignment. The virtual wiggler is for simulation while the actual wiggler is for experiment. We explain the detail reason in context.

after the bend is not desirable for the THz wiggler coherent radiation as we will explain later, we will first perform the FEL simulation assuming that the wiggler is installed at the virtual wiggler place in Fig. 1, where the other experiment takes place. Then we will present an experimental result at the actual wiggler place with simulation data.

FEL SIMULATION OF VIRTUAL WIGGLER

In this section, we present the simulation result of FEL as well as particle tracking, assuming that the wiggler is at the virtual place in Fig. 1. The particle tracking includes the space-charge force that is not negligible and affects particle distributions seriously for energy up to few MeV.

ASTRA Simulation

We use a free code, ASTRA [4] for the particle space-charge tracking. We prepare an initial distribution at the cathode, consisting of a bunch train with four micro-bunches, as in Table 1. This setup is motivated by the realistic situation at KEK LUCX.

Table 1: A micro-bunch distribution at cathode. Each micro-bunch is separated by d_{sep} . The emittance is normalized.

Q	σ_t	$\sigma_{x,y}$	$\epsilon_{x,y}$	d_{sep}
60 pC	50 fs	0.5 mm	1π mrad mm	900 fs

The micro-bunched train is then accelerated by the 3.6-cell S-band RF gun to $E = 10.2$ MeV with 97 MV/m. The phase of RF cavity is chosen such that the peak bunching factor is high enough around 1 THz. The maximum solenoid field value is set at 0.273 T to minimize the transverse size. In Fig. 2, we illustrate the optimization for the wiggler radiation.

The resultant distribution at the entrance of wiggler is illustrated in the upper side of Fig. 3. The space-charge force affects the distribution as seen clearly. Now the beam size and normalized emittance become $\sigma_x \sim 0.197$ mm, $\sigma_y \sim 0.197$ mm, $\epsilon_x \sim 1.99 \pi$ mrad mm, $\epsilon_y \sim 1.99 \pi$ mrad

* sumitomo@post.kek.jp

LUMINOSITY INCREASE IN LASER-COMPTON SCATTERING BY CRAB CROSSING METHOD

Y. Koshiba[†], D. Igarashi, T. Takahashi, S. Ota, M. Washio,
RISE, Waseda University, Tokyo, Japan
K. Sakaue, WIAS, Waseda University, Tokyo, Japan
J. Urakawa, KEK, Ibaraki, Japan

Abstract

In collider experiments such as KEKB, crab crossing is a promising way to increase the luminosity. We are planning to apply crab crossing to laser-Compton scattering (LCS), which is a collision of electron beam and laser, to gain a higher luminosity leading to a higher brilliance X-ray source. It is well known that the colliding angle between electron beam and laser affects the luminosity. It is the best when the collision angle is zero, head-on collision, to get the highest luminosity but difficult to construct such configuration especially when using an optical enhancement cavity. Concerning this difficulty, we are planning crab crossing by tilting the electron beam using an rf-deflector. Although crab crossing in LCS has been already proposed [1], nowhere has demonstrated yet. We are going to demonstrate and conduct experimental studies at our compact accelerator system in Waseda University. In this conference, we will report mainly about expected results of crab crossing LCS.

INTRODUCTION

Nowadays, X-rays are used in various fields such as medical application, biological science, material science and so on. In most cases, X-rays are produced by means of X-ray tubes or synchrotron facilities. X-ray tubes are easy to use and compact, but the brilliance is around 10^8 , relatively low. On the other hand, synchrotron radiation X-rays have high brilliance around 10^{16} , but it needs a GeV class electron beam with a kilometer-long storage ring. Laser-Compton scattering (LCS) X-ray source lies between these two. In other words, it is expected as a compact high brilliance X-ray source. LCS X-ray sources are more compact than synchrotron sources because the energy required is MeV order. In terms of brilliance, $>10^{12}$ has been designed [2].

In Waseda University, LCS experiments had been conducted for the purpose of soft X-ray microscopes for biological observations [3]. Also with the collaboration of KEK, LUCX (Laser Undulator Compact X-ray) has been developing using a 4-mirror optical enhancement cavity [4]. In this report however, we will discuss about crab crossing method in LCS.

Accelerator System in Waseda University

We have been developing a compact (2×3 m) S-band accelerator system based on a photocathode rf electron gun, shown in Fig. 1. The rf gun structure is based on

BNL GUN-IV and can generate 3π mm-mrad, 5MeV, 10ps (FWHM) electron bunch with a 10MW klystron.

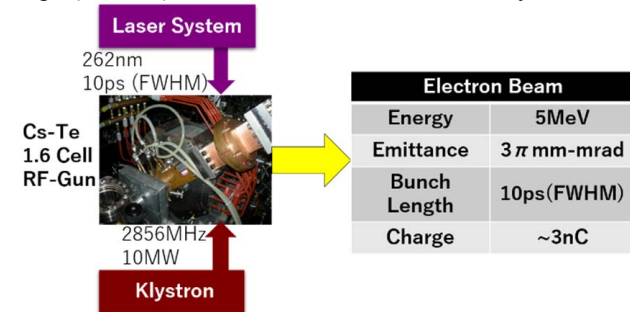


Figure 1: Accelerator system in Waseda University.

Several studies are done using this system such as pulse radiolysis experiment for radiation chemical reactions [5], coherent terahertz Cherenkov radiation [6], ultra-short bunch length measurement using a rf-deflector [7], etc.

Laser-Compton Scattering

LCS (or inverse Compton scattering) is a phenomenon generating higher energy photons through collisions of relativistic electrons and long wavelength laser photons. The scattered photons would be in the region of soft X-ray to gamma ray. Figure 2 shows the schema of LCS.

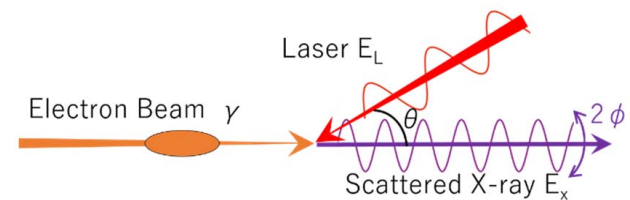


Figure 2: Schema of LCS.

γ , E_L , E_X , θ , ϕ represents the Lorentz factor of electron beam, energy of laser photon, energy of scattered X-ray, colliding angle, and scattering angle, respectively. The maximum X-ray energy E_X^{MAX} would be obtained along the electron beam axis $\phi=0$ and written as

$$E_X^{\text{MAX}} \approx 2\gamma^2(1 + \beta \cos \theta)E_L \quad (1)$$

where β is the velocity of electrons relative to the speed of light. We can see that the maximum X-ray energy is tunable by the electron beam energy and the colliding angle. The total number of scattered photons is given by the product of the total cross section of Compton scattering (σ) and luminosity (L).

$$N = \sigma L = \sigma P G \quad (2)$$

[†] email address: advanced-yuya@asagi.waseda.jp

PRIMARY STUDY OF THE PHOTOCATHODE ELECTRON GUN WITH A CONE CATHODE AND RADIAL POLARIZATION LASER *

R. Huang[†], Qi-ka. Jia[‡]

NSRL, University of Science and Technology of China, Hefei, Anhui, 230029, China

Abstract

The linearly polarized laser with oblique incidence can achieve a higher quantum efficiency (QE) of metal cathodes than that with the normal incidence, which however requires the wavefront shaping for better performance. To maintain the high QE and simplify the system, we propose a cone cathode electron gun with a radial polarization laser at normal incidence. The primary analytical estimation and numerical simulations are explored for its effect on the emittance of the electron beam.

INTRODUCTION

High-brightness electron beam, which can be used for the 4th generation light sources such as X-ray free electron lasers [1], requires the high current and low emittance. In photocathode electron guns, a metal cathode is widely used to emit electrons for its long lifetime. One of the major limitation is the low quantum efficiency(QE), especially for guns with the metal cathodes [2]. It was found that the QE had a significant dependence on the incidence angle and polarization state when the laser illuminated the cathode [3,4]. Early work on Cu showed that the p-polarized laser at 60-70° off normal incidence would give a QE at 5-14 times the normal incidence yield [5]. The primary cause of the QE enhancement is that a surface photoemission is stimulated by the normal electric field of the p-polarized laser with oblique incidence.

The scenario of oblique incidence would result in an ellipsoidal spot on the cathode and a pulse delay in laser wavefront. Thus spatial and temporal laser shaping [6] is required to prevent the distortion of the emitted beam and to improve the initial beam quality. The shaping technique is still challenging and makes the system more complicated and expensive. Some devices still take the normal incidence scheme, which would simplify the system but sacrifice some QE.

To maintain the high QE and also simplify the system, we propose a cone cathode electron gun with a radial polarization laser at normal incidence.

THE PROPOSED SCHEMES

There are two possible schemes of the cone cathode, as shown in Fig. 1. When the laser illuminates a cone cathode at normal incidence, the local incidence angle is an oblique one. The cone is properly designed so that the angle θ equals the optimized oblique angle on a flat cathode which gives a

maximum QE. For the photogun in University of Science and Technology of China (USTC) [7], θ is about 67°.

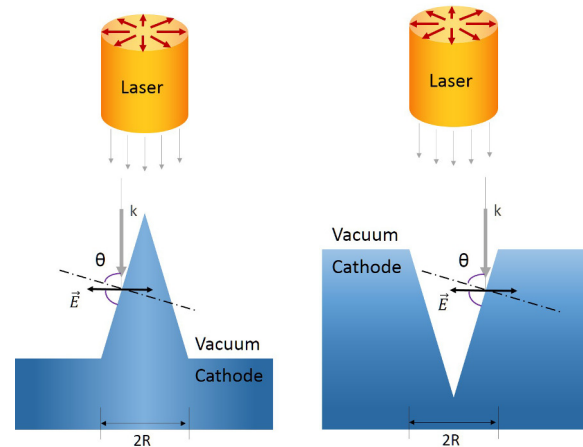


Figure 1: Normal incidence on the cathode like a conical roof (left) and the cathode like a conical sink (right).

The left plot of Fig. 1 shows the normal incidence scheme on a cathode like a conical roof, while the right one shows the scheme on a cathode like a conical sink. In stead of linearly polarized laser on a flat cathode, a radial polarized laser [8] is required for the case of a cone cathode. k is the wavenumber of the incidence laser. \vec{E} is the electric field component of the laser, with an angle θ to the local cathode surface. The radius of circular cone R equals the rms spot size of the laser.

This scheme could enhance the QE as well as achieve a circular laser spot on the cathode. It is also notable that the pulse delay in the proposed scheme is only half the case of the oblique incidence. The cone cathode may also encounter some issues. The uneven cathode surface may bring about a growth in the thermal emittance. Besides, the cone geometry of the cathode could change the field distribution in the gun cavity, which would further influence the beam dynamics.

In the following, we will firstly build a model to analytically evaluate the emittance growth introduced by a cone cathode. Secondly the RF gun design will be studied to analysis the field distribution in the cavity. Finally we will give a primary study on the beam dynamics in the gun.

THE EMITTANCE GROWTH

The thermal emittance for the photoelectric emission in a metal cathode is derived from the Fermi-Dirac model [9]. The dimensionless transverse momentum was found to be

$$\sigma_{p_x} = \sqrt{\frac{h\nu - \phi_{\text{eff}}}{3mc^2}}, \quad (1)$$

* This work is partly supported by the National Nature Science Foundation of China under Grant No. 11375199.

[†] hruxuan@mail.ustc.edu.cn

[‡] jiaqk@ustc.edu.cn

MULTIPLE BUNCH LENGTH OPERATION MODE DESIGN AT HLS-II STORAGE RING*

Weiwei Gao[#], College of Mathematics and Physics, Fujian University of Technology
Fuzhou 350118, China

Wei Li, Lin Wang, NSRL, University of Science & Technology of China, Hefei, 230029, China

Abstract

In this paper we design a simultaneous three bunch length operating mode at the HLS-II (Hefei Light Source II) storage ring by installing two harmonic cavities and minimizing the momentum compaction factor. The short bunches (2.6 mm) presented in this work will meet the requirement of coherent THz radiation experiments, and the long bunches (20 mm) will efficiently increase the total beam current. Therefore, this multiple-bunch-length operating mode allows present synchrotron users and THz users to carry out their experiments simultaneously. Also we analyzed the physical properties such as the CSR effect, RF jitter and Touschek lifetime of this operating mode.

INTRODUCTION

Short pulse electron bunches have been used for decades to satisfy the complex requirements of time resolved experiments. Some of the short electron bunches have been used for producing coherent THz radiation in rapid reaction kinetics experiments. In particular, the combination of THz pump and x-ray probe experiments will offer the opportunity for scientists to separately study the atomic, electronic, and magnetic response of materials. Therefore, generation of coherent THz radiation at a synchrotron radiation facility is a meaningful subject of study.

Previously, the low momentum compaction factor lattice was the preferred scheme for obtaining short electron bunches, because the bunch length is proportional to the square root of the momentum compaction factor [1], as shown in Eq. (1).

$$\sigma_r^2 = \frac{2\pi C_g \alpha R E_0^3}{(mc^2)^2 J_r \rho_0 e \dot{V}_0} \quad (1)$$

Recently, workers at the BESSY-II storage ring proposed a new method for achieving a multiple-bunch-length operating mode by installing harmonic cavities [2]. Based on the BESSY-II proposal we present a scheme for a multiple-bunch-length operating mode at HLS-II, which combines the harmonic cavity and low alpha methods.

* Work supported by NSFC (11305170)

gaomqr@mail.ustc.edu.cn

MULTIPLE-BUNCH-LENGTH OPERATING MODE DESIGN

Low Alpha Lattice Design

In this section we describe the designation work of a reasonable low alpha lattice using a genetic algorithm, which was reported in our previous work [3]. In this optimization, the four groups of quadrupole strengths of one superperiod are varied to obtain a satisfactory low alpha lattice. The first constraint of our optimization is that both the horizontal and vertical betatron functions should be constrained to smaller than 30m. The second constraint is that the maximum dispersion function is restricted to 0.8m. The two objectives are to minimize the momentum compaction factor and the beam emittance. Since that if two lattices with the same momentum compaction factor, we prefer the one with lower emittance. After ascertaining the constraints and objectives, the optimization result gives us a clear picture of HLS-II' lattice properties. The result shows that if the polarity of the four groups of quadrupoles remain the same as in the present HLS-II lattice, the momentum compaction factor will be able to reduced to 10^{-3} when satisfying the above constraints. In addition, the momentum compaction factor can be further reduced (to approximately 10^{-6}) when the polarities of the last two groups of quadrupoles are changed. Synthesizing the injection process and other technologies, we choose a lattice whose momentum compaction factor is 0.0039 and retain the quadrupole polarities of the original HLS-II lattice. The main twiss parameters of this new low alpha lattice are shown in Table 1.

Table 1: Twiss Parameters of the Low Alpha Lattice

Emittance	87nm-rad
Tunes	5.72/2.58
Natural chromaticity	-20.29/-15.95
Momentum compaction factor	0.0039

The one cell betatron functions and dispersion function of the low momentum compaction factor lattice are drawn using ELEGANT program [4], and shown in Fig. 1. In addition, we also studied the nonlinear properties of the newly designed low momentum compaction factor lattice. The dynamic aperture tracking with 1000 turns is shown in Fig. 2.

STATUS OF PLSII OPERATION*

Tae-Yeon Lee[†] on behalf Accelerator Department,
Pohang Accelerator Laboratory, Pohang, Republic of Korea

Abstract

As the upgrade of PLS, PLSII is a 3 GeV light source in 12 super-periods (281.8 m circumference) with 5.8 nm design emittance and can store electron beam up to 400 mA with 3 superconducting RF cavities. Its most unique characteristic is that it has a short straight section and a long straight section for each cell (24 straight sections) and up to 20 insertion devices can be installed. But, as the installed insertion devices, particularly in-vacuum insertion devices, are sources of high impedance, these are quite challenging for high current operation. Current status of PLSII operation and future plans are described in this paper.

INTRODUCTION

PLSII is the upgrade machine of PLS which was a 2.5 GeV light source with a triple bend achromat lattice, and is a 3 GeV machine with a double bend lattice. Certainly, performance of PLSII has been upgraded from PLS, from 18.2 nm emittance to 5.8 nm emittance and PLSII can now store 400 mA compared to 180~190 mA storing of PLS [1]. But, the most special thing of the PLSII lattice is that it has 2 straight sections with different lengths per cell as can be seen in the PLSII lattice of Figure 1. The long straight section (LSS) is 6.88 m long and the short straight section is 3.69 m long. To make these many straight sections, gradient bending magnets were used and only 8 sets of quadrupoles were used in each cell. Parameters of PLSII are listed in Table 1.

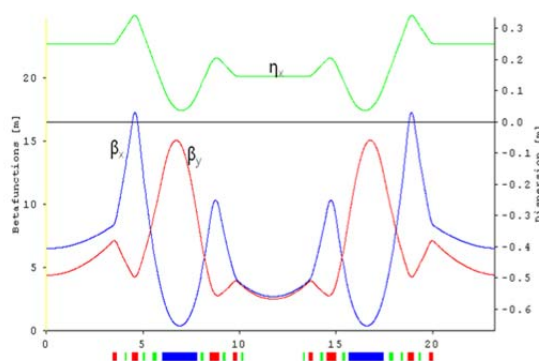


Figure 1: Magnet lattice of PLSII.

The purpose of reserving 2 straight sections per cell was to install as many insertion devices as possible. Hence, of the 24 straight sections of PLSII, 20 straight sections are already used or reserved for insertion devices. Particularly, many in-vacuum insertion devices have been installed to provide hard X-ray capacity to users. Currently, 12 in-vacuum insertion devices are installed. However, these many insertion devices and particularly in-vacuum

insertion devices give difficulties to overcome for smooth operation. First of all, changing gap of the many insertion devices particularly the in-vacuum insertion devices by users is a severe source of orbit perturbation. Next, the insertion devices particularly the in-vacuum insertion devices generate resistive wall impedance high enough to cause transverse multi-bunch instability, when their gap is closed [2]. The instability is so severe that the highest beam current stable is only around 120 mA. The first problem was solved by global orbit feedback and local feed forward while the second problem was solved by a transverse feedback system. Details are explained below.

Table 1: Main Parameters of PLSII

Parameter	Value
Energy	3 GeV
Current	400 mA
Emittance	5.8 nm
Circumference	281.82 m
Tune (h/v)	15.24 / 9.17
Revolution freq.	1.0638 MHz
Harmonic No.	470
RF freq.	499.973 MHz
Cavity type	SC
No. of Cavities	3
Gap Voltage	4.5 MV

ORBIT STABILITY

Now, the PLSII orbit stability is assured by collaboration of the slow orbit feedback (SOFB) system and the fast orbit feedback (FOFB) system. Prior to January, 2016, SOFB was used alone and after January, 2016, SOFB + FOFB is used. Eight beam position monitors (BPM) are placed in a cell.

Slow Orbit Feedback System

SOFB makes use of the 8 correctors, which are actually trim windings on the same number of sextupoles, distributed over a cell. Prior to 2016, SOFB was operated in 1 Hz but is now operated in 2 Hz. With this speed, SOFB alone could not suppress faster orbit perturbations such as ground vibration or insertion device gap changing. Consequently, the unsuppressed orbit errors accumulated and the orbit difference from the reference orbit which is usually chosen twice a year could not maintained within the target value, 1 micron rms, over a long term (for example over the 10 day user service period). The orbit difference from the reference orbit made by SOFB alone over a 10 day period is shown in Fig. 2(a). In this figure, many orbit spikes appearing resulted from insertion device gap changing.

* Work supported by Korean Ministry of Science, ICT & Future Planning

[†] email address

tylee@postech.ac.kr

A POSSIBLE EMITTANCE REDUCTION SCHEME FOR PLSII*

Tae-Yeon Lee[†], Pohang Accelerator Laboratory, Pohang, Republic of Korea

Abstract

As the upgrade of PLS, PLSII is a 3 GeV light source in 12 super-periods (281.8 m circumference) with 5.8 nm design emittance and can store electron beam up to 400 mA with 3 superconducting RF cavities. PLSII lattice is a double bend achromatic (DBA) lattice with 2 straight sections for each cell (24 straight sections). After completion of PLSII, multi-bend achromatic lattice has been widely adopted to accomplish low emittance. This paper discusses how a minimal change can modify the PLSII's DBA to a quadruple bend achromatic (QBA) lattice and reduce the emittance to about a half value.

INTRODUCTION

Construction of PLS (Pohang Light Source) was completed in 1994 and began operation for users in 1995, as a 2 GeV light source with a 12 super-period TBA (triple bend achromatic) lattice giving 12.1 nm rad beam emittance. Later, the PLS electron energy was raised to 2.5 GeV to expand the capacity for hard X-ray emission with the same lattice, which raised the emittance to 18.9 nm rad. In 2011, PLS was upgraded to a 3 GeV light source PLSII in the same storage ring tunnel but with the new lattice. The new lattice adopted DB (double bend) type and was designed to give 5.8 nm rad emittance. Main parameters of PLSII are listed in Table 1.

Table 1: Main Parameters of PLSII Storage Ring

Parameter	Value
Energy	3 GeV
Current	400 mA
Emittance	5.8 nm
Circumference	281.82 m
Tune (h/v)	15.24 / 9.17
Revolution freq.	1.0638 MHz
Harmonic No.	470
RF freq.	499.973 MHz
Cavity type	SC
No. of Cavities	3
Gap Voltage	4.5 MV

PLSII Lattice

The most unique feature of PLSII is that there are two straight sections, a long straight section (LSS) and a short straight section (SSS), for each of the 12 cells, to install as many insertion devices (IDs) as possible. The 6.88 m long LSS is long enough to accommodate the injection system as well as long IDs while the 3.1 m SSS accommodates short IDs. Dispersion is non-zero in both LSS and SSS as can be seen in Fig. 1 which illustrates the PLSII lattice. In order to make this big portion of empty space on the 281.82 m ring circumference, the number of

magnets used was minimized and so only 8 quadrupoles are used in a cell while gradient bending magnets are used. Also, 4 sets of sextupoles are used for chromaticity correction to suppress head-tail instability and for harmonic correction to enlarge the dynamic aperture. Since the completion and commissioning, PLSII has been operated smoothly in the current range of 300~400 mA.

As a price for the unique feature of having two insertion straights and low electron beam emittance, PLSII has relatively high dispersion values on the two straight sections (0.25 m at LSS and 0.14 m at SSS), which increases the effective emittance of the two insertion straights.

After upgrade completion, PLSII has raised its performance step by step and achieved all design goals. It is providing the 300~400 mA top-up service routinely in the submicron rms orbit stability [1].

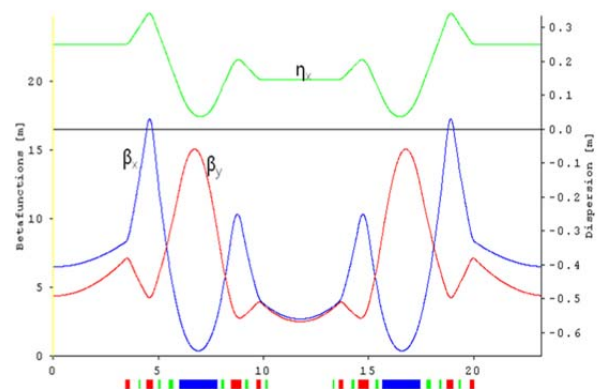


Figure 1: PLSII lattice.

Advent of Multi-bend Lattices

In the meantime, the multi-bend achromatic lattice has been widely accepted by the light source community of the world to obtain even lower (sub-Nano scale emittance or even to the diffraction limit) emittance. While new proposals for sub-Nano scale emittance are made, there are also plans to upgrade existing machines to sub-Nano scale emittance machines.

Motivated by this trend, this paper discusses a possibility that the PLSII lattice can be made a multi-bend lattice through a minimal change leaving the many IDs unchanged and consequently the electron emittance can be reduced substantially. It will be shown below that the DB lattice can be changed to a quadruple bend (QB) lattice only by adding two gradient bending magnets and two quadrupole magnets in each LSS without changing the original PLSII lattice at all. This way, the electron beam emittance can be reduced to about a half value.

NEW LATTICE

The purpose of lattice modification is to change the old DB lattice of PLSII to a quadruple bend lattice, motivat-

* Work supported by Korean Ministry of Science, ICT & Future Planning
[†] email address tylee@postech.ac.kr

CLEARING MAGNET DESIGN FOR APS-U*

M. Abliz†, J. Grimmer, Y. Jaski, F. Westferro and M. Ramanathan
Argonne National Laboratory, Argonne, IL 60439, U.S.A

Abstract

The Advanced Photon Source is in the process of developing an upgrade (APS-U) of the storage ring. The upgrade will be converting the current double bend achromat (DBA) lattice to a multi-bend achromat (MBA) lattice. In addition, the storage ring will be operated at 6 GeV and 200 mA with regular swap-out injection to keep the stored beam current constant [1].

The swap-out injection will take place with beamline shutters open. For radiation safety to ensure that no electrons can exit the storage ring, a passive method of protecting the beamline and containing the electrons inside the storage ring is proposed. A clearing magnet will be located in all beamline front ends inside the storage ring tunnel. This article will discuss the features and design of the clearing magnet scheme for APS-U.

INTRODUCTION

The APS-U will be operating the storage ring with regular swap-out injection as frequently as every 5 seconds. During these injections, the beamlines will be operating with the shutters open, and, as part of radiation safety, no electrons are allowed to exit the storage ring enclosure. Therefore, as part of the beamline, a passive device located inside the storage ring tunnel will be employed to ensure that the electrons cannot exit the storage ring enclosure.

A permanent magnet dipole (clearing magnet) will be located in the front end (part of the beamline between the storage ring exit and the concrete wall to the beamline) to deflect any electrons escaping the storage ring, to prevent them from exiting through the front end apertures and on to the experiment floor.

PRINCIPLE

The front end consists of various masks and shutters to collimate and stop the beam when needed. The main component which can fully contain the beam is the safety shutter, made of tungsten, located at about 22.7 m from the source point. Figure 1 is a schematic representation of the clearing magnet and associated relevant components in the high heat load front end (HHLFE). The clearing magnet is located immediately after a mask (FM2), and is 4 m upstream of the safety shutter. Based on the geometry of possible beam locations at the source, the worst case of mis-steered beam is shown in Fig. 1 below. The worst

case beam trajectory is when the electrons are 0.3 cm below the plane at the source and pass through the top of FM2, resulting in a beam offset of 0.63 cm above the nominal beam plane at the clearing magnet. Given the allowed overlap at the shutter, the required deflection here is 6.08 mrad. Taking the whole picture with the additional 0.44 mrad of the incident electron trajectory, the minimum total deflection to be produced by the clearing magnet is 6.52 mrad downwards. The APS-U storage ring is expected to be operated nominally at 6.0 GeV. However, as part of the safety envelop, the maximum energy of the electron for the magnet design has to be 10% more, resulting in assumptions of 6.6 GeV electrons to be deflected by 6.52 mrad for all calculations.

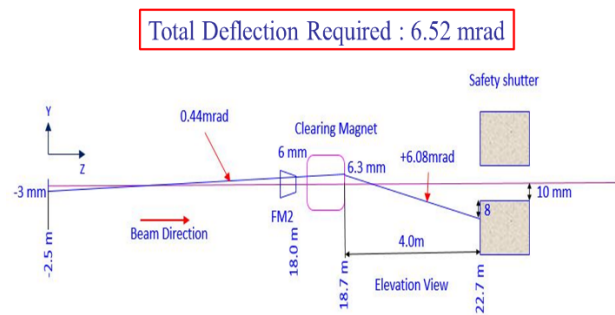


Figure 1: Schematic diagram of the clearing magnet location in the high heat load front end (HHLFE).

Based on these guiding principles the specifications for the clearing magnet are as shown in Table 1 below.

Table 1: Specifications for the Clearing Magnet

Parameter	Value	Unit
Ring Energy	6.6	GeV
Deflecting Angle	6.52	mrad
Gap	1.8	cm
Insertion Length	30	cm
Deflecting direction (electron beam)	Toward floor	---
Distance of the safety shutter from the clearing magnet	400	cm
Deflecting range in vertical (Y)	± 0.6	cm
Field at 20 cm from the magnet center	≤ 1	G

MAGNETIC DESIGN

A permanent magnet (PM) dipole was designed to produce a field of about 1T for a magnetic gap of 1.8 cm. An H-shaped hybrid PM dipole, that creates a B_x field, was designed with Opera 3D as shown in Fig. 2. The beam direction is along the Z-axis and the magnetic gap of 1.8 cm is along the X-axis. For this reference design, the magnet material of choice is NdFeB in grade N42SH, from Shin-Etsu Rare Earth Magnet, and the pole material is 1010 steel (soft iron). The N42SH has the following properties: $B_r = 1.27$ T (20°C) and intrinsic demagnetiza-

5: Beam Dynamics and EM Fields

* Work supported by the U. S. Department of Energy, Office of Science, under Contract No. DE-AC02-06CH11357
† email address: mabliz@aps.anl.gov

SEPTUM MAGNET DESIGN FOR THE APS-U*

M. Abliz†, M. Jaski, A. Xiao, U. Wienands, H. Cease, M. Borland, G. Decker, J. Kerby
Argonne National Laboratory, Argonne, IL 60439, USA

Abstract

The Advanced Photon Source is in the process of upgrading its storage ring from a double-bend to a multi-bend lattice as part of the APS Upgrade Project (APS-U). A swap-out injection scheme is planned for the APS-U to keep a constant beam current and to enable a small dynamic aperture.

A septum magnet with a minimum thickness of 2 mm and an injection field of 1.06 T has been designed, delivering the required total deflecting angle is 89 mrad with a ring energy of 6 GeV. The stored beam chamber has an 8 mm x 6 mm super-ellipsoidal aperture. The magnet is straight; however, it is tilted in yaw, roll, and pitch from the stored beam chamber to meet the on axis swap out injection requirements for the APS-U lattice.

In order to minimize the leakage field inside the stored beam chamber, four different techniques were utilized in the design. As a result, the horizontal deflecting angle of the stored beam was held to only 5 μ rad, and the integrated skew quadrupole inside the stored beam chamber was held to 0.09 T. The detailed techniques that were applied to the design, field multipoles, and resulting trajectories of the injected and stored beams are reported.

INTRODUCTION

On axis swap-out injection [1] is required for APS-U. The electron beam trajectory needs to be deflected in the horizontal and vertical planes before it is injected into the storage ring [2]. The septum needs to be tilted in yaw, pitch, and roll in order to make the required on-axis injection, since the beam comes at an angle from the booster.

To meet the APS-U needs, the septum design must meet the requirements in Table 1. The available space limitation of 178 cm results in a peak field for the injected beam needs of more than 1 T in order to achieve the total deflecting angle of 89 mrad. A thin septum with a high injection field makes the design challenging in terms of the deflecting angle (or field leakage) seen by the stored beam [3]. Furthermore, the required super-ellipsoidal cross-section of the stored beam chamber increases the field leakage in the stored beam chamber compared to the commonly used round beam chamber.

In order to reduce the effect of the field leakage on the stored beam chamber, four different unique ideas were applied to the design of the septum magnet: 1) the top pole was cut shorter than the bottom pole at both US and DS ends; 2) an open space was created around the stored beam chamber; 3) Vanadium Permendur (VP) was selected as the material of the stored beam chamber; 4)

the US end of the stored beam was placed under the side leg.

The combination of these four ideas decreased the field leakage inside stored beam chamber dramatically and decreased the integrated skew quadrupole field inside the stored beam chamber. The detailed design, injection and stored beam trajectories, the field along the injection beam trajectory, and leakage field inside the stored beam chamber will be reported.

Table 1: Specifications

Parameters	Value	Unit	Parameters	Value	Unit
Magnet Type	DC	---	Insertion Length	178	cm
Injected Beam Deflecting Angle	89	mrad	Aperture of the Stored Beam Chamber (H x V)	8 x 6	mm
Injected Field Strength, By	1	T	Septum Thickness at Down Stream End	2	mm
Tilting Angle	93	mrad	Septum Thickness at Up Stream End	4.56	mm
Stored Beam Deflecting Angle	< 100	μ rad	Beam separation at septum	5.5	mm
Injected Field Uniformity	≤ 0.001	---	Septum Thickness Tolerance	50	μ m

MAGNETIC DESIGN

An H-shaped dipole magnet structure was designed with Opera 3D for the septum magnet, as shown in Fig. 1 and Fig. 2. A coil, 4 x 12 turns, was wound around the top pole. The gap between the top and bottom poles was set at 10 mm.

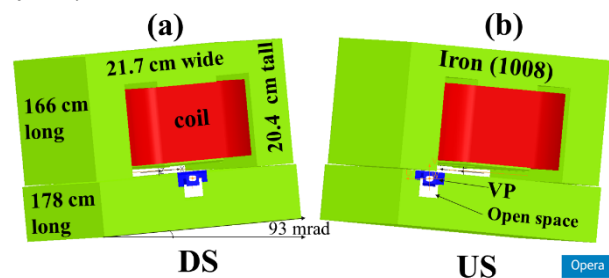


Figure 1: (a) & (b) Views of the septum magnet from the stored beam chamber at the DS and US ends.

The stored beam chamber is located in the bottom pole. The width of the top pole is 6.5 cm, the bottom pole 6 cm, and the thicknesses of the top and side yokes were selected to be 4 cm. The specified septum thicknesses at DS and US are located at the top pole's core length, +/- 83 cm in Z from the magnet center. The upstream and downstream X centers of the stored beam chamber are separated by 7.887 cm, resulting in a 47.5 mrad rotation of the stored beam chamber in the XZ-plane. The iron around the stored beam chamber was cut off and made into an open space, as shown in Fig. 3.

* Work supported by the U. S. Department of Energy, Office of Science, under Contract No. DE-AC02-06CH11357

† email address: mabliz@aps.anl.gov

MAX IV STORAGE RING MAGNET INSTALLATION PROCEDURE

K. Åhnberg*, M. Johansson, P.F. Tavares, L. Thånell, MAX IV Laboratory, Lund, Sweden

Abstract

The MAX IV facility consists of a 3 GeV storage ring, a 1.5 GeV storage ring and a full energy injector linac. The storage ring magnets are based on an integrated “magnet block” concept. Each magnet block holds several consecutive magnet elements. The 3 GeV ring consists of 140 magnet blocks and 1.5 GeV ring has 12 magnet blocks. During the installation, procedures were developed to guarantee block straightness. This article discusses the installation procedure from a mechanical point of view and presents measurement data of block straightness and ring performance.

INTRODUCTION

The MAX IV 3 GeV storage ring consists of 20 achromats [1]. Each achromat consists of five unit cells and two matching cells. The cells consist of one magnet block with several magnet elements. The position of a single magnet element relies on the machined precision of the magnet block [2]. The magnet block is aligned by three vertical, two lateral and one longitudinal adjustment screw. During installation, the magnet block top half is lifted off to allow putting the vacuum chamber in place, but the magnet block bottom half by itself does not maintain its specified straightness. This deflection corresponds to magnet elements being displaced from their ideal locations, some quite far from the specifications.

A procedure for correcting the deflection was developed and implemented in the installation procedure.

INSTALLATION PROCEDURE

- Magnets for a full achromat are lifted to their positions on the concrete stand.
- Each block is aligned with laser tracker according to the global coordinate system.
- The top halves are removed and stored in the storage ring tunnel.
- Vacuum chamber installation starts. The bottom magnet halves are used as a reference for the installation table. Vacuum chambers for a full achromat are assembled and baked together and then lifted to position and mounted in the bottom magnet blocks.
- Magnet top halves re-assembled. This includes correction procedure if needed.
- Cooling water connection.
- Power and interlock cables connected.
- Cables connected at power supply.
- Alignment re-checked according to global coordinate system and magnet to magnet.

Tool for Measuring Straightness

To measure the straightness of the magnet block, a special tool is used. It consists of a long aluminium beam with two struts at the ends and a dial gauge in the middle (see Fig. 1). Through holes in the top half magnet block the split surface is reached, with the dial gauge indicating straightness of three points (see Fig. 2). The tool is equipped with plastic handles and should be operated with gloves to minimize heat transfer. If the tool is touched with a bare hand it could show a reading of 20-30 microns.

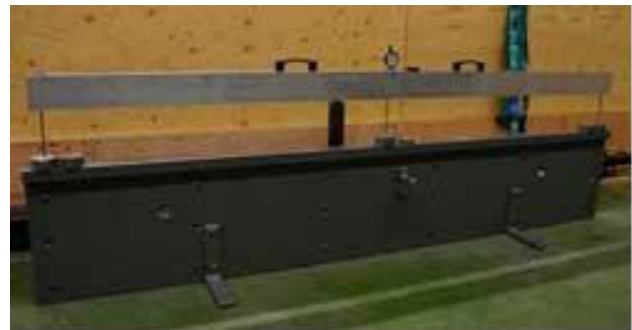


Figure 1: Measurement tool and reference beam.

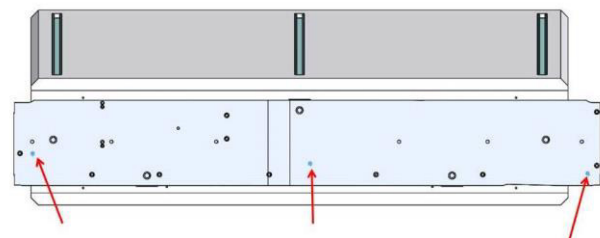


Figure 2: View from top, 3GeV U1 magnet block with points of measure.

Correction Procedure

This procedure corrects for unwanted deflections and it is performed when the bolts between the top and bottom block halves are loose. The correction is locked by tightening all bolts. The bottom magnet block is firmly attached by temporarily adding extra support and turnbuckles at the middle. Dial gauges are used to check that the magnet block is not lifted. This procedure is applied to 3 GeV ring and 1.5 GeV ring magnet blocks.

At both ends adjustable supports and turnbuckles are used to correct the magnet. Dial gauges are used to monitor the motion. The springback from the correction procedure is some 10-30 microns. Time for performing the correction procedure and achieving good results is 1-2h per magnet.

* karl.ahnberg@maxiv.se

DOUBLE TRIPLE BEND ACHROMAT FOR NEXT GENERATION 3 GeV LIGHT SOURCES

A. Alekou*, R. Bartolini, DLS, JAI and University of Oxford, UK,

N. Carmignani, S. M. Liuzzo, P. Raimondi, ESRF, France, T. Pulampong, R. P. Walker, DLS, UK

Abstract

The Double Triple Bend Achromat (DTBA) is a newly designed cell for a next generation 3 GeV synchrotron light source. DTBA is inspired by the Double-Double Bend Achromat (DDBA) cell designed for Diamond and originates from a modification of the ESRF HMBA 6 GeV cell, combining in this way the best characteristics of each lattice. The lattice achieves a natural emittance as low as 131 pm, together with a sufficient Dynamic Aperture (DA) for injection and lifetime. Two cells are designed with different end-drift lengths providing two different Long Straight Sections (LSS) for insertion devices, 5 and 7.5 m long, in addition to a new middle-straight section of 3 m. The characteristics of the lattice together with the results on emittance, DA and Touschek lifetime are presented after extensive linear and non-linear optimisations, with and without the presence of errors and corrections.

INTRODUCTION

Inspired by the DDBA cell studied as an upgrade for the Diamond Light Source [1,2], the 3 GeV Double Triple Bend Achromat (DTBA) lattice is a result of a modification of the ESRF HMBA 6 GeV cell [3] used for the future ESRF upgrade. Profiting from the lower gradients and fields required for 3 GeV, the magnets' lengths are reduced and the central dipole of the HMBA cell is removed creating a new 3 m straight section for an insertion device (ID_B, see Fig. 1).

DTBA LAYOUT

Figure 1 presents the optics and magnets layout of the DTBA cell. It includes longitudinally varying dipoles (DL), optimised for larger dispersion at the sextupoles and minimum horizontal emittance [4]. The central dipoles (DQ) are combined function magnets that allow a -I transformation between the sextupoles, and, as a result of the larger horizontal damping partition number (J_x), they reduce the emittance. A family of octupoles is also required to adjust detuning with amplitude.

Cell-length Adaptation

Several main characteristics of the 3 GeV Diamond Light Source Upgrade (Diamond-II) have been taken into account when designing the DTBA lattice. Diamond-II will have a circumference of close to the existing 561.0 m and will consist of 24 cells placed in a 6-fold symmetry, with a super-period composed as (-C1, C2, C2, C1). The total DTBA length has been adjusted as described in [5]. C2 is symmetric

* androula.alekou@physics.ox.ac.uk

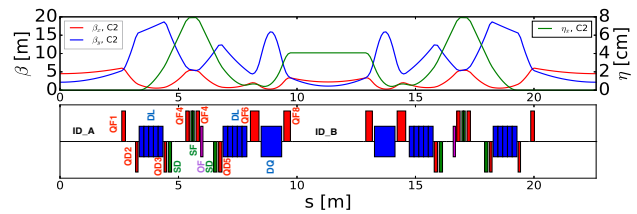


Figure 1: C2 twiss and layout; red: quadrupoles, blue: dipoles, green: sextupoles, magenta: octupoles.

and is created ensuring the quadrupole gradients are below 70 T/m; the DQ has a smaller than 30 T/m quadrupole field and a 0.6 T dipole field. C1 is asymmetric and is obtained from C2 by adding 1.5 m to the last drift.

C1 Design

C1 is asymmetric, with the last straight section longer by 1.5 m compared to C2. To keep the lattice symmetry, as a first approach, the total phase advance of C1 should be as close as possible to that of C2; the achromatic condition should also be preserved.

Two of the options that were considered for the C1 design have been presented in [5]. A third option, incorporating a triplet, is presented here: two quadrupoles were added at the end of C1 drift which help to successfully match the tune to the tune values of C2, and the twiss functions to $\alpha_x = 0$, $\alpha_y = 0$, $\eta'_x = 0$, and $\eta_x = 0$ (see Figure 2). The last 6 quadrupoles participate in the matching, and have practically no impact on the phase-advance between sextupoles; note, however, that this design does not produce a β_x waist in the ID_C. The characteristics of a DTBA lattice with 6 super-periods are given in Table 1 and the layout of one SP is presented in Figure 3.

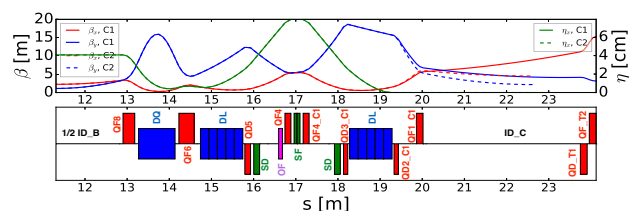


Figure 2: C1 using a triplet at the end of the cell; twiss shown from the middle until the end of the cells.

LATTICE OPTIMISATIONS

Heavy computational linear and non-linear optics optimisations were performed using Elegant [6], Accelerator Toolbox (AT) [7] and Multi-Objective Genetic Algorithms

THE FIRST PARTICLE-BASED PROOF OF PRINCIPLE NUMERICAL SIMULATION OF ELECTRON COOLING

S. Abeyratne, B. Erdelyi

Department of Physics, Northern Illinois University, DeKalb, IL 60115

Abstract

Envisioned particle accelerators such as JLEIC demand unprecedented luminosities of $10^{34} \text{cm}^{-2} \text{s}^{-1}$ and small emittances are key to achieve them. Electron cooling, where a ‘cold’ electron beam and the ‘hot’ proton or ion beam co-propagate in the cooling section of the accelerator, can be used to reduce the emittance growth. It is required to precisely calculate the cooling force among particles to estimate the cooling time accurately. We have developed a novel code, Particles’ High-order Adaptive Dynamics (PHAD), for electron cooling. This code differs from other established methods since it is the first particle-based simulation method employing full particle nonlinear dynamics. In this paper we present the first results obtained that establish electron cooling of heavy ions.

INTRODUCTION

Achieving a high luminosity of $10^{34} \text{cm}^{-2} \text{s}^{-1}$ requires a small emittance of the colliding ion beam. For this emittance reduction we employ electron cooling, which is the recommended cooling method for the JLEIC. In electron cooling, the ion beam (or proton beam) and the electron beam travel in the cooling section of the accelerator at the same average velocity. As a result of Coulomb collisions between electrons and ions, there is a friction force acting on ions. In order to model and simulate electron cooling, this friction force must be calculated precisely. Previous electron cooling simulations were phenomenological (e.g. BETACool, [1]) or parametrization of an average cooling force obtained by several simplifying approximations [2].

The construction cost of JLEIC is over \$1B. Electron cooling is a single point failure of JLEIC. Therefore, Coulomb force calculation, which is required to estimate cooling time, must be very precise in order to raise the confidence of the simulation.

Particle beams typically contain a large number of particles in the order of 10^{11} . The Coulomb force calculation using the exact method or pair-wise method is unrealistic for very large data sets. Therefore, the first challenge is to identify an approximate method to calculate the Coulomb forces efficiently and accurately. We have developed a new code and it is the first particle-based simulation method employing full particle nonlinear dynamics. The new code, Particle’ high-order adaptive dynamis (PHAD), is used to simulate electron cooling.

In this code we use three major techniques to increase the efficiency and accuracy. We use the adaptive fast multipole method to calculate the Coulomb interactions between particles and its computational time and memory usage linearly

scale with the number of particles ($O(N)$). N is the number of particles. The runtime in pair-wise calculation method is $O(N^2)$ and we claim that the adaptive fast multipole method is efficient and accurate [3]. The Picard iteration based integrator [4] is used for time stepping and the Picard order can be used to control the level of accuracy. Strang operator splitting technique is used to increase the efficiency and to maintain the symplecticity [5].

We have developed the serial version and the parallel version of the PHAD code. Using the serial version, we gathered results for over one million time steps. The transverse emittance reduction of protons was observed.

ELECTRON COOLING SIMULATION

Three widespread approximate methods are the basis function method, the particle-mesh method and the hierarchical space decomposition method [6]. Among them, the hierarchical space decomposition method constitutes the fast multipole method (FMM), and we have shown [3, 7] that the adaptive fast multipole method is the most efficient and accurate way to calculate Coulomb forces. The FMM method asserts a priori accuracy. By increasing the FMM order, the accuracy can be increased.

We used a variable order Picard iteration-based integrator [4, 5] to study the propagation of particles with time. Each particle carries an individualized time step size and it is useful for investigating close encounters. The Picard order and the time step size are the two main factors of the integrator which are liable to accuracy of the near range force calculation. However, large Picard orders and too small time step sizes significantly affect the efficiency. Therefore, if small time steps are required, the Picard order must be decreased to maintain the efficiency. On the other hand, when the larger time steps are appropriate, the Picard order can be increased to maintain the accuracy.

Strang operator splitting method is used to solve the differential equations. This is a second order accurate operator splitting method. The particles in the beam experience slow varying forces and fast varying forces. The interaction between a particular particle with other particles in its neighborhood are the fast varying forces. Also, this particle experiences another slow varying force due to the mean field generated by the far away particles. Due to this nature, we need to introduce two time step sizes for fast and slow varying forces. The smaller time step size is determined by the distance between the evaluation point and the source point and the relative speed between them. In this case, each particle has its own time step size. The mean field force is calculated using the FMM. Since this mean field force is

EVOLUTION OF THE DESIGN OF THE MAGNET STRUCTURE FOR THE APS PLANAR SUPERCONDUCTING UNDULATORS*

E. Trakhtenberg, M. Kasa, Y. Ivanyushenkov, APS, Argonne National Lab., Argonne, IL USA

Abstract

A number of superconducting planar undulators (SCU) with different pole gaps and periods were designed, manufactured, and successfully operated at the Advanced Photon Source (APS) storage ring. A key component of the project is the precision machining of the magnet structure and the precision of the coil winding. The design of the magnet core had a number of modifications during the evolution of the design in order to achieve the best magnetic performance. The current design of the magnet structure is based on the assembled jaws with individual poles, while previous designs utilized solid cores with machined coil grooves. The winding procedure also changed from the first test cores to the current final design.

Details of the magnet structure's design, manufacturing, winding and jaw assembly, and changes made from the first prototype system to the production unit, are presented.

INTRODUCTION

In order for an insertion device to be installed onto the APS storage ring it must meet difficult magnetic field specifications, particularly the first and second field integrals and phase errors. [1] Standard hybrid permanent magnet undulators (undulator "A" type) require careful magnet sorting prior to installation of the magnets during undulator assembly. After assembly, the undulator is measured magnetically at all working gaps and the magnetic field is tuned by using multiple shims of different sizes to ensure that the magnetic field will meet the requirements of the APS.

One main advantage of a superconducting undulator (SCU) is that the electric current that creates the magnetic field is the same in each coil pack along the length of the device. Nevertheless, installations of shims inside the SCU cryostat after magnet installation and magnetic field measurements is very time consuming and impractical. Magnetic field errors can be corrected by having multiple built-in correctors or by having a sophisticated correction system, such as the one proposed by Lawrence Berkeley National Lab [2].

Our approach was to fabricate the magnet structure with maximum mechanical precision to preserve uniformity of the magnetic pole width and coil grooves for the superconducting wire to completely avoid shimming and achieve all necessary tolerances with only two small end correctors.

*Work supported by the U.S. Department of Energy, Office of Science, under Contract No. DE-AC02-06CH11357

MAGNET STRUCTURE DESIGN

Several planar SCU magnet structures with lengths of 0.4 meter, 1.1 meters (two), and 1.5 meters have been machined and wound with superconducting wire. We initially considered a core made of one piece with round corners of low carbon steel 1006-1008 for prototyping. This core had continuous grooves for the superconducting wire around the whole core. It required rotation of the core around its longitudinal z-axis to produce such grooves during the machining process. This is acceptable for a short core length, but will create machining challenges for cores of lengths greater than one meter. One other detail, which requires much attention, is the surface finish of the bottom of the coil winding groove and the groove side walls. The surface finish is required to be very smooth in order to avoid damaging the superconducting wire insulation during the coil winding process. Hand polishing of these surfaces could be very labor-intensive, and therefore, costly (see Fig. 1).



Figure 1: Initial core design.

The approach taken at the APS to simplify the manufacturing process and allow for a simpler polishing process is to start with a racetrack core. The racetrack core can be machined precisely with flatness on the face plane (the beam side) better than 50 microns over the whole length, and the surface can easily be polished. This polished surface ends up being the base of the winding groove.

The next operation is to machine precise grooves on the face plane with strict tolerances on the groove width, depth and location. To avoid an accumulated error in the pole location, each groove is machined from the same initial reference plane. The previously precisely grinded, polished, and lapped magnetic poles are then installed into these grooves, which results in an excellent surface finish for the superconducting wire groove. (see Fig. 2).

FNAL ACCELERATOR COMPLEX UPGRADE POSSIBILITIES

I. Kourbanis[#], Fermilab*, Batavia, IL 60510, USA

Abstract

The Fermilab Accelerator Complex is ready to provide 700KW of beam power to the NuMI neutrino target for the first time. The current Accelerator performance will be discussed and then the possibilities for upgrading the beam power up to 4MW will be presented.

ACCELERATOR COMPLEX

The Fermilab Accelerator complex is shown in Figure 1. It has been re-configured for high power operation out of Main Injector and supports an 8 GeV neutrino program out of the Booster.

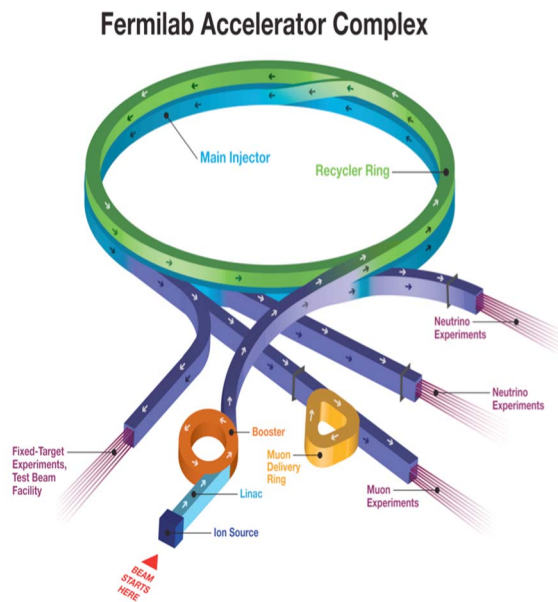


Figure 1: New configuration of the Fermilab Accelerator complex.

Proton Source

The protons source consists of the Pre-Accelerator (Pre-Acc), the 400 MeV Linac and the 8 GeV Booster synchrotron.

The 750 keV Cockcroft-Walton generator was replaced with an RFQ in 2012. The old part of the Linac (up to 116 MeV) uses Drift Tubes powered by RCA 7835 Triodes. The 1971 Booster [1] uses combined function dipoles with exposed laminations. The magnet aperture in the vertical plane is 1.6/2.2 inches in the D/F magnet respectively. It has a lattice with maximum beta functions of 34m and a dispersion of 3.2 m. It crosses transition without a gamma-t jump. The original RF cavities were recently refurbished to allow 15 Hz operations. The RF system was also

upgraded with solid state drivers and new Anode Power supplies. Three additional RF cavities were installed in order to increase reliability. New Booster correctors were installed in 2008 for orbit, tune and chromaticity correction up the ramp. The Proton Source upgrades were part of the Proton Improvement Plan (PIP) [2].

Main Injector and Recycler

The Main Injector Accelerator (MI) [3] was commissioned in 1999. It has seven times the circumference of the Booster. It has a designed admittance of 40 pi-mm-mrad (normalized at 8.0 GeV). It uses all new dipole magnets with sagitta. Most of the quadrupole magnets are recycled from the old Main Ring. It has zero dispersion straight sections, maximum beta of 58 m, and max horizontal dispersion of 1.9 m. It uses the old Main Ring cavities upgraded with solid state drivers. It accelerates protons from 8 GeV to 120 GeV with a maximum acceleration rate of 240 GeV/sec. It crosses transition without a gamma-t jump.

The Recycler [4] is a fixed energy storage Ring located in the Main Injector tunnel. It utilizes 344 combined function dipoles and 86 quadrupoles made out of permanent magnets. Two phase trombones provide tune corrections while Main Injector sextupoles are used for chromaticity correction. The Recycler was built to be a high reliability anti-proton storage Ring. The Recycler aperture is about 20% smaller than the MI aperture.

PRESENT HIGH POWER OPERATION

Slip stacking [5] is used to achieve high intensity. Up to 12 Booster batches can be slip stacked. Slip stacking has an efficiency of ~95% and the losses need to be controlled [6]. To achieve 700 KW we reconfigured the Recycler into a proton machine able to receive protons from the Booster and slip stack 12 Booster batches while the MI is ramping [7]. This reduced the MI cycle time from 2.2 sec to 1.33sec. The MI power and integrated beam to the NuMI target since 2013 when we finished the Recycler modifications are shown in Figure 2. The beam power is gradually increased as we slip stack more bunches. During the current summer shutdown we installing collimators in the Recycler [8] to control the lifetime losses during slip stacking. With the collimators in place we plan to increase the beam power to 700KW.

*Operated by Fermi Research Alliance, LLC under Contact No. DE-AC02-07CH11359 with the United States Department of Energy.

[#]ioanis@fnal.gov

THE ESS ACCELERATOR: MOVING INTO CONSTRUCTION

J.G. Weisend II[†], European Spallation Source ERIC, Lund, Sweden

Abstract

The ESS accelerator construction has started and the tunnel and RF gallery will be handed over to the accelerator division in 2016 with the installation of the cryoplant starting in early 2017. Beam should be delivered in June 2019 at 570 MeV and 1.5 MW with full 5 MW capability being available in 2023. The project is a highly contributed project with more than 50% of the total budget being contributed IK by more than 25 IK partners. This paper will review the project status reflecting the IK nature of the project with the many partners' contributions and with some focus on the cryogenics systems.

INTRODUCTION

The European Spallation Source (ESS) is a new facility currently under construction in Lund, Sweden. Upon completion, ESS will be a neutron source providing world-class capabilities for research in a wide range of topics in materials science and physics.

The neutrons at ESS will be generated via the spallation process when a high power proton beam, produced by a linear accelerator, collides with a rotating Tungsten target. The resulting neutrons then travel to up to 23 instruments where they are use in scientific studies. The overall ESS project is well described in [1].

The ESS proton linac is required to produce a beam of 2 GeV energy with a current of 62.5 mA, a pulse length of 2.86 ms and a repetition rate of 14 Hz. This results in an average beam power of 5 MW with a peak beam power of 125 MW. This will constitute the world's most powerful proton linear accelerator. Figure 1 is a schematic of the ESS accelerator. Additional details on the accelerator may be found in [2 -3].

The ESS accelerator is moving out of the design phase and into construction with almost all of the accelerator components being under construction by May of 2017. This paper will describe the current status of the ESS accelerator components with additional emphasis on the accelerator cryogenics system. A brief overview of the status of the accelerator buildings and tunnel is also presented.

IN-KIND PARTNERS

A significant feature of the ESS project is the use of In-Kind partners. More than 50% of the accelerator project, including almost 100% of the beam line components are provided by 27 different institutions throughout Europe.

The current distribution of In kind partners is shown in Fig. 2. Effective communication and coordination with these partners is a vital aspect of the ESS project. These institutions are not subcontractors but rather are full partners in the ESS project. The In-Kind partner institutions, for example, all have representation on the Accelerator Technical Board which oversees and directs the construction of the accelerator.

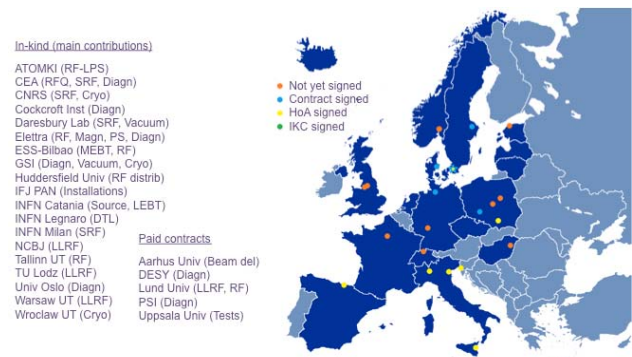


Figure 2: Current In-kind partners for the ESS accelerator.

DESIGN REVIEWS

In order to ensure proper performance, all accelerator components, regardless of their origin, undergo at least one Preliminary Design Review (PDR) and one Critical Design Review (CDR). These reviews examine all aspects of the design including performance, safety, quality and reliability. The review committees consist of members of the ESS project along with external experts when required. Generally speaking, once a component has completed its CDR, it moves from design into procurement and construction. This year represents the peak for accelerator component design reviews at ESS with roughly 50 reviews being held in 2017.

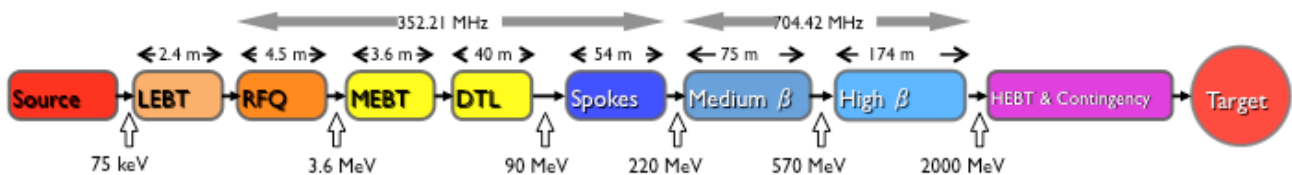


Figure 1: Schematic of the ESS accelerator.

SPACE CHARGE COMPENSATION USING ELECTRON COLUMNS AND ELECTRON LENSES AT IOTA *

Chong Shik Park[†], Vladimir Shiltsev, Giulio Stancari, Jayakar Charles Tobin Thangaraj,
Diletta Milana¹, Fermilab, Batavia, IL, U.S.A.
¹ also at Politecnico/Milano, Milano, Italy

Abstract

The ability to transport a high current proton beam in a ring is ultimately limited by space charge effects. Two novel ways to overcome this limit in a proton ring are by adding low energy, externally matched electron beams (electron lens, e-lens), and by taking advantage of residual gas ionization induced neutralization to create an electron column (e-column). Theory predicts that an appropriately confined electrons can completely compensate the space charge through neutralization, both transversely and longitudinally. In this report, we will discuss the current status of the Fermilab's e-lens experiment for the space charge compensation. In addition, we will show how the IOTA e-column compensates space charge with the WARP simulations. The dynamics of proton beams inside of the e-column is understood by changing the magnetic field of a solenoid, the voltage on the electrodes, and the vacuum pressure, and by looking for electron accumulation, as well as by considering various beam dynamics in the IOTA ring.

INTRODUCTION

High intensity accelerators have been fundamentally limited to their intensities by various sources of instabilities, such as e-cloud, beam halo, space charge effects, etc [1]. There have been many challenges to mitigate the effects of space charge forces, by controlling the beam using solenoidal fields, scrapping the halos, or compensating with opposite charges [2].

The Space Charge Compensation (SCC) methods have been successfully applied to transport high current, low energy proton or H^- beam in linear accelerators. In addition, solenoid based compensations in RF photoinjectors are widely used in most of xFELs. However, SCC schemes in circular machines have not been actively implemented since charge neutralization over the entire circumference of the ring is not practical, and local compensation scheme results in high density profiles of electrons which would also cause another e-p instabilities.

The Integrable Optics Test Accelerator (IOTA) ring is being built at Fermilab to implement nonlinear integrable lattices, which will improve the beam stability to perturbations and mitigations of collective instabilities through Landau damping [3]. The IOTA ring will be also used to study space charge compensation in circular rings, and to demonstrate optical stochastic cooling system. Using newly built IOTA

ring, two novel schemes have been planned to study space charge compensations in circular machines; electron lens and electron column.

For the SCC method with an electron lens, externally generated co-propagating beam of opposite charge collides with the proton beam inside a strong magnetic field, in result, it compensates the space charge tune shift of the proton beam. For an electron column method, however, electrons are generated from the ionization processes of the beam itself with the residual gas in a solenoidal field. Both methods of space charge compensations require to precisely control the density profile of magnetized electrons through propagating or trapping inside strong magnetic fields. In this report, we present these two novel experimental projects to mitigate instabilities induced by space charge effects using electron lens or electron column methods at Fermilab's IOTA ring.

ELECTRON LENS

In the electron lens, a pulsed, magnetically confined, and low energy electron beam interacts with circulating proton beam electromagnetically to mitigate space charge tune shifts [4]. There exists many applications of electron lenses including long-range beam-beam compensation, head-on beam-beam compensation, and halo-scrapping with hollow electron beams [5]. Figure 1 shows the schematic layout of the electron lens previously used in Tevatron.

In an electron lens scheme for the space charge compensation, the externally generated electron beam with matched transverse distributions collides with the circulating proton beam. The transverse density profile of the injected electron beam is shaped by the cathode of the RF photoinjector, and the stability of the electron beam is maintained by strong external solenoidal fields. The longitudinal profile of pulsed electron beam could also match to proton bunch profile, if needed.

We recycle components from the Tevatron electron lenses. Currently, vacuum tests of gun and collector are completed. We aim to assemble the e-lens in straight configuration for checkout by the end of 2018. The electron beam transport

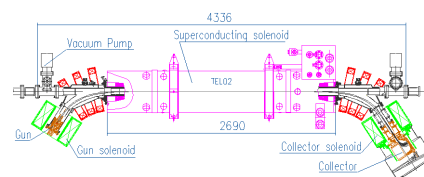


Figure 1: Schematic Layout of an Electron Lens Experimental Setup

* This work was supported by the United States Department of Energy under contract DE-AC02-07CH11359.

[†] cspark@fnal.gov

DEVELOPMENT OF A HIGH BRIGHTNESS SOURCE FOR FAST NEUTRON IMAGING*

B. Rusnak[†], J.M. Hall, P. Fitsos, M. Johnson, D. Bleuel, A. Wiedrick, M. Crank, S. Anderson, R. Marsh, D. Gibson, J. Sain, R. Souza, Lawrence Livermore National Lab, Livermore, USA

Abstract

Lawrence Livermore National Lab is developing an intense, high-brightness fast neutron source to create high resolution neutron radiographs and images. An intense source (10^{11} n/s/sr at 0 degrees) of fast neutrons (10 MeV) allows: penetrating very thick, dense objects; maintaining high scintillator response efficiency; and being just below the air activation threshold for (n,p) reactions. Fast neutrons will be produced using a pulsed 7 MeV, 300 micro-amp average-current commercial ion accelerator that will deliver deuteron bunches to a 3 atmosphere deuterium gas cell target. To achieve high resolution, a small (1.5 mm diameter) beam spot size will be used, and to reduce scattering from lower energy neutrons, a transmission gas cell will be used to produce a quasi-monoenergetic neutron beam in the forward direction. Because of the high power density of such a tightly focused, modest-energy ion beam, the gas target is a major engineering challenge that combines a “windowless” rotating aperture, a rotary valve to meter cross-flowing high pressure gases, a novel gas beam stop, and recirculating gas compressor systems. A summary of the progress of the system design and building effort shall be presented.

INTRODUCTION

Using fast neutrons for radiography enables producing radiographic images of thick, dense objects that are difficult to penetrate with X-rays. For objects with $\rho \cdot l$ areal densities greater than approximately 100-150 g/cm², fast neutrons are more effective than X-rays for producing sub millimeter-scale images with less absorbed dose to the interrogated object than would occur with X-rays [1]. For this reason, fast neutron radiography/imaging is being developed as an advanced non-destructive evaluation (NDE) technique. Areas of potential application include radiographing large assemblies like car engines and heavy machinery that are optically too thick for X-rays to produce images of interior details [2]. A major challenge in advancing the technique for more uses is the inconvenience of having to do the measurements at a large-scale nuclear reactor or at a spallation neutron source. The LLNL system being developed is intended to be a much smaller lab-scale instrument instead of a facility-scale machine. This should facilitate not only easier access, but improve deployment opportunities for potential users.

* This work performed under the auspices of the U. S. Department of Energy by Lawrence Livermore National Laboratory under contract DE-AC52-07NA27344.

[†] rusnak1@llnl.gov

NEUTRON PRODUCTION FOR IMAGING

Fast neutron imaging is accomplished in the same fashion as X-ray shadow radiography, except that an intense, bright source of fast neutrons is used instead of a bright source of bremsstrahlung X-ray photons, shown schematically in Fig. 1.

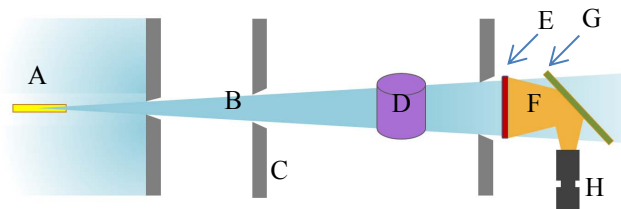


Figure 1: Schematic of neutron imaging approach showing the source (A), neutrons (B), collimators (C), object (D), scintillator (E), light from scintillator (F), turning mirror (G), and CCD camera (H). The location of the object between the source and scintillator sets the magnification of the system.

Achieving high resolution requires a small, bright source spot as the source spot size fundamentally sets the resolution for the system. The LLNL neutron imaging machine is being designed to have a neutron source spot size that is 1.5 mm in diameter and 40 mm in length. Viewed end on, this establishes sub-millimeter image resolution out to 30 cm from the axis 5 m from the source. System resolution is also influenced by the light generation physics in the scintillator, by the scintillator thickness, and the CCD imaging camera. The design has been optimized such that all these elements are consistent with sub-millimeter resolution, and no one element has been over-engineered only to be limited by other elements.

For penetrability, it was determined that the neutron total cross section for most elements drops to the relatively low value of a few barns for neutron energies of 10 MeV and higher. In addition, many heavy elements have a dip in the cross section between 10-15 MeV, suggesting this is a near ideal energy range for fast neutron imaging. Neutrons in this energy range have the added benefits of still having relatively high interaction cross sections with low Z materials inside heavily shielded assemblies, and with the scintillator to produce light that generates the radiograph.

Given this ideal energy range, DT tubes were initially considered for this application given their relative simplicity, modest cost, and ability to produce quasi-monoenergetic neutrons at 14 MeV via the $D(t,p)^4He$

THERMOACOUSTIC RANGE VERIFICATION FOR ION THERAPY

S.K. Patch^{1*}, Y.M. Qadadha, UW-Milwaukee, Milwaukee WI 53211
 M. Kireeff-Covo^{2*}, A. Jackson, K.S. Campbell, R.A. Albright, P. Bloemhard, A.P. Donoghue,
 C.R. Siero, T.L. Gimpel, S.M. Small, B.F. Ninemire, M.B. Johnson, and L. Phair
 Lawrence Berkeley National Laboratory, Berkeley CA 94720
 * corresponding authors for ^{1*}thermoacoustics and ^{2*}chopper engineering

Abstract

The clinical value of particle therapy is limited by inaccurate range verification, currently assumed to be 1 mm + 3.5% of the target depth. The purpose of this work was to correlate the Bragg peak location with target morphology, by overlaying the location of the Bragg peak onto a standard ultrasound image. A fast chopper installed between the ion source and the cyclotron inflector pulsed delivery of 50 MeV protons so that 4 pC were delivered in 2 μ s, depositing 2 Gy in the Bragg peak. The ion pulse generated thermoacoustic pulses that were detected by a cardiac ultrasound array, which also produced a grayscale ultrasound image. A filtered backprojection algorithm focused the received signal to the Bragg peak location with perfect co-registration to the ultrasound images. Data was collected in a room temperature water bath and gelatin phantom with a cavity designed to mimic the intestine, in which gas pockets can displace the Bragg peak. Thermoacoustic range measurements agreed with Monte Carlo simulation and first-order range estimates from CT images to within 1.5 mm.

MOTIVATION/INTRODUCTION

Proton therapy delivers less dose to proximal tissue, and spares distal tissue altogether. Evidence-based medicine currently supports the use of proton therapy only for tumors near the base of the neck, spine, eye and in pediatric patients [1]. Lack of accurate range verification otherwise limits clinical utility of proton therapy [2]. Short-lived positron [3] and prompt gamma emissions [4, 5] can provide fast and real-time feedback, respectively, but do not correlate the Bragg peak location with anatomy. An automated method for correlating PET data to underlying anatomy in CT images [6] is slow and precludes online adaptive planning.

Thermoacoustic range verification is a natural consequence of the conversion of deposited dose to mechanical pressure pulses. Treatment plans are quantified in terms of Grays, 1 Gy = 1 J/kg [7], whereas acoustic pulse amplitudes are quantified by Pascals, 1 Pa = 1 N/m² = 1 J/m³. The units for dose and pressure differ only by a multiplicative factor of target density, ρ . The dimensionless Grüneisen (Γ) is simply the constant of proportionality between energy density and thermally induced pressure change. In soft tissue, $\Gamma \sim 0.1$, so the rule of thumb is that 100 Pa are generated per Gy, provided stress confinement holds and the deposition rate exceeds the rate at which pressure propagates away from the

target. Fig. 1 models pressures generated by single turn delivery of a 2 Gy dose due to a 49 MeV beam.



Figure 1: Pressure and dose in waterbath due to 49 MeV beam. Dose in Gy plotted in yellow, overlaid on a cross-sectional image of pressure due to single turn extraction. Distal transducer location indicated by yellow square.

Regardless of spill time, thermoacoustic pulses measured at distant transducer locations are diminished by several factors. $1/r$ geometric spreading is unavoidable. Fortunately, acoustic absorption and scatter are less significant in the very low frequency regime of thermoacoustic emissions. Thermoacoustic emissions generated by instantaneous, “single turn” delivery of 4 pC are compared to those generated by spill times of 2, 6 and 18 μ s in Fig. 2.

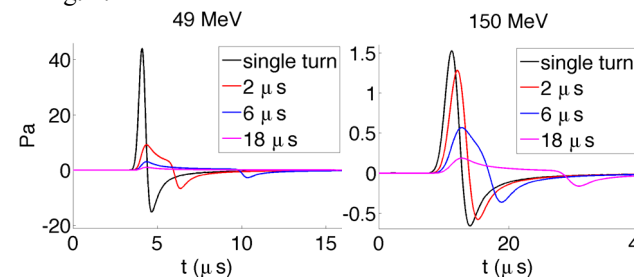


Figure 2: Thermoacoustic measurements at distal transducer locations as a function of spill time. 49 MeV (left) and 150 MeV (right) beams with transducer 6.5 mm and 20 mm distal, respectively.

Long spill times allow pressure to propagate away as ions continue to be deposited. Transit time across the Bragg peak of a 49 MeV beam is less than a 2 μ s spill time, which diminishes measured pressures four-fold, as seen by the red plot in Fig. 2 (left). Straggling broadens the Bragg peak of a 150 MeV beam, increases acoustic transit time so that a 2 μ s spill preserves amplitude, whereas a 6 μ s spill does not as shown in Fig. 2 (right).

Experimentally, 2 μ A of 50 MeV protons were delivered for 2 μ s. An injection line chopper (Fig. 3) limited the energy deposited by low energy beams, delivering 2 Gy in a single pulse. Unlike previous results in which thermoacoustic emissions were detected by single-element transducers or hydrophones without online correlation to anatomy, and recently two different ultrasound arrays were used to receive thermoacoustic emissions and generate ultrasound images of a mouse leg [8]. We used the

AN ULTRA-HIGH RESOLUTION PULSED-WIRE MAGNET MEASUREMENT SYSTEM*

S. G. Biedron, A. D'Audney, S. V. Milton[†], Colorado State University, Fort Collins, CO, USA

Abstract

Traditional magnet measurements systems for undulator magnets have relied on the use of calibrated Hall probes placed on a rigid mechanical arm and passed down the length of the undulator. This works for the most common undulators that have ready access along an entire side of the magnet; however, new magnet designs such as superconducting undulator magnets are not constructed with such convenient access for a Hall probe, and another method is warranted. In this manuscript we explore the use of a dispersion and pulse length corrected pulsed-wire measurement system to measure our undulator magnet. The background and method are described and our results given.

INTRODUCTION

Modern accelerators including accelerator-based light sources rely on the detailed, accurate, and precise measurement of their magnetic devices. Of particular interest in light sources is the measurement of the undulator magnet. The quality of the light being generated from these devices is strongly dependent on the accuracy of the magnetic field profile, and this pushes one to ensure that the fields are accurately measured.

Until recently, the actual design of undulators has followed a historical trend largely driven by the design of the standard 3rd-generation synchrotron light source. In such machines the beam is guided horizontally around the machine circumference by large dipole magnets with their primary magnetic field oriented in the vertical direction. In these 3rd-generation machines the vast majority of the undulators are powered with permanent magnet material and this material is susceptible to radiation damage making it a design criteria to ensure that the undulators are not hit by radiation, be it synchrotron radiation or electron beam losses ([1] and references contained therein). The obvious way to do this is to arrange the out of the plane of the machine and the synchrotron radiation. These criteria have led to a standard undulator design very similar to what is shown in Figure 1 where there is an opening along the entire length of one side of the undulator magnet array. Such a structure not only lends itself well to fitting in standard storage rings, but also to magnetic measurement as a measurement probe can easily be inserted and positioned accurately along the entire length of the structure. But as the light source community has matured and the machines have reached new levels of performance, undulator designs, too, have progressed. The measurement methods have had to adapt to new configurations. These boutique undulators can have very small gaps, exotic geometries, no side gaps and/or can be in vacuum. It is with this in mind that we decided to adapt one of these newer measurement methods to our own undulator.

[†] email address: Stephen.milton@colostate.edu



Figure 1: A common undulator configuration where there is an opening along the entire length of one side.

We have at Colorado State University (CSU) [2] an undulator magnet. The primary undulator parameters are listed in Table 1. This undulator was constructed, measured, and tuned a number of years ago and used for an FEL program at the University of Twente in the Netherlands [3,4]. Since that time it has been shipped across the Atlantic and has been in storage. It is a fixed-gap undulator, and to simplify the construction the gap has been set with gauge blocks along both sides of the gap (Figure 2) thus precluding measurement in a standard undulator magnet measurement configuration.

Table 1: Primary Undulator Parameters

Parameter	Value
K	1
Period	2.5 cm
Gap	8 mm
Material	Sm ₂ CO ₅
Periods	50
Length	1.25 m



Figure 2: Left, the CSU undulator. Right, close-up of the gauge blocks fixing the magnet gap.

Warren developed a pulsed wire magnet measurement system [5]. In this method a thin wire is stretched through the length of the undulator magnet. An electric current is then pulsed through the wire. The resulting Lorentz force generates an impulse that in turn generates a transverse travelling wave along the wire, the amplitude and time structure of which is representative of the magnetic field along the length of the undulator. This motion can then be measured giving a representation of the undulator field.

6D PHASE SPACE MEASUREMENT OF LOW ENERGY, HIGH INTENSITY HADRON BEAM

B. Cathey, A. Aleksandrov, S. Cousineau, A. Zhukov
Oak Ridge National Laboratory, Oak Ridge, TN, 37830, USA

Abstract

The goal of this project is to demonstrate a method for measuring the full six dimensional phase space of a low energy, high intensity hadron beam. This is done by combining four dimensional emittance measurement techniques along with dispersion measurement and a beam shape monitor to provide the energy and arrival time components. The measurement will be performed on the new Beam Test Facility (BTF) at the Spallation Neutron Source (SNS), a 2.5 MeV functional duplicate of the SNS accelerator front end.

INTRODUCTION

For high power, high intensity accelerators, beam loss is one of the limiting factors for performance and achievable beam power [1]. Today's state-of-the-art simulation codes provide accurate tracking for the RMS values of the beam through the beam line for many cases, and in principle should also be able to accurately track the beam halo formation and beam loss through the accelerator. However, successful simulation of beam halo and beam loss have yet to be accomplished [2,3,4,5]. As the capabilities of the simulations should be sufficient, the problem may then lie in an incorrect initial assumption, and the most likely candidate is the initial particle distribution, as it is generally approximated [6,7].

In order to determine the initial particle distribution, the beam must be measured over all six independent spatial and momentum parameters in such a way that correlations between parameters can be seen. However, such a scan would be incredibly time consuming and require an accelerator dedicated to the task. As such, no direct full six dimensional measurement of the distribution has ever been performed. The Beam Test Facility at SNS is a small-scale accelerator with available time, which has already been partially designed for this task. The goals of this thesis are two-fold:

- 1) Complete the design and installation work to allow the full six dimensional measurement
- 2) Perform the first six dimensional phase space measurement.

The measurement will answer questions that have long persisted about the existence of correlations between the six degrees of freedom and will serve as a full and accurate particle distribution for benchmarking simulations and predicting beam dynamics at the level which relates to beam loss.

EMITTANCE MEASUREMENT

Current emittance measurement techniques focus on mainly the transverse plane. As of now the most dimensions measured simultaneously are the four within the transverse plane using the "pepper-pot" technique [8]. But this technique is not effective for higher energy beams. It has been shown that the slit and collector method, which works by passing the beam through two apertures of varying position, is an effective technique to measure a two dimensional phase space for a particular axis of a high energy beam.

In the past, three separate two dimensional phase spaces have been combined to create a six dimensional distribution. However, because the un-measured cross-terms are assumed to be zero in this reconstruction, this distribution is not the same as actually measuring all the dimensions together. In order to determine true six dimensional distributions, all six degrees of freedom must be directly measured together. The technique proposed here is the same principle as the above aperture technique but for all six dimensions simultaneously.

The particles will go through a series of five apertures and a Beam Shape Monitor (BSM). Each aperture will allow particles through at the coordinate being measured. By combining two pairs of apertures, one pair being horizontal slits and the other pair vertical slits, the four dimensional transverse phase space can be measured (Fig. 1).

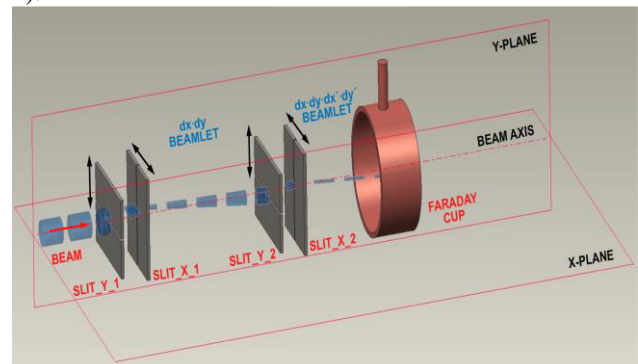


Figure 1: A diagram showing the principle behind a four dimensional scan over the transverse plane.

To find the longitudinal momentum, we use a 90 degree bending magnet. During the turn, the beam spreads as higher momentum and lower momentum particles separate horizontally causing dispersion. This dispersion creates a correlation between the horizontal position and the longitudinal momentum of a particle allowing the selection of particles with certain momentum based on

PROGRESS OF GAS-FILLED MULTI-RF-CAVITY BEAM PROFILE MONITOR FOR INTENSE NEUTRINO BEAMS*

K. Yonehara[†], M. Backfish, A. Moretti, A. V. Tollestrup, A. Watts, R. M. Zwaska,
Fermilab, Batavia, IL 60510, USA

M.A. Cummings, A. Dudas, R. P. Johnson, G. Kazakevich, M. Neubauer,
Muons, Inc., Batavia, IL 60510, USA

B. Freemire, Illinois Institute of Technology, Chicago, IL 60616, USA

Q. Liu, Case Western Reserve University, Cleveland, OH 44106, USA

Abstract

We develop a concept of a novel pressurized gas-filled multi-RF-cavity beam profile monitor that is simple and robust in high-radiation environments. Charged particles passing through each RF-cavity in the monitor produce intensity-dependent ionized plasma, which changes the gas permittivity. The sensitivity to beam intensity is adjustable using gas pressure, concentration of electronegative dopant, and RF gradient. The performance of the RF gas monitor has been numerically simulated to evaluate the sensitivity of permittivity measurements. The range will cover the expected beam intensities in NuMI and LBNF. The critical plasma parameters to design the RF gas monitor and the proposed demonstration test to validate the concept of RF gas monitor are discussed in this presentation.

INTRODUCTION

The Long Baseline Neutrino Facility (LBNF) is the future flagship experiment at Fermilab. Beam profile monitors play an important role to check healthiness of a target which generates the beta-decaying secondary charged particles for neutrino experiments and to diagnose the quality of primary and secondary beams. One of the challenges to realize a multi-MW beam complex such as LBNF is monitoring of the beam profile under extreme radiation environments. Potential radiation damages were found in the present beam profile monitor based on an ionization chamber at NuMI (Neutrinos at the Main Injector) even though the present operating beam power is sub-MW [1].

We propose a radiation-tolerant gas-filled RF cavity beam profile monitor that provides precise measurements of the beam profile downstream of the target. The RF monitor is based on microwave cavity resonators that are a simple metallic box filled with gas. Incident particles interact with the gas to form plasma via the ionization process. As a result, the gas permittivity is changed proportional to the number of ion pairs. The beam profile is reconstructed by measuring the permittivity change in the individual RF cavity of the monitor. The change is measured by observing the modulation of RF signal, e.g. the time domain resonant frequency and quality factor changes in the RF cavity.

Beam-induced plasmas in a high-pressure gas-filled high-gradient RF cavity were studied in experiments at the Muon Test Area (MTA) for muon ionization cooling applications [2, 3]. The multi-RF-cavity beam profile monitor has been evaluated in analytical and numerical simulations by using the experimental result [4]. However, the observed plasma parameters at MTA were taken at quite high RF gradients and gas pressures, i.e. the design RF gradient and gas pressure are 20 MV/m and 160 atm at room temperature, respectively, and a gaseous hydrogen is considered as an ionization material. The RF frequency in the muon ionization cooling channel is 0.2-1 GHz. On the other hand, a present interesting plasma parameter in the RF gas monitor occurs at lower RF gradient and gas pressure than the muon application, i.e. the designed RF gradient and gas pressure are 0.1 MV/m and 10 atm, respectively, and a gaseous nitrogen is considered as an ionization material. The RF frequency for the beam profile monitor is 1-10 GHz. A new beam test is required to study the plasma parameter for the RF monitor.

Current design of the RF gas monitor is optimized for the LBNF application [5]. The primary proton beam power and energy at LBNF are 2.4 MW and 120 GeV, respectively. The beam pulse length is 10 μ s, and the cycle time is 1.2 sec. The number of protons per beam pulse (cycle) is $1.5 \cdot 10^{14}$ protons per pulse. The target will be made of either a 1-meter-long or a 2-meter-long graphite, or using different material, like Be. There are three toroidal magnet horns near the target to focus one-sign of charge pions and other beta decaying particles. The RF gas monitor will be located 200 m downstream from the target. Figure 1 shows the simulated fraction of secondary protons incident into a 3×3 cm² bin, which is the size of single RF cavity in the monitor, per POT (protons on target) at 200 m downstream of a 1-m-long and 2-m-long graphite targets in G4Beamline [6]. It shows that the RF gas monitor should respond to the maximum beam intensity per unit area, that is $5 \cdot 10^{10}$ ppp/cm², without losing a linearity. Ionized plasma due to other charged particles, like pions, kaons, and muons, etc, is two orders of magnitudes lower density than protons. Hence, it is omitted in this analysis.

KEY PARAMETER TO DESIGN RF GAS MONITOR

The essential plasma dynamics in a gas-filled RF cavity is presented in references [2–4]. The critical plasma param-

* Work supported by Fermilab Research Alliance, LLC under Contract No. DE-AC02-07CH11359 and DOE STTR Grant, No. DE-SC0013795.

[†] yonehara@fnal.gov

MEASUREMENT OF COHERENT TRANSITION RADIATION USING INTERFEROMETER AND PHOTOCONDUCTIVE ANTENNA

K. Kan^{#1}, J. Yang, T. Kondoh, M. Gohdo, I. Nozawa, Y. Yoshida^{#2}

The Institute of Scientific and Industrial Research (ISIR), Osaka University, Osaka 567-0047, Japan

Abstract

Ultrashort electron beams are essential for light sources and time-resolved measurements. Electron beams can emit terahertz (THz) pulses using coherent transition radiation (CTR). Michelson interferometer is one of candidates for analyzing the pulse width of an electron beam based on frequency-domain analysis. Recently, electron beam measurement using a photoconductive antenna (PCA) based on time-domain analysis has been investigated. In this presentation, measurement of femtosecond electron beam with 35 MeV energy and < 1 nC from a photocathode based linac will be reported. Frequency- and time-domain analysis of THz pulse of CTR by combining the interferometer and PCA will be carried out.

INTRODUCTION

Short electron bunches with durations of picoseconds to femtoseconds are useful for generation of light in terahertz (THz) range [1]. Such electron beams are used in time-resolved studies of ultrafast phenomena and reactions, including ultrafast electron diffraction (UED) [2] and pulse radiolysis [3-5]. Electro-optic sampling [6], which is one of detection techniques of THz light pulse, is used in diagnostics of electron bunches. In EO samplings for electron bunch length measurement, the birefringence of EO crystals is induced by the beam electric field, and laser polarization corresponding to the longitudinal electron beam profile is detected [7,8]. EO monitors based on the temporal decoding have revealed the Coulomb field of a root mean square (rms) width of 60 fs from femtosecond electron bunches [8]. Interferometers [9] have been also used for the detection of single mode or multimode THz pulses generated by electron bunches and slow-wave structures [10,11]. Smith-Purcell radiation, which uses metallic gratings, has also been analyzed by interferometers [12,13]. Coherent transition radiation (CTR), which is generated by electron bunches crossing a boundary between different media, has been measured by interferometers and grating-type spectrometers [14-16]. Photoconductive antennas (PCAs), which are composed of semi-insulating semiconductor with electrodes, are widely used for both generation and detection of THz pulses in THz time-domain spectroscopy [17-20]. PCAs could be good candidates for analyzing temporal electric field profiles of electron bunches due to the correlation between electric-field-induced current output and THz electric field strength [20]. THz pulses of CTR are radially polarized [21] due to the diverging electric fields from the beam center. Therefore, a PCA with radial polarization charac-

teristics is considered to be useful for the measurement of THz pulse from an electron bunch. Recently, Winnerl *et al.* reported fabrication of a large-aperture PCA, and the radially polarized field pattern of focused THz pulses was measured [22]. Generation of high-power THz pulses from a PCA using a high-voltage source has been studied for acceleration of electron beam [23]. Polarization components of radially polarized THz pulses from a PCA with interdigitated electrodes were also investigated using a wire grid polarizer [24]. Time-domain measurement of CTR using the PCA as a detector has been also conducted. The scheme is based on measurement of radially polarized THz pulses of CTR with a large-aperture PCA [24], which has radial polarization components. The combination of an interferometer and PCA will enable frequency and time-domain analysis of THz pulse of CTR.

In this paper, measurement of CTR from a femtosecond electron beam was conducted based on frequency and time-domain schemes. The energy and charge of the electron beam were 35 MeV and < 1 nC at a repetition rate of 10 Hz, respectively. Frequency spectra of CTR were measured by a Michelson interferometer. On the other hand, time profiles of CTR were measured by a PCA driven by a femtosecond laser.

EXPERIMENTAL ARRANGEMENT

Femtosecond electron bunches were generated by a photocathode-based linac, which consists of a 1.6-cell S-band radio frequency (RF) gun with a copper cathode, a 2-m-long traveling-wave linac, and an arc-type magnetic bunch compressor. The photocathode of RF gun was excited by UV pulses (262 nm) of a picosecond laser with an energy of < 180 μ J/pulse and a pulse width of 5 ps FWHM at 10 Hz. The electron bunches generated in the gun were accelerated in the linac using a 35-MW klystron at a repetition rate of 10 Hz. In the linac, the electron bunches were accelerated to 35 MeV at a linac phase of 100° which is suitable for the bunch compression [16]. The accelerated electron bunches were compressed to femtosecond by the magnetic bunch compressor, which was composed of bending magnets, quadrupole magnets, and sextupole magnets. THz pulses of CTR were generated by the compressed electron bunches and measured.

Schematic diagram and picture of measurement system for CTR using the interferometer and PCA [24] were shown in Fig. 1. CTR was generated on the interface of a mirror (M1) as shown in Fig. 1 (a). The beam energy and bunch charge were 35 MeV and 740 pC/pulse, respectively. Collimated THz pulses of CTR were separated by a beam splitter (BS1). One THz pulse was introduced to the interferometer. In the interferometer, the THz pulse was separated by a beam splitter (BS2) again. Superposed

#1: koichi81@sanken.osaka-u.ac.jp

#2: yoshida@sanken.osaka-u.ac.jp

LIGHT: A LINEAR ACCELERATOR FOR PROTON THERAPY*

A. Degiovanni[†], P. Stabile, D. Ungaro, A.D.A.M. SA, Geneva, Switzerland
on behalf of A.D.A.M. SA

Abstract

ADAM, Application of Detectors and Accelerators to Medicine is a Swiss Company based in Geneva Switzerland established on 20th December 2007. ADAM was founded to promote scientific know-how and innovations in medical technology for cancer treatment. In 2007 a first partnership agreement was signed with CERN and in 2011 ADAM has been officially recognized as CERN spin-off. After the first research results other partnership agreements were signed between ADAM and CERN with the main goal of establishing a framework within which the two parties can collaborate to develop novel technologies for detectors and accelerators. Currently ADAM research activity is mainly focused on the construction and testing of its first linear accelerator for medical application: LIGHT (Linac for Image-Guided Hadron Therapy). LIGHT is an innovative linear accelerator designed to revolutionise hadron therapy facilities by simplifying the infrastructure and make them profitable from an industrial point of view while providing a better quality beam. The current design allows LIGHT to accelerate proton beam up to 230 MeV with several advantages comparing to the current solutions present in the market.

INTRODUCTION

Many of the accelerator and detector technologies developed in the field of particle physics have found an application in industry and medicine. Proton therapy is a very dynamic and growing market for particle accelerators, with 10% increase per year in the number of patients [1].

After ADAM was founded in 2007 a first partnership agreement was signed with CERN and in 2011 ADAM has been officially recognized as CERN spin-off. Examples of projects developed by ADAM in the past years include: i) Intra Operative Radio-Therapy (IORT) linac at high frequency; ii) dosimeter for micro-dosimetry measurements (based on Si detectors used in CMS tracker [2]); iii) X-eye, a compact 6 MeV C-band accelerator for conventional radiotherapy; iv) the First Unit prototype of LIGHT. Currently ADAM research activity is mainly focused on the construction and testing of its first linear accelerator for medical application: LIGHT (Linac for Image-Guided Hadron Therapy). In this work the LIGHT system is described in detail, with a particular emphasis on the technical solutions inspired by technologies either developed or in use at CERN.

THE LIGHT SYSTEM

Electrons linacs are widely spread in hospitals for producing X-rays used in conventional radiation therapy. On the contrary only cyclotrons or synchrotron are used to accelerate protons to energies relevant for the treatment of deep seated tumours. The LIGHT accelerator is the first high frequency linear accelerator working at 3 GHz [3] designed as an industrial product for proton therapy.

The LIGHT accelerator consists of three different linac sections (as shown in Fig. 1): a Radio Frequency Quadrupole (RFQ), a Side Coupled Drift Tube Linac (SCDTL) and a Cell Coupled Linac (CCL) section.

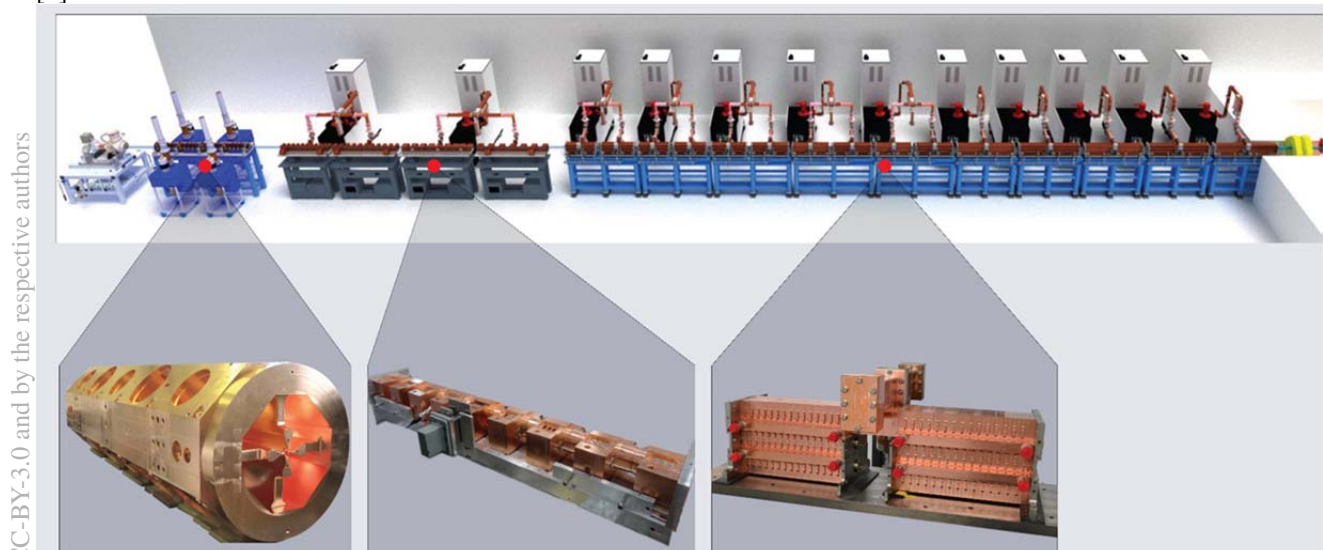


Figure 1: Artistic view of full size LIGHT accelerator. The three different types of cavities used are highlighted with a picture for each type.

DEVELOPMENT AND APPLICATION OF ONLINE OPTIMIZATION ALGORITHMS *

Xiaobiao Huang[†], SLAC, Menlo Park, CA 94025, USA

Abstract

Automated tuning is an online optimization process. It can be faster and more efficient than manual tuning and can lead to better performance. It may also substitute or improve upon model based methods. Noise tolerance is a fundamental challenge to online optimization algorithms. We discuss our experience in developing a high efficiency, noise-tolerant optimization algorithm, the RCDS method, and the successful application of the algorithm to various real-life accelerator problems. Experience with a few other online optimization algorithms are also discussed. A performance stabilizer and an interactive optimization GUI are presented.

BEAM BASED CORRECTION AND BEAM BASED OPTIMIZATION

Modern accelerators are complex systems that consists of many components. The optimal performance of the machine can be achieved only when all of the essential components are working at the proper settings. A major challenge to the accelerator community is to ensure the machines deliver the best possible performance that meets or exceeds the design requirements.

Accelerators are almost always built and operated according to a design model. Ideally, the machine should perform as the model predicts. However, in reality, all kinds of errors come in, causing deviations in operating conditions from the ideal scenario. For example, in a magnet, there are mechanical errors in the machining of the magnet pole pieces; the magnetization curve of the actual magnetic material may differ from the design; and, the current regulation may fluctuate with temperature and humidity. Magnet alignment errors are another major source of magnetic field errors experienced by the beams. In addition, many electromagnetic fields are typically not included in the models, such as beam induced wakefields, insertion devices, and magnet fringe fields.

Differences between the model and the actual machine can be reduced through precise measurements and correction or compensation of errors of each individual component, improved alignment precision, and including as many physical phenomena in the model as accurately as possible. However, despite our best effort and ever-improving precision in accelerator technology, there will always be differences between the model and the real machine. Beam based methods have to be used to mitigate the performance deficiency caused by such differences.

Beam based methods may be divided into two categories - beam based correction (BBC) and beam based optimization

(BBO). Beam based correction refers to methods that use beam based measurements to detect deviations of the operating condition of an accelerator sub-system from the ideal setting and use a deterministic, pre-determined procedure to set the operating condition toward the ideal setting. BBC requires beam diagnostics to monitor the beam conditions which provide sufficient information in order to work out the required adjustments of machine setting with a deterministic method. The correction target, or the ideal setting the beam monitors would indicate at optimal performance, is known a priori.

Take orbit correction as an example, beam position monitors (BPMs) are the diagnostics; the method of inverting an orbit response matrix is the correction calculation method; and, the ideal orbit is determined through beam-based alignment measurements or other requirements. In the orbit correction case, an accelerator model is not required. However, for many cases, BBC requires a model as a representation of the ideal target and to be used in the correction calculation. For example, in storage ring optics correction, the ideal target may be represented by the orbit response matrix, or beta functions and phase advances, calculated with the lattice model; the Jacobian matrix of these representing parameters with respect to the quadrupole correctors is also calculated with the model. BBC typically targets a sub-system because the deterioration of the main performance indicators, such as reduced injection efficiency or beam lifetime, usually does not by itself contain enough information that can lead to a deterministic correction.

When any of the required elements, the diagnostics, the deterministic method, or the ideal target, is absent, BBC cannot be done. However, if the machine performance can be measured and the operating conditions can be adjusted, then beam based optimization can be used to improve the performance. The machine performance may be characterized by one or more performance parameters that are basically functions of the adjustable operating parameters (i.e., knobs). The BBO process is to optimize these functions with the available knobs within the proper parameter space. The functions are evaluated through the system (i.e., the machine); but knowledge of the interior of the system is unnecessary (see Fig. 1).

BBO is frequently performed in machine operation in the form of manual tuning. In this case the parameters are changed by literally turning knobs or manually typing in parameter values through a computer. Data processing and implementation of the optimization algorithm are done with a human brain. Alternatively, BBO can be conducted automatically with a computer. In this sense it may be referred to as automated tuning. Compared to manual tuning, automated tuning has the advantages of being fast, independent

* Work supported by DOE Contract No. DE-AC02-76SF00515

[†] xiahuang@slac.stanford.edu

HIGH PRECISION RF CONTROL FOR THE LCLS-II*

G. Huang[†], K. Campbell, L. Doolittle, Q. Du, J. Jones,
 C. Serrano, V. Vytla, LBNL, Berkeley, CA 94720, USA
 S. Babel, M. Boyes, G. Brown, D. Cha, G. Dalit, J. DeLong, B. Hong, A. McCollough,
 A. Ratti, C. Rivetta, SLAC, Menlo Park, CA 94720, USA
 R. Bachimanchi, C. Hovater, D. Klepec, D. Seidman, JLAB, Newport News, VA 23606, USA
 B. Chase, E. Cullerton, J. Einstein-Curtis, O. Kumar, FNAL, Batavia, IL 60555, USA

ABSTRACT

The LCLS-II is a CW superconducting linac under construction to drive an X-ray FEL. The energy and timing stability requirements of the FEL drive the need for very high precision RF control. This paper summarizes the design considerations and early demonstration of the performance of the modules and system we developed.

INTRODUCTION

LCLS-II is a project to generate high quality, high repetition rate soft X-ray beam for advanced science discovery. The project will construct a 4 GeV superconducting linac in the existing SLAC tunnel. The accelerated electrons will be sent through undulators to produce X-rays.

LCLS-II requires electron beam jitter and energy spread better than 20 fs and 0.014% at the undulator to achieve its X-ray beam quality goals. That, in turn, requires 0.01° in phase and 0.01% amplitude stability for the RF field in each superconducting 1300 MHz cavity. [1]

The superconducting linac will contain 35 cryomodules, each with eight 9-cell 1.3 GHz superconducting cavities. The machine layout is shown in Figure 1.

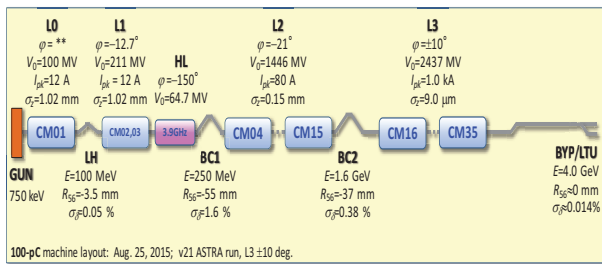


Figure 1: LCLS-II Linac layout.

A system design is a compromise of different parameters, including cost, robustness, noise *etc.* Series of project architectural choices made the high precision RF control possible for the machine. The low level RF collaboration team designed the low noise digital LLRF system to minimize the noise sources within the control bandwidth. Noise or disturbances outside the LLRF system's control bandwidth must be either handled by a beam-based feedback system or be eliminated from the source. [2-4]

* Work supported by the LCLS-II Project and the U.S. Department of Energy, Contract DE-AC02-76SF00515

[†] ghuang@lbl.gov

SYSTEM ARCHITECTURE SELECTION

Digital Low Level RF Control System

The low level RF control system measures the cavity pickup signal and compares it with the vector set point to generate an error signal. The error signal goes through a Proportional and Integral control loop and generates the correction to drive the high power RF system. With the development of ADC, DAC and FPGA technology, the system can be implemented digitally as shown in Figure 2. The flexibility and self-monitoring capability of a digital implementation is so advantageous that analog systems are no longer considered.

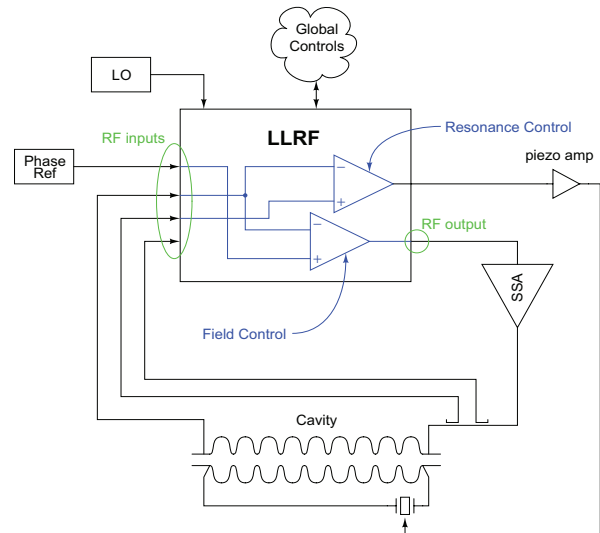


Figure 2: Abstract LLRF feedback topology.

Single Source Single Cavity

In the LCLS-II, the linac RF will run in CW mode with high loaded *Q*. It will be more sensitive to microphonics than pulsed machines. Unlike pulsed machines, the Lorentz Force Detuning effect is static once the amplitude of each cavity is stabilized with feedback.

A single-source single-cavity configuration is selected to give each cavity its own low level RF system. Thus it can combine the piezo and RF power to fight against microphonics. During turn on or recovery from a fault, the system will use Self Excited Loop mode, which is by construction free of ponderomotive instability.

STUDY OF THE ELECTRICAL CENTER OF A RESONANT CAVITY BEAM POSITION MONITOR (RF-BPM) AND ITS INTEGRATION WITH THE MAIN BEAM QUADRUPOLE FOR ALIGNMENT PURPOSES

S. Zorzetti^{1*}, M. Wendt, CERN, Geneva, Switzerland

L. Fanucci, University of Pisa, Pisa, Italy

¹also at University of Pisa, Pisa, Italy

Abstract

To achieve the luminosity goals in a next generation linear collider, acceleration and preservation of ultra-low emittance particle beams is mission critical and requires a precise alignment between the main accelerator components. PACMAN is an innovative doctoral training program, hosted by CERN, with the goal of developing high accuracy metrology and alignment methods and tools to integrate those components in a standalone, automatic test bench. The method will be validated on CLIC components, a proposed Compact Linear Collider currently studied at CERN. The alignment between the electrical center of the Beam Position Monitor (BPM) and the magnetic center of the associated Main Beam Quadrupole (MBQ) is of particular importance to minimize the emittance blow-up, and therefore in the focus of the PACMAN project. On a first stage the two components have been independently characterized on separated test benches by stretched and vibrating wire techniques. Preliminary conclusions are presented in this paper, with emphasis on the characterization of the electrical center of the BPM.

THE PACMAN PROJECT AT CERN

The PACMAN [1] project is an Innovative Training Network (ITN), hosted by CERN and funded by the European Marie Skłodowska-Curie action. It is a multi-disciplinary network, including 10 Early Stage Researchers (ESRs), academic and industrial partners. The purpose is to develop innovative alignment strategies and technologies for the future generation of particle accelerators. The technical development is associated to the CLIC and therefore the tests are associated to its components.

ALIGNMENT STRATEGY

For CLIC, it is required that the main accelerator components, such as Beam Position Monitors (BPM), Accelerating Structures (AS) and Main Beam Quadrupoles (MBQ), are aligned with very tight tolerances, in the order of 14 μm for the main linac. It is foreseen that the modules are pre-aligned on a common girder of 2 m of length, with the final beam-based active alignment taking place in the CLIC tunnel to optimize the beam trajectory. In this scenario, PACMAN is proposing a wire-based pre-alignment methodology. In order to validate its feasibility, an assembly between the cavity BPM and MBQ was developed: the Final PACMAN Alignment Bench (FPAB - Fig. 1). It has the components

mechanically centered on a common support. By means of a stretched-wire the electrical center of the BPM and the magnetic center of the MBQ are located. The wire is made out of copper-beryllium, with 0.1 mm diameter, it is tensioned by a stepper motor and, fixed on two specular end points, passes through the MBQ-BPM assembly. Two lateral 2-DOF stages are used to move the wire with respect to the devices [2].

A GENERAL OVERVIEW OF THE PACMAN MODULE

The following steps were taken to develop the MBQ-BPM pre-aligned system and fiducialize the electromagnetic offset.

1. The single components are separately characterized and calibrated: the MBQ by means of vibrating wire techniques [3], the BPM using stretched-wire methods;
2. The BPM and the MBQ are mechanically aligned on a common axis;
3. Initially, the assembly is studied in a laboratory environment and then moved on the platform of a Coordinate Measuring Machine (CMM) ¹, in a temperature controlled and clean room;
4. The magnetic center of the MBQ and the electrical center of the BPM are located, each with the respective measurement method;
5. Through non-contact sensors the fiducialization process was performed. Two wire positions are recorded, one in point of the MBQ magnetic center, the other in the BPM electrical center.
6. Beyond the non-contact CMM probes, also micro-triangulation and Frequency Scanning Interferometry (FSI) technologies are employed for the fiducialization.

With the knowledge of the offset calibration constant between the magnetic center of the quadrupole and the electrical center of the position cavity BPM, the particle beam position measurements will be referenced to the quadrupole magnetic center and allow to detect beam misalignments with respect to this point. Moreover, as the beam drifts off-center, an active nanopositioning system will automatically operate, correcting the quadrupole position and recentering the beam to its magnetic center.

¹ Maximum uncertainty: $0.3\mu\text{m} + L/1000$, where L is the length of the device under test expressed in [mm]

* silvia.zorzetti@cern.ch

GEM*STAR ACCELERATOR-DRIVEN SUBCRITICAL SYSTEM FOR IMPROVED SAFETY, WASTE MANAGEMENT, AND PLUTONIUM DISPOSITION

M. A. C. Cummings[†], R. Johnson, T. Roberts, R. Abrams, Muons, Inc., Batavia, IL USA

Abstract

The GEM*STAR system employs a high-power SRF proton accelerator with a spallation neutron target to provide a source of neutrons, and a molten salt/graphite core. This results in a lower cost, subcritical nuclear reactor design that has many attractive features, among which are the following. It eliminates the need for a critical core, fuel enrichment, or reprocessing. Fissionable fuel is dissolved in the high-temperature molten-salt fuel. The reactor cannot attain a critical mass and contains almost a million times fewer volatile radioactive fission products than conventional reactors like those at Fukushima.[‡] Volatile radioactive fission products are continuously purged. The GEM*STAR [1] reactor can, without redesign, burn spent nuclear fuel, natural uranium, thorium, or surplus weapons material. A first application is to burn up to 34 tons of excess weapons grade plutonium as an important step in nuclear disarmament under the 2000 Plutonium Management and Disposition Agreement, in which The U.S. and Russia each agreed to dispose of 34 tons of weapons-grade plutonium. The process heat generated by this W-Pu can be used for the Fischer-Tropsch conversion of natural gas and renewable carbon into 1.24 billion gallons of low-CO₂-footprint, drop-in synthetic diesel fuel per ton of W-Pu, for use by the DOD or for other purposes.

GEM*STAR SYSTEM

The Green Energy Multiplier*Subcritical Technology for Alternative Reactors (GEM*STAR) is a subcritical thermal-spectrum reactor operating with a molten salt fuel in a graphite matrix in a continuous flow mode, initially at $k_{\text{eff}} \sim 0.99$. Accelerator-produced neutrons supplement the fission neutrons. The beneficial combination of three reactor technologies (largely neglected since 1970) – molten salts, accelerator-produced neutrons, and the use of a graphite moderator – enable a versatile reactor that addresses multiple problems associated with conventional nuclear reactors and their fuel cycle: safety, nuclear proliferation, nuclear waste, limited fuel, and geologic storage. Unlike the several “Generation IV” reactor technologies, GEM*STAR mitigates or eliminates all of them.

The key point is that GEM*STAR operates in subcritical mode driven by an enormous neutron flux gener-

ated by a proton beam. This means that fission stops within 1 second after the proton beam is turned off, which is a passive response to essentially any accident scenario; without fission, passive air-cooling is sufficient. That flux also means that GEM*STAR can burn fuels no conventional reactor can use: spent nuclear fuel, natural uranium, natural thorium, its own output stream, and even depleted uranium. It burns these fuels without fuel reprocessing or uranium enrichment, greatly reducing proliferation concerns. This turns “waste” into fuel – enormous amounts of it: with a fleet of GEM*STAR reactors there is enough uranium *out of the ground today* to supply 100% of the current U.S. electricity usage for more than 1,000 years.

Accelerator-Driven Reactors

Cyclotrons and electrostatic accelerators played an essential role in the early development of nuclear technology. The first significant quantity of enriched ²⁵³U was produced from “Calutrons”, developed under E.O. Lawrence at Berkeley Laboratory. Later, in the early 1950s, Lawrence constructed much more powerful accelerators for neutron production to produce ²³⁹Pu from neutron capture on ²³⁸U – the “Mark I” of the material test accelerator (MTA). The MTA was a drift tube linear accelerator, designed for both high current and then-high energy, with a diameter of 19m and length of 27m, and reached unprecedented currents of 50 mA of deuterons at 10 MeV for an average power of 0.5 MW – 2 million times larger than that of the Berkeley cyclotrons. A larger version was planned, but discovery of abundant uranium deposits in New Mexico and Colorado, and the success of plutonium production in reactors at Oak Ridge and Hanford, ended the MTA initiative.

For 40 years, accelerator science was driven by basic, rather than applied, science. In the 1990s, Carlo Rubbia proposed an “Energy multiplier” [2], based on a proton cyclotron that produced neutrons to power a thorium-based reactor. Charles Bowman also proposed an accelerator-driven system for waste transmutation [3]. The multi-MW accelerators necessary seemed neither feasible nor practical until the development of superconducting RF. Today, beam power over 1 MW has been achieved at Oak Ridge National Laboratory (ORNL) and the European Spallation Source (ESS). The need for higher intensity beams for future accelerators is driving R&D for powerful proton sources that are increasingly cost effective.

One of the concerns for accelerator-driven subcritical reactor systems (ADSR) is that frequent accelerator trips would cause mechanical fatigue in reactor fuel rods.

[†] macc@muonsinc.com

[‡] There is enough ²³⁹Pu to form a critical mass if it were Pu metal in a sphere, but chemically combined into PuF₄ it cannot achieve a critical mass.